

Correlated 0.01Hz - 40 Hz seismic and Newtonian noise and its impact on future gravitational-wave detectors

Kamiel Janssens^{1,2}, Guillaume Boileau³, Nelson Christensen², Nick van Remortel¹, Francesca Badaracco^{4,5}, Benjamin Canuel⁶, Alessandro Cardini⁷, Andrea Contu⁷, Michael W. Coughlin⁸, Jean-Baptiste Decitre⁹, Rosario De Rosa^{10,11}, Matteo Di Giovanni^{12,13}, Domenico D’Urso^{14,7}, Stéphane Gaffet⁹, Carlo Giunchi¹⁵, Jan Harms^{16,17}, Soumen Koley^{16,17}, Valentina Mangano¹³, Luca Naticchioni¹³, Marco Olivieri¹⁸, Federico Paoletti¹⁹, Davide Rozza^{14,7}, Dylan O. Sabulsky⁹, Shahar Shani-Kadmiel²⁰ and Lucia Trozzo¹¹

¹*Universiteit Antwerpen, Prinsstraat 13, 2000 Antwerpen, Belgium*

²*Université Côte d’Azur, Observatoire de la Côte d’Azur, CNRS, Artemis, 06304 Nice, France*

³*Université Côte d’Azur, Observatoire de la Côte d’Azur, CNRS, Laboratoire Lagrange, 06304 Nice, France*

⁴*Università degli studi di Genova, via Dodecaneso 33, 16146, Italy*

⁵*INFN, Sez. di Genova, via Dodecaneso 33, 16146, Italy*

⁶*LP2N, Laboratoire Photonique, Numérique et Nanosciences, Université Bordeaux–IOGS–CNRS:UMR 5298, rue F. Mitterrand, F-33400 Talence, France*

⁷*INFN, sezione di Cagliari, I-09042, Monserrato (Cagliari), Italy*

⁸*School of Physics and Astronomy, University of Minnesota, Minneapolis, Minnesota 55455, USA*

⁹*Laboratoire Souterrain à Bas Bruit (LSBB), CNRS: UAR3538, Avignon University, Rustrel F-84400, France*

¹⁰*Università Federico II Napoli, 80126 Napoli, Italy*

¹¹*INFN - sezione di Napoli, 80126 Napoli, Italy*

¹²*La Sapienza Università di Roma, I-00185 Roma, Italy*

¹³*INFN, Sezione di Roma, I-00185 Roma, Italy*

¹⁴*Department of Chemistry, Physics, Mathematics and Natural Science, Università degli Studi di Sassari, I-07100, Sassari, Italy*

¹⁵*Istituto Nazionale di Geofisica e Vulcanologia, Sezione di Pisa, Italy*

¹⁶*Gran Sasso Science Institute (GSSI), I-67100 L’Aquila, Italy*

¹⁷*INFN, Laboratori Nazionali del Gran Sasso, I-67100 Assergi, Italy*

¹⁸*Sezione di Bologna, Istituto Nazionale di Geofisica e Vulcanologia, Bologna, Italy*

¹⁹*INFN - sezione di Pisa, 56127 Pisa, Italy*

²⁰*R&D Department of Seismology and Acoustics, KNMI, De Bilt, The Netherlands*

(Dated: February 28, 2024)

We report correlations in underground seismic measurements with horizontal separations of several hundreds of meters to a few kilometers in the frequency range 0.01 Hz to 40 Hz. These seismic correlations could threaten science goals of planned interferometric gravitational-wave detectors such as the Einstein Telescope as well as atom interferometers such as MIGA and ELGAR. We use seismic measurements from four different sites, i.e. the former Homestake mine (USA) as well as two candidate sites for the Einstein Telescope, Sos Enattos (IT) and Euregio Maas-Rhein (NL-BE-DE) and the site housing the MIGA detector, LSBB (FR). At all sites, we observe significant coherence for at least 50% of the time in the majority of the frequency region of interest. Based on the observed correlations in the seismic fields, we predict levels of correlated Newtonian noise from body waves. We project the effect of correlated Newtonian noise from body waves on the capabilities of the triangular design of the Einstein Telescope’s to observe an isotropic gravitational-wave background (GWB) and find that, even in case of the most quiet site, its sensitivity will be affected up to ~ 20 Hz. The resolvable amplitude of a GWB signal with a negatively sloped power-law behaviour would be reduced by several orders of magnitude. However, the resolvability of a power-law signal with a slope of e.g. $\alpha = 0$ ($\alpha = 2/3$) would be more moderately affected by a factor ~ 6 -9 (~ 3 -4) in case of a low noise environment. Furthermore, we bolster confidence in our results by showing that transient noise features have a limited impact on the presented results.

I. INTRODUCTION

Searches for unmodeled and/or long duration gravitational-wave (GW) signals, such as the isotropic GW background (GWB) [1], are more susceptible to be biased by correlated noise. One such example are correlations in magnetic field fluctuations over Earth-scale distances, such as the Schumann resonances [2, 3]. Their potential effect on GWB searches with Earth-based GW

interferometers – LIGO [4], Virgo [5] and KAGRA [6] – has been extensively investigated [7–14]. Moreover, the effect of correlated lightning glitches on searches for GW bursts, such as core collapse supernova, was studied [14, 15]. Furthermore, the effect of Schumann resonances on the Einstein Telescope (ET) was investigated [16] and shown to be a limiting noise source for the search for a GWB below ~ 30 Hz, in case ET has a similar magnetic coupling as LIGO/Virgo.

ET is the European proposal for a third-generation,

Earth-based interferometric GW detector [17]. Its baseline proposal exists out of three nested detectors. Each detector is composed of two interferometers, one optimized for low frequency observations and the other devoted to high frequency observations. This configuration is often referred to as "xylophone". The detectors are arranged in an equilateral triangle with opening angle of $\pi/3$ and arm lengths of 10 km. In this paper, we ignore the details of the xylophone configuration [18] and we treat ET as consisting of three interferometers. This assumption has no effect on our studies. In a proposed alternative design, ET is composed of two separate L-shaped interferometers in xylophone configuration, located in two far sites. Given the large separation of these two separated detector sites, it is deemed that the effect of correlations in seismic noise is negligible in the frequency band of interest for the ET. Therefore the noise projections in this paper are only relevant in case the triangular design is chosen. However, the investigation of correlated noise over a distance of 10km is relevant for both designs as it provides information on potential correlated noise coupling between input and end masses of a singular interferometer.

Official candidate sites for the ET are the area in the vicinity of the Sos Enattos mine in Sardinia[19–24], Italy, and the Euregio Maas-Rhein (EMR) at the intersection of the Belgian, Dutch, and German borders [25–27]. The region of Saxony in Germany has been recently proposed as another possible candidate. The different sites are indicated in the bottom panel of Fig. 1. Moreover, we highlight the USA's proposal for a third generation interferometric GW detector: Cosmic Explorer (CE)[28]. However, we do not consider CE in our study as it is planned to have two widely separated detectors.

Due to the nested design of three almost co-located interferometers in a triangular configuration, there are several potential coupling locations for correlated noise to enter on distance scales of 300 m to 600 m into the different ET interferometers, as illustrated in Fig. 2 [32]. Even though ambient seismic fields rapidly lose coherence over large distances for frequencies higher than 1 Hz [33, 34], in [32] the authors have shown that on distance scales of several hundreds of meters, significant correlations in seismic noise are present at least 50% of the time up to 40 Hz. Please note that the results in [32] are based on surface measurements at EMR and underground measurements at Homestake. The correlations in seismic noise result in correlations in Newtonian noise (NN) [35–37], which is a force exerted on GW test-masses caused by density fluctuations in the surrounding medium. Correlations in NN from body waves could seriously affect the search for a GWB with the ET by orders of magnitude [32]. These results were also considered in a recent study comparing the scientific benefits of a triangular detector configuration versus a configuration with two non co-located, L-shaped detectors [38].

In previous works, potential coupling locations on distance scales of ~ 10.5 km were neglected. However, as

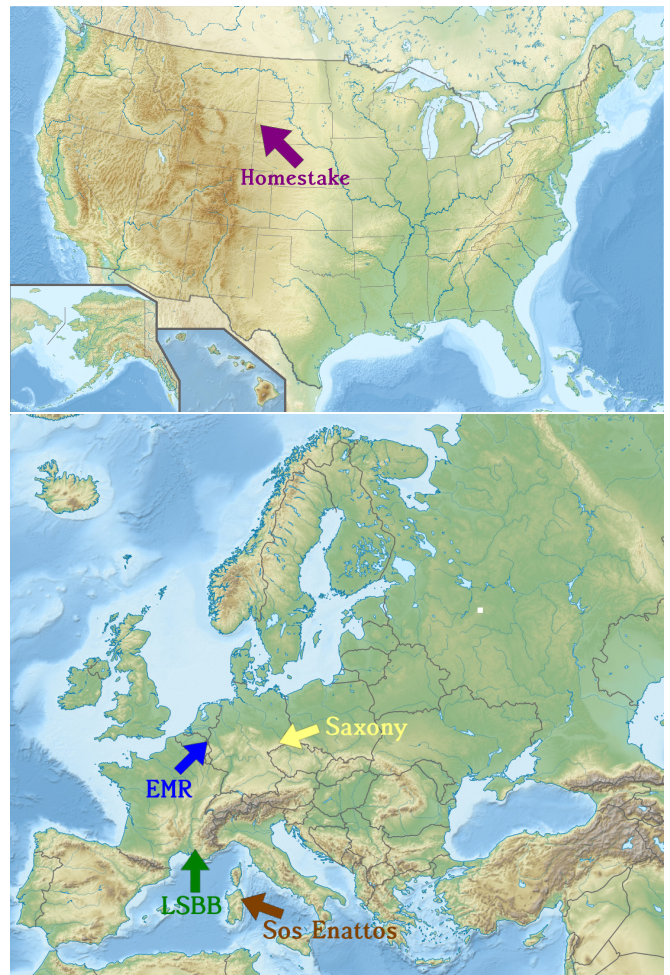


FIG. 1: Top: map of the USA highlighting the location of the former Homestake mine [29]. Bottom: map of Europe with the locations of LSBB (green) and of the two ET candidate sites, namely Sos Enattos (brown) and Euregio Maas-Rhein (EMR) (blue). We also highlight the third ET candidate site in Saxony (yellow) that was not considered for the analyses of this paper. The maps are taken from [30] and [31] and modified according to the creative commons license 3.0.

can be seen on Fig. 2 (not indicated), there are multiple possible coupling locations between the input and end test masses of the different detectors. For these distances, the seismic noise is expected to have lost coherence in the frequency band of relevance for the ET.

In this work, we aim to investigate seismic correlations on distance scales from several hundreds of meters up to tens of kilometers with the goal to provide further insights in potential coupling to the different ET detectors. However, these correlation studies are also of particular interest for GW searches using atom interferometry. Earth-based atom interferometers aim to be sensitive to GWs in the frequency range 0.1 Hz-10 Hz with their peak sensitivity typically around 1Hz-2Hz [39, 40]. At those frequencies, the seismic waves have longer corre-

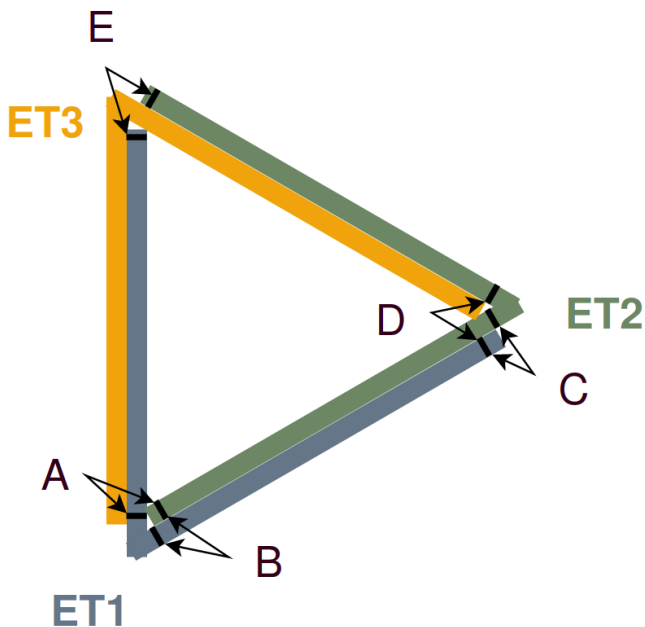


FIG. 2: Scheme of the proposed ET triangular configuration (the low- and the high-frequency detectors are not showed). Considering the ET1-ET2-baseline, we can identify 5 possible coupling locations where seismic and Newtonian noise can correlate on distances between 300m and 600m: A to E [32]. Additionally there are multiple possible coupling locations for correlated noise on distances of about 10.5km (not indicated).

lation lengths up to several kilometers. In Fig. 3, we illustrate the set-up of a proposal for a future atom interferometer, ELGAR¹ [40]. This L-shaped detector consists in a 2D array of atom gradiometers. Each arm is composed of $N=80$ single gradiometers of baseline $L=16,3$ km placed every 200 m. The GW signal is obtained by the difference of the averaged gradiometric signal in each arm. This signal extraction method implies that all NN correlations over distances from 200 m up to tens of kilometers are relevant for the detector sensitivity [41].

In this work, we aim to further understand the effect of correlations in seismic and NN and how they could impact searches for GWs. First of all, we use underground seismic data from four different sites and a total of nine different sensor pairs with horizontal separations between ~ 230 m and ~ 10 km. This reduces the effect of any site dependence that might be present in the earlier results of [32], where underground seismic measurements of a single site were used. Furthermore, we probe correlations on longer distances as in [32], where the largest separation between seismic sensors was 810m. Finally, we do not only focus on the frequency band of interest for the ET

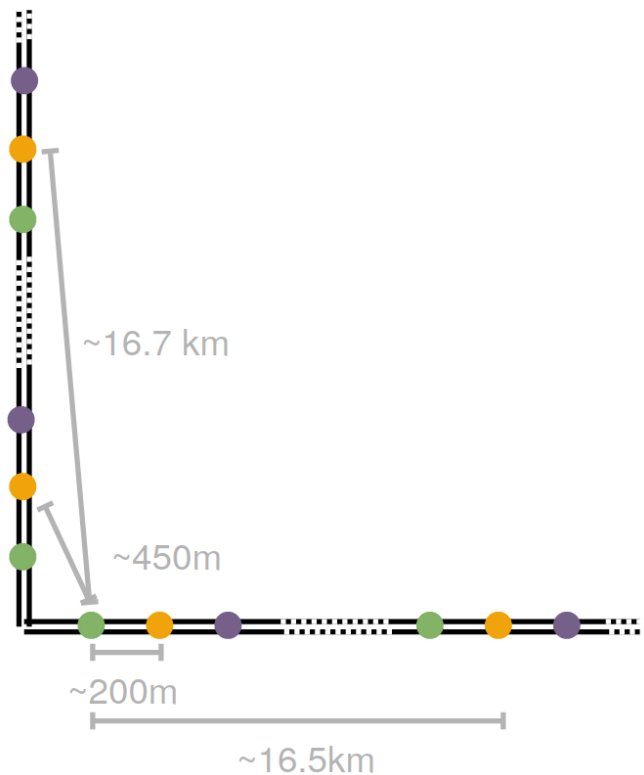


FIG. 3: Scheme of the ELGAR configuration, where the dots represent the atom interferometers. Each color corresponds to a single 16,3 km gradiometer of the 2D array. We give examples of different correlation lengths that must be taken into account to calculate the impact of NN [41]. In this illustration, we have assumed the distance between the beamsplitter and the first atom interferometer to be 200 m.

$(1\text{Hz}-40\text{Hz})^2$, but also on lower frequencies of interest for atom interferometry (0.01Hz-1Hz). In this work we do not make a projection of the correlated seismic and NN on present or future atom interferometers. However, we do discuss seismic correlations over the entire frequency range 0.01Hz-40Hz, which can be used to serve for the calculation of noise projections for atom interferometers, similar to those in earlier work [14, 42].

For GW interferometric detectors we will not discuss the effect of seismic and NN on their instantaneous sensitivity, nor methods to perform NN subtraction as these have been extensively studied in the literature [21, 23, 26, 27, 33, 43–51]. However, we focus on the impact of correlated NN on the search for a GWB, which is (one of) the most sensitive search(es) to correlated noise.

In Sec. II, we highlight the different analyses that are performed. In Sec. III-VI, we present the seismic results

¹ European Laboratory for Gravitation and Atom-interferometric Research

² In the ET community this frequency band is often referred to as the low-frequency (LF) band.

for each site. Afterwards in Sec. VII, we discuss the results of the different sites, by using reference measurement per site. In Sec. VIII, we use the observed seismic correlations to make a projection for the levels of correlated NN. In Sec. IX, we investigate the effect of transient seismic noise and its impact on the results presented in Sec. III-VIII. Finally, in Sec. X, we conclude our results and highlight possibilities for future work.

II. SCOPE OF PERFORMED ANALYSIS

In this study we analyze underground seismic data from four different geographical locations. We only focus on horizontal seismic waves and the subsequent NN from body waves. We focus on these measurements as an earlier study [32] has shown that the effect of correlated NN from Rayleigh waves on the ET and its search for a GWB is modest compared to the effect from NN from body waves. The key factor is that ET will be built underground, drastically reducing the effect from surface waves above 1 Hz. In this earlier study [32], they analysed both vertical and horizontal seismic noise from underground data at the Homestake mine in the USA. Moreover, they used four different sensor pairs with distances between 255 m and 810 m. Because we use slightly different parameters when analysing our data, we re-analyse the data from Homestake to get a one-to-one comparison with this earlier results and have a better comparison with the new results presented in this paper.

As shown on the maps in Fig. 1, the geographical locations from which data are used are: the former Homestake mine in the USA [29], the MIGA³ [39] site at the ‘Laboratoire Souterrain à Bas Bruit’ (LSBB) in France and the two candidate sites for the ET, the former Sos Enattos mine in Italy and the EMR region in the border region of the Netherlands, Belgium and Germany. No data from the third possible candidate site located in the region of Saxony in Germany are used, as at the time of this paper no long term (> 1 month) underground measurements were performed with a horizontal separation of at least several hundreds of meters between two seismometers. It will be interesting to perform a similar analysis when such data becomes available.

The different sensor pairs and the distance between the sensors, as well as their depth with respect to the surface, are listed in Tab. I. For all pairs we only analyse the correlations in seismic noise between the NS seismic measurement of the two sensors. Only for the GAS-RAM pair at LSBB we analyse the three other directionality pairs: EW-EW, NS-EW and EW-NS, to compare these results from LSBB, with a similar analysis for Homestake [32]. Furthermore, in Tab. I we list the range over which the sensors are sensitive. In the discussion of the results

and figures we only show those frequency regions and exclude the frequency bands where the measurements are dominated by e.g. sensor self-noise.

For Homestake and LSBB, we analyse a full year of data and compare the results from different months to establish seasonal variations in the level of seismic noise. For Homestake we use data from 2016⁴ and for LSBB from 2018⁵. The data periods always start and end at 00:00:00 UTC, e.g. for LSBB 1 Jan 00:00:00 UTC 2018 - 1 Jan 00:00:00 UTC 2019. At the time of analysis, the other sites did not always have a continuous data taking period of one year, so only a sub-set of a few months is analyzed. Throughout the paper, we use the months of Jan. and Aug. to present the results and make comparisons between the different sites, where we consider these results to be representative for winter and summer, respectively. For Sos Enattos, we analyzed data from Aug 2021, as well as the month of January from the years 2022 and 2023 for two of the pairs P2-P3 and SOE2-SOE3, respectively. For EMR, we use data recorded during the month of January 2023 as at the time of the analysis no long term high quality data was available for the month of August. The sensors are still actively acquiring more data and future studies could look to include more results.

The data is analyzed with two different sets of parameters optimized for the frequency regions of interest for atom interferometers (0.01Hz - 1Hz) and ET (> 1 Hz). We use a frequency resolution of 0.005Hz and average data in chunks of 6h for the low frequency studies. This enables us to resolve coherence up to $\sim 9.3 \times 10^{-3}$, while still having $\mathcal{O}(100)$ chunks per month to get a good sense of the variability of the data during every month. To be able to resolve smaller coherence up to $\sim 3.8 \times 10^{-4}$, for the high frequency region we use a frequency resolution of 0.1Hz and average data over chunks of 4h, ensuring $\mathcal{O}(200)$ chunks per month. In the interest of being concise, the figures in this work show the results using these two different parameter sets in one unified plot. More specifically, between 0.01Hz and 1Hz the results with 5 mHz resolution are shown, whereas for frequencies above 1Hz the results of the analyses with a frequency resolution of 0.1Hz are presented. This is clearly indicated in the relevant figures. Finally the parameters used for the different analysis are also summarized in Tab. II.

Finally, for the study of transient effects on our results, which is presented in Sec. IX, we analyzed the data with a frequency resolution of 0.1Hz and averaged over 1 min chunks. This duration was inspired based on an earlier study of seismic glitchiness at Sos Enattos [22], where they highlight 1 min is a realistic estimate for a possible signal from a coalescing Intermediate Mass Black Hole

³ Matter-wave laser Interferometric Gravitation Antenna

⁴ We use the entire year of data, excluding Dec 2016, since no high quality data was available for this month.

⁵ The sensors were not operational during the month of May therefore this month can not be include in the analysis.

Location	Name 1	Name 2	Model 1	Model 2	Horizontal distance	Vertical distance	Depth 1	Depth 2	Frequency range
Homestake (US)	D2000	E2000	STS-2	STS-2	~ 405 m	~ 0 m	610 m	610m	0.01Hz-40Hz
LSBB (FR)	GAS	RAM	STS-2	STS-2	~ 600 m	~ 14 m	260 m	500 m	0.01Hz-40Hz
	MGS	RAM	STS-2	STS-2	~ 750 m	~ 4 m	240 m	500 m	0.01Hz-40Hz
	MGS	GAS	STS-2	STS-2	~ 850 m	~ 11 m	240 m	260 m	0.01Hz-40Hz
Sos Enattos (IT)	SOE1	SOE2	T120H	T360	~ 230 m	~ 27 m	84 m	111 m	0.01Hz-10Hz
	SOE1	SOE3	T120H	T240	~ 380 m	~ 76 m	84 m	160 m	0.01Hz-10Hz
	SOE2	SOE3	T360	T240	~ 370 m	~ 49 m	111 m	160 m	0.01Hz-10Hz
	P2	P3	T120Q	T120Q	~ 10000 m	~ 50 m	264 m	252 m	0.01Hz-10Hz
EMR (NL)	TERZ	CTSN	STS-5A	LE3DBH	~ 2417 m	~ 9.4 m	250 m	250 m	0.2Hz-18Hz

TABLE I: Table summarizing the sensor pairs that are used in the correlation analysis in this paper. Please note that the depth is with respect to the surface and not with respect to the sea level. As an example: GAS, RAM and MGS at LSBB are all located at approximately the same sea level height, but have significantly different depths.

	Freq. res. (FFT length)	Chunk length	Resolvable coherence
0.01Hz-1Hz	5mHz (200s)	6h	$\sim 9.3 \times 10^{-3}$
1Hz - 40Hz	0.1Hz (10s)	4h	$\sim 3.8 \times 10^{-4}$
Glitch study	0.1Hz (10s)	1min	N.A.

TABLE II: Summary of the used analysis parameters. Individual fft segments are averaged together to a chunk of data, which forms the starting point of the results described in this work.

(IMBH).

III. HOMESTAKE

In [32], the Homestake data of the sensor pair D2000-E2000 was analysed, as well as several other sensor pairs with different horizontal separations. However, in these earlier results, a frequency resolution of 0.01 Hz was used and data was averaged over 24h segments with a resolvable coherence of about $\sim 10^{-3}$. They used data from Mar 2015 to Dec 2016. In this section we study the seasonal effect, for which we use different analysis parameters, as described in previous section. The parameters are optimized to ensure that we can uncover a sufficiently low coherence, while at the same time have enough data chunks to show the variation within each month in a percentile plot.

Focusing on frequencies below 1 Hz, we see in the left panel of Fig. 4 that during the month of August 2016 the seismic noise is almost fully coherent around the microseismic peak, which is coming from sea activity [52]. To determine whether the observed coherence is significant or not, we compare it to the coherence expected from Gaussian data which goes approximately as $1/N$, where N is the number of time segments over which was averaged. At the lowest frequencies the coherence decreases with decreasing frequency. However at 0.01Hz (0.02Hz), at least 50% (90%) of the time there is significant coherence to the level of $\sim 9.3 \times 10^{-3}$. Here we want to point out that the decrease in coherence below 0.04Hz has most likely a non-physical origin and arises through

data processing leakage. Above 1 Hz, we observe significant coherence 90% of the time up to ~ 40 Hz. This result shows that the month of August has higher coherence compared to the results presented for the period Mar 2015 - Dec 2016 in earlier work [32]. The authors of [32] stated that the lower coherence observed, for the 10% percentile below 1 Hz, in their data was likely due to higher levels of anthropogenic noise leading to degraded coherence. Since this is not observed in any of the months analysed in this paper, these events seem to be limited to the 2015 data.

The right panel of Fig. 14 shows the accompanying cross-spectral density (CSD) of the seismic noise. These correlations in the seismic noise are in agreement with the earlier results [32] if we take into account we do not expect a perfect match as here we only present a small subset of the same data.

Fig. 5 compares median observed coherence (left panel) and CSD (right panel) for the different months of the year. Notice that, as mentioned earlier, the month of Dec is missing due to the absence of good quality data during this period. The only significant difference in coherence across different months is observed below 0.04Hz, which is linked to non-physical effects. However around the first and secondary microseism peaks between 0.04 Hz and 0.3 Hz the observed seismic noise during winter is larger, almost up to an order of magnitude at the secondary microseism peak [23, 42, 53]. At higher frequencies, no clear seasonal pattern is observed.

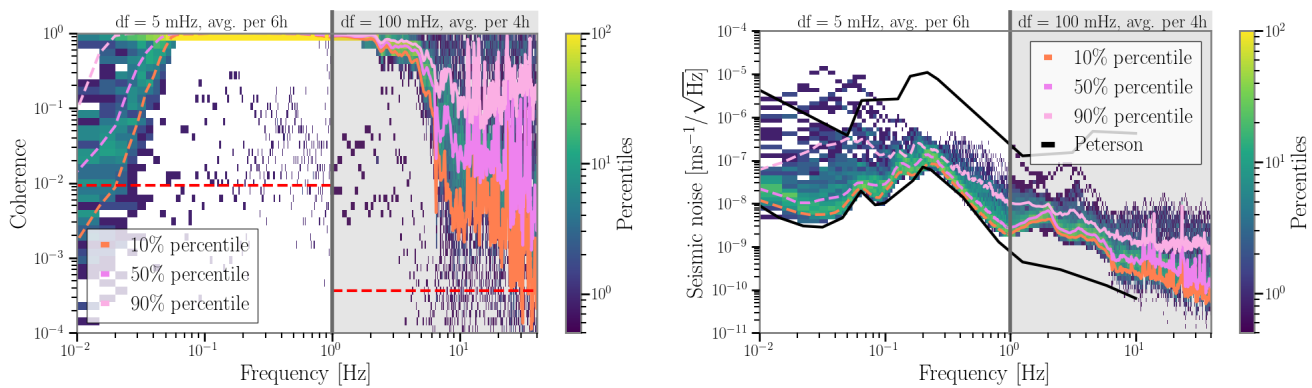


FIG. 4: The coherence (left panel) and CSD (right panel) between the underground seismometers (NS components) D2000 and E2000 (Homestake, USA) during the month of August. The 10th, 50th and 90th percentiles are shown in respectively light pink, dark pink and light orange, where dashed (full) lines are used for the analyses with the different parameters < 1Hz (\geq 1Hz). The red dashed line (left panel) represents the level of coherence expected from Gaussian data. The black curves (right panel) represent the low and high noise models by Peterson [52].

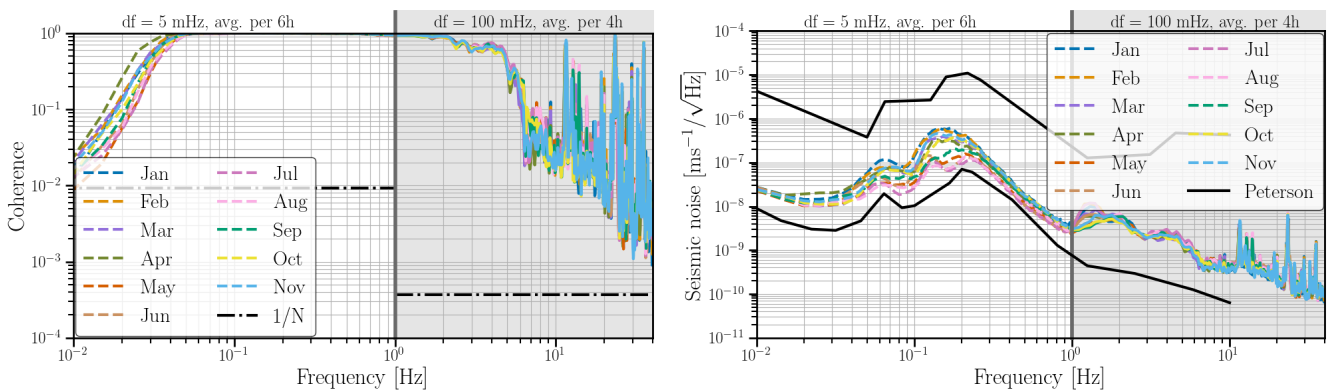


FIG. 5: The median coherence (left panel) and CSD (right panel) of the underground seismometers at Homestake ($\Delta x \approx 405$ m and depth = 610m) as a function of the month of the year 2016. The black dot-dashed line (left panel) represents the level of coherence expected from Gaussian data. In the right panel, the Peterson low and high noise models are shown in black..

IV. LSBB

In this section, we use the shortest distance pair (GAS-RAM, $\Delta x \approx 600$ m) as the reference pair for the LSBB site. For this pair of sensors, we present the coherence and seismic noise percentiles for the NS-NS direction, investigate the seasonal fluctuations as well as the effect of using aligned and perpendicular measurement directions. At the end, we compare the median coherence and median seismic noise for the three pairs at this site.

The left panel of Fig. 6 shows the observed coherence between GAS and RAM. Significant coherence is observed more than 90% of the time in the entire frequency range of 0.01 Hz - 20 Hz. Furthermore, above 20 Hz at least 50% of the time significant coherence is observed. A decrease in coherence is observed around 0.3 Hz for the 10% percentile. Even though we do not have a clear explanation for this feature, it seems likely

there is a site specific noise source at this frequency. The magnitude of this effect depends from month to month with some months being almost unaffected. The accompanying CSD is shown in the right panel of Fig. 6. We notice that the LSBB site is seismically very quiet, where its CSD sometimes is even lower than Peterson's low noise model. However, note that Peterson's low noise model is derived for power spectral density (PSD) values and not for CSDs. The PSDs of GAS and RAM (not shown here) are quiet above ~ 2 Hz with the 10% percentile about a factor 2 or less above Peterson's low noise limit.

The top two panels of Fig. 7 compare median observed coherence (top left panel) and CSD (top right panel) for the different months of the year. Similar to the Homestake analysis, the fluctuation in observed coherence below ~ 0.04 Hz is linked to data processing effects. Similar to Homestake, and as in the literature, higher levels of seismic noise is observed during winter months at the

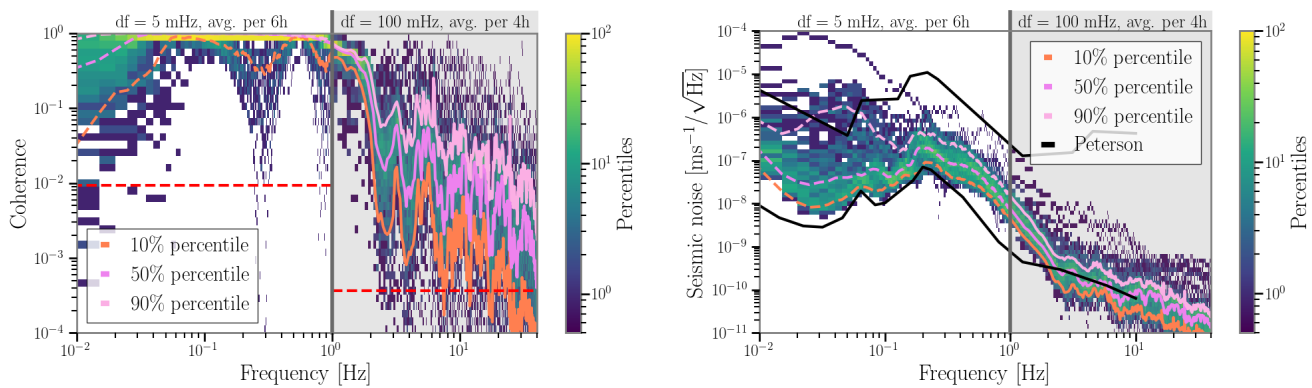


FIG. 6: The coherence (left panel) and CSD (right panel) between the underground seismometers (NS components) GAS and RAM (LSBB, FR) during the month of August. The 10th, 50th and 90th percentiles are shown in respectively light pink, dark pink and light orange, where dashed (full) lines are used for the analyses with the different parameters < 1Hz (\geq 1Hz). The red dashed line (left panel) represents the level of coherence expected from Gaussian data. The black curves (right panel) represent the low and high noise models by Peterson [52].

microseism peaks (0.05Hz - 0.5Hz). In the case of LSBB this excess seismic noise during winter extends up to \sim 1 Hz-2 Hz. This could possibly be explained due to LSBBs close proximity to the Mediterranean sea ($<$ 100 km) whereas Homestake closest ocean is located more than 1500 km away. Furthermore, we also would like to note that LSBB is near to underground natural water masses.

In the two middle panels of Fig. 7 we compare the coherence (middle left panel) and CSD (middle right panel) for the four different combinations one can make between the seismic wave measurements in the horizontal plane: NS-NS, NS-EW, EW-NS and EW-EW. Similar to the results from Homestake presented in earlier work [32]⁶, there is no difference observed in either coherence or CSD for frequencies above \sim 2 Hz. For lower frequencies, the coherence is lower when correlating perpendicular observing directions of the two different sensors. However, the observed coherence is still significant for at least 50% of the time and the CSD is at most a factor two smaller for the perpendicular orientations.

As can be seen in the bottom left panel of Fig. 7, we find a decreased seismic coherence between 0.4 Hz and 2 Hz for more distant sensors. This is similar to what was found for underground seismic coherence at Homestake in earlier work[32]. The CSD presented in the bottom right panel of Fig. 7 experiences a minimal, to negligible effect with respect to distance in the frequency band 0.4 Hz and 2 Hz. Above 2 Hz, no effect is observed. Additionally below 0.1 Hz sensors separated by a larger distance seem to observe lower coherence. The seismic correlated noise in this frequency region is different for the different pairs, however there is no clear pattern with respect to

the horizontal separation.

V. SOS ENATTOS

The coherence between the different sensors with a horizontal separation of several hundreds of meters is shown in the left panel of Fig. 8. Even though the observed coherence below \sim 0.05 Hz is different, there seems to be no distance dependant relationship. As discussed earlier, this is most likely a non-physical effect. Between 1 Hz and \sim 7 Hz, the observed coherence for the shortest distance pair is higher compared to the two other pairs. The correlations in the seismic noise, see right panel of Fig. 8, for this shortest distance pair of sensors are (marginally) larger in the frequency range 3 Hz-7 Hz, compared to the other sensor pairs.

Apart from these three pairs of sensors with a horizontal separation of several hundreds of meters, we also analysed two sensors (P2 and P3) which are located approximately 10 km from each other. This distance is both relevant for the ET as well as atom interferometers. It is namely the distance between two ET end stations in the triangular baseline and the approximate distance scale on which multiple atom gradiometers are deployed in the ELGAR detector, respectively. Furthermore, for both the triangular and two L baseline for the ET, this is the distance between the input and output optics of one single interferometer.

For this long distance pair of underground seismometers, we find 90% (50%) of the time significant coherence in the frequency range 0.02 Hz-0.3 Hz (0.01 Hz-1 Hz) as shown in the left panel of Fig. 9. Between 2 Hz and 10 Hz, there are a number of spectral features which lead to significant coherence over a broader frequency range. Some of these frequencies are most likely caused by electromagnetic interference affecting the digitizer and/or ca-

⁶ Note that in [32] they only presented similar results for frequencies above 0.05 Hz.

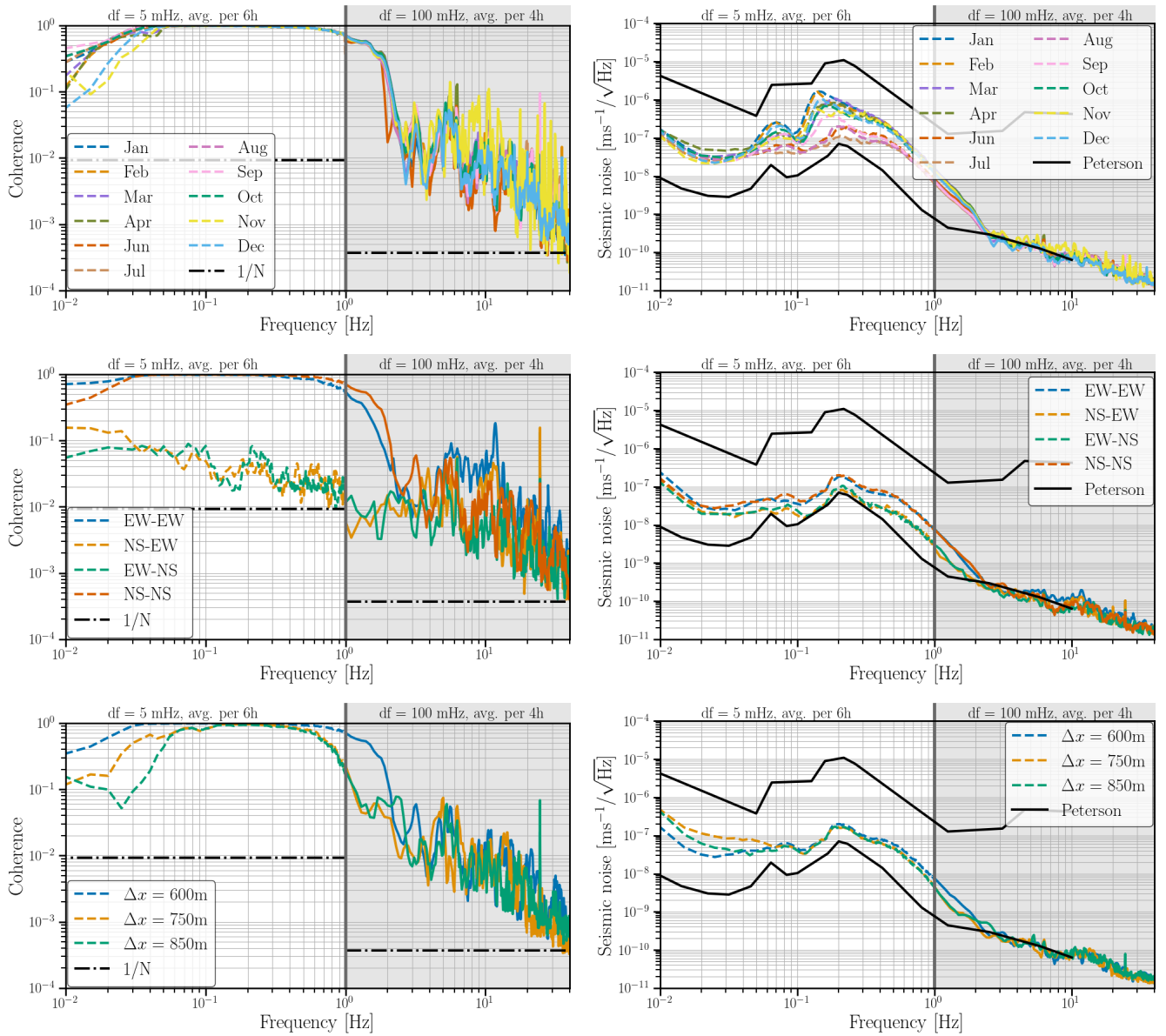


FIG. 7: The median coherence (left panel) and CSD (right panel) of the underground seismometers at LSBB as a function of the month of the year (top panels), the sensors orientations (middle panels) and the horizontal separation (bottom panels). For the top four panels the GAS and RAM sensors were used. For the bottom four panels data from the month of August was used. The black dot-dashed line (left panels) represents the level of coherence expected from Gaussian data. In the right panels, the Peterson low and high noise models are shown in black.

bling. Such an example is the line at 8.3 Hz which is the modulation frequency of the Italian GSM network, i.e. GHz signal packets are transmitted with a frequency of 8.3 Hz [54]. It is likely the other features are from non-seismic origin as well. However, additional research should further investigate this excess coherence and exclude any coherence being from seismological origin.

The right panel of Fig. 9 shows the accompanying levels of correlated seismic noise.

VI. EUREGIO MAAS-RHEIN

For EMR, we only present results for frequencies above 0.2 Hz as one of the sensors (CTSN) is dominated by sensor self-noise for lower frequencies. Furthermore the sensors at EMR are only sampled at 40 Hz and the data has a rapidly decreasing sensitivity for frequencies above 18 Hz.

As can be expected due to the larger horizontal separation between the sensors, the observed coherence is lower compared to the other sites. However, as shown in the

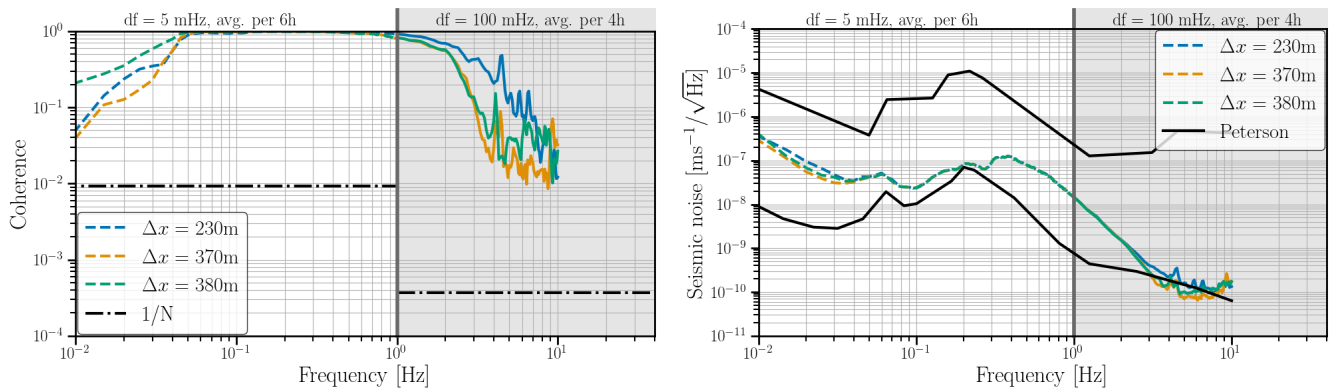


FIG. 8: The median coherence (left panel) and CSD (right panel) of the underground seismometers at Sos Enattos as a function of distance for Aug 2021. The black dot-dashed line (left panel) represents the level of coherence expected from Gaussian data. The Peterson low and high noise models are shown in black (right panel).

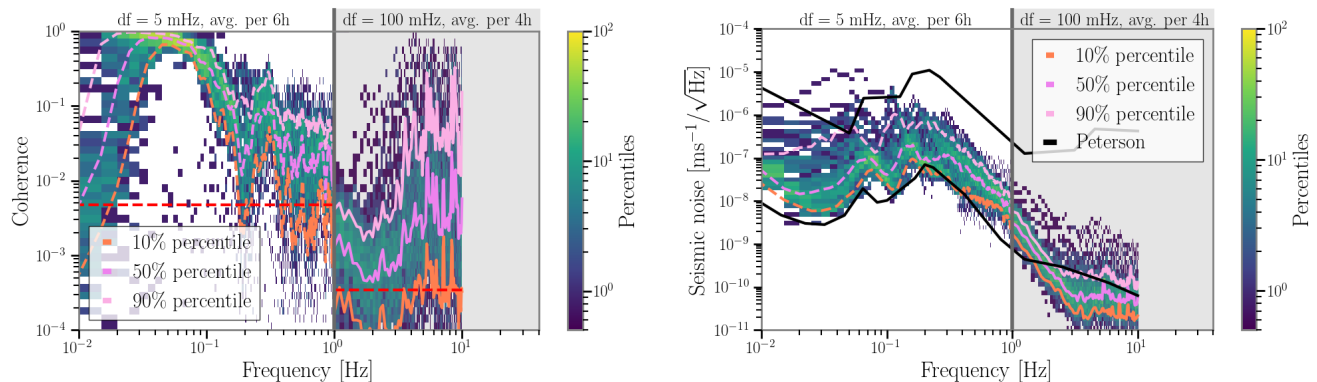


FIG. 9: The coherence (left panel) and CSD (right panel) between the underground seismometers (NS components) P2 and P3 (Sos Enattos, IT) with an approximate horizontal separation of 10km and depth of ≥ 250 m. The 10th, 50th and 90th percentiles are shown in respectively light pink, dark pink and light orange, where dashed (full) lines are used for the analyses with the different parameters < 1 Hz (≥ 1 Hz). The red dashed line (left panel) represents the level of coherence expected from Gaussian data. The black curves (right panel) represent the low and high noise models by Peterson [52].

left panel of Fig. 10, 90% of the time there is still significant coherence up to ~ 2 Hz, as well as at several highly coherent frequencies above 2Hz. Furthermore, 50% of the time there is significant coherence up to ~ 16 Hz. The accompanying CSD is shown in the right panel of Fig. 10.

VII. DISCUSSION

In Sec. III-VI we introduced the data for the four different sites considered in this study. Here we compare the data from the different sites during the months of January. Similar results for August are provided in the Appendix. Making this comparison is very challenging due to the large variety of parameters which are not the same between the different measurements at different sites. Often, more than one of the following rele-

vant parameters are different for each site: location, geographical topology, sensor separation, sensor type, sensor depth, sampling frequency, different year, etc. Based on the available data we try to make some general conclusions by comparing and combining all the seismic data from the different sites. However to really further understand the effect of each individual parameter such as sensor depth or separation etc, a systematic study should be performed where these parameters are carefully controlled for. Currently, such a study is under development at LSBB.

Given all these different parameters the results below should not be considered as a site comparison but rather as a demonstration of possible ranges of the figures of merit involved. We use the following sensor pairs for the different sites: D2000-E2000 (Homestake), GASRAM (LSBB), SOE2-SOE3 (Sos Enattos) and TERZ-CTSN (EMR).

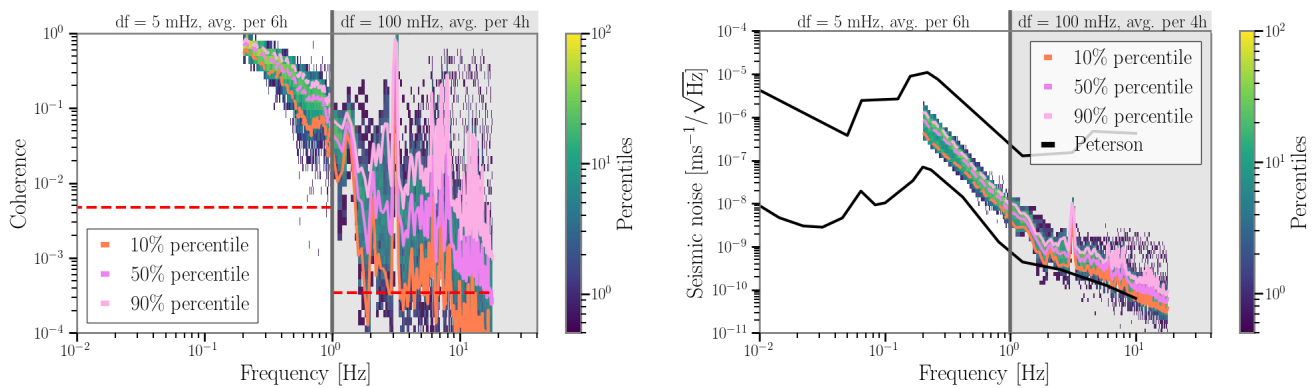


FIG. 10: The coherence (left panel) and CSD (right panel) between the underground seismometers (NS components) TERZ and CTSN (EMR, NL) with an approximate horizontal separation of ~ 2.4 km and depth of ~ 250 m. (Jan 2023) The 10th, 50th and 90th percentiles are shown in respectively light pink, dark pink and light orange, where dashed (full) lines are used for the analyses with the different parameters < 1 Hz (≥ 1 Hz). The red dashed line (left panel) represents the level of coherence expected from Gaussian data. The black curves (right panel) represent the low and high noise models by Peterson [52].

Based on the coherence of the different sites represented in the left panel of Fig. 11, we conclude that we observe significant coherence at least 50% of the time for frequencies between 0.01 Hz and 40 Hz for underground seismometers with a sub kilometer separation. Even in the case of a separation of ~ 2.4 km, as is the case for TERZ-CTSN, we observe significant coherence 50% of the time up to frequencies of about 16 Hz. Furthermore, we would like to point out that the coherence of EMR is high around the microseism peak. In Sec. V, we showed that even on distance scales of ~ 10 km, the seismic noise between 0.01 Hz and 1 Hz is coherent at least 50% of the time. Future investigations might be needed to probe such kilometer-long distance scales in the low frequency region in more detail. However, this is already a first order demonstration that future kilometer-long baseline atom interferometers, such as ELGAR [40], could potentially be impacted by correlated seismic and NN and should investigate this in more detail.

When looking at the observed correlated seismic noise as shown in the right panel of Fig. 11, we find that the levels of correlated seismic noise for all the different sites typically does not differ by more than one order of magnitude. Below 1 Hz Homestake has the lowest levels of seismic noise, apart for the frequency range 0.07 Hz-0.3 Hz when the seismic noise at Sos-Enattos is even lower. This is in line with the expectation that the seismic noise from ocean waves is lower at Homestake due to the large distance to the closest ocean, whereas the Sos-Enattos and LSBB sites are in (very) close proximity to the Mediterranean sea. The reason why Sos Enattos has the lowest CSD between 0.07 Hz and 0.3 Hz, might be linked to the fact that the secondary microseism peak seems to reach its maximum at a slightly higher frequency. This might be due to many different factors which vary for the diverse different sites.

At higher frequencies, Homestake becomes the noisiest site. At the other end, LSBB is an extremely quiet site in the high frequency region and Sos Enattos has low levels of correlated seismic noise up to ~ 8 Hz. However, for the latter, the levels of correlated noise increases between 8 Hz and 10 Hz, even though this correlation may be due to a non-seismic origin as stated in section V. Although the seismometers at the EMR site are located at a much larger separation from each other, the observed levels of correlated seismic noise is somewhere in between the different sites.

VIII. CORRELATED NEWTONIAN NOISE

We calculate the levels of NN from body waves in an identical way to earlier work [32], i.e. we use Eq. 1. Similar to this previous work we assume the bulk density $\rho_{0,\text{Bulk}}$ to be 2800 kg m^{-3} . Additionally, we assume $p = 1/3$, which accounts for the different mixing ratio of P- and S-waves. Choosing the correct value of p is non-trivial, as it strongly depends on the seismic sources (far or close) as well as on the geology. It could be argued that p should be chosen by relying on the equipartitioning of the energy in the assumption of a diffuse field. For a diffuse field the value of p depends on P- and S-wave velocities [55]. However, the presence of close seismic sources makes it difficult to make any assumptions by exploiting the equipartition of the energy. Therefore we use $p = 1/3$ as in this way the correlated NN is at most off by a factor 2 for both of the most extreme values of $p=0$ and $p=1$ (see Eq. 1). Note, the effectiveness with which NN can be subtracted depends on the actual value of p [56]. We purposefully do not use more accurate values, which depends on the site, as the goal of this paper is to probe a site independent order of magnitude rather than

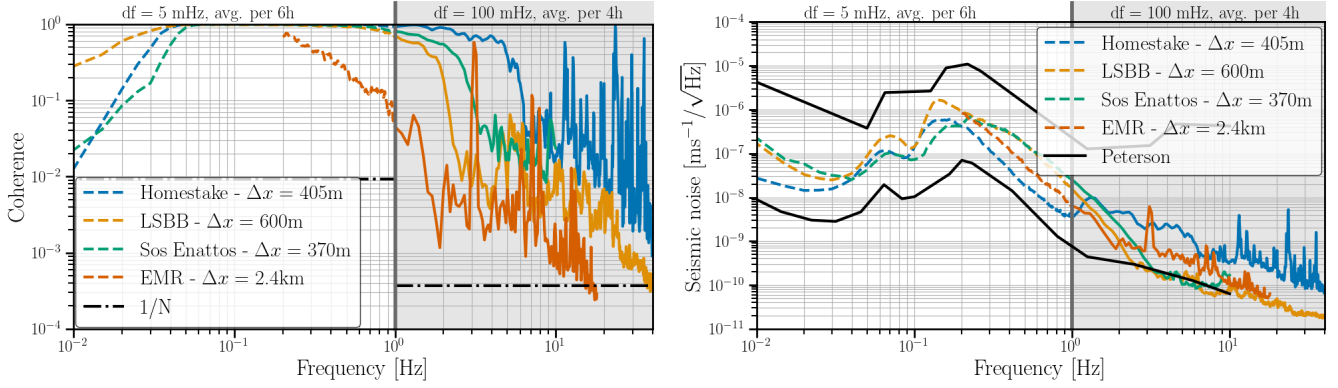


FIG. 11: The median coherence (left panel) and CSD (right panel) of the underground seismometers for the different geographical locations studied in this paper for the month of January. For more details on the sensors specifications, see Tab. I. Note: the data is not from the same year. The data $< 1\text{Hz}$ (dashed curves) are analysed using 200 second long segments which are averaged per 6h-window. Above 1Hz the data (full curves) are analysed using 10 second long segments which are averaged per 4h-window. The black dot-dashed line (left panel) represents the level of coherence expected from Gaussian data. The Peterson low and high noise models are shown in black (right panel).

providing accurate site specific results. S_{ξ_x} represents the PSD, or in our case the CSD, of the displacement caused by the body-waves along the arm direction and L is the length of the interferometer.

$$S_{\text{Body-wave}}(f) = \left(\frac{4\pi}{3} G \rho_{0,\text{Bulk}} \right)^2 (3p+1) \frac{1}{L^2 (2\pi f)^4} S_{\xi_x}(f) \quad (1)$$

A. The search for a GWB

The search for an (isotropic) GWB is very sensitive, if not the most, to correlated noise sources. Therefore, we now describe what one tries to measure when looking for an isotropic GWB and how we can project the effect of correlated noise on this figure of merit. As stated earlier, this projection is only considered to be relevant for the triangular design of the ET. The seismic noise is deemed to be uncorrelated in the relevant frequency band for the two L design, due to the large separation between the separate L-shaped interferometers.

When searching for an isotropic GWB one typically tries to measure its energy density, $d\rho_{\text{GW}}$, contained in a logarithmic frequency interval, $d \ln f$. Furthermore one divides by the critical energy density $\rho_c = 3H_0^2 c^2 / (8\pi G)$ for a flat Universe to construct a dimensionless figure of merit $\Omega_{\text{GW}}(f)$ [1, 57–59]:

$$\Omega_{\text{GW}}(f) = \frac{1}{\rho_c} \frac{d\rho_{\text{GW}}}{d \ln f}, \quad (2)$$

where H_0 is the Hubble-Lemaître constant, c is the speed of light and G is Newton’s constant. We use the 15-year Planck value of $67.9 \text{ km s}^{-1} \text{ Mpc}^{-1}$ for H_0 [60].

When searching for an isotropic, Gaussian, stationary and unpolarized GWB, one can construct the cross-correlation statistic $\hat{C}_{IJ}(f)$,

$$\hat{C}_{IJ}(f) = \frac{2}{T_{\text{obs}}} \frac{\text{Re}[\tilde{s}_I^*(f)\tilde{s}_J(f)]}{\gamma_{IJ}(f)S_0(f)}, \quad (3)$$

which is an unbiased estimator of $\Omega_{\text{GW}}(f)$ in the absence of correlated noise [58, 59]. I and J represent the two interferometers and $\tilde{s}_I(f)$ is the Fourier transform of the time domain strain data $s_I(t)$ measured by interferometer I . γ_{IJ} is the normalized overlap reduction function which encodes the baseline’s geometry [57, 61]. $S_0(f)$ is a normalisation factor given by $S_0(f) = (9H_0^2)/(40\pi^2 f^3)$ and T_{obs} is the total observation time of the data-collecting period⁷.

In line with earlier studies on the impact of correlated noise on the ET [16, 32] we refer to the three different ET interferometers as $\text{ET}_1, \text{ET}_2, \text{ET}_3$, which we assume to have identical sensitivity. Furthermore we neglect the difference in γ_{IJ} between the baseline pairs $IJ = \text{ET}_1\text{ET}_2; \text{ET}_1\text{ET}_3; \text{ET}_2\text{ET}_3$, since the relative difference between the overlap reduction functions of the different arms is smaller than 5×10^{-7} for frequencies under 1 kHz [16]. In the remainder of the paper, we use the ET_1ET_2 -baseline as our default observing baseline.

Similar to earlier work [32], we can construct equivalent cross-correlation statistics for the correlated NN:

$$\hat{C}_{\text{NN},\text{ET}_1\text{ET}_2}(f) \frac{S_{\text{Body-wave}}}{\gamma_{\text{ET}_1\text{ET}_2}(f)S_0(f)}, \quad (4)$$

⁷ The normalisation factor $S_0(f)$ for ET differs from that one of e.g. LIGO-Virgo-KAGRA by a factor of 3/4, due to the different opening angle between the interferometers’ arms ($\pi/2$ for LIGO-Virgo-KAGRA and $\pi/3$ for ET) [61].

where $S_{\text{Body-wave}}$ was introduced in Eq 1.

The sensitivity of a search for an isotropic GWB can be related to the instantaneous sensitivity of the ET interferometer, referred to as the one-sided amplitude spectral density (ASD) $P_{\text{ET}}(f)$, as follows [57–59]:

$$\sigma_{\text{ET}_1\text{ET}_2}(f) \approx \sqrt{\frac{1}{2T_{\text{obs}}\Delta f} \frac{P_{\text{ET}}^2(f)}{\gamma_{\text{ET}_1\text{ET}_2}^2(f)S_0^2(f)}}, \quad (5)$$

with Δf the frequency resolution. Here we have assumed identical sensitivity in the different ET interferometers $\text{ET}_1, \text{ET}_2, \text{ET}_3$. $\sigma_{\text{ET}_1\text{ET}_2}(f)$ is the standard deviation on the cross-correlation statistic defined in Eq. 3, in the small signal-to-noise ratio (SNR) limit and absence of correlated noise. Because the GWB one tries to observe is very weak, the former is a realistic assumption. The effect of the latter is the focus of this section.

As many of the expected signals for an isotropic GWB behave as a power-law, a more appropriate sensitivity to such a signal than $\sigma_{\text{ET}_1\text{ET}_2}(f)$ would be one that takes into account this broadband character of the expected signal. Such a broadband sensitivity is given by the so called power-law integrated (PI) curve: $\Omega_{\text{ET}}^{\text{PI}}(f)$. $\Omega_{\text{ET}}^{\text{PI}}(f)$ is constructed using $\sigma_{\text{ET}_1\text{ET}_2}(f)$ such that at any frequency a power-law signal $\Omega_{\text{GW}}(f)$ with an SNR of 1 for the ET_1ET_2 baseline is tangent to this PI-sensitivity curve [62]. This makes $\Omega_{\text{ET}}^{\text{PI}}(f)$ the relevant figure of merit to identify correlated broadband noise sources that could impact the search for an isotropic GWB.

B. Impact of correlated NN on the search for a GWB

With Fig. 12 we present how correlated NN caused by the observed seismic correlations presented earlier in this paper affects the search for an isotropic GWB with the ET. Fig. 12 shows the noise budget using the seismic data from the month of January. Since in the region of interest for the ET (i.e. $>1\text{Hz}$) there is little difference in the amplitude of seismic noise across seasons, we do not provide the results for August in the main text. However, for completeness, you can find these results in Fig. 16 in the Appendix. Furthermore, we highlight that these budgets are calculated identically to the Homestake results in [32] as well as the results in [38]. The data used for the NN budgets in Fig. 12 is the same as the data used in Fig. 11.

In line with the results presented in [32], correlated NN from body-waves, assuming a seismic environment as observed at Homestake, would dominate the power-law integrated sensitivity curve for broadband GWB signals up to $\sim 40\text{Hz}$ about 50% of the time. This would limit ETs sensitivity to isotropic GWB signals up to 20 Hz–30 Hz to levels similar as planned to be achieved by LIGO and Virgo during their fifth observing run (Design A+). Even in the most optimistic scenario as discussed by the

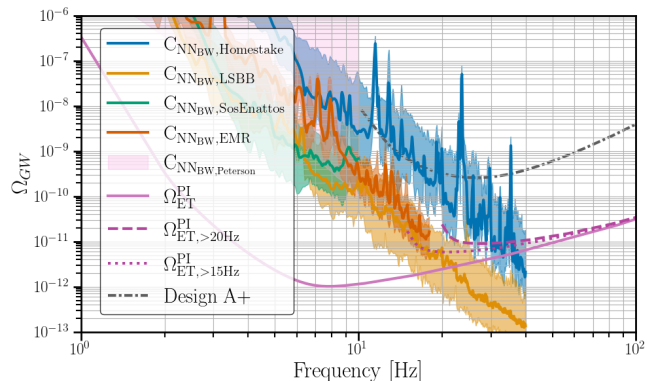


FIG. 12: The projected impact from correlated NN from body-waves, as calculated in this section, for the seismic data from the month of January for the different locations, see the text for details on the used sensors, their distances and depths. As a comparison we make the same projection using the Peterson low noise and high noise models. For the broadband ($\Omega_{\text{ET}}^{\text{PI}}$) sensitivity to a GWB we assumed one year of observation time (100% duty cycle). The one year PI curve of the A+ design for the LIGO Hanford LIGO Livingston and Virgo detectors is represented by the dot-dashed curve. This curve was obtained using the open data provided by the LVK collaborations [63] and was first presented in [64]. Please note: in this paper we present the 1σ PI-curve, whereas in [64] the 2σ PI-curve is shown.

projection of the correlated NN based on observed correlations at LSBB, the search for an isotropic GWB would be limited by correlated NN up to $\sim 20\text{Hz}$ for at least 50% of the time. In [38] a couple of assumptions were used to get an estimate of the lowest possible levels of correlated NN affecting the search for a GWB. For this, the authors of [38] multiplied Peterson’s low noise limit with the observed coherence at Homestake as shown in [32]. This led to a minimal impact of correlated NN above $\sim 10\text{Hz}$. However, based on the results described in this paper, it seems that this assumption is overly optimistic. Neither of the two candidate sites, Sos Enattos and EMR, has correlated seismic noise that low. Even the seismically quiet site LSBB has considerably higher levels of correlated NN which are at least one order of magnitude larger at 10 Hz.

To understand the impact of this noise source on the analysis for an isotropic GWB it is important to understand what the PI curve reflects. As stated earlier, this integrates over $\sigma_{\text{ET}_1\text{ET}_2}(f)$ as a function of frequency. Consider a broadband power-law signal: $\Omega_{\text{GW}}(f) = \Omega_{\text{ref}} \left(\frac{f}{f_{\text{ref}}}\right)^\alpha$. For all negatively sloped (i.e. $\alpha < 0$) signals, the correlated NN noise presents a significant problem seriously limiting the science potential. However, many of the expected signals have positive power-law slopes. Some examples are the GWB from unresolved compact binary coalescence (CBC) events ($\alpha = 2/3$) [65–

67] and the GWB from core collapse supernovae ($\alpha = 3$) [68]. Multiple cosmological GWBs, e.g. cosmic strings [69], predict a flat GWB ,i.e. $\alpha \approx 0$. For such signals the impact of the correlated noise might be less dramatic. Not using the data below 20Hz (15Hz) out of concern of noise contamination results in the dark purple dashed (dotted) PI curves in Fig. 12. The $>20\text{Hz}$ ($>15\text{Hz}$) PI is not affected by the LSBB correlated NN levels up to the 90% (50%) percentiles. This illustrates that in certain circumstances it might be beneficial to disregard the low frequency data in the case of correlated noise contamination. In searching for power-law signals with large positive slopes such as $\alpha = 3$, the low frequency regime (and therefore potential contamination from correlated NN noise) is irrelevant as the dominant contribution to the detectability comes from frequencies above 100Hz. For $\alpha = 0$ ($\alpha = 2/3$) one loses a factor $\sim 6-9$ ($\sim 3-4$) in starting the analysis at 15Hz-20Hz rather than at 1Hz to avoid contamination from correlated noise. This also implies that for certain searches (e.g. $\alpha = 0$) it might be more beneficial to place aggressive data quality vetoes on times with large ambient seismic noise and remove up to 50% of the data to lower the contamination of correlated noise. Namely, the gain from adding more data scales as \sqrt{t} , with t the total observation time and might be outweighed by the gain of reduced noise contamination. See TABLE III for a summary.

Note, here we have not assumed any level of noise subtraction. However, for the noise subtraction as discussed in earlier work [21, 23, 26, 27, 33, 43–50], one typically assumes to construct a Wiener filter. For frequencies above several Hz, the NN of body-waves is below the detector sensitivity on the typical timescales over which the Wiener filter is calculated. The noise sources only becomes problematic for the search for a GWB as in this case one correlates data over very long timescales of $\mathcal{O}(1\text{ yr})$ over which correlated noise sources can accumulate significance. Future research should further investigate the efficiency of these noise subtraction techniques if the NN noise is subthreshold compared to the detector sensitivity when determining the Wiener filter.

IX. GLITCH STUDY

After the presentation of the earlier study investigating the impact of correlated NN based on seismic observations at Homestake [32], some concerns were raised to which extent the multi-hour long averages were dominated by a limited number of short but (very) loud time periods. To address these concerns in this paper, we perform a study of transient seismic noise in this section. For this study, we were inspired by an earlier study of the seismic glitchiness at Sos Enattos [22]. There, they investigate the impact of seismic glitches on the inspiral signal of an intermediate mass black hole binary within a seg-

ment of 1 min⁸. Therefore, in this paper we are looking at the seismic glitchiness on one-minute time segments. For this study, we use data from the month of August for Homestake, LSBB and Sos Enattos and data from the month of January for EMR. Please note that this implies that the EMR results has a higher noise level around the microseism peaks than during summertime at the same location, which is the season considered at the other sites.

We want to state that the study performed in this section and the analysis of [22] serve a different purpose and therefore should not be compared one-to-one. The goal of the authors of [22] was to establish the effect of seismic glitchiness on the ET. On the other hand, the goal of this section is to understand if a small subset of short times lead to a significant bias of our estimate of ambient seismic noise over several hour long time segments. That is, are the percentiles presented in e.g. Figs 11 and 12 a good measure of the ambient seismic noise over several hours, or are they rather dominated by a small amount of large seismic transients. Even though we get some information on the seismic glitchiness as a byproduct of our analysis, more data (e.g. 1yr as in [22]) should be analysed to make clear statements on each site's glitchiness.

The sensor pairs we use are respectively D2000-E2000, GAS-RAM, SOE2-SOE3 and TERZ-CTSN where we only considered the correlation between seismic noise observed in the North-South component of each sensor. In [22] the authors construct a type of SNR indicating the seismic glitchiness compared to ETs sensitivity. However, we make statements on the potential bias on our estimates of the ambient seismic noise caused by the glitchiness of the seismic data of the site itself. To this extent we consider three different frequency regions: 0.1Hz-1Hz, 1Hz-10Hz and 10Hz-40Hz (10Hz-18Hz in the case of the EMR sensor). We use the logarithmic average of the seismic noise in each of these frequency regions as an indicator to study the effect of glitchiness in each one-minute time segment on our estimates of the ambient seismic noise. For the PSD of the first sensor⁹ of each site we present their distributions in Fig. 13. Since the histograms for the PSD of the second sensor have similar behavior, we do not include these figures and focus our discussion on Fig. 13. In case of the low- and mid-frequency region we show the value expected from Peterson's low noise (PLNM), logarithmic average (PA) and high noise models (PHNM).

Based on these histograms a first comment we can make is that neither of the sites seems strongly dominated by a subset of loud outliers¹⁰. We carefully examined the

⁸ As described in [22] the exact signal length depends on many parameters of the system and can range from ten seconds to many tens of seconds. The window of 1 min was chosen as a compromise between the shorter and longer signal duration and only serves as an indicative figure of merit.

⁹ That is respectively D2000, GAS, SOE2 and TERZ for the different sites.

¹⁰ In this context we consider an outlier to be a data point which is

	$\Omega_{\text{ET}>1\text{Hz}}^{\text{PI}}$	$\Omega_{\text{ET}>15\text{Hz}}^{\text{PI}}$	$\Omega_{\text{ET}>20\text{Hz}}^{\text{PI}}$
$\alpha = 0$	1e-12	6e-12	9e-12
$\alpha = 2/3$	2.1e-12	6e-12	7.8e-12
$\alpha = 3$	2e-13	2e-13	2e-13

TABLE III: The approximate amplitude $\Omega_{\text{GW}}(f)$ of the power-law signal tangent to the 1σ PI-curves (as shown in Fig. 12) with different starting frequencies of the analysis. We use $f_{\text{ref}} = 25\text{Hz}$.

time-frequency maps of each associated sensor, allowing us to analyse the behaviour of PSDs, CSDs, and coherence over the duration of a month. These analyses reveal recurring patterns in the PSDs. Specifically, we observed a day-night effect, with nights being significantly quieter than days. This can be attributed to human activity. Additionally, there are a limited number of moments when the PSD and CSD exhibit higher amplitude values, indicating the presence of micro-seismic phenomena that affect ambient measurements. The histograms shown in Fig. 13 highlight the implicated PSD values, which result in an elongation of the distribution tail due to their higher amplitudes.

As a proof of concept, we remove a subset of the loudest one-minute segments and investigate the impact on the observed coherence and CSD. We demonstrate this proof of concept on one site, namely Homestake. We have chosen Homestake as it has a relatively long tail of more noisy segments in the mid- and high frequency range, but compared to LSBB for which this is also the case, Homestake is the site with the loudest predicted levels of correlated seismic noise in these frequency regions. For the PSD of both sensors, we identified in every frequency region the 50 loudest one-minute segments. These 300 noisy segments identified can be described by only 115 unique segments due to large overlap in the noisy segments. This equals to about 0.25% of the total data. This choice of cut-off value is semi-arbitrary. However the distributions of the transient seismic noise are strongly site dependent and therefore it is hard to define an absolute value of which segment should be considered an outlier and which not. At the same time, we do not want to remove a large amount of data as this is expected to impact the observed percentiles just by the mere fact of removing the data. In Fig. 13, we have indicated the 50 loudest bins in that frequency region by the blue dashed line for the histogram of the Homestake data. Please note that in total more bins from the histogram are removed based on the removal criteria in the different frequency regions as well as based on the PSD of the second sensor.

After identifying the loudest segments, we run the analysis for the seismic noise of the month of August at Homestake again with the identified segments removed

significantly disconnected from the bulk of the distribution. As an example the handfull of orange data points near -5.5 for the top left panel and near -7 for the top right and bottom panel are considered outliers.

from the analysis. The coherence and CSD after removal, shown in Fig. 14, should be compared to Fig. 4. The only difference between the data used for these figures is the removal of the loudest segments in Fig. 14.

When comparing the 10% and 50% percentiles for both coherence and the CSD before and after the removal of the loudest transients, almost no effect is observed. The largest effect is observed $> 10\text{Hz}$ for which at all times the seismic CSD after glitch removal is at most 20% smaller compared to the CSD before glitch removal. However, for the 90% percentile a significant difference is observed. The coherence after glitch removal is about two to ten times lower for frequencies above 10Hz. The CSD after glitch removal is up to a factor two lower between 1Hz and 10Hz and up to a factor of four between 10Hz and 40Hz. On average the 90% percentile of the CSD is two times lower after glitch removal. The correlated seismic noise is visibly cleaner after removing the loudest one-minute segments as compared to before.

Furthermore, we want to highlight that we tested the impact of removing 115 one-minute segments by removing the same number of segments arbitrarily chosen. This yields quasi-identical results to the analysis where no data was excluded, shown in Fig. 4. This proves the effect discussed above is indeed due to removing the loudest segments and not due to the act of removing 115 one-minute segments.

Based on the analysis above we can state that whereas the 90% percentile of CSD (and coherence) are significantly impacted by a small number of loud transient time segments, the 10% and 50% percentiles are not. Both in earlier work [32] as well as in this paper, all key conclusions are based on the 50% percentiles. Therefore, we state that all key conclusions of this (and earlier [32]) work were not disproportionately dominated by a small number of noisy segments, but the results form a good representation of the correlated noise of the seismic ambient environment.

X. CONCLUSION

Next generation Earth-based GW atom interferometers, such as ELGAR, as well as interferometric detectors, such as the ET and CE, promise to be powerful instruments to observe GWs in the next decades. With the sensitivity range of atom interferometers to GWs, mainly between 0.1Hz-1Hz, and ET's unprecedented low frequency sensitivity in the range 1 Hz-10 Hz, they could

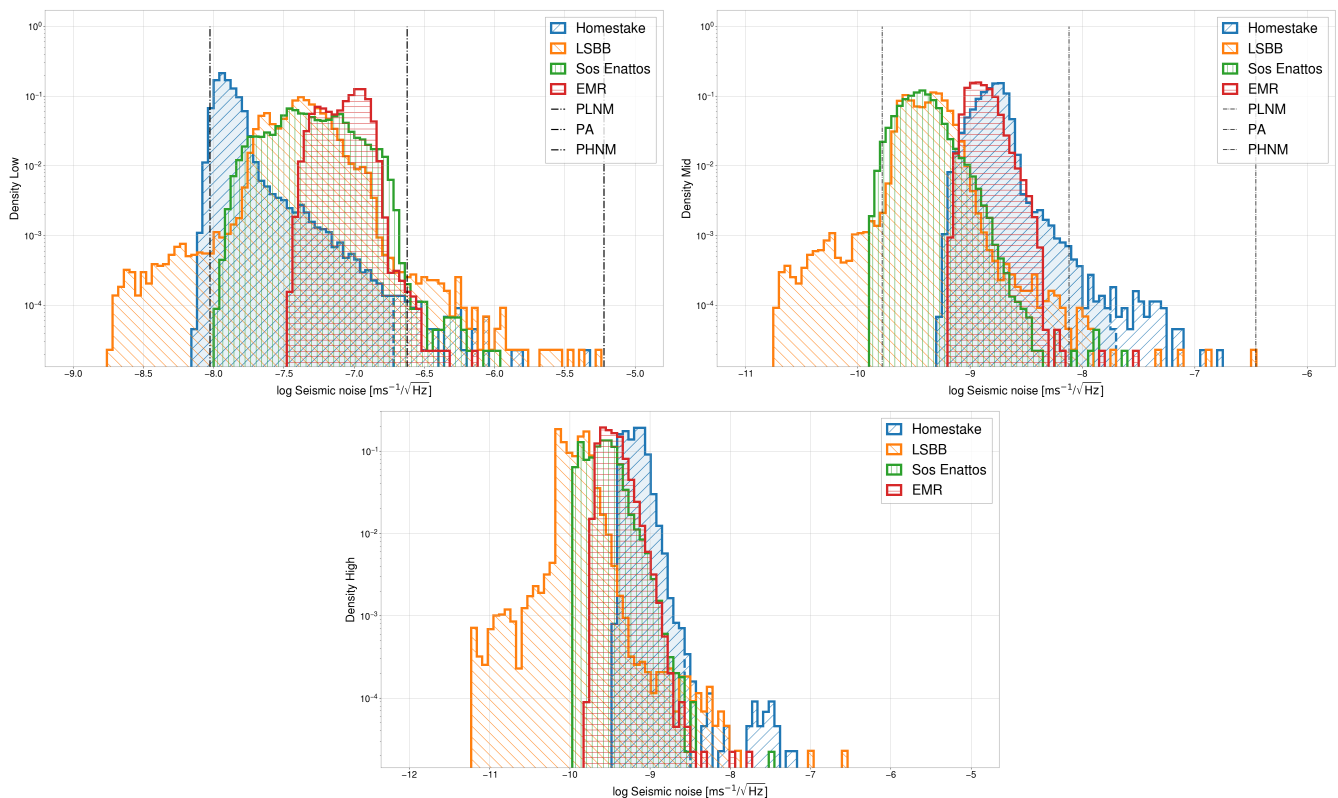


FIG. 13: The logarithmic average seismic noise in the from Homestake (blue), LSBB (orange), Sos Enattos (green) and the EMR (red) for the low frequency band 0.1Hz-1Hz (top left), mid frequency band 1Hz-10Hz (top right) and high frequency band 10Hz-40Hz (bottom). The black curves (top panels) represent the logarithmic average of low and high noise models by Peterson [52], as well as the mean of the Peterson models. Data are analysed using 60-second segments. The blue dashed line corresponds to the cut, we sorted and deleted the 50th highest PSDs.

open new windows into the GW universe.

However, earlier work [32] demonstrated that correlated seismic noise and, particularly, correlated NN could seriously limit the search for an isotropic GWB with co-located ET detectors. In this work, we build further on these earlier results and improve them in multiple ways. Rather than using underground seismic data from one site, we use four geologically different sites, one of which houses the atom interferometer MIGA and two are candidate sites to house the ET. Additionally, we probe a wider range of horizontal separations between the seismic sensors ranging from 230 m to 10 km. The depth of the sensors varies between 84 m and 610 m. Furthermore, we probed the low frequency region 0.01 Hz-0.1 Hz, which is of interest for atom interferometers. Finally we performed a study of the seismic glitches of the sites and prove that seismic transients do not significantly affect our analyses and conclusions.

We analysed data from underground seismometers at the former Homestake mine (USA), the MIGA site at the ‘Laboratoire Souterrain à Bas Bruit’ (FR) and two of the three candidate sites for the ET, the former Sos Enattos mine (IT) and the Euregio Maas-Rhein (NL-BE-DE). The used sensor pairs have a wide variety of analy-

sis parameters such as horizontal separation, depth, sensors model, geological environment, located in a bore-hole or a cavern, etc. Currently a systematic study is being performed at LSBB. However, despite this wide variety, across all these we find (for sensors with a horizontal separation up to 2.4km) significant coherence at least 50% of the time in frequency ranges for both atom interferometers as well as the ET. The levels of correlated seismic noise across these wide variety of sensors is at most about one order of magnitude when comparing the 50% percentiles. More concretely for sensors with a separation less than one kilometer we find at least 50% of the time significant coherence in the entire frequency band 0.01Hz-40Hz. For a sensor pair in the EMR region with a separation of 2.4km we find significant coherence up to ~ 16 Hz for the 50% percentile. Finally, a pair of seismometers separated by 10km at the Sos Enattos site demonstrate that even on this multi kilometer distance we find significant seismic coherence between 0.01Hz and 1Hz for the 50% percentile. For frequencies larger than 1Hz, these results are (almost) independent of the time of the year.

These seismic correlations are important to take into account for next generation atom interferometers and in-

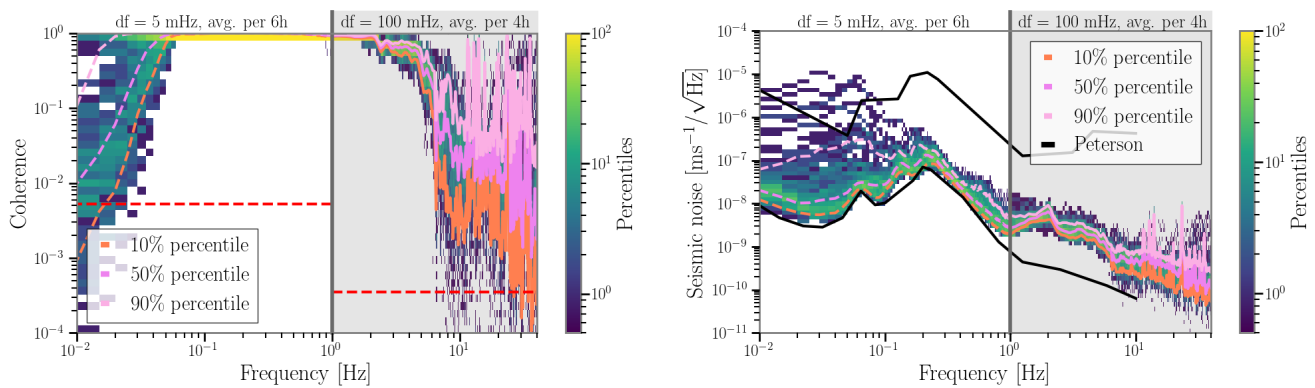


FIG. 14: The coherence (left panel) and CSD (right panel) between the underground seismometers (NS components) D2000 and E2000 at Homestake ($\Delta x \approx 405\text{m}$ and depth = 610m) where 115 noisy 1 min-segments were removed from the analysis as described in the text. The data $< 1\text{Hz}$ (Aug 2016) are analysed using 200 second long segments which are averaged per 6 h-window. Above 1Hz the data are analysed using 10 second long segments which are averaged per 4 h-window. The 10th, 50th and 90th percentiles are shown in respectively light pink, dark pink and light orange, where dashed (full) lines are used for the analyses with the different parameters $< 1\text{Hz}$ ($\geq 1\text{Hz}$). The red dashed line represents the level of coherence expected from Gaussian data which goes approximately as $1/N$, where N is the number of time segments over which was averaged.

terferometric GW detectors. For the former, multiple atomic gradiometers are planned to be placed at distances of several hundred of meters to tens of kilometers. For the ET the baseline configuration consists of an equilateral triangle made up of three nested GW interferometers. In this configuration the end and central station of two different detectors are planned to be separated by a distance of several hundred of meters in the current design [70]. Additionally, 10km is a relevant distance scale for the ET as this is the proposed length-scale for the detector’s arms.

One of the goals from this and earlier [32] research was to provide insight on whether the separation between the corner and end stations of the nested ET detectors would matter for the correlated seismic noise. Based on the results presented in this work it seems that any displacement $< 1\text{km}$ is insufficient to decrease seismic coherence. A distance of $\sim 2.5\text{km}$ does provide significant reduction in seismic coherence. However even in such a case we find significant coherence up to $\sim 16\text{Hz}$ 50% of the time or more. To truly eliminate all seismic coherence (to the level of $\sim 3.8 \times 10^{-4}$) above 1 Hz one should have a horizontal separation between the corner and end stations of different ET detectors between 2.5 km and 10 km. However, such a large separation is rather unlikely.

The effect of the observed correlations of seismic noise, and subsequent NN, on atom interferometers should be projected in future work. However, the results presented in this work could form an ideal starting point to make such projections. Additionally our results demonstrate that one should be cautious and investigate these effects in more detail as we observe seismic correlations over the entire frequency band of interest (0.1 Hz-10 Hz) as well as over the entire range of distances expected for a realistic

set-up ranging from hundreds of meters to $\mathcal{O}(10)$ km.

In the context of the ET, we make a projection of the expected contributions of NN from body waves on the search for an isotropic GWB. This search is the most sensitive to correlated noise sources as one tries to observe a weak background of correlated GW signals for which one typically has to integrate over $\mathcal{O}(1 \text{ year})$ of data. Previous investigations have shown that ET’s instantaneous sensitivity would probably be affected by NN by a factor 3-5, which is considered to be realistically removable by noise subtraction methods such as Wiener filtering [21, 23, 26, 27, 33, 43–50]. However, as shown in [32], the search for an isotropic GWB is subject to very small coherent noise signals. In this work, we have shown that the projections based on underground seismic measurements at Homestake, of which similar results were presented in [32], are probably more pessimistic compared to a realistic situation at one of the ET candidate sites. However, at the same time we demonstrated that the assumptions made in [38] are probably too optimistic as all measurements, even those at extremely low noise seismic sites above 10Hz, predict stronger effects. More concretely, these results predict that during at least 50% of the time the search for an isotropic GWB would be dominated by NN from body-waves up to 20Hz. This assumes our most quiet seismic observations at LSBB. For the Homestake site the effect extends up to 40Hz.

The correlated noise contamination in the low frequency regime has a different impact depending on which type of broadband isotropic GWB one is looking for. The resolvable amplitude for a negatively sloped power-law signal will be reduced by several orders of magnitude. However, most of the signals currently searched for in this frequency band have a flat or positive power-law slope,

e.g. $\alpha = 0, 2/3, 3$ [64]. We demonstrate that by only analysing data above 15Hz-20Hz one would loose up to a factor $\sim 6-9$ ($\sim 3-4$) for a power-law signal with a slope of $\alpha = 0$ ($\alpha = 2/3$). Such analysis could be free of correlated noise in case of low noise levels such as at the LSBB site. The detectability of a signal with $\alpha = 3$ is unaffected as it is dominated by the data at higher frequencies.

Finally, the measurements at Sos Enattos seem to suggest significant seismic correlations on length-scales of 10km are situated below 1Hz. Therefore, any correlation effects between test masses located 10km-far are to be excluded in the frequency band of interest for ET. However, at current detectors increased noise levels are observed above several Hz during times of loud seismic activity at lower frequencies. Such an example are slow scattered light glitches caused by increased microseism activity between 0.1Hz and 0.3Hz [71]. These more complex coupling mechanisms are likely to be detector dependant in which case they are less likely to enter coherently in different interferometers. However, more work might be needed in the future to entirely exclude this additional

pathway for correlated noise to enter into GWB searches with co-located ET detectors. Furthermore, the effect of the correlated seismic noise for frequencies below 1Hz on the angular control of the instruments is to be further understood.

ACKNOWLEDGMENTS

K.J. was supported by FWO-Vlaanderen via grant number 11C5720N during part of this work. M.W.C acknowledges support from the National Science Foundation with grant numbers PHY-2308862 and PHY-2117997. The authors' grateful acknowledgment also goes to the contribution of the Fondi di Ateneo per la ricerca 2019, Fondi di Ateneo per la ricerca 2020 of the University of Sassari and the support of the Italian Ministry of Education, University and Research within the PRIN 2017 Research Program Framework, no. 2017SYRTCN and University of Sassari.

-
- [1] N. Christensen, Reports on Progress in Physics **82**, 016903 (2018).
- [2] W. O. Schumann, Zeitschrift Naturforschung Teil A **7**, 149 (1952).
- [3] W. O. Schumann, Zeitschrift Naturforschung Teil A **7**, 250 (1952).
- [4] J. Aasi *et al.*, Classical and Quantum Gravity **32**, 074001 (2015).
- [5] F. Acernese *et al.* (VIRGO), Class. Quant. Grav. **32**, 024001 (2015), arXiv:1408.3978 [gr-qc].
- [6] Y. Aso, Y. Michimura, K. Somiya, M. Ando, O. Miyakawa, T. Sekiguchi, D. Tatsumi, and H. Yamamoto (The KAGRA Collaboration), Phys. Rev. D **88**, 043007 (2013).
- [7] E. Thrane, N. Christensen, and R. M. S. Schofield, Phys. Rev. D **87**, 123009 (2013), arXiv:1303.2613 [astro-ph.IM].
- [8] E. Thrane, N. Christensen, R. M. S. Schofield, and A. Effler, Phys. Rev. D **90**, 023013 (2014), arXiv:1406.2367 [astro-ph.IM].
- [9] M. W. Coughlin *et al.*, Class. Quant. Grav. **33**, 224003 (2016), arXiv:1606.01011 [gr-qc].
- [10] Y. Himemoto and A. Taruya, Phys. Rev. D **96**, 022004 (2017), arXiv:1704.07084 [astro-ph.IM].
- [11] M. W. Coughlin, A. Cirone, P. Meyers, S. Atsuta, V. Boschi, A. Chincarini, N. L. Christensen, R. De Rosa, A. Effler, I. Fiori, M. Golkowski, M. Guidry, J. Harms, K. Hayama, Y. Kataoka, J. Kubisz, A. Kulak, M. Laxen, A. Matas, J. Mlynarczyk, T. Ogawa, F. Paoletti, J. Salvador, R. Schofield, K. Somiya, and E. Thrane, Phys. Rev. D **97**, 102007 (2018).
- [12] Y. Himemoto and A. Taruya, Phys. Rev. D **100**, 082001 (2019), arXiv:1908.10635 [astro-ph.IM].
- [13] P. M. Meyers, K. Martinovic, N. Christensen, and M. Sakellariadou, Phys. Rev. D **102**, 102005 (2020), arXiv:2008.00789 [gr-qc].
- [14] K. Janssens, M. Ball, R. M. S. Schofield, N. Christensen, R. Frey, N. van Remortel, S. Banagiri, M. W. Coughlin, A. Effler, M. Golkowski, J. Kubisz, and M. Ostrowski, Phys. Rev. D **107**, 022004 (2023).
- [15] I. Kowalska-Leszczynska *et al.*, Class. Quant. Grav. **34**, 074002 (2017), arXiv:1612.01102 [astro-ph.IM].
- [16] K. Janssens, K. Martinovic, N. Christensen, P. M. Meyers, and M. Sakellariadou, Phys. Rev. D **104**, 122006 (2021).
- [17] M. Punturo *et al.*, Class. Quant. Grav. **27**, 194002 (2010).
- [18] S. Hild *et al.*, Class. Quant. Grav. **28**, 094013 (2011), arXiv:1012.0908 [gr-qc].
- [19] L. Naticchioni, M. Perciballi, F. Ricci, E. Coccia, V. Malvezzi, F. Acernese, F. Barone, G. Giordano, R. Romano, M. Punturo, R. D. Rosa, P. Calia, and G. Loddo, Classical and Quantum Gravity **31**, 105016 (2014).
- [20] L. Naticchioni, V. Boschi, E. Calloni, M. Capello, A. Cardini, M. Carpinelli, S. Cuccuru, M. D'Ambrosio, R. de Rosa, M. D. Giovanni, D. d'Urso, I. Fiori, S. Gavigano, C. Giunchi, E. Majorana, C. Migoni, G. Oggiano, M. Olivieri, F. Paoletti, M. Paratore, M. Perciballi, D. Piccinini, M. Punturo, P. Puppo, P. Rapagnani, F. Ricci, G. Saccorotti, V. Sipala, and M. C. Tringali, Journal of Physics: Conference Series **1468**, 012242 (2020).
- [21] M. Di Giovanni, C. Giunchi, G. Saccorotti, A. Berbellini, L. Boschi, M. Olivieri, R. De Rosa, L. Naticchioni, G. Oggiano, M. Carpinelli, D. D'Urso, S. Cuccuru, V. Sipala, E. Calloni, L. Di Fiore, A. Grado, C. Migoni, A. Cardini, F. Paoletti, I. Fiori, J. Harms, E. Majorana, P. Rapagnani, F. Ricci, and M. Punturo, Seismological Research Letters **92**, 352 (2020).
- [22] A. Allocca *et al.*, Eur. Phys. J. Plus **136**, 511 (2021), [Erratum: Eur.Phys.J.Plus 136, 607 (2021)].
- [23] M. Di Giovanni, S. Koley, J. X. Ensing, T. Andric, J. Harms, D. D'Urso, L. Naticchioni, R. De Rosa, C. Giunchi, A. Allocca, M. Cadoni, E. Calloni, A. Cardini, M. Carpinelli, A. Contu, L. Errico, V. Mangano, M. Olivieri, M. Punturo, P. Rapagnani, F. Ricci,

- D. Rozza, G. Saccorotti, L. Trozzo, D. Dell’Aquila, L. Pésenti, V. Sipala, and I. Tosta e Melo, *Geophysical Journal International* **234**, 1943 (2023).
- [24] G. Saccorotti, C. Giunchi, M. D’Ambrosio, S. Gavianio, L. Naticchioni, D. D’Urso, D. Rozza, A. Cardini, A. Contu, F. Dordei, M. Cadeddu, M. Tuveri, C. Migoni, M. Punturo, A. Allocca, E. Calloni, G. L. Cardello, L. D’Onofrio, N. Davari, D. Dell’Aquila, R. D. Rosa, M. Carpinelli, L. D. Fiore, M. di Giovanni, L. Errico, I. Fiori, M. C. Tringali, J. Harms, S. Koley, V. Longo, E. Majorana, V. Mangano, M. Olivieri, F. Paoletti, L. Pésenti, P. Puppo, P. Rapagnani, M. Razzano, F. Ricci, V. Sipala, I. T. e Melo, and L. Trozzo, *The European Physical Journal Plus* **138**, 793 (2023).
- [25] F. Amann *et al.*, *Rev. Sci. Instrum.* **91**, 9 (2020), arXiv:2003.03434 [physics.ins-det].
- [26] S. Koley, M. Bader, J. van den Brand, X. Campman, H. J. Bulten, F. Linde, and B. Vink, *Classical and Quantum Gravity* **39**, 025008 (2022).
- [27] M. Bader, S. Koley, J. van den Brand, X. Campman, H. J. Bulten, F. Linde, and B. Vink, *Classical and Quantum Gravity* **39**, 025009 (2022).
- [28] D. Reitze, R. X. Adhikari, S. Ballmer, B. Barish, L. Barsotti, G. Billingsley, D. A. Brown, Y. Chen, D. Coyne, R. Eisenstein, M. Evans, P. Fritschel, E. D. Hall, A. Lazarini, G. Lovelace, J. Read, B. S. Sathyaprakash, D. Shoemaker, J. Smith, C. Torrie, S. Vitale, R. Weiss, C. Wipf, and M. Zucker, *Bulletin of the AAS* **51** (2019), <https://baas.aas.org/pub/2020n7i035>.
- [29] V. Mandic, V. C. Tsai, G. L. Pavlis, T. Prestegard, D. C. Bowden, P. Meyers, and R. Caton, *Seismological Research Letters* **89**, 2420 (2018).
- [30] TUBS, Wikimedia Commons, “File:USA edcp (+hi +ak) relief location map.png,” https://commons.wikimedia.org/wiki/File:Usa_edcp_%28%2BHI_%2BAK%29_relief_location_map.png (2013).
- [31] TUBS, Wikimedia Commons, “File:blank in ”europe” (relief) (-mini map).svg,” https://commons.wikimedia.org/wiki/File:BLANK_in_Europe_%28relief%29_%28-mini_map%29.svg (2011).
- [32] K. Janssens, G. Boileau, N. Christensen, F. Badaracco, and N. van Remortel, *Phys. Rev. D* **106**, 042008 (2022).
- [33] M. Coughlin, J. Harms, N. Christensen, V. Dergachev, R. DeSalvo, S. Kandhasamy, and V. Mandic, *Classical and Quantum Gravity* **31**, 215003 (2014).
- [34] M. Coughlin, J. Harms, D. C. Bowden, P. Meyers, V. C. Tsai, V. Mandic, G. Pavlis, and T. Prestegard, *Journal of Geophysical Research: Solid Earth* **124**, 2941–2956 (2019).
- [35] J. Harms, *Living Reviews in Relativity* **22** (2019), 10.1007/s41114-019-0022-2.
- [36] P. R. Saulson, *Phys. Rev. D* **30**, 732 (1984).
- [37] S. A. Hughes and K. S. Thorne, *Phys. Rev. D* **58**, 122002 (1998).
- [38] M. Branchesi *et al.*, (2023), arXiv:2303.15923 [gr-qc].
- [39] B. Canuel, A. Bertoldi, L. Amand, E. Pozzo di Borgo, T. Chantrait, C. Danquigny, M. Dovale Álvarez, B. Fang, A. Freise, R. Geiger, J. Gillot, S. Henry, J. Hinderer, D. Holleville, J. Junca, G. Lefèvre, M. Merzougui, N. Mielec, T. Monfret, S. Pelisson, M. Prevedelli, S. Reynaud, I. Riou, Y. Rogister, S. Rosat, E. Cormier, A. Landragin, W. Chaibi, S. Gaffet, and P. Bouyer, *Scientific Reports* **8** (2018), 10.1038/s41598-018-32165-z.
- [40] B. Canuel *et al.*, *Class. Quant. Grav.* **37**, 225017 (2020), arXiv:1911.03701 [physics.atom-ph].
- [41] W. Chaibi, R. Geiger, B. Canuel, A. Bertoldi, A. Landragin, and P. Bouyer, *Phys. Rev. D* **93**, 021101 (2016).
- [42] J. Junca, A. Bertoldi, D. Sabulsky, G. Lefèvre, X. Zou, J.-B. Decitre, R. Geiger, A. Landragin, S. Gaffet, P. Bouyer, and B. Canuel, *Physical Review D* **99** (2019), 10.1103/physrevd.99.104026.
- [43] J. C. Driggers, J. Harms, and R. X. Adhikari, *Phys. Rev. D* **86**, 102001 (2012).
- [44] J. Harms and H. J. Paik, *Phys. Rev. D* **92**, 022001 (2015).
- [45] M. Coughlin, N. Mukund, J. Harms, J. Driggers, R. Adhikari, and S. Mitra, *Classical and Quantum Gravity* **33**, 244001 (2016).
- [46] M. W. Coughlin, J. Harms, J. Driggers, D. J. McManus, N. Mukund, M. P. Ross, B. J. J. Slagmolen, and K. Venkateswara, *Phys. Rev. Lett.* **121**, 221104 (2018).
- [47] M. C. Tringali, T. Bulik, J. Harms, I. Fiori, F. Paoletti, N. Singh, B. Idzkowski, A. Kutynia, K. Nikliborc, M. Suchiński, A. Bertolini, and S. Koley, *Classical and Quantum Gravity* **37**, 025005 (2019).
- [48] F. Badaracco, J. Harms, A. Bertolini, T. Bulik, I. Fiori, B. Idzkowski, A. Kutynia, K. Nikliborc, F. Paoletti, A. Paoli, L. Rei, and M. Suchinski, *Classical and Quantum Gravity* **37**, 195016 (2020).
- [49] F. Badaracco and J. Harms, *Classical and Quantum Gravity* **36**, 145006 (2019).
- [50] T. Andric and J. Harms, *Journal of Geophysical Research: Solid Earth* **125**, e2020JB020401 (2020), e2020JB020401 10.1029/2020JB020401.
- [51] V. van Beveren, M. Bader, J. van den Brand, H. J. Bulten, X. Campman, S. Koley, and F. Linde, *Classical and Quantum Gravity* **40**, 205008 (2023).
- [52] J. Peterson, Open-file report **93-322** (1993).
- [53] E. Stutzmann, M. Schimmel, G. Patau, and A. Maggi, *Geochemistry, Geophysics, Geosystems* **10** (2009), <https://doi.org/10.1029/2009GC002619>, <https://agupubs.onlinelibrary.wiley.com/doi/pdf/10.1029/2009GC002619>.
- [54] J. Misek, J. Jakus, K. Hamza Sladicekova, L. Zastko, M. Veternik, V. Jakusova, and I. Belyaev, *Frontiers in Physics* **11** (2023), 10.3389/fphy.2023.1094921.
- [55] R. Weaver, *Journal of the Acoustical Society of America* **71**, 1608 (1982).
- [56] F. Badaracco, J. Harms, and L. Rei, *Classical and Quantum Gravity* **41**, 025013 (2024).
- [57] N. Christensen, *Phys. Rev. D* **46**, 5250 (1992).
- [58] B. Allen and J. D. Romano, *Phys. Rev. D* **59**, 102001 (1999).
- [59] J. D. Romano and N. J. Cornish, *Living Rev. Relativ.* **20**, 2 (2017).
- [60] P. A. R. Ade *et al.* (Planck), *Astron. Astrophys.* **594**, A13 (2016), arXiv:1502.01589 [astro-ph.CO].
- [61] J. D. Romano and N. J. Cornish, *Living Rev. Rel.* **20**, 2 (2017), arXiv:1608.06889 [gr-qc].
- [62] E. Thrane and J. D. Romano, *Phys. Rev. D* **88**, 124032 (2013), arXiv:1310.5300 [astro-ph.IM].
- [63] LIGO Scientific Collaboration, Virgo Collaboration and KAGRA Collaboration, “Data for upper limits on the isotropic gravitational-wave background from advanced LIGO’s and advanced Virgo’s third observing run,” .
- [64] R. Abbott *et al.* (KAGRA, Virgo, LIGO Scientific), *Phys. Rev. D* **104**, 022004 (2021), arXiv:2101.12130 [gr-qc].
- [65] M. Maggiore, *Gravitational waves - Volume 1: Theory and experiments* (Oxford university press, 2008).

- [66] B. P. Abbott, R. Abbott, T. D. Abbott, *et al.* (LIGO Scientific Collaboration and Virgo Collaboration), *Phys. Rev. Lett.* **116**, 131102 (2016).
- [67] T. Regimbau, *Research in Astronomy and Astrophysics* **11**, 369 (2011).
- [68] V. Ferrari, S. Matarrese, and R. Schneider, *Monthly Notices of the Royal Astronomical Society* **303**, 247 (1999), <https://academic.oup.com/mnras/article-pdf/303/2/247/18630520/303-2-247.pdf>.
- [69] R. Abbott *et al.* (LIGO Scientific, Virgo, KAGRA collaborations), *Phys. Rev. Lett.* **126**, 241102 (2021), [arXiv:2101.12248 \[gr-qc\]](https://arxiv.org/abs/2101.12248).
- [70] ET Steering Committee Editorial Team, (2020), ET-0007B-20.
- [71] D. Davis, J. S. Areeda, *et al.*, *Classical and Quantum Gravity* **38**, 135014 (2021).

APPENDIX: AUGUST RESULTS

In this Appendix we provide the results for the different sites during the month of August. We will however not further discuss these as they are very similar from the January results presented in the main text. The main difference is the lower amplitude of the seismic correlations by about an order magnitude around the micro-seism peaks.

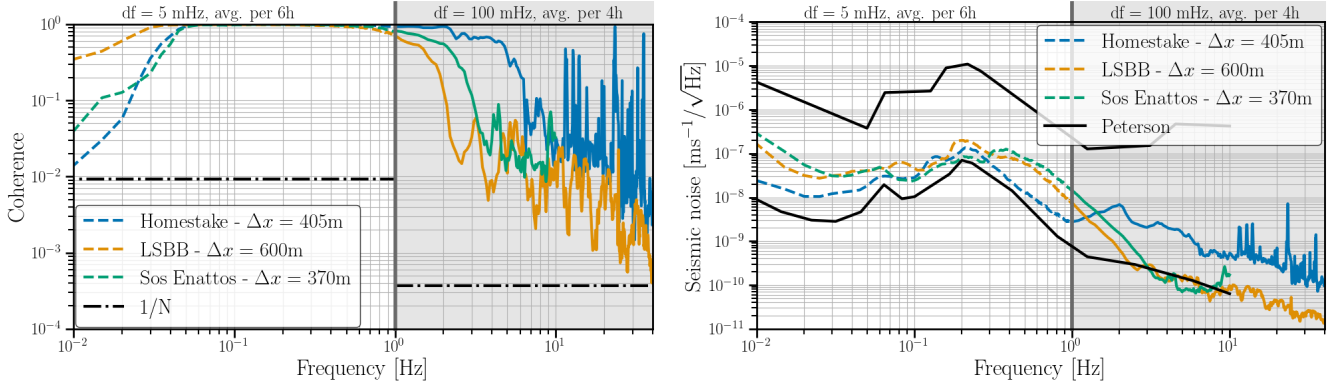


FIG. 15: The median coherence (left panel) and CSD (right panel) of the underground seismometers for the different geographical locations studied in this paper for the month of August. For more details on the sensor’s specifications, see Tab. I. Note: the data is not from the same year. The data $<1\text{Hz}$ (dashed curves) are analysed using 200 second long segments which are averaged per 6 h-window. Above 1Hz the data (full curves) are analysed using 10 second long segments which are averaged per 4 h-window. The black dot-dashed line represents the level of coherence expected from Gaussian data. The Peterson low and high noise models are shown in black (right panel).

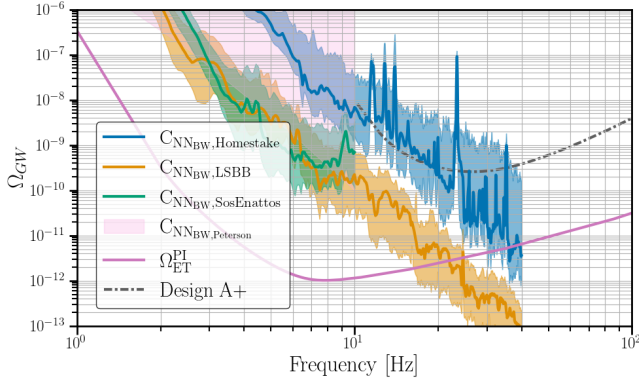


FIG. 16: The projected impact from correlated NN from body-waves, as calculated in this section, for the seismic data from the month of January for the different locations, see the text for details on the used sensors, their distances and depths. As a comparison we make the same projection using the Peterson low noise and high noise models. For the broadband ($\Omega_{\text{ET}}^{\text{PI}}$) sensitivity to a GWB we assumed one year of observation time (100% duty cycle). The one year PI curve of the A+ design for the LIGO Hanford LIGO Livingston and Virgo detectors is represented by the dot-dashed curve. This curve was obtained using the open data provided by the LVK collaborations [63] and was first presented in [64]. Please note: in this paper we present the 1σ PI-curve, whereas in [64] the 2σ PI-curve is shown.

Deep Learning-based Kinetic Analysis in Paper-based Analytical Cartridges Integrated with Field-effect Transistors

Hyun-June Jang^{1,2‡}, Hyou-Arm Joung^{3‡}, Artem Goncharov³, Anastasia Gant Kanegusuku⁴, Clarence W. Chan⁵, Kiang-Teck Jerry Yeo^{5,6}, Wen Zhuang^{1,2}, Aydogan Ozcan^{3,7,8,9*}, Junhong Chen^{1,2*}

¹Pritzker School of Molecular Engineering, University of Chicago, Chicago, IL 60637, USA

²Chemical Sciences and Engineering Division, Physical Sciences and Engineering Directorate, Argonne National Laboratory, Lemont, IL 60439, USA

³Department of Electrical and Computer Engineering, University of California, Los Angeles, CA 90095, USA

⁴Department of Pathology and Laboratory Medicine, Loyola University Medical Center, Maywood, IL 60153

⁵Department of Pathology, The University of Chicago, Chicago, IL 60637, USA

⁶Pritzker School of Medicine, The University of Chicago, Chicago, IL 60637, USA

⁷Department of Bioengineering, University of California, Los Angeles, CA 90095, USA

⁸California NanoSystems Institute (CNSI), University of California, Los Angeles, CA 90095, USA

⁹Department of Surgery, David Geffen School of Medicine, University of California, Los Angeles, CA 90095, USA

‡These authors contributed equally to this work

*Correspondence: ozcan@ucla.edu, junhongchen@uchicago.edu

Keywords: FET Biosensors, Paper Cartridge, Dry Chemistry, Deep Learning, Cholesterol

Summary

This study explores the fusion of a field-effect transistor (FET), a paper-based analytical cartridge, and the computational power of deep learning (DL) for quantitative biosensing via kinetic analyses. The FET sensors address the low sensitivity challenge observed in paper analytical devices, enabling electrical measurements with kinetic data. The paper-based cartridge eliminates the need for surface chemistry required in FET sensors, ensuring economical operation (cost < \$0.15/test). The DL analysis mitigates chronic challenges of FET biosensors such as sample matrix interference, by leveraging kinetic data from target-specific bioreactions. In our proof-of-concept demonstration, our DL-based analyses showcased a coefficient of variation of < 6.46% and a decent concentration measurement correlation with an r^2 value of > 0.976 for cholesterol testing when blindly compared to results obtained from a CLIA-certified clinical laboratory. These integrated technologies can create a new generation of FET-based biosensors, potentially transforming point-of-care diagnostics and at-home testing through enhanced accessibility, ease-of-use, and accuracy.

INTRODUCTION

The landscape of scientific research and technological innovation has witnessed an extraordinary convergence of diverse disciplines, fostering profound advancements across an extensive spectrum of domains. In this dynamic milieu, the emergence of machine learning methodologies heralds a transformative epoch that fundamentally reshapes the contours of medical diagnostics. What is particularly remarkable is the far-reaching impact of this paradigm shift, transcending customary boundaries of laboratory environments to encompass at-home testing, point-of-care (POC) diagnostics, and a broad array of real-world applications. Advanced machine learning methods such as neural networks have been recently emerging in clinical diagnostics with applications in histology, biosensing technologies, and serodiagnosis of cardiovascular diseases, among others.¹⁻⁴ Neural networks can learn from highly multiplexed and non-linear responses of POC sensors and accurately quantify analyte concentrations despite cartridge-to-cartridge variations and the noise present in biological samples (e.g., matrix effect).^{5,6}

Traditional biomedical disciplines have extensively relied on the foundational principles of optical detection techniques and bioimaging, capturing the light signals associated with targeted biomarkers.⁷⁻⁹ Real-time bio-signal measurements and bioimaging technologies offer distinct advantages, including internal quality control through data-driven image analysis¹, improved precision and accuracy^{2, 4-5}, and expedited detection capabilities.⁹ Despite their elegance, optical methodologies are partially encumbered by inherent limitations, particularly in the context of POC and at-home testing scenarios. Some of these limitations include high reagent costs and the need for trained experts/users, instigating an exploration of innovative alternatives in diagnostic platforms.¹⁰

Field-effect transistors (FETs), originally designed for electronic circuitry, have undergone a remarkable evolution, transforming from conventional electronic components into highly sensitive transducers capable of real-time and label-free detection of a diverse array of analytes with unparalleled sensitivity.¹¹ Despite decades of research, FET-based biosensors remain in the proof-of-concept stage, lacking successful market products.^{12,13} The realization of their commercial potential, however, has been hindered by a myriad of challenges: batch variation (i.e., reproducibility)¹⁴, sample matrix effects¹⁰, and packing requirements associated with wet environments on the sensing surface¹⁵, as well as susceptibility to risks such as leakage and contamination of

the sensing zone¹⁶. Recently, a set of FET-based sensor designs has exhibited promising results in overcoming matrix effects and batch variations in sensing metal ions^{14,17,18} by leveraging machine learning. However, these approaches have not been extended to sensing within complex testing environments, such as human blood or plasma, which includes divergent patient-specific proteins, cellular compositions, and ion variations.

While the conventional real-time FET detection captures a snapshot of a bioreaction via monitoring continuous changes in drain current (I_D) at a fixed gate voltage (V_G) application or threshold voltage (V_{th}), its advantages in terms of accuracy and precision have not been thoroughly elucidated as the gate-dependence of the kinetic data is not captured. Additionally, these FET biosensors mandate the incorporation of additional reagent control mechanisms to address issues related to the Debye length^{19,20} for physiological media (e.g., capture-release method²¹ associated with reactions, washing, and measurements under controlled buffers), often facilitated through microfluidic systems for better usability. However, the fabrication of such microfluidic channels frequently encounters challenges, including time-consuming and labor-intensive manufacturing processes, diminished yield and the intricate nature of configuring microfluidic setups involving pumps and valves.²²⁻²⁴ These constraints can complicate operations, contradicting the convenient and straightforward use of POC diagnostic tools, such as lateral-flow assays (LFAs).²⁴⁻²⁵

In this manuscript, we embark on an exploration of the synergism between FET biosensors, paper-based analytical devices, and the computational power of deep learning (DL). We first demonstrate the integration of a porous sensing membrane (PSM), a key component of LFAs, with FET sensors. The platform features a one-step operation for sample injection, a disposable cartridge for introducing plasma samples (cost < \$0.15 per test), and reusable FET sensors. The PSM incorporates dried sensing components that produce electroactive enzymatic signals, such as protons specific to the target biomarkers in plasma. The FET sensor characterizes all-encompassing, target-specific kinetic data occurring within the cartridge through FET transfer curves. Finally, the DL-based analysis of the obtained kinetic data effectively addresses issues related to sample matrix effects and varying rates of chemical reactions from test-to-test, and accurately quantifies the target analyte concentration from the captured data. We showcased a proof-of-concept operation of this platform for cholesterol testing with patient plasma. Cholesterol concentrations blindly predicted by DL exhibited a correlation

(r^2) of > 0.976, with a coefficient of variation (CV) of < 6.42%, when blindly compared against results obtained from a CLIA-certified clinical laboratory for the same samples.

RESULTS

Operating Principle. Our innovative diagnostic platform employs a new dry chemistry approach for FET biosensors. The paper analytical cartridge, housing the desiccated sensing components in the PSM, is electrically connected to the FET (Figure 1a). This synergetic integration offers several advantages: 1) imposing higher sensitivity to paper analytical devices empowered by electrical measurements, 2) enabling the measurement of kinetic data, 3) eliminating the complexities associated with laborious wet chemistry procedures for functionalizing biomolecules on the FET sensing surface, 4) removing the need for traditional microfluidic systems to regulate reagents, 5) facilitating cost-effective testing (~\$0.15 per cartridge, Table S1), 6) mitigating sample matrix effects, 7) achieving easy miniaturization, and 8) ensuring a prolonged shelf-life (the shelf-life of LFAs is up to 2 years²⁵).

As a proof-of-concept demonstration for our diagnostic approach, we selected cholesterol, a standard biomarker in annual blood testing at clinics. The PSM was desiccated with enzymes such as cholesterol esterase (COE), cholesterol oxidase (COx), and peroxidase (POx), along with surfactants, stabilizers, and buffers, eliminating the need for additional functionalization steps (Figure 1b). An ion-sensitive sensing electrode (SE), such as indium-tin-oxide (ITO), was positioned beneath the PSM within the cartridge, with ~50 μm of physical spacing. Injecting 20 μL of plasma into the cartridge's inlet established a connection between the ITO and the FET gate (Figure 1a). Once the plasma contacted the PSM, surfactants broke down lipoproteins, and a series of enzymatic reactions produced protons released into the physical spaces between the PSM and ITO. The real-time release of protons resulting from a series of enzymatic reactions specific to the cholesterol concentration in the plasma was continuously recorded in FET transfer curves repeatedly measured over 5 minutes (Figure 1c). These transfer curves were transformed into a 2D heatmap, encapsulating all enzymatic kinetic details characterized in the sum of transfer curves. The DL analysis further optimized the subset of kinetic signals carrying concentration-specific data to quantify cholesterol concentrations in patient plasma samples (Figure 1c).

Proton Specificity. Proton was the target signal of interest in response to cholesterol. The intrinsic ITO exhibited a Nernstian response of 52.8 mV/pH with an r^2 of 0.997 and CV < 1.3% (Figure S1a) without any changes in the transconductance (G_m) value over all pH ranges (Figure S1b). Due to the significantly higher input impedance of the FET compared with that of an ITO remote gate module²⁶⁻²⁸, there were no changes in V_{th} with increasing contact areas as a result of increasing media volume size (from 20 to 100 μ L) on the ITO surface (Figure S1c). An insignificant drift of 8 μ V/min, measured over 30 minutes (Figure S1d), suggested that the ITO sensing electrode was highly stable for translating enzymatic reactions specifically.

FET Data. Upon injecting human plasma into the cartridge, distinct real-time signal patterns were observed in response to varying cholesterol levels, as indicated by changes in the V_{th} (ΔV_{th}) relative to the V_{th} of lipoprotein-free cholesterol plasma (Figure 2a). The protons generated by each electroactive enzymatic reaction decreased V_{th} levels of n-type FETs due to the positive surface potentials applied on the ITO from protons. The initial V_{th} of the cartridges was largely influenced by the pH and ion concentration of human plasma, as well as batch variations in cartridges, along with diverse proteins and components in plasma that could cause non-specific binding on the ITO surface. Despite injections of different plasma samples, the initial V_{th} values tended to overlap (Figure 2a). This could be attributed to our cartridge design, which incorporated a \sim 50 μ m air gap between the PSM and the ITO electrode (inset of Figure 2a). The presence of this air gap played a pivotal role in facilitating the mixing process between the PSM and plasma samples. It ensured that the mixing process occurred before the original plasma came into direct contact with the ITO electrode (inset of Figure 2a). As a result, any sample matrix effects were significantly diluted by the potent buffer components that were already desiccated within the PSM. Consequently, the PSM efficiently transmitted purified electroenzymatic signals to the ITO surface.

Figure 2b further supports the fluidic dynamics in the cartridge described above by demonstrating the controlled initial V_{th} of each cartridge after the injection of different random human plasma samples using various buffer solutions, such as phosphate-buffered saline (PBS), piperazine-N,N'-bis(2-ethanesulfonic acid) (PIPES), and PIPES/PBS (5:5 ratio), dried onto identical PSMs, with the remaining PSM components being consistent. Small variations in the initial V_{th} levels are shown for each group of cartridges dried with PBS, PIPES/PBS, and PIPES (CV < 10%). Even lipoprotein-free plasma samples with a pH of 5 tend to be controlled by the buffer

solution in the PSM of the cartridge (Figure 2b). For subsequent experiments, we selected PBS (pH 7.4) as the buffer component for the PSM to minimize the pH disparity between plasma (pH 7.35 to 7.45) and the dried buffers.

We further optimized the concentrations of COE, COx, and POx for the PSM by evaluating correlations between the enzyme concentrations and the cholesterol signals (Figure S2). Concentrations of enzymes exceeding 200 U/mL displayed saturated correlations, leading us to choose 300 U/mL enzyme concentrations for COE, COx, and POx in all subsequent experiments. However, without the POx enzyme, no correlative sensing signals were obtained, implying that POx played a critical role in producing electroactive enzymatic signals such as protons (Figure S3). It is noted that the enzyme solutions lacked long-term shelf life without drying them on the PSM, as shown by a large drift in the initial V_{th} levels of the enzyme solution over time (Figure S4).

We further discovered that the use of bovine serum albumin (BSA) coating on the ITO electrode significantly mitigated sample matrix effects without compromising the detection signals (Figure 2c). In contrast, bare ITO electrodes without BSA coating exhibited larger shifts in electroenzymatic signals, even for free cholesterol plasma samples. This might be due to the remaining proteins and ions in lipoprotein-free plasma causing non-specific signals by interacting with the bare ITO surface.

The LOD achieved by our detection platform was assessed in Figure 2d using diluted clinical plasma with lipoprotein-free plasma, ensuring controlled conditions. The estimated LOD for cholesterol is determined to be 28.5 $\mu\text{g/dL}$ (737 nM). This LOD range is exclusively demonstrated by conventional electrochemical detection methods employing sophisticated and complex device fabrications, including the utilization of nanomaterials and mediators.²⁹ The highly sensitive attribute of FET sensors extends this remarkable LOD range to paper-based analytical devices, highlighting the efficacy of the platform even without the need for functionalization.

Lastly, in Figure 2e, we present the distribution of ΔV_{th} values for cholesterol concentrations measured from patient plasma samples across 178 cartridges produced during 15 different sub-batch fabrications. Notably, when enzymes were absent from the PSM, no correlated detection signals were observed, leaving sample matrix effects the only reason for minor variations in ΔV_{th} (Figure S5). While there was a degree of correlation between

cholesterol levels and ΔV_{th} values, relying solely on ΔV_{th} (which is conventionally used in FET sensor analysis to determine target-signals) as the sensor readout presented major challenges. When applied to our dataset, this standard approach displayed a low r^2 of 0.808 (Figure 2e) and a large CV of up to 22.8% within a clinically relevant range (i.e., 100-150 mg/dL, Figure 2f), confirming the challenges of FET biosensor performance on physiological samples, despite optimizations of the diverse fabrication factors listed above.

The conventional FET analysis, focusing solely on ΔV_{th} (Figure 2e) by considering the endpoint and initial point, falls short of providing a comprehensive understanding of variations during enzyme reactions influenced by the time-dependent enzyme reaction rate (Figure 3a) and sample matrix effects. Moreover, the real-time FET measurement (Figure 2a), capturing a cumulative representation of specific snapshots at particular moments over time, also offers limited information about enzyme reactions. For instance, the G_m values, which cannot be obtained from real-time measurement approach in Figure 2a, exhibit significant variations during reactions (Figure 3b). These variations are influenced by factors such as the rate of enzyme reactions, the mixing process within the cartridge, and the presence of sample matrix effects. Interpreting these dynamic behaviors for each specific case can be challenging, underscoring the need for more advanced data-driven analytical techniques, such as DL, to comprehensively capture and interpret the dynamic nature of these biochemical processes, as detailed in the subsequent sections.

Design of DL-based Signal Analysis. DL benefits from the universal function approximation power of neural networks to harness the complex non-linear kinetic data from the FET sensor to measure the analyte concentrations. Here, we employed DL-based analysis and neural networks for two key objectives: 1) optimizing the subset of kinetic signals carrying concentration-specific information, and 2) quantifying the target analyte concentrations in patient plasma samples. The DL models were structured as fully-connected shallow networks with three hidden layers, utilizing continuously measured FET transfer curves as input data. Both the kinetic data input and the network architecture underwent optimization through a 4-fold cross-validation on the validation set of plasma samples (refer to the Data Processing and Deep Learning Analysis section for detailed procedures). The optimized network was subsequently tested on 30 additional samples from the testing set, never used before.

For DL analysis, transfer curves measured over 5 minutes for each plasma sample were transformed into a 2D heatmap (Figure S6). This heatmap for each test visually represented all enzymatic kinetic details, encompassing characteristics observed in the sum of raw transfer curves (Figure S6a), such as potential drifts during the measurement, initial V_{th} , and changes in V_{th} , electronic mobility, and G_m due to enzyme reactions (Figure S6b). Notably, our preliminary observations underscored the significance of subtracting the initial transfer curve data from the raw heatmap in Figure S6b. The initial transfer curves typically serve as a baseline for conventional FET analysis to measure the relative change in target-specific signals, which could be significantly affected by pH, ion concentrations, and sample matrix effects. Thus, the raw heatmap (Figure S6b), after subtracting the initial transfer curve properties and referred to as the signal heatmap (Figure 3c), encapsulated pure kinetic information primarily associated with enzymatic reactions, and remained, by and large, unaffected by interference from varying pH levels in plasma samples. Using this signal heatmap as input resulted in a substantial improvement in the neural network inference, reducing the CV from 20.1% to 8.5% and increasing the r^2 from 0.698 to 0.904 (see Figure 3d).

DL was further applied to optimize the subset of kinetic signals containing concentration-specific information within the signal heatmap. This optimization considered both the size of the V_G window (i.e., within the 0-3 V range, Figure 4a-c) and the time window (i.e., within the 14-343 s range, Figure 4d-f). The selection of the optimal model was based on achieving the lowest mean square error (MSE) and the highest r^2 values when comparing predicted and ground truth cholesterol concentrations for samples from the validation dataset, with variations in the sizes of V_G windows. Consequently, the optimal V_G window was identified to be between 1.15 V and 2.45 V (Figure 4b). The predicted concentrations within this optimal V_G subset still exhibited a high CV of 20.7% and a relatively low r^2 of 0.907. With a fixed V_G window, an optimal time subset was determined to be within the range of 91-119 s (Figure 4e). The network utilizing the optimized subset in Figure 4e demonstrated improved quantification performance on the same validation set in Figure 4c, achieving an r^2 of 0.954 and a CV of 11.4% (Figure 4f). This final optimized network was further utilized to generate blind testing results using plasma samples never seen before, which will be detailed in the next section.

Blinded Testing Results. The optimized neural network model, incorporating the optimal architecture and refined kinetic data input (refer to the Data Processing and Deep Learning Analysis section of the Methods

for detailed model architecture), underwent blind testing to quantify cholesterol concentrations across 30 clinical plasma samples from three distinct testing batches (Figure 4g). For each of the three testing batches, we trained optimized models separately using samples from the same batch to minimize inter-batch variability. The blind testing predictions exhibited a high correlation with the ground truth cholesterol values, with an r^2 value exceeding 0.976 for all three batches (Figure 4h). Additionally, the neural network models' inference results demonstrated low variations in predictions, with a maximum CV of 6.46% over different cholesterol concentration ranges (Figure 4i). Importantly, blind testing predictions from the models using the optimal subset in the signal heatmap (Figure 4g) outperformed other models, including the model that used the entire raw heatmap (Figure S7a), the model with a 2x larger window size than the optimal subset in the signal heatmap (Figure S7b), and the model using the optimal subset in the raw heatmap (Figure S7c). Therefore, this optimized concentration inference method not only better utilized the enzymatic reaction kinetics of our FET-based sensor but also improved the robustness of the network predictions, making them more resistant to variations induced by sample matrix effects.

For the same blind testing set, a single model trained on samples from all three batches (Figure S8) had inferior accuracy (r^2 : 0.886 excluding outliers) and precision (CV of 10.85 %). Higher variations of this single neural network model between different batches originate from additional variabilities in PSM and reagent batches used during different testing days. In future iterations of assay development, incorporating batch-specific information along with the sensor data can be used to create a more robust inference model that generalizes to different batches with the same superior performance.

Scalability to Immunoassay. Our detection platform has the potential to be adapted for immunoassays, which holds significant promise in a wide range of biomedical applications. To illustrate this adaptability, we conducted a proof-of-concept experiment involving electroactive enzymatic signaling on our platform (Figure S9). In this experiment, we utilized the interaction between horseradish peroxidase (HRP)-labeled anti-mouse IgG (Ab-HRP), hydrogen peroxide (H_2O_2), and 3,3',5,5'-tetramethylbenzidine (TMB) — a combination that has long been established and widely used in conventional enzyme-linked immunosorbent assays (ELISA) for detecting biomarkers in sandwich immunoassays using the resultant colored product of TMB.³⁰ TMB and HRP reactions also produce protons³¹, which serve as a target signal in our detection platform. This phenomenon is depicted in Figure S9, where increased concentrations of Ab-HRP decrease V_{th} levels of the FET upon the injection of

H₂O₂ (Figure S9a) or TMB (Figure S9b). TMB and HRP signaling can be integrated into the LFA framework, complemented by zones dedicated to capture antibody, detection antibody, and chemical substrate. This design could be particularly beneficial for immunoassays that require high sensitivity, such as troponin I and metabolite assays, as well as for the rapid detection of infectious diseases.

DISCUSSION

Our integration of an LFA component, specifically the PSM, with a FET yields synergistic benefits and multiple advantages, effectively overcoming limitations inherent in each of the two components when used individually as diagnostic platforms. The FET sensing mechanism can potentially be used to enhance the sensitivity of paper-based analytical devices and enable the measurement of kinetic data within the PSM. On the flip side, the intricate surface chemistry required for FET sensors to immobilize biomolecules like enzymes and antibodies is replaced by the straightforward dry chemistry of the LFA technology. Furthermore, building upon the utilization of an electroactive enzymatic signal, such as protons, as opposed to label-free FET detection, our approach eliminates the requirement for conventional microfluidic systems to regulate reagent supply to FET sensors, effectively addressing Debye length issues. This strategic choice enables a simplified operation down to a single sample injection step, eradicating the need for a complex microfluidic system. This integration goes a step further in mitigating critical commercialization risks associated with FET sensors, including shelf-life, production costs, and contamination of the FET sensing surface, all of which have hindered the widespread adoption of FET biosensors in the market.

Despite effectively addressing the aforementioned risks, some challenges still persist, particularly in terms of reliability, impaired by sample matrix effects and batch-to-batch variations. The enhanced sensitivity of FET sensors, advantageous for detecting target signals, introduces susceptibility to interference from non-specific binding or unintended interactions, which can complicate the interpretation of results and impact the accuracy of the sensor. Various strategies, such as surface modifications, advanced coatings, or the use of blocking agents, have been explored to enhance the specificity of FET sensors. However, the translation of their performance from laboratory-scale studies to practical applications remains a challenge.

Our DL-based analysis, coupled with a meticulous optimization process, proves instrumental in mitigating variation issues arising from sample matrix effects and reaction rates. This approach enhances the ability to discern and interpret complex interactions of the testing environment within the DL model, allowing for a more precise analysis of the intricate but insightful kinetic FET data. While our DL techniques showed competitive cholesterol quantification in samples within the same batch (i.e., models for each of the three batches were trained independently), the scalability of our DL-based FET sensor between different batches was limited (i.e., a single model trained on all three batches showed inferior performance, $r^2 < 0.9$) due to additional factors affecting inter-batch repeatability. These factors include the varying properties of ITO used in different testing batches, variations in enzyme and reagent concentrations due to handling issues, limited control over environmental factors such as temperature and humidity, variability between reagent batches, residual non-specific binding of proteins in plasma on the ITO, and varying enzyme activity influenced by the pH or ion concentrations of plasma samples. These factors can be addressed in future iterations through quality controls implemented in the fabrication and assembly processes. Additionally, assay and environmental factors that have a direct impact on the captured data can be added to the input of future inference models to improve the generalizability of the concentration inference model to different batches.

The potential incorporation of our platform into immunoassay technology will open up a myriad of biomedical applications, including disease diagnosis, biomarker detection, and therapeutic drug monitoring. The demonstration of electroactive enzymatic signaling between anti-HRP and TMB (Figure S9) underscores the versatility of our platform in LFA-based immunoassay techniques. Measuring electrical signals of the commonly used clinical immunoassays by our FET biosensor offers significant advantages, such as high sensitivity, enhanced accuracy through kinetic information, and data-driven analysis. Expanding on the potential benefits, the ability of FET sensors to conduct multiplexed immunoassays could be a critical advancement, enabling the simultaneous detection of multiple biomarkers within a single sample input. This capability is essential for achieving comprehensive disease profiling, providing a more nuanced understanding of an individual's health status. By facilitating the detection of a spectrum of biomarkers within a single diagnostic measurement, our platform, once fully developed, might contribute to more holistic and efficient diagnosis and monitoring of various diseases.

CONCLUSION

Our research showcased a seamless integration of FETs, paper-based analytical devices, and DL methodologies, effectively addressing persistent challenges associated with FET sensors, such as sample matrix effects and variations in reaction rates, while simplifying operational complexities. The inclusion of a PSM in the FET sensing zone streamlined the sensor operation into a single-step, cost-effective testing process. The synergistic interplay between FETs' kinetic data and DL methodologies was further demonstrated through quantitative diagnostics, notably in the proof-of-concept quantification of cholesterol concentration in patient plasma samples. For blinded cholesterol tests, this approach yielded a high precision ($CV < 6.46\%$) and a decent accuracy ($r^2 > 0.976$). The integration of immunoassays into our detection platform could potentially achieve a significant advancement in medical diagnostics, promising improved healthcare outcomes.

EXPERIMENTAL PROCEDURES

Sensing Solution Preparation. A sensing solution included enzymes, a stabilizer, and buffer solutions. 300 U/mL cholesterol esterase (Toyobo, COE-311), 300 U/mL cholesterol oxidase (Toyobo, COO-321), and 300 U/mL peroxidase (Toyobo, POX-301) were dissolved in PBS, piperazine-N,N'-bis(2-ethanesulfonic acid) (PIPES), or PBS/PIPES (45/55% ratio) buffer solution, respectively. Triton X-100 (Sigma Aldrich, SLBM3869V), tween 20 (Surf's Up surfactant Kit, K40000), and 10% BSA (Thermo Scientific, WL335677) were mixed with the enzyme solution at a 0.5% (v/v) for each.

Cartridge Fabrication. ITO (Sigma Aldrich, 639303) cleaned with isopropanol for 20 min was utilized as the SE. ITO was further incubated with 10% BSA solution for 4 hours to achieve a blocking layer on the ITO surface. The final sensing solution described earlier was fully spread over each PSM made of an asymmetric super micron polysulfone membrane (Pall, T9EXPPA0045S00M) with a 0.45 μm average pore size and a nitrocellulose membrane with a 0.22 μm average pore size (Sartorius, 11327-41BL). Each PSM was fully dried for 20 min using nitrogen gas and stored under silica gel for 2 hours. Dried PSM was sliced to a 6 mm diameter circle for the cartridge component. The ITO was taped on an acrylic sheet substrate (1 mm-thick, 1.5 cm by 1.5 cm) using double-sided tape. Another double-sided tape (50 μm thickness) was mounted on the ITO with an opening window for PSM placement. PSM and chamber were sequentially added on the top of double-sided tape. The ITO electrode was connected to the gate of MOSFET using an alligator clip for electrical measurements. All components, including ITO, acrylic sheet and double-sided tapes, were fabricated by a laser cutter (60 W Speedy 100 CO₂ laser, Trotec, USA).

Electrical Measurement System. The ITO of the cartridge was connected to the gate of a commercial n-type metal-oxide-semiconductor field-effect transistor (MOSFET) (CD4007UB) using an alligator clip. The same MOSFET was used over all measurements consistently. A 20 μL volume of plasma was injected into the inlet of the cartridge. An Ag/AgCl reference electrode contacted the plasma, applying the V_G in a range from 0 to 3 V for all measurements. All transfer curves were measured using a Keithley 4200A semiconductor analyzer with a source-drain voltage set at 50 mV, and the V_G fixed in the double-sweep mode. Transfer curves of the FET were repeatedly measured for 5 min under each plasma sample. The V_{th} was calculated as the V_G corresponding to an I_D of 1 μA in each transfer curve. Standard pH buffer solutions were used to evaluate the

pH sensitivity of the ITO in Figure S1. Each solution was removed by pipetting after each measurement. For HRP response tests in Figure S9, 10 mM H₂O₂ in PBS was mixed with IgG-HRP (Southern Biotech, 1030-05) on the bare ITO surface, sequentially, with increasing concentrations of IgG-HRP in a range from 16 ng/mL to 50 µg/mL in PBS. Also, TMB (Thermo Scientific, 34028) was added to goat IgG-HRP solution in a range from 16 ng/mL to 10 µg/mL in PBS before testing.

Clinical Sample Tests. Lithium heparin plasma from leftover patient samples collected at The University of Chicago Medical Center with cholesterol concentrations ranging from 100 to 300 mg/dL were de-identified and stored at -20 °C until use. Samples were collected under a quality assurance protocol, which qualified for an institutional review board waiver and no patient identifiers were collected. Cholesterol concentrations were quantified using the Roche CHOL2 enzymatic colorimetric assay on the c701 module of the Roche Cobas 8000 analyzer system (Indianapolis, IN, USA). After thawing, the samples were stored at 2–8°C for up to seven days. Lipoprotein-free human plasma was purchased from Kalen Biomedical, LLC as control. In order to evaluate LOD (Figure 2d), 312 mg/dL clinical plasma sample was diluted by lipoprotein-free human plasma. The CV values (Figure 2e) were obtained from at least 3 testing cartridges for the same human plasma sample.

A total of 179 plasma samples were tested within 3 testing batches, including 86 plasma samples in the first batch, 57 plasma samples in the second batch, and 36 plasma samples in the third batch. In the first testing batch, 61 plasma samples were used for training, with 17 samples for validation and 8 samples for blind testing of the deep learning model. In the second batch, 42 samples were allocated for training, with 15 samples for blind testing, and in the third batch, 29 samples were reserved for training, with 7 samples for blind testing. This split was dictated by the uniform coverage of cholesterol concentration (in 100-300 mg/dL range).

Data Processing and Deep Learning Analysis. For each sample, the transfer curves of the FET sensor were repeatedly measured over 49 cycles with 7 sec per cycle (i.e., a total of 343 s period). Before applying DL-based analysis, the first captured cycle was subtracted from all 49 cycles within the raw heatmap (Figure S6b), yielding 48 cycles within the heatmap, termed signal heatmap (Figure 3c). For DL analysis, the signal heatmap was converted into a 1D array and input into the processing neural network. The neural network architecture was optimized through a 4-fold cross-validation on the validation set, and the optimal model represented a shallow neural network with a fully-connected architecture with 3 hidden layers (128, 64 and 32 units), each

followed by batch normalization and 0.5 dropout. All three layers used ReLU activation functions and L2 regularization. The loss function (L) was MSE compiled with Adam optimizer, a learning rate of 10^{-3} , and a batch size of 5, i.e.,

$$L = \frac{1}{N} \sum_{i=1}^N (y_i - y'_i)^2,$$

where y_i are the ground truth analyte concentrations, y'_i are the predicted concentrations, and N is the batch size.

The input signals into the neural network were further optimized by selecting a subset of current values from the total operating range (i.e., 14-343 s time range and 0-3 V V_G range). The optimization was done in two steps through a 4-fold cross-validation (see Deep learning-based optimization of the kinetic data for more details) on 17 samples from the validation set (see Clinical Sample Tests section for more details). This optimized model architecture (i.e., the model with optimal input subset and architecture) was further used at the blind testing phase.

The blind testing set included 30 samples (not seen during network optimization) from three different testing batches. For each batch, the final optimized models were independently trained using samples from the same batch (see Clinical Sample Tests). Training times for batches 1 to 3 were 113 s, 143 s, and 145 s, respectively. Irrespective of the batch number, blind testing of the trained model averaged 110 ms per sample for a batch size of 1, and this time decreased to 35 ms per sample when using a batch size of 10. Data preprocessing and training/testing of neural networks were performed in Python, using OpenCV and TensorFlow libraries. Training/testing of the neural networks was done on a desktop computer with a GeForce GT 1080 Ti (NVIDIA).

Deep learning-based Optimization of the Kinetic Data. The neural network input optimization process was performed through a 4-fold cross-validation on the validation set and was conducted in two steps: first, optimizing the V_G subset within 0-3 V range (Figure 4a-c), and second, optimizing the time window within 14-343s range (Figure 4d-f). In each step, the optimal model was selected based on the MSE and r^2 values between the predicted and ground truth cholesterol concentrations for 17 samples from the validation dataset (see the Clinical Sample Tests subsection for further details on the split between training, validation, and testing sets).

At the first step, the optimal V_G operating range was determined to be between 1.15 V and 2.45 V centered at 1.8 V (Figure 4b). The predictions generated by the model with the optimal V_G window exhibited a strong correlation with the ground truth with an r^2 of 0.907, however a CV of 20.7% was still high (Figure 4c). To further enhance the performance, we determined the optimal time range for a fixed optimal V_G window by evaluating MSE and r^2 maps generated on the same validation dataset with 17 samples (Figure 4d). The optimal time range based on lower MSE and higher r^2 was selected between 91 s and 119 s centered at 105 s, reducing the overall assay operation to < 2.5 minutes (Figure 4e). The predictions of the model with optimized V_G and time subsets on the validation set showed an r^2 value of 0.954 and a CV of 11.4% with respect to ground truth measurements (Figure 4f), and the model with this input subset was further used during the blind testing stage.

Author Contributions

Electrical measurements, device fabrication, and interpretation of data were carried out by H.-J. Jang, W. Zhuang, and H. Joung. Computational analysis was carried out by A. Goncharov. The manuscript was prepared by H.-J. Jang, H. Joung., A. Goncharov, A. Ozcan, and J. H. Chen. Plasma samples were prepared and evaluated by A. Kanegusuku, C. Chan, and K.-T. J. Yeo. All authors edited the manuscript and commented on it. The project was supervised by A. Ozcan and J. H. Chen.

Declaration of interests

The authors have a pending patent application on the presented technology.

Acknowledgements

This work was financially supported by a University of Chicago Faculty Start-up fund and the US National Science Foundation (NSF) PATHS-UP Engineering Research Center (Grant #1648451).

Figure captions

Figure 1. Schematic images of (a) the diagnostic platform combining the FET detection system with an actual photo of the components of a single-use paper-based analytical cartridge. (b) Detection mechanism of cholesterol around PSM and SE within the cartridge. (c) Overview of DL signal processing framework.

Figure 2. (a) Representative real-time V_{th} curves in response to enzyme reactions based on the cholesterol concentrations in human plasma. (b) Initial V_{th} distributions of cartridges dried with different buffer components such as PBS, PIPES/PBS, PIPES. CV values of initial V_{th} were compared. (c) ΔV_{th} variation of the cartridge with bare ITO and BSA/ITO for the injection of lipoprotein-free plasma. ΔV_{th} was defined as the difference between the initial V_{th} and V_{th} for a specific time of each cartridge. (d) LOD evaluation measured by using a diluted clinical plasma sample with lipoprotein-free plasma. (e) ΔV_{th} distribution of 178 testing cartridges with plasma samples of varying cholesterol concentrations. (f) CV values of ΔV_{th} in Figure 2(e) calculated from at least 3 repeated tests for the same plasma.

Figure 3. (a) Schematic of transfer curve changes over different stages of the enzymatic reaction on the cartridge. (b) Representative G_m variation over the enzymatic reaction. (c) Transfer curve heatmaps after subtraction of the first cycle signal. (d) Comparison of cholesterol concentrations predicted by the neural network using the pure signal and raw heatmap.

Figure 4. (a) MSE and r^2 maps for the validation dataset from models with different V_G subsets; (b) Optimal V_G subset selected as a local extremum on MSE and r^2 maps. (c) Predictions on the validation dataset for the model with the optimal V_G subset; (d) MSE and r^2 maps for the validation dataset from models with different time subsets. (e) Optimal time subset within V_G subset selected as local extremum on MSE and r^2 maps. (f) Model predictions on the validation dataset for the model with optimal V_G and time subsets. (g) Final model predictions on the blind testing dataset composed of 30 clinical samples from 3 different testing batches. (h) r^2 values expanded over 3 testing batches for models with different input subsets. (i) CV values for the optimal model expanded over different cholesterol ranges for blind tests.

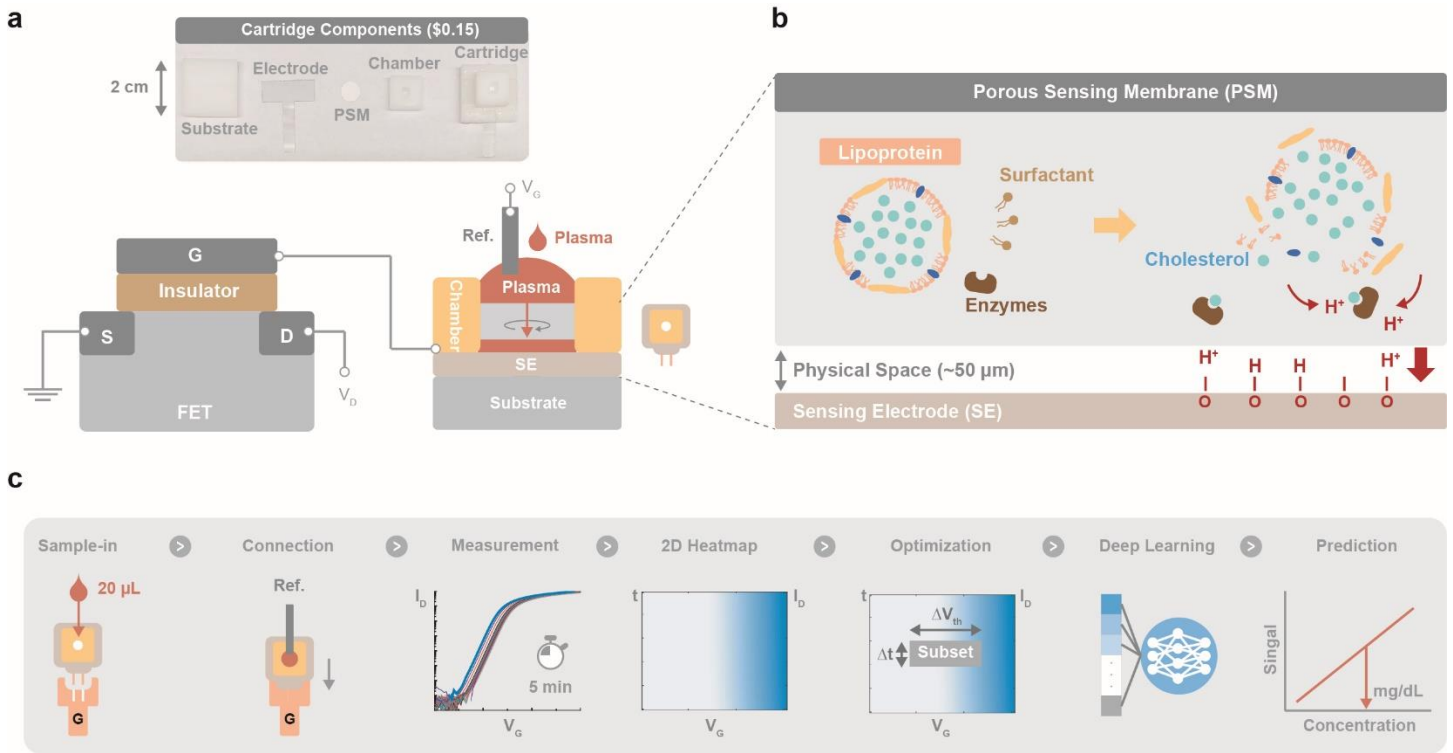


Figure 1

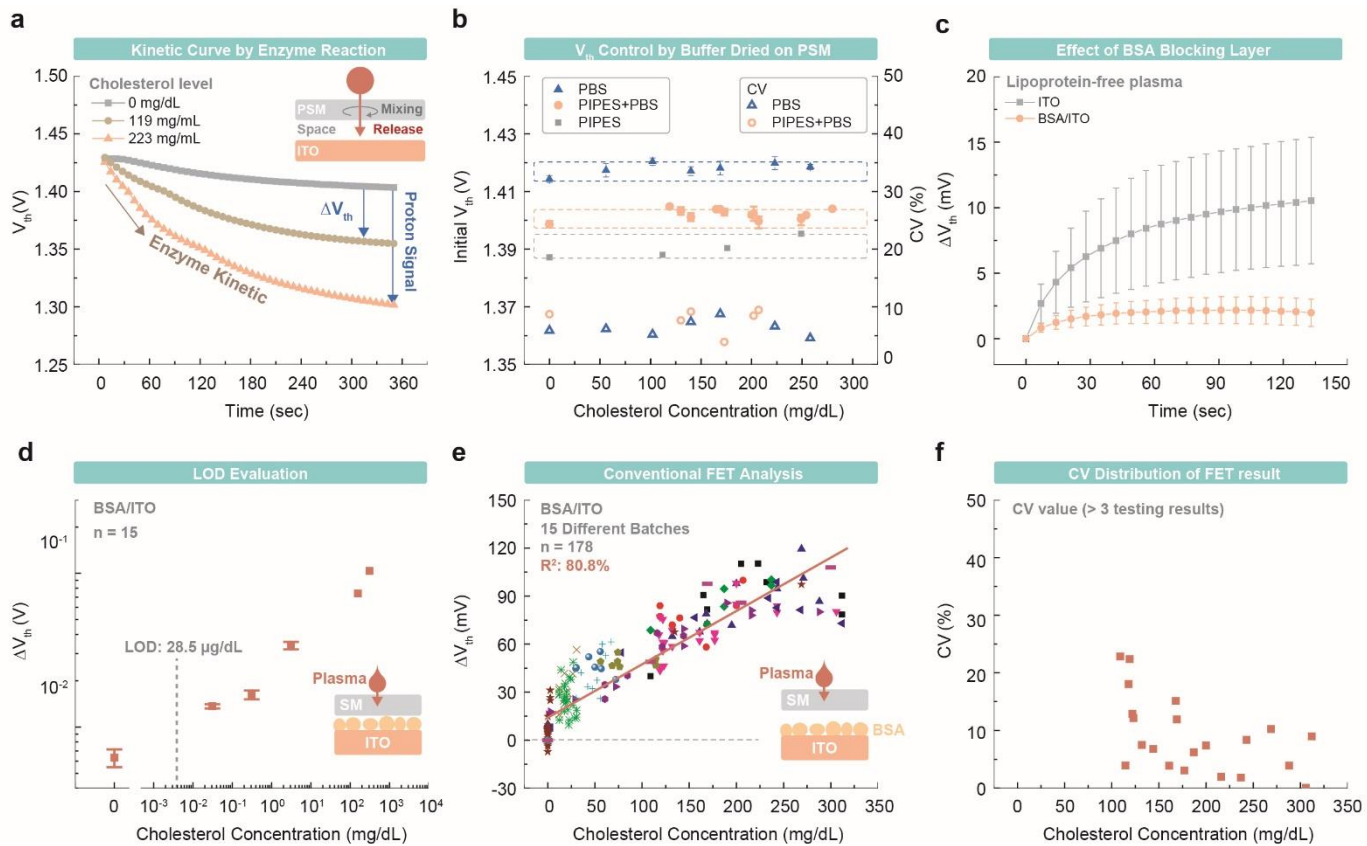


Figure 2

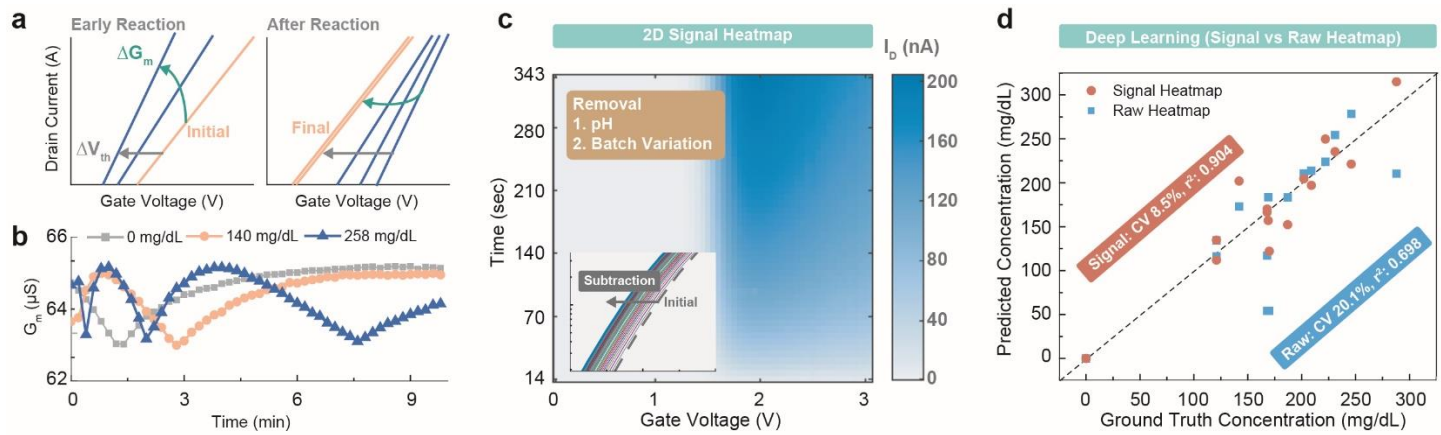


Figure 3

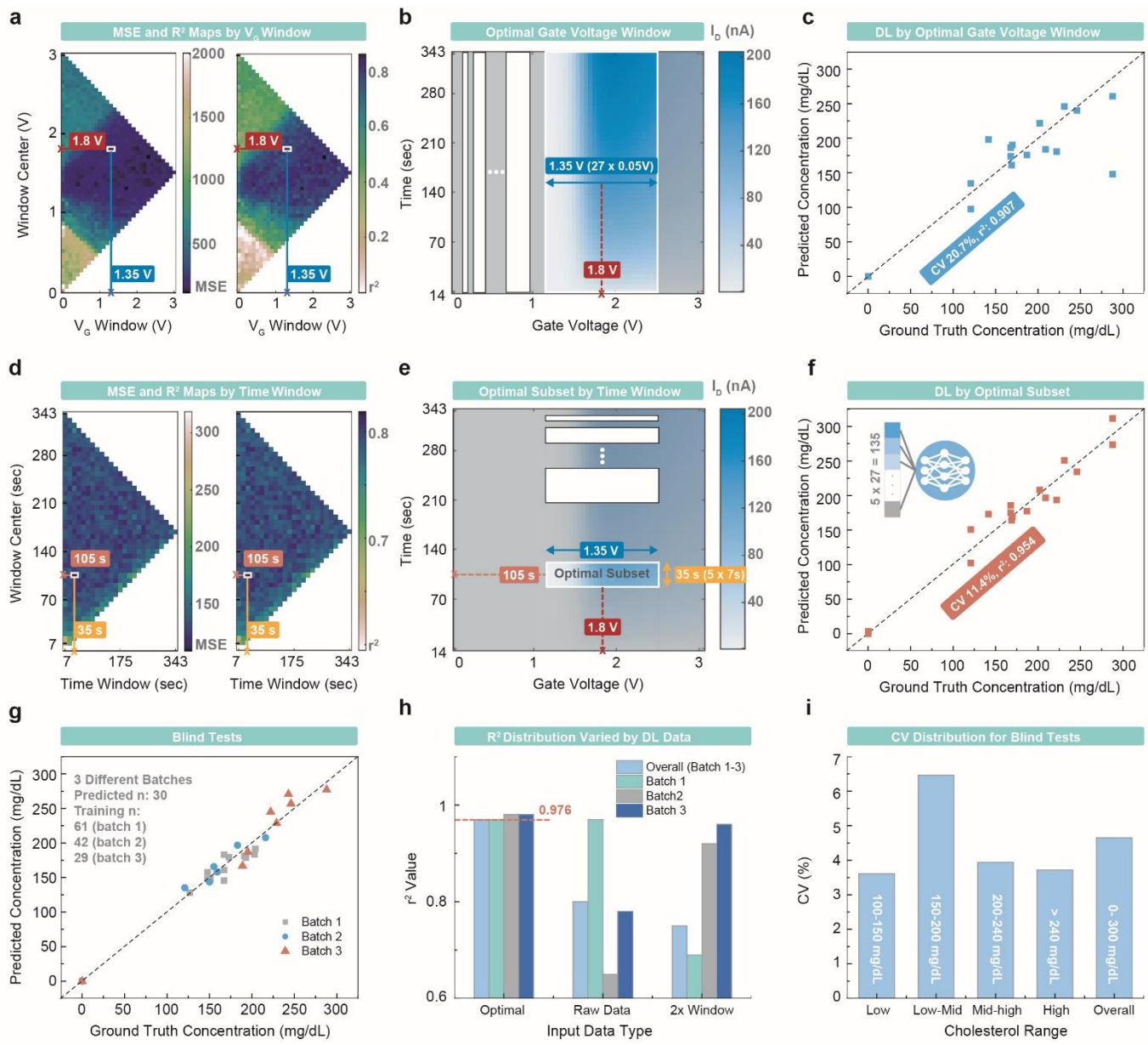


Figure 4

References

1. Rivenson, Y., Wang, H.D., Wei, Z.S., de Haan, K., Zhang, Y.B., Wu, Y.C., Günaydin, H., Zuckerman, J.E., Chong, T., Sisk, A.E., et al. (2019). Virtual histological staining of unlabelled tissue-autofluorescence images via deep learning. *Nat. Biomed. Eng.* **3**, 466-477. 10.1038/s41551-019-0362-y.
2. Goncharov, A., Joung, H.A., Ghosh, R., Han, G.R., Ballard, Z.S., Maloney, Q., Bell, A., Aung, C.T.Z., Garner, O.B., Carlo, D.D., and Ozcan, A. (2023). Deep Learning-Enabled Multiplexed Point-of-Care Sensor using a Paper-Based Fluorescence Vertical Flow Assay. *Small*, **19**, 2300617. 10.1002/smll.202300617.
3. Ballard, Z., Brown, C., Madni, A.M., and Ozcan, A. (2021). Machine learning and computation-enabled intelligent sensor design. *Nat. Mach. Intell.* **3**, 556-565. 10.1038/s42256-021-00360-9.
4. Ghosh, R., Joung, H.A., Goncharov, A., Palanisamy, B., Ngo, K., Pejcinovic, K., Krockenberger, N., Horn, E.J., Garner, O.B., Ghazal, E., et al. (2023). Single-tier point-of-care serodiagnosis of Lyme disease. *bioRxiv*. 10.1101/2023.06.14.544508.
5. Ballard, Z.S., Joung, H.A., Goncharov, A., Liang, J., Nugroho, K., Di Carlo, D., Garner, O.B., and Ozcan, A. (2020). Deep learning-enabled point-of-care sensing using multiplexed paper-based sensors. *NPJ Digit. Med.* **3**, 66. 10.1038/s41746-020-0274-y.
6. Joung, H.A., Ballard, Z.S., Wu, J., Tseng, D.K., Teshome, H., Zhang, L., Horn, E.J., Arnaboldi, P.M., Dattwyler, R.J., Garner, O.B., et al. (2020). Point-of-Care Serodiagnostic Test for Early-Stage Lyme Disease Using a Multiplexed Paper-Based Immunoassay and Machine Learning. *ACS Nano* **14**, 229-240. 10.1021/acsnano.9b08151.
7. Ochoa-Ruiz, A.G., Parra, G., López-Espinoza, D., Astudillo, P., Galyamin, D., Sabaté, N., Esquivel, J.P., and Vallejo-Cardona, A.A. (2023). Electrochemical Immunosensors: The Evolution from Elisa to EμPADs. *Electroanal.* **35**. 2200053. 10.1002/elan.202200053.
8. Yang, M.W., Huang, J.G., Fan, J.L., Du, J.J., Pu, K.Y., and Peng, X.J. (2020). Chemiluminescence for bioimaging and therapeutics: recent advances and challenges. *Chem. Soc. Rev.* **49**, 6800-6815. 10.1039/d0cs00348d.
9. Meng, X.D., Yang, F., Dong, H.F., Dou, L., and Zhang, X.J. (2021). Recent advances in optical imaging of biomarkers in vivo. *Nano Today* **38**. 101156. 10.1016/j.nantod.2021.101156.
10. Tu, J.B., Torrente-Rodríguez, R.M., Wang, M.Q., and Gao, W. (2020). The Era of Digital Health: A Review of Portable and Wearable Affinity Biosensors. *Adv. Funct. Mater.* **30**. 1906713. 10.1002/adfm.201906713.
11. Dai, C.H., Liu, Y.Q., and Wei, D.C. (2022). Two-Dimensional Field-Effect Transistor Sensors: The Road toward Commercialization. *Chem. Rev.* **122**, 10319-10392. 10.1021/acs.chemrev.1c00924.
12. Jang, H.J., Zhuang, W., Sui, X., Ryu, B., Huang, X., Chen, M., Cai, X., Pu, H., Beavis, K., Huang, J., and Chen, J. (2023). Rapid, Sensitive, Label-Free Electrical Detection of SARS-CoV-2 in Nasal Swab Samples. *ACS Appl. Mater. Interfaces* **15**, 15195-15202. 10.1021/acscami.3c00331.
13. Jang, H.J., Sui, X., Zhuang, W., Huang, X., Chen, M., Cai, X., Wang, Y., Ryu, B., Pu, H., Ankenbruck, N., et al. (2022). Remote Floating-Gate Field-Effect Transistor with 2-Dimensional Reduced Graphene Oxide Sensing Layer for Reliable Detection of SARS-CoV-2 Spike Proteins. *ACS Appl. Mater. Interfaces* **14**, 24187-24196. 10.1021/acscami.2c04969.
14. Bian, L., Wang, Z.H., White, D.L., and Star, A. (2021). Machine learning-assisted calibration of Hg²⁺-sensors based on carbon nanotube field-effect transistors. *Biosens. Bioelectron.* **180**. 113085. 10.1016/j.bios.2021.113085.
15. Makowski, M.S., and Ivanisevic, A. (2011). Molecular analysis of blood with micro-/nanoscale field-effect-transistor biosensors. *Small* **7**, 1863-1875. 10.1002/smll.201100211.
16. Sun, J., and Liu, Y. (2018). Matrix Effect Study and Immunoassay Detection Using Electrolyte-Gated Graphene Biosensor. *Micromachines* **9**. 142. 10.3390/mi9040142.
17. Maity, A., Pu, H.H., Sui, X.Y., Chang, J.B., Bottum, K.J., Jin, B., Zhou, G.H., Wang, Y.L., Lu, G.H., and Chen, J.H. (2023). Scalable graphene sensor array for real-time toxins monitoring in flowing water. *Nat. Commun.* **14**. 4184. 10.1038/s41467-023-39701-0.

18. Xue, M.T., Mackin, C., Weng, W.H., Zhu, J.D., Luo, Y.Y., Luo, S.X.L., Lu, A.Y., Hempel, M., McVay, E., Kong, J., and Palacios, T. (2022). Integrated biosensor platform based on graphene transistor arrays for real-time high-accuracy ion sensing. *Nat. Commun.* *13*, 5064. 10.1038/s41467-022-32749-4.
19. Jang, H.J., Lee, T., Song, J., Russell, L., Li, H., Dailey, J., Searson, P.C., and Katz, H.E. (2018). Electronic Cortisol Detection Using an Antibody-Embedded Polymer Coupled to a Field-Effect Transistor. *ACS Appl. Mater. Interfaces* *10*, 16233-16237. 10.1021/acsami.7b18855.
20. Jang, H.J., Ahn, J., Kim, M.G., Shin, Y.B., Jeun, M., Cho, W.J., and Lee, K.H. (2015). Electrical signaling of enzyme-linked immunosorbent assays with an ion-sensitive field-effect transistor. *Biosens. Bioelectron.* *64*, 318-323. 10.1016/j.bios.2014.09.020.
21. Stern, E., Vacic, A., Rajan, N.K., Criscione, J.M., Park, J., Ilic, B.R., Mooney, D.J., Reed, M.A., and Fahmy, T.M. (2010). Label-free biomarker detection from whole blood. *Nat. Nanotechnol.* *5*, 138-142. 10.1038/Nnano.2009.353.
22. Carlborg, C.F., Haraldsson, T., Cornaglia, M., Stemme, G., and van der Wijngaart, W. (2010). A High-Yield Process for 3-D Large-Scale Integrated Microfluidic Networks in PDMS. *J. Microelectromech. S.* *19*, 1050-1057. 10.1109/Jmems.2010.2067203.
23. Halldorsson, S., Lucumi, E., Gómez-Sjöberg, R., and Fleming, R.M.T. (2015). Advantages and challenges of microfluidic cell culture in polydimethylsiloxane devices. *Biosens. Bioelectron.* *63*, 218-231. 10.1016/j.bios.2014.07.029.
24. Pullano, S.A., Critello, C.D., Mahbub, I., Tasneem, N.T., Shamsir, S., Islam, S.K., Greco, M., and Fiorillo, A.S. (2018). EGFET-Based Sensors for Bioanalytical Applications: A Review. *Sensors* *18*, 4042. 10.3390/s18114042.
25. O'Farrell, B. (2009). Evolution in Lateral Flow-Based Immunoassay Systems. *Lateral Flow Immunoassay*, 1-33. 10.1007/978-1-59745-240-3_1.
26. Jang, H.J., Song, Y., Wagner, J., and Katz, H.E. (2020). Suppression of Ionic Doping by Molecular Dopants in Conjugated Polymers for Improving Specificity and Sensitivity in Biosensing Applications. *ACS Appl. Mater. Interfaces* *12*, 45036-45044. 10.1021/acsami.0c11125.
27. Jang, H.J., Wagner, J., Li, H., Zhang, Q., Mukhopadhyaya, T., and Katz, H.E. (2019). Analytical Platform To Characterize Dopant Solution Concentrations, Charge Carrier Densities in Films and Interfaces, and Physical Diffusion in Polymers Utilizing Remote Field-Effect Transistors. *J. Am. Chem. Soc.* *141*, 4861-4869. 10.1021/jacs.8b13026.
28. Jang, H.J., Wagner, J., Song, Y.J., Lee, T., and Katz, H.E. (2020). Carboxylic Acid-Functionalized Conjugated Polymer Promoting Diminished Electronic Drift and Amplified Proton Sensitivity of Remote Gates Compared to Nonpolar Surfaces in Aqueous Media. *Adv. Electron. Mater.* *6*, 1901073. 10.1002/aelm.201901073.
29. Amiri, M., and Arshi, S. (2020). An Overview on Electrochemical Determination of Cholesterol. *Electroanal.* *32*, 1391-1407. 10.1002/elan.201900669.
30. Fanjul-Bolado, P., Gonzalez-Garia, M.B., and Costa-Garcia, A. (2005). Amperometric detection in TMB/HRP-based assays. *Anal. Bioanal. Chem.* *382*, 297-302. 10.1007/s00216-005-3084-9.
31. Bhalla, N., Di Lorenzo, M., Pula, G., and Estrela, P. (2014). Protein phosphorylation analysis based on proton release detection: Potential tools for drug discovery. *Biosens. Bioelectron.* *54*, 109-114. 10.1016/j.bios.2013.10.037.

Capacitive coupling study of the HERD SCD prototype: preliminary results

Ruo-Si Lu, Rui Qiao, Ke Gong, Wen-Xi Peng, Wei-Shuai Zhang, Dong-Ya Guo, Jia-Ju Wei, Yi-Ming Hu, Jian-Hua Guo, Qi Wu, Peng Hu, Xuan Liu, Bing Lu, Yi-Rong Zhang

Abstract—The Silicon Charge Detector (SCD) is a subdetector of the High Energy Cosmic Radiation Detection payload. The dynamic range of the silicon microstrip detector can be extended by the capacitive coupling effect, which is related to the interstrip capacitance and the coupling capacitance. A detector prototype with several sets of parameters was designed and tested in the ion beams at the CERN Super Proton Synchrotron. The capacitive coupling fractions with readout strip and floating strip incidences were studied using the beam test data and SPICE simulation.

Index Terms—Silicon microstrip detectors, Capacitive coupling, Capacitance

I. INTRODUCTION

THE High Energy Cosmic Radiation Detection (HERD) facility is a dedicated particle and astrophysical experiment for the Chinese space station. It aims to achieve several key scientific objectives, including indirect searches for dark matter, precise spectroscopy, and composition measurements of cosmic rays, and monitoring high-energy gamma rays [1]. One of the unresolved phenomena in cosmic ray detection is the “knee”, which refers to the steepening of primary cosmic rays near the PeV energy range [2]. The operation of HERD is expected to make significant contributions to understanding this phenomenon.

The HERD facility comprises a 3-D cubic imaging calorimeter (CALO) surrounded by five sides of trackers, Plastic Scintillator Detector (PSD) and Silicon Charge Detector

This research is supported by the States Key Project of Research and Development Plan (2021YFA0718403, 2021YFA0718404, 2022YFF0503302), the National Natural Science Foundation of China (Projects: 12061131007).

Ruo-Si Lu, Rui Qiao, Ke Gong, Wen-Xi Peng, Wei-Shuai Zhang, Dong-Ya Guo, Qi Wu, Peng Hu, Xuan Liu, Bing Lu and Yi-Rong Zhang are with the Institute of High Energy Physics, Chinese Academy of Sciences, Beijing 100049, China (e-mail: lurs@ihep.ac.cn; qiaorui@ihep.ac.cn; gongk@ihep.ac.cn; pengwx@ihep.ac.cn; zhangws@ihep.ac.cn; guody@ihep.ac.cn; wuqi98@ihep.ac.cn; hupeng@ihep.ac.cn; liuxuan@ihep.ac.cn; lubing@ihep.ac.cn; 2021226055026@stu.scu.edu.cn).

Ruo-Si Lu, Rui Qiao, Ke Gong, Wen-Xi Peng and Qi Wu are with the University of Chinese Academy of Sciences, Beijing 100049, China (e-mail: lurs@ihep.ac.cn; qiaorui@ihep.ac.cn; gongk@ihep.ac.cn; pengwx@ihep.ac.cn; wuqi98@ihep.ac.cn).

Jia-Ju Wei, Yi-Ming Hu, and Jian-Hua Guo are with the Key Laboratory of Dark Matter and Space Astronomy, Purple Mountain Observatory, Chinese Academy of Sciences, Nanjing 210008, China (e-mail: weijj@pmo.ac.cn; huyiming@pmo.ac.cn; jhguo@pmo.ac.cn).

Jian-Hua Guo is with School of Astronomy and Space Science, University of Science and Technology of China, Hefei 230026, China (e-mail: jhguo@pmo.ac.cn).

Wei-Shuai Zhang is with School of Physics and Astronomy, China West Normal University, Nanchong 637002, China (e-mail: zhangws@ihep.ac.cn).

Xuan Liu is with North China University of Technology, Beijing, 100144, China (e-mail: liuxuan@ihep.ac.cn).

Yi-Rong Zhang is with Sichuan University, Chengdu, 610065, China (e-mail: 2021226055026@stu.scu.edu.cn).

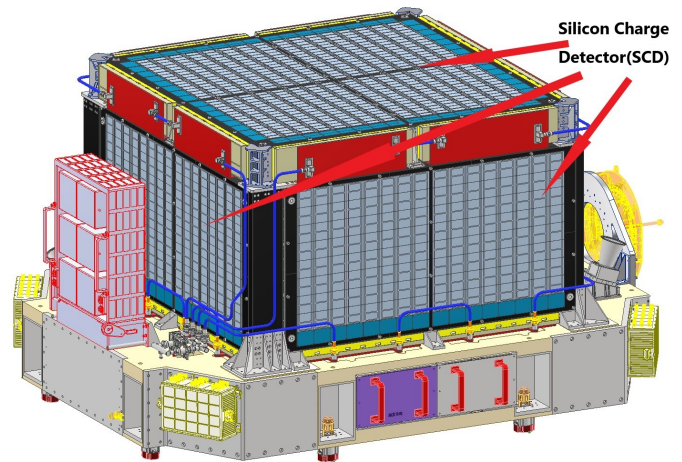


Fig. 1. Schematics of the HERD detector.

(SCD) [3]. The envelope size of the HERD facility is $3.0 \times 2.3 \times 1.7 \text{ m}^3$. SCD is located at the outmost of HERD, as shown in Fig. 1.

The SCD is designed to measure the charge of high-energy cosmic ray nuclei ranging from Z of 1 to about 28. The SCD is composed of a Top-SCD unit covering an area of $1.8 \times 1.8 \text{ m}^2$, and four Side-SCD units with an area of $1.6 \times 1.1 \text{ m}^2$ each. Each SCD unit consists of eight layers of single-sided silicon microstrip detectors. The adjacent layers are installed in orthogonal directions to identify the charge and trajectories of incoming charged particles [4].

A silicon microstrip detector can be modeled as a network of capacitors, which includes the bulk capacitors, the interstrip capacitors, and the coupling capacitors [5,6]. When a charge signal is generated within a strip that has been hit, it can be capacitively coupled to neighboring strips through the capacitor network. This capacitive coupling effect is negligible when the coupling capacitance is significantly larger than the interstrip capacitance. On the contrary, this capacitive coupling effect can be enhanced by using smaller coupling capacitors as discussed in this paper.

The electronic design of SCD is inherited from the Silicon Tungsten Tracker of the Dark Matter Explorer (DAMPE), whose linear dynamic range can only directly measure the signal of $Z = 1 \sim 6$. The SCD is proposed to increase the dynamic range to measure the signal of $Z = 1 \sim 28$ by enhancing the capacitive coupling effect. The small signals from low- Z particles can be easily measured using the fired

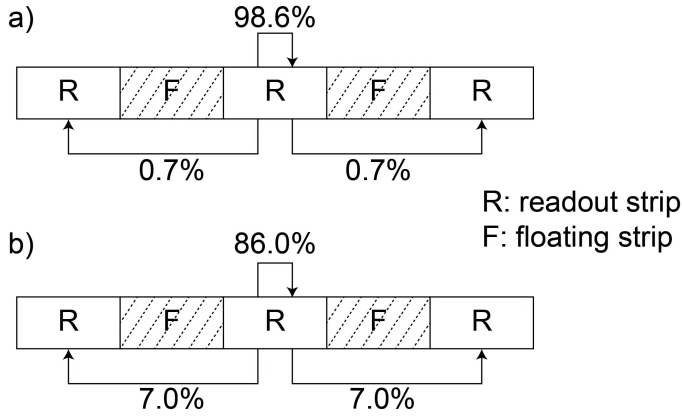


Fig. 2. The capacitive coupling fractions of set 2 a) and set 4 b). The definition of the two sets will be discussed below

strip. The large signals from high-Z particles could saturate the readout electronics of the fired strip, but the capacitively coupled signals of the neighboring strips are not saturated. The total signals can be reconstructed as the coupled signals divided by the coupling fractions. This helps the SCD to measure high-Z particles and extend the dynamic range. However, if the capacitive coupling fractions are too small (Fig. 2a), the coupled signals may be too weak and the signal-to-noise ratios are poor. The capacitive coupling fractions of SCD are preferred to be larger by approximately one order of magnitude than the fractions without external capacitors (Fig. 2b). The dependence of capacitive coupling fractions and the capacitor network of the SCD prototype detector was investigated through ion beam test and SPICE simulation.

II. THE SCD PROTOTYPE DETECTOR

The single-sided AC-coupled prototype detector (Products ID: OOO-2), ordered from MICRON semiconductor in 2021 [7], has a thickness of $300\ \mu\text{m}$ and an active area of $6\ \text{cm} \times 3.2\ \text{cm}$ (Fig. 3). The full depletion voltage of the sensor is $30\ \text{V}$ and it was biased at $80\ \text{V}$ during the experiment. Fig. 4 illustrates a cross-section of the silicon sensor. The junction side of the detector has $400\ \text{p}+$ strips. The implantation and readout pitch are $80\ \mu\text{m}$ and $160\ \mu\text{m}$, respectively. The detector is divided into two groups: the first half with 200 strips have a width of $60\ \mu\text{m}$, while the remaining 200 strips have a width of $25\ \mu\text{m}$. Half of the implantation strips are AC-coupled to the front-end electronics and amplified by four 64-ch IDE1140 ASICs [8], while the other half implantation strips remain floating. These two types of implantation strips are referred to as the readout strips and floating strips, respectively. This interval readout design allows for achieving good spatial resolution using limited readout channels [9,10].

In order to investigate the dependence of capacitive coupling on the coupling capacitors, the 100 readout channels in each group are divided into five sets (Fig. 5). Each set consists of 20 readout channels coupled to various external capacitors, as listed in Table 1.

The readout channels of both set 1 and set 10 (with $68\ \text{pF}$ external capacitors) are connected to two different ASICs.

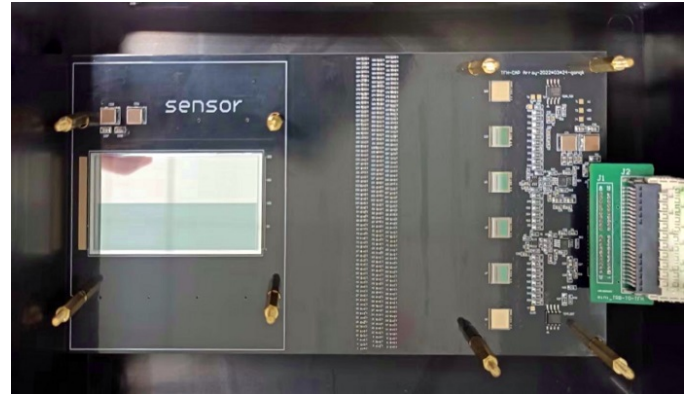


Fig. 3. View of the SCD prototype detector.

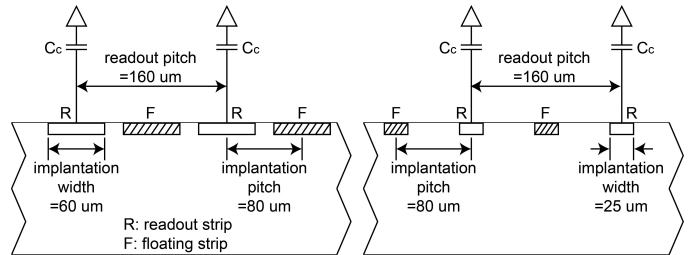


Fig. 4. Layout of the silicon microstrip sensor.

This can introduce a bias in the capacitive coupling effect due to the different ASIC gains. Besides, strip width of $60\ \mu\text{m}$ is closer to the final design. Consequently, only the analysis results of set 2 to set 5 are presented and discussed.

III. CAPACITANCE MEASUREMENT

The bulk capacitance, coupling capacitance, and interstrip capacitance of the SCD were measured using an Agilent 4980A LCR meter. The detector was biased at $80\ \text{V}$ using a Keithley 6487 picoammeter. An Agilent 16065A external voltage bias fixture was used to prevent the bias voltage from damaging the LCR meter. For each type of capacitance, the mean value and the error were calculated through five measurements. In addition, an Agilent 16380A standard capacitor set was used for calibration before each measurement.

The coupling capacitance (C_c) was measured by probing the AC pad and DC pad of the same strip. The equivalent parallel capacitance (C_p) and series capacitance (C_s) were read from

TABLE I
PARAMETERS FOR EACH SET OF THE DETECTOR

Set	Strip width (μm)	External capacitors (pF)
1	60	68
2	60	N/A
3	60	47
4	60	20
5	60	100
6	25	100
7	25	20
8	25	47
9	25	N/A
10	25	68

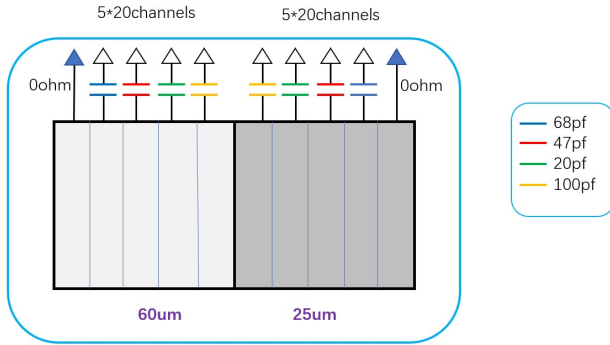


Fig. 5. Schematic diagram of a detector with five sets for each of the two strip widths.

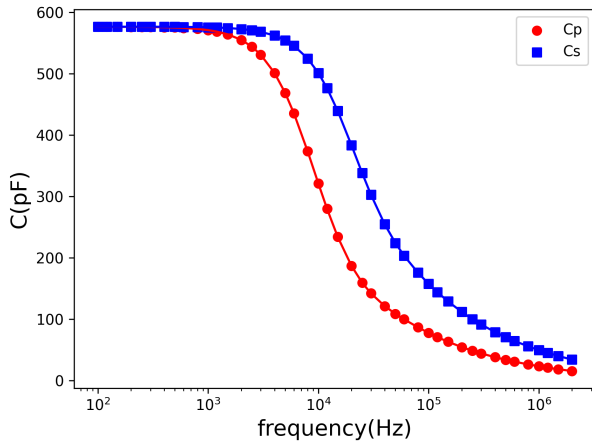


Fig. 6. The coupling capacitance dependence on the frequency.

the LCR meter within a frequency range from 100 Hz to 2 MHz, as shown in Fig. 6. At low frequencies, C_p and C_s were the same and independent of the frequency. As the frequency increased, the resistive implantation strip gradually blocked the AC signal, causing a decrease in the measured capacitance [5]. The measurements at 600 Hz were chosen to evaluate the coupling capacitance.

The total bulk capacitance was measured by probing the bias ring and the backplane of the detector. The bias voltage was scanned from 5 V to 80 V at a frequency of 600 Hz, as shown in Fig. 7. Two linear fits were conducted, and the full depletion voltage was approximately 29.9 V. The bulk capacitance of a single strip (C_b) is calculated by dividing the total bulk capacitance by the number of strips.

Three methods were used to measure the first interstrip capacitance (C_{i1}) by placing the probes on the pads of two adjacent strips: a) AC-AC pads, b) DC-DC pads and c) AC-DC pads. The measurements were conducted with 10 kHz where the capacitance was independent of the frequency. The capacitance obtained from the three methods were 6.18 ± 0.16 pF, 6.27 ± 0.27 pF, and 6.35 ± 0.27 pF, respectively. They

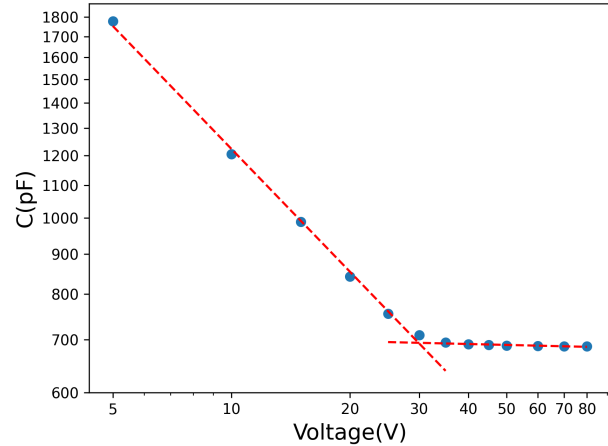


Fig. 7. The total bulk capacitance as a function of the bias voltage.

TABLE II
THE CAPACITANCE MEASUREMENT RESULTS

Capacitance	Value (pF)	Error (pF)
C_c	575	0.65
C_b	1.66	N/A
C_{i1}	6.27	0.29
C_{i2}	0.26	0.30
C_{i3}	0.21	0.12

agreed with each other within the range of error. Therefore, only the AC-AC pads were measured for the second interstrip capacitance (C_{i2}) and third interstrip capacitance (C_{i3}). The final results were shown in Table 2.

IV. ION BEAM TEST RESULTS

A. Experimental setup

An ion beam test was conducted at the CERN Super Proton Synchrotron (SPS) in October 2022 to investigate the response of ions for all the HERD prototype detectors. The test involved a 150 GeV/n lead primary beam directed at a 4 cm thick beryllium target. The secondary particles were selected using magnets and then directed towards the HERD prototype detectors. The SCD was mounted on a moving platform perpendicular to the ion beam, and the height of the platform was adjusted during the test to ensure that most of the detector sets received illumination from the small collimated beams.

B. Raw data process and event selection

The raw data processing consists of three steps: pedestal subtraction, common noise subtraction, and cluster finding. Firstly, the pedestal of each channel was determined by calculating the average ADC value recorded during a pedestal run for that specific channel. This pedestal value was then subtracted from the channel amplitude in every beam run to remove the baseline. Secondly, the common noise, which is caused by power supply fluctuations, was calculated as the average ADC value of each ASIC and then subtracted

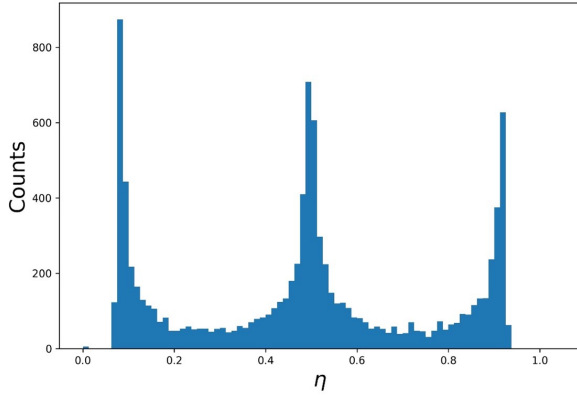


Fig. 8. The η distribution of the detector set 4 with lithium nuclei incidence.

event-by-event [11]. Lastly, a cluster finding algorithm was applied to identify all the clusters [11], and the maximum cluster is selected. The amplitudes of the maximum channel within the cluster (known as the seed channel) along with its eight neighboring channels were preserved for further analysis. Events with readout strips or floating strips incidences were selected based on the impact position η , defined as:

$$\eta = \begin{cases} \frac{PH_{seed}}{PH_{seed-1} + PH_{seed}} & \text{if } PH_{seed-1} \geq PH_{seed+1} \\ \frac{PH_{seed+1}}{PH_{seed} + PH_{seed+1}} & \text{if } PH_{seed-1} < PH_{seed+1} \end{cases} \quad (1)$$

where PH_{seed} , PH_{seed-1} and PH_{seed+1} are the signal amplitudes of the seed channel and its two neighboring channels after pedestal and common noise subtractions, respectively.

When a particle hits a readout strip, the majority of the charge is collected by the seed channel, resulting in the η value close to 0 or 1. On the other hand, when a particle hits the floating strip, the charge is capacitively coupled and distributed almost equally between the two adjacent readout strips, leading to the η value close to 0.5. Fig. 8 illustrates the distribution of η values for incident lithium nuclei on the detector set 4. The readout strip incidence is identified with η values within the range of [0, 0.15] and [0.85, 1], while the floating strip incidence is identified with η values between 0.45 and 0.55.

C. Capacitive coupling analysis

A typical capacitive coupling effect of readout strip incidence is shown in Fig. 9b. The seed channel collects around 90% of the total cluster amplitude. The neighboring channels only share a few percent of the total cluster amplitude, and the sharing fraction decreases as the distance increases. The first neighboring channel contributed approximately 7% of the total cluster amplitude. Fig. 9a depicts the capacitive coupling fractions of each channel when lithium nuclei hit the floating strips of detector set 4. The charge collected by the fired floating strip is shared among its neighboring channels, with the sharing fractions decreasing as the distance increases. The fractions of the first neighboring channels amount to approximately 6% of the total cluster amplitude.

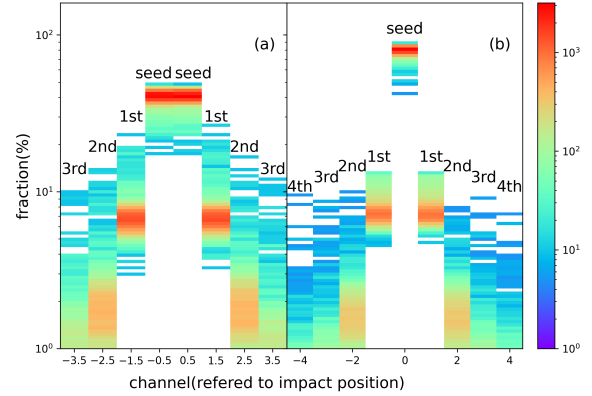


Fig. 9. The capacitive coupling fractions of the detector set 4 with lithium nuclei incidence on the floating strips (a) and the readout strips (b). The color refers to the number of entries in each bin.

The spectra of the capacitive coupling fractions for the first neighboring channels were accumulated for each ion and each detector set with either readout or floating strip incidences. Each spectrum was fitted with a Gaussian distribution and the Gaussian mean and sigma values were evaluated. A Gaussian fit result of the first neighboring channel of detector set 4 with floating strip incidences is shown in Fig. 10. Fig. 11a shows the independence of the capacitive coupling fractions of first neighboring channels on the type of light ions with floating strip incidences. This independence can be explained as follows. The capacitive coupling is affected by the incident angle, the charge diffusion during carrier drifting and the capacitor network. During the ion beam test, the SCD prototype detector was installed perpendicular to the beam direction, and the charge diffusion diameters of light ions are negligible with respect to the implant pitch [12]. As a result, the capacitive coupling should only depend on the detector sets. The final capacitive coupling fractions were evaluated as the weighted mean of the capacitive coupling fractions from $Z = 1 \sim 7$, as shown in Fig. 11 in the dashed lines. It should be noted that the capacitive coupling fractions of ions heavier than nitrogen were not considered due to electronics saturation.

The same evaluation process of the capacitive coupling fractions of detector set 4 was applied to other detector sets. The relationship between the reciprocal of capacitance values and the capacitive coupling fractions of the first neighboring channels will be discussed in the next section. Fig. 12 shows the relationship between the reciprocal of capacitance values and the capacitive coupling fractions of the first neighboring channels of four detector sets with readout strip and float strip incidences. For both readout and floating strip incidences, a smaller external capacitor increases the capacitive coupling fractions of the first neighboring channels.

V. SPICE SIMULATION

In order to obtain the theoretical capacitive coupling fractions, the SCD prototype detector was modelled as a SPICE circuit, as shown in Fig. 13. The second and the third interstrip capacitors were included in the circuit but not shown in Fig.

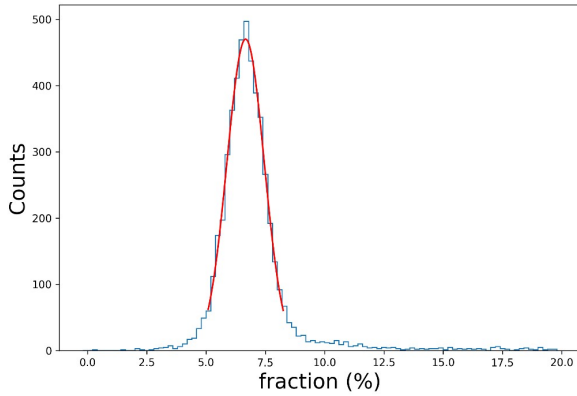


Fig. 10. The capacitive coupling fraction distribution of the first neighboring channels for the detector set 4 with lithium nuclei incidence on the floating strips.

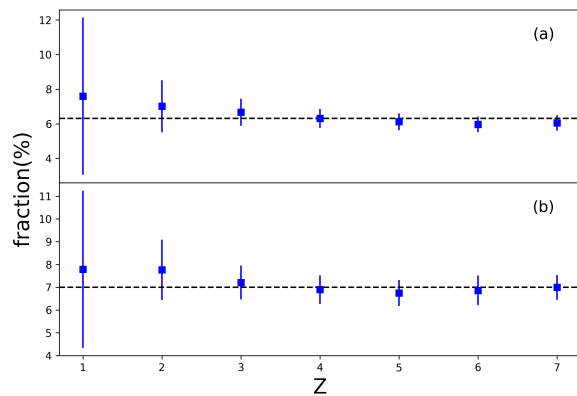


Fig. 11. The capacitive coupling fractions of the first neighboring channels with (a) floating strip and (b) readout strip incidences for the detector set 4.

13 for clear vision. Each readout strip was connected to a preamplifier through an intrinsic coupling capacitor (C_c) and an external coupling capacitor (C_{ce}). The incidence of a charged particle is simulated as a current pulse connected on both sides of a bulk capacitor. The measured capacitance values shown in Table 2 were used in the simulation. The simulation results are shown in Fig. 12 in dashed curves. The SPICE simulation results are consistent with the measured capacitive coupling fractions which depend on the external coupling capacitor.

VI. CONCLUSION

The HERD SCD should have a large dynamic range to measure the charge of $Z = 1 \sim 28$ cosmic rays. The large dynamic range is proposed to be covered by enhancing the capacitive coupling effect. A HERD SCD prototype detector has been designed to study the capacitive coupling effect dependence of the detector parameters. The detector is divided in several detector sets, and each set has various external capacitors. The detector was illuminated by the ion beams in CERN SPS and the capacitive coupling fractions with

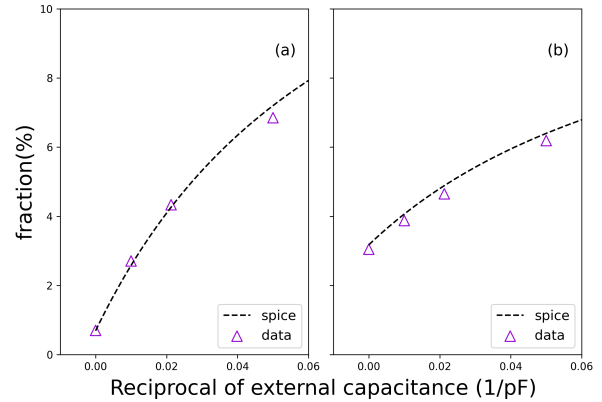


Fig. 12. The relationship between the reciprocal of capacitance values and the capacitive coupling fractions of first neighboring channel with readout strip (a) and floating strip (b) incidences in SPICE simulation and in data.

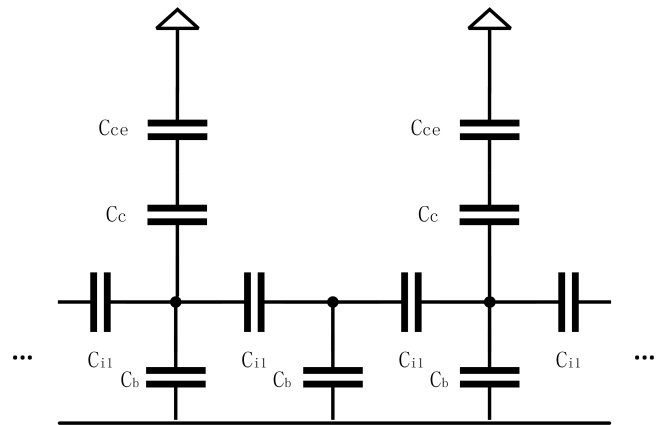


Fig. 13. SPICE equivalent model of the microstrip detector.

readout strip and floating strip incidences were evaluated. The capacitive coupling fractions were not sensitive to the species of ions, but were dependent on the impact position. As the distance to the impact position increases, the capacitive coupling fractions decrease. In addition, the detector parameters and the external coupling capacitors also affect the capacitive coupling fractions. A SPICE simulation has been implemented by modelling the SCD detector as a capacitor network, and the simulation results were consistent with the measurements. The knowledge of the capacitive coupling effect dependence to the detector parameters helps to optimize the design of the SCD detector.

REFERENCES

- [1] S. N. Zhang, O. Adriani, S. Albergo, G. Ambrosi, Q. An, T. W. Bao, *et al.*, "The high energy cosmic-radiation detection (HERD) facility on-board China's Space Station," in *Space Telescopes and Instrumentation 2014: Ultraviolet to Gamma Ray*, Canada: Montréal, 2014.
- [2] J. R. Hörandel, "Models of the knee in the energy spectrum of cosmic rays," *Astropart. Phys.*, vol. 21, no. 3, pp. 241-265, 2004, DOI: 10.1016/j.astropartphys.2004.01.004.
- [3] Y. W. Dong, Z. Quan, J. J. Wang, M. Xu, S. Albergo, F. Ambroglini, *et al.*, "Experimental verification of the HERD prototype at CERN SPS," in *Space Telescopes and Instrumentation 2016*, UK: Ultraviolet to Gamma Ray, Edinburgh, 2016.

- [4] D. Kyratzis, "Latest advancements of the HERD space mission," *Nucl. Instrum. Methods Phys. Res. A*, vol. 1048, pp. 167970, 2023, DOI. 10.1016/j.nima.2022.167970.
- [5] R. Qiao, W. X. Peng, X. Z. Cui, G. Q. Dai, Y. F. Dong, R. R. Fan, *et al.*, "A charge sharing study of silicon microstrip detectors with electrical characterization and SPICE simulation," *Adv. Space Res.*, vol. 64, no. 12, pp. 2627-2633, 2019, DOI. 10.1016/j.asr.2019.07.005.
- [6] M. A. Frautschi, M. R. Hoefkamp and S.C. Seidel, "Capacitance measurements of double-sided silicon microstrip detectors," *Nucl. Instrum. Methods Phys. Res. A*, vol. 378, no. 1-2, pp. 284-296, 1996, DOI. 10.1016/0168-9002(96)00467-6.
- [7] Micron. (2021). Micron strip detectors/ single sided [Online]. Available: <https://www.micronsemiconductor.co.uk/>
- [8] Ideas. (2023). IDE1140 [Online]. Available: <https://ideas.no/>
- [9] M. Krammer and H. Pernegger, "Signal collection and position reconstruction of silicon strip detectors with 200 μm readout pitch," *Nucl. Instrum. Methods Phys. Res. A*, vol. 397, no. 2-3, pp. 232-242, 1997, DOI. 10.1016/S0168-9002(97)00802-4.
- [10] M. Prest, G. Barbiellini, G. Bordignon, G. Fedel, F. Liello, F. Longo, *et al.*, "The AGILE silicon tracker: an innovative γ -ray instrument for space," *Nucl. Instrum. Methods Phys. Res. A*, vol. 501, no. 1, pp. 280-287, 2003, DOI. 10.1016/S0168-9002(02)02047-8.
- [11] Y. F. Dong, F. Zhang, R. Qiao, W. X. Peng, R. R. Fan, K. Gong, *et al.*, "DAMPE silicon tracker on-board data compression algorithm," *Chinese Phys. C*, vol. 39, no. 11, pp. 116202, 2015, DOI. 10.1088/1674-1137/39/11/116202.
- [12] E. Belau, R. Klanner, G. Lutz, E. Neugebauer, H. J. Seebrunner and A. Wylie, "Charge Collection in silicon strip detectors," *Nucl. Instrum. Methods Phys. Res. A*, vol. 214, no. 2, pp. 253-260, 1983, DOI. 10.1016/0167-5087(83)90591-4.

Waveform Simulation for Scintillation Characteristics of NaI(Tl) Crystal

J.J. Choi^a, C. Ha^b, E.J. Jeon^c, K.W. Kim^c, S.K. Kim^a, Y.D. Kim^{c,d}, Y.J. Ko^c,
B.C. Koh^b, H.S. Lee^{c,d}, S.H. Lee^{d,c}, S.M. Lee^a, B.J. Park^{d,c}, G.H. Yu^{e,c}

^a*Department of Physics and Astronomy, Seoul National University,
Seoul 08826, Republic of Korea*

^b*Department of Physics, Chung-Ang University,
Seoul 06973, Republic of Korea*

^c*Center for Underground Physics, Institute for Basic Science (IBS),
Daejeon 34126, Republic of Korea*

^d*IBS School, University of Science and Technology (UST),
Daejeon 34113, Republic of Korea*

^e*Department of Physics, Sungkyunkwan University, Suwon 16419, Republic of Korea*

Abstract

The lowering of the energy threshold in the NaI detector is crucial not only for comprehensive validation of DAMA/LIBRA but also for exploring new possibilities in the search for low-mass dark matter and observing coherent elastic scattering between neutrino and nucleus. Alongside hardware enhancements, extensive efforts have focused on refining event selection to discern noise, achieved through parameter development and the application of machine learning. Acquiring pure, unbiased datasets is crucial in this endeavor, for which a waveform simulation was developed. The simulation data were compared with the experimental data using several pulse shape discrimination parameters to test its performance in describing the experimental data. Additionally, we present the outcomes of multi-variable machine learning trained with simulation data as a scintillation signal sample. The distributions of outcomes for experimental and simulation data show a good agreement. As an application of the waveform simulation, we validate the trigger efficiency alongside estimations derived from the minimally biased measurement data.

Email addresses: kwkim@ibs.re.kr (K.W. Kim), yjko@ibs.re.kr (Y.J. Ko)

Keywords: NaI(Tl), waveform simulation, trigger efficiency

1. Introduction

Since DAMA/LIBRA claimed the observation of an annual modulation signal attributed to dark matter (DM) [1, 2, 3], no signal supporting the DAMA/LIBRA's observation has been substantiated, and the DAMA/LIBRA signal has been invalidated by many experiments based on various models [4, 5, 6, 7, 8]. Several research groups are presently conducting experiments using the same NaI(Tl) crystal detector as DAMA/LIBRA in attempts to replicate and test the signal [9, 10, 11, 12, 13]. Recently, COSINE-100 and ANAIS-112 published results from their model-independent annual modulation analyses [14, 15]. Although inconclusive at present, more definitive results are expected to be reached within the next few years.

When interpreting those results, one noticeable challenge is lowering the analysis threshold. Since DAMA/LIBRA's quenching factor measurements are more than twice as large [16, 17, 18, 19], the direct comparison would require less than half of their analysis threshold. Additionally, DAMA/LIBRA have recently presented the annual modulation results with an energy threshold down to 0.75 keV [20].

The low energy threshold presents additional opportunities, such as the search for weakly interacting massive particles (WIMPs) and the observation of coherent elastic neutrino-nucleus scattering ($\text{CE}\nu\text{NS}$). As sodium and iodine are both odd-proton elements, a synergy with the low energy threshold provides competitive sensitivity for spin-dependent interactions of low-mass WIMPs with protons [21]. Simultaneously, there are efforts to observe $\text{CE}\nu\text{NS}$ of reactor neutrinos using NaI detectors [22]. This experiment aims to enhance our understanding of reactor neutrinos and provide complementary insights into $\text{CE}\nu\text{NS}$ involving relatively lightweight nuclide. The essential element of the $\text{CE}\nu\text{NS}$ observation lies in achieving an extremely low energy threshold. The efforts toward lowering the energy threshold from a hardware perspective have brought

significant enhancements in encapsulation design [23], and concurrent endeavors on the software front via low-energy event analysis need to be pursued alongside.

To improve the analysis of low-energy event, we devised a waveform simulation reflecting the scintillation characteristics and incorporating a data acquisition (DAQ) system. This simulation contributes significantly to refining event selection aimed at lowering the energy threshold by enhancing our understanding of detector responses. This is demonstrated through the development of parameters for pulse shape discrimination (PSD) and their utility in generating pure samples for multi-variable machine learning (ML) applications.

Additionally, the analysis of extremely low-energy events much account for the trigger conditions used to filter out electronic noises. These are more prevalent at lower energies and may obscure the real scintillation events. Thus, the fraction of triggered scintillation events, referred to as trigger efficiency, should be considered in low-energy analysis. Measuring trigger efficiencies requires obtaining minimally biased samples, independent of triggers, and as free from noise as possible. We utilized samples generated from multiple γ rays emitted by a ^{22}Na radioactive source for this purpose.

The waveform simulation was optimized to accurately replicate the experimental data and is detailed in Sec. 2, along with its implementation process. In Sec. 3, we perform a comparative analysis between the experimental and simulation data using several PSD parameters to validate the simulation. Furthermore, we present the outcomes of utilizing the simulated data as a training sample for ML. The dataset used in Secs. 2 and 3 was taken from the NEON experiment, with comprehensive details of the experimental setup available in Ref. [22]. Meanwhile, another experimental setup for measuring trigger efficiencies is outlined in Sec. 4, accompanied by an explanation of the estimation method. We also present trigger efficiencies derived from noise-free simulated data compared to real data for enhanced confidence.

2. Waveform Simulation (WFSim)

We have developed a simulation tool named `WFSim` to thoroughly comprehend the detector response and secure pure samples of scintillation events. Typically, a full simulation for a scintillation calorimeter involves emulating the detector, including the optical process of scintillation photons, and the DAQ process. However, due to the resource-intensive nature of tuning the simulation and generating events, our focus was on crafting a fast and uncomplicated simulation tool tailored specifically to our requirements.

The detector simulation utilizing `GEANT4` [24] yields the energy deposited by the interaction of particles. Photons are then generated according to the light yield of the scintillator, which is the number of photons produced relative to the energy deposited. The generated photons go through an optical process and hit the PMT’s photocathode, which creates photoelectrons (PEs) based on its quantum efficiency. Here, the number of photoelectrons generated within an event is referred to as the NPE , and the number of photoelectrons generated relative to the energy deposited is defined as the “effective light yield”.

`WFSim` focuses on photoelectrons instead of photon, bypassing the optical process. To do this, we derived the expectation value of NPE from experimental data, and a value of NPE serves as input to the `WFSim` for each event, drawn randomly from a Poisson distribution with the expectation value as the mean. Subsequently, `WFSim` generates waveforms identical in dimensions to the experimental data.

The process to compute physics quantities, such as charge and PSD parameters, remains consistent because the simulated waveforms match the dimensions of the physical data. This allows direct comparison between the physics quantities derived from the simulation data and those from the experimental data, enabling the simulation data to function as scintillation signal samples for ML or deep learning (DL). By employing `WFSim`, we can efficiently and precisely simulate the detector response, significantly supporting research and facilitating the development of effective analysis methods for NaI(Tl)-based experiments.

2.1. PMT Simulation

The photomultiplier tube (PMT) serves to amplify PEs emitted upon photon interaction with the photocathode. This amplification, occurring through multiple dynode stages, generates a large quantity of electrons from the PEs, eventually converted into electrical pulses upon reaching the anode. Typically, a single PE (SPE) undergoes amplification by a factor of 10^6 to 10^7 electrons, referred to as the PMT gain G . Various factors, such as voltage differences, material properties, and dynode geometry, influence the amplification factor at each dynode stage. While these factors may vary across stages in real-world scenarios, `WFSim` assumes these as constant values due to complexity.

To stochastically determine the number of electrons amplified at stage i for an electron from stage $i - 1$, it is assumed to follow a Poisson distribution,

$$f_{\text{amp}}(n_{e,i} | G, n_{\text{stage}}) = f_{\text{pois}}(n_{e,i} | A_e = G^{1/n_{\text{stage}}}) = \frac{A_e^{n_{e,i}}}{n_{e,i}!} e^{-A_e}. \quad (1)$$

where $n_{e,i}$ denotes the number of electrons amplified at the i^{th} stage, n_{stage} is the number of dynode stages, and A_e represents the amplification factor of each stage. We assume each stage has the same amplification factor. For each electron obtained in stage $i - 1$, the count of electrons amplified in stage i is randomly drawn from Eq. 1, and their sum constitutes the total electron count in stage i ,

$$N_{e,i} = \sum^{N_{e,i-1}} n_{e,i}^{\text{gen}}, \quad (2)$$

where $n_{e,i}^{\text{gen}}$ represents the random number generated via Eq. 1 for each electron in stage $i - 1$.

SPE pulses are often under-amplified due to cathode/dynode stage skipping or inelastic backscattering [25]. Incorporating under-amplified SPE pulses termed as low-gain (LG) pulses, `WFSim` assumes that these LG pulses have skipped one dynode without amplification. We employ the same A_e as normal-gain (NG) pulses but reducing the number of stages to $n_{\text{stage}} - 1$. Each SPE pulse randomly chooses either NG and LG based on the measured probability

of LG for each PMT, and the PMT amplification process is executed iteratively following Eq. 2.

LG fraction integrated into the simulation is estimated from experimental data through modeling. The dataset used for the analysis is obtained by exposing NaI(Tl) crystal to a ^{241}Am γ ray source, and PE pulses are identified from the waveform via a clustering algorithm introduced in Ref. [26]. To select isolated PE pulses, 59.5-keV γ ray events were selected and a criterion was set with a time window ranging from $2.6\ \mu\text{s}$ after to $4.6\ \mu\text{s}$ after the trigger time. The charge distribution of those pulses can be depicted in Fig. 1, where the ADC count is a charge unit and is covered in detail in Sec. 2.3. The model to describe the data should reflect the characteristics of the NG and LG pulses. Notably, pulses extracted from the data may not exclusively comprise SPE pulses. Overlapping of multi-PE (MPE) pulses may occur making them indistinguishable and potentially biasing the results, so that we should account this effect.

The single-NG pulses can be modeled by a continuous Poisson distribution using Euler Gamma function,

$$f_{X_N}(q|a_q, \mu_n) = f_{\text{CP}}(q/a_q|\mu_n) = \frac{\mu_n^{(q/a_q)}}{\Gamma(q/a_q + 1)} e^{-\mu_n}, \quad (3)$$

where q represents the charge sum of the waveform and a_q is a scaling factor. A random variable X_N formalizes q to describe the charge distribution of NG pulses with μ_n depicting the Poisson mean of q/a_q . With the ratio of the mean charge of NG to LG pulses ρ_{NL} , the charge distribution of single-LG pulses is described as,

$$f_{X_L}(q|a_q, \mu_n, \rho_{NL}) = f_{\text{CP}}(q/a_q \cdot \rho_{NL}|\mu_n). \quad (4)$$

This expression assumes similarity in the charge distribution shapes for LG and NG pulses, as their shapes are primarily determined by the first amplification stage while subsequent stages smear the distribution.

The model to describe MPE pulses should also account for the characteristics of NG and LG pulses. For MPE pulses composed of solely NG or LG pulses, a Poisson distribution with μ_n multiplied by the number of PEs as the mean can

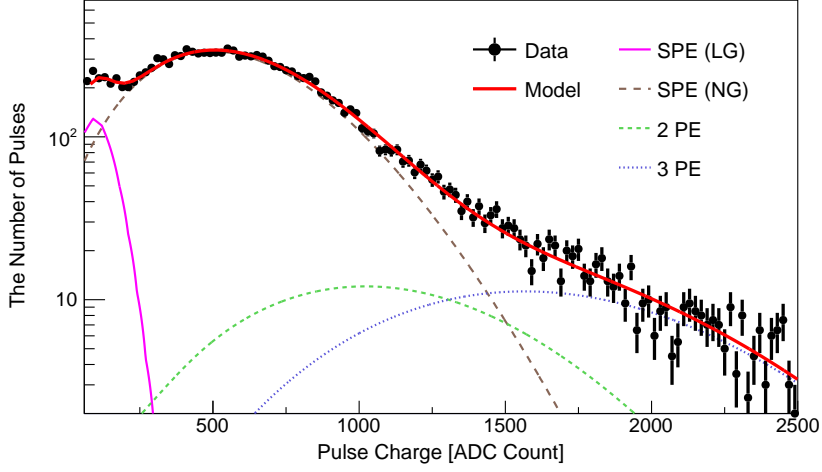


Figure 1: Pulse charge distribution with the N -PE model. The distribution of experimental data (black dots) of 59.5-keV γ rays from a ^{241}Am source are represented by black dots with error bars, while the solid thick red line illustrates the N -PE model as described in Eqs. 3 to 5. The solid magenta, long dashed brown, dashed green, and dotted blue lines represent distributions for low-gain (LG), normal-gain (NG), 2-PE, and 3-PE pulses, respectively. The 2-PE and 3-PE distributions encompass both NG and LG pulses, maintaining an identical fraction of LG pulses.

be used. When MPE pulses are a mix of NG and LG pulses, a distribution with the combination of X_N and X_L as the random variable is needed for modeling. For instance, a distribution like the following can be applied for a 2-PE charge distribution consisting of an NG pulse and an LG pulse,

$$f_Y(q) = \int f_{X_N}(t|a_q, \mu_n) \times f_{X_L}(q-t|a_q, \mu_n, \rho_{NL}) dt, \quad (5)$$

where Y is the random variable representing the sum of X_N and X_L ($Y = X_N + X_L$).

By extending this approach to encompass the charge distribution up to 3-PE pulses, the model adequately represents the data as shown in Fig. 1. The estimated fraction of LG pulses from this model fit is $(6.79 \pm 0.46)\%$, and the

effective light yield given the fraction can be estimated as,

$$NPE/\text{keV} = \frac{Q(59.5 \text{ keV})/(59.5 \text{ keV})}{(1 - f_{\text{LG}}) q_{\text{NG}} + f_{\text{LG}} q_{\text{LG}}}, \quad (6)$$

where $Q(59.5 \text{ keV})$ is the charge corresponding to the 59.5-keV γ ray from ^{241}Am and f_{LG} denotes the LG fraction. The mean charge of NG and LG pulses are represented by q_{NG} and q_{LG} , respectively. These can also be obtained from the model fit as $q_{\text{NG}} = \mu_n a_q$ and $q_{\text{LG}} = \mu_n a_q / \rho_{\text{NL}}$. The information such as SPE gain, LG pulse probability, and effective light yield is used as input to the simulation. These processes are conducted individually to reflect the characteristics of each PMT and the results are utilized in the PMT simulation.

2.2. Waveform Generation

Waveform generation in `WFSim` involves the stacking of SPE and random pulses on the pedestal followed by the analog-to-digital converter's (ADC) sampling. The following subsections explain the implementation of these components and the extraction of essential data-derived information.

2.2.1. Pedestal

The waveform is discretized with a time interval of 2 ns, aligning with the 500-MHz ADC sampling rate of our DAQ system. Each time bin's pedestal value is drawn randomly from a Gaussian distribution,

$$f_{\text{ped}}(q | \mu_{\text{ped}}, \sigma_{\text{ped}}) = \frac{1}{\sqrt{2\pi}\sigma_{\text{ped}}} \exp\left[-\frac{(q - \mu_{\text{ped}})^2}{2\sigma_{\text{ped}}^2}\right], \quad (7)$$

where μ_{ped} and σ_{ped} denote the mean and root-mean-square (RMS) of the pedestal, respectively. During data processing for each event, the pedestal mean is computed and subtracted from the waveform before deriving physics quantities. Therefore, maintaining a constant μ_{ped} does not introduce any difference from the experimental data.

Conversely, if the pedestal RMS differs from the experimental data, it may impact the waveform; thus, it should mirror the data. Given the asymmetric

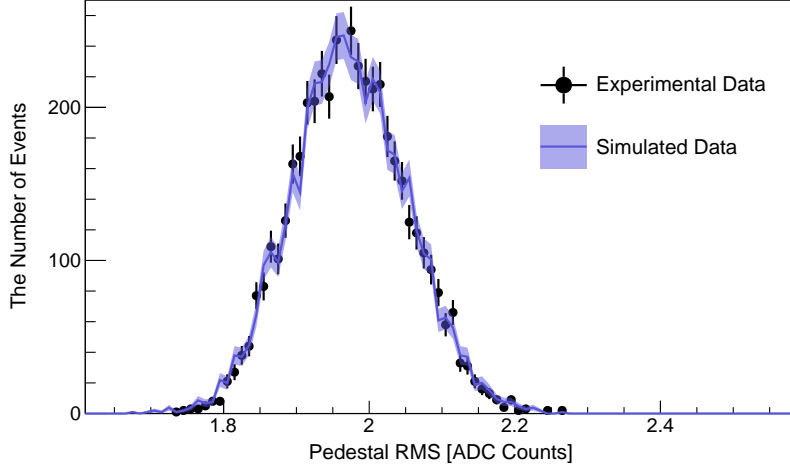


Figure 2: Comparison of the pedestal RMS distributions between the experimental data (black dots) and the simulated data (solid blue line), which are well agreed.

nature of the experimental data's pedestal RMS distribution, we employed an asymmetric Gaussian distribution to model the variations of σ_{ped} ,

$$f_{\sigma_{\text{ped}}}(\sigma_{\text{ped}} | \mu_{\sigma}, \sigma_l, \sigma_r) = \begin{cases} \frac{2}{\sqrt{2\pi}(\sigma_l + \sigma_r)} \exp\left[-\frac{(\sigma_{\text{ped}} - \mu_{\sigma})^2}{2\sigma_l^2}\right] & (\sigma_{\text{ped}} < \mu_{\sigma}), \\ \frac{2}{\sqrt{2\pi}(\sigma_l + \sigma_r)} \exp\left[-\frac{(\sigma_{\text{ped}} - \mu_{\sigma})^2}{2\sigma_r^2}\right] & (\sigma_{\text{ped}} \geq \mu_{\sigma}), \end{cases} \quad (8)$$

where μ_{σ} denote the most probable value of σ_{ped} . The dispersion of σ_{ped} is represented by σ_l and σ_r when it is less or greater than μ_{σ} , respectively. For each event, σ_{ped} is randomly drawn from the distribution in Eq. 8 to generate the pedestal values. These equation parameters were deduced from the experimental data to feed into the simulation. Figure 2 illustrates a comparison between the simulation and experimental data for the pedestal RMS distribution, showing a good agreement between the experimental and simulation data.

2.2.2. SPE Pulse Generation

The initial step in generating an SPE pulse involves selecting the pulse type, either NG or LG pulses, followed by obtaining the SPE charge. By default, the SPE charge is acquired through the PMT simulation outlined in Sec. 2.1 for each

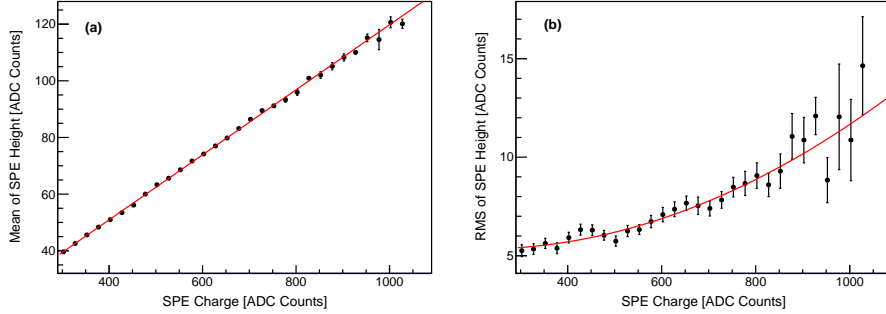


Figure 3: (a) Mean and (b) RMS of the SPE height distribution as functions of the SPE charge. The black dots with error bars depict parameters estimated using a Gaussian model fitted to experimental data. These parameter values are modeled with first and second-order polynomials (red lines) representing the variations in the mean and RMS as the SPE charge changes, respectively.

event. Alternatively, templates obtained from 100 million PMT simulations, including both NG and LG pulses, can be utilized to avoid repeated PMT simulations. In this approach, the SPE charge is randomly extracted from the template corresponding to each pulse type.

The SPE pulse’s height, the maximum amplitude of the pulse, is then determined using a charge-height relationship.

Since the SPE height distribution for a given SPE charge was observed to be Gaussian-like shape in the experimental data, the distribution is modeled by a Gaussian distribution varying its mean and standard deviation depending on the SPE charge q ,

$$f_h(h|q) = f_{\text{gaus}}[h|\mu_h(q), \sigma_h(q)], \quad (9)$$

where h represents the SPE height and μ_h stands for the mean of the SPE height distribution corresponding to a given q , while σ_h represents the standard deviation. The values of μ_h and σ_h in the Gaussian model vary with the change in SPE charge indicating variations in the distribution as demonstrated in Fig. 3. Those values are respectively modeled with first and second-order polynomial functions $\mu_h(q)$ and $\sigma_h(q)$, representing the charge-height relationship. Upon

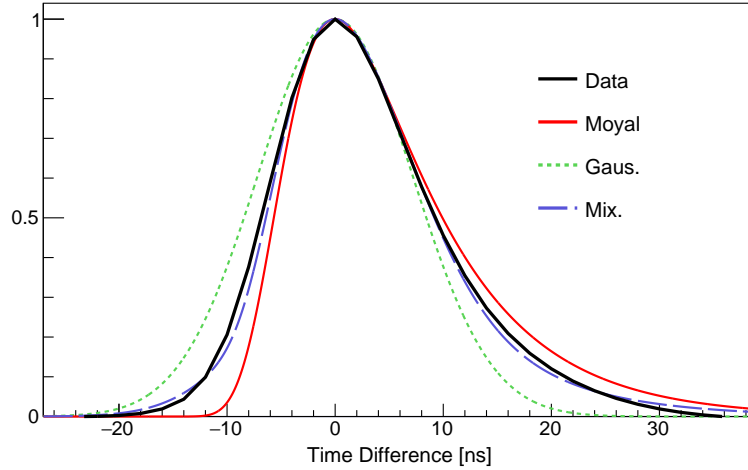


Figure 4: SPE shape distributions. We accumulated isolated pulses zeroing out the time when they maximize for data distribution. The heights of all distributions were normalized to 1, and the widths of the reference distributions were area scaled to be equal to the data.

randomly generating the SPE charge, the height distribution is determined and the SPE height is drawn from this relationship.

To establish the SPE shape for a given SPE charge and height, several reference distributions were compared to the data. Isolated SPE pulses were stacked to get the data distribution. To synchronize the pulse times before stacking, we set the time of maximum pulse amplitude to zero. The reference models used are Gaussian, Moyal [27], and their mixture model expressed as,

$$\begin{aligned}
 & f_{\text{mix}}(t | t_{\text{spe}}, \sigma_{\text{spe}}) \\
 &= \frac{1}{\sqrt{8\pi}\sigma_{\text{spe}}} \left\{ \exp \left[-\frac{1}{2} \left(\frac{t - t_{\text{spe}}}{\sigma_{\text{spe}}} + e^{-\frac{t - t_{\text{spe}}}{\sigma_{\text{spe}}}} \right)^2 \right] + \exp \left[-\frac{(t - t_{\text{spe}})^2}{2\sigma_{\text{spe}}^2} \right] \right\}, \quad (10)
 \end{aligned}$$

where t_{spe} denotes the SPE hit time, and σ_{spe} represents the dispersion of the SPE pulse. As shown in Fig. 4, the mixture model was chosen because it explains the shape such as asymmetry better than the two other models. Once the charge and height of the SPE are determined, the SPE pulse is generated at the specified SPE hit time detailed in the subsequent subsection.

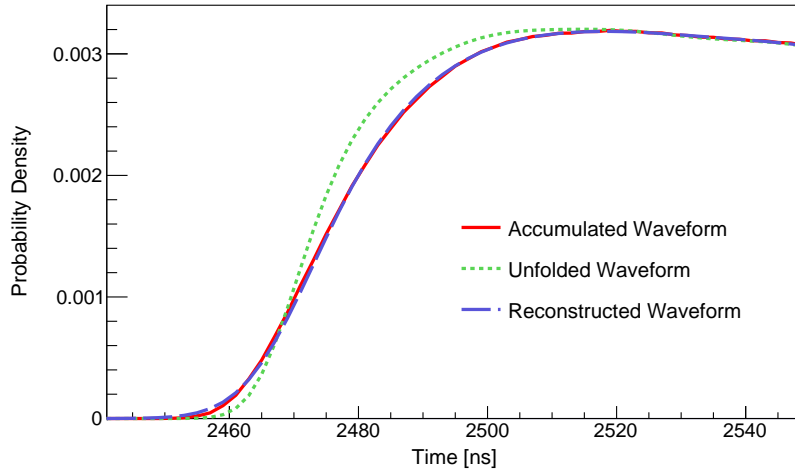


Figure 5: Waveform distribution comparison. The solid red line illustrates the waveform accumulated from scintillation events in experimental data, the dotted green line represents the waveform unfolded from the accumulated waveform, and the dashed blue line shows the waveform reconstructed from the unfolded waveform.

2.2.3. SPE Hit Time

Obtaining the hit time of each SPE typically involves characteristics of scintillation process such as rising and decaying times. However accurate simulation of this process necessitates a comprehensive understanding of the detector response, including scintillation process and optical properties of the NaI(Tl) crystal. It also demands significant simulation time. To bypass these without missing the scintillation characteristics of NaI(Tl) crystal, `WFSim` introduced an alternative method by extracting hit times from a data-driven time distribution generated through a two-step process.

First, an average waveform was derived by accumulating scintillation events within the $[2, 10]$ keV energy range, selected due to its representation of a relatively low-energy area where noise is easily discriminated. To remove the smearing effect caused by the time distribution of the SPE pulses, the iterative Bayesian unfolding (IBU) method [28] was employed. The IBU method unfolded the accumulated waveform, utilizing a migration matrix obtained through

simulations outlined in Sec. 2.2.2.

The unfolded waveform was reconstructed via the migration matrix to be validated,

$$w_i^{\text{recon}} = \sum_j M_{ij} w_j^{\text{unfold}} \quad (11)$$

where w_i^{recon} denotes the amplitude of reconstructed waveform for i^{th} time bin while w_j^{unfold} represents the amplitude of unfolded waveform for j^{th} time bin, and the migration matrix is indicated by M_{ij} . Figure 5 shows that the reconstructed waveform (dashed blue) closely matches the accumulated waveform (solid red). The unfolded waveform is also depicted in the figure as a dotted green line. The t_{spe} values in Eq. 10 are randomly drawn from the unfolded waveform to determine the position of each pulse.

2.2.4. Random Photoelectrons

WFSim includes random PEs originating from sources such as NaI(Tl) phosphorescences [29, 30] and PMT dark current. Given that the waveform recording in the experimental data starts roughly $2.4 \mu\text{s}$ before the trigger time similar as the COSINE-100 DAQ system [31], the rate of random PEs can be estimated by counting pulses within the $[0, 2] \mu\text{s}$ timeframe. These random PEs are assumed to share the same shape and magnitude as the SPE pulses. The position is randomly chosen to ensure an uniform distribution.

2.3. Digitization and Triggering

The PMT generates analog signal measured in volts, which is then digitized by the ADC. The DAQ system used in the COSINE-100 [31] and the NEON [22] experiments has a resolution (σ_{ADC}) of 12 bits and a peak-to-peak voltage (V_{pp}) of 2.5 V. The amplitude of the signal is therefore quantized at a voltage resolution of $2.5/2^{12}$ V (~ 0.61 mV). This quantization occurs at a 500-MHz sampling rate, discretizing the signal at 2-ns intervals. Upon satisfying specific local trigger conditions with the digitized signal, the ADC transmits a trigger decision to the trigger control board (TCB). Given that a NaI(Tl) crystal integrates two PMTs to read scintillation light, the TCB generates a global trigger decision

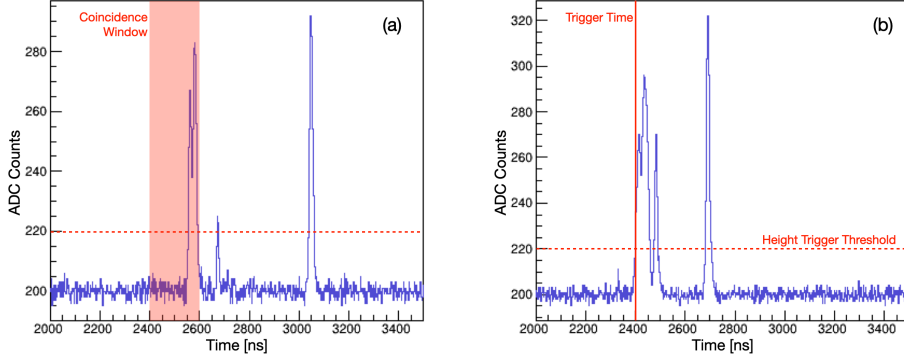


Figure 6: Waveforms generated by WFSim for an event. (a) and (b) represent the waveforms for PMT channel 1 and 2, respectively. The solid red line denotes the trigger time, the dotted red line shows the height trigger threshold, and the red shaded area illustrates the coincidence window. Note that to increase the readability, the waveforms show zoomed-in view from 2000 ns to 3500 ns out of 8000 ns total readout window.

when both PMTs' trigger decisions meet a time coincidence criterion. Upon generating the global trigger decision, the DAQ server records 8- μ s digitized waveforms starting 2.4 μ s before the trigger time.

WFSim includes the discretization process by generating waveforms with 2-ns time interval. The waveform then undergoes a quantization and triggering processes similar to the DAQ system [31]. Since the output from the PMT simulation represents the amplified number of electrons, the amplitude is initially expressed in units of charge, namely pico-Coulomb (pC). It needs a unit conversion to match the quantization standards of the experimental data, and the amplitude is converted into ADC counts, a unit that ensures the ADC's voltage resolution of 1. The factor C_{pC2ADC} accounts for this conversion is expressed as,

$$C_{\text{pC2ADC}} = \frac{2^{\sigma_{\text{ADC}}} R_{\text{ter}}(\Omega)}{w_t(\text{ns}) V_{\text{pp}}(\text{V})} \times 10^{-3}, \quad (12)$$

where R_{ter} is the terminal resistance of 50 Ω .

After converting the waveform amplitudes into ADC count-based values, each time bin's amplitude is quantized into an integer. Local and global triggers

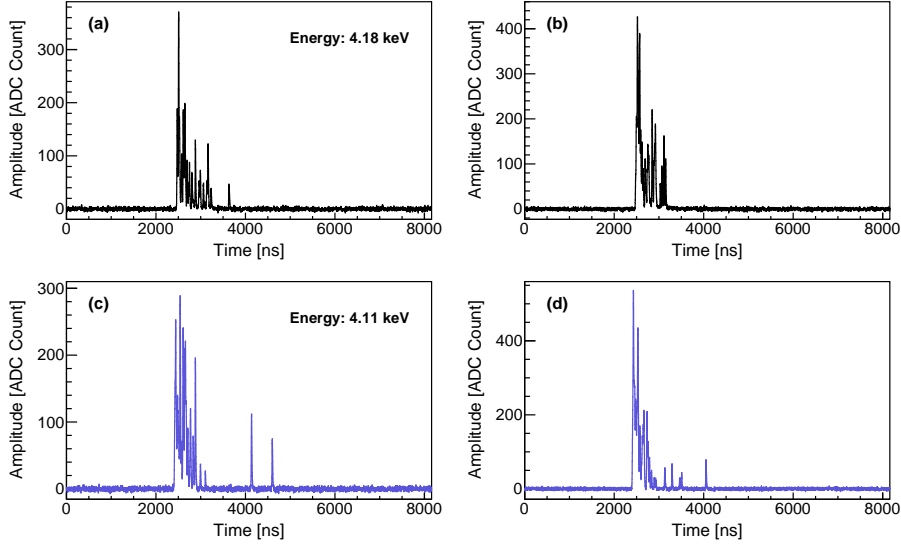


Figure 7: Waveform examples. Pedestal subtracted waveforms from experimental and simulation data are displayed in (a) (b) and (c) (d), respectively, for PMT channel 1 and 2.

that are integrated into the process are implemented as follows: the local trigger deploys a height trigger condition upon amplitude threshold crossing. The global trigger opens a coincidence window (CW) when a local trigger activates on a PMT channel. If another channel triggers while the CW remains open, it flags the event as triggered. The waveform is shifted to align the trigger time with a specified time and is recorded, accompanied by a trigger bit indicating event triggering status.

Figure 6 (b) demonstrates the waveform on channel 2 crossing the height trigger threshold, initiating a 200-ns CW. This event is then triggered because channel 1's waveform also crosses the threshold within the CW as shown in Fig. 6 (a). The local trigger time on channel 2 serves as the global trigger time and is aligned to $2.4 \mu\text{s}$. Figure 7 displays waveforms from experimental and simulation data as an example.

3. Validation of WFSim

The primary objective of `WFSim` is to enhance event selection by analyzing low-energy events. Simulation plays a crucial role in developing PSD parameters by understanding the detector response to scintillation events. It is also essential in training multi-variable ML models using PSD parameters. For this purpose, the simulation must accurately represent the experimental data regarding PSD parameters, ensuring consistency in ML outputs. Here we use boosted decision tree (BDT) as used in the COSINE-100 event selection [32]. Since the simulation generates waveforms based on SPE pulses, several variables characterizing the waveform were compared between the simulation and experimental data.

3.1. SPE Variables

Figure 8 displays three distributions of SPE variables using the dataset selected for Fig. 1 in Sec. 2.1. To generate simulation data comparing with experimental data under the same conditions, the following process was employed: a Poisson distribution was initially defined with the NPE expectation value equivalent to 59.5 keV as the mean. A randomly generated NPE from this distribution was then fed into `WFSim` for each event to produce a waveform. Following identical processing steps as those applied to the experimental data, the charge distribution was obtained with isolated pulses between 2.6 and 4.6 μ s after the trigger time within their respective waveforms.

As shown in Fig. 8 (a), the simulation accounting for only NG pulses (red line) closely approximates the experimental data (black dots) across most regions, but exhibits a noticeable differences in the low-charge region. Conversely, the simulation considering both NG and LG pulses (blue line) aligns well even in the low-charge region. Figure 8 (b) demonstrates the height-to-width ratio distribution of the SPE, showing effective alignment between simulation and experimental data. Here, the SPE width refers to the time interval from the beginning to the end of the pulse. The SPE shape distribution of experimental data is also compared with that of simulation data in Fig. 8 (c). The simulation

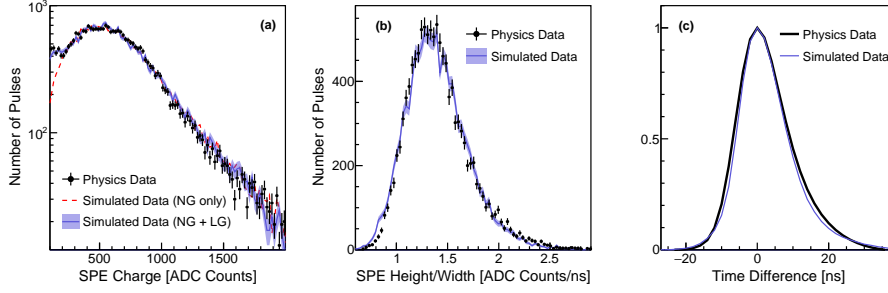


Figure 8: Three SPE distributions. (a) The pulse charge distribution. Experimental data is represented by black dots. The red line illustrates the distribution solely considering NG pulses, while the blue line represents the distribution accounting for both LG and NG pulses. (b) The pulse height-to-width distribution. Experimental data (black dots) is compared with simulation data (solid blue lines). (c) The pulse shape. Data distribution in Fig. 4 compared with simulation distribution. For all distributions, the experimental data used is the same as in Fig. 1.

pulse times were synchronized in the same way as the experimental data by zeroing the time bin when the amplitude was at its maximum.

3.2. PSD Parameters

When a particle deposits energy in a NaI(Tl) crystal, scintillation light is emitted, generating a scintillation signal characterized by a decay time of 250 ns [33]. Conversely, PMT-induced noise (Type-I) exhibit a notably shorter decay time of 50 ns or less. The low-energy region presents a greater challenge in discrimination, as another type of noise events (Type-II) emerges alongside typical noise events. Separating the scintillation events from these noise events is crucial to lowering the energy threshold, thus COSINE-100 has focused on event selection analysis via PSD techniques based on the waveform’s characteristics. In this section, the simulation is compared to the experimental data in terms of several PSD parameters used in COSINE-100’s event selection analysis [32].

NaI(Tl) detectors in the NEON experiment were installed in liquid scintillator (LS) to reduce background by tagging radiation-related events [22]. Events coinciding with LS are categorized as multiple-hit events and excluded when

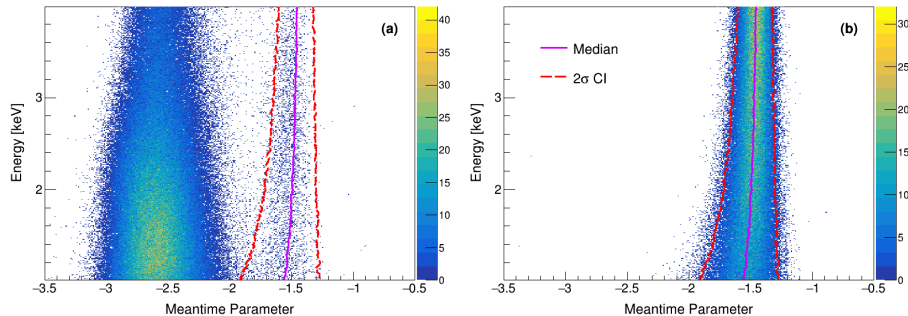


Figure 9: Two-dimensional distributions between the Meantime Parameter and energy. (a) illustrates the distribution of multiple-hit events in experimental data, while (b) shows the distribution of simulation data. The solid purple and dashed red lines denote the median and 2σ confidence interval of the simulation data.

forming the physics-search dataset. However, as these events exhibit relatively low noise, they serve well for comparative distribution analysis with simulation. Conversely, single-hit events without LS coincidences typically contain a higher noise level, especially at lower energies, making them usable as noise samples for BDT training. The analysis in this section uses 42 days of NEON data.

The charge-weighted mean time capitalizes on the differences in decay time, exhibiting strong discrimination power against Type-I noise. Figure 9 displays the two-dimensional distributions between the energy and the Meantime Parameter, which is a combination of charge-weighted mean times for the two PMTs as defined in Ref. [32]. In Fig. 9 (a) derived from experimental data, the scintillation events are distributed on the right, separated from the PMT-noise events. This distribution notably aligns with the 2σ confidence interval from the simulation distribution, indicating the accuracy of `WFSim` in representing the experimental data.

In addition to the Meantime Parameter, we validated the simulation by comparing them to experimental data with six PSD parameters. The first one is the Crystal-based Mean Time, defined as the charge-weighted mean time of stacked waveforms from the two PMTs. The Likelihood Parameter were

also used, which was key to reaching the 1-keV energy threshold in COSINE-100. This parameter is a PSD parameter based on a likelihood method, which was developed with a focus on Type-II noise discrimination [32]. The next parameters used are the Maximum Cluster Ratio and the Charge-to-Height Ratio, defined as the ratio of the charge of the largest pulse within an event to the total event charge and the ratio of the charge integral within the first 5 μ s of the waveform to the maximum amplitude, respectively. Lastly, there are two more PSD parameters utilized for simulation validation through comparison: Slow Charge and Fast Charge. The Slow Charge is defined as the ratio of the charge integrated between 100 and 600 ns to that for the first 600 ns, while the Fast Charge is defined as the ratio of the charge integrated over the first 50 ns to that for the first 600 ns.

Figure 10 displays the comparisons between experimental and simulation data distributions for the aforementioned six PSD parameters. For the comparisons, single-hit and multiple-hit events from experimental data and simulated events were subjected to the two criteria: energies between 2 and 6 keV and a Meantime Parameter greater than -2.2. The single-hit events contain a considerable amount of noise, while notable agreement between experimental and simulation data is observed upon applying BDT conditions described later. Meanwhile, the simulation distributions align well with the multiple-hit event distributions within the scintillation signal region thanks to the relatively lower noise level. Contrary to the first four parameters, the Slow Charge and Fast Charge are PMT-based parameters, thus the distributions are shown for each PMT channel.

BDT stands as one of the multi-variable event selection techniques crucial in achieving a lower energy threshold by effectively distinguishing scintillation and noise events at low energy levels. In COSINE-100, BDT was utilized for event selection, which was a significant improvements [34, 32]. The parameters illustrated in Fig. 10 undergo training through the BDT method and are combined into a single powerful discriminator. The simulated events were used as samples of the scintillation signal for BDT training, while the single-hit events

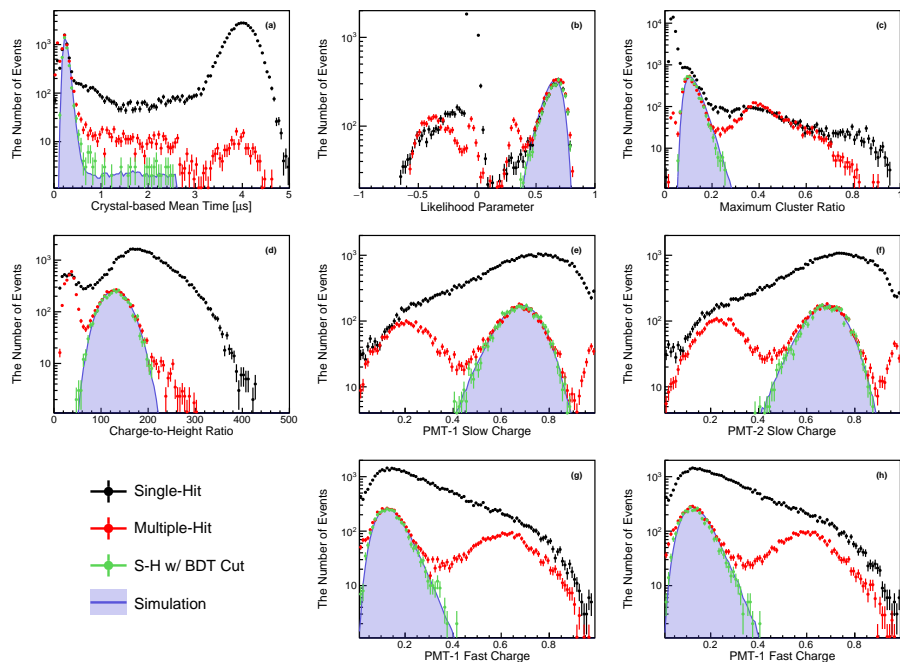


Figure 10: The distributions of PSD parameters used to discriminate scintillation events from noise events. The black and red dots represent single-hit and multiple-hit events in experimental data, while blue lines denote simulation data. The green dots with error bars are single-hit distribution after applying the BDT cut. A condition was set that the Meantime Parameter must exceed -2.2 for all distributions.

from the experimental data were used as background (noise) samples.

As shown in Fig. 11, the region where the BDT output is greater than 0.2 is dominated by scintillation signals and was set to the BDT conditions used in Fig. 10. In this region, the simulation agrees well with the experimental data and the chi-squares between them are 8.2 and 31.8 for the single-hit and multiple-hit events, respectively, with 18 degrees of freedom. The relatively large chi-square with the multiple-hit events is probably due to the fact that the events were mostly triggered by other crystals, while the events in the other data sets were all self-triggered. Consequently, `WFSim` accurately characterizes the experimental data from various perspectives and contributes to lowering the

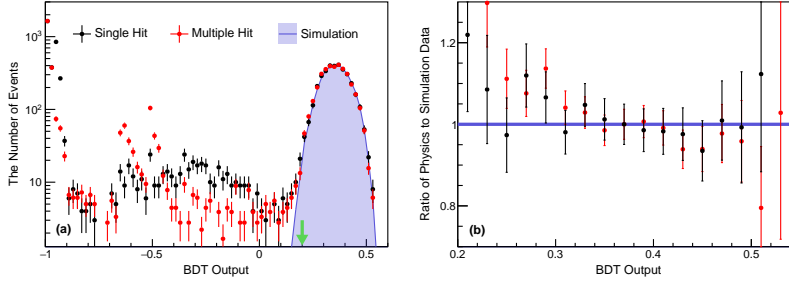


Figure 11: The distribution of BDT outputs and the ratios of experimental to simulation data distribution. Black (red) dots with error bars represent single-hit (multiple-hit) events in experimental data, while the blue line denotes the simulation data. The green arrow points to the BDT cut used for Fig 10. A precondition was set requiring the Meantime Parameter to exceed -2.2 for all distributions.

energy threshold by favoring event selection, especially at lower energies. The potential for an unlimited number of events as samples for ML or DL purposes could lead to substantial improvements.

4. Trigger Efficiency

Measuring trigger efficiencies not only aids in the analysis of low-energy events but also reflects the reliability of understanding the DAQ system and the detector. The main challenge in measuring efficiencies lies in sampling scintillation events that should satisfy two conditions: independence from the trigger condition and inclusion of solely scintillation events without noise events. To meet these criteria, we utilized ^{22}Na data and selected events that met certain criteria as described later. The trigger efficiencies are then estimated from this sample of scintillation events. We also compare the efficiencies estimated via simulation with actual measurements, taking into account that `WFSim` is implemented based on the same DAQ system used for efficiency measurements.

4.1. Experimental Setup

For the trigger efficiency measurement, NaI(Tl) crystals with light yield larger than 25 PE/keV were employed to enhance trigger efficiency assessment below 1 keV region. The crystals were assembled using a new methodology [22], directly attaching them to the PMTs, which minimized optical coupling, reduced light loss, and ensured high effective light yield. Two measurements were conducted: one on a rectangular crystal named Crystal A (20 mm×20 mm×15 mm) and the other on a cylindrical Crystal B (diameter: 25 mm, height: 38 mm). Crystal A shared the same powder as Crystal 2, 5, and 8 in the COSINE-100 crystals, while Crystal B was grown using the powder same to that used for Crystal 3 and 4 in the COSINE-100 crystals [10]. Their effective light yields were 25.9 ± 0.6 and 27.6 ± 0.3 PE/keV for Crystals A and B, respectively. The measurements were conducted in the presence of the CsI(Tl) crystal array, which was used for the KIMS dark matter search experiment at the Yangyang underground laboratory [35, 36, 9] as shown in Fig. 12. Approximately 40 days of data taken from April to May and from October to November in 2020 were used for the trigger efficiency estimation.

To accurately estimate the trigger efficiencies, the NaI(Tl) crystal was exposed to a ^{22}Na radioactive source. The crystal was surrounded by twelve CsI(Tl) crystals, and the source was placed between the NaI(Tl) crystal and one of the CsI(Tl) crystals. About 90% of ^{22}Na decays through positron emission to the 1275-keV level of ^{22}Ne . Thanks to the short half-life (3.7 ps) of excited ^{22}Ne , the γ ray with an energy of 1275 keV is emitted almost simultaneously with the two 511-keV γ rays from electron-positron annihilation. By tagging coincident γ rays, where multiple γ rays from ^{22}Na are detected simultaneously by NaI(Tl) and CsI(Tl) crystals, enabled the collection of minimally biased scintillation event samples for estimating the trigger efficiencies.

The NaI(Tl) and CsI(Tl) crystals each have two PMTs attached and share the trigger condition that both PMTs must be fired within the crystal specific CW. However, due to the difference in decay time of NaI(Tl) and CsI(Tl) crystals, the lengths of the CW are different, 200 ns and 2 μs , respectively, and there

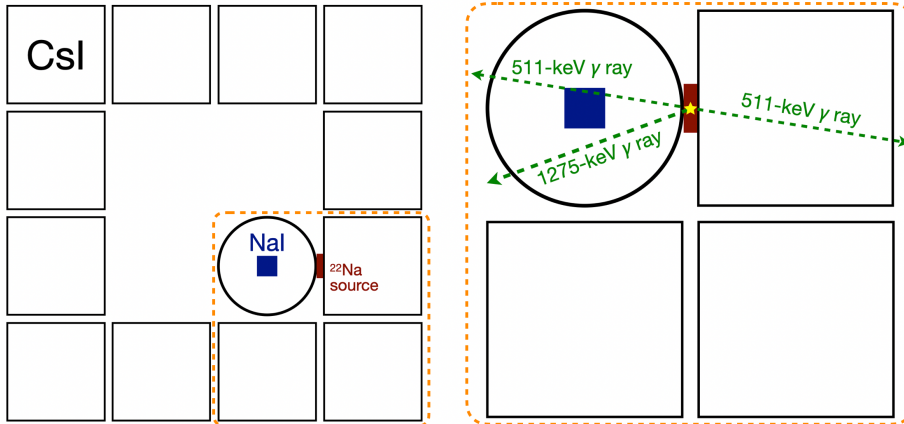


Figure 12: Schematic of the experimental setup for trigger efficiency measurement. The NaI(Tl) crystal (blue filled square) was encapsulated by a copper case (black circle), and it was installed inside twelve CsI(Tl) crystal detector array represented as black squares. ²²Na radioactive source was placed between NaI(Tl) crystal and one of CsI(Tl) crystals.

are differences in the local trigger conditions for the PMTs. The local trigger condition for NaI(Tl) crystal requires at least one PE pulse, as introduced in Sec. 2.3, and is consistent with the COSINE-100 and NEON experiments as well as `WFSim`. On the other hand, the local trigger condition for CsI(Tl) crystal demands at least two PE pulses to be read by each PMT within $2 \mu\text{s}$. Therefore, to define an event, the global trigger is formed by a logical OR condition between the NaI(Tl) and adjacent CsI(Tl) crystals and is recorded as waveforms with a sampling rate of 500 MHz and a length of $8 \mu\text{s}$.

To compare trigger efficiencies among detectors with different effective light yields, we need a variable other than energy. Since the triggering process relies on NPE , it is used as a proxy variable for energy. As the true NPE is an unknown variable, the NPE is converted by dividing the charge by the mean of SPE charge, obtained through modeling of the SPE charge distribution as depicted in Fig. 1. This approach for the NPE calibration was applied equally to simulation and experimental data.

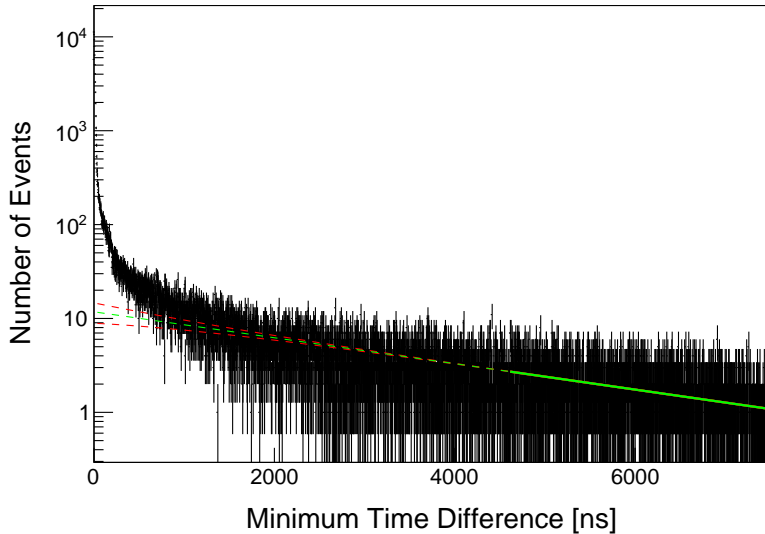


Figure 13: The distribution of the minimum time difference between the two PMTs. The green line is the fitted exponential function to data and the red lines denote its uncertainties. The solid lines show the function and its uncertainties in the fitting range, while the dashed lines represents extrapolations of those.

4.2. Estimation of Trigger Efficiency

As an initial step in event selection, a 511-keV γ ray signal was required at the CsI(Tl) crystal with timing coincidence to the NaI(Tl) crystal. Despite these conditions, there are noise contamination mainly due to direct hits of energetic γ on PMT glasses generating Cherenkov light as well as accidental coincidences enhanced by external γ source. Noise events are identifiable by their distinctive pulse shape characterized by significantly large amplitudes, while randomly coincident events can cause bias as they are not identified. To mitigate the bias caused by these events, we computed a variable termed the Minimum Time Difference (Δt_{\min}). The closest time between the pulse times of the two PMTs was derived as Δt_{\min} by identifying the pulse time of each PMT that represented the moment the waveform crossed the height trigger threshold.

As shown in Fig. 13, the distribution comprises short and long decay compo-

nents. Short decay component indicates strong correlation between the PMTs due to scintillation events, while long decay component denotes accidental coincidence. Modeling with an exponentially decaying function in the longer decay range allowed estimation of the long decay components within the trigger region ($\Delta t_{\min} < CW$) and the entire region. In Fig. 13, the fitted function is shown as a solid line within the range to use for modeling and a dashed line extrapolated outside the range.

There are events that have pulses in only one of the two PMTs. These are not included in Fig. 13, but should be included in the estimation of trigger efficiencies because they could contribute to inefficiencies. Based on the aforementioned description, trigger efficiencies can be estimated using,

$$\epsilon = \frac{n_{\text{trg}} - n_{\text{RC}}|_{\Delta t_{\min} < CW}}{(n_{\text{all}} - n_{\text{RC}}) + n_{\text{SH}}}, \quad (13)$$

where n_{all} denotes the number of events that has timing coincidence with the 511-keV γ ray signal in the CsI(Tl) crystal, while n_{trg} represents the events triggered by DAQ system. The n_{RC} stands for the estimated amount of random coincidence events and n_{SH} is the number of events registered in only one PMT.

Using *NPE* divided into six bins ranging from 3 to 21 PEs, the trigger efficiency for each bin was estimated via Eq. 13. Figure 14 shows the trigger efficiency measurements along with their uncertainties. The uncertainties took into account both uncertainty from noise estimation and statistical uncertainty from event counts such as n_{all} and n_{SH} . The trigger efficiencies measured with Crystals A and B are consistent, revealing low dependence on crystal shapes and light emission quality. At 3 to 6 PEs, the efficiencies are $81.5 \pm 1.2\%$ and $78.6 \pm 1.8\%$ for Crystal A and B, respectively.

Figure 14 also includes a comparison with the trigger efficiencies estimated with *WFSim* introduced in Secs. 2 and 3. With the advantage of noise-free simulation, the trigger efficiencies can be estimated simply by the ratio of triggered to generated events. To account for differences in the SPE size that could be caused by differences in the PMT's gain, the changes in trigger efficiencies for halving and doubling the amplification factor were added to the statistical un-

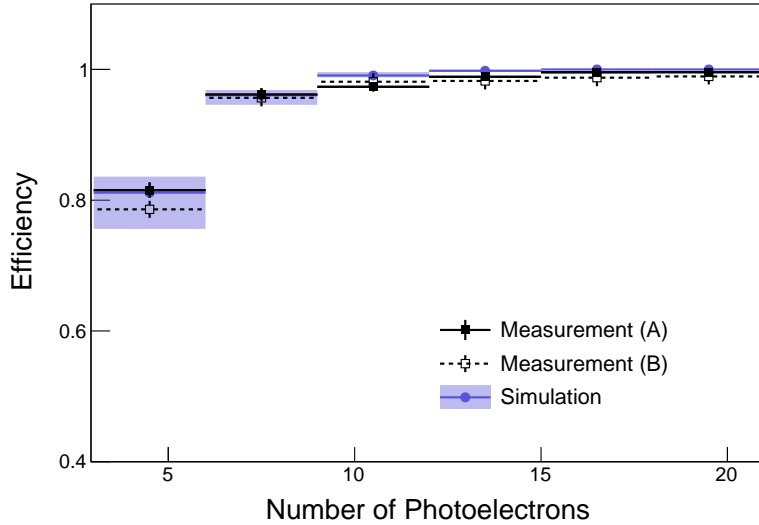


Figure 14: Trigger efficiencies measured via Crystal A (black closed square) and B (open square) together with the simulation (blue circle) as a function of the number of photoelectrons.

certainties and shown as a blue filled area.

Assuming the population has flat distribution and the probabilities of light collection by both PMTs are similar, it is expected that a trigger efficiency can be 85% at the first bin. However, the efficiency from `WFSim` is slightly less than this at 81.15%, and the difference appears to be due to the CW of 200 ns. Since the simulation was tuned to data from NEON, the dependence on the crystal might be more pronounced. Nevertheless, the agreement of the simulation with the measurements within 3% shows a low dependence on the crystal, indicating that the results can be applied to NaI(Tl) detectors in the same DAQ environment.

5. Summary

The NaI(Tl) detector’s low energy threshold is crucial for the full validation of DAMA/LIBRA, the search for low-mass DM, and observations of CE ν NS. To analyze low-energy events, we have developed a data-driven waveform simulation. The simulation generates pedestals, SPE pulses, random photoelectrons, and integrates them. The PMT amplification process is simulated and the pulses are implemented using SPE variables estimated by modeling the experimental data. The waveforms from the experimental data are used to place the pulses, taking into account the scintillation characteristics of the NaI(Tl) crystal.

Our simulation was compared to the experimental data, in terms of SPE variables and PSD parameters as well as results trained with BDT technique, and showed remarkable agreement. The simulation poised to enhance future low-energy analyses in NaI(Tl)-based experiments. Plans to employ DL to train waveform for event selection underscore the simulation’s critical role.

Furthermore, we have measured the trigger efficiencies, which are crucial for characterizing low-energy events. A ^{22}Na source was utilized for minimally biased samples, and the efficiency was estimated to be 80% at 3 to 6 PEs. Comparison with the waveform simulation presents excellent agreement proving reliability of the simulation. Our estimations from the two crystals and the simulation revealed low crystal dependency. These efforts will prove invaluable as we make efforts to achieve to an extremely low energy threshold.

6. Acknowledgments

We thank the Korea Hydro and Nuclear Power (KHNP) Company for providing underground laboratory space at Yangyang and the IBS Research Solution Center (RSC) for providing high-performance computing resources. This work is supported by the Institute for Basic Science (IBS) under project code IBS-R016-A1, NRF-2019R1C1C1005073, NRF-2021R1A2C3010989 and NRF-2021R1A2C1013761, Republic of Korea.

References

- [1] R. Bernabei, et al., [Searching for WIMPs by the annual modulation signature](#), Phys. Lett. B 424 (1) (1998) 195.
- [2] R. Bernabei, et al., [Final model independent result of DAMA/LIBRA-phase1](#), Eur. Phys. J. C 73 (2013) 2648.
- [3] R. Bernabei, et al., [First model independent results from DAMA/LIBRA-phase2](#), Nucl. Phys. Atom. Energy 19 (4) (2018) 307.
- [4] M. Battaglieri, et al., [US Cosmic Visions: New Ideas in Dark Matter 2017: Community Report](#), arXiv:1707.04591 (2017).
- [5] E. Aprile, et al., [Search for Electronic Recoil Event Rate Modulation with 4 Years of XENON100 Data](#), Phys. Rev. Lett. 118 (2017) 101101.
- [6] E. Aprile, et al., [Dark Matter Search Results from a One Ton-Year Exposure of XENON1T](#), Phys. Rev. Lett. 121 (11) (2018) 111302.
- [7] D. S. Akerib, et al., [Search for annual and diurnal rate modulations in the LUX experiment](#), Phys. Rev. D 98 (2018) 062005.
- [8] G. Adhikari, et al., [Strong constraints from COSINE-100 on the DAMA dark matter results using the same sodium iodide target](#), Sci. Adv. 7 (46) (2021) abk2699.
- [9] K. W. Kim, et al., [Tests on NaI\(Tl\) crystals for WIMP search at the Yangyang Underground Laboratory](#), Astropart. Phys. 62 (2015) 249.
- [10] G. Adhikari, et al., [Initial Performance of the COSINE-100 Experiment](#), Eur. Phys. J. C 78 (2) (2018) 107.
- [11] B. Suerfu, et al., [Growth of Ultra-high Purity NaI\(Tl\) Crystal for Dark Matter Searches](#), Phys. Rev. Research 2 (2020) 013223.
- [12] K. Fushimi, et al., [Development of highly radiopure NaI\(Tl\) scintillator for PICOLON dark matter search project](#), PTEP 2021 (4) (2021) 043F01.

- [13] J. Amare, et al., [Assessment of backgrounds of the ANAIS experiment for dark matter direct detection](#), *Eur. Phys. J. C* 76 (2016) 429.
- [14] G. Adhikari, et al., [Three-year annual modulation search with COSINE-100](#), *Phys. Rev. D* 106 (2022) 052005.
- [15] J. Amare, et al., [Annual Modulation Results from Three Years Exposure of ANAIS-112](#), *Phys. Rev. D* 103 (10) (2021) 102005.
- [16] R. Bernabei, et al., [New limits on WIMP search with large-mass low-radioactivity NaI\(Tl\) set-up at Gran Sasso](#), *Phys. Lett. B* 389 (4) (1996) 757.
- [17] J. I. Collar, [Quenching and channeling of nuclear recoils in NaI\(Tl\): Implications for dark-matter searches](#), *Phys. Rev. C* 88 (3) (2013) 035806.
- [18] J. Xu, et al., [Scintillation efficiency measurement of Na recoils in NaI\(Tl\) below the DAMA/LIBRA energy threshold](#), *Phys. Rev. C* 92 (2015) 015807.
- [19] H. W. Joo, et al., [Quenching factor measurement for NaI\(Tl\) scintillation crystal](#), *Astropart. Phys.* 108 (2019) 50.
- [20] R. Bernabei, et al., [Further results from DAMA/LIBRA-phase2 and perspectives](#), *Nucl. Phys. Atom. Energy* 22 (4) (2021) 329.
- [21] G. Adhikari, et al., [Searching for low-mass dark matter via Migdal effect in COSINE-100](#), *Phys. Rev. D* 105 (2022) 042006.
- [22] J. Choi, et al., [Exploring coherent elastic neutrino-nucleus scattering using reactor electron antineutrinos in the NEON experiment](#), *Eur. Phys. J. C* 83 (2023) 226.
- [23] J. Choi, et al., [Improving the light collection using a new NaI\(Tl\) crystal encapsulation](#), *Nucl. Instrum. Meth. A* 981 (2020) 164556.
- [24] S. Agostinelli, et al., [Geant4—a simulation toolkit](#), *Nucl. Instrum. Meth. A* 506 (2003) 250.

- [25] R. Saldanha, et al., [Model independent approach to the single photo-electron calibration of photomultiplier tubes](#), Nucl. Instrum. Meth. A 863 (2017) 35.
- [26] H. Lee, et al., [First limit on WIMP cross section with low background CsI\(Tl\) crystal detector](#), Phys. Lett. B 633 (2) (2006) 201.
- [27] J. Moyal, [XXX. Theory of ionization fluctuations](#), The London, Edinburgh, and Dublin Philosophical Magazine and Journal of Science 46 (374) (1955) 263–280.
- [28] G. D’Agostini, [A multidimensional unfolding method based on Bayes’ theorem](#), Nucl. Phys. Atom. Energy 362 (2) (1995) 487.
- [29] F. Sutanto, et al., [Production and suppression of delayed light in NaI\(Tl\) scintillators](#), Phys. Rev. D 107 (2023) 032010.
- [30] J. Cherwinka, et al., [Measurement of muon annual modulation and muon-induced phosphorescence in NaI\(Tl\) crystals with DM-Ice17](#), Phys. Rev. D 93 (2016) 042001.
- [31] G. Adhikari, et al., [The COSINE-100 data acquisition system](#), J. Instrum. 13 (09) (2018) P09006.
- [32] G. Adhikari, et al., [Lowering the energy threshold in COSINE-100 dark matter searches](#), Astropart. Phys. 130 (2021) 102581.
- [33] M. Tanabashi, et al., [The Review of Particle Physics](#), Phys. Rev. D 98 (2018) 030001.
- [34] G. Adhikari, et al., [An experiment to search for dark-matter interactions using sodium iodide detectors](#), Nature 564 (7734) (2018) 83.
- [35] H. S. Lee, et al., [Limits on Interactions between Weakly Interacting Massive Particles and Nucleons Obtained with CsI\(Tl\) Crystal Detectors](#), Phys. Rev. Lett. 99 (2007) 091301.

- [36] S. C. Kim, et al., [New Limits on Interactions between Weakly Interacting Massive Particles and Nucleons Obtained with CsI\(Tl\) Crystal Detectors](#), Phys. Rev. Lett. 108 (2012) 181301.

Fabrication of ^{108}Cd target for the astrophysical p-process studies

Sukhendu Saha^{a,b}, Mousri Paul^{a,b}, Lalit Kumar Sahoo^{a,b}, Dipali Basak^{a,b},
Tanmoy Bar^{a,b}, Jagannath Datta^c, Sandipan Dasgupta^c, G.L.N. Reddy^d,
Chinmay Basu^a

^a*Nuclear Physics Division, Saha Institute of Nuclear Physics, 1/AF Bidhannagar,
Saltlake, Kolkata-700064, India*

^b*Homi Bhabha National Institute, Anushaktinagar, Mumbai-400094, India*

^c*Analytical Chemistry Division, Bhabha Atomic Research Centre, Variable Energy
Cyclotron Centre, 1/AF Bidhannagar, Saltlake, Kolkata-700064, India*

^d*National Centre for Compositional Characterization of Materials, BARC, ECIL Post,
Hyderabad-500062, India*

Abstract

The detailed process of preparing enriched ^{108}Cd targets on mylar and copper backing using the vacuum evaporation technique is described. These targets were employed in an experiment to measure the proton capture cross-section at energies significantly below the Coulomb barrier, for the astrophysical p-process studies [1][2]. Due to the low melting point and high vapor pressure of cadmium, some adjustments were implemented in the Telemark multipocket e-beam setup. The target thickness was determined through the measurement of alpha particle energy loss from a triple alpha source and also by RBS measurements. The thickness of the ^{108}Cd films varies between 290 to 660 $\mu\text{g}/\text{cm}^2$, with a non-uniformity of approximately 10%. X-ray Photoelectron Spectroscopy (XPS) and X-ray Fluorescence (XRF) analyses were conducted to examine the presence of impurities and to assess surface morphology, phase, and chemical composition.

Keywords:

p-nuclei, vacuum evaporation, RBS, XPS, XRF

1. Introduction

In essence, a laboratory-based nuclear reaction is characterized by the acceleration of mono-energetic particles, referred to as projectiles, which are directed towards a target system consisting of other elements, which can take the form of foil, pellet, or gas system. The resulting products from this interaction are then detected using specialized detectors.

Effective target preparation plays a pivotal role in the success of nuclear reaction cross-section measurements, with critical considerations of purity, composition, thickness, and uniformity. In the context of astrophysical reactions, where reaction cross-sections are of the order of nano-barns to picobarns, the use of thin and enriched targets becomes essential for accurate cross-section measurements [3][4].

Nuclear reaction measurements can be categorized as either online or offline, depending on the resulting product nuclei and the specific measurement objectives. Online experiments, requiring charge particle measurements, necessitate a thin target with a thickness of approximately 10-100 $\mu\text{g}/\text{cm}^2$. For neutron or gamma measurements, thicker targets of several hundreds of $\mu\text{g}/\text{cm}^2$ to mg/cm^2 can be employed [5][6]. If the final product is radioactive with a sufficiently long half-life, typically ranging from a few minutes to days, an offline experiment can be conducted to measure the total reaction cross-section. In the case of offline measurements, it is essential for the product nuclei to remain within the target following the projectile bombardment [7]. Using a target with a catcher foil is a preferable option for these reactions as it helps minimize the loss of product nuclei.

Various methods can be employed for target preparation, including vacuum evaporation and condensation, electrodeposition, rolling, tablet pressing, and others. The selection of the target preparation technique depends on factors such as the material composition, physical form, desired target thickness, uniformity, as well as the purity and availability of the target material [5].

This paper provides a comprehensive description of the preparation of enriched ^{108}Cd deposited on a mylar ($\text{H}_8\text{C}_{10}\text{O}_4$) foil for the measurement of $^{108}\text{Cd}(p,\gamma)^{109}\text{In}$ cross-section, using the activation technique [7]. Additionally, another target consisting of enriched ^{108}Cd on a copper backing was prepared for the investigation of proton elastic scattering near the Coulomb barrier. Both targets were fabricated using vacuum evaporation and condensation method.

The purpose of preparing ^{108}Cd targets was to study Proton capture reaction $^{108}\text{Cd}(p,\gamma)$ using offline activation technique. The inverse reaction occurs in supernova known as the γ -process and the experimental determination of the cross-section of this reaction carries great importance in astrophysics [1][2][8].

2. Deposition setup

Two distinct types of targets were prepared: with depositing Cd on mylar backing, and the other on copper backing. The target fabrication process consists of two primary steps: preparing the backing material and depositing cadmium onto it. For the copper backing, a self-supporting copper layer was deposited using e-beam evaporation and condensation techniques. A commercial mylar foil, with a thickness of $14.3\ \mu\text{m}$, was used for the mylar backing.

The deposition of self-supporting copper was performed using the ‘Hind High Vacuum Pvt Ltd(HHV) Smart Coat 3.0A’ machine as shown in Figure 1. This machine is equipped with three 5cc crucible pockets, and for copper evaporation, a molybdenum crucible was employed, shown in Figure 3. It features a substrate holder positioned 22.3 cm above the crucible pocket, which is attached to a rotating disk. To monitor the thickness of the deposition, a quartz crystal was utilized, and an initial shutter was used to prevent impurities from being deposited onto the substrate. To generate the electron-beam, a tungsten filament was used, and a magnet setup guided the trajectory of the electron-beam through a 270° arc to target the sample, which was maintained at electrical ground potential. The deposited chamber was evacuated using dry roughing (backing) and turbo molecular pump.

For the deposition of cadmium onto backing materials, the ‘Telemark multipocket e-beam setup’ was employed, shown in Figure 2. A graphite crucible compatible with the machine, initially having an opening diameter of $\phi 28\ \text{mm}$, was modified to $\phi 4\ \text{mm}$ and a depth of 8 mm, using pure copper, as shown in Figure 4. A pinhole-type modification was also made to reduce the solid angle, resulting in a high-density vapor stream of cadmium. Furthermore, the substrate holder underwent modification to reduce the separation distance from 17 cm to 5 cm from the crucible pocket and was connected to a rotating disk. Notably, the quartz thickness monitor was not utilized due to the reduced separation between the substrate holder and the crucible pocket. Figure 5 shows a schematic view of the setup.

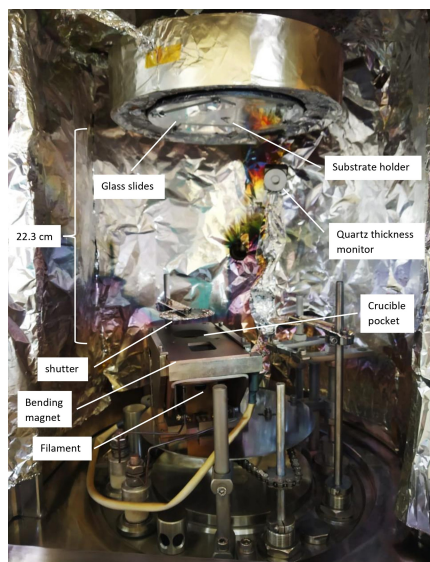


Figure 1: HHV's Smart Coat 3.0A setup

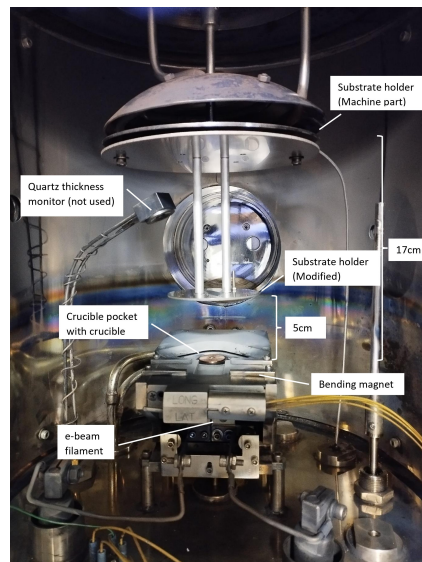


Figure 2: Telemark multipocket e-beam setup

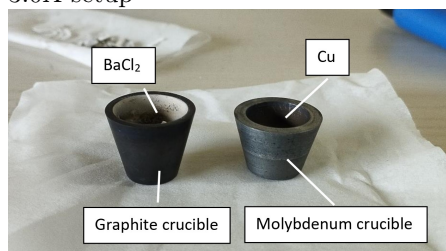


Figure 3: 5cc crucibles has been used for the deposition od $BaCl_2$ and Cu

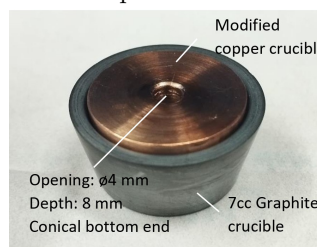


Figure 4: Modified Cu crucible used for Cd deposition

3. Target fabrication methods

Cadmium targets on self-supporting Cu foils and Cd targets on Mylar foils were fabricated using a metal ingot containing 66.3% enriched ^{108}Cd . The isotopic distribution provided by the manufacturer has been tabulated in Table 1.

Cadmium does not readily settle onto the substrate due to its high vapour pressure [5][9] and low melting point of $321^\circ C$. As a result, some changes were made to the Telemark multipocket e-beam setup.

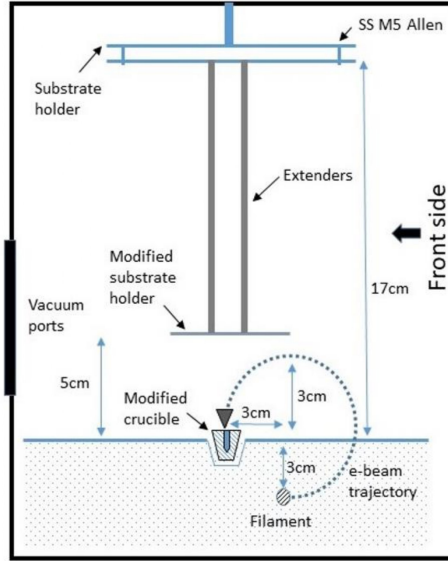


Figure 5: Schematic view of Telemark multipocket e-beam setup

Table 1: Isotopic distribution of 66.30% enriched ^{108}Cd

Isotope	^{106}Cd	^{108}Cd	^{110}Cd	^{111}Cd	$^{112,113,114,116}\text{Cd}$
Content(%)	4.6	66.3	29.1	< 0.0007	< 0.01

3.1. Deposition of Copper

The deposition of self-supporting copper foil for the target backing was conducted using the Hind High Vacuum Pvt Ltd Smartcoat 3.0A setup, shown in Figure 1. In this process, three glass slides, each measuring 76 mm \times 25 mm, were meticulously cleaned with ethanol and were used as substrate.

Before depositing the copper or any self-supporting foil, it is necessary to apply a suitable releasing agent. In this process, BaCl_2 was utilized as a water-soluble releasing agent. Initially, BaCl_2 pellets were prepared using a hydraulic press. These BaCl_2 pallets were then positioned in one graphite crucible, placed in ‘pocket 1’. Simultaneously, a separate molybdenum (Mo) crucible was used to contain a pure copper metal ingot with a purity level of 99.99%. This copper filled crucible was placed in ‘pocket 2’.

The vacuum within the chamber was about 3×10^{-6} mbar. Once the desired pressure was attained, the substrate began to rotate at a speed of 5

revolutions per minute (rpm). Subsequently, a layer of BaCl_2 was deposited, with a thickness of approximately $\sim 3 \mu\text{m}$, using e-beam evaporation. Following a one-hour cooling period of the chamber, ‘pocket 2’ was positioned at the e-beam gun point for the copper evaporation. The filament current was gradually increased until a specific deposition rate was initiated. Initially, the deposition rate was 0.1 \AA/s , when the e-beam current was 60 mA and then slowly increased to 80 mA in 2 mA increments. At this point, the deposition rate reached 2.5 \AA/s . The evaporation process continued until a certain copper thickness, approximately $0.2 \mu\text{m}$, was achieved, as monitored by a quartz crystal. Subsequently, the chamber was allowed to cool before venting.

Table 2: Melting points, current required and the setup used for the e-beam evaporation of different materials

	MP($^{\circ}\text{C}$)	Setup used	Current(mA)
BaCl_2	962	HHV’s Smart Coat 3.0A	10-15
Cd	321.1	Telemark e-beam setup	3-7
Cu	1085	HHV’s Smart Coat 3.0A	60-80

3.2. Fishing and mounting the backing on target frame

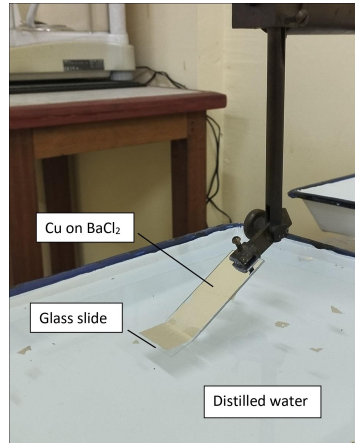


Figure 6: Floating of Cu foils

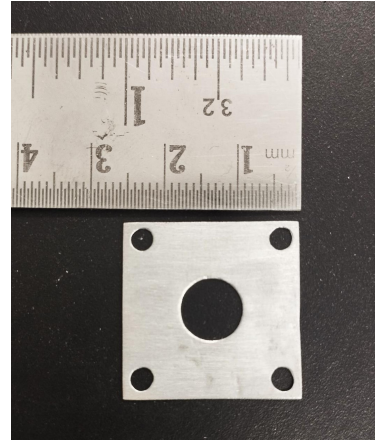


Figure 7: Target frames used to catch the Cu foils

The glass slides were carefully removed and gently immersed in a distilled water bath at an angle of $\sim 35^{\circ}$ with respect to water surface, as shown in

Figure 6. When BaCl_2 dissolved in water, the copper foil floated on the water's surface. Target frames, each with dimensions of $26 \text{ mm} \times 26 \text{ mm}$ and a central hole of diameter approximately $\phi 10 \text{ mm}$, as illustrated in Figure 7, were used to collect the Cu foil. After allowing sufficient time for the foils to dry completely, the thickness of the Cu foil was measured using the energy loss of a known triple-alpha source, detected with $60 \mu\text{m}$ Si surface barrier detectors. The details of the thickness measurement are discussed in Section 4.1.

3.3. Heat test for Mylar backing

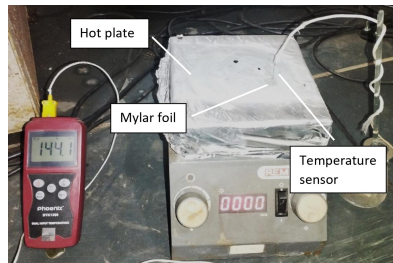


Figure 8: Heat test of Mylar foils using hotplate

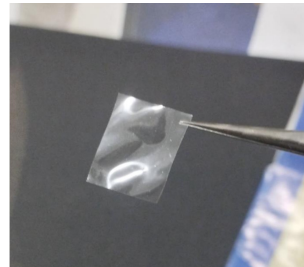


Figure 9: Deformation of Mylar foil at 155°C

While the melting point of Cd is 321°C , Mylar foil has a lower melting point of 254°C . Mylar foil can maintain its shape up to approximately 150°C . However, it starts to deform above this temperature, as depicted in Figure 8 and 9. To assess its sustainability at high temperatures, heat tests were conducted using both an electric hot plate and an infrared (IR) lamp. An electric thermometer was employed to monitor the temperature. The results indicated that the Mylar foil retained its shape for an extended period at temperatures up to 150°C . Beyond this temperature, the foil exhibited deformation.

3.4. Deposition of Cd on Cu and Mylar backing

The deposition of Cd on the backing material was carried out using the Telemark multipocket e-beam setup. For this process, a 38.7 mg sample of enriched ^{108}Cd metal was carefully placed in the modified Cu crucible, as shown in Figure 4. Prior to the deposition, the crucible and the entire chamber were meticulously cleaned using ethanol and isopropanol to ensure a pristine environment. In addition, commercial mylar foil was cut into 25

mm square shapes, and its thickness was verified by measuring the alpha particle energy loss as discussed in Section 4.1. Similarly, the thickness of the self-supporting Cu foil was measured. The mylar foil and the target frame, which contained the Cu foil, were securely attached to the modified substrate holder. This substrate holder was then affixed to the rotating disk.

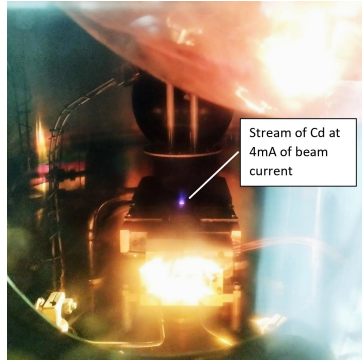


Figure 10: While evaporation of Cd using Telemark multipocket e-beam setup

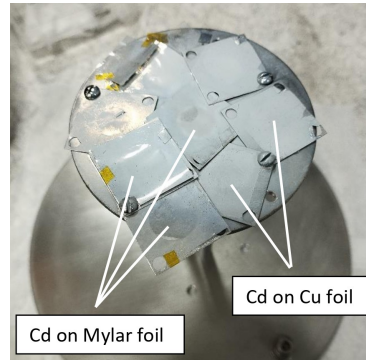


Figure 11: Deposited Cd onto the backing foil attached to the substrate holder

The chamber vacuum 6×10^{-7} mbar. To ensure a uniform Cd deposition, the substrate was set in rotation at 5 rpm. Subsequently, the tungsten filament was powered on with a voltage of 5.95 kV and a current of 17.8 A. Cd evaporation commenced at a beam current of 3 mA, at that time the chamber pressure reached $\sim 3 \times 10^{-6}$ mbar, resulting in the visible appearance of a distinctive blue stream, as depicted in Figure 10. The e^- -beam current was carefully increased to 10 mA, using 1 mA increments, over a period of 30 minutes, during which the blue stream gradually dissipated. After the deposition process was complete, the chamber was allowed to cool for 4 hours. Following this, the chamber was vented, and the targets were carefully removed from the substrate, and subsequently stored in a vacuum desiccator.

Due to the highly toxic nature of cadmium, rigorous safety precautions were meticulously observed throughout the deposition process [10].



Figure 12: Cd deposited on Cu backing and Cd deposited on Mylar backing targets

4. Characterisation of the targets

4.1. Thickness measurement using triple- α source

The target thickness was determined in two stages. Initially, the thickness of the target backing was measured prior to the deposition of cadmium. Subsequently, after the Cd deposition on the backing, the final thickness was measured. The thickness of the Cd layer was estimated by subtracting the backing thickness from the final thickness. The experimental setup and schematic diagram are presented in Figure 13.

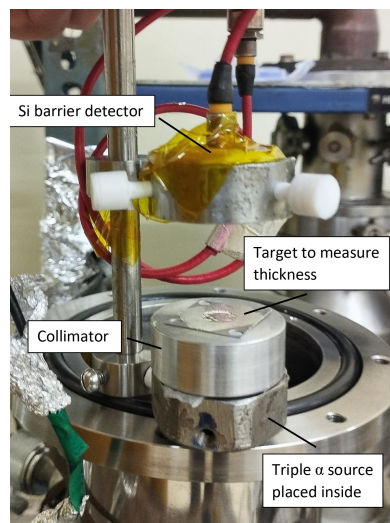


Figure 13: Thickness measurement setup by detecting alpha energy loss by target foil

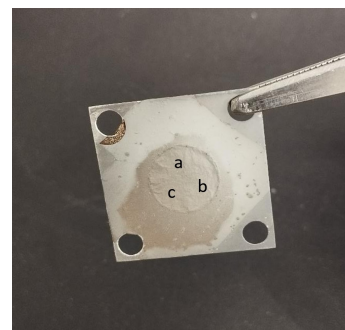


Figure 14: Thickness measurement at different positions of the target

A triple alpha source (containing ^{239}Pu , ^{241}Am and ^{244}Cm) with three distinct alpha energy lines at 5155 keV, 5486 keV, and 5806 keV [11][12], is positioned just below the collimator. The target foil is positioned above the collimator, allowing for the measurement of a specific section of the target's thickness. A $60\mu\text{m}$ Si-surface barrier detector made by EG&G ORTEC, USA was employed to detect alpha particles.

The energies of the three α particles with and without the target were measured using the silicon surface barrier detector. The shift of the energy positions (ΔE) is used to determine the thickness (Δx) of the target from the experiment,

$$\Delta x = \frac{\Delta E}{-(dE/dx)} \quad (1)$$

where $-\frac{dE}{dx}$ is the stopping power of the target at specific alpha energy, E_α . The stopping power is obtained from the code SRIM [13].

The chamber was maintained at a pressure of $\sim 10^{-5}$ mbar. Data acquisition was performed with an MCA featuring MPANT version 2.1 software, manufactured by FAST ComTec, Germany.

Thickness of the target number 'Cd3' (cadmium on mylar) and '317CuCd' (cadmium on copper) has been tabulated in Table 3.

Table 3: Thickness of Cadmium targets by α -energy loss measurement

Backing thickness (material)	α energy(keV)	α -energy loss(backing+ Cd) (keV)	$\frac{dE}{dx}$ of backing (keV/ μm)	α -energy loss in backing (keV)	α -energy loss in Cd (keV)	α -energy falling on Cd layer (keV)	$\frac{dE}{dx}$ of Cd (keV/ μm)	Thickness of Cd (μm)	avg thickness (μm)
14.1 μm (Mylar)	5155	1825.9	116.0	1635.6	190.4	3519.4	361.6	0.53	0.46
	5486	1728.8	110.9	1563.7	165.2	3922.3	343.2	0.48	
	5805	1630.2	106.6	1503.1	127.1	4301.2	327.8	0.39	
0.21 μm (Cu)	5155	205.1	372.3	78.2	126.9	5076.8	300.2	0.42	0.43
	5486	200.0	359.6	75.5	124.5	5410.5	290.2	0.43	
	5805	202.5	384.6	80.7	121.7	5724.2	281.5	0.43	

For the uniformity check, the thickness was measured at three different positions on the same target, as shown in Figure 14. These positions, labeled as (a), (b), and (c), allowed the alpha particles to pass through specific 3 mm areas of the target.

4.2. Rutherford Back-scattering Spectroscopy (RBS)

The ion beam analysis (IBA) experiments involving backscattering spectrometry (BS) were carried out using the 3 MV Tandetron (HVE, Europa) at the Surface and Profile Measurement Laboratory, NCCCM, Hyderabad. The thickness of one of the Cd-deposited targets on Mylar was determined

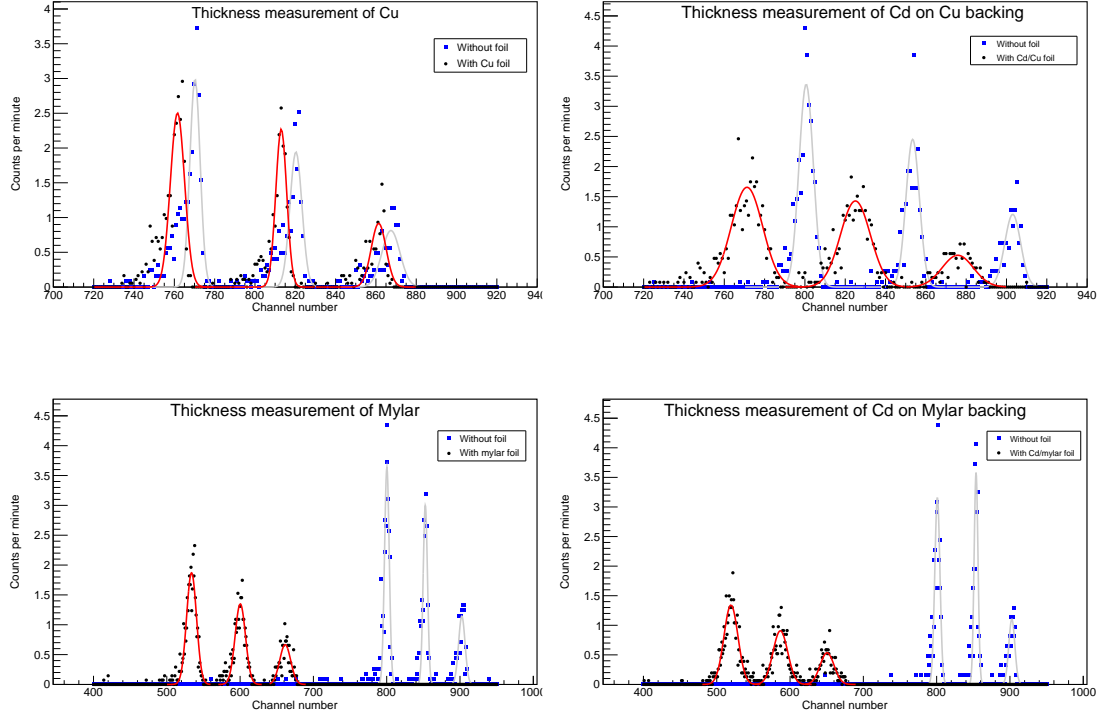


Figure 15: Thickness measurement by measuring energy loss of alpha particle, Cu foil, Cd on Cu foil, Mylar foil and Cd on Mylar foil respectively

using Rutherford Backscattering Spectroscopy (RBS). This involved the use of a 1 MeV proton beam and a 6 MeV Carbon beam, with a beam current of 4 nA.

The Backscattering (EBS) measurements involved, bombardment of the samples with a well-collimated beam of proton and carbons of energy 1 MeV and 6 MeV, respectively, with a beam current of 5 nA ($\Phi = 2.0$ mm). The scattered particles were detected at a backward angle of 170° with a Si surface barrier detector. The detector subtends a solid angle of 1.2×10^{-3} sr. Each spectrum was collected by impinging the sample with about $3.0 \mu\text{C}$ of charge, sufficient to produce statistically significant spectra. The spectra were acquired by 8K-PC based MCA. These were simulated using SIMNRA, a computer code for simulating the energy spectra of charged particles, for qualitative and quantitative analyses [14].

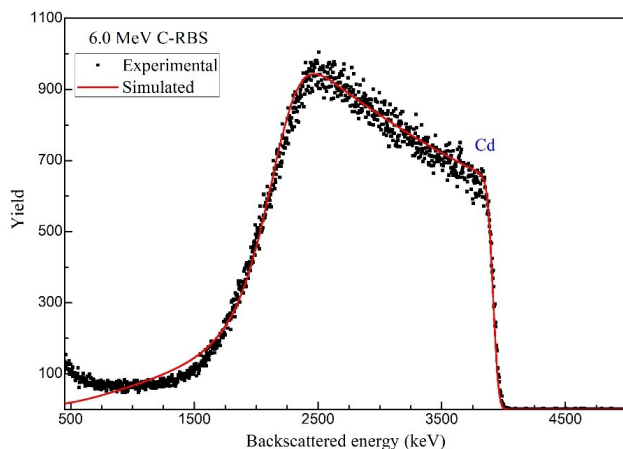


Figure 16: RBS spectrum of enriched ^{108}Cd target deposited on mylar backing

For simulation of RBS spectra using SIMNRA, following conditions were adopted: (a) simulations were continued by refining each layer composition and thickness for the best fit, (b) among the many stopping power data, we have used Ziegler-Biersack data which is more accurate and reliable as the selection of electronic stopping power data has a large influence on the shape of simulated spectra, (c) for Energy-loss straggling, Chu + Yang's theory was used. The refinement of layer composition was stopped when reduced χ^2 (the quadratic deviation between experimental and simulated data) reached less than 5.

The simulation results show that the thickness of the ^{108}Cd layer is approximately 487 nm (areal density $\sim 421 \mu\text{g}/\text{cm}^2$). The measurement come with an associated uncertainty of nearly 10%.

4.3. X-ray Photo-electron Spectroscopy (XPS)

XPS measurements were used to examine the surface chemical composition of the prepared target. For these measurements, the XPS setup provided by VSW Ltd., UK, was utilized. A base pressure of 5×10^{-10} mbar was attained with the aid of a 1250 l/s turbo molecular pump, complemented by a dry-scroll pump during the measurement process. The chamber and X-ray gun were connected to a Varian, Inc. ion pump through a Tee setup, where the X-ray gun was differentially evacuated. A monochromatic Mg K_α X-ray source with an energy of 1253.6 eV was utilized for the XPS analysis. The XPS unit comes with a twin-anode X-ray gun and a hemispherical e-analyzer

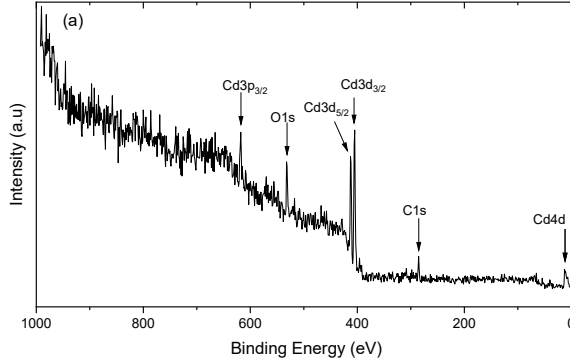


Figure 17: (a) Full survey of XPS spectra

with a radius of 150 mm. Electrons emitted from the target are extracted by a cylindrical electromagnetic lens and directed into the hemispherical analyzer's entrance slit. To capture the photoelectrons, a multichannel detection (MCD) device was used. Using a 20 eV pass energy, XPS spectra of Cd 4d, Cd 3d_{3/2}, Cd 3d_{5/2}, C 1s, and O 1s were obtained within different energy windows. The energy resolution of the XPS system was 1.88 eV, and no charge neutralizer was used throughout the measurements. The XPS spectra were analysed using the XPSpeak41 software, and the binding energy of the C 1s and O 1s peaks was utilised to calibrate the raw spectrum's energy [15][16].

4.4. X-ray Fluorescence (XRF)

The XRF (X-ray Fluorescence) technique was used for the qualitative elemental characterization of the Cd on Mylar and Cd on Cu targets. The experimental setup, built by Moxtek, USA, consists of a 4W MAGNUM X-ray source, a Si-pin detector, and a digital pulse processor. Figure 1 shows a schematic diagram. The X-ray tube is equipped with an Ag anode and a 0.25mm thick beryllium window. The Si-pin detector has a DuraBeryllium window 25 mm thick, with a detector thickness and active area of 625 μ m and 6mm², respectively. The MXDPP50 digital pulse processor, which includes a 4k channel MCA, a detector temperature controller, and a detector power supply, aided in data collecting. The SinerX software was used to control the digitizer, detector, and X-ray tube parameters [17].

The presence of Cd in both targets is confirmed by the Cd L α_1 , Cd K α_1 , and Cd β_1 lines of Cd at 3100 eV, 22180 eV and 26102 eV respectively. In the Cd on Cu backing targets, the Cu K α_1 , and Cu K β_1 of Cu are attributed

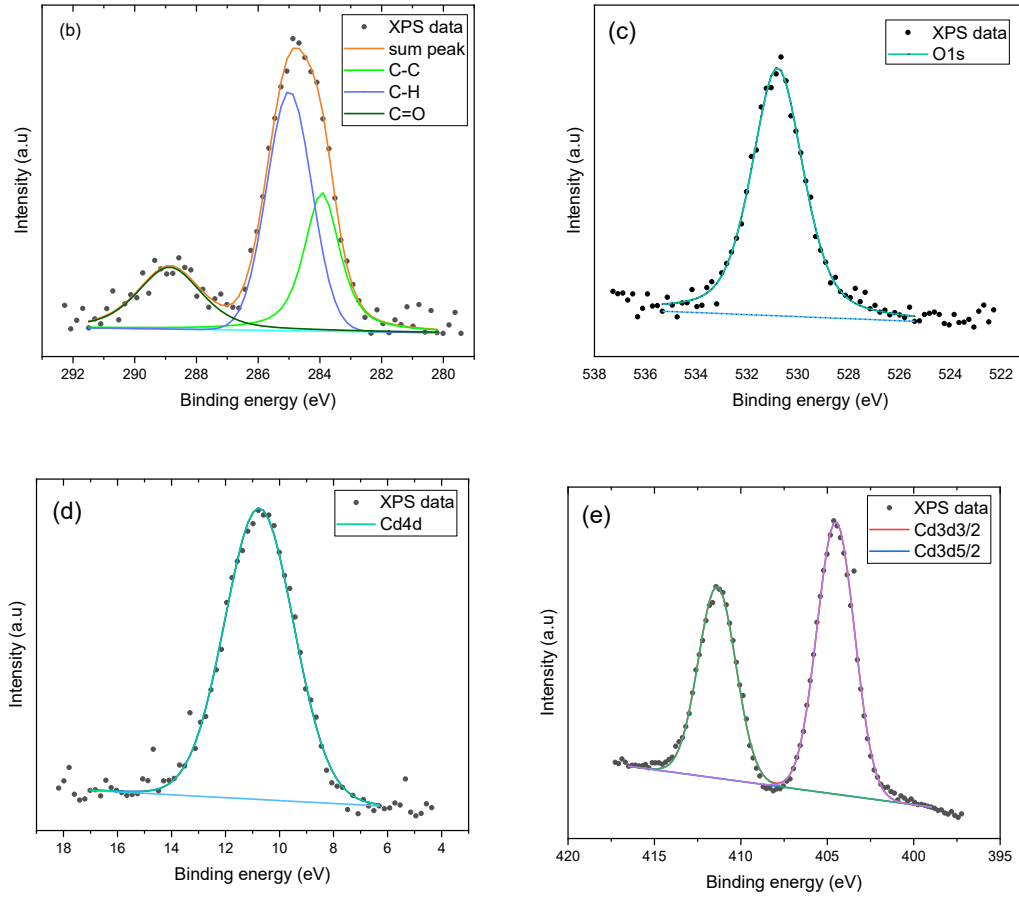


Figure 18: (b),(c) XPS spectra of C1s and O1s for the calibration of raw specrum, (d) and (e) XPS spectra of Cd4d and Cd3d5/2 respectively

to the Cu backing of the target, and no impurity of heavy mass elements are present. The Ag lines are observed due to the presence of the Ag anode in the X-ray tube. The detector was calibrated using a Cu coin, and the experiment was conducted in an on-air condition.

5. $^{108}\text{Cd}(p,\gamma)^{109}\text{In}$ reaction with prepared targets

The cross-section of $^{108}\text{Cd}(p,\gamma)^{109}\text{In}$ was determined through activation techniques. A 7 MeV proton beam was provided by the K130 cyclotron at Variable Energy Cyclotron Centre (VECC), Kolkata, India and then degraded

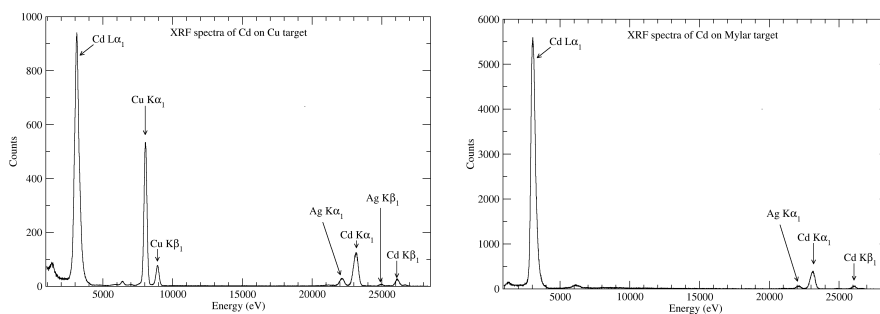


Figure 19: XRF spectra of ‘Cd on Cu’ and ‘Cd on mylar’ targets respectively. Ag $K\alpha_1$ and Ag $K\beta_1$ peaks are coming from machine parts

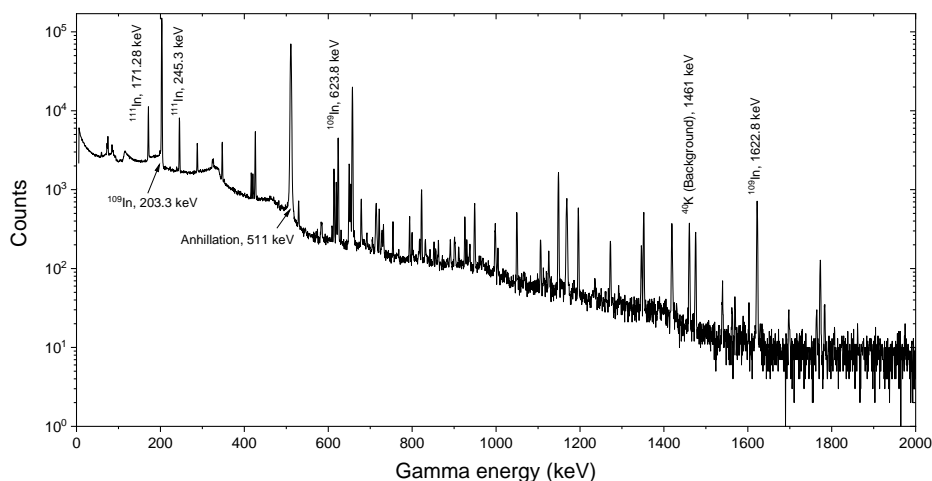


Figure 20: The offline γ -ray spectrum from Cadmium (66.3% enriched ^{108}Cd) on Mylar target irradiated by 5.19 MeV of proton beam

to 6.85 MeV to 2.27 MeV using 99.95% pure Al foils. Each target setup was irradiated for a duration of 10-15 hours at a beam current of 150 enA. Following the irradiation period, the targets were allowed to cool to minimize unnecessary gamma peaks. Subsequently, the targets were placed in front of an HPGe detector at the Analytical Chemistry Division, BARC at VECC, Kolkata, India for gamma counting. Throughout the irradiation, a constant flow of chilled water was maintained for target cooling. After irradiation, no damage was observed on the targets.

Figure 20 illustrates the spectrum of offline gamma rays measured from

target number Cd3 (Cadmium on Mylar) irradiated by a 5.19 MeV proton beam for 6 hours and 7 minutes. The γ -rays were recorded for 1003 seconds after a 2-hour cooling time. The target comprises 29.1% of ^{110}Cd . In the reaction $^{110}\text{Cd}(p,\gamma)^{111}\text{In}$, ^{111}In produces γ -rays at 171.28 keV and 245.35 keV with relative intensities of 90.7% and 94.1%, respectively. Additionally, from the reaction $^{108}\text{Cd}(p,\gamma)^{109}\text{In}$, ^{109}In generated predominantly emits γ -rays with relative intensities greater than 0.2%, with the most prominent ones being at 203.3 keV and 623.8 keV, having relative intensities of 74.2% and 5.64% followed by β^+ decay with a half-life of 4.159 hours [2]. Other gamma rays originate from natural radioactive isotopes.

6. Summary and conclusion

This paper presents the fabrication method of ^{108}Cd on Mylar and ^{108}Cd on copper backing. The optimization process involved adjusting parameters such as the distance between the crucible and substrate holder, the dimensions of the crucible opening, the e-beam current, and the evaporation time. Ultimately, 38.7 mg of 66.3% enriched ^{108}Cd was utilized with a beam current ranging from 3 to 7 mA and a deposition time of 30 minutes. The separation between the crucible and substrate holder was set at 5 cm. The thickness of the cadmium targets was determined through α -energy loss measurements and validated by RBS measurements. We utilized eight different Cadmium targets with thicknesses ranging from 0.33 μm (surface density, 288 $\mu\text{g}/\text{cm}^2$) to 0.76 μm (656 $\mu\text{g}/\text{cm}^2$) on a Mylar backing during the $^{108}\text{Cd}(p,\gamma)^{109}\text{In}$ reaction measurement.

The non-uniformity of the target thickness was observed to be 10%. Adjustments to the thickness of the targets can be made by using an appropriate amount of material during the evaporation process. Alternatively, other processes, such as electrodeposition, can be used for the fabrication of cadmium targets [18][19][20].

The absence of impurities was confirmed through RBS measurements. XPS and XRF measurements provided insights into the quality of the prepared targets, evaluating both surface morphology and bulk composition. The targets exhibited no significant elemental impurities, apart from the presence of carbon, hydrogen and oxygen.

7. Acknowledgements

The authors express their gratitude to Prof. Supratic Chakraborty of the Surface Physics and Material Science division (SPMS), Saha Institute of Nuclear Physics (SINP), Kolkata, India, for their assistance in preparing the target using the Telemark multipocket e-beam facility. Special thanks to Mr. Abhilash S.R. from the Inter-University Accelerator Centre, New Delhi, India, and Gy. Gyurky from ATOMKI, Hungary, for insightful discussions regarding the fabrication of Cadmium. The authors acknowledge Mr. Debraj Dey and Mr. Gautam Sarkar from SPMS division, SINP, for their assistance with XPS measurements. The authors thank to Mr. Arkabrata Gupta from the Indian Institute of Engineering Science and Technology, Shibpur, India, for helping with the XRF measurements. The SINP workshop group is appreciated for their contributions to the setup modifications. Sukhendu Saha expresses thanks to the Council of Scientific & Industrial Research (CSIR), India, for financial support through Senior Research Fellowship (File no: 09/489(0119)/2019-EMR-I).

References

- [1] T. Rauscher, N. Dauphas, I. Dillmann, C. Fröhlich, Z. Fülöp, G. Gyürky, Constraining the astrophysical origin of the p-nuclei through nuclear physics and meteoritic data, *Reports on Progress in Physics* 76 (2013) 066201.
- [2] G. Gyürky, G. Kiss, Z. Elekes, Z. Fülöp, E. Somorjai, 106,108 cd (p, γ) 107,109 in cross-sections for the astrophysical p-process, in: *The 2nd International Conference on Nuclear Physics in Astrophysics: Refereed and selected contributions Debrecen, Hungary May 16–20, 2005*, Springer, 2006, pp. 141–144.
- [3] C. Broggini, D. Bemmerer, A. Guglielmetti, R. Menegazzo, Luna: nuclear astrophysics deep underground, *Annual Review of Nuclear and Particle Science* 60 (2010) 53–73.
- [4] C. Iliadis, *Nuclear physics of stars*, John Wiley & Sons, 2015.
- [5] A. Stolarz, Target preparation for research with charged projectiles, *Journal of radioanalytical and nuclear chemistry* 299 (2014) 913–931.

- [6] W. R. Leo, *Techniques for nuclear and particle physics experiments: a how-to approach*, Springer Science & Business Media, 2012.
- [7] G. Gyürky, Z. Fülöp, F. Käppeler, G. G. Kiss, A. Wallner, The activation method for cross section measurements in nuclear astrophysics, *The European Physical Journal A* 55 (2019) 41.
- [8] G. Gyurky, G. Kiss, Z. Elekes, Z. Fulop, E. Somorjai, A. Palumbo, J. Gorres, H. Lee, W. Rapp, M. Wiescher, et al., Alpha-induced cross sections of ^{106}Cd for the astrophysical p-process, arXiv preprint nucl-ex/0605034 (2006).
- [9] H. Maier, H. Friebel, D. Frischke, R. Grossmann, Special techniques of nuclear target preparation, *Nuclear Instruments and Methods in Physics Research Section A: Accelerators, Spectrometers, Detectors and Associated Equipment* 282 (1989) 128–132.
- [10] Cadmium safety guideline, ??? URL: https://www.teck.com/media/Cadmium_Metal_SDS.pdf.
- [11] C. Yalcin, Thickness measurement using alpha spectroscopy and srim, in: *Journal of Physics: Conference Series*, volume 590, IOP Publishing, 2015, p. 012050.
- [12] L. K. Sahoo, D. Basak, A. K. Mondal, B. Satpati, S. K. Karan, C. Basu, The preparation of ^{7}Li target for reactions involving ^{7}Li target, *Vacuum* 212 (2023) 112055.
- [13] J. F. Ziegler, M. D. Ziegler, J. P. Biersack, Srim—the stopping and range of ions in matter (2010), *Nuclear Instruments and Methods in Physics Research Section B: Beam Interactions with Materials and Atoms* 268 (2010) 1818–1823.
- [14] M. Mayer, *Simnra user’s guide* (1997).
- [15] G. Greczynski, L. Hultman, X-ray photoelectron spectroscopy: towards reliable binding energy referencing, *Progress in Materials Science* 107 (2020) 100591.
- [16] S. R. Achary, S. Agouram, J. F. Sánchez-Royo, M. C. Martínez-Tomás, V. Muñoz-Sanjosé, One-step growth of isolated cdo nanoparticles on

- r-sapphire substrates by using the spray pyrolysis methodology, RSC Advances 4 (2014) 23137–23144.
- [17] A. Gupta, G. Saha, S. Sarkar, A. Bisoi, Characterization of x-ray detection system and its application in the search of contaminations in nuclear astrophysics targets, in: Proceedings of the DAE Symp. On Nucl. Phys, volume 62, 2017, p. 1052.
- [18] P. Scholz, F. Heim, J. Mayer, C. Münker, L. Netterdon, F. Wombacher, A. Zilges, Constraints on the α + nucleus optical-model potential via α -induced reaction studies on ^{108}Cd , Physics Letters B 761 (2016) 247–252.
- [19] T. Bar, D. Basak, S. Saha, C. Basu, Preparation of targets by electro-deposition, in: Proceedings of the DAE-BRNS symposium on nuclear physics. V. 66, 2022.
- [20] R. Biswas, S. Abhilash, G. Umapathy, S. A. Khan, S. Nath, Fabrication and characterization of thin ^{116}Cd target films for fusion measurements, Nuclear Instruments and Methods in Physics Research Section A: Accelerators, Spectrometers, Detectors and Associated Equipment 1046 (2023) 167696.

Cluster Scanning: a novel approach to resonance searches

I. Oleksiyuk,^{a,b} J. A. Raine,^a M. Krämer,^c S. Voloshynovskiy,^b T. Golling^a

^a*Département de Physique Nucléaire et Corpusculaire, University of Geneva, 1211 Geneva, Switzerland*

^b*Centre Universitaire d'Informatique, University of Geneva, 1211 Geneva, Switzerland*

^c*Institute for Theoretical Particle Physics and Cosmology, RWTH Aachen University, 52074 Aachen, Germany*

E-mail: ivan.oleksiyuk@unige.ch, john.raine@unige.ch,
mkraemer@physik.rwth-aachen.de, svyatoslav.voloshynovskyy@unige.ch,
tobias.golling@unige.ch

ABSTRACT: We propose a new model-independent method for new physics searches called Cluster Scanning. It uses the k-means algorithm to perform clustering in the space of low-level event or jet observables, and separates potentially anomalous clusters to construct a signal-enriched region. The invariant mass spectra in these two regions are then used to determine whether a resonant signal is present. A pseudo-analysis on the LHC Olympics dataset with a Z' resonance shows that Cluster Scanning outperforms the widely used 4-parameter functional background fitting procedures, reducing the number of signal events needed to reach a 3σ significant access by a factor of 0.61. Emphasis is placed on the speed of the method, which allows the test statistic to be calibrated on synthetic data.

Contents

1	Introduction	1
2	Dataset	3
2.1	Jet images	3
3	Method	4
3.1	Bump hunt	4
3.1.1	Signal enrichment	4
3.1.2	Background estimation	5
3.1.3	Test Statistic definition and calibration	5
3.1.4	Significance evaluation	6
3.2	Cluster scanning	6
3.3	Discussion	10
3.4	Idealised CS	11
4	Results	12
5	Conclusions and outlook	14
A	Idealised fit and n-parameter fit pseudo-analysis	15
B	Sparsity of the jet images	17
C	Hyperparameter selection and motivation	17
D	Gaussianity of cluster scanning bin entries	20
E	Outlier robust estimators	20
F	Calibration distributions	21

1 Introduction

The Standard Model (SM) is the current apex of theoretical physics, describing the electromagnetic, weak and strong interactions with unparalleled precision. Unfortunately, it is still far from complete, as several phenomena remain unexplained. In order to create a “theory of everything”, one would not only need to combine the SM with general relativity, but also provide an explanation for many other issues, including the existence of neutrino masses, the origin of the matter-antimatter asymmetry, and most importantly, the origin of dark matter. To solve these problems, researchers are collaborating to formalise new

theories, design, build and carry out new experiments, as well as simulate and analyze research data.

One of the most renowned experimental facilities, the Large Hadron Collider (LHC) was constructed with the purpose of testing the SM in the high energy regime. The last elementary particle predicted by the SM, the Higgs boson, was discovered in 2012 [1, 2]. Since then, LHC research has shifted towards precision measurements and searches for beyond the Standard Model (BSM) effects.

Many extensions of the SM imply the existence of as yet undiscovered massive particles, often associated with proposed new symmetry groups. If a new particle has a narrow decay width, the straightforward method is to search for a resonant peak in the spectrum of a mass-like observable, such as the invariant mass of a dijet event. However, such a bump hunt is not completely free of assumptions. Often complex analytical functions need to be chosen to model the background distribution, with the possibility to introduce spurious signals and varying sensitivity under the assumption of different functional forms. Furthermore, additional observables or fiducial cuts need to be chosen and optimised to enhance sensitivity in the case where potential signal yields are low, causing searches to become more model-specific.

Over the past decade, machine learning-based algorithms have become increasingly popular for solving a multitude of problems. Deep learning, in particular, has gained popularity for various tasks, with large neural networks being utilised. For example, many methods were implemented to perform anomaly detection (AD) tasks in various industries. Some of these AD methods have been repurposed and extended to support BSM searches [3–79] (see Refs. [80–83] for a comparison of various ML assisted BSM methods and Refs. [84, 85] for a comparison of weakly supervised and unsupervised approaches). The ATLAS collaboration produced the first experimental results for such searches applied to experimental data using weakly supervised methods [86] and unsupervised ML anomaly detection methods [74, 87]. However, these efforts have not observed any significant deviations from the SM expectation.

Many AD approaches rely on the assumption that any new signal would form a set of outliers. However, in a bump hunt the assumption is instead that any new signal would be localised in some feature space, in particular in an invariant mass spectrum. Weakly supervised approaches, on the other hand, aim to enhance the sensitivity by applying a cut on a classifier trained directly on the data. However, in both instances the same bump hunt restrictions apply with either functional forms or input observables impacting the sensitivity to a model.

In this work we introduce a new data-driven method, cluster scanning (CS), which builds on the foundations of the bump hunt but addresses several limitations. By leveraging more information from the event CS is able to enhance sensitivity to potential signals without enforcing any model specific assumptions, and can also provide a direct estimate of the background distribution. The proposed approach complements existing techniques and is designed to be computationally efficient.

The paper is structured as follows. In Section 2, we briefly describe the LHCO R&D dataset [88], commonly used to benchmark the performance of anomaly detection tech-

niques, and introduce our data preprocessing steps. Section 3 touches on the general topic of bump-hunting strategies in the literature, introduces the novel CS method, and discusses similarities and differences between them. In Section 4 we provide the results of applying CS in an anomaly search. Finally, we draw conclusions in Section 5.

2 Dataset

The LHCO R&D dataset consists of one million background Standard Model dijet events (also subsequently referred to as QCD) and 100 000 signal BSM $Z' \rightarrow XY$ events, where massive particles with $m_X = 500$ GeV and $m_Y = 100$ GeV decay into quark-antiquark pairs. The resonance itself has a mass of $m_{Z'} = 3.5$ GeV. This anomaly model is discussed in detail in Ref. [89].

All the events were produced using PYTHIA 8.219 [90] and DELPHES 3.4.1 [91–93] using default settings. The jets were clustered using an anti- k_T algorithm [94] with $R = 1$ using FASTJET [95] with a `python` interface provided through the `pyjet` library in SCIKIT-HEP [96]. Jets are required to have $p_T > 1.2$ TeV and fall within $|\eta| < 2.5$.

2.1 Jet images

In addition to the di-jet invariant mass (m_{jj}) of the event, used in a bump hunt, we extract additional information from the image representations of the two jets. This allows for a more model agnostic approach than selecting specific jet substructure observables. The jet images are processed following a prescription similar to that used in Ref. [6, 97–99] from the η , ϕ and p_T of the jet constituents. Individual jet images are centred, rotated, and flipped in order to provide a consistent input to a convolutional neural network, reducing the number of symmetries the ML method would need to learn.

The jet images are cropped to $[-0.8, 0.8] \times [-0.8, 0.8]$ in $\eta - \phi$ space relative to the jet centre, binned with a 40×40 pixel grid, and normalised such that the sum of all pixels is equal to one. Fig. 1 shows the average jet images for QCD background, and the separate averages of all lighter (mostly Y) and heavier (mostly X) jets in each Z' event.

Despite being used in many applications, the jet image representation has two main drawbacks, namely the sparsity of non-zero pixels (see app. B) and the imbalance in the magnitudes of their intensities. This is particularly problematic for approaches that depend on the L_2 (Euclidean) distance. We address both of these problems with the solutions introduced in Refs. [57, 100].

To take the soft constituents into account, which have intensities orders of magnitudes lower than hard constituents, we apply a non-linear scaling to all pixels of $I_{ij} \rightarrow I_{ij}^\gamma$. To address sparsity we convolve (smear) the whole image with a two-dimensional Gaussian kernel with an isotropic standard deviation σ_k . We find that using a value of $\gamma = 0.5$ for the pixel scaling alongside $\sigma_k = 1$ for the Gaussian kernel provides an adequate solution to both issues without excessive impact on the structure of the jets.

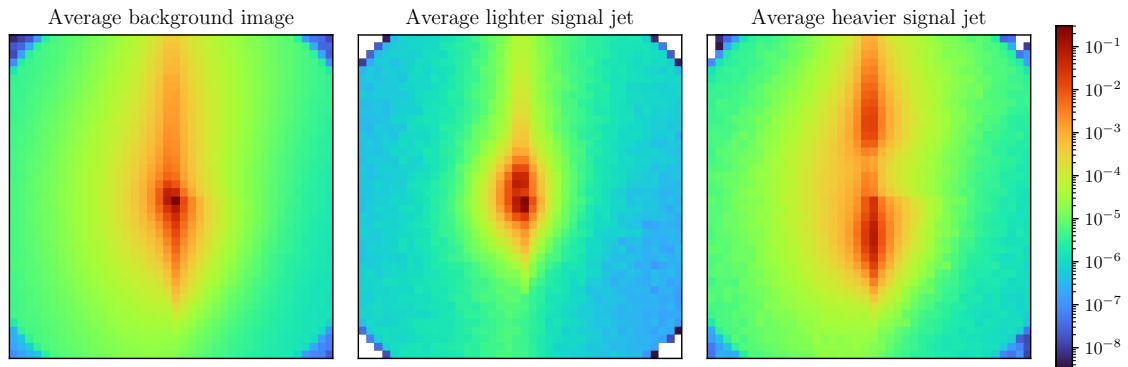


Figure 1: From left to right: average of all 2M available QCD jet images, average image of all 100K lighter jets in a Z' event and average image of all 100K heavier jets in a Z' event before smearing and pixel scaling.

3 Method

3.1 Bump hunt

The bump hunt approach is a standard method used to search for excesses over a non-resonant background in HEP (high-energy physics) data. This method usually follows four main steps that we briefly discuss below. Each of these steps is a complex topic in itself with several different approaches in the literature, thus for our study, we choose only simplified and basic approaches.

3.1.1 Signal enrichment

Signal enrichment, in general, refers to the selection of a subset of experimental data in such a manner that the fraction of signal events in it is increased compared to the initial sample. Most often, this is done by cutting out a region of the observable space where the signal is expected to be abundant compared to the rest of the space, typically using a theoretical model of the signal of interest.

These approaches, despite being sensitive to specific signal processes, make the search less model-agnostic and are ill-suited for general anomaly detection searches. Alternatively, one can hope to define a signal-rich region of the experimental data using a plethora of unsupervised ML (machine learning) techniques, which are expected to provide enhanced sensitivity over a wider range of potential signal processes.

In our particular example of LHCO data, we choose to explore a wide, smoothly falling region of the spectrum of dijet events with invariant dijet mass m_{jj} from 3000 GeV to 4600 GeV. We choose this lower bound to avoid the turn on curve of the mass distribution, resulting from the jet trigger, and the upper bound is selected to remain in a region with relatively high statistics, so that we work in the region where the fit functions from Subsection 3.1.2 are applicable. This interval contains, in total, around 380,000 QCD events and nearly all Z' events. We divide this region into 16 non-intersecting bins with 100 GeV width each, as in Ref. [101, 102].

3.1.2 Background estimation

To perform a hypothesis test, one must first postulate a null hypothesis, which in counting experiments takes form of the expected background coming from the Standard Model processes. Often the background prediction relies on a theoretical basis to calculate the cross sections of the hard process and a simulation to account for detector response and measurement uncertainties. Still there are a number of searches where theory and simulation cannot provide a reliable background estimate. In these cases the background has to be estimated from the data itself in an empiric manner, using some general assumptions.

In dijet-like searches a background is often estimated by fitting a function of the form

$$f(x) = p_1(1-x)^{p_2}x^{p_3+p_4\ln(x)+p_5\ln(x^2)} \quad (3.1)$$

to a smoothly falling part of the dijet mass distribution [103–119], where $x = m_{jj}/\sqrt{s}$. This function is referred to as the “ n -parameter dijet fit function”, where n is the number of nonzero free parameters p_i used in the function. Despite being a good fit to the simulated data, this functional form is still an empirical assumption and thus is subjects to a systematic error. Furthermore, after applying some selection criteria on the events which could be correlated with m_{jj} , this function may no longer well describe the resulting distribution.

More advanced methods of fitting, such as the Sliding Window Fit (SWIFT) [120] and the ABCD method used in [121, 122] are other methods that reduce the assumption of a functional form but introduce their own assumptions instead. However, due to the simplicity and wide use of the n -parameter fit function, we choose to use global 3-parameter and 4-parameter function fits as the benchmark analysis strategy. Further details of the (pseudo-)analysis on the LHCO R&D data performed using these background estimates are given in Appendix A. To access the upper bound on the performance of all background estimation methods, we use the underlying background distribution as an idealised fit, i.e. a fit with no systematic error. The (pseudo-)analysis using this is also described in Appendix A.

3.1.3 Test Statistic definition and calibration

There are several ways to calculate a global test statistic for two spectra. In HEP one of the more popular tests in model agnostic searches, called BumpHunter [123], relies on the maximal local significance (MLS) as the test statistic, where it is computed using a range of different windows over the spectrum. One of the benefits of the MLS test statistic is its simplicity and that it is well suited for signals that give rise to narrow, localised resonances. Here the MLS is applied to the binned m_{jj} distributions of the data. Given a set $\mathcal{B} = \{b_1, \dots, b_{n_{\text{bins}}}\}$ of non-intersecting bins with $N_{\text{sig},b}$ events or jets from the signal-rich (experimental) distribution and $N_{\text{bkg},b}$ events or jets from the background estimation, the MLS can be written as

$$\text{MLS} = \max_{b \in \mathcal{B}} Z_b = \max_{b \in \mathcal{B}} (\text{CDF}_{\mathcal{N}(0,1)}^{-1}(\text{CDF}_{\text{Poisson}(N_{\text{bkg},b})}(N_{\text{sig},b}))), \quad (3.2)$$

where CDF is the cumulative density function of the respective distribution. In equation 3.2 only overdensities are taken into account, i.e. $Z_b > 0$ only for $N_{\text{sig},b} > N_{\text{bkg},b}$ as we are searching for a resonance.

For bins with $N_{\text{sig}/\text{bkg},b} \gg 1$ one can approximate the Poisson distribution with a normal distribution $\mathcal{N}(N_{\text{sig}/\text{bkg},b}, \sqrt{N_{\text{sig}/\text{bkg},b}})$. Equation 3.2 then reduces to a much simpler form

$$\text{MLS} = \max_{b \in \mathcal{B}} Z_b = \max_{b \in \mathcal{B}} \frac{N_{\text{bkg},b} - N_{\text{sig},b}}{\sqrt{N_{\text{bkg},b}}}. \quad (3.3)$$

Although some test statistics, like χ^2 , have well-known distributions, other more unusual test statistics, like the BumpHunter test statistic, require calibration. This is commonly done by modelling its distribution using Monte Carlo simulation.

Moreover, as systematic uncertainties arise from the definition of a signal region selection and the background estimate, this calibration should be performed even in the case where the distribution is known a priori. The calibration for the BumpHunter test statistic is performed in Ref. [123] by running pseudo-experiments in which the counts in each bin are varied according to Poisson's law. This can be extended to higher dimensions by resampling the background events with bootstrapping. By calculating the test statistic for each of our bootstrapped background-only pseudo-experiments, we obtain the distribution of the test statistic in the background-only hypothesis. To ensure good modelling of the tail of the test statistic distribution, which corresponds to large significance values in the presence of signal, a large number of pseudo-experiments is required.

3.1.4 Significance evaluation

To obtain a calibrated p -value for a given value of the test statistic t , one counts the number of background only pseudo-experiments exceeding this value $N_{>t}$ and divides it by the total number of pseudo-experiments done, N_{tot} .

The (one-sided) significance is computed using the inverse cumulative density function of the normal distribution $Z = \text{CDF}_{\mathcal{N}(0,1)}^{-1}(1 - p\text{-value})$.

In the case of $N_{>t} = 0$ arising from the limited number of pseudo-experiments, we instead set a lower bound:

$$p < \frac{1}{N_{\text{tot}}}, \quad Z > \text{CDF}_{\mathcal{N}(0,1)}^{-1}\left(1 - \frac{1}{N_{\text{tot}}}\right). \quad (3.4)$$

For every experiment with added signal events, we still bootstrap the background (for consistency) and combine it with a given number of signal events chosen at random from 100,000 signal events (around 5% of events fall outside of the evaluation region). Due to statistical fluctuations we also perform several pseudo-experiments in the signal enriched case in order to obtain a robust estimate of the significance for each level of signal doping.

3.2 Cluster scanning

In this section we present a novel approach called Cluster Scanning, which follows the same bump hunting scheme, but relies on a distinct set of assumptions than the commonly

employed methods and thus has several favorable characteristics. Our approach can be divided into several key steps given below, with the hyperparameters chosen in order to search for narrow resonances in the m_{jj} spectrum of the LHC0 R&D data. The motivation for these hyperparameters in each step and the argumentation on how to choose them for a different application case is given in App. C.

Training region selection: We select a narrow m_{jj} window [3000, 3100] GeV for training of the k-means algorithm. This window contains 56,486 original background events. In this publication, we focus on relatively small signal injections that include only 5% or less of the total number of Z' signals available. Therefore the training region is expected to contain 89 signal events or less, which can be regarded as negligible. Despite observing a qualitative improvement in performance in case the training region matches the resonant peak and thus has a larger portion of signals events involved in clustering, in an actual analysis the position of the peak will be unknown, thus we choose to discuss a more representative case given here, when the training region happens to be in the tail of the signal peak and thus has a negligible number of signal events.

K-means Clustering: We apply a mini-batch k -means clustering algorithm with $k = 50$ implemented in the SCIKIT-LEARN [124] library, with a batch size of 2048 on the set containing jet images of the leading two jets from each event in this m_{jj} window. The mini-batch implementation is chosen due to its computational speed. The seeding of the cluster centroids is performed using the K-MEANS++ prescription described and motivated in Ref. [125].

Cluster Spectra: After performing the fit of k -centroids to the data in the training region, we fix the centroid positions and evaluate how many jet images from each of the 16 m_{jj} bins of the evaluation region, defined in Subsection 3.1.1, fall into each of the k clusters $N_{i,b}$ where $i \in \{1\dots k\}$, $b \in \{1\dots n_{bins}\}$. Fig. 2 shows the resulting 50 normalised cluster spectra $N_{i,b}/\sum_b(N_{i,b})$ for one pseudo-experiment with signal injection.

Per bin standardisation: We note that in each bin the normalised cluster spectra follow an approximately normal distribution with several outliers from the anomalous clusters (see discussion in App. D). Therefore we standardise the normalised cluster spectra in each bin using outlier robust estimators (described in App. E) for mean and standard deviation with an outlier factor of 0.2. Here we make the assumption that the majority of the signal is located in a small number of clusters, and the rest of the clusters are signal depleted. Figure 3 shows the cluster spectra from Fig. 2 after normalising with the outlier robust estimator.

Selecting anomalous clusters: Utilising the assumption that the signal is localised in m_{jj} , we select potentially signal-rich cluster spectra as those with a deviation of more than a threshold value of $\theta = 3$ standard deviations from the robust mean in the positive direction as we are only interested in a resonance leading to excess of events. The rest of the clusters are labelled as signal-depleted. The threshold and the selected signal-rich clusters are shown in Fig. 3 in red.

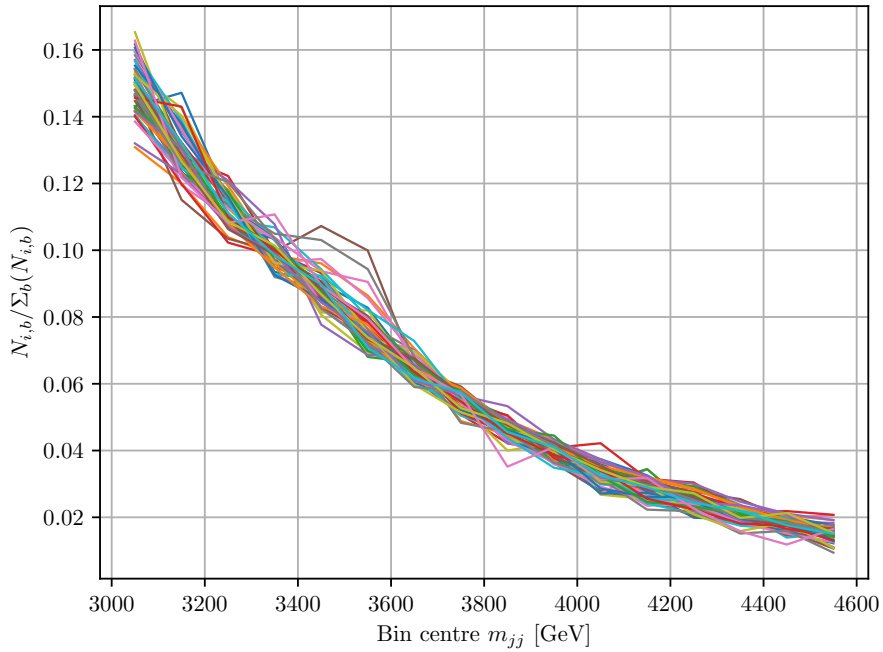


Figure 2: The m_{jj} distributions for the jets in each of the 50 clusters, each normalised to unity. Here, 5,000 signal events have been injected into the evaluation dataset, which corresponds to 5% of the total available signal events.

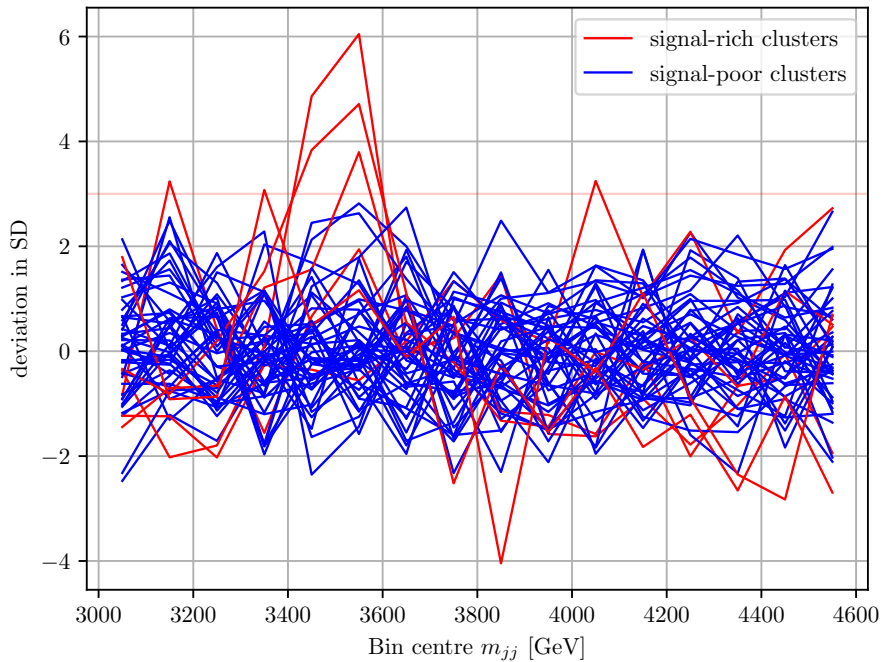


Figure 3: Spectra in Fig. 2 standardised over clusters in each bin. Potentially signal-rich cluster spectra are shown in red.

Signal-rich and signal-depleted regions: After the selection, we combine the non-normalised distributions corresponding to our selected signal-rich clusters. This results in a signal-rich spectrum $N_{\text{sig},b}$ with an example shown in red in Fig. 4.

The remaining cluster spectra are combined to form a signal-depleted spectrum $N_{\text{poor},b}$. The estimate of the background is then constructed by normalising it to the same total entries as in signal-rich spectrum, namely $N_{\text{bkg},b} = N_{\text{poor},b} \frac{\sum_b N_{\text{sig},b}}{\sum_b N_{\text{poor},b}}$. It is shown in blue in Fig. 4.

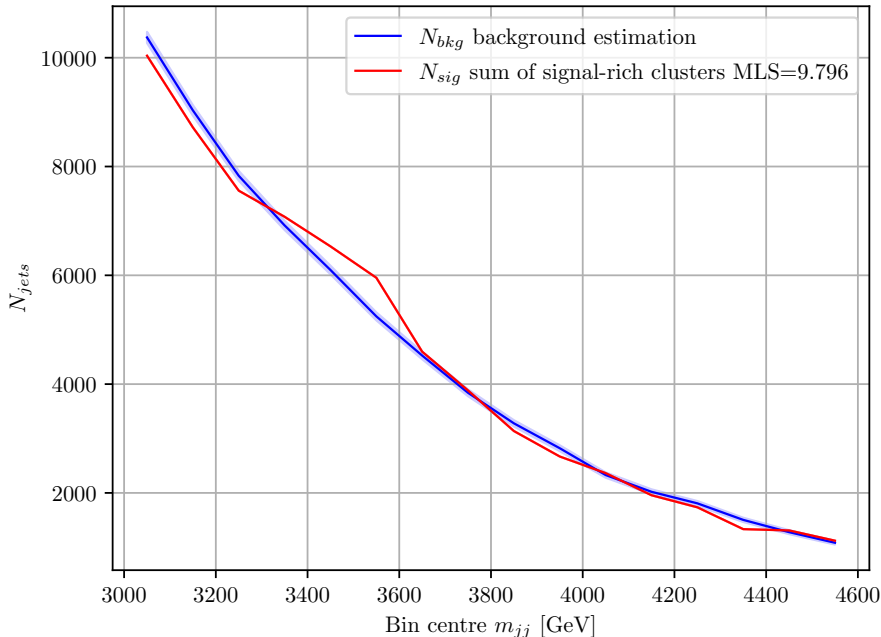


Figure 4: Curves corresponding to the sum of signal-rich and signal-poor spectra in Fig. 3. The blue signal-poor curve is rescaled to have the same total jet number as the signal-rich curve. The coloured region around the blue curve is a $\sigma_{\text{bkg},b} = \sqrt{N_{\text{bkg},b}}$ Poisson deviation after rescaling used to compute MLS.

Test statistic: As previously discussed, to test the significance of an observed excess we use the simple maximum local significance, as defined in Equation 3.2. It may occur that no cluster is selected as anomalous. In this case we assign a default value of 0, in order to show good agreement with the null-hypothesis expectation. This is similar in motivation to setting the value for an observed deficit in events to zero. Following the discussion in Subsection 3.1 for the calibration process, we construct 3,900 pseudo-experiments using bootstrap resampling on 1 million background events. The distribution of the test statistic is discussed in App. F.

Ensembling: Different initialisations lead to a broader distribution over the final test statistic obtained with cluster scanning. In order to obtain a final value for the test statistic, the cluster scanning method is performed 15 times with independent initialisations. The

mean of the test statistic from all the runs forms the final ensembled test statistic. The distribution of this statistic is presented in app. F.

3.3 Discussion

As we can see, CS follows the general bump hunt strategy, but introduces novel approaches for the first two steps of this strategy. First of all, CS selects the most anomalous looking clusters to define the signal-enriched region, and constructs a background estimate from the rest of the clusters. Notably though, this selection is completely data-driven and does not target a specific family of signal models. However, CS relies on a set of assumptions that fundamentally differ from those commonly used in other anomaly detection approaches.

Search for overdensity instead of outliers: Most anomaly search methods like Autoencoders [100] and SVDDs [82] rely on outlier detection, namely, identifying the data instances that lie in a region of very low probability density or outside the support of the “normal” distribution. Notably, while all normal events share similar characteristics and exhibit easily recognisable trends, anomalous data, such as defects or fraud, can differ in numerous ways and are thus given a wide prior. Although model-agnostic searches should accommodate a wide range of possible anomaly models, it is usually assumed that a signal is produced by only one or a few unknown BSM process. Thus, all anomalous events have many features in common and exhibit some similarity to SM events, as any new particle must radiate and decay into SM particles to be detectable.

Therefore we use the localisation of anomalies in both low-level (e.g. jet images) and high-level variable (e.g. m_{jj}) space as the first main assumption of the CS method. Localisation of anomalies in low-level variable space means that only a few out of all clusters contain a fraction of anomalies much higher than the rest of the clusters. This way clustering plays a role of data-driven binning in low-level variable space. Localisation in m_{jj} gives us a possibility to distinguish these anomaly rich clusters from the rest, namely, by searching for an overdensity in m_{jj} in one cluster spectrum compared to all others. Thus, CS is able to select a signal-rich region of events by leveraging the assumption of signal being localised rather than consisting of outliers.

Although semi-supervised methods based on CWoLa (see Refs. [101, 102, 126–130]) and density estimation methods are also sensitive to overdensities, they usually require construction of a background template, which until recent developments [129, 130] was preferably constructed for a smooth distribution of low dimensionality, typically using a few high-level observables. In this publication, we show that CS is able to draw significant improvement from a high-dimensional distribution of low-level jet observables. In this way, it can be considered less signal-model dependent than the methods that rely on hand-crafted high-level observables.

Assume cluster mass independence instead of smoothness: CS proposes a solution to the second step of the analysis, namely, it estimates the form of the background by combining the signal-depleted clusters. In this way, we do not rely on any assumptions on smoothness or on a particular functional form of the background-only spectrum in

m_{jj} , which are heavily relied upon by most other bump hunt methods, such as the global functional fit mentioned in Subsection 3.1, SWIFT [120] and even Gaussian processes [131].

Instead, the second main assumption of CS is that in the background-only case, the assigned cluster centroid is approximately independent from m_{jj} . Ideally, we would want the distribution of background events over m_{jj} in each cluster to be identical within statistical uncertainty, such that the probability of a jet belonging to a cluster and having a specific mass factorises, $p(i, m_{jj}) = p(i)p(m_{jj})$, or at least that the correlation is weak. This would minimise the rate of incorrectly identified signal-enriched clusters. In practice, although Fig. 2 shows that the distributions all follow a similar trend, there are still some systematic deviations. These are a result of the finite width in m_{jj} of the training window and slight correlations between the distribution of the jet constituents and m_{jj} arising from the transverse momenta of the two non-resonant jets depending on m_{jj} . Therefore, for the selection of the clusters, we estimate the full uncertainty (including Poisson fluctuations and uncertainty from mass dependence) separately for each experiment and for bin based on the sample of our k cluster spectra values.

Unlike in methods with sliding window approach [102, 120], in CS the fit only needs to be performed once. Moreover k -means clustering is a simple classical algorithm that typically requires less training than deep learning approaches, making CS a relatively fast analysis method. This is important in the context of the ensembling and calibration, which both require a large number of analysis iterations, and are thus a notable obstacle to incorporating deep learning in HEP analysis under the constraint in computing resources. Fast analysis is also advantageous for testing its efficiency for simulated BSM events in order to produce the exclusion limits (see the RECAST [132] framework). Moreover, CS avoids other disadvantages inherent to sliding window approaches, such as limited search range due to the definition of the sidebands and the need to optimise sideband and signal window widths.

3.4 Idealised CS

Despite choosing a narrow m_{jj} window to reduce mass dependence systematics, the variables that we use for clustering are in general not independent of m_{jj} . Thus, we observe the background-only spectra of some clusters do not just statistically fluctuate around the expected shape of the background, but exhibit some degree of smooth mass sculpting. This affects the performance of the method by introducing false positives at the cluster selection stage and increasing the discrepancy between signal and background spectra when evaluating the test statistic. This may be partially remedied by a more sophisticated method of selecting anomalous clusters or a better background estimate, both of which rely on more assumptions. These studies are outside the scope of this publication. However, to give an upper bound on the performance one may achieve with such improvements we propose an idealised version of clusters scanning.

Idealised CS version requires us to modify the distribution of the jets between the clusters. First, we count the numbers of jets that fall into each cluster in the first m_{jj} bin. If no mass dependence were present, the fractions of QCD jets in each cluster $x_{\text{QCD},i,b} = N_{\text{QCD},i,b} / \sum_i N_{\text{QCD},i,b}$ should be independent of bin number b within statis-

tical uncertainties. To simulate this case in all the consecutive bins except the first we distribute the QCD jets in these bins among clusters using a multinomial distribution with weights equal to the fractions obtained in the first bin $x_{\text{QCD},i,b} = x_{\text{QCD},i,1}$, thus generating cluster spectra that follow the original background spectrum with statistical fluctuations, i.e. the case with no mass dependence. The signal jets are distributed as before according to which cluster they belong to, such that the fractions of Z' jets may differ between different bins. This is done because we assume that only the background is distributed roughly proportionally between clusters, which is equivalent to assumption 2, but not the signal.

This distribution of jets creates idealised cluster spectra for each clustering, and the rest of the algorithm remains unchanged.

4 Results

As a proof of concept we perform an analysis applying CS and global fit based bump-hunting with the above mentioned hyperparameters to the LHCO R&D dataset with different amounts of signal injection, given in figures either as an absolute number of injected events ϵ or as a signal to background ratio S/B of events in the considered [3000, 4600] GeV m_{jj} region. For each pseudo-experiment with signal injection we calculate the significance Z as discussed in Subsection 3.1.4 using the calibration test statistic distribution. For each signal injection level we run 100 pseudo-experiments with bootstrapped background data and randomly sampled signal events. As a reference for the significance and its statistical variation for each contamination level, we report the median significance of these pseudo-experiments and 0.25 and 0.75 quantiles. We define the ratio between the median significance provided by CS to the significance of a baseline method as the significance improvement (SI). We also quote the relation between the number of events needed to obtain a 3σ evidence in each analysis strategy.

Figure 5a shows how the global significance of CS and the parametric fit-based methods depends on the signal contamination in the pseudo-experiment. It characterises the performance of these realistic analysis strategies, which do not use any truth information for the evaluation of the test statistic, thus including all the systematical uncertainties coming from partially fulfilled assumptions needed for the respective method.

We observe that although 3- and 4-parameter fits give approximately the same results, CS outperforms them by a significant margin in the region from 1500 to 4000 signal events. Beyond 3000 signal events, the significance yield from CS is limited by the number of bootstrap pseudo-experiments in the calibration set, but the lower bound on its significance still remains substantially higher than the significance of the parametric fits. This is the most interesting region as there the transition between non-significant signal (below 1σ) and new physics evidence (above 3σ) takes place. Looking at the lower subplot in Fig. 5a we see that CS gives us an SI of 2 and higher on the majority of regions of interest. We can also see that CS produces a 3σ evidence for only 61% of the events needed to obtain this evidence with the parametric fit. This shows that although both suffer from fit and assumption induced systematic uncertainties, CS has a clear advantage over parametric fitting procedures.

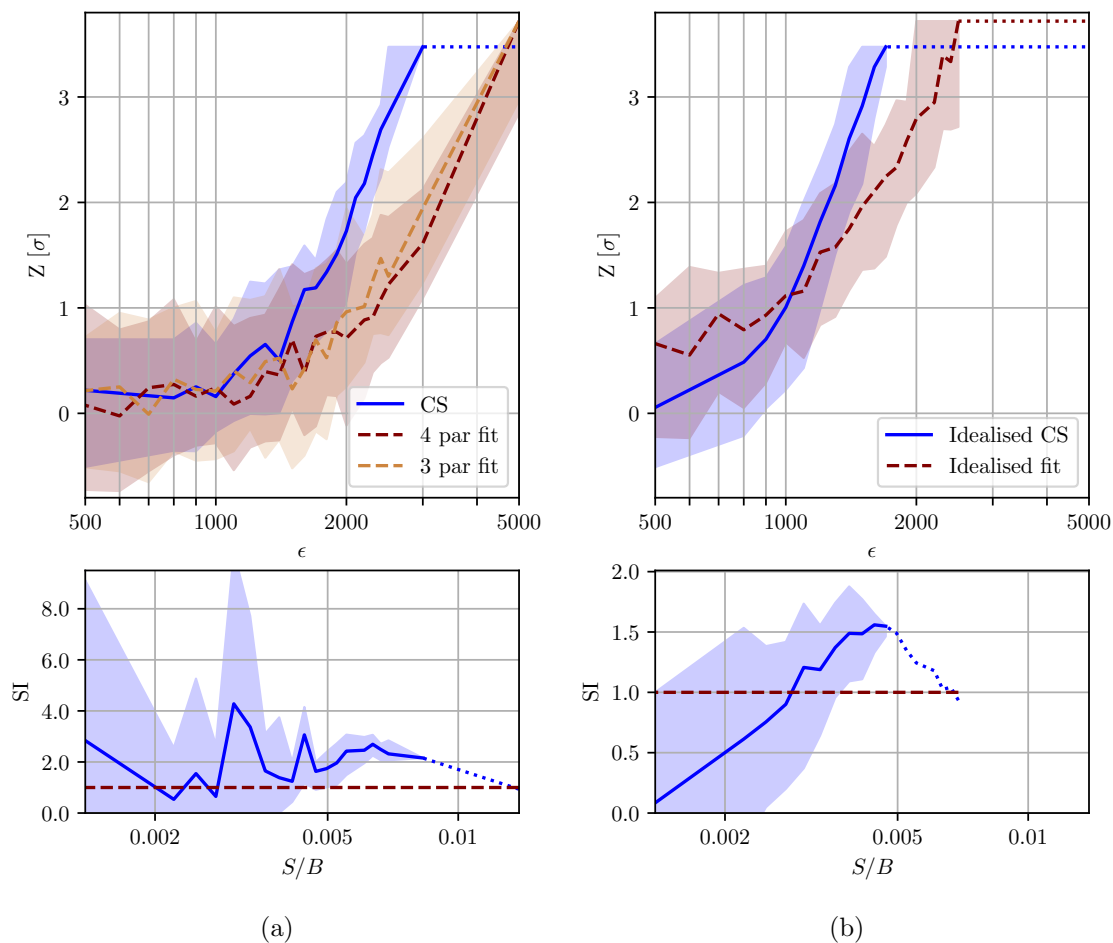


Figure 5: Upper figure: Median and the quartile bounds of global significance of the signal contaminated pseudo-experiments as a function of the number of signal events ϵ injected shown for the (a) realistic and (b) idealised analysis methods. The dotted lines mark lower bounds, as there was not enough statistics to access higher significance levels. Bottom figure: Significance improvement of the CS method compared to the 4-parameter fit for the (a) and the significance improvement of idealised CS compared to idealised fit for the (b) as a function of the signal-to-background ratio S/B .

Above we have also described the idealised version of the cluster scanning method and in Appendix A the analysis with an idealised background fit. Both methods rely on event labels to remove systematic uncertainties introduced by the limitations of the assumptions of our methods and to make the background estimate in both cases close to the true background, with only statistical fluctuation taken in consideration. This is done to separate the influence of additional information, namely the low-level observables used in the analysis, from the systematic uncertainties introduced by the fits, and to construct the upper bound on the performance of our methods.

Figure 5b shows how the global significance of both idealised methods depend on the signal contamination in the pseudo-experiment. It can be seen that one needs substantially

less signal for it to be significant in the idealised methods compared to the realistic methods, as it removes false-positives induced by systematic uncertainties in the fits. Still, we see that the idealised CS outperforms the idealised functional fit on the majority of the interval between 1000 and 2200 signal events. Looking at the lower subplot in Fig. 5b we see that by using CS in the region of interest we gain a significance improvement factor of up to 1.5. We can also see that CS produces a 3σ evidence with only 69% of the events needed to gain this evidence with the idealised fit. This shows that in the case of negligible systematic uncertainties, CS gives an improvement over any smooth fit as, in addition to just using information from m_{jj} , it also makes use of the low-level event information. From the difference between idealised and non-idealised CS we can see that there is some room for improvement of CS to reduce the false positive rate, and improve the analysis efficiency.

5 Conclusions and outlook

This paper is a first proof of concept for the cluster scanning anomaly search method, which is designed to search for resonant overdensities on the distribution of an observable using clustering techniques in auxiliary observables.

We found that it outperforms the widely used bump-hunting method, which relies on the functional background fits, in several metrics relevant to an analysis. In the transition region, where the benchmark algorithm achieves 1σ to 3σ significance, CS improves the result by a factor of 2 or more for the realistic case, or by a factor of 1.5 for the idealised comparison. This reduces the number of signal events required to produce a 3σ significance by a factor of 0.61 in the realistic case and by a factor of 0.69 in the idealised case. The former factor of improvement should be expected in a real application. We also discuss the comparison of cluster scanning with other anomaly detection algorithms in Subsection 3.3, outlining its advantages and limitations.

The CS method should not be seen as a direct competitor to background fitting methods, but rather as a complementary approach that relies on a different set of assumptions about the nature of the anomaly and the background distributions, which are not well known.

There remains a large unexplored field of potential extensions and improvements to this method or synergies with other methods. Straightforward follow-up studies can explore the use of clustering methods other than k -means. One can look for other ways of selecting the anomalous clusters, alternatives to the one proposed in Subsection 3.2, that would rely on different assumptions. For example, one can require that all anomalous clusters are neighbors in the space of clustered inputs. One can also unify the assumptions of CS and functional fits to produce separate background estimates for each of the clusters separately, greatly reducing the m_{jj} dependent systematic uncertainties.

CS could benefit from using features developed by other algorithms that have already been optimised for other tasks, such as flavour tagging, or even using unsupervised learning for feature extraction.

Furthermore, since many other ML approaches to improve sensitivity in model-independent searches rely on a bump hunt for the final statistical analysis, CS could also be used to

further enhance sensitivity. This could be of particular interest when the background distribution is no longer well described by simple, smoothly decreasing functional forms.

Acknowledgments

The authors would like to acknowledge funding through the SNSF Sinergia grant CR-SII5_193716 “Robust Deep Density Models for High-Energy Particle Physics and Solar Flare Analysis (RODEM)” and the SNSF project grant 200020.212127 “At the two upgrade frontiers: machine learning and the ITk Pixel detector”. The research of MK is supported by the DFG under grant 396021762 - TRR 257: Particle Physics Phenomenology after the Higgs Discovery.

Code availability

The code used to produce all results presented in this paper is available at https://github.com/IvanOleksiyuk/jet_cluster_scanning.

Appendix

A Idealised fit and n-parameter fit pseudo-analysis

In general, if a distribution \mathcal{H}_b of a background events is perfectly known a-priori, given a binning for this distribution, one can calculate the expected number of events in each bin. Being provided directly from the true underlying \mathcal{H}_b , this background estimate will on average provide the most efficient tests to discriminate samples drawn from \mathcal{H}_b from samples drawn from an alternative hypothesis \mathcal{H}_{b+s} with signal, compared to any other estimate of the expected background for these samples. Hence we call the expectation from \mathcal{H}_b an “idealised fit”.

As discussed extensively in section 3.1, estimation of the expected background is only one step of the analysis. To create a benchmark, we do pseudo-analysis on LHC0 R&D dataset represented by spectrum $N_{\text{bkg,orig},b}$ using the other choices defined in section 3.1. Namely, we generate pseudo-experiments by bootstrap resampling the events from $N_{\text{bkg,orig},b}$ and add a number of signal events if needed. The “idealised” background estimation for every pseudo-experiment is equal to $N_{\text{bkg,orig},b}$ itself (as the samples were generated with these expected values). Following the discussion in subsection 3.1.3 we use MLS test statistic between this estimate and the generated pseudo-experiments, to generate null-hypothesis test statistic distribution and its value for signal contaminations and thereafter estimate the significance. Depending on the number of doped signal events, the median and quartile region significance given by this test is provided in the main text in Fig. 5b.

Unfortunately the background model is usually unknown, so for each experimental sample the background should be estimated in some less precise way relying on weaker assumptions.

As a realistic benchmark to our method we explore how sensitive the analysis is using global n-parameter functional to the kind of signal presented in LHCO R&D dataset. We use the binning with 16 bins defined in subsection 3.1.2 and count the number of background events in each bin to get an original background spectrum $N_{\text{bkg,orig},b}$.

For all the fits in this studies, we use Trust Region Reflective nonlinear least squares fitting algorithm implementation from SCIPY python package [133]. The chosen bins generally contain more than 5000 counts, so the Poisson distributions of these counts can be well approximated by a Gaussian distributions with the variances equal to the bin counts. Using variances to scale the summands in the least squares objective we make it equivalent to the maximum likelihood objective for this setup.

First, we fit our 3- and 4-parameter functions to the spectrum to see if the fit is valid. Resulting fits with 13 and 12 degrees of freedom score $\frac{\chi^2_{3\text{-par}}}{n_{\text{dof}}} \approx 1.201$ and $\frac{\chi^2_{4\text{-par}}}{n_{\text{dof}}} \approx 1.338$ that correspond to p-values of 0.275 and 0.182 which signify validity of these fits.

Unlike the CS method that doesn't generally rely on the smoothness of the background, global n-parameter takes it as the main assumption, so as $N_{\text{bkg,orig},b}$ already has some statistical fluctuations a distribution resampled from it will have even larger statistical fluctuations than the ones expected for Poisson distribution. To simulate the proper scale Poisson fluctuations in the chosen region for our pseudo-experiments we resample events not from $N_{\text{bkg,orig},b}$ but from the best possible fit. This also negates the systematic error from null-hypothesis not corresponding to the empirical functional form, so these experiments can be viewed as semi-idealised. In a more realistic cases, the space of functions given by all possible parameter values, does not contain the true form of null-hypothesis distribution and can only yield an approximation of it with limited precision. It is usual for fit functions with a small number of parameters, but with increasing number of parameters the function fit problem becomes over-defined and the function can fit the signal bump as well. Experimentally we have observed only insignificant increase in performance when comparing sampling from $N_{\text{bkg,orig},b}$ or from the best fit distributions. On top of the resampled background events we add a number of signal events from signal's original distribution when needed.

The initial parameters of the fit in each experiment are chosen to be equal to the optimal parameters of the initial fit discussed above, so that one gets an "idealised" background fit if no optimisation is done. However, because of the statistical fluctuations and/or added signal contamination, the maximisation of likelihood results in a different set of parameters for this functional form. This error of background mismodeling under its statistical fluctuations and addition of the signal is exactly the type of error we want to demonstrate with this pseudo-analysis.

The results of such analysis for different signal contamination is given in Fig. 5a. We can see that the 3-parameter fit provides a slightly better result than 4-parameter fit as the latter has more flexibility to overfit the signal and the statistical fluctuations. This is so because the samples are drawn from 3- and 4-parameter functions with fixed parameters themselves. If we were to sample from other distribution the error coming from mismatch in true end expected functional forms may switch this ordering but it will reduce both

performances. Therefore, the curves shown in Fig. 5a are upper limits of these realistic n-parameter fit analyses achievable only when the true distribution is described by one of the functions in the chosen parameterised space.

B Sparsity of the jet images

Fig. 6 show that the jet images are very sparsely populated ususally having less tha 100 non-zero pixels per 1600 pixels total.

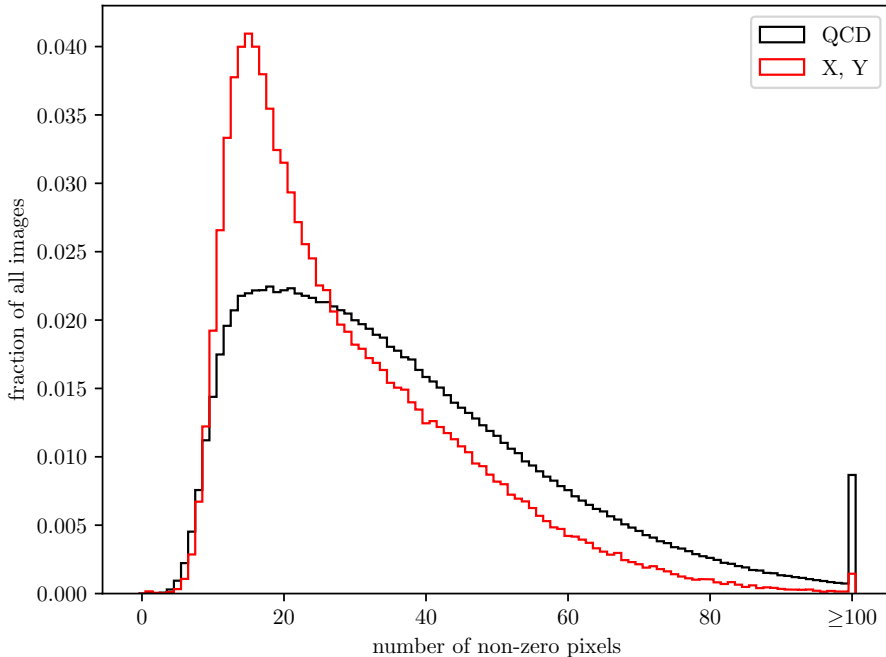


Figure 6: Distribution of images in QCD and top datasets from top-tagging task vs the number of non-0 pixels in them.

C Hyperparameter selection and motivation

In this appendix we give motivation for every not yet discussed choice of hyperparameter in our pseudo-analysis. All the hyperparameter suggestions are done in an unsupervised way coming from general assumptions about signal and background and are not optimised using the truth information from LHC0 R&D data. As such the levels of significance improvements may be further increased by performing a dedicated parameter scan for a specific application, however, we recommend to follow the same reasoning when applying CS in other analyses.

Training region: Training on the full spectrum would likely result in each cluster corresponding to a specific mass region, thus the background spectrum for each cluster would not be close to the original mass spectrum. Therefore we perform clustering in a narrow

mass window [3000, 3100] GeV. We choose this window as it lies in the studied region defined in subsection 3.1.1 and has the largest statistic of all other 100 GeV windows.

Number of clusters: The most important parameter we had to choose is the number of clusters k . Two factors play the key role in this choice. On one hand, the number of clusters has to be as large as possible to better narrow down the anomaly-rich region. On the other hand, for a given number of events in the evaluation region and the binning of this region one has to take the number of clusters sufficiently small so that the least populated clusters in the smallest m_{jj} bin $\min_{i,m_{jj}}(N_i(m_{jj}))$ still has enough statistics for a meaningful statistical analysis. We assume that $\min_{k,m_{jj}}(N_i(m_{jj})) = O(50)$ should be sufficient. Using a coarse search, we determine, that for our choice of binning and overall statistic at hand choosing $k = 50$ gives a good trade-off as it has a median of 55 events in smallest cluster-bin and it goes below 20 only 1 time in 1000 pseudo-experiment runs, as can be seen in Fig. 7.

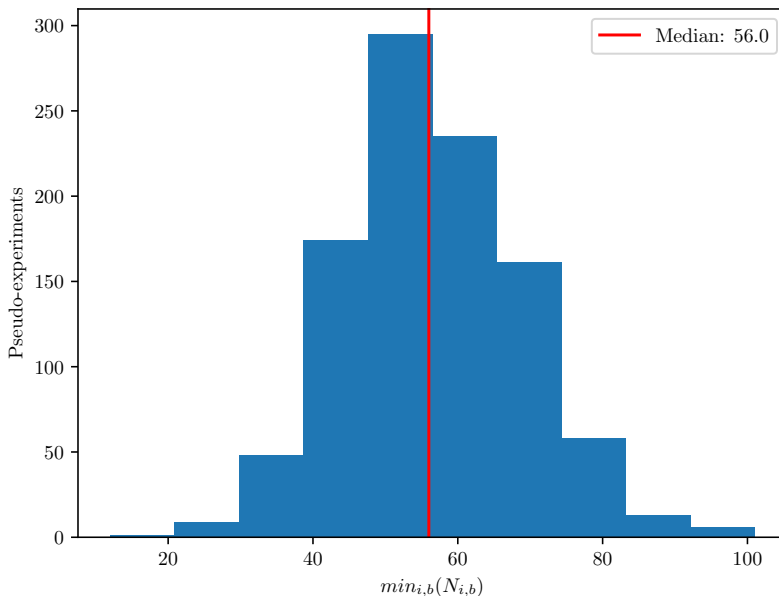


Figure 7: Distribution of the number of jet image counts in the least populated bin of the least populated cluster in each of the 1000 random background only runs of the CS algorithm on background only data.

Batch size: Scikit-learn [124] documentation states that the parallelisation is performed on all available N_{cores} computing cores if the batch size is $N_{cores} \cdot 256$ or larger. We performed all computations with 8 core parallelisation, thus the natural choice of a batch size was 2048. It is also important to maintain the batch size much larger than the number of clusters to ensure faster convergence.

Outlier fraction: To quantify the performance of our method we introduce the signal fraction improvement score (SFI) that characterises a subset \mathcal{S} of the events in evaluation set \mathcal{E} by the relative increase in the signal to background ratio

$$SFI(\mathcal{S}) = \frac{N_{\text{sig}}(\mathcal{S})}{N_{\text{QCD}}(\mathcal{S})} \frac{N_{\text{QCD}}(\mathcal{E})}{N_{\text{sig}}(\mathcal{E})}. \quad (\text{C.1})$$

Our main assumption is that the signal is distributed in clusters unevenly and there only several clusters have a significantly large SFI. To put it in numbers, we assume that not more than 20% of clusters have SFI of 2 or more. Following this assumption we choose the outlier fraction of 0.2 for outlier robust estimators. This is an ad. hoc prior assumption about the data at hand, and it has to be made prior to analysis and has no way to be validated without knowing the truth labels. Still we can show that this assumption is satisfied in our case with a margin for the pseudo-experiment shown on all the figures of section 3. 5000 signal events were giving an overdensity on the original spectrum that was not identifiable as a deviation from smooth background by human eye (without knowing the background truth), but in Fig. 2 one can easily notice two spectra with a significant bump around 3.5 TeV that stand out of the crowd of other spectra. Unsurprisingly these two spectra have SFIs of 9.1 and 8.9. Three more clusters also have a visible overdensity at this position possessing SFIs of 6.3, 5.6, 4.4. In total, exactly 8 clusters have $SFI > 2$. Still as we will see later only 3 of these clusters have a signal significant enough to be selected as anomalous, showing that our assumption is quite conservative in its limit and either the threshold SFI can be increased or the percentage of clusters to pass the threshold reduced for it to still remain a valid assumption. Runs of the analysis on other (pseudo-)experiments behave in the similar manner.

Cluster selection threshold θ : First of all, we use the threshold only for positive deviations as we only search for excesses of events. Apart from the signal-rich outlier clusters the threshold can be passed by signal poor clusters, but only with an expected false positive rate of $1 - (1 - \text{p-value}_{\mathcal{N}(0,1)}(\theta))^{n_{\text{bins}}}$. Then for large enough thresholds the average number of false positives can be estimated as $k \cdot n_{\text{bins}} \cdot \text{p-value}_{\mathcal{N}(0,1)}$. Higher thresholds result in lower false positive and lower true positive rates. To retain the sensitivity for statistically small signal we choose to use $\theta = 3$ that will result in approximately $50 \cdot 16 \cdot 0.00135 = 1.08$ signal poor cluster being assigned a false positive label on average. Fig. 3 shows 4 clusters being chosen using this threshold. Three of them have an overdensity at 3.5 TeV and one does not, implying that it is a likely false positive.

Ensemble size: We recommend to take the ensemble size as high as possible, for given computation resource constrains to reduce the width of the test statistic distribution (see appendix F).

Parameter	value	motivation
k	50	$\min_{i,b}(N_{i,b}) = O(50)$ with binning below
mini-batch	2048	$N_{cores} \cdot 256$, must be $\gg k$
Training region	[3, 3.1] TeV	narrow mass window with high statistic
Evaluation region	[3, 4.6] TeV	the n-parameter fit is applicable excluding low statistic regions
Bin width	100 Gev	broad enough to have sufficient statistics in each bin
outlier fraction f	0.2	consistent with assumption on the maximum number of signal clusters
Cluster selection threshold θ	3σ	low enough to let through many true positives but high enough to filter most false positives
Test statistic	MLS	simple and specialised for local excesses
Default TS	0	minimal test statistic possible
Ensemble size	15	As large as possible realistic compute limitations

Table 1: Summary of the hyperparameters used in cluster scanning.

D Gaussianity of cluster scanning bin entries

Assumption on the Gaussianity of cluster spectra in each bin can be shown to be valid by standardising the background-only cluster counts in each bin and checking if these distributions match $\mathcal{N}(0, 1)$. 50 samples are usually not enough to determine whether the distribution is Gaussian or not, but by marginalising over 16 bins we get 800 samples in total. Fig. 8 shows the said distribution for background only spectra that fits the $\mathcal{N}(0, 1)$ distribution well visually and by a consensus of 3 normality tests Shapiro-Wilk, Kolmogorov-Smirnov and Jarque-Bera (note that the p-values for all the tests are high). The same distribution with added signal has some clear outliers, which reflects in lower p-values for the normality tests, but apart from these it still can be well approximated by a unit Gaussian.

E Outlier robust estimators

While searching for outliers, it is preferred to use outlier robust estimators for standard deviation (SD) and mean. We define them as follows: given a sample of observations $S = \{x_1, x_2, \dots, x_n\}$ we find a median $med(S)$ (which is itself an outlier robust estimator) of this sample and take a subsample \tilde{S}_f that is constructed from S by discarding a fraction $0 < f < 1$ of all samples that have largest absolute distance to this median. In this way we have discarded the outliers. After that we construct estimators $\tilde{\mu}_f = mean(\tilde{S}_f)$ and $\tilde{\sigma}_f = SD(\tilde{S}_f) \cdot g(f)$. If S is a sample from $\mathcal{N}(\mu, \sigma)$ it is obvious that with $\lim_{n \rightarrow \infty} \tilde{\mu}_f = \lim_{n \rightarrow \infty} mean(S) = \mu$. If one takes S from $\mathcal{N}(0, 1)$ and rescales $x_i \rightarrow \sigma x_i$, then both estimators transform as $\tilde{\sigma}_f \rightarrow \sigma \tilde{\sigma}_f$ and $SD(S) \rightarrow \sigma SD(S)$ by definition, so both estimators $\tilde{\sigma}_f$ and $SD(S)$ are proportional to a true σ of the Gaussian distribution.

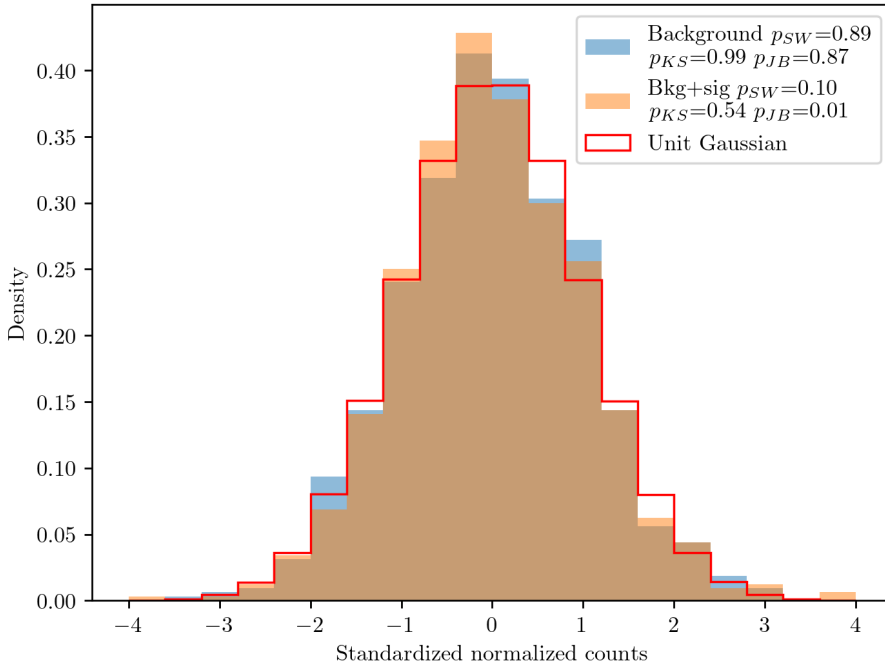


Figure 8: Histogram of deviations from the average of normalised cluster spectra measured in standard deviations of each bin. Blue histogram gives it for signal-free case and orange histogram for case with 5000 injected signal events. Red line show the expected normal distribution.

Both $\tilde{\sigma}_f$ and $SD(S)$ are independent of μ and there are no other parameters of the normal distribution for estimators to depend on, therefore for a family of Gaussian distribution estimators $\tilde{\sigma}_f$ and $SD(S)$ are proportional to each other by some constant factor $g(f)$ in the limit of infinite sample. In other words, adjusting numerically $g(f) = \frac{SD(\mathcal{N}(0,1))}{\tilde{\sigma}_f(\mathcal{N}(0,1))} = \frac{1}{\tilde{\sigma}_f(\mathcal{N}(0,1))}$ is sufficient to satisfy $\lim_{n \rightarrow \infty} \tilde{\sigma}_f = \lim_{n \rightarrow \infty} SD(S) = \sigma$. So $\tilde{\mu}_f$ and $\tilde{\sigma}_f$ are unbiased estimators of μ and σ of a normal distribution, although depending on f they are less efficient than usual non-robust mean and SD.

Fig. 9 shows us the cluster spectra from Fig. 2 with subtracted normalised original spectrum (which is only needed for better visualisation as this step has no effect on the standardisation). Fig. 9 also shows the conventional and the outlier robust estimations of mean and SD of the cluster spectra values in each bin. As expected for lower m_{jj} the SD is higher as these deviations is partially caused by the Poisson fluctuations which are proportional to $\sqrt{N_{i,b}}$. We can also see the conventional estimators have a bump around 3.5 TeV that is induced by our outlier signal-rich clusters, while the robust estimators are unaffected by the outliers.

F Calibration distributions

The distribution of the test statistics given by CS without ensembling for all background only pseudo-experiments is shown in Fig. 10a as a histogram. We see that around 300

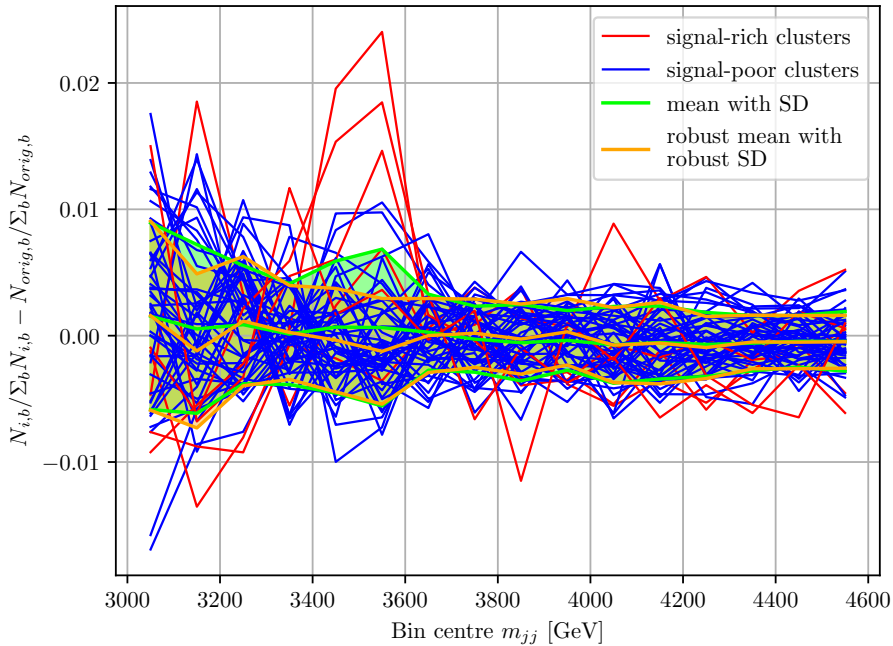


Figure 9: Normalised spectra with subtracted normalised original m_{jj} spectrum. Amount of signal is 5000. The selection of the anomalous clusters is taken from Fig. 4.

of those were assigned test statistic of 0 as they had no clusters selected as anomalous. Other cases where one or more anomalous clusters were selected form a smooth continuous distribution.

The median CS test statistic for 100 signal contaminated pseudo-experiments is represented in Fig. 10a by a vertical line, and the vertical band represent the region between the quartiles of such a test statistic sample. For each signal-doped pseudo-experiment we calculate significance as it is described in subsection 3.1.4. The median significance is quoted in the legend of the figure.

Fig. 10b shows the distribution that is analogous to the one in Fig. 10a, but with an ensemble of 15 runs of CS algorithm for each pseudo-experiment. We notice that the distribution in Fig. 10b is significantly narrower than in 10a which reduces the frequency of background only experiment having large test statistic, thus increasing the sensitivity to signal injection. An additional benefit is that the uncertainty region (between two quarterlies) for each signal doping have significantly decreased which is important for lower uncertainty in the analysis on experimental data on the excess significance or on the exclusion limits.

This motivates, that in general the ensemble size should be taken as large as reasonably possible. Our choice of ensemble size 15 together with the number of pseudo-experiments 3900 were dictated by the computing time and storage memory limits as the amount of full CS algorithm iterations is the product of those numbers (excluding the pseudo-experiments with signal injection)

Finally, Fig. 10c shows that for idealised CS without systematics introduced by mass

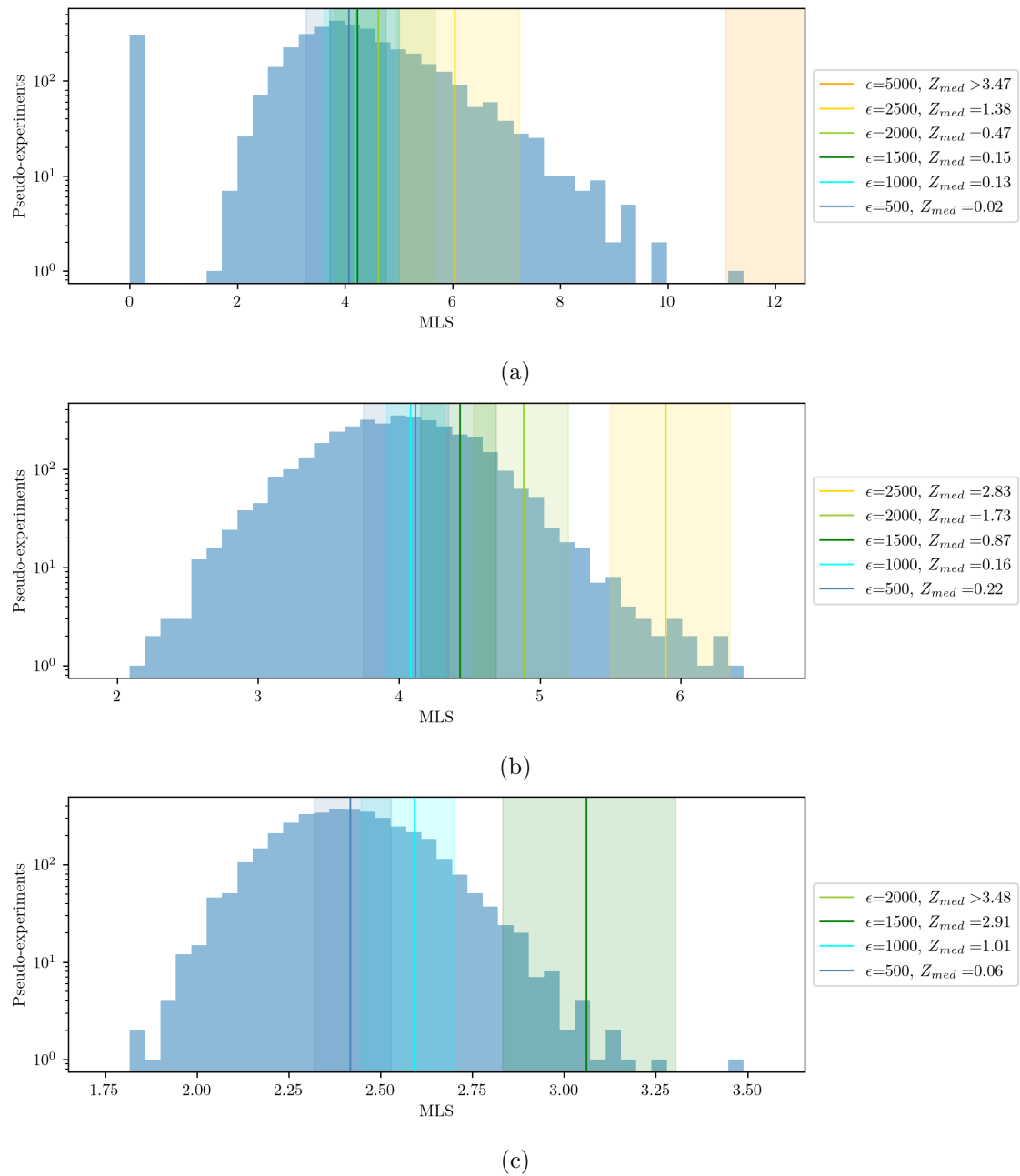


Figure 10: Histogram of the CS test statistic for pseudo-experiments with bootstrapped background only samples. Vertical lines and vertical bands show median and region between lower and higher quartiles of test statistics for pseudo-experiments with signal injection. Several signal injection levels are represented by different colours. Panel (a) shows a case with only 1 initialisation of clusters in CS per pseudo-experiment, panel (b) shows a case for ensembling 15 runs of CS with different initialisations per pseudo-experiment and panel (c) shows a case for ensembling 15 runs of idealised CS with different initialisations per pseudo-experiment.

correlations the MLS between our signal spectrum and background estimate is lower. Moreover, as expected, it improved the sensitivity of the method to the signal. Obviously this technique cannot be utilised in an actual analysis as jet labels are needed to distribute signal and background jets in a different manner. Moreover, as expected, it improved the sensitivity of the method to the signal. Obviously this technique cannot be utilised in an actual analysis as jet labels are needed to distribute signal and background jets in a different manner.

References

- [1] ATLAS Collaboration, *Observation of a new particle in the search for the standard model higgs boson with the ATLAS detector at the LHC*, *Physics Letters B* **716** (2012) 1–29 [[1207.7214](#)].
- [2] CMS Collaboration, *Observation of a new boson at a mass of 125 GeV with the CMS experiment at the LHC*, *Physics Letters B* **716** (2012) 30–61 [[1207.7235](#)].
- [3] R.T. D’Agnolo and A. Wulzer, *Learning New Physics from a Machine*, *Phys. Rev. D* **99** (2019) 015014 [[1806.02350](#)].
- [4] R.T. D’Agnolo, G. Grosso, M. Pierini, A. Wulzer and M. Zanetti, *Learning multivariate new physics*, *Eur. Phys. J. C* **81** (2021) 89 [[1912.12155](#)].
- [5] M. Farina, Y. Nakai and D. Shih, *Searching for New Physics with Deep Autoencoders*, *Phys. Rev. D* **101** (2020) 075021 [[1808.08992](#)].
- [6] T. Heimel, G. Kasieczka, T. Plehn and J.M. Thompson, *QCD or What?*, *SciPost Phys.* **6** (2019) 030 [[1808.08979](#)].
- [7] T.S. Roy and A.H. Vijay, *A robust anomaly finder based on autoencoders*, [1903.02032](#).
- [8] O. Cerri, T.Q. Nguyen, M. Pierini, M. Spiropulu and J.-R. Vlimant, *Variational Autoencoders for New Physics Mining at the Large Hadron Collider*, *JHEP* **05** (2019) 036 [[1811.10276](#)].
- [9] A. Blance, M. Spannowsky and P. Waite, *Adversarially-trained autoencoders for robust unsupervised new physics searches*, *JHEP* **10** (2019) 047 [[1905.10384](#)].
- [10] J. Hajer, Y.-Y. Li, T. Liu and H. Wang, *Novelty Detection Meets Collider Physics*, *Phys. Rev. D* **101** (2020) 076015 [[1807.10261](#)].
- [11] A. De Simone and T. Jacques, *Guiding New Physics Searches with Unsupervised Learning*, *Eur. Phys. J. C* **79** (2019) 289 [[1807.06038](#)].
- [12] A. Mullin, S. Nicholls, H. Pacey, M. Parker, M. White and S. Williams, *Does SUSY have friends? A new approach for LHC event analysis*, *JHEP* **02** (2021) 160 [[1912.10625](#)].
- [13] B.M. Dillon, D.A. Faroughy and J.F. Kamenik, *Uncovering latent jet substructure*, *Phys. Rev. D* **100** (2019) 056002 [[1904.04200](#)].
- [14] J.A. Aguilar-Saavedra, J.H. Collins and R.K. Mishra, *A generic anti-QCD jet tagger*, *JHEP* **11** (2017) 163 [[1709.01087](#)].
- [15] M. Romão Crispim, N.F. Castro, R. Pedro and T. Vale, *Transferability of Deep Learning Models in Searches for New Physics at Colliders*, *Phys. Rev. D* **101** (2020) 035042 [[1912.04220](#)].

- [16] M. Crispim Romão, N.F. Castro, J.G. Milhano, R. Pedro and T. Vale, *Use of a generalized energy Mover's distance in the search for rare phenomena at colliders*, *Eur. Phys. J. C* **81** (2021) 192 [2004.09360].
- [17] O. Amram and C.M. Suarez, *Tag N' Train: a technique to train improved classifiers on unlabeled data*, *JHEP* **01** (2021) 153 [2002.12376].
- [18] T. Cheng, J.-F. Arguin, J. Leissner-Martin, J. Pilette and T. Golling, *Variational autoencoders for anomalous jet tagging*, *Phys. Rev. D* **107** (2023) 016002 [2007.01850].
- [19] C.K. Khosa and V. Sanz, *Anomaly Awareness*, *SciPost Phys.* **15** (2023) 053 [2007.14462].
- [20] P. Thaprasop, K. Zhou, J. Steinheimer and C. Herold, *Unsupervised Outlier Detection in Heavy-Ion Collisions*, *Phys. Scripta* **96** (2021) 064003 [2007.15830].
- [21] S. Alexander, S. Gleyzer, H. Parul, P. Reddy, M.W. Toomey, E. Usai et al., *Decoding Dark Matter Substructure without Supervision*, 2008.12731.
- [22] V. Mikuni and F. Canelli, *Unsupervised clustering for collider physics*, *Phys. Rev. D* **103** (2021) 092007 [2010.07106].
- [23] M. van Beekveld, S. Caron, L. Hendriks, P. Jackson, A. Leinweber, S. Otten et al., *Combining outlier analysis algorithms to identify new physics at the LHC*, *JHEP* **09** (2021) 024 [2010.07940].
- [24] S.E. Park, D. Rankin, S.-M. Udrescu, M. Yunus and P. Harris, *Quasi Anomalous Knowledge: Searching for new physics with embedded knowledge*, *JHEP* **21** (2020) 030 [2011.03550].
- [25] D.A. Faroughy, *Uncovering hidden new physics patterns in collider events using Bayesian probabilistic models*, *PoS ICHEP2020* (2021) 238 [2012.08579].
- [26] T. Golling et al., *The Mass-ive Issue: Anomaly Detection in Jet Physics*, 2303.14134.
- [27] P. Chakravarti, M. Kuusela, J. Lei and L. Wasserman, *Model-Independent Detection of New Physics Signals Using Interpretable Semi-Supervised Classifier Tests*, 2102.07679.
- [28] J. Batson, C.G. Haaf, Y. Kahn and D.A. Roberts, *Topological Obstructions to Autoencoding*, *JHEP* **04** (2021) 280 [2102.08380].
- [29] A. Blance and M. Spannowsky, *Unsupervised event classification with graphs on classical and photonic quantum computers*, *JHEP* **21** (2020) 170 [2103.03897].
- [30] B. Bortolato, A. Smolkovič, B.M. Dillon and J.F. Kamenik, *Bump hunting in latent space*, *Phys. Rev. D* **105** (2022) 115009 [2103.06595].
- [31] J.H. Collins, P. Martín-Ramiro, B. Nachman and D. Shih, *Comparing weak- and unsupervised methods for resonant anomaly detection*, *Eur. Phys. J. C* **81** (2021) 617 [2104.02092].
- [32] B.M. Dillon, T. Plehn, C. Sauer and P. Sorrenson, *Better Latent Spaces for Better Autoencoders*, *SciPost Phys.* **11** (2021) 061 [2104.08291].
- [33] T. Finke, M. Krämer, A. Morandini, A. Mück and I. Oleksiyuk, *Autoencoders for unsupervised anomaly detection in high energy physics*, *JHEP* **06** (2021) 161 [2104.09051].
- [34] D. Shih, M.R. Buckley, L. Necib and J. Tamanas, *via machinae: Searching for stellar streams using unsupervised machine learning*, *Mon. Not. Roy. Astron. Soc.* **509** (2021) 5992 [2104.12789].

- [35] O. Atkinson, A. Bhardwaj, C. Englert, V.S. Ngairangbam and M. Spannowsky, *Anomaly detection with convolutional Graph Neural Networks*, *JHEP* **08** (2021) 080 [2105.07988].
- [36] A. Kahn, J. Gonski, I. Ochoa, D. Williams and G. Brooijmans, *Anomalous jet identification via sequence modeling*, *JINST* **16** (2021) P08012 [2105.09274].
- [37] T. Dorigo, M. Fumanelli, C. Maccani, M. Mojsavska, G.C. Strong and B. Scarpa, *RanBox: anomaly detection in the copula space*, *JHEP* **01** (2023) 008 [2106.05747].
- [38] S. Caron, L. Hendriks and R. Verheyen, *Rare and Different: Anomaly Scores from a combination of likelihood and out-of-distribution models to detect new physics at the LHC*, *SciPost Phys.* **12** (2022) 077 [2106.10164].
- [39] E. Govorkova, E. Puljak, T. Aarrestad, M. Pierini, K.A. Woźniak and J. Ngadiuba, *LHC physics dataset for unsupervised New Physics detection at 40 MHz*, *Sci. Data* **9** (2022) 118 [2107.02157].
- [40] G. Kasieczka, B. Nachman and D. Shih, *New Methods and Datasets for Group Anomaly Detection From Fundamental Physics*, in *Conference on Knowledge Discovery and Data Mining*, 7, 2021 [2107.02821].
- [41] S. Volkovich, F. De Vito Halevy and S. Bressler, *A data-directed paradigm for BSM searches: the bump-hunting example*, *Eur. Phys. J. C* **82** (2022) 265 [2107.11573].
- [42] E. Govorkova et al., *Autoencoders on field-programmable gate arrays for real-time, unsupervised new physics detection at 40 MHz at the Large Hadron Collider*, *Nature Mach. Intell.* **4** (2022) 154 [2108.03986].
- [43] B. Ostdiek, *Deep Set Auto Encoders for Anomaly Detection in Particle Physics*, *SciPost Phys.* **12** (2022) 045 [2109.01695].
- [44] K. Fraser, S. Homiller, R.K. Mishra, B. Ostdiek and M.D. Schwartz, *Challenges for unsupervised anomaly detection in particle physics*, *JHEP* **03** (2022) 066 [2110.06948].
- [45] P. Jawahar, T. Aarrestad, N. Chernyavskaya, M. Pierini, K.A. Wozniak, J. Ngadiuba et al., *Improving Variational Autoencoders for New Physics Detection at the LHC With Normalizing Flows*, *Front. Big Data* **5** (2022) 803685 [2110.08508].
- [46] J. Herrero-Garcia, R. Patrick and A. Scaffidi, *A semi-supervised approach to dark matter searches in direct detection data with machine learning*, *JCAP* **02** (2022) 039 [2110.12248].
- [47] J.A. Aguilar-Saavedra, *Anomaly detection from mass unspecific jet tagging*, *Eur. Phys. J. C* **82** (2022) 130 [2111.02647].
- [48] R. Tombs and C.G. Lester, *A method to challenge symmetries in data with self-supervised learning*, *JINST* **17** (2022) P08024 [2111.05442].
- [49] C.G. Lester and R. Tombs, *Using unsupervised learning to detect broken symmetries, with relevance to searches for parity violation in nature. (Previously: "Stressed GANs snag desserts")*, 2111.00616.
- [50] V. Mikuni, B. Nachman and D. Shih, *Online-compatible unsupervised nonresonant anomaly detection*, *Phys. Rev. D* **105** (2022) 055006 [2111.06417].
- [51] S. Chekanov and W. Hopkins, *Event-Based Anomaly Detection for Searches for New Physics*, *Universe* **8** (2022) 494 [2111.12119].
- [52] R.T. d'Agnolo, G. Grosso, M. Pierini, A. Wulzer and M. Zanetti, *Learning new physics from an imperfect machine*, *Eur. Phys. J. C* **82** (2022) 275 [2111.13633].

- [53] F. Canelli, A. de Cosa, L.L. Pottier, J. Niedziela, K. Pedro and M. Pierini, *Autoencoders for semivisible jet detection*, *JHEP* **02** (2022) 074 [[2112.02864](#)].
- [54] V.S. Ngairangbam, M. Spannowsky and M. Takeuchi, *Anomaly detection in high-energy physics using a quantum autoencoder*, *Phys. Rev. D* **105** (2022) 095004 [[2112.04958](#)].
- [55] L. Bradshaw, S. Chang and B. Ostdiek, *Creating simple, interpretable anomaly detectors for new physics in jet substructure*, *Phys. Rev. D* **106** (2022) 035014 [[2203.01343](#)].
- [56] J.A. Aguilar-Saavedra, *Taming modeling uncertainties with mass unspecific supervised tagging*, *Eur. Phys. J. C* **82** (2022) 270 [[2201.11143](#)].
- [57] T. Buss, B.M. Dillon, T. Finke, M. Krämer, A. Morandini, A. Mück et al., *What's anomalous in LHC jets?*, *SciPost Phys.* **15** (2023) 168 [[2202.00686](#)].
- [58] S. Alvi, C.W. Bauer and B. Nachman, *Quantum anomaly detection for collider physics*, *JHEP* **02** (2023) 220 [[2206.08391](#)].
- [59] B.M. Dillon, R. Mastandrea and B. Nachman, *Self-supervised anomaly detection for new physics*, *Phys. Rev. D* **106** (2022) 056005 [[2205.10380](#)].
- [60] M. Birman, B. Nachman, R. Sebbah, G. Sela, O. Turetz and S. Bressler, *Data-directed search for new physics based on symmetries of the SM*, *Eur. Phys. J. C* **82** (2022) 508 [[2203.07529](#)].
- [61] M. Letizia, G. Losapio, M. Rando, G. Grosso, A. Wulzer, M. Pierini et al., *Learning new physics efficiently with nonparametric methods*, *Eur. Phys. J. C* **82** (2022) 879 [[2204.02317](#)].
- [62] C. Fanelli, J. Giroux and Z. Papandreou, *'Flux+Mutability': a conditional generative approach to one-class classification and anomaly detection*, *Mach. Learn. Sci. Tech.* **3** (2022) 045012 [[2204.08609](#)].
- [63] T. Finke, M. Krämer, M. Lipp and A. Mück, *Boosting mono-jet searches with model-agnostic machine learning*, *JHEP* **08** (2022) 015 [[2204.11889](#)].
- [64] R. Verheyen, *Event Generation and Density Estimation with Surjective Normalizing Flows*, *SciPost Phys.* **13** (2022) 047 [[2205.01697](#)].
- [65] B.M. Dillon, L. Favaro, T. Plehn, P. Sorrenson and M. Krämer, *A Normalized Autoencoder for LHC Triggers*, [2206.14225](#).
- [66] S. Caron, R.R. de Austri and Z. Zhang, *Mixture-of-Theories training: can we find new physics and anomalies better by mixing physical theories?*, *JHEP* **03** (2023) 004 [[2207.07631](#)].
- [67] S.E. Park, P. Harris and B. Ostdiek, *Neural embedding: learning the embedding of the manifold of physics data*, *JHEP* **07** (2023) 108 [[2208.05484](#)].
- [68] J.F. Kamenik and M. Szwec, *Null hypothesis test for anomaly detection*, *Phys. Lett. B* **840** (2023) 137836 [[2210.02226](#)].
- [69] G. Kasieczka, R. Mastandrea, V. Mikuni, B. Nachman, M. Pettee and D. Shih, *Anomaly detection under coordinate transformations*, *Phys. Rev. D* **107** (2023) 015009 [[2209.06225](#)].
- [70] J.Y. Araz and M. Spannowsky, *Quantum-probabilistic Hamiltonian learning for generative modelling & anomaly detection*, [2211.03803](#).

- [71] J. Schuhmacher, L. Boggia, V. Belis, E. Puljak, M. Grossi, M. Pierini et al., *Unravelling physics beyond the standard model with classical and quantum anomaly detection*, *Mach. Learn. Sci. Tech.* **4** (2023) 045031 [2301.10787].
- [72] S. Roche, Q. Bayer, B. Carlson, W. Ouligian, P. Serhiayenka, J. Stelzer et al., *Nanosecond anomaly detection with decision trees for high energy physics and real-time application to exotic Higgs decays*, [2304.03836](#).
- [73] L. Vaslin, V. Barra and J. Donini, *GAN-AE: an anomaly detection algorithm for New Physics search in LHC data*, *Eur. Phys. J. C* **83** (2023) 1008 [2305.15179].
- [74] ATLAS Collaboration, *Anomaly detection search for new resonances decaying into a Higgs boson and a generic new particle X in hadronic final states using $\sqrt{s} = 13$ TeV pp collisions with the ATLAS detector*, *Phys. Rev. D* **108** (2023) 052009 [2306.03637].
- [75] S.V. Chekanov and R. Zhang, *Enhancing the hunt for new phenomena in dijet final-states using anomaly detection filter at High-Luminosity Large Hadron Collider*, [2308.02671](#).
- [76] CMS ECal Collaboration, *Autoencoder-based Anomaly Detection System for Online Data Quality Monitoring of the CMS Electromagnetic Calorimeter*, [2309.10157](#).
- [77] G. Bickendorf, M. Drees, G. Kasieczka, C. Krause and D. Shih, *Combining Resonant and Tail-based Anomaly Detection*, [2309.12918](#).
- [78] M. Freytsis, M. Perelstein and Y.C. San, *Anomaly Detection in Presence of Irrelevant Features*, [2310.13057](#).
- [79] E.M. Metodiev, J. Thaler and R. Wynne, *Anomaly Detection in Collider Physics via Factorized Observables*, [2312.00119](#).
- [80] G. Karagiorgi, G. Kasieczka, S. Kravitz, B. Nachman and D. Shih, *Machine learning in the search for new fundamental physics*, *Nature Reviews Physics* **4** (2022) 399 [2112.03769].
- [81] G. Kasieczka, B. Nachman, D. Shih, O. Amram, A. Andreassen, K. Benkendorfer et al., *The LHC olympics 2020 a community challenge for anomaly detection in high energy physics*, *Reports on Progress in Physics* **84** (2021) 124201 [2101.08320].
- [82] T. Aarrestad, M. van Beekveld, M. Bona, A. Boveia, S. Caron, J. Davies et al., *The Dark Machines Anomaly Score Challenge: Benchmark Data and Model Independent Event Classification for the Large Hadron Collider*, *SciPost Phys.* **12** (2022) 043 [2105.14027].
- [83] V. Belis, P. Odagiu and T.K. Aarrestad, *Machine learning for anomaly detection in particle physics*, *Rev. Phys.* **12** (2024) 100091 [2312.14190].
- [84] J.H. Collins, P. Martín-Ramiro, B. Nachman and D. Shih, *Comparing weak- and unsupervised methods for resonant anomaly detection*, *The European Physical Journal C* **81** (2021) [2104.02092].
- [85] T. Golling, G. Kasieczka, C. Krause, R. Mastandrea, B. Nachman, J.A. Raine et al., *The Interplay of Machine Learning-based Resonant Anomaly Detection Methods*, [2307.11157](#).
- [86] ATLAS Collaboration, *Dijet resonance search with weak supervision using $\sqrt{s} = 13$ TeV pp collisions in the ATLAS detector*, *Physical Review Letters* **125** (2020) 131801 [2005.02983].
- [87] ATLAS Collaboration, *Search for new phenomena in two-body invariant mass distributions using unsupervised machine learning for anomaly detection at $\sqrt{s} = 13$ TeV with the ATLAS detector*, 2023. All figures including auxiliary figures are available at <https://atlas.web.cern.ch/Atlas/GROUPS/PHYSICS/CONFNOTES/ATLAS-CONF-2023-022>.

- [88] G. Kasieczka, B. Nachman and D. Shih, *Official Datasets for LHC Olympics 2020 Anomaly Detection Challenge (Version v6)*, 2019. [10.5281/zenodo.4536624](https://zenodo.org/record/4536624).
- [89] J.H. Kim, K. Kong, B. Nachman and D. Whiteson, *The motivation and status of two-body resonance decays after the LHC run 2 and beyond*, *Journal of High Energy Physics* **2020** (2020) [[1907.06659](https://arxiv.org/abs/1907.06659)].
- [90] T. Sjöstrand, S. Ask, J.R. Christiansen, R. Corke, N. Desai, P. Ilten et al., *An introduction to PYTHIA 8.2*, *Comput. Phys. Commun.* **191** (2015) 159 [[1410.3012](https://arxiv.org/abs/1410.3012)].
- [91] J. de Favereau, C. Delaere, P. Demin, A. Giammanco, V. Lemaître, A. Mertens et al., *DELPHES 3: a modular framework for fast simulation of a generic collider experiment*, *Journal of High Energy Physics* **2014** (2014) 026.
- [92] A. Mertens, *New features in delphes 3*, *Journal of Physics: Conference Series* **608** (2015) 012045.
- [93] M. Selvaggi, *Delphes 3: A modular framework for fast-simulation of generic collider experiments*, *Journal of Physics: Conference Series* **523** (2014) 012033.
- [94] M. Cacciari, G.P. Salam and G. Soyez, *The anti-ktjet clustering algorithm*, *Journal of High Energy Physics* **2008** (2008) 063–063 [[0802.1189](https://arxiv.org/abs/0802.1189)].
- [95] M. Cacciari, G.P. Salam and G. Soyez, *Fastjet user manual*, *The European Physical Journal C* **72** (2012) [[1111.6097](https://arxiv.org/abs/1111.6097)].
- [96] E. Rodrigues et al., *The Scikit HEP Project – overview and prospects*, *EPJ Web Conf.* **245** (2020) 06028 [[2007.03577](https://arxiv.org/abs/2007.03577)].
- [97] L. de Oliveira, M. Kagan, L. Mackey, B. Nachman and A. Schwartzman, *Jet-images — deep learning edition*, *Journal of High Energy Physics* **2016** (2016) [[1511.05190](https://arxiv.org/abs/1511.05190)].
- [98] G. Kasieczka, T. Plehn, A. Butter, K. Cranmer, D. Debnath, B.M. Dillon et al., *The machine learning landscape of top taggers*, *SciPost Physics* **7** (2019) [[1902.09914](https://arxiv.org/abs/1902.09914)].
- [99] S. Macaluso and D. Shih, *Pulling out all the tops with computer vision and deep learning*, *Journal of High Energy Physics* **2018** (2018) [[1803.00107](https://arxiv.org/abs/1803.00107)].
- [100] T. Finke, M. Krämer, A. Morandini, A. Mück and I. Oleksiyuk, *Autoencoders for unsupervised anomaly detection in high energy physics*, *JHEP* **2021** (2021) [[2104.09051](https://arxiv.org/abs/2104.09051)].
- [101] A. Hallin, J. Isaacson, G. Kasieczka, C. Krause, B. Nachman, T. Quadfasel et al., *Classifying anomalies through outer density estimation*, *Phys. Rev. D* **106** (2022) 055006 [[2109.00546](https://arxiv.org/abs/2109.00546)].
- [102] J.A. Raine, S. Klein, D. Sengupta and T. Golling, *CURTAINS for your sliding window: Constructing unobserved regions by transforming adjacent intervals*, *Front. Big Data* **6** (2023) 899345 [[2203.09470](https://arxiv.org/abs/2203.09470)].
- [103] CMS Collaboration, *Search for narrow resonances in the b-tagged dijet mass spectrum in proton-proton collisions at s=13 TeV*, *Phys. Rev. D* **108** (2023) 012009 [[2205.01835](https://arxiv.org/abs/2205.01835)].
- [104] ATLAS Collaboration, *Search for new phenomena in the dijet mass distribution using pp collision data at $\sqrt{s} = 8$ TeV with the atlas detector*, *Phys. Rev. D* **91** (2015) 052007 [[1407.1376](https://arxiv.org/abs/1407.1376)].
- [105] ATLAS Collaboration, *Search for new phenomena in dijet mass and angular distributions from pp collisions at $\sqrt{s} = 13$ tev with the ATLAS detector*, *Physics Letters B* **754** (2016) 302–322 [[1512.01530](https://arxiv.org/abs/1512.01530)].

- [106] CMS Collaboration, *Search for dijet resonances in proton–proton collisions at $\sqrt{s} = 13$ tev and constraints on dark matter and other models*, *Physics Letters B* **769** (2017) 520–542.
- [107] CMS Collaboration, *Search for narrow resonances decaying to dijets in proton-proton collisions at $\sqrt{s} = 13$ tev*, *Physical Review Letters* **116** (2016) [1512.01224].
- [108] CMS Collaboration, *Search for narrow resonances in dijet final states at $\sqrt{s} = 8$ tev with the novel cms technique of data scouting*, *Physical Review Letters* **117** (2016) .
- [109] ATLAS Collaboration, *A search for new physics in dijet mass and angular distributions in pp collisions at $\sqrt{s} = 7$ tev measured with the ATLAS detector*, *New Journal of Physics* **13** (2011) 053044 [1512.01530].
- [110] CMS Collaboration, *Search for resonances and quantum black holes using dijet mass spectra in proton-proton collisions at $\sqrt{s} = 8$ TeV*, *Phys. Rev. D* **91** (2015) 052009 [1501.04198].
- [111] CMS Collaboration, *Search for narrow resonances using the dijet mass spectrum in pp collisions at $\sqrt{s}=8$ TeV*, *Phys. Rev. D* **87** (2013) 114015 [1302.4794].
- [112] CMS Collaboration, *Search for narrow resonances and quantum black holes in inclusive and b-tagged dijet mass spectra from pp collisions at $\sqrt{s} = 7$ tev*, *Journal of High Energy Physics* **2013** (2013) [1210.2387].
- [113] ATLAS Collaboration, *Search for new physics in the dijet mass distribution using 1 fb^{-1} of pp collision data at $\sqrt{s} = 7$ tev collected by the atlas detector*, *Physics Letters B* **708** (2012) 37 [1108.6311].
- [114] ATLAS Collaboration, *Atlas search for new phenomena in dijet mass and angular distributions using pp collisions at $\sqrt{s} = 7$ tev*, *Journal of High Energy Physics* **2013** (2013) [1210.1718].
- [115] CMS Collaboration, *Search for resonances in the dijet mass spectrum from 7 tev pp collisions at cms*, *Physics Letters B* **704** (2011) 123–142 [1107.4771].
- [116] CDF Collaboration, *Search for new particles decaying into dijets in proton-antiproton collisions at $\sqrt{s} = 1.96$ tev*, *Physical Review D* **79** (2009) [0812.4036].
- [117] ATLAS Collaboration, *A search for new physics in dijet mass and angular distributions inppcollisions at $\sqrt{s} = 7$ tev measured with the atlas detector*, *New Journal of Physics* **13** (2011) 053044 [1103.3864].
- [118] CMS Collaboration, *Search for dijet resonances in 7 tev pp collisions at cms*, *Phys. Rev. Lett.* **105** (2010) 211801 [1010.0203].
- [119] ATLAS Collaboration, *Search for low-mass dijet resonances using trigger-level jets with the atlas detector in pp collisions at $\sqrt{s} = 13$ TeV*, *Physical Review Letters* **121** (2018) [1804.03496].
- [120] K. Sekhon, R.C. Edgar and D. Amidei, *SWiFt: Sliding Window Fit Method for Resonance Searches*, Tech. Rep. [ATL-COM-PHYS-2018-161](#), CERN, Geneva (2018).
- [121] J. Alison, F.A. Di Bello, S. Chekanov, A. Coccaro, T. Golling, G. Facini et al., *Search for resonances in the di-jet mass distribution with one or two jets identified as b-jets in proton-proton collisions at $\sqrt{s}=13$ TeV with the ATLAS detector*, Tech. Rep. [ATL-COM-PHYS-2016-1561](#), CERN, Geneva (2016).
- [122] G. Kasieczka, B. Nachman, M.D. Schwartz and D. Shih, *Automating the abcd method with machine learning*, *Phys. Rev. D* **103** (2021) 035021 [2007.14400].

- [123] L. Vaslin, S. Calvet, V. Barra and J. Donini, *pybumphunter: A model independent bump hunting tool in python for high energy physics analyses*, [2208.14760](#).
- [124] F. Pedregosa et al., *Scikit-learn: Machine Learning in Python*, *J. Machine Learning Res.* **12** (2011) 2825 [[1201.0490](#)].
- [125] D. Arthur and S. Vassilvitskii, *K-means++: The advantages of careful seeding*, in *Proceedings of the Eighteenth Annual ACM-SIAM Symposium on Discrete Algorithms, SODA '07, (USA)*, p. 1027–1035, Society for Industrial and Applied Mathematics, 2007.
- [126] A. Andreassen, B. Nachman and D. Shih, *Simulation Assisted Likelihood-free Anomaly Detection*, *Phys. Rev. D* **101** (2020) 095004 [[2001.05001](#)].
- [127] T. Golling, S. Klein, R. Mastandrea and B. Nachman, *Flow-enhanced transportation for anomaly detection*, *Phys. Rev. D* **107** (2023) 096025 [[2212.11285](#)].
- [128] D. Sengupta, S. Klein, J.A. Raine and T. Golling, *CURTAINS Flows For Flows: Constructing Unobserved Regions with Maximum Likelihood Estimation*, [2305.04646](#).
- [129] E. Buhmann, C. Ewen, G. Kasieczka, V. Mikuni, B. Nachman and D. Shih, *Full phase space resonant anomaly detection*, 2023.
- [130] D. Sengupta, M. Leigh, J.A. Raine, S. Klein and T. Golling, *Improving new physics searches with diffusion models for event observables and jet constituents*, [2312.10130](#).
- [131] M. Frate, K. Cranmer, S. Kalia, A. Vandenberg-Rodes and D. Whiteson, *Modeling Smooth Backgrounds and Generic Localized Signals with Gaussian Processes*, [1709.05681](#).
- [132] K. Cranmer and I. Yavin, *RECAST: Extending the Impact of Existing Analyses*, *JHEP* **04** (2011) 038 [[1010.2506](#)].
- [133] P. Virtanen, R. Gommers, T.E. Oliphant, M. Haberland, T. Reddy, D. Cournapeau et al., *SciPy 1.0: Fundamental Algorithms for Scientific Computing in Python*, *Nature Methods* **17** (2020) 261.

T-odd gluon distribution functions in a spectator model

Alessandro Bacchetta,^{1,2,*} Francesco Giovanni Celiberto,^{3,†} and Marco Radici^{2,‡}

¹*Dipartimento di Fisica, Università di Pavia, via Bassi 6, I-27100 Pavia*

²*INFN Sezione di Pavia, via Bassi 6, I-27100 Pavia, Italy*

³*Universidad de Alcalá (UAH), Departamento de Física y Matemáticas, E-28805 Alcalá de Henares, Madrid, Spain*

(Dated: Wednesday 28th February, 2024, 03:00)

We present a model calculation of T-odd transverse-momentum-dependent distributions of gluons in the nucleon. The model is based on the assumption that a nucleon can emit a gluon, and what remains after the emission is treated as a single spectator particle. This spectator particle is considered to be on-shell, but its mass is allowed to take a continuous range of values, described by a spectral function. The final-state interaction that is necessary to generate T-odd functions is modeled as the exchange of a single gluon between the spectator and the outgoing parton.

PACS numbers: 12.38.-t, 12.40.-y, 14.70.Dj

CONTENTS

I. Introduction	2
II. The spectator model	3
A. Tree-level correlator	3
B. Additional single-gluon exchange	4
C. Spectator-gluon-spectator vertex	6
D. Gluon TMD projectors	7
III. T-odd gluon TMDs: Illustrative examples	7
A. Sivers function: g_1 -vertex approximation	7
B. Sivers function: Quark-target model	9
C. Linearity function: g_1 -vertex approximation	11
D. Linearity function: Quark-target model	11
IV. T-odd gluon TMDs: Results of full calculation	11
V. Summary and Outlook	17
Acknowledgments	18
A. Master integrals	18
B. Full calculation of gluon TMDs: The coefficients $C_{ijk}^{[F],l}$	19
1. Sivers function f_{1T}^\perp	19
2. Linearity function h_1	22
3. Propeller function h_{1L}^\perp	25
4. Butterfly function h_{1T}^\perp	27
References	30

* alessandro.bacchetta@unipv.it

† francesco.celiberto@uah.es

‡ marco.radici@pv.infn.it

I. INTRODUCTION

The multi-dimensional distribution of partons within a nucleon can be parametrized in terms of several sets of functions, encoding different correlations between the momentum and spin of the parton and its parent nucleon. In particular, the 3-dimensional distribution in momentum space is encoded in the so-called Transverse-Momentum-Dependent Parton Distributions (TMD PDFs or TMDs) [1]. In simple terms, TMDs extend the conventional 1-dimensional collinear Parton Distribution Functions (PDFs) into three dimensions, including also the dependence on the partonic transverse momentum.

The endeavor to constrain TMDs is a crucial step toward unraveling the multi-dimensional structure of the nucleon, and gaining deeper insight into Quantum ChromoDynamics (QCD) and color confinement. The field of TMDs has witnessed remarkable advancement in recent years, predominantly in the quark sector. Progress within the gluon sector has been relatively restrained, owing to the challenges associated with probing gluons in high-energy processes.

Gluon TMDs at leading twist, first analyzed and classified in Ref. [2], are shown in Tab. I in terms of both the polarization of the gluon and of its parent hadron. In this paper, our focus centers on (naïve) time-reversal odd (T-odd) gluon TMDs, highlighted in red in Tab. I. A notable example of a T-odd TMD is the gluon Sivers function, denoted as $f_{1T}^{\perp g}$. This function describes the distribution of unpolarized gluons in a transversely polarized nucleon and has a crucial role in the description of transverse single-spin asymmetries (see [3] and references therein). As in the case for quark TMDs, T-odd gluon TMDs are generated by the presence of initial and/or final state QCD interactions between incoming or outgoing partons and the target fragments. These interactions also underlie the peculiar process-dependence of gluon TMDs.

		gluon polarization		
		U	circular	linear
nucleon polarization	U	f_1^g		$h_1^{\perp g}$
	L		g_1^g	$h_{1L}^{\perp g}$
	T	$f_{1T}^{\perp g}$	g_{1T}^g	$h_1^g, h_{1T}^{\perp g}$

Table I. Gluon TMD PDFs at twist-2. We adopt here the notation suggested in Ref. [4], similar to the quark case. U , L , T depict unpolarized, longitudinally polarized and transversely polarized nucleons. U , ‘circular’, ‘linear’ describe unpolarized, circularly polarized and linearly polarized gluons. Functions in blue are T-even. Functions in black are T-even and survive transverse-momentum integration. Functions in red are T-odd.

Experimental information on gluon TMDs is very scarce, and particularly so for T-odd ones. Ref. [5] presented the first attempt to reconstruct the unpolarized gluon TMD, f_1^g . Phenomenological studies of the T-odd gluon Sivers function were published in Refs. [6–8], but in processes where TMD factorization is not guaranteed to be applicable. An experimental measurement related to the gluon Sivers function was published by the COMPASS collaboration [9]. Several ways to experimentally access the gluon Sivers function have been discussed in the literature [10–16] and are among the primary goals of new experimental facilities [17–20].

Pioneering calculations of gluon TMD distributions [2, 21, 22] were performed using the *spectator-model* approach (see also Refs. [23, 24] for more recent versions). Originally conceived for studies in the quark-TMD sector [4, 25–29], this approach rests on the assumption that the struck nucleon emits a parton, and the residual fragments are treated as a single spectator particle, considered to be on-shell. At variance with those studies, in Ref. [30] we presented the calculation of all T-even gluon TMDs in the spectator-model approach where the spectator mass is allowed to take a continuous range of values weighted by a flexible spectral function. This modification encapsulates the effect of $q\bar{q}$ contributions, and allows to effectively reproduce both the small- and the moderate- x behavior of the TMDs.

In this paper, we extend the results of Ref. [30] by providing a systematic calculation in the same spectator-model framework of the complete set of all the four T-odd gluon TMDs at leading twist, including their process dependence.

II. THE SPECTATOR MODEL

Our model is based on the assumption that a nucleon can emit a gluon, and what remains after the emission is treated as a single spectator fermionic particle (see Fig. 1). This spectator fermion is considered to be on-shell, but its mass is allowed to take a continuous range of values, described by a spectral function. The nucleon-gluon-spectator coupling is described by an effective vertex containing two form factors, inspired by the standard nucleon form factors. Such model can effectively reproduce the known collinear (un)polarized gluon PDFs (the diagonal black entries f_1^g and g_1^g in Tab. I, that survive integration upon transverse momenta) and can be used to compute all T-even TMDs [30].

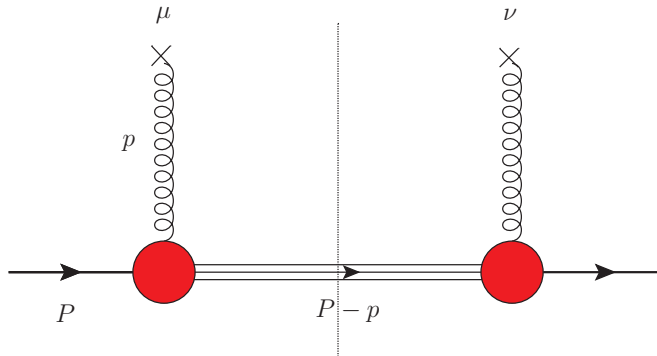


Figure 1. Tree-level cut diagram for the calculation of T-even leading-twist gluon TMDs. The triple line represents a spin- $\frac{1}{2}$ spectator. The red blob represents the nucleon-gluon-spectator vertex.

T-odd gluon TMDs vanish at tree level, because there is no residual interaction between the active parton and the spectator; equivalently, there is no interference between two competing channels producing the complex amplitude whose imaginary part gives the T-odd contribution. We can generate such structures by considering the interference between the tree-level scattering amplitude and the scattering amplitudes with an additional gluon exchange, as shown in Fig. 2. This corresponds to the one-gluon-exchange approximation of the gauge link operator. As we shall discuss in detail, the exact form of the gauge link depends on the process and in our case leads to two different types of functions.

A. Tree-level correlator

Following Ref. [30], we work in the frame where the nucleon momentum P has no transverse component:

$$P = \left[\frac{M^2}{2P^+}, P^+, \mathbf{0} \right], \quad (1)$$

where M is the nucleon mass. The parton momentum is parameterized as

$$p = \left[\frac{p^2 + \mathbf{p}_T^2}{2xP^+}, xP^+, \mathbf{p}_T \right], \quad (2)$$

where evidently $x = p^+/P^+$ is the light-cone (longitudinal) momentum fraction carried by the parton.

In the spectator-model framework one assumes that the nucleon with spin S in the state $|P, S\rangle$ can split into a gluon with momentum p and other remainders, effectively treated as a single spin- $\frac{1}{2}$ spectator particle with momentum $P-p$ and mass M_X . Similarly to Refs. [25, 30], we define a “tree-level” correlator as (see Fig. 1)¹

$$\Phi^{\mu\nu(0)}(x, \mathbf{p}_T, S) = \frac{1}{(2\pi)^3 2(1-x)P^+} \text{Tr} \left[(\not{P} + M) \frac{1 + \gamma^5 \not{\not{p}}}{2} G^{*\nu\sigma}(p, p) \mathcal{Y}_\sigma^{\dagger ab}(p^2) (\not{P} - \not{p} + M_X) \mathcal{Y}_\rho^{ba}(p^2) G^{\mu\rho}(p, p) \right], \quad (3)$$

¹ We remark that in Ref. [30] there is an error in the position of the \mathcal{Y} vertices and a typo in the definition of the $G^{\mu\rho}$ propagator.

where a, b are color indices (in the adjoint representation) and

$$G^{\mu\rho}(p, q) = -\frac{i}{q^2 - m_g^2} \left(g^{\mu\rho} - \frac{q^\mu (n_-)^\rho}{p^+} \right) \quad (4)$$

is a specific Feynman rule for the gluon propagator in the definition of the correlator [31, 32], with n_-^ρ a light-like unit vector of the light-cone basis, and m_g a gluon mass regulator which will be set to zero in our calculations. We model the nucleon-gluon-spectator vertex as

$$\mathcal{Y}_\rho^{ba}(p^2) = \delta^{ba} \left[g_1(p^2) \gamma_\rho + g_2(p^2) \frac{i}{2M} \sigma_{\rho\nu} p^\nu \right], \quad (5)$$

where as usual $\sigma_{\rho\nu} = i[\gamma_\rho, \gamma_\nu]/2$, and $g_{1,2}(p^2)$ are generic form factors. In principle, the expression of $\mathcal{Y}_\rho^{ba}(p^2)$ could contain more Dirac structures. However, with our assumptions the spectator is identified with an on-shell spin- $\frac{1}{2}$ particle, much like the nucleon. Hence, we model the structure of $\mathcal{Y}_\rho^{ba}(p^2)$ similarly to the conserved electromagnetic current of a free nucleon obtained from the Gordon decomposition. The form factors $g_{1,2}(p^2)$ are formally similar to the Dirac and Pauli form factors, but obviously must not be identified with them. Similarly to our previous model description of quark TMDs [25], we use the dipolar expression

$$g_{1,2}(p^2) = \kappa_{1,2} \frac{p^2}{|p^2 - \Lambda_X^2|^2} = \kappa_{1,2} \frac{p^2 (1-x)^2}{(\mathbf{p}_T^2 + L_X^2 (\Lambda_X^2))^2}, \quad (6)$$

where $\kappa_{1,2}$ and Λ_X are normalization and cut-off parameters, respectively, and

$$L_X^2(\Lambda_X^2) = x M_X^2 + (1-x) \Lambda_X^2 - x(1-x) M^2. \quad (7)$$

The dipolar expression of Eq. (6) has several advantages: it cancels the singularity of the gluon propagator, it smoothly suppresses the effect of high \mathbf{p}_T^2 where the TMD formalism cannot be applied, and it compensates also the logarithmic divergences arising after integration upon \mathbf{p}_T .

In our model, the overall color prefactor at tree level is

$$C^{(0)} = \delta^{ab} \delta^{ba} = 8. \quad (8)$$

As a comparison, we will also discuss the quark-target model, which can be obtained from Eq. (3) simply by replacing

$$\mathcal{Y}_\rho^{ba} \rightarrow g_s \gamma_\rho t^a, \quad (9)$$

with g_s the strong coupling constant and t^a a generator of color SU(3) transformations, and by setting $M = M_X \equiv m_q$ everywhere. In this case, the overall color factor is

$$C_q^{(0)} = \frac{1}{N_C} \text{Tr}_C [t^a t^a] = \frac{4}{3}, \quad (10)$$

where N_C is the number of colors and Tr_C indicates the trace upon color indices.

B. Additional single-gluon exchange

In general, T-odd TMDs arise only when there is a residual interaction between the active parton and the spectator. More specifically, they arise from the imaginary part of the interference between the tree-level channel and the channel describing this residual interaction. Following our model calculation for quark TMDs [25], we generate this interference by describing the residual gluon-spectator interaction through the exchange of a soft gluon (see Fig. 2). This one-gluon exchange results from the truncation at the first order in the expansion of the path-ordered exponential that defines the gauge link as the sum of infinite gluon rescatterings [33].

In the general definition of the parton-parton correlator Φ , the gauge link is a necessary ingredient to make the correlator color-gauge invariant. However, the sensitivity of TMDs to the transverse components of the gauge link introduces a process dependence, contrary to the case of collinear PDFs. While T-even quark TMDs are independent from the direction of the color flow in the involved hard scattering, T-odd quark TMDs change sign when moving

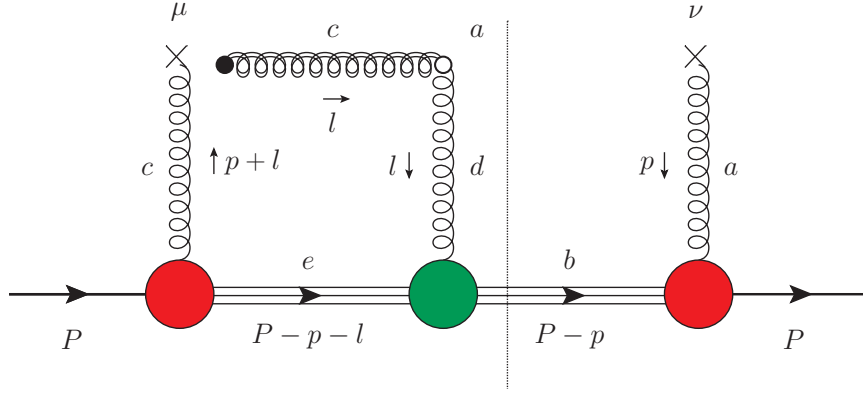


Figure 2. Diagram for the calculation of the gluon-gluon correlator including the single-gluon exchange contribution, necessary to obtain T-odd TMDs. The eikonal propagator arising from the Wilson line in the operator definition of TMDs is indicated by a gluon double line. Only the imaginary part of the box diagram on the left-hand side of the cut is relevant for the calculation of T-odd functions. The red blobs represent the nucleon-gluon-spectator vertex with color indices ce and ba , respectively, while the green blob stands for the spectator-gluon-spectator vertex with color indices edb . The Hermitian-conjugate diagram is not shown.

from final-state interactions with future-pointing ($[+]$) Wilson lines (like in Semi-Inclusive Deep-Inelastic Scattering - SIDIS) to initial-state interactions with past-pointing ($[-]$) Wilson lines (like in Drell-Yan processes) [34–36].

The gluon case is more intricate, due its color-octet structure, and leads to a more diversified form of modified universality with respect to the quark case. There is a gauge link with color flowing through a closed path pointing to the future, corresponding to final-state interactions between the spectator and an outgoing gluon, like in SIDIS production of two jets or heavy-quark pairs [37]. This gauge link is usually denoted with the $[+, +]$ symbol. Conversely, initial-state interactions are described by gauge links with past-pointing close Wilson lines ($[-, -]$) and occur, for example, in Higgs production via gluon fusion ($gg \rightarrow H$) [38, 39]. The gluon TMDs originating from these gauge links are called Weizsäcker–Williams (WW) gluon TMDs, or f -type gluon TMDs because the color structure of the T-odd ones involves the antisymmetric structure constants f of the color gauge group $SU(3)$. It turns out that T-even WW gluon TMDs are symmetric with respect to the different paths ($[+, +] = [-, -]$), while the T-odd WW ones change sign.

Moreover, color can flow through a closed path involving both initial and final states, like in photon-jet production from hadronic collisions or SIDIS [40–42]. We remark that for this class of processes TMD factorization is not expected to hold [43]; however, it is still possible to calculate the corresponding TMDs in the context of our model. Depending on the direction of color flow, we have $[+, -]$ and $[-, +]$ structures and the corresponding gluon TMDs are usually called dipole gluon TMDs, or d -type gluon TMDs because their T-odd color structure involves the symmetric structure constants d of color $SU(3)$.² Similarly to the WW case, the dipole T-even gluon TMDs are symmetric with respect to different color paths ($[+, -] = [-, +]$), while T-odd dipole ones change sign. But, more importantly, WW and dipole gluon TMDs are not related to each other, and contain different physical information.

We first compute the gluon-gluon correlator corresponding to the $[+, +]$ gauge link with future-pointing closed Wilson path. The one-gluon exchange approximation of the gauge link amounts to compute the diagram depicted in Fig. 2. The double gluon line represents the struck gluon described in the eikonal approximation, following the same procedure of the quark case [25]. The Feynman rules to describe the eikonal gluon line and the eikonal vertex are written in detail in Ref. [47].

The expression of the correlator turns out to be

$$\begin{aligned} \Phi^{\mu\nu[+,+]}(x, \mathbf{p}_T, S) &= \frac{1}{(2\pi)^3 2(1-x)P^+} \text{Tr} \left[(\not{P} + M) \frac{1 + \gamma^5 \not{p}}{2} G^{*\nu\sigma}(p, p) \mathcal{Y}_\sigma^{\dagger ab}(p^2) (\not{P} - \not{p} + M_X) (g_s n_-^\alpha f^{dac}) \right. \\ &\quad \times \left. \int \frac{d^4 l}{(2\pi)^4} \left(\frac{-i \mathcal{X}_\alpha^{bde}(l^2)}{l^2 - m_g^2} \right) \left(\frac{-i}{l^+ + i\epsilon} \right) \frac{i(\not{P} - \not{p} - \not{l} + M_X)}{(P-p-l)^2 - M_X^2 + i\epsilon} \mathcal{Y}_\rho^{ec}((p+l)^2) G^{\mu\rho}(p, p+l) \right], \end{aligned} \quad (11)$$

² Due to the connection between the T-odd TMDs at twist-2 and the collinear PDFs at twist-3, the distinction between f -type and d -type gluon TMDs appears already in the correlator of the Qiu–Sterman twist-3 collinear PDF [44–46].

where \mathcal{X}_α^{bde} is the spectator-gluon-spectator vertex to be defined in Section III C.

The correlator $\Phi^{\mu\nu[-,-]}$ for the $[-,-]$ past-pointing closed Wilson path can be obtained by changing the sign of the $+i\epsilon$ term in Eq. (11).

The correlator $\Phi^{\mu\nu[+,-]}$ for the $[+,-]$ gauge link (leading to d -type gluon TMDs [48–50]) can be simply derived by replacing in the eikonal vertex the antisymmetric color structure f^{dac} with the symmetric $-id^{dac}$ in Eq. (11):

$$\begin{aligned} \Phi^{\mu\nu[+,-]}(x, \mathbf{p}_T, S) = & \frac{1}{(2\pi)^3 2(1-x)P^+} \text{Tr} \left[(\not{P} + M) \frac{1 + \gamma^5 \not{g}}{2} G^{*\nu\sigma}(p, p) \mathcal{Y}_\sigma^{\dagger ab}(p^2) (\not{P} - \not{p} + M_X) (-ig_s n_-^\alpha d^{dac}) \right. \\ & \left. \times \int \frac{d^4 l}{(2\pi)^4} \left(\frac{-i\mathcal{X}_\alpha^{bde}(l^2)}{l^2 - m_g^2} \right) \left(\frac{-i}{l^+ + i\epsilon} \right) \frac{i(\not{P} - \not{p} - \not{l} + M_X)}{(P - p - l)^2 - M_X^2 + i\epsilon} \mathcal{Y}_\rho^{ec}((p+l)^2) G^{\mu\rho}(p, p+l) \right]. \end{aligned} \quad (12)$$

As for the WW case, the $[-,+]$ correlator differs from the $[+,-]$ one only by the sign of the $+i\epsilon$ term in Eq. (12).

Our model agrees with the relations between gluon TMDs with different gauge link structures that have been systematically studied in [51]. For example, for the T-even unpolarized function, f_1^g , and for the T-odd gluon Sivers function, f_{1T}^g , one has the following modified-universality relations [11, 40, 51]:

$$f_1^{g[+,+]} = f_1^{g[-,-]}, \quad f_1^{g[+,-]} = f_1^{g[-,+]}, \quad (13)$$

$$f_{1T}^{\perp g[+,+]} = -f_{1T}^{\perp g[-,-]}, \quad f_{1T}^{\perp g[+,-]} = -f_{1T}^{\perp g[-,+]} . \quad (14)$$

As it turns out, in general $f_1^{g[+,+]}$ cannot be related to $f_1^{g[+,-]}$, and likewise for $f_{1T}^{\perp g}$. They encode different information and require different extractions [3].

C. Spectator-gluon-spectator vertex

A key ingredient of our model is the spectator-gluon-spectator vertex \mathcal{X}_α^{bde} , depicted by a green blob in Fig. 2. If the nucleon-gluon-spectator vertex \mathcal{Y}_μ^{ec} (red blob) connects a colorless initial-state (nucleon) to an octet state (gluon) and an anti-octet state (spectator), the spectator-gluon-spectator vertex \mathcal{X}_α^{bde} connects an anti-octet initial state (spectator) to an octet state (gluon) and an anti-octet state (spectator). Since in our model the spectator is assumed to be a spin- $\frac{1}{2}$ particle describing a collection of partons as remainders, the vertex \mathcal{X}_α^{bde} can in principle contain both the f^{bde} and d^{bde} color structure constants, each one multiplying a Dirac structure similar to Eq. (5):

$$\mathcal{X}_\alpha^{bde}(p^2) = f^{bde} \left[g_1^f(p^2) \gamma_\alpha + g_2^f(p^2) \frac{i}{2M} \sigma_{\alpha\beta} p^\beta \right] - i d^{bde} \left[g_1^d(p^2) \gamma_\alpha + g_2^d(p^2) \frac{i}{2M} \sigma_{\alpha\beta} p^\beta \right], \quad (15)$$

where $g_{1,2}^{f,d}(p^2)$ are *a priori* four different functions of p^2 . In principle, they are independent from the $g_{1,2}(p^2)$ form factors entering the nucleon-gluon-spectator vertex of Eq. (5). For the sake of simplicity, we will assume $g_{1,2}^d(p^2) = g_{1,2}^f(p^2)$ and we will get d -type densities equal to the corresponding f -type ones up to a color factor:

$$C^{[+,+]} = f^{acd} f^{dca} = -2C_A^2 C_F = -24, \quad (16)$$

$$C^{[+,-]} = (-i d^{acd}) (-i d^{dca}) = 2(4 - C_A^2) C_F = -\frac{40}{3}. \quad (17)$$

For this reason, in the following we will show results only for f -type gluon TMDs, and we will drop the $[+, +]$ index when not needed.

In the quark-target model, we would replace the spectator-gluon-spectator vertex by $\mathcal{X}_\alpha^{bde} \rightarrow (-ig_s \gamma_\alpha t^d)$ and obtain the color factors

$$C_q^{[+,+]} = -\frac{i}{N_C} \text{Tr}_C [t^a t^c t^d] f^{acd} = \frac{C_A C_F}{2} = -2, \quad (18)$$

$$C_q^{[+,-]} = -\frac{1}{N_C} \text{Tr}_C [t^a t^c t^d] d^{acd} = \frac{C_F}{2} (4 - C_A^2) (C_A - 2C_F) = -\frac{10}{9}. \quad (19)$$

Note that the ratio of the two different gauge link structures remains the same in the two cases: $[+,-]/[+,+] = 5/9$. With our simplified assumptions, therefore, the T-odd d -type functions are always about half of the f -type ones.

We further assume

$$g_{1,2}^d(p^2) = g_{1,2}^f(p^2) \equiv g_{1,2}(p^2) . \quad (20)$$

This means that the parameters entering our model for f -type and d -type T-odd gluon TMDs are fully determined by those ones entering the T-even gluon TMDs that contain $g_{1,2}(p^2)$ through Eq. (5). The latter parameters have been fixed by fitting the integrated T-even gluon TMDs on the known corresponding collinear PDFs [30] (see Tab. II).

D. Gluon TMD projectors

T-odd gluon TMDs can be extracted from the analytic structure of the gluon-gluon correlator by making use of suitable projectors. Using Eqs.(52-54) of Ref. [4] for the general parametrization of the gluon-gluon correlator $\Phi^{\mu\nu}(x, \mathbf{p}_T, S)$ for three different nucleon polarizations $S = 0, S_L, \mathbf{S}_T$, it is possible to show that the four T-odd gluon TMDs of Tab. I can be isolated through the following projections:

$$\begin{aligned} f_{1T}^{\perp g} &= \mathbb{P}_{[f_{1T}^{\perp g}]}^{\mu\nu} [\Phi_{\mu\nu}(x, \mathbf{p}_T, \mathbf{S}_T) - \Phi_{\mu\nu}(x, \mathbf{p}_T, -\mathbf{S}_T)] \\ &= \frac{M}{2} \frac{1}{\epsilon_T^{p_T S_T}} g_T^{\mu\nu} [\Phi_{\mu\nu}(x, \mathbf{p}_T, \mathbf{S}_T) - \Phi_{\mu\nu}(x, \mathbf{p}_T, -\mathbf{S}_T)] , \end{aligned} \quad (21)$$

$$\begin{aligned} h_{1T}^{\perp g} &= \mathbb{P}_{[h_{1T}^{\perp g}]}^{\mu\nu} [\Phi_{\mu\nu}(x, \mathbf{p}_T, \mathbf{S}_T) - \Phi_{\mu\nu}(x, \mathbf{p}_T, -\mathbf{S}_T)] \\ &= \frac{M^3}{p_T^2} \frac{1}{\epsilon_T^{p_T S_T}} \left(\frac{p_T^{\{\mu} S_T^{\nu\}}}{p_T \cdot S_T} - g_T^{\mu\nu} \right) [\Phi_{\mu\nu}(x, \mathbf{p}_T, \mathbf{S}_T) - \Phi_{\mu\nu}(x, \mathbf{p}_T, -\mathbf{S}_T)] , \end{aligned} \quad (22)$$

$$\begin{aligned} h_1^g &= \mathbb{P}_{[h_1^g]}^{\mu\nu} [\Phi_{\mu\nu}(x, \mathbf{p}_T, \mathbf{S}_T) - \Phi_{\mu\nu}(x, \mathbf{p}_T, -\mathbf{S}_T)] \\ &= \frac{M}{2\epsilon_T^{p_T S_T}} \left[\frac{4}{p_T^2} p_T^\mu p_T^\nu + \frac{p_T^{\{\mu} S_T^{\nu\}}}{p_T \cdot S_T} - 3g_T^{\mu\nu} \right] [\Phi_{\mu\nu}(x, \mathbf{p}_T, \mathbf{S}_T) - \Phi_{\mu\nu}(x, \mathbf{p}_T, -\mathbf{S}_T)] , \end{aligned} \quad (23)$$

$$\begin{aligned} h_{1L}^{\perp g} &= \mathbb{P}_{[h_{1L}^{\perp g}]}^{\mu\nu} [\Phi_{\mu\nu}(x, \mathbf{p}_T, S_L) - \Phi_{\mu\nu}(x, \mathbf{p}_T, -S_L)] \\ &= \frac{1}{S_L} \frac{M^2}{2p_T^4} \epsilon_T^{\{\mu} \alpha p_T^{\nu\} \alpha} [\Phi_{\mu\nu}(x, \mathbf{p}_T, S_L) - \Phi_{\mu\nu}(x, \mathbf{p}_T, -S_L)] , \end{aligned} \quad (24)$$

where $\epsilon_T^{vw} \equiv \epsilon^{-+ij} v_i w_j$ with i, j transverse spatial indices and $\epsilon^{\mu\nu\alpha\beta}$ the antisymmetric Levi-Civita tensor, and

$$p_T^{\mu\nu} = p_T^\mu p_T^\nu - \frac{1}{2} p_T^2 g_T^{\mu\nu} , \quad (25)$$

$$g_T^{\mu\nu} = g^{\mu\nu} - n_+^{\{\mu} n_-^{\nu\}} , \quad (26)$$

$$v^{\{\mu} w^{\nu\}} = v^\mu w^\nu + v^\nu w^\mu . \quad (27)$$

III. T-ODD GLUON TMDs: ILLUSTRATIVE EXAMPLES

A. Sivers function: g_1 -vertex approximation

Let us consider first the f -type Sivers function $f_{1T}^{\perp [+,+]}$ with a simpler expression for the nucleon-gluon-spectator vertex, where the term proportional to $\sigma^{\mu\nu} p_\nu$ in Eq. (5) is neglected. In other words, the $g_2(p)$ coupling is set to zero and the vertex reduces to

$$\mathcal{Y}_\rho^{ba} \rightarrow \delta^{ba} g_1(p^2) \gamma_\rho . \quad (28)$$

We name this the “ g_1 -vertex approximation”. We indicate the resulting Sivers function as $f_{1T}^{\perp (g_1)}$, and similarly for all other TMDs computed in this approximation.

Using for $g_1(p^2)$ the dipolar form of Eq. (6), the corresponding projector of Eq. (21) specialized to a f -type gluon Sivers and applied to the correlator of Eq. (11), we obtain

$$\begin{aligned} f_{1T}^{\perp(g_1)}(x, \mathbf{p}_T) &= \mathbb{P}_{[f_{1T}^{\perp g_1}]}^{\mu\nu} \left[\Phi_{\mu\nu}^{[+,+](g_1)}(x, \mathbf{p}_T, \mathbf{S}_T) - \Phi_{\mu\nu}^{[+,+](g_1)}(x, \mathbf{p}_T, -\mathbf{S}_T) \right] \\ &= \frac{48 g_s \kappa_1^3}{(2\pi)^3} \frac{M [M_X - M(1-x)] P^+}{(p^2 - \Lambda_X^2)^2} 2 \text{Re} \int \frac{d^4 l}{(2\pi)^4} \frac{\epsilon_T^{l_T S_T}}{(l^2 - \Lambda_X^2)^2} \frac{1}{l^+ + i\epsilon} \frac{1}{(l+p-P)^2 - M_X^2 + i\epsilon} \frac{1}{[(p+l)^2 - \Lambda_X^2 + i\epsilon]^2}. \end{aligned} \quad (29)$$

In Eq. (29), terms proportional to $\epsilon^{ln-pP} \equiv \epsilon^{\mu\nu\alpha\beta} l_\mu n_{-\nu} p_\alpha P_\beta$ and ϵ^{lpPS} vanish because the only component of l contributing to the integral is the one parallel to p .

Similarly to the calculation of the quark Sivers TMD [25, 52–55], the non vanishing contribution to the integral of Eq. (29) comes from the poles of the two $[l^+ + i\epsilon]$ and $[(l+p-P)^2 - M_X^2 + i\epsilon]$ propagators.

Using the Cutkosky's rules, we can make the replacement

$$\frac{1}{l^+ + i\epsilon} \rightarrow -2\pi i \delta(l^+), \quad \frac{1}{(l+p-P)^2 - M_X^2 + i\epsilon} \rightarrow -2\pi i \delta((l+p-P)^2 - M_X^2). \quad (30)$$

Moreover, we can also make use of the spectator model relation

$$k^2 - \Lambda_X^2 = -\frac{\mathbf{k}_T^2 + L_X^2(\Lambda_X)}{1-x}, \quad (31)$$

where k^2 generically refers to p^2 , l^2 or $(p+l)^2$, and \mathbf{k}_T^2 to the corresponding euclidean transverse parts.

The final result for the WW gluon Sivers function with only g_1 coupling is

$$f_{1T}^{\perp(g_1)}(x, \mathbf{p}_T) = -\frac{48 g_s \kappa_1^3}{(2\pi)^3} \frac{M [M_X - M(1-x)] (1-x)^5 P^+}{[\mathbf{p}_T^2 + L_X^2(\Lambda_X)]^2} \mathcal{D}_2(p), \quad (32)$$

where

$$\mathcal{D}_2(p) = \frac{1}{2P^+} \int \frac{d^2 \mathbf{l}_T}{(2\pi)^2} \frac{\mathbf{l}_T \cdot \mathbf{p}_T}{\mathbf{p}_T^2} \frac{1}{[\mathbf{l}_T^2 + L_X^2(\Lambda_X^2)]^2} \frac{1}{[(\mathbf{l}_T + \mathbf{p}_T)^2 + L_X^2(\Lambda_X^2)]^2}. \quad (33)$$

Introducing the Feynman parametrization, we can rewrite the integral as

$$\mathcal{D}_2(p) = \frac{1}{2P^+} \int \frac{d^2 \mathbf{l}_T}{(2\pi)^2} \frac{\mathbf{l}_T \cdot \mathbf{p}_T}{\mathbf{p}_T^2} \int_0^1 d\alpha \frac{6\alpha(1-\alpha)}{\{\alpha[\mathbf{l}_T^2 + L_X^2(\Lambda_X^2)] + (1-\alpha)[(\mathbf{l}_T + \mathbf{p}_T)^2 + L_X^2(\Lambda_X^2)]\}^4}. \quad (34)$$

After the change of variable $\mathbf{l}_T \rightarrow \mathbf{l}'_T = \mathbf{l}_T + (1-\alpha)\mathbf{p}_T$, we have

$$\begin{aligned} \mathcal{D}_2(p) &= -\frac{1}{2P^+} \int_0^1 d\alpha \int \frac{d^2 \mathbf{l}'_T}{(2\pi)^2} \frac{6\alpha(1-\alpha)^2}{[\mathbf{l}'_T{}^2 + \alpha(1-\alpha)\mathbf{p}_T^2 + L_X^2(\Lambda_X^2)]^4} \\ &= -\frac{1}{4\pi P^+} \int_0^1 d\alpha \frac{\alpha(1-\alpha)^2}{[\alpha(1-\alpha)\mathbf{p}_T^2 + L_X^2(\Lambda_X^2)]^3} \\ &= -\frac{1}{8\pi P^+} \left[\frac{1 - 2L_X^2(\Lambda_X^2)/\mathbf{p}_T^2}{L_X^2(\Lambda_X^2) [\mathbf{p}_T^2 + 4L_X^2(\Lambda_X^2)]^2} + 8 \frac{\mathbf{p}_T^2 + L_X^2(\Lambda_X^2)}{|\mathbf{p}_T|^3 [\mathbf{p}_T^2 + 4L_X^2(\Lambda_X^2)]^{5/2}} \tanh^{-1} \left(\frac{|\mathbf{p}_T|}{\sqrt{\mathbf{p}_T^2 + 4L_X^2(\Lambda_X^2)}} \right) \right]. \end{aligned} \quad (35)$$

Combining Eqs. (32) and (35) we get the final expression for our f -type Sivers function in the g_1 -vertex approximation

$$\begin{aligned} f_{1T}^{\perp(g_1)}(x, \mathbf{p}_T) &= \frac{12 g_s \kappa_1^3}{(2\pi)^4} \frac{M [M_X - M(1-x)] (1-x)^5}{[\mathbf{p}_T^2 + L_X^2(\Lambda_X)]^2} \\ &\times \left[\frac{1 - 2L_X^2(\Lambda_X^2)/\mathbf{p}_T^2}{L_X^2(\Lambda_X^2) [\mathbf{p}_T^2 + 4L_X^2(\Lambda_X^2)]^2} + 8 \frac{\mathbf{p}_T^2 + L_X^2(\Lambda_X^2)}{|\mathbf{p}_T|^3 [\mathbf{p}_T^2 + 4L_X^2(\Lambda_X^2)]^{5/2}} \tanh^{-1} \left(\frac{|\mathbf{p}_T|}{\sqrt{\mathbf{p}_T^2 + 4L_X^2(\Lambda_X^2)}} \right) \right]. \end{aligned} \quad (36)$$

In order to explore the effects of the g_1 -vertex approximation, we fix the model parameters by simultaneously fitting the integrated unpolarized and helicity gluon TMDs onto the corresponding known collinear PDFs. Following

parameter	PVGlue20		PVGlue20g1V	
	mean	replica 11	mean	replica 11
A [GeV ⁻¹]	6.1 ± 2.3	6.0	4.3 ± 1.5	4.29
a	0.82 ± 0.21	0.78	0.73 ± 0.14	0.73
b	1.43 ± 0.23	1.38	1.34 ± 0.13	1.33
C [GeV ⁻¹]	371 ± 58	346	349 ± 24	350
D [GeV]	0.548 ± 0.081	0.548	0.595 ± 0.049	0.586
σ [GeV]	0.52 ± 0.14	0.50	0.42 ± 0.08	0.41
Λ_X [GeV]	0.472 ± 0.058	0.448	0.398 ± 0.035	0.384
κ_1 [GeV ²]	1.51 ± 0.16	1.46	1.33 ± 0.08	1.28
κ_2 [GeV ²]	0.414 ± 0.036	0.414	0.0	0.0

Table II. Mean values of fitted parameters with their 68% uncertainties, and corresponding values for the most representative replica 11 (see text). The original fit of Ref. [30] and the “ g_1 -vertex approximation” are labeled as PVGlue20 and PVGlue20g1V, respectively (see text).

the methodology of Ref. [30], we first allow the spectator mass to take a continuous range of values by weighting the gluon TMDs with the spectral function described in Eqs.(16,17) of Ref. [30], which is a way to effectively take into account $q\bar{q}$ contributions. Then, we integrate the gluon TMDs upon the transverse momenta and we fix all the model parameters by fitting the unpolarized collinear PDF from NNPDF3.1sx [56] and the helicity collinear PDF from NNPDFpol1.1 [57] at the indicated initial scale $Q_0 = 1.64$ GeV and in the range $10^{-3} < x < 0.7$.³ The only exception is the parameter κ_2 in Eq. (6) that controls the strength of the g_2 coupling; here, it is systematically set to zero. Statistical uncertainties are generated using the replica method, widely used in the phenomenological extraction of quark densities from experimental data [56, 59–65].

In Tab. II, we compare the obtained values (labelled PVGlue20g1V in the two rightmost columns) with the original values from Ref. [30] (labelled PVGlue20 in the second and third columns from left). The 68% uncertainties accompanying the central values are obtained by excluding the largest and smallest 16% of all 100 replica values, which would correspond to 1σ standard deviation for a Gaussian distribution. The columns labelled with “replica 11” show the parameters of the most representative replica, because in both fits its parameter values have the minimal distance from the mean values.

In Fig. 3, we show the results for the f -type unpolarized gluon TMD (upper panels) and the gluon Sivers function multiplied by $x|\mathbf{p}_T|/M$ (lower panels), as functions of \mathbf{p}_T^2 , in the g_1 -vertex approximation.⁴ Left (right) plots are for TMDs calculated at $x = 10^{-3}$ ($x = 10^{-1}$) and at $Q_0 = 1.64$ GeV. As for the parameter values, the 68% uncertainty bands are formed by excluding the largest and smallest 16% of 100 computed replicas. The black solid line is the result of the most representative replica 11. Here, and in the following, the strong coupling constant is fixed to $g_s = \sqrt{\alpha_s(Q_0)} = 0.57583$. The qualitative behavior of the TMD f_1^g stays practically the same with respect to the original fit (see upper panels of Fig. 4 in Ref. [30]). The resulting gluon Sivers function decreases at low x . However, this trend can radically change when including also the g_2 vertex, as shown in Sec. IV.

B. Sivers function: Quark-target model

In a similar way, we can also derive the results for the f -type gluon Sivers function in the quark-target model. We indicate it with the superscript (q). In this approximation, the incoming proton in Fig. 2 is replaced by a quark, and similarly for the spectator remnant. Therefore, both the proton and the spectator mass, M and M_X , are set equal to the target-quark mass, m_q , and the effective nucleon-gluon-spectator vertex is replaced by a QCD quark-gluon-quark one. Starting from the expression for the $[+, +]$ gluon correlator in the quark-target model, we obtain

$$f_{1T}^{\perp(q)}(x, \mathbf{p}_T) = -\frac{4g_s^4}{(2\pi)^3} \frac{m_q^2 x(1-x)P^+}{(m_q^2 x^2 + \mathbf{p}_T^2)} \mathcal{D}_q(p), \quad (37)$$

where

$$\mathcal{D}_q(p) = \frac{1}{2(1-x)P^+} \int \frac{d^2\mathbf{l}_T}{(2\pi)^2} \frac{\mathbf{l}_T \cdot \mathbf{p}_T}{\mathbf{p}_T^2} \frac{1}{\mathbf{l}_T^2} \frac{(1-x)}{(\mathbf{l}_T + \mathbf{p}_T)^2 + x^2 m_q^2}. \quad (38)$$

³ The $x > 0.7$ tail was excluded to avoid large uncertainties [58] due to threshold effects and target-mass corrections, not accounted for in our model.

⁴ Preliminary results for the f -type Sivers function in the g_1 -vertex approximation were previously presented in Refs. [66, 67].

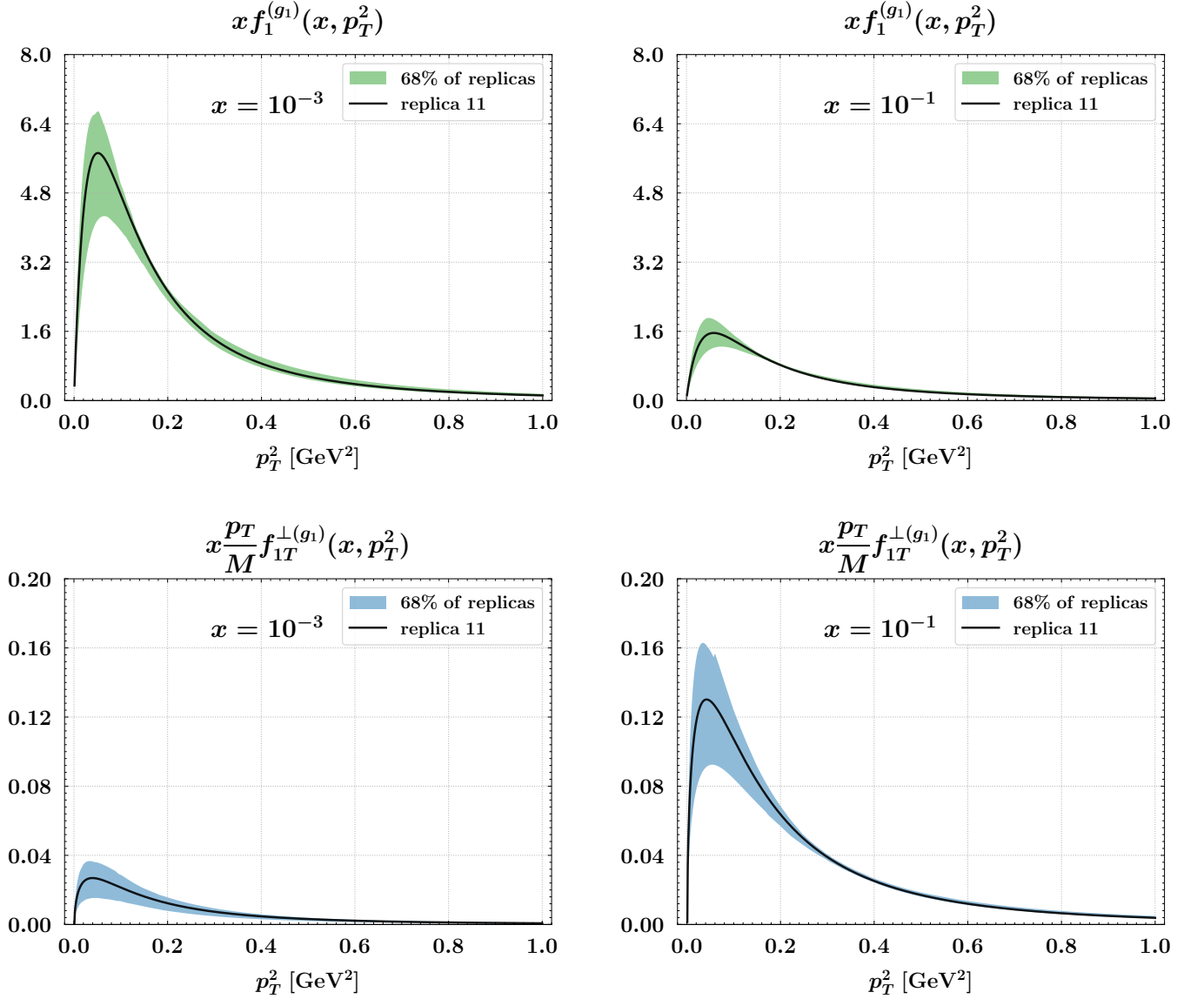


Figure 3. Transverse-momentum dependence of the $[+, +]$ unpolarized TMD (upper panel) and gluon Sivers TMD multiplied by $x|\mathbf{p}_T|/M$ (lower panel) calculated in the g_1 -vertex approximation (see text), at $x = 10^{-3}$ (left panels) and $x = 10^{-1}$ (right panels) and at the initial scale $Q_0 = 1.64$ GeV. Uncertainty band by including the 68% of all computed replicas. Black curves refer to the most representative replica 11 (see text).

Following similar steps as in the previous case, we obtain

$$\mathcal{D}_q(p) = -\frac{1}{8\pi P^+} \frac{1}{\mathbf{p}_T^2} \ln \frac{\mathbf{p}_T^2 + x^2 m_q^2}{x^2 m_q^2}, \quad (39)$$

and we get the final expression for our f -type gluon Sivers function in the quark-target model

$$f_{1T}^{\perp(q)}(x, \mathbf{p}_T) = \frac{g_s^4}{(2\pi)^4} \frac{m_q^2 x (1-x)}{\mathbf{p}_T^2 (m_q^2 x^2 + \mathbf{p}_T^2)} \ln \frac{\mathbf{p}_T^2 + x^2 m_q^2}{x^2 m_q^2}, \quad (40)$$

which corresponds to Eq. (B12) of Ref. [4].

C. Linearity function: g_1 -vertex approximation

Let us consider now the distribution of linearly polarized gluons in a transversely polarized target, denoted as h_1 in Tab. I. For simplicity, we will call it ‘‘linearity function’’ even if this terminology could be used for any h functions in the rightmost column of Tab. I. In spite of the similarity in notation, this function should not be confused with the analogue of the quark transversity distribution. In fact, it does not survive transverse-momentum integration and is T-odd.

In the following, we derive the f -type gluon linearity function in the g_1 -vertex approximation of our spectator model. Using the corresponding projector from Eq. (23), the dipolar form for $g_1(p^2)$ as in Eq. (6), and the $[+, +]$ gluon correlator of Eq. (11), we have

$$\begin{aligned} h_1^{(g_1)}(x, \mathbf{p}_T) &= \mathbb{P}_{[h_1^g]}^{\mu\nu} \left[\Phi_{\mu\nu}^{[+,+](g_1)}(x, \mathbf{p}_T, \mathbf{S}_T) - \Phi_{\mu\nu}^{[+,+](g_1)}(x, \mathbf{p}_T, -\mathbf{S}_T) \right] \\ &= \frac{96 g_s \kappa_1^3 M [M - M_X(1-x)] P^+}{(2\pi)^3 (1-x) \mathbf{p}_T^2 (p^2 - \Lambda_X^2)^2} \\ &\quad \times 2 \operatorname{Re} \int \frac{d^4 l}{(2\pi)^4} \frac{l_T \cdot \mathbf{p}_T}{(l^2 - \Lambda_X^2)^2} \frac{1}{l^+ + i\epsilon} \frac{1}{(l+p-P)^2 - M_X^2 + i\epsilon} \frac{1}{[(p+l)^2 - \Lambda_X^2 + i\epsilon]^2}. \end{aligned} \quad (41)$$

Following the same steps described in Section III A we obtain

$$h_1^{(g_1)}(x, \mathbf{p}_T) = -\frac{96 g_s \kappa_1^3 M [M - M_X(1-x)] (1-x)^4 P^+}{(2\pi)^3 [\mathbf{p}_T^2 + L_X^2(\Lambda_X)^2]} \mathcal{D}_2(p), \quad (42)$$

where $\mathcal{D}_2(p)$ is defined and computed in Eqs. (33)-(35). The final expression for our f -type gluon linearity function in the g_1 -vertex approximation is

$$\begin{aligned} h_1^{(g_1)}(x, \mathbf{p}_T) &= \frac{24 g_s \kappa_1^3 M [M - M_X(1-x)] (1-x)^4}{(2\pi)^4 [\mathbf{p}_T^2 + L_X^2(\Lambda_X)^2]} \\ &\quad \times \left[\frac{1 - 2 L_X^2(\Lambda_X^2)/\mathbf{p}_T^2}{L_X^2(\Lambda_X^2) [\mathbf{p}_T^2 + 4L_X^2(\Lambda_X^2)]^2} + 8 \frac{\mathbf{p}_T^2 + L_X^2(\Lambda_X^2)}{|\mathbf{p}_T|^3 [\mathbf{p}_T^2 + 4L_X^2(\Lambda_X^2)]^{5/2}} \tanh^{-1} \left(\frac{|\mathbf{p}_T|}{\sqrt{\mathbf{p}_T^2 + 4L_X^2(\Lambda_X^2)}} \right) \right]. \end{aligned} \quad (43)$$

Preliminary results on the f -type gluon linearity function in the g_1 -vertex approximation were presented in Refs. [67, 68].

D. Linearity function: Quark-target model

In the quark-target model, following an analogous procedure to the one in Section III B, we get

$$h_1^{(q)}(x, \mathbf{p}_T) = -\frac{8 g_s^4 m_q^2 x P^+}{(2\pi)^3 (m_q^2 x^2 + \mathbf{p}_T^2)} \mathcal{D}_q(p). \quad (44)$$

Combining Eqs. (44) and (39), we get the final expression for our f -type gluon linearity function in the quark-target model

$$h_1^{(q)}(x, \mathbf{p}_T) = \frac{g_s^4}{(2\pi)^4} \frac{2x m_q^2}{\mathbf{p}_T^2 (m_q^2 x^2 + \mathbf{p}_T^2)} \ln \frac{\mathbf{p}_T^2 + x^2 m_q^2}{x^2 m_q^2}, \quad (45)$$

which corresponds to Eq. (B17) of Ref. [4].

IV. T-ODD GLUON TMDs: RESULTS OF FULL CALCULATION

If we include the full structure of the nucleon-gluon-spectator vertex \mathcal{Y}_ρ^{ba} in Eq. (5), a given T-odd gluon TMD, generically indicated by $F(x, \mathbf{p}_T^2)$, can be organized as

$$F(x, \mathbf{p}_T^2) = \sum_{i,j,k}^{1,2} C_{ijk}^{[F]}(x, \mathbf{p}_T^2) g_s \kappa_i \kappa_j \kappa_k, \quad (46)$$

where $\kappa_{i,j,k}$ are the coupling constants encoded in the dipolar form factors of Eq. (6) with the assumption made in Eq. (20), and $C_{ijk}^{[F]}$ are related coefficients. For each T-odd gluon TMD $F(x, \mathbf{p}_T^2)$, the $C_{ijk}^{[F]}$ can be split in eight different contributions $C_{ijk}^{[F],l}$, $l = 1, \dots, 8$, and organized as linear combinations according to

$$C_{ijk}^{[F]}(x, \mathbf{p}_T^2) = \frac{(1-x)^4 P^+}{(2\pi)^3 [\mathbf{p}_T^2 + L_X^2(\Lambda_X)]^2} \sum_{l=1}^8 C_{ijk}^{[F],l}(x, \mathbf{p}_T^2) \mathcal{D}_l(x, \mathbf{p}_T^2), \quad (47)$$

where $\mathcal{D}_l(x, \mathbf{p}_T^2)$ are eight different master integrals that can be found in Appendix A. The final expressions of the $C_{ijk}^{[F],l}$ coefficients for each T-odd gluon TMD F and for $l = 1, \dots, 8$ and $i, j, k = 1, 2$, are listed in Appendix B.

We note that both the T-odd f -type h_{1L}^\perp and h_{1T}^\perp vanish in the g_1 -vertex approximation and in the quark-target model, because the integral describing the loop in Fig. 2 would be proportional to l^+ , which is set to zero by the first of the two Cutkosky rules in Eq. (30). This result is in line with Eqs. (B16) and (B18) of Ref. [4], respectively.

In the following, we show the results of the full calculation of all the four T-odd f -type gluon TMDs that appear at leading twist (see Tab. I). We recall that in our model T-odd d -type gluon TMDs turn out to be equal to the f -type ones up to a color factor computed in Eq. (17), because in the vertices we take the same dipole-like couplings $g_{1,2}(p^2)$ for f -type and d -type functions. Moreover, the parameters of both T-odd f -type and d -type functions are fully determined by those ones entering the T-even gluon TMDs. These parameters were fixed in Ref. [30] by fitting the integrated T-even gluon TMDs onto the corresponding known collinear PDFs at the low scale $Q_0 = 1.64$ GeV; their values are listed in the columns of Tab. II labelled by PVG1ue20.

It is convenient to start from the f -type gluon Sivvers function f_{1T}^\perp in order to compare with the results displayed in the lower panels of Fig. 3 using the g_1 -vertex approximation.

In the upper panels of Fig. 4, we display the T-odd f -type gluon Sivvers function f_{1T}^\perp multiplied by $x|\mathbf{p}_T|/M$, as a function of \mathbf{p}_T^2 at $x = 10^{-3}$ (left) and $x = 10^{-1}$ (right) and at the scale $Q_0 = 1.64$ GeV. As in previous figures, the uncertainty band is constructed by excluding the largest and smallest 16% of all 100 computed replicas, roughly corresponding to 1σ standard deviation. The solid black line is the result of the most representative replica 11. The observed behavior in \mathbf{p}_T^2 clearly does not follow a simple Gaussian pattern, rather it shows a large flattening tail for increasing \mathbf{p}_T^2 . The f -type Sivvers function is regular in $\mathbf{p}_T^2 = 0$, as it can be realized by inspecting the coefficients of Eqs. (46),(47) listed in Tabs. III-VI and the master integrals in Appendix A. Hence, the combination $x|\mathbf{p}_T|/M f_{1T}^\perp$ vanishes at $\mathbf{p}_T^2 = 0$.

By comparing with the lower panels of Fig. 3 where the $x|\mathbf{p}_T|/M f_{1T}^{\perp(g_1)}$ was computed in the g_1 -vertex approximation, we realize that the contribution of the g_2 coupling to the vertices \mathcal{Y}_ρ^{ba} of Eq. (5) and \mathcal{X}_α^{bde} of Eq. (15) completely reverses the situation: the f -type gluon Sivvers function now increases for decreasing x , thus supporting the statement that spin asymmetries generated by this T-odd gluon TMD could be sizable also at small- x .

In the lower panels of Fig. 4, we show the result of the full calculation of the T-odd f -type gluon linearity function h_1 multiplied by $x|\mathbf{p}_T|/M$, as a function of \mathbf{p}_T^2 at $x = 10^{-3}$ (left) and $x = 10^{-1}$ (right) and at the scale $Q_0 = 1.64$ GeV. Notations are the same as in previous panels. The displayed trend is similar to the f -type Sivvers function. Namely, the linearity increases with decreasing x , actually having a size larger than the Sivvers function. The linearity is also regular at $\mathbf{p}_T^2 = 0$, hence vanishes at this point when multiplied by $x|\mathbf{p}_T|/M$.

In Fig. 5, we show for the first time the result of the full calculation of the T-odd f -type gluon h_{1L}^\perp (upper panels) and h_{1T}^\perp (lower panels) functions. In particular, in the upper panel we display $x\mathbf{p}_T^2/M^2 h_{1L}^\perp$ as a function of \mathbf{p}_T^2 at $x = 10^{-3}$ (left) and $x = 10^{-1}$ (right) and at the scale $Q_0 = 1.64$ GeV. Notations are the same as in previous figures. We note that the absolute size increases with decreasing x , but overall it is much smaller than the Sivvers and linearity functions. Interestingly, at $x = 10^{-1}$ the h_{1L}^\perp function shows a very long tail in \mathbf{p}_T^2 but changes sign having a node at $\mathbf{p}_T^2 \approx 0.1$ GeV².

In the lower panels, the $x\mathbf{p}_T^3/M^3 h_{1T}^\perp$ is displayed as a function of \mathbf{p}_T^2 at $x = 10^{-3}$ (left) and $x = 10^{-1}$ (right) and at the scale $Q_0 = 1.64$ GeV. Notations are the same as in previous figures. The absolute size is one order of magnitude smaller, raising doubts on the actual possibility of ever extracting the h_{1T}^\perp from a spin asymmetry measurement. However, it shows an interesting structure with a node at small \mathbf{p}_T^2 and x .

Using the T-odd gluon TMDs computed in our model, we can complete the tomographic picture of the nucleon already discussed in Ref. [30]. To this purpose, we can construct 2-dim \mathbf{p}_T -distributions of gluons at different x for various combinations of their polarization and of the nucleon spin state.

Excluding the case of a circularly polarized gluon for which no T-odd gluon TMDs occur (see Tab. I), we can have in principle six combinations: two polarization states of the gluon (unpolarized, linearly polarized) for each polarization state of the parent nucleon (unpolarized, longitudinally polarized, transversely polarized). However, the

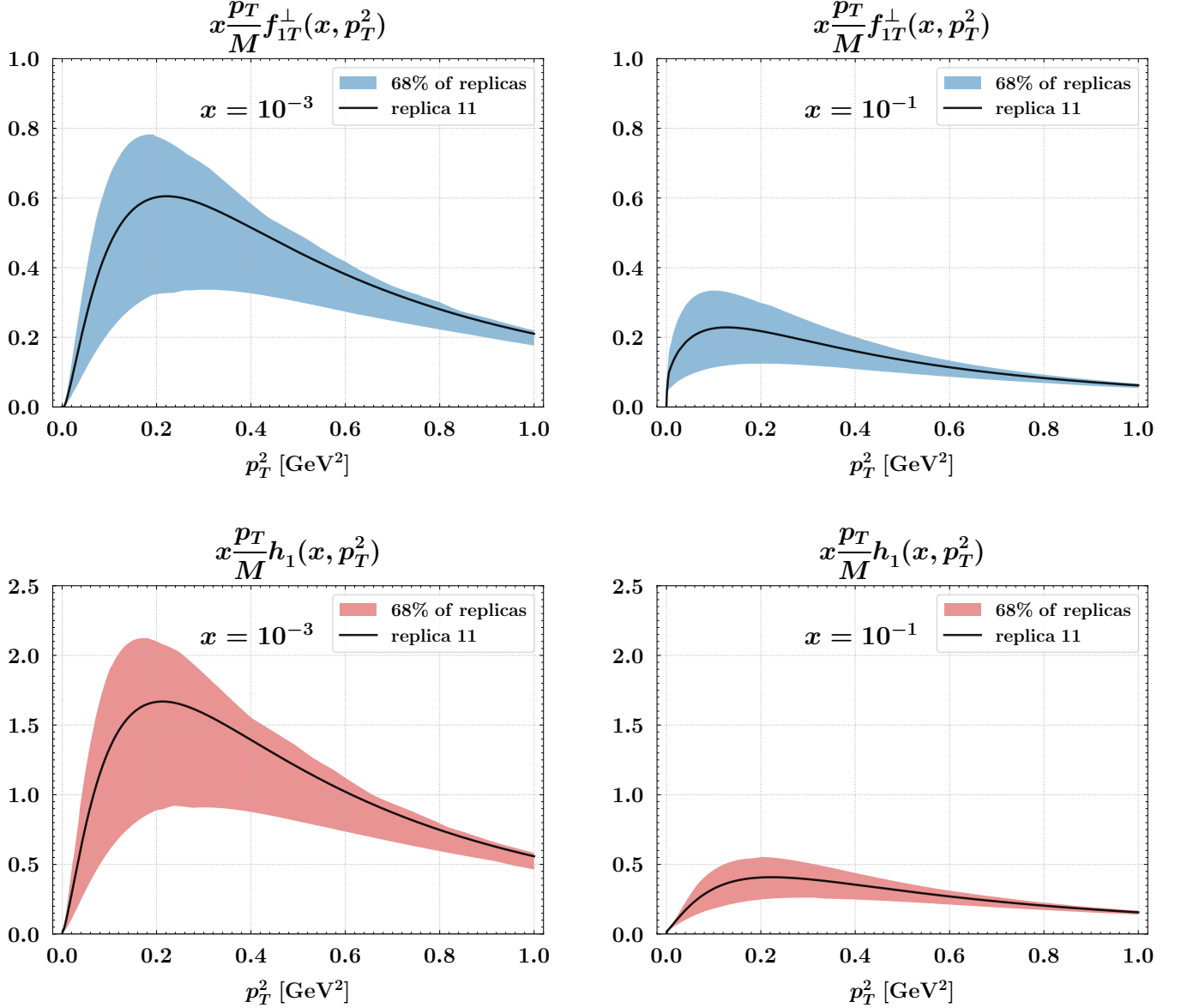


Figure 4. Transverse-momentum dependence of the $[+, +]$ gluon Sivers (upper) and linearity (lower) functions multiplied by $x|\mathbf{p}_T|/M$, as functions of p_T^2 at $x = 10^{-3}$ (left), and $x = 10^{-1}$ (right) and at the initial scale $Q_0 = 1.64$ GeV. Uncertainty band from 68% of all computed replicas. Black curves refer to the most representative replica 11 (see text).

actual combinations are five, since an unpolarized gluon in a longitudinally polarized nucleon is forbidden by parity invariance (see Tab. I).

For a unpolarized gluon in a unpolarized nucleon, we identify the 2-dim density as

$$x\rho(x, p_x, p_y) = x f_1(x, \mathbf{p}_T^2), \quad (48)$$

where f_1 is the leading-twist f -type unpolarized gluon TMD. The upper panels of Fig. 6 show the contour plots for the \mathbf{p}_T -distribution of $x\rho$ from replica 11 at $x = 10^{-3}$ (left) and $x = 10^{-1}$ (right) and at the scale $Q_0 = 1.64$ GeV, for a nucleon moving towards the reader. The color code identifies the size of the oscillations. For a better visualization, ancillary 1-dim plots are attached, representing a “slice” of $x\rho$ at $p_x = 0$ or $p_y = 0$. The 68% uncertainty band is obtained as usual by excluding the largest and smallest 16% of 100 computed replicas; the solid black line is the result of replica 11, actually corresponding to the 2-dim contour plot. Since both nucleon and gluon are unpolarized, the 2-dim density shows a perfect cylindrical symmetry around the direction of motion of the nucleon pointing towards the reader.

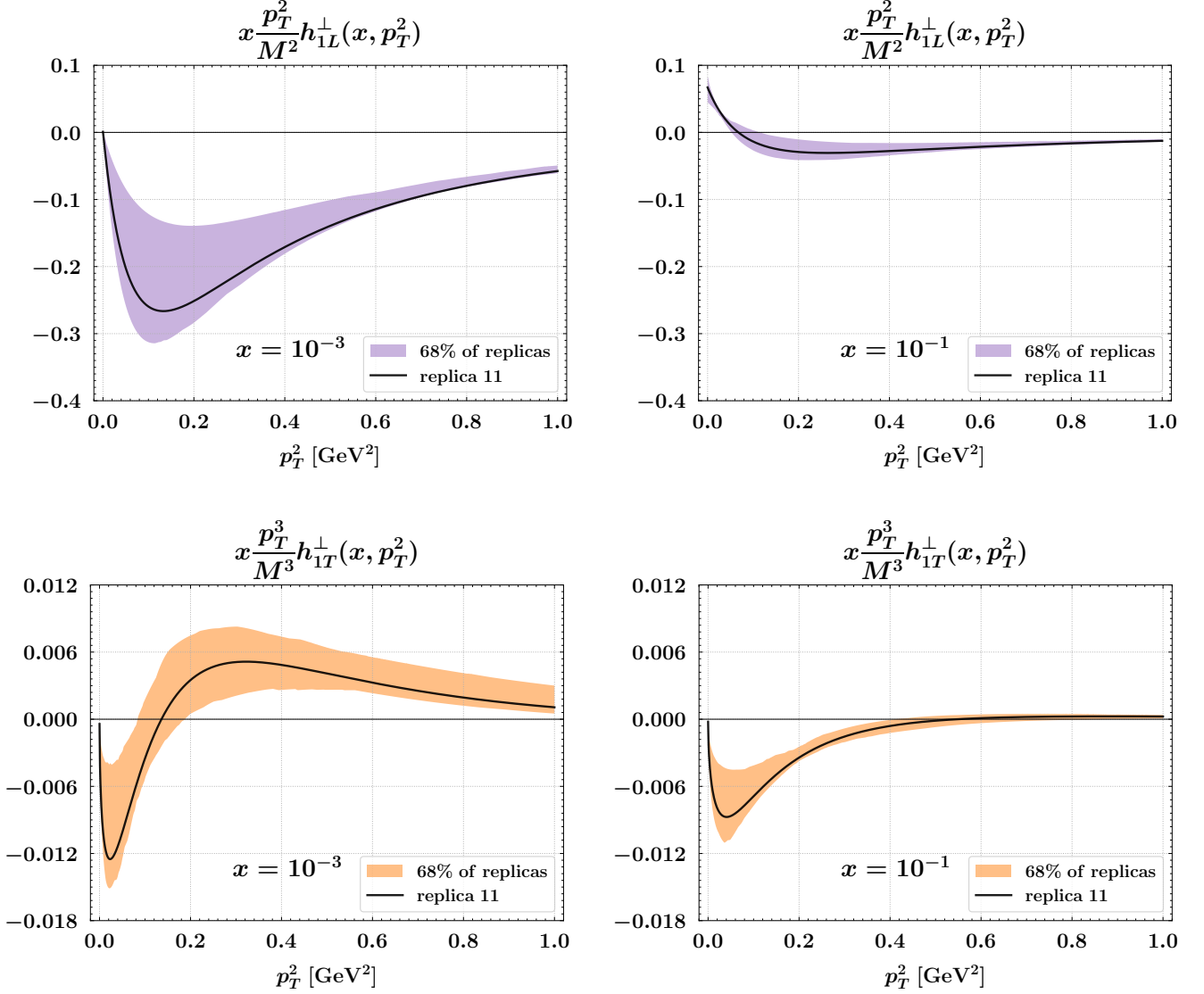


Figure 5. Transverse-momentum dependence of the $[+, +]$ gluon h_{1L}^\perp (upper) and h_{1T}^\perp (lower) functions multiplied by $x p_T^2/M^2$ and $x |p_T|^3/M^3$, respectively, as functions of p_T^2 at $x = 10^{-3}$ (left) and $x = 10^{-1}$ (right) and at the initial scale $Q_0 = 1.64$ GeV. Notations as in previous figures.

For a unpolarized gluon in a nucleon transversely polarized along \hat{x} ($|\mathbf{S}_T| = S_x$), the 2-dim density contains also the f -type gluon Sivers function:

$$x \rho_{p \rightarrow}(x, p_x, p_y) = x f_1(x, \mathbf{p}_T^2) + x \frac{p_y}{M} f_{1T}^\perp(x, \mathbf{p}_T^2). \quad (49)$$

The lower panels of Fig. 6 show such density in the same conditions and with the same notation as before. Since the nucleon is polarized along the \hat{x} axis, the contour plot shows a distortion along the \hat{y} axis. The asymmetry is clearly visible at $x = 10^{-1}$ (right panel), and it is emphasized by the ancillary 1-dim plot at $p_x = 0$. The distortion fades away for decreasing x , as shown in the left panel at $x = 10^{-3}$.

If we consider the gluon also in a linearly polarized state, then the 2-dim densities for various nucleon polarizations can become more complicated. The simplest case is for a unpolarized nucleon: the $x \rho_{p \rightarrow}^{\leftrightarrow}$ is a linear combination of the T-even gluon TMDs f_1 and h_1^\perp , and it has been studied in Ref. [30] (see lower panels of Fig.5 there). If the nucleon has a longitudinal polarization S_L , the 2-dim density $x \rho_{p \rightarrow}^{\leftrightarrow}$ is a linear combination of f_1 , h_1^\perp and h_{1L}^\perp . Finally, if the nucleon has transverse polarization S_T the 2-dim density $x \rho_{p \rightarrow}^{\leftrightarrow}$ is a linear combination of f_1 , h_1^\perp , f_{1T}^\perp , h_1 and h_{1T}^\perp , the latter two ones entering with different coefficients depending on the relative angle between the nucleon and gluon

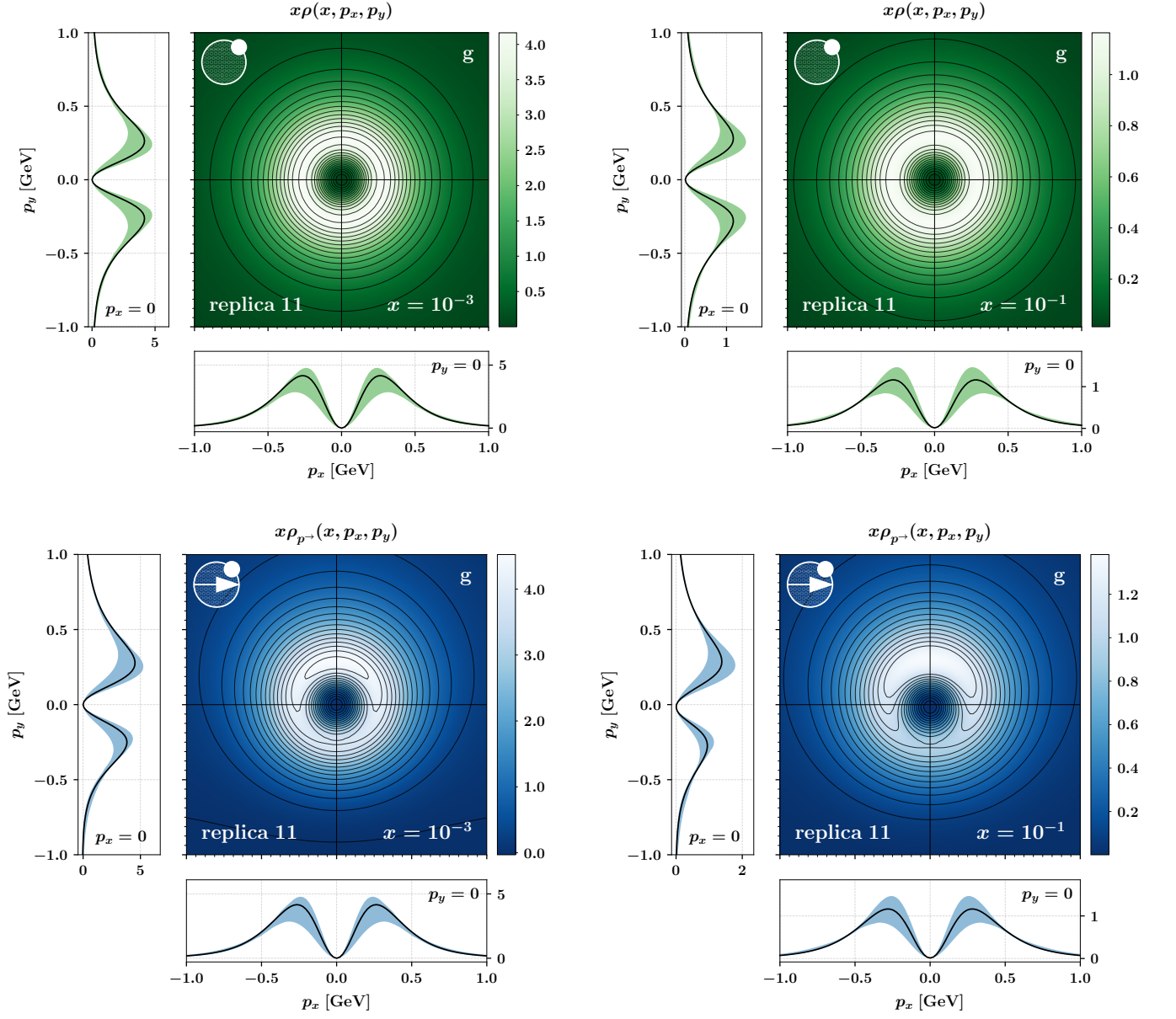


Figure 6. Unpolarized gluon density for a unpolarized (upper panels) or transversely polarized nucleon along \hat{x} (lower panels) as a function of \mathbf{p}_T at $Q_0 = 1.64$ GeV and at $x = 10^{-3}$ (left panels) and $x = 10^{-1}$ (right panels). The nucleon is virtually moving towards the reader. Results from replica 11 (see text). Ancillary 1-dim plots for the density at $p_y = 0$ and $p_x = 0$ with 68% uncertainty band. Solid black line for replica 11 (corresponding to contour plot).

polarizations. Apart for the case of unpolarized nucleon $x\rho^{\leftrightarrow}$, the other 2-dim densities are thus superpositions of three or more gluon TMDs, and their probabilistic interpretation becomes more involved.

Therefore, we prefer to isolate each T-odd TMD for linearly polarized gluons using the projectors discussed in Sec. IID, and we plot them for nucleon polarizations along specific directions.

We first select the nucleon longitudinally polarized along its direction of motion towards the reader, and the gluon linearly polarized along \hat{x} . Using the gluon-gluon correlator $\Phi^{xx}(S_L)$ in Eq.(54) of Ref. [4], the combination $\Phi^{xx}(S_L) - \Phi^{xx}(-S_L)$ isolates the term $h_{1L}^{\perp} p_x p_y / 2M^2$. In the upper panels of Fig. 7, we show the contour plot for the \mathbf{p}_T -distribution of the f -type combination $h_{1L}^{\perp} p_x p_y / 2M^2$ from replica 11 at $x = 10^{-3}$ (left) and $x = 10^{-1}$ (right) and at the scale $Q_0 = 1.64$ GeV, scaled by a factor 10^2 . Because of the $p_x p_y$ weight, the contour plot shows symmetric oscillations along the $p_y = \pm p_x$ directions, emphasized in the 1-dim ancillary plots and becoming more sizeable at $x = 10^{-3}$. Sometimes in the literature, the function h_{1L}^{\perp} is called “T-odd worm-gear” or “pseudo worm-gear” in

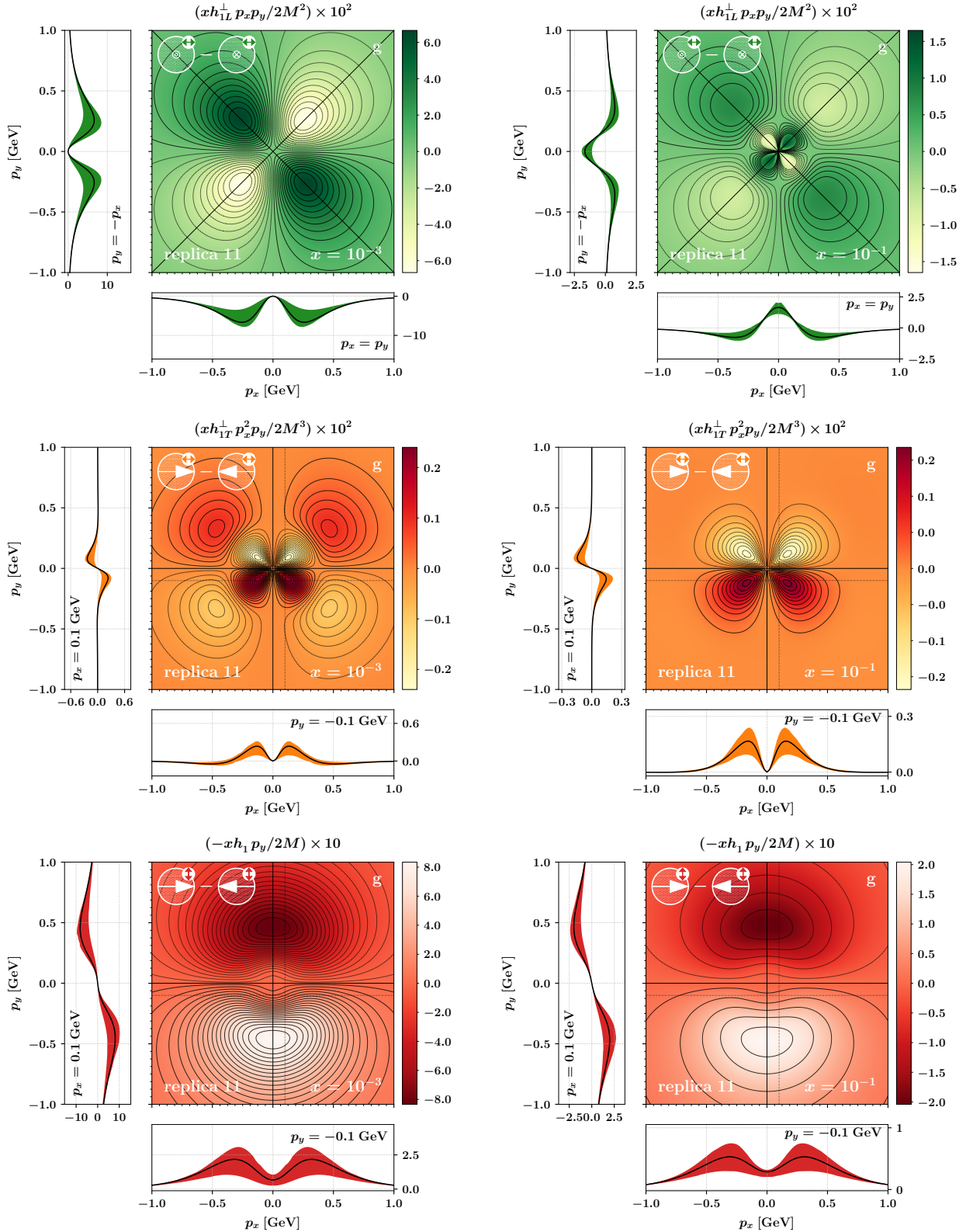


Figure 7. The 2-dim density for linearly polarized gluons in polarized nucleons as a function of \mathbf{p}_T at $Q_0 = 1.64$ GeV and at $x = 10^{-3}$ (left panels) and $x = 10^{-1}$ (right panels). The nucleon is virtually moving towards the reader. Results from replica 11 (see text). Ancillary 1-dim plots for slices of the density at specific values of p_x or p_y , with 68% uncertainty band and solid black line for replica 11. Upper panels: gluon linear polarization along \hat{x} and nucleon longitudinal polarization, proportional to $h_{1L}^\perp p_x p_y / 2M^2$ scaled by 10^2 . Central panels: gluon linear polarization and nucleon polarization along \hat{x} , proportional to $h_{1T}^\perp p_x^2 p_y / 2M^3$ scaled by 10^2 . Lower panels: gluon linear polarization along \hat{y} and nucleon polarization along \hat{x} , proportional to $-h_1 p_y / 2M$ scaled by 10.

analogy with the corresponding quark function. However, we think that this nomenclature does not capture the main characteristics of this function as it emerges from the upper panels of Fig. 7. Since the nucleon is spinning around a direction pointing towards the reader, because of the displayed quadrupolar shape we propose for h_{1L}^\perp the name of “propeller” function.

If we keep the gluon linearly polarized along \hat{x} but we consider the combination $\Phi^{xx}(S_x) - \Phi^{xx}(-S_x)$, we can isolate the term $h_{1T}^\perp p_x^2 p_y / 2M^3$. In the central panels of Fig. 7, we show the contour plot for the \mathbf{p}_T -distribution of the f -type combination $h_{1T}^\perp p_x^2 p_y / 2M^3$, scaled by the factor 10^2 and with the same notations as before. The $p_x^2 p_y$ weight produces oscillations symmetric with respect to the \hat{y} axis, emphasized in the 1-dim ancillary plots with slightly displaced slices at $p_y = -0.1$ GeV and $p_x = 0.1$ GeV. The T-odd gluon TMD h_{1T}^\perp is sometimes referred to as “pretzelosity” in analogy with the quark case. As for h_{1L}^\perp , we think that this nomenclature is misleading. The peculiar shape of the contour plot in the lower panels of Fig. 7 suggests for h_{1T}^\perp the name of “butterfly” function.

Finally, if we turn the gluon linear polarization along the \hat{y} axis but keeping the nucleon polarization along \hat{x} , the combination $\Phi^{yy}(S_x) - \Phi^{yy}(-S_x)$ isolates the linearity function through the term $-h_1 p_y / 2M$. In the lower panels of Fig. 7, we show the contour plot for the \mathbf{p}_T -distribution of the f -type combination $-h_1 p_y / 2M$, scaled by the factor 10 and with the same notations as before. The p_y weight produces oscillations symmetric with respect to the \hat{x} axis, emphasized in the 1-dim ancillary plots with slightly displaced slices at $p_y = -0.1$ GeV and $p_x = 0.1$ GeV.

V. SUMMARY AND OUTLOOK

In this paper, we have presented a model calculation of all four leading-twist T-odd gluon TMDs within a spectator model approach, providing insights into the complex interplay among gluon transverse momentum, gluon polarization, and nucleon spin, and offering a detailed (model-dependent) picture of the distribution of gluons in the nucleon. This paper completes our previous work [30], where we computed all the leading-twist T-even gluon TMDs in the same framework.

The model is based on the idea that a nucleon can split into a gluon and remainders that are treated as a single spectator fermion. This spectator mass is allowed to vary within a continuous range, described by a spectral function. Non vanishing T-odd structures are generated by the interference between the tree-level amplitude and an amplitude with final-state interactions, which in our model are approximated as a single-gluon exchange between the gluon and the spectator. The structure of interaction vertices reflects the nature of the involved particles. Since the spectator has spin- $\frac{1}{2}$, the vertices are modeled resembling the free nucleon electromagnetic current, replacing the Dirac and Pauli form factors with dipolar functions $g_1(p^2)$ and $g_2(p^2)$. For sake of simplicity, all model parameters have been kept the same as in our previous work on T-even gluon TMDs, where they were fixed by fitting the transverse-momentum-integrated gluon TMDs onto known parametrizations of the corresponding collinear unpolarized and helicity gluon PDFs at the lowest scale $Q_0 = 1.64$ GeV [30].

As it is well known, gluon TMDs have a more intricate dependence on the structure of the color flow (gauge link), which in turn introduces a dependence on the involved process. There are two main classes of gluon TMDs, the so-called Weizsäcker–Williams (WW) gluon TMDs (also called f -type) and the dipole gluon TMDs (also called d -type). In general, the two classes cannot be connected, as the WW and dipole gluon TMDs carry different physical information and appear in different processes. Due to the simplifying assumptions in our model, the differences between f -type and d -type gluon TMDs amount only to a calculable color factor: the size of the d -type gluon TMDs is $5/9$ of the f -type ones.

We have provided analytical and numerical results for the f -type T-odd gluon TMDs using two versions of the model: a simpler version with a single form factor (g_1 , taking $g_2 = 0$) for the nucleon-gluon-spectator and spectator-gluon-spectator vertices, and the full calculation with both g_1 and g_2 form factors. In the first case, we obtain nonvanishing results only for the Sivers (f_{1T}^\perp) and linearity (h_1) functions. They turn out to be much smaller than the T-even unpolarized TMD (f_1), and they show a decreasing trend for smaller values of x . In the full calculation, this trend is reversed and the size becomes comparable to f_1 , suggesting that sizeable asymmetries generated by such functions could be measurable at small x . Moreover, we obtain non vanishing results also for the other two T-odd gluon TMDs: the h_{1L}^\perp (which we name “propeller”) and the h_{1T}^\perp (which we name “butterfly”). However, both functions have a very small size, particularly the butterfly function, casting some doubts on the actual possibility of ever extracting them from measured spin asymmetries. We computed the T-odd f -type gluon TMDs also in the quark-target model. Only the Sivers and linearity functions are different from zero, and their expression matches known results in the literature.

As a final remark, the magnitude of the T-odd gluon TMDs crucially depends on the model parameters. For sake of simplicity, in this paper we have taken them equal to the model parameters of the T-even gluon TMDs [30].

However, our model is flexible enough to account for different couplings and different color structures in the interaction vertices, such that the differences between f -type and d -type gluon TMDs would not amount to a simple color factor. Only future data from the Electron-Ion Collider [17, 18, 69–71] and new-generation machines [72–77] will help us to overcome this limitations, and explore also the intriguing connections between our polarized gluon TMDs at small- x and the small- x unintegrated gluon density within a hybrid high-energy and collinear factorization framework (see, e.g., Refs. [78–80]).

ACKNOWLEDGMENTS

This work is supported by the European Research Council (ERC) under the European Union’s Horizon 2020 research and innovation program (grant agreement No. 647981, 3DSPIN), by the Italian MIUR under the FARE program (code n. R16XKPHL3N, 3DGLUE), by the Atracción de Talento Grant (n. 2022-T1/TIC-24176), and by the European Union “Next Generation EU” program through the Italian PRIN 2022 grant n. 20225ZHA7W. F.G.C. thanks the Università degli Studi di Pavia for the warm hospitality.

Appendix A: Master integrals

Here below, we list the master integrals involved in the expressions of our T-odd f -type gluon TMDs. We first define

$$T_h(|\mathbf{p}_T|) = \tanh^{-1} \sqrt{\frac{\mathbf{p}_T^2}{\mathbf{p}_T^2 + 4L_X^2(\Lambda_X^2)}}. \quad (\text{A1})$$

Then, we have

$$\begin{aligned} \mathcal{D}_1(p) &= \frac{1}{2P^+} \int \frac{d^2\mathbf{l}_T}{(2\pi)^2} \frac{1}{[\mathbf{l}_T^2 + L_X^2(\Lambda_X^2)]^2} \frac{1}{[(\mathbf{l}_T + \mathbf{p}_T)^2 + L_X^2(\Lambda_X^2)]^2} \\ &= \frac{1}{8\pi P^+} \left[2 \frac{1 - 2L_X^2(\Lambda_X^2)/\mathbf{p}_T^2}{L_X^2(\Lambda_X^2) [\mathbf{p}_T^2 + 4L_X^2(\Lambda_X^2)]^2} + 16 \frac{\mathbf{p}_T^2 + L_X^2(\Lambda_X^2)}{|\mathbf{p}_T|^3 [\mathbf{p}_T^2 + 4L_X^2(\Lambda_X^2)]^{5/2}} T_h(|\mathbf{p}_T|) \right], \end{aligned} \quad (\text{A2})$$

$$\mathcal{D}_2(p) = \frac{1}{2P^+} \int \frac{d^2\mathbf{l}_T}{(2\pi)^2} \frac{\mathbf{l}_T \cdot \mathbf{p}_T}{\mathbf{p}_T^2} \frac{1}{[\mathbf{l}_T^2 + L_X^2(\Lambda_X^2)]^2} \frac{1}{[(\mathbf{l}_T + \mathbf{p}_T)^2 + L_X^2(\Lambda_X^2)]^2} \equiv -\frac{1}{2} \mathcal{D}_1(p) \quad (\text{A3})$$

$$\begin{aligned} \mathcal{D}_3(p) &= \frac{1}{2P^+} \int \frac{d^2\mathbf{l}_T}{(2\pi)^2} \frac{(\mathbf{l}_T \cdot \mathbf{p}_T)^2}{|\mathbf{p}_T|^4} \frac{1}{[\mathbf{l}_T^2 + L_X^2(\Lambda_X^2)]^2} \frac{1}{[(\mathbf{l}_T + \mathbf{p}_T)^2 + L_X^2(\Lambda_X^2)]^2} \\ &= \frac{1}{8\pi P^+} \left[\frac{1 + 4L_X^2(\Lambda_X^2)/\mathbf{p}_T^2 + 12L_X^4(\Lambda_X^2)/\mathbf{p}_T^4}{L_X^2(\Lambda_X^2) [\mathbf{p}_T^2 + 4L_X^2(\Lambda_X^2)]^2} - 24 \frac{[\mathbf{p}_T^2 + 2L_X^2(\Lambda_X^2)] L_X^2(\Lambda_X^2)}{|\mathbf{p}_T|^5 [\mathbf{p}_T^2 + 4L_X^2(\Lambda_X^2)]^{5/2}} T_h(|\mathbf{p}_T|) \right], \end{aligned} \quad (\text{A4})$$

$$\begin{aligned} \mathcal{D}_4(p) &= \frac{1}{2P^+} \int \frac{d^2\mathbf{l}_T}{(2\pi)^2} \frac{\mathbf{l}_T^2}{\mathbf{p}_T^2} \frac{1}{[\mathbf{l}_T^2 + L_X^2(\Lambda_X^2)]^2} \frac{1}{[(\mathbf{l}_T + \mathbf{p}_T)^2 + L_X^2(\Lambda_X^2)]^2} \\ &= \frac{1}{8\pi P^+} \left[\frac{1 + 2L_X^2(\Lambda_X^2)/\mathbf{p}_T^2 + 4L_X^4(\Lambda_X^2)/\mathbf{p}_T^4}{L_X^2(\Lambda_X^2) [\mathbf{p}_T^2 + 4L_X^2(\Lambda_X^2)]^2} + 4 \frac{\mathbf{p}_T^4 - 4L_X^4(\Lambda_X^2)}{|\mathbf{p}_T|^5 [\mathbf{p}_T^2 + 4L_X^2(\Lambda_X^2)]^{5/2}} T_h(|\mathbf{p}_T|) \right], \end{aligned} \quad (\text{A5})$$

$$\begin{aligned} \mathcal{D}_5(p) &= \frac{1}{2P^+} \int \frac{d^2\mathbf{l}_T}{(2\pi)^2} \frac{\mathbf{l}_T \cdot \mathbf{p}_T}{\mathbf{p}_T^2} \frac{\mathbf{l}_T^2}{\mathbf{p}_T^2} \frac{1}{[\mathbf{l}_T^2 + L_X^2(\Lambda_X^2)]^2} \frac{1}{[(\mathbf{l}_T + \mathbf{p}_T)^2 + L_X^2(\Lambda_X^2)]^2} \\ &= -\frac{1}{8\pi P^+} \left[\frac{1 + 6L_X^2(\Lambda_X^2)/\mathbf{p}_T^2 + 14L_X^4(\Lambda_X^2)/\mathbf{p}_T^4}{L_X^2(\Lambda_X^2) [\mathbf{p}_T^2 + 4L_X^2(\Lambda_X^2)]^2} - 2 \frac{\mathbf{p}_T^4 + 14L_X^2(\Lambda_X^2) \mathbf{p}_T^2 + 28L_X^4(\Lambda_X^2)}{|\mathbf{p}_T|^5 [\mathbf{p}_T^2 + 4L_X^2(\Lambda_X^2)]^{5/2}} T_h(|\mathbf{p}_T|) \right], \end{aligned} \quad (\text{A6})$$

$$\begin{aligned}
\mathcal{D}_6(p) &= \frac{1}{2P^+} \int \frac{d^2\mathbf{l}_T}{(2\pi)^2} \frac{|\mathbf{l}_T|^4}{|\mathbf{p}_T|^4} \frac{1}{[\mathbf{l}_T^2 + L_X^2(\Lambda_X^2)]^2} \frac{1}{[(\mathbf{l}_T + \mathbf{p}_T)^2 + L_X^2(\Lambda_X^2)]^2} \\
&= \frac{1}{8\pi P^+} \left[\frac{[\mathbf{p}_T^2 + 2L_X^2(\Lambda_X^2)][\mathbf{p}_T^4 + 8L_X^2(\Lambda_X^2)\mathbf{p}_T^2 + 22L_X^4(\Lambda_X^2)]}{L_X^2(\Lambda_X^2)\mathbf{p}_T^6[\mathbf{p}_T^2 + 4L_X^2(\Lambda_X^2)]^2} \right. \\
&\quad \left. - 4 \frac{\mathbf{p}_T^6 + 12L_X^2(\Lambda_X^2)\mathbf{p}_T^4 + 40L_X^4(\Lambda_X^2)\mathbf{p}_T^2 + 44L_X^6(\Lambda_X^2)}{|\mathbf{p}_T|^7[\mathbf{p}_T^2 + 4L_X^2(\Lambda_X^2)]^{5/2}} T_h(|\mathbf{p}_T|) \right], \tag{A7}
\end{aligned}$$

$$\begin{aligned}
\mathcal{D}_7(p) &= \frac{1}{2P^+} \int \frac{d^2\mathbf{l}_T}{(2\pi)^2} \frac{(\mathbf{l}_T \cdot \mathbf{p}_T)^2}{|\mathbf{p}_T|^4} \frac{|\mathbf{l}_T|^2}{\mathbf{p}_T^2} \frac{1}{[\mathbf{l}_T^2 + L_X^2(\Lambda_X^2)]^2} \frac{1}{[(\mathbf{l}_T + \mathbf{p}_T)^2 + L_X^2(\Lambda_X^2)]^2} \\
&= \frac{1}{8\pi P^+} \left[\frac{|\mathbf{p}_T|^7 + 10L_X^2(\Lambda_X^2)|\mathbf{p}_T|^5 + 36L_X^4(\Lambda_X^2)|\mathbf{p}_T|^3 + 36L_X^6(\Lambda_X^2)|\mathbf{p}_T|}{L_X^2(\Lambda_X^2)|\mathbf{p}_T|^7[\mathbf{p}_T^2 + 4L_X^2(\Lambda_X^2)]^2} \right. \\
&\quad \left. - 6 \frac{[\mathbf{p}_T^2 + 2L_X^2(\Lambda_X^2)]^2[\mathbf{p}_T^2 + 6L_X^2(\Lambda_X^2)]}{|\mathbf{p}_T|^7[\mathbf{p}_T^2 + 4L_X^2(\Lambda_X^2)]^{5/2}} T_h(|\mathbf{p}_T|) \right], \tag{A8}
\end{aligned}$$

$$\begin{aligned}
\mathcal{D}_8(p) &= \frac{1}{2P^+} \int \frac{d^2\mathbf{l}_T}{(2\pi)^2} \frac{(\mathbf{l}_T \cdot \mathbf{p}_T)^3}{|\mathbf{p}_T|^6} \frac{1}{[\mathbf{l}_T^2 + L_X^2(\Lambda_X^2)]^2} \frac{1}{[(\mathbf{l}_T + \mathbf{p}_T)^2 + L_X^2(\Lambda_X^2)]^2} \\
&= -\frac{1}{8\pi P^+} \left[\frac{1 + 7L_X^2(\Lambda_X^2)/\mathbf{p}_T^2 + 18L_X^4(\Lambda_X^2)/\mathbf{p}_T^4}{L_X^2(\Lambda_X^2)[\mathbf{p}_T^2 + 4L_X^2(\Lambda_X^2)]^2} - 4 \frac{\mathbf{p}_T^4 + 10L_X^2(\Lambda_X^2)\mathbf{p}_T^2 + 18L_X^4(\Lambda_X^2)}{|\mathbf{p}_T|^5[\mathbf{p}_T^2 + 4L_X^2(\Lambda_X^2)]^{5/2}} T_h(|\mathbf{p}_T|) \right]. \tag{A9}
\end{aligned}$$

Appendix B: Full calculation of gluon TMDs: The coefficients $C_{ijk}^{[F],l}$

In the following, we list the final expressions of the $C_{ijk}^{[F],l}$ coefficients in Eqs. (46) and (47) for each T-odd gluon TMD F and for $l = 1, \dots, 8$, $i, j, k = 1, 2$. We note that the $C_{111}^{[F],2}$ coefficients for the f -type gluon Sivers ($[F] \equiv [f_{1T}^\perp]$) and linearity ($[F] \equiv [h_1]$) have already been derived when discussing the computation of these T-odd gluon TMDs in the g_1 -vertex approximation (see Eqs. (32) and (42), respectively).

1. Sivers function f_{1T}^\perp

In Tabs. III-VI, we list the coefficients $C_{ijk}^{[f_{1T}^\perp],l}$ for $i, j, k = 1, 2$ and $l = 1, \dots, 8$.

Table III. Coefficients functions of the f -type gluon Sivers TMD for $ijk = \{111, 112\}$.

$C_{ijk}^{[f_{1T}^\perp],l}$	$ijk = 111$	$ijk = 112$
$l = 1$	0	$\frac{12}{x} [2x (M^2(2-x)x - (M - M_X)^2) + 2\mathbf{p}_T^2(2-x)]$
$l = 2$	$-48M(1-x) [M_X - M(1-x)]$	$-\frac{12}{x} [x(M(1-x) + M_X) (M(1-x)^2 + M_X(1+x)) - \mathbf{p}_T^2(x^2 - 5x + 8)]$
$l = 3$	0	$\frac{24}{x} \mathbf{p}_T^2 (x^2 - 2x + 2)$
$l = 4$	0	$12 \mathbf{p}_T^2 (1-x)$
$l = 5$	0	0
$l = 6$	0	0
$l = 7$	0	0
$l = 8$	0	0

Table IV. Coefficients functions of the f -type gluon Sivers TMD for $ijk = \{121, 122\}$.

$C_{ijk}^{[f_{1T}^\perp],l}$	$ijk = 121$	$ijk = 122$
$l = 1$	0	0
$l = 2$	$\frac{6}{x} [-M^2(2-x)x(1-x)^2 + M_X^2(2-x)x + \mathbf{p}_T^2(x^2 - 10x + 8)]$	$3x \frac{M - M_X}{M} [M^2(1-x)^2 - M_X^2 + \mathbf{p}_T^2]$
$l = 3$	$\frac{48\mathbf{p}_T^2}{x} (1-x)$	0
$l = 4$	$-6\mathbf{p}_T^2 (2-x)$	$\frac{3\mathbf{p}_T^2}{M} [M(4-3x) - M_X(x+4)]$
$l = 5$	0	$\frac{12\mathbf{p}_T^2}{M} [M(1-x) - M_X]$
$l = 6$	0	0
$l = 7$	0	0
$l = 8$	0	0

Table V. Coefficients functions of the f -type gluon Sivers TMD for $ijk = \{211, 212\}$.

$G_{ijk}^{[f_{1T}^\perp],l}$	$ijk = 211$	$ijk = 212$
$l = 1$	$-\frac{24}{x} [x (M_X^2 - M^2(1-x)^2) + (2-x) \mathbf{p}_T^2]$	0
$l = 2$	$-\frac{6}{(1-x)x} [x^2 (M_X - M(1-x)) (M(1-x)x + M_X(4-3x)) - \mathbf{p}_T^2 (x^3 - 8x + 8)]$	$-\frac{3}{M(1-x)} [M^3(2-x)(1-x)^2 + 3M^2 M_X(1-x)^2 x^2 - M (M_X^2 x(3x^2 - 4x + 2) + \mathbf{p}_T^2 (x^2 - 6x + 4)) + M_X^3 x^2 + M_X \mathbf{p}_T^2 (3x^2 - 8x + 4)]$
$l = 3$	0	$\frac{12\mathbf{p}_T^2}{M} [M_X(1-x) - M]$
$l = 4$	$6\mathbf{p}_T^2 \frac{(2-x)^2}{(1-x)}$	$\frac{3x\mathbf{p}_T^2}{M(1-x)} [M(2-x) - M_X x]$
$l = 5$	0	0
$l = 6$	0	0
$l = 7$	0	0
$l = 8$	0	0

Table VI. Coefficients functions of the f -type gluon Sivers TMD for $ijk = \{221, 222\}$.

$C_{ijk}^{[f_{1T}^\perp],l}$	$ijk = 221$	$ijk = 222$
$l = 1$	0	0
$l = 2$	$3x \frac{M^2(1-x)^2 - M_X^2 + \mathbf{p}_T^2}{2M(1-x)}$ $\times [M(1-x)(7-2x) - M_X(7-3x)]$	$\frac{3}{8M^2(1-x)x} [x^2 (M^2(1-x)^2 - M_X^2)]$ $\times (M^2(2x^3 + x^2 - 3) + 4M M_X(3-x)x + M_X^2(3-2x))$ $- 4x\mathbf{p}_T^2 (M^2(1-x)(x^3 - 5x + 6) - M M_X(3-x)x^2$ $+ M_X^2(x^2 + 7x - 6))$ $+ \mathbf{p}_T^4(2x^3 - 3x^2 - 24x + 32)]$
$l = 3$	$\frac{12\mathbf{p}_T^2}{M} [M_X - M(1-x)]$	$-\frac{3\mathbf{p}_T^2}{4M^2(1-x)x} [M^2(1-x)x(2x^3 + 5x^2 - 13x + 4)$ $+ 8M M_X(1-x)x^2 + M_X^2x(2x^2 + 11x - 4)$ $- \mathbf{p}_T^2(2x^3 + 3x^2 - 28x + 32)]$
$l = 4$	$\frac{3x\mathbf{p}_T^2}{2M(1-x)} [M(1-x)(7-2x) - M_X(7-3x)]$	$-\frac{3\mathbf{p}_T^2}{8M^2(1-x)} [M^2(1-x)(2x^3 - 5x^2 - x + 16)$ $+ 4M M_Xx(x^2 + x - 4) + M_X^2x(2x^2 + 13x - 6)$ $- \mathbf{p}_T^2(2x^2 - x + 8)]$
$l = 5$	0	$\frac{3\mathbf{p}_T^2}{8M^2(1-x)} [M^2(1-x)^2(2x^2 - x - 8)$ $+ 16M M_X(1-x)x + M_X^2(2x^2 + 15x - 8)$ $+ \mathbf{p}_T^2(6x^2 - 11x + 32)]$
$l = 6$	0	$\frac{3\mathbf{p}_T^4}{8M^2} \frac{2x^2 - x + 8}{1-x}$
$l = 7$	0	0
$l = 8$	0	$\frac{6\mathbf{p}_T^4}{M^2} \frac{2-x}{x}$

2. Linearity function h_1

In Tabs. VII-X, we list the coefficients $C_{ijk}^{[h_1],l}$ for $i, j, k = 1, 2$ and $l = 1, \dots, 8$.

Table VII. Coefficients functions of the f -type gluon linearity for $ijk = \{111, 112\}$.

$C_{ijk}^{[h_1],l}$	$ijk = 111$	$ijk = 112$
$l = 1$	0	$\frac{6}{x} \left[x(4-3x) \left(M^2(1-x)^2 - M_X^2 \right) + \mathbf{p}_T^2(3x^2 - 12x + 8) \right]$
$l = 2$	$-96M [M_X - M(1-x)]$	$-\frac{6}{x} \left[x \left(M^2(3x^3 - 6x^2 + 11x - 8) + 8M M_X x - M_X^2(8-3x) \right) - \mathbf{p}_T^2(3x^2 - 8x + 16) \right]$
$l = 3$	0	$48\mathbf{p}_T^2 \frac{1-x}{x}$
$l = 4$	0	$48\mathbf{p}_T^2$
$l = 5$	0	0
$l = 6$	0	0
$l = 7$	0	0
$l = 8$	0	0

Table VIII. Coefficients functions of the f -type gluon linearity for $ijk = \{121, 122\}$.

$C_{ijk}^{[h_1],l}$	$ijk = 121$	$ijk = 122$
$l = 1$	0	0
$l = 2$	$\frac{6}{x} \left[x \left(M^2(1-x)^2(2+3x) - 16M M_X(1-x)x - M_X^2(2-13x) \right) + \mathbf{p}_T^2(5x^2 - 2x + 8) \right]$	$\frac{3}{M} \left[M^2 M_X x(7x^2 + 2x - 9) + M x \left(5M^2(1-x)^2 + 11\mathbf{p}_T^2 \right) - M M_X^2 x(5-16x) + 9M_X^3 x + M_X \mathbf{p}_T^2(8+x) \right]$
$l = 3$	$\frac{48\mathbf{p}_T^2}{x}$	$\frac{6\mathbf{p}_T^2}{M} [4Mx + M_X(10+x)]$
$l = 4$	0	$\frac{6\mathbf{p}_T^2}{M} [4M(1-x) + M_X(2+x)]$
$l = 5$	0	$\frac{6\mathbf{p}_T^2}{M} [4M(1-x) + M_X(2-3x)]$
$l = 6$	0	0
$l = 7$	0	0
$l = 8$	0	$-\frac{18\mathbf{p}_T^2 M_X}{M} (2-x)$

Table IX. Coefficients functions of the f -type gluon linearity for $ijk = \{211, 212\}$.

$C_{ijk}^{[h_1],l}$	$ijk = 211$	$ijk = 212$
$l = 1$	$-\frac{6}{x} \left[\left(M^2 (1-x)^2 - M_X^2 \right) (4-3x) x \right. \\ \left. + \mathbf{p}_T^2 (3x^3 - 12x + 8) \right]$	$-9x \left[M^2 (1-x)^2 - M_X^2 - \mathbf{p}_T^2 \right]$
$l = 2$	$-\frac{6}{(1-x)x} \left[x^2 \left(M^2 (1-x)^2 (7-2x) \right. \right. \\ \left. \left. - 8M M_X (1-x) + M_X^2 (1+2x) \right) \right. \\ \left. + \mathbf{p}_T^2 (2x^3 - 7x^2 + 16x - 8) \right]$	$-\frac{3}{M(1-x)} \left[M^3 (1-x)^2 x (9-4x) \right. \\ \left. + M^2 M_X (x^3 + 5x - 6) + 3M M_X^2 (4-3x) x \right. \\ \left. + M \mathbf{p}_T^2 (4x^2 - 9x + 8) + M_X (M_X^2 + \mathbf{p}_T^2) (6-x) \right]$
$l = 3$	0	$-24\mathbf{p}_T^2$
$l = 4$	0	0
$l = 5$	0	0
$l = 6$	0	0
$l = 7$	0	0
$l = 8$	0	0

Table X. Coefficients functions of the f -type gluon linearity for $ijk = \{221, 222\}$.

$C_{ijk}^{[h_1],l}$	$ijk = 221$	$ijk = 222$
$l = 1$	0	0
$l = 2$	$\frac{3}{M(1-x)} \left[2M_X \left(M^2 x (3+2x) (1-x)^2 \right. \right.$ $\left. \left. + \mathbf{p}_T^2 (2x^2 + 5x - 4) \right) \right.$ $\left. + M(1-x)x \left(-M^2 (6-x) (1-x)^2 - \mathbf{p}_T^2 (10+x) \right) \right.$ $\left. + M M_X^2 (17x^2 - 23x + 6)x - 6M_X^3 (1-2x)x \right]$	$-\frac{3}{4M^2(1-x)x} \left[\mathbf{p}_T^2 x \left(M^2 (1-x) (6x^3 - 31x^2 + 6x - 4) \right. \right.$ $\left. \left. + 2M M_X (x^2 + 21x - 16)x + 2M_X^2 (2+x) (1+3x) \right) \right.$ $\left. - x^2 (M(1-x) - M_X) \left(M^3 (x^2 + x - 2)^2 - M_X^3 (4 - 17x) \right) \right.$ $\left. + M^2 M_X (3x^2 - 18x + 4) (1-x) + M M_X (17x^2 - x - 4) \right]$ $+ \mathbf{p}_T^4 (5x^3 - 30x^2 + 52x - 16)]$
$l = 3$	$-12\mathbf{p}_T^2 (2-x)$	$-\frac{3\mathbf{p}_T^2}{2M^2(1-x)x} \left[M^2 (2x^3 - 15x^2 + 8x + 2) (1-x)x \right.$ $\left. - 4M M_X (1-x)x^2 + M_X^2 (4x^2 + 5x - 2) \right]$ $+ \mathbf{p}_T^2 (2x^3 - 9x^2 + 30x - 16)]$
$l = 4$	$-12x \mathbf{p}_T^2$	$-\frac{3\mathbf{p}_T^2}{4M^2(1-x)} \left[M^2 (3x^3 - 7x^2 + 2x - 8) (1-x) \right.$ $\left. - 24M M_X (1-x)x - M_X^2 (x^2 + 8x - 8) \right]$ $+ \mathbf{p}_T^2 (3x^2 - 12x + 8)]$
$l = 5$	0	$\frac{3\mathbf{p}_T^2}{2M^2(1-x)} \left[M^2 (1-x)^2 (x^2 - 7x + 2) + 8M M_X (1-x)x \right.$ $\left. - M_X^2 (7x^2 - 11x + 2) - \mathbf{p}_T^2 (x^2 - x - 6) \right]$
$l = 6$	0	$\frac{3\mathbf{p}_T^4}{M^2} \frac{x}{1-x}$
$l = 7$	0	$-\frac{3\mathbf{p}_T^4}{M^2} \frac{x}{1-x}$
$l = 8$	0	$\frac{3\mathbf{p}_T^2}{2M^2(1-x)x} \left[3(2-x)x \left(M_X^2 (1-2x) - M^2 (1-x)^2 \right) \right.$ $\left. + \mathbf{p}_T^2 (3x^2 - 18x + 8) \right]$

3. Propeller function h_{1L}^\perp

In Tabs. [XI-XIV](#), we list the coefficients $C_{ijk}^{[h_{1L}^\perp],l}$ for $i, j, k = 1, 2$ and $l = 1, \dots, 8$.

Table XI. Coefficients functions of the f -type gluon propeller for $ijk = \{111, 112\}$.

$C_{ijk}^{[h_{1L}^\perp],l}$	$ijk = 111$	$ijk = 112$
$l = 1$	0	$96(1-x)M^2$
$l = 2$	0	$48M[3M(1-x) - M_X]$
$l = 3$	0	$96M[M(1-x) - M_X]$
$l = 4$	0	$-48M[M(1-x) - M_X]$
$l = 5$	0	0
$l = 6$	0	0
$l = 7$	0	0
$l = 8$	0	0

Table XII. Coefficients functions of the f -type gluon propeller for $ijk = \{121, 122\}$.

$C_{ijk}^{[h_{1L}^\perp],l}$	$ijk = 121$	$ijk = 122$
$l = 1$	0	0
$l = 2$	$96(1-x)M[M(1-x) - M_X]$	$-24[M(1-x)(M(1-x) - 2M_X x) - M_X^2(1-2x) + \mathbf{p}_T^2]$
$l = 3$	$96(1-x)M[M(1-x) - M_X]$	$\frac{48}{x}[M M_X(1-x)x^2 - M_X^2 x^2 + \mathbf{p}_T^2(1-x)]$
$l = 4$	$-48(1-x)M[M(1-x) - M_X]$	$-\frac{24}{x}[M M_X(1-x)x^2 - M_X^2 x^2 + 2\mathbf{p}_T^2]$
$l = 5$	0	$-24\mathbf{p}_T^2$
$l = 6$	0	0
$l = 7$	0	0
$l = 8$	0	0

Table XIII. Coefficients functions of the f -type gluon propeller for $ijk = \{211, 212\}$.

$C_{ijk}^{[h_{1L}^\perp],l}$	$ijk = 211$	$ijk = 212$
$l = 1$	$-96(1-x)M^2$	0
$l = 2$	$-48M[M(1-x) + M_X]$	$-48[M(1-x) - M_X]$
$l = 3$	0	$-\frac{48}{x}[x(M + M_X)(M(1-x) - M_X) - \mathbf{p}_T^2]$
$l = 4$	0	$\frac{24}{x}[x(M + M_X)(M(1-x) - M_X) - 2\mathbf{p}_T^2]$
$l = 5$	0	0
$l = 6$	0	0
$l = 7$	0	0
$l = 8$	0	0

Table XIV. Coefficients functions of the f -type gluon propeller for $ijk = \{221, 222\}$.

$C_{ijk}^{[h_{1L}^\perp],l}$	$ijk = 221$	$ijk = 222$
$l = 1$	0	0
$l = 2$	$-24[M^2(1-x)^2 - 2M M_X(1-x)x - M_X^2(1-2x) + \mathbf{p}_T^2]$	$\frac{24}{M}(M_X + M)[x M_X(M_X - M(1-x)) + \mathbf{p}_T^2]$
$l = 3$	$\frac{48(1-x)}{x}[x(M + M_X)(M_X - M(1-x)) + \mathbf{p}_T^2]$	$\frac{24M_X}{M}[x(M_X + M)(M_X - M(1-x)) + 2\mathbf{p}_T^2]$
$l = 4$	$-\frac{24}{x}[(1-x)x(M + M_X)(M_X - M(1-x)) + \mathbf{p}_T^2(2-x)]$	$-\frac{12}{M}[x^2 M_X M(M_X + M) + x M_X(M_X^2 - M^2) + (M_X - 3M)\mathbf{p}_T^2]$
$l = 5$	0	$\frac{12\mathbf{p}_T^2}{M}(M + M_X)$
$l = 6$	0	0
$l = 7$	0	0
$l = 8$	0	0

4. Butterfly function h_{1T}^\perp

In Tabs. XV-XVIII, we list the coefficients $C_{ijk}^{[h_{1T}^\perp],l}$ for $i, j, k = 1, 2$ and $l = 1, \dots, 8$.

Table XV. Coefficients functions of the f -type gluon butterfly for $ijk = \{111, 112\}$.

$C_{ijk}^{[h_{1T}^+],l}$	$ijk = 111$	$ijk = 112$
$l = 1$	0	$-\frac{M^2}{2\mathbf{p}_T^2(1-x)x} \left[(1-x)^2 (M^2 x(x^2 - 5x + 4) - 2M_X^2 x + 2\mathbf{p}_T^2(4-x)) + x(x^2 + x - 2)(M_X^2 + \mathbf{p}_T^2) \right]$
$l = 2$	0	$-\frac{M^2}{2\mathbf{p}_T^2(1-x)x} \left[(1-x)^2 (M^2 x(x^2 - 5x + 4) - 2M_X^2 x + 2\mathbf{p}_T^2(8-x)) + x(x^2 + x - 2)(M_X^2 + \mathbf{p}_T^2) \right]$
$l = 3$	0	$-4M^2 \frac{1-x}{x}$
$l = 4$	0	0
$l = 5$	0	0
$l = 6$	0	0
$l = 7$	0	0
$l = 8$	0	0

Table XVI. Coefficients functions of the f -type gluon butterfly for $ijk = \{121, 122\}$.

$C_{ijk}^{[h_{1T}^+],l}$	$ijk = 121$	$ijk = 122$
$l = 1$	0	0
$l = 2$	$\frac{M^2}{2x\mathbf{p}_T^2} \left[(2-x)x(M_X^2 + \mathbf{p}_T^2) - (1-x)^2 (M^2(2-x)x + 8\mathbf{p}_T^2) \right]$	$\frac{M}{4\mathbf{p}_T^2} \left[M^3 x(1-x)^2 + M(\mathbf{p}_T^2(3x^2 - 8x + 4) - M_X^2 x^2) - (1-x)(M^2 M_X(1-x)x + M M_X^2 x + M \mathbf{p}_T^2(4-3x) + 4M_X \mathbf{p}_T^2) + M_X^3 x - M_X \mathbf{p}_T^2(4-5x) \right]$
$l = 3$	$-\frac{4M^2(1-x)^2}{x}$	$-\frac{2-3x}{2} M M_X$
$l = 4$	0	$-\frac{2-x}{2} M M_X$
$l = 5$	0	$-\frac{2-x}{2} M M_X$
$l = 6$	0	0
$l = 7$	0	0
$l = 8$	0	$\frac{2-x}{2} M M_X$

Table XVII. Coefficients functions of the f -type gluon butterfly for $ijk = \{211, 212\}$.

$C_{ijk}^{[h\bar{1}T],l}$	$ijk = 211$	$ijk = 212$
$l = 1$	$\frac{M^2}{2x\mathbf{p}_T^2} \left[(1-x) \left(4M^2 (1-x)^2 x + 4\mathbf{p}_T^2 (2-x) \right) \right. \\ \left. + 3M^2 x^2 (1-x)^2 - x \left(M_X^2 (4-x) + 3\mathbf{p}_T^2 x \right) \right]$	$\frac{xM^2}{4\mathbf{p}_T^2} \left[M^2 (1-x)^2 - M_X^2 - \mathbf{p}_T^2 \right]$
$l = 2$	$-\frac{M^2}{\mathbf{p}_T^2(1-x)x} \left[(1-x)^2 \left(M^2 x^2 - 4\mathbf{p}_T^2 (2-x) \right) \right. \\ \left. - x \left(M_X^2 x + \mathbf{p}_T^2 (4x^2 - 7x + 4) \right) \right]$	$\frac{M}{4(1-x)\mathbf{p}_T^2} \left[(1-x)^2 \left(M^3 x (2x^2 - 4x + 3) + 2M\mathbf{p}_T^2 (2-x) \right) \right. \\ \left. + 2M^3 x^2 (1-x)^3 - M_X (2-x) (1-x) \left(2\mathbf{p}_T^2 + M^2 x (1-x) \right) \right. \\ \left. - M M_X^2 x (3-2x) + M\mathbf{p}_T^2 (2x^3 - 6x^2 + 7x - 4) \right. \\ \left. + M_X^3 (2-x)x + M_X \mathbf{p}_T^2 (x^2 + 4x - 4) \right]$
$l = 3$	0	$-2MM_X$
$l = 4$	0	0
$l = 5$	0	0
$l = 6$	0	0
$l = 7$	0	0
$l = 8$	0	0

Table XVIII. Coefficients functions of the f -type gluon butterfly for $ijk = \{221, 222\}$.

$C_{ijk}^{[h_{1T}^+],l}$	$ijk = 221$	$ijk = 222$
$l = 1$	0	0
$l = 2$	$\frac{M}{4(1-x)\mathbf{p}_T^2} \left[M^3 x(3-x)(1-x)^3 - (1-x) \left(2M M_X^2 x^2 \right. \right.$ $\left. \left. - 2M \mathbf{p}_T^2 (x^2 - 4x + 2) - 3M_X^3 x + M_X \mathbf{p}_T^2 (4 - 7x) \right) \right.$ $\left. - M(1-x)^2 (M_X x (3M_X + M(3-x)) + \mathbf{p}_T^2 (4-x) \right.$ $\left. + 2M_X^3 x^2 - 2M_X \mathbf{p}_T^2 (x^2 - 4x + 2) \right]$	$-\frac{1}{16(1-x)x\mathbf{p}_T^2} \left[\mathbf{p}_T^2 x \left(M^2 (1-x) (2x^3 - 3x^2 + 8x - 4) \right. \right.$ $\left. \left. - 2M M_X (3-x) x^2 + 2M_X^2 (9x^2 - 10x + 2) \right) \right.$ $\left. + x^2 \left(M^2 (1-x)^2 - M_X^2 \right) \left(-M^2 (1-x^3) \right. \right.$ $\left. \left. + 2M M_X (3-x) x + M_X^2 (1-x) \right) \right.$ $\left. + \mathbf{p}_T^4 (x^3 - 3x^2 + 20x - 16) \right]$
$l = 3$	$-2MM_X$	$-\frac{1}{8x} \left[M^2 x (2x^2 - x - 2) \right.$ $\left. - M_X^2 x (1 + 3x) - 2\mathbf{p}_T^2 (8 - 3x) \right]$
$l = 4$	0	$\frac{1}{16(1-x)} \left[M^2 (1-x) (x^3 - x^2 + 6x - 8) \right.$ $\left. + M_X^2 (5x^2 - 12x + 8) + \mathbf{p}_T^2 (x^2 + 8x - 8) \right]$
$l = 5$	0	$-\frac{1}{16(1-x)} \left[(1-x) \left(x \left(M^2 (1-x)^2 - M_X^2 \right) \right. \right.$ $\left. \left. + \mathbf{p}_T^2 (8-x) \right) + (2-x) \left(M^2 (2-x) (1-x)^2 \right. \right.$ $\left. \left. - M_X^2 (2-5x) + \mathbf{p}_T^2 (2+x) \right) \right]$
$l = 6$	0	0
$l = 7$	0	0
$l = 8$	0	$\frac{2-x}{8(1-x)x} \left[M^2 (1-x)^2 x - M_X (1-2x) x \right.$ $\left. - \mathbf{p}_T^2 (4-5x) \right]$

REFERENCES

- [1] R. Angeles-Martinez *et al.*, *Acta Phys. Polon. B* **46**, 2501 (2015), arXiv:1507.05267 [hep-ph].
- [2] P. J. Mulders and J. Rodrigues, *Phys. Rev.* **D63**, 094021 (2001), arXiv:hep-ph/0009343 [hep-ph].
- [3] D. Boer, C. Lorcé, C. Pisano, and J. Zhou, *Adv. High Energy Phys.* **2015**, 371396 (2015), arXiv:1504.04332 [hep-ph].
- [4] S. Meissner, A. Metz, and K. Goeke, *Phys. Rev.* **D76**, 034002 (2007), arXiv:hep-ph/0703176 [HEP-PH].
- [5] J.-P. Lansberg, C. Pisano, F. Scarpa, and M. Schlegel, *Phys. Lett. B* **784**, 217 (2018), [Erratum: Phys.Lett.B 791, 420–421 (2019)], arXiv:1710.01684 [hep-ph].
- [6] U. D’Alesio, F. Murgia, C. Pisano, and P. Taels, *Phys. Rev.* **D96**, 036011 (2017), arXiv:1705.04169 [hep-ph].
- [7] U. D’Alesio, C. Flore, F. Murgia, C. Pisano, and P. Taels, *Phys. Rev. D* **99**, 036013 (2019), arXiv:1811.02970 [hep-ph].
- [8] U. D’Alesio, L. Maxia, F. Murgia, C. Pisano, and S. Rajesh, *Phys. Rev. D* **102**, 094011 (2020), arXiv:2007.03353 [hep-ph].
- [9] C. Adolph *et al.* (COMPASS), *Phys. Lett. B* **772**, 854 (2017), arXiv:1701.02453 [hep-ex].
- [10] F. Yuan, *Phys. Rev. D* **78**, 014024 (2008), arXiv:0801.4357 [hep-ph].
- [11] D. Boer, P. J. Mulders, C. Pisano, and J. Zhou, *JHEP* **08**, 001 (2016), arXiv:1605.07934 [hep-ph].
- [12] L. Zheng, E. C. Aschenauer, J. H. Lee, B.-W. Xiao, and Z.-B. Yin, *Phys. Rev.* **D98**, 034011 (2018), arXiv:1805.05290 [hep-ph].
- [13] R. M. Godbole, A. Kaushik, A. Misra, and V. S. Rawoot, *Phys. Rev.* **D91**, 014005 (2015), arXiv:1405.3560 [hep-ph].

- [14] A. Mukherjee and S. Rajesh, *Eur. Phys. J.* **C77**, 854 (2017), arXiv:1609.05596 [hep-ph].
- [15] A. Bacchetta, D. Boer, C. Pisano, and P. Taels, *Eur. Phys. J. C* **80**, 72 (2020), arXiv:1809.02056 [hep-ph].
- [16] U. D'Alesio, F. Murgia, C. Pisano, and P. Taels, *Phys. Rev.* **D100**, 094016 (2019), arXiv:1908.00446 [hep-ph].
- [17] D. Boer *et al.*, (2011), arXiv:1108.1713 [nucl-th].
- [18] A. Accardi *et al.*, *Eur. Phys. J. A* **52**, 268 (2016), arXiv:1212.1701 [nucl-ex].
- [19] S. J. Brodsky, F. Fleuret, C. Hadjidakis, and J. P. Lansberg, *Phys. Rept.* **522**, 239 (2013), arXiv:1202.6585 [hep-ph].
- [20] C. A. Aidala *et al.*, *Proceedings, 27th International Workshop on Deep Inelastic Scattering and Related Subjects (DIS 2019): Torino, Italy, April 8-12, 2019*, *PoS DIS2019*, 233 (2019), arXiv:1901.08002 [hep-ex].
- [21] Z. Lu and B.-Q. Ma, *Phys. Rev.* **D94**, 094022 (2016), arXiv:1611.00125 [hep-ph].
- [22] J. M. Pereira-Resina-Rodrigues, *Modelling quark and gluon correlation functions*, Ph.D. thesis, Vrije Univ. Amsterdam (2001).
- [23] D. Chakrabarti, P. Choudhary, B. Gurjar, R. Kishore, T. Maji, C. Mondal, and A. Mukherjee, *Phys. Rev. D* **108**, 014009 (2023), arXiv:2304.09908 [hep-ph].
- [24] X. Xie and Z. Lu, *Phys. Lett. B* **842**, 137973 (2023), arXiv:2210.16532 [hep-ph].
- [25] A. Bacchetta, F. Conti, and M. Radici, *Phys. Rev.* **D78**, 074010 (2008), arXiv:0807.0323 [hep-ph].
- [26] A. Bacchetta, M. Radici, F. Conti, and M. Guagnelli, *Eur. Phys. J.* **A45**, 373 (2010), arXiv:1003.1328 [hep-ph].
- [27] L. P. Gamberg and G. R. Goldstein, *Phys. Lett. B* **650**, 362 (2007), arXiv:hep-ph/0506127.
- [28] L. P. Gamberg, G. R. Goldstein, and M. Schlegel, *Phys. Rev. D* **77**, 094016 (2008), arXiv:0708.0324 [hep-ph].
- [29] R. Jakob, P. J. Mulders, and J. Rodrigues, *Nucl. Phys.* **A626**, 937 (1997), arXiv:hep-ph/9704335 [hep-ph].
- [30] A. Bacchetta, F. G. Celiberto, M. Radici, and P. Taels, *Eur. Phys. J. C* **80**, 733 (2020), arXiv:2005.02288 [hep-ph].
- [31] K. Goeke, S. Meissner, A. Metz, and M. Schlegel, *Phys. Lett.* **B637**, 241 (2006), arXiv:hep-ph/0601133 [hep-ph].
- [32] J. Collins, *Camb. Monogr. Part. Phys. Nucl. Phys. Cosmol.* **32**, 1 (2011).
- [33] A. Efremov and A. Radyushkin, *Theor. Math. Phys.* **44**, 774 (1981).
- [34] S. J. Brodsky, D. S. Hwang, and I. Schmidt, *Phys. Lett.* **B530**, 99 (2002), arXiv:hep-ph/0201296 [hep-ph].
- [35] J. C. Collins, *Phys. Lett. B* **536**, 43 (2002), arXiv:hep-ph/0204004.
- [36] A. V. Belitsky, X. Ji, and F. Yuan, *Nucl. Phys. B* **656**, 165 (2003), arXiv:hep-ph/0208038.
- [37] C. Pisano, D. Boer, S. J. Brodsky, M. G. Buffing, and P. J. Mulders, *JHEP* **10**, 024 (2013), arXiv:1307.3417 [hep-ph].
- [38] D. Boer, W. J. den Dunnen, C. Pisano, and M. Schlegel, *Phys. Rev. Lett.* **111**, 032002 (2013), arXiv:1304.2654 [hep-ph].
- [39] M. G. Echevarria, T. Kasemets, P. J. Mulders, and C. Pisano, *JHEP* **07**, 158 (2015), [Erratum: *JHEP*05,073(2017)], arXiv:1502.05354 [hep-ph].
- [40] C. Bomhof, P. Mulders, and F. Pijlman, *Eur. Phys. J. C* **47**, 147 (2006), arXiv:hep-ph/0601171.
- [41] A. Bacchetta, C. Bomhof, U. D'Alesio, P. Mulders, and F. Murgia, *Phys. Rev. Lett.* **99**, 212002 (2007), arXiv:hep-ph/0703153.
- [42] M. G. Buffing, Z.-B. Kang, K. Lee, and X. Liu, (2018), arXiv:1812.07549 [hep-ph].
- [43] T. C. Rogers, *Phys. Rev. D* **88**, 014002 (2013), arXiv:1304.4251 [hep-ph].
- [44] J.-w. Qiu and G. F. Sterman, *Phys. Rev. Lett.* **67**, 2264 (1991).
- [45] J.-w. Qiu and G. F. Sterman, *Nucl. Phys. B* **378**, 52 (1992).
- [46] J.-w. Qiu and G. F. Sterman, *Phys. Rev. D* **59**, 014004 (1999), arXiv:hep-ph/9806356.
- [47] M. G. A. Buffing, M. Diehl, and T. Kasemets, *JHEP* **01**, 044 (2018), arXiv:1708.03528 [hep-ph].
- [48] D. Khazeev, Y. V. Kovchegov, and K. Tuchin, *Phys. Rev. D* **68**, 094013 (2003), arXiv:hep-ph/0307037.
- [49] F. Dominguez, B.-W. Xiao, and F. Yuan, *Phys. Rev. Lett.* **106**, 022301 (2011), arXiv:1009.2141 [hep-ph].
- [50] F. Dominguez, C. Marquet, B.-W. Xiao, and F. Yuan, *Phys. Rev. D* **83**, 105005 (2011), arXiv:1101.0715 [hep-ph].
- [51] M. G. A. Buffing, A. Mukherjee, and P. J. Mulders, *Phys. Rev.* **D88**, 054027 (2013), arXiv:1306.5897 [hep-ph].
- [52] S. J. Brodsky, D. S. Hwang, and I. Schmidt, *Nucl. Phys. B* **642**, 344 (2002), arXiv:hep-ph/0206259.
- [53] L. P. Gamberg, G. R. Goldstein, and K. A. Oganessyan, *Phys. Rev. D* **67**, 071504 (2003), arXiv:hep-ph/0301018.
- [54] D. Boer, S. J. Brodsky, and D. S. Hwang, *Phys. Rev. D* **67**, 054003 (2003), arXiv:hep-ph/0211110.
- [55] A. Bacchetta, A. Schaefer, and J.-J. Yang, *Phys. Lett. B* **578**, 109 (2004), arXiv:hep-ph/0309246.
- [56] R. D. Ball, V. Bertone, M. Bonvini, S. Marzani, J. Rojo, and L. Rottoli, *Eur. Phys. J.* **C78**, 321 (2018), arXiv:1710.05935 [hep-ph].
- [57] E. R. Nocera, R. D. Ball, S. Forte, G. Ridolfi, and J. Rojo (NNPDF), *Nucl. Phys.* **B887**, 276 (2014), arXiv:1406.5539 [hep-ph].
- [58] R. D. Ball *et al.* (NNPDF), *JHEP* **04**, 040 (2015), arXiv:1410.8849 [hep-ph].
- [59] S. Forte, L. Garrido, J. I. Latorre, and A. Piccione, *JHEP* **05**, 062 (2002), arXiv:hep-ph/0204232.
- [60] A. Bacchetta, F. Delcarro, C. Pisano, M. Radici, and A. Signori, *JHEP* **06**, 081 (2017), [Erratum: *JHEP* 06, 051 (2019)], arXiv:1703.10157 [hep-ph].
- [61] I. Scimemi and A. Vladimirov, *JHEP* **06**, 137 (2020), arXiv:1912.06532 [hep-ph].
- [62] A. Bacchetta, V. Bertone, C. Bissolotti, G. Bozzi, F. Delcarro, F. Piacenza, and M. Radici, *JHEP* **07**, 117 (2020), arXiv:1912.07550 [hep-ph].
- [63] A. Bacchetta, V. Bertone, C. Bissolotti, G. Bozzi, M. Cerutti, F. Piacenza, M. Radici, and A. Signori (MAP), *JHEP* **10**, 127 (2022), arXiv:2206.07598 [hep-ph].
- [64] M. Bury, F. Hautmann, S. Leal-Gomez, I. Scimemi, A. Vladimirov, and P. Zurita, *JHEP* **10**, 118 (2022), arXiv:2201.07114 [hep-ph].
- [65] V. Moos, I. Scimemi, A. Vladimirov, and P. Zurita, (2023), arXiv:2305.07473 [hep-ph].
- [66] A. Bacchetta, F. G. Celiberto, and M. Radici, *PoS EPS-HEP2021*, 376 (2022), arXiv:2111.01686 [hep-ph].

-
- [67] A. Bacchetta, F. G. Celiberto, and M. Radici, *JPS Conf. Proc.* **37**, 020124 (2022), arXiv:2201.10508 [hep-ph].
- [68] A. Bacchetta, F. G. Celiberto, and M. Radici, *PoS PANIC2021*, 378 (2022), arXiv:2111.03567 [hep-ph].
- [69] R. Abdul Khalek *et al.*, *Nucl. Phys. A* **1026**, 122447 (2022), arXiv:2103.05419 [physics.ins-det].
- [70] R. Abdul Khalek *et al.*, in *2022 Snowmass Summer Study* (2022) arXiv:2203.13199 [hep-ph].
- [71] R. Abir *et al.*, (2023), arXiv:2305.14572 [hep-ph].
- [72] A. Arbuzov *et al.*, *Prog. Part. Nucl. Phys.* **119**, 103858 (2021), arXiv:2011.15005 [hep-ex].
- [73] E. Chapon *et al.*, *Prog. Part. Nucl. Phys.* **122**, 103906 (2022), arXiv:2012.14161 [hep-ph].
- [74] S. Amoroso *et al.*, *Acta Phys. Polon. B* **53**, A1 (2022), arXiv:2203.13923 [hep-ph].
- [75] L. A. Anchordoqui *et al.*, *Phys. Rept.* **968**, 1 (2022), arXiv:2109.10905 [hep-ph].
- [76] J. L. Feng *et al.*, *J. Phys. G* **50**, 030501 (2023), arXiv:2203.05090 [hep-ex].
- [77] A. Accardi *et al.*, (2023), arXiv:2306.09360 [nucl-ex].
- [78] F. G. Celiberto, *Phys. Rev. D* **105**, 114008 (2022), arXiv:2204.06497 [hep-ph].
- [79] M. Deak, A. van Hameren, H. Jung, A. Kusina, K. Kutak, and M. Serino, *Phys. Rev. D* **99**, 094011 (2019), arXiv:1809.03854 [hep-ph].
- [80] F. Silveti and M. Bonvini, *Eur. Phys. J. C* **83**, 267 (2023), arXiv:2211.10142 [hep-ph].

A case study of sending graph neural networks back to the test bench for applications in high-energy particle physics

Emanuel Pfeffer  · Michael Waßmer  ·
Yee-Ying Cung · Roger Wolf  ·
Ulrich Husemann 

Abstract In high-energy particle collisions, the primary collision products usually decay further resulting in tree-like, hierarchical structures with a priori unknown multiplicity. At the stable-particle level all decay products of a collision form permutation invariant sets of final state objects. The analogy to mathematical graphs gives rise to the idea that graph neural networks (GNNs), which naturally resemble these properties, should be best-suited to address many tasks related to high-energy particle physics. In this paper we describe a benchmark test of a typical GNN against neural networks of the well-established deep fully-connected feed-forward architecture. We aim at performing this comparison maximally unbiased in terms of nodes, hidden layers, or trainable parameters of the neural networks under study. As physics case we use the classification of the final state X produced in association with top quark-antiquark pairs in proton-proton collisions at the Large Hadron Collider at CERN, where X stands for a bottom quark-antiquark pair produced either non-resonantly or through the decay of an intermediately produced Z or Higgs boson.

Keywords Graph Neural Networks · Deep Neural Networks · High-Energy Particle Physics · LHC

Emanuel Pfeffer¹ (corresponding author)
E-mail: emanuel.pfeffer@kit.edu

Michael Waßmer¹
E-mail: michael.wassmer@kit.edu

Yee-Ying Cung
E-mail: yeeying.cung@web.de

Roger Wolf¹
E-mail: roger.wolf@kit.edu

Ulrich Husemann¹
E-mail: ulrich.husemann@kit.edu

¹ Karlsruhe Institute of Technology, Institute of Experimental Particle Physics, Karlsruhe, Germany

1 Introduction

The continuous rise and flourish of deep learning has significantly impacted also the community of high-energy particle physics, where modern algorithms of deep learning —mostly in the form of various neural network (NN) architectures— find applications as automation tools, for (multiclass) classification, parameter regression, or universal function approximation. The Large Hadron Collider (LHC) at CERN offers a unique test environment for such algorithms providing a large amount of independent identically distributed (i.i.d.) data from proton-proton (pp) collisions under well controlled laboratory conditions. These data feature a rich hierarchical structure, optimally suited for the application of all kinds of general methods of statistical data analysis. Moreover, the underlying physics laws and statistical models, which have emerged over many decades of research, are scrutinized to a level that allows the reliable estimation of particle properties with a relative accuracy ranging far below the per-mille level, in rare cases even below 10^{-10} [1]. This circumstance offers a toolbox for generating a large amount of perfectly known, complex, synthetic data, with a high relation to experimental observations, through the application of Monte Carlo (MC) methods [2,3]. These data are usually obtained as samples from an intractable though well-known likelihood function \mathcal{L} . This setup provides a unique opportunity to thoroughly benchmark any kinds of machine learning (ML) algorithms under complex, real-life laboratory conditions.

At the LHC, data analysts strive for the application of more and more sophisticated ML-models with more and more not further processed —and in this sense “raw”— input data. This strategy is fed by the belief that automated algorithms might find ways of extracting information of interest to the analyst, which are superior to selection strategies that are vulnerable to the bias of human prejudice. On the other hand, ML-algorithms should not be forced to learn already known and well-established physics principles, like symmetries inherent to the presented task. While such information can only be insufficiently passed through the necessarily finite training samples, it can be intrinsically incorporated either into the loss functions used for training, or in the NN architectures.

At the large multi-purpose LHC experiments, ATLAS [4] and CMS [5], pp collisions at a center-of-mass energy of, e.g., 13 TeV result in the creation of thousands of collision products to be recorded by the experiments. Primary collision products might decay further resulting in tree-like, hierarchical structures with a priori unknown multiplicity. The collision process can be described in a factorized approach:

During the hard scattering process, the fundamental constituents of the protons, i.e., the quarks and gluons which are also collectively referred to as partons, interact via the fundamental interactions under investigation. We refer to the result of these interactions as the partonic final state. It cannot be observed directly in an experiment. Rather, each parton undergoes a series of theoretically well-known processes, setting in at lower energy scales, resulting in stable particles. The inverse problem usually subject of high-energy particle physics is to infer the presence and properties of the stable particles and eventually the partonic final state from their observable energy deposits in the detectors.

At the stable particle level all decay products of a collision form permutation invariant sets of final state objects, which may emerge from the collision in the form

of collimated particle jets [6], forming well-suited proxies for strongly-interacting final state partons, or individual, spatially isolated particles, like leptons. From the preparation of the collision’s initial state and energy and momentum conservation, physicists may infer the presence of non- or weakly-interacting particles, like neutrinos, in the collision’s final state, through the principle of missing transverse energy (MET) [7]. A natural representation of this richly structured data is in the form of mathematical graphs \mathcal{G} , which are indeed also the basis of theoretical amplitude calculations of the quantum-mechanical wave function in the form of Feynman graphs [8].

Within the high-energy particle physics community, this observation has led to an increased interest in NNs based on mathematical graphs (GNNs) [9,10,11,12,13], where nodes are usually identified by particles and edges potentially by relations across particles. A comprehensive review can be found in Ref. [14]. However, on closer inspection, several features of GNNs that count for seemingly obvious advantages reveal subtle challenges:

- The mathematical model to match physics entities like stable particles to the graph \mathcal{G} of the GNN, which is subject to mathematical operations, bears ambiguities. The representation of particles by the nodes of \mathcal{G} appears as an obvious choice. This choice raises the question of the (potentially physical) meaning to the connecting edges, which could represent mother-daughter relations, or proximity in an arbitrarily defined space. This issue is emphasized once mathematical weights or even trainable parameters (TPs) used during node aggregation are assigned to the edges.
- Training and application imply the potentially complex and computationally time-consuming task of building \mathcal{G} , based on the physics inputs.
- In general, the more complex structure of the GNN compared to other NN architectures complicates the users’ comprehension of how the GNN arrives at its prediction.

In this paper we describe a comparison of typical GNN architectures with NN models based on the deep fully-connected feed-forward architecture (DNN), which has been studied intensely in the past. We aim at comparisons that are to best effort unbiased in terms of expressiveness and information provided to the NN models to solve a given task. In Section 2 we give an introduction to the task that serves as benchmark for this comparison. In Section 3 the architectures and training setups of the NNs under study are described. In Section 4 we present the results of the comparison. We conclude the paper with a summary in Section 5.

2 Neural network task

2.1 Physics processes

As benchmark for the comparison we use the classification of the final state X produced in association with top (t) quark-antiquark pairs ($t\bar{t}$) in pp collisions at the LHC, where X stands for a bottom (b) quark-antiquark pair ($b\bar{b}$) produced either through non-resonant gluon exchange or through the decay of a massive Z or Higgs (H) boson as intermediate particle, as discussed, e.g., in Ref. [15]. Under realistic conditions, the collision of interest might be overlaid by several tens of

additional collisions, referred to as pileup. The complete detectable final state of a collision of interest, including pileup, is referred to as an event, whose feature vector \mathbf{x} would be presented to the NN. An arbitrary number of such events may be generated synthetically by evaluating \mathcal{L} of the full process via the MC method. In this study, we focus on the classification of the underlying hard process neglecting the effects of pileup.

The interest in the chosen classification task arose from studies of H production in association with $t\bar{t}$ in the subsequent $H \rightarrow b\bar{b}$ decay ($ttH(bb)$), for which $t\bar{t}$ associated Z boson production (ttZ) in the $Z \rightarrow b\bar{b}$ decay channel ($ttZ(bb)$) and non-resonant $b\bar{b}$ production in association with $t\bar{t}$ ($ttbb$) are important background processes. Exemplary Feynman diagrams of these processes in leading-order (LO) of perturbation theory are shown in Figure 1. The decay products, resembled by the outgoing lines in the diagrams, shown in Figure 1, represent the partonic final state of interest to this study, which is the same for all processes. Therefore, the processes can only be distinguished by the kinematic properties of the particles, in particular b quarks. This situation is complicated by the fact that the t quark also decays into b quarks radiating a quasi-real W boson with a branching fraction of nearly 100% [16]. The W boson subsequently decays either into quarks, which further on form jets in the detector, or leptons. For the presented study the semi-leptonic $t\bar{t}$ final state has been chosen, in which the W boson of one t decays into an electron or muon, further on referred to as ℓ , and a corresponding neutrino ν_ℓ . The other W boson decays into quarks. Due to the radiation of additional gluons and the splitting of gluons into quark-antiquark pairs additional colored particles and consequently jets might emerge from the process. This constellation implies a richly structured final state of an event with at least four b quark- and two predominantly light-quark-induced jets; an ℓ , which is spatially isolated from any other activity originating from the hard scattering process in the detector; and MET, due to the emitted ν_ℓ . The b quark-induced jets, referred to as b jets in the following, may be identified experimentally with a finite purity and efficiency, as, e.g., described in Ref. [17]; the methods of how to achieve this are not subject of this paper.

2.2 Sample preparation

Samples for all processes in question have been generated synthetically from a corresponding likelihood \mathcal{L} using the MC technique. The tools used for event generation are the matrix-element generator MadGraph5_aMC@NLO [18,19] in ver-

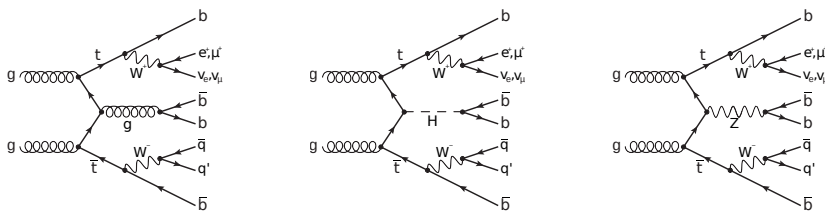


Fig. 1 Exemplary Feynman diagrams for the processes of interest to this study: (left) $ttbb$, (middle) $ttH(bb)$, and (right) $ttZ(bb)$.

Table 1 Selection requirements on the reconstructed final-state objects. The quantity $I_{\text{rel}}^{\Delta R}$ corresponds to the scalar sum of energy deposits detected within the radius ΔR around ℓ in η - ϕ divided by the p_{T} of ℓ , as defined in the text. A lower value of $I_{\text{rel}}^{\Delta R}$ implies less activity in the spacial vicinity of ℓ , indicating that ℓ originates from $W \rightarrow \ell\nu_{\ell}$. The variable β refers to the working points of a specific b jet identification algorithm, as described in the text.

Object	p_{T} (GeV)	$ \eta $	$I_{\text{rel}}^{\Delta R}$	β
Electron	≥ 25	< 2.5	< 0.12 ($\Delta R = 0.3$)	–
Muon	≥ 25	< 2.4	< 0.25 ($\Delta R = 0.4$)	–
Jet (anti- k_{T} , $R_0=0.4$ [22])	≥ 20	< 2.4	–	–
b jet	≥ 20	< 2.4	–	$\beta \geq 2$

sion 2.9.9 interfaced with the Pythia event generator [20] in version 8.306 to map the partonic final state to the stable-particle level. All processes in consideration have been generated at LO in perturbative quantum chromodynamics (QCD), in the four-flavor scheme. The same setup has been used for the generation of all samples to avoid spurious differences due to the use of different generation tools.

All generated events have been passed through a simplified simulation of the CMS detector as configured during the LHC Run-2 data-taking period in the years 2016–2018, using the DELPHES simulation package [21]. For this study only reconstructed leptons, jets, and MET are considered. All detected and reconstructed final-state objects have been selected to fulfill a set of selection criteria typically used for the analysis of data collected by the CMS experiment, as summarized in Table 1. These selection criteria comprise the following observables:

- The transverse momentum p_{T} and pseudorapidity η of the reconstructed ℓ and jets.
- A variable $I_{\text{rel}}^{\Delta R}$ that corresponds to the scalar sum of energy deposits E_i detected within the radius $\Delta R = \sqrt{\Delta\eta^2 + \Delta\phi^2}$ around ℓ , divided by the p_{T} of ℓ , where $\Delta\eta$ refers to the difference between E_i and ℓ in η and $\Delta\phi$ to the corresponding difference in azimuthal angle ϕ , based on the coordinate system deployed by CMS [5]. For ℓ originating from $W \rightarrow \ell\nu_{\ell}$ low values of $I_{\text{rel}}^{\Delta R}$ are expected.
- The output of a specific b jet identification algorithm represented by the discrete observable $\beta \in \{0, 1, 2, 3\}$ indicating whether an object has been identified as a b jet under a specific working point α ($\beta \geq \alpha$). The value of α represents ($\alpha = 1$) loose, ($\alpha = 2$) medium, and ($\alpha = 3$) tight selection criteria, corresponding to a rate of non-b jets wrongly identified as a b jet (false-positive rate), of approximately 10%, 1%, and 0.1%, respectively.

All events have been selected to exhibit at least six and not more than eight jets, at least four of which are assumed to be correctly identified as b jets according to $\beta \geq 2$, and exactly one ℓ , matching all selection criteria. The selection of one ℓ and six jets, of which at least four are identified as b jets, is motivated by the partonic final state under study, as depicted in Figure 1. The selection of up to two additional jets, increases the chance that the complete partonic final state can be matched to the selected jets.

For each reconstructed jet the attempt is made to assign the initiating particle of the partonic final state, based on the distance ΔR between the jet and the corresponding parton. Only partonic final state objects with transverse momentum of $p_{\text{T}} > 20$ GeV and $|\eta| < 2.4$ are considered for this assignment. From the

Table 2 Requirements for the jet-class definition, according to the matching to the partonic final state, where b_{add} corresponds to a b quark not originating from a t decay, $b_{t_{\text{had}}}$ ($b_{t_{\text{lep}}}$) to a b quark originating from $t \rightarrow bW(qq')$ ($t \rightarrow bW(\ell\nu_\ell)$), and $q_{W_{\text{had}}}$ to a quark originating from $W \rightarrow qq'$. We note that the classes ADDB and HTQ comprise two jets. Jets not assigned to any other class are assigned to the NA class and sorted by decreasing p_T . If no jet is found to fulfill the corresponding ΔR criterion, the leading jet from the NA class is re-assigned to the classes HTB, HTL, HTQ, in that order.

Class label	Assignment	Description
ADDB	$\Delta R(\text{jet}, b_{\text{add}}) < 0.4$	b jets not from t decays
HTB	$\Delta R(\text{jet}, b_{t_{\text{had}}}) < 0.4^\dagger$	b jet from t_{had}
LTB	$\Delta R(\text{jet}, b_{t_{\text{lep}}}) < 0.4^\dagger$	b jet from t_{lep}
HTQ	$\Delta R(\text{jet}, q_{W_{\text{had}}}) < 0.4^\dagger$	q jet from W
NA	No match	Additional jet

[†] If no assignment by ΔR is found, the leading jet from NA is assigned.

assignment five mutually exclusive jet classes are build, referring to the (ADDB) b quarks not originating from any t decay; the b quark originating from the (HTB) hadronic and (LTB) leptonic t decay, (HTQ) quarks originating from the hadronic W decay; and (NA) jets not assigned to the partonic final state.

The assignment of the partonic final state to the reconstructed jets may be incomplete, for a given event. Events for which no or only one jet is assigned to the ADDB class are discarded from the training and test samples. In all other cases, if the assignment by ΔR did not result in one jet of class LTB, one jet of class HTB, and two jets of class HTQ, the remaining not associated jets of class NA are ordered by decreasing p_T and the leading jets in p_T are re-assigned to these classes in the order of LTB, HTB, HTQ. A summary of all jet classes is given in Table 2

2.3 Task definition

The NN models are supposed to perform a classification task, in which a given event should be assigned either to $ttbb$, $ttH(bb)$, or $ttZ(bb)$. The physics process from which the event was generated constitutes the ground truth information for this task.

To simplify the task, the reconstructed jets are assumed to perfectly match the initiating partons, whenever possible, through the parton association algorithm, as described in Section 2.2. The ADDB class contains jets which stem directly from the intermediate particle to distinguish the processes under study. The features of these jets are assumed to provide the most decisive contribution to the classification.

2.4 Training setup

All NN models are subject to a supervised training. The generated samples used for this are split into a training, validation, and test sample, containing 60, 20, and 20% of the generated events, respectively. Event numbers, split by process and sample, are given in Table 3.

Each training is performed for an ensemble of ten statistically independent repetitions to obtain a rough estimate of the statistical spread of the trained models, due to random choices in the training setup. Performance measures of each model are reported as sample means μ , of which the corresponding uncertainty $\Delta\mu$ is estimated from the square root of the sample variance. All repetitions are based on the same training, validation, and test samples. Due to the large number of events in these samples, randomization through data shuffling is assumed not to change the conclusions of the studies significantly.

Each training is performed on CPUs through a distributed computing infrastructure, where each training is performed on a dedicated CPU. We ensure that each step affected by random choices is based on a different random seed. The library used to build the GNNs is PyTorch Geometric v2.0.3 [23] based on the PyTorch library [24]. The same library is used, to construct the corresponding DNNs under study. Further parameter choices of the training setups are given in the upper part of Table 4. They are the same for both NN architectures.

3 Neural networks under study

3.1 Architectures

For the GNN models, a graph representation of the final state is obtained from the reconstructed jets, ℓ , and MET in an event. Each of these objects is represented by a node i in \mathcal{G} . This set of nodes may be complemented by nodes for up to two more jets in the selection. Accordingly, \mathcal{G} has 8–10 nodes. For each i , a vector \mathbf{a}_i of attributes with $\dim(\mathbf{a}_i) = n$, $\forall i$ is defined, forming the embedding space. At initialization time, the \mathbf{a}_i are initialized by the feature vectors \mathbf{x}_i with $\dim(\mathbf{x}_i) = n_{\text{feat}}$, $\forall i$. The following studies also comprise configurations with $n > n_{\text{feat}}$. In these cases, attributes in the \mathbf{a}_i without correspondence in \mathbf{x}_i are set to zero (zero padding), at initialization time.

Table 3 Numbers of events for each process, in the training, validation, and test samples.

Process	Training	Validation	Test	Sum
ttbb	41650	13883	13803	69336
ttH(bb)	99695	33329	33229	166253
ttZ(bb)	88107	29272	29453	146832

Table 4 Common parameter choices for the NN architectures under study and their training setup.

Parameter	Setting(s)
Loss function	Binary cross-entropy
Optimizer	Adam [25] ($\gamma = 0.01$)
Mini-batch size	200
Maximum number of epochs	200
Early-stopping	$\Delta\text{epochs} = 15$, $\Delta\text{loss} = 0.001$
Use of weights and biases	Yes
Number of outputs	1 (binary)
Activation function (for hidden layers)	ReLU
Activation function (for output layer)	Sigmoid

All nodes are connected with edges, resulting in a fully-connected non-directed graph without self-loops. Relational information between nodes i and j may be assigned, in form of edge weights ω_{ij} . For this purpose three physics motivated choices are made: (i) the invariant mass m ; (ii) the distance ΔR ; and (iii) the reciprocal distance ΔR^{-1} of the connected final-state objects. In addition, the cases of a (one) constant, (rnd) random, and (zero) no edge connection at all are studied, resulting in a total of six variants of edge connections. An illustration of a resulting graph for an event with eight nodes and no additional jets is given in Figure 2.

The GNN algorithm to process the graph data is based on the layered GraphConv operation, as introduced and described in Ref. [26], using the sum over all i as aggregation function. After initialization, k GraphConv operations are applied, after which the resulting \mathbf{a}_i are transformed into a single vector of length n , averaging over all i . A linear combination of the components of this vector, which is scaled to values between 1 (indicating ttbb as signal) and 0, for binary classification, eventually forms the output \hat{y} of the GNN. A graphical illustration of this model is given in the lower part of Figure 2.

In a first study, the GNN are compared with corresponding DNN models with k hidden layers, containing n hidden nodes, each. The values of k , n , and the choice of weights, steering the exploitation of relational information by the GNN models are varied, resulting in 36 variants of parameter choices, as summarized in Table 5. We note that here, as in the following, n represents a tuple of length k . For a GNN this tuple indicates the dimension of the embedding space per GraphConv operation; for a DNN it represents the number of nodes per hidden layer. Other parameter choices related to the NN architectures under study or the setup of the NN training are made common and summarized in Table 4. Special care is taken to compare the GNN with the corresponding DNN models on the same footing, especially in terms of information about the feature space presented to them, as discussed in the following section.

3.2 Presentation of the feature space

Primary features passed to the NNs are the invariant mass (m), energy (E), η , and ϕ of each reconstructed final state object. The reconstructed final state objects comprise ℓ , MET, at least four b jets, two additional jets, all of which are

Table 5 Parameters varied for the comparison of GNN with corresponding DNN models, where n corresponds to the dimension of the embedding space during a GraphConv operation (number of nodes in a hidden layer) and k to the number of GraphConv operations (hidden layers) in the GNN (DNN) case. The choices of n are motivated by the size of the input vector n_{feat} to the GNN, as described in Section 3.2. The choices of **one**, **rnd**, and **zero** for the use of edge information in GNN models are compared to DNN models without relational information between individual objects. These DNN models are indicated by the label **none**, in corresponding figures.

Parameter	Setting(s)
k	1, 2
n	13, 26, 39
Edge weights (ω_{ij})	m , ΔR , ΔR^{-1} , one , rnd , zero

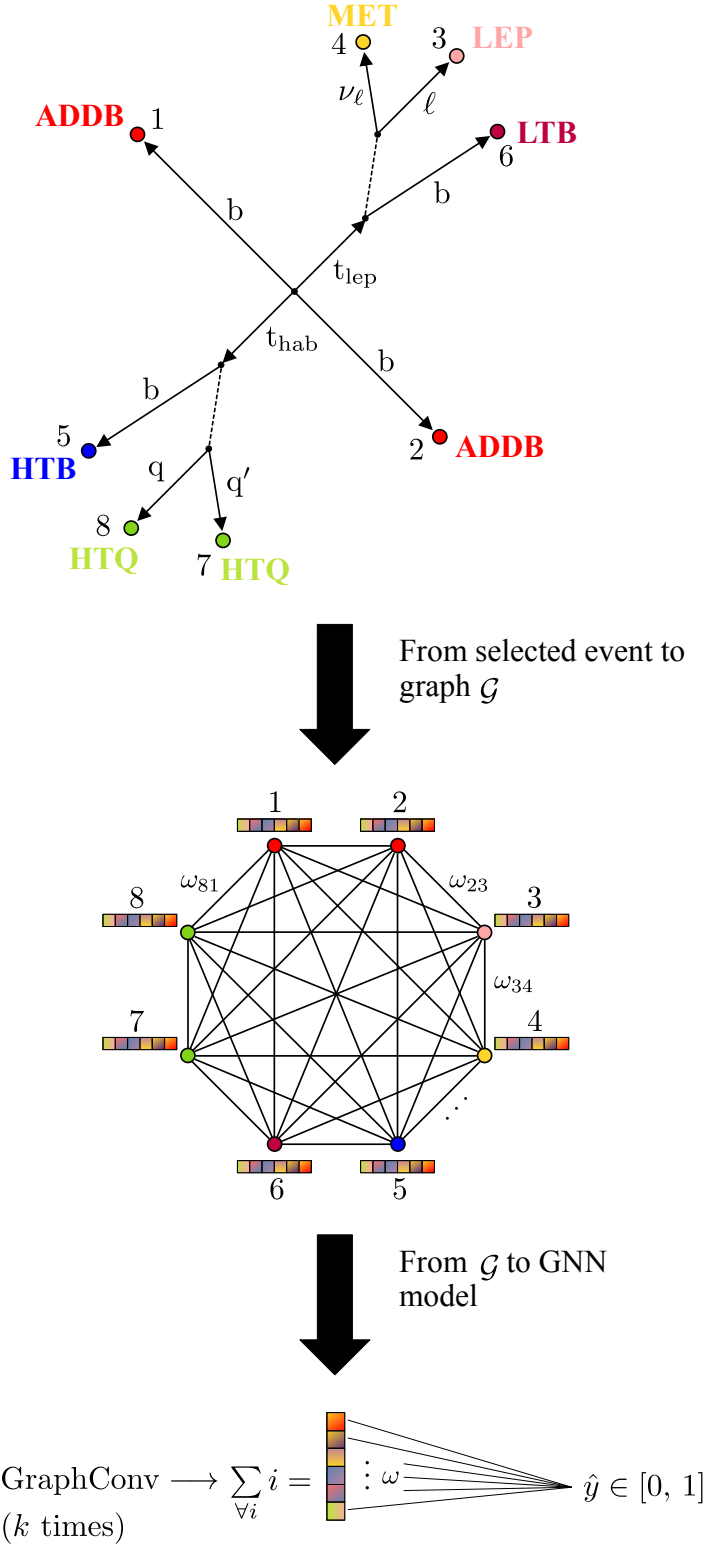


Fig. 2 Translation of an (upper part) selected event (without jets in the NA jet-class in this case) into a (middle part) graph \mathcal{G} and finally into the (lower part) GNN model. For the indication of the partonic final state we do not distinguish particles from anti-particles. The individual object-classes are indicated by different colors. The nodes of \mathcal{G} are labelled by $i = 1 \dots 8$ and colored the same way as the object-classes. The boxes next to the nodes indicate the embedding space of the GNN model. The GNN output is indicated by \hat{y} .

associated with the partonic final state, and potentially two more non-associated jets from the event selection. For MET the features E and m are set to zero. The primary features are complemented by β . The selection requires values of $\beta \geq 2$ for identified b jets. For ℓ and MET β is set to zero.

We note that both NN architectures may profit from additional information, which is not passed explicitly through \mathbf{x}_i , but implicitly through the way the features are presented to the NNs. An obvious difference between the NN architectures arises from the fact that the GNN naturally supports processing of events with arbitrary object multiplicities. The \mathbf{x}_i are transferred to the GNN through the \mathbf{a}_i , during initialization. During the GNN processing the information per i is aggregated over all nodes. In the DNN case such an aggregation step is absent. Instead, the \mathbf{x}_i are concatenated into an enlarged feature vector \mathbf{x}^{DNN} of length $10 \times n_{\text{feat}}$, comprising the \mathbf{x}_i of the eight reconstructed objects, of which all jets have been associated to the partonic final state, plus potentially two additional selected jets. The order in which these objects are concatenated has been chosen to follow the association to the partonic final state. For events that contain fewer than two jets in addition to those that have been matched to the partonic final state, the corresponding entries in \mathbf{x}^{DNN} are filled with zeros. We point out two subtleties, which are related to these choices:

One subtlety, in favor of the GNN, arises from incorporating relational information through ω_{ij} . This advantage is compensated for by appending equivalent information to \mathbf{x}^{DNN} . For up to ten selected objects in an event this results in up to 45 additional features. The choices of `one`, `rnd`, and `zero` for the use of edge information in GNN models are compared to DNN models without relational information between individual objects. These DNN models are indicated by the label `none`, in corresponding figures.

Another subtlety, related to the same fundamental difference, but this time in favor of the DNN, arises from the fact that through the concatenation of the \mathbf{x}_i into \mathbf{x}^{DNN} , according to the association to the partonic final state, the DNN receives extra information through the positions of the \mathbf{x}_i in \mathbf{x}^{DNN} which is not accessible to the GNN. This advantage is compensated for by adding information about the association of the i to the partonic final state via one-hot encoding. For the five jet-classes defined in Table 2 plus one label (LEP) for ℓ and one label (MET) for MET this extension increases n_{feat} by seven, leading to the dimension of \mathbf{x}_i , $\forall i$ of $n_{\text{feat}} = 13$.

For \mathbf{x}^{DNN} the \mathbf{x}_i are concatenated for all i assuming two more jets in the NA class. For events with fewer than two jets in the NA class the foreseen features are initialized with zero. Together with the relational information between all potential objects in an event, this results in a dimension of \mathbf{x}^{DNN} of 175 features, of which up to 47 features might potentially be filled with zeros.

In this configuration the information about the association to the partonic final state is presented in the form of one-hot encoding to both NN architectures. To confirm to what extent the DNN may infer this information already from the position of the \mathbf{x}_i within \mathbf{x}^{DNN} we also investigate configurations of the DNNs without this information in form of one-hot encoding, resulting in a reduced input vector $\mathbf{x}_{\text{red}}^{\text{DNN}}$ with dimension 105. All input features in use are listed in Table 6. All non-integer features are standardized to a mean of zero and a standard deviation of one.

Table 6 Input features used for the studies described in the text. Columns 2–4 indicate whether a given feature is continuous, discrete, or presented via one-hot encoding. The given features form the feature vectors \mathbf{x}_i per object i . For the DNNs the \mathbf{x}_i for potentially ten selected objects are concatenated into an extended feature vector \mathbf{x}^{DNN} , according to their association to the partonic final state; for events with fewer than ten objects the \mathbf{x}_i of the missing objects are filled with zeros. In addition, relational information between all potential objects is added to \mathbf{x}^{DNN} . In a reduced configuration, the one-hot encoded information about the association of the objects to the partonic final state is omitted to form a reduced input vector $\mathbf{x}_{\text{red}}^{\text{DNN}}$ to the DNNs.

Input feature	Continuous	Discrete	One-hot	Comment
m	✓	–	–	} Primary features
E	✓	–	–	
p_T	✓	–	–	
ϕ	✓	–	–	
η	✓	–	–	
β	–	✓	–	
LEP	–	–	✓	Assoc. to ℓ
MET	–	–	✓	Assoc. to MET
ADDB	–	–	✓	Assoc. to additional b quarks
HTB	–	–	✓	Assoc. to $t_{b_{\text{had}}}$
LTB	–	–	✓	Assoc. to $t_{b_{\text{lep}}}$
HTQ	–	–	✓	Assoc. to $q_{W_{\text{had}}}$
NA	–	–	✓	Not associated

4 Results

To be able to draw fair conclusions from a comparison of different NN architectures (of potentially different complexity) special care has to be taken for this comparison to be based on the same ground. For this study we have focused on a common choice of non-tunable (hyper-)parameters, which are not subject to the NN training, as well as on an equal level of information primarily passed to the NNs, through training conditions and input features.

An inevitable difference remains in the organization and layering of hidden nodes, which when kept similar, may well lead to a different number of TPs and therefore a priori different expressiveness of the NN models. Vice versa, keeping the number of TPs similar, implies differences in the layering and organization of hidden nodes. Since differences of one or the other kind may not be overcome, both configurations, (i) similar layering of hidden nodes; and (ii) similar number of TPs, are studied. In any case, the enlarged size of \mathbf{x}^{DNN} ($\mathbf{x}_{\text{red}}^{\text{DNN}}$) with respect to \mathbf{x} will give higher emphasis to the first DNN layer compared to the corresponding GNN architecture. In addition, the DNN architecture features the less complex pre-processing of the inputs, since it does not imply the creation of graphs. On the other hand, the potentially more constrained GNN may have advantages over the DNN architecture in terms of convergence properties of the training.

4.1 Comparison of neural networks with similar layering of hidden nodes

4.1.1 Neural networks with one layer of hidden nodes

A first comparison of GNN with corresponding DNN models, based on a similar layering of hidden nodes, is shown in Figure 3. The metric by which to judge the

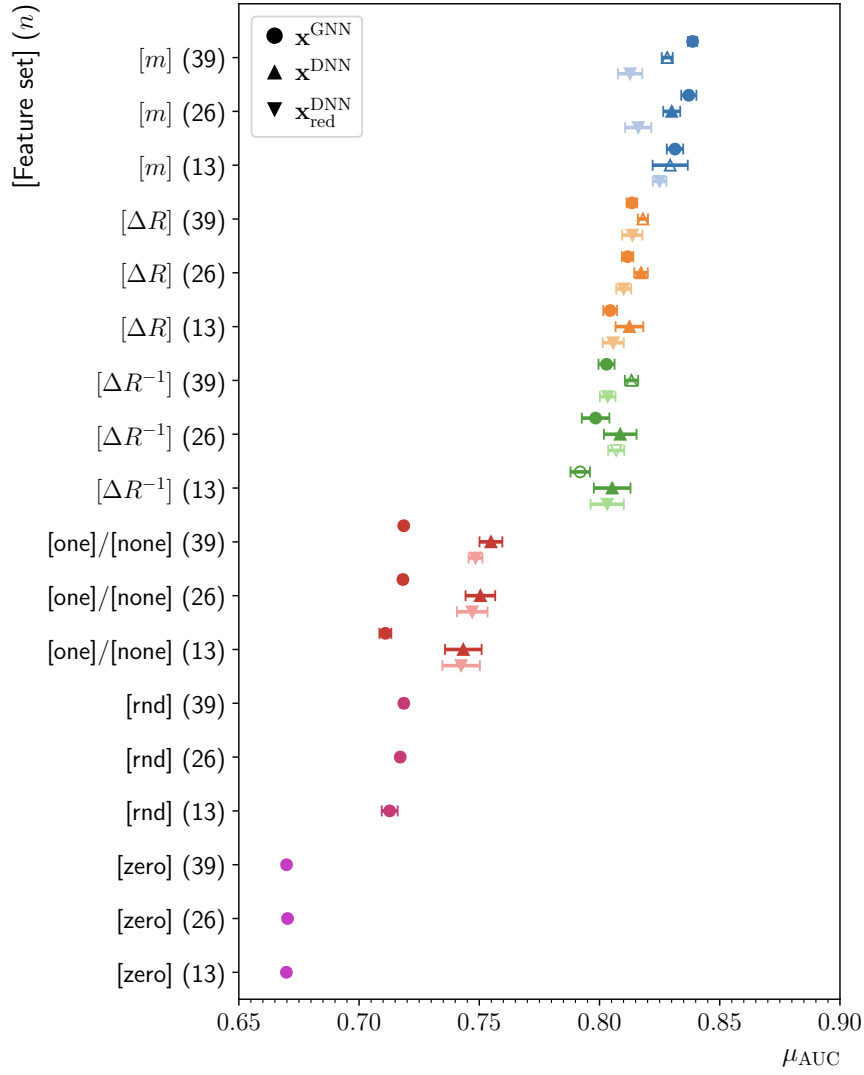


Fig. 3 Mean ROC-AUC μ_{AUC} as obtained for 18 different configurations of GNN and 24 corresponding configurations of DNN models with $k = 1$. The labels in brackets on the vertical axis indicate the use of relational information, as discussed in Section 3.2, the numbers in parentheses correspond to the choices of n . The circles refer to GNN and the upward (downward) pointing triangles to DNN models with a default (reduced) set of input features \mathbf{x}^{DNN} ($\mathbf{x}_{\text{red}}^{\text{DNN}}$), as discussed in Section 3.2. For better readability, markers of the same configuration are shifted vertically along the y-axis. The bars are obtained from the sample variance of an ensemble, as described in Section 2.4. Those NN architectures which belong to the same choices of varying parameters are spatially grouped and shown in the same color. Open markers indicate that significant outliers of the corresponding distribution of ROC-AUC values have been removed from the calculation of μ_{AUC} and its variance, as described in the text.

success of an NN to fulfill the task is chosen to be the mean of the ROC-AUC μ_{AUC} based on the training setup, as described in Section 2.4. The results are presented for the variation of parameters as summarized in Table 5. For the presentation in Figure 3 a simple architecture with one hidden layer for the DNN models and one GraphConv operation of the GNN models ($k = 1$) has been chosen. For the GNN architecture this implies that there is only one exchange of information across adjacent nodes of \mathcal{G} , i.e., each node receives information only of its nearest and not the next to nearest neighbor in \mathcal{G} . Since \mathcal{G} has been chosen to be fully connected, there is no strict suppression of information that way, in the sense that each node i receives information from any other node $j \neq i$ in \mathcal{G} . The input features presented to each corresponding NN architecture are chosen, as described in Section 3.2 and summarized in Table 6.

The results for the GNN models are represented by circles, the results for the DNN models with \mathbf{x}^{DNN} ($\mathbf{x}_{\text{red}}^{\text{DNN}}$) as input vector by upward (downward) pointing triangles. The bars associated with the points indicate the uncertainty $\Delta\mu_{\text{AUC}}$ in μ_{AUC} due to random choices in the training, as described in Section 2.4. Open markers indicate that at least one training repetition in an ensemble has been removed as an outlier from the calculations of μ_{AUC} and $\Delta\mu_{\text{AUC}}$. Candidates for outliers have been identified by their μ_{AUC} values exceeding $1.5\Delta\mu_{\text{AUC}}$, as obtained from the full ensemble. An outlier candidate has been definitely removed and the ensemble size reduced accordingly, if doing so changed $\Delta\mu_{\text{AUC}}$ by a value of at least 0.0025. Following this procedure, 54 outliers have been removed from a total of 1840, which corresponds to a rate of 2.9%. Split by NN architectures, it corresponds to 17 (37) removed outliers for GNN (DNN) models from a total of 800 (1040). In no case more than two outliers have been removed from the original ten training repetitions of any individually model.

On the x -axis of the figure the corresponding values of μ_{AUC} , ranging from 0.67 to 0.83, are shown. On the y -axis the individual NN models are labelled, such that brackets indicate, what relational information between final state objects has been used, and the values in parentheses indicate the choices of n .

We conclude that all training setups have succeeded in the sense that all NN models result in values of $\mu_{\text{AUC}} > 0.5$. The worst separation of signal from background we observe for the GNN models for which no relational information is exploited, indicated by three groups of NN architectures shown in pink, purple and red colors in the lower part of the figure. It is noted that the feature set **zero** refers to the case where the node convolution in the GraphConv operation is forcefully suppressed, and deliberately no information across nodes is exchanged at all. We anticipate that this approach counteracts the whole GNN idea. We still keep this configuration as part of the study, to gauge the effect and importance of the GraphConv operation itself. Compared to the feature set **zero**, the feature sets **one** and **rnd** single out cases in which information exchange across nodes takes place, but no real relational information is associated with it. Instead, the embedding spaces of the individual nodes are just mixed without particular prevalence. We note that even when allowing node convolution the GNN architecture falls significantly behind the comparable DNN architecture, even with a reduced input vector $\mathbf{x}_{\text{red}}^{\text{DNN}}$, as long as no mindful relational information across adjacent nodes i and j is provided according to ω_{ij} . This is true for assigning (**one**) the same or (**rnd**) random weights to each edge, irrespective of the expressiveness of the NNs, indicated by n . The superiority of the DNN architecture in this case cannot be

attributed to the additional information about the jet parton association, since this information is available to all NN architectures under study. In particular it is passed on to the GNNs, in the explicit form of one-hot encoding, which is not even the case for the DNNs with $\mathbf{x}_{\text{red}}^{\text{DNN}}$ as input vector. At this occasion, we note that the additional (and in fact in this case redundant) information of the parton association in form of one-hot encoding to the DNN does not lead to a significant increase of μ_{AUC} , compared to the implicit knowledge already provided by the positional information in $\mathbf{x}_{\text{red}}^{\text{DNN}}$. Hence, if the way this information is presented to the DNN were of influence, this influence is not significant in the scope of our study. We also observe that $\Delta\mu_{\text{AUC}}$ is considerably larger for the DNNs.

In conclusion, if the advantage of the GNN over the DNN architecture were that potentially excessive degrees of freedom in the DNN architecture are replaced by built-in constraints, the GNN architecture appears too confined, until these constraints are introduced mindfully. In turn the additional degrees of freedom of the DNN architecture result in a larger spread $\Delta\mu_{\text{AUC}}$ due to random choices in the training setup.

The upper part of Figure 3 reveals that, as soon as a domain-knowledge motivated ranking of information exchange across neighboring nodes is introduced, the GNN architecture significantly gains in separation power. Also here, this gain comes with an increase in $\Delta\mu_{\text{AUC}}$. The choices of (green) ΔR^{-1} , (orange) ΔR , and (blue) m as weights leads to an increase in separation power in the given order, where for each choice the values of μ_{AUC} can be grouped with a corresponding internal spread. On the other hand, a significant gain in μ_{AUC} , when increasing the expressiveness of an NN within a certain configuration group in terms of n , for the utilized NN models, is not observed.

We note that, as in the case of the positional encoding of parton association in $\mathbf{x}_{\text{red}}^{\text{DNN}}$, all choices of relational information are intrinsic to the training sample and implicitly accessible to all NNs through their feature vectors. For ΔR this is, e.g., the case through ϕ and η in the primary features of each reconstructed object. However, the information of $\Delta\phi$ and $\Delta\eta$ between pairs of reconstructed objects appears too subtle in the high-dimensional feature space, so that none of the chosen architectures could grasp it without the assistance of an accordingly conditioned representation of \mathbf{x} and \mathbf{x}^{DNN} , even from a training sample with more than 200,000 events.

We further note that when turning the edge-weights of the GNN structure into TPs we did not obtain a separation of signal from background better than the domain-knowledge supported use of m . At the same time we observed a significantly increased spread in the achieved separation power based on random choices of the training setup.

Our physics prior assigns more physical meaning to the choice of ΔR over ΔR^{-1} , since due to causality we expect a closer relation between objects with smaller than larger spatial distance in ΔR . The observation that both choices of relational information lead to nearly similar results in μ_{AUC} we explain by a special characteristic of NN-based classification tasks in the given setup. For the NN decision, downgrading information from further-away objects is equivalent to upgrading close-by objects. The fact that corresponding DNN architectures follow the trends of the GNN architectures, as long as equipped with the same information, supports the assumption that it is this additional relational information

between objects, rather than the GNN-specific operation of mixing features across nodes that leads to the increase of μ_{AUC} .

We note that, consistently for all architectures, the highest values of μ_{AUC} are obtained with an energy-weighted distance measure like m , which again follows our prior physics intuition. It is noteworthy that in this case the DNN architecture with \mathbf{x}_{red}^{DNN} seems to significantly lose in separation power, compared to the other architectures. In fact μ_{AUC} even decreases for increasing values of n . Also $\Delta\mu_{AUC}$ appears consistently higher for all DNN compared to the GNN architectures. These observations may be interpreted as indications of the advantage of careful guidance of the NN training- and model-setup over just confronting a highly expressive NN architecture, represented by a large number of TPs, with an even excessively large training sample. This guidance may be provided through the choice and representation of input features, as well as through the choice of a more constrained NN architecture. We note that the highest value of μ_{AUC} with the smallest spread $\Delta\mu_{AUC}$ is indeed obtained from the GNN architecture with highest expressiveness, given for $n = 39$.

4.1.2 Neural networks with two layers of hidden nodes

Moving on to an NN architecture with $k = 2$ introduces the ambiguity of how to choose n for each individual layer. To prevent any kinds of potential selection biases, all ways of allocating the tested values of $n = 13, 26, 39$ to the individual layers/embedding spaces are shown in Figure 4.

For the case of completely suppressed relational information for the GNN architectures (**zero**) μ_{AUC} remains lowest and unaffected by the choice of k , as expected for a setup in which any information transfer through a GaphConv operation is deliberately suppressed. At the same time we generally observe that no superior choice of allocating n across layers can be pointed to, throughout all tested architecture configurations. Especially the gain of using a configuration with $n = (39, 39)$ for both hidden layers/GraphConv operations over a configuration with $n = (13, 13)$ within a given architecture appears marginal.

However, the increase in k consistently mitigates the previously observed, clearly inferior separation of signal from background, of the GNN compared to the corresponding DNN architectures, for randomly (**rnd**) and unweighted (**one**) relational information. The μ_{AUC} values of these groups of GNN models start to clearly supersede the μ_{AUC} values of the one-layered DNN models with unweighted relational information, labeled by **none** in Figure 3, even slightly taking the lead over the two-layered DNNs of the same kind, in terms of μ_{AUC} .

We note that all two-layered NN architectures without use of relational information still result in lower values of μ_{AUC} than all tested one-layered NN models that profit from the use of relational information, as presented in Figure 3. At the same time, they are subject to an increased spread $\Delta\mu_{AUC}$ compared to their one-layered counterparts, in most cases. In this sense, the wise choice of relational information outweighs the presumable advantage in expressiveness provided by $k = 2$, irrespective of the allocated values of n .

For the NN architectures including relational information, we observe no further, dramatic gains, with respect to their one-layered counterparts in μ_{AUC} , apart from a slight advantage of the GNN over the corresponding DNN architectures that seems to become more manifest. While this advantage is below the 1%-level it is

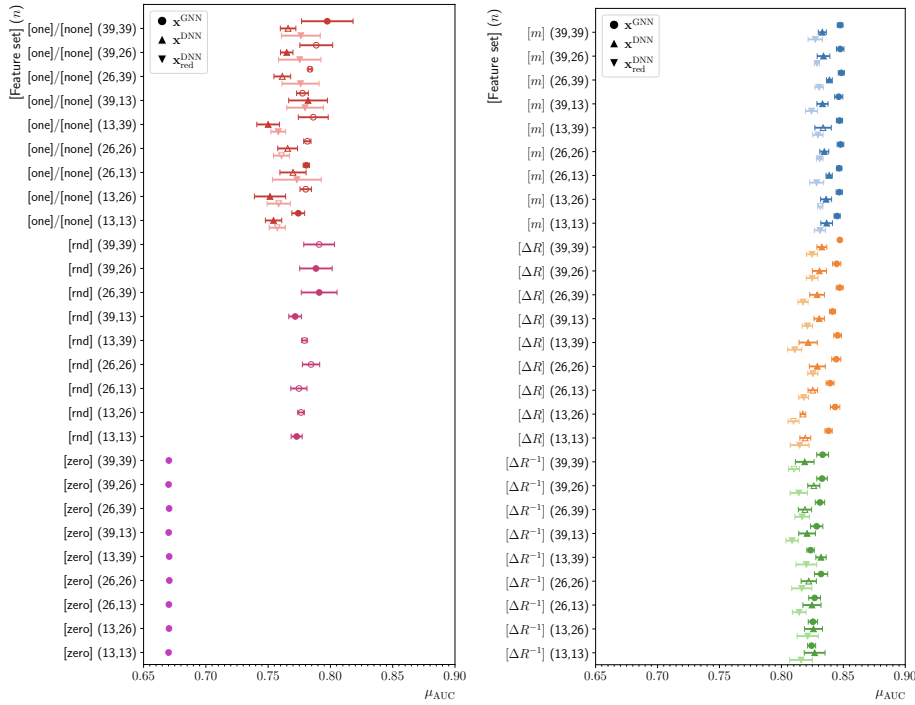


Fig. 4 Mean ROC-AUC μ_{AUC} as obtained for 54 different GNN and 72 corresponding DNN models with $k = 2$. The labels in brackets on the vertical axis indicate the use of relational information, as discussed in Section 3.2, the numbers in parentheses correspond to n . The circles refer to GNN and the upward (downward) pointing triangles to DNN models with a default (reduced) set of input features \mathbf{x}^{DNN} ($\mathbf{x}_{\text{red}}^{\text{DNN}}$), as discussed in Section 3.2. For better readability, markers of the same configuration are shifted vertically along the y-axis. The bars are obtained from the sample variance of an ensemble, as described in Section 2.4. NN architectures which belong to the same choices of varying parameters are spatially grouped and shown in the same color. Open markers indicate that significant outliers of the corresponding distribution of ROC-AUC values have been removed from the calculation of μ_{AUC} and its variance, as described in the text.

still significant compared to $\Delta\mu_{\text{AUC}}$. A summary of the achieved values of μ_{AUC} for the one- and two-layered GNN models is shown in Figure 5. An equivalent summary for the corresponding DNN models is shown in Figure 6.

From the study we conclude that the external information of the ω_{ij} seems to give slight advantages to the GNNs with $k = 2$. We note that two subsequent GraphConv operations indeed convey more information than a DNN model with two hidden layers. Viewing ΔR^{-1} , ΔR , and m as distance measures, the first GraphConv operation conveys information about the nearest neighborhood of each i . The second GraphConv operation conveys information about the nearest neighborhood of the nearest neighbors, which is not the same as in the case of the first operation. This information is indeed not primarily accessible to the DNN architectures, but it emerges from the definition of the GraphConv operation. Along this line, once again, we conclude that not the mixing of features across neighboring nodes i during the GraphConv operation, but the additional

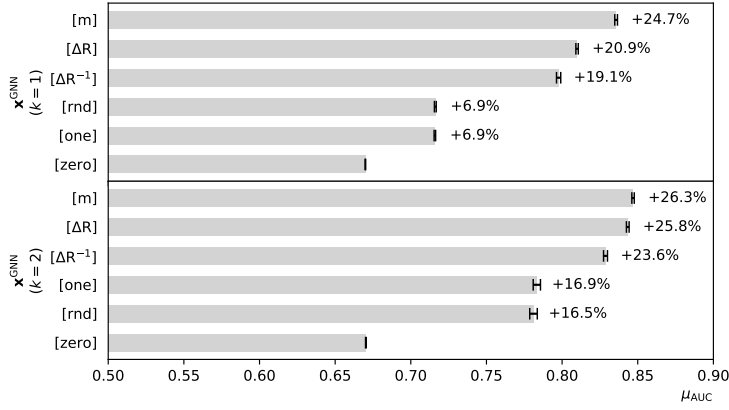


Fig. 5 Summary of the achieved values of μ_{AUC} for the GNN models with (upper half) one and (lower half) two GraphConv operations, with different use of relational information. For this summary, the associations of n with the highest values of μ_{AUC} in each group of GNN models have been used. The value of μ_{AUC} is displayed on the x -axis. Improvements relative to the least separating GNN with no relational information at all (zero) is given in numbers to the right of the bars. The use of relational information, as defined in Table 5, is indicated in brackets, on the y -axis.

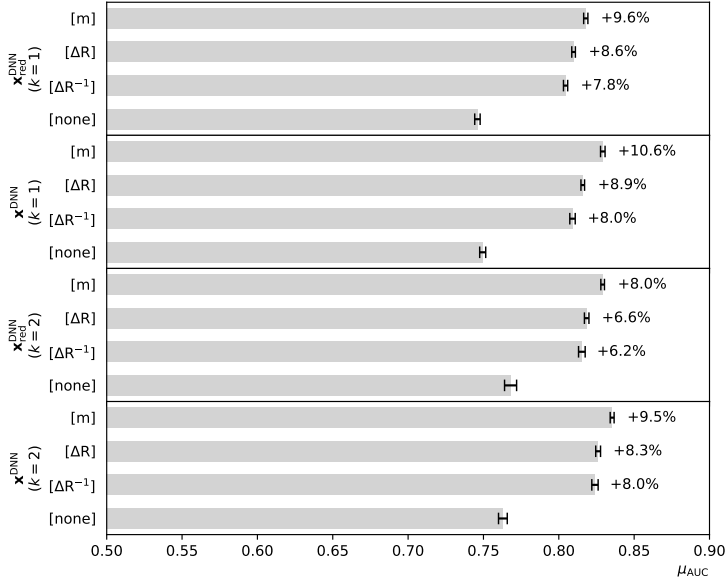


Fig. 6 Summary of the achieved values of μ_{AUC} for the DNN models with (upper half) one and (lower half) two hidden layers, with different use of relational information. For this summary, the associations of n with the highest values of μ_{AUC} in each group of DNN models have been used. The DNN configurations with \mathbf{x}^{DNN} and \mathbf{x}^{DNN}_{red} are shown separately. The values of μ_{AUC} are displayed on the x -axis. Improvements relative to the least separating DNN with no relational information (none) is given in numbers to the right of the bars. The use of relational information, as defined in Table 5, is indicated in brackets, on the y -axis.

(implicit) information accessible to the GNN through this operation is the source for the slight gain in μ_{AUC} . This interpretation is supported by the observation that an increase in n does not lead to any significant improvements in μ_{AUC} despite the increase in expressiveness of the models. This also explains why the GNN models with constant (one) or randomly associated (rnd) weights suffer in their performance: Through both ways of assigning weights across the nodes i the information about any kind of distance measure across nodes, in what ever space, is omitted.

A summary of the GNN and DNN configurations with the highest values of μ_{AUC} is given in Table 7.

4.2 Neural networks with comparable numbers of trainable parameters

As stated before, two principally different NN architectures lack comparability in the sense that it might be more natural to pick up certain information from the training sample through one or the other architecture. As long as it addresses an intrinsic property of one or the other architecture, such a difference is part of the benchmark comparison. If, on the other hand, such an inequality results from withholding primary information from one or the other architecture, or potentially inappropriate advantages in terms of expressiveness, an effort should be made to study and estimate the effect of it.

We have identified and noted such an inequality, in the beginning of Section 4, in terms of the number of TPs (N_{TP}), which turns out to be naturally higher for the DNN compared to the GNN architecture, due to the usually much larger input layer. We therefore complete our study by three additional setups, for which we drop the restrictions on the layered structure of the trained NN models in favor of comparable numbers of TPs.

As shown in Table 7, the GNN model with the highest value of μ_{AUC} (labelled as $\text{GNN}_{k=2}$) is based on $k = 2$ and $n = (26, 39)$, with $N_{\text{TP}}(\text{GNN}_{k=2}) = 2809$ and a value of $\mu_{\text{AUC}} = 0.8484 \pm 0.0008$. The DNN with the highest result of μ_{AUC}

Table 7 Summary of n , number of TPs (N_{TP}), and μ_{AUC} of the (upper part) GNN and (lower part) DNN models with the highest results in μ_{AUC} . For the DNN models a number of effective TPs $N_{\text{TP}}^{\text{eff}}$, as defined in the text, is also given in parentheses. Corresponding summaries are given for the cases of $k = 1$ and 2. In all cases m has been used as relational information between nodes/physics objects. Also shown are the configurations of three additional NN models discussed in Section 4.2: the GNN^\uparrow model with N_{TP} comparable within 1% with $N_{\text{TP}}(\text{DNN}_{k=2})$ and the DNN^\downarrow ($\text{DNN}_{\text{eff}}^\downarrow$) model with N_{TP} ($N_{\text{TP}}^{\text{eff}}$) comparable within 1% with $N_{\text{TP}}(\text{GNN}_{k=2})$.

NN arch.	n	N_{TP} ($N_{\text{TP}}^{\text{eff}}$)	μ_{AUC}	Label
GNN	(39)	1093	0.8387 ± 0.0006	$\text{GNN}_{k=1}$
	(26, 39)	2809	0.8484 ± 0.0008	$\text{GNN}_{k=2}$
	(29, 28, 29, 29)	5829	0.8546 ± 0.0006	GNN^\uparrow
DNN	(26)	5773 (4753)	0.8300 ± 0.0011	$\text{DNN}_{k=1}$
	(26, 39)	6839 (5819)	0.8388 ± 0.0007	$\text{DNN}_{k=2}$
	(13, 14, 14)	3294 (2784)	0.8400 ± 0.0006	$\text{DNN}_{\text{eff}}^\downarrow$
	(11, 10, 11, 11)	2816 (2385)	0.8386 ± 0.0007	DNN^\downarrow

(labelled as $\text{DNN}_{k=2}$) is based on the same configuration in terms of k and n , with $N_{\text{TP}}(\text{DNN}_{k=2}) = 6839$ and a value of $\mu_{\text{AUC}} = 0.8388 \pm 0.0007$. One may argue that for the DNN model, not the full set of TPs is really actively contributing to the solution of the task, since part of the input space is regularly filled with zeros, e.g., if fewer than eight jets are selected in an event. Therefore, we estimate, in addition to N_{TP} , a number of effective TPs ($N_{\text{TP}}^{\text{eff}}$) from the product of N_{TP} with the average number of nonzero input nodes in \mathbf{x}^{DNN} , evaluated on the training dataset. This results in a value of $N_{\text{TP}}^{\text{eff}}(\text{DNN}_{k=2}) = 5819$.

In a first approach we survey varying DNN structures with N_{TP} ($N_{\text{TP}}^{\text{eff}}$) comparable to $N_{\text{TP}}(\text{GNN}_{k=2})$. We do this based on the following algorithm: We allow $k \leq 4$ and any number of nodes per hidden layer (n). Of all DNN configurations for which $N_{\text{TP}}(\text{GNN}_{k=2})$ is matched by N_{TP} ($N_{\text{TP}}^{\text{eff}}$) within a margin of 1%, the model with the smallest spread of n across layers is selected. If no DNN configuration with N_{TP} ($N_{\text{TP}}^{\text{eff}}$) within a 1% margin of the target value can be found the closest possible model is chosen. This situation occurs only in models with one hidden layer.

This procedure ensures a homogeneous structure of hidden layers. As a result, e.g., a DNN configuration with $k = 4$ and $n = (11, 10, 11, 11)$, with $N_{\text{TP}} = 2816$, further on referred to as DNN^{\downarrow} , is preferred over a model with $k = 4$ and $n = (10, 8, 14, 24)$, even though the latter results in an exact match with $N_{\text{TP}}(\text{GNN}_{k=2})$. The DNN^{\downarrow} model achieves a value of $\mu_{\text{AUC}} = 0.8386 \pm 0.0007$. A second DNN configuration with $k = 3$ and $n = (13, 14, 14)$, with $N_{\text{TP}}^{\text{eff}} = 2784$ within the 1% margin of $N_{\text{TP}}(\text{GNN}_{k=2})$ is also considered and further on referred to as $\text{DNN}_{\text{eff}}^{\downarrow}$. This model achieves a value of $\mu_{\text{AUC}} = 0.8400 \pm 0.0006$. We observe that, although the DNN^{\downarrow} ($\text{DNN}_{\text{eff}}^{\downarrow}$) model uses only 41% (48%) of N_{TP} ($N_{\text{TP}}^{\text{eff}}$) of $\text{DNN}_{k=2}$, this does not result in any significant loss in separation power, after training.

In a second approach we survey varying GNN structures with N_{TP} comparable to $N_{\text{TP}}^{\text{eff}}(\text{DNN}_{k=2})$. For this purpose we exploit the same algorithm as described above, resulting in a GNN with $k = 4$ and $n = (29, 28, 29, 29)$ with $N_{\text{TP}} = 5829$, further on referred to as GNN^{\uparrow} . This model achieves a value of $\mu_{\text{AUC}} = 0.8546 \pm 0.0006$. It reveals the highest value of μ_{AUC} across all tested models. The difference in μ_{AUC} with respect to other NN configurations is only at the 1%-level, but it is still significant in terms of $\Delta\mu_{\text{AUC}}$.

From this finding we conclude that the GNN model with the same expressiveness as a maximally comparable DNN must have intrinsic advantages over the DNN model in extracting additional information from the given, large training sample. For the benchmark setup in use, this advantage is small but significant in the scope of the study. It emerges after external augmentation with an energy-weighted distance measure like m between the input objects/nodes, and more clearly manifests itself in the study for $k > 1$. We anticipate that this gain originates from the hierarchically structured information about nearest neighbors and the nearest neighborhood of nearest neighbors of node i , when viewing the edge weights ω_{ij} as a distance measure. This information is an intrinsic property of the GNN model and not easily accessible through the more simplistic DNN structure. An increase of TPs of the simpler DNN structure does not compensate for this informational advantage. In this interpretation the gain of GNN^{\uparrow} over all other configurations should mostly be attributed to the increase in k over the associa-

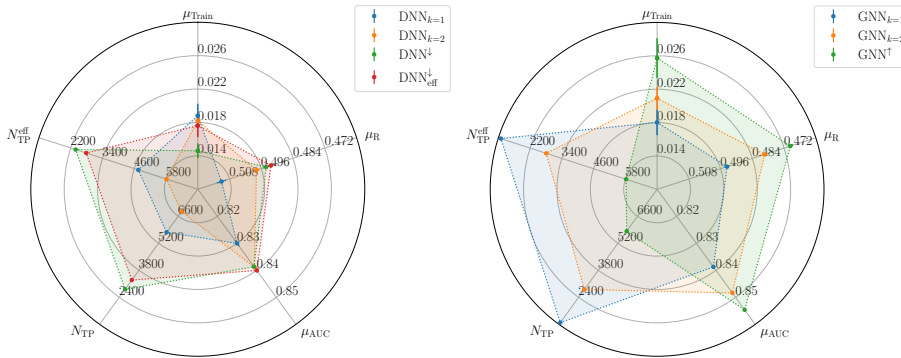


Fig. 7 Visualization of GNN and DNN models with the highest values in μ_{AUC} and $k = 1$ ($\text{GNN}_{k=1}$, $\text{DNN}_{k=1}$) and $k = 2$ ($\text{GNN}_{k=2}$, $\text{DNN}_{k=2}$). Also shown are the DNN models DNN^{\downarrow} and $\text{DNN}^{\downarrow}_{\text{eff}}$ with a comparable number of (effective) TPs as the $\text{GNN}_{k=2}$ model, and the GNN model GNN^{\uparrow} with a comparable number of effective TPs as the $\text{DNN}_{k=2}$ model. Five different metrics to evaluate the properties of an NN model are shown: N_{TP} ($N_{\text{TP}}^{\text{eff}}$), the mean convergence rate μ_{Train} , the mean empirical risk evaluated on the test sample μ_R , and μ_{AUC} . The spanned area in the figures indicates the capability of an NN model to fulfill the task.

tion of n per GraphConv operation. The parameter choices of the DNN^{\downarrow} , $\text{DNN}^{\downarrow}_{\text{eff}}$, and GNN^{\uparrow} models and correspondingly achieved values of μ_{AUC} are also given in Table 7.

4.3 Convergence behavior

In this study we have investigated the capacities of GNN and DNN models to fulfill their primary target, i.e., to provide the best possible solutions to the classification task defined in Section 2.3. We anticipate that, in particular in practical life, the properties of an NN architecture may be evaluated in other terms, viz. the mean of the training speed μ_{Train} , which we evaluate as the inverse of the epoch with the highest value of the ROC-AUC on the validation dataset and the mean of the empirical risk obtained from the test dataset μ_R , which we take as a measure of the generalization property of the given NN model under study. To conclude our studies we provide a visualization of these properties and all other properties of the NN models that have been discussed throughout the paper so far, in Figure 7. In Figure 7 (left) μ_{Train} , μ_R , μ_{AUC} , N_{TP} , and $N_{\text{TP}}^{\text{eff}}$ for the $\text{DNN}_{k=1}$, $\text{DNN}_{k=2}$, DNN^{\downarrow} , and $\text{DNN}^{\downarrow}_{\text{eff}}$ models are shown, on five independent axes. The axes are defined such that values closer to the common origin of the figure are disfavored. This is in particular true for N_{TP} , $N_{\text{TP}}^{\text{eff}}$, and μ_R , where the values are given in descending order when moving away from the origin. In this sense a larger size of the correspondingly colored area indicates the larger capability of a given NN model to adequately solve the presented task. In Figure 7 (right) the same quantities are shown for the $\text{GNN}_{k=1}$, $\text{GNN}_{k=2}$, and GNN^{\uparrow} models. The axes ranges are kept the same to ease comparison between both architectures.

In terms of μ_{Train} the DNN models usually fall behind their corresponding GNN counterparts. This finding, as well as the observation that the GNN models usually achieve a comparable or slightly larger value of μ_{AUC} , after training,

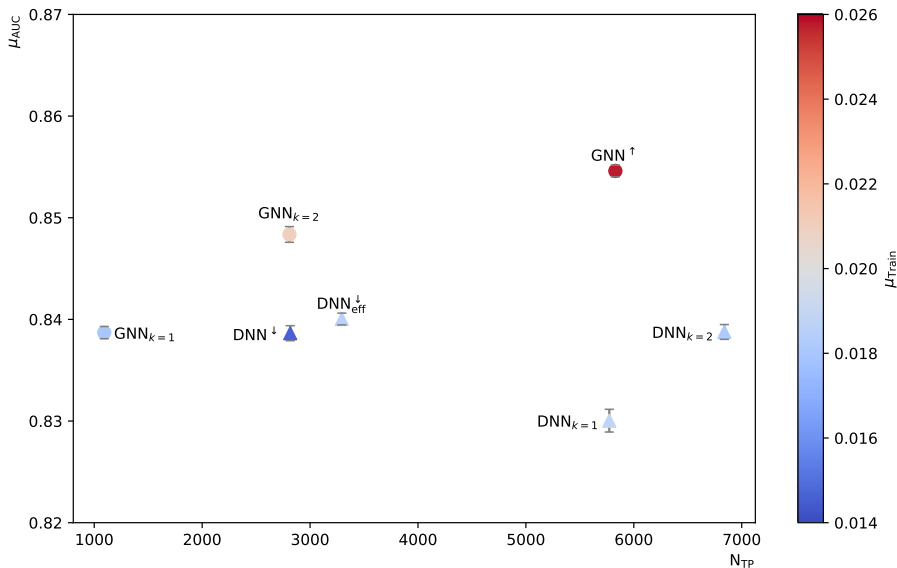


Fig. 8 Overview of the GNN and DNN models with $k = 1$ and 2 , and the highest achieved values of μ_{AUC} , as well as a GNN model with an increased number of TPs (GNN^\dagger) and a DNN model DNN^\dagger ($\text{DNN}_{\text{eff}}^\dagger$) with a restricted (effective) number of TPs. The GNN models are indicated by circles and the DNN models by triangles. The models are shown in a three-dimensional space built from μ_{AUC} , N_{TP} and μ_{Train} . The bars in μ_{AUC} are obtained from the sample variance of a training ensemble, as described in Section 2.4. The quantity μ_{Train} , indicated by the color code of the points corresponds to the inverse of the epoch with the highest value of the ROC-AUC on the validation dataset.

indicates the assumed effect of guiding the convergence by constraints, which are built-in to the GNN architecture. This property allows the GNN architecture not only to converge to a solution that is equally good or slightly better than the solution found by corresponding DNN architectures, but also to converge faster and typically with a smaller number of TPs. We note though that a clear correlation between μ_{Train} and N_{TP} ($N_{\text{TP}}^{\text{eff}}$) cannot be deduced from our study. We understand this situation such that a less expressive NN model, with fewer degrees of freedom for the minimization process, may well lead to a more pronounced landscape of the expected risk and thus reduced μ_{Train} . In addition we note that also μ_R for the DNN models falls behind, compared to their GNN counterparts. Here we observe the benefit of a regularizing effect of the built-in constraints, which correlates with reduced numbers of (effective) TPs. It is obvious that an NN model with more TPs reveals a higher vulnerability to specific properties of the training sample. A summary of all NN configurations that have been discussed in this section is shown in Figure 8.

5 Summary

With this paper we have made an effort to put the comparison of graph neural network (GNN) and equivalent fully-connected feed-forward neural network (DNN)

architectures on a maximally fair ground. Under the laboratory conditions of a high-energy physics process of interest, at the CERN LHC, we have controlled the definition of the task, choice of non-tunable (hyper-)parameters of the models, which are not subject to the training, and amount of information primarily presented to the neural network models, through their input feature vectors.

Within the scope of the study we have demonstrated clear evidence that the presumable advantage of the more complex GNN over an equivalent DNN structure does not originate from an uncontrolled mixture of features in the embedding space of the graph nodes, but from the extra relational information between nodes, that we have added based on domain-knowledge. Without this extra knowledge the GNN models fall behind equivalent DNN models in terms of their capability to separate signal from background. Neither are the GNN models superior in terms of their separation power to equivalent DNN models, as long as these are equipped with the same information in the input space.

Both, the built-in permutation invariance and the circumstance that the GNN architecture a priori is not bound to a fixed number of nodes might be viewed as advantages. They might also have positive influence on the convergence behavior of the training. On the other hand it cannot be deduced that either of these properties significantly contributes to an increase, e.g., in the power to separate a given signal from background. Any advantage of the GNN over the DNN architecture that we observed in our studies could be traced back to the access to more information, which, when given to the other architecture lead to the same performance also for the other architecture.

The real advantage of the GNN over the DNN structure emerges as soon as more than one GraphConv operations are applied, during which the GNN structure naturally accesses more relational information between nodes than a DNN has access to. In the configurations investigated in our study this gain is tied to the use of relational information that can be interpreted as a distance measure to define proximity between two nodes. Apart from that we observe significant advantages of the GNN over the DNN architecture in terms of convergence and generalizability that we attribute to a level of built-in implicit constraints to the GNN model resulting in a better ratio of accessible information over trainable parameters of the model. We anticipate that these advantages might be more pronounced the more hierarchical the training data are. We assume that this property is the basis for the success of GNN structures when applied to particle physics jets, which are highly hierarchical objects. In conclusion we expect the highest gain of a GNN over a DNN structure for tasks based on hierarchically structured data, ideally based a known distance measure.

ACKNOWLEDGEMENTS

This research was supported by the German Federal Ministry of Education and Research (BMBF) under grant 05H21VKCCB.

References

1. D. Aguillard, T. Albahri, et al. Measurement of the Positive Muon Anomalous Magnetic Moment to 0.20 ppm. *Phys. Rev. Lett.*, 131(16):161802, 2023.

2. N. Metropolis, A. Rosenbluth, et al. Equation of State Calculations by Fast Computing Machines. *The Journal of Chemical Physics*, 21(6):1087, 2004.
3. M. Rosenbluth. Genesis of the Monte Carlo Algorithm for Statistical Mechanics. *AIP Conference Proceedings*, 690(1):22, 2003.
4. G. Aad, E. Abat, et al. The ATLAS Experiment at the CERN Large Hadron Collider. *JINST*, 3:S08003, 2008.
5. S. Chatrchyan, G. Hmayakyan, et al. The CMS Experiment at the CERN LHC. *JINST*, 3:S08004, 2008.
6. G. Salam. Towards Jetography. *Eur.Phys.J.*, C67:637–686, 2010.
7. A. Sirunyan, A. Tumasyan, et al. Performance of missing transverse momentum reconstruction in proton-proton collisions at $\sqrt{s} = 13$ TeV using the CMS detector. *JINST*, 14(07):P07004, 2019.
8. R. Feynman. The theory of positrons. *Phys. Rev.*, 76:749–759, Sep 1949.
9. F. Scarselli, M. Gori, et al. The graph neural network model. *IEEE Transactions on Neural Networks*, 20(1):61–80, 2009.
10. A. Micheli. Neural network for graphs: A contextual constructive approach. *IEEE Transactions on Neural Networks*, 20(3):498–511, 2009.
11. T. Kipf and M. Welling. Semi-Supervised Classification with Graph Convolutional Networks. *arXiv e-prints*, page arXiv:1609.02907, September 2016.
12. W. Hamilton, R. Ying, et al. Inductive representation learning on large graphs. In *Proceedings of the 31st International Conference on Neural Information Processing Systems, NIPS’17*, page 1025–1035, Red Hook, NY, USA, 2017. Curran Associates Inc.
13. P. Veličković, G. Cucurull, et al. Graph Attention Networks. *International Conference on Learning Representations*, 2018.
14. J. Shlomi, P. Battaglia, et al. Graph Neural Networks in Particle Physics. 7 2020.
15. A. Sirunyan, A. Tumasyan, et al. Search for $t\bar{t}H$ production in the $H \rightarrow b\bar{b}$ decay channel with leptonic $t\bar{t}$ decays in proton-proton collisions at $\sqrt{s} = 13$ TeV. *JHEP*, 03:026, 2019.
16. R. Workman, V. Burkert, et al. Review of Particle Physics. *PTEP*, 2022:083C01, 2022.
17. A. Sirunyan, A. Tumasyan, et al. Identification of heavy-flavour jets with the CMS detector in pp collisions at 13 TeV. *JINST*, 13(05):P05011, 2018.
18. J. Alwall, R. Frederix, et al. The automated computation of tree-level and next-to-leading order differential cross sections, and their matching to parton shower simulations. *JHEP*, 07:079, 2014.
19. J. Alwall, M. Herquet, et al. MadGraph 5 : Going Beyond. *JHEP*, 06:128, 2011.
20. T. Sjöstrand, S. Ask, et al. An introduction to PYTHIA 8.2. *Comput. Phys. Commun.*, 191:159–177, 2015.
21. J. de Favereau, C. Delaere, et al. DELPHES 3, A modular framework for fast simulation of a generic collider experiment. *JHEP*, 02:057, 2014.
22. M. Cacciari, G. Salam, et al. The anti- k_t jet clustering algorithm. *JHEP*, 04:063, 2008.
23. M. Fey and J. Lenssen. Fast graph representation learning with pytorch geometric, 2019.
24. A. Paszke, S. Gross, et al. Pytorch: An imperative style, high-performance deep learning library, 2019.
25. D. Kingma and J. Ba. Adam: A Method for Stochastic Optimization. 12 2014.
26. C. Morris, M. Ritzert, et al. Weisfeiler and leman go neural: Higher-order graph neural networks. *Proceedings of the AAAI Conference on Artificial Intelligence*, 33(01):4602–4609, Jul. 2019.

A comparative study of flavour-sensitive observables in hadronic Higgs decays

Benjamin Campillo Avelaira^{a,1,2}, Aude Gehrman–De Ridder^{b,1,3},
Christian T Preuss^{c,1,4}

¹Institute for Theoretical Physics, ETH, 8093 Zürich, Switzerland

²Institute for Theoretical Physics, KIT, 76131 Karlsruhe, Germany

³Department of Physics, University of Zürich, 8057 Zürich, Switzerland

⁴Department of Physics, University of Wuppertal, 42119 Wuppertal, Germany

Received: date / Accepted: date

Abstract Jet production from hadronic Higgs decays at future lepton colliders will have significantly different phenomenological implications than jet production via off-shell photon and Z -boson decays, owing to the fact that Higgs bosons decay to both pairs of quarks and gluons. We compute observables involving flavoured jets in hadronic Higgs decays to three partons at Born level including next-to-leading order corrections in QCD (i.e. up to $\mathcal{O}(\alpha_s^2)$). The calculation is performed in the framework of an effective theory in which the Higgs boson couples directly to gluons and massless b -quarks retaining a non-vanishing Yukawa coupling. For the following flavour sensitive observables: the energy of the leading and subleading flavoured jet, the angular separation and the invariant mass of the leading $b\bar{b}$ pair, we contrast the results obtained in both Higgs decay categories and using either of the infrared-safe flavoured jet algorithms flavour- k_T and flavour-dressing.

Keywords flavoured jets · hadronic Higgs decays · NLO QCD

1 Introduction

Precision studies of the Higgs boson discovered at LHC by CMS and ATLAS [1,2] will become possible at future lepton colliders such as [3,4], all aiming to operate as Higgs factories. In this clean experimental environment, where interactions take place at well-defined centre-of mass energies, it is expected to enable model-independent measurements of the Higgs couplings to

gauge bosons and fermions at the level of a few percent. At these future lepton colliders, in particular it will become possible to have access to so-far unobserved hadronic decay channels such as Higgs decays to gluons. The latter is currently inaccessible in hadron-collider environments due to the presence of overwhelming QCD backgrounds. Only the $H \rightarrow b\bar{b}$ decay was observed to date [5,6] in associated vector-boson production where the leptonic decay signature of the vector boson helps to identify the $H \rightarrow b\bar{b}$ decay.

Hadronic Higgs decays to at least two final state hard partons proceed via two main decay modes; either as Yukawa-induced decay to a bottom-quark pair, $H \rightarrow b\bar{b}$, or as a heavy-quark-loop induced decay to two gluons, $H \rightarrow gg$. In the latter category, observables are computed in the framework of an effective field theory, in which the top-quark loop is integrated out into an effective point-like Hgg vertex.

So far these two categories of Higgs decay processes have been considered together in the computation of flavour-agnostic event-shape observables, i.e., for three-jet-like final states in [7,8,9,10,11] and for four jet-like final states in [12]. It was also recently suggested to determine branching ratios in hadronic Higgs decays via fractional energy correlators [13]. Flavour-sensitive jet observables related to the presence of a flavoured jet in the final state have so far been computed for the following LHC processes: VH production, with $H \rightarrow b\bar{b}$ or $Z + b$ -jet and $Z/W + c$ -jet, with the vector boson decaying leptonically in all cases. More precisely, parton-level predictions including up to NNLO QCD corrections using massless charm or bottom quarks at the origin of the flavoured jet have been computed most re-

^ae-mail: benjamin.campillo@kit.edu

^be-mail: gehra@phys.ethz.ch

^ce-mail: preuss@uni-wuppertal.de

cently for VH in [14,15,16,17], and for $Z/W + c/b$ in [18,19,20,21,22,23].

In a lepton collider environment, flavour-sensitive jet observables associated to Z decays have been lately considered in [24,25] while colour-sensitive observables have been used to disentangle bottom quarks stemming from Higgs decays against those stemming from QCD background in [26].

All of these computations employ an infrared-safe procedure to define flavoured jets from massless partons. The latter procedure requires the use of an infrared-safe recombination algorithm to cluster flavourless and flavoured partons into final states including well-defined flavoured jets. Up to very recently, only the flavour- k_T algorithm [27] was used in theoretical computations at hadron colliders. Lately, a number of flavour-sensitive jet algorithms have been designed [24,25,28,29], with increased interest in providing modified versions of the anti- k_T algorithm [24,25,29], to improve the data versus theory comparisons at LHC.

All of these algorithms share the principle that, at least up to a certain order in the strong coupling, they can be proven to be infrared flavour safe, i.e., that the flavour assignment of a given jet is not spoiled by the emission of unresolved (soft or collinear) massless partons. A detailed comparison of currently available algorithms has been presented in [25].

In this paper, we compute a range of flavour-sensitive three-jet like observables in hadronic Higgs decays, including NLO QCD corrections for both decay categories, i.e related to $H \rightarrow b\bar{b}$ and $H \rightarrow gg$, as alluded to above. To define flavour-sensitive observables we employ the flavour- k_T algorithm [27] and the flavour-dressing algorithm [24] which can both be applied in a lepton collider environment.

The study is organised as follows: In section 2 we give a brief overview of the definition of flavoured jets using either of the two infrared flavour-safe jet algorithms before describing our computational setup in section 3. In section 4, in a first part presented in section 4.2 we compute the so-called “misidentified cross section” to check the correctness of our implementation using both infrared-safe and flavour-safe jet algorithms. In the second part of section 4, i.e., in section 4.3, we present theoretical predictions up to second order in QCD for four different flavour-sensitive observables related to both Higgs-decay categories and compare the results using both flavour-safe jet algorithms. We conclude and give an outlook on future work in section 5.

2 Flavoured jets

In experimental analyses as well as theoretical calculations, final-state particle configurations are often described by so-called jets. While the definition of jets is fixed by the choice of a sequential recombination algorithm known as a jet algorithm, the association of the jet with a given parton (or hadron) flavour is a more complicated endeavour. Naïvely, it may be tempting to define the jet flavour as the sum of the constituent flavours of each jet, i.e,

$$\text{Jet flavour} = f - \bar{f}, \quad (1)$$

where f is the number of particles with a given a flavour and \bar{f} is the number of particles with the corresponding anti-flavour. However, this naïve approach violates an important property known as infrared flavour safety [27], which describes whether an algorithm respects physically meaningful flavour assignments when one or more particles become unresolved. The problem is that jet algorithms may in general cluster the flavoured daughters of a soft wide-angle gluon splitting $g \rightarrow q\bar{q}$ into different jets, changing their flavour association. In effect, the flavours of the two jets, and therefore any flavour-dependent observables, become explicitly dependent on the presence of a pair of unresolved particles, in violation of infrared safety. It is thus mandatory for a jet-flavour definition to respect infrared flavour safety, meaning that the presence of a pair of unresolved flavoured particles to an event must not change the flavours of the jets.

As mentioned in the introduction, several approaches to infrared-safe flavoured jet algorithms have been explored [24,25,27,28,29], of which only the flavour- k_T [27] and the flavour-dressing algorithm [24] explicitly describe an implementation compatible with the use of the Durham (k_T) algorithm. In the present study we therefore limit the discussion to these two flavoured jet algorithms, which we briefly describe below.

The flavour- k_T algorithm [27] achieves infrared flavour safety by modifying the Durham distance measure valid for all unflavoured partons (i, j) [30] into two cases defined depending whether the softer particles to be clustered are flavoured or not. In the flavour- k_T algorithm, the distance measure is given by:

$$y_{ij}^F = \frac{2(1 - \cos \theta_{ij})}{E_{\text{tot}}^2} \min(E_i, E_j)^{2-\alpha} \max(E_i, E_j)^\alpha \quad (2)$$

if the softer of i, j is flavoured. Instead the regular Durham distance given by,

$$y_{ij}^F = \frac{2(1 - \cos \theta_{ij})}{E_{\text{tot}}^2} \min(E_i, E_j)^2, \quad (3)$$

is kept if the softer of i, j is flavourless. Here, $\alpha \in (0, 2]$ is an arbitrary parameter. In this study, the value $\alpha = 2$ is chosen everywhere. The distance measure in eq. (2) ensures that soft pairs of flavoured particles are recombined first and thus avoids the previously discussed infrared-safety problem present in the standard (flavour-agnostic) Durham (k_T) algorithm. The main draw-back to the use of this algorithm is that it requires the flavour information of all particles, thus making it difficult to use in experimental analyses. Indeed, so far, it has not been used in measurements of flavour-sensitive jet observables.

The flavour-dressing algorithm [24] on the other hand does not change the underlying jet algorithm but instead alters the way flavours are assigned to jets. Instead of using the naïve jet-flavour definition, a more complex definition is invoked which ensures infrared flavour safety of the jet algorithm at hand. The basic idea is to first cluster an event into jets using a flavour-agnostic jet algorithm of choice, and, in a second step, cluster flavoured objects into so-called flavour clusters using a technique akin to soft-drop grooming [31]. In the final, “association” step the flavour clusters of step two are assigned to the jets of step one. A striking and important feature of the flavour-dressing algorithm is that it is equally applicable to theoretical calculations (and full particle-level simulations) as to experimental analyses, as discussed in [24]. It can in particular be used together with the anti- k_T algorithm, mostly used in experimental analyses at LHC but also in combination with the Durham k_T algorithm as explored in this paper.

3 Computational setup

We perform the computation of flavoured observables related to hadronic Higgs decays using the parton-level Monte-Carlo generator EERAD3 [32, 33], which was originally developed to compute NNLO QCD corrections to event-shape observables in hadronic Z -decays. This generator was recently extended to compute event shapes related to hadronic Higgs decays with three- and four-jet configurations at Born level in [7, 12]. In both cases, the antenna subtraction method is used to regulate infrared divergences related to real radiation contributions.

The hadronic Higgs-decay observables are computed in the framework of an effective theory including two Higgs decay categories. In the first category, the Higgs boson couples directly to gluons via an effective Higgs-gluon-gluon vertex and in the other, Standard-Model-like category, the Higgs boson decays into a massless b -quark pair retaining a non-vanishing Yukawa coupling

[7, 12]. This can be recasted into the following effective Lagrangian

$$\mathcal{L}_{\text{Higgs}} = -\frac{\lambda(M_t, \mu_R)}{4} H G_{\mu\nu}^a G^{a, \mu\nu} + \frac{y_b(\mu_R)}{\sqrt{2}} H \bar{\psi}_b \psi_b. \quad (4)$$

In this context, the effective Higgs-gluon-gluon coupling is given in terms of the Higgs vacuum expectation value v by

$$\lambda(M_t, \mu_R) = -\frac{\alpha_s(\mu_R) C(M_t, \mu_R)}{3\pi v} \quad (5)$$

and the $Hb\bar{b}$ Yukawa coupling reads

$$y_b(\mu_R) = \bar{m}_b(\mu_R) \frac{4\pi\alpha}{\sqrt{2}M_W \sin\theta_W}. \quad (6)$$

Both λ and y_b are subject to renormalisation, which we perform at scale μ_R in the $\overline{\text{MS}}$ scheme using $N_F = 5$. The top-quark Wilson coefficient is evaluated at first order in α_s using the results of [34, 35, 36, 37, 38, 39, 40], and the running of the Yukawa mass \bar{m}_b is performed using the results of [41].

It is important to highlight that the terms in eq. (4) do not interfere under the assumption of kinematically massless quarks. In particular, they do not mix under renormalisation [9]. This allows to define two separate Higgs-decay categories and to compute higher-order corrections independently for each. Throughout, we therefore consider predictions for the $H \rightarrow b\bar{b}$ and $H \rightarrow gg$ categories separately. All partonic contributions yielding three hard partons in the final state at Born level and needed for the computation presented in this paper, have been presented in detail for both categories up to $\mathcal{O}(\alpha_s^2)$ in [7]. In particular, it is worth mentioning that the Born-level partonic processes contributing at $\mathcal{O}(\alpha_s)$ are: $H \rightarrow b\bar{b}g$ in the $H \rightarrow b\bar{b}$ category and $H \rightarrow ggg$, $H \rightarrow gq\bar{q}$ in the $H \rightarrow gg$ category. In the latter case, q stands for any quark with specific flavour, including the bottom quark.

For any infrared-safe observables O , the parton-level generator EERAD3 calculates the LO coefficient \bar{A} and the NLO coefficient \bar{B} in a perturbative expansion of the differential decay width,

$$\frac{1}{\Gamma_{2j}^{(n)}(\mu_R)} \frac{d\Gamma}{dO} = \left(\frac{\alpha_s(\mu_R^2)}{2\pi} \right) \frac{d\bar{A}}{dO} + \left(\frac{\alpha_s(\mu_R^2)}{2\pi} \right)^2 \left(\frac{d\bar{B}}{dO} + \beta_0 \log \left(\frac{\mu_R^2}{M^2} \right) \frac{d\bar{A}}{dO} \right). \quad (7)$$

Here, $\Gamma_{2j}^{(n)}$ is the partial two-body decay width to order n ; specifically, $n = 0$ at LO and $n = 1$ at NLO.

In eq. (7), the LO coefficient \bar{A} involves only an integration over the three-particle phase space, while the NLO contribution \bar{B} involves an integration over the

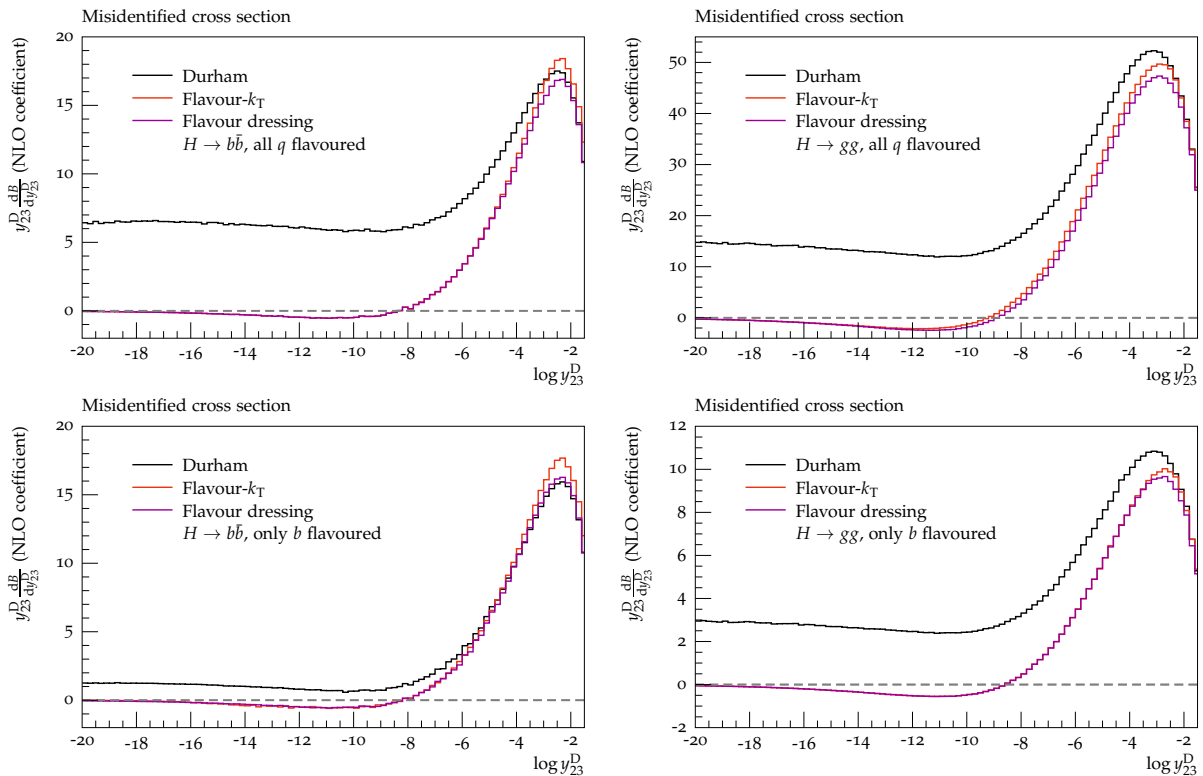


Fig. 1 Misidentified cross section in the $H \rightarrow b\bar{b}$ (left) and $H \rightarrow gg$ (right) category, considering all quarks as flavoured (top row) and only b -quarks as flavoured (bottom row). Both flavour- k_T and flavour dressing use $\alpha = 2$, as defined in the text.

four-particle phase space related to the real-radiation contribution and real subtraction terms, and an integration over the three-particle phase space, pertaining to one-loop contributions and virtual subtraction terms. Within this study, we employ the antenna subtraction scheme to construct real and virtual subtraction terms. Explicit expressions for the perturbative coefficients \bar{A} and \bar{B} can be found in [7].

In order to compute flavour-sensitive observables related to hadronic Higgs decays, as in this paper, on top of the ingredients needed to compute flavour-agnostic observables as described above, a new flavour layer needs to be implemented in the parton-level event generator EERAD3. This parton-level flavour-tracking procedure implemented here in EERAD3 for the first time can be summarized as follows: For each momentum configuration all contributing flavour configurations are generated and matrix elements as well as subtraction terms are evaluated separately for each flavoured parton configuration. In particular, this means that the calculation is split into different flavour contributions across all layers in eq. (7). Because the subtraction terms involve mapped configurations in which one parton is clustered into a “reduced” particle configuration, this has the consequence that the subtraction scheme is only viable if a flavour-safe jet algorithm is used. For each

flavour configuration, the flavour layer then acts as an additional input to the jet algorithm and parton-level contributions needed to be considered for the evaluation of the observables.

To conclude this section, we wish to define the theoretical framework in which our predictions are valid and numerically stable. Fixed-order calculations are accurate only in phase-space regions in which hard, well-separated jets dominate. We therefore devise a resolution cut, y_{cut} on the (flavoured) jet algorithm and define three-jet states to have three particles with $\min_{i,j}(y_{ij}) \geq y_{\text{cut}}$, where y_{ij} denotes the distance measure of the respective jet algorithm. Similarly, four-jet states are defined to have four particles with $\min_{i,j}(y_{ij}) \geq y_{\text{cut}}$. Furthermore, to avoid large numerical cancellations between the real contribution and the corresponding real subtraction term in unresolved phase-space regions, we implement a technical cut-off of $y_0 = 10^{-8}$ on the smallest dimensionless two-particle invariant $y_{ij} = 2p_i p_j / s$ in real configurations. We have verified that our predictions are independent of the choice of this theoretical cut-off.

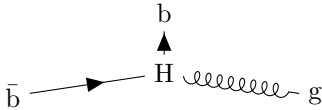


Fig. 2 Momentum-space diagram in the Higgs rest frame of a $H \rightarrow b\bar{b}g$ decay in which flavour- k_T allows for an arbitrarily soft b -quark.

4 Results

We here focus on presenting theoretical predictions for the following flavour-sensitive observables: the energy of the leading and subleading flavoured jet, the angular separation and invariant mass of the leading $b\bar{b}$ pair. We shall present results obtained in both Higgs-decay categories and using either of the infrared-safe flavoured jet algorithms flavour- k_T and flavour-dressing. After presenting the numerical set-up in section 4.1 we divide the discussion of our results into two subsections. In section 4.2 we validate the infrared flavour safety of the flavour- k_T and flavour-dressing algorithms before presenting and comparing our predictions for flavour-sensitive observables in section 4.3.

4.1 Numerical set-up and scale-variation prescription

We consider on-shell Higgs decays with $M_H = 125 \text{ GeV}$ and calculate all observables in the resonance centre-of-mass frame. We use $\alpha_s(M_Z) = 0.1179$ with either one- or two-loop running at LO and NLO, respectively. Electroweak quantities are considered constant and we use the G_μ -scheme with

$$\begin{aligned} G_F &= 1.20495 \times 10^{-5} \text{ GeV}^{-2}, \\ M_Z &= 91.1876 \text{ GeV}, \\ M_W &= 80.385 \text{ GeV}, \end{aligned} \quad (8)$$

corresponding to $\alpha = \frac{1}{128}$. To estimate theoretical uncertainties from missing higher-order corrections in our calculation, we vary the renormalisation scale around the Higgs mass, i.e., consider $\mu_R = k_\mu M_H$ with $0.5 \leq k_\mu \leq 2$.

4.2 Infrared flavour safety

To guarantee infrared flavour safety for flavour-sensitive observables, the jet algorithms that are employed in the computation need to correctly assign flavours to jets in the deep infrared region. Correct flavour assignment is determined by the underlying two parton process, i.e., by either two flavourless jets in the $H \rightarrow gg$ category

or by one flavoured and one anti-flavoured jet in the $H \rightarrow b\bar{b}$ category.

The study of infrared-flavour safety was first conducted for hadronic Z -decays in [27], in which it was highlighted that the Durham algorithm violates infrared flavour safety and a flavour-safe modification in terms of the flavour- k_T algorithm was suggested. As a measure of infrared flavour safety, the so-called misidentified cross section was defined in terms of the three-jet resolution variable y_{23} . The latter variable, measures the departure from two-jet-like into three-jet-like topologies.

In [24] the same criterion was used to validate the infrared flavour safety of the flavour-dressing algorithm. As a validation of our implementation, we thus apply the same criterion but here for hadronic Higgs decays. In this case, the misidentified cross section collects two-jet like events for which the flavour does not correspond to the flavour of the original two parton like topology in either of the Higgs categories. In fig. 1, we present the NLO coefficient \bar{B} differential in the Durham resolution y_{23}^D using jet definitions according to the plain Durham, flavour- k_T , and flavour-dressing algorithm. We employ two different flavour definitions; in the top row all quarks are counted as flavoured, in line with the definitions used in [24,27], while in the bottom row only b -quarks are treated as flavoured with all other quarks being flavourless. The former (in $H \rightarrow b\bar{b}$) can be used as a fundamental cross-check of our implementation with the original papers [24,27], whereas the latter is the flavour definition used in the remainder of this paper, since it allows for a straightforward experimental adaption in terms of b -tagging, see e.g. [42,43,44]. In fig. 1, to probe the deep infrared region, we have used the value of the theoretical cut y_0 to be 10^{-13} .

For an infrared-safe flavour jet algorithm, one expects the probability for flavour misidentification to vanish as the variable y_{23} tends to zero. In both Higgs-decay categories and regardless of the flavour-definition, in fig. 1 it is clearly visible that the Durham algorithm has a non-zero probability for an incorrect flavour assignment in the deep infrared region, whereas both the flavour- k_T and flavour-dressing algorithm yield a vanishing cross section for misidentified events. Confirming the findings in [24,27], both the flavour- k_T and flavour-dressing algorithms provide infrared-safe flavour jet definitions in hadronic Higgs decays, whereas the flavour-agnostic Durham algorithm does not. Thus, we shall present predictions only using these two jet algorithms in the remainder of this section.

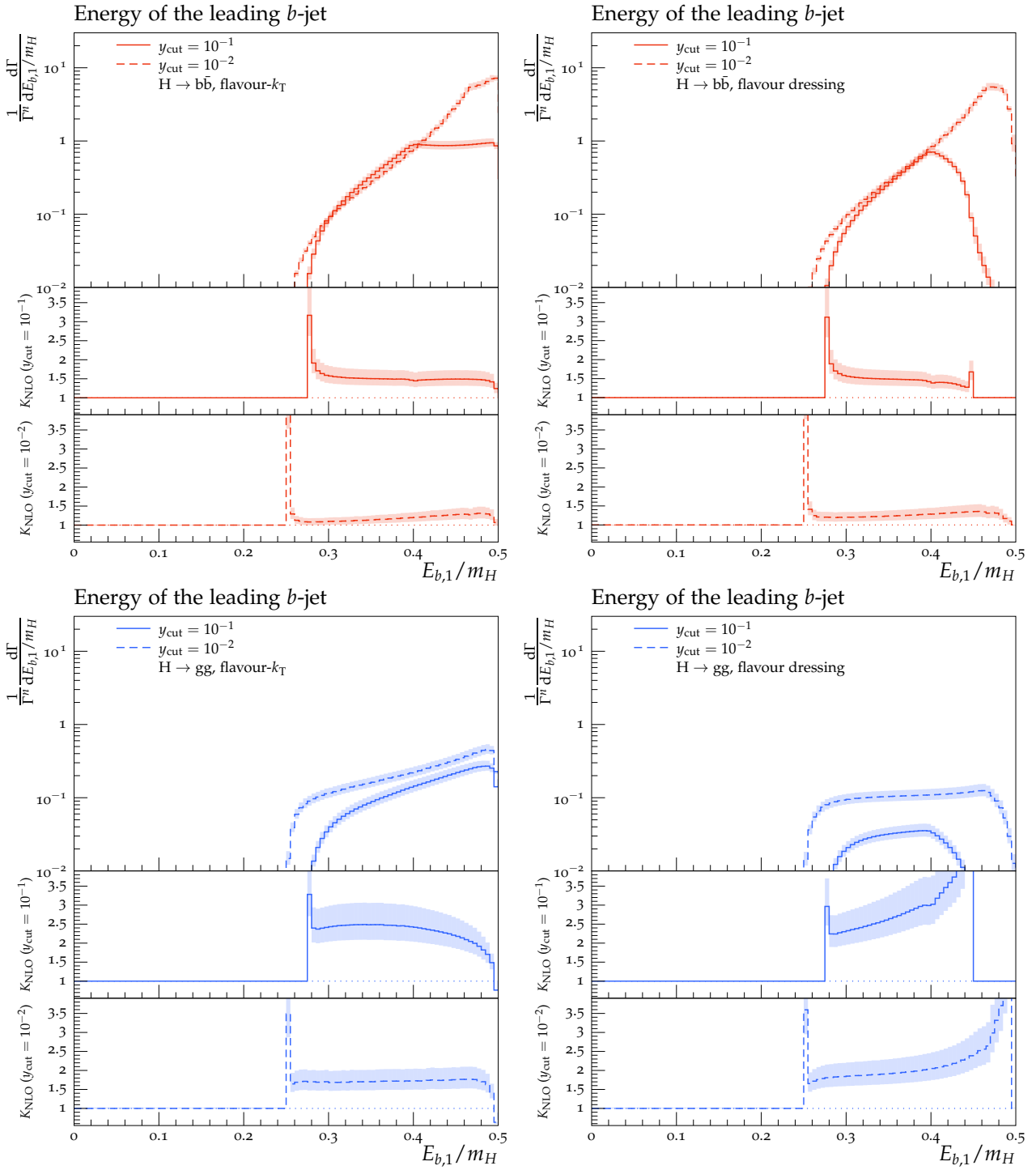


Fig. 3 Energy of the leading b -jet in the $H \rightarrow b\bar{b}$ (top row) and $H \rightarrow gg$ (bottom row) decay category using the flavour- k_T (left column) and flavour dressing (right column) algorithm.

4.3 Flavour-sensitive observables

We consider flavour-sensitive observables in both Higgs decay categories yielding three-jet-like configurations at Born level. For a given experimental resolution parameter y_{cut} and for each pair of final state partons i, j (quark or gluon), present in the partonic subprocesses at leading and next-to-leading order, we impose that $\min_{i,j}(y_{ij}) \geq y_{\text{cut}}$ in the respective flavoured jet algorithm. We then calculate NLO QCD, i.e. ($\mathcal{O}(\alpha_s^2)$), predictions for the following observables

- (a) the energy of the leading flavoured jet, $E_{b,1}$;
- (b) the energy of the subleading flavoured jet, $E_{b,2}$;
- (c) the angular separation of the leading b - and \bar{b} -jet, $\cos \theta_{b\bar{b}}$;
- (d) the invariant mass of the leading b - and \bar{b} -jet, $m_{b\bar{b}}$.

Except for the angular separation, we only consider scaled observables, normalised to the Higgs mass m_H . In all cases, we choose $\alpha = 2$ in the flavour- k_T and flavour-dressing algorithm and consider only b -quarks (\bar{b} -quarks) as flavoured (anti-flavoured).

Theoretical predictions for the four flavour-sensitive observables defined above are shown in figs. 3 to 6 for two different jet-algorithm resolution parameter, $y_{\text{cut}} = 0.1$ (solid lines) and $y_{\text{cut}} = 0.01$ (dashed lines). In all figures, predictions in the $H \rightarrow b\bar{b}$ category are shown in the top row in red, while predictions for the $H \rightarrow gg$ category are shown in the bottom row in blue. Similarly, we show results using the flavour- k_T algorithm in the left-hand column and results using the flavour-dressing algorithm in the right-hand column. Each plot consists of two panels, with the upper panel showing the NLO distributions and the lower panels showing the differential K -factor NLO/LO for the two values of the jet-algorithm resolution parameter y_{cut} .

Scale variations are included by a lighter shaded band around the central predictions.

Generally, we observe larger rates in the $H \rightarrow b\bar{b}$ decay, owing to the fact that events in this category always contain at least one $b\bar{b}$ pair, whereas most events in $H \rightarrow gg$ decays contain only unflavoured partons. We find larger NLO K -factors in the $H \rightarrow gg$ decay category, owing to the fact that our calculation employs the HEFT coupling between the Higgs and gluons, making it susceptible to large corrections. This is also reflected in the larger uncertainty band in predictions in the $H \rightarrow gg$ decay category. In both Higgs decay categories, the magnitude of the NLO corrections is comparable between the flavour- k_T and flavour-dressing algorithms, with somewhat larger corrections visible in the latter. It can be seen that predictions calculated with larger values of y_{cut} generally also receive larger NLO corrections. In all cases, lowering y_{cut} leads to wider

distributions, owing to the larger kinematically allowed phase space.

Before moving on to discussing features specific to the individual observables, we wish to highlight a peculiar behaviour of the flavour- k_T algorithm that results in some interesting phenomenology. For all observables shown here, distributions in the flavour- k_T algorithm span a significantly larger value range than predictions employing the flavour-dressing algorithm. Although it might appear as if the flavour- k_T algorithm allows to probe phase-space regions with infrared sensitive configurations, this is not the case. The reason for the large allowed value range can be found in the definition of the modified distance measure of the flavour- k_T algorithm, eq. (2), which takes the maximum whenever the softer of the two partons is flavoured. In three-parton configurations $b\bar{b}g$ which contain a soft b -quark (or \bar{b} -quark), $E_b \ll E_g, E_{\bar{b}}$, cf. fig. 2, all distances involving this quark involve the maximum of the energies, $y_{bj} \propto \max(E_b, E_j)$. As no singularity is associated with a single (anti-)quark becoming soft, this definition allows for arbitrarily small (anti-)quark energies, in principle below the order of the cut-off y_{cut} , while still retaining $\min_{i,j}(y_{ij}) > y_{\text{cut}}$. In other words, the flavour- k_T algorithm counts three-particle configuration with a single arbitrarily soft quark as three-jet configurations, in contrast to the naïve expectation that a soft particle, regardless of its flavour, does not constitute a jet. We shall explore the consequence of this peculiar behaviour of the application of the flavour- k_T algorithm in analysing thoroughly the shape and normalisation of the distributions presented below.

The energy of the leading flavoured jet, $E_{b,1}$:

Figure 3 shows the energy of the leading flavoured jet. In both decay categories and for both choices of the experimental resolution parameter y_{cut} , we observe similar results in the distributions using the flavour- k_T and flavour-dressing algorithm at lower energies. Towards the kinematical limit on the right-hand side of the plots, however, we find substantial differences between the two jet algorithms: The flavour-dressing algorithm assigns a vanishing probability to configurations with $E_{b,1} \approx m_H/2$, whereas such configurations have a non-zero probability in the flavour- k_T algorithm. This is related to the treatment of three-particle configurations containing a single soft quark in the flavour- k_T algorithm.

For the $H \rightarrow b\bar{b}$ category we find the following K -factors for the two y_{cut} values: With a y_{cut} value of 0.1 we find K -factors around 1.4 – 1.9 for flavour- k_T and 1.3 to 1.9 for flavour-dressing.

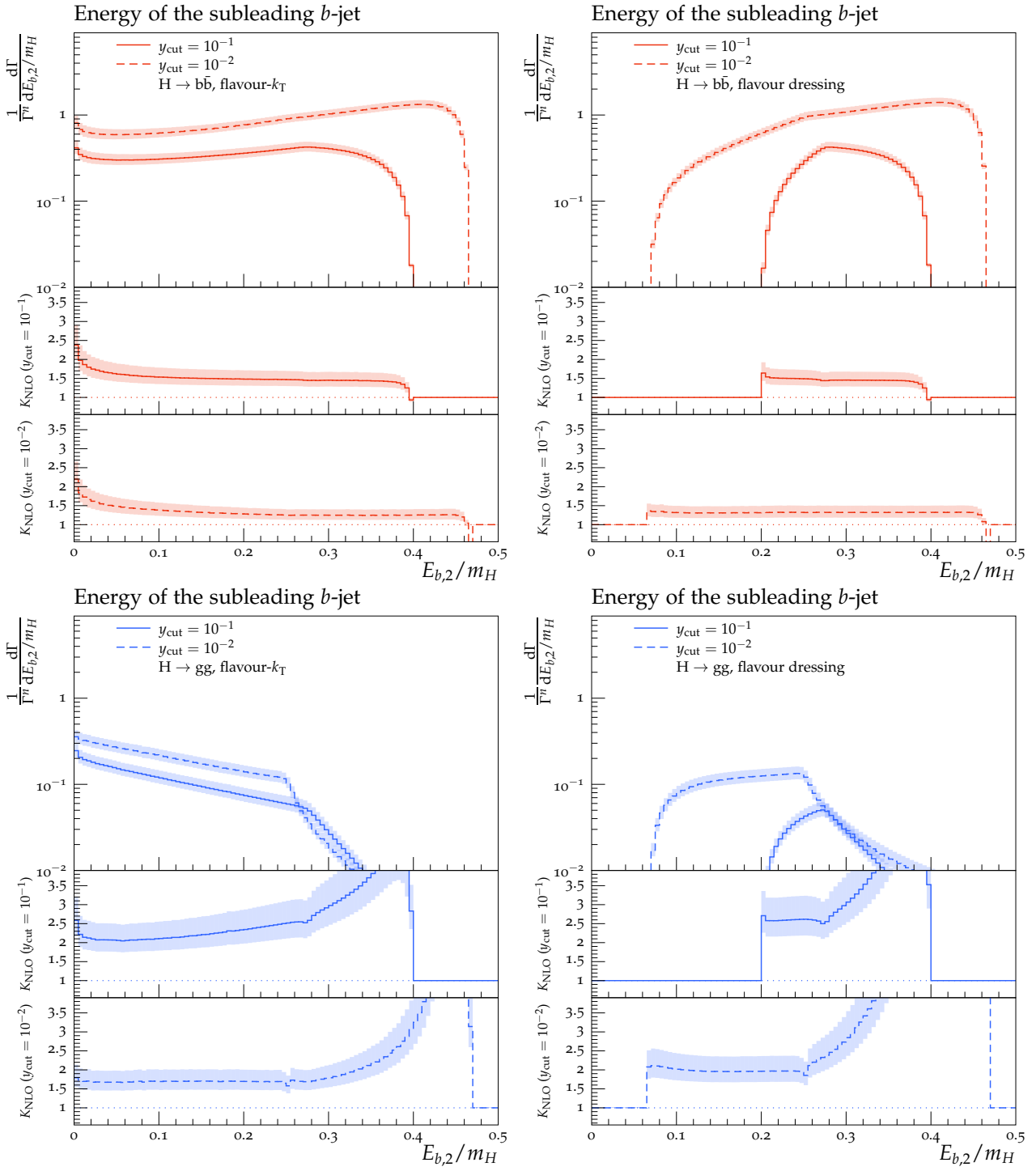


Fig. 4 Energy of the subleading b -jet in the $H \rightarrow b\bar{b}$ (top row) and $H \rightarrow gg$ (bottom row) decay category using the flavour- k_T (left column) and flavour dressing (right column) algorithm.

For $y_{\text{cut}} = 0.01$, we find K -factors ranging from 1.1 (1.2) to 1.3 (1.3) for flavour- k_T (flavour-dressing). In the $H \rightarrow gg$ category, we find higher NLO corrections, which are also reflected in the K -factors. For flavour- k_T and a y_{cut} of 0.1, we find K -factors from 1.5 to 2.5, where we start on the left side with a small increase from 2.4 up to 2.5 at an energy of $E_{b,1}/m_H = 0.34$, followed by a decrease to 1.5 for higher energies. The K -factors are more constant for a y_{cut} value of 0.01, varying around 1.4–1.7. Flavour-dressing with a y_{cut} of 0.1 starts with K -factors of around 2.2 and then rapidly increases. A similar behaviour is observed for a y_{cut} value of 0.01, where we start at 1.7 and then diverge again. Flavour- k_T does not have these diverging NLO corrections, because of the previously discussed three-particle configurations containing a single soft quark. Analysing the situation regarding the size of the QCD corrections observed with both algorithms further, the following can be said: Already at LO, flavour- k_T allows one quark to have large energies (and thus the other quark has almost no energy), whereas flavour-dressing does not allow for such configurations. Only at NLO, flavoured jets are allowed to have large energies in flavour dressing, and thus the K -factors receive large contributions there.

The energy of the subleading flavoured jet, $E_{b,2}$:
The distribution of the energy of the subleading flavoured jet, shown in fig. 4 can be explained by a similar reasoning as before for the leading flavoured jet distribution. Due to the peculiar behaviour for pathological $b\bar{b}g$ configurations, the flavour- k_T algorithm has a non-vanishing probability to find a flavoured jet with (almost) zero energy. As such however, the situation for the subleading flavoured jet is inverse to the situation of the leading flavoured jet. Indeed the corresponding subleading jet distribution now extends all the way to the maximum of $E_{b,1} \rightarrow m_H/2$, while $E_{b,2} \rightarrow 0$. For this subleading jet distribution, the gluonic decay category is subject to rather large NLO corrections at higher energies. Understanding that flavoured quarks in the $H \rightarrow gg$ decay are exclusively generated by secondary gluon decays, it becomes clear that the high-energy tail of the subleading-energy distribution receives large corrections from real corrections in which both gluons decay to a $b\bar{b}$ pair. The K -factors for the fermionic decay category have a small increase for very low energies in the flavour- k_T algorithm and a decrease for high-energies for both algorithms. The ranges are from 1.3 (1.2) at to 2.0 (1.9) for flavour- k_T with $y_{\text{cut}} = 0.1$ ($y_{\text{cut}} = 0.01$). For flavour-dressing the ranges are from 1.3 (1.3) to 1.5 (1.4) with $y_{\text{cut}} = 0.1$ ($y_{\text{cut}} = 0.01$). The increase is for all algorithms and y_{cut} values towards

lower energies. The gluonic channel has diverging K -factors for high energies, as alluded to above. Otherwise, the K -factors range for a y_{cut} of 0.1 from 2.1 to 3.0 for flavour- k_T and 2.6 to 3.0 for flavour-dressing, where for both the K -factor of 3.0 is obtained at an energy of $E_{b,2}/m_H = 0.3$. For a y_{cut} of 0.01 the ranges are from 1.7 to 1.8 for flavour- k_T and around 2.0 – 2.8 for flavour dressing, where again the upper value is obtained at an energy of $E_{b,2}/m_H = 0.3$. Afterwards the K -factors diverge, as alluded to above.

The angular separation of the leading b - and \bar{b} -jet, $\cos\theta_{b\bar{b}}$:

Figure 5 shows the angular separation of the leading b - and leading \bar{b} -jet. We see that the peak of the distributions is located at large angles ($\cos\phi \rightarrow -1$) in the $H \rightarrow b\bar{b}$ category, whereas it is located at small angles ($\cos\phi \rightarrow 1$) in $H \rightarrow gg$ decays. The reason is that in Yukawa-induced $H \rightarrow b\bar{b}$, the quark-antiquark pair directly stems from the Higgs decay and is thus expected to favour a large angular separation, whereas quark-antiquark pairs stem from gluon decays in the $H \rightarrow gg$ category and, as such, are divergent in the collinear limit. In $H \rightarrow gg$ decays, we see another peak towards $\cos\phi = -1$, which originates from decays $H \rightarrow gg \rightarrow b\bar{b}b\bar{b}$, in which the leading b and leading \bar{b} originate from different gluons. Since this only happens at NLO, these obtain large NLO-corrections. The same is not visible in $H \rightarrow b\bar{b}$ decays, as the leading $b\bar{b}$ pair almost exclusively stems from the primary Higgs-decay vertex. The peculiar behaviour of the flavour- k_T algorithm for the three-parton configurations with a single soft b -quark again allows the distributions to span further into the infrared region, as is visible by the numerically larger upper limit in the distributions obtained with flavour- k_T . Except for the peak towards $\cos\phi = -1$, the K -factors for the $H \rightarrow b\bar{b}$ channel are ranging from 1.3 (0.8) to 1.7 (1.3) for flavour- k_T and a y_{cut} of 0.1 (0.01), while the range for flavour-dressing with a y_{cut} of 0.1 is from 1.2 to 1.6, where the decrease is towards higher $\cos\phi$. The distribution is ended by a sudden increase in the NLO corrections. Flavour-dressing with a y_{cut} of 0.01 starts around a K -factor of 1.3 at low energies and then slowly decreases to a K -factor of 1.0 for higher energies. For $H \rightarrow gg$ we find the already discussed explosion of NLO correction towards $\cos\phi = -1$ and have otherwise K -factors in a range from 2.1 (1.5) to 2.2 (1.9) for a y_{cut} value of 0.1 (0.01), where for $y_{\text{cut}} = 0.01$ the minimal K -factor of 1.5 is obtained around $\cos\phi = 0$ and possesses a steady increase of the NLO corrections in both directions. Flavour-dressing again features huge NLO corrections towards $\cos\phi = -1$. The descent for a y_{cut} of 0.1 leads at $\cos\phi = -0.5$ to a K -factor of

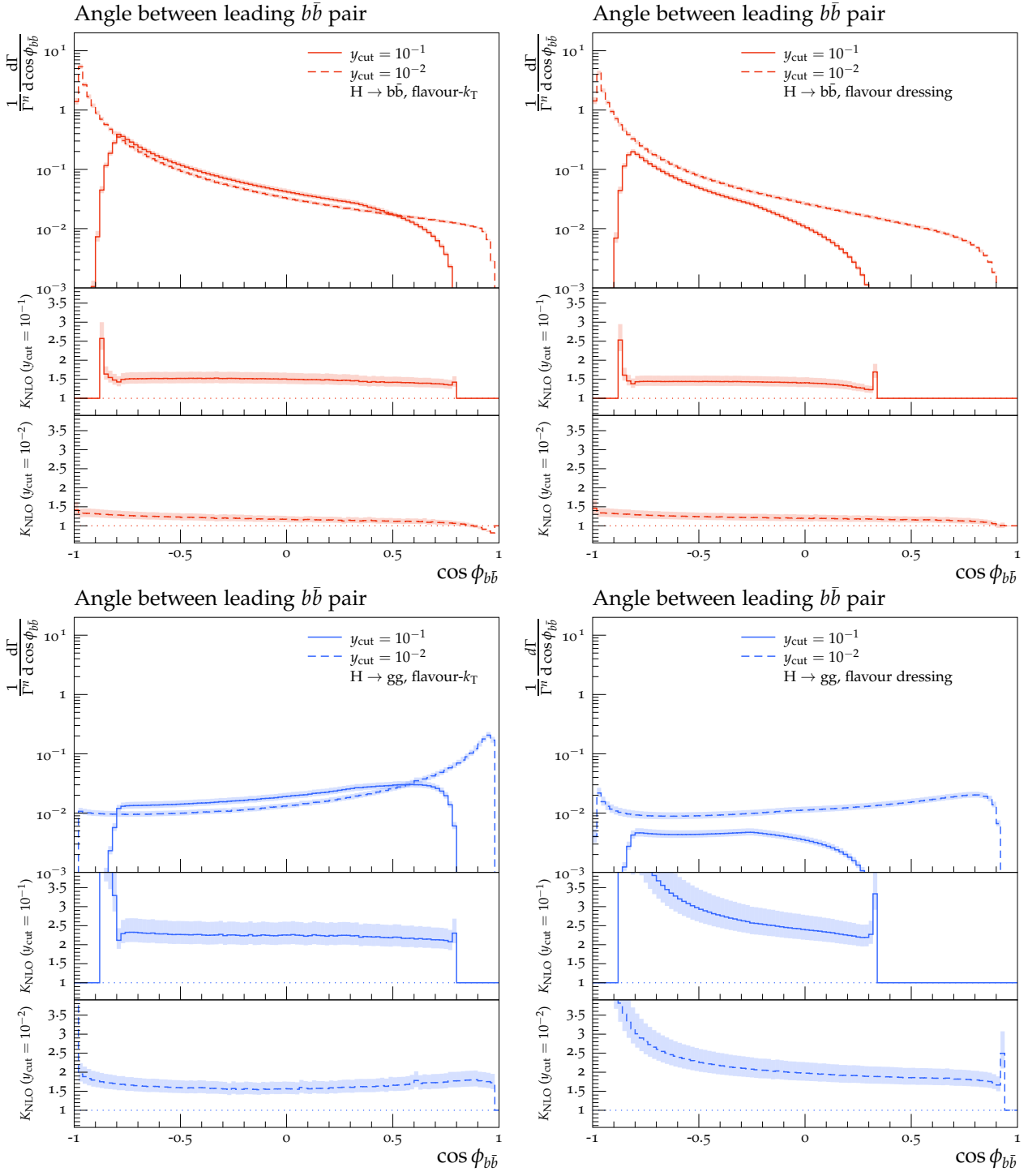


Fig. 5 Angular separation of the leading b - and \bar{b} -jet pair in the $H \rightarrow b\bar{b}$ (top row) and $H \rightarrow gg$ (bottom row) decay category using the flavour- k_T (left column) and flavour dressing (right column) algorithm.

3.0, and yields at $\cos\phi = 0$ a K -factor of 2.4. It then falls further to around 2.2 followed by a sharp increase again. For a y_{cut} of 0.01, the K -factors have a flatter distribution, where after the explosion on the left-hand side, it reaches at $\cos\phi = -0.5$ a K -factor of 2.3 and slowly decreases afterwards down to a K -factor of 1.7 followed again by a sharp spike.

The invariant mass of the leading b - and \bar{b} -jet, $m_{b\bar{b}}$:

Figure 6 shows the invariant mass of the leading b - and leading \bar{b} -jet, $m_{b\bar{b}}$. While Yukawa-induced decays favour quarks with a high invariant mass, $H \rightarrow gg$ decays favour quark-antiquark pairs with a small invariant mass. Again this can be understood by noting that the quarks in $H \rightarrow b\bar{b}$ decays originate directly from the primary Higgs-decay vertex, whereas they stem from secondary gluon splittings in $H \rightarrow gg$ decays and will thus have a smaller invariant mass $m_{b\bar{b}} \sim (1 - \cos\theta_{b\bar{b}})$, due to the form of the $g \rightarrow q\bar{q}$ splitting amplitude. The difference becomes more pronounced for lower values of y_{cut} , where the distribution shifts to larger angles in Yukawa-induced decays and towards smaller angles in gluonic decays. The main difference between the jet algorithms is that the flavour- k_{T} allows for smaller values of $m_{b\bar{b}}$, which again is explained by the maximum in the distance measure in equation (2). The K -factors for a y_{cut} of 0.1 in the fermionic decay category start by a peak at low invariant mass, where the peak for the flavour-dressing goes below a K -factor of 1. Both algorithms then do not have too much variation in the K -factors. For flavour- k_{T} the values range from 1.5, at higher invariant mass, to 1.6 at lower invariant mass. In flavour-dressing the increase is in the opposite direction with values ranging from 1.3, obtained around $m_{b\bar{b}} = 0.4$, to 1.5 for higher invariant mass. Both algorithms then end the distributions with another peak. Lowering the y_{cut} value to 0.01 again flattens the distribution a bit. Flavour- k_{T} starts for low invariant mass at a K -factor of 1.1 and then increases to a maximum of 1.4. Thereafter it slowly decreases to a K -factor of 1.3 for higher invariant mass. The flavour-dressing algorithm has a small K -factor of 0.2 for very low invariant mass, but then quickly increases again until reaching a K -factor of 1.2 around $m_{b\bar{b}}/m_H = 0.3$ followed by further increase to 1.3 for higher invariant mass.

The $H \rightarrow gg$ decay channel has big variations in the K -factors and need a careful analysis. Starting with flavour- k_{T} and $y_{\text{cut}} = 0.1$, we observe that the NLO corrections diverge towards negative infinity for small invariant mass, leaving thereby the region where the fixed order prediction can be trusted. Increasing the invariant mass also increases the NLO corrections, and the K -

factor crosses a value of 1.0 around $m_{b\bar{b}}/m_H = 0.03$ and further rapidly increases to 1.8 around $m_{b\bar{b}}/m_H = 0.1$, 2.4 at $m_{b\bar{b}}/m_H = 0.3$, 2.7 at $m_{b\bar{b}}/m_H = 0.5$ and further to 4.0 at $m_{b\bar{b}}/m_H = 0.7$, where it then starts to diverge towards positive infinity.

The distribution is similar for flavour- k_{T} with a y_{cut} value of 0.01 with the main difference, that after reaching a peak in the K -factor of 2.3 around $m_{b\bar{b}}/m_H = 0.16$, it starts to decrease again to a K -factor of 1.7, before the NLO-corrections get larger again for higher invariant mass. For flavour-dressing the distributions are similar to flavour- k_{T} , where again for $y_{\text{cut}} = 0.1$, we start with very small NLO-corrections at low invariant mass followed by a quick increase and a divergence towards positive infinity. Similarly for $y_{\text{cut}} = 0.01$, the NLO-corrections are low at small invariant mass. After a rapid increase to a K -factor of 1.8 at $m_{b\bar{b}}/m_H = 0.2$, the NLO-corrections increases to 2.8 at $m_{b\bar{b}}/m_H = 0.6$ and then start to diverge again.

5 Summary and outlook

In this paper, for the first time, we have computed flavour-sensitive observables related to hadronic Higgs decays including both Higgs decay categories, i.e. stemming from the underlying processes $H \rightarrow b\bar{b}$ and $H \rightarrow gg$ including higher order corrections up to $\mathcal{O}(\alpha_s^2)$ in perturbative QCD. The calculation was carried out in an effective theory in which the Higgs couples directly to gluons, while massless b -quarks retain a non-vanishing Yukawa coupling. Specifically, we considered the following observables: the energy of the leading and subleading flavoured jet, the angular separation and the invariant mass of the leading $b\bar{b}$ pair at relative $\mathcal{O}(\alpha_s^2)$ in QCD. Using the antenna-subtraction framework, the computations were performed with the parton-level event generator EERAD3, extended to account for hadronic Higgs decays. A new flavour layer was implemented in EERAD3 to allow for the computation of observables with identified flavoured jets. Flavoured jets were defined using both the flavour- k_{T} and flavour-dressing algorithm. For both algorithms, infrared flavour safety was explicitly verified in section 4.2. For each observable, predictions obtained in both Higgs-decay categories, using both flavoured jet algorithms and for two values of the experimental resolution parameter y_{cut} , i.e., $y_{\text{cut}} = 0.1$ and $y_{\text{cut}} = 0.01$ were compared. In all cases, lowering the parameter y_{cut} leads to wider distributions, owing to the larger kinematically allowed phase space.

Comparing the two Higgs decay modes, we observe larger rates in the $H \rightarrow b\bar{b}$ decay category. This is related to the fact that events in this category always

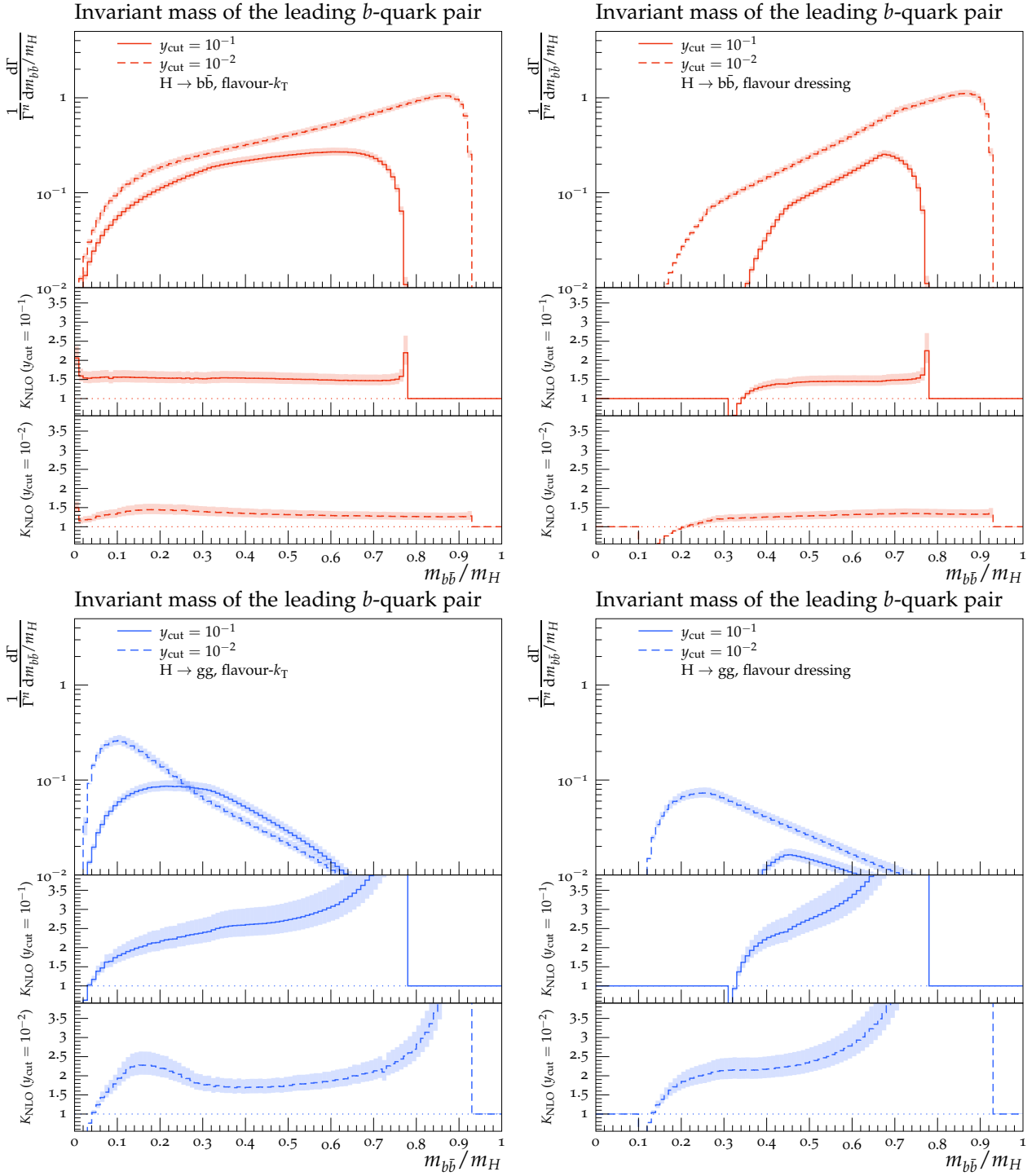


Fig. 6 Invariant mass of the leading b - and \bar{b} -jet pair in the $H \rightarrow b\bar{b}$ (top row) and $H \rightarrow gg$ (bottom row) decay category using the flavour- k_T (left column) and flavour dressing (right column) algorithm.

contain at least one $b\bar{b}$ pair, whereas most events in $H \rightarrow gg$ decays contain only unflavoured partons. We find larger NLO K -factors in the $H \rightarrow gg$ decay category, owing to the fact that our calculation employs the HEFT coupling between the Higgs and the gluons. Comparing the results obtained using the two flavoured jet algorithms, it was highlighted that the use of the flavour- k_T algorithm introduces counter-intuitive phenomenological implications, owing to its treatment of pathological three-parton configurations containing a single soft flavoured quark. While states with a single soft quark do not correspond to infrared singularities in physical matrix elements, it has the effect that these configurations are identified as three-jet like despite containing an, in principle, arbitrarily soft quark.

Away from phase-space regions dominated by configurations with a single soft flavoured quark, we find qualitatively good agreement between the flavour- k_T and the flavour-dressing algorithm, with generally slightly larger NLO corrections in the latter. Using the flavour dressing algorithm in particular, the shape and normalisation of the individual distributions in both decay categories have characteristic fixed-order behaviour over the whole kinematical range. In particular the behaviour at the kinematical edges, i.e., the drop or peak in the cross section, can be understood considering only hard final states in both Higgs decay categories. It is worth mentioning though, that the drop or the peak of the distributions seen at the kinematical edges are systematically exchanged in one or the other Higgs decay categories. This analysis demonstrates in particular the practical applicability of the flavour-dressing algorithm to compute flavour-sensitive observables in hadronic Higgs decays including both decay modes.

Our study marks the first step towards a more complete treatment of flavour-induced effects in hadronic Higgs decays. Obtaining a solid theoretical understanding of these effects will be vital for Higgs precision studies at future lepton colliders. Among these efforts, two avenues for future work are particularly worth mentioning: the study of flavour-tagged event shapes and the analysis of the phenomenological impact gained by the inclusion of NNLO-type corrections to flavour-sensitive observables in hadronic Higgs decays. We anticipate to return to both avenues in the future.

Acknowledgements We would like to thank Giovanni Stagnitto for useful discussions and a careful reading of the manuscript. AG and CTP acknowledge support by the Swiss National Science Foundation (SNF) under contract 200021-197130 and by the Swiss National Supercomputing Centre (CSCS) under project ID ETH5f. BCA is supported by the Deutsche Forschungsgemeinschaft (DFG, German Research Foundation) under grant 396021762 - TRR257. Parts of the computations

were carried out on the PLEIADES cluster at the University of Wuppertal, supported by the Deutsche Forschungsgemeinschaft (DFG, grant No. INST 218/78-1 FUGG) and the Bundesministerium für Bildung und Forschung (BMBF).

References

1. G. Aad, et al., Phys. Lett. B **716**, 1 (2012). DOI 10.1016/j.physletb.2012.08.020
2. S. Chatrchyan, et al., Phys. Lett. B **716**, 30 (2012). DOI 10.1016/j.physletb.2012.08.021
3. A. Abada, et al., Eur. Phys. J. ST **228**(2), 261 (2019). DOI 10.1140/epjst/e2019-900045-4
4. A. Arbey, et al., Eur. Phys. J. C **75**(8), 371 (2015). DOI 10.1140/epjc/s10052-015-3511-9
5. M. Aaboud, et al., Phys. Lett. B **786**, 59 (2018). DOI 10.1016/j.physletb.2018.09.013
6. A.M. Sirunyan, et al., Phys. Rev. Lett. **121**(12), 121801 (2018). DOI 10.1103/PhysRevLett.121.121801
7. G. Coloretti, A. Gehrmann-De Ridder, C.T. Preuss, JHEP **06**, 009 (2022). DOI 10.1007/JHEP06(2022)009
8. J. Gao, JHEP **01**, 038 (2018). DOI 10.1007/JHEP01(2018)038
9. J. Gao, Y. Gong, W.L. Ju, L.L. Yang, JHEP **03**, 030 (2019). DOI 10.1007/JHEP03(2019)030
10. M.X. Luo, V. Shtabovenko, T.Z. Yang, H.X. Zhu, JHEP **06**, 037 (2019). DOI 10.1007/JHEP06(2019)037
11. J. Gao, V. Shtabovenko, T.Z. Yang, JHEP **02**, 210 (2021). DOI 10.1007/JHEP02(2021)210
12. A. Gehrmann-De Ridder, C.T. Preuss, C. Williams, (2023)
13. M. Knobbe, F. Krauss, D. Reichelt, S. Schumann, Eur. Phys. J. C **84**(1), 83 (2024). DOI 10.1140/epjc/s10052-024-12430-4
14. R. Gauld, A. Gehrmann-De Ridder, E.W.N. Glover, A. Huss, I. Majer, JHEP **10**, 002 (2019). DOI 10.1007/JHEP10(2019)002
15. W. Bizoń, E. Re, G. Zanderighi, JHEP **06**, 006 (2020). DOI 10.1007/JHEP06(2020)006
16. S. Zanolini, M. Chiesa, E. Re, M. Wiesemann, G. Zanderighi, JHEP **07**, 008 (2022). DOI 10.1007/JHEP07(2022)008
17. A. Behring, W. Bizoń, F. Caola, K. Melnikov, R. Rötsch, Phys. Rev. D **101**(11), 114012 (2020). DOI 10.1103/PhysRevD.101.114012
18. R. Gauld, A. Gehrmann-De Ridder, E.W.N. Glover, A. Huss, I. Majer, Phys. Rev. Lett. **125**(22), 222002 (2020). DOI 10.1103/PhysRevLett.125.222002
19. M. Czakon, A. Mitov, M. Pellen, R. Poncelet, JHEP **06**, 100 (2021). DOI 10.1007/JHEP06(2021)100
20. M. Czakon, A. Mitov, M. Pellen, R. Poncelet, JHEP **02**, 241 (2023). DOI 10.1007/JHEP02(2023)241
21. R. Gauld, A. Gehrmann-De Ridder, E.W.N. Glover, A. Huss, A.R. Garcia, G. Stagnitto, Eur. Phys. J. C **83**(4), 336 (2023). DOI 10.1140/epjc/s10052-023-11530-x
22. A. Gehrmann-De Ridder, T. Gehrmann, E.W.N. Glover, A. Huss, A.R. Garcia, G. Stagnitto, (2023)
23. O. Fedkevych, C.K. Khosa, S. Marzani, F. Sforza, Phys. Rev. D **107**(3), 034032 (2023). DOI 10.1103/PhysRevD.107.034032
24. R. Gauld, A. Huss, G. Stagnitto, Phys. Rev. Lett. **130**(16), 161901 (2023). DOI 10.1103/PhysRevLett.130.161901

-
25. F. Caola, R. Grabarczyk, M.L. Hutt, G.P. Salam, L. Scyboz, J. Thaler, *Phys. Rev. D* **108**(9), 094010 (2023). DOI 10.1103/PhysRevD.108.094010
 26. L. Cavallini, A. Coccaro, C.K. Khosa, G. Manco, S. Marzani, F. Parodi, D. Rebuffi, A. Rescia, G. Stagnitto, *Eur. Phys. J. C* **82**(5), 493 (2022). DOI 10.1140/epjc/s10052-022-10447-1
 27. A. Banfi, G.P. Salam, G. Zanderighi, *Eur. Phys. J. C* **47**, 113 (2006). DOI 10.1140/epjc/s2006-02552-4
 28. S. Caletti, A.J. Larkoski, S. Marzani, D. Reichelt, *Eur. Phys. J. C* **82**(7), 632 (2022). DOI 10.1140/epjc/s10052-022-10568-7
 29. M. Czakon, A. Mitov, R. Poncelet, *JHEP* **04**, 138 (2023). DOI 10.1007/JHEP04(2023)138
 30. S. Catani, Y.L. Dokshitzer, M. Olsson, G. Turnock, B.R. Webber, *Phys. Lett. B* **269**, 432 (1991). DOI 10.1016/0370-2693(91)90196-W
 31. A.J. Larkoski, S. Marzani, G. Soyez, J. Thaler, *JHEP* **05**, 146 (2014). DOI 10.1007/JHEP05(2014)146
 32. A. Gehrmann-De Ridder, T. Gehrmann, E.W.N. Glover, G. Heinrich, *JHEP* **12**, 094 (2007). DOI 10.1088/1126-6708/2007/12/094
 33. A. Gehrmann-De Ridder, T. Gehrmann, E.W.N. Glover, G. Heinrich, *Comput. Phys. Commun.* **185**, 3331 (2014). DOI 10.1016/j.cpc.2014.07.024
 34. T. Inami, T. Kubota, Y. Okada, *Z. Phys. C* **18**, 69 (1983). DOI 10.1007/BF01571710
 35. A. Djouadi, J. Kalinowski, P.M. Zerwas, *Z. Phys. C* **54**, 255 (1992). DOI 10.1007/BF01566654
 36. K.G. Chetyrkin, B.A. Kniehl, M. Steinhauser, *Phys. Rev. Lett.* **79**, 353 (1997). DOI 10.1103/PhysRevLett.79.353
 37. K.G. Chetyrkin, B.A. Kniehl, M. Steinhauser, *Nucl. Phys. B* **510**, 61 (1998). DOI 10.1016/S0550-3213(97)00649-4
 38. K.G. Chetyrkin, J.H. Kuhn, C. Sturm, *Nucl. Phys. B* **744**, 121 (2006). DOI 10.1016/j.nuclphysb.2006.03.020
 39. Y. Schroder, M. Steinhauser, *JHEP* **01**, 051 (2006). DOI 10.1088/1126-6708/2006/01/051
 40. P.A. Baikov, K.G. Chetyrkin, J.H. Kühn, *Phys. Rev. Lett.* **118**(8), 082002 (2017). DOI 10.1103/PhysRevLett.118.082002
 41. J.A.M. Vermaseren, S.A. Larin, T. van Ritbergen, *Phys. Lett. B* **405**, 327 (1997). DOI 10.1016/S0370-2693(97)00660-6
 42. A.M. Sirunyan, et al., *JINST* **13**(05), P05011 (2018). DOI 10.1088/1748-0221/13/05/P05011
 43. G. Aad, et al., *JINST* **11**(04), P04008 (2016). DOI 10.1088/1748-0221/11/04/P04008
 44. R. Aaij, et al., *JINST* **10**(06), P06013 (2015). DOI 10.1088/1748-0221/10/06/P06013

Impact of strong magnetic field, baryon chemical potential, and medium anisotropy on polarization and spin alignment of hadrons

Bhagyarathi Sahoo,* Captain R. Singh,† and Raghunath Sahoo‡

Department of Physics, Indian Institute of Technology Indore, Simrol, Indore 453552, India

(Dated: February 28, 2024)

The recent observation of global polarization of Λ ($\bar{\Lambda}$) hyperons and spin alignment of ϕ and K^{*0} vector mesons create remarkable interest in investigating the particle polarization in the relativistic fluid produced in heavy-ion collisions at GeV/TeV energies. Among other sources of polarization, the Debye mass of a medium plays a crucial role in particle polarization. Any modification brought to the effective mass due to the temperature, strong magnetic field (eB), baryonic chemical potential (μ_B), and medium anisotropy (ξ), vorticity, etc., certainly affects the particle polarization. In this work, we explore the global hyperon polarization and the spin alignment of vector mesons corresponding to the strong magnetic field, baryonic chemical potential, and medium anisotropy. We find that the degree of polarization is flavor-dependent for hyperons. Meanwhile, vector meson spin alignment depends on the hadronization mechanisms of initially polarized quarks and anti-quarks. Medium anisotropy significantly changes the degree of polarization in comparison with the magnetic field and baryon chemical potential.

I. INTRODUCTION

So far, the thermalized state of strongly interacting partons, called quark-gluon plasma (QGP), is probed in heavy-ion collisions through a baseline, the pp collisions. It was assumed that QGP existence in pp collisions is next to impossible because it lacks the necessary conditions for QGP to be formed. On the contrary, in recent LHC events, ultra-relativistic pp collision experiments have reported behavior similar to heavy-ion collisions, e.g., collective flow, strangeness enhancement, etc [1, 2]. However, other studies suggest similar phenomena may arise due to the other QCD processes [3, 4]. These studies raise a question concerning the present QGP signatures and a need for the next generation of probes. In the quest for such a baseline-independent probe, polarization comes into picture and can have implications for understanding hot QCD matter. The particle production mechanisms lead to a finite polarization of the light/heavy baryons and vector mesons [5]. However, there are various sources by which hadrons can get polarized in ultra-relativistic collisions. One such primary source could be the initial state polarization, which arises due to the motion and spin of the constituent quarks of the colliding nucleons. This initial state polarization can be transmitted to the quarks participating in the collision process. The magnetic field produced by the charged spectator protons in such collisions interacts with the electric charge and spin of the quarks, which may lead to quark polarization. A topological charge imbalance in the presence of an external magnetic field leads to the charge separation in the direction of the magnetic field. This phenomenon

is known as the chiral magnetic effect (CME) [6, 7]. If QGP exhibits chiral symmetry restoration, then CME could lead to quark polarization along the direction of the magnetic field. A similar phenomenon called chiral vortical effect (CVE) is expected due to the non-zero local vorticity, which also contributes to the hadron polarization [8, 9]. The hydrodynamic behavior or collective motion of QGP can also induce polarization in the quark distribution due to the anisotropic expansion [10, 11]. Determining the precise sources and types of polarization in ultra-relativistic collisions requires sophisticated theoretical studies with corresponding experimental observations.

In 2005, Liang and Wang predicted in non-central heavy-ion collisions, the orbital angular momentum (OAM) of the partonic system polarizes the quarks and anti-quarks through spin-orbit coupling. They asserted that the initial partons created in the collisions could generate a longitudinal fluid shear distribution representing the local relative OAM in the same direction as global OAM at a finite impact parameter. This quark polarization manifests the polarization of the hadrons (with finite spin) along the direction of OAM during the process of hadronization [12–15]. Apart from global polarization of hadrons, such global quark polarization has many observable consequences, such as left-right asymmetry in hadron spectra and global transverse polarization of thermal photons, dileptons, etc. [16, 17]. They have studied the global polarization of hyperons [12] and spin alignment of vector mesons [13] in different hadronization scenarios. Following, in 2013, Becattini et al. predicted the global spin polarization of Λ hyperons due to the OAM-manifested thermal vorticity [18]. Various theoretical predictions of global Λ hyperons polarization by different hydrodynamic and transport models are well agreed with the experimental results available at Relativistic Heavy Ion Collider (RHIC) [19–27]. These hydrodynamic and transport

* Bhagyarathi.Sahoo@cern.ch

† captainriturajsingh@gmail.com

‡ Raghunath.Sahoo@cern.ch (Corresponding Author)

models considered the thermal equilibrated distribution of spin degrees of freedom for polarization studies [28–35].

In addition to Λ hyperons, the averaged global polarization measurement of Ω and Ξ hyperons are obtained using the polarization transfer method in STAR [36]. Similarly, the polarization of quarkonium states is obtained by measuring the angular distribution of dileptons [5, 37–40]. Furthermore, the global spin alignment of ϕ , K^{*0} , K_S^0 mesons is observed at the LHC and RHIC from the angular distribution of decay daughters in the mother particles’s rest frame [41–46]. Recent spin alignment measurements for ϕ vector mesons by the STAR collaboration initiate a spark in the theoretical communities to investigate the source of large positive spin alignment for ϕ vector meson, while K^{*0} shows no such spin-alignment within uncertainties [41].

Some theoretical studies claim that in addition to vorticity and electromagnetic fields, a strong vector meson force field is responsible for hyperon polarization [47] as well as spin alignment of vector mesons [48, 49]. Recently, Sheng et al. [49] explain the large spin alignment of ϕ vector meson in a quark polarization mechanism by a strong force field, in which quarks interact with the dense medium through a strong force and become polarized. The strong force field is proposed to polarize the vector meson with the hidden flavor quantum number. Apart from these sources, there could be various other possible sources for vector meson spin-alignment, which need further investigation. Moreover, recent observation of longitudinal local polarization of Λ hyperons at LHC and RHIC mismatches with the theoretical predictions [11], which opens a new door for the heavy-ion community to have intense investigations on this topic. However, various studies have been developed to solve this puzzle through different aspects [50, 51]. Similar to hyperons, the local polarization of quarks and anti-quarks due to anisotropic expansion of the medium contributes to the spin alignment of vector meson [52]. The authors have argued that the deviation of ρ_{00} from 1/3 is not solely coming from global spin alignment but also has the contribution of quarks and/or anti-quarks, which are locally polarized. However, the contribution of local quark polarization requires the measurement of off-diagonal elements of the spin density matrix.

In the experiment, the methods used to measure polarization for hyperons and vector mesons are different. However, both depend on the angular distribution of decay daughters in the mother particles’ rest frame. The hyperons undergo parity-violating weak decays, while the vector mesons mainly decay through the parity, conserving strong decay. The Λ hyperon polarization is estimated by the projection of the daughter proton’s momentum along the OAM (or vorticity axis) direction. On the other hand, the spin alignment of vector meson has been studied by measuring the ρ_{00} element of the

spin density matrix. The detailed explanation of the spin density matrix is discussed in section II.

Ultra-peripheral heavy-ion collisions have several consequences; one such example is that they produce a strong magnetic field. This magnetic field decays with time and can, in principle, affect the QGP medium evolution, thermodynamic, and transport properties [53–55]. The magnetic field is believed to affect the Λ polarization, specifically on the polarization splitting of Λ and $\bar{\Lambda}$ at the lower center of mass energies. The effect of magnetic field on polarization and spin alignment of hadrons is discussed in Ref. [56–64]. Recent observation of global polarization of Λ hyperons indicate that hyperon polarization decreases with the increasing center of mass energy [19–21]. So, at lower energies, the probability of particles getting polarized is large, which could be a consequence of baryon stopping. This high baryon chemical potential may affect the evolution process and particle polarization. Further, due to the rapid longitudinal expansion of the fireball created in heavy-ion collisions, a high degree of momentum-space anisotropy is produced in the QGP medium in its local rest frame [65]. This momentum-space anisotropy has many novel consequences; for example, it is essential in modeling heavy-quark dynamics, making the inter-quark potentials spatially anisotropic. This anisotropy in the QGP medium may affect the particle yield, flow coefficients, particle polarization, etc.

In this work, we investigate the effect of static strong magnetic field, baryon chemical potential, and momentum-space anisotropy parameter on the polarization of hyperons and spin alignment of vector mesons through Debye screening mass. Please note that in the rest of the paper, we shall refer to Debye screening mass as Debye mass. The individual and combined effect of eB , μ_B and ξ on the polarization and spin-alignment of hadrons is studied. It is important to mention that the magnetic field may generate an additional anisotropy in the medium, which is not explicitly considered in this study. We consider two different hadronization mechanisms, i.e., the recombination and fragmentation processes, for both hyperons and vector mesons.

The structure of this work is as follows. The section II gives a detailed overview of the formalism used in this work. We briefly examine the results in section III and provide a summary in section IV

II. FORMULATION

The global quark polarization is obtained through parton elastic scattering within the framework of an effective static potential model. This model uses effective mass or Debye mass to incorporate the parton scattering, which induces the quark polarization [12–15], given as,

$$P_q = -\frac{\pi}{2} \frac{m_D p}{E(E + m_q)} \quad (1)$$

where $E = \sqrt{p^2 + m^2}$, p and m_q are the energy, momentum, and mass of quark in the center of mass frame of the parton scattering, m_D is the Debye mass.

Assuming $P_u = P_d \equiv P_q$, recent studies [56] calculated the polarization of hyperons using a spin density matrix. The following study is consistent with the previous findings [12], where the authors have calculated the polarization of hyperons using recombination and fragmentation processes.

This global quark polarization leads to the global hyperons polarization at the hadronization stage. The global polarization due to exclusive recombination process for Λ , Σ^\pm , Ξ^- , Ω^- , and Δ^{++} hyperons are given as [12, 56];

$$P_\Lambda^{rec} = P_s, \quad P_{\Sigma^\pm}^{rec} = \frac{4P_q - P_s - 3P_s P_q^2}{3 - 4P_q P_s + P_q^2} \quad (2)$$

$$P_{\Xi^-}^{rec} = \frac{4P_s - P_q - 3P_q P_s^2}{3 - 4P_q P_s + P_s^2}, \quad P_{\Omega^-}^{rec} = \frac{P_s(5 + P_s^2)}{1 + P_s^2} \quad (3)$$

$$P_{\Delta^{++}}^{rec} = \frac{P_u(5 + P_u^2)}{1 + P_u^2} \quad (4)$$

The hyperon polarization from inclusive recombination is difficult to estimate. However, at the extreme limit of inclusive recombination (i.e., fragmentation), the hyperon polarization due to polarized quarks is estimated in Ref. [12]. The fragmentation of hyperons is given by;

$$P_\Lambda^{frag} = \frac{n_s P_s}{n_s + 2f_s}, \quad P_{\Sigma^\pm}^{frag} = \frac{4f_s P_q - n_s P_s}{3(n_s + 2f_s)} \quad (5)$$

$$P_{\Xi^-}^{frag} = \frac{4n_s P_s - f_s P_q}{3(2n_s + f_s)}, \quad P_{\Omega^-}^{frag} = \frac{P_s}{3}, \quad P_{\Delta^{++}}^{frag} = \frac{P_u}{3} \quad (6)$$

Such global polarization of quarks and anti-quarks also describes the spin alignment of vector mesons through different hadronization scenarios [13].

Unlike spin-polarization for hyperons, the spin alignment of vector meson is described by the spin density matrix $\rho_{m,m'}$, where m and m' label the spin component along the quantization axis. The spin alignment for vector meson is mostly measured by the 00^{th} element of the spin density matrix, i.e., ρ_{00} . It can be measured experimentally through the angular distribution of the decay products of the particles rest frame [43]. The deviation of ρ_{00} from $1/3$ (i.e. $\rho_{00} - 1/3$) determines

the degree of alignment of vector meson. In Ref. [13], the authors have described the spin alignment of vector mesons in different hadronization scenarios.

In this work, we consider two scenarios of the hadronization process; the first one is due to the recombination of polarized quarks and anti-quarks. The second one is due to the recombination of polarized quarks and anti-quarks, in which either of them is created in the fragmentation process. The 00^{th} element of spin density matrix for ρ , ϕ and K^* mesons in recombination and fragmentation processes in which both quarks and anti-quarks are polarized are obtained as,

$$\rho_{00}^{\rho(rec)} = \frac{1 - P_q^2}{3 + P_q^2}, \quad \rho_{00}^{\phi(rec)} = \frac{1 - P_s^2}{3 + P_s^2}, \quad \rho_{00}^{K^*(rec)} = \frac{1 - P_q P_s}{3 + P_q P_s} \quad (7)$$

$$\rho_{00}^{\rho(frag)} = \frac{1 + \beta P_q^2}{3 - \beta P_q^2}, \quad \rho_{00}^{\phi(frag)} = \frac{1 + \beta P_s^2}{3 - \beta P_s^2} \quad (8)$$

$$\rho_{00}^{K^*(frag)} = \frac{f_s}{n_s + f_s} \frac{1 + \beta P_q^2}{3 - \beta P_q^2} + \frac{n_s}{n_s + f_s} \frac{1 + \beta P_s^2}{3 - \beta P_s^2} \quad (9)$$

where $\beta \simeq 0.5$. n_s and f_s are the strange quark abundances relative to up and down quarks in QGP and quark fragmentation, respectively.

Further, we have briefly outlined the formalism to explore the effect of magnetic field, baryon chemical potential, and anisotropic parameters on the polarization of hyperons and mesons.

A. Debye Mass under Strong Magnetic Field

The magnetic field produced in the peripheral heavy-ion collisions is believed to decay very quickly. So, it is expected to only affect the partonic phase during the early stage of the evolution process. Magnetic fields tend to align charged particles in a specific direction, resulting in the polarization of the system. Given that quarks possess a fractional electric charge, it is anticipated that a magnetic field could potentially modify the orientation of quarks within the QGP phase. Consequently, in the presence of a strong magnetic field, the total Debye mass for fermions or quarks in the static limit has been calculated through the temporal component of one loop vacuum self-energy diagram and has the following form [66–69];

$$m_D^2(T, eB) = 4\pi\alpha_s(\Lambda^2, |eB|) \left[T^2 \frac{N_c}{3} + \sum_f \frac{|q_f eB|}{4\pi^2} \right] \quad (10)$$

here, $\alpha_s(\Lambda^2, |eB|)$ is the running coupling constant, which depends on the magnetic field and temperature. It can be written as [68],

$$\alpha_s(\Lambda^2, |eB|) = \frac{g_s^2}{4\pi} = \frac{\alpha_s(\Lambda^2)}{1 + b_1 \alpha_s(\Lambda^2) \ln \left(\frac{\Lambda^2}{\Lambda^2 + |eB|} \right)} \quad (11)$$

with

$$\alpha_s(\Lambda^2) = \frac{1}{b_1 \ln \left(\frac{\Lambda^2}{\Lambda_{MS}^2} \right)} \quad (12)$$

where $b_1 = \frac{11N_c - 2N_f}{12\pi}$, $\Lambda_{MS} = 0.176$ GeV for $N_f = 3$ and renormalization scale $\Lambda = 2\pi T$ [70].

B. Debye Mass with Baryon Chemical Potential

Finite μ_B dictates the dominance of the number of quarks over anti-quarks, such an imbalance affects the final production yield of hadrons. In nature, any order parameter or disparity ultimately leads to the polarization of the system. Likewise, a non-zero baryon chemical potential can be the source of a polarized QGP medium. Any change brought to the QGP affects its effective mass, as a consequence, μ_B is incorporated in the Debye mass. In a hot and high baryon density medium ($T, \mu_B \gg m_q$, with m_q as the light quark mass), the leading order HTL/HDL calculation predicts resultant Debye mass which has the following form [71–74];

$$m_D^2(T, \mu_B) = 4\pi\alpha_s(\Lambda^2) \left[T^2 \left(\frac{N_c}{3} + \frac{N_f}{6} \right) + \sum_f \frac{\mu_B^2}{18\pi^2} \right] \quad (13)$$

Here, the strong coupling constant $\alpha_s(\Lambda^2)$ takes the form given in Eq. 12, and in the presence of baryon chemical

potential, the renormalization scale is modified into

$$\Lambda = 2\pi \sqrt{T^2 + \frac{\mu_B^2}{\pi^2}} \quad (14)$$

C. Effect of Anisotropy on Debye Mass

Momentum space anisotropy originated due to the collision geometry causing differential expansions of the fireball along the longitudinal and transverse directions. As a consequence, it also alters the effective mass of the medium. The effect of momentum-space anisotropy of the medium on Debye mass is given as [65, 75–79];

$$m_D(T, \xi) = m_D(T) \left[f_1(\xi) \cos^2 \theta + f_2(\xi) \right]^{-\frac{1}{4}} \quad (15)$$

and,

$$m_D(T) = \sqrt{4\pi\alpha_s(\Lambda^2)T^2 \left(\frac{N_c}{3} + \frac{N_f}{6} \right)} \quad (16)$$

The parameter ξ measures the degree of momentum-space anisotropy, defined as;

$$\xi = \frac{1 \langle \mathbf{k}_\perp^2 \rangle}{2 \langle k_z^2 \rangle} - 1 \quad (17)$$

where $k_z \equiv \mathbf{k} \cdot \mathbf{n}$, $\mathbf{k}_\perp \equiv \mathbf{k} - \mathbf{n}(\mathbf{k} \cdot \mathbf{n})$ correspond to the particle momenta along and perpendicular to the direction of anisotropy, and θ is the angle between quark pair alignment (\mathbf{r}) with respect to direction of anisotropy (\mathbf{n}). The $f_1(\xi)$ and $f_2(\xi)$ are parameterized in such a way that Eq. 15 remains always true under small and large values of ξ ,

$$f_1(\xi) = \frac{9\xi(1+\xi)^{\frac{3}{2}}}{2\sqrt{3+\xi}(3+\xi^2)} \frac{\pi^2(\sqrt{2} - (1+\xi)^{\frac{1}{8}}) + 16(\sqrt{3+\xi} - \sqrt{2})}{(\sqrt{6} - \sqrt{3})\pi^2 - 16(\sqrt{6} - 3)} \quad (18)$$

$$f_2(\xi) = \xi \left(\frac{16}{\pi^2} - \frac{\sqrt{2}(\frac{16}{\pi^2} - 1) + (1+\xi)^{\frac{1}{8}}}{\sqrt{3+\xi}} \right) \left(1 - \frac{(1+\xi)^{\frac{3}{2}}}{1 + \frac{\xi^2}{3}} \right) + f_1(\xi) + 1 \quad (19)$$

D. Net Debye Mass

In previous sections, we have discussed the Debye mass for individual cases now combining all together (eB , μ_B , and ξ), we have obtained the resultant Debye mass;

$$m_D(T, \mu_B, B, \xi) = m_D(T, \mu_B, B) \left[f_1(\xi) \cos^2 \theta + f_2(\xi) \right]^{-\frac{1}{4}} \quad (20)$$

and

$$m_D(T, \mu_B, B) = \sqrt{4\pi\alpha_s(\Lambda^2, |eB|) \left[T^2 \frac{N_c}{3} + \sum_f \frac{|q_f eB|}{4\pi^2 T} \int_0^\infty dp_z \{n^+(E)(1 - n^+(E)) + n^-(E)(1 - n^-(E))\} \right]} \quad (21)$$

with

$$n^\pm(E) = \left[\exp \left(\frac{E \mp \mu_B}{T} \right) + 1 \right]^{-1} \quad (22)$$

The $n^+(E)$ and $n^-(E)$ are the phase-space distribution functions of quarks and anti-quarks, respectively.

III. RESULTS AND DISCUSSION

Following the discussed formulation, we studied the influence of magnetic field (eB), baryon chemical potential (μ_B), and anisotropic parameter (ξ) on the polarization of hyperons and spin alignment of vector mesons. As quark-antiquark polarization leads to global hadron polarization, based on that, we have predicted the global polarization of various hadrons. Further, The spin alignment of vector mesons and polarization of hyperons are obtained corresponding to two different hadronization processes: (i) recombination and (ii) fragmentation. Firstly, the hyperon polarization prediction is given and discussed. Subsequently, the spin-alignment of vector mesons is presented. But before that, the change in the Debye mass due to magnetic field, baryon chemical potential, and the anisotropic parameter is depicted in Fig 1 to ensure the validity of our results. It shows the variation of effective Debye mass with the magnetic field (left panel), baryon chemical potential (middle panel), and anisotropic parameter (right panel) for three different values of temperature, i.e., $T = 200$ MeV, $T = 250$ MeV, and $T = 300$ MeV.

The left panel of Fig. 1 shows that the Debye mass increases with magnetic field and temperature. However, the impact of the external magnetic field on the rate of change in Debye mass is stronger at lower temperatures. The observed enhancement in the Debye mass with the external magnetic field is in qualitative agreement with the findings reported in Refs. [80–82]. The middle panel of Fig. 1 reveals a modest decrease in the Debye mass with increasing baryon chemical potential in a baryon-rich medium. Although its decrease is very small in magnitude, the effect of baryon chemical potential is a bit prominent at lower temperatures compared to higher temperatures. In the right panel of Fig. 1, we found that the Debye mass decreases significantly as the anisotropy parameter increases. The decrease in the Debye mass with the momentum anisotropy agrees well with the finding reported in Refs. [65, 75].

Based on these observations, it can be said that the medium effects are encoded in the Debye mass. It is

more sensitive to the anisotropy parameter than the magnetic field and baryon chemical potential. The Debye mass of the medium represents the change in the degree of freedom of the systems, if the Debye mass of the system is very small, then the color degrees of freedom would reduce to the hadron degree of freedom. The Debye mass depends on two things: the medium's temperature (energy) and the coupling strength of the medium. The magnetic field in the medium gives an additional boost to the energy level and strengthens the coupling constant. Due to this, a positive change in Debye mass with increasing field can be seen in the left panel of Fig. 1. On the other hand, finite baryon chemical potential also provides additional energy to the medium but reduces the coupling strengths. Consequently, in Fig. 1, we observe the negative change in the Debye mass with increasing baryon chemical potential. Meanwhile, the anisotropy of the medium does not affect the coupling strength of the medium. However, an uneven distribution of the partons in the medium measured in terms of ξ reduces the net effective mass of the medium. Therefore, a visible reduction in the Debye mass with large values of ξ is observed in Fig. 1. The combined effect of the magnetic field, baryon chemical potential, and medium anisotropy on Debye mass can be estimated using Eq. 21, which is not explicitly illustrated in this work. But one can easily infer the combined effect of these parameters on Debye mass from Fig. 1.

Furthermore, it is noteworthy to mention that in the quark recombination model, the hyperon polarization and spin alignment of vector meson from polarized quarks and anti-quarks does not include momentum dependence explicitly. This momentum dependence is introduced in a non-relativistic quark-coalescence model through the spin-density matrix [56], with which the polarization of vector meson and baryon of spin-1/2 and spin-3/2 is calculated systematically. However, the conventional quark coalescence or recombination models do not include the spin degrees of freedom. Again, the quark coalescence model is improved in Ref. [57].

A. Polarization of hyperons

To understand the polarization dynamics of hyperons, it is crucial to understand how these polarized quarks recombine to produce the final polarized hyperons. The polarization of hyperons depends on the process of hadronization. Here, we estimate the individual and combined effect of magnetic field, baryon chemical potential, and medium anisotropy on the global polar-

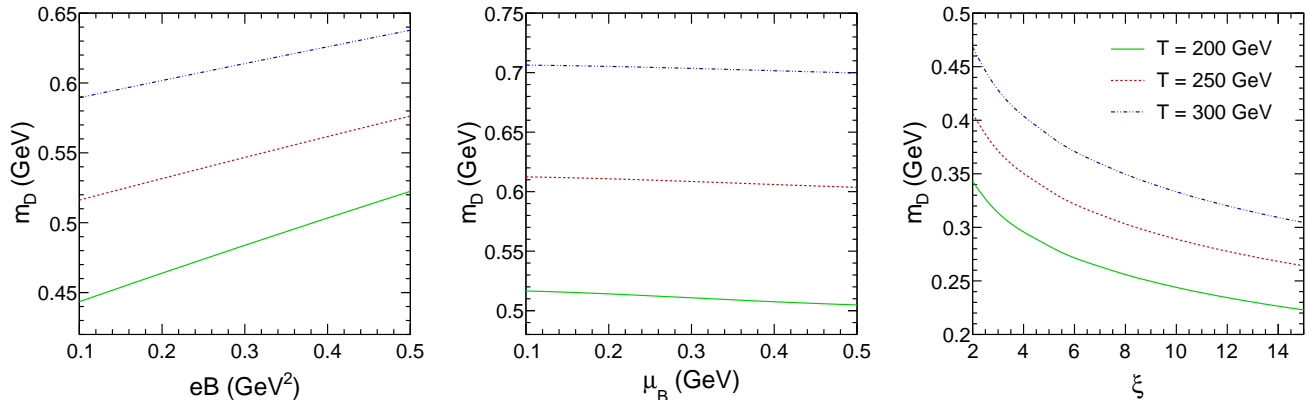


FIG. 1: (Color online) The variation of Debye screening mass (m_D) as a function of magnetic field (eB)(left panel), baryon chemical potential (μ_B)(middle panel) and anisotropic parameter (ξ)(right panel) for three different values of temperatures, i.e $T = 200$ MeV, $T=250$ MeV, and $T = 300$ MeV.

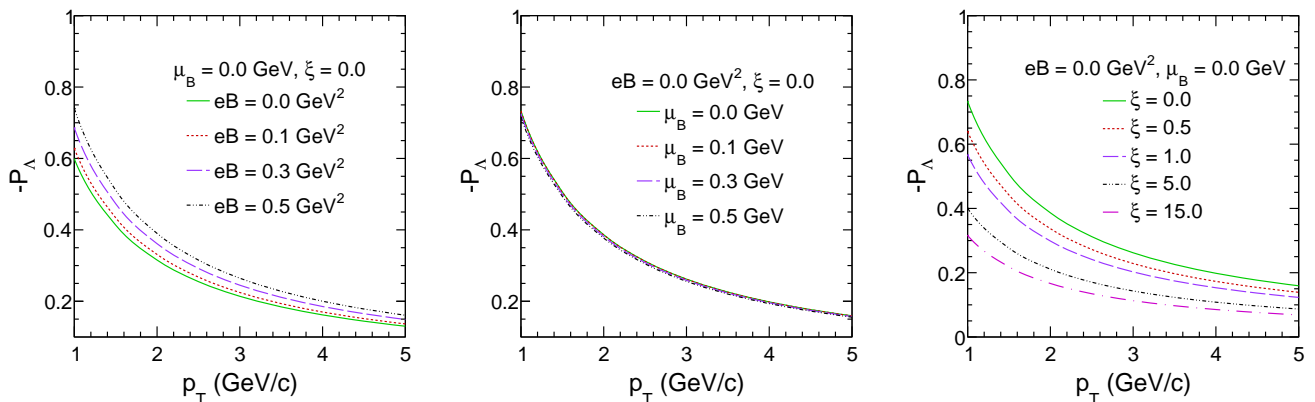


FIG. 2: (Color online) The variation of Λ hyperon polarization as a function of transverse momentum due to recombination process in the presence of magnetic field (eB)(left panel), baryon chemical potential (μ_B)(middle panel) and anisotropic parameter (ξ)(right panel) at temperature $T = 200$ MeV.

ization of hyperons.

The polarization of Λ , Σ^\pm , Ξ^- , Δ^{++} , and Ω^- hyperons in quark recombination process is calculated using the Eqs. 2, 3, 4. The left panel of Fig. 2 shows the variation of Λ hyperon polarization as a function of the transverse momentum (p_T) for different values of the magnetic field at $\mu_B = 0$ GeV and $\xi = 0$ in recombination process of hadronization. We consider three finite values of the magnetic field, i.e., $eB = 0.1$, 0.3 , and 0.5 GeV^2 . Figure 2 indicates the polarization of Λ hyperon decreases as a function of the p_T for all values of the magnetic field. It is observed that the increase in polarization of the Λ hyperon with a magnetic field can be attributed to the corresponding increase in the Debye mass. Apart from that, the magnetic field helps

to polarize the particle and anti-particle through their magnetic moments. The Λ hyperon has a negative magnetic moment, whereas the $\bar{\Lambda}$ hyperon has a positive magnetic moment. In the presence of a magnetic field, the spin of the $\bar{\Lambda}$ is strongly aligned along the direction of the field, while the Λ spin is relatively poorly aligned against the direction of the field. This argument could qualitatively describe the splitting of Λ and $\bar{\Lambda}$ hyperon with $P_{\bar{\Lambda}} > P_\Lambda$. However, current formalism predicts the same polarization for Λ and $\bar{\Lambda}$. Moreover, various phenomenological studies suggest that hyperon polarization is directly proportional to the magnetic field and plays a crucial role in particle polarization [56, 58].

During the exclusive recombination process of hadronization, it has been observed that the polarization

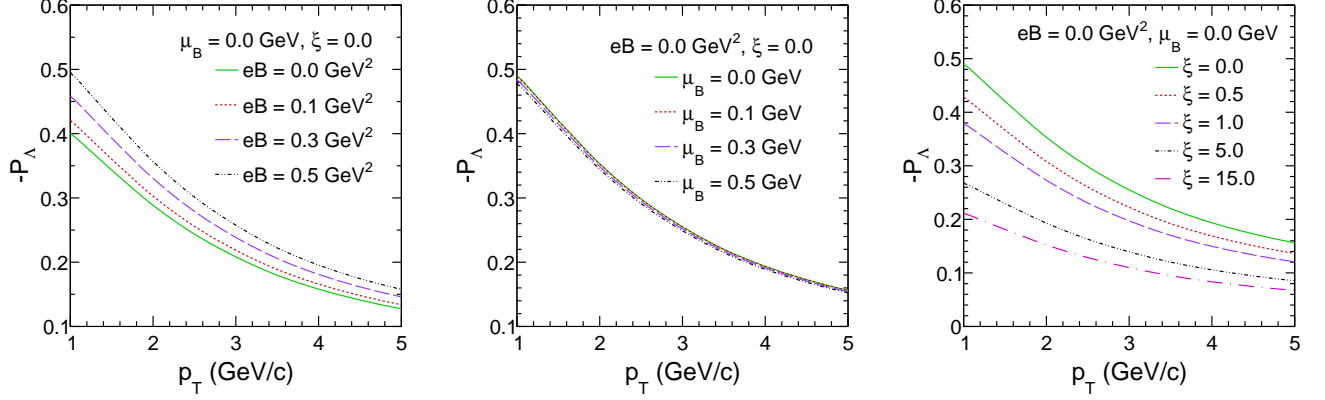


FIG. 3: (Color online) The variation of Λ hyperon polarization as a function of transverse momentum due to fragmentation process in the presence of magnetic field (eB)(left panel), baryon chemical potential (μ_B)(middle panel) and anisotropic parameter (ξ)(right panel) at temperature $T = 200$ MeV.

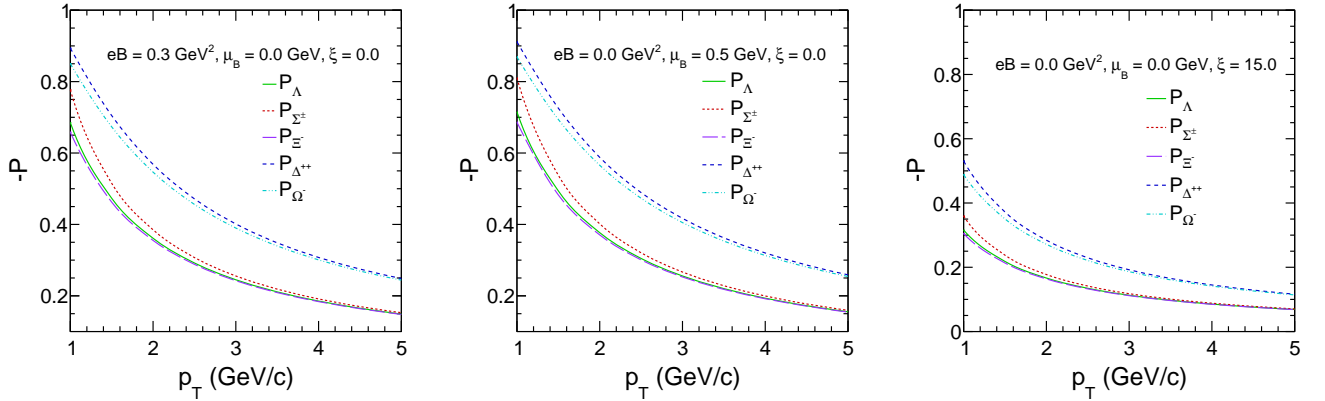


FIG. 4: (Color online)The variation of baryon polarization as a function of transverse momentum in the recombination process due to magnetic field (eB)(left panel), baryon chemical potential (μ_B)(middle panel) and anisotropic parameter (ξ)(right panel) at temperature $T = 200$ MeV.

of Λ hyperons aligns with the polarization of the initial strange quark. The initial strange quarks with lower momentum have higher values of Λ polarization after recombining to Λ hyperons and vice-versa. The middle panel of Fig. 2 illustrates the dependence of Λ hyperon polarization as a function of p_T for various values of chemical potential in the recombination scenario of hadronization. Three finite values of chemical potential are considered with $\mu_B = 0.1, 0.3,$ and 0.5 GeV. It can be seen here that there is no notable effect of baryon chemical potential on the polarization of Λ . The right panel of Fig. 2 depicts the variation of Λ polarization as a function of p_T for various values of the anisotropic parameter. Anisotropy in the medium is believed to restrict the alignment of particle spins along a specific

direction. Here, we considered four different values of anisotropic parameters, i.e., $\xi = 0.5, 1.0, 5.0, 15.0$, along with the isotropic case, i.e., $\xi = 0$. It is observed that the Λ hyperon polarization decreases with the anisotropy parameter. It is an intriguing observation that the medium anisotropy plays a significant role in influencing the polarization of Λ hyperons.

Figure 3 depicts the change in the Λ polarization with p_T corresponding to the fragmentation process of hadronization. The polarization of $\Lambda, \Sigma^\pm, \Xi^-, \Delta^{++},$ and Ω^- hyperons due to fragmentation is obtained using Eqs. 5, 6. The polarization corresponding to the fragmentation process is obtained using the n_s and f_s parameters. The values of these parameters

are extracted from Ref. [83]. Similar to Fig. 2, the polarization is shown for the same values of eB (left panel), μ_B (middle panel), and ξ (right panel) in Fig. 3. The p_T dependence of Λ hyperon polarization in the presence of an external magnetic field, baryon chemical potential, and medium anisotropy in the fragmentation process follow the same trend as the recombination process, except a change in the slope is observed at low p_T . However, the magnitude of Λ polarization due to fragmentation is comparably less than the recombination process.

Further, in Fig. 4, the variation in the polarization because of recombination is shown as a function of p_T at $eB = 0.3 \text{ GeV}^2$, $\mu_B = 0 \text{ GeV}$ and $\xi = 0$ for Λ , Σ^\pm , Ξ^- , Δ^{++} , and Ω^- hyperons. Moreover, we observe that the hyperon spin-polarization is dominant at low p_T . The middle and right panel of Fig. 4 shows Λ , Σ^\pm , Ξ^- , Δ^{++} , and Ω^- polarization with p_T for baryon chemical potential $\mu_B = 0.5 \text{ GeV}$ and anisotropic parameter $\xi = 15$, respectively. The role of baryon chemical potential on particle polarization is quite similar to the magnetic field. Fig. 4 indicates a quark flavor-dependent polarization of hyperons in the heavy-ion collisions. We found that there is grouping among the particles of baryon octet with spin-1/2 and baryon decouplet with spin-3/2 during the spin-orbit coupling. Particles having the same quark flavor, for example, Ω^- (sss) and Δ^{++} (uuu) have similar spin-orientation along the direction of OAM as compared to particles having mixed quark flavor, e.g., Λ (uds), Σ^\pm (uus/dds), and Ξ^- (dss). Therefore, particles of the same species possibly have some correlation among themselves, which drives the spin polarization. This correlation might be absent in mixed species particles; such an observation is recently reported for ϕ meson in Ref. [49]. In addition, the baryon-decouplet of spin-3/2 has higher polarization as compared to the baryon-octet of spin-1/2. Therefore, particle spin might play a role in its polarization. However, to confirm the importance of spin in the global polarization picture and to better understand the polarization mechanism in heavy-ion collisions, the experimental verification of global polarization for different particles with different spin and/or magnetic moments is required. Although the recent measurement global polarization of Ξ and Ω hyperons at STAR hint at a possible hierarchy in the global polarization, i.e., $P_\Lambda < P_\Xi < P_\Omega$ [36]. The large systematic and statistical uncertainties raise a question as to whether the difference is either due to the mass, lifetime, strangeness quantum number, differential freeze-out, etc.

Similarly, Fig. 5 shows the dependence of Λ , Σ^\pm , Ξ^- , Δ^{++} , and Ω^- hyperon polarization as a function of p_T in the presence of external magnetic field (left panel), baryon chemical potential (middle panel) and medium anisotropy parameters (right panel) in the fragmentation process of hadronization. In the fragmentation process, the polarization of Δ^{++} and Ω^-

is 1/3 of the polarization due to the u and s quarks, respectively. Therefore, baryons having the same quark flavor, each quark contributes equally to the final state baryon polarization. Meanwhile, baryons of mixed quark flavors have linear combinations due to each flavor. As consequence, a significant decrease in the Δ^{++} , and Ω^- polarization is observed compared to Λ , Σ^\pm , and Ξ^- in Fig 5. However, the polarization in the fragmentation process is always less compared to recombination for all baryons. The change in the polarization due to fragmentation in the presence of the magnetic field, baryon chemical potential, and medium anisotropy follow the same trend of the polarization obtained from the recombination process.

The left panel of Fig. 6 shows the combined effect of the magnetic field, baryon chemical potential, and medium anisotropy on Λ hyperon polarization. The interplay of these three effects is examined in Fig 6. We found that the medium anisotropy has a prevalent impact on the polarization observable as compared to the magnetic field and baryon chemical potential. The observed feature of medium anisotropy on polarization is due to the influence of anisotropy on Debye mass. Medium anisotropy plays a crucial role in controlling the spin-polarization of hyperon, which needs an extensive investigation from a theoretical standpoint. The right panel of Fig. 6 shows change in the polarization for Λ along with Σ^\pm , Ξ^- , Ω^- , and Δ^{++} baryons corresponding to the combined effect of the magnetic field, baryon chemical potential, and medium momentum-space anisotropy.

B. Spin alignment of vector mesons

Similar to the global polarization of hyperon, the spin-alignment of vector meson is also based on the same mechanism of spin-orbit coupling. Since a vector meson with spin one can have three different spin orientations, the probability for its spin to align in a given direction is 1/3. Any value of the spin alignment differs from 1/3, which means the polarization of the vector meson is along that direction. With the recent large spin alignment measurement of ϕ vector meson at RHIC [41, 42] and LHC [44], it becomes a challenging and active area of research for the theoretical community to know the possible sources of spin alignment for ϕ vector meson. The spin alignment of vector meson comes from both constituent quark and anti-quark and hence its polarization is quadratic in vorticity [56].

The left panel of Fig. 7 shows the effect of magnetic field on the spin alignment of ϕ meson for two different hadronization scenarios as described in formalism section II. The curves below line 1/3 depict the spin alignment of ϕ -meson due to the recombination of polarized

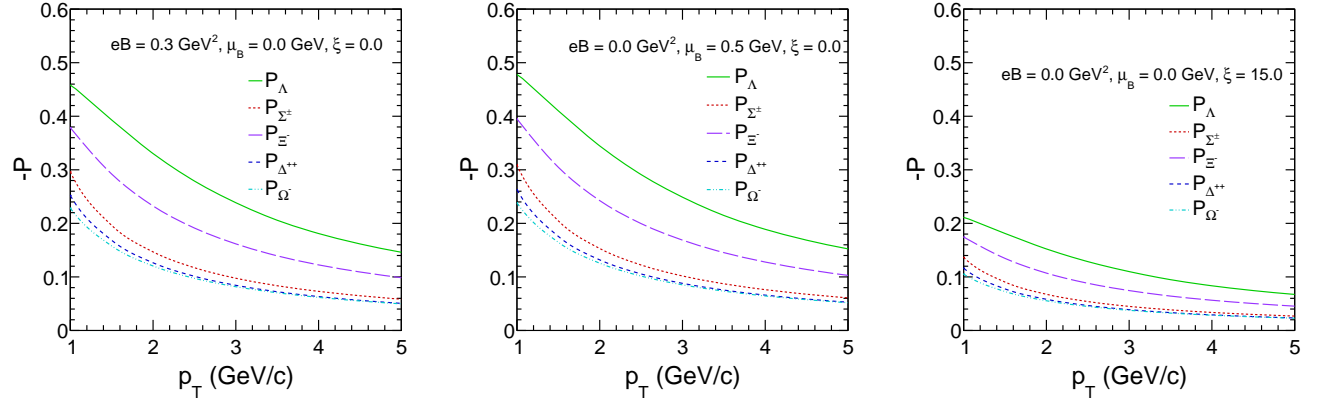


FIG. 5: (Color online) The variation of hyperon polarization as a function of transverse momentum due to the fragmentation process in the presence of magnetic field (eB)(left panel), baryon chemical potential (μ_B)(middle panel) and anisotropic parameter (ξ)(right panel) at temperature $T = 200$ MeV.

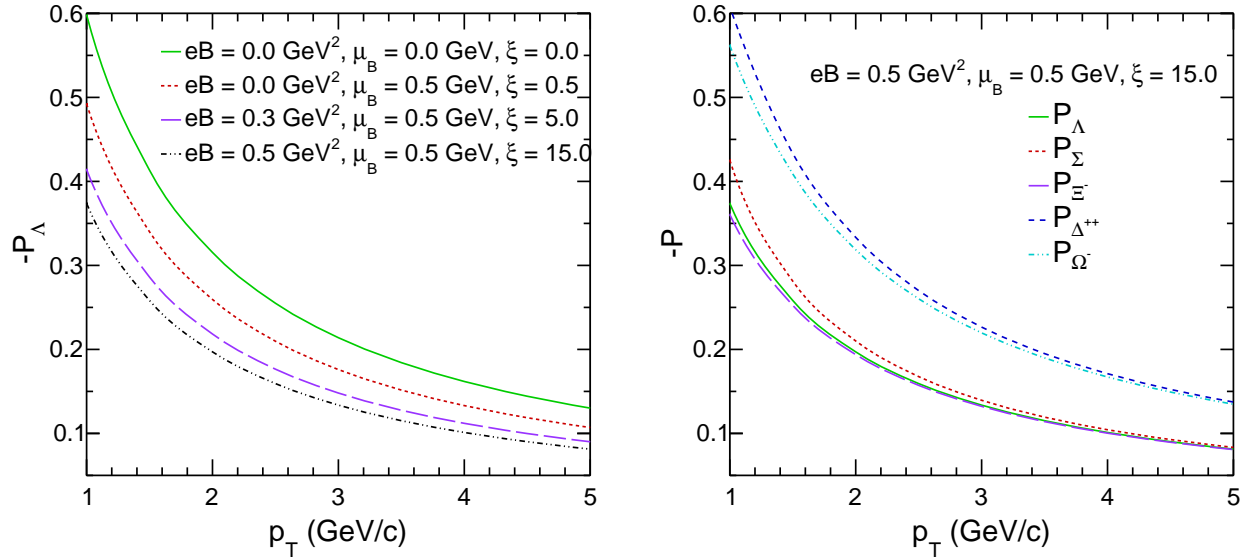


FIG. 6: (Color online) The variation of hyperon polarization as a function of transverse momentum due to magnetic field (left panel), baryon chemical potential (middle panel), and anisotropic parameter (right panel) at temperature $T = 200$ MeV.

quarks and anti-quarks. The curves above line 1/3 show the hadronization process of quark and anti-quark pairs in which either of them is created in the fragmentation process. We compare the obtained results with the STAR Collaboration data for Au+Au collisions for various centers of mass energies in (20-60)% bin [41]. The choice of center of mass energy selection of STAR data for Au+Au collisions in Fig 7 and Fig. 8 is just for illustration pur-

poses, and it has nothing specific relation with the magnetic field and anisotropy. It is found that the absolute deviation of ρ_{00} from 1/3 ($|\rho_{00} - 1/3|$) for ϕ vector meson increases with magnetic field for both cases of hadronization processes. The magnetic field aligns the particle spin in a specific direction; hence, it helps to enhance the degree of spin alignment. It is evident that the spin alignment of vector meson is directly proportional to

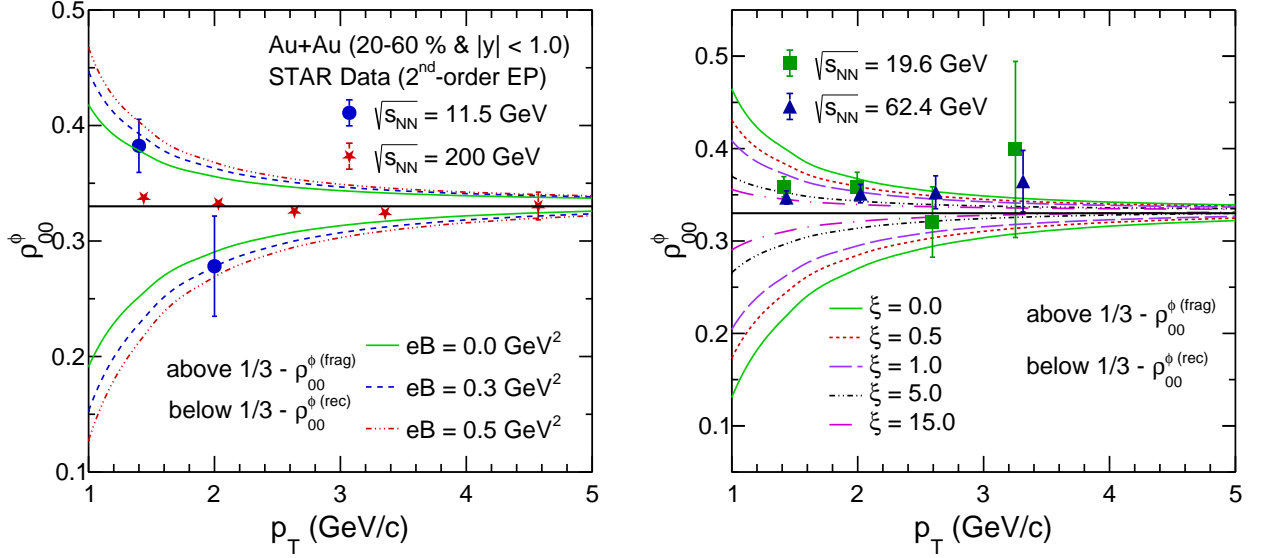


FIG. 7: (Color online) The variation of spin alignment of ϕ vector meson as a function of transverse momentum due to the magnetic field (left panel) and anisotropic parameter (right panel) at temperature $T = 200$ MeV. The results are compared with STAR measurements taken from Ref. [41].

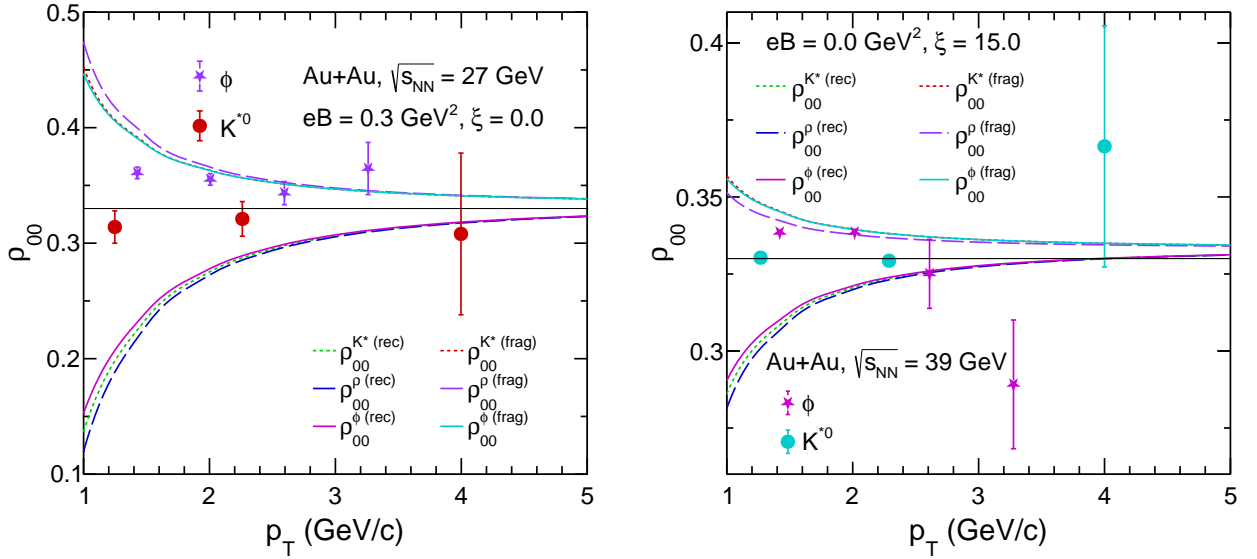


FIG. 8: (Color online) The variation of spin alignment of ϕ , K^{*0} , ρ vector meson as a function of transverse momentum due to the magnetic field (left panel), and anisotropic parameter (right panel) at temperature $T = 200$ MeV. The results are compared with STAR measurements taken from Ref. [41].

the square of the magnetic field. Since baryon chemical potential does not have a substantial effect on hyperon polarization, we have neglected the effect of baryon chemical potential on the spin alignment measurement of vector meson. The right panel of Fig. 7 shows the effect of ξ on the spin alignment of ϕ meson with a set of ξ values. From the figure, it is evident that medium anisotropy significantly modifies the vector meson spin alignment. The left panel of Fig. 8 shows the spin alignment of ϕ , K^* , and ρ meson at $eB = 0.5 \text{ GeV}^2$ for corresponding to fragmentation and recombination hadronization scenarios. The right panel of Fig. 8 shows the spin alignment of ϕ , K^* , and ρ meson for $\xi = 15$. Figure 7 and 8 depicts the absolute deviation of ρ_{00} from $1/3$ is more at low p_T for the recombination process as compared to the fragmentation. This implies that the degree of spin alignment is more at low p_T in the recombination process for ϕ , K^* , and ρ vector mesons. The value of ρ_{00} is close to $1/3$ towards high p_T showing zero spin alignment for ϕ , K^* , and ρ mesons. In the quark polarization model, the polarization of a quark is inversely proportional to the square of its mass, which suggests a mass ordering in the spin alignment effect of vector mesons due to their constituent quark composition. Figure 8 depicts $\rho_{00}^\rho > \rho_{00}^{K^*} > \rho_{00}^\phi$ at low p_T in the recombination scenario.

IV. CONCLUSION

In summary, we explored the global polarization of hyperons and spin-alignment of vector mesons in the presence of magnetic field, baryon chemical potential, and medium momentum-space anisotropy. The individual and combined effect of these parameters on hyperons and vector mesons polarization have been studied in the recombination and fragmentation process of hadronization. We found that the polarization of hyperons and spin-alignment of vector mesons increases with the increase in magnetic field. In this study, the baryon chemical potential has negligible dependence on hyperon polarization. The medium anisotropy significantly affects the polarization and spin alignment of

hadrons. It is interesting to note that the recombination process dominates at low p_T in comparison with the fragmentation process. The Debye mass-based polarization may have a substantial implication on particle production yield. Therefore, for a comprehensive study, one may include such an effect to study the hadron production in heavy-ion collisions.

The hyperon polarization obtained through the global quark polarization method is comparably higher than the experimentally measured hyperon polarization in heavy-ion collisions at RHIC. In addition to the magnetic field, baryon chemical potential, and medium momentum-space anisotropy used in this work, there may be various other sources that may affect the hyperon polarization. Such sources could be medium rotation, hadronic interactions, anisotropic flows in the medium, and fluctuation of other force fields such as vorticity, temperature gradient, shear tensor, strong force field, etc. However, the contribution of these sources on hyperon polarization has yet to be studied collectively. The qualitative prediction of global polarization is an open challenge and requires further investigation.

ACKNOWLEDGEMENT

Bhagyarathi Sahoo acknowledges the financial aid from CSIR, Government of India. The authors gratefully acknowledge the DAE-DST, Government of India funding under the mega-science project "Indian Participation in the ALICE experiment at CERN" bearing Project No.SR/MF/PS-02/2021-IITI (E-37123).

-
- [1] J. Adam *et al.* [ALICE Collaboration], *Nature Phys.* **13**, 535 (2017).
 - [2] V. Khachatryan *et al.* [CMS Collaboration], *Phys. Lett. B* **765**, 193 (2017).
 - [3] A. Ortiz Velasquez, P. Christiansen, E. Cuautle Flores, I. Maldonado Cervantes and G. Paić, *Phys. Rev. Lett.* **111**, 042001 (2013).
 - [4] C. Zhang, A. Behera, S. Bhatta and J. Jia, *Phys. Lett. B* **822**, 136702 (2021).
 - [5] B. Sahoo, D. Sahu, S. Deb, C. R. Singh and R. Sahoo, [arXiv:2308.15151 [hep-ph]].
 - [6] K. Fukushima, D. E. Kharzeev and H. J. Warringa, *Phys. Rev. D* **78**, 074033 (2008).
 - [7] D. E. Kharzeev, L. D. McLerran and H. J. Warringa, *Nucl. Phys. A* **803** 227 (2008).
 - [8] O. Rogachevsky, A. Sorin and O. Teryaev, *Phys. Rev. C* **82**, 054910 (2010).
 - [9] D. Kharzeev and A. Zhitnitsky, *Nucl. Phys. A* **797**, 67 (2007).
 - [10] F. Becattini and I. Karpenko, *Phys. Rev. Lett.* **120**, 012302 (2018).
 - [11] J. Adam *et al.* [STAR Collaboration], *Phys. Rev. Lett.* **123**, 132301 (2019).

- [12] Z. T. Liang and X. N. Wang, Phys. Rev. Lett. **94**, 102301 (2005). [erratum: Phys. Rev. Lett. **96** (2006), 039901]
- [13] Z. T. Liang and X. N. Wang, Phys. Lett. B **629**, 20 (2005).
- [14] Z. t. Liang, J. Phys. G **34**, S323-330 (2007).
- [15] J. H. Gao, S. W. Chen, W. t. Deng, Z. T. Liang, Q. Wang and X. N. Wang, Phys. Rev. C **77**, 044902 (2008).
- [16] D. L. Adams *et al.* [FNAL-E704], Phys. Lett. B **264**, 462(1991).
- [17] A. Ipp, A. Di Piazza, J. Evers and C. H. Keitel, Phys. Lett. B **666**, 315 (2008).
- [18] F. Becattini, V. Chandra, L. Del Zanna and E. Grossi, Annals Phys. **338** 32 (2013).
- [19] B. I. Abelev *et al.* [STAR Collaboration], Phys. Rev. C **76**, 024915 (2007).
- [20] L. Adamczyk *et al.* [STAR Collaboration], Nature **548** 62 (2017).
- [21] J. Adam *et al.* [STAR Collaboration], Phys. Rev. C **98**, 014910 (2018).
- [22] S. Alzhrani, S. Ryu and C. Shen, Phys. Rev. C **106**, 014905 (2022).
- [23] O. Vitiuk, L. V. Bravina and E. E. Zabrodin, Phys. Lett. B **803**, 135298 (2020).
- [24] Y. Jiang, Z. W. Lin and J. Liao, Phys. Rev. C **94** (2016) no.4, 044910 [erratum: Phys. Rev. C **95** (2017) no.4, 049904]
- [25] Y. Sun and C. M. Ko, Phys. Rev. C **96**, 024906 (2017).
- [26] Y. B. Ivanov, V. D. Toneev and A. A. Soldatov, Phys. Rev. C **100**, 014908 (2019).
- [27] K. K. Pradhan, B. Sahoo, D. Sahu and R. Sahoo, [arXiv:2304.05190 [hep-ph]].
- [28] L. P. Csernai, V. K. Magas and D. J. Wang, Phys. Rev. C **87**, 034906 (2013).
- [29] L. P. Csernai, D. J. Wang, M. Bleicher and H. Stöcker, Phys. Rev. C **90**, 021904 (2014).
- [30] L. G. Pang, H. Petersen, Q. Wang and X. N. Wang, Phys. Rev. Lett. **117**, 192301 (2016).
- [31] H. Li, L. G. Pang, Q. Wang and X. L. Xia, Phys. Rev. C **96**, 054908 (2017).
- [32] B. Fu, K. Xu, X. G. Huang and H. Song, Phys. Rev. C **103**, 024903 (2021).
- [33] I. Karpenko and F. Becattini, Nucl. Phys. A **967**, 764 (2017).
- [34] F. Becattini and M. A. Lisa, Ann. Rev. Nucl. Part. Sci. **70**, 395 (2020).
- [35] Xie, Y., Wang, D. and Csernai, L.P., Eur. Phys. J. C **80**, 39 (2020).
- [36] J. Adam *et al.* [STAR Collaboration], Phys. Rev. Lett. **126**, 162301 (2021).
- [37] S. Acharya *et al.*, [ALICE Collaboration], Phys. Lett. B **815**, 136146 (2021).
- [38] S. Acharya *et al.*, [ALICE Collaboration], Phys. Rev. Lett. **131**, 042303 (2023).
- [39] L. Adamczyk *et al.*, [STAR Collaboration], Phys. Lett. B **739**, 180 (2014).
- [40] J. Adam *et al.*, [STAR Collaboration], Phys. Rev. D **102**, 092009 (2020).
- [41] M. S. Abdallah *et al.* [STAR Collaboration], Nature **614** 244 (2023).
- [42] S. Singha [STAR Collaboration], Nucl. Phys. A **1005**, 121733 (2021).
- [43] B. I. Abelev *et al.* [STAR Collaboration], Phys. Rev. C **77**, 061902 (2008).
- [44] S. Acharya *et al.* [ALICE Collaboration], Phys. Rev. Lett. **125**, 012301 (2020).
- [45] R. Singh [ALICE Collaboration], Nucl. Phys. A **982**, 515 (2019).
- [46] B. Mohanty, S. Kundu, S. Singha and R. Singh, Mod. Phys. Lett. A **36**, 2130026 (2021).
- [47] L. P. Csernai, J. I. Kapusta and T. Welle, Phys. Rev. C **99**, 021901 (2019).
- [48] X. L. Sheng, L. Oliva and Q. Wang, Phys. Rev. D **101**, 096005 (2020). [erratum: Phys. Rev. D **105**, 099903 (2022).]
- [49] X. L. Sheng, L. Oliva, Z. T. Liang, Q. Wang and X. N. Wang, Phys. Rev. Lett. **131**, 042304 (2023).
- [50] F. Becattini, M. Buzzegoli, G. Inghirami, I. Karpenko and A. Palermo, Phys. Rev. Lett. **127**, 272302 (2021).
- [51] H. Z. Wu, L. G. Pang, X. G. Huang and Q. Wang, Phys. Rev. Research. **1**, 033058 (2019).
- [52] X. L. Xia, H. Li, X. G. Huang and H. Zhong Huang, Phys. Lett. B **817** (2021), 136325
- [53] V. Skokov, A. Y. Illarionov and V. Toneev, Int. J. Mod. Phys. A **24**, 5925 (2009).
- [54] B. Sahoo, C. R. Singh, D. Sahu, R. Sahoo and J. e. Alam, Eur. Phys. J. C **83**, 873 (2023).
- [55] B. Sahoo, K. K. Pradhan, D. Sahu and R. Sahoo, Phys. Rev. D **108**, 074028 (2023).
- [56] Y. G. Yang, R. H. Fang, Q. Wang and X. N. Wang, Phys. Rev. C **97**, 034917 (2018).
- [57] X. L. Sheng, Q. Wang and X. N. Wang, Phys. Rev. D **102**, 056013 (2020).
- [58] F. Becattini, I. Karpenko, M. Lisa, I. Upsal and S. Voloshin, Phys. Rev. C **95**, 054902 (2017).
- [59] S. Wu and Y. Xie, Eur. Phys. J. A **59**, 108 (2023).
- [60] Z. Z. Han and J. Xu, Phys. Lett. B **786**, 255 (2018).
- [61] K. Xu, F. Lin, A. Huang and M. Huang, Phys. Rev. D **106**, L071502 (2022).
- [62] A. Ayala, M. A. Ayala Torres, E. Cuautle, I. Domínguez, M. A. Fontaine Sanchez, I. Maldonado, E. Moreno-Barbosa, P. A. Nieto-Marín, M. Rodríguez-Cahuantzi and J. Salinas, *et al.* Phys. Lett. B **810**, 135818 (2020).
- [63] X. Guo, J. Liao and E. Wang, Sci. Rep. **10**, 2196 (2020).
- [64] J. H. Gao, Z. T. Liang, S. Pu, Q. Wang and X. N. Wang, Phys. Rev. Lett. **109**, 232301 (2012).
- [65] L. Dong, Y. Guo, A. Islam and M. Strickland, Phys. Rev. D **104**, 096017 (2021).
- [66] B. Karmakar, A. Bandyopadhyay, N. Haque and M. G. Mustafa, Eur. Phys. J. C **79**, 658 (2019).
- [67] H. X. Zhang, J. W. Kang and B. W. Zhang, Eur. Phys. J. C **81**, 623 (2021).
- [68] A. Bandyopadhyay, B. Karmakar, N. Haque and M. G. Mustafa, Phys. Rev. D **100**, 034031 (2019).
- [69] B. Singh, L. Thakur and H. Mishra, Phys. Rev. D **97**, 096011 (2018).
- [70] N. Haque, A. Bandyopadhyay, J. O. Andersen, M. G. Mustafa, M. Strickland and N. Su, JHEP **05**, 027 (2014).
- [71] J. Zhao and B. Chen, Phys. Rev. C **107**, 044909 (2023).
- [72] D. Lafferty and A. Rothkopf, Phys. Rev. D **101**, 056010 (2020).
- [73] G. Huang and P. Zhuang, Phys. Rev. D **104**, 074001 (2021).
- [74] M. Le Bellac, Thermal Field Theory (Cambridge University Press, Cambridge, England, 1996).
- [75] L. Dong, Y. Guo, A. Islam, A. Rothkopf and M. Strickland, JHEP **09**, 200 (2022).

- [76] M. Strickland and D. Bazow, Nucl. Phys. A **879**, 25-58 (2012).
- [77] P. Romatschke and M. Strickland, Phys. Rev. D **68**, 036004 (2003).
- [78] P. Romatschke and M. Strickland, Phys. Rev. D **70**, 116006 (2004).
- [79] M. Strickland, Anisotropic hydrodynamics: Three lectures, Acta Phys. Pol. B 45, 2355 (2014).
- [80] C. Bonati, M. D'Elia, M. Mariti, M. Mesiti, F. Negro, A. Rucci and F. Sanfilippo, Phys. Rev. D **95**, 074515 (2017).
- [81] A. Bandyopadhyay, C. A. Islam and M. G. Mustafa, Phys. Rev. D **94**, 114034 (2016).
- [82] A. Bandyopadhyay, R. L. S. Farias, B. S. Lopes and R. O. Ramos, Phys. Rev. D **100**, 076021 (2019).
- [83] J. w. Zhang, H. h. Li, F. l. Shao and J. Song, Chin. Phys. C **44**, 014101 (2020).

Constraining Asymmetric Dark Matter using Colliders and Direct Detection

Arnab Roy , ^{a,b} Basudeb Dasgupta , ^a and Monoranjan Guchait  ^a

^a *Tata Institute of Fundamental Research, Homi Bhabha Road, Colaba, Mumbai 400005, India*

^b *School of Physics and Astronomy, Monash University,
Wellington Road, Clayton, Victoria 3800, Australia*

E-mail: arnab.roy1@monash.edu, bdasgupta@theory.tifr.res.in,
guchait@tifr.res.in

ABSTRACT: We reappraise the viability of asymmetric dark matter (ADM) realized as a Dirac fermion coupling dominantly to the Standard Model fermions. Treating the interactions of such a DM particle with quarks/leptons in an effective-interactions framework, we derive updated constraints using mono-jet searches from the Large Hadron Collider (LHC) and mono-photon searches at the Large Electron-Positron (LEP) collider. We carefully model the detectors used in these experiments, which is found to have significant impact. The constraint of efficient annihilation of the symmetric part of the ADM, as well as other observational constraints are synthesized to produce a global picture. Consistent with previous work, we find that ADM with mass in the range 1–100 GeV is strongly constrained, thus ruling out its best motivated mass range. However, we find that leptophilic ADM remains allowed for $\gtrsim 10$ GeV DM, including bounds from colliders, direct detection, and stellar heating. We forecast that the Future Circular Collider for electron-positron collisions (FCC-ee) will improve sensitivity to DM-lepton interactions by almost an order of magnitude.

Contents

1	Introduction	1
2	Dark Matter Interactions and Production	3
2.1	Effective interactions	3
2.2	Relic density and the asymmetry criterion	4
3	Constraining ADM-Quark Interactions	6
3.1	Mono-jet searches at hadron colliders	6
3.2	Direct detection experiments	7
3.3	Constraints on the $\Lambda - m_\chi$ plane	8
4	Constraining ADM-Lepton Interactions	11
4.1	Mono-photon searches at LEP	11
4.2	Discovery potential of ADM at FCC-ee	14
4.3	Constraints from compact stars and direct detection	15
4.4	Constraints and discovery potential for leptophilic ADM	16
5	Summary and Outlook	18
A	Expressions of $\langle\sigma v\rangle$ for different operators	21

1 Introduction

Despite the significant asymmetry between the cosmological abundances of matter and antimatter, we observe comparable abundances of ordinary matter, dominated by baryons (b), and of dark matter (DM), namely $\Omega_b \simeq \Omega_{\text{DM}}/5$ [1]. This observation has motivated the Asymmetric Dark Matter (ADM) hypothesis [2–5]. Here, the similar baryon and DM abundances are a consequence of both densities arising from an asymmetry of the corresponding Dirac fermion over its anti-fermion, with the two asymmetries related to each other in some way [6–11]. Similar to models of weakly interacting massive particle type DM, where the DM is produced via thermal freeze-out and traditionally thought of as having mass near the electroweak scale, the models for ADM are also testable at particle colliders because the expected mass-range for ADM particles is around the GeV scale or close to it. This is because ADM models predict that the number abundances, n_{DM} and n_b , are similar and the ratio of observed mass abundances then predicts ADM particles at the GeV-scale [12–21].

The ADM hypothesis therefore presents a theoretical alternative to WIMPs, retaining almost all of its strengths. These models are well-motivated from the ultraviolet considerations, such as GUTs and additional confined gauge sectors [22–31]. They are conceptually

minimal, employing the mathematical structures and physical mechanisms that are believed to already underlie the Standard Model, e.g., Dirac fermions, particle-antiparticle asymmetry, gauge interactions, anomalies, and sphalerons. And importantly, they predict GeV-scale masses for the DM particle, with observable signals not only at direct detection (DD) experiments and colliders, but also constraints from astrophysics and cosmology.

While considerable attention has been devoted to the theories of ADM, its detectability in particle colliders remains relatively less well-explored. A previous study by March-Russell et al. (2012) [32] presented collider and DD constraints on ADM, together with the constraints imposed by the model itself. The key idea being that efficient annihilation of the symmetric part of the ADM relic density requires that the coupling between DM and SM fermions cannot be too weak. This is under the usual simplifying assumption that the dark matter annihilates into and scatters off SM fermions, and these processes are mediated by the same elementary interaction. Quite remarkably, already in this early work, it was found that collider data and direct detection searches practically rule out ADM with mass all the way up to 100 GeV or more.

Developments over the past decade motivate a reappraisal. Continued data-taking at the LHC as well as at the significantly more sensitive and diverse set of DD searches now allow a more comprehensive study of ADM couplings to SM fermions. Further, there is a renewed interest in ADM, especially in connection to their dramatic impact on compact stars [33–52]. And finally, several new DM experiments [53], as well as experiments at the HL-LHC, aim to search widely for DM, which motivate an updated idea of *‘where to look for new physics’*.

In this study, we revisit collider constraints on ADM and provide new and updated bounds on the interactions between ADM and quarks/leptons. Our analysis includes a careful incorporation of detector efficiencies, corresponding to different phase space regions of the final state particles. For DM-quark interactions, our collider limits are based on the outcomes of mono-jet searches conducted at the LHC. Further, by combining other DD and collider bounds on DM with the prerequisites of the ADM hypothesis, we find that all the operators we consider are ruled out for DM mass up to a few hundred GeV; for some operators the exclusion stretches almost to TeV masses. *Prima facie* the basic ADM scenario appears strongly disfavored.

We then turn our attention to a leptophilic variant of the ADM scenario, where ADM couples to SM leptons but not to quarks. Such ADM models may be motivated by theory, and are poised to take advantage of the upcoming experiments. In some ADM models, the DM asymmetry fundamentally arises due to new sphalerons that transform the lepton asymmetry created by leptogenesis into a DM asymmetry. Here, a chiral gauge interaction shared by DM and leptons directly leads to the above phenomenology and does not necessarily need to involve quarks. On the observational side, DM interactions with leptons (electrons, in particular) has gained interest over the past decade. Unsurprisingly, DM-lepton interactions have been studied in depth [13, 54–68] and a gamut of experiments have already produced interesting limits on leptophilic DM [69–72]. More importantly, there are now several novel proposals that promise to make significant progress in this direction in the near future [73–89]. Limits on DM-lepton interactions from the heating of neutron stars

(NS) [90] and white dwarfs (WD) [91] happen to provide some of the strongest constraints. On the collider front, mono-photon searches at LEP have been set bounds on four effective operators (three of which are independent) [92], which are more stringent than the NS or WD bounds for DM masses in the 1-100 GeV range. Investigations have also focused on the prospects of identifying leptophilic dark matter through future lepton colliders, mainly the International Linear Collider (ILC) [93–95]. In the latter part of this paper, we update the bounds on DM-lepton interactions using the LEP mono-photon searches, compare with other constraints as for the quark case, and appraise the viability of leptophilic ADM. We also forecast discovery prospects at the prospective FCC-ee.

The structure of this paper is as follows. In Section 2, we start by establishing the EFT framework and provide a brief introduction to the ADM hypothesis and review the existing constraints on interactions between ADM and quarks. In Section 3, we calculate new bounds on the ADM-quark interactions from the mono-jet searches at the LHC and present the constraints on ADM-quark interactions for all EFT operators. Additionally, in Section 4, we investigate the DM-lepton interactions. Here, a comprehensive methodology to calculate the LEP bounds are presented, followed by the FCC-ee discovery prospects. The combined pictures of the allowed (and excluded) regions of ADM-lepton interactions from all relevant searches are presented at the end of section 4. Lastly, Section 5 summarizes our findings and concludes.

2 Dark Matter Interactions and Production

2.1 Effective interactions

We assume the DM is a Dirac fermion and the mediators responsible for its interactions with the SM particles are heavier than the DM itself. The interactions are thus encoded in higher-dimensional operators within the framework of an effective field theory (EFT) involving SM and DM degrees of freedom. However, we will ignore the dimension-5 couplings of DM to the SM Higgs, which is already very well studied and constrained. See, for example, the stringent upper limits of $H_{\text{SM}} \rightarrow$ invisible branching fractions [96, 97].¹ With these considerations, in Table 1 we write down all allowed EFT operators at dimension-6. These operators are of the form

$$\mathcal{O}_{\Gamma\Gamma'} = \frac{1}{\Lambda^2} (\bar{\psi}\Gamma\psi)(\bar{\chi}\Gamma'\chi), \quad (2.1)$$

where ψ and χ are Dirac fermion SM and DM particles, respectively, whereas $\Gamma^{(\prime)}$ s are strings of gamma matrices,

$$\Gamma = \{1, \gamma^5, \gamma^\mu, \gamma^\mu\gamma^5, \sigma^{\mu\nu}, \sigma^{\mu\nu}\gamma^5\}. \quad (2.2)$$

¹Note that the Higgs portal for fermionic DM of mass smaller than ~ 20 GeV, consistent with $\text{BR}(H_{\text{SM}} \rightarrow \text{invisible}) < 10\%$, leads to DM-nucleon scattering cross-section below the “neutrino floor” [98–100], which is uninteresting from DD perspective [101]. Alternatively, though a higher mass region of DM allows parameter regions above the neutrino floor, they are excluded by the DD limits [101].

Table 1: List of dimension-6 operators connecting SM fermions to Dirac DM with flavor-universal couplings, along with the dependence of the scattering cross section on the spin of the SM target (and the leading dependence on q or v), as well as the leading partial-wave contribution to the corresponding annihilation rate; q and v denote the magnitude of transferred momentum and the relative velocity between the target and the DM, respectively.

Operator	Definition	Scattering	Annihilation
\mathcal{O}_{ss}	$\bar{\psi}\psi\bar{f}f$	SI (1)	p -wave
\mathcal{O}_{pp}	$\bar{\psi}\gamma^5\psi\bar{f}\gamma^5f$	SD (q^2)	s -wave
\mathcal{O}_{sp}	$\bar{\psi}\psi\bar{f}i\gamma^5f$	SD (q)	p -wave
\mathcal{O}_{ps}	$\bar{\psi}i\gamma^5\psi\bar{f}f$	SI (q)	s -wave
\mathcal{O}_{vv}	$\bar{\psi}\gamma^\mu\psi\bar{f}\gamma_\mu f$	SI (1)	s -wave
\mathcal{O}_{aa}	$\bar{\psi}\gamma^\mu\gamma^5\psi\bar{f}\gamma_\mu\gamma^5f$	SD (1)	s -wave $\propto m_q^2/m_\chi^2$
\mathcal{O}_{va}	$\bar{\psi}\gamma^\mu\psi\bar{f}\gamma_\mu\gamma^5f$	SD (v)	s -wave
\mathcal{O}_{av}	$\bar{\psi}\gamma^\mu\gamma^5\psi\bar{f}\gamma_\mu f$	SD (v)	p -wave
\mathcal{O}_{tt}	$\bar{\psi}\sigma^{\mu\nu}\psi\bar{f}\sigma_{\mu\nu}f$	SD (1)	s -wave
\mathcal{O}_{pt}	$\bar{\psi}i\sigma^{\mu\nu}\gamma^5\psi\bar{f}\sigma_{\mu\nu}f$	SI (q)	s -wave

Among the tensor operators, $\bar{\psi}\sigma^{\mu\nu}\psi\bar{f}i\sigma_{\mu\nu}\gamma^5f$ is rewritable as $\bar{\psi}i\sigma^{\mu\nu}\gamma^5\psi\bar{f}\sigma_{\mu\nu}f \equiv \mathcal{O}_{pt}$ and $\bar{\psi}i\sigma^{\mu\nu}\gamma^5\psi\bar{f}i\sigma_{\mu\nu}\gamma^5f$ as $\bar{\psi}\sigma^{\mu\nu}\psi\bar{f}\sigma_{\mu\nu}f \equiv \mathcal{O}_{tt}$. So they are not separately considered. Moreover, operators enter the Lagrangian along with respective Wilson coefficients (WC). In this work, we will consider that the WCs are absorbed into the Λ .

Using available data, we will determine the viability of each of these operators as a function of the DM mass m_χ and the EFT expansion scale Λ . Note that the operators, \mathcal{O}_{ss} , \mathcal{O}_{vv} , \mathcal{O}_{aa} and \mathcal{O}_{tt} present velocity-unsuppressed interactions with nucleon, while the other interactions are suppressed. On the other hand, operators marked as SI are spin independent (i.e., do not depend on the spin of the target SM fermion), and thus allow more sensitive searches that can take advantage of coherent enhancement. For a detailed discussion of these non-relativistic dependencies of DM, see Ref. [102]. The annihilation rate, $\langle\sigma v\rangle$, also depends on the velocity of DM. While s -wave annihilation is independent of velocity, p -wave annihilation is velocity-dependent and thus suppressed. As a result, \mathcal{O}_{ss} , \mathcal{O}_{sp} , and \mathcal{O}_{av} lead to a velocity-suppressed annihilation rate. It is worth noting that, although annihilation for \mathcal{O}_{aa} occurs through s -wave, it is suppressed by a factor proportional to m_q^2/m_χ^2 .

2.2 Relic density and the asymmetry criterion

The asymmetric dark matter paradigm assumes that both DM (χ) and the anti-DM ($\bar{\chi}$) are present up to some era of the evolution of the Universe, as in the case of baryonic matter. Then by some mechanism, an asymmetry is generated between DM and anti-DM sectors, which gets frozen out with the departure from thermal equilibrium, and the symmetric part

gets annihilated out. In this study we remain agnostic about the asymmetry generation and sharing mechanisms.

The total dark-abundance can be written as the sum of the yields of DM and anti-DM, i.e., $Y_\chi + Y_{\bar{\chi}}$, where the yield $Y = n/s$ is defined as the number density scaled by the entropy density of the early universe. This, in turn can be expressed as a symmetric and an asymmetric component:

$$Y_{\text{tot}} = Y_\chi + Y_{\bar{\chi}} = (Y_\chi - Y_{\bar{\chi}}) + 2Y_{\bar{\chi}} = Y_{\text{asy}} + Y_{\text{sym}}, \quad (2.3)$$

where, Y_{asy} is the asymmetric yield, and Y_{sym} is the yield of the symmetric component.

For the symmetric part, following [103], we take

$$Y_{\text{sym}} = 2Y_{\bar{\chi}} = \frac{2Y_{\text{asy}}}{\exp\left[Y_{\text{asy}}\lambda\left(\frac{a}{x_F} + \frac{3b}{x_F^2}\right)\right] - 1}, \quad (2.4)$$

where a and b are coefficients in the partial wave expansion of $\langle\sigma v\rangle$, λ is a function of DM mass:

$$\lambda = \frac{4\pi}{\sqrt{90}} m_\chi M_{\text{pl}} \sqrt{g_*}, \quad (2.5)$$

with reduced Planck mass $M_{\text{pl}} = 2.4 \times 10^{18}$ GeV, and $g_* \sim 100$ being the number of available relativistic degrees of freedom at freeze-out. Also, the shifted coordinate x_F is given by [103]

$$x_F = x_{F_0} \left(1 + 0.285 \frac{a\lambda Y_{\text{asy}}}{x_{F_0}^3} + 1.35 \frac{b\lambda Y_{\text{asy}}}{x_{F_0}^4} \right), \quad (2.6)$$

with $x_{F_0} = m_\chi/T_F$ being the usual coordinate at freeze-out. The difference between x_F and x_{F_0} encodes the ADM correction to the $\bar{\chi}$ abundance, which is otherwise under-predicted by the standard WIMP treatment. The expressions of the annihilation cross-sections times velocity for each of the operators in Table 1 are given in Appendix A.

The constraint imposed in ADM model is that the symmetric part, as in Eq. 2.4, must be decidedly sub-leading to the asymmetric part. We implement this by restricting Y_{sym} to contribute $\leq 1\%$ (say) to $\Omega_{\text{DM}} h^2$ [32]:

$$Y_{\text{sym}} \leq \frac{1}{100} \times \frac{\Omega_{\text{DM}} h^2}{2.76 \times 10^8} \left(\frac{\text{GeV}}{m_\chi} \right). \quad (2.7)$$

This is to be achieved by annihilating out the symmetric component ($Y_{\text{sym}} \rightarrow 0$) into SM fermions using the operators presented in Table 1. When there is a stronger interaction between DM and SM particles, it becomes easier to annihilate the symmetric part. However, it also makes more challenging to pass the constraints set by various experiments. For instance, at a specific value of the DM mass m_χ , a large Λ implies less effective scattering interactions (SI or SD) with quarks, but at the same time, it also indicates less efficient annihilation in the early universe. Consequently, the requirement for efficient annihilation sets an upper limit on Λ (say, $\Lambda < \Lambda_1$) via Eq. 2.7. In contrast, null results from DD

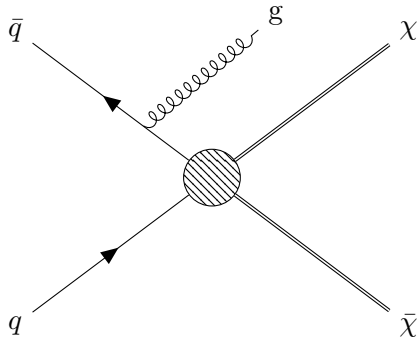


Figure 1: Representative Feynman diagram of mono-jet production along with DM.

experiments establish a lower limit ($\Lambda > \Lambda_2$). The space that lies in-between, if it exists (i.e., $\Lambda_1 > \Lambda_2$), defines the permissible range for ADM scenarios. However, if one finds $\Lambda_1 \leq \Lambda_2$ in a particular mass range, it rules out the feasibility of an ADM scenario within that region. Operators that lead to p -wave annihilation, such as \mathcal{O}_{ss} , \mathcal{O}_{sp} , and \mathcal{O}_{av} , require a lower value of Λ to satisfy the ADM requirement, resulting in stronger exclusions.

3 Constraining ADM-Quark Interactions

In this section, we first revisit the constraints on the DM-quark effective interactions and then find their implications on ADM scenario. The DM-quark interactions are mainly constrained by the DD experiments and the results of mono-jet searches at the LHC, where direct interaction of DM with quarks is present. These constraints were already shown in Ref. [32]. More extensive experimental results and several new searches have come up since, which are expected to impose stronger and more robust constraints. In this section, we update the bounds derived from mono-jet searches at LHC using latest data and by taking relevant detector effects into account. We then present the big picture for ADM-quark interactions, comparing with constraints from the asymmetry, and including other important constraints, especially those from recent DD experiments.

3.1 Mono-jet searches at hadron colliders

Any non-vanishing effective interactions between DM and quarks, listed in Table 1, should pair-produce DM through p - p collision at the LHC, if its mass is within the reach of LHC energy, $\sqrt{s} = 13$ TeV. However, production of solely DM particles does not yield any detectable signals within the detector, since they do not interact with the detector. Only if the DM particles are accompanied by some visible particles, then the imbalance of the transverse momentum (p_T) can be measured by detecting the visible particles, such as mono-jet, where one extra jet is produced along with the DM (see Fig. 1 for a representative Feynman diagram), and results in signals of energetic jets with missing p_T (\cancel{E}_T),

$$pp \rightarrow \chi\bar{\chi}j \rightarrow \cancel{E}_T j. \quad (3.1)$$

At the LHC Run-II experiment, both ATLAS and CMS experiments have reported their results of mono-jet searches [104, 105]. Ref. [104] looks for jets with high p_T with

Table 2: 95% CL upper limits on the visible mono-jet production cross-section at the LHC ($\sqrt{s} = 13$ TeV) [104].

Selection criteria	$\sigma^{95}(\text{fb})$
$p_T^j > 200$ GeV	736
$p_T^j > 1200$ GeV	0.3

different selection criteria on p_T of the jet. Since the mono-jet cross-section drops with the p_T of jet, a lower p_T selection includes a larger fraction of events in the low p_T region, but fewer events in the high p_T region. Contrarily, a higher p_T cut includes the fraction of events from the higher p_T phase space only. As the scaling of the cross-section of SM backgrounds with p_T may not necessarily be identical to the DM signal, mono-jet analyses with different p_T cuts result in different levels of exclusion on the DM-quark interactions. In order to interpret results of mono-jet searches within the framework of effective interactions considered here, we closely follow analysis strategy described in Ref. [104], as shown in Table 2.

The hard-scattering matrix elements are generated in MG5aMC_atNLO-3.3.0 [106] using Feynrules UFO [107] package, which is required to include the effective interactions for a given set of parameters (Λ, m_χ). Events are produced up to one jet in Madgraph, and MLM-matching is used to avoid double counting, which is essential in reproducing a mono-jet analysis. The showering and hadronization are performed using PYTHIA8 [108, 109]. Unlike the previous study [32], we consider the ATLAS detector effects using Delphes [110] ATLAS-card. After applying specific cuts on p_T^j (see Table 2), we can determine the acceptance rate of the signal. It is obtained by dividing the number of events that meet the criteria on p_T^j (N) by the total number of simulated events (N_0), i.e., $\mathcal{A} = N/N_0$. However, it is important to note that various detector efficiencies (ϵ) are already applied during the simulation, and their impacts are already included in the value of N . Therefore, for a given parameter space, taking into account the effects of DM-EFT, we calculate the measurable cross-section, $\sigma_{\text{mes}} = \sigma \times \mathcal{A}$. If σ_{mes} is greater than the experimentally determined 95% upper limit, then we claim that the given choice of $\{\Lambda, m_\chi\}$ is excluded. Repeating this procedure for various values of $\{\Lambda, m_\chi\}$, finally we obtain the excluded region in the $\Lambda - m_\chi$ plane due to the mono-jet searches, as shown in Figs. 2-6.

3.2 Direct detection experiments

DM can interact with the nucleon via the effective interactions listed in the Table 1. The strength ($1/\Lambda$) of the interactions affect the DM-nucleon scattering cross-section. Thus, the bounds on the DM-nucleon scattering cross-section can be recast as constraints on these interactions in terms of Λ and mass of DM (m_χ). Notice that, the spin-dependence of the scattering cross-section significantly impacts the bounds placed on each effective operator in Table 1. Some of the interactions get suppressed by the powers of DM velocity (v). For

example, the vector current singles out the temporal component of a spinor and the axial-vector current picks up the spatial component. Consequently, the combinations of these two (\mathcal{O}_{av} or \mathcal{O}_{va}) are velocity suppressed, and eventually leading to weaker bounds from the DD experiments. On the other hand, spin-independent DM-nucleon scattering cross-section often turn out to be restricted severely. Considering universal coupling to quarks, the scattering cross-section for each of the non-suppressed spin-independent interactions listed in Table 1 are given by [32],

$$\sigma_{\text{SI}}^{\mathcal{O}_{ss}} \sim \frac{1}{\pi\Lambda^4} \mu_p^2 f_p^2, \quad (3.2)$$

$$\sigma_{\text{SI}}^{\mathcal{O}_{vv}} \sim \frac{9}{\pi\Lambda^4} \mu_p^2, \quad (3.3)$$

where, $\mu_p = m_\chi m_p / (m_\chi + m_p)$ is the reduced mass of the nucleon-DM system and f_p is the DM effective coupling to protons. Here we use $f_p = 0.3$ [111]. The non-suppressed scattering cross-section for the spin-dependent operators listed in Table 1 is [32]:

$$\sigma_{\text{SD}}^{\mathcal{O}_{tt}} \sim 4 \times \sigma_{\text{SD}}^{\mathcal{O}_{aa}} \sim \frac{16}{\pi\Lambda^4} \mu_p^2 \left(\sum_q \Delta_q^p \right)^2, \quad (3.4)$$

where Δ_q^p accounts for the spin content of the nucleon and $(\sum_q \Delta_q^p)^2 \simeq 0.32$ [112].

The LUX-ZEPLIN (LZ) experiment currently provides the most stringent constraint on the cross-section for SI scattering between DM and nucleons. Specifically, they reported a limit of $6.5 \times 10^{-48} \text{ cm}^2$ on σ_{SI} at 90% CL for 19 GeV DM mass [113]. In parallel, the DarkSide-50 experiment excluded a cross-section of 10^{-41} cm^2 for DM-nucleon SI interactions with a 90% CL, for a DM particle mass of 1.8 GeV [114]. The constraints on the SD scattering cross-sections of dark matter with protons and neutrons have also improved for large ranges of DM particle masses. Notably, the most stringent limits on DM-neutron interactions originate from the XENON- n T experiment [115], having a minimum of $6.3 \times 10^{-42} \text{ cm}^2$ for DM mass 30 GeV at 90% CL. Whereas, for DM-proton interactions the PICO-60 experiment [116] sets the strongest constraints, e.g., $2.5 \times 10^{-41} \text{ cm}^2$ for DM mass 25 GeV at 90% CL.

To interpret these findings in the EFT context, we have converted the limits on DM-nucleon scattering cross-sections to the plane defined by the dark matter particle mass (m_χ) and the EFT scale (Λ), using Eqns. (3.3) and (3.4). Additionally, for the sake of comparison against the constraints outlined in Ref. [32], we have included the bounds predicted by the XENON-100 experiment [117]. These comparisons are illustrated in Figs. 2 and 3.

3.3 Constraints on the $\Lambda - m_\chi$ plane

In Figs. 2-6, the exclusion on Λ as a function of ADM mass are shown along with the results due to various DD experiments, such as LZ, Xenon, Darkside. The bounds from the mono-jet searches are presented for two jet- p_T selection criteria, $p_T(j) > 200 \text{ GeV}$ (LHC-200) and $p_T(j) > 1200 \text{ GeV}$ (LHC-1200). The current DD exclusions are also presented in the same plot to gather an idea of the overall picture of the exclusions.

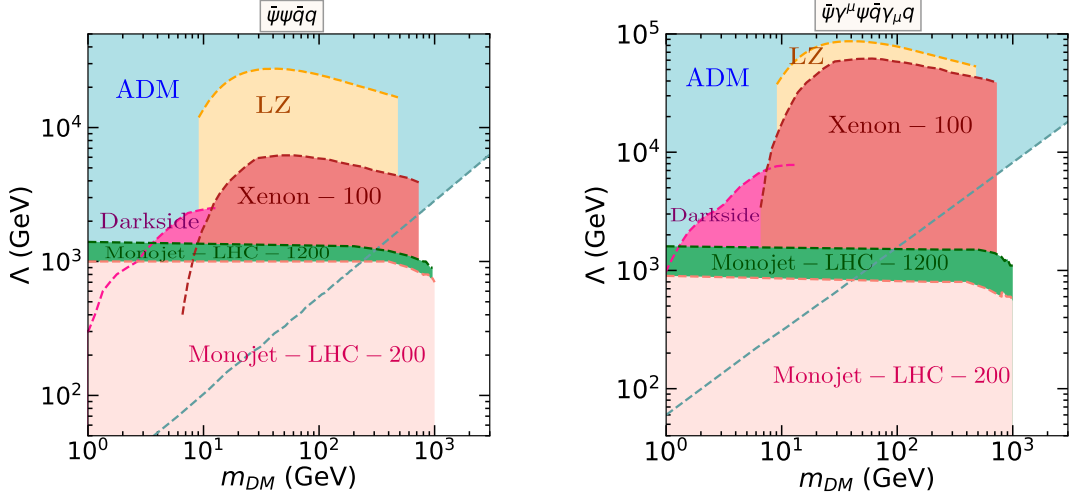


Figure 2: Current exclusion limits on the scale Λ at different DM mass (m_{DM}) for the scalar ($\mathcal{O}_{ss} \equiv \frac{1}{\Lambda^2}\bar{\psi}\psi\bar{q}q$) (left) and vector ($\mathcal{O}_{vv} \equiv \frac{1}{\Lambda^2}\bar{\psi}\gamma^\mu\psi\bar{q}\gamma_\mu q$) (right) type interaction of DM with quarks from different experimental observations and ADM considerations, labeled on the respective regions with darker shades. The experimental exclusions extends up to the bottom of the plots and overlapping regions are implicit.

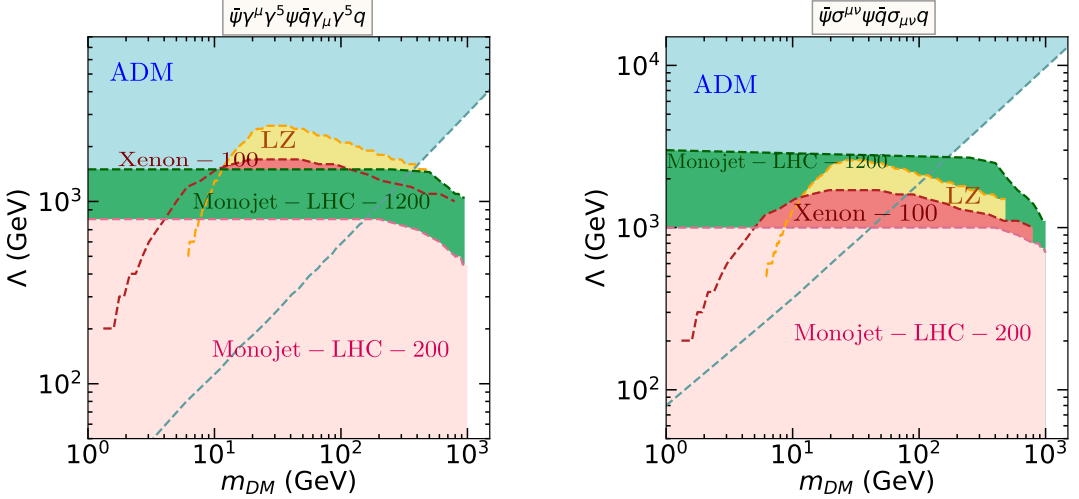


Figure 3: Same as Fig. 2 but for axial-vector ($\mathcal{O}_{aa} \equiv \frac{1}{\Lambda^2}\bar{\psi}\gamma^\mu\gamma^5\psi\bar{q}\gamma_\mu\gamma^5q$) (left) and tensor ($\mathcal{O}_{tt} \equiv \frac{1}{\Lambda^2}\bar{\psi}\sigma^{\mu\nu}\psi\bar{q}\sigma_{\mu\nu}q$) (right) type interaction of DM with quarks.

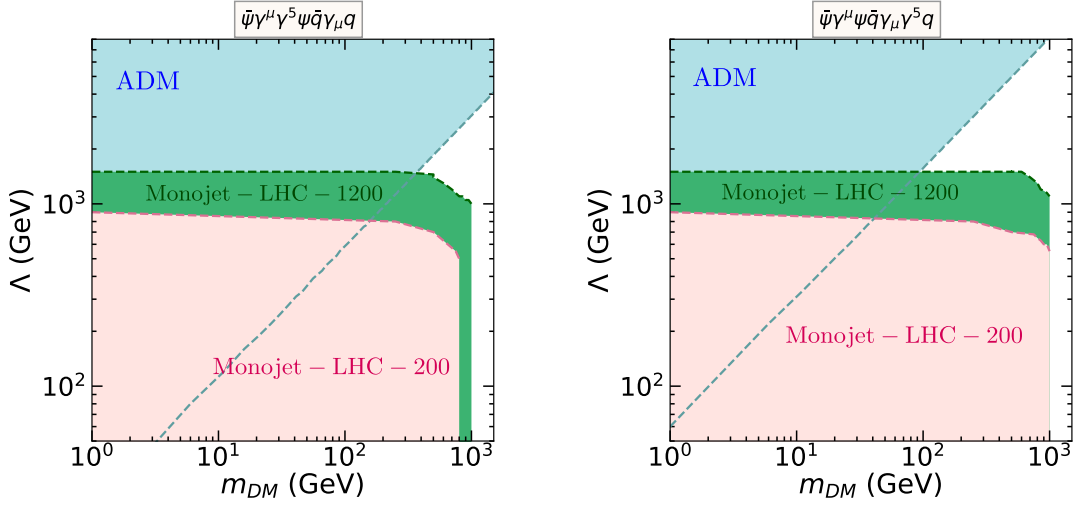


Figure 4: Same as Fig. 2 but for axial-vector–vector ($\mathcal{O}_{av} \equiv \frac{1}{\Lambda^2} \bar{\psi} \gamma^\mu \gamma^5 \psi \bar{q} \gamma_\mu q$) (left) and vector–axial-vector ($\mathcal{O}_{va} \equiv \frac{1}{\Lambda^2} \bar{\psi} \gamma^\mu \psi \bar{q} \gamma_\mu \gamma^5 q$) (right) type interaction of DM with quarks.

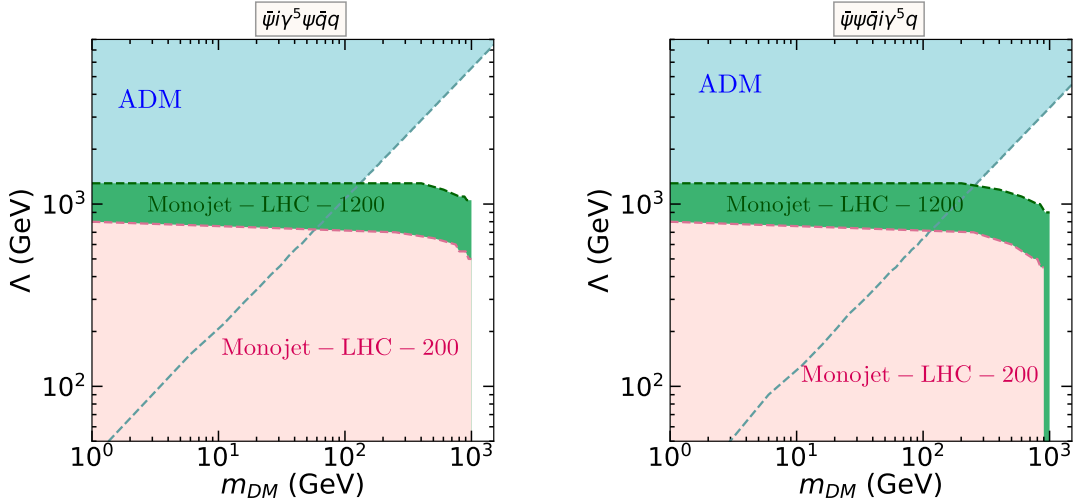


Figure 5: Same as Fig. 2 but for pseudo-scalar–scalar ($\mathcal{O}_{ps} \equiv \frac{1}{\Lambda^2} \bar{\psi} i \gamma^5 \psi \bar{q} q$) (left) and scalar–pseudo-scalar ($\mathcal{O}_{sp} \equiv \frac{1}{\Lambda^2} \bar{\psi} \psi \bar{q} i \gamma^5 q$) (right) type interaction of DM with quarks.

Clearly, the current DD limits are found to be much stronger compared to those presented in the Ref. [32]. For large part of the mass region, the DD bounds dominate the exclusion on the DM-quark interactions. However, in low DM-mass regions, even in case of the non-suppressed interactions, we found that the bounds coming from the mono-jet searches supersede the DD limits. Especially for the \mathcal{O}_{aa} and \mathcal{O}_{tt} operator, the current limits exclude a good fraction of region. Indeed, the DD measurements are found to be not sensitive for operators with suppressed interactions. In these cases the mono-jet searches put the dominant constraints for these interactions (see Figs. 4-6).

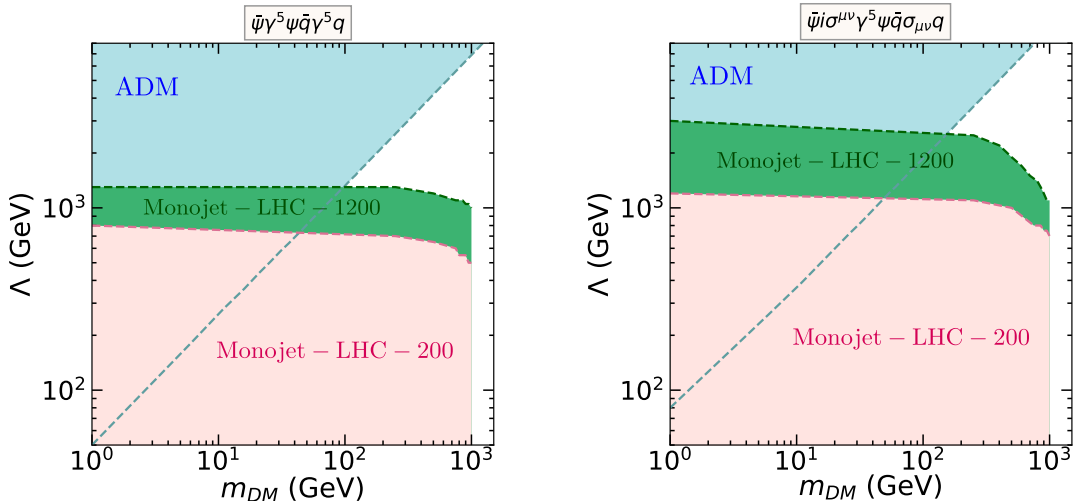


Figure 6: Same as Fig. 2 but for pseudo-scalar–pseudo-scalar ($\mathcal{O}_{pp} \equiv \frac{1}{\Lambda^2} \bar{\psi} \gamma^5 \psi \bar{q} \gamma^5 q$) (left) and pseudo-tensor–tensor ($\mathcal{O}_{pt} \equiv \frac{1}{\Lambda^2} \bar{\psi} i \sigma^{\mu\nu} \gamma^5 \psi \bar{q} \sigma_{\mu\nu} q$) (right) type interaction of DM with quarks.

4 Constraining ADM-Lepton Interactions

In this section we consider the case of leptophilic DM. Note in these models DM-quark interactions occur only at the loop level. Consequently, the limits obtained based on the mono-jet searches at hadron colliders and nuclear recoil dependent DD experiments become much weaker in this case. Moreover, the LHC being a hadron collider, the production of DM, which is not coupled to quarks or gluons, is suppressed. On the other hand, leptophilic DM attracts bounds from monophoton production at lepton colliders, such as LEP, or may be searched at future lepton colliders, e.g., ILC, FCC-ee. Interestingly, studies of effects of DM capture in compact stars help constrain DM-lepton interactions strongly, which we will discuss in Section 4.3.

4.1 Mono-photon searches at LEP

Similar to the mono-jet production in association with DM at the LHC, in an electron-positron collider, e.g., at LEP, DM can be produced accompanied by a photon radiated off from the electron or positron (see Fig. 7 (left)), namely,

$$e^+ e^- \rightarrow \chi \bar{\chi} \gamma \rightarrow \cancel{E}_T \gamma. \quad (4.1)$$

The SM counterpart of it involves production of neutrinos in place of DM (see Fig. 7 (right)), such as,

$$e^+ e^- \rightarrow \nu \bar{\nu} \gamma \rightarrow \cancel{E}_T \gamma. \quad (4.2)$$

These processes give rise to a mono-photon signal at the detector, a potentially robust way to look for DM in $e^+ e^-$ collider. In Ref. [92], the authors studied the mono-photon

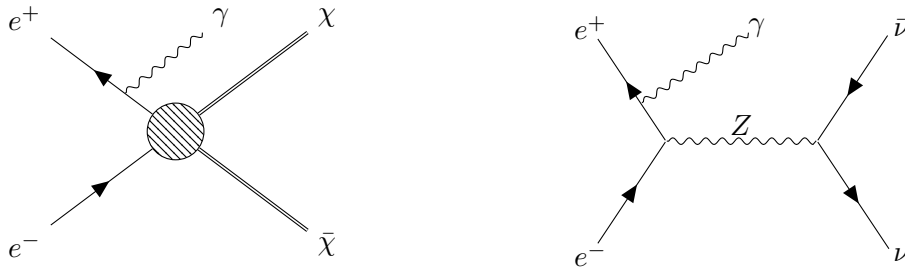


Figure 7: (Left) Feynman diagram of DM production from e^+e^- through effective interaction with additional photon from ISR; (right) Feynman diagram for the SM mono-photon production process.

production in the e^+e^- collider and predicted the excluded region in the $\Lambda - m_\chi$ plane for four effective operators (three of which are independent) of the DM-lepton interactions, considering the mono-photon analysis of the DELPHI experiment at LEP [118], including a simulation of the effects of the DELPHI detector.

In this section, we revisit this LEP exclusions including all possible DM-lepton contact interactions (same as Table 1, with $f = e$). Moreover, while presenting these LEP exclusions, we also include the limits from DD or indirect detection experiments, to review the overall picture of the current limits on leptophilic DM. Using these limits, we also infer the exclusions for the case of ADMs. This approach permits us to delineate the parameter spaces for viable ADM scenarios, similar to the analysis in the previous section.

In the following, we document our methodology to find the exclusions due to the LEP data. To start with, we performed a Monte-Carlo (MC) simulation of the SM mono-photon process, as in Eq. (4.2). This simulation is tailored to closely replicate the experimental data. We factor in all the relevant aspects such as detector efficiencies, resolutions, and effects of smearing. Then we validated our MC simulation with the experimental data. Post-validation, we proceeded to employ the same configuration to generate events associated with dark matter for a wide range of parameter values, Λ and m_χ . Subsequently, we evaluated the degree of excess that could potentially manifest at LEP as a result of these dark matter events. Finally, this allows us to exclude regions in the $\Lambda - m_\chi$ plane.

We closely follow the original LEP analysis Ref. [118], describing the measurements of the mono-photon events with the DELPHI detector corresponding to luminosity $\mathcal{L} = 650 \text{ pb}^{-1}$. These measurements are presented in bins of,

$$X_\gamma = \frac{E_\gamma}{E_{\text{beam}}}, \quad (4.3)$$

where E_γ and E_{beam} are the energies of the photon and the colliding beams respectively. The DM events are generated using Madgraph5-aMC@NLO-3.3.0[106] including the ISR photon, using a UFO model file for leptophilic DM produced using the Feynrules package [107]. Finally, mono-photon events are passed through PYTHIA8 [108, 109] for showering. It is important to emphasize here that accurate measurements of photons arising from initial state radiation (ISR) is crucial to model a mono-photon process. In our analysis, we ensure that all final state photons pass the requirements for identification with

Table 3: Efficiencies and energy resolutions of various components of the DELPHI detector. Trigger and acceptance efficiencies increase linearly, with specified values at the given energies. Energy units are in GeV.

Detector	Angular coverage	Overall efficiency	Trigger efficiency	Acceptance efficiency	Angular requirement	Energy resolution
HPC	$45^\circ < \theta < 135^\circ$	$X_\gamma > 0.6$	52% at $E_\gamma = 6$; 72% at $E_\gamma = 30$; 84% at $E_\gamma = 100$	41% at $E_\gamma = 6$; 78% at $E_\gamma = 80$, and above	-	$0.043 \oplus 0.32/\sqrt{E}$
FEMC	$12^\circ < \theta < 32^\circ$, or ($148^\circ < \theta < 168^\circ$)	$X_\gamma > 0.1$	93% at $E_\gamma = 10$; 100% at $E_\gamma = 15$; and above	57% at $E_\gamma = 10$; 75% at $E_\gamma = 100$; \times const. factor 89%	$\theta > 28^\circ - 80^\circ X_\gamma$	$0.03 \oplus 0.12/\sqrt{E} \oplus 0.11/E$
STIC	$3.8^\circ < \theta < 8^\circ$, or ($172^\circ < \theta < 176.2^\circ$)	$X_\gamma > 0.3$	Const. 48% all over	-	$\theta > 9.2^\circ - 9^\circ X_\gamma$	$0.0152 \oplus 0.135/\sqrt{E}$

the DELPHI detector. For completeness and clarity, we provide a brief overview of the detector efficiencies and resolutions in the following.

The DELPHI detector had three parts, namely, High-Density Projection Chamber (HPC), Forward Electromagnetic Calorimeter (FEMC), and Small Angle Tile Calorimeter (STIC). We present the energy resolutions and different efficiencies of various sub-detector in Table 3. There is an overall efficiency for each sub-detector components which depends on X_γ , followed by energy-dependent trigger and acceptance efficiencies. The trigger and acceptance efficiencies increase linearly with energy. The slope of the increase can be obtained using a few fixed values at certain energies, which are presented in Table 3. To reduce the large background of radiative Bhabha events in FEMC, and due to beam-gas interactions in STIC, an energy-dependent angular requirement is imposed. The energy resolution adds an energy-dependent smearing for each of the photon that have passed all the selection criteria. Following Ref. [92], we have added a Lorentzian smearing with a width of $0.052E_\gamma$ GeV, which is necessary to obtain a more realistic distribution.

In order to demonstrate whether our simulated data correctly mimics the LEP measurements, we compare the p-value of X_γ distribution corresponding to the SM mono-photon production (Eq. 4.2) with the DELPHI measurements. We obtain the data-MC agreement for X_γ as shown in Fig. 8. Some erroneous data can be found in the last bin, most likely due to inaccurate detector resolution modeling. We remove this bin from the χ^2 -analysis. The χ^2/dof is $\sim 14/19$ for 19 d.o.f corresponding to yields in 19 bins. A good agreement is found, confirming our simulation methodology. In the same figure, the distribution for the DM signal is also plotted considering $m_\chi = 10$ GeV and $\Lambda = 300$ GeV, where the lower X_γ bins show deviations due to DM effects.

Now we use this setup to generate the mono-photon energy distribution for the mono-photon production for DM (Eq. 4.1) for each choice of m_χ and Λ . Calculation of χ^2 between the photon energy distributions for SM-MC and the DM, it is possible to predict the allowed and ruled out DM parameter space. Results are shown for different operators in Figs. 10-14. Notice that, these bounds are the strongest one for leptophilic dark matter in the 1-100 GeV mass range, which are discussed later.

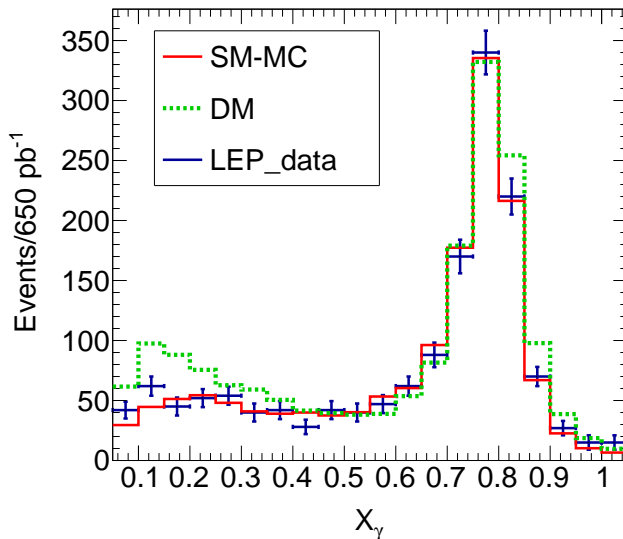


Figure 8: Distribution of $X_\gamma = E_\gamma/E_{\text{beam}}$ for single photon event, where the agreement of the SM Monte-Carlo (red histogram) with the DELPHI-data (blue points with error bar) can be observed. The DM signal (green histogram), with vector-like interaction with $\Lambda = 300$ GeV and $m_\chi = 10$ GeV, shows excess for the lower values of X_γ and otherwise consistent with the SM.

4.2 Discovery potential of ADM at FCC-ee

In this section we discuss the discovery potential of leptophilic DM in the FCC-ee (Future Circular Collider - electron-positron) corresponding to the allowed region of parameter space. The FCC-ee is a proposed e^+e^- collider with relatively higher center of mass (COM) energies and luminosities, measuring observables at unprecedented precision [119]. The FCC-ee collider is proposed to operate in several stages, with different COM energies, such as $\sqrt{s} = 91, 160, 240$ and 365 GeV. In our study, we have used the highest energy option ($\sqrt{s} = 365$ GeV) to calculate the discovery reach of ADM scenarios. It is to be noted that, this sensitivity study is applicable to any leptophilic DM with contact interactions of Table 1, and not limited to ADM.

The FCC-ee experiment should produce mono-photon events similar to LEP. However, the new detector set-up with increased COM energy is expected to probe wider ranges of parameters (Λ, m_χ).

The production cross-sections of both the signal and backgrounds depend highly on the polarization of the e^+ and e^- beams. For the sake of demonstration, we compute the cross-section of the SM mono-photon background using Madgraph5-aMC@NLO-3.4.1[106], varying the polarization of the beams. The variation of the cross-section with different choices of beam polarizations are presented in Fig. 9 (left). As the beam polarization setting of FCC-ee is not fixed yet, we used an unpolarized (50%-L and 50%-R combination) beam for representative purposes.

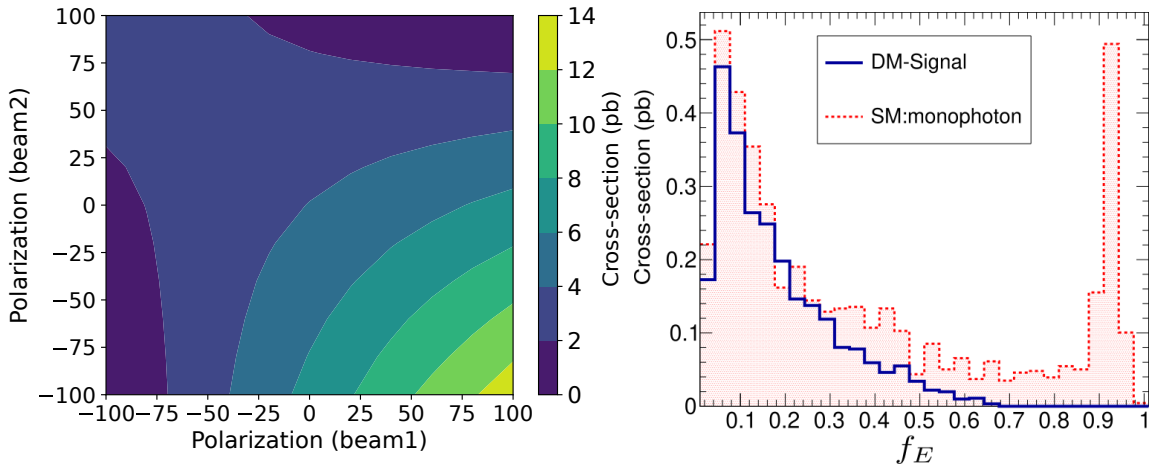


Figure 9: (Left) Variation of the SM mono-photon production cross-section ($e^+e^- \rightarrow \nu\nu\gamma$) at FCC-ee with variation of beam-polarization; (right) distribution of the energy fraction of photon in the mono-photon events, for DM-signal (choosing $\Lambda = 400$ GeV, $m_\chi = 100$ GeV, and vector-like interaction) and SM-background.

For the signal, we essentially have one detectable object, namely the photon in the final state. All other kinematic variables such as \cancel{E}_T and the transverse mass, $M_T(\gamma, \cancel{E}_T)$, are strongly correlated to the energy of the photon. Hence a selection for photon energy results in the effective discrimination between signal and background. Hence, a selection as

$$f_E = E_\gamma/E_{\text{beam}} < 0.3, \quad (4.4)$$

is found to be very powerful to suppress backgrounds as shown in Fig. 9 (right panel). The resulting signal significances, $S/\sqrt{S+B}$, are estimated at $\mathcal{L} = 340 \text{ fb}^{-1}$ for each of the given parameter spaces $\{m_\chi, \Lambda\}$. Repeating this analysis for different choices of $\{m_\chi, \Lambda\}$, we present the region for which $S/\sqrt{S+B} > 3.0$, i.e., the $3\text{-}\sigma$ reach. The results are presented in the following subsection.

4.3 Constraints from compact stars and direct detection

As seen in the previous sections, lepton-colliders are sensitive to a relatively smaller range of leptophilic ADM masses. Comparatively, DM capture in compact objects can be used to set bounds on a wider range of DM mass [48, 120–125]. Especially, neutron stars (NS) [90, 91, 124, 126–133] and white dwarfs (WD) [91, 123, 134–137] constrains DM-lepton interactions strongly for a MeV to TeV range of DM mass. Due to their high density, NS can capture dark matter very efficiently and can lead to the heating of NS [128, 132]. Since old, isolated NS can naturally cool to temperatures below 1000 K, this heating can be utilized to establish constraints on the strength of DM interactions. For instance, Refs. [90, 91] have calculated these limits in detail for DM-electron interactions.

A comparable scenario can arise with white dwarfs (WDs) as well. The core of a WD is primarily composed of a degenerate electron gas. Consequently, if there is interaction

between DM and electrons, it would likely be more pronounced at the core of the WD. The DM can then scatter off the electrons and can heat up the WD. Also, a DM-dense WD core may result in DM annihilation, another source of rising the temperature of WD. The presence of DM would then prevent the natural cooling of the old, isolated WDs. Conversely, the absence of anomalous cooling in WDs can lead to stringent constraints on the strength of the interaction between DM and electrons. Following this, Ref. [91] calculated the limits on DM-lepton interactions from WDs.

On the other hand, among different DD experiments, DAMIC [76, 138] and SuperCDMS [139] put the strongest constraint on DM-lepton interactions for MeV to GeV range of DM mass. However, these DD bounds are generally not competitive in the preferred mass range for ADM. Nevertheless, the upcoming DAMIC-M-1kg-yr experiment is expected to have a promising sensitivity [138], and we consider this projected constraint for illustrative purposes. Finally, we present an overall picture of the constraints on DM-lepton interactions from all possible sources.

4.4 Constraints and discovery potential for leptophilic ADM

In this subsection, we discuss the constraints on the ADM-lepton interactions imposed by the experimental measurements, as discussed in section 4.1. In order to achieve a comprehensive perspective on the global exclusions associated with these interactions, we also incorporate important constraints originating from both indirect and direct searches. These additional constraints, gathered from Refs. [90, 91], are presented alongside the new collider-based bounds. It is worth noting that the constraints arising from dark matter-nucleon scattering experiments are relatively weak. This is because these interactions can only occur at the loop-level. Conversely, experiments focusing on dark matter-electron scattering probe a range of much lower dark matter masses, a region that is not highly motivated by the ADM hypothesis.

We present the overall picture of the allowed and excluded parameter spaces for DM-electron interaction in Figs. 10-14. Each of the shaded regions within the presented figures signify exclusion due to specific hypotheses. For instance, the blue shaded region eliminates the possibility of dark matter being asymmetric, while the dark red portion is excluded based on the outcomes of the LEP mono-photon searches, and so on. Interestingly, for $\mathcal{O}_{ss}, \mathcal{O}_{sp}, \mathcal{O}_{aa}, \mathcal{O}_{av}$, where $\chi\bar{\chi} \rightarrow e^+e^-$ occurs through velocity suppressed p -wave (s -wave annihilation is either absent or has m_q^2 suppression), the ADM requirement excludes a larger parameter space in the $\Lambda - m_\chi$ plane. It is important to note here that the other exclusions, which are not restricted to the ADM hypothesis, hold for any DM with these effective interactions, and all the regions above the shaded region (except blue) are allowed. Our study reveals that, though the constraints from the NS or WDs on the DM-lepton interactions are overall strong, the bounds coming from the mono-photon searches at the LEP experiments surpasses all those in the sensitive region, $m_\chi \sim 1 - 100$ GeV. Considering the ADM hypothesis, we find that most of the operators fail to provide an ADM solution for any value of Λ in the region $m_\chi \sim 1 - 100$ GeV, sensitive to the LEP experiment. Only for operators $\mathcal{O}_{vv}, \mathcal{O}_{av}$, and \mathcal{O}_{ps} , the bounds are somewhat weak ~ 50 GeV, while for $\mathcal{O}_{va}, \mathcal{O}_{pt}, \mathcal{O}_{sp}$, and \mathcal{O}_{pp} they are much weaker ~ 10 GeV. Notice that, for the interactions $\mathcal{O}_{ss},$

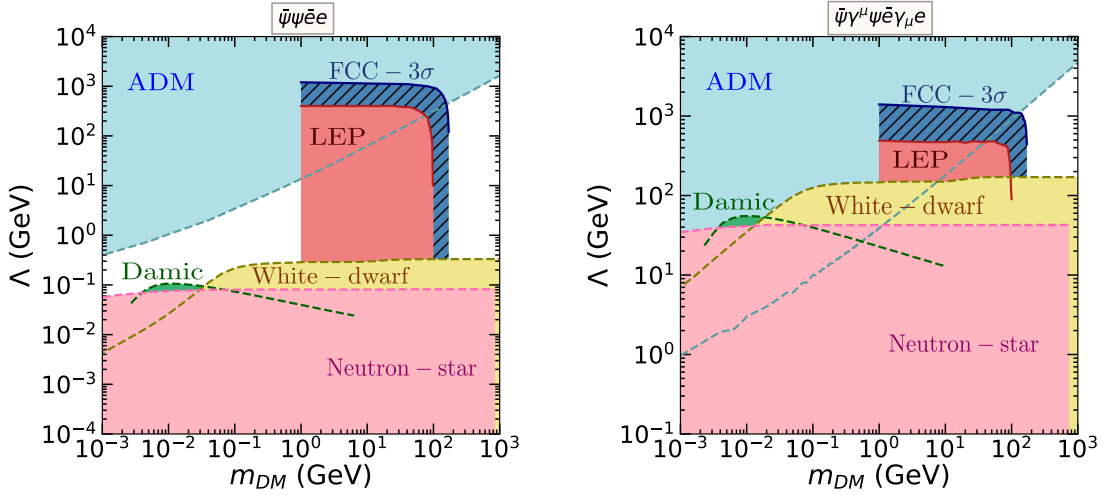


Figure 10: Limits on Λ_e for scalar ($\mathcal{O}_{ss} \equiv \frac{1}{\Lambda^2} \bar{\psi}\psi\bar{e}e$) (left) and vector ($\mathcal{O}_{vv} \equiv \frac{1}{\Lambda^2} \bar{\psi}\gamma^\mu\psi\bar{e}\gamma_\mu e$) (right) type interaction of DM with electrons from different experimental observations and ADM scenario, labeled on the respective regions with darker shades. The striped dark blue region corresponds to the FCC-3 σ reach. The experimental exclusions/reach extends up to the bottom of the plots and overlapping regions are implicit.

\mathcal{O}_{sp} , \mathcal{O}_{ps} , and \mathcal{O}_{pp} the LEP bounds are the only ones that can completely exclude ADM possibility of a certain mass.

The blue striped region in Figs. 10-14 presents the 3- σ reach of the upcoming FCC-ee experiment in the mono-photon search channel in the $m_\chi - \Lambda$ plane. The pattern of the probing parameter region is similar to the LEP mono-photon bounds, as expected. However, owing to higher COM energy, the reach extends to $m_\chi \sim 175$ GeV and constraints may strengthen by a factor of 2 or so.

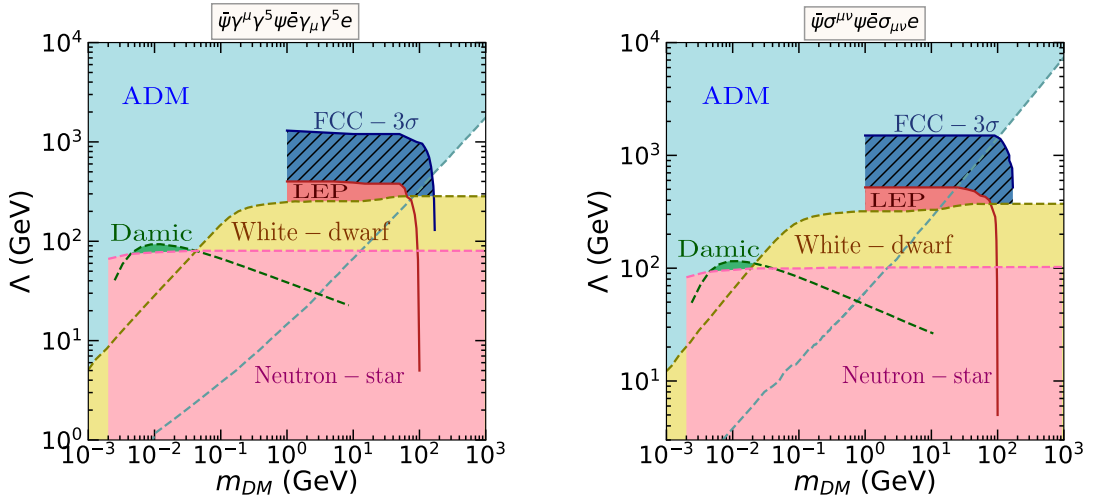


Figure 11: Same as Fig. 10 but for axial-vector ($\mathcal{O}_{aa} \equiv \frac{1}{\Lambda^2} \bar{\psi} \gamma^\mu \gamma^5 \psi \bar{e} \gamma_\mu \gamma^5 e$) (left) and tensor ($\mathcal{O}_{tt} \equiv \frac{1}{\Lambda^2} \bar{\psi} \sigma^{\mu\nu} \psi \bar{e} \sigma_{\mu\nu} e$) (right) type interaction of DM with electrons.

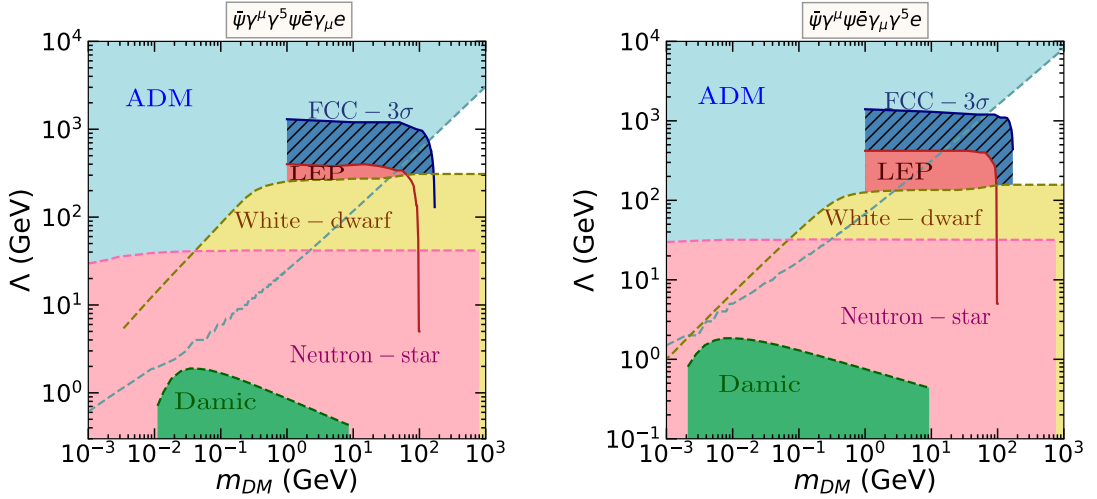


Figure 12: Same as Fig. 10 but for axial-vector–vector ($\mathcal{O}_{av} \equiv \frac{1}{\Lambda^2} \bar{\psi} \gamma^\mu \gamma^5 \psi \bar{e} \gamma_\mu e$) (left) and vector–axial-vector ($\mathcal{O}_{va} \equiv \frac{1}{\Lambda^2} \bar{\psi} \gamma^\mu \psi \bar{e} \gamma_\mu \gamma^5 e$) (right) type interaction of DM with electrons.

5 Summary and Outlook

In this paper, we present a detailed study of the current status of the effective interactions of ADM with quarks and leptons, with a future projection of the sensitivity of FCC-ee in probing leptophilic ADM. We start with the ADM-quark interactions, where the DD constraints often become most stringent. Considering the strongest exclusions from different DD experiments, we find the excluded and allowed region corresponding to each interaction in the $\Lambda - m_\chi$ plane. However, for several effective interactions, the DM-nucleon scattering cross-sections are suppressed. In these cases, the constraints from monojet

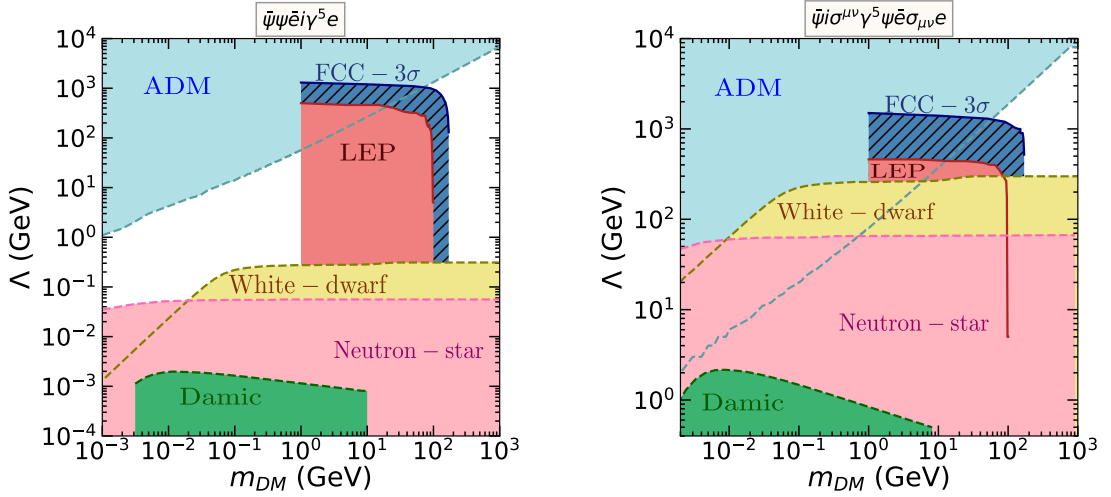


Figure 13: Same as Fig. 10 but for scalar–pseudo-scalar ($\mathcal{O}_{sp} \equiv \frac{1}{\Lambda^2} \bar{\psi} \psi \bar{e} i \gamma^5 e$) (left) and pseudo-tensor–tensor ($\mathcal{O}_{pt} \equiv \frac{1}{\Lambda^2} \bar{\psi} i \sigma^{\mu\nu} \gamma^5 \psi \bar{e} \sigma_{\mu\nu} e$) (right) type interaction of DM with electrons.

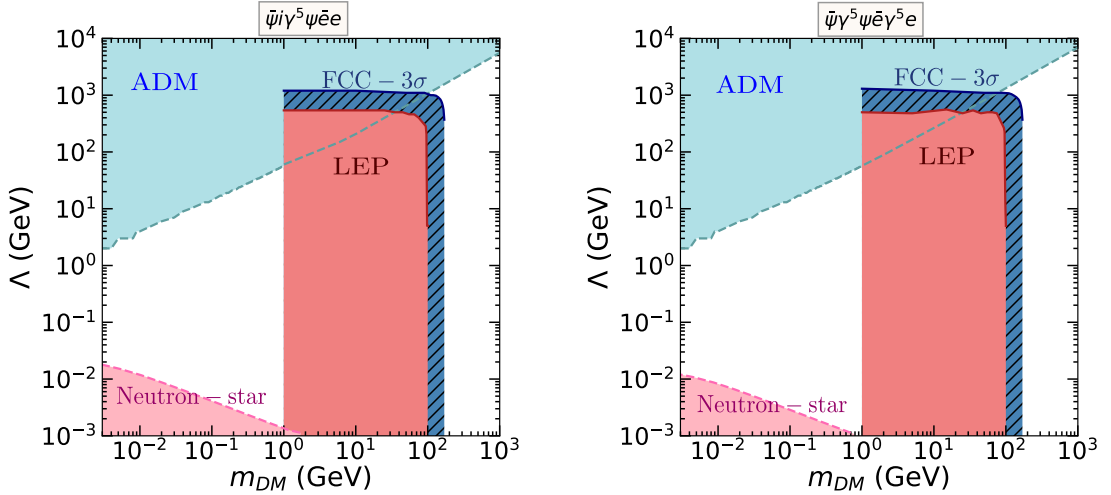


Figure 14: Same as Fig. 10 but for pseudo-scalar–scalar ($\mathcal{O}_{ps} \equiv \frac{1}{\Lambda^2} \bar{\psi} i \gamma^5 \psi \bar{e} e$) (left) and pseudo-scalar–pseudo-scalar ($\mathcal{O}_{pp} \equiv \frac{1}{\Lambda^2} \bar{\psi} \gamma^5 \psi \bar{e} \gamma^5 e$) (right) type interaction of DM with electrons.

searches are dominant. We calculate the exclusions from the monojet searches using the most recent LHC measurements and including detector effects. We find that, for scalar ($\mathcal{O}_{ss} \equiv \frac{1}{\Lambda^2} \bar{\psi} \psi \bar{e} e$) and vector ($\mathcal{O}_{vv} \equiv \frac{1}{\Lambda^2} \bar{\psi} \gamma^\mu \psi \bar{e} \gamma_\mu e$) type of interactions, the possibility of ADM is ruled out almost up to ~ 1 TeV. Whereas, for other types of interactions, ADM of mass larger than a few hundred GeV are still allowed in a narrow range of Λ . None of the searches exclude the viability of ADM above ~ 1 TeV. Note that the exclusion regions from the experimental searches are not restricted to the ADM but are also applicable to any DM with the interactions in Table 1.

Next, we concentrate on the ADM-lepton interactions. In this case, the strongest bounds generally come from NS or WD studies. However, we found that the constraints from the monophoton searches at the LEP experiment, which we have calculated in detail for each interaction, overshoot those from the NS or WD for all types of interactions in the 1-100 GeV mass range. According to our study, the possibility of a leptophilic ADM is ruled out by the LEP experiment for ~ 1 -100 GeV mass range of the ADM, except for the vector–axial-vector operator ($\mathcal{O}_{va} \equiv \frac{1}{\Lambda^2} \bar{\psi} \gamma^\mu \psi \bar{e} \gamma_\mu \gamma^5 e$), the pseudo-tensor–tensor operator ($\mathcal{O}_{pt} \equiv \frac{1}{\Lambda^2} \bar{\psi} \sigma^{\mu\nu} i \gamma^5 \psi \bar{e} \sigma_{\mu\nu} e$), the scalar–pseudo-scalar operator ($\mathcal{O}_{sp} \equiv \frac{1}{\Lambda^2} \bar{\psi} \psi \bar{e} i \gamma^5 e$), and the pseudo-scalar–pseudo-scalar operator ($\mathcal{O}_{pp} \equiv \frac{1}{\Lambda^2} \bar{\psi} \gamma^5 \psi \bar{e} \gamma^5 e$) mediated interactions, where the constraints are loose $\sim \mathcal{O}(10)$ GeV. Again, the constraints apply to any DM having the considered effective interactions (Table 1).

As a possible successor of e^+e^- colliders, the FCC-ee experiment will be interesting to probe the still viable regions of the ADM-lepton interactions. In our analysis, we calculate the region of parameter spaces where the monophoton searches at the FCC-ee will obtain the $3\text{-}\sigma$ sensitivity. This study indicates that FCC-ee can probe up to ~ 200 GeV mass range of any general kind of DM for EFT expansion scale up to ~ 1 TeV, which, though not a significant improvement, seems attractive from the aspect of possible FCC-ee physics goals.

Acknowledgements

The authors are thankful to Dr. Nishita Desai for useful discussions and suggestions. The authors acknowledge support from the Department of Atomic Energy (DAE), Government of India, under Project Identification No. RTI4002. BD acknowledges partial support through a Swarnajayanti Fellowship of the Department of Science and Technology (DST), Government of India. AR thanks the support of Monash University, where he moved at the end of the writing stage of this manuscript, for support towards completing this work.

A Expressions of $\langle\sigma v\rangle$ for different operators

The expressions of the annihilation rates for the operators in Table 1 can be obtained as,

$$\sigma^{\mathcal{O}_{ss}v} = \frac{3m_\chi^2}{8\pi\Lambda^4} \sum_q \left(1 - \frac{m_q^2}{m_\chi^2}\right)^{3/2} v^2 \quad (\text{A.1})$$

$$\sigma^{\mathcal{O}_{pp}v} = \frac{3m_\chi^2}{\pi\Lambda^4} \sum_q \left(1 - \frac{m_q^2}{m_\chi^2}\right)^{1/2} \left[1 + \frac{v^2}{8} \left(\frac{2m_\chi^2 - m_q^2}{m_\chi^2 - m_q^2}\right)\right] \quad (\text{A.2})$$

$$\sigma^{\mathcal{O}_{sp}v} = \frac{3m_\chi^2}{4\pi\Lambda^4} \sum_q \left(1 - \frac{m_q^2}{m_\chi^2}\right)^{1/2} v^2 \quad (\text{A.3})$$

$$\sigma^{\mathcal{O}_{ps}v} = \frac{3m_\chi^2}{4\pi\Lambda^4} \sum_q \left(1 - \frac{m_q^2}{m_\chi^2}\right)^{3/2} \left[1 + v^2 \left(\frac{2m_q^2 - m_\chi^2}{m_\chi^2 - m_q^2}\right)\right] \quad (\text{A.4})$$

$$\sigma^{\mathcal{O}_{vv}v} = \frac{3m_\chi^2}{2\pi\Lambda^4} \sum_q \left(1 - \frac{m_q^2}{m_\chi^2}\right)^{1/2} \left[\left(2 + \frac{m_q^2}{m_\chi^2}\right) + v^2 \left(\frac{8m_\chi^4 - 4m_q^2 m_\chi^2 + 5m_q^4}{24m_\chi^2(m_\chi^2 - m_q^2)}\right)\right] \quad (\text{A.5})$$

$$\sigma^{\mathcal{O}_{aa}v} = \frac{3m_\chi^2}{2\pi\Lambda^4} \sum_q \left(1 - \frac{m_q^2}{m_\chi^2}\right)^{1/2} \left[\frac{m_q^2}{m_\chi^2} + v^2 \left(\frac{8m_\chi^4 - 22m_q^2 m_\chi^2 + 17m_q^4}{24m_\chi^2(m_\chi^2 - m_q^2)}\right)\right] \quad (\text{A.6})$$

$$\sigma^{\mathcal{O}_{va}v} = \frac{3m_\chi^2}{\pi\Lambda^4} \sum_q \left(1 - \frac{m_q^2}{m_\chi^2}\right)^{1/2} \left[\left(1 - \frac{m_q^2}{m_\chi^2}\right) + \frac{v^2}{24} \left(4 + 5\frac{m_q^2}{m_\chi^2}\right)\right] \quad (\text{A.7})$$

$$\sigma^{\mathcal{O}_{av}v} = \frac{m_\chi^2}{4\pi\Lambda^4} \sum_q \left(1 - \frac{m_q^2}{m_\chi^2}\right)^{1/2} \left(2 + \frac{m_q^2}{m_\chi^2}\right) v^2 \quad (\text{A.8})$$

$$\sigma^{\mathcal{O}_{tt}v} = \frac{3m_\chi^2}{\pi\Lambda^4} \sum_q \left(1 - \frac{m_q^2}{m_\chi^2}\right)^{1/2} \left[\left(1 + 2\frac{m_q^2}{m_\chi^2}\right) + v^2 \left(\frac{4m_\chi^4 - 11m_q^2 m_\chi^2 + 16m_q^4}{24m_\chi^2(m_\chi^2 - m_q^2)}\right)\right] \quad (\text{A.9})$$

$$\sigma^{\mathcal{O}_{pt}v} = \frac{6m_\chi^2}{\pi\Lambda^4} \sum_q \left(1 - \frac{m_q^2}{m_\chi^2}\right)^{1/2} \left[\left(1 - \frac{m_q^2}{m_\chi^2}\right) + \frac{v^2}{24} \left(4 + 11\frac{m_q^2}{m_\chi^2}\right)\right] \quad (\text{A.10})$$

References

- [1] PLANCK collaboration, *Planck 2018 results. VI. Cosmological parameters*, [1807.06209](#).
- [2] S. Nussinov, *TECHNOCOSMOLOGY: COULD A TECHNIBARYON EXCESS PROVIDE A 'NATURAL' MISSING MASS CANDIDATE?*, *Phys. Lett. B* **165** (1985) 55.
- [3] G.B. Gelmini, L.J. Hall and M.J. Lin, *What Is the Cosmion?*, *Nucl. Phys. B* **281** (1987) 726.
- [4] K.M. Zurek, *Asymmetric Dark Matter: Theories, Signatures, and Constraints*, *Phys. Rept.* **537** (2014) 91 [[1308.0338](#)].
- [5] K. Petraki and R.R. Volkas, *Review of asymmetric dark matter*, *Int. J. Mod. Phys. A* **28** (2013) 1330028 [[1305.4939](#)].

- [6] S.M. Barr, R.S. Chivukula and E. Farhi, *Electroweak Fermion Number Violation and the Production of Stable Particles in the Early Universe*, *Phys. Lett. B* **241** (1990) 387.
- [7] S.M. Barr, *Baryogenesis, sphalerons and the cogeneration of dark matter*, *Phys. Rev. D* **44** (1991) 3062.
- [8] D.B. Kaplan, *A Single explanation for both the baryon and dark matter densities*, *Phys. Rev. Lett.* **68** (1992) 741.
- [9] S.B. Gudnason, C. Kouvaris and F. Sannino, *Towards working technicolor: Effective theories and dark matter*, *Phys. Rev. D* **73** (2006) 115003 [[hep-ph/0603014](#)].
- [10] S.B. Gudnason, C. Kouvaris and F. Sannino, *Dark Matter from new Technicolor Theories*, *Phys. Rev. D* **74** (2006) 095008 [[hep-ph/0608055](#)].
- [11] G.D. Kribs, T.S. Roy, J. Terning and K.M. Zurek, *Quirky Composite Dark Matter*, *Phys. Rev. D* **81** (2010) 095001 [[0909.2034](#)].
- [12] D.E. Kaplan, M.A. Luty and K.M. Zurek, *Asymmetric Dark Matter*, *Phys. Rev. D* **79** (2009) 115016 [[0901.4117](#)].
- [13] T. Cohen and K.M. Zurek, *Leptophilic Dark Matter from the Lepton Asymmetry*, *Phys. Rev. Lett.* **104** (2010) 101301 [[0909.2035](#)].
- [14] T. Cohen, D.J. Phalen, A. Pierce and K.M. Zurek, *Asymmetric Dark Matter from a GeV Hidden Sector*, *Phys. Rev. D* **82** (2010) 056001 [[1005.1655](#)].
- [15] H. An, S.-L. Chen, R.N. Mohapatra and Y. Zhang, *Leptogenesis as a Common Origin for Matter and Dark Matter*, *JHEP* **03** (2010) 124 [[0911.4463](#)].
- [16] E.J. Chun, *Leptogenesis origin of Dirac gaugino dark matter*, *Phys. Rev. D* **83** (2011) 053004 [[1009.0983](#)].
- [17] J. Shelton and K.M. Zurek, *Darkogenesis: A baryon asymmetry from the dark matter sector*, *Phys. Rev. D* **82** (2010) 123512 [[1008.1997](#)].
- [18] H. Davoudiasl, D.E. Morrissey, K. Sigurdson and S. Tulin, *Hylogenesis: A Unified Origin for Baryonic Visible Matter and Antibaryonic Dark Matter*, *Phys. Rev. Lett.* **105** (2010) 211304 [[1008.2399](#)].
- [19] N. Haba and S. Matsumoto, *Baryogenesis from Dark Sector*, *Prog. Theor. Phys.* **125** (2011) 1311 [[1008.2487](#)].
- [20] P.-H. Gu, M. Lindner, U. Sarkar and X. Zhang, *WIMP Dark Matter and Baryogenesis*, *Phys. Rev. D* **83** (2011) 055008 [[1009.2690](#)].
- [21] M. Blennow, B. Dasgupta, E. Fernandez-Martinez and N. Rius, *Aidnogenesis via Leptogenesis and Dark Sphalerons*, *JHEP* **03** (2011) 014 [[1009.3159](#)].
- [22] K. Agashe and G. Servant, *Baryon number in warped GUTs: Model building and (dark matter related) phenomenology*, *JCAP* **02** (2005) 002 [[hep-ph/0411254](#)].
- [23] R. Kitano and I. Low, *Grand unification, dark matter, baryon asymmetry, and the small scale structure of the universe*, [hep-ph/0503112](#).
- [24] N. Cosme, L. Lopez Honorez and M.H.G. Tytgat, *Leptogenesis and dark matter related?*, *Phys. Rev. D* **72** (2005) 043505 [[hep-ph/0506320](#)].
- [25] D. Suematsu, *Nonthermal production of baryon and dark matter*, *Astropart. Phys.* **24** (2006) 511 [[hep-ph/0510251](#)].

- [26] M.H.G. Tytgat, *Relating leptogenesis and dark matter*, in *41st Rencontres de Moriond on Electroweak Interactions and Unified Theories*, pp. 320–323, 6, 2006 [[hep-ph/0606140](#)].
- [27] T. Banks, S. Echols and J.L. Jones, *Baryogenesis, dark matter and the Pentagon*, *JHEP* **11** (2006) 046 [[hep-ph/0608104](#)].
- [28] V. Page, *Non-thermal right-handed sneutrino dark matter and the $\Omega(\text{DM})/\Omega(b)$ problem*, *JHEP* **04** (2007) 021 [[hep-ph/0701266](#)].
- [29] D. Hooper, J. March-Russell and S.M. West, *Asymmetric sneutrino dark matter and the $\Omega(b) / \Omega(\text{DM})$ puzzle*, *Phys. Lett. B* **605** (2005) 228 [[hep-ph/0410114](#)].
- [30] R. Kitano and I. Low, *Dark matter from baryon asymmetry*, *Phys. Rev. D* **71** (2005) 023510 [[hep-ph/0411133](#)].
- [31] A. Belyaev, M.T. Frandsen, S. Sarkar and F. Sannino, *Mixed dark matter from technicolor*, *Phys. Rev. D* **83** (2011) 015007 [[1007.4839](#)].
- [32] J. March-Russell, J. Unwin and S.M. West, *Closing in on Asymmetric Dark Matter I: Model independent limits for interactions with quarks*, *JHEP* **08** (2012) 029 [[1203.4854](#)].
- [33] S.D. McDermott, H.-B. Yu and K.M. Zurek, *Constraints on Scalar Asymmetric Dark Matter from Black Hole Formation in Neutron Stars*, *Phys. Rev. D* **85** (2012) 023519 [[1103.5472](#)].
- [34] C. Kouvaris and P. Tinyakov, *Excluding Light Asymmetric Bosonic Dark Matter*, *Phys. Rev. Lett.* **107** (2011) 091301 [[1104.0382](#)].
- [35] C. Kouvaris, *Limits on Self-Interacting Dark Matter*, *Phys. Rev. Lett.* **108** (2012) 191301 [[1111.4364](#)].
- [36] C. Kouvaris and P. Tinyakov, *(Not)-constraining heavy asymmetric bosonic dark matter*, *Phys. Rev. D* **87** (2013) 123537 [[1212.4075](#)].
- [37] J. Bramante, K. Fukushima and J. Kumar, *Constraints on bosonic dark matter from observation of old neutron stars*, *Phys. Rev. D* **87** (2013) 055012 [[1301.0036](#)].
- [38] N.F. Bell, A. Melatos and K. Petraki, *Realistic neutron star constraints on bosonic asymmetric dark matter*, *Phys. Rev. D* **87** (2013) 123507 [[1301.6811](#)].
- [39] I. Goldman, R.N. Mohapatra, S. Nussinov, D. Rosenbaum and V. Teplitz, *Possible Implications of Asymmetric Fermionic Dark Matter for Neutron Stars*, *Phys. Lett. B* **725** (2013) 200 [[1305.6908](#)].
- [40] J. Bramante, K. Fukushima, J. Kumar and E. Stopnitzky, *Bounds on self-interacting fermion dark matter from observations of old neutron stars*, *Phys. Rev. D* **89** (2014) 015010 [[1310.3509](#)].
- [41] J. Bramante and T. Linden, *Detecting Dark Matter with Imploding Pulsars in the Galactic Center*, *Phys. Rev. Lett.* **113** (2014) 191301 [[1405.1031](#)].
- [42] J. Bramante and F. Elahi, *Higgs portals to pulsar collapse*, *Phys. Rev. D* **91** (2015) 115001 [[1504.04019](#)].
- [43] C. Kouvaris and N.G. Nielsen, *Asymmetric Dark Matter Stars*, *Phys. Rev. D* **92** (2015) 063526 [[1507.00959](#)].
- [44] J. Bramante, T. Linden and Y.-D. Tsai, *Searching for dark matter with neutron star mergers and quiet kilonovae*, *Phys. Rev. D* **97** (2018) 055016 [[1706.00001](#)].

- [45] C. Kouvaris, P. Tinyakov and M.H.G. Tytgat, *NonPrimordial Solar Mass Black Holes*, *Phys. Rev. Lett.* **121** (2018) 221102 [[1804.06740](#)].
- [46] M.I. Gresham and K.M. Zurek, *Asymmetric Dark Stars and Neutron Star Stability*, *Phys. Rev. D* **99** (2019) 083008 [[1809.08254](#)].
- [47] R. Garani, Y. Genolini and T. Hambye, *New Analysis of Neutron Star Constraints on Asymmetric Dark Matter*, *JCAP* **05** (2019) 035 [[1812.08773](#)].
- [48] B. Dasgupta, A. Gupta and A. Ray, *Dark matter capture in celestial objects: light mediators, self-interactions, and complementarity with direct detection*, *JCAP* **10** (2020) 023 [[2006.10773](#)].
- [49] B. Dasgupta, R. Laha and A. Ray, *Low Mass Black Holes from Dark Core Collapse*, *Phys. Rev. Lett.* **126** (2021) 141105 [[2009.01825](#)].
- [50] N. Rutherford, G. Raaijmakers, C. Prescod-Weinstein and A. Watts, *Constraining bosonic asymmetric dark matter with neutron star mass-radius measurements*, *Phys. Rev. D* **107** (2023) 103051 [[2208.03282](#)].
- [51] S. Bhattacharya, B. Dasgupta, R. Laha and A. Ray, *Can LIGO Detect Nonannihilating Dark Matter?*, *Phys. Rev. Lett.* **131** (2023) 091401 [[2302.07898](#)].
- [52] J. Bramante and N. Raj, *Dark matter in compact stars*, *Phys. Rept.* **1052** (2024) 1 [[2307.14435](#)].
- [53] S. Cebrián, *Review on dark matter searches*, *J. Phys. Conf. Ser.* **2502** (2023) 012004 [[2205.06833](#)].
- [54] E.A. Baltz and L. Bergstrom, *Detection of leptonic dark matter*, *Phys. Rev. D* **67** (2003) 043516 [[hep-ph/0211325](#)].
- [55] C.-R. Chen and F. Takahashi, *Cosmic rays from Leptonic Dark Matter*, *JCAP* **02** (2009) 004 [[0810.4110](#)].
- [56] P.J. Fox and E. Poppitz, *Leptophilic Dark Matter*, *Phys. Rev. D* **79** (2009) 083528 [[0811.0399](#)].
- [57] Q.-H. Cao, E. Ma and G. Shaughnessy, *Dark Matter: The Leptonic Connection*, *Phys. Lett. B* **673** (2009) 152 [[0901.1334](#)].
- [58] A. Ibarra, A. Ringwald, D. Tran and C. Weniger, *Cosmic Rays from Leptophilic Dark Matter Decay via Kinetic Mixing*, *JCAP* **08** (2009) 017 [[0903.3625](#)].
- [59] X.-J. Bi, X.-G. He and Q. Yuan, *Parameters in a class of leptophilic models from PAMELA, ATIC and FERMI*, *Phys. Lett. B* **678** (2009) 168 [[0903.0122](#)].
- [60] J. Kopp, V. Niro, T. Schwetz and J. Zupan, *DAMA/LIBRA and leptonically interacting Dark Matter*, *Phys. Rev. D* **80** (2009) 083502 [[0907.3159](#)].
- [61] P. Ko and Y. Omura, *Supersymmetric $U(1)_B \times U(1)_L$ model with leptophilic and leptophobic cold dark matters*, *Phys. Lett. B* **701** (2011) 363 [[1012.4679](#)].
- [62] W. Chao, *Pure Leptonic Gauge Symmetry, Neutrino Masses and Dark Matter*, *Phys. Lett. B* **695** (2011) 157 [[1005.1024](#)].
- [63] D. Schmidt, T. Schwetz and T. Toma, *Direct Detection of Leptophilic Dark Matter in a Model with Radiative Neutrino Masses*, *Phys. Rev. D* **85** (2012) 073009 [[1201.0906](#)].

- [64] M. Das and S. Mohanty, *Leptophilic dark matter in gauged $L_\mu - L_\tau$ extension of MSSM*, *Phys. Rev. D* **89** (2014) 025004 [[1306.4505](#)].
- [65] P. Schwaller, T.M.P. Tait and R. Vega-Morales, *Dark Matter and Vectorlike Leptons from Gauged Lepton Number*, *Phys. Rev. D* **88** (2013) 035001 [[1305.1108](#)].
- [66] Y. Bai and J. Berger, *Lepton Portal Dark Matter*, *JHEP* **08** (2014) 153 [[1402.6696](#)].
- [67] P. Agrawal, Z. Chacko and C.B. Verhaaren, *Leptophilic Dark Matter and the Anomalous Magnetic Moment of the Muon*, *JHEP* **08** (2014) 147 [[1402.7369](#)].
- [68] J. Kopp, L. Michaels and J. Smirnov, *Loopy Constraints on Leptophilic Dark Matter and Internal Bremsstrahlung*, *JCAP* **04** (2014) 022 [[1401.6457](#)].
- [69] XENON100 collaboration, *Exclusion of Leptophilic Dark Matter Models using XENON100 Electronic Recoil Data*, *Science* **349** (2015) 851 [[1507.07747](#)].
- [70] LZ collaboration, *Projected sensitivities of the LUX-ZEPLIN experiment to new physics via low-energy electron recoils*, *Phys. Rev. D* **104** (2021) 092009 [[2102.11740](#)].
- [71] C.-Y. Chen, J. Kozaczuk and Y.-M. Zhong, *Exploring leptophilic dark matter with NA64- μ* , *JHEP* **10** (2018) 154 [[1807.03790](#)].
- [72] L. Marsicano, M. Battaglieri, A. Celentano, R. De Vita and Y.-M. Zhong, *Probing Leptophilic Dark Sectors at Electron Beam-Dump Facilities*, *Phys. Rev. D* **98** (2018) 115022 [[1812.03829](#)].
- [73] CRESST collaboration, *Results on MeV-scale dark matter from a gram-scale cryogenic calorimeter operated above ground*, *Eur. Phys. J. C* **77** (2017) 637 [[1707.06749](#)].
- [74] SUPERCDMS collaboration, *Light Dark Matter Search with a High-Resolution Athermal Phonon Detector Operated Above Ground*, *Phys. Rev. Lett.* **127** (2021) 061801 [[2007.14289](#)].
- [75] SENSEI collaboration, *SENSEI: Direct-Detection Results on sub-GeV Dark Matter from a New Skipper-CCD*, *Phys. Rev. Lett.* **125** (2020) 171802 [[2004.11378](#)].
- [76] DAMIC-M collaboration, *First Constraints from DAMIC-M on Sub-GeV Dark-Matter Particles Interacting with Electrons*, *Phys. Rev. Lett.* **130** (2023) 171003 [[2302.02372](#)].
- [77] A. Aguilar-Arevalo, F.A. Bessia, N. Avalos, D. Baxter, X. Bertou, C. Bonifazi et al., *The oscura experiment*, *arXiv preprint arXiv:2202.10518* (2022) .
- [78] M.C. Marshall, M.J. Turner, M.J.H. Ku, D.F. Phillips and R.L. Walsworth, *Directional detection of dark matter with diamond*, *Quantum Sci. Technol.* **6** (2021) 024011 [[2009.01028](#)].
- [79] S.A. Hertel, A. Biekert, J. Lin, V. Velan and D.N. McKinsey, *Direct detection of sub-GeV dark matter using a superfluid ^4He target*, *Phys. Rev. D* **100** (2019) 092007 [[1810.06283](#)].
- [80] SPICE, HERALD collaboration, *Applying Superfluid Helium to Light Dark Matter Searches: Demonstration of the HeRALD Detector Concept*, [2307.11877](#).
- [81] G.-B. Kim, *Self-absorption and Phonon Pulse Shape Discrimination in Scintillating Bolometers*, *Journal of Low Temperature Physics* **199** (2020) 1004.
- [82] Y. Hochberg, Y. Zhao and K.M. Zurek, *Superconducting Detectors for Superlight Dark Matter*, *Phys. Rev. Lett.* **116** (2016) 011301 [[1504.07237](#)].

- [83] Y. Hochberg, I. Charaev, S.-W. Nam, V. Verma, M. Colangelo and K.K. Berggren, *Detecting Sub-GeV Dark Matter with Superconducting Nanowires*, *Phys. Rev. Lett.* **123** (2019) 151802 [[1903.05101](#)].
- [84] R.M. Geilhufe, F. Kahlhoefer and M.W. Winkler, *Dirac Materials for Sub-MeV Dark Matter Detection: New Targets and Improved Formalism*, *Phys. Rev. D* **101** (2020) 055005 [[1910.02091](#)].
- [85] Y. Kahn and T. Lin, *Searches for light dark matter using condensed matter systems*, *Rept. Prog. Phys.* **85** (2022) 066901 [[2108.03239](#)].
- [86] C. Blanco, R. Essig, M. Fernandez-Serra, H. Ramani and O. Slone, *Dark matter direct detection with quantum dots*, *Phys. Rev. D* **107** (2023) 095035 [[2208.05967](#)].
- [87] Z. Huang, C. Lane, S.E. Grefe, S. Nandy, B. Fauseweh, S. Paschen et al., *Dark Matter Detection with Strongly Correlated Topological Materials: Flatband Effect*, [2305.19967](#).
- [88] A. Das, J. Jang and H. Min, *Sub-MeV Dark Matter Detection with Bilayer Graphene*, [2312.00866](#).
- [89] B. Carew, A.R. Caddell, T.N. Maity and C.A.J. O'Hare, *The neutrino fog for dark matter-electron scattering experiments*, [2312.04303](#).
- [90] N.F. Bell, G. Busoni and S. Robles, *Capture of Leptophilic Dark Matter in Neutron Stars*, *JCAP* **06** (2019) 054 [[1904.09803](#)].
- [91] N.F. Bell, G. Busoni, M.E. Ramirez-Quezada, S. Robles and M. Virgato, *Improved treatment of dark matter capture in white dwarfs*, *JCAP* **10** (2021) 083 [[2104.14367](#)].
- [92] P.J. Fox, R. Harnik, J. Kopp and Y. Tsai, *LEP Shines Light on Dark Matter*, *Phys. Rev. D* **84** (2011) 014028 [[1103.0240](#)].
- [93] S. Dutta, D. Sachdeva and B. Rawat, *Signals of Leptophilic Dark Matter at the ILC*, *Eur. Phys. J. C* **77** (2017) 639 [[1704.03994](#)].
- [94] B. Barman, S. Bhattacharya, S. Girmohanta and S. Jahedi, *Effective Leptophilic WIMPs at the $e+e-$ collider*, *JHEP* **04** (2022) 146 [[2109.10936](#)].
- [95] S. Kundu, A. Guha, P.K. Das and P.S.B. Dev, *EFT analysis of leptophilic dark matter at future electron-positron colliders in the mono-photon and mono-Z channels*, *Phys. Rev. D* **107** (2023) 015003 [[2110.06903](#)].
- [96] CMS collaboration, *Search for invisible decays of the Higgs boson produced via vector boson fusion in proton-proton collisions at $s=13$ TeV*, *Phys. Rev. D* **105** (2022) 092007 [[2201.11585](#)].
- [97] ATLAS collaboration, *Search for invisible Higgs-boson decays in events with vector-boson fusion signatures using 139 fb^{-1} of proton-proton data recorded by the ATLAS experiment*, *JHEP* **08** (2022) 104 [[2202.07953](#)].
- [98] L.E. Strigari, *Neutrino Coherent Scattering Rates at Direct Dark Matter Detectors*, *New J. Phys.* **11** (2009) 105011 [[0903.3630](#)].
- [99] J. Billard, L. Strigari and E. Figueroa-Feliciano, *Implication of neutrino backgrounds on the reach of next generation dark matter direct detection experiments*, *Phys. Rev. D* **89** (2014) 023524 [[1307.5458](#)].
- [100] J. Monroe and P. Fisher, *Neutrino Backgrounds to Dark Matter Searches*, *Phys. Rev. D* **76** (2007) 033007 [[0706.3019](#)].

- [101] G. Arcadi, A. Djouadi and M. Kado, *The Higgs-portal for dark matter: effective field theories versus concrete realizations*, *Eur. Phys. J. C* **81** (2021) 653 [[2101.02507](#)].
- [102] J. Fan, M. Reece and L.-T. Wang, *Non-relativistic effective theory of dark matter direct detection*, *JCAP* **11** (2010) 042 [[1008.1591](#)].
- [103] H. Iminiyaz, M. Drees and X. Chen, *Relic Abundance of Asymmetric Dark Matter*, *JCAP* **07** (2011) 003 [[1104.5548](#)].
- [104] ATLAS collaboration, *Search for new phenomena in events with an energetic jet and missing transverse momentum in pp collisions at $\sqrt{s} = 13$ TeV with the ATLAS detector*, *Phys. Rev. D* **103** (2021) 112006 [[2102.10874](#)].
- [105] CMS collaboration, *Search for new particles in events with energetic jets and large missing transverse momentum in proton-proton collisions at $\sqrt{s} = 13$ TeV*, *JHEP* **11** (2021) 153 [[2107.13021](#)].
- [106] J. Alwall, R. Frederix, S. Frixione, V. Hirschi, F. Maltoni, O. Mattelaer et al., *The automated computation of tree-level and next-to-leading order differential cross sections, and their matching to parton shower simulations*, *JHEP* **07** (2014) 079 [[1405.0301](#)].
- [107] A. Alloul, N.D. Christensen, C. Degrande, C. Duhr and B. Fuks, *FeynRules 2.0 - A complete toolbox for tree-level phenomenology*, *Comput. Phys. Commun.* **185** (2014) 2250 [[1310.1921](#)].
- [108] T. Sjostrand, S. Mrenna and P.Z. Skands, *PYTHIA 6.4 Physics and Manual*, *JHEP* **05** (2006) 026 [[hep-ph/0603175](#)].
- [109] T. Sjostrand, S. Mrenna and P.Z. Skands, *A Brief Introduction to PYTHIA 8.1*, *Comput. Phys. Commun.* **178** (2008) 852 [[0710.3820](#)].
- [110] DELPHES 3 collaboration, *DELPHES 3, A modular framework for fast simulation of a generic collider experiment*, *JHEP* **02** (2014) 057 [[1307.6346](#)].
- [111] G. Belanger, F. Boudjema, A. Pukhov and A. Semenov, *Dark matter direct detection rate in a generic model with micrOMEGAs 2.2*, *Comput. Phys. Commun.* **180** (2009) 747 [[0803.2360](#)].
- [112] COMPASS collaboration, *The Polarised Valence Quark Distribution from semi-inclusive DIS*, *Phys. Lett. B* **660** (2008) 458 [[0707.4077](#)].
- [113] LZ collaboration, *First Dark Matter Search Results from the LUX-ZEPLIN (LZ) Experiment*, [2207.03764](#).
- [114] DARKSIDE collaboration, *Low-Mass Dark Matter Search with the DarkSide-50 Experiment*, *Phys. Rev. Lett.* **121** (2018) 081307 [[1802.06994](#)].
- [115] XENON collaboration, *Constraining the spin-dependent WIMP-nucleon cross sections with XENON1T*, *Phys. Rev. Lett.* **122** (2019) 141301 [[1902.03234](#)].
- [116] PICO collaboration, *Dark Matter Search Results from the Complete Exposure of the PICO-60 C_3F_8 Bubble Chamber*, *Phys. Rev.* **D100** (2019) 022001 [[1902.04031](#)].
- [117] XENON100 collaboration, *Dark Matter Results from 100 Live Days of XENON100 Data*, *Phys. Rev. Lett.* **107** (2011) 131302 [[1104.2549](#)].
- [118] DELPHI collaboration, *Photon events with missing energy in $e^+ e^-$ collisions at $s^{*(1/2)} = 130\text{-GeV}$ to 209-GeV* , *Eur. Phys. J. C* **38** (2005) 395 [[hep-ex/0406019](#)].

- [119] FCC collaboration, *FCC-ee: The Lepton Collider: Future Circular Collider Conceptual Design Report Volume 2*, *Eur. Phys. J. ST* **228** (2019) 261.
- [120] W.H. Press and D.N. Spergel, *Capture by the sun of a galactic population of weakly interacting, massive particles*, *APJ* **296** (1985) .
- [121] A. Gould, *Weakly Interacting Massive Particle Distribution in and Evaporation from the Sun*, *APJ* **321** (1987) 560.
- [122] A. Gould, *Resonant Enhancements in Weakly Interacting Massive Particle Capture by the Earth*, *APJ* **321** (1987) 571.
- [123] G. Bertone and M. Fairbairn, *Compact Stars as Dark Matter Probes*, *Phys. Rev. D* **77** (2008) 043515 [[0709.1485](#)].
- [124] J. Bramante, A. Delgado and A. Martin, *Multiscatter stellar capture of dark matter*, *Phys. Rev. D* **96** (2017) 063002 [[1703.04043](#)].
- [125] B. Dasgupta, A. Gupta and A. Ray, *Dark matter capture in celestial objects: Improved treatment of multiple scattering and updated constraints from white dwarfs*, *JCAP* **08** (2019) 018 [[1906.04204](#)].
- [126] C. Kouvaris, *WIMP Annihilation and Cooling of Neutron Stars*, *Phys. Rev. D* **77** (2008) 023006 [[0708.2362](#)].
- [127] C. Kouvaris and P. Tinyakov, *Can Neutron stars constrain Dark Matter?*, *Phys. Rev. D* **82** (2010) 063531 [[1004.0586](#)].
- [128] M. Baryakhtar, J. Bramante, S.W. Li, T. Linden and N. Raj, *Dark Kinetic Heating of Neutron Stars and An Infrared Window On WIMPs, SIMPs, and Pure Higgsinos*, *Phys. Rev. Lett.* **119** (2017) 131801 [[1704.01577](#)].
- [129] N.F. Bell, G. Busoni and S. Robles, *Heating up Neutron Stars with Inelastic Dark Matter*, *JCAP* **09** (2018) 018 [[1807.02840](#)].
- [130] C.-S. Chen and Y.-H. Lin, *Reheating neutron stars with the annihilation of self-interacting dark matter*, *JHEP* **08** (2018) 069 [[1804.03409](#)].
- [131] J.F. Acevedo, J. Bramante, R.K. Leane and N. Raj, *Warming Nuclear Pasta with Dark Matter: Kinetic and Annihilation Heating of Neutron Star Crusts*, *JCAP* **03** (2020) 038 [[1911.06334](#)].
- [132] N. Raj, P. Tanedo and H.-B. Yu, *Neutron stars at the dark matter direct detection frontier*, *Phys. Rev. D* **97** (2018) 043006 [[1707.09442](#)].
- [133] A. de Lavallaz and M. Fairbairn, *Neutron Stars as Dark Matter Probes*, *Phys. Rev. D* **81** (2010) 123521 [[1004.0629](#)].
- [134] M. McCullough and M. Fairbairn, *Capture of Inelastic Dark Matter in White Dwarves*, *Phys. Rev. D* **81** (2010) 083520 [[1001.2737](#)].
- [135] D. Hooper, D. Spolyar, A. Vallinotto and N.Y. Gnedin, *Inelastic Dark Matter As An Efficient Fuel For Compact Stars*, *Phys. Rev. D* **81** (2010) 103531 [[1002.0005](#)].
- [136] J.F. Acevedo and J. Bramante, *Supernovae Sparked By Dark Matter in White Dwarfs*, *Phys. Rev. D* **100** (2019) 043020 [[1904.11993](#)].
- [137] P.W. Graham, R. Janish, V. Narayan, S. Rajendran and P. Riggins, *White Dwarfs as Dark Matter Detectors*, *Phys. Rev. D* **98** (2018) 115027 [[1805.07381](#)].

- [138] DAMIC-M collaboration, *The DAMIC-M experiment: Status and first results*, *SciPost Phys. Proc.* **12** (2023) 014 [[2210.12070](#)].
- [139] SUPERCDMS collaboration, *First Dark Matter Constraints from a SuperCDMS Single-Charge Sensitive Detector*, *Phys. Rev. Lett.* **121** (2018) 051301 [[1804.10697](#)].

Direct Detection of Dark Photon Dark Matter with the James Webb Space Telescope

Haipeng An,^{1,2,3,4,*} Shuailiang Ge,^{3,5,†} Jia Liu,^{5,3,‡} and Zhiyao Lu^{5,§}

¹*Department of Physics, Tsinghua University, Beijing 100084, China*

²*Center for High Energy Physics, Tsinghua University, Beijing 100084, China*

³*Center for High Energy Physics, Peking University, Beijing 100871, China*

⁴*Frontier Science Center for Quantum Information, Beijing 100084, China*

⁵*School of Physics and State Key Laboratory of Nuclear Physics and Technology, Peking University, Beijing 100871, China*

(Dated: February 28, 2024)

Abstract

In this study, we propose an investigation into dark photon dark matter (DPDM) within the infrared frequency band, utilizing highly sensitive infrared light detectors commonly integrated into space telescopes, such as the James Webb Space Telescope (JWST). The presence of DPDM induces electron oscillations in the reflector of these detectors. Consequently, these oscillating electrons can emit monochromatic electromagnetic waves with a frequency almost equivalent to the mass of DPDM. By employing the stationary phase approximation, we can demonstrate that when the size of the reflector significantly exceeds the wavelength of the electromagnetic wave, the contribution to the electromagnetic wave field at a given position primarily stems from the surface unit perpendicular to the relative position vector. This simplification results in the reduction of electromagnetic wave calculations to ray optics. By applying this concept to JWST, our analysis of observational data demonstrates the potential to establish constraints on the kinetic mixing between the photon and dark photon within the range [10, 500] THz. Despite JWST not being optimized for DPDM searches, our findings reveal constraints comparable to those obtained from the XENON1T experiment in the laboratory, as well as astrophysical constraints from solar emission. Additionally, we explore strategies to optimize future experiments specifically designed for DPDM searches.

* anhp@mail.tsinghua.edu.cn

† sge@pku.edu.cn

‡ jialiu@pku.edu.cn

§ 2000011457@stu.pku.edu.cn

CONTENTS

I. Introduction	2
II. High Frequency Approximation	4
A. Monochromatic DPDM	5
B. Non-monochromatic DPDM	9
III. The Optical Telescope Element (OTE) of JWST	11
IV. Calculating the Equivalent Flux Density	13
V. Constraints from JWST Observation Data	16
VI. Summary and Outlook	19
Acknowledgement	20
A. Detailed derivation of Eq. (21)	20
B. A Brief Proof of Eq. (8)	21
C. Ray Transfer Matrix Analysis	23
D. Data Analysis Method	26
References	28

I. INTRODUCTION

The elusive nature of dark matter has thus far eluded detection through various non-gravitational search efforts. The scope of potential candidates has expanded beyond traditional weakly interacting massive particles (WIMPs) to encompass a broad range of mass scales. One intriguing category comprises ultralight bosonic dark matter, which has garnered significant attention as the lightest dark matter candidate. Among these, the dark photon is a notable ultralight vector dark matter candidate due to its kinetic mixing marginal operator coupling with the photon field, serving as one of the simplest extensions of the Standard

Model [1–6]. The kinetic mixing dark photon could have been generated in the early universe and holds promise as a viable dark matter candidate [7–10]. Various mechanisms facilitate its plausibility, including the misalignment mechanism coupled with a non-minimal Ricci scalar coupling [8, 9, 11–13], inflationary fluctuations [10, 14–23], parametric resonances [24–29], or the decay of cosmic strings [30].

Due to the vast range of unknown mass of the dark photon dark matter (DPDM), there are various detecting methods accordingly [31, 32]. The relevant searches for dark photon DM are haloscope experiments [33–38], dish antenna experiments [39–42], plasma telescopes [43], CMB spectrum distortion [9, 44] and radio telescopes [45–47]. The searches include direct detection of local DPDM in laboratories and observation on its impact in the early universe.

Recently, we proposed to search for Dark Photon Dark Matter (DPDM) conversion, specifically $A' \rightarrow \gamma$, locally using radio telescopes such as FAST and LOFAR [46]. For instance, the FAST radio telescope, equipped with a large dish antenna, converts DPDM into a regular photon field. In each small surface area of FAST, an oscillating electric dipole is generated by the DPDM field, with a frequency matching the DPDM mass. Summing up the contributions from each surface area yields the total converted electromagnetic field. The original proposal utilized a spherical reflector, causing the electromagnetic field to constructively focus on the spherical center [39, 41, 48]. This concept has been previously employed in shielded room-sized experiments by various works, utilizing variations such as plane/parabolic reflectors or dipole antennas [42, 49–55].

In this article, we would like to explore this idea with the recent new telescope, the James Webber Science Telescope (JWST), which is running in space. JWST covers the frequency range of 10–500 THz for infrared astronomy. Our searches for DPDM benefit from JWST’s high frequency resolution $R = f/\Delta f$, which ranges from 4 to 3000, depending on different observation modes [56]. Also, since it works in space, we expect it to have a much lower noise background than terrestrial facilities. The Near Infrared Spectrograph (NISpec) and the Mid-Infrared Instrument (MIRI), two instruments carried by JWST, are especially useful for searching for DPDM. By analyzing data collected by the two instruments, we get the upper limits for the DPDM-photon coupling constant, $\epsilon \sim 10^{-10} - 10^{-12}$ in the frequency range 10 – 500 THz at 95% confidence level (C.L.).

The Lagrangian of the dark photon model in this work is a vector boson that couples to the SM particles through its kinetic mixing with photon, and the Lagrangian is described

by the equation

$$\mathcal{L} = -\frac{1}{4}F'_{\mu\nu}F'^{\mu\nu} + \frac{1}{2}m_{A'}^2 A'_\mu A'^\mu - \frac{1}{2}\epsilon F_{\mu\nu}F'^{\mu\nu}, \quad (1)$$

where F and F' are the dark photon and photon field strength, ϵ is the kinematic mixing. After proper rotation and redefinition, one can eliminate the kinematic mixing term and arrive at the interaction Lagrangian for A' , the SM photon A , and the electromagnetic current j_{em}^μ ,

$$\mathcal{L}_{\text{int}} = e j_{\text{em}}^\mu (A_\mu - \epsilon A'_\mu), \quad (2)$$

where e is the electromagnetic coupling. Therefore, the DPDM electric field, $\mathbf{E}' = -\dot{\mathbf{A}}' - \nabla A'^0$, can accelerate the charge carriers in a reflector and thus be converted to SM electromagnetic waves.

This work is structured as follows: In Section I, we present the background of DPDM conversion. In Section II, we offer a mathematical proof of the reduction from complex electroweak wave calculation to ray optics using the stationary phase approximation. Section III applies the simplified calculation to JWST, obtaining the equivalent flux density of the electromagnetic field in Section IV. Section V establishes limits on the kinetic mixing parameter of the dark photon using JWST observational data. Finally, in Section VI, we draw our conclusions.

II. HIGH FREQUENCY APPROXIMATION

In order to calculate the EM signals induced by DPDM on a metal reflector plate, the most direct way is to divide the reflector into many small patches and sum up the induced EM signals over all of them. The length of each small patch is required to be much smaller than the wavelength λ of the induced EW signal while at the same time much larger than the reflector thickness. Consequently, to ensure enough accuracy, the simulation mesh must be fine enough for the distance between mesh points to be smaller than the wavelength. This method works well in the case of FAST telescope [57]. The FAST detects radio photons around 1 GHz and has a reflector roughly 500 m in diameter. Therefore, we only need to divide the FAST reflector into $\sim 10^6$ patches for an accurate simulation. On the other hand, JWST works at a much higher frequency range, 10 – 500 THz (i.e., the photon wavelength $\lambda \sim 0.6 - 30 \mu\text{m}$), and the diameter of the JWST's primary mirror is $D = 6.6$ meter. To achieve an acceptable level of accuracy in simulating the JWST case, we require over 10^{15}

patches, which is finer than the FAST case by orders of magnitude. However, such a fine mesh imposes an immense computational burden, rendering it unfeasible to simulate signal strength using available computer resources.

Fortunately, as we will see, we can theoretically demonstrate that calculating the induced EM signals becomes considerably more straightforward in the high-frequency regime, $D \gg \lambda$. Similar to the case of reaching the ray optics at the high-frequency limit of the wave optics, we can establish that the strength of the DPDM-induced signal can be obtained using a ray-optical method. This simplification ultimately leads to a set of algebraic equations that can be easily calculated, even manually without the need of a fine-mesh simulation. The physical interpretation of such a simplification is that, in the high-frequency regime, interferences between different patches on the reflector have a negligible impact on the final result.

To be more specific, this simplification works primarily due to two key factors. Firstly, the phases of the electric fields contributed by different patches on a plate vary significantly, while their strengths remain relatively the same. This results in significant cancellations between the electric fields generated by different patches. Secondly, one significant parameter is the coherence length of DPDM. The DPDM and the induced photon have the same energy, but the coherent length of DPDM, λ' , is much larger than the wavelength of the induced photons, λ . This is due to the non-relativistic nature of dark matter with a low speed $v_{\text{DM}} \sim 10^{-3}$, which gives $\lambda' \sim \lambda/v_{\text{DM}}$. Importantly, λ' is still significantly smaller than the diameter of the JWST's mirrors. As a result, the interferences between different patches are dampened by incoherence.

In the following, we are going to prove that the ray optics is indeed applicable here in calculating the EM signals induced by DPDM for the JWST case which locates in the high-frequency regime, $D/\lambda \sim 10^6$ and $D/\lambda' \sim 10^3$. Finally, a formula for computing the strength of the induced signal will be introduced.

A. Monochromatic DPDM

Firstly, we consider a simplified case that DPDM is monochromatic in frequency. Then, in the next subsection, we discuss the more realistic case where the velocity distribution of dark matter is included. Under the effect of the DPDM's dark electric field, each small

patch on a reflector plate can be treated as an electric dipole,

$$\mathbf{p} = 2\epsilon\mathbf{A}'_{\tau}\Delta S, \quad (3)$$

where \mathbf{A}'_{τ} is the component of \mathbf{A}' parallel with the patch and ΔS is the area of the patch [57]. The dipole is oscillating as a result of the oscillation of the DPDM field. Then, summing up the EM radiations from all the dipoles, we arrive at the expressions of the induced EM fields at position \mathbf{r} [57],

$$\mathbf{E}(\mathbf{r}) = -\frac{\epsilon m_{A'}^2 |\mathbf{A}'|}{2\pi} \int [\boldsymbol{\tau} \times (\mathbf{r} - \mathbf{r}')] \times (\mathbf{r} - \mathbf{r}') \frac{e^{im_{A'}|\mathbf{r}-\mathbf{r}'| + ik' \cdot (\mathbf{r}' - \mathbf{r})}}{|\mathbf{r} - \mathbf{r}'|^3} dS', \quad (4)$$

$$\mathbf{B}(\mathbf{r}) = -\frac{\epsilon m_{A'}^2 |\mathbf{A}'|}{2\pi} \int \boldsymbol{\tau} \times (\mathbf{r} - \mathbf{r}') \frac{e^{im_{A'}|\mathbf{r}-\mathbf{r}'| + ik' \cdot (\mathbf{r}' - \mathbf{r})}}{|\mathbf{r} - \mathbf{r}'|^2} dS'. \quad (5)$$

\mathbf{k}' is the wave vector of DPDM. $\mathbf{A}'_{\tau} = \boldsymbol{\tau}|\mathbf{A}'|$ where the tangent vector $\boldsymbol{\tau}$ can be calculated as $\boldsymbol{\tau} \equiv \mathbf{n}_0 - (\mathbf{n}_0 \cdot \mathbf{n})\mathbf{n}$. The two unit vectors, \mathbf{n}_0 and \mathbf{n} , represent the direction of \mathbf{A}' and the normal direction of dS , respectively. The magnitude of oscillations, $|\mathbf{A}'|$, is determined by the dark matter energy density ρ_{DM} , that is,

$$\rho_{\text{DM}} = \frac{1}{2}m_{A'}^2 |\mathbf{A}'|^2 = \frac{1}{2}|\mathbf{E}'|^2. \quad (6)$$

Then, we can calculate the energy flux density,

$$\langle \mathbf{S}' \rangle_t = \frac{1}{2} \text{Re}(\mathbf{E} \times \mathbf{B}^*). \quad (7)$$

$\langle \dots \rangle_t$ here means the average over time. In principle, for any reflectors, we can numerically simulate the DPDM-induced EM waves using these formulas. However, as we discussed above, such a simulation requires a very fine mesh that is hard to realize in computers for the JWST case. As we are going to see below, we figure out a more analytical method applicable in the high-frequency regime.

The key to simplifying our formulas in the high-frequency regime is to use the stationary phase approximation. In general, the stationary phase approximation works in solving the following integral as α tends to infinity [58],

$$\begin{aligned} & \int_{\mathbb{R}^n} g(\mathbf{x}) e^{i\alpha f(\mathbf{x})} d^n \mathbf{x} \\ &= \sum_{\mathbf{x}_0 \in \Sigma} e^{i\alpha f(\mathbf{x}_0)} |\det(\text{Hess}(f(\mathbf{x}_0)))|^{-1/2} e^{\frac{i\pi}{4} \text{sgn}(\text{Hess}(f(\mathbf{x}_0)))} \left(\frac{2\pi}{\alpha} \right)^{\frac{n}{2}} g(\mathbf{x}_0) + o(\alpha^{-\frac{n}{2}}), \quad \alpha \rightarrow \infty. \end{aligned} \quad (8)$$

where the function $g(\mathbf{x})$ is either zero or exponentially suppressed when \mathbf{x} is large, (the condition where $g(\mathbf{x})$ is zero when \mathbf{x} is large, can be more accurately described by the mathematical terminology of “compactly supported”). Σ is the set of points where $\nabla f = 0$. $\text{Hess}(f(x_0))$ is the Hessian of f , and $\text{sgn}(\text{Hess}(f(\mathbf{x}_0)))$ is the signature of the Hessian,

$$\text{Hess}(f(\mathbf{x}_0))_{ij} = \left. \frac{\partial^2 f}{\partial x_i \partial x_j} \right|_{\mathbf{x}=\mathbf{x}_0}, \quad (9)$$

$$\text{sgn}(\text{Hess}(f(\mathbf{x}_0))) = \#(\text{positive eigenvalues}) - \#(\text{negative eigenvalues}). \quad (10)$$

Note that Eq. (8) is only valid when we assume $\nabla f = 0$ has only discrete solutions, otherwise $\text{Hess}(f(x_0))$ is non-degenerate at $x_0 \in \Sigma$.

This stationary-phase approximation (8) can be intuitively understood in the following way: when k is large, the exponential oscillates rapidly with a small change of \mathbf{x} , while $g(\mathbf{x})$ changes very little. Therefore, the integral vanishes unless we are considering a small patch in \mathbb{R}^n around $\nabla f = 0$, which is the stationary point of the phase factor. A rigorous proof of Eq. (8) is provided in Appendix B.

In the JWST case, the phase factor is $m_{A'}|\mathbf{r} - \mathbf{r}'| + \mathbf{k}' \cdot (\mathbf{r}' - \mathbf{r})$. Given that the dark photon’s wave vector is approximately 10^{-3} times its frequency, the phase factor is dominated by the first term. By rewriting the first term as $m_{A'}D \times (|\mathbf{r} - \mathbf{r}'|/D)$, with D being the characteristic length of JWST optical elements, the second factor becomes an $\mathcal{O}(1)$ function of spacial coordinates, and $m_{A'}D \gg 1$ by assumption. This is equivalent to the case $\alpha \gg 1$ in Eq. (8). Consequently, we can apply the stationary-phase approximation (8) to calculate Eq. (4). The process of calculating Eq. (5) is the same, so it will not be shown here for the sake of conciseness. In the most general setup, a conductor is a closed surface. In Eq. (4), the domain of integration is the whole conductor surface. By assumption, this integral can be split into several integrals in compact subsets of \mathbb{R}^2 , with the surface element dS re-expressed in the form $J(\mathbf{r}')dudv$ where J is the Jacobian determined by the equation of the surface. We study each of these integrals separately, and denote by Ω the domain of integration. Define

$$g(\mathbf{r}') = \begin{cases} -\frac{\epsilon m_{A'}^2 |\mathbf{A}'| [\boldsymbol{\tau}(\mathbf{r}') \times (\mathbf{r} - \mathbf{r}')] \times (\mathbf{r} - \mathbf{r}')}{2\pi |\mathbf{r} - \mathbf{r}'|^3} J(\mathbf{r}') & \mathbf{r}' \in \Omega \\ 0 & \mathbf{r}' \notin \Omega \end{cases}. \quad (11)$$

Clearly, $g(\mathbf{r}')$ is compactly supported. Applying the stationary phase approximation, the

only contribution to the integral comes from points where

$$\frac{\partial}{\partial u}|\mathbf{r} - \mathbf{r}'(u, v)| = 0, \quad \frac{\partial}{\partial v}|\mathbf{r} - \mathbf{r}'(u, v)| = 0, \quad (12)$$

or equivalently,

$$(\mathbf{r} - \mathbf{r}') \cdot \frac{\partial \mathbf{r}'}{\partial u} = 0, \quad (\mathbf{r} - \mathbf{r}') \cdot \frac{\partial \mathbf{r}'}{\partial v} = 0. \quad (13)$$

u and v can be understood as two parameters describing a certain patch of the surface, so $\partial \mathbf{r}' / \partial u$ and $\partial \mathbf{r}' / \partial v$ are tangent vectors at \mathbf{r}' . Therefore, Eq. (13) tells us that $\mathbf{r} - \mathbf{r}'$ is perpendicular to the tangent plane at \mathbf{r}' . This result can be interpreted in a more intuitive way. Considering a conductor surface, at each point \mathbf{r}' on the surface, a light ray is only emitted in the normal direction, then the signal received at the position \mathbf{r} is the sum of the light rays passing through the position \mathbf{r} . Therefore, we see the calculations in the JWST case can be accomplished within the framework of ray optics. The key difference with conventional ray optics is that a light ray induced by DPDM is always perpendicular to the local surface from which it is emitted, regardless of the direction in which the DPDM is incident.

We denote by $\hat{\mathbf{r}}_j$ the j th point on the conductor surface such that $\mathbf{r} - \hat{\mathbf{r}}_j$ is perpendicular to the tangent plane at $\hat{\mathbf{r}}_j$. Using the stationary-phase method, Eq. (4) becomes

$$\mathbf{E}(\mathbf{r}) = \sum_j i e^{i m_{A'} |\mathbf{r} - \hat{\mathbf{r}}_j|} \epsilon m_{A'} \hat{\mathbf{A}}'(\hat{\mathbf{r}}_j) \quad (14)$$

where $\hat{\mathbf{A}}'(\hat{\mathbf{r}}_j) = |\mathbf{A}'| \boldsymbol{\tau}(\hat{\mathbf{r}}_j)$ is the projection of \mathbf{A}' onto the tangent plane at $\hat{\mathbf{r}}_j$. The expression for \mathbf{B} is similar which is not present here for the purpose of conciseness. Putting everything together, we get

$$\langle \mathbf{S}(\mathbf{r}) \rangle_t = \sum_j \frac{1}{2} \epsilon^2 m_{A'}^2 \hat{\mathbf{A}}'(\hat{\mathbf{r}}_j)^2 \hat{\mathbf{n}}(\hat{\mathbf{r}}_j) + \text{interference terms} \quad (15)$$

where $\hat{\mathbf{n}}(\hat{\mathbf{r}}_j)$ is the out-pointing normal direction of the conductor surface at $\hat{\mathbf{r}}_j$. The interference term comes from the cross products of contributions from $\hat{\mathbf{r}}_j$ and $\hat{\mathbf{r}}_k$, with $j \neq k$. If there is only one $\hat{\mathbf{r}}_j$, there is only one term in the summation and the interference term drops out. As a consistency check, one can compare (15) with the result of infinitely large metal plate given in appendix I-A of Ref. [57].

In the most extreme case, the conductor is a sphere and the detector is placed at the center of the sphere. Then, for the detector, the phase is stationary everywhere on the

sphere and no simplification can be made to Eqs. (4) and (5). Note that this is not the case with JWST, because the reflectors in JWST are not spherical, and the points $\hat{\mathbf{r}}_j$ are indeed discrete. In addition, in the frequency range of JWST, the correlation length is much smaller than the characteristic length of the reflectors, and the interference between different patches is further suppressed. This will be discussed in more detail in the following section.

B. Non-monochromatic DPDM

According to the Standard Halo Model, dark matter has a truncated Maxwellian distribution in the momentum space. Consequently, we should take into consideration the effect of finite coherence length of DPDM. The dark photon field at a location \mathbf{x} can be expressed as,

$$\mathbf{E}'(\mathbf{x}, t) = \int_{<k_{\text{esc}}} \frac{d^3\mathbf{k}'}{(2\pi)^3} b e^{-\frac{k'^2}{k_0^2}} \times \mathbf{E}'_0 e^{i(\mathbf{k}' \cdot \mathbf{x} - \omega t + \theta(\mathbf{k}'))} \quad (16)$$

where $\theta(\mathbf{k}')$ is a random phase associated with the \mathbf{k}' mode and $\omega = \sqrt{\mathbf{k}'^2 + m_{A'}^2}$ is the energy. b is a normalization factor. We have $k_0 = m_{A'} v_0$ and $k_{\text{esc}} = m_{A'} v_{\text{esc}}$, where $v_0 \approx 235$ km/s is the most probable velocity and v_{esc} is the escape velocity of leaving the Galaxy at the position of the solar system which is about 500 km/s [59, 60]. Due to randomness, we assume that there is no correlation between different momentum modes,

$$\langle e^{i(\theta(\mathbf{k}'_1) - \theta(\mathbf{k}'_2))} \rangle_t = a (2\pi)^3 \delta^3(\mathbf{k}'_1 - \mathbf{k}'_2) \quad (17)$$

where a is a dimensionful constant. Then, analogous to Eqs. (4) and (5), the full expressions for the induced electric and magnetic fields read

$$\mathbf{E} = - \int_{<k_{\text{esc}}} \frac{d^3\mathbf{k}'}{(2\pi)^3} \frac{\epsilon m_{A'} |\mathbf{E}'_0|}{2\pi} b e^{-\frac{k'^2}{k_0^2}} \int dS' [\boldsymbol{\tau}(\mathbf{r}') \times (\mathbf{r} - \mathbf{r}')] \times (\mathbf{r} - \mathbf{r}') \frac{e^{i(\omega|\mathbf{r}-\mathbf{r}'| + \mathbf{k}' \cdot \mathbf{r}' + \theta(\mathbf{k}'))}}{|\mathbf{r} - \mathbf{r}'|^3}, \quad (18)$$

$$\mathbf{B} = - \int_{<k_{\text{esc}}} \frac{d^3\mathbf{k}'}{(2\pi)^3} \frac{\epsilon m_{A'} |\mathbf{E}'_0|}{2\pi} b e^{-\frac{k'^2}{k_0^2}} \int dS' \boldsymbol{\tau}(\mathbf{r}') \times (\mathbf{r} - \mathbf{r}') \frac{e^{i(\omega|\mathbf{r}-\mathbf{r}'| + \mathbf{k}' \cdot \mathbf{r}' + \theta(\mathbf{k}'))}}{|\mathbf{r} - \mathbf{r}'|^2}. \quad (19)$$

One can further obtain the full expression for the energy flux density,

$$\begin{aligned} \langle \mathbf{S} \rangle_t = \frac{1}{2} \int_{<k_{\text{esc}}} \frac{d^3\mathbf{k}'}{(2\pi)^3} \left(\frac{\epsilon m_{A'} |\mathbf{E}'_0|}{2\pi} \right)^2 a b^2 e^{-\frac{2k'^2}{k_0^2}} \int dS' dS'' \{ [\boldsymbol{\tau}(\mathbf{r}') \times (\mathbf{r} - \mathbf{r}')] \times (\mathbf{r} - \mathbf{r}') \} \\ \times [\boldsymbol{\tau}(\mathbf{r}'') \times (\mathbf{r} - \mathbf{r}'')] \text{Re} \left(\frac{e^{im_{A'}(|\mathbf{r}-\mathbf{r}'| - |\mathbf{r}-\mathbf{r}''|) + i\mathbf{k}' \cdot (\mathbf{r}' - \mathbf{r}'')}}{|\mathbf{r} - \mathbf{r}'|^3 |\mathbf{r} - \mathbf{r}''|^2} \right). \end{aligned} \quad (20)$$

This expression can be simplified after some computation, the detail is given in appendix A.

$$\langle \mathbf{S} \rangle_t = \rho_{\text{DM}} \left(\frac{\epsilon}{\lambda} \right)^2 \int dS' dS'' \{ [\boldsymbol{\tau}(\mathbf{r}') \times (\mathbf{r} - \mathbf{r}')] \times (\mathbf{r} - \mathbf{r}') \} \times [\boldsymbol{\tau}(\mathbf{r}'') \times (\mathbf{r} - \mathbf{r}'')] \times e^{-\frac{1}{8}k_0^2 |\mathbf{r}' - \mathbf{r}''|^2} \text{Re} \left(\frac{e^{im_{A'}(|\mathbf{r} - \mathbf{r}'| - |\mathbf{r} - \mathbf{r}''|)}}{|\mathbf{r} - \mathbf{r}'|^3 |\mathbf{r} - \mathbf{r}''|^2} \right) \quad (21)$$

If we choose the reflector to be spherical, some analytic results can be derived. In the $k_0 \rightarrow 0$ limit, i.e. the infinite correlation length limit, the result is

$$\frac{\langle \mathbf{S} \rangle_t}{\rho_{\text{DM}}} = \frac{1}{3} \pi^2 \epsilon^2 \frac{R^2}{\lambda^2} s_\gamma s_{\theta_0}^2 \sqrt{c_\gamma^2 (2 - 3c_{\theta_0} + c_{\theta_0}^3)^2 + 4s_\gamma^2 (c_{\theta_0}^3 - 1)^2} \quad (22)$$

where γ is the angle between the polarization vector \mathbf{n}_0 and z-direction, θ_0 describes how large the spherical surface is, with $\theta_0 = 0$ for the surface shrinking to a point and $\theta_0 = \pi$ for the surface becoming a full sphere. This is the same as what we obtained in [57]. We are also interested in the $k_0 \rightarrow \infty$ limit, i.e. the zero correlation length limit, the result is

$$\frac{\langle \mathbf{S} \rangle_t}{\rho_{\text{DM}}} = \frac{\epsilon^2}{2v_0^2} s_{\theta_0}^2 \sqrt{4s_\gamma^2 c_\gamma^2 s_{\theta_0}^4 + (2(1 + c_{\theta_0}^2) s_\gamma^2 + (1 + c_\gamma^2) s_{\theta_0}^2)^2} \quad (23)$$

Interestingly, the flux in the high frequency limit doesn't depend on the radius of the sphere, but it does depend on θ_0 . Note that (23) only applies when the radius of the reflector is much larger than the dark photon wavelength, which is 10^3 times the same-frequency EM wavelength. Naively, larger reflectors produce stronger signal, but (23) tells us that the signal saturates when the reflector is much larger than the dark photon wavelength.

Coming back to the JWST case, we apply again the stationary phase approximation. In order that the integration is not suppressed, \mathbf{r}' has to satisfy two conditions:

$$\mathbf{r} - \mathbf{r}' \perp \text{tangent plane at } \mathbf{r}', \quad \mathbf{r}' = \mathbf{r}'' \quad (24)$$

This means that due to finite correlation length, the contribution from interference terms completely vanishes. We denote by $\hat{\mathbf{r}}_i$ the i th solution to the perpendicular condition (24), and the total flux density is,

$$\langle \mathbf{S}(\mathbf{r}) \rangle_t = \sum_i \frac{1}{2} \epsilon^2 m_{A'}^2 \hat{\mathbf{A}}'(\hat{\mathbf{r}}_i) \hat{\mathbf{n}}(\hat{\mathbf{r}}_i) \quad (25)$$

Again, $\hat{\mathbf{n}}(\hat{\mathbf{r}}_i)$ is the out-directed normal vector at $\hat{\mathbf{r}}_i$, and $\hat{\mathbf{A}}'(\hat{\mathbf{r}}_i) = |\mathbf{A}'| \boldsymbol{\tau}(\hat{\mathbf{r}}_i)$. Note that if the set of solutions to (24) is not discrete, we should change the sum into an integration. If one wishes to average over all possible polarization, the result is

$$\langle \mathbf{S}(\mathbf{r}) \rangle_t = \sum_i \frac{2}{3} \epsilon^2 \rho_{\text{DM}}(\hat{\mathbf{r}}_i) \hat{\mathbf{n}}(\hat{\mathbf{r}}_i) \quad (26)$$

Component	RoC(mm)	Surface	Conic	V_1 (mm)	V_2 (mm)	V_3 (mm)	Size(mm)
Primary	15879.7	concave	-0.9967	0	0	0	6605.2(diameter)
Secondary	1778.9	convex	-1.6598	7169.0	0	0	738(diameter)
Tertiary	3016.2	concave	-0.6595	-796.3	0	-0.19	728(length) \times 517(width)
Fine Steering Mirror		flat		1047.8	0	-2.36	172.5(diameter)

Table I: Parameters for the optical elements of JWST. The data can be found in JWST documentation [61].

In the JWST case, all approximation conditions applied in this section are satisfied, so one may directly use (26) to compute the dark photon flux density.

III. THE OPTICAL TELESCOPE ELEMENT (OTE) OF JWST

The Optical Telescope Element (OTE) of the James Webb Space Telescope (JWST) comprises a primary mirror, a secondary mirror, a tertiary mirror, and a fine steering mirror. A sketch of the mirror system is shown in Figure 1. Detailed parameters for these optical components are available in JWST documentation [61], and we have also summarized them in Table I. In the table, ‘RoC’ denotes the radius of curvature, and ‘conic’ denotes the conic constant K which can be related to eccentricity e_{cone} as

$$K = -e_{\text{cone}}^2. \quad (27)$$

Table I provides insights into the optical characteristics of the JWST’s optical elements. The primary and tertiary mirrors exhibit elliptical shapes, while the secondary mirror is hyperbolic and the fine steering mirror is flat. The primary, secondary and fine steering mirrors are rounded, while the tertiary mirror is rectangular[62]. Their sizes are listed in Table I. V_1 , V_2 and V_3 are the spacial displacements of the mirrors, as shown in Fig. 1.

The EM energy flux density induced by DPDM originates from several sources within the optical system. DPDM can interact with different components of the optical train, including the primary mirror. The light emitted from the primary mirror is then sequentially reflected by the secondary mirror, the tertiary mirror, and the fine steering mirror before reaching the detector. Additionally, DPDM can also directly interact with the secondary mirror, leading

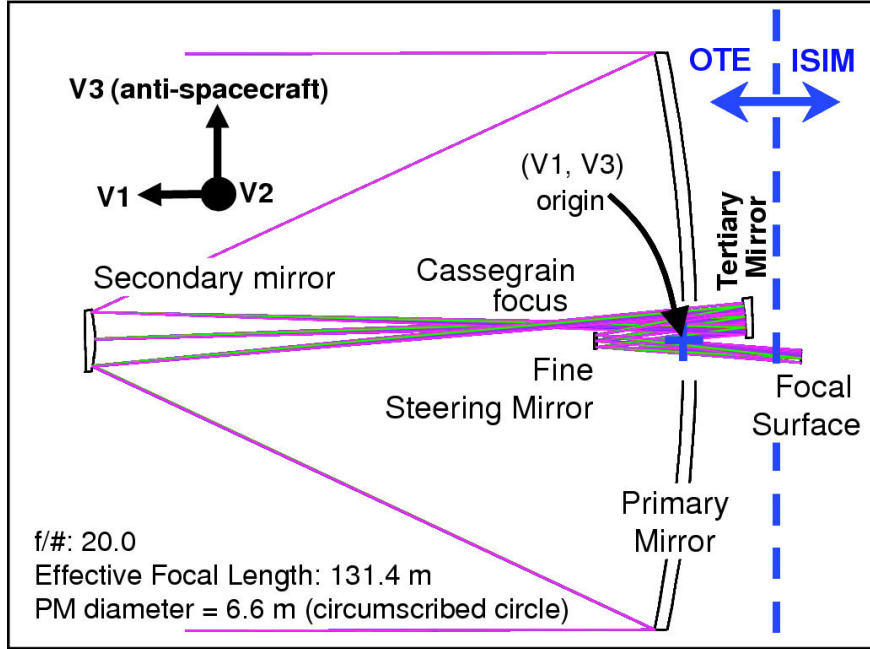


Figure 1: The OTE of JWST. Everything is drawn to scale. Figure taken from Ref. [56].

to a ‘double’ reflection before being detected. The same principle applies to interactions with the tertiary and fine steering mirrors. However, it is important to note that not all the lights induced by DPDM on the mirrors will reach the detector. Some of them may stray and cannot be focused on the detector after multiple reflections between the mirrors. After all, the JWST mirror system is designed to focus parallel lights from distant sources, while our light rays are always perpendicular to the mirror surface at which they are induced. To quantify the amount of the induced flux that can reach the detector, a detailed analysis of light propagation within the mirror system is necessary.

In the following section, we are going to carry out such an analysis based on the ray-transfer-matrix method. This method is applicable when the paraxial condition is satisfied, which means that the rays should be within a small angle to the optical axis throughout the system. We will show that the paraxial condition is indeed met in our case. It’s important to note that while the mirrors’ absolute sizes may not be significantly smaller than their radii of curvature, their effective sizes are small so that can satisfy the paraxial condition. Here, ‘effective’ refers to the portion of the mirror surface that make contributions to the flux finally detected.

IV. CALCULATING THE EQUIVALENT FLUX DENSITY

In this section, we are going to use the ray-transfer-matrix method to calculate the induced flux that can finally be detected by the JWST detector. A technical review of the ray-transfer-matrix method is shown in Appendix C. Firstly, we can alter the direction of light rays to make them move to the right for convenience, while at the same time we replace each reflector with a corresponding type of lens as depicted in Figure 2. The radii of curvature for the first three lenses are denoted by ρ_1 , ρ_2 , and ρ_3 , respectively. In this section, we will use subscripts P , S , T and F for the shorthand of “primary mirror”, “secondary mirror”, “tertiary mirror” and “fine steering mirror” respectively.

In ray-transfer-matrix method, a ray is described with a 2-component vector X , the first component being the angle between the ray and the optical axis, the second being its vertical displacement from the optical axis. Each optical operation that a ray undergoes—such as free travel or refraction through a lens—is represented by a 2×2 matrix. Specifically, within this section, free travel over a distance L_i will be symbolized by the matrix U_i , while refraction on the primary mirror will be denoted by the matrix U_P , and likewise for other mirrors in the optical system.

We can write out the transition matrix of each lens and interval,

$$U_P = \begin{bmatrix} 1 & -\frac{2}{\rho_1} \\ 0 & 1 \end{bmatrix} \quad U_S = \begin{bmatrix} 1 & \frac{2}{\rho_2} \\ 0 & 1 \end{bmatrix} \quad U_T = \begin{bmatrix} 1 & -\frac{2}{\rho_3} \\ 0 & 1 \end{bmatrix}, \quad (28)$$

$$U_1 = \begin{bmatrix} 1 & 0 \\ L_1 & 1 \end{bmatrix} \quad U_2 = \begin{bmatrix} 1 & 0 \\ L_2 & 1 \end{bmatrix} \quad U_3 = \begin{bmatrix} 1 & 0 \\ L_3 & 1 \end{bmatrix}. \quad (29)$$

Light is emitted from each reflector, and the corresponding vectors are

$$X_P = \begin{bmatrix} -\frac{y}{\rho_1} \\ y \end{bmatrix}, \quad X_S = \begin{bmatrix} \frac{y}{\rho_2} \\ y \end{bmatrix}, \quad X_T = \begin{bmatrix} -\frac{y}{\rho_3} \\ y \end{bmatrix}, \quad X_F = \begin{bmatrix} 0 \\ y \end{bmatrix}. \quad (30)$$

Here y represents the height of the emission point relative to the optical axis.

We require that the light emitted from the primary mirror can reach the other three mirrors. For example, to check whether the light emitted from the primary mirror can reach the fine steering mirror, we use the following vector,

$$X = U_3 U_T U_2 U_S U_1 X_P. \quad (31)$$

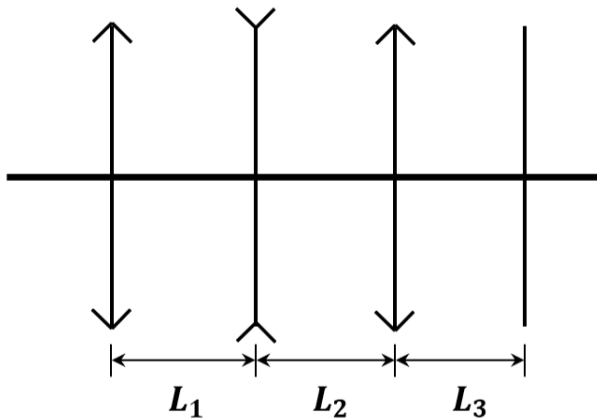


Figure 2: The OTE of JWST can be simplified to a set of lenses. The configuration comprises two convex lenses, positioned as the first and third lenses, with the second lens being concave and the fourth being flat.

If the light can be received by the fine steering mirror, then the absolute value of the second component of vector X has to be smaller than the radius of the fine steering mirror, which yields an inequality restricting the possible values of y . Therefore, by requiring that the light emitted by the primary mirror can be reflected three times and finally get into the detector, we have three inequalities which cut out an effective region on the surface of the primary mirror. Direct calculations show that this effective region is a rectangle with the length as 146.795 mm and the width as 104.248 mm. However, the primary mirror of JWST is hollowed in the center. The hollowed region is a hexagon with the side length as 762mm, which entirely encloses the effective region. Therefore, EM waves emitted by the primary mirror can't be received by the detector.

We can perform a similar analysis for the the other three mirrors. The effective region is also rectangular, with the length and width as

$$a_S = 132.904, \quad b_S = 94.3834. \quad (32)$$

The effective region of the tertiary mirror is rounded, with the diameter as

$$d_T = 443.9 \quad (33)$$

In addition, the whole area of the fine steering mirror is effective.

We also need to analyze the focusing ability. After a direct calculation, we find that

$$X_S \Rightarrow \begin{bmatrix} -0.00307001y \\ -6.20097y \end{bmatrix}, \quad X_T \Rightarrow \begin{bmatrix} -0.000331543y \\ -0.261223y \end{bmatrix}, \quad X_F \Rightarrow \begin{bmatrix} 0 \\ y \end{bmatrix} \quad (34)$$

where the unit of y is millimeter. Let us take X_s for example. After a series of reflections, the light emitted at the height y goes into the detector at height $6.20097y$. This means that the energy emitted by a disk with radius y is redistributed into a disk with radius $6.20097y$, and thus the energy flux density is $(6.20097)^{-2}$ the flux density emitted.

To sum up, the flux density induced by dark photon can be written as

$$I_{DM} = \frac{2}{3}\epsilon^2\rho_{DM} \times (1 + 6.20097^{-2} + 0.261223^{-2}) \quad (35)$$

In order to compare our calculated result of the DPDM-induced EM signal with the real data recorded by JWST, we need to translate the induced signal into the equivalent flux density of the incoming astronomical EM signals. This means that we need to further calculate the focusing ability for the case of the incoming planar EM waves. The incoming plane waves can be described by a vector

$$X_0 = \begin{bmatrix} 0 \\ y \end{bmatrix}. \quad (36)$$

We again use the transition matrices to calculate the light at the receiver,

$$X_0 \Rightarrow \begin{bmatrix} 7.52946 \times 10^{-6}y \\ -0.0080392y \end{bmatrix} \quad (37)$$

Noting that the first entry is very small, we conclude that indeed the incoming planar wave is transformed into another planar wave. From the second entry, we get the enhancement factor $(0.0080392)^{-2}$. Thus, we can calculate the equivalent flux density by

$$I_{\text{eqv}} \times (0.0080392)^{-2} = I_{DM} \quad (38)$$

which gives

$$I_{\text{eqv}} = 6.75618 \times 10^{-4}\epsilon^2\rho_{DM}. \quad (39)$$

However, there is one more subtlety. We have calculated the effective range of the secondary mirror and the tertiary mirror, the light emitted from the secondary mirror can indeed

cover the whole receiver, but light emitted from the tertiary mirror is concentrated in a smaller region, and can only be observed with a well-chosen observation angle. To be very conservative, we simply assume that the light emitted by the tertiary mirror cannot go into the detector, and we have

$$I'_{\text{eqv}} = 4.42064 \times 10^{-5} \epsilon^2 \rho_{\text{DM}}. \quad (40)$$

V. CONSTRAINTS FROM JWST OBSERVATION DATA

The James Webb Space Telescope (JWST) stands as the cutting-edge space telescope, equipped with various detectors and versatile observation modes. In our study, we harnessed data from 972 distinct observation projects to establish constraints on the Dark Photon-Dark Matter coupling constant. Out of these projects, 713 relied on the Near-Infrared Spectrograph (NIRSpec) [cite], while 259 made use of the Mid-Infrared Instrument (MIRI) [cite]. It is worth noting that the data selected for analysis excludes background subtraction, ensuring its suitability for our research.

The JWST data we collected from the Mikulski Archive for Space Telescopes (MAST) database [63] includes two crucial parameters: the measured spectral flux density, denoted as \bar{O}_i , and the associated statistical uncertainty, denoted as $\sigma_{\bar{O}_i}$. In our effort to establish upper limits on the coupling of Dark Photon with the Standard Model electromagnetic current, denoted as ϵ , we followed the data analysis approach detailed in previous works [46, 57, 64].

To provide a concise overview, we summarize the key aspects of our method here, while reserving more detailed information for Appendix A. Our analysis begins by applying a local polynomial function to model the background surrounding a selected frequency bin, i_0 , while considering neighboring bins. We estimate systematic uncertainties by comparing data deviations to the background fit. Next, we introduce a hypothetical Dark Photon Dark Matter signal with a strength denoted as S at the specific bin, i_0 . This allows us to construct a likelihood function, L , that incorporates S into the comparison between data and the background function. Nuisance parameters are introduced to account for the coefficients of the background polynomial function.

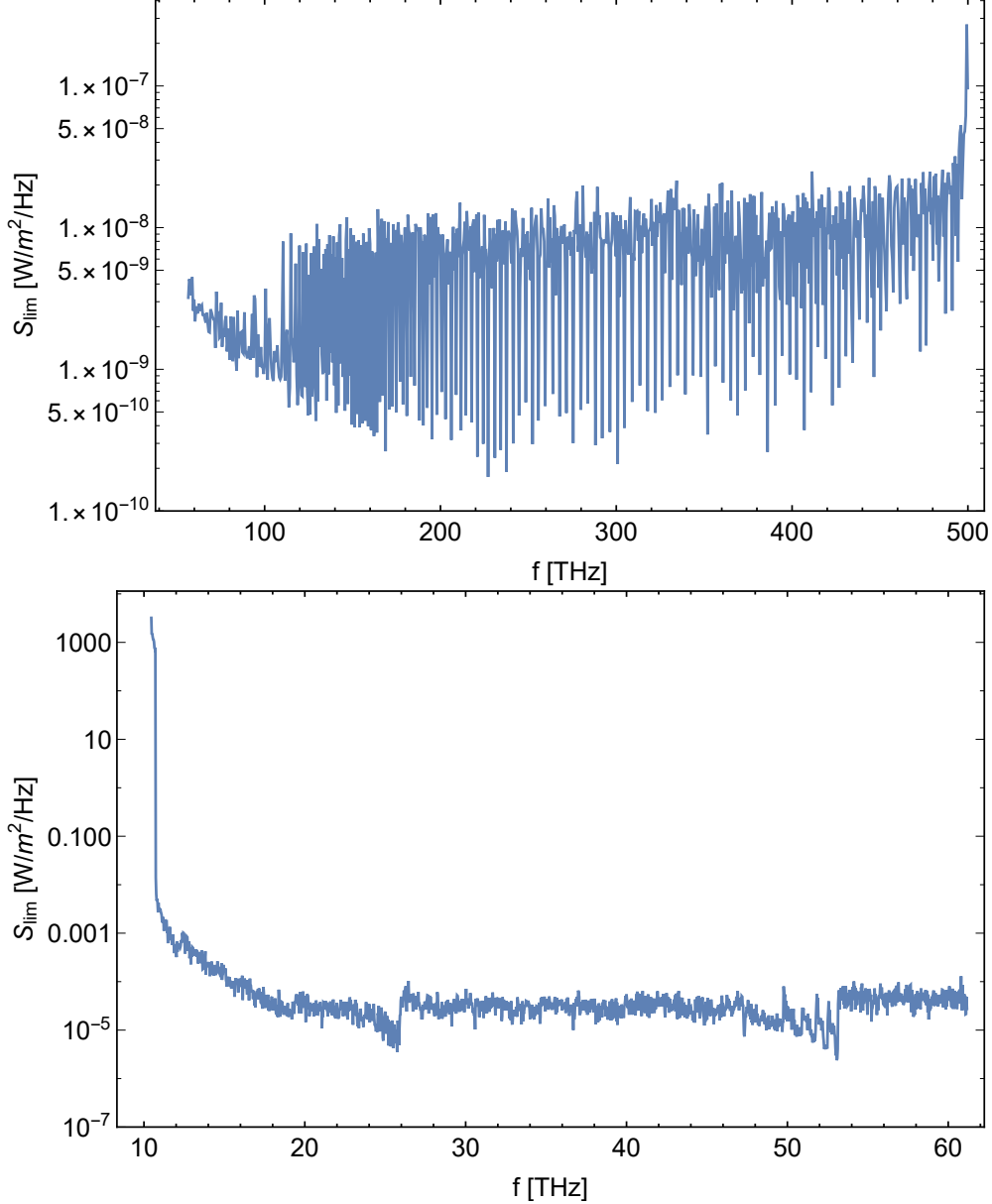


Figure 3: Model-independent 95% C.L. upper limits on a constant monochromatic signal from JWST data. The first figure corresponds to NIRSpec observation data, and the lower one MIRI. It shows the strongest limit from the all projects at each frequency bin.

Following the statistical method developed in Ref. [64], we compute the ratio, λ_S , between the maximized likelihood under two conditions: first, when only the nuisance parameters are varied to maximize L while keeping S constant, and second, when both the nuisance parameters and S are varied to maximize L . The test statistic, $-2 \log(\lambda_S)$, follows a half- χ^2 distribution [64]. This analysis allows us to derive the 95% confidence level upper limit, S_{lim} ,

for a constant monochromatic signal. The results are illustrated in Fig. 3.

We establish upper limits on the mixing parameter ϵ as $S_{\text{lim}} = S'_{\text{eqv}}$, where S'_{eqv} represents the signal strength from theoretical calculations for Dark Photon Dark Matter. Different datasets from NIRSpec and MIRI yield varying constraints on the signal strength coupling ϵ , and we select the most stringent among them. The constraint on ϵ and its comparison with previous experiments are illustrated in Fig. 4.

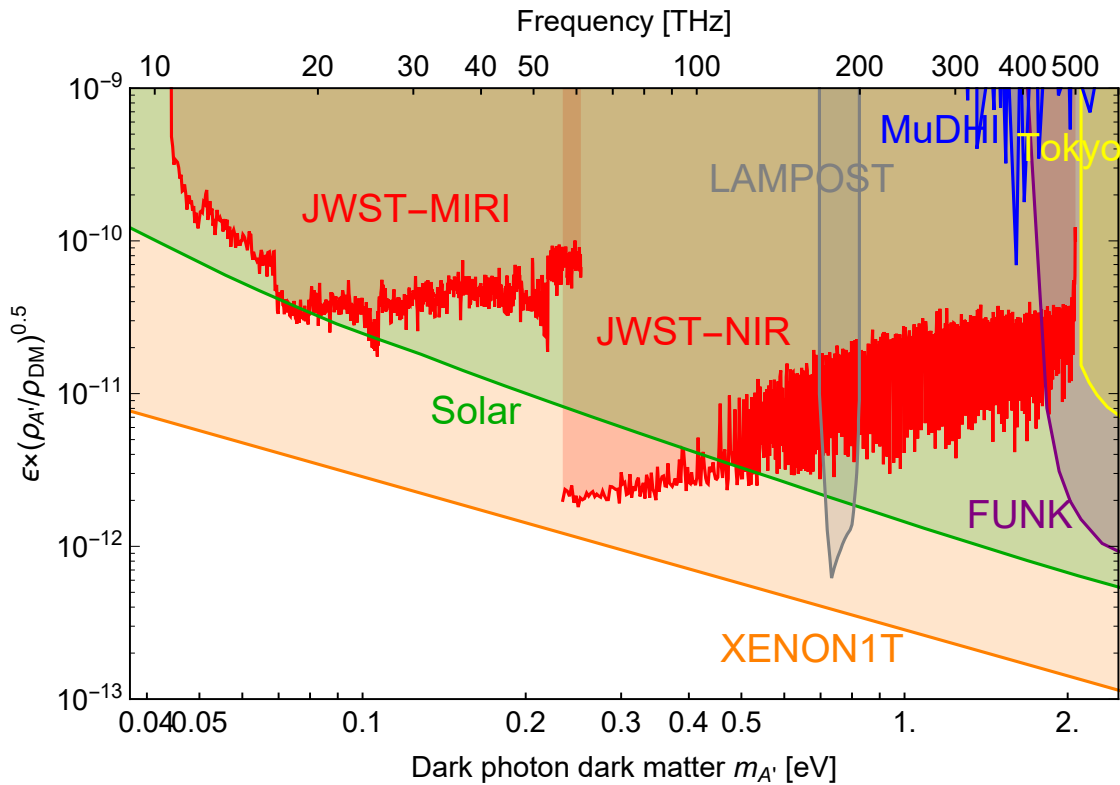


Figure 4: Constraints on the kinematic mixing parameter ϵ between Dark Photon Dark Matter (DPDM) and photons in the randomized polarization scheme. The solid red curve represents the 95% confidence level (C.L.) exclusion limit for DPDM using JWST data. The left and right sections display constraints derived from NIRSpec and MIRI observation data, respectively. Additionally, we provide a comparison with existing limits, including those from Solar [65], XENON1T [66], Lampost [67], Mudhi [68], Funk [54], and Tokyo [50].

VI. SUMMARY AND OUTLOOK

In this study, we conducted a direct detection search for dark photon dark matter (DPDM) using a haloscope setup. Our approach involved converting local DPDM into a normal electromagnetic field at the mirrors of the James Webb Space Telescope (JWST), which was then detected by its receiver. Due to the frequency match between the electromagnetic field and the DPDM mass, the resulting signal took the form of a monochromatic electromagnetic wave. Typically, accounting for the contribution of each surface area on the mirror to the electromagnetic field is necessary. The final electromagnetic energy received by the receiver encompasses the interference from each surface unit. We demonstrated that for high-mass DPDM, the contribution to the electromagnetic wave field at a given position primarily stems from the surface unit perpendicular to the separation vector, allowing us to calculate the electromagnetic flux at the receiver using ray-optics.

We utilized data from JWST observations to search for a monochromatic signal within the continuous background in the 10-500 terahertz (THz) range. Both the JWST Mid-Infrared Instrument (MIRI) and Near Infrared Spectrograph (NIRSpec) data were employed. Our analysis enabled us to establish limits on the DPDM kinetic mixing coupling at approximately $\epsilon \sim 3 \times 10^{-11}$ and $\epsilon \sim \mathcal{O}(10^{-12})$ respectively. This broadband search for DPDM yielded valuable lower-frequency constraints, complementing other experiments conducted in room-sized laboratories, such as Lampost, Mudhi, FUNK, and TOKYO. However, our results indicated a coupling weaker by about one order of magnitude compared to the XENON1T results, which utilized the potential dark photon flux generated by the Sun, without assuming that the dark photon is the dark matter. Our results are also comparable with the astrophysical bound from the solar emission of the dark photon particles.

While our results are slightly weaker than XENON1T constraints, there exists potential for improvement given that JWST is not specifically designed for the direct detection of DPDM. JWST boasts an outstanding receiver capable of detecting THz signals. By incorporating a spherical mirror as the reflector, as proposed in Refs. [39, 41, 48], or adopting a flat reflector along with a parabolic collection mirror, akin to the design in the TOKYO experiment [42, 51] and the BRASS-p experiment [55], it is possible to enhance sensitivity by orders of magnitude due to the right focus on the DPDM signal.

ACKNOWLEDGEMENT

JL would like to thank Le Hoang Nguyen for the helpful discussions. The work of HA is supported in part by the National Key R&D Program of China under Grant No. 2023YFA1607104 and 2021YFC2203100, the NSFC under Grant No. 11975134, and the Tsinghua University Initiative Scientific Research Program. The work of SG is supported by NSFC under Grant No. 12247147, the International Postdoctoral Exchange Fellowship Program, and the Boya Postdoctoral Fellowship of Peking University. The work of JL is supported by NSFC under Grant No. 12075005, 12235001.

Appendix A: Detailed derivation of Eq. (21)

Starting from equation (20), the integration over \mathbf{k}' can be done analytically,

$$\int_{<k_{\text{esc}}} \frac{d^3 \mathbf{k}'}{(2\pi)^3} e^{-\frac{2k'^2}{k_0^2}} e^{i\mathbf{k}' \cdot (\mathbf{r}' - \mathbf{r}'')} = \frac{k_0^2 e^{-2z^2} e^{-iyz}}{32\sqrt{2}\pi^2 \Delta r} \left[2\sqrt{2}i(-1 + e^{2iyz}) + \sqrt{\pi}y e^{-(y-4iz)^2/8} \left(\text{erf}\left(\frac{4z+iy}{2\sqrt{2}}\right) + \text{erf}\left(\frac{4z-iy}{2\sqrt{2}}\right) \right) \right] \quad (\text{A1})$$

where $\Delta r = |\mathbf{r}' - \mathbf{r}''|$, $z = k_{\text{esc}}/k_0$, and $y = k_0 \Delta r$. When z or k_{esc} is large, the expression above can be expanded as

$$\int_{<k_{\text{esc}}} \frac{d^3 \mathbf{k}'}{(2\pi)^3} e^{-\frac{2k'^2}{k_0^2}} e^{i\mathbf{k}' \cdot (\mathbf{r}' - \mathbf{r}'')} \approx \frac{k_0^3}{16\sqrt{2}\pi^{3/2}} \left(e^{-\frac{1}{8}y^2} - \frac{2\sqrt{2}}{\sqrt{\pi}y} e^{-2z^2} \sin(yz) \right). \quad (\text{A2})$$

The next-to-leading order term is suppressed by e^{-2z^2} , and can be neglected. In addition, note that that

$$\rho_{\text{DM}} = \frac{1}{2} \langle \mathbf{E}'(\mathbf{r}, t) \mathbf{E}'^*(\mathbf{r}, t) \rangle = \frac{ab^2}{64\pi^2} k_0^3 |\mathbf{E}'_0|^2 \left(\sqrt{2\pi} \text{erf}(\sqrt{2}z) - 4ze^{-2z^2} \right) \quad (\text{A3})$$

which, under the large z approximation, becomes

$$\rho_{\text{DM}} = \frac{ab^2}{32\sqrt{2}\pi^{3/2}} k_0^3 |\mathbf{E}'_0|^2. \quad (\text{A4})$$

So the expression for $\langle \mathbf{S} \rangle_t$ reads

$$\langle \mathbf{S} \rangle_t = \rho_{\text{DM}} \left(\frac{\epsilon}{\lambda} \right)^2 \int dS' dS'' \{ [\boldsymbol{\tau}(\mathbf{r}') \times (\mathbf{r} - \mathbf{r}')] \times (\mathbf{r} - \mathbf{r}') \} \times [\boldsymbol{\tau}(\mathbf{r}'') \times (\mathbf{r} - \mathbf{r}'')] \times e^{-\frac{1}{8}k_0^2 |\mathbf{r}' - \mathbf{r}''|^2} \text{Re} \left(\frac{e^{im_{A'}(|\mathbf{r} - \mathbf{r}'| - |\mathbf{r} - \mathbf{r}''|)}}{|\mathbf{r} - \mathbf{r}'|^3 |\mathbf{r} - \mathbf{r}''|^2} \right) \quad (\text{A5})$$

Appendix B: A Brief Proof of Eq. (8)

We demonstrate the one-dimensional case; extending to higher dimensions is straightforward.

We wish to evaluate

$$\lim_{\alpha \rightarrow \infty} \sqrt{\alpha} \int_{-\infty}^{\infty} g(x) e^{i\alpha f(x)} dx \quad (\text{B1})$$

in the large α limit. In this analysis, we assume that $f(x)$ is second order differentiable, $g(x)$ is continuous. We also assume that $g(x)$ is either compactly supported or exhibits exponential decay and that $f'(x) = 0$ has only a discrete set of solutions. Here, we will focus on proving the case where $g(x)$ is compactly supported, noting that a similar approach can be applied when $g(x)$ has exponential decay.

Denote by Σ the set of points where $f'(x) = 0$. Define

$$\Delta = \min\{x_i - x_j | x_i, x_j \in \Sigma\} \quad (\text{B2})$$

Denote by I the set on which $g(x)$ is supported. Define a set A as follows,

$$A = \left\{ [a, b] \mid [a, b] = \left[x_0 - \frac{\delta}{2}, x_0 + \frac{\delta}{2} \right] \cap I, x_0 \in \Sigma \right\} \quad (\text{B3})$$

where δ is a positive real number that satisfies $\delta < \min\{\Delta, \alpha^{-1/2+\epsilon}\}$, with ϵ being a real number in the range $0 < \epsilon < 1/8$. Due to the continuity of $f'(x)$, it follows that $f(x)$ is monotonic between any two adjacent points in Σ . Consequently, we can divide the interval I into a finite set of closed intervals, each of which is either an element of A or an interval on which $f(x)$ is strictly monotonic.

Let's begin by examining the integral over intervals where $f(x)$ is monotonic.

$$\sqrt{\alpha} \int_c^d g(x) e^{i\alpha f(x)} dx \quad (\text{B4})$$

Where c and d are two real numbers. Since $f(x)$ is monotonic, it has an inverse, here denoted by $f^{-1}(x)$. We define $y = f^{-1}(x)$, and the integral can be expressed as

$$\sqrt{\alpha} \int_{c'}^{d'} \tilde{g}(y) e^{i\alpha y} dy \quad (\text{B5})$$

where $c' = f(c)$, $d' = f(d)$, and $\tilde{g}(y) = g(f^{-1}(y))(f^{-1})'(y)$. It can be shown that this expression goes to zero as $\alpha \rightarrow \infty$. By dividing the interval $[c', d']$ into a set of intervals with length $2\pi/\alpha$, integrating on each small interval contributes a result of order $\mathcal{O}(\alpha^{-3/2})$.

Summing over all intervals gives an additional factor of α , resulting in the overall order $\mathcal{O}(\alpha^{-1/2})$. Consequently, (B5) vanishes in the large α limit.

Next consider the integral on elements of A :

$$\sqrt{\alpha} \int_{x_0-a}^{x_0+b} g(x) e^{i\alpha f(x)} dx \quad (\text{B6})$$

where $x_0 \in \Sigma$ and $\delta \geq a$, $b \geq 0$. Notice that

$$\sqrt{\alpha} \left| \int_{x_0-a}^{x_0+b} (g(x) - g(x_0)) e^{i\alpha f(x)} dx \right| \leq \sqrt{\alpha}(a+b) \sup_{x_0-a \leq x \leq x_0+b} \{g(x) - g(x_0)\} = \mathcal{O}(\alpha^{-1/2+2\epsilon}) \quad (\text{B7})$$

As α approaches infinity, the expression above tends to zero. Therefore, the integral we aim to evaluate can be replaced by the following expression,

$$\sqrt{\alpha} \int_{x_0-a}^{x_0+b} g(x_0) e^{i\alpha f(x)} dx \quad (\text{B8})$$

In the vicinity of x_0 , $f(x)$ can be Taylor-expanded as

$$f(x) = f(x_0) + \frac{1}{2} f''(x_0)(x - x_0)^2 + R_2(x) \quad (\text{B9})$$

where $R_2(x)$ represents the remainder term. Divide the integral into two parts

$$\begin{aligned} \sqrt{\alpha} \int_{x_0-a}^{x_0+b} g(x_0) e^{i\alpha f(x)} dx &= \sqrt{\alpha} \int_{x_0-a}^{x_0+b} g(x_0) \exp \left[i\alpha \left(f(x_0) + \frac{1}{2} f''(x_0)(x - x_0)^2 \right) \right] dx \\ &+ \sqrt{\alpha} \int_{x_0-a}^{x_0+b} g(x_0) [\exp(i\alpha R_2(x)) - 1] \exp \left[i\alpha \left(f(x_0) + \frac{1}{2} f''(x_0)(x - x_0)^2 \right) \right] dx \end{aligned} \quad (\text{B10})$$

As $\alpha R_2(x) = \mathcal{O}(\alpha^{-1/2+3\epsilon})$, the second term is of order $\mathcal{O}(\alpha^{-1/2+4\epsilon})$, and therefore vanishes in the large α limit. Furthermore, in the large α limit, it can be demonstrated that the first term is equal to

$$\sqrt{\alpha} \int_{-\infty}^{\infty} g(x_0) \exp \left[i\alpha \left(f(x_0) + \frac{1}{2} f''(x_0)(x - x_0)^2 \right) \right] dx \quad (\text{B11})$$

We just have to prove that both

$$\sqrt{\alpha} \int_{-\infty}^{x_0-a} g(x_0) \exp \left[i\alpha \left(f(x_0) + \frac{1}{2} f''(x_0)(x - x_0)^2 \right) \right] dx \quad (\text{B12})$$

and

$$\sqrt{\alpha} \int_{x_0+b}^{\infty} g(x_0) \exp \left[i\alpha \left(f(x_0) + \frac{1}{2} f''(x_0)(x - x_0)^2 \right) \right] dx \quad (\text{B13})$$

tends to zero as $\alpha \rightarrow \infty$. Take (B13) for example. Let's define $t = \alpha(x - x_0)^2$, substitute x with t , and (B13) becomes

$$g(x_0)e^{i\alpha f(x_0)} \int_{\alpha b^2}^{\infty} \frac{1}{2\sqrt{t}} \exp \left[\frac{1}{2} i f''(x_0) t \right] dt \quad (\text{B14})$$

When α is sufficiently large, we have $\alpha b^2 = \alpha^{2\epsilon}$. Therefore, as α approaches infinity, (B13) tends to zero.

To sum up, we have

$$\int_{-\infty}^{\infty} g(x)e^{i\alpha f(x)} dx = \sum_{x_0 \in \Sigma} \int_{-\infty}^{\infty} g(x_0) \exp \left[i\alpha \left(f(x_0) + \frac{1}{2} f''(x_0)(x - x_0)^2 \right) \right] dx \quad (\text{B15})$$

The integral on the right-hand side is nothing but a Gaussian integral, so the result is

$$\int_{-\infty}^{\infty} g(x)e^{i\alpha f(x)} dx = \sum_{x_0 \in \Sigma} \sqrt{\frac{2\pi}{\alpha}} |f''(x_0)|^{-1/2} e^{\frac{i\pi}{4} \text{sgn}(f''(x_0))} g(x_0) e^{i\alpha f(x_0)} \quad (\text{B16})$$

It is straight forward to generalize to higher dimensional case. We can use the same method to prove that

$$\int_{\mathbb{R}^n} g(\mathbf{x}) e^{i\alpha f(\mathbf{x})} d^n \mathbf{x} = \sum_{\mathbf{x}_0 \in \Sigma} \int_{\mathbb{R}^n} g(\mathbf{x}_0) \exp \left[i\alpha \left(f(\mathbf{x}_0) + \frac{1}{2} (\mathbf{x} - \mathbf{x}_0)^T \text{Hess}(f(\mathbf{x}_0)) (\mathbf{x} - \mathbf{x}_0) \right) \right] d^n \mathbf{x} \quad (\text{B17})$$

Here Σ is defined to be the set of points where $\nabla f = 0$, and the Hessian matrix is defined to be

$$\text{Hess}(f(\mathbf{x})) = \begin{bmatrix} \frac{\partial^2 f}{\partial x_1^2} & \frac{\partial^2 f}{\partial x_1 \partial x_2} & \cdots & \frac{\partial^2 f}{\partial x_1 \partial x_n} \\ \frac{\partial^2 f}{\partial x_2 \partial x_1} & \frac{\partial^2 f}{\partial x_2^2} & \cdots & \frac{\partial^2 f}{\partial x_2 \partial x_n} \\ \vdots & \vdots & \ddots & \vdots \\ \frac{\partial^2 f}{\partial x_n \partial x_1} & \frac{\partial^2 f}{\partial x_n \partial x_2} & \cdots & \frac{\partial^2 f}{\partial x_n^2} \end{bmatrix} \quad (\text{B18})$$

To evaluate the multidimensional Gaussian integral, we diagonalize the Hessian matrix. This transforms the integral into the product of n one dimensional Gaussian integrals, ultimately leading to equation (8).

Appendix C: Ray Transfer Matrix Analysis

In systems satisfying paraxial condition, we can utilize "ray transfer matrix analysis" to simplify the calculations. A beam of light can be characterized by two parameters:

the angle(counterclockwise) between the light and the optical axis, and the vertical distance(upward) between the light and the optical axis. These two parameters can be organized into a column vector

$$\mathbf{v} = \begin{bmatrix} \theta \\ y \end{bmatrix} \quad (\text{C1})$$

Here we assume that the light is travelling from left to right.

We can perform various operations on the light. First, it can travel a distance L through free space, as depicted in Figure 5. During free travel, the angle θ remains unchanged, while the height y increases by θL . This process can be described by the left multiplication of a matrix

$$\mathbf{v} \Rightarrow \mathbf{v}' = \begin{bmatrix} 1 & 0 \\ L & 1 \end{bmatrix} \mathbf{v} \quad (\text{C2})$$

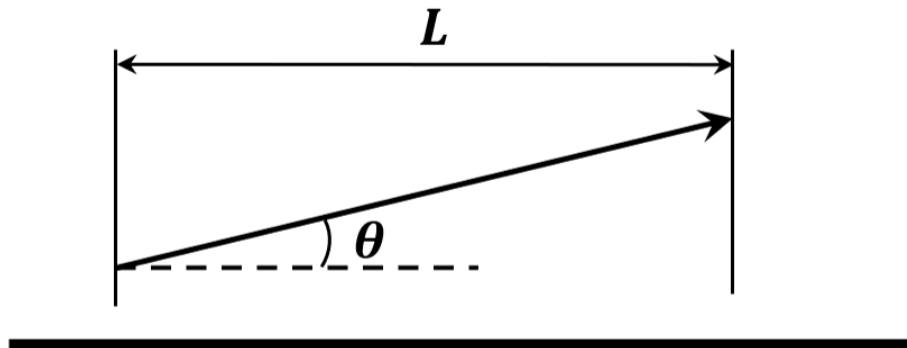


Figure 5: A beam of light travelling in free space

We can also represent the effects of reflectors using matrices. Reflecting changes the direction of the light from right-going to left-going, which can introduce complications. To simplify matters, we reflect the direction of the light, ensuring that it always travels rightward, as shown in figure 6.

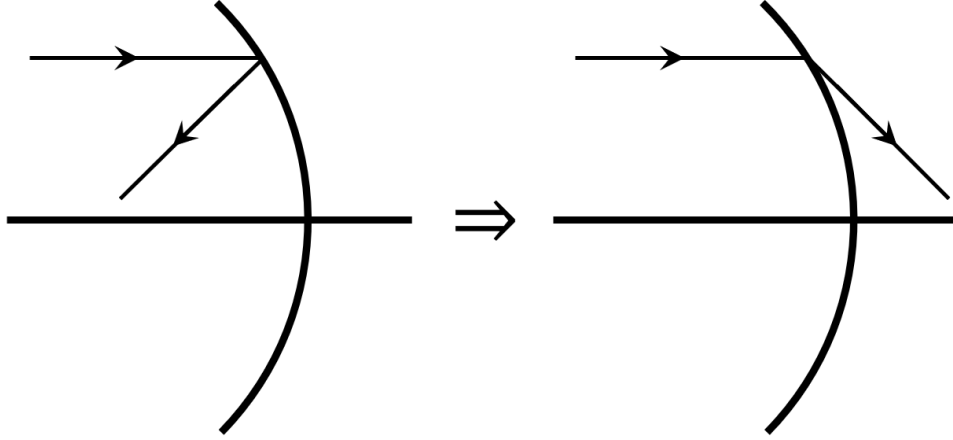


Figure 6: Reflecting the light so that it is always right-going

We are now prepared to analyze the effect of a reflector. When a beam of light is reflected by the reflector, its height remains unchanged while the direction θ is altered. Given that the paraxial condition is met, the reflector can be approximated by a spherical mirror, with its radius equal to the radius of curvature. Through direct analysis, we find that the effect of a reflector can be described by the following matrices

$$\begin{bmatrix} 1 & -\frac{2}{\rho} \\ 0 & 1 \end{bmatrix} \text{ (concave)} \quad \begin{bmatrix} 1 & \frac{2}{\rho} \\ 0 & 1 \end{bmatrix} \text{ (convex)} \quad (\text{C3})$$

In the JWST setup, the axis of symmetry of the reflectors may differ from the optical axis, as shown in Figure 7 and Figure 8. Fortunately, the system is linear, so both of these effects simply add an overall constant to the beams of light we are considering.

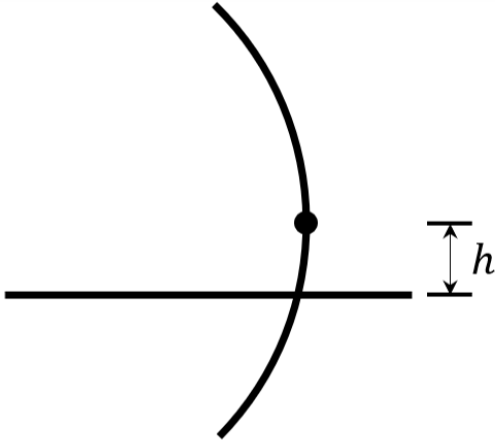


Figure 7: The center of the reflector is higher than the optical axis.

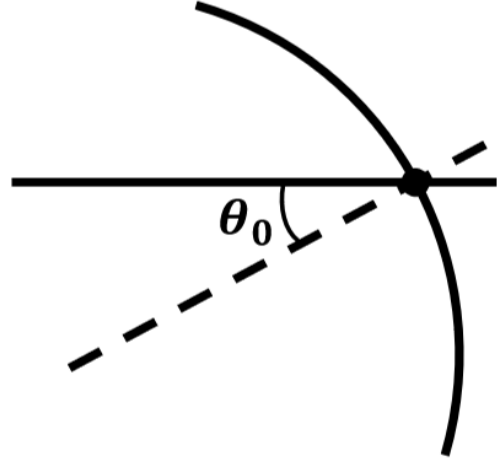


Figure 8: The axis of symmetry is not parallel to the optical axis.

First, if the center of the mirror is higher than the optical axis, the effect of the mirror is

$$\begin{bmatrix} \theta \\ y \end{bmatrix} \Rightarrow \begin{bmatrix} \theta - \frac{2y}{\rho} + \frac{2h}{\rho} \\ y \end{bmatrix} \quad (\text{C4})$$

So there is an overall angle $2h/\rho$, which can only cause overall vertical or angular displacement.

In the second case, where the axis of symmetry is not parallel to the optical axis, we have

$$\begin{bmatrix} \theta \\ y \end{bmatrix} \Rightarrow \begin{bmatrix} \theta - \frac{2y}{\rho} - 2\theta_0 \\ y \end{bmatrix} \quad (\text{C5})$$

Similarly, the $2\theta_0$ term can only cause overall vertical or angular displacements. As a result, the displacement of mirrors has no effect on the signal strength, allowing us to disregard the displacements and permitting light to pass through some mirrors if necessary.

Appendix D: Data Analysis Method

The data analysis method adopted in the present work follows that in [46, 57, 64]. Utilizing JWST observation [63], we have a dataset of spectral flux density \bar{O}_i (mean value) along with the associated statistical error $\sigma_{\bar{O}_i}$ at a series of frequency bins indexed by i . To model the local flux background around bin i_0 , We apply a polynomial function $B(a, f)$, fitting the data from bin $i_0 - k$ to bin $i_0 + k$,

$$B(a, f) = a_0 + a_1 f + a_2 f^2 + \dots + a_n f^n. \quad (\text{D1})$$

$a = \{a_0, a_1, a_2, \dots, a_n\}$ are the coefficients of the polynomial terms. The weighted sum of squared residuals,

$$\sum_{i=i_0-k}^{i_0+k} \frac{1}{\sigma_{\bar{O}_i}^2} [B(a, f_i) - \bar{O}_i]^2, \quad (\text{D2})$$

is minimized at $a = \tilde{a}$. The deviations of the data points from the background fitting result, $\delta_i \equiv B(\tilde{a}, f_i) - \bar{O}_i$, can be modeled as a systematic error at bin i_0 , that is

$$\sigma_{i_0}^{\text{sys}} = \sqrt{\frac{1}{2k-1} \sum_{i=i_0-k}^{i_0+k} (\delta_i - \bar{\delta})^2}. \quad (\text{D3})$$

$\bar{\delta}$ is the average of the list δ_i . Note that in computing Eqs. (D2)-(D3), we do not include the bin i_0 in the calculations. Additionally, for practical purposes, we set $n = 3$ and $k = 5$. By adding these two kinds of uncertainties in quadrature, we get the total uncertainty at bin i_0 ,

$$\sigma_{i_0}^{\text{sys}} = \sqrt{(\sigma_{i_0}^{\text{sys}})^2 + \sigma_{\bar{O}_{i_0}}^2}. \quad (\text{D4})$$

Next, to set upper limits on the coupling of DPDM with photon, we employ a likelihood-based statistical method [64]. A likelihood function is constructed around bin i_0 as follows,

$$L(S, a) = \prod_{i=i_0-k}^{i_0+k} \frac{1}{\sqrt{2\pi}\sigma_i^{\text{tot}}} \exp \left[-\frac{1}{2} \left(\frac{B(a, f_i) + S\delta_{i_0} - \bar{O}_i}{\sigma_i^{\text{tot}}} \right)^2 \right]. \quad (\text{D5})$$

Here, we consider the parameter a 's as nuisance parameters. S represents the DPDM-induced signal, and we assume its location to be in bin i_0 . It's worth noting that the frequency dispersion of DPDM is $\mathcal{B}_{\text{DPDM}} \sim 0.15 \text{ kHz} \times (m_{A'}/\mu\text{eV})$. This is much smaller than the instrumental spectral resolution which ranges from 10 GHz to 40 THz, depending on different observation modes [56], so the DPDM-induced signal can be safely confined within a single frequency bin.

Then, we build the test statistic as

$$q_S = \begin{cases} -2 \ln \frac{L(S, \hat{a})}{L(\hat{S}, \hat{a})}, & \hat{S} \leq S \\ 0, & \hat{S} > S \end{cases}. \quad (\text{D6})$$

L is maximized at $a = \hat{a}$ and $S = \hat{S}$; it is conditionally maximized at $a = \hat{a}$ for a fixed S . As has been demonstrated in Ref. [64], the test statistic q_S satisfies the half-chi-squared distribution,

$$f(q_S|S) = \frac{1}{2} \delta(q_S) + \frac{1}{2} \frac{1}{\sqrt{2\pi}} \frac{1}{\sqrt{q_S}} \exp(-q_S/2), \quad (\text{D7})$$

the cumulative distribution of which is labeled as $\Phi(\sqrt{q_S})$. Then, we define the p-value function as $p_S = [1 - \Phi(\sqrt{q_S})]/[1 - \Phi(\sqrt{q_0})]$ which measures the deviation of the assumed signal S to the null $S = 0$. We set $p_S = 5\%$ and then determine the value of S corresponding to this p_S , which we denote as S_{lim} . Consequently, if an assumed signal has a strength $S > S_{\text{lim}}$, we can exclude it at the 95% confidence level.

-
- [1] Bob Holdom, “Two U(1)’s and Epsilon Charge Shifts,” *Phys. Lett.* **166B**, 196–198 (1986).
 - [2] Keith R. Dienes, Christopher F. Kolda, and John March-Russell, “Kinetic mixing and the supersymmetric gauge hierarchy,” *Nucl. Phys. B* **492**, 104–118 (1997), arXiv:hep-ph/9610479.
 - [3] S. A. Abel and B. W. Schofield, “Brane anti-brane kinetic mixing, millicharged particles and SUSY breaking,” *Nucl. Phys. B* **685**, 150–170 (2004), arXiv:hep-th/0311051.
 - [4] S. A. Abel, M. D. Goodsell, J. Jaeckel, V. V. Khoze, and A. Ringwald, “Kinetic Mixing of the Photon with Hidden U(1)s in String Phenomenology,” *JHEP* **07**, 124 (2008), arXiv:0803.1449 [hep-ph].
 - [5] Steven A. Abel, Joerg Jaeckel, Valentin V. Khoze, and Andreas Ringwald, “Illuminating the Hidden Sector of String Theory by Shining Light through a Magnetic Field,” *Phys. Lett. B* **666**, 66–70 (2008), arXiv:hep-ph/0608248.
 - [6] Mark Goodsell, Joerg Jaeckel, Javier Redondo, and Andreas Ringwald, “Naturally Light Hidden Photons in LARGE Volume String Compactifications,” *JHEP* **11**, 027 (2009), arXiv:0909.0515 [hep-ph].
 - [7] Javier Redondo and Marieke Postma, “Massive hidden photons as lukewarm dark matter,” *JCAP* **02**, 005 (2009), arXiv:0811.0326 [hep-ph].
 - [8] Ann E. Nelson and Jakub Scholtz, “Dark Light, Dark Matter and the Misalignment Mechanism,” *Phys. Rev.* **D84**, 103501 (2011), arXiv:1105.2812 [hep-ph].
 - [9] Paola Arias, Davide Cadamuro, Mark Goodsell, Joerg Jaeckel, Javier Redondo, and Andreas Ringwald, “WISPy Cold Dark Matter,” *JCAP* **1206**, 013 (2012), arXiv:1201.5902 [hep-ph].
 - [10] Peter W. Graham, Jeremy Mardon, and Surjeet Rajendran, “Vector Dark Matter from Inflationary Fluctuations,” *Phys. Rev.* **D93**, 103520 (2016), arXiv:1504.02102 [hep-ph].
 - [11] Gonzalo Alonso-Álvarez, Thomas Hugle, and Joerg Jaeckel, “Misalignment & Co.: (Pseudo-)scalar and vector dark matter with curvature couplings,” (2019), arXiv:1905.09836 [hep-ph].

- [12] Kazunori Nakayama, “Vector Coherent Oscillation Dark Matter,” *JCAP* **1910**, 019 (2019), arXiv:1907.06243 [hep-ph].
- [13] Kazunori Nakayama, “Constraint on Vector Coherent Oscillation Dark Matter with Kinetic Function,” *JCAP* **08**, 033 (2020), arXiv:2004.10036 [hep-ph].
- [14] Yohei Ema, Kazunori Nakayama, and Yong Tang, “Production of Purely Gravitational Dark Matter: The Case of Fermion and Vector Boson,” *JHEP* **07**, 060 (2019), arXiv:1903.10973 [hep-ph].
- [15] Edward W. Kolb and Andrew J. Long, “Completely dark photons from gravitational particle production during the inflationary era,” *JHEP* **03**, 283 (2021), arXiv:2009.03828 [astro-ph.CO].
- [16] Borna Salehian, Mohammad Ali Gorji, Hassan Firouzjahi, and Shinji Mukohyama, “Vector dark matter production from inflation with symmetry breaking,” *Phys. Rev. D* **103**, 063526 (2021), arXiv:2010.04491 [hep-ph].
- [17] Aqeel Ahmed, Bohdan Grzadkowski, and Anna Socha, “Gravitational production of vector dark matter,” *JHEP* **08**, 059 (2020), arXiv:2005.01766 [hep-ph].
- [18] Yuichiro Nakai, Ryo Namba, and Ziwei Wang, “Light Dark Photon Dark Matter from Inflation,” *JHEP* **12**, 170 (2020), arXiv:2004.10743 [hep-ph].
- [19] Kazunori Nakayama and Yong Tang, “Gravitational Production of Hidden Photon Dark Matter in Light of the XENON1T Excess,” *Phys. Lett. B* **811**, 135977 (2020), arXiv:2006.13159 [hep-ph].
- [20] Hassan Firouzjahi, Mohammad Ali Gorji, Shinji Mukohyama, and Borna Salehian, “Dark photon dark matter from charged inflaton,” *JHEP* **06**, 050 (2021), arXiv:2011.06324 [hep-ph].
- [21] Mar Bastero-Gil, Jose Santiago, Lorenzo Ubaldi, and Roberto Vega-Morales, “Dark photon dark matter from a rolling inflaton,” *JCAP* **02**, 015 (2022), arXiv:2103.12145 [hep-ph].
- [22] Hassan Firouzjahi, Mohammad Ali Gorji, Shinji Mukohyama, and Alireza Talebian, “Dark matter from entropy perturbations in curved field space,” *Phys. Rev. D* **105**, 043501 (2022), arXiv:2110.09538 [gr-qc].
- [23] Takanori Sato, Fuminobu Takahashi, and Masaki Yamada, “Gravitational production of dark photon dark matter with mass generated by the Higgs mechanism,” (2022), arXiv:2204.11896 [hep-ph].
- [24] Raymond T. Co, Aaron Pierce, Zhengkang Zhang, and Yue Zhao, “Dark Photon Dark Matter

- Produced by Axion Oscillations,” (2018), arXiv:1810.07196 [hep-ph].
- [25] Jeff A. Dror, Keisuke Harigaya, and Vijay Narayan, “Parametric Resonance Production of Ultralight Vector Dark Matter,” (2018), arXiv:1810.07195 [hep-ph].
- [26] Mar Bastero-Gil, Jose Santiago, Lorenzo Ubaldi, and Roberto Vega-Morales, “Vector dark matter production at the end of inflation,” (2018), arXiv:1810.07208 [hep-ph].
- [27] Prateek Agrawal, Naoya Kitajima, Matthew Reece, Toyokazu Sekiguchi, and Fuminobu Takahashi, “Relic Abundance of Dark Photon Dark Matter,” (2018), arXiv:1810.07188 [hep-ph].
- [28] Raymond T. Co, Keisuke Harigaya, and Aaron Pierce, “Gravitational waves and dark photon dark matter from axion rotations,” JHEP **12**, 099 (2021), arXiv:2104.02077 [hep-ph].
- [29] Kazunori Nakayama and Wen Yin, “Hidden photon and axion dark matter from symmetry breaking,” JHEP **10**, 026 (2021), arXiv:2105.14549 [hep-ph].
- [30] Andrew J. Long and Lian-Tao Wang, “Dark Photon Dark Matter from a Network of Cosmic Strings,” (2019), arXiv:1901.03312 [hep-ph].
- [31] Marco Fabbrichesi, Emidio Gabrielli, and Gaia Lanfranchi, “The Dark Photon,” (2020), 10.1007/978-3-030-62519-1, arXiv:2005.01515 [hep-ph].
- [32] Andrea Caputo, Alexander J. Millar, Ciaran A. J. O’Hare, and Edoardo Vitagliano, “Dark photon limits: A handbook,” Phys. Rev. D **104**, 095029 (2021), arXiv:2105.04565 [hep-ph].
- [33] S. De Panfilis, A. C. Melissinos, B. E. Moskowitz, J. T. Rogers, Y. K. Semertzidis, Walter Wuensch, H. J. Halama, A. G. Prodell, W. B. Fowler, and F. A. Nezrick, “Limits on the Abundance and Coupling of Cosmic Axions at 4.5-Microev $\leq m(a) \leq$ 5.0-Microev,” Phys. Rev. Lett. **59**, 839 (1987).
- [34] Walter Wuensch, S. De Panfilis-Wuensch, Y. K. Semertzidis, J. T. Rogers, A. C. Melissinos, H. J. Halama, B. E. Moskowitz, A. G. Prodell, W. B. Fowler, and F. A. Nezrick, “Results of a Laboratory Search for Cosmic Axions and Other Weakly Coupled Light Particles,” Phys. Rev. **D40**, 3153 (1989).
- [35] C. Hagmann, P. Sikivie, N. S. Sullivan, and D. B. Tanner, “Results from a search for cosmic axions,” Phys. Rev. **D42**, 1297–1300 (1990).
- [36] Stephen J. Asztalos *et al.* (ADMX), “Large scale microwave cavity search for dark matter axions,” Phys. Rev. **D64**, 092003 (2001).
- [37] S. J. Asztalos *et al.* (ADMX), “A SQUID-based microwave cavity search for dark-matter axions,” Phys. Rev. Lett. **104**, 041301 (2010), arXiv:0910.5914 [astro-ph.CO].

- [38] Le Hoang Nguyen, Andrei Lobanov, and Dieter Horns, “First results from the WISPDMMX radio frequency cavity searches for hidden photon dark matter,” *JCAP* **1910**, 014 (2019), arXiv:1907.12449 [hep-ex].
- [39] Dieter Horns, Joerg Jaeckel, Axel Lindner, Andrei Lobanov, Javier Redondo, and Andreas Ringwald, “Searching for WISPy Cold Dark Matter with a Dish Antenna,” *JCAP* **04**, 016 (2013), arXiv:1212.2970 [hep-ph].
- [40] Joerg Jaeckel and Javier Redondo, “An antenna for directional detection of WISPy dark matter,” *JCAP* **11**, 016 (2013), arXiv:1307.7181 [hep-ph].
- [41] Joerg Jaeckel and Stefan Knirck, “Directional Resolution of Dish Antenna Experiments to Search for WISPy Dark Matter,” *JCAP* **01**, 005 (2016), arXiv:1509.00371 [hep-ph].
- [42] Stefan Knirck, Takayuki Yamazaki, Yoshiki Okesaku, Shoji Asai, Toshitaka Idehara, and Toshiaki Inada, “First results from a hidden photon dark matter search in the meV sector using a plane-parabolic mirror system,” *JCAP* **1811**, 031 (2018), arXiv:1806.05120 [hep-ex].
- [43] Graciela B. Gelmini, Alexander J. Millar, Volodymyr Takhistov, and Edoardo Vitagliano, “Probing dark photons with plasma haloscopes,” *Phys. Rev. D* **102**, 043003 (2020), arXiv:2006.06836 [hep-ph].
- [44] Samuel D. McDermott and Samuel J. Witte, “Cosmological evolution of light dark photon dark matter,” *Phys. Rev. D* **101**, 063030 (2020), arXiv:1911.05086 [hep-ph].
- [45] Haipeng An, Fa Peng Huang, Jia Liu, and Wei Xue, “Radio-frequency Dark Photon Dark Matter across the Sun,” *Phys. Rev. Lett.* **126**, 181102 (2021), arXiv:2010.15836 [hep-ph].
- [46] Haipeng An, Xingyao Chen, Shuailiang Ge, Jia Liu, and Yan Luo, “Searching for Ultralight Dark Matter Conversion in Solar Corona using LOFAR Data,” (2023), arXiv:2301.03622 [hep-ph].
- [47] Haipeng An, Shuailiang Ge, and Jia Liu, “Solar Radio Emissions and Ultralight Dark Matter,” *Universe* **9**, 142 (2023), arXiv:2304.01056 [hep-ph].
- [48] Joerg Jaeckel and Javier Redondo, “Resonant to broadband searches for cold dark matter consisting of weakly interacting slim particles,” *Phys. Rev. D* **88**, 115002 (2013), arXiv:1308.1103 [hep-ph].
- [49] Jun’ya Suzuki, Yoshizumi Inoue, Tomoki Horie, and Makoto Minowa, “Hidden photon CDM search at Tokyo,” in *11th Patras Workshop on Axions, WIMPs and WISPs* (2015) pp. 145–148, arXiv:1509.00785 [hep-ex].

- [50] J. Suzuki, T. Horie, Y. Inoue, and M. Minowa, “Experimental Search for Hidden Photon CDM in the eV mass range with a Dish Antenna,” *JCAP* **09**, 042 (2015), arXiv:1504.00118 [hep-ex].
- [51] Nozomu Tomita, Shugo Oguri, Yoshizumi Inoue, Makoto Minowa, Taketo Nagasaki, Jun’ya Suzuki, and Osamu Tajima, “Search for hidden-photon cold dark matter using a K-band cryogenic receiver,” *JCAP* **09**, 012 (2020), arXiv:2006.02828 [hep-ex].
- [52] Benjamin Godfrey *et al.*, “Search for dark photon dark matter: Dark E field radio pilot experiment,” *Phys. Rev. D* **104**, 012013 (2021), arXiv:2101.02805 [physics.ins-det].
- [53] Pierre Brun, Laurent Chevalier, and Christophe Flouzat, “Direct Searches for Hidden-Photon Dark Matter with the SHUKET Experiment,” *Phys. Rev. Lett.* **122**, 201801 (2019), arXiv:1905.05579 [hep-ex].
- [54] A. Andrianavalomahefa *et al.* (FUNK Experiment), “Limits from the Funk Experiment on the Mixing Strength of Hidden-Photon Dark Matter in the Visible and Near-Ultraviolet Wavelength Range,” *Phys. Rev. D* **102**, 042001 (2020), arXiv:2003.13144 [astro-ph.CO].
- [55] Fayez Bajjali *et al.*, “First results from BRASS-p broadband searches for hidden photon dark matter,” *JCAP* **08**, 077 (2023), arXiv:2306.05934 [hep-ex].
- [56] Jonathan P. Gardner *et al.*, “The James Webb Space Telescope,” *Space Sci. Rev.* **123**, 485 (2006), arXiv:astro-ph/0606175.
- [57] Haipeng An, Shuailiang Ge, Wen-Qing Guo, Xiaoyuan Huang, Jia Liu, and Zhiyao Lu, “Direct detection of dark photon dark matter using radio telescopes,” *Phys. Rev. Lett.* **130**, 181001 (2023).
- [58] N. Bleistein and R.A. Handelsman, *Asymptotic Expansions of Integrals*, Dover Books on Mathematics Series (Dover Publications, 1986).
- [59] A. K. Drukier, Katherine Freese, and D. N. Spergel, “Detecting Cold Dark Matter Candidates,” *Phys. Rev. D* **33**, 3495–3508 (1986).
- [60] N. Wyn Evans, Ciaran A. J. O’Hare, and Christopher McCabe, “Refinement of the standard halo model for dark matter searches in light of the Gaia Sausage,” *Phys. Rev. D* **99**, 023012 (2019), arXiv:1810.11468 [astro-ph.GA].
- [61] Paul Lightsey, Charles Atkinson, Mark Clampin, and Lee Feinberg, “James webb space telescope: Large deployable cryogenic telescope in space,” *Optical Engineering* **51**, 1003– (2012).

- [62] Paul A. Lightsey, J. Scott Knight, and Gary Golnik, “Status of the optical performance for the James Webb Space Telescope,” in *Space Telescopes and Instrumentation 2014: Optical, Infrared, and Millimeter Wave*, Society of Photo-Optical Instrumentation Engineers (SPIE) Conference Series, Vol. 9143, edited by Jr. Oschmann, Jacobus M., Mark Clampin, Giovanni G. Fazio, and Howard A. MacEwen (2014) p. 914304.
- [63] MAST 2021, JWST Archive Manual, eds. R.A. Shaw, B. Cherinka, P. Forshay, J. Yoon (Baltimore: STScI).
- [64] Glen Cowan, Kyle Cranmer, Eilam Gross, and Ofer Vitells, “Asymptotic formulae for likelihood-based tests of new physics,” *The European Physical Journal C* **71** (2011), 10.1140/epjc/s10052-011-1554-0.
- [65] Shao-Ping Li and Xun-Jie Xu, “Production rates of dark photons and z' in the sun and stellar cooling bounds,” (2023), arXiv:2304.12907 [hep-ph].
- [66] E. Aprile *et al.* (XENON), “Emission of single and few electrons in XENON1T and limits on light dark matter,” *Phys. Rev. D* **106**, 022001 (2022), arXiv:2112.12116 [hep-ex].
- [67] Jeff Chiles *et al.*, “New Constraints on Dark Photon Dark Matter with Superconducting Nanowire Detectors in an Optical Haloscope,” *Phys. Rev. Lett.* **128**, 231802 (2022), arXiv:2110.01582 [hep-ex].
- [68] Laura Manenti *et al.*, “Search for dark photons using a multilayer dielectric haloscope equipped with a single-photon avalanche diode,” *Phys. Rev. D* **105**, 052010 (2022), arXiv:2110.10497 [hep-ex].

Theoretical Highlights of CP Violation in B Decays

Eleftheria Malami^{a,b,*}

^a*Center for Particle Physics Siegen (CPPS), Theoretische Physik 1, Universität Siegen,
D-57068 Siegen, Germany*

^b*Nikhef,
Science Park 105, 1098 XG Amsterdam, Netherlands*

E-mail: Eleftheria.Malami@uni-siegen.de, emalami@nikhef.nl

In this presentation, we discuss recent key topics in theoretical analyses of CP violation in benchmark decays of the B meson. We provide the most updated values of the mixing phases and discuss the importance of including the penguin contributions in their studies. Exploring intriguing patterns in purely tree decays, interesting new methodologies can be developed and applied. New data related to the CP asymmetries of key modes like $B_d^0 \rightarrow \pi^0 K_S$ and $B_s^0 \rightarrow K^+ K^-$ lead to interesting results. The new $R_{K^{(*)}}$ measurement, compatible with the Standard Model, can still allow for electron-muon symmetry violation through new sources of CP violation.

*16th International Conference on Heavy Quarks and Leptons (HQL2023)
28 November-2 December 2023
TIFR, Mumbai, Maharashtra, India*

*Speaker

1. First Few Words

The concept of CP violation in the B -meson system is important in order to test the Standard Model (SM) as well as to search for hints of New Physics (NP). Central role in the studies of CP violation plays the Cabibbo–Kobayashi–Maskawa (CKM) matrix [1, 2], and an important topic linked to this matrix is the Unitarity triangle (UT). We provide recent highlights in the studies of CP violation and discuss benchmark modes.

2. Topic 1: Mixing Phases and Penguin Contributions

An important feature of neutral B mesons is the oscillation between B_q^0 and \bar{B}_q^0 , which may lead to interference effects if both B_q^0 and \bar{B}_q^0 decay into the same final state. These interference effects give rise to CP-violating asymmetries. Associated to the B_q^0 – \bar{B}_q^0 mixing phenomenon are the CP-violating mixing phases ϕ_d and ϕ_s for the B_d and B_s systems, respectively. Benchmark decays for determining these phases are the $B_d^0 \rightarrow J/\psi K_s^0$ and $B_s^0 \rightarrow J/\psi \phi$ modes. The theoretical precision is limited by doubly-Cabibbo suppressed penguin contributions, which are difficult to calculate. So, instead of calculating these penguin topologies, we use control channels to determine them, exploiting the SU(3) flavour symmetry of strong interactions. The corresponding analysis is given in Ref. [3] and allows us to extract the values of the mixing phases, taking the penguin contributions into account. The experimental input for the phases is:

$$\phi_s^{\text{eff}} = (-4.1 \pm 1.3)^\circ, \quad \phi_d^{\text{eff}} = (43.6 \pm 1.4)^\circ, \quad (1)$$

where $\phi_q^{\text{eff}} = \phi_q + \Delta\phi_q$ with $\Delta\phi_q$ indicating the hadronic phase shift. The extracted penguin parameters $a_{(V)}$ and $\theta_{(V)}$ and mixing phases are the following [4]:

$$\text{vector-pseudoscalar states } a = 0.14_{-0.11}^{+0.17}, \quad \theta = \left(173_{-45}^{+35}\right)^\circ, \quad \phi_d = \left(44.4_{-1.5}^{+1.6}\right)^\circ, \quad (2)$$

$$\text{vector-vector states } a_V = 0.044_{-0.038}^{+0.085}, \quad \theta_V = \left(306_{-112}^{+48}\right)^\circ, \quad \phi_s = (-4.2 \pm 1.4)^\circ. \quad (3)$$

We note that updated measured values for ϕ_s^{eff} and ϕ_d^{eff} have recently been provided by the LHCb Collaboration and the Belle II experiment in Refs. [5–7], respectively. In future analyses, achieving much higher precision, it is important that the penguin contributions are properly included.

Having provided the mixing phases, we move on to the UT and the determination of its apex. For this aim, special attention needs to be given to the determination of the CKM input parameters. As presented in Ref. [8], one way of determining the UT is through the angle γ and the side R_b . Concerning the angle γ , it is measured by the LHCb collaboration through $B \rightarrow DK$ modes. An alternative way of obtaining this angle is via the isospin analysis of $B \rightarrow \pi\pi, \rho\pi, \rho\rho$ decays, yielding the UT angle α . Utilising the ϕ_d phase, the value of α is converted into γ . The two results agree with each other, thus with the current precision, we can make an average of these γ values:

$$\gamma_{\text{avg}} = (68.4 \pm 3.3)^\circ. \quad (4)$$

Regarding R_b , tensions arise between the inclusive and exclusive determinations of the $|V_{ub}|$ and $|V_{cb}|$ matrix elements. The essential point is to avoid making averages between these values but to

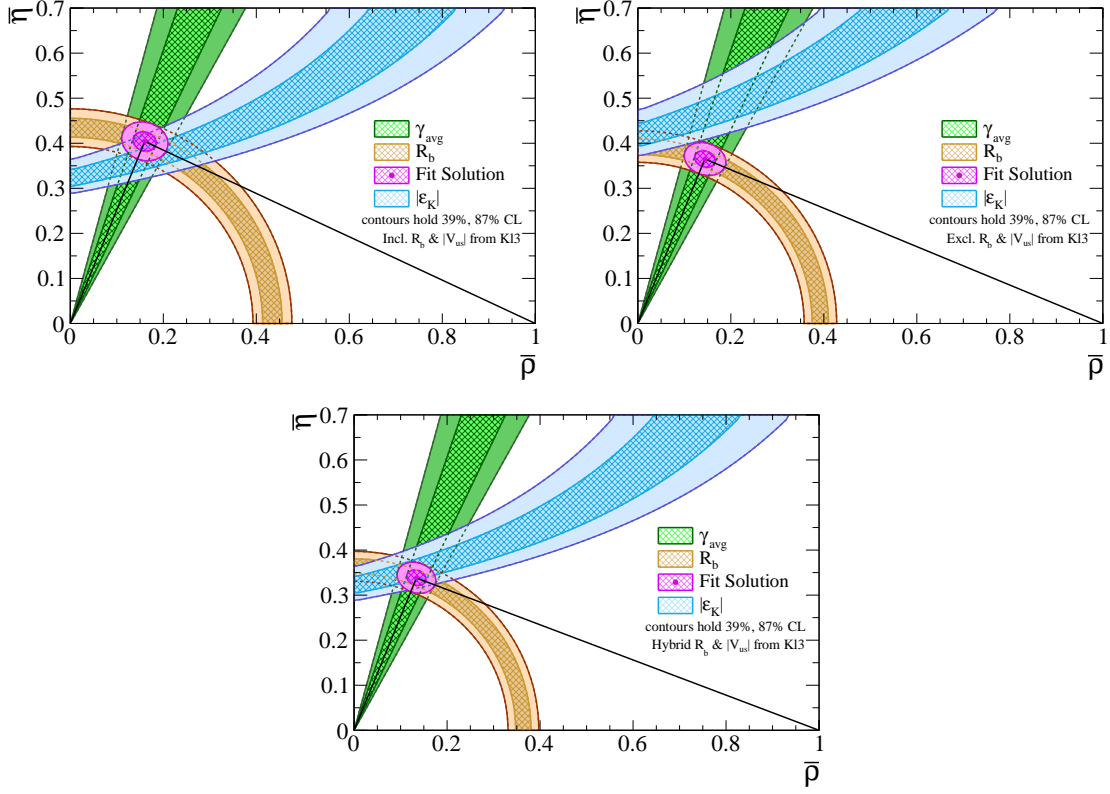


Figure 1: Determination of the UT apex. Top left: inclusive case, top right: exclusive case and bottom plot: hybrid case with excl. $|V_{ub}|$ and incl. $|V_{cb}|$ [3].

perform separate analysis for the two different approaches. On top of that, we can explore a hybrid option; the case of exclusive $|V_{ub}|$ and inclusive $|V_{cb}|$, as presented in [8]. An illustration of the UT for these three cases is given in Fig. 1. In the same figure, the ϵ_K hyperbola (blue contour), coming from indirect CP violation in the neutral kaon system, is also shown.

The studies of the UT are a key input for obtaining SM predictions of the B_q mixing parameters and eventually, exploring the corresponding space for NP left through the current data. As discussed in [8], the corresponding results have interesting applications in rare leptonic decays. In particular, we can minimise the impact of the CKM parameters when constraining NP in $B_s^0 \rightarrow \mu^+ \mu^-$ by creating ratios of the branching fraction of this decay and the mass difference Δm_s [9, 10]:

$$R_{s\mu} = \bar{\mathcal{B}}(B_s^0 \rightarrow \mu^+ \mu^-) / \Delta m_s, \quad (5)$$

where the CKM elements drop out in the SM.

3. Topic 2: Puzzles in Tree Decays

The pure tree decays $\bar{B}_s^0 \rightarrow D_s^+ K^-$ and $B_s^0 \rightarrow D_s^+ K^-$ (and their CP conjugates) offer a powerful probe for testing the SM description of CP violation [11–13]. Intriguing puzzles arise in the angle γ of the UT and the individual branching ratios, which complement each other. A strategy that

allows us to study these anomalies and search for hints of NP is discussed in Refs. [14, 15]. Let us summarise the key points of this methodology.

As a first step, we explore CP violation. Due to $B_q^0-\bar{B}_q^0$ mixing, interference effects arise between the $\bar{B}_s^0 \rightarrow D_s^+ K^-$ and $B_s^0 \rightarrow D_s^+ K^-$ channels. These interference effects lead to a time-dependent CP asymmetry, which yields the observables C , S , $\mathcal{A}_{\Delta\Gamma}$ and their CP conjugates. A measure of the strength of the interference effects is given by the quantities ξ and $\bar{\xi}$. Therefore, one can use the observables C , S , $\mathcal{A}_{\Delta\Gamma}$ and \bar{C} , \bar{S} , $\bar{\mathcal{A}}_{\Delta\Gamma}$, in order to determine ξ and $\bar{\xi}$, respectively, from the experimental data in an unambiguous way. Within the SM, in the product $\xi \times \bar{\xi}$ hadronic matrix elements cancel out allowing a theoretically clean extraction to $(\phi_s + \gamma)$. In the presence of NP, the generalisation of this relation takes the following form:

$$\xi \times \bar{\xi} = \sqrt{1 - 2 \left[\frac{C + \bar{C}}{(1 + C)(1 + \bar{C})} \right]} e^{-i[2(\phi_s + \gamma_{\text{eff}})]}, \quad (6)$$

where again hadronic uncertainties cancel. In particular, here it is possible that $C + \bar{C}$ is not equal to 0, as in the SM. The above expression leads to a theoretically clean determination of the angle:

$$\gamma_{\text{eff}} \equiv \gamma + \gamma_{\text{NP}}, \quad (7)$$

where γ_{NP} is a function of the NP parameters ρ , φ , δ , and $\bar{\rho}$, $\bar{\varphi}$, $\bar{\delta}$ (for the CP conjugate case). Here, $\rho = [A(\bar{B}_s^0 \rightarrow D_s^+ K^-)_{\text{NP}}/A(\bar{B}_s^0 \rightarrow D_s^+ K^-)_{\text{SM}}]$ measures the strength of NP, while δ and φ denote the CP-conserving and CP-violating phases, and similarly for $\bar{\rho}$, $\bar{\varphi}$, $\bar{\delta}$. Using information on γ [16] from other processes, we extract γ_{NP} .

The second step corresponds to information from the branching ratios. We create ratios by combining the branching fractions of the non-leptonic decays we study with differential branching ratios of their semi-leptonic partner channels. These ratios with the semileptonic decays minimize the dependence on the CKM matrix elements and the hadronic form factors. Therefore, they provide a useful setup which permits the extraction of the colour factors $|a_1|$ from the data in the theoretically cleanest possible manner. Comparing these experimental results with theoretical predictions, we find tensions even up to the 4.8σ level. This intriguing pattern is in line with what we expect from the puzzling situation with γ . In order to interpret these $|a_1|$ deviations, we introduce the quantities:

$$\bar{b} \equiv \frac{\langle \mathcal{B}(\bar{B}_s^0 \rightarrow D_s^+ K^-)_{\text{th}} \rangle}{\mathcal{B}(\bar{B}_s^0 \rightarrow D_s^+ K^-)_{\text{th}}^{\text{SM}}} = 1 + 2 \bar{\rho} \cos \bar{\delta} \cos \bar{\varphi} + \bar{\rho}^2, \quad (8)$$

$$b \equiv \frac{\langle \mathcal{B}(B_s^0 \rightarrow D_s^- K^+)_{\text{th}} \rangle}{\mathcal{B}(B_s^0 \rightarrow D_s^- K^+)_{\text{th}}^{\text{SM}}} = 1 + 2 \rho \cos \delta \cos \varphi + \rho^2, \quad (9)$$

where now we use as input the theoretical expectation of $|a_1|$. The extracted values of b and \bar{b} deviate from the SM. We highlight that making use of other control channels, we are able to constrain the contributions from exchange diagrams and no anomalous enhancement is observed due to these topologies.

Last but not least, we explore how much room there is for NP utilising all three γ_{eff} , b and \bar{b} . More specifically, we obtain correlations between the NP parameters $\rho(\varphi)$ and $\bar{\rho}(\bar{\varphi})$, assuming that the strong phases equal to 0. Constraining these NP parameters, we find that it is possible to accommodate the current data with new contributions of moderate size.

We note that for the numerical analysis in Refs. [14, 15] the values presented by the LHCb Collaboration in Ref. [17] have been used. A new standalone measurement by LHCb using only Run II has recently been reported [18], which is interesting to explore further.

4. Topic 3: $B_d^0 \rightarrow \pi^0 K_S$ and $B_s \rightarrow K^+ K^-$

Another powerful probe for CP violation studies is given by charmless two-body B decays, such as $B \rightarrow \pi K$, $B_{(s)} \rightarrow KK$ and $B \rightarrow \pi\pi$ [19–21]. Here, we will present updates related to two of these channels, $B_d^0 \rightarrow \pi^0 K_S$ and $B_s \rightarrow K^+ K^-$, which are dominated by penguin topologies.

The $B_d^0 \rightarrow \pi^0 K_S$ decay is one of the most interesting $B \rightarrow \pi K$ channels, as this is the only one exhibiting mixing-induced CP violation. Therefore, it is important to measure CP violation with the highest precision in this system, and especially the mixing-induced CP violation. This mode is extensively studied in Refs. [22–25].

Following the analysis in Ref. [22], utilising an isospin relation and complementing it with a minimal SU(3) input, we obtain correlations between the CP asymmetries, given by the following expression [26]:

$$S_{\pi^0 K_S} = \sqrt{1 - A_{\pi^0 K_S}^2} \sin(\phi_d - \phi_{00}). \quad (10)$$

Here, $S_{\pi^0 K_S}$ is the mixing-induced and $A_{\pi^0 K_S}$ the direct CP asymmetry, ϕ_d is the $B_d^0 - \bar{B}_d^0$ mixing phase and ϕ_{00} denotes the angle between the decay amplitude $B_d^0 \rightarrow \pi^0 K^0$ and its CP-conjugate $\bar{B}_d^0 \rightarrow \pi^0 \bar{K}^0$. Interestingly, tensions arise with the SM picture. Thus, we need to explore how this puzzle can be resolved. Two are the options: either the data should change or NP physics contributions might enter the penguin sector.

An update on the time-dependent CP violation in $B_d^0 \rightarrow \pi^0 K_S$ was recently provided by Belle II. The new new results for the mixing induced and direct CP asymmetries are the following [27]:

$$A_{\pi^0 K_S}^{\text{Belle II}} = 0.04_{-0.14}^{+0.15} \pm 0.05, \quad S_{\pi^0 K_S}^{\text{Belle II}} = 0.75_{-0.23}^{+0.20} \pm 0.04. \quad (11)$$

These results can be compared with the current world average:

$$A_{\pi^0 K_S}^{\text{world average}} = -0.01 \pm 0.10, \quad S_{\pi^0 K_S}^{\text{world average}} = 0.57 \pm 0.17. \quad (12)$$

The new Belle II data become competitive with the world's most precise measurements. In comparison with the theoretical results for the CP asymmetries derived from Eq. 10, this new measurement has been shifted towards the theory predictions, showing a better agreement within the uncertainties. This is an interesting point as it can play a key role in resolving the longstanding $B \rightarrow \pi K$ puzzle.

The second interesting channel we discuss is the $B_s \rightarrow K^+ K^-$ [28], where the first observation of CP violation in this decay was recently reported by the LHCb collaboration [29]. The new LHCb measurements reveal surprising differences between the direct CP asymmetries in the following modes [29]:

$$\mathcal{A}_{\text{CP}}^{\text{dir}}(B_s^0 \rightarrow K^- K^+) - \mathcal{A}_{\text{CP}}^{\text{dir}}(B_d^0 \rightarrow \pi^- K^+) = 0.089 \pm 0.031, \quad (13)$$

$$\mathcal{A}_{\text{CP}}^{\text{dir}}(B_d^0 \rightarrow \pi^- \pi^+) - \mathcal{A}_{\text{CP}}^{\text{dir}}(B_s^0 \rightarrow K^- \pi^+) = -0.095 \pm 0.040. \quad (14)$$

These decays differ only via the spectator quark thus, it is unlikely that this pattern indicates NP. An analysis performed in Ref. [30] shows that these differences can be accommodated in the SM through exchange and penguin-annihilation topologies, that are sizeable – at the level of 20%.

On top of that, the analysis in Ref. [30] provides an interesting way of extracting the angle γ of the UT. The proposed strategy relies only on CP asymmetries without requiring information on branching ratios. The result:

$$\gamma = (65_{-7}^{+11})^\circ, \quad (15)$$

agrees excellently with the γ values from the $B \rightarrow DK$ decays, which are pure tree transitions. As an alternative, the $B_s^0-\bar{B}_s^0$ mixing phase ϕ_s can also be determined if now one uses the value of γ as an input. For this purpose, the methodology of using ratios of non-leptonic and semileptonic $B_{(s)}$ decay rates is utilised, providing a clean way of obtaining ϕ_s .

5. Topic 4: CP Violation in Rare Decays. What about $R_{K^{(*)}}$ and the Electron-Muon Symmetry Violation?

The new results for $R_{K^{(*)}}$ presented by the LHCb collaboration in 2022 [31, 32]:

$$\langle R_K \rangle = 0.949 \pm 0.05, \quad \text{for momentum transfer } q^2 \in [1.1, 6.0] \text{ GeV}, \quad (16)$$

brought new perspectives for testing the electron–muon universality. These results agree with Lepton Flavour Universality (LFU). The differential rates for $B \rightarrow K\mu^+\mu^-$ are small compared to the SM predictions, deviating at the 3.5σ level, thereby still indicating possible NP through these decays. How much electron-muon universality violation is possibly left for this NP, now constrained by R_K ? As shown in the analysis in Ref. [33] due to new CP-violating effects, there is still significant room for violation of the electron–muon universality.

More specifically, this analysis explores the CP-violating effects in the NP studies of rare decays making use of the muonic Wilson coefficients. The experimental branching ratio and the direct CP asymmetry of the $B^- \rightarrow K^- \mu^+ \mu^-$ mode constrains the corresponding muonic Wilson coefficients $C_{i\mu}$. Combining this constrain with the new $\langle R_K \rangle$ measurement allows the determination of the Wilson coefficient C_{ie} in the electronic sector. Having determined C_{ie} , the electronic direct and mixing-induced CP asymmetry are also obtained. The following conclusions are drawn:

- i) NP Wilson coefficients entering the electronic modes can strongly differ from the corresponding ones entering the muonic channels and
- ii) CP violating phases can be significantly different, therefore also the CP asymmetries between the electronic and muonic modes, which are the observables that they experimentalists should utilize in order to test the violation of LFU.

Therefore, it is still possible to have significant electron–muon universality violation, if NP effects are associated with new sources of CP violation, which are encoded in Wilson coefficients. In the era of high-precision B physics, it is important to perform experimental searches focusing on differences in CP asymmetries between the $b \rightarrow se^+e^-$ and $b \rightarrow s\mu^+\mu^-$ transitions. These studies will be essential for further testing LFU.

6. Epilogue

A lot of progress has been achieved over the last years in the studies of CP violation, which was possible through the synergy between theorists and experimentalists. There are exciting new perspectives to further explore CP violation. Moving towards the high precision era of B physics and monitoring the evolution of the data will lead to a much sharper picture.

Acknowledgements

I would like to thank the organisers of the HQL2023 for the invitation and the opportunity to attend such a great conference.

References

- [1] N. Cabibbo, Phys. Rev. Lett. **10** (1963), 531-533 doi:10.1103/PhysRevLett.10.531
- [2] M. Kobayashi and T. Maskawa, Prog. Theor. Phys. **49** (1973), 652-657 doi:10.1143/PTP.49.652
- [3] M. Z. Barel, K. De Bruyn, R. Fleischer and E. Malami, J. Phys. G **48** (2021) no.6, 065002
- [4] M. Z. Barel, K. De Bruyn, R. Fleischer and E. Malami, PoS **CKM2021** (2023), 111 doi:10.22323/1.411.0111 [arXiv:2203.14652 [hep-ph]].
- [5] R. Aaij *et al.* [LHCb], [arXiv:2308.01468 [hep-ex]].
- [6] R. Aaij *et al.* [LHCb], Phys. Rev. Lett. **132** (2024) no.2, 021801
- [7] I. Adachi *et al.* [Belle-II], [arXiv:2302.12898 [hep-ex]].
- [8] K. De Bruyn, R. Fleischer, E. Malami and P. van Vliet, J. Phys. G **50** (2023) no.4, 045003
- [9] A. J. Buras, Phys. Lett. B **566** (2003), 115-119
- [10] A. J. Buras and E. Venturini, Acta Phys. Polon. B **53** no.6, 6-A1
- [11] R. Aleksan, I. Dunietz and B. Kayser, Z. Phys. C **54** (1992), 653-660
- [12] R. Fleischer, Nucl. Phys. B **671** (2003), 459-482
- [13] K. De Bruyn, R. Fleischer, R. Knegjens, M. Merk, M. Schiller and N. Tuning, Nucl. Phys. B **868** (2013), 351-367
- [14] R. Fleischer and E. Malami, Eur. Phys. J. C **83** (2023) no.5, 420
- [15] R. Fleischer and E. Malami, Phys. Rev. D **106** (2022) no.5, 056004
- [16] Y. S. Amhis *et al.* [HFLAV], Eur. Phys. J. C **81**, no.3, 226 (2021)
- [17] R. Aaij *et al.* [LHCb Collaboration], JHEP **1803**, 059 (2018)

- [18] [LHCb], LHCb-CONF-2023-004.
- [19] M. Neubert and J. L. Rosner, Phys. Lett. B **441** (1998), 403-409
- [20] A. J. Buras and R. Fleischer, Eur. Phys. J. C **11** (1999), 93-109
- [21] T. Huber and G. Tetlalmatzi-Xolocotzi, Eur. Phys. J. C **82** (2022) no.3, 210
- [22] R. Fleischer, R. Jaarsma, E. Malami and K. K. Vos, Eur. Phys. J. C **78** (2018) no.11, 943
- [23] R. Fleischer, R. Jaarsma and K. K. Vos, Phys. Lett. B **785** (2018), 525-529
- [24] R. Fleischer, S. Jager, D. Pirjol and J. Zupan, Phys. Rev. D **78** (2008), 111501
- [25] A. J. Buras, R. Fleischer, S. Recksiegel and F. Schwab, Nucl. Phys. B **697** (2004), 133-206
- [26] S. Faller, R. Fleischer and T. Mannel, Phys. Rev. D **79** (2009), 014005
- [27] M. Veronesi [BELLE II], [arXiv:2305.09153 [hep-ex]].
- [28] R. Fleischer, Phys. Lett. B **459** (1999), 306-320
- [29] R. Aaij *et al.* [LHCb], JHEP **03** (2021), 075
- [30] R. Fleischer, R. Jaarsma and K. K. Vos, JHEP **02** (2023), 081
- [31] R. Aaij *et al.* [LHCb], Phys. Rev. Lett. **131** (2023) no.5, 051803
- [32] R. Aaij *et al.* [LHCb], Phys. Rev. D **108** (2023) no.3, 032002
- [33] R. Fleischer, E. Malami, A. Rehult and K. K. Vos, JHEP **06** (2023), 033

The symmetry approach to quark and lepton masses and mixing

Gui-Jun Ding^a*, José W.F. Valle^b†

^a*Department of Modern Physics, University of Science and Technology of China,
Hefei, Anhui 230026, China*

^b*AHEP Group, Instituto de Física Corpuscular - CSIC/Universitat de València, Parque Científico
C/Catedrático José Beltrán, 2, E-46980 Paterna (València) - SPAIN*

Abstract

The Standard Model lacks an organizing principle to describe quark and lepton “flavours”. We review the impact of neutrino oscillation experiments, which show that leptons mix very differently from quarks, placing a major challenge, but also providing a key input to the flavour puzzle. We briefly sketch the seesaw and “scotogenic” approaches to neutrino mass, the latter including also WIMP dark matter. We discuss the limitations of popular neutrino mixing patterns and examine the possibility that they arise from symmetry, giving a bottom-up approach to residual flavour and CP symmetries. We show how family and/or CP symmetries can generate novel viable and predictive mixing patterns. We review the model-independent ways to predict lepton mixing and test both mixing predictions as well as mass sum rules. We also discuss UV-complete flavour theories in four and more space-time dimensions, and their predictions. Benchmarks given include an A_4 scotogenic construction with trimaximal mixing pattern TM2. Higher-dimensional completions are also reviewed, such as 5-D warped flavordynamics. We present a T' warped flavordynamics theory with TM1 mixing pattern, detectable neutrinoless double beta decay rates and providing a very good fit of flavour observables, including quarks. We also review how 6-D orbifolds offer a way to determine the structure of the 4-D family symmetry from the symmetries between the extra-D branes. We describe a scotogenic A_4 orbifold predicting the “golden” quark-lepton mass relation, large neutrino mass with normal ordering, higher atmospheric octant, restricted reactor angle, and an excellent global flavour fit, including quark observables. Finally, we discuss promising recent progress in tackling the flavor issue through the use of modular symmetries.

Keywords: Fermion mixing, CP violation, generalized CP, flavor and modular symmetry, orbifolds, warped-flavordynamics.

*E-mail: dinggj@ustc.edu.cn

†E-mail: valle@ific.uv.es

Contents

1	Introduction	4
1.1	Quark masses and mixing	6
1.2	Lepton masses and mixing	7
1.3	Neutrino oscillation recap	9
1.4	Neutrinoless double beta decay	12
2	Origin of neutrino masses and flavour puzzle	16
2.1	Effective neutrino masses	16
2.2	The seesaw paradigm	16
2.3	Dark matter as the source of neutrino mass	18
2.4	Missing partner seesaw and dark matter: the scoto-seesaw	18
2.5	The low-scale inverse and linear seesaw mechanisms	19
2.6	Dark inverse and linear seesaw mechanisms	20
2.7	Neutrinos and the flavour puzzle	21
3	Lepton mixing patterns	24
3.1	Tri-bimaximal mixing (TBM)	24
3.2	Generalizations of tri-bimaximal mixing	25
3.3	Golden ratio mixing pattern	26
3.4	Bi-maximal mixing pattern	27
4	Flavour and CP symmetries from the bottom-up	29
4.1	Residual symmetries of leptons	29
4.2	Reconstructing lepton mixing from remnant CP symmetry	33
4.3	Residual symmetries of quarks	36
5	Viable lepton mixing patterns	39
5.1	Revamped TBM mixing	39
5.1.1	Case a: G_1 flavour and X_1, X_4 CP symmetries	41
5.1.2	Case b: G_2 flavour and X_2, X_4 CP symmetries	43
5.2	Revamped Golden-Ratio mixing scheme	44
5.3	Bi-large mixing	46
5.3.1	Bi-large mixing from abelian family symmetry	47
5.3.2	Confronting bi-large mixing with oscillation data	51
6	Lepton mixing from flavour and CP symmetry	54
6.1	Lepton mixing from flavour symmetry alone	54
6.1.1	Fully preserved residual symmetry $G_\nu = K_4$	56
6.1.2	Partially preserved residual symmetry $G_\nu = Z_2$	57

6.2	Combining flavour and CP symmetry	59
6.2.1	Mathematical consistency	60
6.2.2	Implications of residual flavour and CP symmetries	63
6.3	Predictive scenarios with CP symmetry	64
6.3.1	$\mathcal{G}_l = Z_n$ ($n \geq 3$), $\mathcal{G}_\nu = Z_2 \times CP$	65
6.3.2	$\mathcal{G}_l = Z_2 \times CP$, $\mathcal{G}_\nu = Z_2 \times CP'$	72
6.4	Quark and lepton mixing from a common flavour group	75
6.5	Geometrical CP violation	79
7	Testing flavor and CP symmetries	81
7.1	Testing mixing predictions	81
7.2	Testing mass sum rules	84
7.3	Flavor symmetry toolkit	88
8	Benchmark UV-complete models in 4-D	89
8.1	A_4 family symmetry in a scotogenic model	89
8.1.1	Charged lepton masses	90
8.1.2	Dark fermion masses	91
8.1.3	Scotogenic neutrino masses	92
8.2	A benchmark model with both flavour and CP symmetries	95
8.2.1	Flavon superpotential	96
8.2.2	The charged lepton sector	97
8.2.3	The neutrino sector	98
9	Family symmetry in 5-D models with a warped extra dimension	102
9.1	Warped flavourdynamics with the T' family group	102
9.1.1	Lepton masses and mixing	103
9.1.2	Quark masses and CKM matrix	107
9.2	Global flavour fit	108
10	Family symmetry from 6-D orbifolds	111
10.1	General preliminaries	111
10.2	Scotogenic orbifold	113
10.3	Symmetry breaking and fermion masses	115
10.3.1	Quark and lepton masses	116
10.3.2	Scotogenic neutrino masses	117
10.4	Global fit of flavour observables	118
10.4.1	Preliminaries	118
10.4.2	Fit procedure	119
10.5	Flavour predictions of the scotogenic orbifold model	119

10.5.1 Golden quark-lepton mass relation	119
10.5.2 Neutrino oscillation predictions	120
10.5.3 Neutrinoless double beta decay predictions	121
11 Recent progress: modular symmetry	123
11.1 The modular group	123
11.2 Modular invariance	125
11.3 Generalized CP in modular symmetry	126
11.4 Modular symmetry from top-down	127
11.5 Quark-lepton mass relations from modular symmetry	127
11.6 Modular versus traditional flavor symmetry	128
12 Summary and outlook	129
A The A_4 group	133
B The S_4 group	135
C The dihedral group	138
D Diagonalization of a 2×2 complex symmetric matrix	141

1 Introduction

Elucidating the spontaneous mechanism of symmetry breaking [1] within the Standard Model (SM) [2–5], i.e. the existence of a physical Higgs boson [6–8], has so far been the main accomplished goal of the successful LHC programme. This was achieved, at least partially, with the discovery of a scalar particle with properties closely resembling those of the SM Higgs, by the ATLAS [9] and CMS [10] experiments at CERN. More is expected from future studies, for example, at the upcoming FCC facility [11, 12] and other complementary lepton accelerators [13–17].

Another major milestone in elementary particle physics has been the discovery of neutrino oscillations in solar and atmospheric neutrino experiments [18, 19]. These were followed by reactor- and accelerator-based studies, e.g. [20–23] which, altogether, imply nonzero neutrino masses, as well as large mixing angles in the lepton sector [24, 25]¹. This comes as a surprise, when compared with the pattern seen in the Cabibbo-Kobayashi-Maskawa matrix describing quark mixing and CP violation [28]. It also means that, even after the discovery of the Higgs boson, the architecture of particle physics is still quite far from “complete”.

The origin of neutrino masses is one of the deepest secrets of modern particle physics [29]. The most general neutrino mass generation template is given by the $SU(3)_c \otimes SU(2)_L \otimes U(1)_Y$ gauge theory framework characterizing the SM [30–32]. In this review we will be mainly concerned with bottom-up

¹There is a fairly good agreement with the other determinations, by the Bari group [26] and NuFit [27].

approaches, for which this is the most appropriate choice. However the seesaw can also be discussed in terms of left-right theories and $SO(10)$ [33–38].

Following the gauge principle that underlies the SM construction, neutrinos should also get mass through spontaneous symmetry breaking (SSB). Small neutrino masses would be understood dynamically through new vacuum expectation values (VEVs). A specially interesting case is that of spontaneous violation of lepton number [32, 39]. Besides the high-scale seesaw, we stress that one can also have dynamical generation of neutrino masses at low scales [40–42].

Within the SM picture three of the fundamental interactions of nature (electromagnetic, weak and strong) all have a gauge description. It would be very appealing if these could also have a common origin at very high energies [34, 43–47], though no hard evidence for this beautiful idea has ever been found. Despite their potential in providing an all-encompassing unified description including also gravity [48–50], superstring theories have so far also failed to provide a phenomenologically convincing roadmap.

Another major drawback of the SM construction is that it fails to explain family replication, fermion mass hierarchies and mixing pattern. The discovery of oscillations has only exacerbated this fact. The disparity observed in the pattern of quark and lepton mixing parameters appears to us unlikely to be the result of pure chance. As a result, we will not examine the possibility of neutrino mixing anarchy [51, 52]. Although viable, we find this hypothesis theoretically unsatisfactory. Instead, our main common thread in this review will be the symmetry approach to the “flavour problem”.

Here we will be mainly concerned with explaining the detailed pattern of the weak interactions of quarks and leptons within family-symmetry extended theories based on the $SU(3)_c \otimes SU(2)_L \otimes U(1)_Y$ gauge group, with special emphasis on the case of leptons. Early attempts to understand the lepton mixing pattern starting from the quark sector have now become obsolete, since the discovery of neutrino oscillations. A fully successful flavour theory should explain not only the observed large mixing angles in the lepton sector but also the CKM mixing pattern governing quark mixing and CP violation. Likewise, it should also account for the pattern of quark and lepton masses. In this review we will illustrate how this may, at least partially, be achieved either within 4-dimensional renormalizable gauge field theories [53–69] or in the context of theories with extra spacetime dimensions [70–84]. To set up notation for the following chapters here we start with some preliminaries on the gauge-theoretic description of quark and lepton mixing, followed by a very brief critique of the SM drawbacks.

We should stress that there are already several excellent reviews on the discrete flavor symmetry approach to address the SM flavor puzzle [85–93]. Apart from providing an update to these, the present review will focus on how the residual flavor and CP symmetries can constrain the fermion mixing angles and CP violation phases independently of the details of a specific implementation. We discuss in detail both theory and phenomenological predictions. In addition, we discuss several other topics and predictive benchmark flavor model examples, both in four dimensions and extra dimensions. The latter include warped 5D flavordynamics as well as orbifold-based scenarios, which are reviewed here for the first time. We discuss extensively the predictions of a broad class of symmetry-based theories of flavor. Finally, we also give a brief discussion of theories based on modular symmetries and how these may help with the

vacuum alignment problem.

1.1 Quark masses and mixing

We recall that in a gauge field theory like the Standard Model all the fermion masses arise from spontaneous symmetry breaking. The most general quark Yukawa interactions with the Higgs doublet H allowed by symmetry are given by [94–96],

$$\mathcal{L}_{\text{Yuk}}^q = -(y_D)_{ij} \overline{D_R^i} H^\dagger Q_L^j - (y_U)_{ij} \overline{U_R^i} \tilde{H}^\dagger Q_L^j + \text{h.c.}, \quad (1.1)$$

where $\tilde{H} = i\tau_2 H^*$ and $Q_L^i = (U_L^i, D_L^i)^T$. The Yukawa matrices y_D and y_U are arbitrary complex matrices in flavour space. Upon electroweak symmetry breaking, the Higgs vacuum expectation value (VEV) $\langle H \rangle = (0, v/\sqrt{2})^T$ with $v \simeq 246\text{GeV}$ gives us the quark mass terms

$$\mathcal{L}_{\text{mass}}^q = -\overline{U}_R m_U U_L - \overline{D}_R m_D D_L + \text{h.c.}, \quad (1.2)$$

where $U_L \equiv (u_L, c_L, t_L)^T$, $D_L \equiv (d_L, s_L, b_L)^T$, $U_R \equiv (u_R, c_R, t_R)^T$ and $D_R \equiv (d_R, s_R, b_R)^T$ denote the three generations of left and right-handed up- and down-type quark fields, respectively. The mass matrices are determined by the Yukawa couplings and the Higgs VEV as follows

$$m_U = \frac{v}{\sqrt{2}} y_U, \quad m_D = \frac{v}{\sqrt{2}} y_D. \quad (1.3)$$

Gauge invariance does not constrain the flavour structure of the Yukawa couplings y_D and y_U and therefore m_U and m_D are arbitrary complex matrices. These matrices can be brought into diagonal form by separate unitary transformations on the left and right fermions, i.e.

$$W_u^\dagger m_U V_u = \text{diag}(m_u, m_c, m_t), \quad W_d^\dagger m_D V_d = \text{diag}(m_d, m_s, m_b), \quad (1.4)$$

which implies

$$V_u^\dagger m_U^\dagger m_U V_u = \text{diag}(m_u^2, m_c^2, m_t^2), \quad (1.5)$$

$$V_d^\dagger m_D^\dagger m_D V_d = \text{diag}(m_d^2, m_s^2, m_b^2). \quad (1.6)$$

By performing such unitary transformations $U_L \rightarrow V_u U_L$, $D_L \rightarrow V_d D_L$, $U_R \rightarrow W_u U_R$ and $D_R \rightarrow W_d D_R$ one can go to the physical mass eigenstates. The resulting flavour-changing quark charged current weak interaction reads

$$\mathcal{L}_{CC}^q = \frac{g}{\sqrt{2}} \overline{U}_L \gamma^\mu V_{CKM} D_L W_\mu^+ + \text{h.c.}, \quad (1.7)$$

where $V_{CKM} \equiv V_u^\dagger V_d$ is the Cabibbo-Kobayshi-Maskawa (CKM) mixing matrix [97, 98]. In what follows we adopt the standard form for the CKM matrix describing quark mixing, i.e.

$$V_{CKM} = \begin{pmatrix} c_{12}^q c_{13}^q & s_{12}^q c_{13}^q & s_{13}^q e^{-i\delta^q} \\ -s_{12}^q c_{23}^q - c_{12}^q s_{13}^q s_{23}^q e^{i\delta^q} & c_{12}^q c_{23}^q - s_{12}^q s_{13}^q s_{23}^q e^{i\delta^q} & c_{13}^q s_{23}^q \\ s_{12}^q s_{23}^q - c_{12}^q s_{13}^q c_{23}^q e^{i\delta^q} & -c_{12}^q s_{23}^q - s_{12}^q s_{13}^q c_{23}^q e^{i\delta^q} & c_{13}^q c_{23}^q \end{pmatrix}, \quad (1.8)$$

with $c_{ij}^q \equiv \cos \theta_{ij}^q$, $s_{ij}^q \equiv \sin \theta_{ij}^q$. This parameterization is the one adopted by the Review of Particle Physics of the Particle Data Group (PDG) [28], and supplements the original proposal in Ref. [30] by specifying a convenient factor ordering. Notice that only one physical phase remains after the allowed quark phase redefinitions. The CKM-phase-parameter δ_q is expressed in a neat and rephasing-invariant way as [99],

$$\delta^q = \phi_{13}^q - \phi_{12}^q - \phi_{23}^q, \quad (1.9)$$

in terms of the fundamental ϕ_{ij}^q phases. These are the relative phases between up- and down-type diagonalization matrices. From Ref. [28] we extract the following allowed ranges [100, 101] for the CKM parameters,

$$V_{CKM} = \begin{pmatrix} 0.97431 \pm 0.00012 & 0.22514 \pm 0.00055 & (0.00365 \pm 0.00010)e^{i(-66.8 \pm 2.0)^\circ} \\ (-0.22500 \pm 0.00054)e^{i(0.0351 \pm 0.0010)^\circ} & (0.97344 \pm 0.00012)e^{i(-0.001880 \pm 0.000052)^\circ} & 0.04241 \pm 0.00065 \\ (0.00869 \pm 0.00014)e^{i(-22.23 \pm 0.63)^\circ} & (-0.04124 \pm 0.00056)e^{i(1.056 \pm 0.032)^\circ} & 0.999112 \pm 0.000024 \end{pmatrix}. \quad (1.10)$$

1.2 Lepton masses and mixing

It is a characteristic feature of the Standard Model that spontaneous gauge symmetry breaking leaves neutrinos as massless fermions. However, the discovery of neutrino oscillations [18, 19] implies non-zero neutrino masses and neutrino mixing. One can introduce three right-handed neutrino fields ν_R^i for $i = 1, 2, 3$ as full $SU(3)_c \otimes SU(2)_L \otimes U(1)_Y$ singlets. In analogy with the quark sector the neutrino and charged lepton masses are described by the Yukawa interactions,

$$\mathcal{L}_{\text{Yuk}}^l = -(y_l)_{ij} \bar{l}_R^i H^\dagger L_L^j - (y_\nu)_{ij} \bar{\nu}_R^i \tilde{H}^\dagger L_L^j + \text{h.c.}, \quad (1.11)$$

where $L_L^i = (\nu_L^i, l_L^i)^T$ are the lepton doublet fields. In this case neutrinos would be Dirac particles. This requires the *ad hoc* imposition of lepton number symmetry to forbid the right-handed Majorana mass term $M_{ij} \overline{\nu_R^i} (\nu_R^j)^c$ allowed by SM gauge invariance. Moreover, the Yukawa coupling y_ν should be of order 10^{-11} in order to accommodate the neutrino masses below the eV scale.

Under the assumption of lepton number conservation one gets, after electroweak symmetry breaking, the following charged lepton and neutrino mass terms,

$$\mathcal{L}_{\text{mass}}^l = -\bar{l}_R m_l l_L - \bar{\nu}_R m_\nu \nu_L + \text{h.c.}. \quad (1.12)$$

However, without *a priori* assumptions, gauge theories suggest that neutrinos are Majorana particles [30]². However, this important issue of the nature of neutrinos must be settled by experiment. A prime example is to search for neutrinoless double beta decay [106–109]. A positive detection would imply, by the black-box theorem, the Majorana nature of at least one of the neutrinos [110].

Majorana neutrino masses can be effectively described by the non-renormalizable Weinberg operator $(y_\nu)_{ij} \left(\overline{(L_L^i)^c} i\tau_2 H \right) \left(H^T i\tau_2 L_L^j \right) / (2\Lambda)$ [29]. As a result the charged lepton and neutrino mass terms take of the following form

$$\mathcal{L}_{\text{mass}}^l = -\bar{l}_R m_l l_L - \frac{1}{2} \overline{\nu_L^c} m_\nu \nu_L + \text{h.c.}, \quad (1.13)$$

where $m_\nu = y_\nu v^2 / (2\Lambda)$. The smallness of neutrino mass may be ascribed to the large new physics scale Λ . There are also attractive low-scale realizations of the seesaw mechanism, as we comment below. Both charged lepton and neutrino mass matrices are diagonalized through unitary transformations as follows

$$U_l^\dagger m_l^\dagger m_l U_l = \text{diag} (m_e^2, m_\mu^2, m_\tau^2), \quad (1.14)$$

and

$$\begin{aligned} U_\nu^T m_\nu U_\nu &= \text{diag} (m_1, m_2, m_3), & \text{for Majorana neutrinos,} \\ U_\nu^\dagger m_\nu^\dagger m_\nu U_\nu &= \text{diag} (m_1^2, m_2^2, m_3^2), & \text{for Dirac neutrinos.} \end{aligned} \quad (1.15)$$

where the light neutrino masses $m_{1,2,3}$ are real and non-negative. The nonzero mass squared differences measured in neutrino oscillation experiments imply a non-degenerate mass spectrum $m_1 \neq m_2 \neq m_3$. As a consequence, we can express the lepton mass matrices in terms of U_l , U_ν and the mass eigenvalues as

$$m_l^\dagger m_l = U_l \text{diag} (m_e^2, m_\mu^2, m_\tau^2) U_l^\dagger, \quad (1.16)$$

$$m_\nu = U_\nu^* \text{diag} (m_1, m_2, m_3) U_\nu^\dagger, \quad \text{for Majorana neutrinos,} \quad (1.17)$$

$$m_\nu^\dagger m_\nu = U_\nu \text{diag} (m_1^2, m_2^2, m_3^2) U_\nu^\dagger, \quad \text{for Dirac neutrinos.} \quad (1.18)$$

Transforming to the charged lepton and neutrino mass eigenstates, one obtains the leptonic charged-current weak interaction as [30]

$$\mathcal{L}_{CC}^l = \frac{g}{\sqrt{2}} \bar{l}_L \gamma^\mu U_l^\dagger U_\nu \nu_L W_\mu^- + \text{h.c.}, \quad (1.19)$$

where the combination $U_l^\dagger U_\nu$ defines the lepton mixing matrix, i.e.

$$U = U_l^\dagger U_\nu. \quad (1.20)$$

²Note that the most general description of neutrinos is in terms of two-component spinors, Dirac fermions being just a particular case of Majorana [102]. Although the two-component approach is universal and often more insightful, in this review we will adopt the more familiar four-component formalism used in most textbooks, for example [103–105], in which Majorana and Dirac neutrinos appear as separate “cases”.

Like the CKM matrix describing quark mixing, the lepton mixing matrix U arises from the mismatch between the diagonalizations of charged leptons and neutrinos. Assuming unitarity, the matrix U is characterized by three angles and three physical CP phases [30],

$$U = \begin{pmatrix} c_{12}^\ell c_{13}^\ell & s_{12}^\ell c_{13}^\ell e^{-i\phi_{12}} & s_{13}^\ell e^{-i\phi_{13}} \\ -s_{12}^\ell c_{23}^\ell e^{i\phi_{12}} - c_{12}^\ell s_{13}^\ell s_{23}^\ell e^{-i(\phi_{23}-\phi_{13})} & c_{12}^\ell c_{23}^\ell - s_{12}^\ell s_{13}^\ell s_{23}^\ell e^{-i(\phi_{23}+\phi_{12}-\phi_{13})} & c_{13}^\ell s_{23}^\ell e^{-i\phi_{23}} \\ s_{12}^\ell s_{23}^\ell e^{i(\phi_{23}+\phi_{12})} - c_{12}^\ell s_{13}^\ell c_{23}^\ell e^{i\phi_{13}} & -c_{12}^\ell s_{23}^\ell e^{i\phi_{23}} - s_{12}^\ell s_{13}^\ell c_{23}^\ell e^{-i(\phi_{12}-\phi_{13})} & c_{13}^\ell c_{23}^\ell \end{pmatrix}, \quad (1.21)$$

with the abbreviation $c_{ij}^\ell \equiv \cos \theta_{ij}^\ell$ and $s_{ij}^\ell \equiv \sin \theta_{ij}^\ell$. The above universal symmetrical presentation for the matrix U in Eq. (1.21) is very convenient both for the description of quark as well as lepton mixing [30]. Notice that there is an important difference between leptons and quarks concerning CP violation, namely, all three CP phases in Eq. (1.21) are physical parameters. One of them is the lepton analogue of the CKM phase in Eq. (1.9), also called *Dirac phase*.

$$\delta^\ell = \phi_{13} - \phi_{12} - \phi_{23}. \quad (1.22)$$

The others are the so-called *Majorana phases*, which can not be eliminated by field redefinitions [30] if neutrinos are Majorana particles. Only the Dirac phase affects conventional neutrino oscillation probabilities, while the Majorana phases can only affect lepton number violating processes [111, 112]. Note that in what follows we will also use the notation δ_{CP} for the lepton Dirac CP phase δ^ℓ . It will be an experimental challenge to obtain robust information on their magnitudes.

Current neutrino oscillation data restrict the elements of the lepton mixing matrix. One finds, at 3σ , the following ranges [24, 25]

$$U^{\text{NO}} = \begin{pmatrix} 0.7838 \rightarrow 0.8442 & 0.5133 \rightarrow 0.6004 & (-0.1568 \rightarrow 0.1489) + i(-0.1182 \rightarrow 0.1520) \\ (-0.4831 \rightarrow -0.2394) + i(-0.0749 \rightarrow 0.0963) & (0.4635 \rightarrow 0.6749) + i(-0.0521 \rightarrow 0.0668) & 0.6499 \rightarrow 0.7719 \\ (0.3068 \rightarrow 0.5391) + i(-0.0643 \rightarrow 0.0933) & (-0.6897 \rightarrow -0.4821) + i(-0.0446 \rightarrow 0.0644) & 0.6161 \rightarrow 0.7434 \end{pmatrix} \quad (1.23)$$

for the case of normal neutrino mass-ordering. On the other hand, for inverted-ordered neutrino masses one has [24, 25],

$$U^{\text{IO}} = \begin{pmatrix} 0.7835 \rightarrow 0.8440 & 0.5133 \rightarrow 0.6005 & (-0.1423 \rightarrow 0.1490) + i(0.0191 \rightarrow 0.1553) \\ (-0.4806 \rightarrow -0.2682) + i(0.0114 \rightarrow 0.0990) & (0.4546 \rightarrow 0.6395) + i(0.0074 \rightarrow 0.0695) & 0.6493 \rightarrow 0.7711 \\ (0.3102 \rightarrow 0.5133) + i(0.0094 \rightarrow 0.0947) & (-0.6956 \rightarrow -0.5248) + i(0.0057 \rightarrow 0.0654) & 0.6171 \rightarrow 0.7436 \end{pmatrix} \quad (1.24)$$

Current determinations of the mass-ordering and the atmospheric octant are not yet fully robust. On the other hand we still struggle with a very poor determination of the magnitude of the Dirac CP phase (see below).

1.3 Neutrino oscillation recap

We now give a ‘‘drone view’’ of the current status of neutrino oscillation parameters. The basic discovery made in solar and atmospheric studies was soon followed by reactor and accelerator-based experiments that have not only provided independent confirmation, but also improved parameter determination. Current experimental data mainly converge towards a consistent global picture – the three-neutrino paradigm – in which the oscillation parameters are determined as shown in figure 1.

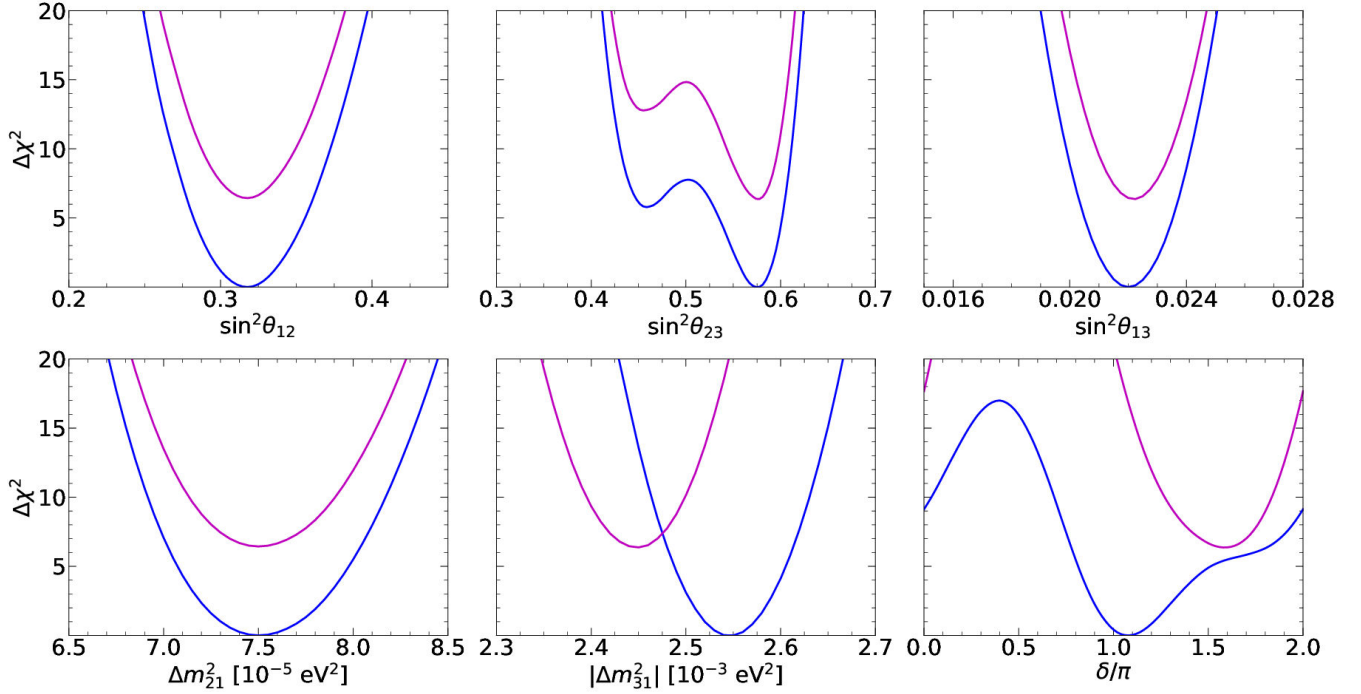


Figure 1: Current summary of neutrino oscillation parameters, where $\delta \equiv \delta_{CP}$. From [24, 25].

The top-three panels show that two mixing angles are fairly large, at odds with the corresponding mixing angles observed in the quark sector. In fact, it is the smallest lepton mixing angle, θ_{13} , that lies intriguingly close in magnitude to the largest of the quark mixing angles, i.e. the Cabibbo angle. Currently we have no explanation for this fact.

The global oscillation parameter determinations can also be shown as the “matrix” in figure 2. Besides the individual oscillation parameter determinations, given by the “diagonal” entries, the “off-diagonal” entries of figure 2 show all pairwise parameter correlations³, very useful for model-builders. Indeed, any flavour model leads to predictions for various entries of the above triangular matrix. The zenodo website in [25] will be used extensively in this review in order to examine the allowed parameter regions in different theoretical setups.

At this point one should stress that, although the overall picture provided by the “three-neutrino paradigm” is mostly robust, there are still loose ends. As already mentioned, the determination of the neutrino spectrum and the octant of the atmospheric angle is not fully robust yet, while the precise value of the leptonic CP phase also remains an open challenge. A robust CP determination will be a key objective of the Deep Underground Neutrino Experiment (DUNE) [113]. The experiment will have two detector systems placed along Fermilab’s Long Baseline Neutrino Facility (LBNF) beam. One of them will be near the beam source, while a much larger one will be placed underground 1300 km away at the Sanford Underground Research Laboratory in South Dakota, in the same mine where Ray Davis

³Numerical tables for the relevant χ^2 profiles can be downloaded from Ref. [25], including all pairwise correlations. These tables can be used to test various neutrino mixing patterns predicted by different flavour theories, such as those in Refs. [53–56, 59–84].

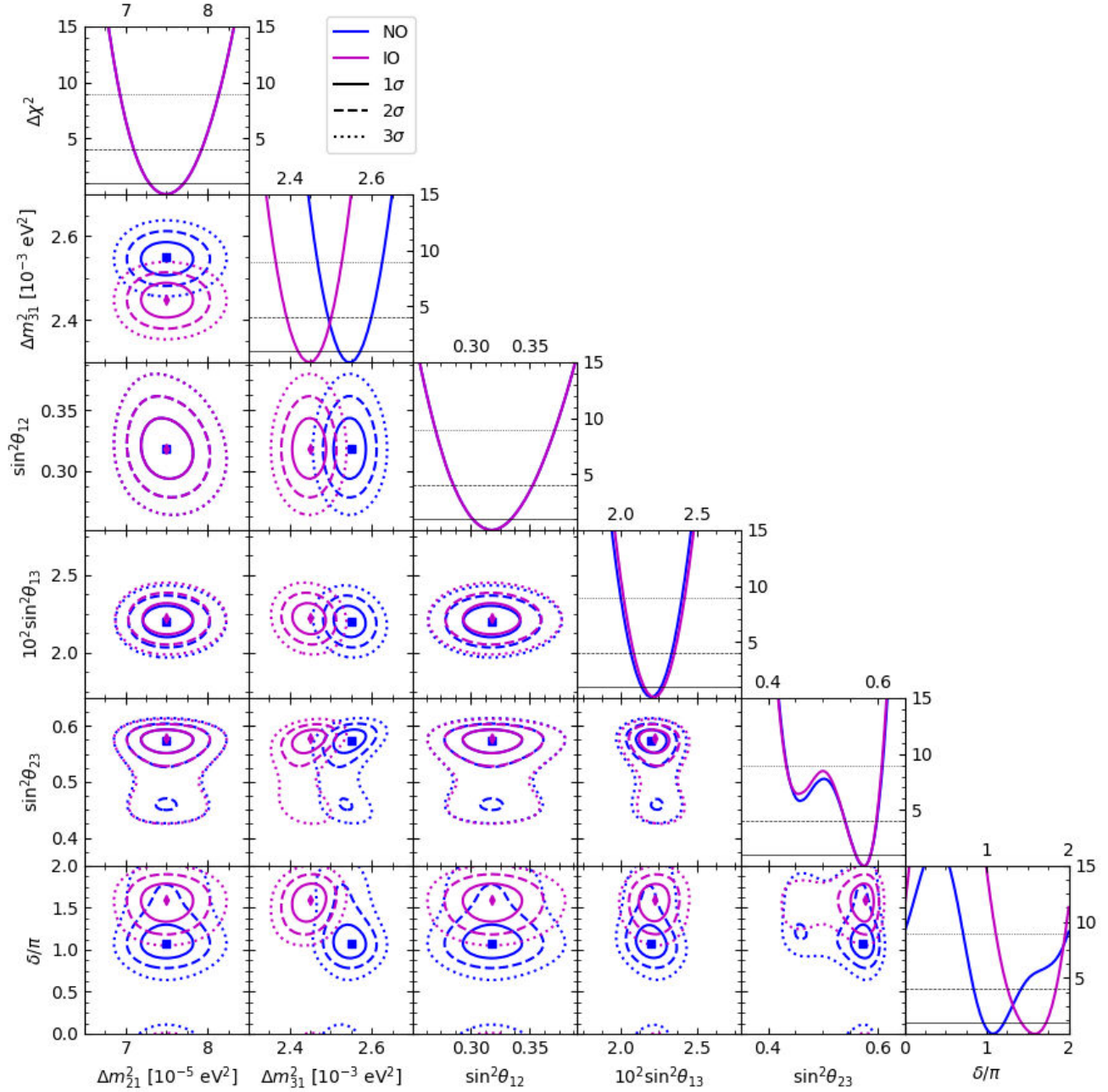


Figure 2: Neutrino oscillation parameters pair-correlations. As before $\delta \equiv \delta_{CP}$. From [24, 25].

pioneered neutrino oscillation studies in the sixties. Further improvements are expected at the ambitious T2HK proposal in Japan [114]. Reaching a precise CP phase determination will be a challenge for the coming years. Likewise, underpinning the mass ordering [115]. Octant resolution may be harder, if the preferred θ_{23} value lies close to maximality. See for example Refs. [116, 117] for details and related references. Altogether, octant discrimination, underpinning the mass-ordering and performing a precise CP determination constitute the target of the next generation of oscillation searches [118].

Last, but not least, we mention that there are also some experimental anomalies in neutrino physics

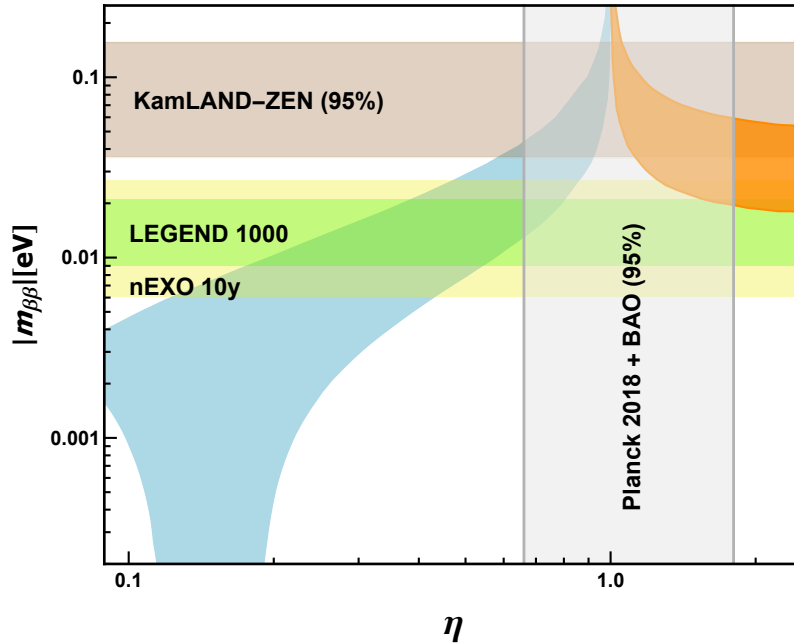


Figure 3: The $0\nu\beta\beta$ decay amplitude in a generic three-neutrino scheme versus the degeneracy parameter η . The curved bands are the normal and inverted ordering branches allowed by neutrino oscillations respectively [124]. The current experimental bound $|m_{\beta\beta}| < (36 - 156)$ meV at 90% confidence level (C.L.) from KamLAND-Zen [125] and the future sensitivity ranges $|m_{\beta\beta}| < (9.0 - 21)$ meV from LEGEND-1000 [126] and $|m_{\beta\beta}| < (6.1 - 27)$ meV from nEXO [127] are indicated by light brown, light yellow and light green horizontal bands respectively. The vertical grey band is excluded by the 95% C.L. limit $\Sigma_i m_i < 0.120$ eV from Planck [128, 129].

that challenge the simple picture provided by the “three-neutrino paradigm” suggesting, perhaps, a four-neutrino oscillation scenario [119]. They will not be discussed in this review, the interested readers can see Refs. [120–123].

1.4 Neutrinoless double beta decay

Neutrinoless double-beta decay (or $0\nu\beta\beta$ for short) is the prime lepton number violating process [106–109]. Given that neutrinos are observed to be massive fermions, and expected to be Majorana-type [30], it follows that $0\nu\beta\beta$ decay should take place, as a consequence of neutrino exchange. In this case, the effective mass parameter characterizing the amplitude is given as

$$|m_{\beta\beta}| = \left| \sum_{j=1}^3 U_{ej}^2 m_j \right| = \left| c_{12}^{\ell 2} c_{13}^{\ell 2} m_1 + s_{12}^{\ell 2} c_{13}^{\ell 2} m_2 e^{-2i\phi_{12}} + s_{13}^{\ell 2} m_3 e^{-2i\phi_{13}} \right|. \quad (1.25)$$

Here we note that, in contrast with the parametrization adopted by the PDG, the symmetrical form of the lepton mixing matrix provides a conceptually transparent description of $0\nu\beta\beta$ in which, as it should, only Majorana phases appear [99]. Altogether, the original symmetrical form of the lepton mixing matrix, Eq. (1.21), provides an insightful description both for the Dirac phase, Eq. (1.22), as well as the Majorana phases, Eq. (1.25).

An important point to notice from Eq. (1.25) is that, thanks to the Majorana phases, the $0\nu\beta\beta$ amplitude can vanish due to possible destructive interference among the three individual neutrino amplitudes. This is clearly seen in the blue branch of figure 3, taken from Ref. [124], which shows the $0\nu\beta\beta$ decay amplitude versus the degeneracy parameter η . When $\eta \rightarrow 1$ neutrino masses become degenerate, and the two bands correspond to the two possible mass orderings. The most favorable case for $0\nu\beta\beta$ decay detectability happens when neutrinos are nearly degenerate, as predicted in some UV-complete flavour theories [53–55]. The $\eta \equiv 1$ case corresponds to the idealized limit where neutrinos would be strictly degenerate. In order to generate oscillations neutrino masses must deviate from exact degeneracy. This can happen in two ways, corresponding to the two curved branches seen in the figure. The normal-ordered (NO) neutrino region is indicated in the left (blue) band, while inverted ordering (IO) gives the upper-right (orange) branch. One sees that, thanks to the presence of the Majorana phases [30], the $0\nu\beta\beta$ amplitude can vanish for normal ordering (but not for inverted). The horizontal band denotes the current KamLAND-Zen limit [125], while the vertical one is excluded [124] by cosmological observations [128,129] e.g. by the Planck collaboration. Altogether, one sees current data strongly disfavour nearly degenerate neutrinos.

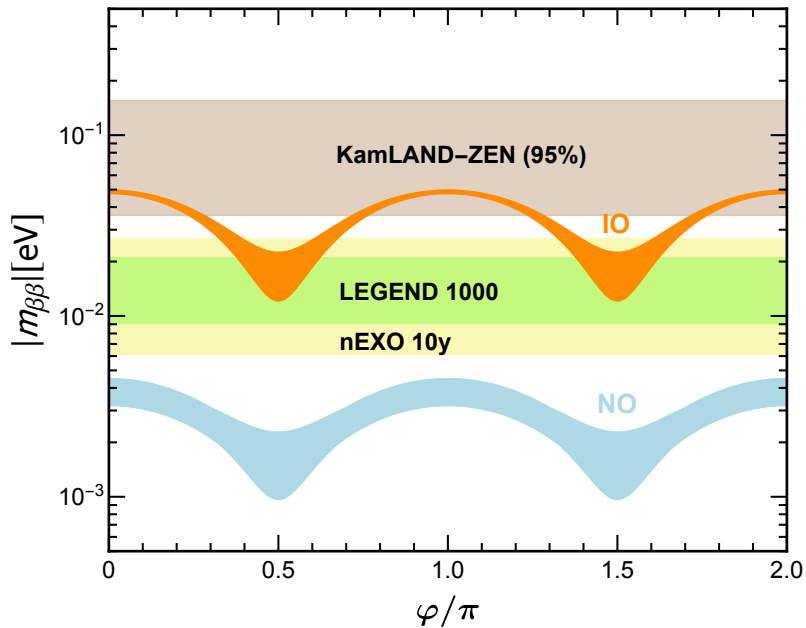


Figure 4: $0\nu\beta\beta$ decay amplitude when one neutrino is massless. The light-blue and light-orange bands are the current 3σ C.L. regions for normal and inverted mass-ordering. The current bound from KamLAND-ZEN [125] and projected sensitivities of LEGEND 1000 [126] and nEXO [127] are indicated.

Another interesting situation happens if one (or two) of the three neutrinos is massless or nearly so, as in the “missing partner” seesaw mechanism [30] and other “incomplete-multiplet” schemes ⁴. The minimal viable tree-level type-I seesaw has only two right-handed neutrinos [131–133]. In such a scheme no cancellation is possible, even for normal-ordering [134–138]. The resulting regions are the two periodic

⁴A massless neutrino may also arise from the presence of anti-symmetric Yukawa couplings, see e.g. [130].

bands seen in figure 4, which are expressed in terms of the only free parameter available, namely, the relative neutrino Majorana phase φ ⁵. The colored horizontal bands show current experimental limits of KamLAND-ZEN and the expected sensitivities of LEGEND 1000 and nEXO, where the width of the bands reflects nuclear matrix element uncertainties [108, 109]. Notice in this case the existence of a predicted theoretical lower bound on $|m_{\beta\beta}|$. Taking into account the sensitivities expected at upcoming $0\nu\beta\beta$ experiments, one sees that this lower bound for NO lies below detectability in the foreseeable future.

In contrast, inverse mass-ordering provides a lower bound that lies higher than the one generically expected for the IO three-massive-neutrino case. This implies a guaranteed discovery in the next round of experiments [139, 140]. In fact, for this case, the recent KamLAND-Zen limit [125] already probes the Majorana phase, as seen by the magenta band in figure 4. In short, for the one-massless-neutrino case there is a chance, perhaps, that one could be able to extract the value of the relevant Majorana phase from experiment.

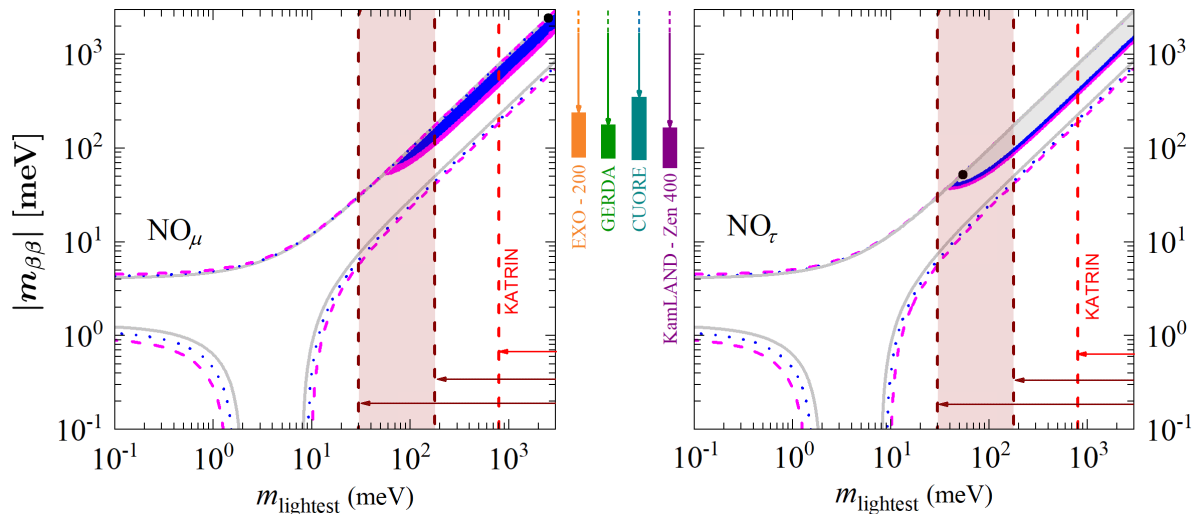


Figure 5: The solid (dotted) [dashed] lines delimit the 1σ (2σ) [3σ] $|m_{\beta\beta}|$ regions allowed by oscillations. Predictions of two normal-ordered \mathcal{Z}_8 schemes are given [148]. Vertical bars in mid-panels indicate current 95%CL $|m_{\beta\beta}|$ upper bounds from KamLAND-Zen 400 [149], GERDA [150], CUORE [151] and EXO-200 [152].

We now turn to the general three-massive-neutrino case. Although there is no guaranteed minimum value for $|m_{\beta\beta}|$ in this case, there can still be a lower-bound, even for normal mass-ordering, provided the cancellation of the amplitudes is prevented by the structure of the leptonic weak interaction vertex [66, 68, 69, 141–144]. This can happen as a result of the imposition of a family symmetry to account for the mixing pattern seen in oscillations. As an example, figure 5 shows the predictions of a \mathcal{Z}_8 family symmetry scheme. The hollow solid (dotted) [dashed] lines delimit the 1σ (2σ) [3σ] $|m_{\beta\beta}|$ regions allowed in the general three-neutrino case. The sub-regions shown in gray, blue and magenta, respectively, are the flavour-model predictions. The black dots correspond to best-fits. The vertical shaded band indicates the current sensitivity of cosmological data [128]. The vertical dashed red line corresponds to the KATRIN

⁵For vanishing lightest neutrino mass the relevant Majorana phase is $\varphi = \phi_{12} - \phi_{13}$ for NO and $\varphi = \phi_{12}$ for IO.

tritium beta decay [145] upper limit $m_\beta < 0.8$ eV (90% CL) [146,147]. The heights of the bars shown in the mid-part of figure 5 reflect the uncertainties in the nuclear matrix elements relevant for the computation of the decay rates. The flavour predictions for $|m_{\beta\beta}|$ illustrate our point. For example, one sees how the preferred flavour-predicted point in the right panel sits right inside the cosmologically interesting band, and close to the current $0\nu\beta\beta$ limits, as indicated in between the panels. Similar predictions for $0\nu\beta\beta$ amplitudes occur in other family symmetry models, some of which will be discussed in this review, see for instance discussions given in Chapters 8 and 10.

In short, oscillations have left an important imprint upon neutrinoless double beta decay studies. The results of the negative searches conducted so-far imply that we must consider both the possibilities of Dirac or Majorana neutrinos, as we do in this review. Nonetheless, there is a reasonable chance that, perhaps, $0\nu\beta\beta$ could be seen in the coming round of experiments. This would constitute a major breakthrough. Indeed, a positive $0\nu\beta\beta$ decay detection would imply, as a consequence of the black box theorem, that at least one of the neutrinos has Majorana nature [110]. The argument is illustrated in figure 6. Note that the black-box argument holds irrespective of the underlying physics responsible for generating the process [153, 154].

In some cases, as we saw in figure 4, the discovery of $0\nu\beta\beta$ decay might allow us to underpin also the value of the relevant Majorana phase. Note however that, although a positive $0\nu\beta\beta$ discovery would imply that at least one of the neutrinos is a Majorana particle, a negative result would not imply that neutrinos are Dirac-type, as the amplitude can be suppressed even for Majorana-type neutrinos, due to the effect of the Majorana phases. It has been argued that if a null $0\nu\beta\beta$ decay signal was accompanied by a positive $0\nu 4\beta$ quadruple beta decay signal [155, 156], then at least one neutrino should be a Dirac particle [157].

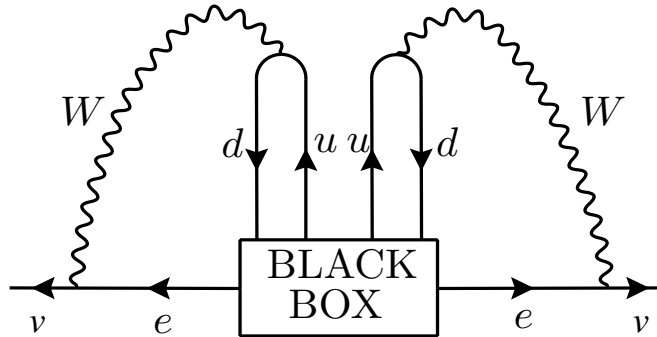


Figure 6: The observation of $0\nu\beta\beta$ decay implies that at least one neutrino is a Majorana fermion [110].

2 Origin of neutrino masses and flavour puzzle

Despite its amazing success in describing three out of the four known fundamental forces of nature, there are many drawbacks and open issues in the Standard Model. Altogether, they imply that the theory of particle physics needs a completion beyond its current form. Here we start with one of the most important issues, i.e. the lack of neutrino masses.

2.1 Effective neutrino masses

Although the Standard Model lacks neutrino masses, these can arise effectively from a unique dimension-five operator characterizing lepton number non-conservation [29], as illustrated in figure 7. In this case neutrinos are Majorana fermions, as generally expected in gauge theories. Indeed, on general grounds it was argued in [30], within the $SU(3)_c \otimes SU(2)_L \otimes U(1)_Y$ setup, that neutrinos are expected to be Majorana fermions.

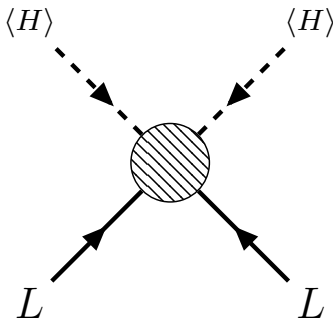


Figure 7: Majorana neutrino mass generation from the dimension-five operator.

However, neutrinos could also be Dirac fermions, this is currently an open experimental question. Dirac neutrinos can indeed emerge in the presence of extra symmetries, that could be discrete or continuous, global or local. For example, the imposition of $U(1)_{B-L}$ symmetry, where B and L are baryon and lepton numbers respectively, would forbid the Majorana mass terms of the right-handed neutrinos [158–161]. Alternatively, as mentioned below, the Dirac nature of neutrinos could result from the presence of an underlying Peccei-Quinn symmetry [162, 163] or be associated with dark matter stability [164–171]. Small Dirac-type neutrino masses as in Eq. (1.11), could arise from effective dimension-five [172–175] as well as dimension-six operators [176, 177], that have by now been classified.

2.2 The seesaw paradigm

An attractive ultraviolet completion of the dimension-five operator is provided by the seesaw mechanism. It is specially interesting, as it gives a simple *dynamical* understanding of small neutrino masses by minimizing the Higgs potential, as well as the possibility of having a stable electroweak vacuum [178–183].

It has become usual to distinguish three main seesaw varieties, namely type-I [30–35], type-II [30–32, 36–38] and type-III [184], illustrated in figure 8. These generate neutrino masses at tree level from the mediation of new heavy singlet fermion (ν_R), triplet scalar (Δ) and triplet fermion (Σ_R), respectively. In the simplest seesaw neutrinos acquire masses through the exchange of heavy scalars, called type-I in [30] and today called type-II. Such seesaw realization allows one to reconstruct the parameters characterizing the neutrino sector from various experiments [185], in particular those from high energy colliders [186,187]. Moreover, the type-II seesaw opens the really tantalizing possibility of probing the absolute neutrino mass and mass ordering in collider experiments [188].

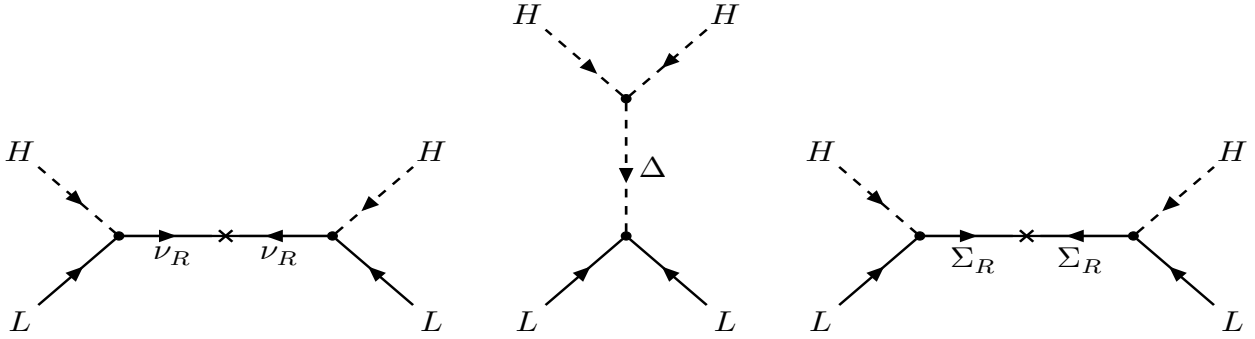


Figure 8: Feynman diagrams for the conventional seesaw types, where the mediators ν_R and Σ_R are SM singlet and triplet fermions respectively, while Δ is a SM triplet scalar.

Here we focus on the type-I seesaw mechanism, where neutrinos acquire masses through the exchange of heavy gauge-singlet fermions, as illustrated in the left panel of figure 8. Seesaw mediators were originally thought to lie at a high mass scale, associated to $\text{SO}(10)$ unification or left-right symmetry. The associated physics has been covered in several textbooks [102–105] and reviews [189]. Note that, following Ref. [30], here we do not assume left-right symmetry in the seesaw mechanism, but simply the minimal well-tested $\text{SU}(3)_c \otimes \text{SU}(2)_L \otimes \text{U}(1)_Y$ gauge structure. Notice that this seesaw description of neutrino mass generation can be made fully dynamical in the presence of a singlet vacuum expectation value (VEV) driving the spontaneous violation of lepton number symmetry. The theory is then accompanied by a Nambu-Goldstone boson, dubbed Majoron [32,39].

Notice that the most general realization of the seesaw mechanism leads most naturally to Majorana neutrinos. However, in the presence of adequate extra symmetries, Dirac neutrinos can emerge from the seesaw [190]. Indeed, there may be good reasons for neutrinos to be Dirac-type. For example, the Dirac nature of neutrinos could also be associated to the existence of an underlying Peccei-Quinn symmetry [162,163]. Moreover, it could signal the stability of dark matter [164–171]. Finally, there are interesting scenarios where the Dirac nature of neutrinos is associated with a family symmetry [191,192].

2.3 Dark matter as the source of neutrino mass

It is well-known that about 85% of the matter in the universe is “dark” in the sense that it does not appear to interact with the electromagnetic field and is, as a consequence, very hard to detect. It is not our purpose to provide a comprehensive discussion of the observational aspects of cosmological dark matter; for a review see Ref. [193]. The first point we note is that the existence of such cosmological Dark matter is totally unaccounted for within the Standard Model. A very interesting possibility is that dark matter is made up of a novel weakly interacting massive particle, dubbed WIMP, typically present in the case of supersymmetric theories with conserved R-parity [194].

Underpinning the mechanism yielding small neutrino masses and/or dark matter is of paramount importance in particle physics, as it may select which new physics to expect as the next step. This is a very broad subject which we will not try to review. Rather, in this review we just comment on the issue of particle dark matter candidates, and how they may be simply related to the mechanism of neutrino mass generation. We focus on the very interesting possibility that the dark matter sector mediates neutrino mass generation, as postulated within the scotogenic picture [195–201]. An interesting twist is to imagine the existence of a universal “hidden” dark matter sector that *seeds* neutrino mass generation, which proceeds *a la seesaw*, as in the dark inverse seesaw [202] mechanism. Alternatively, one can envisage a dark linear seesaw mechanism [203, 204].

Both dark inverse and dark linear seesaw realizations will be described below. In either case dark matter will be WIMP-like. Instead of being related to supersymmetry, WIMP dark matter in these models is closely related to neutrino physics, either as mediator or as seed of neutrino mass generation. Flavored scotogenic dark matter may also be implemented [205], providing an attractive way to reconcile low-scale radiative neutrino mass generation with dark matter, while addressing the flavour problem at the same time, see Sec. 2.7.

Last, but not least, we mention that particle physics theories where neutrino masses arise from the spontaneous breaking of a continuous global lepton number symmetry have a natural dark matter candidate [206, 207], namely the associated Nambu-Goldstone boson, dubbed majoron [32, 39]. Indeed, the majoron is likely to pick up a mass from gravitational instanton effects, that explicitly violate global symmetries [208]. The majoron necessarily decays to neutrinos, with an amplitude proportional to their tiny mass, which typically gives it cosmologically long lifetimes [32]. The associated restrictions on the decaying warm dark matter picture coming from the CMB [209] as well as mono-energetic photon emission in astrophysics have been examined in detail [210]. Using N-body simulations it has also been shown that the warm majoron dark matter model provides a viable alternative to the Λ CDM scenario, with predictions that can differ substantially on small scales [211].

2.4 Missing partner seesaw and dark matter: the scoto-seesaw

In contrast to a left-right symmetric SO(10)-based seesaw mechanism, where the number of “left” and “right” neutrinos must match as a consequence of gauge invariance, in the most general SM-based seesaw mechanism [30] one can have any number (m) of “right-handed” neutrino mediators, since they are gauge

singlets. Theories with $m < 3$ in the classification of [30] could simplify substantially the form of the lepton mixing matrix ⁶.

Such “missing partner” seesaw schemes with less “right” than “left” neutrinos, imply that some of the active “left” neutrinos remain massless [30, 131, 132]. The (3,2) choice corresponds to the minimal viable type-I seesaw, in which there are only two mass parameters corresponding to the experimentally measured solar and atmospheric splittings. The lightest neutrino is massless, leading to the $0\nu\beta\beta$ prediction discussed in Sec. 1.4.

On the other hand, the minimal (3,1) seesaw leads to the same $0\nu\beta\beta$ prediction as (3,2), but has only one neutrino mass parameter [30]. Although such setup is not consistent with current neutrino data, as it lacks solar neutrino oscillations, the later may arise from a completion in which the degeneracy between the lowest-mass neutrinos is lifted by some other mechanism, for example, as a result of radiative corrections.

Indeed, the (3,1) setup offers a template to reconcile the seesaw paradigm and the WIMP dark matter paradigm within a minimal hybrid construction called “scoto-seesaw” mechanism. Such simplest (3,1) “scoto-seesaw” scheme provides a comprehensive theory of neutrino mass generation as well as WIMP dark matter, in which the relative magnitudes of solar and atmospheric oscillation lengths are explained due to a loop factor [136, 137].

2.5 The low-scale inverse and linear seesaw mechanisms

As a final example, one may consider having more “right-” than “left-handed” neutrinos in the seesaw mechanism, for example, two isosinglets for each “active” isodoublet family. This can be implemented with explicit [213] as well as spontaneous violation of lepton number [40]. In the lepton-number-conserving limit one finds that the three light neutrinos remain massless, as in the Standard Model [214–216]. In contrast to the Standard Model, however, lepton flavour and lepton CP symmetries can be substantially violated ⁷. This shows that flavour and CP violation can exist in the leptonic weak interaction despite the masslessness of neutrinos, implying that such processes need not be suppressed by the small neutrino masses, and hence can have large rates [214–216, 222, 223] ⁸. Such “(3,6)” setup [30], where the 3 doublet neutrinos are accompanied by 6 heavy singlet neutral leptons, provides the template for building genuine “low-scale” realizations of the seesaw mechanism in which lepton number is restored at low values of the lepton number violation scale. The models are natural in *t’Hooft* sense, leading to small, symmetry-protected neutrino masses. Realizations of such genuine “low-scale” seesaw mechanisms include the inverse [40, 213] as well as the linear seesaw [229–231]. Last, but not least, we notice that a dynamical realization of the seesaw mechanism involving the spontaneous violation of lepton number symmetry can improve the consistency properties of the electroweak vacuum [178–183].

If realized at low-scale, the type-I seesaw mechanism may also lead to signals at high-energy colliders. Already back in the LEP days, it was suggested that the neutrino mass mediators could be produced

⁶For an early example, with lepton number symmetry conservation, see [212].

⁷General discussions of leptonic flavour and CP violation are given in [217–221].

⁸For generic references on lepton flavour violation and seesaw schemes see, for example [224–228].

at high energy colliders [232–237]. This proposal was indeed taken up by subsequent experiments, for example the ATLAS and CMS experiments at the LHC [238–240] as well as future proposals [12, 241–243]. These have also taken into account the possibility of having displaced vertices [244–246]⁹ coming from the fact that the couplings responsible for the mediator decays can be neutrino-mass-suppressed.

2.6 Dark inverse and linear seesaw mechanisms

The symmetry protection provided by the above schemes can be upgraded into a “double protection”, by having the seed of lepton number violation to arise radiatively. Indeed, a very interesting possibility has been suggested, namely the dark inverse [202] and also the dark linear seesaw mechanism [203, 204]. In the former case there is a universal gauge-singlet or “hidden” dark matter sector that *seeds* neutrino mass generation, which proceeds *a la seesaw*. The same idea can be used to promote the linear seesaw mechanism into a mechanism sourced by a dark sector. The latter is not unique, interesting examples were given in [203] and [204].

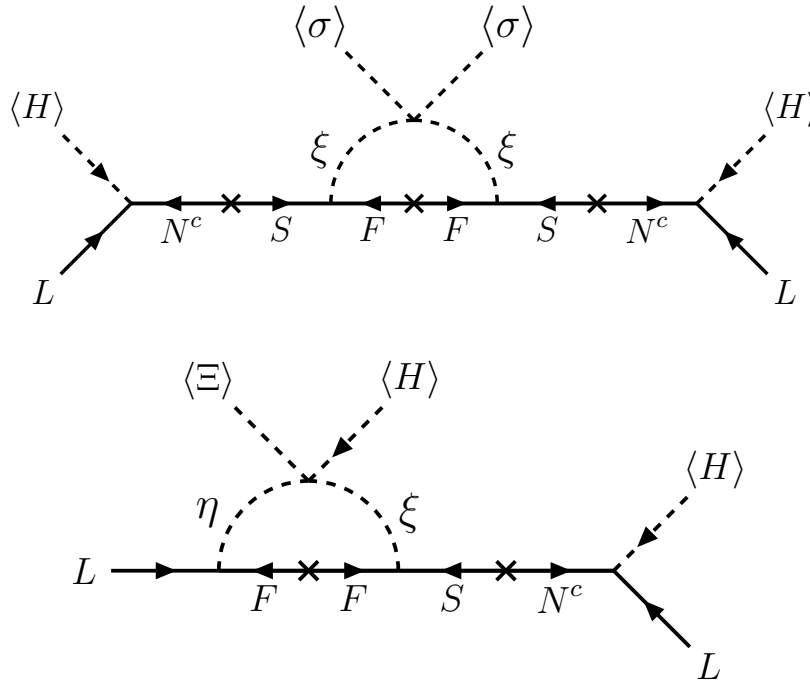


Figure 9: Feynman diagrams for “dark” inverse seesaw (upper panel) [202], and the “dark” linear seesaw mechanism (lower one) [203]. For another realization of the linear seesaw see [204].

The dark inverse seesaw is illustrated in the upper panel of figure 9. The lepton number violation loop that “seeds” neutrino mass is mediated by the “dark” gauge singlet fermion F and dark singlet scalar ξ [202]. This provides an elegant way to reconcile the seesaw and dark matter paradigms, providing an interesting dynamical seesaw theory where dark matter and neutrino mass generation are closely

⁹Other neutrino mass mediator searches can also lead to displaced vertices [247–249].

inter-connected. Scenarios have also been proposed where a dark sector seeds neutrino mass generation radiatively within the linear seesaw mechanism [203, 204], as illustrated in the lower panel. Neutrino masses are also calculable, since tree-level contributions are forbidden by symmetry. By having the seesaw realized at low-scale [40, 213], as indicated in figure 9, in either case one has charged lepton flavour violating processes e.g. $\mu \rightarrow e\gamma$ with accessible rates [202]. We stress that these can be large, despite the tiny neutrino masses. Interesting dark-matter and collider physics implications have also been discussed.

2.7 Neutrinos and the flavour puzzle

We now turn to the issue of understanding the pattern of the weak interactions of quarks and leptons from first principles. Such “flavour problem” constitutes a major challenge in modern particle physics. Why three families of quarks and leptons? How to explain their mass hierarchies e.g. why, though otherwise so similar, the muon is about 200 times heavier than the electron? Why is the top quark mass so large compared with the masses of the other fermions? On the other hand, we also face the question of explaining why do the fermion mixing matrices follow the peculiar pattern observed? In particular, why do leptons mix so differently from the way quarks do? All of these shortcomings pose a real challenge on unified descriptions of nature.

As it stands, the Standard Model of particle physics lacks an organizing principle in terms of which to understand the flavour problem. Hence it can not be a complete theory of nature. Although the Standard Model suffers from many other drawbacks, in this review we focus mainly on explaining the fermion mixing pattern and CP violation, though we also discuss some ideas to account for the fermion mass hierarchies. A “flavour completion” of the SM would have potentially important tests in the laboratory. Moreover, a deep understanding of the flavour problem and CP violation may prove crucial in understanding the baryon asymmetry of the universe [250, 251].

In this review we cover some recent attempts to account for the pattern of neutrino mixing indicated by oscillation experiments. Our key ingredient in formulating a theory of flavour is the imposition of an extra symmetry G_f relating the families. The leading Lagrangian for the lepton masses should be invariant under both the SM gauge symmetry as well as the flavour symmetry, and it can be generally written as

$$\mathcal{L}_m^l = -[y_l(\Phi_l)]_{ij} \bar{l}_R^i H^\dagger L_L^j - \frac{1}{2\Lambda} [y_\nu(\Phi_\nu)]_{ij} \overline{(L_L^i)^c} i\sigma_2 H H^T i\sigma_2 L_L^j + \text{h.c.}, \quad (2.1)$$

where $\sigma_2 = \begin{pmatrix} 0 & -i \\ i & 0 \end{pmatrix}$ is Pauli’s conjugation matrix, $y(\Phi)$ generically denotes the Yukawa couplings, which are determined as functions of the flavons, and the neutrino masses are described by the Weinberg operator [29]. Here Φ_l and Φ_ν denote the flavon fields with vacuum expectation values that break G_f down to the residual subgroups G_l and G_ν in the charged lepton and neutrino sectors respectively. In concrete models the higher-order terms can lead to subleading corrections. As a result, the mismatch of the residual symmetries G_l and G_ν allows one to make model-independent symmetry predictions for the lepton mixing matrix $U = U_l^\dagger U_\nu$, as illustrated in figure 10.

Within the bottom-up approach one may consider remnant flavour symmetries and/or remnant CP

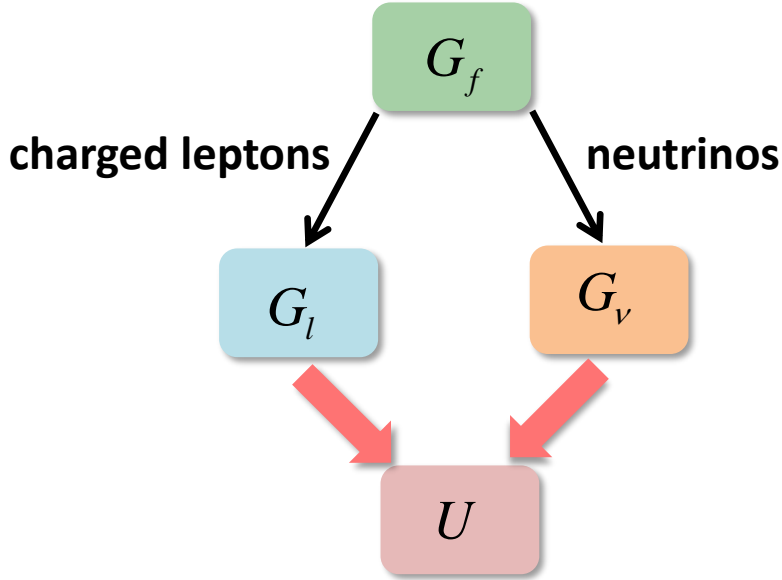


Figure 10: Predicting lepton flavour mixing from the flavour group G_f breaking to different subgroups.

symmetries, such as generalizations of the $\mu - \tau$ reflection symmetry [252–258], as a way to restrict the lepton mass matrices, irrespective of the details of the underlying flavour symmetry. This can be used in turn to constrain the lepton flavour mixing parameters, such as mixing angles [259–263] and especially the CP phases [264–268]. In what follows we call this approach “residual symmetry method” [269–272]. We notice that such $\mu - \tau$ reflection symmetry can emerge within UV-complete theories, e.g. [54, 264]. Indeed, one may seek to constrain the flavour mixing parameters within a complete flavour theory. Attaining a satisfactory theory that explains both quark and lepton sectors together remains an open challenge [273, 274], especially within a quark-lepton unified framework [34, 43–47, 275]. This difficulty [85–93] follows mainly due to the disparity between quark and lepton mixing angles. A possible idea is that lepton mixing angles are large with respect to quark mixing angles because neutrino masses are degenerate in the family symmetry limit [54]. However, nearly degenerate neutrinos are now strongly disfavored by cosmological restrictions [124].

There have been many efforts to approach the flavour problem in the quark sector in terms of an underlying family symmetry, either within a bottom-up or top-down approach [276–286]. For example, the Cabibbo mixing angle can be described by a flavour symmetry [263, 270, 278, 281, 287]. Similarly, quark mixing angles and CP violation may also be accounted for in the framework of generalized CP symmetries [282–286].

Turning now to mass predictions, we note that some quark-lepton relations may emerge naturally from the imposition of family symmetries, even in the absence of a genuine unification group. A prime example is the “golden” formula,

$$\frac{m_\tau}{\sqrt{m_\mu m_e}} \approx \frac{m_b}{\sqrt{m_s m_d}}, \quad (2.2)$$

relating charged-lepton and down-type quark masses. This successful relation may constitute, perhaps, part of any complete theory of flavour. The golden formula could be associated to an underlying Peccei-Quinn symmetry [287]. Alternatively, it could arise within UV-complete family-symmetry-based theories such as [288–290] or [65, 66]. Finally, we note that distinct variants of the golden formula can arise from modular symmetries [291].

We stress that the golden-type relations involve mass ratios, stable under renormalization-group evolution, and allow us to relate quarks and leptons without invoking a genuine unified gauge group such as SU(5) or SO(10). More ambitious approaches to the flavour problem have been proposed within extra spacetime dimensions. For example, 5-D warped schemes were proposed in which mass hierarchies are accounted for by adequate choices of the bulk mass parameters, while quark and lepton mixing angles are restricted by the imposition of a flavour symmetry [70–84]. Predictions for neutrino mixing, CP violation and $0\nu\beta\beta$ decay, as well as a good global fit of flavour observables emerge in warped flavordynamics [78, 79].

On the other hand, 6-dimensional orbifold compactification has been suggested as a promising way to determine the structure of the family symmetry in four dimensions. In this approach the 4-dimensional flavour group emerges from the symmetries between the branes in extra dimensions [292, 293]. Interesting flavour and CP predictions have been obtained from 6-dimensional orbifold compactification schemes, including neutrino oscillation and $0\nu\beta\beta$ decay predictions, as well as a successful global description of the flavour observables [143, 144, 294, 295].

3 Lepton mixing patterns

The most striking implications of the oscillation experiments is that leptons mix quite differently from quarks. Here we consider the interpretation of the oscillation results in terms of phenomenological neutrino mixing patterns. Several of these were suggested, largely motivated by the desire to shed light on the neutrino oscillation parameters. The most salient features of the oscillation phenomenon are captured by the so-called tri-bimaximal (TBM) mixing pattern [296–298]. However there are other interesting mixing patterns, some of which we survey below ¹⁰.

3.1 Tri-bimaximal mixing (TBM)

The Tri-bimaximal lepton mixing pattern embodies bi-maximal mixing of atmospheric neutrinos, tri-maximal solar mixing, no reactor mixing and hence no CP violation. It has been taken very seriously until the Daya Bay collaboration [21,303,304] provided a robust measurement of the angle θ_{13} in 2012. The latest and most precise measurement of Daya Bay gives $\sin^2 2\theta_{13} = 0.0851 \pm 0.0024$ [305,306]. Nevertheless, the TBM pattern still remains as an interesting first step towards a full description of neutrino mixing. Its mixing matrix is given by

$$U_{TBM} = \begin{pmatrix} \sqrt{\frac{2}{3}} & \frac{1}{\sqrt{3}} & 0 \\ -\frac{1}{\sqrt{6}} & \frac{1}{\sqrt{3}} & \frac{1}{\sqrt{2}} \\ -\frac{1}{\sqrt{6}} & \frac{1}{\sqrt{3}} & -\frac{1}{\sqrt{2}} \end{pmatrix}, \quad (3.1)$$

which gives

$$\theta_{23} = 45^\circ, \quad \theta_{12} = \arctan \frac{1}{\sqrt{2}} \simeq 35.26^\circ, \quad \theta_{13} = 0^\circ. \quad (3.2)$$

Under the assumption of Majorana neutrinos, the most general form of the associated neutrino mass matrix in the charged lepton diagonal basis is

$$\begin{aligned} m_\nu^{TBM} &= U_{TBM} \text{diag}(m_1, m_2, m_3) U_{TBM}^T \\ &= \frac{1}{6} \begin{pmatrix} 4m_1 + 2m_2 & -2m_1 + 2m_2 & -2m_1 + 2m_2 \\ -2m_1 + 2m_2 & m_1 + 2m_2 + 3m_3 & m_1 + 2m_2 - 3m_3 \\ -2m_1 + 2m_2 & m_1 + 2m_2 - 3m_3 & m_1 + 2m_2 + 3m_3 \end{pmatrix}. \end{aligned} \quad (3.3)$$

It is easy to check that the above neutrino mass matrix is invariant under the following residual flavour transformations

$$G_1^{TBM} = \frac{1}{3} \begin{pmatrix} 1 & -2 & -2 \\ -2 & -2 & 1 \\ -2 & 1 & -2 \end{pmatrix}, \quad G_2^{TBM} = \frac{1}{3} \begin{pmatrix} -1 & 2 & 2 \\ 2 & -1 & 2 \\ 2 & 2 & -1 \end{pmatrix}, \quad G_3^{TBM} = - \begin{pmatrix} 1 & 0 & 0 \\ 0 & 0 & 1 \\ 0 & 1 & 0 \end{pmatrix}, \quad (3.4)$$

¹⁰Note that, within a UV-complete theory framework, there can be radiative corrections to the TBM predictions [299–302]. This issue lies beyond the scope of the model-independent approach followed here.

up to an overall sign. In other words, the neutrino mass matrix m_ν^{TBM} fulfills

$$(G_i^{TBM})^T m_\nu^{TBM} G_i^{TBM} = m_\nu^{TBM}. \quad (3.5)$$

The symmetry transformation G_3^{TBM} exchanges the second and third columns as well as the second and third rows of the neutrino mass matrix, it is the well-known $\mu - \tau$ permutation symmetry [307–311], and it enforces maximal θ_{23} and vanishing θ_{13} . This symmetry emerges in some UV-complete theories, e.g. [54].

The second transformation G_2^{TBM} requires that the sum of the entries in each row of the light neutrino mass matrix should be equal to that of the corresponding column, the so-called magic symmetry [255, 312]. The invariance under G_2^{TBM} determines one column of the lepton mixing matrix to be $(1, 1, 1)^T / \sqrt{3}$. The residual symmetry transformation G_e of the charged lepton mass matrix is a generic diagonal phase matrix in the flavour basis¹¹. The simplest choice for G_e which can distinguish the three charged leptons is

$$G_e^{TBM} = \begin{pmatrix} 1 & 0 & 0 \\ 0 & \omega^2 & 0 \\ 0 & 0 & \omega \end{pmatrix} \quad (3.6)$$

where ω is the cubic root of one, i.e. $\omega = e^{2\pi i/3}$.

The group generated by G_1^{TBM} , G_2^{TBM} , G_3^{TBM} and G_e^{TBM} turns out to be S_4 group. Consequently, the minimal flavour symmetry group capable of yielding the tri-bimaximal mixing is S_4 [269, 270]. However, in the absence of symmetry breaking by flavons in the $\mathbf{1}'$ and $\mathbf{1}''$ representations the A_4 flavor symmetry can also give rise to the tri-bimaximal mixing pattern [53, 54, 59, 70, 313–315].

3.2 Generalizations of tri-bimaximal mixing

Soon after the tri-bimaximal mixing ansatz was proposed, possible deviations were considered. A simple generalization is obtained by assuming that just one given row or column of the lepton mixing matrix takes the same form as for tri-bimaximal [252]. If the first column of the tri-bimaximal mixing is retained, this is known as the TM1 mixing pattern [316–318], and the associated mixing matrix can be parameterized as

$$U_{TM1} = \frac{1}{\sqrt{6}} \begin{pmatrix} 2 & \sqrt{2} \cos \theta & \sqrt{2} e^{-i\delta} \sin \theta \\ -1 & \sqrt{2} \cos \theta - \sqrt{3} e^{i\delta} \sin \theta & \sqrt{3} \cos \theta + \sqrt{2} e^{-i\delta} \sin \theta \\ -1 & \sqrt{2} \cos \theta + \sqrt{3} e^{i\delta} \sin \theta & -\sqrt{3} \cos \theta + \sqrt{2} e^{-i\delta} \sin \theta \end{pmatrix}. \quad (3.7)$$

The predictions for the lepton mixing angles and leptonic Jarlskog invariant are expressed in terms of just two free parameters δ and θ as

$$\sin^2 \theta_{13} = \frac{1}{3} \sin^2 \theta, \quad \sin^2 \theta_{12} = \frac{1 + \cos 2\theta}{5 + \cos 2\theta},$$

¹¹If G_e is a non-abelian subgroup, the charged lepton mass spectrum would be completely or partially degenerate. Thus G_e should be a cyclic group Z_n with the index $n \geq 3$ or a product of cyclic groups such as $Z_2 \times Z_2$ in order to distinguish among the generations.

$$\sin^2 \theta_{23} = \frac{1}{2} + \frac{\sqrt{6} \cos \delta \sin 2\theta}{5 + \cos 2\theta}, \quad J_{CP} = \frac{1}{6\sqrt{6}} \sin \delta \sin 2\theta. \quad (3.8)$$

One finds that the lepton mixing angles and Dirac CP phases are correlated as follows

$$3 \cos^2 \theta_{12} \cos^2 \theta_{13} = 2, \quad \tan 2\theta_{23} \cos \delta^\ell = \frac{5 \sin^2 \theta_{13} - 1}{2 \sin \theta_{13} \sqrt{2 - 6 \sin^2 \theta_{13}}}. \quad (3.9)$$

We notice that this TM1 pattern emerges as a prediction of the UV-complete models proposed in Refs. [64, 79, 319, 320].

On the other hand, by retaining the second column of the tri-bimaximal mixing matrix one obtains the TM2 [316–318] pattern, a particular case of trimaximal mixing [252, 321–323], given as

$$U_{TM2} = \frac{1}{\sqrt{6}} \begin{pmatrix} 2 \cos \theta & \sqrt{2} & 2e^{-i\delta} \sin \theta \\ -\cos \theta - \sqrt{3} e^{i\delta} \sin \theta & \sqrt{2} & \sqrt{3} \cos \theta - e^{-i\delta} \sin \theta \\ -\cos \theta + \sqrt{3} e^{i\delta} \sin \theta & \sqrt{2} & -\sqrt{3} \cos \theta - e^{-i\delta} \sin \theta \end{pmatrix}. \quad (3.10)$$

All the lepton mixing parameters depend on just two free parameters δ and θ ,

$$\begin{aligned} \sin^2 \theta_{13} &= \frac{2}{3} \sin^2 \theta, & \sin^2 \theta_{12} &= \frac{1}{2 + \cos 2\theta}, \\ \sin^2 \theta_{23} &= \frac{1}{2} - \frac{\sqrt{3} \cos \delta \sin 2\theta}{2(2 + \cos 2\theta)}, & J_{CP} &= \frac{1}{6\sqrt{3}} \sin \delta \sin 2\theta, \end{aligned} \quad (3.11)$$

which implies the following correlations

$$3 \sin^2 \theta_{12} \cos^2 \theta_{13} = 1, \quad \tan 2\theta_{23} \cos \delta^\ell = \frac{\cos 2\theta_{13}}{\sin \theta_{13} \sqrt{2 - 3 \sin^2 \theta_{13}}}. \quad (3.12)$$

Here we note also that this TM2 neutrino mixing pattern emerges within the UV-complete models described in Refs. [61, 62, 78, 205, 323–325].

3.3 Golden ratio mixing pattern

Within the standard golden ratio (GR) mixing pattern¹², the lepton mixing angles are given by $\theta_{23} = 45^\circ$, $\theta_{13} = 0^\circ$ and $\cot \theta_{12} = \phi_g$, where $\phi_g = (1 + \sqrt{5})/2$ is the golden ratio [328, 329]. The lepton mixing matrix is of the form

$$U_{GR} = \begin{pmatrix} c_{12} & s_{12} & 0 \\ -\frac{s_{12}}{\sqrt{2}} & \frac{c_{12}}{\sqrt{2}} & \frac{1}{\sqrt{2}} \\ -\frac{s_{12}}{\sqrt{2}} & \frac{c_{12}}{\sqrt{2}} & -\frac{1}{\sqrt{2}} \end{pmatrix} \equiv \frac{1}{\sqrt{2\sqrt{5}\phi_g}} \begin{pmatrix} \sqrt{2}\phi_g & \sqrt{2} & 0 \\ -1 & \phi_g & \sqrt{\sqrt{5}\phi_g} \\ -1 & \phi_g & -\sqrt{\sqrt{5}\phi_g} \end{pmatrix}. \quad (3.13)$$

¹²Another proposal for the golden ratio mixing has the solar mixing angle given as $\cos \theta_{12} = \phi_g/2$ [326, 327].

In this case, the neutrino mass matrix is given by

$$m_\nu^{GR} = \frac{m_1}{2\sqrt{5}} \begin{pmatrix} 2\phi_g & -\sqrt{2} & -\sqrt{2} \\ -\sqrt{2} & -1/\phi_g & -1/\phi_g \\ -\sqrt{2} & -1/\phi_g & -1/\phi_g \end{pmatrix} + \frac{m_2}{2\sqrt{5}} \begin{pmatrix} 2/\phi_g & \sqrt{2} & \sqrt{2} \\ \sqrt{2} & \phi_g & \phi_g \\ \sqrt{2} & \phi_g & \phi_g \end{pmatrix} + \frac{m_3}{2} \begin{pmatrix} 0 & 0 & 0 \\ 0 & 1 & -1 \\ 0 & -1 & 1 \end{pmatrix}. \quad (3.14)$$

The residual flavour symmetry transformations of m_ν^{GR} take the form

$$G_1^{GR} = \frac{1}{\sqrt{5}} \begin{pmatrix} 1 & -\sqrt{2} & -\sqrt{2} \\ -\sqrt{2} & -\phi_g & 1/\phi_g \\ -\sqrt{2} & 1/\phi_g & -\phi_g \end{pmatrix}, \quad G_2^{GR} = \frac{1}{\sqrt{5}} \begin{pmatrix} -1 & \sqrt{2} & \sqrt{2} \\ \sqrt{2} & -1/\phi_g & \phi_g \\ \sqrt{2} & \phi_g & -1/\phi_g \end{pmatrix},$$

$$G_3^{GR} = - \begin{pmatrix} 1 & 0 & 0 \\ 0 & 0 & 1 \\ 0 & 1 & 0 \end{pmatrix}. \quad (3.15)$$

The minimal flavour symmetry that can produce the golden ratio mixing pattern is the A_5 group [330–332]. Accordingly, a finite Z_5 subgroup is preserved by the charged lepton mass term with

$$G_e = \begin{pmatrix} 1 & 0 & 0 \\ 0 & e^{2\pi i/5} & 0 \\ 0 & 0 & e^{-2\pi i/5} \end{pmatrix}. \quad (3.16)$$

In order to be phenomenologically viable, the golden-ratio pattern would certainly require a revamping, along the lines considered in section 5.

3.4 Bi-maximal mixing pattern

For the bi-maximal mixing, both solar angle and atmospheric mixing angles are maximal $\theta_{12} = \theta_{23} = 45^\circ$ while the reactor angle is vanishing [333]. In the basis where the charged lepton mass matrix is diagonal, the corresponding neutrino mass matrix is given by

$$m_\nu^{BM} = \frac{1}{4} \begin{pmatrix} 2(m_1 + m_2) & \sqrt{2}(m_2 - m_1) & \sqrt{2}(m_2 - m_1) \\ \sqrt{2}(m_2 - m_1) & m_1 + m_2 + 2m_3 & m_1 + m_2 - 2m_3 \\ \sqrt{2}(m_2 - m_1) & m_1 + m_2 - 2m_3 & m_1 + m_2 + 2m_3 \end{pmatrix}. \quad (3.17)$$

The residual flavour symmetry transformations of the above neutrino mass matrix are

$$G_1^{BM} = \frac{1}{2} \begin{pmatrix} 0 & -\sqrt{2} & -\sqrt{2} \\ -\sqrt{2} & -1 & 1 \\ -\sqrt{2} & 1 & -1 \end{pmatrix}, \quad G_2^{BM} = \frac{1}{2} \begin{pmatrix} 0 & \sqrt{2} & \sqrt{2} \\ \sqrt{2} & -1 & 1 \\ \sqrt{2} & 1 & -1 \end{pmatrix}, \quad G_3^{BM} = - \begin{pmatrix} 1 & 0 & 0 \\ 0 & 0 & 1 \\ 0 & 1 & 0 \end{pmatrix}. \quad (3.18)$$

We can choose the residual flavour symmetry of the charged lepton mass matrix to be a Z_4 subgroup with

$$G_e^{BM} = \begin{pmatrix} 1 & 0 & 0 \\ 0 & i & 0 \\ 0 & 0 & -i \end{pmatrix}. \quad (3.19)$$

The group generated by G_1^{BM} , G_2^{BM} , G_3^{BM} and G_e^{BM} is also the S_4 group [334, 335]. Therefore the S_4 flavour symmetry can also be used to produce the bimaximal mixing.

Note, however, that the solar angle θ_{12} and reactor angle θ_{13} would have to undergo very large corrections in order to be compatible with current neutrino oscillation data [24, 25], making this pattern very problematic. As a result, Bi-maximal mixing should be discarded or generalized in a radical way. One of its possible radical generalizations is the Bi-large mixing pattern discussed in section 5.3.

Besides the tri-bimaximal, golden ratio and bi-maximal mixing patterns, there are other constant mixing patterns compatible with experimental data with nonzero θ_{13} [259, 336–338]. They could be derived from the breaking of large flavor symmetry groups such as $\Delta(96)$, $\Delta(384)$ etc. No sizable corrections are necessary for these mixing patterns, however the required vacuum configuration and symmetry breaking are more complicated.

As shown above, the neutrino mass matrices corresponding to the simple tri-bimaximal, golden ratio and bi-maximal mixing patterns obey certain residual flavour symmetries. In the following section, we will show that the neutrino and charged lepton mass matrices generally can have both residual flavour and residual CP symmetries, and also that a residual flavour symmetry can be generated by a residual CP symmetry. In particular, residual symmetries can provide a method to revamp all mixing patterns discussed above. Indeed, in the next section we will show how to revamp them in a systematic manner by using the residual symmetry method. The generalized patterns are not only phenomenologically viable, but also predictive, since the form of the resulting lepton mixing matrices can be restricted.

4 Flavour and CP symmetries from the bottom-up

In this section, we will examine quark and lepton mass matrices that have both remnant flavour and CP symmetry. Remnant flavour symmetries can be generated by performing two remnant CP transformations in succession, with explicit forms of the remnant CP symmetry derived from the experimentally measured mixing matrix. On the other hand, the fermion mixing matrices can be constructed from the postulated residual CP transformations of the quark and lepton mass matrices. In the following, we present the remnant flavour and CP symmetries of the quark and lepton mass matrices, their parametrization and the master formula to construct the mixing matrix from the remnant CP symmetry.

4.1 Residual symmetries of leptons

In the absence of a fundamental theory of flavour we study the effect of possible remnant symmetries G_ν and G_l of the neutrino and charged lepton mass terms. Their existence may provide a model-independent approach towards underpinning the ultimate nature of the underlying theory. Let us now focus on this point.

The lepton masses terms are given in Eq. (1.12) and Eq. (1.13) for Dirac and Majorana neutrinos respectively. Since in the SM the only physical mixing matrix relates to left-handed fermions, we are concerned with the hermitian mass matrix $m_l^\dagger m_l$ connecting left-handed charged leptons on both sides. Under generic unitary transformations of the left-handed lepton fields l_L and ν_L ,

$$l_L \rightarrow G_l l_L, \quad \nu_L \rightarrow G_\nu \nu_L, \quad (4.1)$$

where both G_l and G_ν are three-dimensional unitary matrices, the charged lepton and neutrino mass matrices transform as

$$m_l^\dagger m_l \rightarrow G_l^\dagger m_l^\dagger m_l G_l, \quad (4.2)$$

$$m_\nu \rightarrow G_\nu^T m_\nu G_\nu, \quad \text{for Majorana neutrinos,} \quad (4.3)$$

$$m_\nu^\dagger m_\nu \rightarrow G_\nu^\dagger m_\nu^\dagger m_\nu G_\nu, \quad \text{for Dirac neutrinos.} \quad (4.4)$$

In order for the symmetry to hold, the mass matrices must satisfy

$$G_l^\dagger m_l^\dagger m_l G_l = m_l^\dagger m_l, \quad (4.5)$$

$$G_\nu^T m_\nu G_\nu = m_\nu, \quad \text{for Majorana neutrinos,} \quad (4.6)$$

$$G_\nu^\dagger m_\nu^\dagger m_\nu G_\nu = m_\nu^\dagger m_\nu, \quad \text{for Dirac neutrinos.} \quad (4.7)$$

Applying these invariance conditions to Eqs. (1.16, 1.17, 1.18) and assuming no mass eigenvalue vanishes we obtain

$$U_l^\dagger G_l U_l = \text{diag} (e^{i\alpha_e}, e^{i\alpha_\mu}, e^{i\alpha_\tau}), \quad (4.8)$$

$$U_\nu^\dagger G_\nu U_\nu = \text{diag}(\pm 1, \pm 1, \pm 1), \quad \text{for Majorana neutrinos,} \quad (4.9)$$

$$U_\nu^\dagger G_\nu U_\nu = \text{diag}(e^{i\alpha_{\nu e}}, e^{i\alpha_{\nu \mu}}, e^{i\alpha_{\nu \tau}}), \quad \text{for Dirac neutrinos,} \quad (4.10)$$

where $\alpha_{e,\mu,\tau}$ and $\alpha_{\nu e,\nu\mu,\nu\tau}$, are arbitrary real parameters. It follows that the residual flavour symmetry transformations G_l and G_ν are of the following form [263, 265]:

$$G_l = U_l \text{diag}(e^{i\alpha_e}, e^{i\alpha_\mu}, e^{i\alpha_\tau}) U_l^\dagger, \quad (4.11)$$

$$G_\nu = U_\nu \text{diag}(\pm 1, \pm 1, \pm 1) U_\nu^\dagger, \quad \text{for Majorana neutrinos,} \quad (4.12)$$

$$G_\nu = U_\nu \text{diag}(e^{i\alpha_{\nu e}}, e^{i\alpha_{\nu \mu}}, e^{i\alpha_{\nu \tau}}) U_\nu^\dagger, \quad \text{for Dirac neutrinos.} \quad (4.13)$$

One sees that the charged lepton mass term generically admits a $U(1) \times U(1) \times U(1)$ remnant flavour symmetry. For the neutrino mass matrix the remnant flavour symmetry depends on the nature of neutrinos. For the case of Dirac neutrinos it is also $U(1) \times U(1) \times U(1)$ [263]. For Majorana neutrinos, the eight possible choices of G_ν in Eq. (4.12) correspond to $Z_2 \times Z_2 \times Z_2$. Notice that G_ν and $-G_\nu$ should be identified as the same residual flavour symmetry transformation, since the minus sign can be absorbed as a neutrino field redefinition. Indeed, they both lead to the same constraint on the neutrino mass matrix. We are therefore left with four possible solutions for G_ν , which can be chosen as [269–272],

$$G_i = U_\nu d_i U_\nu^\dagger, \quad i = 1, 2, 3, 4, \quad (4.14)$$

where the d_i are given as

$$\begin{aligned} d_1 &= \text{diag}(1, -1, -1), & d_2 &= \text{diag}(-1, 1, -1), \\ d_3 &= \text{diag}(-1, -1, 1), & d_4 &= \text{diag}(1, 1, 1). \end{aligned} \quad (4.15)$$

One sees that G_4 is simply the trivial identity matrix, and we can further check that

$$G_i^2 = 1, \quad G_i G_j = G_j G_i = G_k \quad \text{with} \quad i \neq j \neq k \neq 4. \quad (4.16)$$

It follows that the residual flavour symmetry of the Majorana neutrino mass matrix is a Klein group isomorphic to $Z_2 \times Z_2$. In the flavour basis where the charged lepton mass matrix m_l is diagonal, U_l would be trivial, so that the lepton mixing comes just from the neutrino sector, i.e. $U = U_\nu$. Hence the residual symmetries of the neutrino and charged lepton mass matrices are determined in terms of the mixing angles and CP violation phases contained in the mixing matrix.

An important observation is that, besides the above residual flavour symmetry, the lepton mass matrices can have residual CP (or charge conjugation parity) symmetry. The CP transformation properties of the left-handed neutrino and charged lepton fields are given by

$$l_L(x) \xrightarrow{CP} i X_l \gamma^0 C \bar{l}_L^T(\mathcal{P}x), \quad \nu_L(x) \xrightarrow{CP} i X_\nu \gamma^0 C \bar{\nu}_L^T(\mathcal{P}x), \quad (4.17)$$

where $\mathcal{P}x = (t, -\vec{x})$, C is the charge-conjugation matrix [94–96], X_l and X_ν are 3×3 unitary matrices acting in family space. Notice that the matrices X_l and X_ν generalize the conventional CP transformation prescription. As a result, they are referred to in the literature as generalized CP transformations [264, 339–344].

Requiring that X_l and X_ν are symmetries of the lepton mass terms in Eqs. (1.12, 1.13) implies that the lepton mass matrices m_l and m_ν should satisfy [265, 345]

$$X_l^\dagger m_l^\dagger m_l X_l = \left(m_l^\dagger m_l\right)^* , \quad (4.18)$$

$$X_\nu^T m_\nu X_\nu = m_\nu^* , \quad \text{for Majorana neutrinos} , \quad (4.19)$$

$$X_\nu^\dagger m_\nu^\dagger m_\nu X_\nu = \left(m_\nu^\dagger m_\nu\right)^* , \quad \text{for Dirac neutrinos} . \quad (4.20)$$

Plugging Eqs. (1.16, 1.17, 1.18) into the above invariance conditions, one sees that the unitary transformations U_l and U_ν must be subject to the following conditions

$$U_l^\dagger X_l U_l^* = \text{diag} \left(e^{i\beta_e}, e^{i\beta_\mu}, e^{i\beta_\tau} \right) , \quad (4.21)$$

$$U_\nu^\dagger X_\nu U_\nu^* = \text{diag} (\pm 1, \pm 1, \pm 1) , \quad \text{for Majorana neutrinos} , \quad (4.22)$$

$$U_\nu^\dagger X_\nu U_\nu^* = \text{diag} \left(e^{i\beta_{\nu e}}, e^{i\beta_{\nu\mu}}, e^{i\beta_{\nu\tau}} \right) , \quad \text{for Dirac neutrinos} , \quad (4.23)$$

where $\beta_{e,\mu,\tau}$ and $\beta_{\nu e,\nu\mu,\nu\tau}$ are real free parameters. Hence the residual CP transformations X_l and X_ν should be of the form [263–268]

$$X_l = U_l \text{diag} \left(e^{i\beta_e}, e^{i\beta_\mu}, e^{i\beta_\tau} \right) U_l^T , \quad (4.24)$$

$$X_\nu = U_\nu \text{diag} (\pm 1, \pm 1, \pm 1) U_\nu^T , \quad \text{for Majorana neutrinos} , \quad (4.25)$$

$$X_\nu = U_\nu \text{diag} \left(e^{i\beta_{\nu e}}, e^{i\beta_{\nu\mu}}, e^{i\beta_{\nu\tau}} \right) U_\nu^T , \quad \text{for Dirac neutrinos} . \quad (4.26)$$

Clearly, both X_l and X_ν are unitary and symmetric matrices [264, 265]

$$X_l = X_l^T , \quad X_\nu = X_\nu^T , \quad X_l X_l^\dagger = X_\nu X_\nu^\dagger = 1 . \quad (4.27)$$

From the expressions of remnant flavor symmetry in Eqs. (4.11, 4.12, 4.13) and remnant CP transformations in Eqs. (4.24, 4.25, 4.26), one can check that the residual flavour and CP symmetries satisfy the following restricted consistency conditions

$$\begin{aligned} X_l G_l^* X_l^{-1} &= G_l^{-1} , \\ X_\nu G_\nu^* X_\nu^{-1} &= G_\nu , \quad \text{for Majorana neutrinos} , \\ X_\nu G_\nu^* X_\nu^{-1} &= G_\nu^{-1} , \quad \text{for Dirac neutrinos} . \end{aligned} \quad (4.28)$$

If we successively perform two CP transformations on the left-handed charged lepton fields, characterized

by $X_l = U_l \text{diag}(e^{i\beta_e}, e^{i\beta_\mu}, e^{i\beta_\tau}) U_l^T$ and $X_l' = U_l \text{diag}(e^{i\beta_e'}, e^{i\beta_\mu'}, e^{i\beta_\tau'}) U_l^T$ we obtain ¹³

$$l_L(x) \xrightarrow{CP} iX_l \gamma^0 C \bar{l}_L^T(\mathcal{P}x) \xrightarrow{CP} X_l X_l'^* l_L(x), \quad (4.29)$$

with

$$X_l X_l'^* = U_l \text{diag}(e^{i(\beta_e - \beta_e')}, e^{i(\beta_\mu - \beta_\mu')}, e^{i(\beta_\tau - \beta_\tau')}) U_l^\dagger. \quad (4.30)$$

Moreover, from the invariance condition of $m_l^\dagger m_l$ under the residual CP symmetry, Eq. (4.18), it is easy to show that

$$X_l'^T X_l^\dagger m_l^\dagger m_l X_l X_l'^* = m_l^\dagger m_l. \quad (4.31)$$

This means that performing two CP transformations in succession is equivalent to a flavour symmetry transformation $X_l X_l'^* \equiv G_l$ [265]. The same conclusion also holds true for neutrinos if they are Dirac particles.

For the case of Majorana neutrinos, there are eight possibilities for X_ν . In this case one should take X_ν and $-X_\nu$ as the same CP transformation, since the minus sign can be absorbed into the neutrino fields since the mass term involves a product of two neutrino fields. As a result only four of them are relevant. Without loss of generality they can be chosen to be [265–267]

$$X_i = U_\nu d_i U_\nu^T, \quad i = 1, 2, 3, 4, \quad (4.32)$$

with d_i given in Eq. (4.15). The remaining four can be obtained from the above by multiplying an overall -1 factor. It is straightforward to check that the neutrino mass matrix m_ν satisfies

$$X_j^\dagger X_i^T m_\nu X_i X_j^* = m_\nu. \quad (4.33)$$

As a result, remnant flavour symmetries can be generated by remnant CP symmetries as well. Explicitly, we have the following relations [265]:

$$\begin{aligned} X_2 X_3^* &= X_3 X_2^* = X_4 X_1^* = X_1 X_4^* = G_1, \\ X_1 X_3^* &= X_3 X_1^* = X_4 X_2^* = X_2 X_4^* = G_2, \\ X_1 X_2^* &= X_2 X_1^* = X_4 X_3^* = X_3 X_4^* = G_3, \\ X_1 X_1^* &= X_2 X_2^* = X_3 X_3^* = X_4 X_4^* = G_4 = 1. \end{aligned} \quad (4.34)$$

As a result, once we impose a set of generalized CP transformations, there is always an associated flavour symmetry. Furthermore, Eq. (4.34) implies that any residual CP transformation can be expressed in terms of the remaining ones as follows [265],

$$X_i = X_j X_m^* X_n, \quad i \neq j \neq m \neq n. \quad (4.35)$$

¹³Notice that an overall minus sign is dropped in the last step, as it can be absorbed into the lepton field.

In other words, only three of the four remnant CP transformations are independent. In the flavour basis where m_l is diagonal, the residual CP transformation X_l is an arbitrary diagonal phase matrix, while $X_\nu = U \text{diag}(\pm 1, \pm 1, \pm 1) U^T$. Hence the remnant CP symmetry can be constructed from the neutrino mixing matrix, and its explicit form can be determined more precisely with the improved measurement of the mixing angles and CP phases [24, 25].

Here we have so far assumed that the three light neutrino masses are non-vanishing. If the lightest neutrino is massless one can analyze the residual symmetry of the neutrino mass matrix in the same way. This interesting situation occurs generically in the “missing partner” seesaw mechanism [30] in which there are less “right” than “left”-handed neutrinos¹⁴ (a massless neutrino also emerges in theories where anti-symmetric Yukawa couplings are involved in generating neutrino mass [130]). Note that an incomplete fermion multiplet structure¹⁵ can also be interesting in cosmology [134–138].

With one neutrino massless one has $m_1 = 0$ for normal ordered (NO) neutrino mass spectrum, and $m_3 = 0$ for the inverted ordered (IO) spectrum. If neutrinos have Dirac nature, one finds that the residual CP transformation X_ν would still be given by Eq. (4.26). On the other hand, if neutrinos are Majorana particles, one must use Eq. (4.25) replacing the diagonal entry “ ± 1 ” in the position (11) for NO and (33) for IO with an arbitrary phase factor [348], i.e.

$$X_\nu = \begin{cases} U_\nu \text{diag}(e^{i\beta}, \pm 1, \pm 1) U_\nu^T, & \text{for NO,} \\ U_\nu \text{diag}(\pm 1, \pm 1, e^{i\beta}) U_\nu^T, & \text{for IO,} \end{cases} \quad (4.36)$$

where β is real. Similarly the residual flavour symmetry G_ν becomes [265, 348]

$$G_\nu = \begin{cases} U_\nu \text{diag}(e^{i\alpha}, \pm 1, \pm 1) U_\nu^\dagger, & \text{for NO,} \\ U_\nu \text{diag}(\pm 1, \pm 1, e^{i\alpha}) U_\nu^\dagger, & \text{for IO,} \end{cases} \quad (4.37)$$

with real α . Hence the generalized CP and residual flavour symmetry groups have the structure $U(1) \times Z_2$ (instead of $Z_2 \times Z_2$) modulo a possible overall factor -1 in this case. On the other hand, this kind of residual symmetry can enforce a massless Majorana neutrino. The breaking of finite discrete groups into this form of G_ν in the neutrino sector was analyzed in [349–351], where the angle α was a rational multiple of π .

4.2 Reconstructing lepton mixing from remnant CP symmetry

As shown in above, residual CP symmetries can be derived from the mixing matrix, and conversely, the lepton mixing matrix can be constructed from the remnant CP symmetries in the neutrino and the charged lepton sectors. In concrete models, we can start from a set of CP transformations $\mathcal{X}_{\mathcal{CP}}$ respected by the Lagrangian at some high energy scale. Subsequently $\mathcal{X}_{\mathcal{CP}}$ is spontaneously broken by some scalar fields into different remnant symmetries in the neutrino and the charged lepton sectors. The misalignment

¹⁴The present neutrino data allows the possibility that the lightest neutrino is massless, consequently at least two right-handed neutrinos are necessary in type-I seesaw [131–133].

¹⁵For a discussion of seesaw leptogenesis with two and three right-handed neutrinos see [346, 347].

between the two remnant symmetries is responsible for the mismatch of the rotations which diagonalize the neutrino and charged lepton matrices, leading to the lepton mixing matrix. We now present the general parametrization for the remnant CP symmetries of the neutrino and charged lepton sector, and the corresponding restrictions on the unitary transformations U_ν and U_l .

We start from the simplest nontrivial case in which a single remnant CP transformation X_R is preserved by the neutrino mass matrix. As shown in section 4.1, X_R should be a symmetric unitary matrix, otherwise the light neutrino masses would be degenerate. Thus X_R can be parameterized as follows [265]:

$$X_R = e^{i\kappa_1} v_1 v_1^T + e^{i\kappa_2} v_2 v_2^T + e^{i\kappa_3} v_3 v_3^T, \quad (4.38)$$

where the phases κ_1 , κ_2 and κ_3 can be taken in the range of 0 and 2π without loss of generality, v_1 , v_2 and v_3 are mutually orthogonal vectors with

$$\begin{aligned} v_1 &= \begin{pmatrix} \cos \varphi \\ \sin \varphi \cos \phi \\ \sin \varphi \sin \phi \end{pmatrix}, & v_2 &= \begin{pmatrix} \sin \varphi \cos \rho \\ -\sin \phi \sin \rho - \cos \varphi \cos \phi \cos \rho \\ \cos \phi \sin \rho - \cos \varphi \sin \phi \cos \rho \end{pmatrix}, \\ v_3 &= \begin{pmatrix} \sin \varphi \sin \rho \\ \sin \phi \cos \rho - \cos \varphi \cos \phi \sin \rho \\ -\cos \phi \cos \rho - \cos \varphi \sin \phi \sin \rho \end{pmatrix}. \end{aligned} \quad (4.39)$$

Invariance of the neutrino mass matrix under X_R implies that U_ν should be subject to the constraint in Eq. (4.22) and Eq. (4.23) for Majorana and Dirac neutrinos. As a consequence, U_ν is fixed to be [265]

$$U_\nu = (v_1, v_2, v_3) \text{diag}(e^{i\frac{\kappa_1}{2}}, e^{i\frac{\kappa_2}{2}}, e^{i\frac{\kappa_3}{2}}) O_3(\theta_1, \theta_2, \theta_3) Q_\nu, \quad (4.40)$$

where O_3 is a generic real orthogonal matrix,

$$O_3(\theta_1, \theta_2, \theta_3) = \begin{pmatrix} 1 & 0 & 0 \\ 0 & \cos \theta_1 & \sin \theta_1 \\ 0 & -\sin \theta_1 & \cos \theta_1 \end{pmatrix} \begin{pmatrix} \cos \theta_2 & 0 & \sin \theta_2 \\ 0 & 1 & 0 \\ -\sin \theta_2 & 0 & \cos \theta_2 \end{pmatrix} \begin{pmatrix} \cos \theta_3 & \sin \theta_3 & 0 \\ -\sin \theta_3 & \cos \theta_3 & 0 \\ 0 & 0 & 1 \end{pmatrix}, \quad (4.41)$$

where the rotation angles $\theta_{1,2,3}$ are free. The matrix Q_ν is diagonal, and its entries are ± 1 and $\pm i$ which encode the CP parity of the neutrinos, while it is unphysical for Dirac neutrinos.

If two remnant CP transformations X_{R1} and X_{R2} out of the original CP symmetry are preserved in the neutrino sector, they can generally be written as [265]

$$\begin{aligned} X_{R1} &= e^{i\kappa_1} v_1 v_1^T + e^{i\kappa_2} v_2 v_2^T + e^{i\kappa_3} v_3 v_3^T, \\ X_{R2} &= e^{i\kappa_1} v_1 v_1^T - e^{i\kappa_2} v_2 v_2^T - e^{i\kappa_3} v_3 v_3^T, \end{aligned} \quad (4.42)$$

for Majorana neutrinos¹⁶. A remnant flavour transformation G_R can be obtained from X_{R1} and X_{R2} as

$$G_R = X_{R1}X_{R2}^* = X_{R2}X_{R1}^* = 2v_1v_1^T - 1, \quad (4.43)$$

which satisfies $G_R^2 = 1$. Hence a remnant Z_2 flavor symmetry generated by G_R is induced and it fixes one column of U_ν to be v_1 . Besides the parameters characterizing the remnant CP symmetry, U_ν is determined just by a free rotation angle θ [265],

$$U_\nu = (v_1, v_2, v_3) \text{diag}(e^{i\frac{\kappa_1}{2}}, e^{i\frac{\kappa_2}{2}}, e^{i\frac{\kappa_3}{2}}) R_{23}(\theta) P_\nu Q_\nu, \quad (4.44)$$

where $R_{23}(\theta)$ denotes a rotation matrix through an angle θ in the (23)-plane with $0 \leq \theta < \pi$,

$$R_{23}(\theta) = \begin{pmatrix} 1 & 0 & 0 \\ 0 & \cos \theta & \sin \theta \\ 0 & -\sin \theta & \cos \theta \end{pmatrix}. \quad (4.45)$$

Since the remnant symmetry can not constrain the ordering of the light neutrino mass eigenvalues, U_ν is determined up to independent column permutations, and consequently P_ν is a generic permutation matrix which can take six possible forms 1, P_{12} , P_{13} , P_{23} , $P_{23}P_{12}$, $P_{23}P_{13}$ with

$$P_{12} = \begin{pmatrix} 0 & 1 & 0 \\ 1 & 0 & 0 \\ 0 & 0 & 1 \end{pmatrix}, \quad P_{13} = \begin{pmatrix} 0 & 0 & 1 \\ 0 & 1 & 0 \\ 1 & 0 & 0 \end{pmatrix}, \quad P_{23} = \begin{pmatrix} 1 & 0 & 0 \\ 0 & 0 & 1 \\ 0 & 1 & 0 \end{pmatrix}. \quad (4.46)$$

We see that the unitary transformations U_ν for the two permutations P_ν and $P_{23}P_\nu$ are related by the redefinitions $\theta \rightarrow \theta - \pi/2$ and $Q_\nu \rightarrow P_\nu^T \text{diag}(1, 1, -1) P_\nu Q_\nu$. Hence only three inequivalent permutations of the columns are relevant in this case. In other words, the fixed vector $(\cos \varphi, \sin \varphi \cos \phi, \sin \varphi \sin \phi)^T$ can be the first column, the second column or the third column of the matrix U_ν .

For the case of Majorana neutrinos, we consider the scenario that all independent remnant CP transformations are preserved by the neutrino mass matrix. The remnant CP transformations can be parameterized as [267]

$$\begin{aligned} X_{R1} &= e^{i\kappa_1} v_1 v_1^T + e^{i\kappa_2} v_2 v_2^T + e^{i\kappa_3} v_3 v_3^T, \\ X_{R2} &= e^{i\lambda_1} v_1 v_1^T + e^{i\lambda_2} w_2 w_2^T + e^{i\lambda_3} w_3 w_3^T, \\ X_{R3} &= e^{i\lambda_1} v_1 v_1^T - e^{i\lambda_2} w_2 w_2^T - e^{i\lambda_3} w_3 w_3^T, \\ X_{R4} &= e^{i\kappa_1} v_1 v_1^T - e^{i\kappa_2} v_2 v_2^T - e^{i\kappa_3} v_3 v_3^T, \end{aligned} \quad (4.47)$$

¹⁶For Dirac neutrinos, the neutrino mixing matrix U_ν would be completely fixed up to column permutations, if the order of the remnant flavour transformation $G_R = X_{R1}X_{R2}^* = X_{R2}X_{R1}^*$ is greater than or equal to three, so as to distinguish the three families.

where v_1 , w_2 and w_3 also form another set of real orthonormal vectors with

$$w_2 = \cos \xi v_2 - \sin \xi v_3, \quad w_3 = \sin \xi v_2 + \cos \xi v_3, \quad (4.48)$$

and the phases $e^{i\lambda_1}$, $e^{i\lambda_2}$ and $e^{i\lambda_3}$ are given by

$$e^{i\lambda_1} = -e^{i\kappa_1}, \quad e^{i\lambda_2} = -\frac{e^{i\kappa_2} \cos^2 \xi + e^{i\kappa_3} \sin^2 \xi}{|e^{i\kappa_2} \cos^2 \xi + e^{i\kappa_3} \sin^2 \xi|}, \quad e^{i\lambda_3} = \frac{e^{i\kappa_2} \sin^2 \xi + e^{i\kappa_3} \cos^2 \xi}{|e^{i\kappa_2} \sin^2 \xi + e^{i\kappa_3} \cos^2 \xi|}. \quad (4.49)$$

A remnant Klein four flavour symmetry $K_4 \equiv \{1, G_{R1}, G_{R2}, G_{R3}\}$ can be generated by performing two CP transformations, and the three nontrivial residual flavour symmetry transformations G_{Ri} for $i = 1, 2, 3$ can be expressed as

$$\begin{aligned} G_{R1} &= X_{R1} X_{R4}^* = v_1 v_1^T - v_2 v_2^T - v_3 v_3^T, \\ G_{R2} &= X_{R1} X_{R3}^* = -v_1 v_1^T - c_{22} v_2 v_2^T - c_{33} v_3 v_3^T - c_{23} v_2 v_3^T - c_{32} v_3 v_2^T, \\ G_{R3} &= X_{R1} X_{R2}^* = -v_1 v_1^T + c_{22} v_2 v_2^T + c_{33} v_3 v_3^T + c_{23} v_2 v_3^T + c_{32} v_3 v_2^T, \end{aligned} \quad (4.50)$$

with

$$c_{22} = -c_{33} = -\frac{\cos 2\xi}{|e^{i\kappa_2} \cos^2 \xi + e^{i\kappa_3} \sin^2 \xi|}, \quad c_{23} = c_{32}^* = \frac{\cos\left(\frac{\kappa_2 - \kappa_3}{2}\right) e^{i\frac{\kappa_2 - \kappa_3}{2}} \sin 2\xi}{|e^{i\kappa_2} \cos^2 \xi + e^{i\kappa_3} \sin^2 \xi|}. \quad (4.51)$$

In this case, the neutrino mixing matrix U_ν is completely determined by the remnant CP transformations without additional free parameters [267],

$$U_\nu = (v_1, v_2, v_3) \text{diag}(e^{i\frac{\kappa_1}{2}}, e^{i\frac{\kappa_2}{2}}, e^{i\frac{\kappa_3}{2}}) R_{23}(\chi) P_\nu Q_\nu, \quad (4.52)$$

where the angle χ fulfills

$$\tan 2\chi = \cos\left(\frac{\kappa_2 - \kappa_3}{2}\right) \tan 2\xi. \quad (4.53)$$

Notice that the lepton mixing angles and the three CP violating phases are completely fixed by the remnant CP symmetry in this case. Moreover, note that the master *formulae* of Eqs. (4.40, 4.44, 4.52) for U_ν hold irrespective of how the remnant CP symmetry is dynamically realized.

4.3 Residual symmetries of quarks

In this section, we turn to the residual flavour and CP symmetries of the quark mass matrices. The Lagrangian for the quark masses is given in Eq. (1.2). One can easily check that the hermitian combinations $m_U^\dagger m_U$ and $m_D^\dagger m_D$ are invariant under the following unitary transformations [263],

$$U_L \rightarrow G_u U_L, \quad D_L \rightarrow G_d D_L, \quad (4.54)$$

with

$$G_u = V_u \text{diag}(e^{i\alpha_u}, e^{i\alpha_c}, e^{i\alpha_t}) V_u^\dagger, \quad G_d = V_d \text{diag}(e^{i\alpha_d}, e^{i\alpha_s}, e^{i\alpha_b}) V_d^\dagger, \quad (4.55)$$

where α_q ($q = u, d, c, s, t, b$) are arbitrary phase parameters. Hence the following equalities are satisfied,

$$G_u^\dagger m_U^\dagger m_U G_u = m_U^\dagger m_U, \quad G_d^\dagger m_D^\dagger m_D G_d = m_D^\dagger m_D. \quad (4.56)$$

In other words, both the up-quark mass matrix m_U and down-quark mass matrix m_D have a residual $U(1) \times U(1) \times U(1)$ flavour symmetry [263]. Notice that the same conclusion holds true for any Dirac fermion mass matrix, hence it also applies for the charged lepton mass term.

Let us now turn to the discussion of residual CP symmetries of the quark mass term. Assuming the left-handed quarks U_L and D_L transform as

$$U_L(x) \xrightarrow{CP} iX_u \gamma^0 C \bar{U}_L^T(\mathcal{P}x), \quad D_L(x) \xrightarrow{CP} iX_d \gamma^0 C \bar{D}_L^T(\mathcal{P}x), \quad (4.57)$$

this is a symmetry of the quark mass matrices m_U and m_D if and only if $m_U^\dagger m_U$ and $m_D^\dagger m_D$ fulfill the conditions

$$X_u^\dagger m_U^\dagger m_U X_u = (m_U^\dagger m_U)^*, \quad X_d^\dagger m_D^\dagger m_D X_d = (m_D^\dagger m_D)^*. \quad (4.58)$$

Similarly to the charged lepton sector, one can show that X_u and X_d must take the following form

$$X_u = V_u \text{diag} \left(e^{i\beta_u}, e^{i\beta_c}, e^{i\beta_t} \right) V_u^T, \quad X_d = V_d \text{diag} \left(e^{i\beta_d}, e^{i\beta_s}, e^{i\beta_b} \right) V_d^T, \quad (4.59)$$

where β_q ($q = u, d, c, s, t, b$) are real. It is easy to see that both X_u and X_d are unitary symmetric matrices, and that residual flavour symmetries G_u and G_d will be generated by X_u and X_d , respectively. In the basis where the up-quark mass matrix is diagonal, V_u is diagonal, so that V_d coincides with the CKM matrix, $V_d = V_{CKM}$. As a result, the explicit form of the remnant flavour symmetries G_u , G_d and the remnant CP symmetries X_u , X_d can be fixed in terms of the measured values of the CKM matrix elements [28]. As in section 4.2 for lepton sector, the quark mixing matrix can also be fixed by the remnant CP symmetry.

So far we have shown that lepton and quark mass terms generically admit residual flavour and CP symmetries. These are associated to the charged current flavour mixing matrix. One may ask about the origin of these residual symmetries. It is well known that the spontaneous breaking of the $SU(3)_c \otimes SU(2)_L \otimes U(1)_Y$ gauge symmetry preserves the $U(1)$ gauge symmetry associated to electromagnetism. Likewise, one may conjecture that at some high energy scale the true underlying theory has a flavour and CP symmetry which is subsequently broken down to the residual symmetry or a subgroup of it. This gives a further motivation for introducing flavour and CP symmetries, i.e. to explain flavour mixing and CP violation in a model-independent manner. We also saw that the residual flavour symmetry of the charged leptons and quarks should be contained in $U(1) \times U(1) \times U(1)$. The same holds for neutrinos if they are Dirac particles. In contrast, the residual flavour symmetry of the neutrino sector should be a subgroup of $Z_2 \times Z_2 \times Z_2$ if they are Majorana fermions.

In a pioneering work [276], Froggatt and Nielsen originally took the $G_f = U(1)$ flavor symmetry in order to explain the quark mass ratios and the CKM mixing angles, which are expressed as powers of small G_f breaking parameters. This is the so-called FN mechanism. Concerning the lepton sector,

broken flavor symmetries based on non-abelian discrete groups were found to reproduce certain interesting mixing patterns, such as TBM as a first order approximation [53, 54, 70, 313]. Continuous Lie groups $U(2)$ [277, 352–354], $SO(3)$ [287, 355, 356] and $SU(3)$ [293, 357–359] as flavor symmetries were also studied to address the flavor puzzles. Typically, they must be strongly broken.

Besides the use of full-fledged flavor symmetries, there are more phenomenological approaches to the flavor puzzle involving, e.g., the use of texture zeros in the fermion mass matrices [360–363]. Alternatively the assumption of lepton mixing “anarchy” [51, 52]. In the present review, we shall focus on the approach of discrete flavor symmetry as well as generalized CP symmetry.

5 Viable lepton mixing patterns

The “constant” lepton mixing patterns discussed in section 3, such as the tri-bimaximal, golden ratio and bi-maximal mixing, characterized by numerical predictions for the mixing angles and phase, are all ruled out by neutrino oscillation data [24, 25], especially by the precise measurement of the “reactor angle” θ_{13} [305, 306]. They all need to be “revamped” in order to be compatible with experimental data and to enable meaningful theoretical predictions for CP violation.

In this section we assume that neutrinos are Majorana particles and show how the imposition of residual flavour and CP symmetries [257, 258, 265, 364–366] can be used to produce systematic generalizations of the patterns discussed in the section 3. Indeed, imposing the residual symmetries G_i in Sec. 4 fixes the i -th column of the mixing matrix. In this way one can obtain generalized patterns which can be not only viable, but also predictive, in which the mixing matrix is described by just a few parameters. This model-independent approach of predicting new mixing patterns holds irrespective of how the relevant mass matrices arise from first principles. We now describe some examples.

5.1 Revamped TBM mixing

Working in the charged lepton diagonal basis, we start our discussion with the “complex TBM” matrix (cTBM) [367], which is given by

$$U_{cTBM} = \begin{pmatrix} \sqrt{\frac{2}{3}} & \frac{e^{-i\rho}}{\sqrt{3}} & 0 \\ -\frac{e^{i\rho}}{\sqrt{6}} & \frac{1}{\sqrt{3}} & \frac{e^{-i\sigma}}{\sqrt{2}} \\ \frac{e^{i(\rho+\sigma)}}{\sqrt{6}} & -\frac{e^{i\sigma}}{\sqrt{3}} & \frac{1}{\sqrt{2}} \end{pmatrix}. \quad (5.1)$$

This cTBM mixing matrix predicts the same mixing angles as the usual real TBM pattern in Eq. (3.2), though the Majorana phases are non-vanishing. Within the symmetrical parametrization of the lepton mixing matrix in Eqs. (1.21) and (1.22) they are given by

$$\phi_{12} = \rho, \quad \phi_{23} = \sigma. \quad (5.2)$$

The TBM matrix in Eq. (3.1) corresponds to zero Majorana phases $\rho = \sigma = 0$ and hence we call it real TBM¹⁷. From Eq. (4.32), we know the four CP symmetry matrices $X_{1,2,3,4}$ associated with the cTBM mixing pattern are

$$X_i = U_{cTBM} d_i U_{cTBM}^T, \quad (5.3)$$

¹⁷The minus sign of the third row is absorbed into the charged leptons.

where $d_{1,2,3,4}$ are diagonal matrices with entries ± 1 given in Eq. (4.15). Thus the above four CP symmetries are given in matrix form as

$$\begin{aligned}
X_1 &= \frac{1}{6} \begin{pmatrix} 4 - 2e^{-2i\rho} & -2e^{-i\rho} - 2e^{i\rho} & 2e^{i(\rho+\sigma)} + 2e^{-i(\rho-\sigma)} \\ -2e^{-i\rho} - 2e^{i\rho} & -2 + e^{2i\rho} - 3e^{-2i\sigma} & -3e^{-i\sigma} - e^{i(2\rho+\sigma)} + 2e^{i\sigma} \\ 2e^{i(\rho+\sigma)} + 2e^{-i(\rho-\sigma)} & -3e^{-i\sigma} - e^{i(2\rho+\sigma)} + 2e^{i\sigma} & -3 + e^{2i(\rho+\sigma)} - 2e^{2i\sigma} \end{pmatrix}, \\
X_2 &= \frac{1}{6} \begin{pmatrix} -4 + 2e^{-2i\rho} & 2e^{-i\rho} + 2e^{i\rho} & -2e^{i(\rho+\sigma)} - 2e^{-i(\rho-\sigma)} \\ 2e^{-i\rho} + 2e^{i\rho} & 2 - e^{2i\rho} - 3e^{-2i\sigma} & -3e^{-i\sigma} + e^{i(2\rho+\sigma)} - 2e^{i\sigma} \\ -2e^{i(\rho+\sigma)} - 2e^{-i(\rho-\sigma)} & -3e^{-i\sigma} + e^{i(2\rho+\sigma)} - 2e^{i\sigma} & -3 - e^{2i(\rho+\sigma)} + 2e^{2i\sigma} \end{pmatrix}, \\
X_3 &= \frac{1}{6} \begin{pmatrix} -4 - 2e^{-2i\rho} & -2e^{-i\rho} + 2e^{i\rho} & -2e^{i(\rho+\sigma)} + 2e^{-i(\rho-\sigma)} \\ -2e^{-i\rho} + 2e^{i\rho} & -2 - e^{2i\rho} + 3e^{-2i\sigma} & 3e^{-i\sigma} + e^{i(2\rho+\sigma)} + 2e^{i\sigma} \\ -2e^{i(\rho+\sigma)} + 2e^{-i(\rho-\sigma)} & 3e^{-i\sigma} + e^{i(2\rho+\sigma)} + 2e^{i\sigma} & 3 - e^{2i(\rho+\sigma)} - 2e^{2i\sigma} \end{pmatrix}, \\
X_4 &= \frac{1}{6} \begin{pmatrix} 4 + 2e^{-2i\rho} & 2e^{-i\rho} - 2e^{i\rho} & 2e^{i(\rho+\sigma)} - 2e^{-i(\rho-\sigma)} \\ 2e^{-i\rho} - 2e^{i\rho} & 2 + e^{2i\rho} + 3e^{-2i\sigma} & 3e^{-i\sigma} - e^{i(2\rho+\sigma)} - 2e^{i\sigma} \\ 2e^{i(\rho+\sigma)} - 2e^{-i(\rho-\sigma)} & 3e^{-i\sigma} - e^{i(2\rho+\sigma)} - 2e^{i\sigma} & 3 + e^{2i(\rho+\sigma)} + 2e^{2i\sigma} \end{pmatrix}. \tag{5.4}
\end{aligned}$$

The CP symmetries corresponding to the ‘‘standard’’ real TBM matrix of Eq. (3.1) are obtained simply by taking the limit of $\rho, \sigma \rightarrow 0$ in Eq. (5.4). These CP symmetries are therefore given by

$$\begin{aligned}
X_1 &= \frac{1}{3} \begin{pmatrix} 1 & -2 & 2 \\ -2 & -2 & -1 \\ 2 & -1 & -2 \end{pmatrix}, & X_2 &= \frac{1}{3} \begin{pmatrix} -1 & 2 & -2 \\ 2 & -1 & -2 \\ -2 & -2 & -1 \end{pmatrix}, \\
X_3 &= \begin{pmatrix} -1 & 0 & 0 \\ 0 & 0 & 1 \\ 0 & 1 & 0 \end{pmatrix}, & X_4 &= \begin{pmatrix} 1 & 0 & 0 \\ 0 & 1 & 0 \\ 0 & 0 & 1 \end{pmatrix}. \tag{5.5}
\end{aligned}$$

As shown in Eq. (4.34), the residual flavour symmetry can be generated by the CP transformations,

$$\begin{aligned}
G_1 &= X_2 X_3^* = X_3 X_2^* = X_4 X_1^* = X_1 X_4^*, & G_2 &= X_1 X_3^* = X_3 X_1^* = X_4 X_2^* = X_2 X_4^*, \\
G_3 &= X_1 X_2^* = X_2 X_1^* = X_4 X_3^* = X_3 X_4^*, & G_4 &= X_1 X_1^* = X_2 X_2^* = X_3 X_3^* = X_4 X_4^*. \tag{5.6}
\end{aligned}$$

It is our goal here to obtain generalized but restricted forms for the mixing matrices starting from the ‘‘original’’ ones by exploiting residual flavour and CP symmetries. Notice that only three of the four CP and flavour symmetries are really independent [265, 267]. If any three of the four CP symmetries in Eq. (5.4) are imposed simultaneously, the neutrino mixing matrix would be the cTBM matrix in Eq. (5.1) with $\theta_{13} = 0$. Therefore, we will impose only two or only one of these CP symmetries, so that realistic mixing patterns with non-vanishing θ_{13} and CP violation are obtained.

5.1.1 Case a: G_1 flavour and X_1, X_4 CP symmetries

The requirement that the CP transformations X_1 and X_4 are symmetries of the neutrino mass matrix m_ν implies that the G_1 flavour symmetry is preserved and m_ν satisfies

$$X_1^T m_\nu X_1 = m_\nu^*, \quad X_4^T m_\nu X_4 = m_\nu^*. \quad (5.7)$$

Consequently the light neutrino mass matrix is of the following form

$$m'_\nu = U_{cTBM}^T m_\nu U_{cTBM} = \begin{pmatrix} m_1 & 0 & 0 \\ 0 & m_2 & \delta m \\ 0 & \delta m & m_3 \end{pmatrix}, \quad (5.8)$$

where the parameters m_1, m_2, m_3 and δm are real. The mass matrix m'_ν can be diagonalized by a real orthogonal matrix $R_{23}(\theta)$ given by

$$R_{23}(\theta) = \begin{pmatrix} 1 & 0 & 0 \\ 0 & \cos \theta & \sin \theta \\ 0 & -\sin \theta & \cos \theta \end{pmatrix} \quad \text{with} \quad \tan 2\theta = \frac{2\delta m}{m_3 - m_2}. \quad (5.9)$$

As a result, in this case the lepton mixing matrix is given as

$$\begin{aligned} U &= U_{cTBM} R_{23} Q_\nu \\ &= \frac{1}{\sqrt{6}} \begin{pmatrix} 2 & \sqrt{2}e^{-i\rho} \cos \theta & \sqrt{2}e^{-i\rho} \sin \theta \\ -e^{i\rho} & \sqrt{2} \cos \theta - \sqrt{3}e^{-i\sigma} \sin \theta & \sqrt{2} \sin \theta + \sqrt{3}e^{-i\sigma} \cos \theta \\ e^{i(\rho+\sigma)} & -\sqrt{3} \sin \theta - \sqrt{2}e^{i\sigma} \cos \theta & \sqrt{3} \cos \theta - \sqrt{2}e^{i\sigma} \sin \theta \end{pmatrix} Q_\nu, \end{aligned} \quad (5.10)$$

where $Q_\nu = \text{diag}(e^{ik_1\pi/2}, e^{ik_2\pi/2}, e^{ik_3\pi/2})$ is a diagonal unitary matrix with $k_{1,2,3} = 0, 1, 2, 3$. The entries ± 1 and $\pm i$ encode the CP parities of the neutrino states and render the neutrino mass eigenvalues non-negative. From Eq. (5.10) one can then extract the expressions of lepton mixing angles and CP violating phases as follows,

$$\begin{aligned} \sin^2 \theta_{13} &= \frac{\sin^2 \theta}{3}, \quad \sin^2 \theta_{12} = \frac{\cos^2 \theta}{\cos^2 \theta + 2}, \quad \sin^2 \theta_{23} = \frac{1}{2} + \frac{\sqrt{6} \sin 2\theta \cos \sigma}{2 \cos^2 \theta + 4}, \\ \sin \delta^\ell &= -\frac{\text{sign}(\sin 2\theta)(\cos^2 \theta + 2) \sin \sigma}{\sqrt{(\cos^2 \theta + 2)^2 - 6 \sin^2 2\theta \cos^2 \sigma}}, \quad \tan \delta^\ell = \frac{2 + \cos^2 \theta}{2 - 5 \cos^2 \theta} \tan \sigma, \\ \phi_{12} &= \rho + \frac{(k_1 - k_2)\pi}{2}, \quad \phi_{13} = \rho + \frac{(k_1 - k_3)\pi}{2}. \end{aligned} \quad (5.11)$$

Notice that in the symmetric parametrization the CP violating phase characterizing neutrino oscillations is given by the invariant combination $\delta^\ell = \phi_{13} - \phi_{12} - \phi_{23}$ [99], see Eq. (1.22). We see that the first column of the lepton mixing matrix in Eq. (5.10) is $(2, -e^{i\rho}, e^{i(\rho+\sigma)})^T/\sqrt{6}$ which is in common with that of the cTBM mixing pattern. This arises from the preserved G_1 symmetry. Eliminating the parameters

θ and σ in Eq. (5.11), we see that the lepton mixing angles and CP phases are correlated with each other according to

$$\cos^2 \theta_{12} \cos^2 \theta_{13} = \frac{2}{3}, \quad \tan 2\theta_{23} \cos \delta^\ell = \frac{5 \sin^2 \theta_{13} - 1}{2 \sin \theta_{13} \sqrt{2 - 6 \sin^2 \theta_{13}}}. \quad (5.12)$$

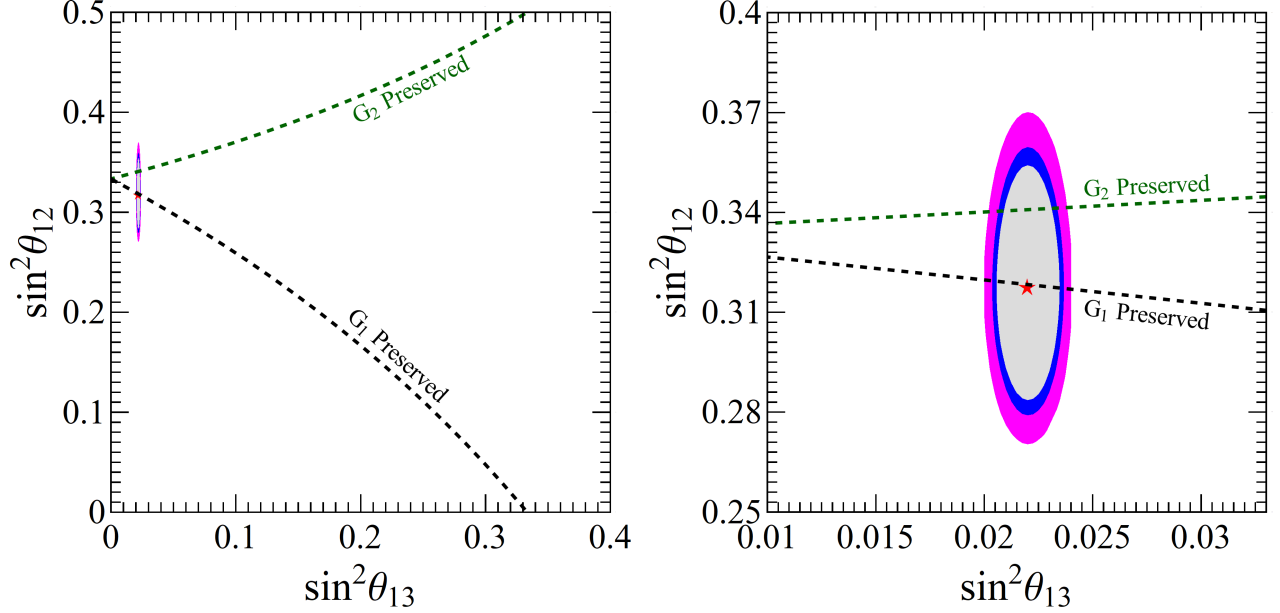


Figure 11: Predicted correlation between $\sin^2 \theta_{12}$ and $\sin^2 \theta_{13}$ in the revamped TBM scheme. The black-dashed line corresponds to the case where G_1 is preserved by the neutrino sector (Eq. (5.12), left), while the green-dashed one refers to the case where G_2 is preserved (Eq. (5.18), left). The right panel is a zoom of the left one. The global fit regions correspond to 90%, 95% and 99% confidence levels [24, 25].

The first equation in Eq. (5.12) relates the solar and the reactor angles while, for given values of the latter, the second equation correlates the CP phase δ^ℓ and the atmospheric angle. These correlations can be used to test the mixing matrix of Eq. (5.10) at current and future oscillation experiments. Notice that these correlations are a generic feature of mass matrices which preserve the G_1 symmetry. These are displayed in figure 11 and figure 12. In the limit of $\rho, \sigma \rightarrow 0$, we see that the mixing angles θ_{12} and θ_{13} remain the same, while the Dirac CP phase vanishes $\sin \delta^\ell \rightarrow 0$, so that CP would be conserved in neutrino oscillations. Notice that both Majorana phases [111] become some integer multiples of $\pi/2$ and therefore they correspond to just CP signs [368, 369].

When the two CP symmetries X_2 and X_3 are imposed, the neutrino mass matrix preserves the flavour symmetry $G_1 = X_2 X_3^* = X_3 X_2^*$ as well. The resulting predictions for lepton mixing parameters are obtained from Eq. (5.11) by redefining $\rho \rightarrow \rho + \pi/2$ and $\sigma \rightarrow \sigma - \pi/2$.

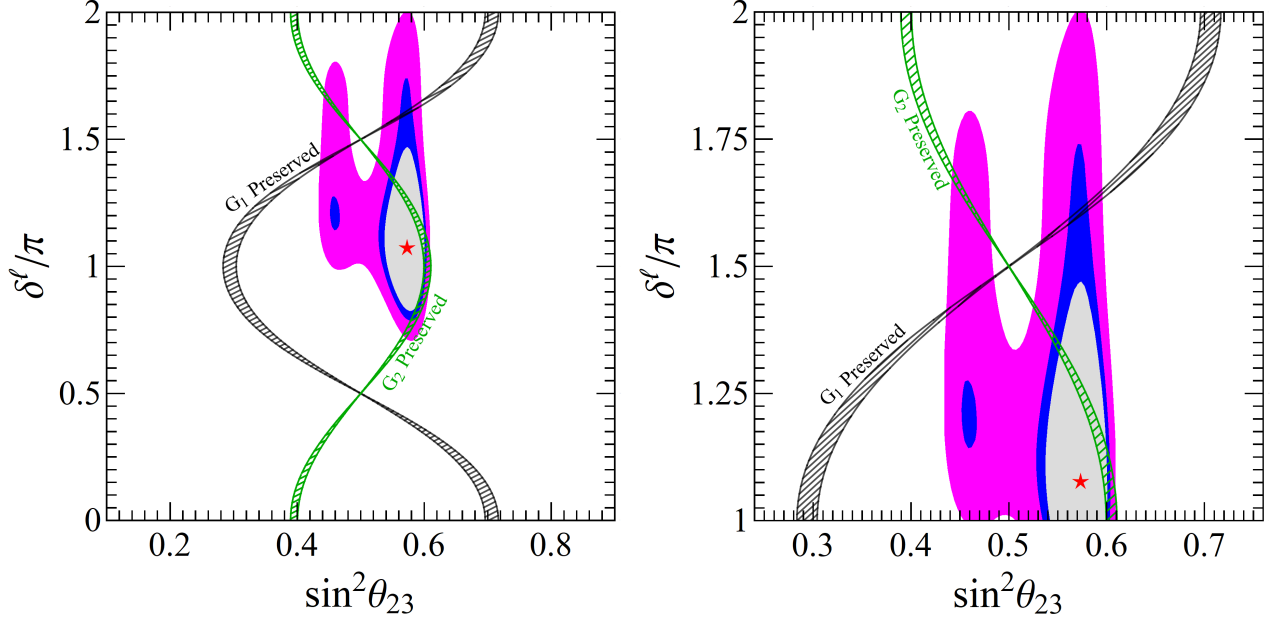


Figure 12: Predicted correlation between δ^ℓ and $\sin^2 \theta_{23}$ in the revamped TBM scheme. The black region corresponds to the case where G_1 is preserved by the neutrino sector, as given by Eq. (5.12), right. The green region corresponds to the case where G_2 is preserved, as given by Eq. (5.18), right. The right panel is a zoom of the left one. The global fit regions correspond to 90%, 95% and 99% confidence levels [24,25].

5.1.2 Case b: G_2 flavour and X_2, X_4 CP symmetries

The combination of X_2 and X_4 leads to the conservation of $G_2 = X_2 X_4^* = X_4 X_2^*$ flavour symmetry. The invariance of neutrino mass matrix under the action of X_2 and X_4 requires

$$X_2^T m_\nu X_2 = m_\nu^*, \quad X_4^T m_\nu X_4 = m_\nu^*, \quad (5.13)$$

from which we can determine the neutrino mass matrix to be of the following form

$$m'_\nu = U_{cTBM}^T m_\nu U_{cTBM} = \begin{pmatrix} m_1 & 0 & \delta m \\ 0 & m_2 & 0 \\ \delta m & 0 & m_3 \end{pmatrix}, \quad (5.14)$$

where $m_{1,2,3}$ and δm are generic real parameters. The matrix m'_ν can be diagonalized by a rotation matrix $R_{13}(\theta)$ in the (13)-plane,

$$R_{13}(\theta) = \begin{pmatrix} \cos \theta & 0 & \sin \theta \\ 0 & 1 & 0 \\ -\sin \theta & 0 & \cos \theta \end{pmatrix} \quad \text{with} \quad \tan 2\theta = \frac{2 \delta m}{m_3 - m_1}. \quad (5.15)$$

Consequently the residual CP symmetries X_2 and X_4 fix the lepton mixing matrix to be

$$\begin{aligned}
U &= U_{cTBM} R_{13}(\theta) Q_\nu \\
&= \frac{1}{\sqrt{6}} \begin{pmatrix} 2 \cos \theta & \sqrt{2} e^{-i\rho} & 2 \sin \theta \\ -e^{i\rho} \cos \theta - \sqrt{3} e^{-i\sigma} \sin \theta & \sqrt{2} & -e^{i\rho} \sin \theta + \sqrt{3} e^{-i\sigma} \cos \theta \\ e^{i(\rho+\sigma)} \cos \theta - \sqrt{3} \sin \theta & -\sqrt{2} e^{i\sigma} & e^{i(\rho+\sigma)} \sin \theta + \sqrt{3} \cos \theta \end{pmatrix} Q_\nu. \quad (5.16)
\end{aligned}$$

Note that the second column of the mixing matrix is $(e^{-i\rho}, 1, -e^{i\sigma})^T / \sqrt{3}$ which matches with that of the cTBM mixing pattern. We can extract the mixing angles and the predicted CP violation phases from Eq. (5.16) in the usual way, leading to

$$\begin{aligned}
\sin^2 \theta_{13} &= \frac{2 \sin^2 \theta}{3}, \quad \sin^2 \theta_{12} = \frac{1}{2 \cos^2 \theta + 1}, \quad \sin^2 \theta_{23} = \frac{1}{2} - \frac{\sqrt{3} \sin 2\theta \cos(\rho + \sigma)}{4 \cos^2 \theta + 2}, \\
\sin \delta^\ell &= -\frac{\text{sign}(\sin 2\theta)(2 \cos^2 \theta + 1) \sin(\rho + \sigma)}{\sqrt{(2 \cos^2 \theta + 1)^2 - 3 \cos^2(\rho + \sigma) \sin^2 2\theta}}, \quad \tan \delta^\ell = \frac{(2 \cos^2 \theta + 1) \tan(\rho + \sigma)}{1 - 4 \cos^2 \theta}, \\
\phi_{12} &= \rho + \frac{(k_1 - k_2)\pi}{2}, \quad \phi_{13} = \frac{(k_1 - k_3)\pi}{2}. \quad (5.17)
\end{aligned}$$

The mixing parameters are again correlated with each other, as follows

$$\sin^2 \theta_{12} \cos^2 \theta_{13} = \frac{1}{3}, \quad \tan 2\theta_{23} \cos \delta^\ell = \frac{\cos 2\theta_{13}}{\sin \theta_{13} \sqrt{2 - 3 \sin^2 \theta_{13}}}. \quad (5.18)$$

These correlations lead to predictions for the oscillations parameters, given in figures 11 and 12.

For the case that the CP symmetries X_1 and X_3 are preserved, the flavour symmetry $G_2 = X_1 X_3^* = X_3 X_1^*$ would be preserved as well¹⁸. The resulting predictions for lepton mixing matrix and mixing parameters can be obtained from Eqs. (5.16, 5.17) by redefining $\rho \rightarrow \rho + \pi/2$, $\sigma \rightarrow \sigma - \pi$.

Finally, if a single CP symmetry is preserved by the neutrino mass matrix, the lepton mixing matrix is determined up to a three dimensional orthogonal matrix. The resulting lepton flavour mixing predictions can be analyzed in a similar fashion [365]. The simple TBM mixing matrix can also be revamped by exploiting the generalized CP symmetries of the charged lepton mass matrix [370].

5.2 Revamped Golden-Ratio mixing scheme

In a way analogous to what we did for the TBM mixing matrix, we can also revamp the Golden-Ratio (GR) mixing pattern. We start from the complex GR mixing matrix, in the charged lepton diagonal basis,

$$U_{cGR} = \frac{1}{\sqrt{2\sqrt{5}\phi_g}} \begin{pmatrix} \sqrt{2}\phi_g & \sqrt{2}e^{-i\rho} & 0 \\ -e^{i\rho} & \phi_g & \sqrt{\sqrt{5}\phi_g} e^{-i\sigma} \\ -e^{i(\rho+\sigma)} & \phi_g e^{i\sigma} & -\sqrt{\sqrt{5}\phi_g} \end{pmatrix}, \quad (5.19)$$

¹⁸The imposition of G_3 is uninteresting here, as it leads to $\theta_{13} = 0$.

which reduces to the real GR mixing matrix of Eq. (3.13) in the limit of $\rho = \sigma = 0$. The four CP symmetry matrices $X_i = U_{cGR} d_i U_{cGR}^T$ associated with the cGR mixing pattern are of the following form,

$$\begin{aligned}
X_1 &= \frac{1}{\sqrt{5}} \begin{pmatrix} 1 + \frac{2i \sin \rho}{\phi_g} e^{-i\rho} & -\sqrt{2} \cos \rho & -\sqrt{2} e^{i\sigma} \cos \rho \\ -\sqrt{2} \cos \rho & -\frac{1+\sqrt{5}e^{-2i\sigma}}{2} + \frac{i \sin \rho}{\phi_g} e^{i\rho} & -\frac{e^{i\sigma} + \sqrt{5}e^{-i\sigma}}{2} + \frac{i \sin \rho}{\phi_g} e^{i(\rho+\sigma)} \\ -\sqrt{2} e^{i\sigma} \cos \rho & -\frac{e^{i\sigma} + \sqrt{5}e^{-i\sigma}}{2} + \frac{i \sin \rho}{\phi_g} e^{i(\rho+\sigma)} & -\frac{e^{2i\sigma} + \sqrt{5}}{2} + \frac{i \sin \rho}{\phi_g} e^{i(\rho+2\sigma)} \end{pmatrix}, \\
X_2 &= \frac{1}{\sqrt{5}} \begin{pmatrix} -1 - \frac{2i \sin \rho}{\phi_g} e^{-i\rho} & \sqrt{2} \cos \rho & \sqrt{2} e^{i\sigma} \cos \rho \\ \sqrt{2} \cos \rho & \frac{1-\sqrt{5}e^{-2i\sigma}}{2} - \frac{i \sin \rho}{\phi_g} e^{i\rho} & \frac{e^{i\sigma} + \sqrt{5}e^{-i\sigma}}{2} - \frac{i \sin \rho}{\phi_g} e^{i(\rho+\sigma)} \\ \sqrt{2} e^{i\sigma} \cos \rho & \frac{e^{i\sigma} + \sqrt{5}e^{-i\sigma}}{2} - \frac{i \sin \rho}{\phi_g} e^{i(\rho+\sigma)} & \frac{e^{2i\sigma} - \sqrt{5}}{2} - \frac{i \sin \rho}{\phi_g} e^{i(\rho+2\sigma)} \end{pmatrix}, \\
X_3 &= \frac{1}{\sqrt{5}} \begin{pmatrix} -1 - \frac{2 \cos \rho}{\phi_g} e^{-i\rho} & \sqrt{2} i \sin \rho & \sqrt{2} i e^{i\sigma} \sin \rho \\ \sqrt{2} i \sin \rho & -\frac{1+\sqrt{5}e^{-2i\sigma}}{2} - \frac{\cos \rho}{\phi_g} e^{i\rho} & -\frac{e^{i\sigma} + \sqrt{5}e^{-i\sigma}}{2} - \frac{\cos \rho}{\phi_g} e^{i(\rho+\sigma)} \\ \sqrt{2} i e^{i\sigma} \sin \rho & -\frac{e^{i\sigma} + \sqrt{5}e^{-i\sigma}}{2} - \frac{\cos \rho}{\phi_g} e^{i(\rho+\sigma)} & -\frac{e^{2i\sigma} + \sqrt{5}}{2} - \frac{\cos \rho}{\phi_g} e^{i(\rho+2\sigma)} \end{pmatrix}, \\
X_4 &= \frac{1}{\sqrt{5}} \begin{pmatrix} 1 + \frac{2 \cos \rho}{\phi_g} e^{-i\rho} & -\sqrt{2} i \sin \rho & -\sqrt{2} i e^{i\sigma} \sin \rho \\ -\sqrt{2} i \sin \rho & \frac{1+\sqrt{5}e^{-2i\sigma}}{2} + \frac{\cos \rho}{\phi_g} e^{i\rho} & \frac{e^{i\sigma} - \sqrt{5}e^{-i\sigma}}{2} + \frac{\cos \rho}{\phi_g} e^{i(\rho+\sigma)} \\ -\sqrt{2} i e^{i\sigma} \sin \rho & \frac{e^{i\sigma} - \sqrt{5}e^{-i\sigma}}{2} + \frac{\cos \rho}{\phi_g} e^{i(\rho+\sigma)} & \frac{e^{2i\sigma} + \sqrt{5}}{2} + \frac{\cos \rho}{\phi_g} e^{i(\rho+2\sigma)} \end{pmatrix}. \tag{5.20}
\end{aligned}$$

Taking the limit of $\rho, \sigma \rightarrow 0$, we obtain

$$\begin{aligned}
X_1 &= \frac{1}{\sqrt{5}} \begin{pmatrix} 1 & -\sqrt{2} & -\sqrt{2} \\ -\sqrt{2} & -\phi_g & 1/\phi_g \\ -\sqrt{2} & 1/\phi_g & -\phi_g \end{pmatrix}, \quad X_2 = \frac{1}{\sqrt{5}} \begin{pmatrix} -1 & \sqrt{2} & \sqrt{2} \\ \sqrt{2} & -1/\phi_g & \phi_g \\ \sqrt{2} & \phi_g & -1/\phi_g \end{pmatrix}, \\
X_3 &= - \begin{pmatrix} 1 & 0 & 0 \\ 0 & 0 & 1 \\ 0 & 1 & 0 \end{pmatrix}, \quad X_4 = \begin{pmatrix} 1 & 0 & 0 \\ 0 & 1 & 0 \\ 0 & 0 & 1 \end{pmatrix}. \tag{5.21}
\end{aligned}$$

The relations between residual flavour and CP symmetries in Eq. (5.6) are fulfilled. If all the four remnant CP transformations in Eq. (5.20) are preserved by the neutrino mass matrix, the complex GR mixing pattern with vanishing θ_{13} would be produced.

Similarly to section 5.1, we consider the scenario of partially preserved remnant CP symmetries. If the CP symmetries X_1, X_4 or X_2, X_3 are preserved in the neutrino sector, the remnant flavour symmetry $G_1 = X_1 X_4^* = X_4 X_1^* = X_2 X_3^* = X_3 X_2^*$ would be conserved as well. As a consequence, the first column of the lepton mixing matrix would be determined to be $(\sqrt{2}\phi_g, -e^{i\rho}, -e^{i(\rho+\sigma)})^T / \sqrt{2\sqrt{5}\phi_g}$, the same as in the cGR mixing. It follows that the relation $\cos^2 \theta_{12} \cos^2 \theta_{13} = \frac{\phi_g}{\sqrt{5}}$ is fulfilled. Using the 3σ allowed range $2.000 \times 10^{-2} \leq \sin^2 \theta_{13} \leq 2.405 \times 10^{-2}$ [24, 25], we find the solar mixing angle must lie in the region $0.2586 \leq \sin^2 \theta_{12} \leq 0.2616$ which doesn't overlap with the experimental 3σ range of θ_{12} [24, 25].

The phenomenologically viable case is found when the CP symmetries X_2, X_4 or X_1, X_3 are preserved by the neutrino mass matrix. The mixing parameters for the latter CP transformation can be obtained from those of the former by redefining $\rho \rightarrow \rho + \pi/2, \sigma \rightarrow \sigma - \pi$. Without loss of generality, we shall focus on preserved CP transformations X_2, X_4 which leads to conservation of the flavour symmetry generated

by the $G_2 = X_2 X_4^* = X_4 X_2^*$ transformation¹⁹. The lepton mixing matrix is found to be

$$U = U_{cGR} R_{13}(\theta) Q_\nu$$

$$= \frac{1}{\sqrt{2\sqrt{5}\phi_g}} \begin{pmatrix} \sqrt{2}\phi_g \cos \theta & \sqrt{2}e^{-i\rho} & \sqrt{2}\phi_g \sin \theta \\ -e^{i\rho} \cos \theta - 5^{1/4}e^{-i\sigma} \sqrt{\phi_g} \sin \theta & \phi_g & -e^{i\rho} \sin \theta + 5^{1/4}e^{-i\sigma} \sqrt{\phi_g} \cos \theta \\ -e^{i(\rho+\sigma)} \cos \theta + 5^{1/4} \sqrt{\phi_g} \sin \theta & e^{i\sigma} \phi_g & -e^{i(\rho+\sigma)} \sin \theta - 5^{1/4} \sqrt{\phi_g} \cos \theta \end{pmatrix} Q_\nu. \quad (5.22)$$

The mixing angles and CP violating phases read as

$$\sin^2 \theta_{13} = \frac{\phi_g \sin^2 \theta}{\sqrt{5}}, \quad \sin^2 \theta_{12} = \frac{1}{1 + \phi_g^2 \cos^2 \theta}, \quad \sin^2 \theta_{23} = \frac{1}{2} - \frac{\sqrt{\sqrt{5}\phi_g \sin 2\theta \cos(\rho + \sigma)}}{2\phi_g^2 \cos^2 \theta + 2},$$

$$\sin \delta^\ell = -\frac{\text{sign}(\sin 2\theta)(\phi_g^2 \cos^2 \theta + 1) \sin(\rho + \sigma)}{\sqrt{(\phi_g^2 \cos^2 \theta + 1)^2 - \sqrt{5}\phi_g \sin^2 2\theta \cos^2(\rho + \sigma)}},$$

$$\tan \delta^\ell = -\frac{(\phi_g^2 \cos^2 \theta + 1) \tan(\rho + \sigma)}{\cos 2\theta + \phi_g^2 \cos^2 \theta}, \quad \phi_{12} = \rho + \frac{(k_1 - k_2)\pi}{2}, \quad \phi_{13} = \frac{(k_1 - k_3)\pi}{2}. \quad (5.23)$$

As a consequence, we can derive the following exact relations among the mixing parameters

$$\sin^2 \theta_{12} \cos^2 \theta_{13} = \frac{1}{\sqrt{5}\phi_g}, \quad \tan 2\theta_{23} \cos \delta^\ell = \frac{\phi_g^2 \cot^2 \theta_{13} - 2}{2\sqrt{\phi_g^2 \cot^2 \theta_{13} - 1}}. \quad (5.24)$$

For the best fit value $\sin^2 \theta_{13} = 2.200 \times 10^{-2}$ [24, 25], we find the solar mixing angle $\sin^2 \theta_{12} = 0.2826$ which is within the 3σ range. The correlations of Eq. (5.24) are displayed in figure 13.

5.3 Bi-large mixing

It is unlikely that any revamping procedure can make the bi-maximal mixing pattern of section 3.4 consistent with the oscillation data, since the measured value of the solar angle θ_{12} deviates too much from the maximal value [24, 25]. The bi-large pattern is phenomenologically motivated by the fact that the smallest lepton mixing angle θ_{13} is similar in magnitude to the largest of the elements of the quark mixing matrix, the Cabibbo angle. It suggests that the latter may act as the universal seed for quark and lepton mixings [371–375]. Bi-large neutrino mixing implies that the lepton and quark sectors may be related with each other, a possible new strategy in the quest for quark-lepton symmetry and unification.

Within the simplest bi-large mixing hypothesis, the solar and atmospheric mixing angles are expressed as [371],

$$\sin \theta_{13} = \lambda, \quad \sin \theta_{12} = s\lambda, \quad \sin \theta_{23} = a\lambda, \quad (5.25)$$

where the small parameter λ is the reactor angle, s and a are free parameters of order one. Using the best fit values of the mixing angles [24, 25], one finds $\lambda \simeq 0.148$, $s \simeq 3.802$ and $a \simeq 5.108$ for normal neutrino mass ordering. Since the bi-large approach describes the structure of the lepton mixing matrix in terms of θ_{13} as input, no revamping is needed.

¹⁹Notice again that imposing G_3 is uninteresting here, as it leads to $\theta_{13} = 0$.

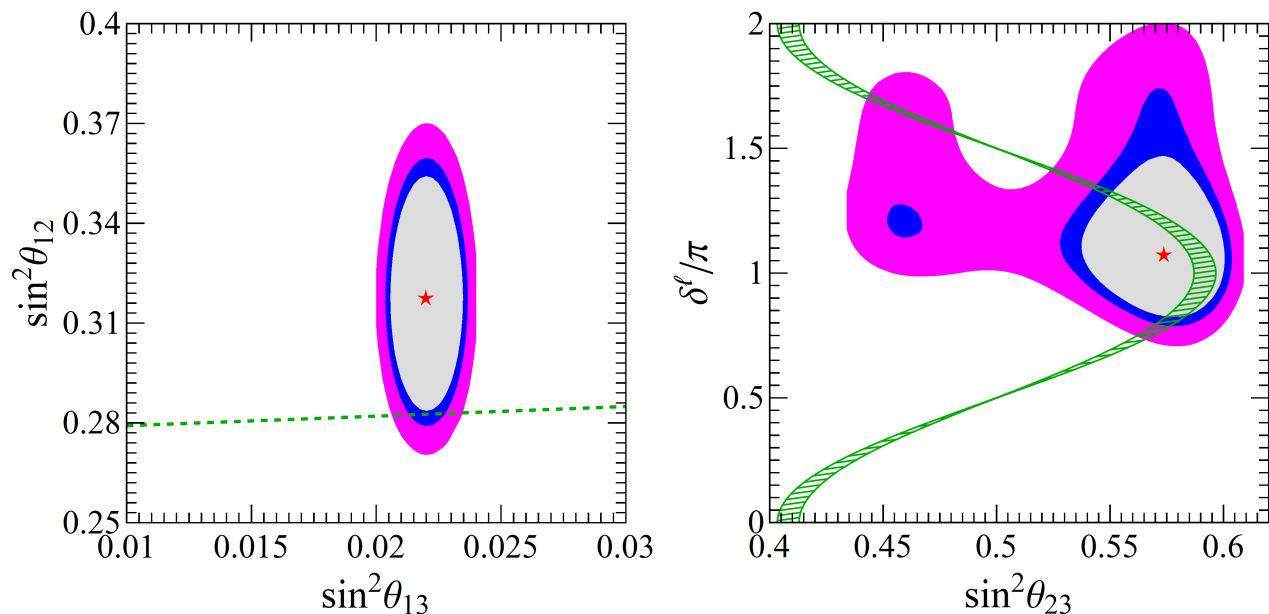


Figure 13: Predicted oscillation parameter correlations in the revamped GR scheme. The “generic” global-fit allowed regions corresponding to 90%, 95% and 99% confidence level are displayed [24, 25].

5.3.1 Bi-large mixing from abelian family symmetry

As shown above, the bi-large mixing ansatz assumes that the three lepton mixing angles are of the same order of magnitude, to first approximation,

$$\text{BL}_1 : \quad \sin \theta_{12} \sim \lambda_c, \quad \sin \theta_{13} \sim \lambda_c, \quad \sin \theta_{23} \sim \lambda_c, \quad (5.26)$$

where $\lambda_c \simeq 0.23$ is the Cabibbo angle [28], and the notation “ \sim ” implies that the above relations contain unknown factors of order one. The freedom in these factors can be used to obtain an adequate description of neutrino mixing. Although global analyses of neutrino oscillation data show preference for the second octant of the atmospheric mixing angle θ_{23} [24, 25], the significance is not yet overwhelming. For θ_{23} in the preferred higher octant, it has been proposed [372] that the bi-large mixing ansatz could be

$$\text{BL}_2 : \quad \sin \theta_{12} \sim \lambda_c, \quad \sin \theta_{13} \sim \lambda_c, \quad \sin \theta_{23} \sim 1 - \lambda_c. \quad (5.27)$$

Here we will show how the above variants of the bi-large mixing patterns can be achieved in a Froggatt-Nielsen-type scenario [276] with an Abelian flavour symmetry. Assuming the presence of two Higgs doublets $H_{u,d}$, and that neutrino masses are described by an effective Weinberg operator we generalize the well-known $U(1)$ flavour symmetry to a larger $U(1) \times Z_m \times Z_n \subset U(1) \times U(1)' \times U(1)''$ family symmetry. In order to break the $U(1)$, Z_m and Z_n flavour groups we assume three flavons Θ_1 , Θ_2 and Θ_3 with horizontal charges $\Theta_1 : (-1, 0, 0)$, $\Theta_2 : (0, -1, 0)$, $\Theta_3 : (0, 0, -1)$, respectively, and their VEVs $\langle \Theta_{1,2,3} \rangle / \Lambda$ scaled by the cutoff Λ are of order λ_c . We assume the horizontal charges of $H_{u,d}$ to be zero.

Fermion masses are then described by the following effective Yukawa couplings [372],

$$\begin{aligned}
\mathcal{W} = & (y_u)_{ij} Q_i U_j^c H_u \left(\frac{\Theta_1}{\Lambda} \right)^{F(Q_i)+F(U_j^c)} \left(\frac{\Theta_2}{\Lambda} \right)^{[Z_m(Q_i)+Z_m(U_j^c)]} \left(\frac{\Theta_3}{\Lambda} \right)^{[Z_n(Q_i)+Z_n(U_j^c)]} \\
& + (y_d)_{ij} Q_i D_j^c H_d \left(\frac{\Theta_1}{\Lambda} \right)^{F(Q_i)+F(D_j^c)} \left(\frac{\Theta_2}{\Lambda} \right)^{[Z_m(Q_i)+Z_m(D_j^c)]} \left(\frac{\Theta_3}{\Lambda} \right)^{[Z_n(Q_i)+Z_n(D_j^c)]} \\
& + (y_e)_{ij} L_i E_j^c H_d \left(\frac{\Theta_1}{\Lambda} \right)^{F(L_i)+F(E_j^c)} \left(\frac{\Theta_2}{\Lambda} \right)^{[Z_m(L_i)+Z_m(E_j^c)]} \left(\frac{\Theta_3}{\Lambda} \right)^{[Z_n(L_i)+Z_n(E_j^c)]} \\
& + (y_\nu)_{ij} \frac{1}{\Lambda} L_i L_j H_u H_u \left(\frac{\Theta_1}{\Lambda} \right)^{F(L_i)+F(L_j)} \left(\frac{\Theta_2}{\Lambda} \right)^{[Z_m(L_i)+Z_m(L_j)]} \left(\frac{\Theta_3}{\Lambda} \right)^{[Z_n(L_i)+Z_n(L_j)]}, \quad (5.28)
\end{aligned}$$

where $F(\psi)$ denotes the $U(1)$ charge of the field ψ , $Z_{m,n}(\psi)$ stand for the $Z_{m,n}$ charge of ψ , and the brackets [...] around the exponents denote that we are modding out by m (n) according to the Z_m (Z_n) addition rule, i.e., $[Z_m(Q_i) + Z_m(U_j^c)] = Z_m(Q_i) + Z_m(U_j^c) \pmod{m}$. Hence fermion mass matrices are expressed in terms of the horizontal charges as follows,

$$\begin{aligned}
(M_u)_{ij} &= (y_u)_{ij} \lambda_c^{F(Q_i)+F(U_j^c)+[Z_m(Q_i)+Z_m(U_j^c)]+[Z_n(Q_i)+Z_n(U_j^c)]} v_u, \\
(M_d)_{ij} &= (y_d)_{ij} \lambda_c^{F(Q_i)+F(D_j^c)+[Z_m(Q_i)+Z_m(D_j^c)]+[Z_n(Q_i)+Z_n(D_j^c)]} v_d, \\
(M_e)_{ij} &= (y_e)_{ij} \lambda_c^{F(L_i)+F(E_j^c)+[Z_m(L_i)+Z_m(E_j^c)]+[Z_n(L_i)+Z_n(E_j^c)]} v_d, \\
(M_\nu)_{ij} &= (y_\nu)_{ij} \lambda_c^{F(L_i)+F(L_j)+[Z_m(L_i)+Z_m(L_j)]+[Z_n(L_i)+Z_n(L_j)]} \frac{v_u^2}{\Lambda}. \quad (5.29)
\end{aligned}$$

If all the horizontal charges are positive, the hierarchical structure of the mass matrices allows a simple order-of-magnitude estimate of the various mass ratios and mixing angles. For instance, the entries of the CKM matrix are estimated to be,

$$(V_{CKM})_{ij} \sim \lambda_c^{F_{\text{eff}}(Q_i)-F_{\text{eff}}(Q_j)\pm\alpha m\pm\beta n}, \quad (5.30)$$

where $F_{\text{eff}}(\psi) = F(\psi) + Z_m(\psi) + Z_n(\psi)$, and $\alpha, \beta = 0, 1$ depends on the charge assignment under Z_m and Z_n . Likewise for the lepton sector, one obtains

$$\sin \theta_{ij} \sim \lambda_c^{F_{\text{eff}}(L_i)-F_{\text{eff}}(L_j)\pm\alpha m\pm\beta n}. \quad (5.31)$$

Notice that the mixing angles can be enhanced or suppressed by $\lambda^{\pm m \pm n}$ relative to the scaling predictions obtained with the continuous $U(1) \times U(1)' \times U(1)''$ family symmetry. Moreover, $U(1) \times Z_m \times Z_n$ reduces to $U(1) \times Z_m$ if $n = 1$, and to the usual $U(1)$ if $m = n = 1$.

- Model for BL_1 mixing

The family symmetry group is $U(1) \times Z_3 \times Z_4$, and we assign the lepton fields to transform under the

flavour symmetry as follows [372],

$$\begin{aligned} L_1 &: (4, 1, 3), & L_2 &: (3, 2, 2), & L_3 &: (1, 1, 1), \\ E_1^c &: (3, 2, 2), & E_2^c &: (1, 2, 2), & E_3^c &: (0, 0, 0). \end{aligned} \quad (5.32)$$

One can then read out the pattern of charged lepton and neutrino mass matrices,

$$M_e \sim \begin{pmatrix} \lambda_c^8 & \lambda_c^6 & \lambda_c^8 \\ \lambda_c^7 & \lambda_c^5 & \lambda_c^7 \\ \lambda_c^7 & \lambda_c^5 & \lambda_c^3 \end{pmatrix} v_d, \quad M_\nu \sim \begin{pmatrix} \lambda_c^{12} & \lambda_c^8 & \lambda_c^7 \\ \lambda_c^8 & \lambda_c^7 & \lambda_c^7 \\ \lambda_c^7 & \lambda_c^7 & \lambda_c^6 \end{pmatrix} \frac{v_u^2}{\Lambda}. \quad (5.33)$$

These give rise to the following mass ratios and lepton mixing angles,

$$\begin{aligned} \frac{m_e}{m_\mu} &\sim \lambda_c^3, & \frac{m_\mu}{m_\tau} &\sim \lambda_c^2, \\ m_1 &\sim \lambda_c^8 \frac{v_u^2}{\Lambda}, & m_2 &\sim \lambda_c^7 \frac{v_u^2}{\Lambda}, & m_3 &\sim \lambda_c^6 \frac{v_u^2}{\Lambda}, \\ \sin \theta_{12} &\sim \lambda_c, & \sin \theta_{13} &\sim \lambda_c, & \sin \theta_{23} &\sim \lambda_c. \end{aligned} \quad (5.34)$$

This way we obtain the BL₁ mixing pattern. A simple numerical analysis with different seed procedures for the order-one Yukawa coefficients, leads to the θ_{23} distributions given in figure 14. One sees that $\sin^2 \theta_{23} < 1/2$ (first octant) is preferred in this case.

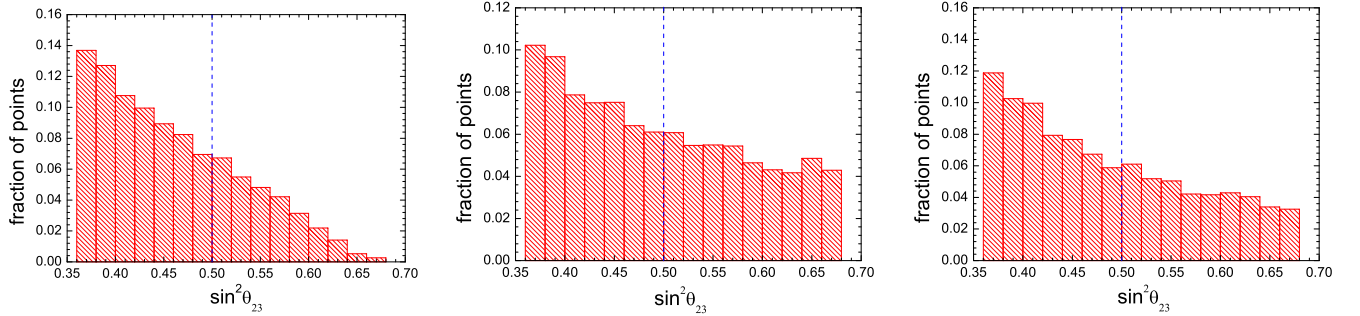


Figure 14: Distributions of the atmospheric neutrino mixing angle θ_{23} in the BL₁ model. The left, middle and right panels are obtained with flat, exponential and Gaussian seed procedures. From [372].

We now extend the model to the quark sector along the lines of $SU(5)$ unification. Each family of standard quarks and leptons is embedded in $SU(5)$ multiplets $\mathbf{10} = (Q, U^c, E^c)$ and $\bar{\mathbf{5}} = (D^c, L)$. The fields within a single $SU(5)$ multiplet transform in the same way under the family symmetry. Therefore the lepton assignment in Eq. (5.32) implies that the quark charges under the flavour group $U(1) \times Z_3 \times Z_4$ should be

$$Q_1 : (3, 2, 2), \quad Q_2 : (1, 2, 2), \quad Q_3 : (0, 0, 0),$$

$$\begin{aligned}
U_1^c &: (3, 2, 2), & U_2^c &: (1, 2, 2), & U_3^c &: (0, 0, 0), \\
D_1^c &: (4, 1, 3), & D_2^c &: (3, 2, 2), & D_3^c &: (1, 1, 1).
\end{aligned} \tag{5.35}$$

Consequently, the up-type and down-type quark mass matrices are given as

$$M_u \sim \begin{pmatrix} \lambda_c^7 & \lambda_c^5 & \lambda_c^7 \\ \lambda_c^5 & \lambda_c^3 & \lambda_c^5 \\ \lambda_c^7 & \lambda_c^5 & 1 \end{pmatrix} v_u, \quad M_d \sim \begin{pmatrix} \lambda_c^8 & \lambda_c^7 & \lambda_c^7 \\ \lambda_c^6 & \lambda_c^5 & \lambda_c^5 \\ \lambda_c^8 & \lambda_c^7 & \lambda_c^3 \end{pmatrix} v_d, \tag{5.36}$$

The resulting quark masses and CKM mixing matrix are determined to follow the pattern

$$\begin{aligned}
m_u &\sim \lambda_c^7 v_u, & m_c &\sim \lambda_c^3 v_u, & m_t &\sim v_u, \\
m_d &\sim \lambda_c^8 v_d, & m_s &\sim \lambda_c^5 v_d, & m_b &\sim \lambda_c^3 v_d, \\
|V_{us}| &\sim \lambda_c^2, & |V_{cb}| &\sim \lambda_c^2, & |V_{ub}| &\sim \lambda_c^4,
\end{aligned} \tag{5.37}$$

which are in agreement with experimental data except $|V_{us}|$, for which an accidental enhancement of $\mathcal{O}(\lambda^{-1})$ amongst the free order-one coefficients is needed so as to reproduce the correct Cabibbo angle.

- Model for BL_2 mixing

Here the flavour symmetry is $U(1) \times Z_2$, and the charge assignments for the quarks and leptons are taken as [372]

$$\begin{aligned}
D_1^c, L_1 &: (3, 0), & D_2^c, L_2 &: (3, 1), & D_3^c, L_3 &: (2, 0), \\
Q_1, U_1^c, E_1^c &: (4, 0), & Q_2, U_2^c, E_2^c &: (2, 1), & Q_3, U_3^c, E_3^c &: (0, 1).
\end{aligned} \tag{5.38}$$

Consequently the neutrino and charged lepton mass matrices take the following form

$$M_e \sim \begin{pmatrix} \lambda_c^7 & \lambda_c^6 & \lambda_c^4 \\ \lambda_c^8 & \lambda_c^5 & \lambda_c^3 \\ \lambda_c^6 & \lambda_c^5 & \lambda_c^3 \end{pmatrix} v_d, \quad M_\nu \sim \begin{pmatrix} \lambda_c^6 & \lambda_c^7 & \lambda_c^5 \\ \lambda_c^7 & \lambda_c^6 & \lambda_c^6 \\ \lambda_c^5 & \lambda_c^6 & \lambda_c^4 \end{pmatrix} \frac{v_u^2}{\Lambda}. \tag{5.39}$$

The charged lepton mass matrix M_e has a ‘‘lopsided’’ structure, and can give the correct order-of-magnitude for the charged lepton masses and a large 2-3 mixing. Combining neutrino and charged lepton diagonalization matrices, the resulting BL_2 lepton mixing pattern is determined as,

$$\sin \theta_{12} \sim \lambda_c, \quad \sin \theta_{13} \sim \lambda_c, \quad \sin \theta_{23} \sim 1. \tag{5.40}$$

Using the master formula of Eq. (5.29) we can easily read off the quark mass matrices as

$$M_u \sim \begin{pmatrix} \lambda_c^8 & \lambda_c^7 & \lambda_c^5 \\ \lambda_c^7 & \lambda_c^4 & \lambda_c^2 \\ \lambda_c^5 & \lambda_c^2 & 1 \end{pmatrix} v_u, \quad M_d \sim \begin{pmatrix} \lambda_c^7 & \lambda_c^8 & \lambda_c^6 \\ \lambda_c^6 & \lambda_c^5 & \lambda_c^5 \\ \lambda_c^4 & \lambda_c^3 & \lambda_c^3 \end{pmatrix} v_d. \quad (5.41)$$

This leads to the following pattern of CKM matrix elements and quark mass ratios,

$$\begin{aligned} |V_{us}| &\sim \lambda_c, & |V_{cb}| &\sim \lambda_c^2, & |V_{ub}| &\sim \lambda_c^3, \\ \frac{m_u}{m_c} &\sim \lambda_c^4, & \frac{m_c}{m_t} &\sim \lambda_c^4, & \frac{m_d}{m_s} &\sim \lambda_c^2, & \frac{m_s}{m_b} &\sim \lambda_c^2, & \frac{m_b}{m_t} &\sim \lambda_c^3, \end{aligned} \quad (5.42)$$

in very good qualitative agreement with observed values.

5.3.2 Confronting bi-large mixing with oscillation data

We now make the bi-large mixing ansatz more predictive. We assume a CP conserving neutrino diagonalization matrix U_ν , with its three angles related to the Cabibbo angle in a simple manner, and a CKM-like charged lepton diagonalization. Under these assumptions we illustrate the predictive power of bi-large mixing [374].

- Constraining bi-large mixing: pattern I

Here the neutrino mixing angles are assumed to be related to the Cabibbo angle as follows [374]

$$\sin \theta_{13} = \lambda_c, \quad \sin \theta_{12} = 2\lambda_c, \quad \sin \theta_{23} = 1 - \lambda_c. \quad (5.43)$$

The Dirac CP phase is taken as $\delta_{CP}^\nu = \pi$ with vanishing Majorana phases. The resulting neutrino diagonalization matrix is given by

$$U_\nu \simeq \begin{pmatrix} 1 - \frac{5\lambda_c^2}{2} & 2\lambda_c & -\lambda_c \\ \lambda_c - 2\sqrt{2}\lambda_c^{3/2} & \sqrt{2}\lambda_c - \frac{\lambda_c^{3/2}}{2\sqrt{2}} & 1 - \lambda_c - \frac{\lambda_c^2}{2} \\ 2\lambda_c + \sqrt{2}\lambda_c^{3/2} & -1 + \lambda_c & \sqrt{2}\lambda_c - \frac{\lambda_c^{3/2}}{2\sqrt{2}} \end{pmatrix}. \quad (5.44)$$

Motivated by $SO(10)$, we take a CKM-type charged lepton diagonalization matrix

$$U_l = R_{23}(\theta_{23}^{CKM}) \Phi R_{12}(\theta_{12}^{CKM}) \Phi^\dagger \simeq \begin{pmatrix} 1 - \frac{\lambda_c^2}{2} & \lambda_c e^{-i\phi} & 0 \\ -\lambda_c e^{i\phi} & 1 - \frac{\lambda_c^2}{2} & A\lambda_c^2 \\ A\lambda_c^3 e^{i\phi} & -A\lambda_c^2 & 1 \end{pmatrix}, \quad (5.45)$$

where $\sin \theta_{12}^{CKM} = \lambda_c$, $\sin \theta_{23}^{CKM} = A\lambda_c^2$, $\lambda_c = 0.22453 \pm 0.00044$ and $A = 0.836 \pm 0.015$ are the Wolfenstein parameters [28], and $\Phi = \text{diag}(e^{-i\phi/2}, e^{i\phi/2}, 1)$ where ϕ is a free phase parameter. One sees that the lepton mixing matrix $U = U_l^\dagger U_\nu$ only depends on a single free phase parameter ϕ , which can in general

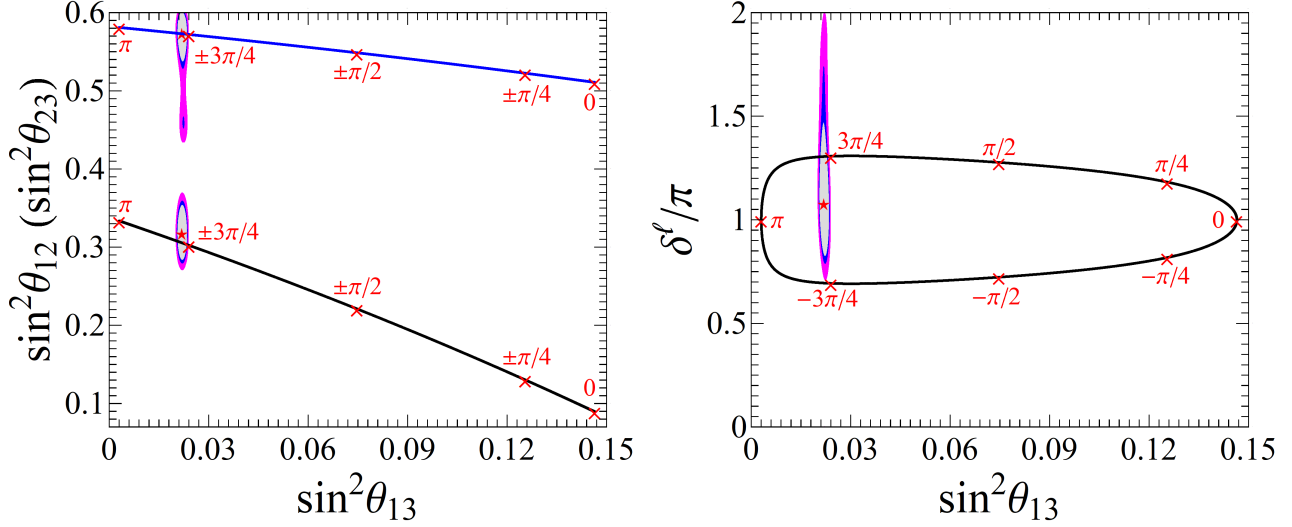


Figure 15: Predicting the solar and atmospheric mixing parameters $\sin^2 \theta_{12}$ (lower, black line) and $\sin^2 \theta_{23}$ (upper, blue line) versus $\sin^2 \theta_{13}$ in the first kind of constrained bi-large mixing scheme. The right panel shows δ^ℓ versus $\sin^2 \theta_{13}$. The allowed 90%, 95% and 99% CL regions of the global oscillation fit are displayed [24, 25]. The crosses correspond to $\phi = 0, \pi, \pm\pi/4, \pm\pi/2, \pm 3\pi/4$.

take values between $-\pi$ and π . The leptonic mixing angles and Jarlskog invariant are found to be

$$\begin{aligned}
\sin^2 \theta_{13} &\simeq 4\lambda_c^2(1 - \lambda_c) \cos^2 \frac{\phi}{2}, \\
\sin^2 \theta_{12} &\simeq 2\lambda_c^2(2 - 2\sqrt{2\lambda_c} \cos \phi + \lambda_c), \\
\sin^2 \theta_{23} &\simeq (1 - \lambda_c)^2 - 2\sqrt{2}A\lambda_c^{\frac{5}{2}} - 2\lambda_c^3(1 + 2 \cos \phi), \\
J_{CP} &\simeq -2(\sqrt{2} + \sqrt{\lambda}) \lambda_c^{5/2} \sin \phi.
\end{aligned} \tag{5.46}$$

We show these correlations in figure 15. They show how the precise measurement of the reactor angle can be promoted to sharp predictions for solar and atmospheric mixing angles. Similarly, the Dirac CP phase is also predicted, up to a two-fold degeneracy.

- Constraining bi-large mixing: pattern II

In this case the bi-large ansatz for the neutrino mixing angles is [374]

$$\sin \theta_{13}^\nu = \lambda_c, \quad \sin \theta_{12}^\nu = 2\lambda_c, \quad \sin \theta_{23}^\nu = 3\lambda_c, \tag{5.47}$$

with $\delta_{CP}^\nu = \pi$ and vanishing Majorana phases. Motivated by $SU(5)$ unification, we take the charged-lepton diagonalization matrix to be of the form

$$U_l = \Phi^\dagger R_{12}^T(\theta_{12}^{CKM}) \Phi R_{23}^T(\theta_{23}^{CKM}) \simeq \begin{pmatrix} 1 - \frac{1}{2}\lambda_c^2 & -\lambda_c e^{i\phi} & A\lambda_c^3 e^{i\phi} \\ \lambda_c e^{-i\phi} & 1 - \frac{1}{2}\lambda_c^2 & -A\lambda_c^2 \\ 0 & A\lambda_c^2 & 1 \end{pmatrix}. \tag{5.48}$$

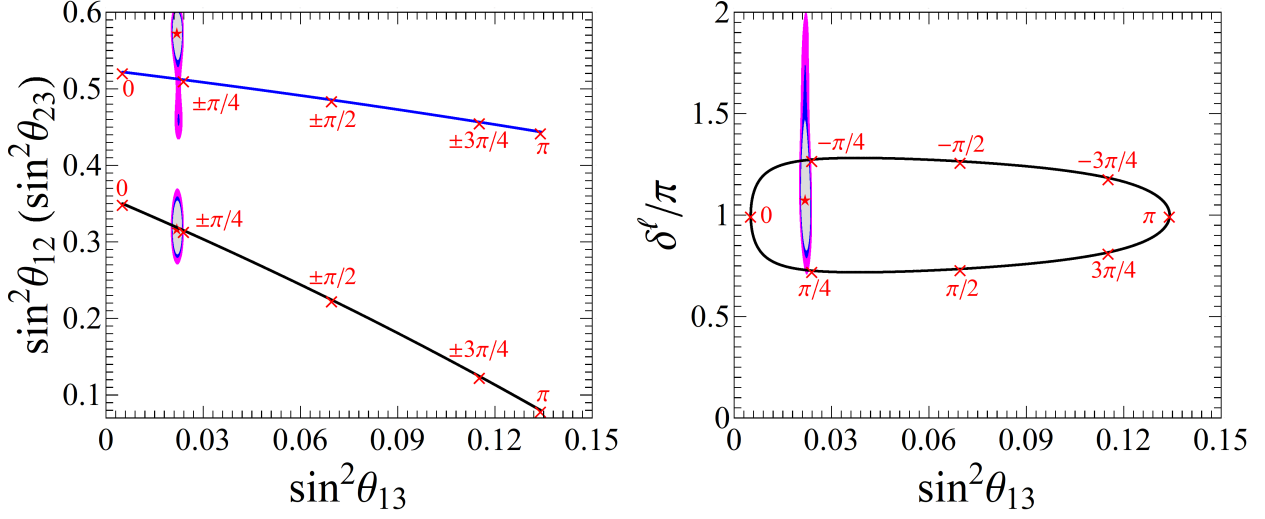


Figure 16: Predicting the solar and atmospheric mixing angles and Dirac phase in the second constrained bi-large mixing scheme. We adopt the same convention as in figure 15.

Taking into account both charged and neutral diagonalizations we can extract the following results for the lepton mixing angles and leptonic Jarlskog invariant,

$$\begin{aligned}
 \sin^2 \theta_{13} &\simeq \lambda_c^2 - 6\lambda_c^3 \cos \phi + 8\lambda_c^4, \\
 \sin^2 \theta_{12} &\simeq \lambda_c^2(5 + 4 \cos \phi) - 2\lambda_c^4(8 + 13 \cos \phi), \\
 \sin^2 \theta_{23} &\simeq 9\lambda_c^2 + 6\lambda_c^3(A + \cos \phi) - \lambda_c^4(8 - 2A \cos \phi - A^2), \\
 J_{CP} &\simeq -[3 + (16 + A)\lambda_c] \lambda_c^3 \sin \phi.
 \end{aligned} \tag{5.49}$$

The resulting correlations between mixing parameters are displayed in figure 16. As before, requiring $\sin^2 \theta_{13}$ in the 3σ range [24, 25], we find that the other oscillation parameters θ_{12} , θ_{23} and δ_{CP} vary in the following regions

$$\begin{aligned}
 0.02000 \leq \sin^2 \theta_{13} \leq 0.02405, & \quad 0.314824 \leq \sin^2 \theta_{12} \leq 0.322459, \\
 0.511755 \leq \sin^2 \theta_{23} \leq 0.513969, & \quad 1.26643 \leq \delta_{CP}/\pi \leq 1.27402.
 \end{aligned} \tag{5.50}$$

6 Lepton mixing from flavour and CP symmetry

Symmetries have been widely used to address the family puzzle. Early attempts employed a $U(1)$ flavour symmetry [276], spontaneously broken by the vacuum expectation value of a singlet scalar field. This would qualitatively account for the small quark mass ratios, as well as mixing angles. With the discovery of neutrino oscillations the idea of flavour symmetry was substantially extended, with many symmetry groups and breaking patterns studied. It has been found that finite discrete flavour groups [376] are particularly suitable to reproduce the large lepton mixing angles and provide non-trivial predictions. The basic theory is assumed to be invariant under a flavour group G_f , but G_f is spontaneously broken into different subgroups G_ν and G_l in the neutrino and charged lepton sectors respectively. This is achieved by the VEVs of a set of scalar fields, and the misalignment between neutrino and charged lepton mass matrices arises from the non-trivial breaking pattern of the flavour symmetry.

Neutrino model building using non-abelian discrete flavor symmetries has been surveyed in a number of dedicated reviews [85–93]. A prime non-abelian discrete flavour symmetry is A_4 [53, 54, 70, 313] which, under some circumstances, leads to the celebrated tri-bimaximal mixing pattern. Although no longer compatible with the experimental measurement of the reactor angle $\theta_{13} \simeq 8.5^\circ$ [21, 22, 303, 305, 306, 377], the simplest A_4 symmetry can, as we saw, be revamped so as to produce viable and predictive patterns of neutrino mixing.

All in all, the idea that lepton mixing emerges from the mismatch of the embedding of the two residual subgroups G_ν and G_l into of the flavour group G_f is still viable, interesting and predictive. In particular, if combining flavour symmetry with the generalized CP symmetry, one can not only accommodate lepton mixing angles but also predict leptonic CP violating phases in terms of few free parameters. In what follows, we shall review the possible schemes of predicting lepton mixing from residual symmetry, emphasizing the role of generalized CP symmetry. The results only depend on the assumed symmetry breaking pattern and are independent of the details of the residual symmetry and the particle content of the flavor symmetry breaking sector, or possible additional symmetries of the theory.

6.1 Lepton mixing from flavour symmetry alone

Within a top-down approach, one imposes a certain flavour symmetry group G_f at some high energy scale. The full Lagrangian is invariant under G_f , which is subsequently broken down to different subgroups G_ν and G_l in the neutrino and charged lepton sectors respectively. The residual symmetry G_l can be any abelian subgroup of G_f , and the same holds for G_ν if neutrinos are Dirac particles. On the other hand G_ν can only be the Klein group K_4 (or a subgroup) for the case of Majorana neutrinos. Throughout this review, we shall focus on the scenario in which G_f is a non-abelian finite discrete group. In general, the three families of left-handed lepton doublets are assigned to an irreducible faithful three-dimensional representation $\rho_{\mathbf{3}}$ of G_f . We assume that the charged lepton and neutrino mass matrices are invariant under the action of the elements of G_l and G_ν , i.e.

$$\rho_{\mathbf{3}}^\dagger(g_l)m_l^\dagger m_l \rho_{\mathbf{3}}(g_l) = m_l^\dagger m_l, \quad g_l \in G_l, \quad (6.1)$$

and

$$\begin{aligned}\rho_{\mathbf{3}}^\dagger(g_\nu)m_\nu^\dagger m_\nu \rho_{\mathbf{3}}(g_\nu) &= m_\nu^\dagger m_\nu, & g_\nu \in G_\nu, & \text{ for Dirac neutrinos,} \\ \rho_{\mathbf{3}}^T(g_\nu)m_\nu \rho_{\mathbf{3}}(g_\nu) &= m_\nu, & g_\nu \in G_\nu, & \text{ for Majorana neutrinos.}\end{aligned}\quad (6.2)$$

Notice that it is sufficient to impose the conditions in Eqs. (6.1) and (6.2) on the generators of G_l and G_ν . Moreover, we see that these conditions imply

$$\left[\rho_{\mathbf{3}}(g_l), m_l^\dagger m_l\right] = 0, \quad \left[\rho_{\mathbf{3}}(g_\nu), m_\nu^\dagger m_\nu\right] = 0. \quad (6.3)$$

As $\rho_{\mathbf{3}}(g_l)$ and $m_l^\dagger m_l$ commute with each other, the unitary transformation U_l that diagonalizes $m_l^\dagger m_l$ also diagonalizes $\rho_{\mathbf{3}}(g_l)$ up to permutations and phases of columns

$$U_l^\dagger \rho_{\mathbf{3}}(g_l) U_l = \text{diag}(e^{i\alpha_e}, e^{i\alpha_\mu}, e^{i\alpha_\tau}). \quad (6.4)$$

Since g_l is an element of the discrete flavour symmetry group G_f , the $e^{i\alpha_{e,\mu,\tau}}$ are all roots of unity. Analogously $\rho_{\mathbf{3}}(g_\nu)$ and $m_\nu^\dagger m_\nu$ (or m_ν) are diagonalized by the same matrix U_ν ,

$$U_\nu^\dagger \rho_{\mathbf{3}}(g_\nu) U_\nu = \begin{cases} \text{diag}(e^{i\beta_e}, e^{i\beta_\mu}, e^{i\beta_\tau}), & \text{for Dirac neutrinos,} \\ \text{diag}(\pm 1, \pm 1, \pm 1), & \text{for Majorana neutrinos,} \end{cases} \quad (6.5)$$

where $\beta_{e,\mu,\tau}$ are rational multiples of π . Then the lepton mixing matrix U is determined as

$$U = U_l^\dagger U_\nu \quad (6.6)$$

up to independent row and column permutations. In short, given a family symmetry group G_f and the residual subgroups G_l and G_ν , the unitary transformations U_l and U_ν as well as the lepton matrix U can be obtained by diagonalizing the representation matrices of the generators of G_l and G_ν , as illustrated in the figure 17. In practice, we only need to find the eigenvectors of $\rho_{\mathbf{3}}(g_l)$ and $\rho_{\mathbf{3}}(g_\nu)$ that form the column vectors of U_l and U_ν . In this approach, it is not necessary to construct the explicit form of the mass matrices $m_l^\dagger m_l$ and $m_\nu^\dagger m_\nu$ (or m_ν) although this can be accomplished in a straightforward manner. Since the lepton masses cannot be predicted in this framework, in particular the neutrino mass spectrum can have either normal ordering or inverted ordering, the unitary matrices U_l and U_ν are uniquely fixed up to permutations and phases of their column vectors. As a consequence, the lepton mixing matrix U is determined up to independent row and column permutations and arbitrary phase matrices multiplied from the left and right sides. Therefore the Majorana CP phases are not constrained by the residual flavour symmetry.

Notice that if we switch the roles of the subgroups G_ν and G_l , the lepton matrix U would become its Hermitian conjugate. If two pairs of subgroups $\{G_l, G_\nu\}$ and $\{G'_l, G'_\nu\}$ are conjugate²⁰, both residual

²⁰The two pairs of groups are conjugate if their generators g_e, g_ν and g'_e, g'_ν are related by group conjugacy, i.e., $g'_l = h g_l h^{-1}$,

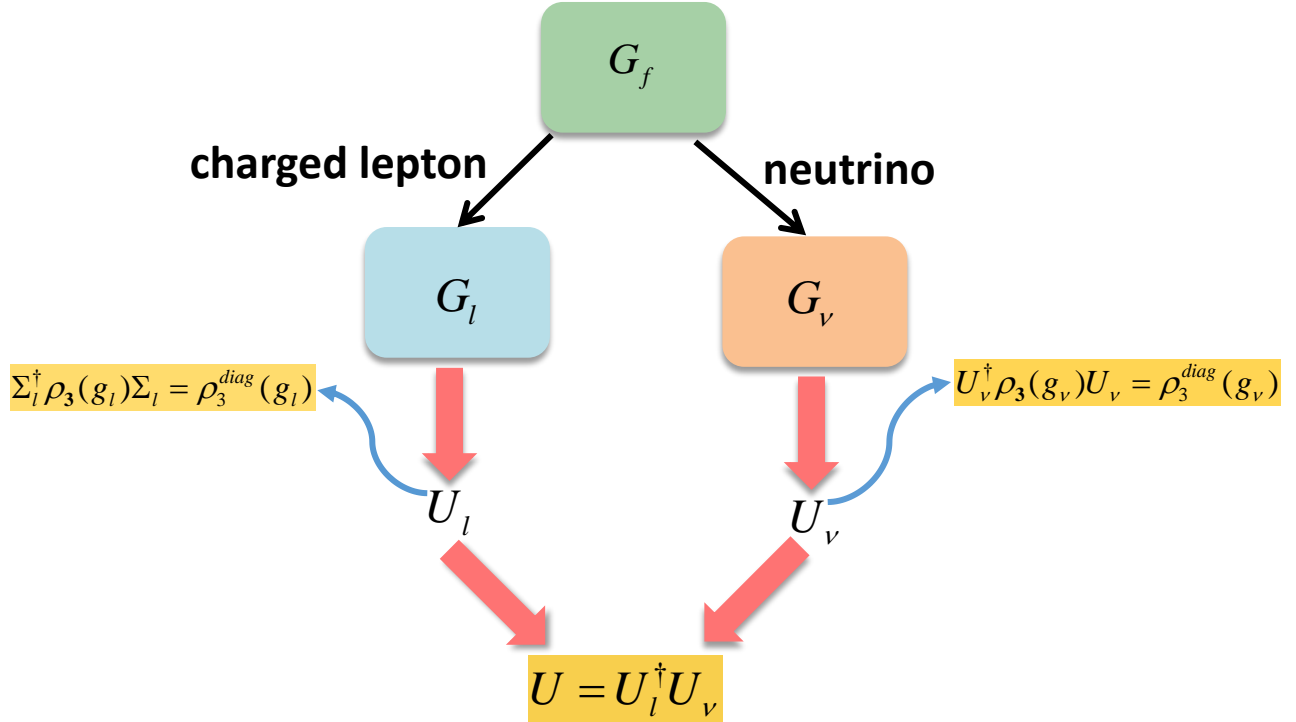


Figure 17: Model-independent predictions for the lepton mixing matrix from the flavour symmetry G_f broken to different residual subgroups G_l and G_ν in the neutrino and charged lepton sectors. Here g_l and g_ν are G_l and G_ν generators, respectively. See text for details.

symmetries would lead to the same result for the lepton mixing matrix. The reason is that if the generators of G_l and G_ν are diagonalized by U_l and U_ν respectively, $\rho_3(h)U_l$ and $\rho_3(h)U_\nu$ would diagonalize those of G'_l and G'_ν . On the other hand, if the left-handed lepton fields are assigned to the complex-conjugate of the triplet representation, the lepton mixing matrix would be complex conjugated, so that the predictions for the lepton mixing angles are unchanged and the signs of the CP violation phases are inverted.

6.1.1 Fully preserved residual symmetry $G_\nu = K_4$

As already mentioned, if the flavour group G_f is of finite order and the residual symmetries G_l and G_ν distinguish the three families of charged leptons and neutrinos then the lepton mixing matrix would be completely determined by the residual symmetries, regardless of the lepton masses or any other parameter of the underlying theory [259–263]. This is the so-called direct model building approach [88, 378]. This happens, for instance, if G_ν is the Klein group K_4 and G_l is a cyclic group Z_n with $n \geq 3$ or the product of several cyclic groups. A complete classification of all resulting mixing matrices has been performed by using theorems on roots of unity [261]. One finds that the lepton mixing matrix can take 17 sporadic patterns plus one infinite series, and only the latter could be compatible with the experimental data,

$g'_\nu = hg_\nu h^{-1}$, where h is an element of G_f .

given as [261, 263]

$$U = \frac{1}{\sqrt{3}} \begin{pmatrix} \sqrt{2} \cos \theta & 1 & -\sqrt{2} \sin \theta \\ -\sqrt{2} \cos(\theta - \frac{\pi}{3}) & 1 & \sqrt{2} \sin(\theta - \frac{\pi}{3}) \\ -\sqrt{2} \cos(\theta + \frac{\pi}{3}) & 1 & \sqrt{2} \sin(\theta + \frac{\pi}{3}) \end{pmatrix}, \quad (6.7)$$

where θ is a rational multiple of π , with its exact value completely determined by group-theoretical considerations. This result is consistent with comprehensive scanning over the finite groups and possible symmetry breaking patterns [262, 263, 379]. We obtain the following expressions for the lepton mixing angles

$$\sin^2 \theta_{13} = \frac{2}{3} \sin^2 \theta, \quad \sin^2 \theta_{12} = \frac{1}{1 + 2 \cos^2 \theta}, \quad \sin^2 \theta_{23} = \frac{2 \sin^2(\theta - \frac{\pi}{3})}{1 + 2 \cos^2 \theta}. \quad (6.8)$$

Combining the above equations one sees that the three mixing angles depend on a single parameter θ , consequently the following relations must be satisfied,

$$3 \sin^2 \theta_{12} \cos^2 \theta_{13} = 1, \quad \sin^2 \theta_{23} = \frac{1}{2} \pm \frac{1}{2} \tan \theta_{13} \sqrt{2 - \tan^2 \theta_{13}}. \quad (6.9)$$

Using the best fit value of the reactor mixing angle $\sin^2 \theta_{13} \simeq 0.022$ for NO [24, 25] we get

$$\sin^2 \theta_{12} \simeq 0.341, \quad \sin^2 \theta_{23} \simeq 0.605 \text{ or } 0.395. \quad (6.10)$$

The value of solar mixing angle is within the experimentally preferred 2σ region, the atmospheric angle $\sin^2 \theta_{23} \simeq 0.605$ lies in the 3σ region, while another possible value $\sin^2 \theta_{23} \simeq 0.395$ is disfavored by the present data [24, 25]. As regards the CP violation phases, the Majorana phases are unconstrained²¹ and the Dirac CP phase vanishes

$$\sin \delta_{CP} = 0. \quad (6.11)$$

Notice that current measurements still do not provide a fully robust global CP determination [24, 25].

In order to reproduce the experimentally favored mixing angles the minimal flavour symmetry group is $G_f = (Z_{18} \times Z_6) \times S_3$ [260, 263] for Majorana neutrinos, while for Dirac neutrinos the minimal flavour group is $G_f = (Z_9 \times Z_3) \times S_3$ [263]. Hence the order of the flavour symmetry group should be at least 648 and 162 for Majorana and Dirac neutrinos, respectively, leading to a realistic value of $\theta = \pi/18$. In concrete models, the residual symmetries G_l and G_ν are spoiled by higher order terms involving flavon fields. These induce corrections suppressed by the flavon VEVs with respect to the flavor scale.

6.1.2 Partially preserved residual symmetry $G_\nu = Z_2$

The idea of partially preserved residual symmetry was proposed [381–384] in order to accommodate a non-zero Dirac CP violation phase δ^ℓ and degrade the order of the flavour symmetry. In this approach, part of the residual symmetry of the neutrino mass matrix arises from the assumed flavour symmetry at

²¹One can predict the values of Majorana phases by including the generalized CP symmetry. For instance, for the flavor symmetry $\Delta(6n^2) = (Z_n \times Z_n) \times S_3$ in combination with CP, the Majorana phase ϕ_{12} can take several discrete values for each n , namely ϕ_{13} is a multiple of $\pi/2$ [380] if residual K_4 flavor symmetry and CP symmetry are preserved by neutrino mass matrix.

high the energy scale. A widely studied scenario is that a Z_2 (instead of K_4) subgroup is preserved in the neutrino sector, i.e. the residual group is $G_\nu = Z_2^{g_\nu}$, where g_ν refers to the generator of G_ν . Note that the presentation rule of the cyclic group Z_n^g is $Z_n^g \equiv \{1, g, g^2, \dots, g^{n-1}\}$.

The invariance of the neutrino mass matrix under $Z_2^{g_\nu}$ requires that Eq. (6.2) holds. Consequently the residual flavour symmetry imposes the following restriction on the unitary transformation

$$U_\nu^\dagger \rho_{\mathbf{3}}(g_\nu) U_\nu = \pm P_\nu^T \text{diag}(1, -1, -1) P_\nu, \quad (6.12)$$

where P_ν is a permutation matrix, and we have taken into account that the eigenvalues of $\rho_{\mathbf{3}}(g_\nu)$ is $+1$ or -1 , since g_ν is of order two. Let us denote U_0 as a diagonalization matrix of $\rho_{\mathbf{3}}(g_\nu)$ with

$$U_0^\dagger \rho_{\mathbf{3}}(g_\nu) U_0 = \pm \text{diag}(1, -1, -1), \quad (6.13)$$

Then the unitary transformation U_ν would be of the form

$$U_\nu = U_0 U_{23}(\theta, \delta) P_\nu, \quad (6.14)$$

where $U_{23}(\theta, \delta)$ is a block diagonal complex unitary rotation,

$$U_{23}(\theta, \delta) = \begin{pmatrix} 1 & 0 & 0 \\ 0 & \cos \theta & \sin \theta e^{-i\delta} \\ 0 & -\sin \theta e^{i\delta} & \cos \theta \end{pmatrix}. \quad (6.15)$$

Notice that, since the residual Z_2 flavour symmetry can not fully distinguish the three neutrino families in this case, only one column of U_ν is numerically fixed. In the charged lepton sector, a residual subgroup G_l is preserved, so that the unitary transformation U_l obeys the condition $U_l^\dagger \rho_{\mathbf{3}}(g_l) U_l = \text{diag}(e^{i\alpha_e}, e^{i\alpha_\mu}, e^{i\alpha_\tau})$ as shown in Eq. (6.4), where $\alpha_{e,\mu,\tau}$ are rational multiples of π . Thus the assumed residual symmetry allows us to determine the lepton mixing matrix in terms of two free parameters as

$$U = U_l^\dagger U_0 U_{23}(\theta, \delta) P_\nu. \quad (6.16)$$

Hence only one column is fixed by residual symmetry in this case, and this is dubbed semi-direct approach in [88]. For example, if the flavour group is S_4 and the residual symmetries are chosen as $G_\nu = Z_2^{SU}$ and $G_l = Z_3^T$, then $U_0 = U_{TBM}$ and the lepton mixing is

$$U = \frac{1}{\sqrt{6}} \begin{pmatrix} 2 & \sqrt{2} \cos \theta & \sqrt{2} e^{-i\delta} \sin \theta \\ -1 & \sqrt{2} \cos \theta - \sqrt{3} e^{i\delta} \sin \theta & \sqrt{3} \cos \theta + \sqrt{2} e^{-i\delta} \sin \theta \\ -1 & \sqrt{2} \cos \theta + \sqrt{3} e^{i\delta} \sin \theta & -\sqrt{3} \cos \theta + \sqrt{2} e^{-i\delta} \sin \theta \end{pmatrix}. \quad (6.17)$$

We see that the first column is $(2/\sqrt{6}, -1/\sqrt{6}, -1/\sqrt{6})^T$ which is in common with the TBM mixing pattern [296–298]. In fact, this is exactly the TM1 lepton mixing matrix in Eq. (3.7) [316–318]. In

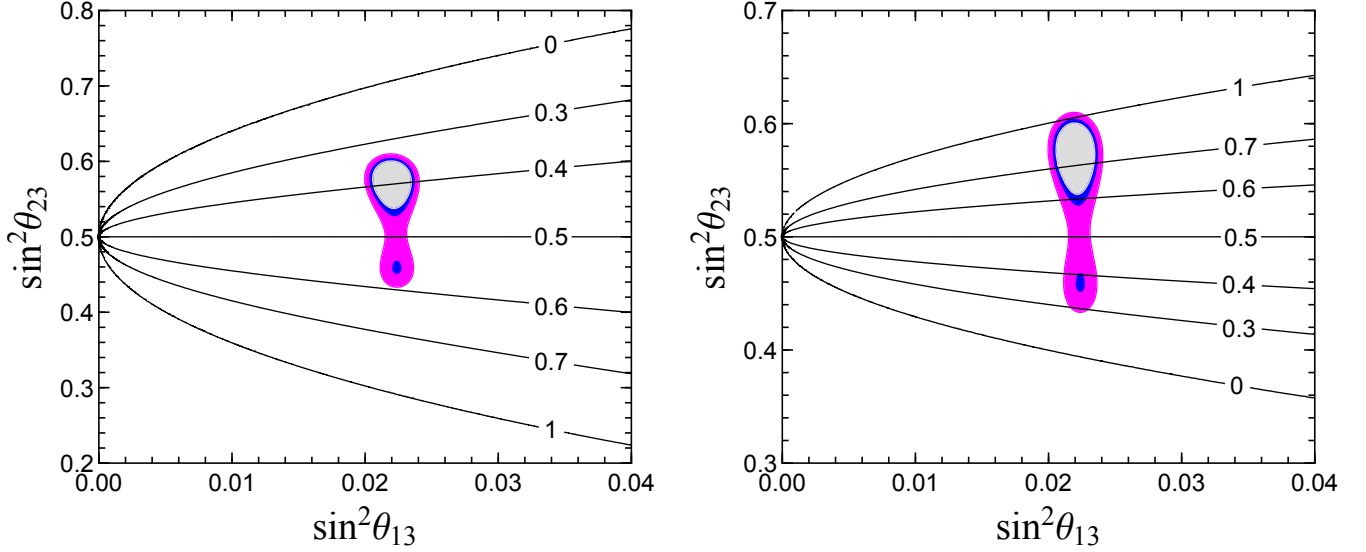


Figure 18: Contours of $|\delta_{CP}/\pi|$ in the $\sin^2 \theta_{23} - \sin^2 \theta_{13}$ plane. The left panel is for the case that the fixed column is $(2/\sqrt{6}, -1/\sqrt{6}, -1/\sqrt{6})^T$ (TM1), and the right panel is for $(1/\sqrt{3}, 1/\sqrt{3}, 1/\sqrt{3})^T$ (TM2). The global-fit allowed oscillation regions corresponding to 90%, 95% and 99% confidence level are shown [24, 25]

figure 18 we plot the contour of $|\delta_{CP}|$ in the plane $\sin^2 \theta_{23}$ versus $\sin^2 \theta_{13}$. The value of the Dirac CP phase δ_{CP} is not too constrained, as long as the atmospheric mixing angle θ_{23} remains poorly measured.

On the other hand, if the residual groups are $G_\nu = Z_2^S$ and $G_l = Z_3^T$ for either A_4 or S_4 flavour symmetry, one column of the lepton mixing matrix is enforced to be $(1/\sqrt{3}, 1/\sqrt{3}, 1/\sqrt{3})^T$ with,

$$U = \frac{1}{\sqrt{6}} \begin{pmatrix} 2 \cos \theta & \sqrt{2} & 2e^{-i\delta} \sin \theta \\ -\cos \theta - \sqrt{3} e^{i\delta} \sin \theta & \sqrt{2} & \sqrt{3} \cos \theta - e^{-i\delta} \sin \theta \\ -\cos \theta + \sqrt{3} e^{i\delta} \sin \theta & \sqrt{2} & -\sqrt{3} \cos \theta - e^{-i\delta} \sin \theta \end{pmatrix}, \quad (6.18)$$

which is exactly the tri-maximal mixing pattern TM2 in Eq. (3.10) [252, 321–323]. The predictions for the Dirac phase δ_{CP} are shown in figure 18. The figure refers to the case of normal mass ordering, with very similar results for the case of inverse-ordered masses.

6.2 Combining flavour and CP symmetry

We saw how a non-vanishing Dirac CP phase can be obtained if a Z_2 rather than the Klein group K_4 is the residual flavour symmetry preserved by the neutrino mass matrix. However, δ_{CP} can vary within a wide region. Moreover, the Majorana phases can not be predicted just from the flavour symmetry. In order to understand the CP violating phases, one can impose a generalized CP (gCP) symmetry [341–343], see [264, 344, 385] for discussions of gCP to the lepton flavor mixing problem. A simple example is the $\mu - \tau$ reflection symmetry [252–256], see Ref. [386] for review. The $\mu - \tau$ reflection symmetry is a combination of the canonical CP transformation with the $\mu - \tau$ exchange symmetry, which exchanges a muon (tau)

neutrino with a tau (muon) antineutrino,

$$\begin{pmatrix} \nu_e \\ \nu_\mu \\ \nu_\tau \end{pmatrix} \mapsto \begin{pmatrix} \nu_e^c \\ \nu_\tau^c \\ \nu_\mu^c \end{pmatrix} = \begin{pmatrix} 1 & 0 & 0 \\ 0 & 0 & 1 \\ 0 & 1 & 0 \end{pmatrix} \begin{pmatrix} \nu_e^c \\ \nu_\mu^c \\ \nu_\tau^c \end{pmatrix}. \quad (6.19)$$

Notice that the generalized CP transformation matrix is not diagonal in family space. In the charged lepton mass basis, the neutrino mass matrix invariant under $\mu - \tau$ reflection has the following form

$$m_\nu = \begin{pmatrix} a & b & b^* \\ b & c & d \\ b^* & d & c^* \end{pmatrix}, \quad (6.20)$$

where a and d are real, b and c are complex numbers. As a result, both atmospheric mixing angle θ_{23} and Dirac CP phase would be maximal, while Majorana phases take CP conserving values. These should be contrasted with present neutrino oscillation data [24, 25]. Deviations of θ_{23} and δ_{CP} from maximal values can easily arise from a more general $\mu - \tau$ reflection symmetry acting on the neutrino sector. Such CP transformation is of the following form [257],

$$\begin{pmatrix} \nu_e \\ \nu_\mu \\ \nu_\tau \end{pmatrix} \mapsto \begin{pmatrix} \nu_e^c \\ \cos \Theta \nu_\mu^c + i \sin \Theta \nu_\tau^c \\ \cos \Theta \nu_\tau^c + i \sin \Theta \nu_\mu^c \end{pmatrix} = \begin{pmatrix} 1 & 0 & 0 \\ 0 & \cos \Theta & i \sin \Theta \\ 0 & i \sin \Theta & \cos \Theta \end{pmatrix} \begin{pmatrix} \nu_e^c \\ \nu_\mu^c \\ \nu_\tau^c \end{pmatrix}, \quad (6.21)$$

where the angle Θ characterizes the CP transformation. It reduces to the $\mu - \tau$ reflection symmetry in the limit of $\Theta = \pi/2$. The atmospheric mixing angle θ_{23} and Dirac phase δ_{CP} are predicted to be strongly correlated as follows [257],

$$\sin^2 \delta_{CP} \sin^2 2\theta_{23} = \sin^2 \Theta, \quad (6.22)$$

while the Majorana phases take on trivial CP conserving values. The correlation in Eq. (6.22) allows us to predict the range of the Dirac CP violating phase $|\sin \delta_{CP}|$ as a function of the parameter Θ as shown in figure 19. Note that the sign of δ_{CP} can not be fixed.

6.2.1 Mathematical consistency

Family symmetries can be generated if one successively performs two generalized CP transformations. Hence generalized CP symmetries can be thought of as associated to some underlying flavour symmetry. A convenient strategy for defining such CP transformations is to start from a flavour symmetry group G_f and find all possible CP transformations H_{CP} which can generate the given flavour group transformations. The purpose of this section is to determine the restricted lepton mixing matrices that can be obtained from discrete flavour and CP symmetries.

It is highly non-trivial to define a CP transformation consistently in the presence of a family symmetry G_f [264, 344, 385, 387]. Let us consider a set of fields φ in a generic irreducible representation \mathbf{r} of G_f ,

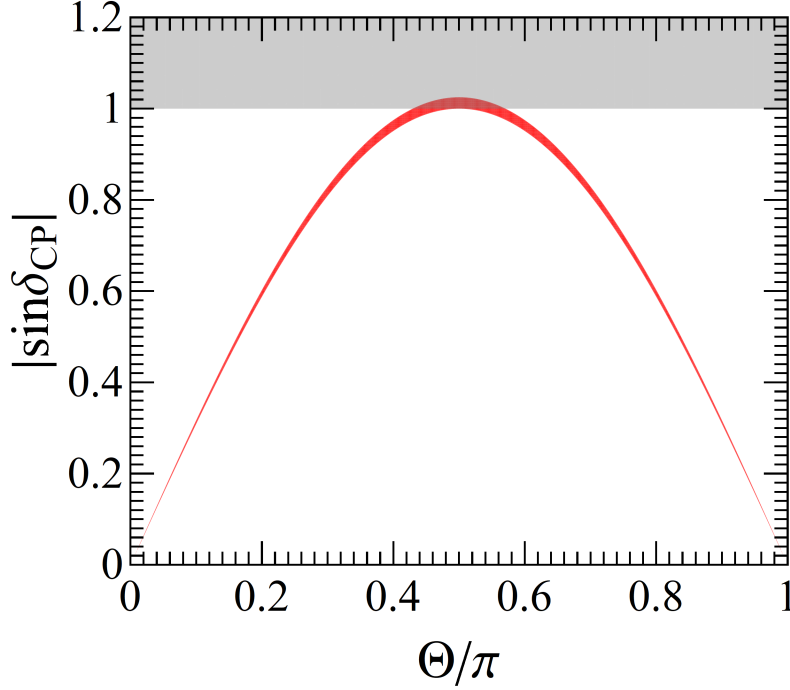


Figure 19: $|\sin \delta_{CP}|$ regions versus Θ characterizing the generalized $\mu - \tau$ reflection, where θ_{23} is required to lie in its 3σ allowed range [24, 25].

transforming under the action of G_f as

$$\varphi(x) \xrightarrow{G_f} \rho_{\mathbf{r}}(g)\varphi(x), \quad g \in G_f, \quad (6.23)$$

where $\rho_{\mathbf{r}}(g)$ denotes the representation matrix for any element g in the irreducible representation \mathbf{r} . The generalized CP acts on φ as

$$\varphi(x) \xrightarrow{\mathcal{CP}} X_{\mathbf{r}} \varphi^*(x_{\mathcal{P}}), \quad (6.24)$$

where $x_{\mathcal{P}} = (t, -\vec{x})$, and $X_{\mathbf{r}}$ is the CP transformation matrix in flavor space, assumed to be a unitary matrix, so as to leave the kinetic term invariant²². A physical CP transformation should map each field $\varphi(x)$ in any irreducible representation \mathbf{r} of G_f into its complex conjugate $\varphi^*(x_{\mathcal{P}})$ in the complex representation \mathbf{r}^* [387]. If we first perform a CP transformation, then apply a flavour symmetry transformation, and subsequently an inverse CP transformation we obtain

$$\varphi(x) \xrightarrow{\mathcal{CP}} X_{\mathbf{r}} \varphi^*(x_{\mathcal{P}}) \xrightarrow{G_f} X_{\mathbf{r}} \rho_{\mathbf{r}^*}(g) \varphi^*(x_{\mathcal{P}}) \xrightarrow{\mathcal{CP}^{-1}} X_{\mathbf{r}} \rho_{\mathbf{r}^*}(g) X_{\mathbf{r}}^{-1} \varphi(x). \quad (6.25)$$

As shown in figure 20, the theory should still be invariant since it is invariant under each transformation individually. To make the theory consistent the resulting net transformation should be equivalent to a flavour symmetry transformation $\rho_{\mathbf{r}}(g')$ of some flavour group element g' , i.e.

$$X_{\mathbf{r}} \rho_{\mathbf{r}^*}(g) X_{\mathbf{r}}^{-1} = \rho_{\mathbf{r}}(g'), \quad g, g' \in G_f \quad (6.26)$$

²²When φ denotes a spinor, the obvious action of CP on the spinor indices is understood.

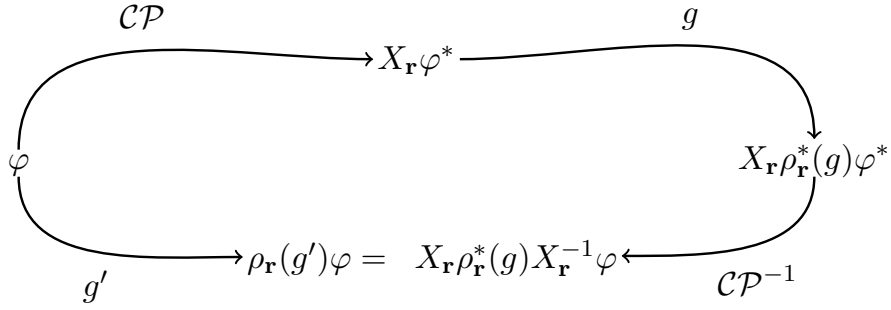


Figure 20: The consistency condition for flavour and generalized CP symmetries.

where the elements g and g' are independent of the representation \mathbf{r} . Eq. (6.26) is the important consistency condition which must be fulfilled for all irreducible representations of G_f in order to ensure generalized CP and flavour symmetry invariance simultaneously. If the condition Eq. (6.26) is not fulfilled, the group G_f is not the full symmetry group of the Lagrangian, and one would have to consider a larger group, which closes under CP transformations. The allowed form of the generalized CP transformations is strongly restricted by the consistency condition of Eq. (6.26).

In practice, it suffices to consider the consistency conditions for the generators of G_f . It is remarkable that both $e^{i\theta}X_{\mathbf{r}}$ and $\rho_{\mathbf{r}}(h)X_{\mathbf{r}}$ satisfy the consistency condition Eq. (6.26) for a generalized CP transformation $X_{\mathbf{r}}$, where θ is real and h is any element of G_f . For a well-defined CP transformation $X_{\mathbf{r}}$, $\rho_{\mathbf{r}}(h)X_{\mathbf{r}}$ is also a viable CP transformation for any $h \in G_f$. The two CP transformations $X_{\mathbf{r}}$ and $\rho_{\mathbf{r}}(h)X_{\mathbf{r}}$ differ by a flavour symmetry transformation $\rho_{\mathbf{r}}(h)$. Since the latter is certainly a symmetry of the Lagrangian, these two CP transformations are indistinguishable. Moreover, Eq. (6.26) implies that the generalized CP transformation $X_{\mathbf{r}}$ maps the group element g into g' and the flavour group multiplication is preserved under this mapping, i.e. $X_{\mathbf{r}}\rho_{\mathbf{r}}^*(g_1g_2)X_{\mathbf{r}}^{-1} = X_{\mathbf{r}}\rho_{\mathbf{r}}^*(g_1)X_{\mathbf{r}}^{-1}X_{\mathbf{r}}\rho_{\mathbf{r}}^*(g_2)X_{\mathbf{r}}^{-1}$. Therefore the CP transformation $X_{\mathbf{r}}$ defines a homomorphism $\mathbf{u} : g \rightarrow g'$, $g, g' \in G_f$ of the family symmetry group G_f . Note that the homomorphism \mathbf{u}' associated with the CP transformation $\rho_{\mathbf{r}}(h)X_{\mathbf{r}}$ for any $h \in G_f$ is related to \mathbf{u} by conjugation:

$$\mathbf{u}'(g) = h\mathbf{u}(g)h^{-1}, \quad \forall h, g \in G_f. \quad (6.27)$$

Notice that when $\rho_{\mathbf{r}}$ is a faithful representation, the elements g and g' have the same order, the mapping defined in Eq. (6.26) is bijective, and thus the associated CP transformation becomes an automorphism, see Ref. [344] for a more formal treatment. Furthermore, taking trace on both sides of the consistency condition in Eq. (6.26), we find that the group characters $\chi_{\mathbf{r}}$ fulfill

$$\chi_{\mathbf{r}}(g') = \text{tr}[\rho_{\mathbf{r}}(g')] = \text{tr}[X_{\mathbf{r}}\rho_{\mathbf{r}}^*(g)X_{\mathbf{r}}^{-1}] = \text{tr}[\rho_{\mathbf{r}}^*(g)] = \text{tr}[\rho_{\mathbf{r}}^\dagger(g)] = \chi_{\mathbf{r}}(g^{-1}). \quad (6.28)$$

Hence g' and g^{-1} should be in the same conjugacy class, that is to say the CP transformation corresponds to a class-inverting automorphism of G_f . As a consequence, when determining the generalized CP transformation compatible with a flavour symmetry group G_f it is sufficient to focus on the class-inverting automorphisms. Because g and g' in Eq. (6.26) are generally different group elements, flavour transfor-

mations and CP transformations in general do not commute. Hence the mathematical structure of the group comprising G_f and generalized CP is in general a semi-direct product, and the full symmetry is $G_f \rtimes H_{CP}$ [264], where H_{CP} is the group generated by generalized CP transformations. The semi-direct product would reduce to a direct product in the case $g = g'$.

6.2.2 Implications of residual flavour and CP symmetries

The presence of generalized CP allows for more symmetry breaking patterns than flavor symmetry alone. In this approach, the parent flavour and CP symmetries are broken down to different residual subgroups $G_l \rtimes H_{CP}^l$ and $G_\nu \rtimes H_{CP}^\nu$ in the charged lepton and neutrino sectors respectively. The mismatch between the residual symmetries $G_l \rtimes H_{CP}^l$ and $G_\nu \rtimes H_{CP}^\nu$ gives rise to a certain lepton mixing pattern. It is remarkable that the lepton flavour mixing is fixed by the group structure of $G_f \rtimes H_{CP}$ and the residual symmetries [265, 267]. The details of the breaking mechanisms realizing the assumed residual symmetries are irrelevant. In the following, we present the formalism to determine the residual symmetries on the charged lepton and neutrino mass matrices. We shall assume neutrinos to be Majorana particles, thus the residual flavour symmetry G_ν is a Z_2 or Klein subgroup K_4 (Dirac neutrinos can be discussed in a very similar way). As usual the three generations of left-handed leptons are assumed to transform as a faithful irreducible triplet $\mathbf{3}$ of the G_f symmetry.

For the residual symmetry $G_l \rtimes H_{CP}^l$ to hold, the Hermitian combination $m_l^\dagger m_l$ of the charged lepton mass matrix should be invariant under the action of $G_l \rtimes H_{CP}^l$, i.e.,

$$\rho_{\mathbf{3}}^\dagger(g_l) m_l^\dagger m_l \rho_{\mathbf{3}}(g_l) = m_l^\dagger m_l, \quad g_l \in G_l, \quad (6.29)$$

$$X_{l\mathbf{3}}^\dagger m_l^\dagger m_l X_{l\mathbf{3}} = (m_l^\dagger m_l)^*, \quad X_{l\mathbf{3}} \in H_{CP}^l, \quad (6.30)$$

where the charged lepton mass matrix m_l is given in the convention in which the left-handed (right-handed) fields are on the right-hand (left-hand) side of m_l . We denote the unitary diagonalization matrix of $m_l^\dagger m_l$ as U_l which satisfies $U_l^\dagger m_l^\dagger m_l U_l = \text{diag}(m_e^2, m_\mu^2, m_\tau^2)$. Once the residual symmetry $G_l \rtimes H_{CP}^l$ and the triplet representation $\mathbf{3}$ are specified, the explicit form of $m_l^\dagger m_l$ can be constructed from Eqs. (6.29, 6.30) in a straightforward way, and thus U_l can be determined. In fact, one can also directly extract the restrictions on U_l from Eqs. (6.29, 6.30) without working out the explicit form of $m_l^\dagger m_l$ as follows

$$U_l^\dagger \rho_{\mathbf{3}}(g_l) U_l = \rho_{\mathbf{3}}^{diag}(g_l), \quad U_l^\dagger X_{l\mathbf{3}} U_l^* = X_{l\mathbf{3}}^{diag}, \quad (6.31)$$

where both $\rho_{\mathbf{3}}^{diag}(g_l)$ and $X_{l\mathbf{3}}^{diag}$ are diagonal phase matrices.

The first identity in Eq. (6.31) comes from imposing the residual flavour symmetry G_l , and the latter arises from the residual CP symmetry H_{CP}^l . We see that both $\rho_{\mathbf{3}}(g_l)$ and $m_l^\dagger m_l$ can be diagonalized by the same unitary matrix U_l , and the residual CP transformation $X_{l\mathbf{3}} = U_l X_{l\mathbf{3}}^{diag} U_l^T$ should be a symmetric unitary matrix. Moreover, Eq. (6.31) implies that the residual flavour and CP symmetries should satisfy

the following restricted consistency conditions:

$$X_{l\mathbf{r}}\rho_{\mathbf{r}}^*(g_l)X_{l\mathbf{r}}^{-1} = \rho_{\mathbf{r}}(g_l^{-1}), \quad g_l \in G_l, \quad (6.32)$$

If the residual flavour symmetry G_l distinguishes the three families, the inclusion of generalized CP H_{CP}^l would not add any information as far as lepton mixing is concerned [335, 388]. Likewise, the requirement that $G_\nu \times H_{CP}^\nu$ is preserved in the neutrino sector implies that the neutrino mass matrix m_ν must be invariant under the action of $G_\nu \times H_{CP}^\nu$, i.e.,

$$\begin{aligned} \rho_{\mathbf{3}}^T(g_\nu)m_\nu\rho_{\mathbf{3}}(g_\nu) &= m_\nu, \quad g_\nu \in G_\nu, \\ X_{\nu\mathbf{3}}^T m_\nu X_{\nu\mathbf{3}} &= m_\nu^*, \quad X_{\nu\mathbf{3}} \in H_{CP}^\nu. \end{aligned} \quad (6.33)$$

Since G_ν is a Z_2 or K_4 subgroup for Majorana neutrinos, the eigenvalues of the representation matrix $\rho_{\mathbf{3}}(g_\nu)$ can only be $+1$ or -1 . The diagonalization matrix of m_ν is denoted as U_ν and satisfies $U_\nu^T m_\nu U_\nu = \text{diag}(m_1, m_2, m_3)$. From Eq. (6.33), we find that the residual symmetry $G_\nu \times H_{CP}^\nu$ leads to the following restrictions on the unitary transformation U_ν ,

$$U_{\nu\mathbf{3}}^\dagger \rho_{\mathbf{3}}(g_\nu) U_\nu = \text{diag}(\pm 1, \pm 1, \pm 1), \quad U_{\nu\mathbf{3}}^\dagger X_{\nu\mathbf{3}} U_\nu^* = \text{diag}(\pm 1, \pm 1, \pm 1). \quad (6.34)$$

Hence the residual CP transformation $X_{\nu\mathbf{3}}$ should be a symmetric matrix [264, 265, 267] and the restricted consistency condition in the neutrino sector is

$$X_{\nu\mathbf{r}}\rho_{\mathbf{r}}^*(g_\nu)X_{\nu\mathbf{r}}^{-1} = \rho_{\mathbf{r}}(g_\nu), \quad g_\nu \in G_\nu, \quad X_{\nu\mathbf{r}} \in H_{CP}^\nu, \quad (6.35)$$

which implies that the residual flavour symmetry G_ν and residual CP symmetry H_{CP}^ν in the neutrino sector commute with each other. Consequently, for Majorana neutrinos the mathematical structure of the residual symmetry is a direct product $G_\nu \times H_{CP}^\nu$. Solving the constraints Eqs. (6.31, 6.34) imposed by the residual symmetry, one can fix the unitary transformations U_l , U_ν and hence the lepton mixing matrix, as

$$U = U_l^\dagger U_\nu. \quad (6.36)$$

In the following, we present several different choices for the residual scheme and the corresponding predictions for the lepton mixing matrix.

6.3 Predictive scenarios with CP symmetry

Assuming a generalized CP symmetry, the Majorana CP violation phases can be predicted and we have more choices for the possible residual symmetries. In particular, some scenarios are quite predictive, with the lepton mixing matrix elements depending only on few free parameters, as shown in table 1. For notational simplicity, we denote $\mathcal{G}_l \equiv G_l \times H_{CP}^l$ and $\mathcal{G}_\nu \equiv G_\nu \times H_{CP}^\nu$ which are the residual symmetries

of the charged lepton and neutrino sectors respectively ²³. We have assumed that the residual flavour symmetry Z_n with $n \geq 3$ is sufficient to distinguish the three generations of charged leptons, otherwise it can be taken to be a product of cyclic groups. The unitary transformations Σ_l and Σ_ν are the Takagi factorizations of the residual CP transformations H_{CP}^l and H_{CP}^ν respectively, in the presence of residual CP. They should also diagonalize the residual flavour symmetry transformations G_l and G_ν respectively. Moreover, $R_{23}(\theta)$ is a rotation matrix in the (23)-plane, Eq. (4.45), while $O_3(\theta_1, \theta_2, \theta_3)$ is a general three-dimensional rotation matrix, Eq. (4.41). Both P_l and P_ν are permutation matrices since the neutrino and charged lepton masses are not constrained by the residual symmetry. Furthermore, Q_l and Q_ν are diagonal phase matrices, Q_l can be absorbed into the charged lepton fields, the non-zero elements of Q_ν encoding the CP parity of neutrinos are equal to ± 1 and $\pm i$ and they can shift the Majorana phases ϕ_{12} and ϕ_{13} by $\pm\pi/2$ or $\pm\pi$. In what follows, we present two predictive scenarios for illustration.

\mathcal{G}_l	\mathcal{G}_ν	U	number of parameters
Z_n	$K_4 \times CP$	$Q_l^\dagger P_l^T \Sigma_l^\dagger \Sigma_\nu P_\nu Q_\nu$	0
Z_n	$Z_2 \times CP$	$Q_l^\dagger P_l^T \Sigma_l^\dagger \Sigma_\nu R_{23}(\theta) P_\nu Q_\nu$	1
$Z_2 \times CP$	$K_4 \times CP'$	$Q_l^\dagger P_l^T R_{23}^T(\theta_l) \Sigma_l^\dagger \Sigma_\nu P_\nu Q_\nu$	
$Z_2 \times CP$	$Z_2 \times CP'$	$Q_l^\dagger P_l^T R_{23}^T(\theta_l) \Sigma_l^\dagger \Sigma_\nu R_{23}(\theta_\nu) P_\nu Q_\nu$	2
Z_2	$K_4 \times CP$	$Q_l^\dagger P_l^T U_{23}^\dagger(\theta_l, \delta_l) \Sigma_l^\dagger \Sigma_\nu P_\nu Q_\nu$	3
Z_n	CP	$Q_l^\dagger P_l^T \Sigma_l^\dagger \Sigma_\nu O_3(\theta_1, \theta_2, \theta_3) Q_\nu$	
CP	$K_4 \times CP'$	$Q_l^\dagger O_3^T(\theta_1, \theta_2, \theta_3) \Sigma_l^\dagger \Sigma_\nu Q_\nu$	
Z_2	$Z_2 \times CP$	$Q_l^\dagger P_l^T U_{23}^\dagger(\theta_l, \delta_l) \Sigma_l^\dagger \Sigma_\nu R_{23}(\theta_\nu) P_\nu Q_\nu$	

Table 1: Possible choices of residual symmetries and corresponding predictions for lepton mixing matrix, when the latter depends on up to three free parameters. If the residual CP is absent from \mathcal{G}_ν , the Majorana CP phases are not restricted.

6.3.1 $\mathcal{G}_l = Z_n$ ($n \geq 3$), $\mathcal{G}_\nu = Z_2 \times CP$

We consider the scenario where the three families of left-handed leptons transform inequivalently as one-dimensional representations under the residual flavour symmetry $G_l = Z_n$ with $n \geq 3$, so that they are distinguished by the abelian subgroup G_l . The representation matrix $\rho_3(g_l)$ can be diagonalized by a unitary matrix Σ_l fulfilling $\Sigma_l^\dagger \rho_3(g_l) \Sigma_l = \rho_3^{diag}(g_l)$, where the three columns of Σ_l are formed by the three eigenvectors of $\rho_3(g_l)$ and Σ_l is determined up to an arbitrary diagonal unitary matrix Q_l and a permutation matrix P_l . Eq. (6.31) implies that the charged lepton diagonalization matrix U_l coincides with Σ_l , i.e.,

$$U_l = \Sigma_l P_l Q_l. \quad (6.37)$$

Concerning the neutrino sector, since $X_{\nu\mathbf{3}}$ is a symmetric and unitary matrix, by performing the Takagi factorization $X_{\nu\mathbf{3}}$ can be written as

$$X_{\nu\mathbf{3}} = \Sigma_\nu \Sigma_\nu^T, \quad \text{with} \quad \Sigma_\nu^\dagger \rho_3(g_\nu) \Sigma_\nu = \pm \text{diag}(1, -1, -1). \quad (6.38)$$

²³In concrete model building, one could possibly have more branches of residual symmetry [389–392].

The procedure of obtaining the unitary matrix Σ_ν has been given in [345]. The neutrino diagonalization matrix U_ν satisfying the conditions in Eq. (6.34) is determined to be of the following form [264, 345]

$$U_\nu = \Sigma_\nu R_{23}(\theta) P_\nu Q_\nu, \quad (6.39)$$

where $R_{23}(\theta)$ stands for a rotation matrix through an angle θ in the (23)-plane and it takes the form of Eq. (4.45), and P_ν is a generic permutation matrix. Here Q_ν in Eq. (6.39) is a diagonal matrix with elements equal to ± 1 and $\pm i$. Hence, without loss of generality it can be given as,

$$Q_\nu = \begin{pmatrix} 1 & 0 & 0 \\ 1 & i^{k_1} & 0 \\ 0 & 0 & i^{k_2} \end{pmatrix} \quad (6.40)$$

with $k_{1,2} = 0, 1, 2, 3$. Hence the lepton mixing matrix U is of the form [264, 265, 345]

$$U = U_l^\dagger U_\nu = Q_l^\dagger P_l^T \Sigma_l^\dagger \Sigma_\nu R_{23}(\theta) P_\nu Q_\nu. \quad (6.41)$$

Notice that, as usual, the phase matrix Q_l can be absorbed into the charged lepton fields [30], while the effect of Q_ν is to shift the Majorana CP phases ϕ_{12} and ϕ_{13} by integral multiples of $\pi/2$. It is remarkable that the lepton mixing matrix is constrained to only depend on a single free parameter θ , whose value can be fixed by the precisely measured reactor mixing angle θ_{13} . We can therefore predict the values of the other two mixing angles θ_{12} , θ_{23} as well as the CP violation phases. The lepton mixing matrix is determined up to possible permutations of rows and columns, since both neutrino and charged lepton masses are not constrained in this approach. Moreover, the Z_2 residual flavour symmetry can only distinguish one neutrino family from the other two generations, so that only one column of the lepton mixing matrix is fixed through the choice of residual symmetry, as can be seen from Eq. (6.41). Comparing with the oscillation data in Eqs. (1.23, 1.24), one can determine the phenomenologically allowed permutation matrices P_l and P_ν .

It follows from the above that, for any postulated residual symmetry subgroups G_l and $Z_2 \times CP$, the lepton mixing matrix can be extracted by using Eq. (6.41) in a simple manner, the recipe is summarized in figure 21. The predicted lepton mixing matrix only depends on the structure of the symmetry group $G_f \times H_{CP}$ and the assumed residual symmetry, regardless of the underlying dynamics which breaks $G_f \times H_{CP}$ down to the residual subgroup.

As an illustration, we consider the S_4 flavor symmetry in combination with the generalized CP symmetry. The group theory and representation of S_4 are given in B. The outer automorphism group of S_4 is trivial [320, 344], all the automorphisms of S_4 are inner automorphisms which are group conjugations. Without loss of generality it is sufficient to consider the representative automorphism $\mathbf{u} : (s, t, u) \rightarrow (s, t^{-1}, u)$, where s , t and u are the generators of S_4 , the corresponding generalized CP transformation $X_{\mathbf{r}}^0$ is determined

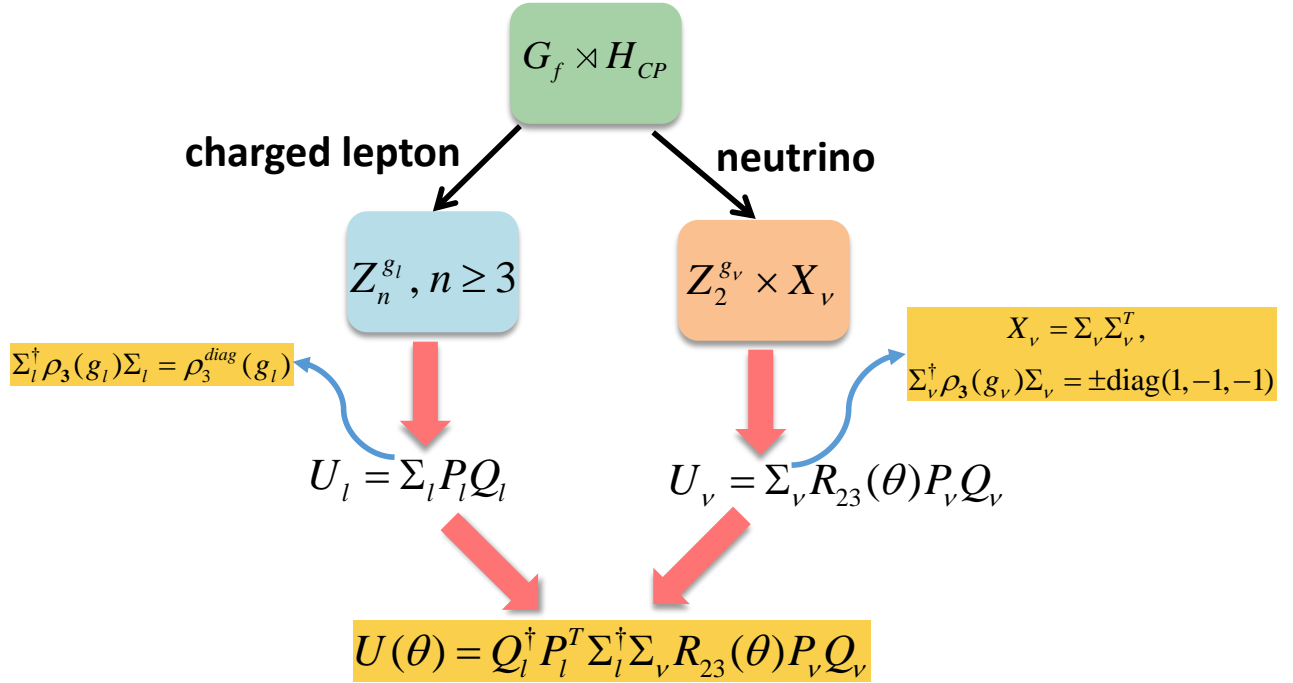


Figure 21: The model independent predictions for lepton mixing matrix for the preserved residual symmetry abelian subgroup G_l and $Z_2 \times CP$ in the charged lepton and neutrino sectors respectively.

by the following consistency equations

$$\begin{aligned}
X_{\mathbf{r}}^0 \rho_{\mathbf{r}}^*(s) (X_{\mathbf{r}}^0)^{-1} &= \rho_{\mathbf{r}}(\mathbf{u}(s)) = \rho_{\mathbf{r}}(s), \\
X_{\mathbf{r}}^0 \rho_{\mathbf{r}}^*(t) (X_{\mathbf{r}}^0)^{-1} &= \rho_{\mathbf{r}}(\mathbf{u}(t)) = \rho_{\mathbf{r}}(t^2), \\
X_{\mathbf{r}}^0 \rho_{\mathbf{r}}^*(u) (X_{\mathbf{r}}^0)^{-1} &= \rho_{\mathbf{r}}(\mathbf{u}(u)) = \rho_{\mathbf{r}}(u).
\end{aligned} \tag{6.42}$$

From the explicit form of the representation matrices in Eqs. (B.3, B.4, B.5), it follows that $X_{\mathbf{r}}^0$ is the unit matrix up to an arbitrary overall phase,

$$X_{\mathbf{r}}^0 = 1. \tag{6.43}$$

Including the family symmetry transformation, the generalized CP transformation consistent with the S_4 symmetry is given by [320, 325, 335]

$$X_{\mathbf{r}} = \rho_{\mathbf{r}}(g) X_{\mathbf{r}}^0 = \rho_{\mathbf{r}}(g), \quad g \in S_4. \tag{6.44}$$

It was found that three sets of residual symmetries are compatible with the experimental data [264]. Notice that a fourth residual symmetry with $G_l = Z_3^t$, $G_\nu = Z_2^{su}$, $X_\nu = 1$ is not phenomenologically viable, since the reactor and atmospheric angles can not be accommodated simultaneously.

- (i) $G_l = Z_3^t$, $G_\nu = Z_2^s$, $X_\nu = 1$

In this case, the unitary transformation Σ_l is the unit matrix since the representation matrix $\rho_{\mathbf{3}}(t)$ is diagonal, and the Takagi factorization matrix Σ_ν is found to be

$$\Sigma_\nu = \frac{1}{\sqrt{6}} \begin{pmatrix} \sqrt{2} & 2 & 0 \\ \sqrt{2} & -1 & \sqrt{3} \\ \sqrt{2} & -1 & -\sqrt{3} \end{pmatrix}. \quad (6.45)$$

Hence the lepton mixing matrix is determined to be

$$U = \frac{1}{\sqrt{6}} \begin{pmatrix} 2 \cos \theta & \sqrt{2} & 2 \sin \theta \\ -\cos \theta - \sqrt{3} \sin \theta & \sqrt{2} & \sqrt{3} \cos \theta - \sin \theta \\ -\cos \theta + \sqrt{3} \sin \theta & \sqrt{2} & -\sqrt{3} \cos \theta - \sin \theta \end{pmatrix} Q_\nu, \quad (6.46)$$

where we have taken $P_\nu = P_{12}$ such that $(1, 1, 1)^T/\sqrt{3}$ is in the second column, in order to be consistent with experimental data. We can extract the lepton mixing parameters as follows,

$$\begin{aligned} \sin^2 \theta_{13} &= \frac{2}{3} \sin^2 \theta, & \sin^2 \theta_{23} &= \frac{1}{2} - \frac{\sqrt{3} \sin 2\theta}{2(2 + \cos 2\theta)} = \frac{1}{2} \pm \frac{1}{2} \tan \theta_{13} \sqrt{2 - \tan^2 \theta_{13}}, \\ \sin^2 \theta_{12} &= \frac{1}{2 + \cos 2\theta} = \frac{1}{3 \cos^2 \theta_{13}}, & \sin 2\phi_{12} &= \sin 2\phi_{13} = \sin \delta_{CP} = 0. \end{aligned} \quad (6.47)$$

Using the experimental best fit value $(\sin^2 \theta_{13})^{\text{bf}} = 0.022$ [24, 25], we find the solar mixing angle $\sin^2 \theta_{12} \simeq 0.341$ and the atmospheric angle

$$\sin^2 \theta_{23} \simeq \begin{cases} 0.426 & \text{for } \theta < \pi/2 \\ 0.574 & \text{for } \theta > \pi/2 \end{cases}. \quad (6.48)$$

The Dirac and Majorana CP phases are determined to take on CP conserving values in this case.

(ii) $G_l = Z_3^t$, $G_\nu = Z_2^s$, $X_\nu = u$

This case differs from the previous one in the residual CP X_ν . The unitary matrix Σ_ν is

$$\Sigma_\nu = \frac{1}{\sqrt{6}} \begin{pmatrix} \sqrt{2}i & 2i & 0 \\ \sqrt{2}i & -i & \sqrt{3} \\ \sqrt{2}i & -i & -\sqrt{3} \end{pmatrix}. \quad (6.49)$$

Consequently, for $P_\nu = P_{12}$, the lepton mixing matrix is fixed to be

$$U = \frac{1}{\sqrt{6}} \begin{pmatrix} 2 \cos \theta & \sqrt{2} & 2 \sin \theta \\ -\cos \theta + i\sqrt{3} \sin \theta & \sqrt{2} & -\sin \theta - i\sqrt{3} \cos \theta \\ -\cos \theta - i\sqrt{3} \sin \theta & \sqrt{2} & -\sin \theta + i\sqrt{3} \cos \theta \end{pmatrix} Q_\nu. \quad (6.50)$$

We can extract the lepton mixing parameters as

$$\begin{aligned}\sin^2 \theta_{13} &= \frac{2}{3} \sin^2 \theta, & \sin^2 \theta_{12} &= \frac{1}{2 + \cos 2\theta} = \frac{1}{3 \cos^2 \theta_{13}}, \\ \sin^2 \theta_{23} &= \frac{1}{2}, & |\sin \delta_{CP}| &= 1, & \sin 2\phi_{12} &= \sin 2\phi_{13} = 0.\end{aligned}\quad (6.51)$$

Because the $\mu - \tau$ reflection symmetry $X_\nu = u$ is imposed on the neutrino mass matrix [252–255], both atmospheric angle θ_{23} and Dirac CP phase δ_{CP} are maximal, while the Majorana CP phases ϕ_{12} and ϕ_{13} are trivial.

(iii) $G_l = Z_3^t, G_\nu = Z_2^{su}, X_\nu = u$

The Takagi factorization matrix Σ_ν is determined to be

$$\Sigma_\nu = \frac{1}{\sqrt{6}} \begin{pmatrix} 2i & \sqrt{2}i & 0 \\ -i & \sqrt{2}i & -\sqrt{3} \\ -i & \sqrt{2}i & \sqrt{3} \end{pmatrix}. \quad (6.52)$$

Using the mater formula Eq. (6.41), we obtain the lepton mixing matrix as

$$U = \frac{1}{\sqrt{6}} \begin{pmatrix} 2 & \sqrt{2} \cos \theta & \sqrt{2} \sin \theta \\ -1 & \sqrt{2} \cos \theta - i\sqrt{3} \sin \theta & \sqrt{2} \sin \theta + i\sqrt{3} \cos \theta \\ -1 & \sqrt{2} \cos \theta + i\sqrt{3} \sin \theta & \sqrt{2} \sin \theta - i\sqrt{3} \cos \theta \end{pmatrix} Q_\nu. \quad (6.53)$$

The predictions for mixing angles and CP violation phases are

$$\begin{aligned}\sin^2 \theta_{13} &= \frac{1}{3} \sin^2 \theta, & \sin^2 \theta_{12} &= \frac{1 + \cos 2\theta}{5 + \cos 2\theta} = \frac{1 - 3 \sin^2 \theta_{13}}{3 \cos^2 \theta_{13}}, \\ \sin^2 \theta_{23} &= \frac{1}{2}, & |\sin \delta_{CP}| &= 1, & \sin 2\phi_{12} &= \sin 2\phi_{13} = 0.\end{aligned}\quad (6.54)$$

For $(\sin^2 \theta_{13})^{\text{bf}} = 0.022$ [24, 25] we find, from Eq. (6.54), the solar mixing angle as $\sin^2 \theta_{12} \simeq 0.318$. Similar to case ii, the $\mu - \tau$ reflection symmetry $X_\nu = u$ implies maximal values of θ_{23} and δ_{CP} , and CP conserving values of ϕ_{12}, ϕ_{13} .

The values of the effective $|m_{\beta\beta}|$ parameter characterizing the $0\nu\beta\beta$ decay amplitude can be determined for the viable cases associated to the lepton mixing matrices in Eqs. (6.46, 6.50, 6.53). This effective mass parameter depends on the CP parity encoded in Q_ν . Since the rotation angle θ is strongly constrained by the reactor angle θ_{13} and the Majorana phases can be predicted, the effective mass $|m_{\beta\beta}|$ is severely restricted, as shown in figure 22. The narrow width of each band comes from varying θ_{13} and the neutrino mass squared differences over their allowed 3σ ranges [24].

For inverted neutrino mass ordering, the term proportional to m_3 in $|m_{\beta\beta}|$ is suppressed by the small values of m_3 and $\sin^2 \theta_{13}$, consequently the value of k_2 is almost irrelevant. For $(k_1, k_2) = (0, 0), (0, 1)$, the effective mass $m_{\beta\beta}$ is close to the upper boundary of the IO region obtained by using the 3σ global

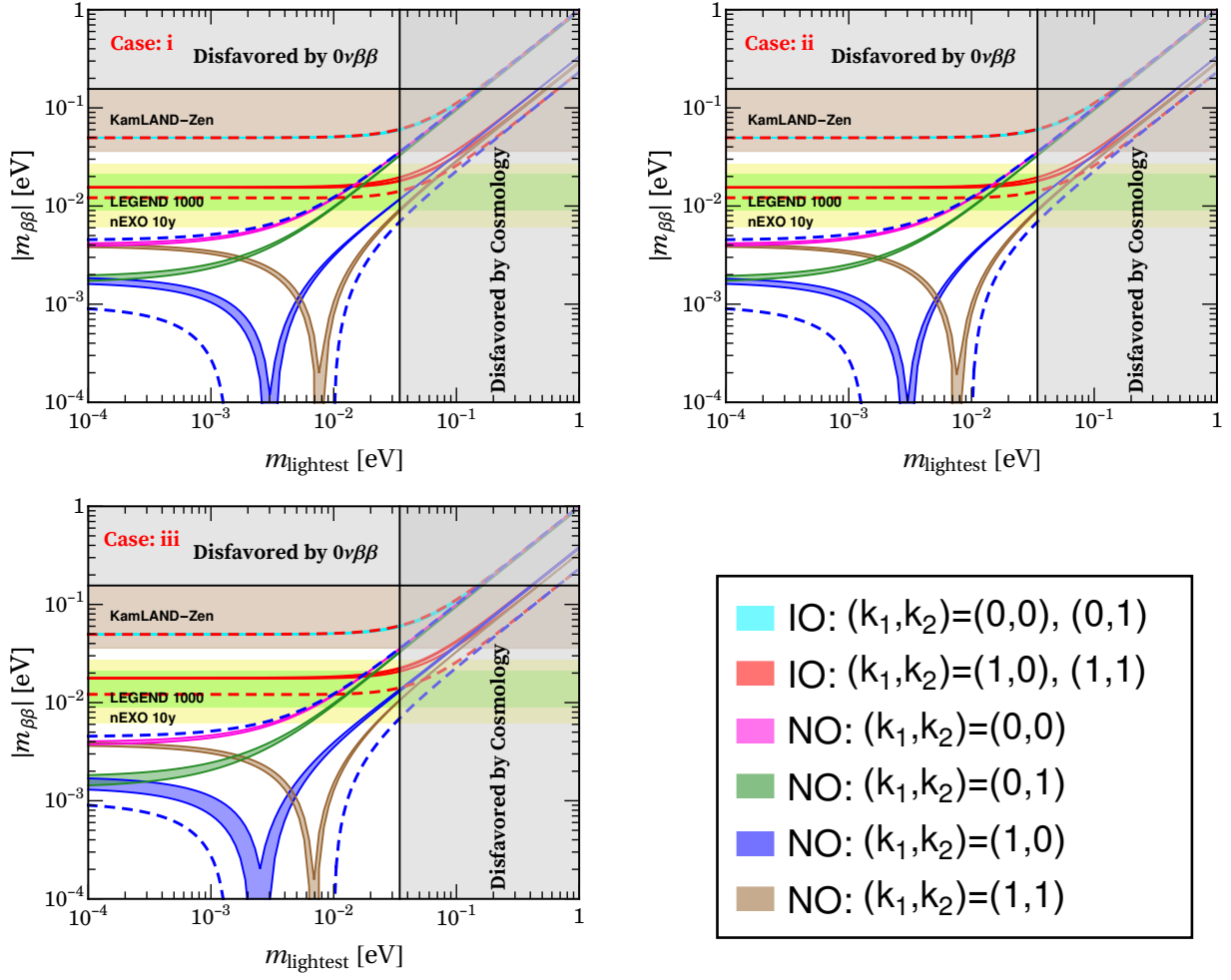


Figure 22: Predicted effective Majorana neutrino mass $|m_{\beta\beta}|$ for three viable mixing patterns when the S_4 flavour symmetry and CP symmetry are broken to an Abelian subgroup and $Z_2 \times CP$ in the charged lepton sector and neutrino sector respectively. The red (blue) dashed lines indicate the most general allowed regions for IO (NO) neutrino mass ordering obtained by varying the mixing parameters in their 3σ ranges [24, 25]. The current experimental bound $|m_{\beta\beta}| < (36 - 156)$ meV at 90% C.L. from KamLAND-Zen [125] and the future sensitivity ranges $|m_{\beta\beta}| < (9.0 - 21)$ meV from LEGEND-1000 [126] and $|m_{\beta\beta}| < (6.1 - 27)$ meV from nEXO [127] are indicated by light brown, light yellow and light green horizontal bands respectively. The vertical grey exclusion band represents the bound $\sum_i m_i < 0.120$ eV from Planck at 95% C.L. [128, 129].

data, while $|m_{\beta\beta}|$ is close to the lower boundary of IO for $(k_1, k_2) = (1, 0), (1, 1)$.

Symmetry breaking patterns of abelian subgroups in the charged lepton sector and $Z_2 \times CP$ in the neutrino sector have also been studied for many flavour symmetry groups combined with generalized CP, such as A_4 [264, 388, 393], S_4 [264, 320, 325, 335, 394–396], $\Delta(27)$ [397, 398], $\Delta(48)$ [399, 400], A_5 [401–405], $\Delta(96)$ [406] and the infinite group series $\Delta(3n^2) = (Z_n \times Z_n) \rtimes Z_3$ [407, 408], $\Delta(6n^2) = (Z_n \times Z_n) \rtimes S_3$ [407, 409] and $D_{9n, 3n}^{(1)} = (Z_{9n} \times Z_{3n}) \rtimes S_3$ [410]. For popular flavour symmetries A_4 , S_4 and A_5 , the Dirac CP phase is predicted to take simple values $\delta_{CP} = 0, \pi, \pm\pi/2$, and the Majorana phases take on CP conserving values for the experimentally viable mixing patterns. Moreover, the values of the Dirac

CP phase and atmospheric mixing angle are correlated in flavor groups A_4 , S_4 and A_5 , the atmospheric angle is maximal for $\delta_{CP} = \pm\pi/2$ and non-maximal for $\delta_{CP} = 0, \pi$. Both Dirac and Majorana CP phases can depend nontrivially on the parameter θ for larger flavour symmetry groups such as $\Delta(96)$ [406]. A systematical classification of the possible mixing patterns resulting from the pair of residual symmetry subgroups $\{G_l, Z_2 \times CP\}$ has been performed [345]. The neutrino mixing patterns compatible with oscillation data are given as follows [345]:

$$\begin{aligned}
U^{I(a)} &= \frac{1}{\sqrt{3}} \begin{pmatrix} \sqrt{2} \sin \varphi_1 & e^{i\varphi_2} & \sqrt{2} \cos \varphi_1 \\ \sqrt{2} \cos(\varphi_1 - \frac{\pi}{6}) & -e^{i\varphi_2} & -\sqrt{2} \sin(\varphi_1 - \frac{\pi}{6}) \\ \sqrt{2} \cos(\varphi_1 + \frac{\pi}{6}) & e^{i\varphi_2} & -\sqrt{2} \sin(\varphi_1 + \frac{\pi}{6}) \end{pmatrix} R_{23}(\theta) Q_\nu, \\
U^{I(b)} &= \frac{1}{\sqrt{3}} \begin{pmatrix} \sqrt{2} \cos \varphi_1 & e^{i\varphi_2} & \sqrt{2} \sin \varphi_1 \\ -\sqrt{2} \sin(\varphi_1 - \frac{\pi}{6}) & -e^{i\varphi_2} & \sqrt{2} \cos(\varphi_1 - \frac{\pi}{6}) \\ -\sqrt{2} \sin(\varphi_1 + \frac{\pi}{6}) & e^{i\varphi_2} & \sqrt{2} \cos(\varphi_1 + \frac{\pi}{6}) \end{pmatrix} R_{12}(\theta) Q_\nu, \\
U^{II} &= \frac{1}{\sqrt{3}} \begin{pmatrix} e^{i\varphi_1} & 1 & e^{i\varphi_2} \\ \omega e^{i\varphi_1} & 1 & \omega^2 e^{i\varphi_2} \\ \omega^2 e^{i\varphi_1} & 1 & \omega e^{i\varphi_2} \end{pmatrix} R_{13}(\theta) Q_\nu, \\
U^{III} &= \frac{1}{\sqrt{3}} \begin{pmatrix} \sqrt{2} e^{i\varphi_1} \sin \varphi_2 & 1 & \sqrt{2} e^{i\varphi_1} \cos \varphi_2 \\ \sqrt{2} e^{i\varphi_1} \cos(\varphi_2 + \frac{\pi}{6}) & 1 & -\sqrt{2} e^{i\varphi_1} \sin(\varphi_2 + \frac{\pi}{6}) \\ -\sqrt{2} e^{i\varphi_1} \cos(\varphi_2 - \frac{\pi}{6}) & 1 & \sqrt{2} e^{i\varphi_1} \sin(\varphi_2 - \frac{\pi}{6}) \end{pmatrix} R_{13}(\theta) Q_\nu, \\
U^{IV(a)} &= \frac{1}{\sqrt{2\sqrt{5}\phi_g}} \begin{pmatrix} -\sqrt{2}\phi_g & \sqrt{2} & 0 \\ 1 & \phi_g & -\sqrt{\sqrt{5}\phi_g} \\ 1 & \phi_g & \sqrt{\sqrt{5}\phi_g} \end{pmatrix} R_{13}(\theta) Q_\nu, \\
U^{IV(b)} &= \frac{1}{\sqrt{2\sqrt{5}\phi_g}} \begin{pmatrix} -\sqrt{2}\phi_g i & \sqrt{2} & 0 \\ i & \phi_g & -\sqrt{\sqrt{5}\phi_g} \\ i & \phi_g & \sqrt{\sqrt{5}\phi_g} \end{pmatrix} R_{13}(\theta) Q_\nu, \\
U^V &= \frac{1}{2} \begin{pmatrix} \phi_g & 1 & \phi_g - 1 \\ \phi_g - 1 & -\phi_g & 1 \\ 1 & 1 - \phi_g & -\phi_g \end{pmatrix} R_{23}(\theta) Q_\nu, \\
U^{VI} &= \frac{1}{2\sqrt{3}} \begin{pmatrix} (\sqrt{3}-1)e^{i\varphi} & 2 & -(\sqrt{3}+1)e^{i(\varphi+\frac{3\pi}{4})} \\ -(\sqrt{3}+1)e^{i\varphi} & 2 & (\sqrt{3}-1)e^{i(\varphi+\frac{3\pi}{4})} \\ 2e^{i\varphi} & 2 & 2e^{i(\varphi+\frac{3\pi}{4})} \end{pmatrix} R_{13}(\theta) Q_\nu, \\
U^{VII} &= \frac{1}{2\sqrt{6}} \begin{pmatrix} -\frac{\sqrt{3}}{s_3} & 2\sqrt{2} & \frac{s_2-s_1}{s_1s_2} \\ \frac{\sqrt{3}}{s_2} & 2\sqrt{2} & -\frac{s_1+s_3}{s_1s_3} \\ \frac{\sqrt{3}}{s_1} & 2\sqrt{2} & \frac{s_2+s_3}{s_2s_3} \end{pmatrix} R_{23}(\theta) Q_\nu, \tag{6.55}
\end{aligned}$$

up to row and column permutations, where $s_n \equiv \sin(2n\pi/7)$ with $n = 1, 2, 3$ and $R_{ij}(\theta)$ is the rotation

matrix through an angle θ in the (ij) -plane. The parameters φ_1 , φ_2 and φ are group theoretical indices characterizing the flavour group and the residual symmetry and they can only take some discrete values for a given flavour symmetry. The possible values of φ_1 , φ_2 and φ for different finite flavour group G_f up to order 2000 and the corresponding predictions for lepton mixing parameters are given in [345]. It is remarkable that the above mixing patterns can be obtained from the flavour groups $\Delta(6n^2)$, $D_{9n,3n}^{(1)}$, A_5 and $\Sigma(168)$ in combination with generalized CP symmetry.

As shown in table 1, if the residual symmetries $K_4 \times CP$ and $Z_2 \times CP'$ are preserved in the neutrino and charged lepton sectors respectively, the lepton mixing matrix would only depends on a single real parameter θ as well. In this case, one row of the mixing matrix is completely fixed by residual symmetry, regardless of the free parameter θ .

It turns out that only one type of mixing pattern can accommodate the oscillation data [345]:

$$U^{VIII} = \frac{1}{2} R_{13}^T(\theta) \begin{pmatrix} \sqrt{2}e^{i\varphi_1} & -\sqrt{2}e^{i\varphi_1} & 0 \\ 1 & 1 & -\sqrt{2}e^{i\varphi_2} \\ 1 & 1 & \sqrt{2}e^{i\varphi_2} \end{pmatrix} Q_\nu, \quad (6.56)$$

where φ_1 and φ_2 take discrete values determined by the choice of the residual symmetry and the flavour symmetry group.

6.3.2 $\mathcal{G}_l = Z_2 \times CP$, $\mathcal{G}_\nu = Z_2 \times CP'$

The residual subgroups in both the neutrino and charged lepton sectors are of the structure $Z_2 \times CP$ in this scheme [282, 284, 395]. Since the neutrino sector still preserves the residual symmetry $Z_2^{g_\nu} \times X_\nu$, the unitary transformation U_ν is given by Eq. (6.39). The residual symmetry of the charged lepton sector is denoted as $Z_2^{g_l} \times X_l$ in this scheme, and the constrained consistency condition in Eq. (6.32) should be fulfilled, i.e., $X_{l\mathbf{r}}\rho_{\mathbf{r}}^*(g_l)X_{l\mathbf{r}}^{-1} = \rho_{\mathbf{r}}(g_l)$. The three families of left-handed lepton doublets are assigned to transform as a faithful triplet ρ of the flavour group G_f , where the representation ρ can be either irreducible or reducible. The residual symmetry $Z_2^{g_l} \times X_l$ of the charged lepton sector requires that $m_l^\dagger m_l$ is invariant under $Z_2^{g_l} \times X_l$, where m_l is the charged lepton mass matrix. Thus the unitary transformation U_l of the charged leptons should fulfill

$$U_l^\dagger \rho(g_l) U_l = \text{diag}(\pm 1, \pm 1, \pm 1), \quad U_l^\dagger X_l U_l^* = \text{diag}(e^{-i\alpha_e}, e^{-i\alpha_\mu}, e^{-i\alpha_\tau}) \equiv Q_l^{\dagger 2}, \quad (6.57)$$

where $Q_l = \text{diag}(e^{i\alpha_e/2}, e^{i\alpha_\mu/2}, e^{i\alpha_\tau/2})$ is a diagonal phase matrix with $\alpha_{e,\mu,\tau}$ real. Notice that the eigenvalue of $\rho(g_l)$ is +1 or -1 because the generator g_l is of order 2. The residual CP transformation X_l should be a symmetric matrix, otherwise the charged lepton masses would be partially degenerate. Likewise, for the neutrino sector we can perform the Takagi factorization for X_l as follows

$$X_l = \Sigma_l \Sigma_l^T, \quad \Sigma_l^\dagger \rho(g_l) \Sigma_l = \pm \text{diag}(1, -1, -1). \quad (6.58)$$

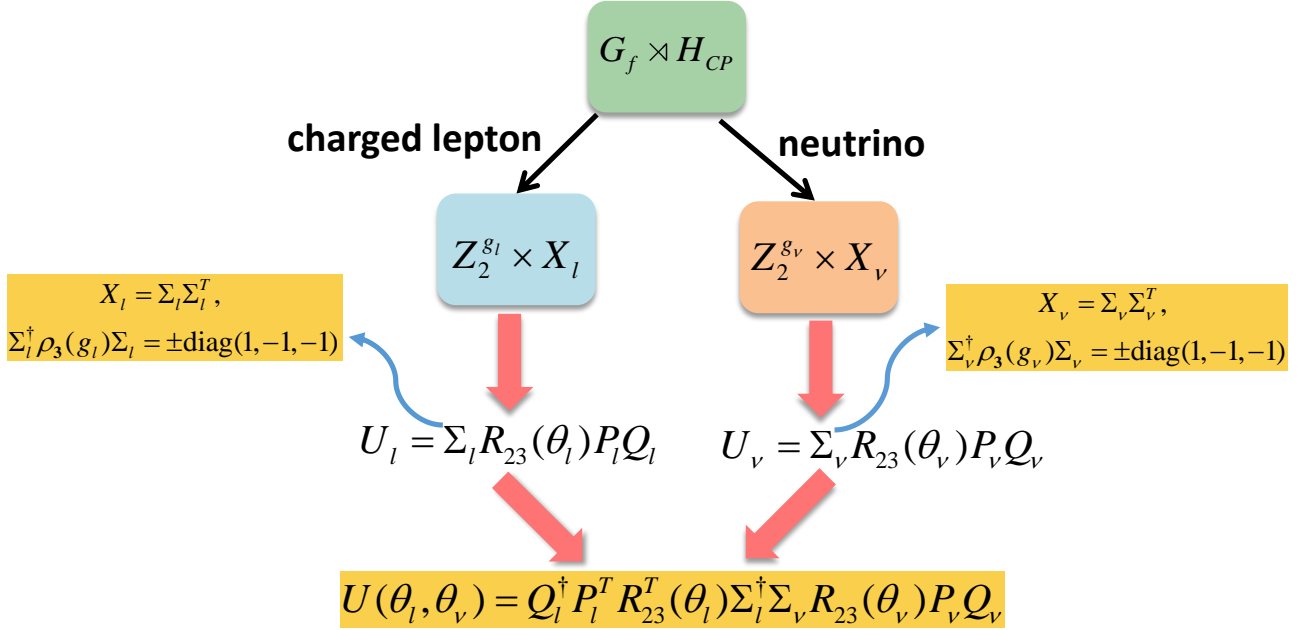


Figure 23: Model-independent predictions for the lepton mixing matrix when the residual symmetry has the structure $Z_2 \times CP$ in both neutrino and charged lepton sectors.

Then the residual symmetry constrains U_l to be

$$U_l = \Sigma_l R_{23}(\theta_l) P_l Q_l \quad (6.59)$$

where P_l is a generic three-dimensional permutation matrix, since the charged lepton masses are not predicted in this scheme. Hence the lepton mixing matrix is determined to be of the following form

$$U = U_l^\dagger U_nu = Q_l^\dagger P_l^T R_{23}^T(\theta_l) \Sigma_l^\dagger \Sigma_nu R_{23}(\theta_nu) P_nu Q_nu, \quad (6.60)$$

where the phase matrix Q_l can be absorbed into the charged lepton fields. In this scenario, the recipe for extracting the predicted lepton mixing matrix from the residual symmetry is summarized in figure 23. One sees that the resulting lepton mixing matrix only depends on two free rotation angles θ_l and θ_nu , lying in the range $0 \leq \theta_{l,\nu} < \pi$. The precisely measured reactor angle θ_{13} and the solar angle θ_{12} can be accommodated for certain values of θ_l and θ_nu , leading to relations for the other mixing parameters. Notice that in this scheme only one element of the mixing matrix is fixed to a constant value by the residual subgroups.

A comprehensive study of the lepton mixing patterns which can arise from the breaking of S_4 and CP symmetries into two distinct $Z_2 \times CP$ subgroups in the neutrino and charged lepton sectors leads to eighteen phenomenologically viable cases [395]. In the following, we give one typical example which predicts non-trivial CP violation phases. The three families of left-handed leptons are embedded in a triplet $\mathbf{3}$ of S_4 , and the residual symmetries of the neutrino and charged lepton mass matrices are $Z_2^{st^2su} \times X_l$ and $Z_2^s \times X_nu$ respectively, with $X_l = t^2$ and $X_nu = su$. The Takagi factorization Σ_l and Σ_nu are

found to be

$$\Sigma_l = \frac{1}{\sqrt{6}} \begin{pmatrix} 2 & 0 & -\sqrt{2} \\ e^{\frac{i\pi}{3}} & -\sqrt{3} e^{\frac{i\pi}{3}} & \sqrt{2} e^{\frac{i\pi}{3}} \\ e^{-\frac{i\pi}{3}} & \sqrt{3} e^{-\frac{i\pi}{3}} & \sqrt{2} e^{-\frac{i\pi}{3}} \end{pmatrix}, \quad \Sigma_\nu = \frac{1}{\sqrt{6}} \begin{pmatrix} \sqrt{2} i & 0 & -2 \\ \sqrt{2} i & -\sqrt{3} i & 1 \\ \sqrt{2} i & \sqrt{3} i & 1 \end{pmatrix} \quad (6.61)$$

The lepton mixing matrix can be easily obtained by using the master formula of Eq. (6.60), one of its elements is fixed to be $1/\sqrt{2}$. In order to be compatible with experimental data, the fixed element can be either the (23) or (33) entry, so that we can take the permutation matrices $(P_l, P_\nu) = (P_{12}, P_{13})$ or (P_{13}, P_{12}, P_{13}) . For the first case, $(P_l, P_\nu) = (P_{12}, P_{13})$, we find that the lepton mixing parameters are

$$\sin^2 \theta_{13} = \frac{1}{2} \cos^2 \theta_l, \quad \sin^2 \theta_{12} = \frac{1}{2} + \frac{(1 - 3 \cos 2\theta_l) \sin 2\theta_\nu}{6 - 2 \cos 2\theta_l}, \quad \sin^2 \theta_{23} = \frac{1}{2 - \cos^2 \theta_l}, \quad (6.62)$$

while the CP invariants are determined as

$$J_{CP} = \frac{\sin 2\theta_l \cos 2\theta_\nu}{8\sqrt{2}}, \quad I_1 = \frac{(2 \sin 2\theta_l - 3 \sin 4\theta_l) \cos 2\theta_\nu}{16\sqrt{2}}, \quad I_2 = \frac{\sin \theta_l \cos^3 \theta_l \cos 2\theta_\nu}{2\sqrt{2}}. \quad (6.63)$$

The Jarlskog invariant J_{CP} of neutrino oscillations is related to δ^ℓ in Eq. (1.22), while the other two invariants I_1 and I_2 are given in terms of the basic Majorana phases ϕ_{12}, ϕ_{13} involved in $0\nu\beta\beta$ decay, see section 1. One finds the following expressions [219, 411–413],

$$\begin{aligned} J_{CP} &= \text{Im}(U_{11}U_{33}U_{13}^*U_{31}^*) = \frac{1}{8} \sin 2\theta_{12} \sin 2\theta_{13} \sin 2\theta_{23} \cos \theta_{13} \sin \delta^\ell, \\ I_1 &= \text{Im}(U_{11}^{2*}U_{12}^2) = -\sin^2 \theta_{12} \cos^2 \theta_{12} \cos^4 \theta_{13} \sin 2\phi_{12}, \\ I_2 &= \text{Im}(U_{11}^{2*}U_{13}^2) = -\cos^2 \theta_{12} \cos^2 \theta_{13} \sin^2 \theta_{13} \sin 2\phi_{13}. \end{aligned} \quad (6.64)$$

The lepton mixing matrices corresponding to the two kinds of permutations $(P_l, P_\nu) = (P_{13}, P_{12}, P_{13})$ and $(P_l, P_\nu) = (P_{12}, P_{13})$ are related to each other by the exchange of the second and third rows. Thus the atmospheric angle θ_{23} and Dirac CP violation phase δ^ℓ become $\pi/2 - \theta_{23}$ and $\delta^\ell + \pi$ respectively, while the other mixing angles θ_{12}, θ_{13} and the Majorana CP phases ϕ_{12} and ϕ_{13} remain unchanged.

The results of the χ^2 analysis are presented in table 2. Moreover, a numerical analysis is performed, with both θ_l and θ_ν varying freely in the range of 0 to π , requiring all the three lepton mixing angles to lie in the experimental 3σ regions [24, 25]. In figure 24 we display the 3σ contour regions for $\sin^2 \theta_{12}$, $\sin^2 \theta_{13}$ and $\sin^2 \theta_{23}$, as well as their experimental best fit values in the $\theta_l - \theta_\nu$ plane. Dashed (solid) lines are the best fit mixing-angle values [24, 25]. Left (right) panels are for $(P_l, P_\nu) = (P_{12}, P_{13})$ and $(P_l, P_\nu) = (P_{13}, P_{12}, P_{13})$, respectively. One sees that the lepton mixing angles can be accommodated in the small regions around the best fit points.

In figure 25 we show the contour plots of the CP violation phases δ^ℓ, ϕ_{12} and ϕ_{13} in the plane θ_ν versus θ_l . The black areas denote the regions where the lepton mixing angles are compatible with oscillation data within 3σ . These will be testable at forthcoming long baseline neutrino oscillation experiments. Since all the lepton mixing angles and CP phases are predicted to lie in narrow regions, we also have tight predictions for the effective Majorana mass of neutrinoless double beta decay, as shown in figure 26.

	(P_l, P_ν)	χ^2_{\min}	$(\theta_l^{\text{bf}}, \theta_\nu^{\text{bf}})/\pi$	$\sin^2 \theta_{13}$	$\sin^2 \theta_{12}$	$\sin^2 \theta_{23}$	δ^ℓ/π	ϕ_{12}/π (mod 1/2)	ϕ_{13}/π (mod 1/2)	
NO	(P_{12}, P_{13})	20.078	(0.433, 0.938)	0.022	0.318	0.511	0.539	0.397	0.468	
			(0.567, 0.562)							
			(0.433, 0.562)							
			(0.567, 0.938)							
	(P_{13}, P_{12}, P_{13})	37.057	37.057	(0.433, 0.938)	0.022	0.318	0.489	1.539	0.397	0.468
				(0.567, 0.562)						
				(0.433, 0.562)						
				(0.567, 0.938)						
IO	(P_{12}, P_{13})	15.352	(0.432, 0.938)	0.022	0.318	0.511	0.539	0.396	0.468	
			(0.568, 0.562)							
			(0.432, 0.562)							
			(0.568, 0.938)							
	(P_{13}, P_{12}, P_{13})	27.629	27.629	(0.432, 0.938)	0.022	0.318	0.489	1.539	0.396	0.468
				(0.568, 0.562)						
				(0.432, 0.562)						
				(0.568, 0.938)						

Table 2: χ^2 analysis for the residual symmetries $Z_2^{st^2su} \times X_l$ in the charged lepton sector and $Z_2^s \times X_\nu$ in the neutrino sector with $X_l = t^2$ and $X_\nu = su$. We give the best fit values θ_l^{bf} and θ_ν^{bf} for θ_l and θ_ν corresponding to χ^2_{\min} . We also list the mixing angles and CP violating phases at the best fit point.

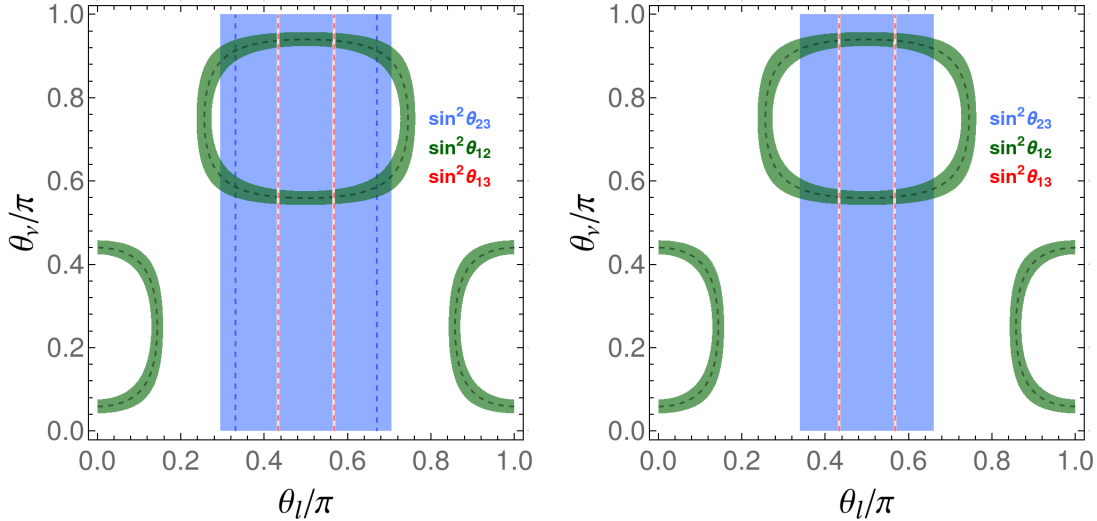


Figure 24: Contour plots of $\sin^2 \theta_{ij}$ in the plane θ_ν versus θ_l for the residual symmetries $Z_2^{st^2su} \times X_l$ in the charged lepton sector and $Z_2^s \times X_\nu$ in the neutrino sector with $X_l = t^2$ and $X_\nu = su$. The red, blue and green areas are the 3σ regions of $\sin^2 \theta_{13}$, $\sin^2 \theta_{23}$ and $\sin^2 \theta_{12}$ respectively. The dashed lines correspond to the best fit mixing angle values taken from [24, 25].

6.4 Quark and lepton mixing from a common flavour group

Discrete flavour symmetries are particularly suitable to account for the large lepton mixing angles. As discussed in [259, 263, 270, 278–281] they can also address the quark mixing pattern. Assuming that the flavour group of quarks is broken down to different residual subgroups in the up- and down-quark sectors, only the Cabibbo mixing between the first two quark families can be generated with only flavour symmetry [263, 270, 278, 280, 281]. It is remarkable that the hierarchical quark mixing angles and CP

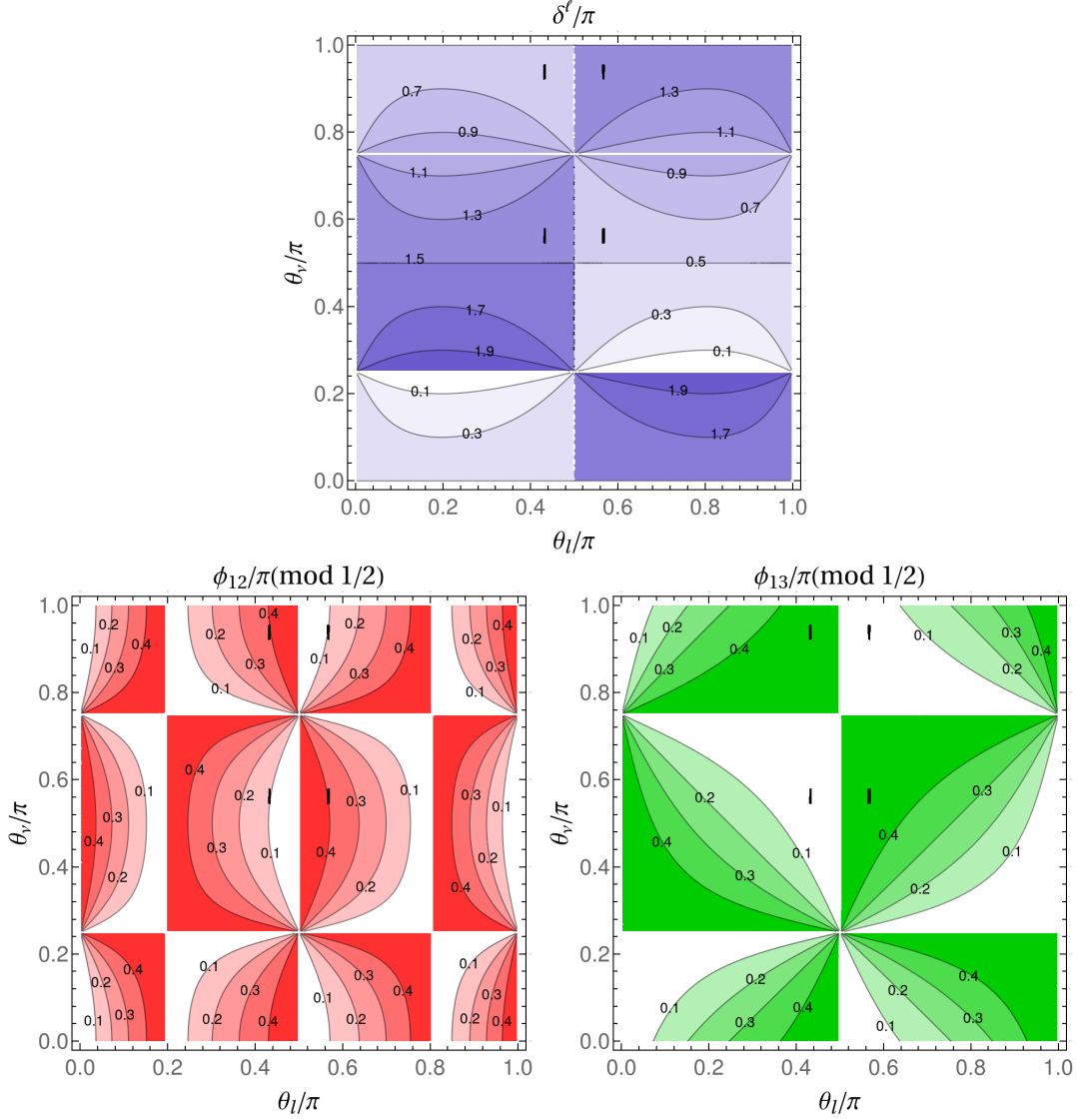


Figure 25: Contour plots of the CP violation phases δ^ℓ , ϕ_{12} and ϕ_{13} in the $\theta_l - \theta_\nu$ plane, where the residual symmetries are $Z_2^{st^2su} \times X_l$ in the charged lepton sector and $Z_2^s \times X_\nu$ in the neutrino sector with $X_l = t^2$ and $X_\nu = su$. In the black areas all three lepton mixing angles lie within their experimental 3σ ranges. Here we choose the row and column permutations $(P_l, P_\nu) = (P_{12}, P_{13})$, the Dirac CP phase δ^ℓ changes to $\delta^\ell + \pi$ while the Majorana phases ϕ_{12} and ϕ_{13} are invariant for $(P_l, P_\nu) = (P_{13}, P_{12}, P_{13})$.

violation can be explained if the flavour symmetry is extended with CP symmetry and the residual subgroups of the up- and down-quark sectors are $Z_2^{g_u} \times X_u$ and $Z_2^{g_d} \times X_d$ respectively [282, 284], where both CP transformations X_u and X_d are unitary and symmetric. The diagonalization matrices U_u and U_d would be restricted to be of the following form

$$U_u = \Sigma_u R_{23}(\theta_u) P_u Q_u, \quad U_d = \Sigma_d R_{23}(\theta_d) P_d Q_d \quad (6.65)$$

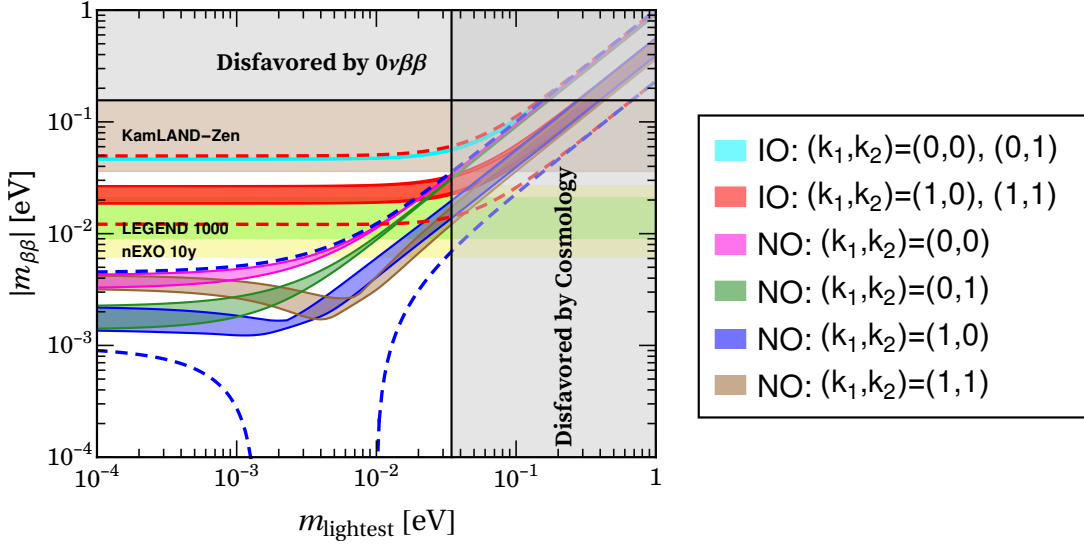


Figure 26: The effective Majorana neutrino mass $m_{\beta\beta}$ versus the lightest neutrino mass, for residual symmetries $Z_2^{st^2 su} \times X_l$ in the charged lepton and $Z_2^s \times X_\nu$ in the neutrino sector, with $X_l = t^2$ and $X_\nu = su$. Here we adopt the same convention for the different bands as used in figure 22.

where $P_{u,d}$ are three dimensional permutation matrices, $Q_{u,d}$ are generic phase matrices, and $\Sigma_{u,d}$ are the Takagi factorizations of $X_{u,d}$, fulfilling

$$\begin{aligned} X_u &= \Sigma_u \Sigma_u^T, & \Sigma_u^\dagger \rho(g_u) \Sigma_u &= \pm \text{diag}(1, -1, -1), \\ X_d &= \Sigma_d \Sigma_d^T, & \Sigma_d^\dagger \rho(g_d) \Sigma_d &= \pm \text{diag}(1, -1, -1). \end{aligned} \quad (6.66)$$

As a consequence, the CKM mixing matrix is predicted as

$$V_{CKM} = U_u^\dagger U_d = Q_u^\dagger P_u^T R_{23}^T(\theta_u) \Sigma_u^\dagger \Sigma_d R_{23}(\theta_d) P_d Q_d, \quad (6.67)$$

which only depends on two free rotation angles θ_u and θ_d , limited in the range $0 \leq \theta_{u,d} < \pi$. Notice that both Q_u and Q_d are unphysical, as they can be absorbed into quark fields. We take the flavour symmetry as the dihedral group D_n which has only one- and two-dimensional irreducible representations, as shown in C.

Since the top quark is much heavier than the others, the first two families of left-handed quarks are assigned to a doublet of D_n , while the third generation is a D_n singlet. Without loss of generality, we can take

$$\begin{pmatrix} Q_1 \\ Q_2 \end{pmatrix} \sim \mathbf{2}_1, \quad Q_3 \sim \mathbf{1}_1, \quad (6.68)$$

where $Q_1 \equiv (u_L, d_L)^T$, $Q_2 \equiv (c_L, s_L)^T$, and $Q_3 \equiv (t_L, b_L)^T$. The dihedral group and CP symmetry are broken down to $Z_2^{SR^{z_u}} \times X_u$ in up-quark sector and $Z_2^{SR^{z_d}} \times X_d$ in down-quark sector with $X_u = R^{-z_u + x_u}$ and $X_d = R^{-z_d + x_d}$, where $z_u, z_d = 0, 1, \dots, n-1$, $x_u = x_d = 0$ for odd n and $x_u, x_d = 0, n/2$ if the group

index n is even. The Takagi factorization of the residual symmetry $Z_2^{SR^z} \times R^{-z+x}$ is determined to be

$$\Sigma = \frac{i^{2x/n}}{\sqrt{2}} \begin{pmatrix} -e^{-\frac{i\pi z}{n}} & 0 & e^{-\frac{i\pi z}{n}} \\ e^{\frac{i\pi z}{n}} & 0 & e^{\frac{i\pi z}{n}} \\ 0 & \sqrt{2} i^{-2x/n} & 0 \end{pmatrix}. \quad (6.69)$$

From our master formula in Eq. (6.67), we find that the quark mixing matrix takes the following form,

$$V_{CKM} = \begin{pmatrix} \cos \varphi_1 & -c_d \sin \varphi_1 & s_d \sin \varphi_1 \\ c_u \sin \varphi_1 & s_d s_u e^{i\varphi_2} + c_d c_u \cos \varphi_1 & c_d s_u e^{i\varphi_2} - s_d c_u \cos \varphi_1 \\ -s_u \sin \varphi_1 & s_d c_u e^{i\varphi_2} - c_d s_u \cos \varphi_1 & c_d c_u e^{i\varphi_2} + s_d s_u \cos \varphi_1 \end{pmatrix}, \quad (6.70)$$

up to row and column permutations with

$$\varphi_1 = \frac{(z_u - z_d)\pi}{n}, \quad \varphi_2 = \frac{(x_u - x_d)\pi}{n} \quad (6.71)$$

and $c_d \equiv \cos \theta_d$, $s_d \equiv \sin \theta_d$, $c_u \equiv \cos \theta_u$, $s_u \equiv \sin \theta_u$. The parameters φ_1 and φ_2 depend on the choice of residual symmetry, and they can take the following discrete values

$$\begin{aligned} \varphi_1 \pmod{2\pi} &= 0, \frac{1}{n}\pi, \frac{2}{n}\pi, \dots, \frac{2n-1}{n}\pi, \\ \varphi_2 \pmod{2\pi} &= 0, \frac{1}{2}\pi, \frac{3}{2}\pi. \end{aligned} \quad (6.72)$$

One can straightforwardly extract the quark mixing parameters from Eq. (6.70). Eliminating the free parameters θ_u and θ_d , one obtains the following correlations among the quark mixing angles and CP phase [284],

$$\cos^2 \theta_{13}^q \cos^2 \theta_{12}^q = \cos^2 \varphi_1, \quad \sin \delta^q \simeq \frac{\sin 2\varphi_1 \sin \varphi_2}{\sin 2\theta_{12}^q \cos^2 \theta_{13}^q \cos \theta_{23}^q}. \quad (6.73)$$

The experimental data on the CKM matrix can be well accommodated for $\varphi_1 = \pi/14$, $\varphi_2 = \pi/2$, which can be achieved from the D_{14} flavour group with the residual symmetry indices $z_u = 1$, $z_d = 0$, $x_u = 7$, $x_d = 0$. The best-fit values of $\theta_{u,d}$ and mixing parameters are determined to be,

$$\begin{aligned} \theta_u &= 0.01237\pi, & \theta_d &= 0.99473\pi, & \sin \theta_{12}^q &= 0.22249, \\ \sin \theta_{13}^q &= 0.00369, & \sin \theta_{23}^q &= 0.04206, & J_{CP}^q &= 3.104 \times 10^{-5}. \end{aligned} \quad (6.74)$$

Notice that $\sin \theta_{13}^q$, $\sin \theta_{23}^q$ and J_{CP}^q are consistent with the global fit results of the UTfit collaboration [101]. The mixing angle $\sin \theta_{12}^q$ is about 1% smaller than its measured value, so that higher-order corrections in a concrete model are needed to reconcile it with the data.

The D_{14} flavour group can also explain the lepton flavour structure if it is broken down to $Z_2^{SR^{z_l}} \times X_l$ and $Z_2^{SR^{z_\nu}} \times X_\nu$ in the charged lepton and neutrino sector, respectively, where $X_l = R^{-z_l+x_l}$, $X_\nu = R^{-z_\nu+x_\nu}$ with $z_{l,\nu} = 0, 1, \dots, 13$ and $x_{l,\nu} = 0, 7$. The lepton mixing matrix has the same form as Eq. (6.70), the rotation angles θ_u and θ_d should be replaced with θ_l and θ_ν respectively. Choosing the residual

symmetry indices $z_l = 4$, $z_\nu = 0$, $x_l = 7$ and $x_\nu = 0$, we have $\varphi_1 = 2\pi/7$ and $\varphi_2 = \pi/2$. Choosing the permutations as $P_l = P_{12}P_{23}$ and $P_\nu = P_{13}$, the lepton mixing angles can be accommodated for certain values of the free parameters $\theta_{l,\nu}$:

$$\begin{aligned} \theta_e^{\text{bf}} &= 0.439\pi, \quad \theta_\nu^{\text{bf}} = 0.811\pi, \quad \chi_{\text{min}}^2 = 4.147, \quad \sin^2 \theta_{13} = 0.0220, \quad \sin^2 \theta_{12} = 0.318, \\ \sin^2 \theta_{23} &= 0.603, \quad \delta^\ell/\pi = 1.530, \quad \phi_{12}/\pi = -0.082 \pmod{1/2}, \quad \phi_{13}/\pi = 1.474 \pmod{1/2}. \end{aligned} \quad (6.75)$$

In summary, one sees how the dihedral group as well as the residual symmetry $Z_2 \times CP$ provide an interesting opportunity for model building. Indeed, we saw how the D_{14} flavour symmetry can provide a unified description of flavour mixing for both quarks and leptons.

If both left-handed quarks and leptons are assigned as irreducible triplets of the flavour symmetry and the residual symmetry is $Z_2 \times CP$, one finds that $\Delta(294)$ is the minimal flavour group that can generate realistic quark and lepton flavour mixing patterns [283]. In contrast, the singlet plus doublet assignment seems better than the triplet assignment. Once the CP symmetry is included, the order of the flavour symmetry group can be reduced considerably, i.e. 28 versus 294 in this scheme.

There are also other schemes to explain the mixing patterns of quarks and leptons using flavour and CP symmetries. For instance, quark and lepton mixing patterns can arise from the stepwise breaking of these symmetries to different residual subgroups in different sectors of the theory [285, 286], with charged fermion mass hierarchies generated by operators with different numbers of flavons. For a concrete model with $\Delta(384)$ flavour symmetry see [286].

6.5 Geometrical CP violation

It is well-known that CP symmetry is broken by complex Yukawa couplings in the SM, which leads to the CP violation in charged current interactions through the CKM matrix. However, the origin of CP violation is still a mystery. Analogous to the electroweak symmetry, the CP symmetry could be spontaneously broken by the VEVs of some scalar fields [414]. In models of spontaneous CP violation, the Lagrangian is invariant under the CP symmetry so that all parameters of the scalar potential are real in a certain basis. Spontaneous CP violation is achieved through complex VEVs for the Higgs multiplets which also break the gauge symmetry. Usually the phases of the fields depend on the coupling constants in the scalar potential.

The phases of the Higgs multiplets could have geometrical values, independently of the potential parameters if there is an additional (accidental) CP symmetry of the potential. The resulting CP breaking vacua lead to the so-called geometrical CP violation or calculable phases [415]. It has been shown that more than two Higgs doublets and non-abelian symmetry relating the Higgs multiplets are necessary conditions in order to realize the geometrical CP violation. It turns out that $\Delta(27)$ and $\Delta(54)$ are the smallest groups which lead to calculable phases [415, 416].

If one assigns three Higgs doublets $H \equiv (H_1, H_2, H_3)$ to a triplet of $\Delta(27)$ or $\Delta(54)$, the scalar potential

has only one relevant phase dependent term, i.e.

$$V = V_0 + \left[\lambda_4 \sum_{i \neq j \neq k} (H_i^\dagger H_j)(H_i^\dagger H_k) + \text{h.c.} \right]. \quad (6.76)$$

The traditional CP transformation $H_i \xrightarrow{CP} H_i^*$ forces the coupling λ_4 to be real. Then one can obtain the following two possible vacua with calculable phases [415]

$$\begin{aligned} \langle H \rangle &= \frac{v}{\sqrt{3}} \begin{pmatrix} 1 \\ \omega \\ \omega^2 \end{pmatrix}, & \lambda_4 < 0, \\ \langle H \rangle &= \frac{v}{\sqrt{3}} \begin{pmatrix} \omega^2 \\ 1 \\ 1 \end{pmatrix}, & \lambda_4 > 0. \end{aligned} \quad (6.77)$$

The same scalar potential as Eq. (6.76) and calculable phases in Eq. (6.77) can be obtained from other non-abelian symmetry groups such as $\Delta(3n^2)$ [417] and $\Delta(6n^2)$ [418], where n is a multiple of 3.

The observed fermion masses and flavor mixings could possibly be accommodated if one properly assigns the transformations of fermion fields under the symmetry group [416]. In short, the geometrical CP violation arises from the correct interplay among the scalar content, non-abelian symmetry group and CP symmetry.

7 Testing flavor and CP symmetries

As shown above, discrete flavor and generalized CP symmetries allow us to predict the lepton mixing matrix in terms of few parameters. Eliminating free parameters generally leads to correlations among the lepton mixing angles and CP violation phases. Such predictions are often called lepton mixing *sum rules* in the literature, though they are not always strictly so. For example, for the residual symmetry $\mathcal{G}_l = Z_n$ ($n \geq 3$), $\mathcal{G}_\nu = Z_2 \times CP$ discussed in section 6.3.1, the lepton mixing matrix depends on a unique real parameter θ , as shown in Eq. (6.41). The parameter θ becomes determined in terms of the precisely measured reactor mixing angle θ_{13} , leading to sharp predictions for the leptonic mixing angles and CP violation phases that can be tested at current and future neutrino oscillation experiments.

Ultimately they could be used to distinguish different symmetry-based flavor models. It is remarkable that, besides the mixing angles, flavor symmetry in combination with generalized CP symmetry allows us to predict both the Dirac and Majorana leptonic CP violation phases. Hence the effective neutrino mass $|m_{\beta\beta}|$ is constrained to lie within narrow regions, as can be seen from figures 22 and 26.

As a result one could also test flavor and CP symmetries by confronting with the data of the current and forthcoming $0\nu\beta\beta$ experiments. In fact, some flavor models relate the Majorana phases to the neutrino masses, which could also lead to restrictions on the effective mass $|m_{\beta\beta}|$, and a very powerful tool to test and discriminate flavour models.

7.1 Testing mixing predictions

Neutrino physics has entered the precision era, providing a good opportunity for probing different flavor models. The reactor angle θ_{13} is the best-measured leptonic mixing parameter. The precise measurement of nonzero θ_{13} by Daya Bay [21, 419], Double Chooz [420, 421], and RENO [22, 422] has excluded many flavor models predicting θ_{13} close to zero. The long baseline neutrino oscillation experiments NO ν A [423] and T2K [424] give measurements of the leptonic mixing angle θ_{23} and also the first hint of leptonic CP violation [425–427] associated to the leptonic Dirac CP violation phase δ_{CP} . However, the value of δ_{CP} has not been significantly constrained by neutrino oscillation experiments. The latest data of T2K favor near-maximal Dirac CP violation phase, the atmospheric mixing angle $\theta_{23} > 45^\circ$ and normal mass ordering [428]. The data of T2K constrain the CP phase δ_{CP} in the range $\delta_{CP} = -1.97_{-0.70}^{+0.97}$, and $\delta_{CP} = 0, \pi$ is excluded at more than 90% confidence level [428]. In comparison with T2K, the data of NO ν A exclude the CP phase in the vicinity of $\delta_{CP} = \pi/2$ at more than 3σ for the inverted mass ordering, and the values around $\delta_{CP} = 3\pi/2$ in the normal ordering are disfavored at 2σ confidence [429]. Improved CP measurements constitute the target of upcoming experiments such as DUNE. The future long baseline neutrino oscillation experiments DUNE [113, 430] and T2HK [431] should measure θ_{23} and δ_{CP} with very good precision. It is expected that DUNE can observe the signal of lepton CP violation with 5σ significance after about 7 years if $\delta_{CP} = -\pi/2$ and after about 10 years for 50% of δ_{CP} values, and CP violation can be observed with 3σ significance for 75% of δ_{CP} values after about 13 years of running [113, 430]. T2HK has shown that it can expect a discovery of CP violation over 76%(58%) of the parameter space at $3\sigma(5\sigma)$ [431]. The forthcoming medium baseline reactor neutrino experiment JUNO

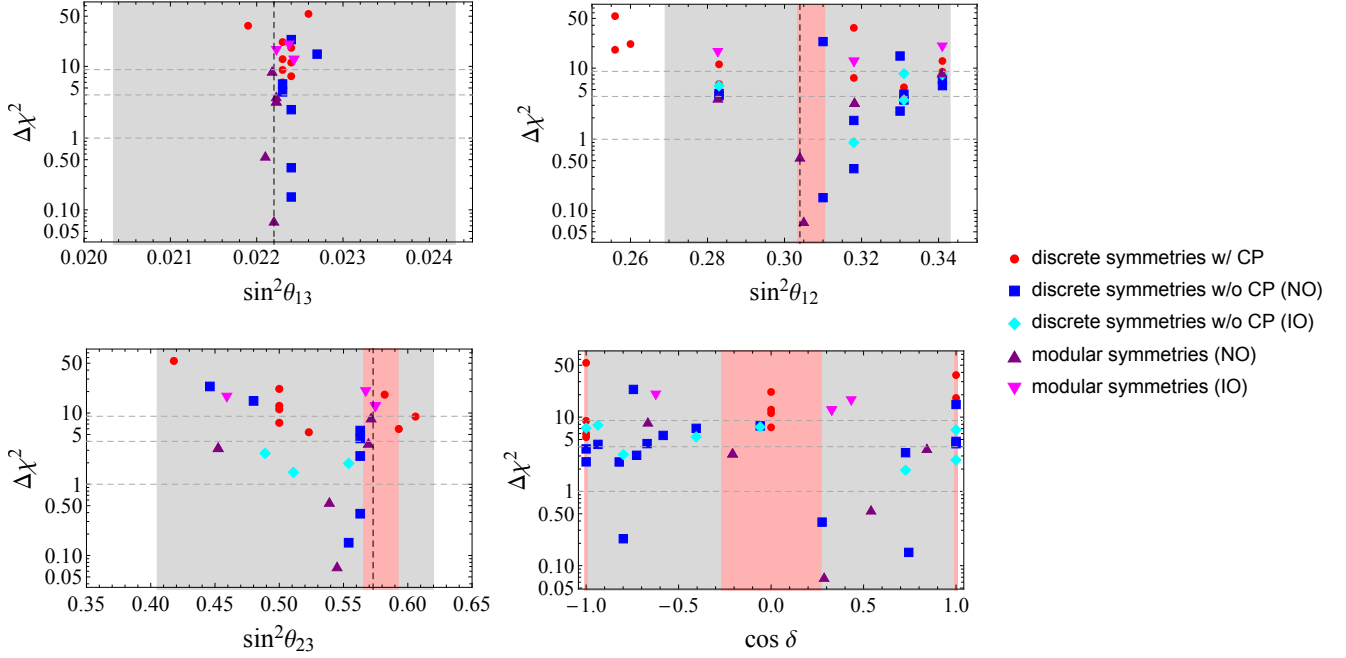


Figure 27: Best-fit predictions of the models based on discrete symmetries broken to certain residual symmetries of the lepton mass matrices [432, 433], and the models based on modular symmetries discussed in [434–436]. The gray regions are the 3σ ranges and the dashed line is the best fit value for normal-ordered neutrino masses. The red band in the panel of $\sin^2\theta_{12}$ is the prospective 3σ range after 6 years of JUNO running [115], and the red regions in the panels of $\sin^2\theta_{23}$ and $\cos\delta$ are the prospective 3σ ranges after 15 years of DUNE running [430]. This figure is taken from [437].

can make very precise measurement of the solar angle θ_{12} , and the error of $\sin^2\theta_{12}$ can be reduced to the level of 0.5% – 0.7% [115].

We show in figure 27 the best fit predictions for the mixing parameters in some typical models based on discrete flavor symmetry with or without generalized CP symmetry and modular symmetry. We see that the synergy between JUNO and long baseline neutrino experiments DUNE and T2HK will be extremely powerful for testing the huge number of flavor symmetry models.

As an illustration, we give an extensively discussed prediction for lepton mixing angles as follows [438, 439],

$$\cos\delta_{CP} = \frac{\tan\theta_{23}}{\sin 2\theta_{12} \sin\theta_{13}} [\cos 2\theta'_{12} + (\sin^2\theta_{12} - \cos^2\theta'_{12}) (1 - \cot^2\theta_{23} \sin^2\theta_{13})], \quad (7.1)$$

which generally arises when considering charged-lepton corrections to neutrino mixing matrices which are completely fixed by symmetry with the neutrino angle $\theta'_{13} = 0$ and charged lepton rotation angle $\theta^e_{13} = 0$. This prediction gives $\cos\delta_{CP}$ as a function of the measured lepton mixing angles and one fixed parameter θ'_{12} determined by the underlying discrete symmetry. It is noticeable that Eq. (7.1) is specified by fixing the value of just one parameter, the angle θ'_{12} . Thus one can enumerate the viable models of this type by deriving the values of θ'_{12} from symmetry considerations. This leads us the following well-motivated sum rules characterized by specific values of θ'_{12} , namely the one based on TBM mixing with

	Ranges of δ_{CP} obtained by varying			
	θ_{12} in 3σ	θ_{23} in 3σ	θ_{13} in 3σ	$\theta_{12}\&\theta_{23}\&\theta_{13}$ in 3σ
TBM	$\pm[240.54^\circ, 289.19^\circ]$	$\pm[264.58^\circ, 268.06^\circ]$	$\pm[264.86^\circ, 265.89^\circ]$	$\pm[235.27^\circ, 291.21^\circ]$
GRA	$\pm[271.01^\circ, 322.93^\circ]$	$\pm[289.72^\circ, 295.36^\circ]$	$\pm[292.95^\circ, 294.82^\circ]$	$\pm[270.22^\circ, 332.89^\circ]$
GRB	$\pm[233.08^\circ, 283.21^\circ]$	$\pm[258.11^\circ, 263.51^\circ]$	$\pm[258.57^\circ, 260.20^\circ]$	$\pm[226.19^\circ, 284.41^\circ]$
HG	$\pm[284.70^\circ, 360^\circ]$	$\pm[300.64^\circ, 312.11^\circ]$	$\pm[307.15^\circ, 310.98^\circ]$	$\pm[283.21^\circ, 360^\circ]$

Table 3: The prediction of the sum rule Eq. (7.1) for the allowed ranges of $|\delta_{CP}|$ due to the present 3σ uncertainties in the values of the neutrino mixing angles. Here we vary at least one lepton mixing angle in its corresponding 3σ intervals for the NO spectrum [24].

$\theta_{12}^\nu = \arcsin(1/\sqrt{3}) \approx 35.26^\circ$ [296–298], the one based on BM mixing with $\theta_{12}^\nu = 45^\circ$ [333], the one based on the type A golden ratio mixing (GRA) with $\theta_{12}^\nu = \arctan(1/\phi_g) \approx 31.72^\circ$ [328, 329], the one based on the type B golden ratio mixing (GRB) with $\theta_{12}^\nu = \arccos(\phi_g/2) = 36^\circ$ [326, 327], and the one based on hexagonal (HEX) mixing with $\theta_{12}^\nu = 30^\circ$ [317, 440].

Using the sum rule of Eq. (7.1) and plugging into the best fit values of the neutrino mixing angles for NO [24], one can straightforwardly determine the value of $\cos \delta_{CP}$ and the CP phase δ_{CP} for the above mentioned values of θ_{12}^ν ,

$$\begin{aligned}
\text{TBM : } & \cos \delta_{CP} \approx -0.08, \quad \delta_{CP} \approx \pm 94.65^\circ, \\
\text{GRA : } & \cos \delta_{CP} \approx 0.41, \quad \delta_{CP} \approx \pm 66.09^\circ, \\
\text{GRB : } & \cos \delta_{CP} \approx -0.18, \quad \delta_{CP} \approx \pm 100.65^\circ, \\
\text{HG : } & \cos \delta_{CP} \approx 0.63, \quad \delta_{CP} \approx \pm 50.90^\circ,
\end{aligned} \tag{7.2}$$

Notice that there are two values of δ_{CP} of opposite sign for each value of $\cos \delta_{CP}$. The sum rule of Eq. (7.1) for the BM case, $\theta_{12}^\nu = 45^\circ$, is not compatible with the current best fit values of the lepton mixing angles [24], and will be dropped hereafter. We also take into account the experimental uncertainties of the three lepton mixing angles by varying θ_{12} , θ_{23} , and θ_{13} in their 3σ experimentally allowed regions. The ranges of the CP violation δ_{CP} obtained from Eq. (7.1) are summarized in table 3. We see that out of all mixing angles, the 3σ allowed range of θ_{12} causes the largest uncertainty in δ_{CP} resulting from Eq. (7.1).

Future long baseline experiments DUNE and T2HK will be able to make precision measurement of δ_{CP} and θ_{23} . The combination of DUNE and T2HK provides better sensitivity to δ_{CP} than either of these two experiments in isolation. The prospective DUNE+T2HK data should allow one to test the predictions for $\cos \delta_{CP}$, as shown in figure 28. Given the 3σ range $\delta_{CP} \in [127.80^\circ, 358.20^\circ]$ of the Dirac phase δ_{CP} from the latest global analysis [24], only δ_{CP} values in the interval of 180° to 360° are considered in figure 28. We see that a significant part of the true value of δ_{CP} gets disfavoured at more than 3σ for each symmetry predicted value of the angle θ_{12}^ν . Furthermore, detailed analysis showed that future facilities DUNE and T2HK in combination with JUNO could distinguish the different cases of θ_{12}^ν [439, 441].

In summary, the existence of mixing predictions is a characteristic feature of flavor symmetry models, as explicitly shown in Eqs. (5.12, 5.18, 5.24, 6.9, 6.22, 6.47, 6.51, 6.54, 6.73). These relations highlight

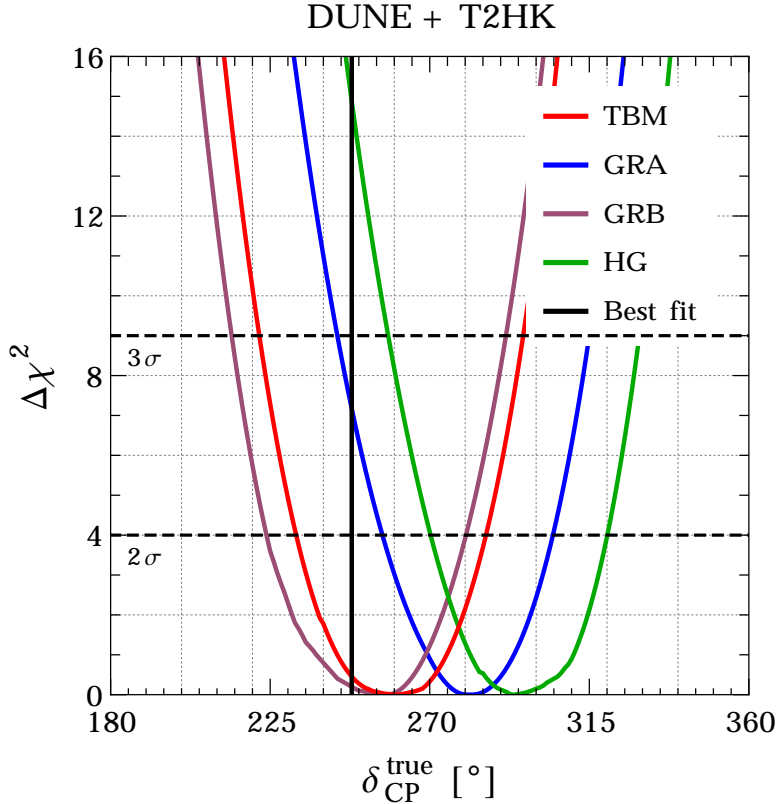


Figure 28: Compatibility of the prediction in Eq. (7.1) with any potentially true value of the Dirac CP phase δ_{CP} in the range $\delta_{CP} \in [180^\circ, 360^\circ]$. Four values of θ'_{12} are considered: $\theta'_{12} = \arcsin(1/\sqrt{3}) \approx 35.26^\circ$ for TBM, $\theta'_{12} = \arctan(1/\phi_g) \approx 31.72^\circ$ for GRA, $\theta'_{12} = 36^\circ$ for GRB, and $\theta'_{12} = 30^\circ$ for HG. From [441].

the testability of flavor symmetry, and there are many other possible relations among the lepton mixing parameters in the literature [355, 438, 439, 442–445]. The phenomenological implications of these sum rules and the prospects of testing them at precision neutrino facilities have been extensively discussed [433, 439, 441, 444, 446, 447].

7.2 Testing mass sum rules

The neutrino mass matrix leading to the three neutrino masses in discrete flavor symmetry models typically involves a reduced set of parameters. Indeed, several discrete flavor-symmetry-based models yield a constrained neutrino mass matrix, leading to specific neutrino mass sum-rules. This in turn is phenomenologically interesting, as it can lead to predictions for the effective neutrinoless double beta mass parameter [141]. For example, one can have a $0\nu\beta\beta$ lower bound on even for normal ordered neutrino spectrum [142].

If the light neutrino mass matrix depends on two complex parameters [448] one can extract a relation between the three complex neutrino mass eigenvalues, leading to a neutrino mass sum rule. Typically neutrino mass sum rules can arise from any neutrino mass generation mechanism in which the structure of the mass matrix is generated by two flavons. Prime examples neutrino mass sum rules are $2\tilde{m}_2 + \tilde{m}_3 = \tilde{m}_1$ and $2\tilde{m}_2^{-1} + \tilde{m}_3^{-1} = \tilde{m}_1^{-1}$ predicted by early A_4 models [70, 313, 449]. For systematic categorisation and

consequences of neutrino mass sum rules in beta decay, $0\nu\beta\beta$ decay and cosmology see Refs. [141,450–453]. A sample of the flavor models in the literature, includes the following twelve different neutrino mass sum rules [451]:

$$\begin{aligned}
\tilde{m}_1 + \tilde{m}_2 &= \tilde{m}_3, & \tilde{m}_1 + \tilde{m}_3 &= 2\tilde{m}_2, \\
2\tilde{m}_2 + \tilde{m}_3 &= \tilde{m}_1, & \tilde{m}_1 + \tilde{m}_2 &= 2\tilde{m}_3, \\
\tilde{m}_1 + \frac{\sqrt{3}+1}{2}\tilde{m}_3 &= \frac{\sqrt{3}-1}{2}\tilde{m}_2, & \tilde{m}_1^{-1} + \tilde{m}_2^{-1} &= \tilde{m}_3^{-1}, \\
2\tilde{m}_2^{-1} + \tilde{m}_3^{-1} &= \tilde{m}_1^{-1}, & \tilde{m}_1^{-1} + \tilde{m}_3^{-1} &= 2\tilde{m}_2^{-1}, \\
\tilde{m}_3^{-1} \pm 2i\tilde{m}_2^{-1} &= \tilde{m}_1^{-1}, & \tilde{m}_1^{1/2} - \tilde{m}_3^{1/2} &= 2\tilde{m}_2^{1/2}, \\
\tilde{m}_1^{1/2} + \tilde{m}_3^{1/2} &= 2\tilde{m}_2^{1/2}, & \tilde{m}_1^{-1/2} + \tilde{m}_2^{-1/2} &= 2\tilde{m}_3^{-1/2}, \tag{7.3}
\end{aligned}$$

where \tilde{m}_i stand for the complex neutrino mass eigenvalues, which can be expressed in terms of the Majorana phases $\phi_i \in [0, 2\pi)$ and the physical mass eigenvalues $m_i \geq 0$ as $\tilde{m}_i = m_i e^{-i\phi_i}$ with ϕ_3 chosen to be unphysical. These sum rules appeared in models based on A_4 , S_4 , A_5 , T' , T_7 , $\Delta(54)$ and $\Delta(96)$ flavor symmetry, when the three neutrino mass eigenvalues can be described by two model parameters only, see Ref. [451] for a very good discussion and references on models predicting these sum rules. In addition, five new mass sum rules have been identified in flavor models based on modular symmetries with residual symmetries [434]. From Eq. (7.3) one sees that all neutrino mass sum rules can be parametrized in the following manner [451, 452]:

$$c_1 \left(m_1 e^{-i\phi_1}\right)^d e^{i\Delta\chi_{13}} + c_2 \left(m_2 e^{-i\phi_2}\right)^d e^{i\Delta\chi_{23}} + m_3^d = 0, \tag{7.4}$$

with $c_1, c_2 > 0$, where ϕ_1 and ϕ_2 are the Majorana phases. The parameters c_1 , c_2 , d , $\Delta\chi_{13}$, and $\Delta\chi_{23}$ characterize the sum rule, and they can be straightforwardly read out for any of the above twelve known sum rules. Interpreting the complex numbers as vectors in the complex plane, the neutrino mass sum rule can be geometrically understood as a sum of three vectors which form a triangle in the complex plane [450]. Since the sum rule in Eq. (7.4) is a complex equation, it requires both real part and imaginary parts to be vanishing, i.e.,

$$\begin{aligned}
c_1 m_1^d \cos \beta + c_2 m_2^d \cos \alpha + m_3^d &= 0, \\
c_1 m_1^d \sin \beta + c_2 m_2^d \sin \alpha &= 0, \tag{7.5}
\end{aligned}$$

with the angles $\alpha \equiv -d\phi_2 + \Delta\chi_{23}$ and $\beta \equiv -d\phi_1 + \Delta\chi_{13}$. Eq. (7.5) allows to express α and β in terms of the parameters of the sum rule,

$$\cos \alpha = \frac{c_1^2 m_1^{2d} - c_2^2 m_2^{2d} - m_3^{2d}}{2c_2 m_2^d m_3^d}, \quad \cos \beta = \frac{c_2^2 m_2^{2d} - c_1^2 m_1^{2d} - m_3^{2d}}{2c_1 m_1^d m_3^d},$$

$$\begin{aligned}
\sin \alpha &= \pm \frac{\sqrt{4c_2^2 m_2^{2d} m_3^{2d} - (c_1^2 m_1^{2d} - c_2^2 m_2^{2d} - m_3^{2d})^2}}{2c_2 m_2^d m_3^d}, \\
\sin \beta &= \mp \frac{\sqrt{4c_2^2 m_2^{2d} m_3^{2d} - (c_1^2 m_1^{2d} - c_2^2 m_2^{2d} - m_3^{2d})^2}}{2c_1 m_1^d m_3^d},
\end{aligned} \tag{7.6}$$

which relate Majorana CP phases with light neutrino masses. Given that $|\cos \alpha| \leq 1$, $|\sin \alpha| \leq 1$, $|\cos \beta| \leq 1$ and $|\sin \beta| \leq 1$, it follows that the validity of the sum rule requires the three neutrino masses to satisfy the following triangle inequalities,

$$\begin{aligned}
|c_1 m_1^d e^{i\beta}| &\leq |c_2 m_2^d e^{i\alpha}| + |c_3 m_3^d|, \\
\text{and } |c_2 m_2^d e^{i\alpha}| &\leq |c_1 m_1^d e^{i\beta}| + |c_3 m_3^d|, \\
\text{and } |c_3 m_3^d| &\leq |c_1 m_1^d e^{i\beta}| + |c_2 m_2^d e^{i\alpha}|,
\end{aligned} \tag{7.7}$$

which implies a triangle formed out of the three vectors $c_1 m_1^d e^{i\beta}$, $c_2 m_2^d e^{i\alpha}$ and $c_3 m_3^d$ in the complex plane. Given the solar and atmospheric neutrino mass squared differences $\Delta m_{\text{sol}}^2 \equiv m_2^2 - m_1^2 = 7.50_{-0.20}^{+0.22} \times 10^{-5} \text{ eV}^2$ and $\Delta m_{\text{atm}}^2 \equiv |m_3^2 - m_1^2| = 2.55 (2.45)_{-0.03}^{+0.02} \times 10^{-3} \text{ eV}^2$ [24] for NO (IO), the light neutrino masses are related to the smallest mass m_1 (m_3) as follows,

$$\begin{aligned}
\text{NO : } m_2 &= \sqrt{\Delta m_{\text{sol}}^2 + m_1^2}, \quad m_3 = \sqrt{\Delta m_{\text{atm}}^2 + m_1^2}, \\
\text{IO : } m_1 &= \sqrt{\Delta m_{\text{atm}}^2 + m_3^2}, \quad m_2 = \sqrt{\Delta m_{\text{atm}}^2 + \Delta m_{\text{sol}}^2 + m_3^2}.
\end{aligned} \tag{7.8}$$

Thus mass rules usually lead to a lower limit on the lightest neutrino mass through the triangle inequalities in Eq. (7.7), and some sum rules may only allow for a certain mass ordering. For instance, neutrino masses can only be normal ordered for the sum rule $2\tilde{m}_2 + \tilde{m}_3 = \tilde{m}_1$ since the triangle inequality $m_3 + m_1 \geq 2m_2$ cannot be fulfilled for IO. Solving the inequality $m_3 \leq m_1 + 2m_2$ in the case of NO, one obtain the lower limit on m_1 ,

$$m_1 \geq \sqrt{\frac{\Delta m_{\text{atm}}^2}{8}} (1 - 3r) \simeq 0.016 \text{ eV}, \tag{7.9}$$

where the exact result has been expanded in terms of the small ratio $r \equiv \Delta m_{\text{sol}}^2 / \Delta m_{\text{atm}}^2$. Another benchmark sum rule $2\tilde{m}_2^{-1} + \tilde{m}_3^{-1} = \tilde{m}_1^{-1}$ works for both mass orderings, and the limits on the lightest neutrino mass from the triangle inequalities are found to be

$$\begin{aligned}
\text{NO : } 0.0043 \text{ eV} &\simeq \sqrt{\frac{\Delta m_{\text{sol}}^2}{3}} \left(1 - \frac{4\sqrt{3r}}{9}\right) \leq m_1 \leq \sqrt{\frac{\Delta m_{\text{sol}}^2}{3}} \left(1 + \frac{4\sqrt{3r}}{9}\right) \simeq 0.0057 \text{ eV}, \\
\text{IO : } m_3 &\geq \sqrt{\frac{\Delta m_{\text{atm}}^2}{8}} \left(1 + \frac{r}{3}\right) \simeq 0.018 \text{ eV}.
\end{aligned} \tag{7.10}$$

One sees that certain mass sum rules predict a value of the lightest neutrino mass close to the current upper limit from cosmology and therefore they could be probed in the near future. Moreover, the lower

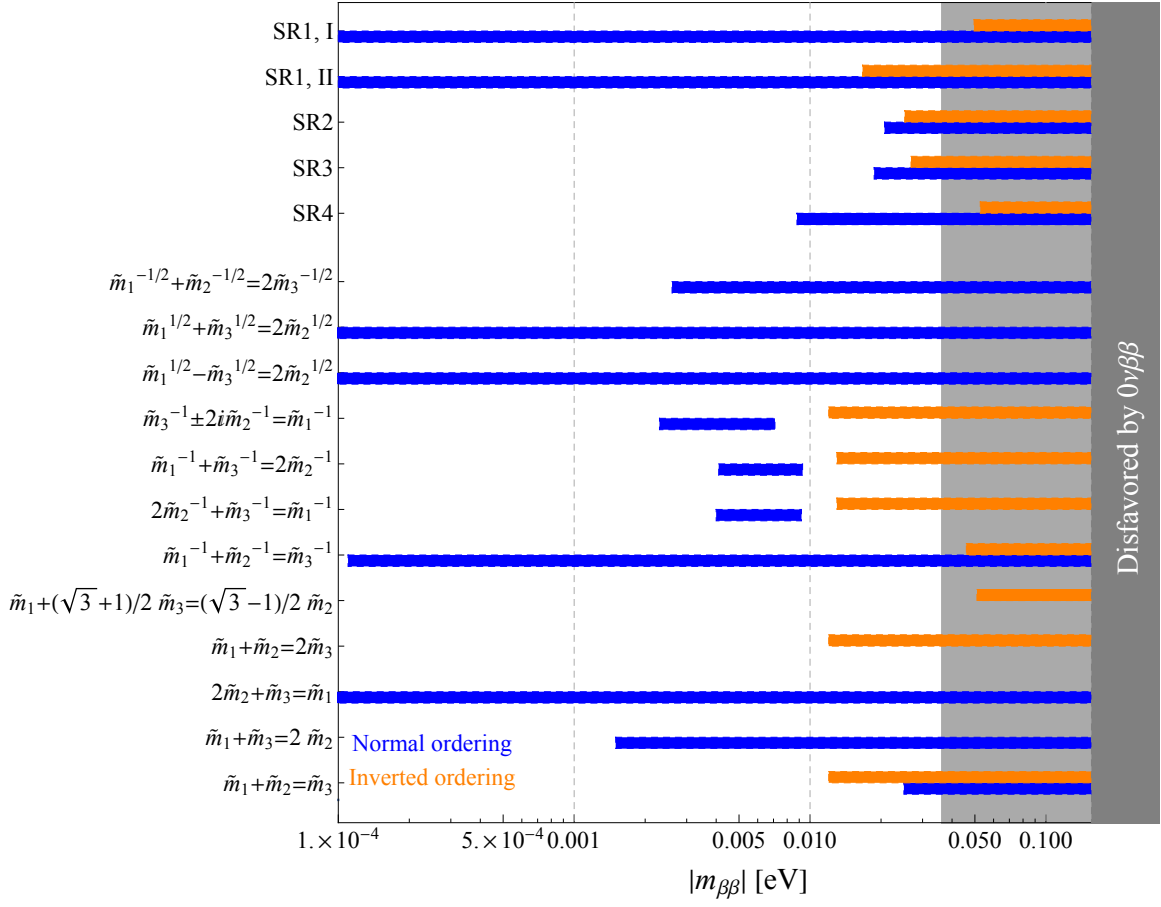


Figure 29: Predictions for $|m_{\beta\beta}|$ from different neutrino mass sum rules. The upper five mass sum rules have been derived in models based on modular symmetries [434], the lower twelve mass sum rules come from models based on discrete symmetries [451]. The grey regions show the constraints on $|m_{\beta\beta}|$ from Ref. [125] using commonly-adopted nuclear matrix-element calculations. Taken from [107].

bound on the lightest neutrino mass obtained in this way combined with the predictions for Majorana phases in Eq. (7.6) can be used to estimate the lower bound for the effective mass $|m_{\beta\beta}|$ from the general expression in Eq. (1.25). A detailed description of the analysis procedure can be found in Refs. [450, 451]. The predictions for the effective Majorana neutrino mass $|m_{\beta\beta}|$ for the different sum rules are displayed in figure 29.

One sees that certain sum rules can be fully or partially probed by the next generation of $0\nu\beta\beta$ decay experiments even taking into account the large uncertainties in the nuclear matrix element calculations. The exact mass sum rule could be violated by the higher-order terms resulting from flavour symmetry breaking or by the renormalization group evolution effects [452]. It was shown that the predictions of the sum rules are still valid at least qualitatively [452, 453]. To sum up one can say that, precision measurements of mixing angles, an observation of neutrinoless double beta decay can also provide insights into underlying flavor symmetries.

7.3 Flavor symmetry toolkit

One can check the validity of flavor symmetry models and constrain their predicted mixing parameters by comparing them those extracted from global oscillation fit results [24–27]. Nevertheless, numerical simulation of neutrino experiments and statistical analysis are often necessary to test and discriminate theoretical models in the current and future neutrino oscillation experiments such as NO ν A, T2K, JUNO, DUNE and T2HK. The public available software such as GLOBES [454, 455], Prob3++ [456], nuCRAFT [457] and nuSQuIDS [458] have been widely used to simulate the experimental characteristics of neutrino oscillation experiments. The compatibility between the experimental data and the expected outcome of a given neutrino experiment is frequently evaluated by the chi-square test. The involved simulation and analysis with GLOBES is quite involved and time-consuming. In order to facilitate the analysis of leptonic flavour symmetry models in neutrino oscillation experiments, a dedicated package FaSE-GLOBES has been recently developed [459] and is available via the link https://github.com/tcwphy/FASE_GLOBES. FaSE-GLOBES is a supplemental tool for GLOBES, written in c/c++ language, and allows users to assign any flavour symmetry model and analyze how it can be constrained and tested by the simulated neutrino oscillation experiments.

8 Benchmark UV-complete models in 4-D

In addition to the model-independent approaches described in previous chapters, the flavour problem may be tackled in a more complete, UV-complete manner, by guessing the structure of the underlying family symmetry and building explicit models on a case-by-case basis, for reviews see, e.g. Refs. [86–91]. In this chapter we present two simple extensions of the Standard Model implementing family symmetry within the renormalisable $SU(3)_c \otimes SU(2)_L \otimes U(1)_Y$ gauge field theoretic framework.

8.1 A_4 family symmetry in a scotogenic model

Here A_4 is used as flavour symmetry within the scotogenic picture [196] in which the neutrino masses are generated radiatively, and the lightest of the mediators is identified with the dark matter particle. We adopt the singlet-triplet extension [197–201] of the original model [196], making it substantially richer in the associated phenomenology [138]. We employ the Ma-Rajasekaran basis [53], the representation matrices of the generators and the Clebsch-Gordon coefficients are listed in table 12.

We now present a flavored extension of the theory proposed in [205]. The basic fields and their symmetry transformation properties are summarized in table 4. The left-handed leptons form an A_4 triplet, while right-handed ones come in as inequivalent singlets. Besides the SM fields, the original singlet-triplet scotogenic model [197] contains new weak iso-triplet and iso-singlet fermions Σ and F . Together with the Higgs scalars ϕ and Ω , these transform as triplets under the action of the family group A_4 , while the dark scalar η is a flavour singlet.

A characteristic prediction of this model is the lower bound for the $0\nu\beta\beta$ decay amplitude, discussed in section 1.4. This follows from its incomplete fermion multiplet nature, see figure 4. In contrast to its original form, both charged lepton and neutrino mass matrices will now have a non-trivial structure, predicting trimaximal neutrino mixing. As usual, the \mathbb{Z}_2 parity is imposed in order to ensure the stability of the dark matter candidate and the radiative nature of neutrino mass generation. With the fields and

	Standard Model		dark fermions		scalars		
	L	e_R, μ_R, τ_R	Σ	F	ϕ	η	Ω
multiplicity	3	3	3	3	3	1	3
$SU(3)_c$	1	1	1	1	1	1	1
$SU(2)_L$	2	1	3	1	2	2	3
$U(1)_Y$	-1	-2	0	0	1	1	0
\mathbb{Z}_2	1	1	-1	-1	1	-1	1
A_4	3	1, 1', 1''	3	3	3	1	3

Table 4: Transformation properties of the fields in the scotogenic model with A_4 family symmetry [205].

symmetry assignments in table 4, we can read out the Yukawa terms relevant to fermion masses as follows,

$$\begin{aligned}
 \mathcal{L}_Y \supset & -y_e(\bar{L}\phi)_1 e_R - y_\mu(\bar{L}\phi)_{1'} \mu_R - y_\tau(\bar{L}\phi)_{1''} \tau_R - Y_F (\bar{L}F)_1 \tilde{\eta} - Y_\Sigma (\bar{L}\tilde{\Sigma}^c)_1 \tilde{\eta} \\
 & - Y_{\Omega,1} \left(\text{Tr} \left[(\bar{\Sigma}\Omega)_{\mathbf{3}_S} \right] F \right)_1 - Y_{\Omega,2} \left(\text{Tr} \left[(\bar{\Sigma}\Omega)_{\mathbf{3}_A} \right] F \right)_1 + \text{h.c.} .
 \end{aligned} \tag{8.1}$$

In addition we have the bare mass terms

$$\mathcal{L}_{\mathcal{M}} \supset -\frac{1}{2}M_{\Sigma}\text{Tr}((\bar{\Sigma}\tilde{\Sigma}^c)_1) - \frac{1}{2}M_F(\bar{F}^c F)_1 + \text{h.c.}, \quad (8.2)$$

where $\tilde{\eta} = i\sigma_2\eta^*$. The $SU(2)_L$ triplets Σ and Ω are written in 2×2 matrix notation as

$$\Omega = \begin{pmatrix} \Omega^0/\sqrt{2} & \Omega^+ \\ \Omega^- & -\Omega^0/\sqrt{2} \end{pmatrix}, \quad \Sigma = \begin{pmatrix} \Sigma^0/\sqrt{2} & \Sigma^+ \\ \Sigma^- & -\Sigma^0/\sqrt{2} \end{pmatrix} \quad (8.3)$$

with $\tilde{\Sigma}^c \equiv i\sigma_2\Sigma^c i\sigma_2$. The scalar triplet Ω is assumed to be real.

The A_4 flavour symmetry is broken by the VEVs of the scalar fields ϕ and Ω , with the following VEV alignment in flavour space

$$\langle\phi\rangle = \begin{pmatrix} 1 \\ 1 \\ 1 \end{pmatrix} v_{\phi}, \quad \langle\Omega\rangle = \begin{pmatrix} 1 \\ 0 \\ 0 \end{pmatrix} v_{\Omega}, \quad \langle\eta\rangle = 0, \quad (8.4)$$

which can be a global minimum of the A_4 -invariant scalar potential in certain regions of parameter space [205]. Notice that the VEVs of ϕ and Ω break the A_4 flavour symmetry down to the subgroups Z_3^t and Z_2^s respectively, where the superscripts denote the generators of the subgroups. The ρ parameter constrains the VEV v_{Ω} to be small, and the current electroweak precision tests lead to [28]

$$v_{\Omega} \leq 4.5 \text{ GeV} \quad \text{at } 3\sigma \text{ CL} \quad (8.5)$$

8.1.1 Charged lepton masses

The first three terms in the Yukawa Lagrangian are responsible for the charged lepton masses. Inserting the VEV of ϕ and using the multiplication law for the contraction of two triplets in table 12, one can straightforwardly read out the charged lepton mass matrix as

$$M_{\ell} = \begin{pmatrix} y_e & y_{\mu} & y_{\tau} \\ y_e & \omega y_{\mu} & \omega^2 y_{\tau} \\ y_e & \omega^2 y_{\mu} & \omega y_{\tau} \end{pmatrix} v_{\phi}. \quad (8.6)$$

The matrix $M_{\ell}M_{\ell}^{\dagger}$ can be diagonalized to $\text{diag}(3|y_e v_{\phi}|^2, 3|y_{\mu} v_{\phi}|^2, 3|y_{\tau} v_{\phi}|^2)$ by means of the unitary transformation

$$U_{\ell} = \frac{1}{\sqrt{3}} \begin{pmatrix} 1 & 1 & 1 \\ 1 & \omega & \omega^2 \\ 1 & \omega^2 & \omega \end{pmatrix}, \quad (8.7)$$

which is a constant matrix.

8.1.2 Dark fermion masses

With the alignment of Ω in Eq. (8.4), we find the mass matrix of the dark fermions F and Σ^0 is of the following form

$$M_\chi = \begin{pmatrix} M_\Sigma & 0 & 0 & 0 & 0 & 0 \\ 0 & M_F & 0 & 0 & 0 & 0 \\ 0 & 0 & M_\Sigma & (Y_{\Omega,1} - Y_{\Omega,2})v_\Omega & 0 & 0 \\ 0 & 0 & (Y_{\Omega,1} - Y_{\Omega,2})v_\Omega & M_F & 0 & 0 \\ 0 & 0 & 0 & 0 & M_\Sigma & (Y_{\Omega,1} + Y_{\Omega,2})v_\Omega \\ 0 & 0 & 0 & 0 & (Y_{\Omega,1} + Y_{\Omega,2})v_\Omega & M_F \end{pmatrix} \quad (8.8)$$

in the convention of $-\frac{1}{2}(\overline{\Sigma}_1^0, \overline{F}_1^c, \overline{\Sigma}_2^0, \overline{F}_3^c, \overline{\Sigma}_3^0, \overline{F}_2^c)M_\chi(\Sigma_1^{0c}, F_1, \Sigma_2^{0c}, F_3, \Sigma_3^{0c}, F_2)^T$. The last block in Eq. (8.8) determines the masses of the dark Majorana fermions F and Σ . The symmetric complex 6×6 matrix M_χ can be diagonalized by a 6×6 block-diagonal matrix V :

$$V^T M_\chi V = \text{diag}(m_{\chi_1^0}, m_{\chi_2^0}, m_{\chi_3^0}, m_{\chi_4^0}, m_{\chi_5^0}, m_{\chi_6^0}), \quad (8.9)$$

with

$$V = \begin{pmatrix} 1 & 0 & 0 & 0 & 0 & 0 \\ 0 & 1 & 0 & 0 & 0 & 0 \\ 0 & 0 & \cos \theta_1 e^{i(\phi_1 + \varrho_1)/2} & \sin \theta_1 e^{i(\phi_1 + \sigma_1)/2} & 0 & 0 \\ 0 & 0 & -\sin \theta_1 e^{i(-\phi_1 + \varrho_1)/2} & \cos \theta_1 e^{i(-\phi_1 + \sigma_1)/2} & 0 & 0 \\ 0 & 0 & 0 & 0 & \cos \theta_2 e^{i(\phi_2 + \varrho_2)/2} & \sin \theta_2 e^{i(\phi_2 + \sigma_2)/2} \\ 0 & 0 & 0 & 0 & -\sin \theta_2 e^{i(-\phi_2 + \varrho_2)/2} & \cos \theta_2 e^{i(-\phi_2 + \sigma_2)/2} \end{pmatrix}. \quad (8.10)$$

Following the method described in D, one finds that the rotation angles θ_1 and θ_2 are given as

$$\tan 2\theta_1 = \frac{\Delta_{34}}{M_F^2 - M_\Sigma^2}, \quad \tan 2\theta_2 = \frac{\Delta_{56}}{M_F^2 - M_\Sigma^2}, \quad (8.11)$$

with

$$\begin{aligned} \Delta_{34} &= 2Y_- \sqrt{M_\Sigma^2 + M_F^2 + 2M_\Sigma M_F \cos 2\phi_{34}}, \\ \Delta_{56} &= 2Y_+ \sqrt{M_\Sigma^2 + M_F^2 + 2M_\Sigma M_F \cos 2\phi_{56}}, \\ Y_- &\equiv |(Y_{\Omega,1} - Y_{\Omega,2})v_\Omega|, \quad \phi_{34} \equiv \arg((Y_{\Omega,1} - Y_{\Omega,2})v_\Omega), \\ Y_+ &\equiv |(Y_{\Omega,1} + Y_{\Omega,2})v_\Omega|, \quad \phi_{56} \equiv \arg((Y_{\Omega,1} + Y_{\Omega,2})v_\Omega). \end{aligned} \quad (8.12)$$

The eigenvalues $M_{\chi_{1,2,3,4,5,6}^0}$ are given by

$$m_{\chi_1^0} = M_\Sigma, \quad m_{\chi_2^0} = M_F,$$

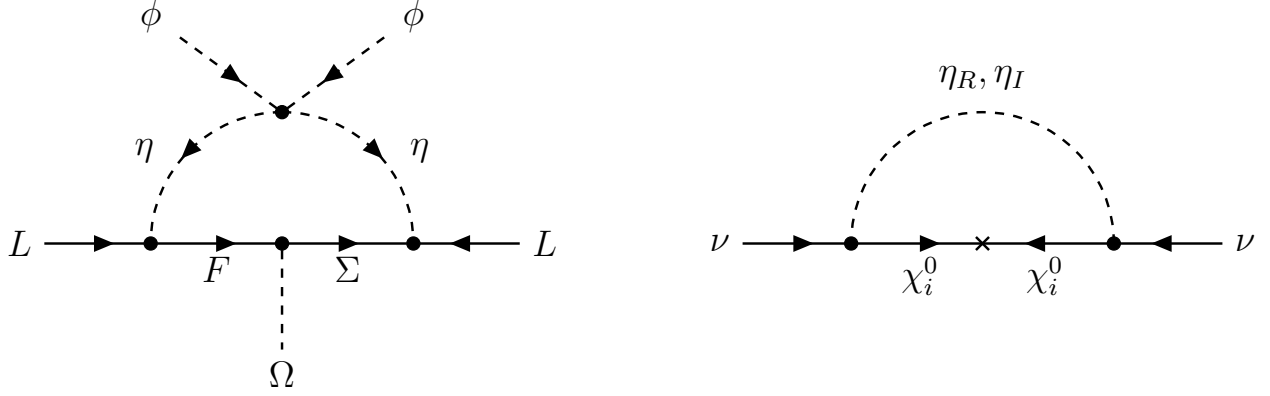


Figure 30: Feynman diagrams for scotogenic neutrino mass generation in the weak- (left panel) and mass-eigenstate basis (right panel).

$$\begin{aligned}
m_{\chi_3^0}^2 &= \frac{1}{2} \left(M_\Sigma^2 + M_F^2 + 2Y_-^2 - \sqrt{(M_F^2 - M_\Sigma^2)^2 + \Delta_{34}^2} \right), \\
m_{\chi_4^0}^2 &= \frac{1}{2} \left(M_\Sigma^2 + M_F^2 + 2Y_-^2 + \sqrt{(M_F^2 - M_\Sigma^2)^2 + \Delta_{34}^2} \right), \\
m_{\chi_5^0}^2 &= \frac{1}{2} \left(M_\Sigma^2 + M_F^2 + 2Y_+^2 - \sqrt{(M_F^2 - M_\Sigma^2)^2 + \Delta_{56}^2} \right), \\
m_{\chi_6^0}^2 &= \frac{1}{2} \left(M_\Sigma^2 + M_F^2 + 2Y_+^2 + \sqrt{(M_F^2 - M_\Sigma^2)^2 + \Delta_{56}^2} \right),
\end{aligned} \tag{8.13}$$

The Majorana fermion mass eigenstates $\chi_{1,2,3,4,5,6}^0$ are related with Σ_0^c and F by the unitary transformation V via

$$\begin{pmatrix} \Sigma_1^{0c} \\ F_1 \\ \Sigma_2^{0c} \\ F_3 \\ \Sigma_3^{0c} \\ F_2 \end{pmatrix} = V \begin{pmatrix} \chi_1^0 \\ \chi_2^0 \\ \chi_3^0 \\ \chi_4^0 \\ \chi_5^0 \\ \chi_6^0 \end{pmatrix}. \tag{8.14}$$

8.1.3 Scotogenic neutrino masses

We now turn to neutrino masses. These arise radiatively, at the one-loop level, as shown in figure 30, mediated by a “dark sector”, within a scotogenic setup. In contrast to the “flavour-blind” singlet-triplet scotogenic model, the dark fermions now transform as A_4 triplets and all of the six dark fermions mediate the one-loop diagrams. The interactions contributing to neutrino mass generation arise from the Yukawa terms involving Y_F and Y_Σ .

In the mass-eigenstate basis of dark Majorana fermions, the relevant Lagrangian is of the following

form

$$\mathcal{L}_\nu = -\frac{1}{\sqrt{2}}h_{\alpha i}\bar{\nu}_\alpha\eta_R\chi_i^0 + \frac{i}{\sqrt{2}}h_{\alpha i}\bar{\nu}_\alpha\eta_I\chi_i^0 - \frac{1}{\sqrt{2}}h_{\alpha i}^*\bar{\chi}_i^0\eta_R\nu_\alpha - \frac{i}{\sqrt{2}}h_{\alpha i}^*\bar{\chi}_i^0\eta_I\nu_\alpha, \quad (8.15)$$

where α is the family index and the rectangular matrix h is given by

$$h = \begin{pmatrix} \frac{Y_\Sigma}{\sqrt{2}} & Y_F & 0 & 0 & 0 & 0 \\ 0 & 0 & \frac{Y_\Sigma}{\sqrt{2}} & 0 & 0 & Y_F \\ 0 & 0 & 0 & Y_F & \frac{Y_\Sigma}{\sqrt{2}} & 0 \end{pmatrix} V. \quad (8.16)$$

Calculating the one-loop diagram in figure 30, we find that the radiatively generated neutrino mass matrix is given by

$$(m_\nu)_{\alpha\beta} = i \sum_i \frac{h_{\alpha i}h_{\beta i}}{32\pi^2} m_{\chi_i^0} \left(-\frac{m_{\eta_R}^2 \ln\left(\frac{m_{\eta_R}^2}{m_{\chi_i^0}^2}\right)}{m_{\eta_R}^2 - m_{\chi_i^0}^2} + \frac{m_{\eta_I}^2 \ln\left(\frac{m_{\eta_I}^2}{m_{\chi_i^0}^2}\right)}{m_{\eta_I}^2 - m_{\chi_i^0}^2} \right), \quad (8.17)$$

where m_{η_R} and m_{η_I} denote the masses of η_R and η_I respectively. Note that η_R and η_I are the real and imaginary parts of the neutral field $\eta^0 = (\eta_R + i\eta_I)/\sqrt{2}$. It is notable that the light neutrino mass matrix is predicted to be block-diagonal,

$$m_\nu = \begin{pmatrix} \times & 0 & 0 \\ 0 & \times & \times \\ 0 & \times & \times \end{pmatrix}, \quad (8.18)$$

where the symbol “ \times ” indicates a non-vanishing element. The reason is that only the flavon Ω is involved in the neutrino sector and its VEV preserves the Z_2^s subgroup, so that the light neutrino mass matrix is invariant under the action of the A_4 generator s , i.e., $\rho_{\mathbf{3}}^\dagger(s)m_\nu\rho_{\mathbf{3}}^*(s) = m_\nu$. This implies the form in Eq. (8.18). The corresponding neutrino diagonalization matrix is of the form

$$U_\nu = \begin{pmatrix} 1 & 0 & 0 \\ 0 & \cos\theta_\nu & \sin\theta_\nu e^{i\delta_\nu} \\ 0 & -\sin\theta_\nu e^{-i\delta_\nu} & \cos\theta_\nu \end{pmatrix}, \quad (8.19)$$

which satisfies $U_\nu^\dagger \mathcal{M}_\nu U_\nu^* = \text{diag}(m_1, m_2, m_3)$.

One sees that at this level there is no solar mixing. However, including the contribution from the charged lepton sector one obtains a realistic lepton mixing matrix given as

$$U = \frac{1}{\sqrt{3}} \begin{pmatrix} \cos\theta_\nu - \sin\theta_\nu e^{-i\delta_\nu} & 1 & \cos\theta_\nu + \sin\theta_\nu e^{i\delta_\nu} \\ \omega^2 \cos\theta_\nu - \omega \sin\theta_\nu e^{-i\delta_\nu} & 1 & \omega \cos\theta_\nu + \omega^2 \sin\theta_\nu e^{i\delta_\nu} \\ \omega \cos\theta_\nu - \omega^2 \sin\theta_\nu e^{-i\delta_\nu} & 1 & \omega^2 \cos\theta_\nu + \omega \sin\theta_\nu e^{i\delta_\nu} \end{pmatrix}. \quad (8.20)$$

with non-vanishing solar mixing angle. One sees the full lepton mixing matrix is predicted in terms of two free parameters θ_ν and δ_ν . Without loss of generality, these can be taken in the regions $0 \leq \theta_\nu \leq \pi$ and $0 \leq \delta_\nu \leq \pi$.

One also notes that the lepton mixing matrix U has the so-called trimaximal **TM2** form [205], since the second column is fixed to be $\frac{1}{\sqrt{3}}(1, 1, 1)^T$ [316–318]. From the mixing matrix (8.20) one can express the lepton mixing angles and the leptonic Jarlskog invariant in terms of just two free parameters

$$\begin{aligned}\sin^2 \theta_{13} &= \frac{1 + \sin 2\theta_\nu \cos \delta_\nu}{3}, & \sin^2 \theta_{12} &= \frac{1}{2 - \sin 2\theta_\nu \cos \delta_\nu}, \\ \sin^2 \theta_{23} &= \frac{1}{2} - \frac{\sqrt{3} \sin 2\theta_\nu \sin \delta_\nu}{4 - 2 \sin 2\theta_\nu \cos \delta_\nu}, & J_{CP} &= \frac{\cos 2\theta_\nu}{6\sqrt{3}}.\end{aligned}$$

One predicts the following relations amongst the mixing angles and the CP phase,

$$\cos^2 \theta_{13} \sin^2 \theta_{12} = \frac{1}{3}, \quad \cos \delta_{CP} = \frac{2(3 \cos^2 \theta_{12} \cos^2 \theta_{23} + 3 \sin^2 \theta_{12} \sin^2 \theta_{13} \sin^2 \theta_{23} - 1)}{3 \sin 2\theta_{23} \sin 2\theta_{12} \sin \theta_{13}}. \quad (8.21)$$

Using the 3σ range of the reactor angle $2.000 \times 10^{-2} \leq \sin^2 \theta_{13} \leq 2.405 \times 10^{-2}$ for NO and $2.018 \times 10^{-2} \leq \sin^2 \theta_{13} \leq 2.424 \times 10^{-2}$ for IO [24, 25], we predict narrow ranges for the solar mixing angle [205],

$$\text{NO: } 0.3401 \leq \sin^2 \theta_{12} \leq 0.3415, \quad \text{IO: } 0.3402 \leq \sin^2 \theta_{12} \leq 0.3416, \quad (8.22)$$

These predictions are very close to the 1σ upper limits from the general neutrino oscillation global fit [24, 25] and should be testable in forthcoming neutrino oscillation experiments.

To sum up we have obtained the three lepton mixing angles and the Dirac CP phase in terms of just two parameters θ_ν and δ_ν as given in figure 31. The resulting predictions for the two most poorly determined oscillation parameters $\sin^2 \theta_{23}$ and δ_{CP} are given in figure 32, where the star and dot stand

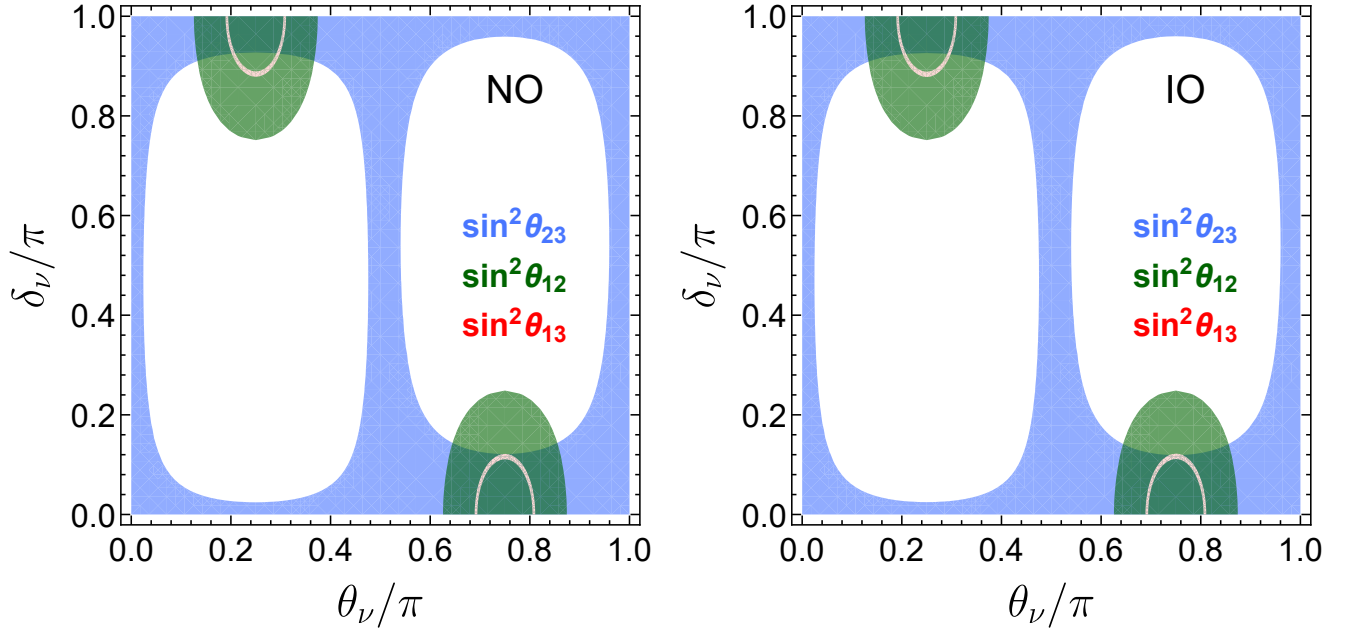


Figure 31: Contour plots of $\sin^2 \theta_{12}$, $\sin^2 \theta_{13}$, and $\sin^2 \theta_{23}$ in the $\theta_\nu - \delta_\nu$ plane. The red, green and blue areas denote the allowed 3σ regions of $\sin^2 \theta_{13}$, $\sin^2 \theta_{12}$ and $\sin^2 \theta_{23}$ respectively.

for the global best fit points for NO and IO respectively.

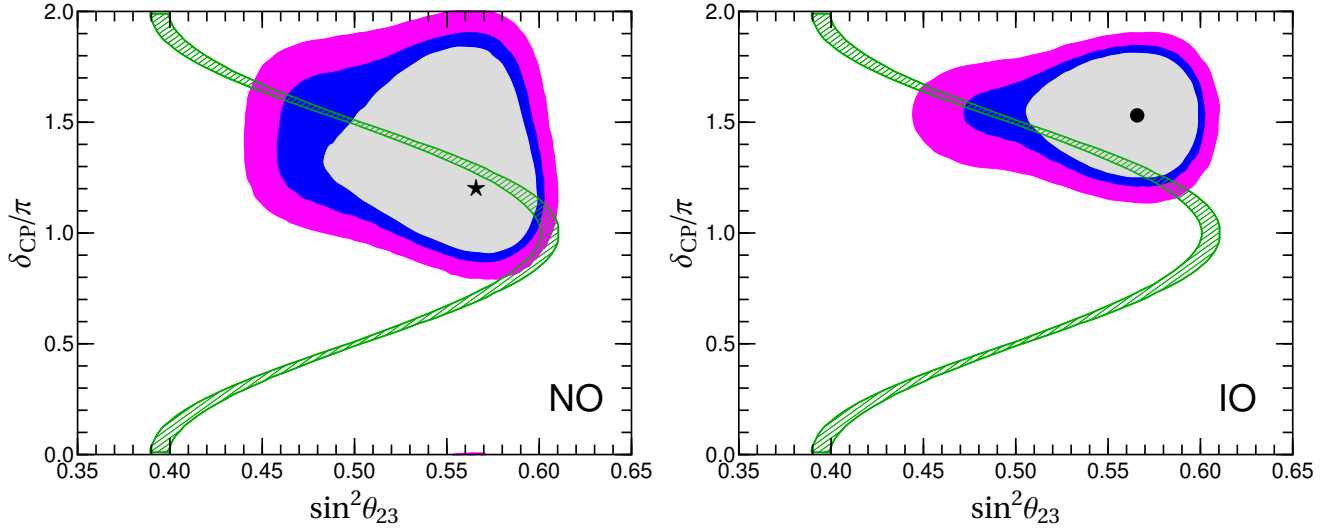


Figure 32: The hatched green bands indicate the predicted correlations between δ_{CP} and $\sin^2 \theta_{23}$ for both neutrino mass orderings. The undisplayed parameters $\sin^2 \theta_{13}$ and $\sin^2 \theta_{12}$ are required to lie within their 3σ regions from the current oscillation global fit [24, 25]. The generic 1σ , 2σ and 3σ regions from the current neutrino oscillation global fit are indicated by the shaded areas [24, 25].

One sees also that the CP phase δ_{CP} is predicted to lie in a range narrower than that obtained in the generic global fits of neutrino oscillations. We also mention that in this model the smallness of the reactor angle θ_{13} and CP violation parameter J_{CP} has a dynamical origin, given by the small ratio $v_\Omega/(M_F + M_\Sigma)$ involving the triple Higgs VEV, see [205] for details. Finally, as already mentioned, the incomplete fermion multiplet structure implies that one of the neutrinos is massless, leading to the $0\nu\beta\beta$ decay predictions in figure 4. All in all, this construction offers a serious benchmark theory for neutrino oscillations and dark matter.

8.2 A benchmark model with both flavour and CP symmetries

In this section, we describe a model implementing both the S_4 flavour symmetry and the generalized CP symmetry [325]. See Refs. [320, 394] for alternative models. It realizes the breaking patterns of flavour and CP symmetry analyzed in subsection 6.3.1. We adopt a supersymmetric (SUSY) formulation of the model in four dimensional space-time. The model is renormalizable at high energies, it gives rise to tri-bimaximal neutrino mixing at leading order, and the next-to-leading order contributions break the tri-bimaximal to a trimaximal mixing pattern. We introduce the auxiliary symmetry $Z_3 \times Z_4$ so as to generate charged lepton mass hierarchies and forbid unwanted operators.

In order to construct the superpotential responsible for the alignment of the flavon vacuum expectation values, we use the standard supersymmetric driving field mechanism [313]. We assume the existence of an R -symmetry $U(1)_R$ containing the usual R -parity, under which the Higgs and flavon fields are uncharged, while matter fields carry a $+1$ R -charge. In addition, the so-called driving fields are necessary and they

carry two units of R -charge. Therefore all terms in the superpotential should be bilinear in the matter superfields or linear in the driving field.

8.2.1 Flavon superpotential

The matter and flavon fields and their transformation properties under the flavour symmetry are summarized in table 5. On the other hand the driving fields in our model and their transformation rules under

Field	L	N^c	e^c	μ^c	τ^c	$H_{u,d}$	φ_T	η	φ_S	ϕ	ξ	Δ
S_4	3	3	1	1'	1	1	3	2	3'	2	1	1'
Z_3	ω	ω^2	ω^2	1	ω	1	ω	ω	ω^2	ω^2	ω^2	1
Z_4	1	1	i	-1	$-i$	1	i	i	1	1	1	1
$U(1)_R$	1	1	1	1	1	0	0	0	0	0	0	0

Table 5: Transformation properties of matter, Higgs and flavon fields.

the flavour symmetry group are listed in table 6. The most general driving superpotential \mathcal{W}_d invariant under $S_4 \times Z_3 \times Z_4$ with $R = 2$ is given by [325]

$$\begin{aligned}
\mathcal{W}_d = & g_1 (\varphi_T^0 (\varphi_T \varphi_T)_{\mathbf{3}'})_{\mathbf{1}} + g_2 (\varphi_T^0 (\eta \varphi_T)_{\mathbf{3}'})_{\mathbf{1}} + g_3 \zeta^0 (\varphi_T \varphi_T)_{\mathbf{1}} + g_4 \zeta^0 (\eta \eta)_{\mathbf{1}} \\
& + f_1 (\varphi_S^0 (\varphi_S \varphi_S)_{\mathbf{3}'})_{\mathbf{1}} + f_2 (\varphi_S^0 (\phi \varphi_S)_{\mathbf{3}'})_{\mathbf{1}} + f_3 (\varphi_S^0 \varphi_S)_{\mathbf{1}} \xi + f_4 (\tilde{\varphi}_S^0 (\phi \varphi_S)_{\mathbf{3}})_{\mathbf{1}} \\
& + f_5 \xi^0 (\varphi_S \varphi_S)_{\mathbf{1}} + f_6 \xi^0 (\phi \phi)_{\mathbf{1}} + f_7 \xi^0 \xi^2 + M^2 \Delta^0 + f_8 \Delta^0 \Delta^2.
\end{aligned} \tag{8.23}$$

Since we impose CP symmetry on the theory in the unbroken phase, all couplings in w_d are real. In the limit of unbroken supersymmetry, the minimum of the scalar potential is determined by vanishing F -terms for the driving fields. As a result, the VEVs of the flavons are aligned as follows [325]

$$\begin{aligned}
\langle \varphi_T \rangle &= \begin{pmatrix} 0 \\ 1 \\ 0 \end{pmatrix} v_T, & \langle \eta \rangle &= \begin{pmatrix} 0 \\ 1 \end{pmatrix} v_\eta, & \langle \Delta \rangle &= v_\Delta, \\
\langle \varphi_S \rangle &= \begin{pmatrix} 1 \\ 1 \\ 1 \end{pmatrix} v_S, & \langle \phi \rangle &= \begin{pmatrix} 1 \\ 1 \end{pmatrix} v_\phi, & \langle \xi \rangle &= v_\xi,
\end{aligned} \tag{8.24}$$

Field	φ_T^0	ζ^0	φ_S^0	$\tilde{\varphi}_S^0$	ξ^0	Δ^0	Ω_1	Ω_1^c	Ω_2	Ω_2^c	Ω_3	Ω_3^c	Σ	Σ^c
S_4	3'	1	3'	3	1	1	2	2	2	2	3	3	3'	3'
Z_3	ω	ω	ω^2	ω^2	ω^2	1	1	1	ω	ω^2	ω^2	ω	ω^2	ω
Z_4	-1	-1	1	1	1	1	-1	-1	$-i$	i	1	1	1	1
$U(1)_R$	2	2	2	2	2	2	1	1	1	1	1	1	1	1

Table 6: Transformation rules for driving and messenger fields under the $S_4 \times Z_4 \times Z_3$ and $U(1)_R$ symmetries.

with

$$v_T = \frac{g_2}{2g_1} v_\eta, \quad v_S^2 = -\frac{1}{6f_2^2 f_5} (f_3^2 f_6 + 2f_2^2 f_7) v_\xi^2, \quad v_\phi = -\frac{f_3}{2f_2} v_\xi, \quad v_\Delta^2 = -M^2/f_8, \quad (8.25)$$

where v_η and v_ξ are undetermined, as they are related to a flat direction. The phase of v_η can be absorbed into the lepton fields, thus we can take the VEVs v_η and v_T real without loss of generality. The common phase of v_S , v_ϕ and v_ξ does not affect neutrino masses and mixing, because it can be factored out in the light neutrino mass matrix. As a consequence, v_ϕ and v_ξ can be considered real while v_S is real or purely imaginary depending on the coefficient $-(f_3^2 f_6 + 2f_2^2 f_7)/(f_2^2 f_5)$ being positive or negative. Furthermore, the VEV v_Δ is real for $f_8 < 0$ and purely imaginary for $f_8 > 0$.

8.2.2 The charged lepton sector

The renormalizable Yukawa superpotential terms involving charged leptons is obtained by integrating out the three pairs of messengers Ω_i and Ω_i^c ($i = 1, 2, 3$). These are chiral superfields with non-vanishing hypercharge $+2(-2)$ for Ω_i (Ω_i^c). Given the field content and the symmetry assignments in tables 5 and 6, one can read off the superpotential for the charged leptons as follows,

$$\begin{aligned} \mathcal{W}_\ell = & z_1 (L\Omega_3)_1 H_d + z_2 (\Omega_3^c \varphi_T)_1 \tau^c + z_3 ((\Omega_3^c \varphi_T)_2 \Omega_2)_1 + z_4 (\Omega_2^c \eta)_1 \mu^c \\ & + z_5 ((\Omega_2^c \eta)_2 \Omega_1)_1 + z_6 (\Omega_1^c \eta)_1 e^c + M_{\Omega_1} (\Omega_1 \Omega_1^c)_1 + z_7 \Delta (\Omega_1 \Omega_1^c)_1 \\ & + M_{\Omega_2} (\Omega_2 \Omega_2^c)_1 + z_8 \Delta (\Omega_2 \Omega_2^c)_1 + M_{\Omega_3} (\Omega_3 \Omega_3^c)_1, \end{aligned} \quad (8.26)$$

where CP invariance requires all coupling constants z_i and messenger masses M_{Ω_1} , M_{Ω_2} and M_{Ω_3} to be real. The terms $\Delta (\Omega_1 \Omega_1^c)_1$ and $\Delta (\Omega_2 \Omega_2^c)_1$, lead to corrections to the Ω_1 and Ω_2 masses respectively. The mass scales of the messenger fields are much larger than the flavon VEVs, hence the contributions of these two operators can be safely neglected. Integrating out the messenger pairs Ω_i and Ω_i^c as shown in figure 33, we obtain the effective superpotential for the charged lepton masses as

$$\mathcal{W}_\ell^{eff} = -\frac{z_1 z_2}{M_{\Omega_3}} (L\varphi_T)_1 H_d \tau^c + \frac{z_1 z_3 z_4}{M_{\Omega_2} M_{\Omega_3}} ((L\varphi_T)_2 \eta)_1 \mu^c - \frac{z_1 z_3 z_5 z_6}{M_{\Omega_1} M_{\Omega_2} M_{\Omega_3}} ((L\varphi_T)_2 (\eta\eta)_2)_1 H_d e^c. \quad (8.27)$$

Using the flavon VEVs in Eq. (8.24), we find a diagonal charged lepton mass matrix with

$$m_\tau = -z_1 z_2 \frac{v_T}{M_{\Omega_3}} v_d, \quad m_\mu = z_1 z_3 z_4 \frac{v_T v_\eta}{M_{\Omega_2} M_{\Omega_3}} v_d, \quad m_e = -z_1 z_3 z_5 z_6 \frac{v_T v_\eta^2}{M_{\Omega_1} M_{\Omega_2} M_{\Omega_3}} v_d, \quad (8.28)$$

where $v_d = \langle H_d \rangle$ is the VEV of the Higgs field H_d . We see that the electron, muon and tau masses are suppressed by different powers of v_T and v_η , so that the mass hierarchies among the charged leptons are naturally reproduced.

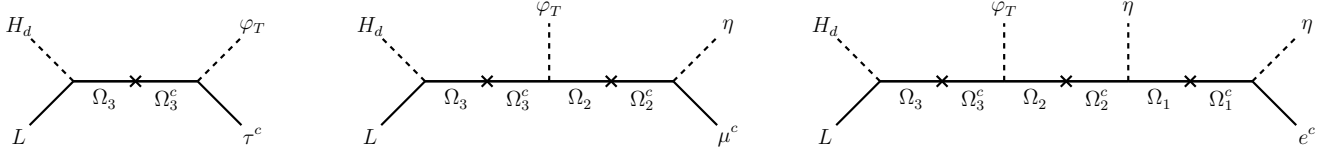


Figure 33: Diagrams for charged-lepton-mass effective operators, crosses indicating fermion mass insertions.

8.2.3 The neutrino sector

The renormalizable superpotential responsible for generating the light neutrino masses can be written as the sum of the leading-order terms and the relevant messenger terms:

$$\mathcal{W}_\nu = \mathcal{W}_\nu^{LO} + \mathcal{W}_\nu^\Sigma, \quad (8.29)$$

where

$$\begin{aligned} \mathcal{W}_\nu^{LO} &= y (LN^c)_1 H_u + y_1 ((N^c N^c)_{\mathbf{3}'})_1 \varphi_S + y_2 (N^c N^c)_1 \xi + y_3 ((N^c N^c)_2 \phi)_1, \\ \mathcal{W}_\nu^\Sigma &= x_1 ((N^c \Sigma)_{\mathbf{3}'})_1 \varphi_S + x_2 ((N^c \Sigma)_2 \phi)_1 + x_3 (N^c \Sigma^c)_1 \Delta + M_\Sigma (\Sigma \Sigma^c)_1. \end{aligned} \quad (8.30)$$

where the couplings x_i and y_i are real due to CP invariance and the messenger field Σ (Σ^c) is a chiral superfield with vanishing hypercharge. The first term of \mathcal{W}_ν^{LO} gives rise to a very simple form for the Dirac neutrino mass matrix,

$$m_D = y v_u \begin{pmatrix} 1 & 0 & 0 \\ 0 & 0 & 1 \\ 0 & 1 & 0 \end{pmatrix}, \quad (8.31)$$

with $v_u = \langle H_u \rangle$. On the other hand, the last three terms of \mathcal{W}_ν^{LO} lead to the mass matrix m_M^{LO} of the right-handed neutrinos. Given the alignment of φ_S , ϕ and ξ shown in Eq. (8.24), we have

$$m_M^{LO} = y_1 v_s \begin{pmatrix} 2 & -1 & -1 \\ -1 & 2 & -1 \\ -1 & -1 & 2 \end{pmatrix} + y_2 v_\xi \begin{pmatrix} 1 & 0 & 0 \\ 0 & 0 & 1 \\ 0 & 1 & 0 \end{pmatrix} + y_3 v_\phi \begin{pmatrix} 0 & 1 & 1 \\ 1 & 1 & 0 \\ 1 & 0 & 1 \end{pmatrix}. \quad (8.32)$$

The effective light neutrino mass matrix is given by the simplest type-I seesaw formula [32]

$$m_\nu^{LO} = -m_D (m_M^{LO})^{-1} m_D^T$$

which is exactly diagonalized by the tri-bimaximal mixing matrix U_{TBM} ,

$$U_{TBM}^T m_\nu^{LO} U_{TBM} = \text{diag}(m_1^{LO}, m_2^{LO}, m_3^{LO}), \quad (8.33)$$

so we obtain

$$m_1^{LO} = -\frac{y^2 v_u^2}{3y_1 v_S + y_2 v_\xi - y_3 v_\phi}, \quad m_2^{LO} = -\frac{y^2 v_u^2}{y_2 v_\xi + 2y_3 v_\phi}, \quad m_3^{LO} = -\frac{y^2 v_u^2}{3y_1 v_S - y_2 v_\xi + y_3 v_\phi}.$$

Note that the tri-bimaximal mixing pattern is produced at leading order. This follows from the fact that the VEVs of the flavons φ_S , ϕ and ξ involved in the neutrino mass term are invariant under the action of the Klein subgroup generated by the tri-bimaximal s and u generators.

The leading-order and next-to-leading order (NLO) contributions to the right-handed neutrino masses are depicted in figure 34.

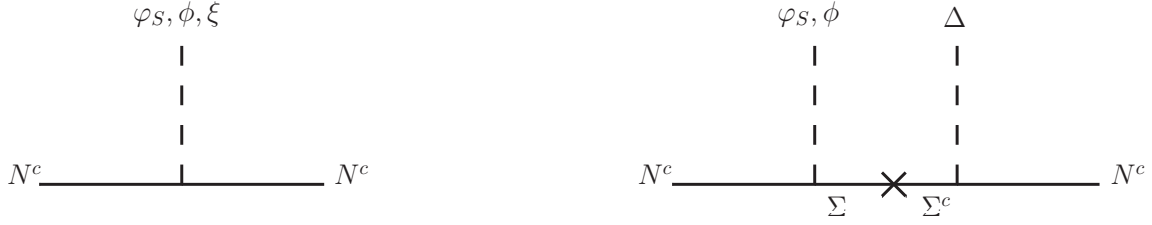


Figure 34: The diagrams for the RH neutrino masses, where the cross indicates a fermionic mass insertion.

Integrating out the messenger fields Σ and Σ^c , we obtain the following NLO effective operator

$$\mathcal{W}_\nu^{NLO} = -\frac{x_2 x_3}{M_\Sigma} \Delta ((N^c N^c)_2 \phi)_{1'}. \quad (8.34)$$

Notice that the VEV of the flavon Δ breaks the residual Klein symmetry down to a Z_2 subgroup generated by s at NLO. Consequently, the corrected right-handed neutrino mass matrix is given as

$$m_M = a \begin{pmatrix} 2 & -1 & -1 \\ -1 & 2 & -1 \\ -1 & -1 & 2 \end{pmatrix} + b \begin{pmatrix} 1 & 0 & 0 \\ 0 & 0 & 1 \\ 0 & 1 & 0 \end{pmatrix} + c \begin{pmatrix} 0 & 1 & 1 \\ 1 & 1 & 0 \\ 1 & 0 & 1 \end{pmatrix} + d \begin{pmatrix} 0 & 1 & -1 \\ 1 & -1 & 0 \\ -1 & 0 & 1 \end{pmatrix}, \quad (8.35)$$

with

$$a = y_1 v_S, \quad b = y_2 v_\xi, \quad c = y_3 v_\phi, \quad d = x_2 x_3 \frac{v_\Delta v_\phi}{M_\Sigma}. \quad (8.36)$$

Therefore, up to an overall factor $y^2 v_u^2$, the corrected light neutrino mass matrix obtained from the seesaw formula has the form

$$m_\nu = \alpha \begin{pmatrix} 2 & -1 & -1 \\ -1 & 2 & -1 \\ -1 & -1 & 2 \end{pmatrix} + \beta \begin{pmatrix} 1 & 0 & 0 \\ 0 & 0 & 1 \\ 0 & 1 & 0 \end{pmatrix} + \gamma \begin{pmatrix} 0 & 1 & 1 \\ 1 & 1 & 0 \\ 1 & 0 & 1 \end{pmatrix} + \epsilon \begin{pmatrix} 0 & 1 & -1 \\ 1 & -1 & 0 \\ -1 & 0 & 1 \end{pmatrix}, \quad (8.37)$$

where the parameters α , β , γ and ϵ are given by,

$$\alpha = \frac{a}{-9a^2 + (b-c)^2 + 3d^2}, \quad \beta = -\frac{1}{3(b+2c)} + \frac{2(b-c)}{3[9a^2 - (b-c)^2 - 3d^2]},$$

$$\gamma = -\frac{1}{3(b+2c)} - \frac{b-c}{3[9a^2 - (b-c)^2 - 3d^2]}, \quad \epsilon = \frac{d}{-9a^2 + (b-c)^2 + 3d^2}, \quad (8.38)$$

The first three terms in the light neutrino matrix of Eq. (8.37) preserve the tri-bimaximal mixing form. The last term, which is proportional to ϵ , violates it. The associated parameter ϵ is induced by the NLO contributions suppressed by v_Δ/M_Σ with respect to α , β and γ . This naturally accounts for the small reactor mixing angle θ_{13} and the small deviation from the maximal atmospheric mixing.

As shown in section 8.2.1, the VEVs v_ϕ and v_ξ can be assumed real, while v_S and v_Δ can be real or purely imaginary due to the generalized CP symmetry. If v_S and v_Δ are real, the vacuum alignment of the flavons φ_S , ϕ , ξ and Δ is invariant under the CP transformation $X_{\mathbf{r}} = 1$ and the residual flavour symmetry Z_2^s . The parameters α , β , γ and ϵ are all real, the lepton mixing matrix has the form of Eq. (6.46) with the rotation angle θ given by

$$\tan 2\theta = \frac{\sqrt{3}\epsilon}{\gamma - \beta}. \quad (8.39)$$

The lepton mixing angles and CP violation phases are given in Eq. (6.47). The light neutrino masses are

$$\begin{aligned} m_1 &= \left| 3\alpha - \text{sign}(\epsilon \sin 2\theta) \sqrt{(\gamma - \beta)^2 + 3\epsilon^2} \right|, \\ m_2 &= |\beta + 2\gamma|, \\ m_3 &= \left| 3\alpha + \text{sign}(\epsilon \sin 2\theta) \sqrt{(\gamma - \beta)^2 + 3\epsilon^2} \right|. \end{aligned} \quad (8.40)$$

This model allows for both neutrino mass orderings, either NO or IO.

Moreover, if the VEV v_S is real while v_Δ is pure imaginary, the neutrino sector would preserve the residual flavour symmetry Z_2^s and CP symmetry $X_{\mathbf{r}} = u$ which corresponds to the $\mu - \tau$ reflection symmetry. The parameters α , β , γ in Eq. (8.37) are real, and ϵ is pure imaginary. We find that the lepton mixing matrix is given by Eq. (6.50) with the rotation angle θ given as

$$\tan 2\theta = \frac{i\epsilon}{\sqrt{3}\alpha}. \quad (8.41)$$

Both the atmospheric angle θ_{23} and the CP violation phase δ_{CP} are maximal, as shown in Eq. (6.51). The light neutrino masses are given by

$$\begin{aligned} m_1 &= \left| \beta - \gamma + \text{sign}(\alpha \cos 2\theta) \sqrt{9\alpha^2 - 3\epsilon^2} \right|, \\ m_2 &= |\beta + 2\gamma|, \\ m_3 &= \left| \beta - \gamma - \text{sign}(\alpha \cos 2\theta) \sqrt{9\alpha^2 - 3\epsilon^2} \right|, \end{aligned} \quad (8.42)$$

Again, this is consistent with both neutrino mass orderings, either NO or IO.

All in all, this model implements the first two symmetry breaking patterns analyzed in detail in section 6.3.1. The reader is addressed to that section for a discussion of the corresponding neutrino

mixing, CP violation and $0\nu\beta\beta$ decay predictions. See Ref. [320] for an S_4 model realizing the third breaking pattern and the lepton mixing matrix of Eq. (6.53).

9 Family symmetry in 5-D models with a warped extra dimension

Extra dimensions [460] provide an interesting way to address the so-called hierarchy problem [461–463], by making the fundamental scale of gravity exponentially reduced from the Planck mass down to the TeV scale. This follows as a result of having the Standard Model fields localized near the boundary of the extra dimensions. Here we stress that the fermion mass hierarchies can also be addressed through the localization of fermion profiles which are fixed by the bulk mass parameters.

As we have shown in the previous section, the lepton and quark mixing angles can be well explained by using a discrete flavour symmetry within concrete 4-D models. One can also implement flavour symmetry in the context of extra dimensions, so that the structure of both mass hierarchies as well as mixing angles can be addressed in a clear manner. There has been intense activity using discrete family symmetries to build UV-complete 4-D gauge theories [85–93], describing the masses and mixing matrices of leptons and quarks. The pattern of fermion mixing could also arise from the imposition of family symmetries in extra dimensions, including holographic models [70–84].

In this section we consider warped flavourdynamics schemes, of which there have been two recent proposals in the literature [78, 79]. The first warped flavourdynamics model is based on the $\Delta(27)$ family symmetry, with neutrinos as Dirac fermions, and a predicted TM2 mixing pattern [78]. An alternative proposal for a warped flavourdynamics scheme is based on the T' family group [79]. Here neutrinos are Majorana fermions with a predicted TM1 mixing pattern. In what follows we develop the key features of this second example, and refer the interested reader to the original work in [78] for the other case.

9.1 Warped flavourdynamics with the T' family group

Here we present our benchmark extra-dimensional model with T' flavour symmetry [79]. The T' group is the double covering of A_4 . The relation between T' and A_4 is quite similar to the familiar relation between $SU(2)$ and $SO(3)$. Although $SU(2)$ and $SO(3)$ possess the same Lie algebra, $SO(3)$ has only odd-dimensional representations, while $SU(2)$ possesses both even and odd-dimensional representations. Likewise T' has three doublet representations $\mathbf{2}$, $\mathbf{2}'$ and $\mathbf{2}''$ besides the singlets $\mathbf{1}$, $\mathbf{1}'$, $\mathbf{1}''$ and triplet $\mathbf{3}$ of A_4 .

We formulate our model in the framework of the Randall-Sundrum model [462]. The bulk geometry is described by the following metric

$$ds^2 = e^{-2ky} \eta_{\mu\nu} dx^\mu dx^\nu - dy^2. \quad (9.1)$$

This extra dimension y is compactified, and the two 3-branes with opposite tension are located at $y = 0$, the UV brane, and the infra-red (IR) brane at $y = L$.

In order to comply with electroweak precision measurement constraints, the electroweak symmetry of the model is promoted to $G_{\text{bulk}} = SU(2)_L \otimes SU(2)_R \otimes U(1)_{B-L}$ [464, 465] and it is broken down to the standard model gauge group $G_{\text{SM}} = SU(2)_L \otimes U(1)_Y$ on the UV brane by the boundary conditions (BCs) of the gauge bosons. The Higgs field lives in the bulk, and it is in the $(\mathbf{2}, \mathbf{2})$ bi-doublet representation of

$SU(2)_L \otimes SU(2)_R$. The Kaluza-Klein (KK) Higgs field decomposition is [466]

$$H(x^\mu, y) = H(x^\mu) \frac{f_H(y)}{\sqrt{L}} + \text{heavy KK Modes}, \quad (9.2)$$

where $f_H(y)$ is the zero mode profile. For an adequate choice of BCs, we have

$$f_H(y) = \sqrt{\frac{2kL(1-\beta)}{1-e^{-2(1-\beta)kL}}} e^{kL} e^{(2-\beta)k(y-L)}, \quad (9.3)$$

with $\beta = \sqrt{4 + m_H^2/k^2}$ and m_H is the bulk mass of the Higgs field.

The three families of leptons and quarks transform under $SU(2)_L \otimes SU(2)_R$ in the following way,

$$\Psi_{\ell_i} = \begin{pmatrix} \nu_i^{[++]} \\ e_i^{[++]} \end{pmatrix} \sim (\mathbf{2}, \mathbf{1}), \quad \Psi_{e_i} = \begin{pmatrix} \tilde{\nu}_i^{[+-]} \\ e_i^{[--]} \end{pmatrix} \sim (\mathbf{1}, \mathbf{2}), \quad \Psi_{\nu_i} = \begin{pmatrix} N_i^{[--]} \\ \tilde{e}_i^{[+-]} \end{pmatrix} \sim (\mathbf{1}, \mathbf{2}), \quad (9.4)$$

$$\Psi_{Q_i} = \begin{pmatrix} u_i^{[++]} \\ d_i^{[++]} \end{pmatrix} \sim (\mathbf{2}, \mathbf{1}), \quad \Psi_{d_i} = \begin{pmatrix} \tilde{u}_i^{[+-]} \\ d_i^{[--]} \end{pmatrix} \sim (\mathbf{1}, \mathbf{2}), \quad \Psi_{u_i} = \begin{pmatrix} u_i^{[--]} \\ \tilde{d}_i^{[+-]} \end{pmatrix} \sim (\mathbf{1}, \mathbf{2}). \quad (9.5)$$

where the two signs in the bracket indicate Neumann (+) or Dirichlet (−) boundary conditions for the left-handed component of the corresponding field on UV and IR branes respectively. The Kaluza-Klein decomposition of a 5D fermion for the two different BCs are

$$\psi^{[++]}(x^\mu, y) = \frac{e^{2ky}}{\sqrt{L}} \left\{ \psi_L(x^\mu) f_L(y, c_L) + \text{heavy KK modes} \right\}, \quad (9.6)$$

$$\psi^{[--]}(x^\mu, y) = \frac{e^{2ky}}{\sqrt{L}} \left\{ \psi_R(x^\mu) f_R(y, c_R) + \text{heavy KK modes} \right\}. \quad (9.7)$$

The 5D fields with [++] BCs only have left-handed zero modes, while those with [--] BCs only have right-handed ones. The functions $f_L(y, c_L)$ and $f_R(y, c_R)$ are the zero mode profiles [467, 468]

$$f_L(y, c_L) = \sqrt{\frac{(1-2c_L)kL}{e^{(1-2c_L)kL}-1}} e^{-c_L ky}, \quad f_R(y, c_R) = \sqrt{\frac{(1+2c_R)kL}{e^{(1+2c_R)kL}-1}} e^{c_R ky}, \quad (9.8)$$

where c_L and c_R denote the bulk mass of the 5D fermions in units of the AdS_5 curvature k . As usual, we adopt the zero mode approximation which identifies the standard model fields with the zero modes of corresponding 5D fields.

9.1.1 Lepton masses and mixing

The field content and the symmetry assignment are given in table 7. The zero mode of Ψ_L is the left-handed lepton doublet, and the zero modes of $\Psi_{e,\mu,\tau}$ and Ψ_ν are the right-handed charged leptons and neutrinos respectively. The left-handed lepton fields are assumed to transform as a triplet under flavour symmetry group.

Field	Ψ_l	Ψ_e	Ψ_μ	Ψ_τ	Ψ_ν	H	$\varphi_l(IR)$	$\sigma_l(IR)$	$\varphi_\nu(UV)$	$\rho_\nu(UV)$
$SU(2)_L \times SU(2)_R \times U(1)_{B-L}$	(2, 1, -1)	(1, 2, -1)	(1, 2, -1)	(1, 2, -1)	(1, 2, -1)	(2, 2, 0)	(1, 1, 0)	(1, 1, 0)	(1, 1, 0)	(1, 1, 0)
T'	3	1'	1''	1	3	1	2	1''	3	3
Z_3	ω^2	1	1	1	ω^2	1	ω	ω	ω	ω
Z_4	i	i	i	i	i	1	-1	-1	i	$-i$

Table 7: Lepton and flavon fields under the $SU(2)_L \times SU(2)_R \times U(1)_{B-L}$ gauge group and the $T' \times Z_3 \times Z_4$ family symmetry, with $\omega = e^{2\pi i/3}$. Flavons φ_l , σ_l and φ_ν , ρ_ν lie on the IR and UV branes respectively.

Note that in order to forbid dangerous terms, besides the flavour group T' , we introduce the auxiliary symmetry $Z_3 \times Z_4$. Four flavons φ_l , σ_l , φ_ν and ρ_ν are introduced to break the T' family symmetry. The flavons φ_l and σ_l couple to the charged lepton sector, and are localized on the IR brane, while φ_ν and ρ_ν are localized on the UV brane. The vacuum expectation values of these flavons are aligned along the following directions

$$\langle \varphi_l \rangle = (1, 0)v_{\varphi_l}, \quad \langle \sigma_l \rangle = v_{\sigma_l}, \quad \langle \varphi_\nu \rangle = (1, -2\omega^2, -2\omega)v_{\varphi_\nu}, \quad \langle \rho_\nu \rangle = (1, -2\omega, -2\omega^2)v_{\rho_\nu}, \quad (9.9)$$

with $\omega = e^{2i\pi/3}$. The above vacuum alignment can be the global minimum of the scalar potential in certain regions of parameters [79]. At leading order, the lepton mass terms respecting both gauge symmetry as well as the flavour symmetry $T' \times Z_3 \times Z_4$ take the following form

$$\mathcal{L}_Y^l = \frac{\sqrt{G}}{\Lambda^3} \left[y_e (\varphi_l^2 \bar{\Psi}_l)_{\mathbf{1}''} H \Psi_e + y_\mu (\varphi_l^2 \bar{\Psi}_l)_{\mathbf{1}'} H \Psi_\mu + y_\tau (\varphi_l^2 \bar{\Psi}_l)_{\mathbf{1}} H \Psi_\tau \right] \delta(y-L) + \text{h.c.}, \quad (9.10)$$

$$\begin{aligned} \mathcal{L}_Y^\nu &= y_{\nu_1} \frac{\sqrt{G}}{\Lambda'} (\bar{\Psi}_l H \Psi_\nu)_{\mathbf{1}} \delta(y-L) + \frac{1}{2} \frac{\sqrt{G}}{\Lambda^2} \left[y_{\nu_2} (\bar{N}^C N)_{\mathbf{1}} (\varphi_\nu^2)_{\mathbf{1}} + y_{\nu_3} (\bar{N}^C N)_{\mathbf{1}} (\rho_\nu^2)_{\mathbf{1}} \right. \\ &\quad \left. + y_{\nu_4} \left((\bar{N}^C N)_{\mathbf{3}_S} (\varphi_\nu^2)_{\mathbf{3}_S} \right)_{\mathbf{1}} + y_{\nu_5} \left((\bar{N}^C N)_{\mathbf{3}_S} (\rho_\nu^2)_{\mathbf{3}_S} \right)_{\mathbf{1}} \right] \delta(y) + \text{h.c.}, \end{aligned} \quad (9.11)$$

where $G = e^{-8ky}$ is the determinant of the 5D metric.

For the vacuum configuration in Eq. (9.9), the charged lepton mass matrix is diagonal and the three charged lepton masses are

$$m_e = \tilde{y}_e \frac{v_{\varphi_l}^2}{\Lambda'^2} v, \quad m_\mu = \tilde{y}_\mu \frac{v_{\varphi_l}^2}{\Lambda'^2} v, \quad m_\tau = \tilde{y}_\tau \frac{v_{\varphi_l}^2}{\Lambda'^2} v, \quad (9.12)$$

with

$$\tilde{y}_{e,\mu,\tau} = \frac{y_{e,\mu,\tau}}{L\Lambda'} f_L(L, c_\ell) f_R(L, c_{e,\mu,\tau}). \quad (9.13)$$

Neutrino masses are generated by the type-I seesaw mechanism, and the large seesaw scale arises naturally, since the Majorana mass terms of the right-handed neutrinos are UV-localized. The first term in Eq. (9.11) leads to a diagonal Dirac neutrino mass matrix $m_D = \tilde{y}_{\nu_1} v \mathbb{1}_3$ where $\tilde{y}_{\nu_1} = \frac{y_{\nu_1}}{L\Lambda'} f_L(L, c_\ell) f_R(L, c_\nu)$ and $\mathbb{1}_3$ is the 3×3 unit matrix. The last four are the Majorana mass terms for the right-handed neutrinos, leading

to the mass matrix

$$\begin{aligned}
m_N = & \left(\tilde{y}_{\nu_2} \frac{v_{\varphi\nu}^2}{\Lambda} + \tilde{y}_{\nu_3} \frac{v_{\rho\nu}^2}{\Lambda} \right) \begin{pmatrix} 1 & 0 & 0 \\ 0 & 0 & 1 \\ 0 & 1 & 0 \end{pmatrix} + \tilde{y}_{\nu_4} \frac{v_{\varphi\nu}^2}{\Lambda} \begin{pmatrix} 2 & 2\omega & 2\omega^2 \\ 2\omega & -4\omega^2 & -1 \\ 2\omega^2 & -1 & -4\omega \end{pmatrix} \\
& + \tilde{y}_{\nu_5} \frac{v_{\rho\nu}^2}{\Lambda} \begin{pmatrix} 2 & 2\omega^2 & 2\omega \\ 2\omega^2 & -4\omega & -1 \\ 2\omega & -1 & -4\omega^2 \end{pmatrix}, \tag{9.14}
\end{aligned}$$

where

$$\tilde{y}_{\nu_{2,3,4,5}} = \frac{y_{\nu_{2,3,4,5}}}{L\Lambda} f_R^2(0, c_\nu). \tag{9.15}$$

The light neutrino mass matrix is given by the simple type-I seesaw formula

$$m_\nu = -m_D m_N^{-1} m_D^T$$

After performing a tri-bimaximal transformation on the neutrino fields, m_ν acquires block diagonal form,

$$m'_\nu = U_{TBM}^\dagger m_\nu U_{TBM}^* = m_0 \begin{pmatrix} \frac{-1}{1+3(y_4+y_5)} & 0 & 0 \\ 0 & \frac{1-3(y_4+y_5)}{18(y_4-y_5)^2+3(y_4+y_5)-1} & \frac{3\sqrt{2}i(y_4-y_5)}{18(y_4-y_5)^2+3(y_4+y_5)-1} \\ 0 & \frac{3\sqrt{2}i(y_4-y_5)}{18(y_4-y_5)^2+3(y_4+y_5)-1} & \frac{-1}{18(y_4-y_5)^2+3(y_4+y_5)-1} \end{pmatrix}, \tag{9.16}$$

with $m_0 = \frac{\tilde{y}_{\nu_1}^2 \Lambda v^2}{\tilde{y}_{\nu_2} v_{\varphi\nu}^2 + \tilde{y}_{\nu_3} v_{\rho\nu}^2}$, $y_4 = \frac{\tilde{y}_{\nu_4} v_{\varphi\nu}^2}{\tilde{y}_{\nu_2} v_{\varphi\nu}^2 + \tilde{y}_{\nu_3} v_{\rho\nu}^2}$ and $y_5 = \frac{\tilde{y}_{\nu_5} v_{\rho\nu}^2}{\tilde{y}_{\nu_2} v_{\varphi\nu}^2 + \tilde{y}_{\nu_3} v_{\rho\nu}^2}$.

One sees from Eq. (9.16) that the light neutrino mass matrix only depends on two complex parameters y_4 and y_5 and on the overall scale m_0 . As a result one expects sharp predictions both for neutrino masses as well as mixing parameters. As shown in D, the above block-diagonal matrix is exactly diagonalized as

$$U_\nu'^\dagger m'_\nu U_\nu'^* = \text{diag}(m_1, m_2, m_3), \quad U_\nu' = \begin{pmatrix} 1 & 0 & 0 \\ 0 & \cos \theta_\nu & \sin \theta_\nu e^{i\delta_\nu} \\ 0 & -\sin \theta_\nu e^{-i\delta_\nu} & \cos \theta_\nu \end{pmatrix}, \tag{9.17}$$

The charged lepton mass matrix m_l is already in diagonal form, consequently the lepton mixing matrix is determined to be

$$U = U_{TBM} U_\nu' = \frac{1}{\sqrt{6}} \begin{pmatrix} 2 & \sqrt{2} \cos \theta_\nu & \sqrt{2} \sin \theta_\nu e^{i\delta_\nu} \\ -1 & \sqrt{2} \cos \theta_\nu - \sqrt{3} \sin \theta_\nu e^{-i\delta_\nu} & \sqrt{3} \cos \theta_\nu + \sqrt{2} \sin \theta_\nu e^{i\delta_\nu} \\ -1 & \sqrt{2} \cos \theta_\nu + \sqrt{3} \sin \theta_\nu e^{-i\delta_\nu} & -\sqrt{3} \cos \theta_\nu + \sqrt{2} \sin \theta_\nu e^{i\delta_\nu} \end{pmatrix}. \tag{9.18}$$

We notice that the first column of the lepton mixing matrix is fixed to be $(2, -1, -1)^T/\sqrt{6}$ which coincides with the first column of the TBM mixing pattern. In other words, the lepton mixing matrix has trimaximal TM1 form [316–318].

From Eq. (9.18) one can extract the mixing angles and the leptonic Jarlskog invariant in the usual way, to find

$$\begin{aligned} \sin^2 \theta_{13} &= \frac{1}{3} \sin^2 \theta_\nu, & \sin^2 \theta_{12} &= \frac{1 + \cos 2\theta_\nu}{5 + \cos 2\theta_\nu}, \\ \sin^2 \theta_{23} &= \frac{1}{2} + \frac{\sqrt{6} \sin 2\theta_\nu \cos \delta_\nu}{5 + \cos 2\theta_\nu}, & J_{CP} &= -\frac{\sin 2\theta_\nu \sin \delta_\nu}{6\sqrt{6}}. \end{aligned} \quad (9.19)$$

One sees from Eq. (9.19) that all the three mixing angles and the Dirac CP phase δ_{CP} are given in terms of just two free parameters δ_ν and θ_ν . The above relations imply two predicted correlations amongst the mixing angles and the Dirac CP violation phase,

$$\cos^2 \theta_{12} \cos^2 \theta_{13} = \frac{2}{3}, \quad \cos \delta_{CP} = \frac{(3 \cos 2\theta_{12} - 2) \cos 2\theta_{23}}{3 \sin 2\theta_{23} \sin 2\theta_{12} \sin \theta_{13}}. \quad (9.20)$$

that characterize the TM1 mixing pattern.

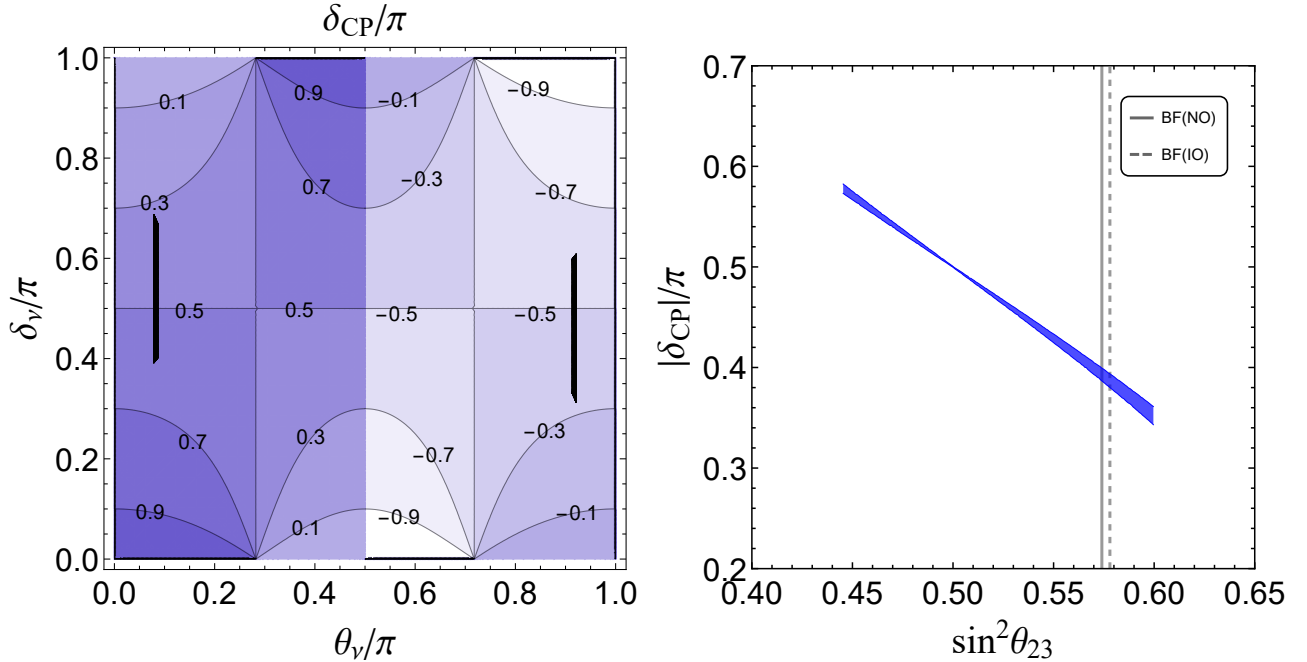


Figure 35: Contour plots of δ_{CP} in the $\theta_\nu - \delta_\nu$ plane (left) and predicted correlation between $|\delta_{CP}|$ and $\sin^2 \theta_{23}$ (right). The vertical solid/dashed lines in the right panel are the best-fit $\sin^2 \theta_{23}$ values for NO/IO spectra, respectively [24, 25].

In the left panel of figure 35 we display the contour plot of δ_{CP} in the plane δ_ν versus θ_ν . The small black areas in the left panel indicate the regions in which all three lepton mixing angles lie within their experimentally allowed 3σ ranges. The right panel of figure 35 shows a very tight correlation between $|\delta_{CP}|$ and the magnitude of the atmospheric angle θ_{23} . One sees that both octants are consistent, and that the CP phase parameter is predicted to lie in the restricted range $[0.325\pi, 0.592\pi]$. Upcoming long-baseline experiments will be able to test these predictions for θ_{23} and δ_{CP} [113, 114, 118].

We now turn to neutrinoless double beta decay. In figure 36 we display the expected values for the

effective Majorana neutrino mass $|m_{\beta\beta}|$ characterizing the $0\nu\beta\beta$ decay amplitude. If the neutrino mass spectrum is inverted-ordered (IO), the effective Majorana mass has a lower limit $|m_{\beta\beta}| \geq 0.0162$ eV, while the lightest neutrino mass satisfies $m_{\text{lightest}} \geq 0.0133$ eV. For the case of normal-ordering (NO), the effective mass $|m_{\beta\beta}|$ lies in the narrow interval $[5.2\text{meV}, 9.6\text{meV}]$, and the allowed range of m_{lightest} is $[4.8\text{meV}, 7.2\text{meV}]$. Clearly, as indicated in the figure, the predicted regions for the lightest neutrino mass and $|m_{\beta\beta}|$ are quite restricted. The existing experimental bounds as well as the estimated experimental sensitivities are also indicated by the horizontal bands [125–127] in figure 36. The predicted decay amplitudes do suggest a guaranteed $0\nu\beta\beta$ discovery at the forthcoming round of experiments [107].

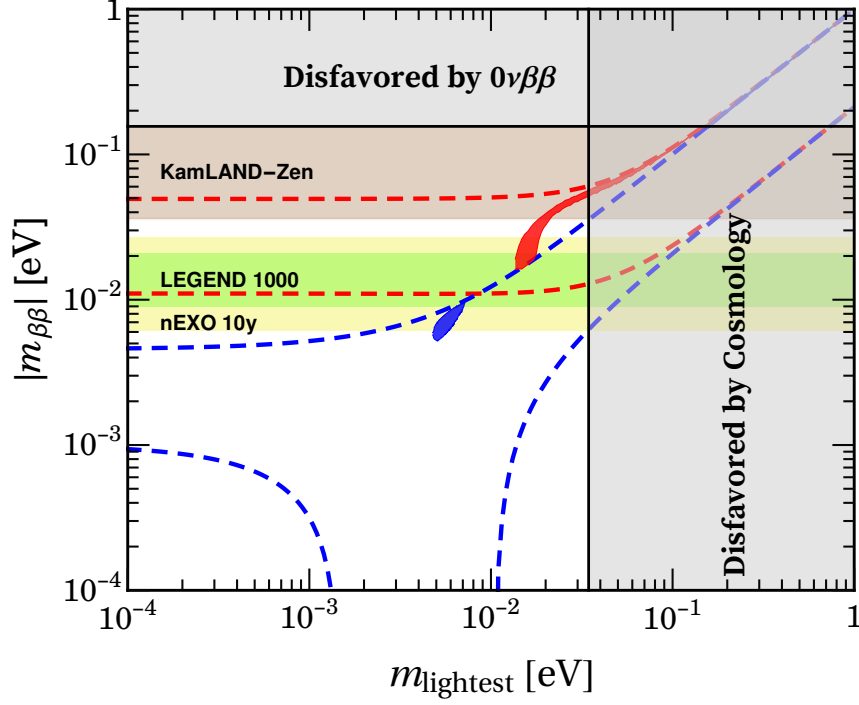


Figure 36: Predicted mass parameter characterizing the $0\nu\beta\beta$ decay amplitude; red and blue regions are for IO and NO neutrino mass spectra, respectively. Here we adopt the same convention as figure 22 for different bands and boundaries.

9.1.2 Quark masses and CKM matrix

This model can be extended to include quarks, the transformation properties of the quark fields under the family symmetry $T' \times Z_3 \times Z_4$ are listed in table 8. Note that no new scalars are needed, beyond the flavons φ_l and σ_l characterizing the lepton sector.

Field	Ψ_{UC}	Ψ_T	Ψ_u	Ψ_c	Ψ_t	Ψ_{ds}	Ψ_b	H	$\varphi_l(IR)$	$\sigma_l(IR)$
$SU(2)_L \times SU(2)_R \times U(1)_{B-L}$	$(2, 1, 1/3)$	$(2, 1, 1/3)$	$(1, 2, 1/3)$	$(1, 2, 1/3)$	$(1, 2, 1/3)$	$(1, 2, 1/3)$	$(1, 2, 1/3)$	$(2, 2, 0)$	$(1, 1, 0)$	$(1, 1, 0)$
T'	$\mathbf{2}$	$\mathbf{1}$	$\mathbf{1}'$	$\mathbf{1}''$	$\mathbf{1}'$	$\mathbf{2}'$	$\mathbf{1}''$	$\mathbf{1}$	$\mathbf{2}$	$\mathbf{1}''$
Z_3	ω^2	ω	1	ω^2	1	ω	ω^2	1	ω	ω
Z_4	1	-1	1	-1	-1	1	-1	1	-1	-1

Table 8: Classification of the quark fields under the bulk gauge group $SU(2)_L \times SU(2)_R \times U(1)_{B-L}$ and the flavour symmetry $T' \times Z_3 \times Z_4$.

The quark Yukawa interactions are localized on the IR brane and constrained by the T' flavour symmetry to be of the following form,

$$\begin{aligned}\mathcal{L}_Y^d &= \frac{\sqrt{G}}{\Lambda^3} \left[y_{ds_1} (\bar{\Psi}_{UC} H \Psi_{ds})_{\mathbf{3}} \varphi_l^{*2} + y_{ds_2} (\bar{\Psi}_{UC} H \Psi_{ds})_{\mathbf{1}'} \sigma_l^{*2} + y'_b (\bar{\Psi}_T H \Psi_b)_{\mathbf{1}''} \sigma_l^2 \right] \delta(y-L) + \text{h.c.} + \dots \\ \mathcal{L}_Y^u &= \frac{\sqrt{G}}{\Lambda^3} \left[y'_u \Lambda' (\bar{\Psi}_T H \Psi_u)_{\mathbf{1}'} \sigma_l + y_t \Lambda' (\bar{\Psi}_{UC} H \Psi_t)_{\mathbf{2}} \varphi_l^* + y_u (\bar{\Psi}_{UC} H \Psi_u)_{\mathbf{2}} \varphi_l \sigma_l \right. \\ &\quad \left. + y'_c (\bar{\Psi}_T H \Psi_c)_{\mathbf{1}''} \sigma_l^2 + y'_t (\bar{\Psi}_T H \Psi_t)_{\mathbf{1}'} \sigma_l^{*2} \right] \delta(y-L) + \text{h.c.} + \dots,\end{aligned}\quad (9.21)$$

for the down-type and up-type quark masses respectively. One can read out the mass matrices for the zero modes of the quark fields as

$$m^d = v \begin{pmatrix} \tilde{y}_{ds_2} v_{\sigma_1}^{*2} / \Lambda'^2 & 0 & 0 \\ \tilde{y}_{ds_1} v_{\varphi_1}^{*2} / \Lambda'^2 & \tilde{y}_{ds_2} v_{\sigma_1}^{*2} / \Lambda'^2 & 0 \\ 0 & 0 & \tilde{y}'_b v_{\sigma_1}^2 / \Lambda'^2 \end{pmatrix}, \quad (9.22)$$

$$m^u = v \begin{pmatrix} \tilde{y}_u v_{\varphi_1} v_{\sigma_1} / \Lambda'^2 & 0 & 0 \\ 0 & 0 & \tilde{y}_t v_{\varphi_1}^* / \Lambda' \\ \tilde{y}'_u v_{\sigma_1} / \Lambda' & \tilde{y}'_c v_{\sigma_1}^2 / \Lambda'^2 & \tilde{y}'_t v_{\sigma_1}^{*2} / \Lambda'^2 \end{pmatrix}. \quad (9.23)$$

where the parameters with tilde are given by

$$\tilde{y}_{u,t,ds_{1,2}} = \frac{y_{u,t,ds_{1,2}}}{L\Lambda'} f_L(L, c_{UC}) f_R(L, c_{u,t,ds}), \quad \tilde{y}'_{u,c,t,b} = \frac{y'_{u,c,t,b}}{L\Lambda'} f_L(L, c_T) f_R(L, c_{u,c,t,b}). \quad (9.24)$$

Notice that the down-quark mass matrix is block diagonal and the (11) and (22) entries are exactly equal. Note also that the up-quark sector gives a negligible contribution to the Cabibbo angle θ_c but is responsible for generating V_{ub} and V_{cb} . As a result this model gives rise to the well-known Gatto-Sartori relation $m_d/m_s \simeq \tan^2 \theta_c$ [469].

9.2 Global flavour fit

Let us now perform a global fit of the masses and flavour mixing parameters of both quarks and leptons within this model. The fundamental 5D scales on the UV and IR branes are taken to be $\Lambda \simeq k \simeq 2.44 \times 10^{18}$ GeV and $\Lambda' = k e^{-kL} \simeq 1.5$ TeV respectively. The vacuum expectation value of the Higgs field is fixed to its SM value $v \simeq 174$ GeV, and we choose the flavon VEVs as $v_{\varphi_1} / \Lambda' = v_{\sigma_1} / \Lambda' = v_{\varphi_\nu} / \Lambda = v_{\rho_\nu} / \Lambda = 0.2$. In what follows we give a typical set of values for the free parameters. The bulk mass parameters and the Yukawa coupling constants of the charged lepton and quarks are given by

$$\begin{aligned}c_l &= 0.460, \quad c_e = -0.725, \quad c_\mu = -0.553, \quad c_\tau = -0.117, \\ c_{UC} &= 0.587, \quad c_T = -0.980, \quad c_u = -0.516, \quad c_c = -0.555, \\ c_t &= 0.966, \quad c_{ds} = -0.503, \quad c_b = -0.532, \\ y_e &= y_\mu = y_\tau = 1.0, \quad y_u = 6.321, \quad y_t = 6.20, \quad y'_u = 4.00,\end{aligned}$$

$$y'_c = 1.00, \quad y'_t = 8.30, \quad y_{ds1} = 4.00, \quad y_{ds2} = 0.892, \quad y'_b = 4.00. \quad (9.25)$$

The values of the parameters in the neutrino sector depend on the neutrino mass ordering,

$$\begin{aligned} \text{NO} : c_\nu &= -0.404, \quad y_{\nu 1} = y_{\nu 2} = y_{\nu 3} = 1, \quad y_{\nu 4} = 0.235 + 0.0770i, \quad y_{\nu 5} = 0.340 + 0.0710i, \\ \text{IO} : c_\nu &= -0.383, \quad y_{\nu 1} = y_{\nu 2} = y_{\nu 3} = 1, \quad y_{\nu 4} = -0.354 + 0.275i, \quad y_{\nu 5} = -0.562 + 0.270i. \end{aligned} \quad (9.26)$$

The resulting predictions for flavour observables such as lepton and quark mass and mixing parameters are all listed in table 9. One sees that all Standard Model fermion masses and mixings can be very well reproduced.

parameters	best-fit $\pm 1\sigma$	predictions
$\sin \theta_{12}^q$	0.22500 ± 0.00100	0.22503
$\sin \theta_{13}^q$	0.003675 ± 0.000095	0.003668
$\sin \theta_{23}^q$	0.04200 ± 0.00059	0.04205
$\delta_{CP}^q / ^\circ$	66.9 ± 2	68.2
m_u [MeV]	$2.16^{+0.49}_{-0.26}$	2.16
m_c [GeV]	1.27 ± 0.02	1.27
m_t [GeV]	172.9 ± 0.4	172.90
m_d [MeV]	$4.67^{+0.48}_{-0.17}$	4.21
m_s [MeV]	93^{+11}_{-5}	93.00
m_b [GeV]	$4.18^{+0.03}_{-0.02}$	4.18
$\sin^2 \theta_{12}^l / 10^{-1}$ (NO)	$3.20^{+0.20}_{-0.16}$	3.19
$\sin^2 \theta_{12}^l / 10^{-1}$ (IO)		3.18
$\sin^2 \theta_{23}^l / 10^{-1}$ (NO)	$5.47^{+0.20}_{-0.30}$	5.47
$\sin^2 \theta_{23}^l / 10^{-1}$ (IO)		5.51
$\sin^2 \theta_{13}^l / 10^{-2}$ (NO)	$2.160^{+0.083}_{-0.069}$	2.160
$\sin^2 \theta_{13}^l / 10^{-2}$ (IO)		2.220
δ_{CP}^l / π (NO)	$1.32^{+0.21}_{-0.15}$	1.567
δ_{CP}^l / π (IO)		1.571
m_e [MeV]	$0.511 \pm 3.1 \times 10^{-9}$	0.511
m_μ [MeV]	$105.658 \pm 2.4 \times 10^{-6}$	105.658
m_τ [MeV]	1776.86 ± 0.12	1776.86
Δm_{21}^2 [10^{-5}eV^2] (NO)	$7.55^{+0.20}_{-0.16}$	7.55
Δm_{21}^2 [10^{-5}eV^2] (IO)		
$ \Delta m_{31}^2 $ [10^{-3}eV^2] (NO)	2.50 ± 0.03	2.50
$ \Delta m_{31}^2 $ [10^{-3}eV^2] (IO)		
χ^2 (NO)	—	7.65
χ^2 (IO)		7.66

Table 9: Global warped flavordynamics fit: neutrino oscillation parameters are taken from the global analysis in [24, 25], while the quark parameters are taken from the Review of Particle Physics [28].

All in all the model provides a consistent scenario for the flavour problem, in which fermion mass hierarchies are accounted for by adequate choices of the bulk mass parameters, while quark and lepton mixing angles are restricted by the assumed T' flavour symmetry. Note that in this model neutrinos are

Majorana particles, the tiny neutrino masses are generated by the type-I seesaw mechanism with “right-handed” neutrino masses in the range of $[10^{12}, 10^{13}]$ GeV and relatively sizeable rates for $0\nu\beta\beta$ decay, accessible within the next round of experiments. For an alternative warped flavourdynamics construction along the similar lines, see Ref. [78]. In that case the model uses the $\Delta(27)$ family symmetry, neutrinos are Dirac fermions, and the predicted neutrino mixing pattern is TM2.

10 Family symmetry from 6-D orbifolds

Underpinning the nature of the underlying family symmetry of particle physics amongst the huge plethora of possibilities constitutes a formidable task. As already seen in the previous section, a promising approach to the flavour problem is to imagine the existence of new dimensions in spacetime. In the present section we illustrate how the existence of extra dimensions may shed light on the nature of the family symmetry in four dimensions. The idea was suggested within six-dimensional setups compactified on a torus [292, 293].

The resulting theories share a realistic A_4 family symmetry, featuring the “golden” quark-lepton mass formula

$$\frac{m_\tau}{\sqrt{m_\mu m_e}} \approx \frac{m_b}{\sqrt{m_s m_d}}. \quad (10.1)$$

This formula was proposed in [288], and emerges also in other 4-D flavour schemes such as those in Refs. [289, 290] and [65, 66], as well as in implementations of the Peccei-Quinn symmetry [287]. It is remarkable that it also comes out neatly in scenarios where the family symmetry arises from the compactification of 6-dimensional orbifolds, as proposed in Refs. [143, 144, 294, 295] and considered next. Fermions are nicely arranged in terms of the A_4 family symmetry. Different setups can be identified, with very interesting phenomenology. Indeed, they bring in the possibility of predicting neutrino mixing angles and CP phases, as well as providing a good global description of flavour observables.

10.1 General preliminaries

Here we summarize the theory framework and survey its main features. First of all we have a 6-dimensional version of the standard $SU(3)_c \otimes SU(2)_L \otimes U(1)_Y$ gauge symmetry, supplemented with orbifold compactification, as outlined below. In the full six-dimensional theory, the spacetime manifold \mathcal{M} is identified as the direct product $\mathcal{M} = \mathbb{M}^4 \times (T^2/\mathbb{Z}_2)$, where \mathbb{M}^4 is the four-dimensional Minkowski spacetime, and T^2/\mathbb{Z}_2 is a one-parameter family (given by θ) of 2-D toroidal orbifolds defined by the following relations satisfied by the extra-dimensional coordinates

$$(x^5, x^6) = (x^5 + 2\pi R_1, x^6), \quad (10.2)$$

$$(x^5, x^6) = (x^5 + 2\pi R_2 \cos \theta, x^6 + 2\pi R_2 \sin \theta). \quad (10.3)$$

$$(x^5, x^6) = (-x^5, -x^6), \quad (10.4)$$

The first two equations define a torus, with θ describing its twist angle, and the third equation defines the \mathbb{Z}_2 orbifolding. For simplicity we assume that the characteristic radii of the compact extra dimensions are similar, i.e.

$$R_1 \sim R_2 \sim 1/M_c, \quad (10.5)$$

in terms of the compactification scale M_c . Moreover, the twist angle is assumed to be $\theta = 2\pi/3$. To simplify the analysis we define the scaled complex coordinate $z = M_c(x_5 + ix_6)/(2\pi)$ and rewrite Eqs. (10.2)-(10.4) as

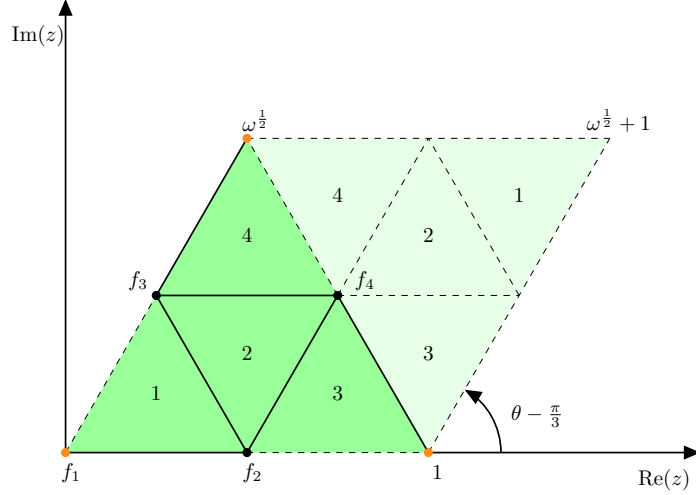


Figure 37: The fundamental domain of the T^2/\mathbb{Z}_2 orbifold is the darkest region, obtained after the compactification of the corresponding domain of the twisted torus, which includes the lightest region. The resulting space is reminiscent of a tetrahedron, and can be visualized by identifying the three orange dots into a single vertex. The fixed points of the orbifold are located at the vertices of the tetrahedron.

$$z = z + 1, \quad (10.6)$$

$$z = z + \omega, \quad (10.7)$$

$$z = -z, \quad (10.8)$$

where ω is the cubic root of unity

$$\omega \equiv e^{i\theta} = e^{i2\pi/3}. \quad (10.9)$$

A key feature of orbifolds is that they have singular points. In our case there are four of these, located at the points that remain fixed by the transformations in Eqs. (10.6)-(10.8), namely

$$f_1 = 0, \quad f_2 = \frac{1}{2}, \quad f_3 = \frac{\omega}{2}, \quad f_4 = \frac{1 + \omega}{2}. \quad (10.10)$$

These fixed points define the location of 4-dimensional branes embedded in the 6-dimensional space \mathcal{M} . In figure 37 we display both the fundamental domain of the twisted torus T^2 (light shaded green), as well as the fundamental domain of the T^2/\mathbb{Z}_2 orbifold (dark shaded green). After compactification, the continuous Poincaré symmetry of the two extra dimensions is broken, leaving a residual A_4 symmetry of the branes [314]. The appearance of the discrete A_4 symmetry can be understood as the invariance under permutations displayed by the four fixed points of the orbifold. Any of these can be written in terms of two independent transformations

$$S : z \longrightarrow z + 1/2, \quad T : z \longrightarrow \omega^2 z. \quad (10.11)$$

These can be also expressed as elements of the permutation group S_4 .

$$S = (12)(34), \quad T = (1)(243), \quad (10.12)$$

This way S and T are related to the generators of the A_4 group, satisfying

$$S^2 = T^3 = (ST)^3 = 1, \quad (10.13)$$

which are exactly the multiplication rules of the A_4 group in Eq. (A.1).

The model is based on this remnant A_4 as a family symmetry. Same-charge fields located on the four different branes would transform into each other by the remnant A_4 transformations. These four branes transform as the reducible representation $\mathbf{4}$, which decomposes as a sum of irreducible representations $\mathbf{4} \rightarrow \mathbf{3} + \mathbf{1}$. Thus, the brane-localized fields must transform under the flavour group as A_4 triplets or singlets, so the family symmetry is spontaneously broken. Below we show how this can provide a realistic pattern for the three families of leptons and quarks in a rather predictive and economical way.

Notice that the assumption of extra dimensions implies the existence of infinitely many 4-D fields associated with every bulk field, called a Kaluza-Klein (KK) tower. Their masses $(n^2 + m^2)M_c$ are determined by positive integers n, m . In our case, the fields in the bulk are the SM gauge fields g_μ, W_μ, B_μ , the right-handed quarks u_i^c and the gauge singlet scalar σ .

The tower of massive KK modes from the vector $SU(2)_L$ triplets can affect the Peskin-Takeuchi oblique parameters S, T and U in an important way. The current experimental bound for our setup (2 non-universal extra dimensions) is [470, 471]

$$M_c > 2.1 \text{ TeV}.$$

For a compactification scale sufficiently close to 2 TeV, the electroweak precision tests could in principle probe the extra dimensions at the High Luminosity LHC run.

10.2 Scotogenic orbifold

Our basic setup is a 6-dimensional extension of the Standard $SU(3)_c \otimes SU(2)_L \otimes U(1)_Y$ Model, featuring the orbifold compactification described in the previous section, and inheriting the A_4 discrete family symmetry in a natural manner. Its simplest model-realization includes three right-handed neutrinos, mediating neutrino mass generation through the type-I seesaw mechanism [143, 144]. Instead of pursuing such an approach, however, here we focus on a more complete, yet equally economical, scotogenic variant that also provides a WIMP dark matter candidate [294, 295].

The field content and transformation properties of our benchmark scotogenic variant under the various symmetry groups are shown in table 10. Note that all fermionic fields, except for the right-handed quarks, transform as flavour triplets and are localized in the orbifold branes.

Field	SU(3) _C	SU(2) _L	U(1) _Y	\mathbb{Z}_4	A_4	Location
L	1	2	-1	1	3	Brane
d^c	3	1	2/3	1	3	Brane
e^c	1	1	2	1	3	Brane
Q	3	2	1/3	1	3	Brane
$u_{1,2,3}^c$	3	1	-4/3	-1	1'', 1', 1	Bulk
F	1	1	0	i	3	Brane
H_u	1	2	1	-1	3	Brane
H_d	1	2	-1	1	3	Brane
η	1	2	1	$-i$	1	Brane
σ	1	1	0	-1	3	Bulk

Table 10: Field representation content and symmetries of the scotogenic orbifold model [295].

The model assumes an auxiliary lepton quarticity symmetry [165, 167]. This \mathbb{Z}_4 is spontaneously broken to a residual \mathbb{Z}_2 symmetry, defining the “dark sector” which comprises the dark fermion F and scalar η . Both transform non-trivially under the “dark symmetry” ensuring stability of the lightest \mathbb{Z}_2 -charged field. This makes it a potentially viable dark matter candidate, whose stability is directly related to the radiative origin of neutrino masses, Fig. 38.

The Higgs sector consists of two flavour-triplet weak iso-doublets, H_u and H_d and a SM singlet scalar σ driving the spontaneous breaking of both lepton number [32, 39], as well as family symmetry, a sort of “flavoured” Majoron scheme.

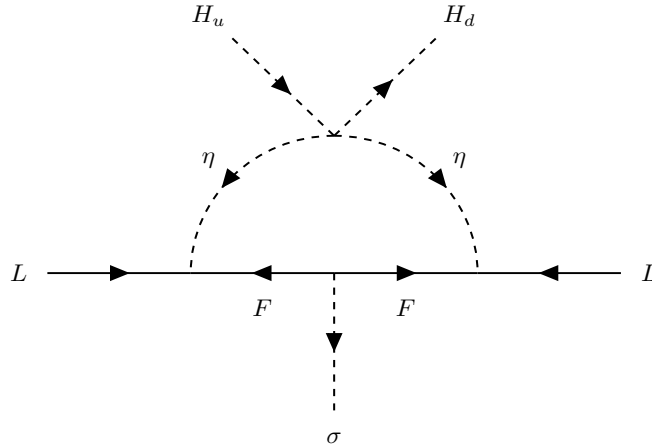


Figure 38: One-loop diagram for Majorana neutrino masses, mediated by the “dark sector” particles [295].

Given the defining symmetries of the model, one can write the most general effective Yukawa Lagrangian below the compactification scale. The Yukawa interaction terms of down-type quarks and charged leptons have the same structure, given by

$$\mathcal{L}_{H_d}^{\text{Yukawa}} = y_1^e (LH_d e^c)_{1_1} + y_2^e (LH_d e^c)_{1_2} + y_1^d (QH_d d^c)_{1_1} + y_2^d (QH_d d^c)_{1_2} + \text{H.c.}, \quad (10.14)$$

while the transformation properties of the up-type quark fields under A_4 yield

$$\mathcal{L}_{H_u}^{\text{Yukawa}} = y_1^u (QH_u)_{\mathbf{1}'} u_1^c + y_2^u (QH_u)_{\mathbf{1}''} u_2^c + y_3^u (QH_u)_{\mathbf{1}} u_3^c + \text{H.c.} \quad (10.15)$$

Notice that the bold subscripts in each term indicate its transformation properties under the remnant A_4 family symmetry. The explicit expressions for the invariant multiplet products are given in [A](#).

The dark fermion triplet F couples to the scalar field σ . The latter acquires a vacuum expectation value which drives the spontaneous breaking of lepton number symmetry, \mathbb{Z}_4 , and the A_4 family symmetry, giving rise to Majorana mass terms for the dark fermions,

$$\mathcal{L}_{\sigma}^{\text{Yukawa}} = y^{\sigma} (F^T F \sigma)_{\mathbf{1}_1} + \text{H.c.} \quad (10.16)$$

The dark scalar η plays a crucial role in the model, as it couples with both dark fermions and neutrinos

$$\mathcal{L}_{\eta}^{\text{Yukawa}} = y_1^{\eta} (L \eta F)_{\mathbf{1}} + \text{H.c.} \quad (10.17)$$

In the following, we will assume that all Yukawa couplings are real, and therefore that the model preserves a trivial CP symmetry.

10.3 Symmetry breaking and fermion masses

The scalar potential $V(H_d, H_u, \eta, \sigma)$ comprises all terms up to quartic interactions consistent with all the symmetries. Apart from the Higgs scalars H_d, H_u, σ it contains also the dark scalar η which does not develop a vacuum expectation value (VEV). The symmetry breakdown of the model proceeds in two steps. At high energies the electroweak singlet scalar field σ develops a VEV compatible with the extra-dimensional boundary conditions. Subsequently, at lower energies, the electroweak Higgs doublets H_u, H_d acquire VEVs according to the minimization of the scalar potential.

In order to describe the high-scale A_4 symmetry breaking produced by σ we introduce a boundary condition P , consistent with the orbifold construction. It defines a non-trivial gauge/Poincaré twist of the orbifold, and must be a symmetry of the Lagrangian. We assume that the transformation P acts trivially on the A_4 singlet bulk fields. Hence the only bulk field transforming non-trivially under P is the flavour triplet scalar σ , obeying the boundary condition

$$\sigma(x, z) = P\sigma(x, -z). \quad (10.18)$$

so as to be consistent with Eq. (10.8). The invariance of the kinetic term of the σ field in the 6-D Lagrangian implies that $P \in SU(3)$, while the condition in Eq. (10.18) ensures that the matrix P will leave invariant the interactions of fields in the brane. Thus the boundary condition matrix must satisfy

$$P \in SU(3), \quad P^2 = \mathbf{1}_{3 \times 3}, \quad P^\dagger = P. \quad (10.19)$$

The boundary condition on the σ field applies also to its VEV alignment. As a result, the masses of the dark fermions F are a direct outcome of the boundary condition of the bulk field σ in the two extra dimensions

$$\langle \sigma \rangle = P \langle \sigma \rangle. \quad (10.20)$$

The boundary condition matrix P is a property of the orbifold, its form is given explicitly in [295]. Here we adopt the most general VEV alignment consistent with the spontaneous breaking of lepton number and the A_4 family symmetry, expressed as

$$\langle \sigma \rangle = v_\sigma \begin{pmatrix} \epsilon_1^\sigma e^{i\varphi} \\ \epsilon_2^\sigma \\ 1 \end{pmatrix}, \quad \text{with} \quad v_\sigma, \epsilon_1^\sigma, \epsilon_2^\sigma \in \mathbb{R} \quad \text{and} \quad 0 \leq \varphi < \pi. \quad (10.21)$$

Here we will not present a dedicated analysis of the scalar potential, except to stress the importance of the λ_5 term for the neutrino mass generation mechanism, namely

$$V(H_u, H_d, \eta) \supset \frac{1}{2} \lambda_5 \left[(H_d^T (i\sigma_2) \eta)_{\mathbf{3}} (H_u^\dagger \eta)_{\mathbf{3}_1} \right] + \text{H.c.} \quad (10.22)$$

Here λ_5 is a coupling constant and σ_2 is the second Pauli matrix. This term lifts the degeneracy of the mass eigenstates of the neutral components of η , denoted as $\sqrt{2} \text{Re}(\eta^0)$ and $\sqrt{2} \text{Im}(\eta^0)$, playing a key role in the scotogenic generation of neutrino masses at the one-loop level, as illustrated in Fig. 38. One can show that there is enough freedom in parameter space to drive the spontaneous breaking of the gauge symmetries down to $U(1)_{\text{EM}}$.

10.3.1 Quark and lepton masses

Since A_4 breaks spontaneously at the v_σ scale, in the second stage of spontaneous symmetry breaking, we assume that the weak iso-doublets H_u and H_d obtain the most general A_4 breaking VEVs consistent with trivial CP symmetry. For real $v_u, v_d, \epsilon_{1,2}^{u,d}$ it is given as

$$\langle H_u \rangle = v_u \begin{pmatrix} \epsilon_1^u \\ \epsilon_2^u \\ 1 \end{pmatrix}, \quad \langle H_d \rangle = v_d \begin{pmatrix} \epsilon_1^d \\ \epsilon_2^d \\ 1 \end{pmatrix}. \quad (10.23)$$

After spontaneous symmetry breaking, the up-quark mass matrix becomes

$$M_u = v_u \begin{pmatrix} y_1^u \epsilon_1^u & y_2^u \epsilon_1^u & y_3^u \epsilon_1^u \\ y_1^u \epsilon_2^u \omega^2 & y_2^u \epsilon_2^u \omega & y_3^u \epsilon_2^u \\ y_1^u \omega & y_2^u \omega^2 & y_3^u \end{pmatrix}, \quad (10.24)$$

while the down-quark and charged lepton mass matrices take the form

$$\begin{aligned}
M_d &= v_d \begin{pmatrix} 0 & y_1^d \epsilon_1^d & y_2^d \epsilon_2^d \\ y_2^d \epsilon_1^d & 0 & y_1^d \\ y_1^d \epsilon_2^d & y_2^d & 0 \end{pmatrix}, \\
M_e &= v_d \begin{pmatrix} 0 & y_1^e \epsilon_1^d & y_2^e \epsilon_2^d \\ y_2^e \epsilon_1^d & 0 & y_1^e \\ y_1^e \epsilon_2^d & y_2^e & 0 \end{pmatrix}.
\end{aligned} \tag{10.25}$$

All Yukawa couplings in the last two equations are assumed to be real due to our imposition of trivial CP symmetry.

10.3.2 Scotogenic neutrino masses

The A_4 flavour symmetry structure of the Yukawa term in Eq. (10.16) implies that the Majorana mass matrix of the dark fermions M_F must have the following structure

$$M_F = y_\sigma v_\sigma \begin{pmatrix} 0 & 1 & \epsilon_2^\sigma \\ 1 & 0 & \epsilon_1^\sigma e^{i\varphi} \\ \epsilon_2^\sigma & \epsilon_1^\sigma e^{i\varphi} & 0 \end{pmatrix}. \tag{10.26}$$

In order to describe our one-loop scotogenic mechanism for neutrino masses we write the dark fermion F fields in the mass eigenstate basis (\tilde{F}) by performing the singular value decomposition of the dark fermion mass matrix M_F . Since the latter is symmetric, only one unitary matrix V is needed in the Takagi decomposition [30],

$$y^\sigma (F^T F \sigma)_{\mathbf{1}_1} = F^T M_F F = F^T V^T D V F = (V F)^T D (V F) \equiv \tilde{F}^T D \tilde{F}, \tag{10.27}$$

where $D = \text{diag}(m_{F_1}, m_{F_2}, m_{F_3})$ and $\tilde{F} \equiv V F$ denotes the dark fermion triplet expressed in the mass eigenstate basis. We can then rewrite Eq. (10.17) as

$$\mathcal{L}_\eta^{\text{Yukawa}} = y_1^\eta \eta \left(L V^\dagger \tilde{F} \right) + \text{H.c.} \tag{10.28}$$

As already mentioned, neutrino masses are forbidden at tree-level due to the auxiliary \mathbb{Z}_4 symmetry. However, thanks to the mediation of the dark fields η and F , neutrino masses emerge at one-loop through the diagram depicted in Fig. 38, which has the basic scotogenic structure [196].

Defining $y_1^\eta V^\dagger \equiv h$ in Eq. (10.27) we can write the expression for the one-loop neutrino mass matrix M_ν as

$$(M_\nu)_{ij} = \sum_k^3 \frac{h_{ik} (h^T)_{kj}}{16\pi^2} S(m_{F_k}), \tag{10.29}$$

where $S(m_{F_k})$ is for the loop factor

$$S(m_{F_k}) = m_{F_k} \left(\frac{m_R^2}{m_R^2 - m_{F_k}^2} \ln \frac{m_R^2}{m_{F_k}^2} - \frac{m_I^2}{m_I^2 - m_{F_k}^2} \ln \frac{m_I^2}{m_{F_k}^2} \right), \quad (10.30)$$

with $m_R = m(\sqrt{2} \operatorname{Re} \eta^0)$, $m_I = m(\sqrt{2} \operatorname{Im} \eta^0)$ with

$$m_R^2 - m_I^2 \equiv 2\lambda_5 (\langle H_u \rangle_{\mathbf{3}} \langle H_d \rangle_{\mathbf{3}})_1. \quad (10.31)$$

Neutrino masses are not only loop-suppressed, but also symmetry-protected, as they vanish in the limit $\lambda_5 \rightarrow 0$, see Eq. (10.22).

After spontaneous symmetry breaking, the auxiliary \mathbb{Z}_4 breaks down to a residual \mathbb{Z}_2 that stabilizes the lightest dark particle. There are two possible dark matter candidates: the lightest state in the complex neutral scalar η , or the lightest Majorana fermion in the flavour triplet F . In either case, the phenomenology of dark matter is qualitatively similar to that of other scotogenic scenarios, which has been extensively discussed, see for example Ref. [138] and references therein.

10.4 Global fit of flavour observables

Before describing the global fit of flavour observables, some preliminaries are necessary. The bottom line is that, due to the reduced number of parameters, the model makes strong flavour predictions.

10.4.1 Preliminaries

Here we adopt the symmetrical parametrization of the quark and lepton mixing matrices [30], described in Sect. 1. For the case of quarks, choosing the PDG ordering prescription, the symmetrical form leads to the standard Cabibbo-Kobayashi-Maskawa (CKM) matrix in Eq. (1.8). On the other hand, for the mixing of leptons, it is described by Eq. (1.21)²⁴. In both cases the mixing matrix description is supplemented by the PDG factor ordering convention. However, in the leptonic case the symmetrical form provides a neater description of CP violation than the PDG form. In this case the Dirac CP phase that enters in neutrino oscillations is the leptonic analogue of the quark Jarlskog parameter, identified with the “rephasing-invariant” combination

$$\delta^\ell = \phi_{13} - \phi_{12} - \phi_{23}.$$

Notice that this phase must not be present in the effective mass parameter $\langle m_{\beta\beta} \rangle$ characterizing the amplitude for neutrinoless double beta decay, which involves only the two Majorana phases, Eq. (1.25). Hence the symmetrical presentation is more transparent for describing the $0\nu\beta\beta$ decay amplitude [99].

²⁴In both cases we assume unitarity, neglecting therefore possible mixing with exotic fermions that could be relevant, say, within a low-scale seesaw scheme [472].

10.4.2 Fit procedure

The above model is characterized by 16 independent parameters in the flavour sector, identified as follows: 8 real Yukawa couplings $y_{1,2}^{e,d}$, $y_{1,2,3}^u$, y_1^η , 6 real VEV ratios $\epsilon_{1,2}^{u,d}$, $\epsilon_{1,2}^\sigma$, one quartic coupling λ_5 and one CP violating phase φ contained in $\langle\sigma\rangle$. These parameters describe 22 observables, namely, 12 masses, 4 CKM matrix elements, plus 6 lepton mixing matrix parameters including the 2 Majorana phases.

In order to explore the predictivity of the model, we perform a global flavour fit to the available experimental data, by minimizing the chi-square function defined as

$$\chi^2 = \sum (\mu_{\text{exp}} - \mu_{\text{model}})^2 / \sigma_{\text{exp}}^2, \quad (10.32)$$

where the sum runs through the 19 measured physical parameters, i.e. 6 quark masses, 3 CKM mixing angles, 1 CKM CP phase, 3 charged lepton masses, 3 lepton mixing angles, 1 lepton CP violating phase and 2 neutrino squared mass splittings. Note that we have only limits on the lightest neutrino mass from experiment and no direct information on the Majorana $0\nu\beta\beta$ phases. The fit is performed by scanning the values of the 16 independent model parameters that provide a description of the above 22 flavour observables.

In our chi-square minimization with respect to the 16 independent model parameters, all quark and charged-lepton masses were evaluated at the same energy scale, chosen as M_Z [473]. This assumption was shown to be consistent with the golden mass relation [143]. Coming to the neutrino oscillation parameters, these were extracted from the global fit in [24, 25], neglecting the effect of running to M_Z [473, 474]. The remaining observables were taken from the PDG [28]. In order to extract the flavour observables from the mass matrices in Eqs. (10.24) and (10.25) we use the Mathematica Mixing Parameter Tools package [475].

The results of our flavour fit are summarized in table 11. The minimum at $\chi^2 \approx 2$ shows that the model reproduces the observed pattern of fermion masses and mixing rather well. From Table 11 one can read directly the predictions of the model concerning the mass of the lightest neutrino and the values of the CP phases characterizing the lepton sector.

10.5 Flavour predictions of the scotogenic orbifold model

We now discuss in more detail the flavour predictions of our scotogenic orbifold model, both in the quark and lepton sectors. These follow directly from the A_4 family symmetry that results from the orbifold compactification of the extra dimensions.

10.5.1 Golden quark-lepton mass relation

This is a key feature of the model that results from the down-type quarks and charged lepton assignments under the A_4 flavour symmetry. Indeed, after spontaneous symmetry breaking these obtain masses from the same common Higgs doublet H_d , leading to the mass matrices in Eq.(10.25). After diagonalization

to physical mass-eigenstates, one obtains the golden quark-lepton mass relation

$$\frac{m_\tau}{\sqrt{m_\mu m_e}} \approx \frac{m_b}{\sqrt{m_s m_d}}, \quad (10.33)$$

This relation emerges in models with SO(3) family symmetry implementing a Peccei-Quinn symmetry [287], and in the theories proposed in Refs. [65, 66] and [288–290].

In our case the golden relation is a common feature of the models with A_4 family symmetry arising from the compactification of 6-Dimensional orbifolds, proposed in Refs. [143, 144] and further discussed in [294, 295]. One can show that, given the current experimental measurements of the relevant masses, the golden relation holds with good precision, see for example, Fig.1 in [143]. Besides, it constitutes a very robust prediction under the renormalization group evolution, as it involves only fermion mass ratios.

Parameter	Value	Observable	Data		Model best fit
			Central value	1 σ range	
$y_1^e v_d / \text{GeV}$	-1.745	$\theta_{12}^\ell / ^\circ$	34.3	33.3 \rightarrow 35.3	33.0
$y_2^e v_d / (10^{-1} \text{GeV})$	1.021	$\theta_{13}^\ell / ^\circ$	8.45	8.31 \rightarrow 8.61	8.52
$y_1^d v_d / (10^{-2} \text{GeV})$	-5.039	$\theta_{23}^\ell / ^\circ$	49.26	48.47 \rightarrow 50.05	50.44
$y_2^d v_d / \text{GeV}$	2.852	$\delta^\ell / ^\circ$	194	172 \rightarrow 218	192
$y_1^u v_u / (10^{-1} \text{GeV})$	6.074	m_e / MeV	0.486	0.486 \rightarrow 0.486	0.486
$y_2^u v_u / (10^2 \text{GeV})$	1.712	m_μ / GeV	0.102	0.102 \rightarrow 0.102	0.102
$y_3^u v_u / \text{GeV}$	7.157	m_τ / GeV	1.745	1.743 \rightarrow 1.747	1.745
$\epsilon_1^u / 10^{-4}$	7.055	$\Delta m_{21}^2 / (10^{-5} \text{eV}^2)$	7.50	7.30 \rightarrow 7.72	7.50
$\epsilon_2^u / 10^{-2}$	-5.044	$\Delta m_{31}^2 / (10^{-3} \text{eV}^2)$	2.55	2.52 \rightarrow 2.57	2.54
$\epsilon_1^d / 10^{-3}$	-2.814	m_1 / meV			135.35
$\epsilon_2^d / 10^{-3}$	5.833	m_2 / meV			135.63
ϵ_1^σ	1.501	m_3 / meV			144.43
ϵ_2^σ	-0.654	$\phi_{12} / ^\circ$			87.01
φ	3.527	$\phi_{13} / ^\circ$			190.30
$(y_1^n)^2 y_\sigma v_\sigma / (\text{KeV})$	1.813	$\phi_{23} / ^\circ$			271.05
$2\lambda_5 \langle H_u \rangle \langle H_d \rangle / (\text{KeV})^2$	0.012	$\theta_{12}^q / ^\circ$	13.04	12.99 \rightarrow 13.09	13.04
		$\theta_{13}^q / ^\circ$	0.20	0.19 \rightarrow 0.22	0.20
		$\theta_{23}^q / ^\circ$	2.38	2.32 \rightarrow 2.44	2.38
		$\delta^q / ^\circ$	68.75	64.25 \rightarrow 73.25	60.23
		m_u / MeV	1.28	0.76 \rightarrow 1.55	1.28
		m_c / GeV	0.626	0.607 \rightarrow 0.645	0.626
		m_t / GeV	171.6	170 \rightarrow 173	171.6
		m_d / MeV	2.74	2.57 \rightarrow 3.15	2.49
		m_s / MeV	54	51 \rightarrow 57	54
		m_b / GeV	2.85	2.83 \rightarrow 2.88	2.85
		χ^2			1.96

Table 11: Flavour parameters and observables: measured versus predicted values for the best fit point.

10.5.2 Neutrino oscillation predictions

In order to identify the predictions of the model concerning the oscillation parameters we have randomly varied the parameters around the global best fit point in Table 11, while requiring compatibility with all measured flavour observables at 3σ . The results of the analysis are given in Fig 39, where the blue contours represent the 90, 95, and 99% C.L. profiles from the Valencia global oscillation fit in [24, 25], while the purple dots indicate regions compatible at 3σ with all experimental data. The best fit point of the global oscillation fit is marked with a black star, while that of the global flavour fit is indicated by a white cross. One sees from Fig. 39 how the predicted values of the leptonic Dirac CP phase are restricted

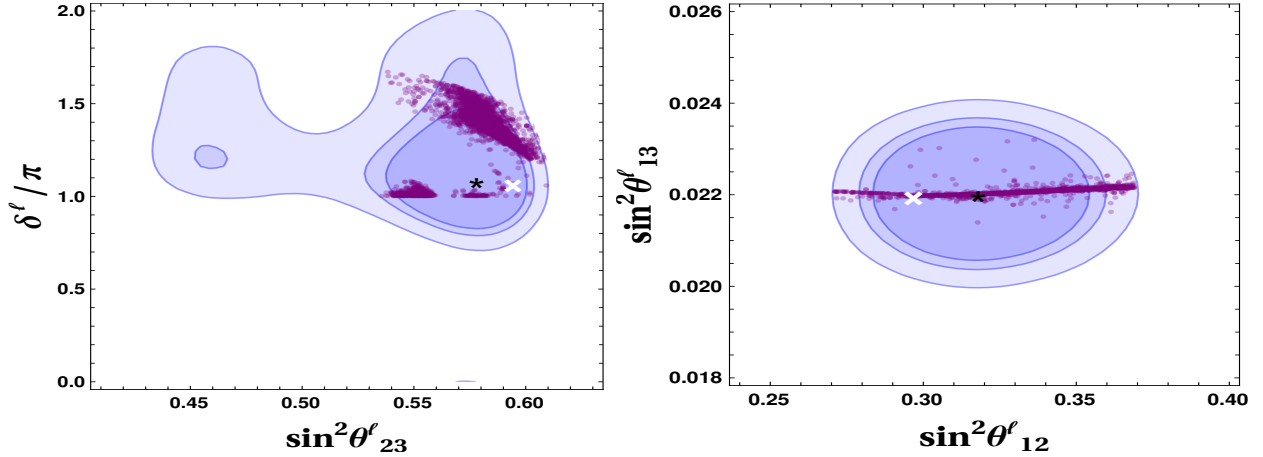


Figure 39: Allowed values for the mixing angles and the leptonic Dirac CP phase. The purple points are compatible at 3σ with all flavour observables, while the blue shades are the generic 90, 95 and 99% C.L. regions of the global oscillation fit in [24, 25]. The black star is the central point of the global oscillation fit, while the white cross stands for the best fit point in Table 11.

to the range $\delta^\ell \geq \pi$, while the atmospheric angle θ_{23}^ℓ is required to lie in the higher octant. Besides, one sees from the right panel in Fig. 39 a sharp prediction for the reactor angle θ_{13}^ℓ , see also table 11.

A scan of the parameter space of the model consistent at 3σ with all current experiments reveals that only the Normal Ordered (NO) neutrino mass spectrum is possible. Indeed, the best fit point in table 11 has positive Δm_{31}^2 , corresponding to NO, and a rather high absolute scale for the neutrino masses.

10.5.3 Neutrinoless double beta decay predictions

Concerning neutrinoless double beta decay, using the Majorana phase and neutrino mass predictions of table 11 in Eq. (1.25), one finds the preferred effective amplitude parameter:

$$|m_{\beta\beta}| = 58.08 \text{ meV}. \quad (10.34)$$

A detailed analysis is presented in figure 40, where we show in purple the region of predicted $|m_{\beta\beta}|$ values as a function of the lightest neutrino mass m_1 . To be conservative, we randomly varied the model parameters within the allowed 3σ range. The best fit point from table 11 is marked in red. One sees that the predicted central value of $|m_{\beta\beta}|$ lies inside the current exclusion band of Kamland-Zen (36 – 156 meV) [125].

shown in orange in Fig. 40. This will also be probed by cosmological observations and possibly by future beta decay endpoint studies. We also display the projected sensitivities of the next round of $0\nu\beta\beta$ experiments LEGEND [476] and nEXO [477] as the colored horizontal bands.

Notice that the central value of the lightest neutrino mass m_1 obtained from the global fit is disfavored by the latest results of the Planck collaboration on the sum of light neutrino masses [128]. This tension is further enhanced by the addition of Baryon Acoustic Oscillations (BAO) data [124], see vertical band in lighter gray in figure 40. Beyond the central prediction, however, there is a broad parameter region consistent both with measured flavour observables as well as with the cosmological bounds.

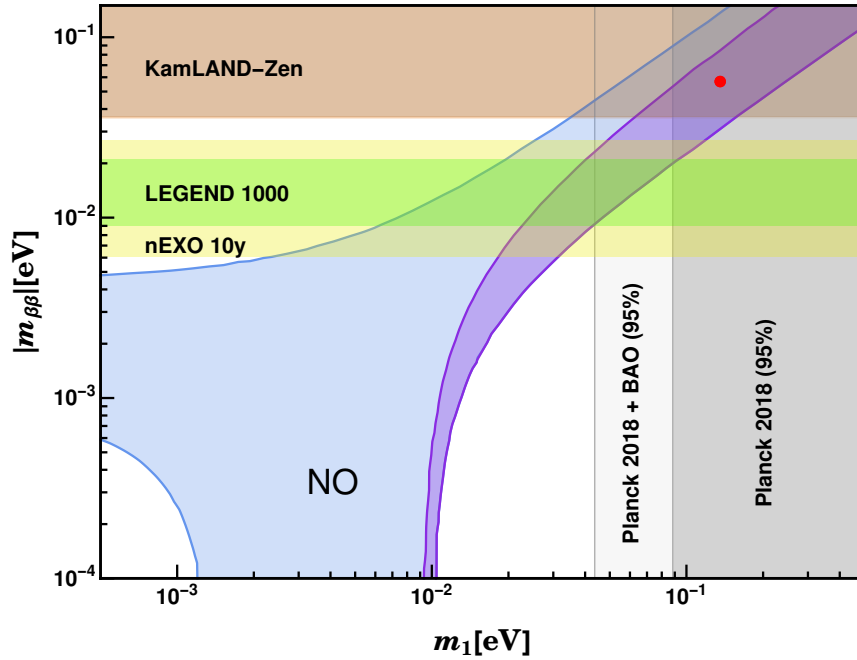


Figure 40: Effective $0\nu\beta\beta$ decay amplitude versus the lightest neutrino mass m_1 . From the global fit one finds that only normal ordering is allowed. The blue region is the generic one consistent with oscillations at 2σ . The purple region is the one allowed at 3σ around the global best fit point in table 11, marked in red. The current KamLAND-Zen limit is shown in brown, and the projected sensitivities of future experiments LEGEND-1000 and nEXO are indicated with light yellow and light green horizontal bands respectively. The vertical gray bands represent the current sensitivity of cosmological data from the Planck collaboration (dark gray), and in combination with BAO data (light gray) [128, 129]

11 Recent progress: modular symmetry

In flavour symmetry models, complicated vacuum alignment assumptions are often required to break the flavor symmetry. The vacuum expectation values of the associated flavons should be conveniently oriented in family space. Moreover, higher-dimensional operators with flavon insertions and unknown coefficients are often present, affecting the resulting model predictions. In order to alleviate these shortcomings modular invariance as flavor symmetry has been recently proposed [478]. In what follows we briefly sketch recent work, for dedicated reviews on modular symmetries see Refs. [91, 479, 480].

11.1 The modular group

The modular group $SL(2, \mathbb{Z})$ is the group of 2×2 integer matrices with determinant one,

$$SL(2, \mathbb{Z}) = \left\{ \begin{pmatrix} a & b \\ c & d \end{pmatrix} \middle| a, b, c, d \in \mathbb{Z}, ad - bc = 1 \right\}. \quad (11.1)$$

The modular group $SL(2, \mathbb{Z})$ acts on the complex variable τ in the upper-half plane as the linear fractional transformation [481]

$$\gamma\tau = \frac{a\tau + b}{c\tau + d} \quad \text{for } \gamma = \begin{pmatrix} a & b \\ c & d \end{pmatrix} \in SL(2, \mathbb{Z}) \quad \text{and } \text{Im}(\tau) > 0. \quad (11.2)$$

One sees that γ and $-\gamma$ induce the same linear fraction transformation.

The modular group can be generated by the two generators S and T ,

$$S = \begin{pmatrix} 0 & 1 \\ -1 & 0 \end{pmatrix}, \quad T = \begin{pmatrix} 1 & 1 \\ 0 & 1 \end{pmatrix}, \quad (11.3)$$

which lead to duality and shift symmetries of τ as follows,

$$\tau \xrightarrow{S} -\frac{1}{\tau}, \quad \tau \xrightarrow{T} \tau + 1. \quad (11.4)$$

Any value of τ in the upper half complex plane can be shifted in to the region of $-\frac{1}{2} \leq \text{Re}(\tau) < \frac{1}{2}$ by multiple T transformations. Moreover, it can be mapped to the region $|\tau| \leq 1$ by an S transformation. As a consequence, the complex modulus τ could be restricted to the fundamental domain \mathcal{F} of the modular group,

$$\mathcal{F} = \left\{ \tau \middle| -\frac{1}{2} \leq \text{Re}(\tau) < \frac{1}{2}, \text{Im}(\tau) > 0, |\tau| > 1 \right\} \cup \left\{ \tau \middle| -\frac{1}{2} \leq \text{Re}(\tau) \leq 0, \text{Im}(\tau) > 0, |\tau| = 1 \right\}, \quad (11.5)$$

which is displayed in figure 41. Every complex modulus τ can be mapped into the fundamental domain by a modular transformation of Eq. (11.2), and no two points in \mathcal{F} can be related by modular transformations. Notice the right half boundary of \mathcal{F} is not included into the fundamental domain, since it can related

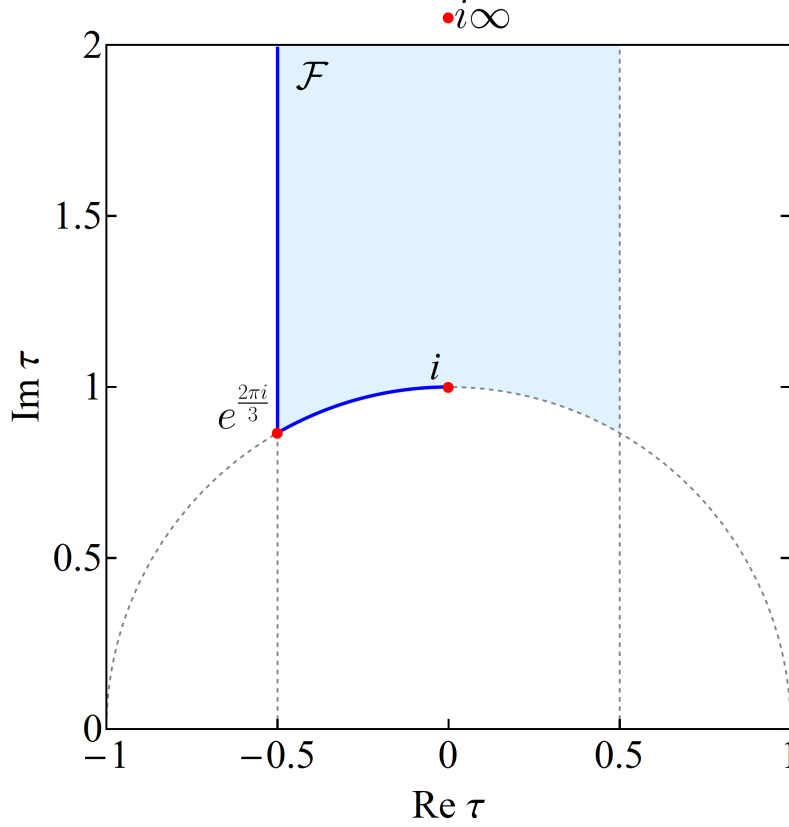


Figure 41: The fundamental domain \mathcal{F} of the modular group, where the red points denote the three fixed points $\tau_0 = i, e^{2\pi i/3}, i\infty$ which preserve a residual modular symmetry.

to the left half boundary by some modular transformation. Moreover, no value of τ is left invariant by the whole modular group action of Eq. (11.2). In the fundamental domain, there are only three fixed points $\tau_0 = i, e^{2\pi i/3}, i\infty$ which break the modular group $SL(2, \mathbb{Z})$ partially. These are invariant under the modular transformations S, ST and T respectively [481–483]. Notice that each τ is trivially invariant under S^2 which is a negative identity matrix.

Modular symmetry provides a novel origin of discrete flavor symmetry through the quotient of $SL(2, \mathbb{Z})$ by the principal congruence subgroup of level N which is defined as,

$$\Gamma(N) = \left\{ \begin{pmatrix} a & b \\ c & d \end{pmatrix} \in SL(2, \mathbb{Z}) \left| a, d = 1 \pmod{N}, b, c = 0 \pmod{N} \right. \right\}, \quad (11.6)$$

which is a normal subgroup of finite index in $SL(2, \mathbb{Z})$. The finite modular groups are the quotient groups $\Gamma_N = SL(2, \mathbb{Z}) / \pm \Gamma(N)$ which play the role of discrete flavor symmetry. Remarkably, for $N \leq 5$ the finite modular groups Γ_N are isomorphic to the permutation groups [259, 478]

$$\Gamma_2 \cong S_3, \quad \Gamma_3 \cong A_4, \quad \Gamma_4 \cong S_4, \quad \Gamma_5 \cong A_5, \quad (11.7)$$

which have been widely used as traditional flavor symmetries.

11.2 Modular invariance

A key concept of the theory of modular symmetries [478] is that of modular forms of level N and weight $2k$, denoted $Y(\tau)$. These are holomorphic functions of the modulus τ with the following transformation property

$$Y(\gamma\tau) = (c\tau + d)^{2k}Y(\tau), \quad \gamma = \begin{pmatrix} a & b \\ c & d \end{pmatrix} \in \Gamma(N), \quad (11.8)$$

where the integer $k \geq 0$ determines the weight $2k$.

There are only a finite number of linearly independent modular forms, denoted as $Y_i(\tau)$, and one can always choose a basis such that the transformation of the modular forms can be described by a unitary representation ρ of Γ_N :

$$Y_i(\gamma\tau) = (c\tau + d)^{2k} \rho_{ij}(\gamma) Y_j(\tau), \quad (11.9)$$

where $\gamma = \begin{pmatrix} a & b \\ c & d \end{pmatrix}$ refers to a representative element of Γ_N . Likewise, the modular transformation properties of matter fields $\varphi^{(I)}$ are completely specified by the weight k_I and the unitary representation $\rho^{(I)}$ of the finite modular group Γ_N ,

$$\varphi^I \rightarrow (c\tau + d)^{k_I} \rho^{(I)} \varphi^{(I)}. \quad (11.10)$$

Note that the modular flavor symmetry requires supersymmetry to preserve the holomorphicity of the modular form. Then the superpotential can be expanded in a power series of the matter fields $\varphi^{(I)}$ as follows,

$$\mathcal{W} = \sum_n Y_{I_1 I_2 \dots I_n}(\tau) \varphi^{(I_1)} \varphi^{(I_2)} \dots \varphi^{(I_n)}. \quad (11.11)$$

Modular invariance requires $Y_{I_1 I_2 \dots I_n}(\tau)$ to be a modular form of weight k_Y and level N transforming in the representation ρ of Γ_N ,

$$Y_{I_1 I_2 \dots I_n}(\gamma\tau) = (c\tau + d)^{k_Y} \rho(\gamma) Y_{I_1 I_2 \dots I_n}(\tau), \quad (11.12)$$

with the conditions

$$k_Y + k_{I_1} + k_{I_2} + \dots + k_{I_n} = 0, \quad \rho \otimes \rho^{(I_1)} \otimes \rho^{(I_2)} \otimes \dots \otimes \rho^{(I_n)} \supset \mathbf{1}, \quad (11.13)$$

where $\mathbf{1}$ denotes the invariant singlet representation of Γ_N . One sees that the modular flavor symmetry requires the Yukawa couplings to be modular forms $Y_{I_1 I_2 \dots I_n}(\tau)$. In the simplest implementation, flavons are not necessary and the complex modulus τ is the unique symmetry breaking parameter, greatly simplifying the alignment problem. Moreover, modular invariance requires the Yukawa couplings and fermion mass matrices to be combinations of modular forms, holomorphic functions of τ , all higher-dimensional operators are unambiguously determined in the limit of unbroken supersymmetry. As a result, flavour models with modular invariance depend on fewer parameters, enhancing their predictive power.

The above formalism of modular flavor symmetry has been extended to the double covers [435, 484–487] or the metaplectic covers [487, 488] of the finite group Γ_N , then the modular weights can take integer values or more general rational values.

11.3 Generalized CP in modular symmetry

The interplay of modular symmetry and generalized CP symmetry (gCP) has been studied [489–491]. The consistency between the modular symmetry and gCP fixes the CP transformation of the modulus τ to be [489, 492–495]

$$\tau \xrightarrow{CP} -\tau^* \quad (11.14)$$

up to modular transformations. For any modular transformation

$$\gamma = \begin{pmatrix} a & b \\ c & d \end{pmatrix} \in SL(2, \mathbb{Z}),$$

one can check that the action of the transformation chain $CP \rightarrow \gamma \rightarrow CP^{-1}$ on τ is,

$$\tau \xrightarrow{CP} -\tau^* \xrightarrow{\gamma} -\frac{a\tau^* + b}{c\tau^* + d} \xrightarrow{CP^{-1}} \frac{a\tau - b}{-c\tau + d}. \quad (11.15)$$

This implies that the CP transformation corresponds to an automorphism of the modular group, and it maps any modular transformation γ to another modular transformation $u(\gamma)$,

$$u(\gamma) \equiv CP \circ \gamma \circ CP^{-1} = \begin{pmatrix} a & -b \\ -c & d \end{pmatrix}. \quad (11.16)$$

In particular, one has

$$u(S) = CP \circ S \circ CP^{-1} = S^{-1}, \quad u(T) = CP \circ T \circ CP^{-1} = T^{-1}. \quad (11.17)$$

We proceed to consider the gCP transformation of an arbitrary chiral superfield multiplet $\varphi(x)$ in the representation \mathbf{r} of the finite modular group Γ_N ,

$$\varphi(x) \xrightarrow{CP} X_{\mathbf{r}} \bar{\varphi}(x_P), \quad (11.18)$$

where a bar denotes the Hermitian conjugate superfield, and where $x = (t, \mathbf{x})$, $x_P = (t, -\mathbf{x})$ and $X_{\mathbf{r}}$ is a unitary matrix acting on flavour space. Applying the consistency condition chain of Eq. (11.16) to the matter multiplet φ , one find that the CP transformation matrix $X_{\mathbf{r}}$ has to satisfy the following constraint [489],

$$X_{\mathbf{r}} \rho_{\mathbf{r}}^*(\gamma) X_{\mathbf{r}}^{-1} = \rho_{\mathbf{r}}(u(\gamma)). \quad (11.19)$$

It is sufficient to just consider the modular generators $\gamma = S, T$, namely

$$X_{\mathbf{r}} \rho_{\mathbf{r}}^*(S) X_{\mathbf{r}}^{-1} = \rho(S^{-1}), \quad X_{\mathbf{r}} \rho_{\mathbf{r}}^*(T) X_{\mathbf{r}}^{-1} = \rho(T^{-1}), \quad (11.20)$$

which fixes $X_{\mathbf{r}}$ up to an overall phase by Schur's lemma, for each irreducible representation \mathbf{r} . In the basis where both S and T are represented by symmetric and unitary matrices, $X_{\mathbf{r}} = \mathbb{1}_{\mathbf{r}}$ solves the consistency condition. As a consequence, CP symmetry imposition enforces all coupling constants to be real in such basis. The VEV of τ is the unique source breaking both modular and gCP symmetries. The combination of modular and CP symmetries allows one to construct quite predictive flavor models. Indeed, it is remarkable that all the lepton masses, mixing angles and CP violation phases could be described in terms of only four real couplings plus the complex modulus τ in the minimal modular model of Refs. [496, 497]. The gCP symmetry can also be consistently implemented in the context of multiple moduli [491].

11.4 Modular symmetry from top-down

The idea of modular flavor symmetry is inspired by top-down considerations from string theory. The modular symmetry can naturally appear in orbifold compactifications of the heterotic string [492, 498] and magnetized toroidal compactification [499–505]. The double covers and metaplectic covers of the finite modular groups could be reproduced from top-down constructions. Given the fact that string compactification generally yields several moduli, the modular invariance has been extended to involve multiple moduli based on the direct product of several $SL(2, \mathbb{Z})$ [506] or the Symplectic modular group $Sp(2g, \mathbb{Z})$ [507], where g is a generic positive integer called genus. Note that $Sp(2g, \mathbb{Z})$ can arise as the duality group in string Calabi-Yau compactifications [508–510], and the group $Sp(2, \mathbb{Z})$ is isomorphic to the modular group $SL(2, \mathbb{Z})$. Moreover, it has been found that the modular symmetry and traditional flavor symmetry appear together in top-down constructions. This leads to the concept of eclectic flavor group [511, 512], a maximal extension of the traditional flavor group by finite modular group. It is more predictive than the finite modular group and also the traditional flavor group by itself, combining the advantages of both approaches. In particular, the interplay of modular symmetry and traditional flavor symmetry can restrict the Kähler potential more severely than the modular symmetry by itself. The possibility of eclectic flavor group can also be consistently combined with the gCP symmetry [511].

11.5 Quark-lepton mass relations from modular symmetry

Quite generally, the problem of understanding the pattern of fermion masses and mixings presents a two-fold challenge. While predicting fermion mixings through the imposition of flavor symmetries is relatively straightforward, formulating a convincing theory of fermion masses seems tougher.

It has recently been shown that realistic fermion mass relations can arise naturally in modular invariant models [436, 513–515], without relying on *ad hoc* flavon alignments. As an example, Ref. [291] gave a set of viable fermion mass relations based on the $\Gamma_4 \cong S_4$ symmetry. The new versions exhibit calculable deviations from the usual Golden Mass Relation in Eq. (10.1). They were derived from modular flavor

symmetry in a rather general manner, relying only on the modular flavor group and its vector-valued modular forms, rather than *ad hoc* flavon alignments²⁵. The new relations were shown to be viable and experimentally testable, distinguishing modular models from the conventional flavon-based prediction in Eq. (10.1).

The method is largely model-independent, and can be adapted also to obtain predictions in the up-quark sector and neutrinos. It may also prove useful for more comprehensive modular invariant models and for top-down constructions.

11.6 Modular versus traditional flavor symmetry

We now comment on the predictive power of traditional flavor symmetry and modular symmetry. As we have shown in section 6, traditional flavor symmetry in combination with generalized CP symmetry allows one to predict lepton mixing angles and CP violation phases in terms of just one or two real free parameters when certain residual symmetry is preserved. In general, however, lepton masses are unconstrained by the residual symmetry.

In the case of modular symmetry, the fermion mass matrices exhibit certain symmetry-determined flavor structure through the modular forms which are functions of the modulus τ . One finds that both fermion masses as well as flavor mixing parameters can be determined within specific models. However, one must resort to numerical analysis to reveal the possible correlations amongst the flavor parameters, since a residual modular symmetry with a single modulus has not led to phenomenologically viable models. Concerning vacuum alignment, it is notoriously difficult to dynamically realize the alignment required by the residual symmetry within traditional flavor symmetry constructions. On the other hand, determining the VEV of the modulus τ from a dynamical principle is also an open question, some possible schemes have been proposed to stabilize the modular VEV [516–524]. In modular flavor models, the VEV of τ is usually treated as free parameter, and its value is determined by confronting the model predictions with experimental data.

In short, modular flavor symmetries may shed light on the ultimate symmetry underlying the flavor problem. They have been studied from both the bottom-up and top-down approaches. There are still some unsolved problems such as modulus stabilization and the Kähler potential problem. However, invoking modular symmetry seems a useful tool towards formulating theories of flavor. A comprehensive description of these recent developments lies outside the scope of the present work, see Refs. [91, 479, 480] dedicated modular symmetry reviews.

²⁵They are determined by the Clebsch-Gordan coefficients of the given finite modular group as well as the expansion coefficients of its modular forms.

12 Summary and outlook

The flavour problem constitutes perhaps one of the major open issues and deepest challenges of particle physics. Even more so after the revolutionary discovery and confirmation of neutrino oscillations. The main legacy of these experiments has been to show that leptons mix rather differently from quarks, providing a key input on the flavour issue. Indeed, it seems unlikely that the peculiar pattern of neutrino mixing angles extracted from experiment is just a random coincidence. Rather, it should have its roots in some, perhaps subtle, underlying symmetry of nature.

By itself, the Standard Model lacks an organizing principle in terms of which to understand the “flavours” of the fundamental building blocks of matter. First of all, the flavour challenge comprises an understanding of family replication, i.e. why nature repeats itself three times. Moreover, it also requires an explanation for the pattern of fermion masses and mixings. This review examined the possibility that the flavour puzzle has a symmetry explanation.

To set up the stage we started with an introductory section in which we gave basic preliminaries on the description of lepton and quark mixing, as well as a recap on the status of neutrino oscillations, Fig. 1 and Fig. 2, and neutrinoless double beta decay, e.g. Fig. 3. We discussed ways to have detectable $0\nu\beta\beta$ decay rates, in particular theories where the lightest neutrino is massless or nearly so, see Fig. 4, as occurs, for example, in the missing partner seesaw mechanism, where there are less “right” than “left”-handed neutrinos. We also commented on the detectability of $0\nu\beta\beta$ decay in schemes with family symmetries, e.g. Fig. 5, and also on the significance of a possible $0\nu\beta\beta$ discovery for particle physics, Fig. 6.

In Section 2 we briefly discussed the origin of neutrino masses, both from point of view of effective theories, e.g. the Weinberg operator in Fig. 7, as well as, for instance, the type-I realization of the seesaw paradigm, Fig. 8, or the “scotogenic” paradigm. In the latter dark matter mediates neutrino mass generation through radiative corrections. We also briefly discussed the idea that dark matter *seeds* neutrino mass generation that proceeds *a la seesaw*, as in the recent recently proposed low-scale seesaw variants dubbed “dark inverse” and “dark linear seesaw” Fig. 9. Finally, we mentioned the *flavour problem*, a major SM drawback and main thread of this review, and how it may be approached by symmetry, as illustrated in Fig. 10.

In Sect. 3 we described various phenomenological lepton mixing patterns, showing how most of them are at odds with current experimental data, especially from Daya Bay. In Sect. 4 we gave a bottom-up description of residual flavour and CP symmetries, both for the case of leptons as well as quarks. Indeed, the residual CP and flavor symmetries of quark and lepton mass terms are determined in terms of the experimentally measured mixing matrix, as given in Eqs. (4.11, 4.12, 4.13, 4.24, 4.25, 4.26) and Eqs. (4.55, 4.59). On the other hand, they may arise from the breaking of flavour and CP symmetries at high energies. It is remarkable that one can fix the quark and lepton mixing matrices from the structure of the flavour symmetry group and the residual symmetries, irrespective of the flavour symmetry breaking dynamics. Residual symmetries can restrict the mixing matrix as summarized in table 1. Moreover, remnant symmetries are quite useful as a guide to construct concrete flavour models. They can also

provide adequate revampings of various neutrino mixing patterns at odds with experiment so as to yield generalizations that are not only viable, but also predictive, as discussed in Sect. 5. For example, viable and predictive generalizations of the TBM mixing pattern are given in Figs. 11 and 12. On the other hand, similar generalizations of the Golden-ratio mixing pattern are given in Fig. 13. Soon after the first Daya-Bay results indicating a nonzero value of θ_{13} the bi-large mixing pattern was suggested, in which solar and atmospheric mixing angles as well as the Dirac CP phase are determined in terms of θ_{13} , as seen in Figs. 15 and 16.

Within the family symmetry paradigm, the symmetry group is usually broken down to different subgroups in the neutrino and charged lepton sectors, the lepton mixing matrix arises from the mismatch of the symmetry breaking patterns, as shown in Fig. 17 in Sect. 6. If a Klein subgroup is preserved by the (Majorana) neutrino mass term and the residual abelian subgroup of the charged lepton sector distinguishes the three generations, the lepton mixing matrix would be completely fixed from group theory up to row and column permutations. On the other hand, the Dirac CP phase δ_{CP} is predicted to take on CP conserving values, while the Majorana phases cannot be constrained. Instead, if a Z_2 subgroup is preserved in the neutrino sector, then only one column of the lepton mixing matrix is determined and δ_{CP} can lie in a relative large region, e.g. see Fig. 18. Generalized CP symmetries are very powerful to constrain the CP phase. For instance, the $\mu - \tau$ reflection symmetry on the neutrino fields enforces δ_{CP} to be maximal, while the predicted δ_{CP} values for the generalized $\mu - \tau$ reflection are displayed in Fig. 19.

A flavour symmetry transformation can be generated by performing two CP transformations, the interplay of flavour symmetry and generalized CP symmetry is highly nontrivial, requiring that the consistency condition in Fig. 20 must hold. The inclusion of generalized CP symmetry in flavour symmetry provides richer symmetry breaking patterns. For example, one usually assumes that the flavour and CP symmetry are broken to an abelian subgroup in the charged lepton sector and $Z_2 \times CP$ in the neutrino sector. In this case all the lepton mixing parameters depend only on a single real rotation angle θ in Fig. 21. The value of θ is fixed by the precisely measured reactor angle θ_{13} , leading to a determination of the other lepton mixing angles and CP violation phases, see, e.g. Eq. (6.47). This also implies definite predictions for the $0\nu\beta\beta$ decay amplitude, as shown in Fig. 22. Another possibility is that the remnant subgroup preserved by both neutrino and charged lepton mass terms has the structure $Z_2 \times CP$. In this case the lepton mixing matrix depends on two free rotation angles θ_l and θ_ν , see Fig. 23. All the mixing angles and CP violation phases as well as the effective $0\nu\beta\beta$ mass parameter are predicted to lie in very restricted regions, as shown in Figs. 24, 25, 26. It is remarkable that this scheme can be extended to the quark sector, both quark and lepton mixings can be accommodated using a single flavour group, in terms of total four free parameters. Generalized flavour and CP symmetries may also be employed for the case of Dirac neutrinos. Similar results hold true, except that the remnant flavour symmetry of neutrino sector can be an arbitrary abelian subgroup. In particular, the master formulas in Figs. 21 and 23 also hold for Dirac neutrinos.

In section 7 we gave a panoramic view illustrating possible tests of flavor symmetry models. The

existence of mixing predictions is a characteristic feature of flavor symmetry models. This follows from the fact that typically they have less free parameters than physical observables, therefore correlations between light neutrino observables are predicted. This is explicitly shown in Eqs. (5.12, 5.18, 5.24, 6.9, 6.22, 6.47, 6.51, 6.54, 6.73). For example the ranges of the CP violation δ_{CP} obtained from Eq. (7.1) are summarized in table 3. The predictions of some typical flavor models are displayed in figure 27. One can see that a precise measurement of the lepton mixing parameters at forthcoming neutrino facilities JUNO, DUNE and T2HK should provide a test of flavor models, see also figure 28. On the other hand, neutrino mass sum rules are generally parameterized as Eq. (7.4), providing another type of correlation. It relates the three complex light neutrino mass eigenvalues amongst each other and thus also relate the Majorana CP phases to the neutrino masses. The mass sum rules lead to strong restrictions on the lightest neutrino mass and to distinct predictions for the effective mass $|m_{\beta\beta}|$ probed in $0\nu\beta\beta$ decay, as shown in figure 29. Finally, we commented on a recently developed toolkit to contrast flavor models with upcoming oscillation experiments.

So far we have confined ourselves to model-independent approaches to the flavour puzzle, in which the underlying theory is unspecified and only the predictive power of symmetry is explored. As a next step we turned to various UV-complete approaches to the flavour puzzle. In Sect. 8 we gave two benchmarks for UV-complete constructions in 4 dimensions. The first incorporates dark matter in a “scotogenic” manner, Fig. 30 together with a successful family symmetry leading to the so-called trimaximal pattern TM2. The neutrino oscillation predictions are illustrated in Figs. 31 and 32. An alternative example given puts together family and CP symmetry within the same construction.

More ambitious approaches to the flavor problem have been proposed within extra spacetime dimensions. For example, in Sect. 9 we described a five-dimensional warped flavordynamics scenario in which mass hierarchies are accounted for by adequate choices of the bulk mass parameters, while quark and lepton mixing angles are restricted by the imposition of a family symmetry. We presented a T' model leading to Majorana neutrinos, with the TM1 mixing pattern and tight neutrino oscillation correlations, given in Fig. 35. The $0\nu\beta\beta$ decay rates lie within the sensitivities of the next round of experiments, as indicated in Fig. 36. Finally, one has a good global fit of all flavour observables, including quarks, see table 9.

Finally, in Sect. 10 we described orbifold compactification as a promising way to determine the structure of the family symmetry in four dimensions. The construction is illustrated in Fig. 37. We illustrated the idea with a benchmark 6-dimensional scotogenic (see Fig. 38) orbifold scenario, in which a 4-dimensional A_4 flavour group emerges from the symmetries between the branes in extra dimensions. Predictions include the “golden” quark-lepton mass relation, Eq. (10.33), and a very good global description of all flavour observables, including quarks, table 11. Concerning neutrino oscillations, the mass ordering and atmospheric octant are predicted, together with the reactor angle, see Fig. 39. The lightest neutrino mass can be probed in neutrinoless double beta decay searches as well as cosmology, Fig. 40.

We have also stressed that adequate vacuum alignment is required in flavour symmetry models. Generally one must introduce additional large shaping symmetries and many new fields so as to cleverly design the flavon potential needed to obtain the correct vacuum alignment. In Sec. 11 we discussed how

modular symmetry provides an interesting way to overcome this drawback [478]. In this case the role of flavor symmetry is played by the modular invariance, and the complex modulus τ could be the unique source of modular symmetry breaking. Modular invariance requires the Yukawa couplings to be modular forms, thus a small number of free parameters are involved in modular models. Such modular symmetry approach has been comprehensively reviewed elsewhere [91, 479, 480] within the bottom-up as well as top-down approaches.

Recent progress in the formulation of flavor models involving the use of modular symmetry is discussed in Sec. 11. This idea opens the door to a simpler description and deeper understanding of the flavor symmetry breaking required for obtaining viable flavor predictions without the need to invoke *flavons* in an *ad hoc* manner.

All in all, the legacy of the oscillation program over the past two decades has been a tremendous progress in the field, bringing neutrinos to the center of the particle physics stage. Indeed, addressing the dynamical origin of small neutrino masses touches the heart of the electroweak theory, such as the consistency of symmetry breaking. Moreover, the precise measurement of the neutrino mixing parameters could shed light into the flavor problem. One might have expected that this would bring a decisive boost towards the formulation of a comprehensive theory of fermion masses and mixings. It is somewhat frustrating, however, that so far no decisive flavor road map has emerged. One can reproduce the observations in many different ways, within a wide range of models that go all the way from anarchy to discrete family symmetries. While the latter seems intellectually more appealing, we have not yet been able to underpin a convincing final theory of flavor. Despite many interesting ideas and the formulation of a plethora elegant models, the structure of the three families of fermions remains mysterious.

From the experimental viewpoint in the coming decade we expect a vibrant period for oscillation studies, within and beyond the minimum paradigm. Current neutrino facilities as well as future ones, such as JUNO, DUNE and T2HK should be capable of measuring the solar angle θ_{12} , the atmospheric angle θ_{23} and the Dirac CP phase δ_{CP} with high sensitivity. The next generation of ton-scale $0\nu\beta\beta$ decay experiments will probe the Majorana nature of neutrinos, exploring the whole region associated with the inverted ordering spectrum. These experiments should provide important insights into the mysteries behind flavor mixing, fermion mass hierarchies and CP violation.

A The A_4 group

A_4 is the even permutation group of four objects, and it is isomorphic to the symmetry group of a regular tetrahedron. The A_4 group can be generated by two generators s and t which satisfy the following multiplication rules ²⁶,

$$s^2 = t^3 = (st)^3 = 1. \quad (\text{A.1})$$

The 12 elements of A_4 belong to four conjugacy classes:

$$\begin{aligned} 1C_1 &= \{1\}, & 3C_2 &= \{s, tst^2, t^2st\}, \\ 4C_3 &= \{t, st, ts, sts\}, & 4C'_3 &= \{t^2, st^2, t^2s, st^2s\}, \end{aligned} \quad (\text{A.2})$$

where the conjugacy class is denoted by kC_n , k is the number of elements belonging to it, and the subscript n is the order of the elements contained in it. A_4 has a unique Klein group $K_4^{(s, tst^2)}$ and three Z_3 subgroups generated by t , st , ts and sts respectively. The A_4 group has four inequivalent irreducible representations: three singlets $\mathbf{1}$, $\mathbf{1}'$, $\mathbf{1}''$ and a triplet $\mathbf{3}$. Two different bases are used in the literature, the Ma-Rajasekaran (MR) basis [53] and the Altarelli-Feruglio (AF) basis [313]. They differ in the three-dimensional irreducible representation $\mathbf{3}$, the representation matrix of the generator t is real in the MR basis [53] while it is complex and diagonal in AF basis [313]. The explicit form of the representation matrices are summarized in table 12. The two bases are related through a unitary transformation,

$$s_{AF} = V^\dagger s_{MR} V, \quad t_{AF} = V^\dagger t_{MR} V, \quad (\text{A.3})$$

where

$$V = \frac{1}{\sqrt{3}} \begin{pmatrix} 1 & 1 & 1 \\ 1 & \omega & \omega^2 \\ 1 & \omega^2 & \omega \end{pmatrix}. \quad (\text{A.4})$$

If we have two triplets $\alpha \sim (\alpha_1, \alpha_2, \alpha_3)$ and $\beta \sim (b_1, b_2, b_3)$, their product decomposes as the sum

$$\mathbf{3} \otimes \mathbf{3} = \mathbf{1} \oplus \mathbf{1}' \oplus \mathbf{1}'' \oplus \mathbf{3}_s \oplus \mathbf{3}_a, \quad (\text{A.5})$$

where $\mathbf{3}_s$ and $\mathbf{3}_a$ denote the symmetric and the antisymmetric triplet combinations respectively. The results for the contractions in the above two bases are summarized in table 12.

²⁶We use small s , t , u for the generators of A_4 and S_4 flavour groups in order to avoid confusion with oblique parameters S , T , U .

Representation matrices of A_4 generators				
	Ma-Rajasekaran basis		Altarelli-Feruglio basis	
	s	t	s	t
$\mathbf{1}$	1	1	1	1
$\mathbf{1}'$	1	ω	1	ω
$\mathbf{1}''$	1	ω^2	1	ω^2
$\mathbf{3}$	$\begin{pmatrix} 1 & 0 & 0 \\ 0 & -1 & 0 \\ 0 & 0 & -1 \end{pmatrix}$	$\begin{pmatrix} 0 & 1 & 0 \\ 0 & 0 & 1 \\ 1 & 0 & 0 \end{pmatrix}$	$\frac{1}{3} \begin{pmatrix} -1 & 2 & 2 \\ 2 & -1 & 2 \\ 2 & 2 & -1 \end{pmatrix}$	$\begin{pmatrix} 1 & 0 & 0 \\ 0 & \omega & 0 \\ 0 & 0 & \omega^2 \end{pmatrix}$
Tensor products of two A_4 triplets				
	Ma-Rajasekaran basis		Altarelli-Feruglio basis	
$(\alpha \otimes \beta)_{\mathbf{1}}$	$\alpha_1\beta_1 + \alpha_2\beta_2 + \alpha_3\beta_3$		$\alpha_1\beta_1 + \alpha_2\beta_3 + \alpha_3\beta_2$	
$(\alpha \otimes \beta)_{\mathbf{1}'}$	$\alpha_1\beta_1 + \omega^2\alpha_2\beta_2 + \omega\alpha_3\beta_3$		$\alpha_3\beta_3 + \alpha_1\beta_2 + \alpha_2\beta_1$	
$(\alpha \otimes \beta)_{\mathbf{1}''}$	$\alpha_1\beta_1 + \omega\alpha_2\beta_2 + \omega^2\alpha_3\beta_3$		$\alpha_2\beta_2 + \alpha_3\beta_1 + \alpha_1\beta_3$	
$(\alpha \otimes \beta)_{\mathbf{3}_s}$	$\begin{pmatrix} \alpha_2\beta_3 + \alpha_3\beta_2 \\ \alpha_3\beta_1 + \alpha_1\beta_3 \\ \alpha_1\beta_2 + \alpha_2\beta_1 \end{pmatrix}$		$\begin{pmatrix} 2\alpha_1\beta_1 - \alpha_2\beta_3 - \alpha_3\beta_2 \\ 2\alpha_3\beta_3 - \alpha_1\beta_2 - \alpha_2\beta_1 \\ 2\alpha_2\beta_2 - \alpha_3\beta_1 - \alpha_1\beta_3 \end{pmatrix}$	
$(\alpha \otimes \beta)_{\mathbf{3}_a}$	$\begin{pmatrix} \alpha_2\beta_3 - \alpha_3\beta_2 \\ \alpha_3\beta_1 - \alpha_1\beta_3 \\ \alpha_1\beta_2 - \alpha_2\beta_1 \end{pmatrix}$		$\begin{pmatrix} \alpha_2\beta_3 - \alpha_3\beta_2 \\ \alpha_1\beta_2 - \alpha_2\beta_1 \\ \alpha_3\beta_1 - \alpha_1\beta_3 \end{pmatrix}$	

Table 12: The representation matrices of the A_4 generators s and t in the different irreducible representations. We also give the tensor product rule of two A_4 triplets $\alpha = (\alpha_1, \alpha_2, \alpha_3) \sim \mathbf{3}$ and $\beta = (\beta_1, \beta_2, \beta_3) \sim \mathbf{3}$, where $\omega = e^{i2\pi/3} = -1/2 + i\sqrt{3}/2$ is a cubic root of unity.

B The S_4 group

S_4 is the permutation group of four distinct objects; geometrically it is the symmetry group of a regular octahedron. Its generators s , t and u obey the following multiplication rules [325, 395, 525],

$$s^2 = t^3 = u^2 = (st)^3 = (su)^2 = (tu)^2 = (stu)^4 = 1. \quad (\text{B.1})$$

Note that the generators s and t alone generate the group A_4 , while the generators t and u alone generate the group S_3 . The S_4 group elements can be divided into 5 conjugacy classes

$$\begin{aligned} 1C_1 &= \{1\}, \\ 3C_2 &= \{s, tst^2, t^2st\}, \\ 6C'_2 &= \{u, tu, su, ut, stsu, st^2su\}, \\ 8C_3 &= \{t, st, ts, sts, t^2, st^2, t^2s, st^2s\}, \\ 6C_4 &= \{stu, tsu, t^2su, st^2u, tst^2u, t^2stu\}, \end{aligned} \quad (\text{B.2})$$

The group structure of S_4 has been studied in detail in [526], it has thirty proper subgroups of orders 1, 2, 3, 4, 6, 8, 12 or 24. Since the number of inequivalent irreducible representations is equal to the number of conjugacy classes and the sum of the squares of the dimensions of the irreducible representations must be equal to the order of the group, it is easy to see that S_4 has two singlet irreducible representations $\mathbf{1}$ and $\mathbf{1}'$, one doublet representation $\mathbf{2}$ and two triplet representations $\mathbf{3}$ and $\mathbf{3}'$. In the singlet representations $\mathbf{1}$ and $\mathbf{1}'$, we have

$$\begin{aligned} \mathbf{1} &: s = t = u = 1, \\ \mathbf{1}' &: s = t = 1, \quad u = -1. \end{aligned} \quad (\text{B.3})$$

For the doublet representation $\mathbf{2}$, the generators are represented by

$$s = \begin{pmatrix} 1 & 0 \\ 0 & 1 \end{pmatrix}, \quad t = \begin{pmatrix} \omega & 0 \\ 0 & \omega^2 \end{pmatrix}, \quad u = \begin{pmatrix} 0 & 1 \\ 1 & 0 \end{pmatrix}, \quad (\text{B.4})$$

with $\omega = e^{2\pi i/3}$. In the triplet representations $\mathbf{3}$ and $\mathbf{3}'$, the generators are

$$\begin{aligned} \mathbf{3} : s &= \frac{1}{3} \begin{pmatrix} -1 & 2 & 2 \\ 2 & -1 & 2 \\ 2 & 2 & -1 \end{pmatrix}, \quad t = \begin{pmatrix} 1 & 0 & 0 \\ 0 & \omega^2 & 0 \\ 0 & 0 & \omega \end{pmatrix}, \quad u = - \begin{pmatrix} 1 & 0 & 0 \\ 0 & 0 & 1 \\ 0 & 1 & 0 \end{pmatrix}, \\ \mathbf{3}' : s &= \frac{1}{3} \begin{pmatrix} -1 & 2 & 2 \\ 2 & -1 & 2 \\ 2 & 2 & -1 \end{pmatrix}, \quad t = \begin{pmatrix} 1 & 0 & 0 \\ 0 & \omega^2 & 0 \\ 0 & 0 & \omega \end{pmatrix}, \quad u = \begin{pmatrix} 1 & 0 & 0 \\ 0 & 0 & 1 \\ 0 & 1 & 0 \end{pmatrix}. \end{aligned} \quad (\text{B.5})$$

Classes	$1C_1$	$3C_2$	$6C'_2$	$8C_3$	$6C_4$
1	1	1	1	1	1
1'	1	1	-1	1	-1
2	2	2	0	-1	0
3	3	-1	-1	0	1
3'	3	-1	1	0	-1

Table 13: Character table of the S_4 group.

Notice that the representations **3** and **3'** differ in the overall sign of the generator u . The character of an element is the trace of its representation matrix, then we can straightforwardly obtain the character table of S_4 , as shown in table 13. Moreover, the decompositions of the tensor product of the S_4 irreducible representations are as follows,

$$\begin{aligned}
\mathbf{1} \otimes \mathbf{r} &= \mathbf{r}, & \mathbf{1}' \otimes \mathbf{1}' &= \mathbf{1}, & \mathbf{1}' \otimes \mathbf{2} &= \mathbf{2}, & \mathbf{1}' \otimes \mathbf{3} &= \mathbf{3}', & \mathbf{1}' \otimes \mathbf{3}' &= \mathbf{3}, \\
\mathbf{2} \otimes \mathbf{2} &= \mathbf{1} \oplus \mathbf{1}' \oplus \mathbf{2}, & \mathbf{2} \otimes \mathbf{3} &= \mathbf{2} \otimes \mathbf{3}' = \mathbf{3} \otimes \mathbf{3}', \\
\mathbf{3} \otimes \mathbf{3} &= \mathbf{3}' \otimes \mathbf{3}' = \mathbf{1} \oplus \mathbf{2} \oplus \mathbf{3} \oplus \mathbf{3}', & \mathbf{3} \otimes \mathbf{3}' &= \mathbf{1}' \oplus \mathbf{2} \oplus \mathbf{3} \oplus \mathbf{3}',
\end{aligned} \tag{B.6}$$

where \mathbf{r} stands for any irreducible representation of S_4 . We proceed to present the Clebsch-Gordan (CG) coefficients in the above basis. The entries of the two multiplets in the tensor product are denoted by α_i and β_i respectively. For the product of the singlet $\mathbf{1}'$ with a doublet or a triplet, we have [325, 395, 525]

$$\mathbf{1}' \otimes \mathbf{2} = \mathbf{2} = \begin{pmatrix} \alpha\beta_1 \\ -\alpha\beta_2 \end{pmatrix}, \quad \mathbf{1}' \otimes \mathbf{3} = \mathbf{3}' = \begin{pmatrix} \alpha\beta_1 \\ \alpha\beta_2 \\ \alpha\beta_3 \end{pmatrix}, \quad \mathbf{1}' \otimes \mathbf{3}' = \mathbf{3} = \begin{pmatrix} \alpha\beta_1 \\ \alpha\beta_2 \\ \alpha\beta_3 \end{pmatrix}. \tag{B.7}$$

The CG coefficients for the products involving the doublet representation $\mathbf{2}$ are found to be

$$\mathbf{2} \otimes \mathbf{2} = \mathbf{1} \oplus \mathbf{1}' \oplus \mathbf{2}, \quad \text{with} \quad \begin{cases} \mathbf{1} = \alpha_1\beta_2 + \alpha_2\beta_1 \\ \mathbf{1}' = \alpha_1\beta_2 - \alpha_2\beta_1 \\ \mathbf{2} = \begin{pmatrix} \alpha_2\beta_2 \\ \alpha_1\beta_1 \end{pmatrix} \end{cases} \tag{B.8}$$

$$\mathbf{2} \otimes \mathbf{3} = \mathbf{3} \oplus \mathbf{3}', \quad \text{with} \quad \begin{cases} \mathbf{3} = \begin{pmatrix} \alpha_1\beta_2 + \alpha_2\beta_3 \\ \alpha_1\beta_3 + \alpha_2\beta_1 \\ \alpha_1\beta_1 + \alpha_2\beta_2 \end{pmatrix} \\ \mathbf{3}' = \begin{pmatrix} \alpha_1\beta_2 - \alpha_2\beta_3 \\ \alpha_1\beta_3 - \alpha_2\beta_1 \\ \alpha_1\beta_1 - \alpha_2\beta_2 \end{pmatrix} \end{cases} \tag{B.9}$$

$$\mathbf{2} \otimes \mathbf{3}' = \mathbf{3} \oplus \mathbf{3}', \quad \text{with} \quad \begin{cases} \mathbf{3} = \begin{pmatrix} \alpha_1\beta_2 - \alpha_2\beta_3 \\ \alpha_1\beta_3 - \alpha_2\beta_1 \\ \alpha_1\beta_1 - \alpha_2\beta_2 \end{pmatrix} \\ \mathbf{3}' = \begin{pmatrix} \alpha_1\beta_2 + \alpha_2\beta_3 \\ \alpha_1\beta_3 + \alpha_2\beta_1 \\ \alpha_1\beta_1 + \alpha_2\beta_2 \end{pmatrix} \end{cases} \quad (\text{B.10})$$

Similarly, for the tensor products among the triplet representations $\mathbf{3}$ and $\mathbf{3}'$, we have

$$\mathbf{3} \otimes \mathbf{3} = \mathbf{3}' \otimes \mathbf{3}' = \mathbf{1} \oplus \mathbf{2} \oplus \mathbf{3} \oplus \mathbf{3}', \quad \text{with} \quad \begin{cases} \mathbf{1} = \alpha_1\beta_1 + \alpha_2\beta_3 + \alpha_3\beta_2 \\ \mathbf{2} = \begin{pmatrix} \alpha_2\beta_2 + \alpha_1\beta_3 + \alpha_3\beta_1 \\ \alpha_3\beta_3 + \alpha_1\beta_2 + \alpha_2\beta_1 \end{pmatrix} \\ \mathbf{3} = \begin{pmatrix} \alpha_2\beta_3 - \alpha_3\beta_2 \\ \alpha_1\beta_2 - \alpha_2\beta_1 \\ \alpha_3\beta_1 - \alpha_1\beta_3 \end{pmatrix} \\ \mathbf{3}' = \begin{pmatrix} 2\alpha_1\beta_1 - \alpha_2\beta_3 - \alpha_3\beta_2 \\ 2\alpha_3\beta_3 - \alpha_1\beta_2 - \alpha_2\beta_1 \\ 2\alpha_2\beta_2 - \alpha_1\beta_3 - \alpha_3\beta_1 \end{pmatrix} \end{cases} \quad (\text{B.11})$$

$$\mathbf{3} \otimes \mathbf{3}' = \mathbf{1}' \oplus \mathbf{2} \oplus \mathbf{3} \oplus \mathbf{3}', \quad \text{with} \quad \begin{cases} \mathbf{1}' = \alpha_1\beta_1 + \alpha_2\beta_3 + \alpha_3\beta_2 \\ \mathbf{2} = \begin{pmatrix} \alpha_2\beta_2 + \alpha_1\beta_3 + \alpha_3\beta_1 \\ -(\alpha_3\beta_3 + \alpha_1\beta_2 + \alpha_2\beta_1) \end{pmatrix} \\ \mathbf{3} = \begin{pmatrix} 2\alpha_1\beta_1 - \alpha_2\beta_3 - \alpha_3\beta_2 \\ 2\alpha_3\beta_3 - \alpha_1\beta_2 - \alpha_2\beta_1 \\ 2\alpha_2\beta_2 - \alpha_1\beta_3 - \alpha_3\beta_1 \end{pmatrix} \\ \mathbf{3}' = \begin{pmatrix} \alpha_2\beta_3 - \alpha_3\beta_2 \\ \alpha_1\beta_2 - \alpha_2\beta_1 \\ \alpha_3\beta_1 - \alpha_1\beta_3 \end{pmatrix} \end{cases} \quad (\text{B.12})$$

C The dihedral group

The dihedral group D_n is the symmetry group of an n -sided regular polygon, which includes rotations and reflections. For instance, D_3 is the symmetry group of the regular triangle, and consequently it is isomorphic to S_3 . A regular polygon with n sides is invariant under a rotation of multiples of $2\pi/n$ about the origin. If n is odd, each reflection axis connects the midpoint of one side to the opposite vertex. If n is even, there are $n/2$ reflection axes connecting the midpoints of opposite sides and $n/2$ axes of symmetry connecting opposite vertices. Consequently the group D_n has $2n$ elements. The group D_n can be generated by a rotation R of order n and a reflection S of order 2, and they satisfy the following multiplication rules

$$R^n = S^2 = (RS)^2 = 1, \quad (\text{C.1})$$

where R denotes a rotation of $2\pi/n$ about the origin, and S is a reflection across n lines through the origin. Notice that D_1 is Z_2 group generated by S and D_2 is isomorphic to $Z_2 \times Z_2$. All the group elements of D_n can be expressed as

$$g = S^\alpha R^\beta \quad (\text{C.2})$$

where $\alpha = 0, 1$ and $\beta = 0, 1, \dots, n-1$. Then it is straightforward to determine the conjugacy classes of the dihedral group. Depending on whether the group index n is even or odd, the $2n$ group elements of D_n can be classified into three or five types of conjugacy classes.

- odd n

$$\begin{aligned} 1C_1 &= \{1\}, \\ 2C_m^{(\rho)} &= \{R^\rho, R^{-\rho}\}, \quad \text{with } \rho = 1, \dots, \frac{n-1}{2}, \\ nC_2 &= \{S, SR, SR^2, \dots, SR^{n-1}\}, \end{aligned} \quad (\text{C.3})$$

where m refers to the order of the element R^ρ .

- even n

$$\begin{aligned} 1C_1 &= \{1\}, \\ 1C_2 &= \{R^{n/2}\}, \\ 2C_m^{(\rho)} &= \{R^\rho, R^{-\rho}\}, \quad \text{with } \rho = 1, \dots, \frac{n-2}{2}, \\ \frac{n}{2}C_2 &= \{S, SR^2, SR^4, \dots, SR^{n-4}, SR^{n-2}\}, \\ \frac{n}{2}C_2 &= \{SR, SR^3, \dots, SR^{n-3}, SR^{n-1}\}. \end{aligned} \quad (\text{C.4})$$

The subgroups of D_n are either dihedral groups or cyclic groups, and they are given by

$$\begin{aligned} Z_j &= \langle R^{\frac{n}{j}} \rangle \quad \text{with } j|n, \\ Z_2^{(m)} &= \langle SR^m \rangle \quad \text{with } m = 0, 1, \dots, n-1, \\ D_j^{(m)} &= \langle R^{\frac{n}{j}}, SR^m \rangle \quad \text{with } j|n, m = 0, 1, \dots, \frac{n}{j} - 1, \end{aligned} \quad (\text{C.5})$$

where the elements inside the angle brackets denote the generators of the subgroups. We see that the total number of dihedral subgroups is the sum of positive divisors of n .

The group D_n is a subgroup of $SO(2)$, and it has only one-dimensional and two-dimensional irreducible representations. The representations of D_n crucially depend on the value of the group index n .

- odd n

If n is an odd integer, the group D_n has two singlet representations $\mathbf{1}_i$ and $\frac{n-1}{2}$ doublet representations $\mathbf{2}_j$, where the subscripts i and j take values $i = 1, 2$ and $j = 1, \dots, \frac{n-1}{2}$. The sum of the squares of the dimensions of the irreducible representations is

$$1^2 + 1^2 + 2^2 \times \frac{n-1}{2} = 2n, \quad (\text{C.6})$$

which is exactly the number of elements of the D_n group. In the singlet representations, the generators R and S are represented by

$$\mathbf{1}_1 : R = S = 1, \quad \mathbf{1}_2 : R = 1, S = -1. \quad (\text{C.7})$$

For the doublet representations, we have

$$\mathbf{2}_j : R = \begin{pmatrix} e^{2\pi i \frac{j}{n}} & 0 \\ 0 & e^{-2\pi i \frac{j}{n}} \end{pmatrix}, \quad S = \begin{pmatrix} 0 & 1 \\ 1 & 0 \end{pmatrix}, \quad (\text{C.8})$$

with $j = 1, \dots, \frac{n-1}{2}$.

- even n

For the case that the index n an even integer, the group D_n has four singlet representations $\mathbf{1}_i$ with $i = 1, 2, 3, 4$ and $\frac{n}{2} - 1$ doublet representations $\mathbf{2}_j$ with $j = 1, \dots, \frac{n}{2} - 1$. It is straightforward to obtain the generators R and S in the singlet representations

$$\begin{aligned} \mathbf{1}_1 : R = S = 1, & & \mathbf{1}_2 : R = 1, S = -1, \\ \mathbf{1}_3 : R = -1, S = 1, & & \mathbf{1}_4 : R = S = -1. \end{aligned} \quad (\text{C.9})$$

The explicit forms of these generators in the irreducible two-dimensional representations are

$$\mathbf{2}_j : R = \begin{pmatrix} e^{2\pi i \frac{j}{n}} & 0 \\ 0 & e^{-2\pi i \frac{j}{n}} \end{pmatrix}, \quad S = \begin{pmatrix} 0 & 1 \\ 1 & 0 \end{pmatrix}, \quad (\text{C.10})$$

with $j = 1, \dots, \frac{n}{2} - 1$. Notice that the doublet representation $\mathbf{2}_j$ and the complex conjugate $\bar{\mathbf{2}}_j$ are equivalent, and they are related through a similarity transformation, i.e., $R^* = VRV^{-1}$ and $S^* = VSV^{-1}$ with $V = \begin{pmatrix} 0 & 1 \\ 1 & 0 \end{pmatrix}$. Hence all the doublet representations of D_n are real, although the representation matrix of R is complex in our basis. Moreover, if $a = (a_1, a_2)^T$ is a doublet

transforming as $\mathbf{2}_j$, then $(a_2^*, a_1^*)^T$ transform as $\mathbf{2}_j$ under D_n as well.

The D_n group has a class-inverting outer automorphism \mathbf{u} , and its action on the generators R and S is

$$R \xrightarrow{\mathbf{u}} R^{-1}, \quad S \xrightarrow{\mathbf{u}} S. \quad (\text{C.11})$$

The CP transformation corresponding to \mathbf{u} is denoted by $X_{\mathbf{r}}^0$, its concrete form is determined by the following consistency conditions,

$$\begin{aligned} X_{\mathbf{r}}^0 \rho_{\mathbf{r}}^*(R) X_{\mathbf{r}}^{0\dagger} &= \rho_{\mathbf{r}}(\mathbf{u}(R)) = \rho_{\mathbf{r}}(R^{-1}), \\ X_{\mathbf{r}}^0 \rho_{\mathbf{r}}^*(S) X_{\mathbf{r}}^{0\dagger} &= \rho_{\mathbf{r}}(\mathbf{u}(S)) = \rho_{\mathbf{r}}(S). \end{aligned} \quad (\text{C.12})$$

Since both $\rho_{\mathbf{r}}(R)$ and $\rho_{\mathbf{r}}(S)$ are symmetric and unitary, $X_{\mathbf{r}}^0$ coincides the canonical CP transformation up to an overall irrelevant phase, i.e.,

$$X_{\mathbf{r}}^0 = \mathbb{1}. \quad (\text{C.13})$$

From $X_{\mathbf{r}}^0$ and the flavor symmetry transformations of D_n , we can obtain other generalized CP transformations $X_{\mathbf{r}} = \rho_{\mathbf{r}}(g) X_{\mathbf{r}}^0 = \rho_{\mathbf{r}}(g)$, $g \in D_n$, yet they don't impose any new restrictions.

D Diagonalization of a 2×2 complex symmetric matrix

A generic complex symmetric 2×2 matrix can be written as

$$M = \begin{pmatrix} a & c \\ c & b \end{pmatrix}, \quad (\text{D.1})$$

where a , b and c are complex. It can be diagonalized by a two dimensional unitary matrix U via

$$U^T M U = \text{diag}(\lambda_1, \lambda_2), \quad U = \begin{pmatrix} \cos\theta & e^{i\phi}\sin\theta \\ -e^{-i\phi}\sin\theta & \cos\theta \end{pmatrix} \begin{pmatrix} e^{-i\alpha} & 0 \\ 0 & e^{-i\beta} \end{pmatrix}. \quad (\text{D.2})$$

The eigenvalues $\lambda_{1,2}$ are non-negative with

$$\begin{aligned} \lambda_1^2 &= \frac{1}{2} \left[|a|^2 + |b|^2 + 2|c|^2 - \sqrt{(|b|^2 - |a|^2)^2 + 4|a^*c + bc^*|^2} \right] \\ \lambda_2^2 &= \frac{1}{2} \left[|a|^2 + |b|^2 + 2|c|^2 + \sqrt{(|b|^2 - |a|^2)^2 + 4|a^*c + bc^*|^2} \right] \end{aligned} \quad (\text{D.3})$$

Without loss of generality, the rotation angle θ can be limited in the region $0 \leq \theta \leq \pi/2$ and it satisfies

$$\tan 2\theta = \frac{2|a^*c + bc^*|}{|b|^2 - |a|^2}. \quad (\text{D.4})$$

The expressions of the phases ϕ , α and β are

$$\begin{aligned} \phi &= \arg(a^*c + bc^*), \\ \alpha &= \frac{1}{2} \arg [a(|b|^2 - |\lambda_1|^2) - b^*c^2], \\ \beta &= \frac{1}{2} \arg [b(|\lambda_2|^2 - |a|^2) + a^*c^2]. \end{aligned} \quad (\text{D.5})$$

The general case of an arbitrary dimension is given in Ref. [30].

Acknowledgements

This review is based on the fruitful collaboration with many friends and colleagues worldwide. We have also benefited from useful discussions with many others. We express our sincere gratitude to all of them. This work was supported by the Spanish grants PID2020-113775GB-I00 (AEI/10.13039/501100011033) and Prometeo CIPROM/2021/054 and by the National Natural Science Foundation of China under Nos. 12375104, 11975224, 11835013.

References

- [1] C.-N. Yang, R. L. Mills, Conservation of Isotopic Spin and Isotopic Gauge Invariance, *Phys. Rev.* 96 (1954) 191–195. [doi:10.1103/PhysRev.96.191](https://doi.org/10.1103/PhysRev.96.191).
- [2] S. L. Glashow, Partial Symmetries of Weak Interactions, *Nucl. Phys.* 22 (1961) 579–588. [doi:10.1016/0029-5582\(61\)90469-2](https://doi.org/10.1016/0029-5582(61)90469-2).
- [3] S. Weinberg, A Model of Leptons, *Phys. Rev. Lett.* 19 (1967) 1264–1266. [doi:10.1103/PhysRevLett.19.1264](https://doi.org/10.1103/PhysRevLett.19.1264).
- [4] A. Salam, Weak and Electromagnetic Interactions, *Conf. Proc. C 680519* (1968) 367–377. [doi:10.1142/9789812795915_0034](https://doi.org/10.1142/9789812795915_0034).
- [5] S. L. Glashow, J. Iliopoulos, L. Maiani, Weak Interactions with Lepton-Hadron Symmetry, *Phys. Rev. D* 2 (1970) 1285–1292. [doi:10.1103/PhysRevD.2.1285](https://doi.org/10.1103/PhysRevD.2.1285).
- [6] G. S. Guralnik, C. R. Hagen, T. W. B. Kibble, Global Conservation Laws and Massless Particles, *Phys. Rev. Lett.* 13 (1964) 585–587. [doi:10.1103/PhysRevLett.13.585](https://doi.org/10.1103/PhysRevLett.13.585).
- [7] F. Englert, R. Brout, Broken Symmetry and the Mass of Gauge Vector Mesons, *Phys. Rev. Lett.* 13 (1964) 321–323. [doi:10.1103/PhysRevLett.13.321](https://doi.org/10.1103/PhysRevLett.13.321).
- [8] P. W. Higgs, Spontaneous Symmetry Breakdown without Massless Bosons, *Phys. Rev.* 145 (1966) 1156–1163. [doi:10.1103/PhysRev.145.1156](https://doi.org/10.1103/PhysRev.145.1156).
- [9] G. Aad, et al., Observation of a new particle in the search for the Standard Model Higgs boson with the ATLAS detector at the LHC, *Phys. Lett. B* 716 (2012) 1–29. [arXiv:1207.7214](https://arxiv.org/abs/1207.7214), [doi:10.1016/j.physletb.2012.08.020](https://doi.org/10.1016/j.physletb.2012.08.020).
- [10] S. Chatrchyan, et al., Observation of a New Boson at a Mass of 125 GeV with the CMS Experiment at the LHC, *Phys. Lett. B* 716 (2012) 30–61. [arXiv:1207.7235](https://arxiv.org/abs/1207.7235), [doi:10.1016/j.physletb.2012.08.021](https://doi.org/10.1016/j.physletb.2012.08.021).
- [11] A. Abada, et al., HE-LHC: The High-Energy Large Hadron Collider: Future Circular Collider Conceptual Design Report Volume 4, *Eur. Phys. J. ST* 228 (5) (2019) 1109–1382. [doi:10.1140/epjst/e2019-900088-6](https://doi.org/10.1140/epjst/e2019-900088-6).
- [12] A. Abada, et al., FCC Physics Opportunities: Future Circular Collider Conceptual Design Report Volume 1, *Eur. Phys. J. C* 79 (6) (2019) 474. [doi:10.1140/epjc/s10052-019-6904-3](https://doi.org/10.1140/epjc/s10052-019-6904-3).
- [13] T. K. Charles, et al., The Compact Linear Collider (CLIC) - 2018 Summary Report 2/2018. [arXiv:1812.06018](https://arxiv.org/abs/1812.06018), [doi:10.23731/CYRM-2018-002](https://doi.org/10.23731/CYRM-2018-002).
- [14] P. Bambade, et al., The International Linear Collider: A Global Project [arXiv:1903.01629](https://arxiv.org/abs/1903.01629).

- [15] The International Linear Collider Technical Design Report - Volume 2: Physics [arXiv:1306.6352](#).
- [16] Physics and Detectors at CLIC: CLIC Conceptual Design Report [arXiv:1202.5940](#), [doi:10.5170/CERN-2012-003](#).
- [17] M. Dong, et al., CEPC Conceptual Design Report: Volume 2 - Physics & Detector [arXiv:1811.10545](#).
- [18] A. B. McDonald, Nobel Lecture: The Sudbury Neutrino Observatory: Observation of flavor change for solar neutrinos, *Rev. Mod. Phys.* 88 (3) (2016) 030502. [doi:10.1103/RevModPhys.88.030502](#).
- [19] T. Kajita, Nobel Lecture: Discovery of atmospheric neutrino oscillations, *Rev. Mod. Phys.* 88 (3) (2016) 030501. [doi:10.1103/RevModPhys.88.030501](#).
- [20] K. Eguchi, et al., First results from KamLAND: Evidence for reactor anti-neutrino disappearance, *Phys. Rev. Lett.* 90 (2003) 021802. [arXiv:hep-ex/0212021](#), [doi:10.1103/PhysRevLett.90.021802](#).
- [21] F. P. An, et al., Observation of electron-antineutrino disappearance at Daya Bay, *Phys. Rev. Lett.* 108 (2012) 171803. [arXiv:1203.1669](#), [doi:10.1103/PhysRevLett.108.171803](#).
- [22] J. K. Ahn, et al., Observation of Reactor Electron Antineutrino Disappearance in the RENO Experiment, *Phys. Rev. Lett.* 108 (2012) 191802. [arXiv:1204.0626](#), [doi:10.1103/PhysRevLett.108.191802](#).
- [23] K. Abe, et al., Indication of Electron Neutrino Appearance from an Accelerator-produced Off-axis Muon Neutrino Beam, *Phys. Rev. Lett.* 107 (2011) 041801. [arXiv:1106.2822](#), [doi:10.1103/PhysRevLett.107.041801](#).
- [24] P. F. de Salas, D. V. Forero, S. Gariazzo, P. Martínez-Miravé, O. Mena, C. A. Ternes, M. Tórtola, J. W. F. Valle, 2020 global reassessment of the neutrino oscillation picture, *JHEP* 02 (2021) 071. [arXiv:2006.11237](#), [doi:10.1007/JHEP02\(2021\)071](#).
- [25] P. F. De Salas, et al., *Chi2 profiles from Valencia neutrino global fit*, <http://globalfit.astroparticles.es/> (2021). [doi:10.5281/zenodo.4726908](#).
URL <https://doi.org/10.5281/zenodo.4726908>
- [26] F. Capozzi, E. Di Valentino, E. Lisi, A. Marrone, A. Melchiorri, A. Palazzo, Unfinished fabric of the three neutrino paradigm, *Phys. Rev. D* 104 (8) (2021) 083031. [arXiv:2107.00532](#), [doi:10.1103/PhysRevD.104.083031](#).
- [27] I. Esteban, M. C. Gonzalez-Garcia, M. Maltoni, T. Schwetz, A. Zhou, The fate of hints: updated global analysis of three-flavor neutrino oscillations, *JHEP* 09 (2020) 178. [arXiv:2007.14792](#), [doi:10.1007/JHEP09\(2020\)178](#).
- [28] R. L. Workman, Others, Review of Particle Physics, *PTEP* 2022 (2022) 083C01. [doi:10.1093/ptep/ptac097](#).
- [29] S. Weinberg, Baryon and Lepton Nonconserving Processes, *Phys. Rev. Lett.* 43 (1979) 1566–1570. [doi:10.1103/PhysRevLett.43.1566](#).
- [30] J. Schechter, J. W. F. Valle, Neutrino Masses in $SU(2) \times U(1)$ Theories, *Phys. Rev. D* 22 (1980) 2227. [doi:10.1103/PhysRevD.22.2227](#).
- [31] T. P. Cheng, L.-F. Li, Neutrino Masses, Mixings and Oscillations in $SU(2) \times U(1)$ Models of Electroweak Interactions, *Phys. Rev. D* 22 (1980) 2860. [doi:10.1103/PhysRevD.22.2860](#).
- [32] J. Schechter, J. W. F. Valle, Neutrino Decay and Spontaneous Violation of Lepton Number, *Phys. Rev. D* 25 (1982) 774. [doi:10.1103/PhysRevD.25.774](#).

- [33] P. Minkowski, $\mu \rightarrow e\gamma$ at a Rate of One Out of 10^9 Muon Decays?, Phys. Lett. B 67 (1977) 421–428. doi:[10.1016/0370-2693\(77\)90435-X](https://doi.org/10.1016/0370-2693(77)90435-X).
- [34] M. Gell-Mann, P. Ramond, R. Slansky, Complex Spinors and Unified Theories, Conf. Proc. C 790927 (1979) 315–321. arXiv:[1306.4669](https://arxiv.org/abs/1306.4669).
- [35] R. N. Mohapatra, G. Senjanovic, Neutrino Mass and Spontaneous Parity Nonconservation, Phys. Rev. Lett. 44 (1980) 912. doi:[10.1103/PhysRevLett.44.912](https://doi.org/10.1103/PhysRevLett.44.912).
- [36] M. Magg, C. Wetterich, Neutrino Mass Problem and Gauge Hierarchy, Phys. Lett. B 94 (1980) 61–64. doi:[10.1016/0370-2693\(80\)90825-4](https://doi.org/10.1016/0370-2693(80)90825-4).
- [37] G. Lazarides, Q. Shafi, C. Wetterich, Proton Lifetime and Fermion Masses in an SO(10) Model, Nucl. Phys. B 181 (1981) 287–300. doi:[10.1016/0550-3213\(81\)90354-0](https://doi.org/10.1016/0550-3213(81)90354-0).
- [38] R. N. Mohapatra, G. Senjanovic, Neutrino Masses and Mixings in Gauge Models with Spontaneous Parity Violation, Phys. Rev. D 23 (1981) 165. doi:[10.1103/PhysRevD.23.165](https://doi.org/10.1103/PhysRevD.23.165).
- [39] Y. Chikashige, R. N. Mohapatra, R. D. Peccei, Are There Real Goldstone Bosons Associated with Broken Lepton Number?, Phys. Lett. B 98 (1981) 265–268. doi:[10.1016/0370-2693\(81\)90011-3](https://doi.org/10.1016/0370-2693(81)90011-3).
- [40] M. C. Gonzalez-Garcia, J. W. F. Valle, Fast Decaying Neutrinos and Observable Flavor Violation in a New Class of Majoron Models, Phys. Lett. B 216 (1989) 360–366. doi:[10.1016/0370-2693\(89\)91131-3](https://doi.org/10.1016/0370-2693(89)91131-3).
- [41] S. M. Boucenna, S. Morisi, J. W. F. Valle, The low-scale approach to neutrino masses, Adv. High Energy Phys. 2014 (2014) 831598. arXiv:[1404.3751](https://arxiv.org/abs/1404.3751), doi:[10.1155/2014/831598](https://doi.org/10.1155/2014/831598).
- [42] Y. Cai, J. Herrero-García, M. A. Schmidt, A. Vicente, R. R. Volkas, From the trees to the forest: a review of radiative neutrino mass models, Front. in Phys. 5 (2017) 63. arXiv:[1706.08524](https://arxiv.org/abs/1706.08524), doi:[10.3389/fphy.2017.00063](https://doi.org/10.3389/fphy.2017.00063).
- [43] H. Georgi, S. L. Glashow, Unity of All Elementary Particle Forces, Phys. Rev. Lett. 32 (1974) 438–441. doi:[10.1103/PhysRevLett.32.438](https://doi.org/10.1103/PhysRevLett.32.438).
- [44] H. Georgi, H. R. Quinn, S. Weinberg, Hierarchy of Interactions in Unified Gauge Theories, Phys. Rev. Lett. 33 (1974) 451–454. doi:[10.1103/PhysRevLett.33.451](https://doi.org/10.1103/PhysRevLett.33.451).
- [45] H. Fritzsch, P. Minkowski, Unified Interactions of Leptons and Hadrons, Annals Phys. 93 (1975) 193–266. doi:[10.1016/0003-4916\(75\)90211-0](https://doi.org/10.1016/0003-4916(75)90211-0).
- [46] H. Georgi, C. Jarlskog, A New Lepton - Quark Mass Relation in a Unified Theory, Phys. Lett. B 86 (1979) 297–300. doi:[10.1016/0370-2693\(79\)90842-6](https://doi.org/10.1016/0370-2693(79)90842-6).
- [47] S. Dimopoulos, H. Georgi, Softly Broken Supersymmetry and SU(5), Nucl. Phys. B 193 (1981) 150–162. doi:[10.1016/0550-3213\(81\)90522-8](https://doi.org/10.1016/0550-3213(81)90522-8).
- [48] M. B. Green, J. H. Schwarz, E. Witten, SUPERSTRING THEORY. VOL. 1: INTRODUCTION, Cambridge Monographs on Mathematical Physics, 1988.
- [49] J. Polchinski, String theory. Vol. 2: Superstring theory and beyond, Cambridge Monographs on Mathematical Physics, Cambridge University Press, 2007. doi:[10.1017/CB09780511618123](https://doi.org/10.1017/CB09780511618123).
- [50] S. T. a. Dieter Lust, **Lectures on String Theory**, Lecture Notes in Physics 346, Springer Berlin Heidelberg, 1989.
URL <http://gen.lib.rus.ec/book/index.php?md5=a63659a291b19c9e6abc9856b960f536>

- [51] L. J. Hall, H. Murayama, N. Weiner, Neutrino mass anarchy, Phys. Rev. Lett. 84 (2000) 2572–2575. [arXiv:hep-ph/9911341](#), [doi:10.1103/PhysRevLett.84.2572](#).
- [52] A. de Gouvea, H. Murayama, Neutrino Mixing Anarchy: Alive and Kicking, Phys. Lett. B 747 (2015) 479–483. [arXiv:1204.1249](#), [doi:10.1016/j.physletb.2015.06.028](#).
- [53] E. Ma, G. Rajasekaran, Softly broken A_4 symmetry for nearly degenerate neutrino masses, Phys. Rev. D 64 (2001) 113012. [arXiv:hep-ph/0106291](#), [doi:10.1103/PhysRevD.64.113012](#).
- [54] K. S. Babu, E. Ma, J. W. F. Valle, Underlying A_4 symmetry for the neutrino mass matrix and the quark mixing matrix, Phys. Lett. B 552 (2003) 207–213. [arXiv:hep-ph/0206292](#), [doi:10.1016/S0370-2693\(02\)03153-2](#).
- [55] M. Hirsch, J. C. Romao, S. Skadhauge, J. W. F. Valle, A. Villanova del Moral, Phenomenological tests of supersymmetric $A(4)$ family symmetry model of neutrino mass, Phys. Rev. D 69 (2004) 093006. [arXiv:hep-ph/0312265](#), [doi:10.1103/PhysRevD.69.093006](#).
- [56] E. Ma, H. Sawanaka, M. Tanimoto, Quark Masses and Mixing with A_4 Family Symmetry, Phys. Lett. B 641 (2006) 301–304. [arXiv:hep-ph/0606103](#), [doi:10.1016/j.physletb.2006.08.062](#).
- [57] M. Hirsch, S. Morisi, J. W. F. Valle, Modelling tri-bimaximal neutrino mixing, Phys. Rev. D 79 (2009) 016001. [arXiv:0810.0121](#), [doi:10.1103/PhysRevD.79.016001](#).
- [58] M. Hirsch, S. Morisi, J. W. F. Valle, Tri-bimaximal neutrino mixing and neutrinoless double beta decay, Phys. Rev. D 78 (2008) 093007. [arXiv:0804.1521](#), [doi:10.1103/PhysRevD.78.093007](#).
- [59] M. Hirsch, S. Morisi, J. W. F. Valle, A_4 -based tri-bimaximal mixing within inverse and linear seesaw schemes, Phys. Lett. B 679 (2009) 454–459. [arXiv:0905.3056](#), [doi:10.1016/j.physletb.2009.08.003](#).
- [60] G.-J. Ding, D. Meloni, A Model for Tri-bimaximal Mixing from a Completely Broken A_4 , Nucl. Phys. B 855 (2012) 21–45. [arXiv:1108.2733](#), [doi:10.1016/j.nuclphysb.2011.10.001](#).
- [61] S. F. King, C. Luhn, Trimaximal neutrino mixing from vacuum alignment in A_4 and S_4 models, JHEP 09 (2011) 042. [arXiv:1107.5332](#), [doi:10.1007/JHEP09\(2011\)042](#).
- [62] Y. Shimizu, M. Tanimoto, A. Watanabe, Breaking Tri-bimaximal Mixing and Large θ_{13} , Prog. Theor. Phys. 126 (2011) 81–90. [arXiv:1105.2929](#), [doi:10.1143/PTP.126.81](#).
- [63] M. S. Boucenna, M. Hirsch, S. Morisi, E. Peinado, M. Taoso, J. W. F. Valle, Phenomenology of Dark Matter from A_4 Flavor Symmetry, JHEP 05 (2011) 037. [arXiv:1101.2874](#), [doi:10.1007/JHEP05\(2011\)037](#).
- [64] I. de Medeiros Varzielas, L. Lavoura, Flavour models for TM_1 lepton mixing, J. Phys. G 40 (2013) 085002. [arXiv:1212.3247](#), [doi:10.1088/0954-3899/40/8/085002](#).
- [65] S. Morisi, M. Nebot, K. M. Patel, E. Peinado, J. W. F. Valle, Quark-Lepton Mass Relation and CKM mixing in an A_4 Extension of the Minimal Supersymmetric Standard Model, Phys. Rev. D 88 (2013) 036001. [arXiv:1303.4394](#), [doi:10.1103/PhysRevD.88.036001](#).
- [66] S. F. King, S. Morisi, E. Peinado, J. W. F. Valle, Quark-Lepton Mass Relation in a Realistic A_4 Extension of the Standard Model, Phys. Lett. B 724 (2013) 68–72. [arXiv:1301.7065](#), [doi:10.1016/j.physletb.2013.05.067](#).
- [67] S. Morisi, D. V. Forero, J. C. Romão, J. W. F. Valle, Neutrino mixing with revamped A_4 flavor symmetry, Phys. Rev. D 88 (1) (2013) 016003. [arXiv:1305.6774](#), [doi:10.1103/PhysRevD.88.016003](#).

- [68] M. Hirsch, A. Villanova del Moral, J. W. F. Valle, E. Ma, Predicting neutrinoless double beta decay, *Phys. Rev. D* 72 (2005) 091301, [Erratum: *Phys.Rev.D* 72, 119904 (2005)]. [arXiv:hep-ph/0507148](#), [doi:10.1103/PhysRevD.72.091301](#).
- [69] M. Hirsch, A. S. Joshipura, S. Kaneko, J. W. F. Valle, Predictive flavour symmetries of the neutrino mass matrix, *Phys. Rev. Lett.* 99 (2007) 151802. [arXiv:hep-ph/0703046](#), [doi:10.1103/PhysRevLett.99.151802](#).
- [70] G. Altarelli, F. Feruglio, Tri-bimaximal neutrino mixing from discrete symmetry in extra dimensions, *Nucl. Phys. B* 720 (2005) 64–88. [arXiv:hep-ph/0504165](#), [doi:10.1016/j.nuclphysb.2005.05.005](#).
- [71] G. Altarelli, F. Feruglio, C. Hagedorn, A SUSY SU(5) Grand Unified Model of Tri-Bimaximal Mixing from A_4 , *JHEP* 03 (2008) 052. [arXiv:0802.0090](#), [doi:10.1088/1126-6708/2008/03/052](#).
- [72] C. Csaki, C. Delaunay, C. Grojean, Y. Grossman, A Model of Lepton Masses from a Warped Extra Dimension, *JHEP* 10 (2008) 055. [arXiv:0806.0356](#), [doi:10.1088/1126-6708/2008/10/055](#).
- [73] M.-C. Chen, K. T. Mahanthappa, F. Yu, A Viable Randall-Sundrum Model for Quarks and Leptons with T-prime Family Symmetry, *Phys. Rev. D* 81 (2010) 036004. [arXiv:0907.3963](#), [doi:10.1103/PhysRevD.81.036004](#).
- [74] T. J. Burrows, S. F. King, A(4) Family Symmetry from SU(5) SUSY GUTs in 6d, *Nucl. Phys. B* 835 (2010) 174–196. [arXiv:0909.1433](#), [doi:10.1016/j.nuclphysb.2010.04.002](#).
- [75] A. Kadosh, E. Pallante, An A(4) flavor model for quarks and leptons in warped geometry, *JHEP* 08 (2010) 115. [arXiv:1004.0321](#), [doi:10.1007/JHEP08\(2010\)115](#).
- [76] A. Kadosh, E. Pallante, CP violation and FCNC in a warped A_4 flavor model, *JHEP* 06 (2011) 121. [arXiv:1101.5420](#), [doi:10.1007/JHEP06\(2011\)121](#).
- [77] A. Kadosh, Θ_3 and charged Lepton Flavor Violation in "warped" A_4 models, *JHEP* 06 (2013) 114. [arXiv:1303.2645](#), [doi:10.1007/JHEP06\(2013\)114](#).
- [78] P. Chen, G.-J. Ding, A. D. Rojas, C. A. Vaquera-Araujo, J. W. F. Valle, Warped flavor symmetry predictions for neutrino physics, *JHEP* 01 (2016) 007. [arXiv:1509.06683](#), [doi:10.1007/JHEP01\(2016\)007](#).
- [79] P. Chen, et al., Predictions from warped flavor dynamics based on the T' family group, *Phys. Rev. D* 102 (9) (2020) 095014. [arXiv:2003.02734](#), [doi:10.1103/PhysRevD.102.095014](#).
- [80] F. del Aguila, A. Carmona, J. Santiago, Neutrino Masses from an A_4 Symmetry in Holographic Composite Higgs Models, *JHEP* 08 (2010) 127. [arXiv:1001.5151](#), [doi:10.1007/JHEP08\(2010\)127](#).
- [81] C. Hagedorn, M. Serone, Leptons in Holographic Composite Higgs Models with Non-Abelian Discrete Symmetries, *JHEP* 10 (2011) 083. [arXiv:1106.4021](#), [doi:10.1007/JHEP10\(2011\)083](#).
- [82] G.-J. Ding, Y.-L. Zhou, Dirac Neutrinos with S_4 Flavor Symmetry in Warped Extra Dimensions, *Nucl. Phys. B* 876 (2013) 418–452. [arXiv:1304.2645](#), [doi:10.1016/j.nuclphysb.2013.08.011](#).
- [83] C. Hagedorn, M. Serone, General Lepton Mixing in Holographic Composite Higgs Models, *JHEP* 02 (2012) 077. [arXiv:1110.4612](#), [doi:10.1007/JHEP02\(2012\)077](#).
- [84] A. E. Cárcamo Hernández, I. de Medeiros Varzielas, N. A. Neill, Novel Randall-Sundrum model with S_3 flavor symmetry, *Phys. Rev. D* 94 (3) (2016) 033011. [arXiv:1511.07420](#), [doi:10.1103/PhysRevD.94.033011](#).
- [85] H. Ishimori, T. Kobayashi, H. Ohki, Y. Shimizu, H. Okada, M. Tanimoto, Non-Abelian Discrete Symmetries in Particle Physics, *Prog. Theor. Phys. Suppl.* 183 (2010) 1–163. [arXiv:1003.3552](#), [doi:10.1143/PTPS.183.1](#).

- [86] G. Altarelli, F. Feruglio, Discrete Flavor Symmetries and Models of Neutrino Mixing, *Rev. Mod. Phys.* 82 (2010) 2701–2729. [arXiv:1002.0211](#), [doi:10.1103/RevModPhys.82.2701](#).
- [87] S. Morisi, J. W. F. Valle, Neutrino masses and mixing: a flavour symmetry roadmap, *Fortsch. Phys.* 61 (2013) 466–492. [arXiv:1206.6678](#), [doi:10.1002/prop.201200125](#).
- [88] S. F. King, C. Luhn, Neutrino Mass and Mixing with Discrete Symmetry, *Rept. Prog. Phys.* 76 (2013) 056201. [arXiv:1301.1340](#), [doi:10.1088/0034-4885/76/5/056201](#).
- [89] S. F. King, A. Merle, S. Morisi, Y. Shimizu, M. Tanimoto, Neutrino Mass and Mixing: from Theory to Experiment, *New J. Phys.* 16 (2014) 045018. [arXiv:1402.4271](#), [doi:10.1088/1367-2630/16/4/045018](#).
- [90] S. F. King, Unified Models of Neutrinos, Flavour and CP Violation, *Prog. Part. Nucl. Phys.* 94 (2017) 217–256. [arXiv:1701.04413](#), [doi:10.1016/j.pnpnp.2017.01.003](#).
- [91] F. Feruglio, A. Romanino, Lepton flavor symmetries, *Rev. Mod. Phys.* 93 (1) (2021) 015007. [arXiv:1912.06028](#), [doi:10.1103/RevModPhys.93.015007](#).
- [92] Z.-z. Xing, Flavor structures of charged fermions and massive neutrinos, *Phys. Rept.* 854 (2020) 1–147. [arXiv:1909.09610](#), [doi:10.1016/j.physrep.2020.02.001](#).
- [93] G. Chauhan, P. S. B. Dev, I. Dubovyk, B. Dziewit, W. Flieger, K. Grzanka, J. Gluza, B. Karmakar, S. Zieba, Phenomenology of Lepton Masses and Mixing with Discrete Flavor Symmetries, [arXiv:2310.20681](#).
- [94] M. E. Peskin, D. V. Schroeder, *An Introduction to quantum field theory*, Addison-Wesley, Reading, USA, 1995.
- [95] C. P. Burgess, G. D. Moore, *The standard model: A primer*, Cambridge University Press, 2006.
- [96] J. F. Donoghue, E. Golowich, B. R. Holstein, *Dynamics of the standard model*, Vol. 2, CUP, 2014. [doi:10.1017/CB09780511524370](#).
- [97] N. Cabibbo, Unitary Symmetry and Leptonic Decays, *Phys. Rev. Lett.* 10 (1963) 531–533. [doi:10.1103/PhysRevLett.10.531](#).
- [98] M. Kobayashi, T. Maskawa, CP Violation in the Renormalizable Theory of Weak Interaction, *Prog. Theor. Phys.* 49 (1973) 652–657. [doi:10.1143/PTP.49.652](#).
- [99] W. Rodejohann, J. W. F. Valle, Symmetrical Parametrizations of the Lepton Mixing Matrix, *Phys. Rev. D* 84 (2011) 073011. [arXiv:1108.3484](#), [doi:10.1103/PhysRevD.84.073011](#).
- [100] M. Bona, et al., The Unitarity Triangle Fit in the Standard Model and Hadronic Parameters from Lattice QCD: A Reappraisal after the Measurements of $\Delta m(s)$ and $\text{BR}(B \rightarrow \tau \nu(\tau))$, *JHEP* 10 (2006) 081. [arXiv:hep-ph/0606167](#), [doi:10.1088/1126-6708/2006/10/081](#).
- [101] M. Bona, et al., *Ufit website*.
URL <http://www.utfit.org/UTfit/>
- [102] J. W. F. Valle, J. C. Romao, *Neutrinos in high energy and astroparticle physics*, Physics textbook, Wiley-VCH, Weinheim, 2015.
URL <https://www.wiley.com/WileyCDA/WileyTitle/productCd-3527411976,descCd-buy.html>
- [103] M. Fukugita, T. Yanagida, *Physics of neutrinos and applications to astrophysics*, 2003.
- [104] C. Giunti, C. W. Kim, *Fundamentals of Neutrino Physics and Astrophysics*, 2007.

- [105] Z.-z. Xing, S. Zhou, Neutrinos in particle physics, astronomy and cosmology, 2011.
- [106] B. J. P. Jones, The Physics of Neutrinoless Double Beta Decay: A Primer, in: Theoretical Advanced Study Institute in Elementary Particle Physics: The Obscure Universe: Neutrinos and Other Dark Matters, 2021. [arXiv:2108.09364](#).
- [107] V. Cirigliano, et al., Neutrinoless Double-Beta Decay: A Roadmap for Matching Theory to Experiment [arXiv:2203.12169](#).
- [108] M. J. Dolinski, A. W. P. Poon, W. Rodejohann, Neutrinoless Double-Beta Decay: Status and Prospects, *Ann. Rev. Nucl. Part. Sci.* 69 (2019) 219–251. [arXiv:1902.04097](#), [doi:10.1146/annurev-nucl-101918-023407](#).
- [109] J. D. Vergados, H. Ejiri, F. Simkovic, Theory of Neutrinoless Double Beta Decay, *Rept. Prog. Phys.* 75 (2012) 106301. [arXiv:1205.0649](#), [doi:10.1088/0034-4885/75/10/106301](#).
- [110] J. Schechter, J. W. F. Valle, Neutrinoless Double beta Decay in $SU(2) \times U(1)$ Theories, *Phys. Rev. D* 25 (1982) 2951. [doi:10.1103/PhysRevD.25.2951](#).
- [111] J. Schechter, J. W. F. Valle, Neutrino Oscillation Thought Experiment, *Phys. Rev. D* 23 (1981) 1666. [doi:10.1103/PhysRevD.23.1666](#).
- [112] S. M. Bilenky, J. Hosek, S. T. Petcov, On Oscillations of Neutrinos with Dirac and Majorana Masses, *Phys. Lett. B* 94 (1980) 495–498. [doi:10.1016/0370-2693\(80\)90927-2](#).
- [113] R. Acciarri, et al., Long-Baseline Neutrino Facility (LBNF) and Deep Underground Neutrino Experiment (DUNE): Conceptual Design Report, Volume 2: The Physics Program for DUNE at LBNF [arXiv:1512.06148](#).
- [114] K. Abe, et al., Hyper-Kamiokande Design Report [arXiv:1805.04163](#).
- [115] F. An, et al., Neutrino Physics with JUNO, *J. Phys. G* 43 (3) (2016) 030401. [arXiv:1507.05613](#), [doi:10.1088/0954-3899/43/3/030401](#).
- [116] S. S. Chatterjee, P. Pasquini, J. W. F. Valle, Resolving the atmospheric octant by an improved measurement of the reactor angle, *Phys. Rev. D* 96 (1) (2017) 011303. [arXiv:1703.03435](#), [doi:10.1103/PhysRevD.96.011303](#).
- [117] R. Srivastava, C. A. Ternes, M. Tórtola, J. W. F. Valle, Zooming in on neutrino oscillations with DUNE, *Phys. Rev. D* 97 (9) (2018) 095025. [arXiv:1803.10247](#), [doi:10.1103/PhysRevD.97.095025](#).
- [118] M. S. Athar, et al., Status and perspectives of neutrino physics, *Prog. Part. Nucl. Phys.* 124 (2022) 103947. [arXiv:2111.07586](#), [doi:10.1016/j.pnpnp.2022.103947](#).
- [119] M. Maltoni, T. Schwetz, M. A. Tortola, J. W. F. Valle, Status of global fits to neutrino oscillations, *New J. Phys.* 6 (2004) 122. [arXiv:hep-ph/0405172](#), [doi:10.1088/1367-2630/6/1/122](#).
- [120] M. Drewes, et al., A White Paper on keV Sterile Neutrino Dark Matter, *JCAP* 01 (2017) 025. [arXiv:1602.04816](#), [doi:10.1088/1475-7516/2017/01/025](#).
- [121] C. Giunti, T. Lasserre, eV-scale Sterile Neutrinos, *Ann. Rev. Nucl. Part. Sci.* 69 (2019) 163–190. [arXiv:1901.08330](#), [doi:10.1146/annurev-nucl-101918-023755](#).
- [122] S. Böser, C. Buck, C. Giunti, J. Lesgourgues, L. Ludhova, S. Mertens, A. Schukraft, M. Wurm, Status of Light Sterile Neutrino Searches, *Prog. Part. Nucl. Phys.* 111 (2020) 103736. [arXiv:1906.01739](#), [doi:10.1016/j.pnpnp.2019.103736](#).

- [123] B. Dasgupta, J. Kopp, Sterile Neutrinos, *Phys. Rept.* 928 (2021) 1–63. [arXiv:2106.05913](#), [doi:10.1016/j.physrep.2021.06.002](#).
- [124] M. Lattanzi, M. Gerbino, K. Freese, G. Kane, J. W. F. Valle, Cornering (quasi) degenerate neutrinos with cosmology, *JHEP* 10 (2020) 213. [arXiv:2007.01650](#), [doi:10.1007/JHEP10\(2020\)213](#).
- [125] S. Abe, et al., Search for the Majorana Nature of Neutrinos in the Inverted Mass Ordering Region with KamLAND-Zen, *Phys. Rev. Lett.* 130 (5) (2023) 051801. [arXiv:2203.02139](#), [doi:10.1103/PhysRevLett.130.051801](#).
- [126] N. Abgrall, et al., The Large Enriched Germanium Experiment for Neutrinoless $\beta\beta$ Decay: LEGEND-1000 Preconceptual Design Report [arXiv:2107.11462](#).
- [127] G. Adhikari, et al., nEXO: neutrinoless double beta decay search beyond 10^{28} year half-life sensitivity, *J. Phys. G* 49 (1) (2022) 015104. [arXiv:2106.16243](#), [doi:10.1088/1361-6471/ac3631](#).
- [128] N. Aghanim, et al., Planck 2018 results. VI. Cosmological parameters, *Astron. Astrophys.* 641 (2020) A6, [Erratum: *Astron. Astrophys.* 652, C4 (2021)]. [arXiv:1807.06209](#), [doi:10.1051/0004-6361/201833910](#).
- [129] M. Gerbino, et al., Synergy between cosmological and laboratory searches in neutrino physics, *Phys. Dark Univ.* 42 (2023) 101333. [arXiv:2203.07377](#), [doi:10.1016/j.dark.2023.101333](#).
- [130] J. Leite, et al., A theory for scotogenic dark matter stabilised by residual gauge symmetry, *Phys. Lett. B* 802 (2020) 135254. [arXiv:1909.06386](#), [doi:10.1016/j.physletb.2020.135254](#).
- [131] S. F. King, Large mixing angle MSW and atmospheric neutrinos from single right-handed neutrino dominance and U(1) family symmetry, *Nucl. Phys. B* 576 (2000) 85–105. [arXiv:hep-ph/9912492](#), [doi:10.1016/S0550-3213\(00\)00109-7](#).
- [132] P. H. Frampton, S. L. Glashow, T. Yanagida, Cosmological sign of neutrino CP violation, *Phys. Lett. B* 548 (2002) 119–121. [arXiv:hep-ph/0208157](#), [doi:10.1016/S0370-2693\(02\)02853-8](#).
- [133] M. Raidal, A. Strumia, Predictions of the most minimal seesaw model, *Phys. Lett. B* 553 (2003) 72–78. [arXiv:hep-ph/0210021](#), [doi:10.1016/S0370-2693\(02\)03124-6](#).
- [134] M. Reig, D. Restrepo, J. W. F. Valle, O. Zapata, Bound-state dark matter with Majorana neutrinos, *Phys. Lett. B* 790 (2019) 303–307. [arXiv:1806.09977](#), [doi:10.1016/j.physletb.2019.01.023](#).
- [135] D. M. Barreiros, R. G. Felipe, F. R. Joaquim, Combining texture zeros with a remnant CP symmetry in the minimal type-I seesaw, *JHEP* 01 (2019) 223. [arXiv:1810.05454](#), [doi:10.1007/JHEP01\(2019\)223](#).
- [136] N. Rojas, R. Srivastava, J. W. F. Valle, Simplest Scoto-Seesaw Mechanism, *Phys. Lett. B* 789 (2019) 132–136. [arXiv:1807.11447](#), [doi:10.1016/j.physletb.2018.12.014](#).
- [137] S. Mandal, R. Srivastava, J. W. F. Valle, The simplest scoto-seesaw model: WIMP dark matter phenomenology and Higgs vacuum stability, *Phys. Lett. B* 819 (2021) 136458. [arXiv:2104.13401](#), [doi:10.1016/j.physletb.2021.136458](#).
- [138] I. M. Ávila, et al., Phenomenology of scotogenic scalar dark matter, *Eur. Phys. J. C* 80 (10) (2020) 908. [arXiv:1910.08422](#), [doi:10.1140/epjc/s10052-020-08480-z](#).
- [139] M. Agostini, et al., Probing Majorana neutrinos with double- β decay, *Science* 365 (2019) 1445. [arXiv:1909.02726](#), [doi:10.1126/science.aav8613](#).

- [140] M. Agostini, G. Benato, J. A. Detwiler, J. Menéndez, F. Vissani, Toward the discovery of matter creation with neutrinoless $\beta\beta$ decay, *Rev. Mod. Phys.* 95 (2) (2023) 025002. [arXiv:2202.01787](#), [doi:10.1103/RevModPhys.95.025002](#).
- [141] L. Dorame, D. Meloni, S. Morisi, E. Peinado, J. W. F. Valle, Constraining Neutrinoless Double Beta Decay, *Nucl. Phys. B* 861 (2012) 259–270. [arXiv:1111.5614](#), [doi:10.1016/j.nuclphysb.2012.04.003](#).
- [142] L. Dorame, S. Morisi, E. Peinado, J. W. F. Valle, A. D. Rojas, A new neutrino mass sum rule from inverse seesaw, *Phys. Rev. D* 86 (2012) 056001. [arXiv:1203.0155](#), [doi:10.1103/PhysRevD.86.056001](#).
- [143] F. J. de Anda, J. W. Valle, C. A. Vaquera-Araujo, Flavour and CP predictions from orbifold compactification, *Phys.Lett. B* 801 (2020) 135195. [arXiv:1910.05605](#), [doi:10.1016/j.physletb.2019.135195](#).
- [144] F. J. de Anda, et al., Probing the predictions of an orbifold theory of flavor, *Phys. Rev. D* 101 (11) (2020) 116012. [arXiv:2004.06735](#), [doi:10.1103/PhysRevD.101.116012](#).
- [145] J. A. Formaggio, A. L. C. de Gouvêa, R. G. H. Robertson, Direct Measurements of Neutrino Mass, *Phys. Rept.* 914 (2021) 1–54. [arXiv:2102.00594](#), [doi:10.1016/j.physrep.2021.02.002](#).
- [146] M. Aker, et al., Direct neutrino-mass measurement with sub-electronvolt sensitivity, *Nature Phys.* 18 (2) (2022) 160–166. [arXiv:2105.08533](#), [doi:10.1038/s41567-021-01463-1](#).
- [147] M. Aker, et al., Improved Upper Limit on the Neutrino Mass from a Direct Kinematic Method by KATRIN, *Phys. Rev. Lett.* 123 (22) (2019) 221802. [arXiv:1909.06048](#), [doi:10.1103/PhysRevLett.123.221802](#).
- [148] D. M. Barreiros, F. R. Joaquim, R. Srivastava, J. W. F. Valle, Minimal scoto-seesaw mechanism with spontaneous CP violation, *JHEP* 04 (2021) 249. [arXiv:2012.05189](#), [doi:10.1007/JHEP04\(2021\)249](#).
- [149] A. Gando, et al., Search for Majorana Neutrinos near the Inverted Mass Hierarchy Region with KamLAND-Zen, *Phys. Rev. Lett.* 117 (8) (2016) 082503, [Addendum: *Phys.Rev.Lett.* 117, 109903 (2016)]. [arXiv:1605.02889](#), [doi:10.1103/PhysRevLett.117.082503](#).
- [150] M. Agostini, et al., Final Results of GERDA on the Search for Neutrinoless Double- β Decay, *Phys. Rev. Lett.* 125 (25) (2020) 252502. [arXiv:2009.06079](#), [doi:10.1103/PhysRevLett.125.252502](#).
- [151] D. Q. Adams, et al., Improved Limit on Neutrinoless Double-Beta Decay in ^{130}Te with CUORE, *Phys. Rev. Lett.* 124 (12) (2020) 122501. [arXiv:1912.10966](#), [doi:10.1103/PhysRevLett.124.122501](#).
- [152] G. Anton, et al., Search for Neutrinoless Double- β Decay with the Complete EXO-200 Dataset, *Phys. Rev. Lett.* 123 (16) (2019) 161802. [arXiv:1906.02723](#), [doi:10.1103/PhysRevLett.123.161802](#).
- [153] M. Duerr, M. Lindner, A. Merle, On the Quantitative Impact of the Schechter-Valle Theorem, *JHEP* 06 (2011) 091. [arXiv:1105.0901](#), [doi:10.1007/JHEP06\(2011\)091](#).
- [154] L. Gráf, M. Lindner, O. Scholer, Unraveling the $0\nu\beta\beta$ decay mechanisms, *Phys. Rev. D* 106 (3) (2022) 035022. [arXiv:2204.10845](#), [doi:10.1103/PhysRevD.106.035022](#).
- [155] J. Heeck, W. Rodejohann, Neutrinoless Quadruple Beta Decay, *EPL* 103 (3) (2013) 32001. [arXiv:1306.0580](#), [doi:10.1209/0295-5075/103/32001](#).
- [156] R. Arnold, et al., Search for neutrinoless quadruple- β decay of ^{150}Nd with the NEMO-3 detector, *Phys. Rev. Lett.* 119 (4) (2017) 041801. [arXiv:1705.08847](#), [doi:10.1103/PhysRevLett.119.041801](#).
- [157] M. Hirsch, R. Srivastava, J. W. F. Valle, Can one ever prove that neutrinos are Dirac particles?, *Phys. Lett. B* 781 (2018) 302–305. [arXiv:1711.06181](#), [doi:10.1016/j.physletb.2018.03.073](#).

- [158] R. E. Marshak, R. N. Mohapatra, Quark - Lepton Symmetry and B-L as the U(1) Generator of the Electroweak Symmetry Group, *Phys. Lett. B* 91 (1980) 222–224. doi:[10.1016/0370-2693\(80\)90436-0](https://doi.org/10.1016/0370-2693(80)90436-0).
- [159] R. N. Mohapatra, R. E. Marshak, Local B-L Symmetry of Electroweak Interactions, Majorana Neutrinos and Neutron Oscillations, *Phys. Rev. Lett.* 44 (1980) 1316–1319, [Erratum: *Phys.Rev.Lett.* 44, 1643 (1980)]. doi:[10.1103/PhysRevLett.44.1316](https://doi.org/10.1103/PhysRevLett.44.1316).
- [160] C. Wetterich, Neutrino Masses and the Scale of B-L Violation, *Nucl. Phys. B* 187 (1981) 343–375. doi:[10.1016/0550-3213\(81\)90279-0](https://doi.org/10.1016/0550-3213(81)90279-0).
- [161] J. Leite, et al., Scotogenic dark matter and Dirac neutrinos from unbroken gauged B – L symmetry, *Phys. Lett. B* 807 (2020) 135537. arXiv:[2003.02950](https://arxiv.org/abs/2003.02950), doi:[10.1016/j.physletb.2020.135537](https://doi.org/10.1016/j.physletb.2020.135537).
- [162] E. Peinado, M. Reig, R. Srivastava, J. W. F. Valle, Dirac neutrinos from Peccei–Quinn symmetry: A fresh look at the axion, *Mod. Phys. Lett. A* 35 (21) (2020) 2050176. arXiv:[1910.02961](https://arxiv.org/abs/1910.02961), doi:[10.1142/S021773232050176X](https://doi.org/10.1142/S021773232050176X).
- [163] A. G. Dias, J. Leite, J. W. F. Valle, C. A. Vaquera-Araujo, Reloading the axion in a 3-3-1 setup, *Phys. Lett. B* 810 (2020) 135829. arXiv:[2008.10650](https://arxiv.org/abs/2008.10650), doi:[10.1016/j.physletb.2020.135829](https://doi.org/10.1016/j.physletb.2020.135829).
- [164] Y. Farzan, E. Ma, Dirac neutrino mass generation from dark matter, *Phys. Rev. D* 86 (2012) 033007. arXiv:[1204.4890](https://arxiv.org/abs/1204.4890), doi:[10.1103/PhysRevD.86.033007](https://doi.org/10.1103/PhysRevD.86.033007).
- [165] S. Centelles Chuliá, E. Ma, R. Srivastava, J. W. F. Valle, Dirac Neutrinos and Dark Matter Stability from Lepton Quarticity, *Phys.Lett. B* 767 (2017) 209–213. arXiv:[1606.04543](https://arxiv.org/abs/1606.04543), doi:[10.1016/j.physletb.2017.01.070](https://doi.org/10.1016/j.physletb.2017.01.070).
- [166] C. Bonilla, E. Ma, E. Peinado, J. W. F. Valle, Two-loop Dirac neutrino mass and WIMP dark matter, *Phys. Lett. B* 762 (2016) 214–218. arXiv:[1607.03931](https://arxiv.org/abs/1607.03931), doi:[10.1016/j.physletb.2016.09.027](https://doi.org/10.1016/j.physletb.2016.09.027).
- [167] R. Srivastava, C. A. Ternes, M. Tórtola, J. W. F. Valle, Testing a lepton quarticity flavor theory of neutrino oscillations with the DUNE experiment, *Phys. Lett. B* 778 (2018) 459–463. arXiv:[1711.10318](https://arxiv.org/abs/1711.10318), doi:[10.1016/j.physletb.2018.01.014](https://doi.org/10.1016/j.physletb.2018.01.014).
- [168] S. Centelles Chuliá, R. Srivastava, J. W. F. Valle, Generalized Bottom-Tau unification, neutrino oscillations and dark matter: predictions from a lepton quarticity flavor approach, *Phys. Lett. B* 773 (2017) 26–33. arXiv:[1706.00210](https://arxiv.org/abs/1706.00210), doi:[10.1016/j.physletb.2017.07.065](https://doi.org/10.1016/j.physletb.2017.07.065).
- [169] M. Reig, D. Restrepo, J. W. F. Valle, O. Zapata, Bound-state dark matter and Dirac neutrino masses, *Phys. Rev. D* 97 (11) (2018) 115032. arXiv:[1803.08528](https://arxiv.org/abs/1803.08528), doi:[10.1103/PhysRevD.97.115032](https://doi.org/10.1103/PhysRevD.97.115032).
- [170] C. Bonilla, S. Centelles-Chuliá, R. Cepedello, E. Peinado, R. Srivastava, Dark matter stability and Dirac neutrinos using only Standard Model symmetries, *Phys. Rev. D* 101 (3) (2020) 033011. arXiv:[1812.01599](https://arxiv.org/abs/1812.01599), doi:[10.1103/PhysRevD.101.033011](https://doi.org/10.1103/PhysRevD.101.033011).
- [171] C. Alvarado, C. Bonilla, J. Leite, J. W. F. Valle, Phenomenology of fermion dark matter as neutrino mass mediator with gauged B-L, *Phys. Lett. B* 817 (2021) 136292. arXiv:[2102.07216](https://arxiv.org/abs/2102.07216), doi:[10.1016/j.physletb.2021.136292](https://doi.org/10.1016/j.physletb.2021.136292).
- [172] M. Roncadelli, D. Wyler, Naturally Light Dirac Neutrinos in Gauge Theories, *Phys. Lett. B* 133 (1983) 325–329. doi:[10.1016/0370-2693\(83\)90156-9](https://doi.org/10.1016/0370-2693(83)90156-9).
- [173] P.-H. Gu, H.-J. He, Neutrino Mass and Baryon Asymmetry from Dirac Seesaw, *JCAP* 12 (2006) 010. arXiv:[hep-ph/0610275](https://arxiv.org/abs/hep-ph/0610275), doi:[10.1088/1475-7516/2006/12/010](https://doi.org/10.1088/1475-7516/2006/12/010).

- [174] C.-Y. Yao, G.-J. Ding, Systematic analysis of Dirac neutrino masses from a dimension five operator, *Phys. Rev. D* 97 (9) (2018) 095042. [arXiv:1802.05231](#), [doi:10.1103/PhysRevD.97.095042](#).
- [175] S. Centelles Chuliá, R. Srivastava, J. W. F. Valle, Seesaw roadmap to neutrino mass and dark matter, *Phys. Lett. B* 781 (2018) 122–128. [arXiv:1802.05722](#), [doi:10.1016/j.physletb.2018.03.046](#).
- [176] C.-Y. Yao, G.-J. Ding, Systematic Study of One-Loop Dirac Neutrino Masses and Viable Dark Matter Candidates, *Phys. Rev. D* 96 (9) (2017) 095004, [Erratum: *Phys.Rev.D* 98, 039901 (2018)]. [arXiv:1707.09786](#), [doi:10.1103/PhysRevD.96.095004](#).
- [177] S. Centelles Chuliá, R. Srivastava, J. W. F. Valle, Seesaw Dirac neutrino mass through dimension-six operators, *Phys. Rev. D* 98 (3) (2018) 035009. [arXiv:1804.03181](#), [doi:10.1103/PhysRevD.98.035009](#).
- [178] J. Elias-Miro, J. R. Espinosa, G. F. Giudice, G. Isidori, A. Riotto, A. Strumia, Higgs mass implications on the stability of the electroweak vacuum, *Phys. Lett. B* 709 (2012) 222–228. [arXiv:1112.3022](#), [doi:10.1016/j.physletb.2012.02.013](#).
- [179] C. Bonilla, R. M. Fonseca, J. W. F. Valle, Consistency of the triplet seesaw model revisited, *Phys. Rev. D* 92 (7) (2015) 075028. [arXiv:1508.02323](#), [doi:10.1103/PhysRevD.92.075028](#).
- [180] C. Bonilla, R. M. Fonseca, J. W. F. Valle, Vacuum stability with spontaneous violation of lepton number, *Phys. Lett. B* 756 (2016) 345–349. [arXiv:1506.04031](#), [doi:10.1016/j.physletb.2016.03.037](#).
- [181] S. Mandal, R. Srivastava, J. W. F. Valle, Consistency of the dynamical high-scale type-I seesaw mechanism, *Phys. Rev. D* 101 (11) (2020) 115030. [doi:10.1103/PhysRevD.101.115030](#).
- [182] S. Mandal, R. Srivastava, J. W. F. Valle, Electroweak symmetry breaking in the inverse seesaw mechanism, *JHEP* 03 (2021) 212. [arXiv:2009.10116](#), [doi:10.1007/JHEP03\(2021\)212](#).
- [183] S. Mandal, J. C. Romão, R. Srivastava, J. W. F. Valle, Dynamical inverse seesaw mechanism as a simple benchmark for electroweak breaking and Higgs boson studies, *JHEP* 07 (2021) 029. [arXiv:2103.02670](#), [doi:10.1007/JHEP07\(2021\)029](#).
- [184] R. Foot, H. Lew, X. G. He, G. C. Joshi, Seesaw Neutrino Masses Induced by a Triplet of Leptons, *Z. Phys. C* 44 (1989) 441. [doi:10.1007/BF01415558](#).
- [185] S. Mandal, O. G. Miranda, G. Sanchez Garcia, J. W. F. Valle, X.-J. Xu, Toward deconstructing the simplest seesaw mechanism, *Phys. Rev. D* 105 (9) (2022) 095020. [arXiv:2203.06362](#), [doi:10.1103/PhysRevD.105.095020](#).
- [186] P. Fileviez Perez, T. Han, G.-y. Huang, T. Li, K. Wang, Neutrino Masses and the CERN LHC: Testing Type II Seesaw, *Phys. Rev. D* 78 (2008) 015018. [arXiv:0805.3536](#), [doi:10.1103/PhysRevD.78.015018](#).
- [187] Y. Cai, T. Han, T. Li, R. Ruiz, Lepton Number Violation: Seesaw Models and Their Collider Tests, *Front. in Phys.* 6 (2018) 40. [arXiv:1711.02180](#), [doi:10.3389/fphy.2018.00040](#).
- [188] S. Mandal, O. G. Miranda, G. S. Garcia, J. W. F. Valle, X.-J. Xu, High-energy colliders as a probe of neutrino properties, *Phys. Lett. B* 829 (2022) 137110. [arXiv:2202.04502](#), [doi:10.1016/j.physletb.2022.137110](#).
- [189] J. W. F. Valle, Neutrino physics overview, *J. Phys. Conf. Ser.* 53 (2006) 473–505. [arXiv:hep-ph/0608101](#), [doi:10.1088/1742-6596/53/1/031](#).
- [190] J. W. F. Valle, C. A. Vaquera-Araujo, Dynamical seesaw mechanism for Dirac neutrinos, *Phys. Lett. B* 755 (2016) 363–366. [arXiv:1601.05237](#), [doi:10.1016/j.physletb.2016.02.031](#).

- [191] A. Aranda, C. Bonilla, S. Morisi, E. Peinado, J. W. F. Valle, Dirac neutrinos from flavor symmetry, *Phys. Rev. D* 89 (3) (2014) 033001. [arXiv:1307.3553](#), [doi:10.1103/PhysRevD.89.033001](#).
- [192] D. Borah, B. Karmakar, A_4 flavour model for Dirac neutrinos: Type I and inverse seesaw, *Phys. Lett. B* 780 (2018) 461–470. [arXiv:1712.06407](#), [doi:10.1016/j.physletb.2018.03.047](#).
- [193] G. Bertone, D. Hooper, J. Silk, Particle dark matter: Evidence, candidates and constraints, *Phys. Rept.* 405 (2005) 279–390. [arXiv:hep-ph/0404175](#), [doi:10.1016/j.physrep.2004.08.031](#).
- [194] G. Jungman, M. Kamionkowski, K. Griest, Supersymmetric dark matter, *Phys. Rept.* 267 (1996) 195–373. [arXiv:hep-ph/9506380](#), [doi:10.1016/0370-1573\(95\)00058-5](#).
- [195] Z.-j. Tao, Radiative seesaw mechanism at weak scale, *Phys. Rev. D* 54 (1996) 5693–5697. [arXiv:hep-ph/9603309](#), [doi:10.1103/PhysRevD.54.5693](#).
- [196] E. Ma, Verifiable radiative seesaw mechanism of neutrino mass and dark matter, *Phys. Rev. D* 73 (2006) 077301. [arXiv:hep-ph/0601225](#), [doi:10.1103/PhysRevD.73.077301](#).
- [197] M. Hirsch, R. A. Lineros, S. Morisi, J. Palacio, N. Rojas, J. W. F. Valle, WIMP dark matter as radiative neutrino mass messenger, *JHEP* 10 (2013) 149. [arXiv:1307.8134](#), [doi:10.1007/JHEP10\(2013\)149](#).
- [198] A. Merle, M. Platscher, N. Rojas, J. W. F. Valle, A. Vicente, Consistency of WIMP Dark Matter as radiative neutrino mass messenger, *JHEP* 07 (2016) 013. [arXiv:1603.05685](#), [doi:10.1007/JHEP07\(2016\)013](#).
- [199] M. A. Díaz, N. Rojas, S. Urrutia-Quiroga, J. W. F. Valle, Heavy Higgs Boson Production at Colliders in the Singlet-Triplet Scotogenic Dark Matter Model, *JHEP* 08 (2017) 017. [arXiv:1612.06569](#), [doi:10.1007/JHEP08\(2017\)017](#).
- [200] S. Choubey, S. Khan, M. Mitra, S. Mondal, Singlet-Triplet Fermionic Dark Matter and LHC Phenomenology, *Eur. Phys. J. C* 78 (4) (2018) 302. [arXiv:1711.08888](#), [doi:10.1140/epjc/s10052-018-5785-1](#).
- [201] D. Restrepo, A. Rivera, Phenomenological consistency of the singlet-triplet scotogenic model, *JHEP* 04 (2020) 134. [arXiv:1907.11938](#), [doi:10.1007/JHEP04\(2020\)134](#).
- [202] S. Mandal, N. Rojas, R. Srivastava, J. W. F. Valle, Dark matter as the origin of neutrino mass in the inverse seesaw mechanism, *Phys. Lett. B* 821 (2021) 136609. [arXiv:1907.07728](#), [doi:10.1016/j.physletb.2021.136609](#).
- [203] A. E. Cárcamo Hernández, V. K. N., J. W. F. Valle, Linear seesaw mechanism from dark sector, *JHEP* 09 (2023) 046. [arXiv:2305.02273](#), [doi:10.1007/JHEP09\(2023\)046](#).
- [204] A. Batra, H. B. Câmara, F. R. Joaquim, Dark linear seesaw mechanism, *Phys. Lett. B* 843 (2023) 138012. [arXiv:2305.01687](#), [doi:10.1016/j.physletb.2023.138012](#).
- [205] G.-J. Ding, J.-N. Lu, J. W. F. Valle, Trimaximal neutrino mixing from scotogenic A_4 family symmetry, *Phys. Lett. B* 815 (2021) 136122. [arXiv:2009.04750](#), [doi:10.1016/j.physletb.2021.136122](#).
- [206] V. Berezhinsky, J. W. F. Valle, The KeV majoron as a dark matter particle, *Phys. Lett. B* 318 (1993) 360–366. [arXiv:hep-ph/9309214](#), [doi:10.1016/0370-2693\(93\)90140-D](#).
- [207] M. Lattanzi, R. A. Lineros, M. Taoso, Connecting neutrino physics with dark matter, *New J. Phys.* 16 (12) (2014) 125012. [arXiv:1406.0004](#), [doi:10.1088/1367-2630/16/12/125012](#).
- [208] S. R. Coleman, Why There Is Nothing Rather Than Something: A Theory of the Cosmological Constant, *Nucl. Phys. B* 310 (1988) 643–668. [doi:10.1016/0550-3213\(88\)90097-1](#).

- [209] M. Lattanzi, J. W. F. Valle, Decaying warm dark matter and neutrino masses, *Phys. Rev. Lett.* 99 (2007) 121301. [arXiv:0705.2406](#), [doi:10.1103/PhysRevLett.99.121301](#).
- [210] M. Lattanzi, S. Riemer-Sorensen, M. Tortola, J. W. F. Valle, Updated CMB and x- and γ -ray constraints on Majoron dark matter, *Phys. Rev. D* 88 (6) (2013) 063528. [arXiv:1303.4685](#), [doi:10.1103/PhysRevD.88.063528](#).
- [211] J.-L. Kuo, M. Lattanzi, K. Cheung, J. W. F. Valle, Decaying warm dark matter and structure formation, *JCAP* 12 (2018) 026. [arXiv:1803.05650](#), [doi:10.1088/1475-7516/2018/12/026](#).
- [212] J. Schechter, J. W. F. Valle, Comment on the Lepton Mixing Matrix, *Phys. Rev. D* 21 (1980) 309. [doi:10.1103/PhysRevD.21.309](#).
- [213] R. N. Mohapatra, J. W. F. Valle, Neutrino Mass and Baryon Number Nonconservation in Superstring Models, *Phys. Rev. D* 34 (1986) 1642. [doi:10.1103/PhysRevD.34.1642](#).
- [214] J. Bernabeu, A. Santamaria, J. Vidal, A. Mendez, J. W. F. Valle, Lepton Flavor Nonconservation at High-Energies in a Superstring Inspired Standard Model, *Phys. Lett. B* 187 (1987) 303–308. [doi:10.1016/0370-2693\(87\)91100-2](#).
- [215] G. C. Branco, M. N. Rebelo, J. W. F. Valle, Leptonic CP Violation With Massless Neutrinos, *Phys. Lett. B* 225 (1989) 385–392. [doi:10.1016/0370-2693\(89\)90587-X](#).
- [216] N. Rius, J. W. F. Valle, Leptonic CP Violating Asymmetries in Z^0 Decays, *Phys. Lett. B* 246 (1990) 249–255. [doi:10.1016/0370-2693\(90\)91341-8](#).
- [217] H. Nunokawa, S. J. Parke, J. W. F. Valle, CP Violation and Neutrino Oscillations, *Prog. Part. Nucl. Phys.* 60 (2008) 338–402. [arXiv:0710.0554](#), [doi:10.1016/j.pnpnp.2007.10.001](#).
- [218] A. de Gouvea, B. Kayser, R. N. Mohapatra, Manifest CP Violation from Majorana Phases, *Phys. Rev. D* 67 (2003) 053004. [arXiv:hep-ph/0211394](#), [doi:10.1103/PhysRevD.67.053004](#).
- [219] G. C. Branco, R. G. Felipe, F. R. Joaquim, Leptonic CP Violation, *Rev. Mod. Phys.* 84 (2012) 515–565. [arXiv:1111.5332](#), [doi:10.1103/RevModPhys.84.515](#).
- [220] A. Vicente, Lepton flavor violation beyond the MSSM, *Adv. High Energy Phys.* 2015 (2015) 686572. [arXiv:1503.08622](#), [doi:10.1155/2015/686572](#).
- [221] A. Abada, J. Kriewald, A. M. Teixeira, On the role of leptonic CPV phases in cLFV observables, *Eur. Phys. J. C* 81 (11) (2021) 1016. [arXiv:2107.06313](#), [doi:10.1140/epjc/s10052-021-09754-w](#).
- [222] F. Deppisch, J. W. F. Valle, Enhanced lepton flavor violation in the supersymmetric inverse seesaw model, *Phys. Rev. D* 72 (2005) 036001. [arXiv:hep-ph/0406040](#), [doi:10.1103/PhysRevD.72.036001](#).
- [223] F. Deppisch, T. S. Kosmas, J. W. F. Valle, Enhanced μ - e conversion in nuclei in the inverse seesaw model, *Nucl. Phys. B* 752 (2006) 80–92. [arXiv:hep-ph/0512360](#), [doi:10.1016/j.nuclphysb.2006.06.032](#).
- [224] A. Ilakovac, A. Pilaftsis, Flavor violating charged lepton decays in seesaw-type models, *Nucl. Phys. B* 437 (1995) 491. [arXiv:hep-ph/9403398](#), [doi:10.1016/0550-3213\(94\)00567-X](#).
- [225] E. Arganda, M. J. Herrero, A. M. Teixeira, μ - e conversion in nuclei within the CMSSM seesaw: Universality versus non-universality, *JHEP* 10 (2007) 104. [arXiv:0707.2955](#), [doi:10.1088/1126-6708/2007/10/104](#).
- [226] A. Abada, V. De Romeri, S. Monteil, J. Orloff, A. M. Teixeira, Indirect searches for sterile neutrinos at a high-luminosity Z-factory, *JHEP* 04 (2015) 051. [arXiv:1412.6322](#), [doi:10.1007/JHEP04\(2015\)051](#).

- [227] A. Abada, M. Lucente, Looking for the minimal inverse seesaw realisation, Nucl. Phys. B 885 (2014) 651–678. [arXiv:1401.1507](#), [doi:10.1016/j.nuclphysb.2014.06.003](#).
- [228] A. Abada, V. De Romeri, A. M. Teixeira, Impact of sterile neutrinos on nuclear-assisted cLFV processes, JHEP 02 (2016) 083. [arXiv:1510.06657](#), [doi:10.1007/JHEP02\(2016\)083](#).
- [229] E. K. Akhmedov, M. Lindner, E. Schnapka, J. W. F. Valle, Dynamical left-right symmetry breaking, Phys. Rev. D 53 (1996) 2752–2780. [arXiv:hep-ph/9509255](#), [doi:10.1103/PhysRevD.53.2752](#).
- [230] E. K. Akhmedov, M. Lindner, E. Schnapka, J. W. F. Valle, Left-right symmetry breaking in NJL approach, Phys. Lett. B 368 (1996) 270–280. [arXiv:hep-ph/9507275](#), [doi:10.1016/0370-2693\(95\)01504-3](#).
- [231] M. Malinsky, J. C. Romao, J. W. F. Valle, Novel supersymmetric SO(10) seesaw mechanism, Phys. Rev. Lett. 95 (2005) 161801. [arXiv:hep-ph/0506296](#), [doi:10.1103/PhysRevLett.95.161801](#).
- [232] W.-Y. Keung, G. Senjanovic, Majorana Neutrinos and the Production of the Right-handed Charged Gauge Boson, Phys. Rev. Lett. 50 (1983) 1427. [doi:10.1103/PhysRevLett.50.1427](#).
- [233] M. Dittmar, A. Santamaria, M. C. Gonzalez-Garcia, J. W. F. Valle, Production Mechanisms and Signatures of Isosinglet Neutral Heavy Leptons in Z^0 Decays, Nucl. Phys. B 332 (1990) 1–19. [doi:10.1016/0550-3213\(90\)90028-C](#).
- [234] M. C. Gonzalez-Garcia, A. Santamaria, J. W. F. Valle, Isosinglet Neutral Heavy Lepton Production in Z Decays and Neutrino Mass, Nucl. Phys. B 342 (1990) 108–126. [doi:10.1016/0550-3213\(90\)90573-V](#).
- [235] J. A. Aguilar-Saavedra, F. Deppisch, O. Kittel, J. W. F. Valle, Flavour in heavy neutrino searches at the LHC, Phys. Rev. D 85 (2012) 091301. [arXiv:1203.5998](#), [doi:10.1103/PhysRevD.85.091301](#).
- [236] S. P. Das, F. F. Deppisch, O. Kittel, J. W. F. Valle, Heavy Neutrinos and Lepton Flavour Violation in Left-Right Symmetric Models at the LHC, Phys. Rev. D 86 (2012) 055006. [arXiv:1206.0256](#), [doi:10.1103/PhysRevD.86.055006](#).
- [237] F. F. Deppisch, N. Desai, J. W. F. Valle, Is charged lepton flavor violation a high energy phenomenon?, Phys. Rev. D 89 (5) (2014) 051302. [arXiv:1308.6789](#), [doi:10.1103/PhysRevD.89.051302](#).
- [238] G. Aad, et al., Search for heavy neutral leptons in decays of W bosons produced in 13 TeV pp collisions using prompt and displaced signatures with the ATLAS detector, JHEP 10 (2019) 265. [arXiv:1905.09787](#), [doi:10.1007/JHEP10\(2019\)265](#).
- [239] A. M. Sirunyan, et al., Search for heavy neutral leptons in events with three charged leptons in proton-proton collisions at $\sqrt{s} = 13$ TeV, Phys. Rev. Lett. 120 (22) (2018) 221801. [arXiv:1802.02965](#), [doi:10.1103/PhysRevLett.120.221801](#).
- [240] A. Tumasyan, et al., Inclusive nonresonant multilepton probes of new phenomena at $\sqrt{s}=13$ TeV, Phys. Rev. D 105 (11) (2022) 112007. [arXiv:2202.08676](#), [doi:10.1103/PhysRevD.105.112007](#).
- [241] A. Abada, et al., FCC-ee: The Lepton Collider: Future Circular Collider Conceptual Design Report Volume 2, Eur. Phys. J. ST 228 (2) (2019) 261–623. [doi:10.1140/epjst/e2019-900045-4](#).
- [242] J. L. Feng, et al., The Forward Physics Facility at the High-Luminosity LHC, J. Phys. G 50 (3) (2023) 030501. [arXiv:2203.05090](#), [doi:10.1088/1361-6471/ac865e](#).
- [243] A. M. Abdullahi, et al., The present and future status of heavy neutral leptons, J. Phys. G 50 (2) (2023) 020501. [arXiv:2203.08039](#), [doi:10.1088/1361-6471/ac98f9](#).

- [244] J. C. Helo, M. Hirsch, S. Kovalenko, Heavy neutrino searches at the LHC with displaced vertices, Phys. Rev. D 89 (2014) 073005, [Erratum: Phys.Rev.D 93, 099902 (2016)]. [arXiv:1312.2900](#), [doi:10.1103/PhysRevD.89.073005](#).
- [245] M. Drewes, J. Hajer, Heavy Neutrinos in displaced vertex searches at the LHC and HL-LHC, JHEP 02 (2020) 070. [arXiv:1903.06100](#), [doi:10.1007/JHEP02\(2020\)070](#).
- [246] R. Beltrán, G. Cottin, J. C. Helo, M. Hirsch, A. Titov, Z. S. Wang, Long-lived heavy neutral leptons at the LHC: four-fermion single- N_R operators, JHEP 01 (2022) 044. [arXiv:2110.15096](#), [doi:10.1007/JHEP01\(2022\)044](#).
- [247] A. Datta, B. Mukhopadhyaya, F. Vissani, Tevatron signatures of an R-parity violating supersymmetric theory, Phys. Lett. B 492 (2000) 324–330. [arXiv:hep-ph/9910296](#), [doi:10.1016/S0370-2693\(00\)01104-7](#).
- [248] W. Porod, M. Hirsch, J. Romao, J. W. F. Valle, Testing neutrino mixing at future collider experiments, Phys. Rev. D 63 (2001) 115004. [arXiv:hep-ph/0011248](#), [doi:10.1103/PhysRevD.63.115004](#).
- [249] F. de Campos, O. J. P. Eboli, M. B. Magro, W. Porod, D. Restrepo, J. W. F. Valle, Probing neutrino mass with displaced vertices at the Tevatron, Phys. Rev. D 71 (2005) 075001. [arXiv:hep-ph/0501153](#), [doi:10.1103/PhysRevD.71.075001](#).
- [250] A. D. Sakharov, Violation of CP Invariance, C asymmetry, and baryon asymmetry of the universe, Pisma Zh. Eksp. Teor. Fiz. 5 (1967) 32–35. [doi:10.1070/PU1991v034n05ABEH002497](#).
- [251] M. Fukugita, T. Yanagida, Baryogenesis Without Grand Unification, Phys. Lett. B 174 (1986) 45–47. [doi:10.1016/0370-2693\(86\)91126-3](#).
- [252] P. F. Harrison, W. G. Scott, Symmetries and generalizations of tri - bimaximal neutrino mixing, Phys. Lett. B 535 (2002) 163–169. [arXiv:hep-ph/0203209](#), [doi:10.1016/S0370-2693\(02\)01753-7](#).
- [253] P. F. Harrison, W. G. Scott, μ - τ reflection symmetry in lepton mixing and neutrino oscillations, Phys. Lett. B 547 (2002) 219–228. [arXiv:hep-ph/0210197](#), [doi:10.1016/S0370-2693\(02\)02772-7](#).
- [254] W. Grimus, L. Lavoura, A Nonstandard CP transformation leading to maximal atmospheric neutrino mixing, Phys. Lett. B 579 (2004) 113–122. [arXiv:hep-ph/0305309](#), [doi:10.1016/j.physletb.2003.10.075](#).
- [255] P. F. Harrison, W. G. Scott, The Simplest neutrino mass matrix, Phys. Lett. B 594 (2004) 324–332. [arXiv:hep-ph/0403278](#), [doi:10.1016/j.physletb.2004.05.039](#).
- [256] Y. Farzan, A. Y. Smirnov, Leptonic CP violation: Zero, maximal or between the two extremes, JHEP 01 (2007) 059. [arXiv:hep-ph/0610337](#), [doi:10.1088/1126-6708/2007/01/059](#).
- [257] P. Chen, G.-J. Ding, F. Gonzalez-Canales, J. W. F. Valle, Generalized $\mu - \tau$ reflection symmetry and leptonic CP violation, Phys. Lett. B 753 (2016) 644–652. [arXiv:1512.01551](#), [doi:10.1016/j.physletb.2015.12.069](#).
- [258] P. Chen, S. Centelles Chuliá, G.-J. Ding, R. Srivastava, J. W. F. Valle, Neutrino Predictions from Generalized CP Symmetries of Charged Leptons, JHEP 07 (2018) 077. [arXiv:1802.04275](#), [doi:10.1007/JHEP07\(2018\)077](#).
- [259] R. de Adelhart Toorop, F. Feruglio, C. Hagedorn, Finite Modular Groups and Lepton Mixing, Nucl. Phys. B 858 (2012) 437–467. [arXiv:1112.1340](#), [doi:10.1016/j.nuclphysb.2012.01.017](#).

- [260] M. Holthausen, K. S. Lim, M. Lindner, Lepton Mixing Patterns from a Scan of Finite Discrete Groups, *Phys. Lett. B* 721 (2013) 61–67. [arXiv:1212.2411](#), [doi:10.1016/j.physletb.2013.02.047](#).
- [261] R. M. Fonseca, W. Grimus, Classification of lepton mixing matrices from finite residual symmetries, *JHEP* 09 (2014) 033. [arXiv:1405.3678](#), [doi:10.1007/JHEP09\(2014\)033](#).
- [262] J. Talbert, [Re]constructing Finite Flavour Groups: Horizontal Symmetry Scans from the Bottom-Up, *JHEP* 12 (2014) 058. [arXiv:1409.7310](#), [doi:10.1007/JHEP12\(2014\)058](#).
- [263] C.-Y. Yao, G.-J. Ding, Lepton and Quark Mixing Patterns from Finite Flavor Symmetries, *Phys. Rev. D* 92 (9) (2015) 096010. [arXiv:1505.03798](#), [doi:10.1103/PhysRevD.92.096010](#).
- [264] F. Feruglio, C. Hagedorn, R. Ziegler, Lepton Mixing Parameters from Discrete and CP Symmetries, *JHEP* 07 (2013) 027. [arXiv:1211.5560](#), [doi:10.1007/JHEP07\(2013\)027](#).
- [265] P. Chen, C.-C. Li, G.-J. Ding, Lepton Flavor Mixing and CP Symmetry, *Phys. Rev. D* 91 (2015) 033003. [arXiv:1412.8352](#), [doi:10.1103/PhysRevD.91.033003](#).
- [266] L. L. Everett, T. Garon, A. J. Stuart, A Bottom-Up Approach to Lepton Flavor and CP Symmetries, *JHEP* 04 (2015) 069. [arXiv:1501.04336](#), [doi:10.1007/JHEP04\(2015\)069](#).
- [267] P. Chen, C.-Y. Yao, G.-J. Ding, Neutrino Mixing from CP Symmetry, *Phys. Rev. D* 92 (7) (2015) 073002. [arXiv:1507.03419](#), [doi:10.1103/PhysRevD.92.073002](#).
- [268] L. L. Everett, A. J. Stuart, Lepton Sector Phases and Their Roles in Flavor and Generalized CP Symmetries, *Phys. Rev. D* 96 (3) (2017) 035030. [arXiv:1611.03020](#), [doi:10.1103/PhysRevD.96.035030](#).
- [269] C. S. Lam, Determining Horizontal Symmetry from Neutrino Mixing, *Phys. Rev. Lett.* 101 (2008) 121602. [arXiv:0804.2622](#), [doi:10.1103/PhysRevLett.101.121602](#).
- [270] C. S. Lam, Symmetry of Lepton Mixing, *Phys. Lett. B* 656 (2007) 193–198. [arXiv:0708.3665](#), [doi:10.1016/j.physletb.2007.09.032](#).
- [271] C. S. Lam, Group Theory and Dynamics of Neutrino Mixing, *Phys. Rev. D* 83 (2011) 113002. [arXiv:1104.0055](#), [doi:10.1103/PhysRevD.83.113002](#).
- [272] C. S. Lam, Horizontal Symmetry: Bottom Up and Top Down [arXiv:1105.5166](#).
- [273] S. Antusch, I. de Medeiros Varzielas, V. Maurer, C. Sluka, M. Spinrath, Towards predictive flavour models in SUSY SU(5) GUTs with doublet-triplet splitting, *JHEP* 09 (2014) 141. [arXiv:1405.6962](#), [doi:10.1007/JHEP09\(2014\)141](#).
- [274] F. Björkeröth, F. J. de Anda, I. de Medeiros Varzielas, S. F. King, Towards a complete $A_4 \times SU(5)$ SUSY GUT, *JHEP* 06 (2015) 141. [arXiv:1503.03306](#), [doi:10.1007/JHEP06\(2015\)141](#).
- [275] M. Reig, J. W. F. Valle, C. A. Vaquera-Araujo, F. Wilczek, A Model of Comprehensive Unification, *Phys. Lett. B* 774 (2017) 667–670. [arXiv:1706.03116](#), [doi:10.1016/j.physletb.2017.10.038](#).
- [276] C. D. Froggatt, H. B. Nielsen, Hierarchy of Quark Masses, Cabibbo Angles and CP Violation, *Nucl. Phys. B* 147 (1979) 277–298. [doi:10.1016/0550-3213\(79\)90316-X](#).
- [277] R. Barbieri, G. R. Dvali, L. J. Hall, Predictions from a U(2) flavor symmetry in supersymmetric theories, *Phys. Lett. B* 377 (1996) 76–82. [arXiv:hep-ph/9512388](#), [doi:10.1016/0370-2693\(96\)00318-8](#).

- [278] A. Blum, C. Hagedorn, M. Lindner, Fermion Masses and Mixings from Dihedral Flavor Symmetries with Preserved Subgroups, *Phys. Rev. D* 77 (2008) 076004. [arXiv:0709.3450](#), [doi:10.1103/PhysRevD.77.076004](#).
- [279] M. Holthausen, K. S. Lim, Quark and Leptonic Mixing Patterns from the Breakdown of a Common Discrete Flavor Symmetry, *Phys. Rev. D* 88 (2013) 033018. [arXiv:1306.4356](#), [doi:10.1103/PhysRevD.88.033018](#).
- [280] T. Araki, H. Ishida, H. Ishimori, T. Kobayashi, A. Ogasahara, CKM matrix and flavor symmetries, *Phys. Rev. D* 88 (2013) 096002. [arXiv:1309.4217](#), [doi:10.1103/PhysRevD.88.096002](#).
- [281] I. de Medeiros Varzielas, R. W. Rasmussen, J. Talbert, Bottom-Up Discrete Symmetries for Cabibbo Mixing, *Int. J. Mod. Phys. A* 32 (06n07) (2017) 1750047. [arXiv:1605.03581](#), [doi:10.1142/S0217751X17500476](#).
- [282] C.-C. Li, J.-N. Lu, G.-J. Ding, Toward a unified interpretation of quark and lepton mixing from flavor and CP symmetries, *JHEP* 02 (2018) 038. [arXiv:1706.04576](#), [doi:10.1007/JHEP02\(2018\)038](#).
- [283] J.-N. Lu, G.-J. Ding, Quark and lepton mixing patterns from a common discrete flavor symmetry with a generalized CP symmetry, *Phys. Rev. D* 98 (5) (2018) 055011. [arXiv:1806.02301](#), [doi:10.1103/PhysRevD.98.055011](#).
- [284] J.-N. Lu, G.-J. Ding, Dihedral flavor group as the key to understand quark and lepton flavor mixing, *JHEP* 03 (2019) 056. [arXiv:1901.07414](#), [doi:10.1007/JHEP03\(2019\)056](#).
- [285] C. Hagedorn, J. König, Lepton and quark mixing from a stepwise breaking of flavor and CP , *Phys. Rev. D* 100 (7) (2019) 075036. [arXiv:1811.07750](#), [doi:10.1103/PhysRevD.100.075036](#).
- [286] C. Hagedorn, J. König, Lepton and quark masses and mixing in a SUSY model with $\Delta(384)$ and CP, *Nucl. Phys. B* 953 (2020) 114953. [arXiv:1811.09262](#), [doi:10.1016/j.nuclphysb.2020.114953](#).
- [287] M. Reig, J. W. F. Valle, F. Wilczek, $SO(3)$ family symmetry and axions, *Phys. Rev. D* 98 (9) (2018) 095008. [arXiv:1805.08048](#), [doi:10.1103/PhysRevD.98.095008](#).
- [288] S. Morisi, E. Peinado, Y. Shimizu, J. W. F. Valle, Relating quarks and leptons without grand-unification, *Phys. Rev. D* 84 (2011) 036003. [arXiv:1104.1633](#), [doi:10.1103/PhysRevD.84.036003](#).
- [289] C. Bonilla, S. Morisi, E. Peinado, J. W. F. Valle, Relating quarks and leptons with the T_7 flavour group, *Phys. Lett. B* 742 (2015) 99–106. [arXiv:1411.4883](#), [doi:10.1016/j.physletb.2015.01.017](#).
- [290] C. Bonilla, J. M. Lamprea, E. Peinado, J. W. F. Valle, Flavour-symmetric type-II Dirac neutrino seesaw mechanism, *Phys. Lett. B* 779 (2018) 257–261. [arXiv:1710.06498](#), [doi:10.1016/j.physletb.2018.02.022](#).
- [291] M.-C. Chen, S. F. King, O. Medina, J. W. F. Valle, Quark-lepton mass relations from modular flavor symmetry [arXiv:2312.09255](#).
- [292] F. J. de Anda, S. F. King, An $S_4 \times SU(5)$ SUSY GUT of flavour in 6d, *JHEP* 07 (2018) 057. [arXiv:1803.04978](#), [doi:10.1007/JHEP07\(2018\)057](#).
- [293] F. J. de Anda, S. F. King, $SU(3) \times SO(10)$ in 6d, *JHEP* 10 (2018) 128. [arXiv:1807.07078](#), [doi:10.1007/JHEP10\(2018\)128](#).
- [294] F. J. de Anda, I. Antoniadis, J. W. F. Valle, C. A. Vaquera-Araujo, Scotogenic dark matter in an orbifold theory of flavor, *JHEP* 10 (2020) 190. [arXiv:2007.10402](#), [doi:10.1007/JHEP10\(2020\)190](#).
- [295] F. J. de Anda, O. Medina, J. W. F. Valle, C. A. Vaquera-Araujo, Scotogenic Majorana neutrino masses in a predictive orbifold theory of flavor, *Phys. Rev. D* 105 (5) (2022) 055030. [arXiv:2110.06810](#), [doi:10.1103/PhysRevD.105.055030](#).

- [296] P. F. Harrison, D. H. Perkins, W. G. Scott, Tri-bimaximal mixing and the neutrino oscillation data, Phys. Lett. B 530 (2002) 167. [arXiv:hep-ph/0202074](#), [doi:10.1016/S0370-2693\(02\)01336-9](#).
- [297] Z.-z. Xing, Nearly tri bimaximal neutrino mixing and CP violation, Phys. Lett. B 533 (2002) 85–93. [arXiv:hep-ph/0204049](#), [doi:10.1016/S0370-2693\(02\)01649-0](#).
- [298] X. G. He, A. Zee, Some simple mixing and mass matrices for neutrinos, Phys. Lett. B 560 (2003) 87–90. [arXiv:hep-ph/0301092](#), [doi:10.1016/S0370-2693\(03\)00390-3](#).
- [299] S. Luo, Z.-z. Xing, Generalized tri-bimaximal neutrino mixing and its sensitivity to radiative corrections, Phys. Lett. B 632 (2006) 341–348. [arXiv:hep-ph/0509065](#), [doi:10.1016/j.physletb.2005.10.068](#).
- [300] F. Plentinger, W. Rodejohann, Deviations from tribimaximal neutrino mixing, Phys. Lett. B 625 (2005) 264–276. [arXiv:hep-ph/0507143](#), [doi:10.1016/j.physletb.2005.08.092](#).
- [301] M. Hirsch, E. Ma, J. C. Romao, J. W. F. Valle, A. Villanova del Moral, Minimal supergravity radiative effects on the tri-bimaximal neutrino mixing pattern, Phys. Rev. D 75 (2007) 053006. [arXiv:hep-ph/0606082](#), [doi:10.1103/PhysRevD.75.053006](#).
- [302] P. Wilina, M. S. Singh, N. N. Singh, Deviations from tribimaximal and golden ratio mixings under radiative corrections of neutrino masses and mixings, Int. J. Mod. Phys. A 37 (25) (2022) 2250156. [arXiv:2205.01936](#), [doi:10.1142/S0217751X22501561](#).
- [303] F. P. An, et al., Improved Measurement of Electron Antineutrino Disappearance at Daya Bay, Chin. Phys. C 37 (2013) 011001. [arXiv:1210.6327](#), [doi:10.1088/1674-1137/37/1/011001](#).
- [304] F. P. An, et al., Spectral measurement of electron antineutrino oscillation amplitude and frequency at Daya Bay, Phys. Rev. Lett. 112 (2014) 061801. [arXiv:1310.6732](#), [doi:10.1103/PhysRevLett.112.061801](#).
- [305] K. Luk, [Daya-bay talk on final 3158-day data](#) (International Conference on Neutrino Physics and Astrophysics, 2022).
URL <https://neutrino2022.org/>
- [306] F. P. An, et al., Precision Measurement of Reactor Antineutrino Oscillation at Kilometer-Scale Baselines by Daya Bay, Phys. Rev. Lett. 130 (16) (2023) 161802. [arXiv:2211.14988](#), [doi:10.1103/PhysRevLett.130.161802](#).
- [307] T. Fukuyama, H. Nishiura, Mass matrix of Majorana neutrinos [arXiv:hep-ph/9702253](#).
- [308] E. Ma, M. Raidal, Neutrino mass, muon anomalous magnetic moment, and lepton flavor nonconservation, Phys. Rev. Lett. 87 (2001) 011802, [Erratum: Phys.Rev.Lett. 87, 159901 (2001)]. [arXiv:hep-ph/0102255](#), [doi:10.1103/PhysRevLett.87.011802](#).
- [309] K. R. S. Balaji, W. Grimus, T. Schwetz, The Solar LMA neutrino oscillation solution in the Zee model, Phys. Lett. B 508 (2001) 301–310. [arXiv:hep-ph/0104035](#), [doi:10.1016/S0370-2693\(01\)00532-9](#).
- [310] C. S. Lam, A 2-3 symmetry in neutrino oscillations, Phys. Lett. B 507 (2001) 214–218. [arXiv:hep-ph/0104116](#), [doi:10.1016/S0370-2693\(01\)00465-8](#).
- [311] W. Grimus, L. Lavoura, Softly broken lepton numbers and maximal neutrino mixing, JHEP 07 (2001) 045. [arXiv:hep-ph/0105212](#), [doi:10.1088/1126-6708/2001/07/045](#).
- [312] C. S. Lam, Magic neutrino mass matrix and the Bjorken-Harrison-Scott parameterization, Phys. Lett. B 640 (2006) 260–262. [arXiv:hep-ph/0606220](#), [doi:10.1016/j.physletb.2006.08.007](#).

- [313] G. Altarelli, F. Feruglio, Tri-bimaximal neutrino mixing, A_4 and the modular symmetry, Nucl. Phys. B 741 (2006) 215–235. [arXiv:hep-ph/0512103](#), [doi:10.1016/j.nuclphysb.2006.02.015](#).
- [314] G. Altarelli, F. Feruglio, Y. Lin, Tri-bimaximal neutrino mixing from orbifolding, Nucl. Phys. B 775 (2007) 31–44. [arXiv:hep-ph/0610165](#), [doi:10.1016/j.nuclphysb.2007.03.042](#).
- [315] G. Altarelli, F. Feruglio, L. Merlo, Tri-Bimaximal Neutrino Mixing and Discrete Flavour Symmetries, Fortsch. Phys. 61 (2013) 507–534. [arXiv:1205.5133](#), [doi:10.1002/prop.201200117](#).
- [316] C. H. Albright, W. Rodejohann, Comparing Trimaximal Mixing and Its Variants with Deviations from Tri-bimaximal Mixing, Eur. Phys. J. C 62 (2009) 599–608. [arXiv:0812.0436](#), [doi:10.1140/epjc/s10052-009-1074-3](#).
- [317] C. H. Albright, A. Dueck, W. Rodejohann, Possible Alternatives to Tri-bimaximal Mixing, Eur. Phys. J. C 70 (2010) 1099–1110. [arXiv:1004.2798](#), [doi:10.1140/epjc/s10052-010-1492-2](#).
- [318] X.-G. He, A. Zee, Minimal Modification to Tri-bimaximal Mixing, Phys. Rev. D 84 (2011) 053004. [arXiv:1106.4359](#), [doi:10.1103/PhysRevD.84.053004](#).
- [319] C. Luhn, Trimaximal TM_1 neutrino mixing in S_4 with spontaneous CP violation, Nucl. Phys. B 875 (2013) 80–100. [arXiv:1306.2358](#), [doi:10.1016/j.nuclphysb.2013.07.003](#).
- [320] C.-C. Li, G.-J. Ding, Generalised CP and trimaximal TM_1 lepton mixing in S_4 family symmetry, Nucl. Phys. B 881 (2014) 206–232. [arXiv:1312.4401](#), [doi:10.1016/j.nuclphysb.2014.02.002](#).
- [321] J. D. Bjorken, P. F. Harrison, W. G. Scott, Simplified unitarity triangles for the lepton sector, Phys. Rev. D 74 (2006) 073012. [arXiv:hep-ph/0511201](#), [doi:10.1103/PhysRevD.74.073012](#).
- [322] X.-G. He, A. Zee, Minimal modification to the tri-bimaximal neutrino mixing, Phys. Lett. B 645 (2007) 427–431. [arXiv:hep-ph/0607163](#), [doi:10.1016/j.physletb.2006.11.055](#).
- [323] W. Grimus, L. Lavoura, A Model for trimaximal lepton mixing, JHEP 09 (2008) 106. [arXiv:0809.0226](#), [doi:10.1088/1126-6708/2008/09/106](#).
- [324] W. Grimus, L. Lavoura, A. Singraber, Trimaximal lepton mixing with a trivial Dirac phase, Phys. Lett. B 686 (2010) 141–145. [arXiv:0911.5120](#), [doi:10.1016/j.physletb.2010.02.032](#).
- [325] G.-J. Ding, S. F. King, C. Luhn, A. J. Stuart, Spontaneous CP violation from vacuum alignment in S_4 models of leptons, JHEP 05 (2013) 084. [arXiv:1303.6180](#), [doi:10.1007/JHEP05\(2013\)084](#).
- [326] W. Rodejohann, Unified Parametrization for Quark and Lepton Mixing Angles, Phys. Lett. B 671 (2009) 267–271. [arXiv:0810.5239](#), [doi:10.1016/j.physletb.2008.12.010](#).
- [327] A. Adulpravitchai, A. Blum, W. Rodejohann, Golden Ratio Prediction for Solar Neutrino Mixing, New J. Phys. 11 (2009) 063026. [arXiv:0903.0531](#), [doi:10.1088/1367-2630/11/6/063026](#).
- [328] A. Datta, F.-S. Ling, P. Ramond, Correlated hierarchy, Dirac masses and large mixing angles, Nucl. Phys. B 671 (2003) 383–400. [arXiv:hep-ph/0306002](#), [doi:10.1016/j.nuclphysb.2003.08.026](#).
- [329] Y. Kajiyama, M. Raidal, A. Strumia, The Golden ratio prediction for the solar neutrino mixing, Phys. Rev. D 76 (2007) 117301. [arXiv:0705.4559](#), [doi:10.1103/PhysRevD.76.117301](#).
- [330] L. L. Everett, A. J. Stuart, Icosahedral ($A(5)$) Family Symmetry and the Golden Ratio Prediction for Solar Neutrino Mixing, Phys. Rev. D 79 (2009) 085005. [arXiv:0812.1057](#), [doi:10.1103/PhysRevD.79.085005](#).

- [331] F. Feruglio, A. Paris, The Golden Ratio Prediction for the Solar Angle from a Natural Model with A_5 Flavour Symmetry, *JHEP* 03 (2011) 101. [arXiv:1101.0393](#), [doi:10.1007/JHEP03\(2011\)101](#).
- [332] G.-J. Ding, L. L. Everett, A. J. Stuart, Golden Ratio Neutrino Mixing and A_5 Flavor Symmetry, *Nucl. Phys. B* 857 (2012) 219–253. [arXiv:1110.1688](#), [doi:10.1016/j.nuclphysb.2011.12.004](#).
- [333] V. D. Barger, S. Pakvasa, T. J. Weiler, K. Whisnant, Bimaximal mixing of three neutrinos, *Phys. Lett. B* 437 (1998) 107–116. [arXiv:hep-ph/9806387](#), [doi:10.1016/S0370-2693\(98\)00880-6](#).
- [334] G. Altarelli, F. Feruglio, L. Merlo, Revisiting Bimaximal Neutrino Mixing in a Model with $S(4)$ Discrete Symmetry, *JHEP* 05 (2009) 020. [arXiv:0903.1940](#), [doi:10.1088/1126-6708/2009/05/020](#).
- [335] C.-C. Li, G.-J. Ding, Deviation from bimaximal mixing and leptonic CP phases in S_4 family symmetry and generalized CP, *JHEP* 08 (2015) 017. [arXiv:1408.0785](#), [doi:10.1007/JHEP08\(2015\)017](#).
- [336] R. de Adelhart Toorop, F. Feruglio, C. Hagedorn, Discrete Flavour Symmetries in Light of T2K, *Phys. Lett. B* 703 (2011) 447–451. [arXiv:1107.3486](#), [doi:10.1016/j.physletb.2011.08.013](#).
- [337] G.-J. Ding, TFH Mixing Patterns, Large θ_{13} and $\Delta(96)$ Flavor Symmetry, *Nucl. Phys. B* 862 (2012) 1–42. [arXiv:1201.3279](#), [doi:10.1016/j.nuclphysb.2012.04.002](#).
- [338] C. Hagedorn, A. Meroni, L. Vitale, Mixing patterns from the groups $\Sigma(n\phi)$, *J. Phys. A* 47 (2014) 055201. [arXiv:1307.5308](#), [doi:10.1088/1751-8113/47/5/055201](#).
- [339] G. Ecker, W. Grimus, W. Konetschny, Quark Mass Matrices in Left-right Symmetric Gauge Theories, *Nucl. Phys. B* 191 (1981) 465–492. [doi:10.1016/0550-3213\(81\)90309-6](#).
- [340] G. Ecker, W. Grimus, H. Neufeld, Spontaneous CP Violation in Left-right Symmetric Gauge Theories, *Nucl. Phys. B* 247 (1984) 70–82. [doi:10.1016/0550-3213\(84\)90373-0](#).
- [341] J. Bernabeu, G. C. Branco, M. Gronau, CP Restrictions on Quark Mass Matrices, *Phys. Lett. B* 169 (1986) 243–247. [doi:10.1016/0370-2693\(86\)90659-3](#).
- [342] G. Ecker, W. Grimus, H. Neufeld, A Standard Form for Generalized CP Transformations, *J. Phys. A* 20 (1987) L807. [doi:10.1088/0305-4470/20/12/010](#).
- [343] H. Neufeld, W. Grimus, G. Ecker, Generalized CP Invariance, Neutral Flavor Conservation and the Structure of the Mixing Matrix, *Int. J. Mod. Phys. A* 3 (1988) 603–616. [doi:10.1142/S0217751X88000254](#).
- [344] M. Holthausen, M. Lindner, M. A. Schmidt, CP and Discrete Flavour Symmetries, *JHEP* 04 (2013) 122. [arXiv:1211.6953](#), [doi:10.1007/JHEP04\(2013\)122](#).
- [345] C.-Y. Yao, G.-J. Ding, CP Symmetry and Lepton Mixing from a Scan of Finite Discrete Groups, *Phys. Rev. D* 94 (7) (2016) 073006. [arXiv:1606.05610](#), [doi:10.1103/PhysRevD.94.073006](#).
- [346] A. Abada, G. Arcadi, V. Domcke, M. Drewes, J. Klarić, M. Lucente, Low-scale leptogenesis with three heavy neutrinos, *JHEP* 01 (2019) 164. [arXiv:1810.12463](#), [doi:10.1007/JHEP01\(2019\)164](#).
- [347] M. Drewes, Y. Georis, J. Klarić, Mapping the Viable Parameter Space for Testable Leptogenesis, *Phys. Rev. Lett.* 128 (5) (2022) 051801. [arXiv:2106.16226](#), [doi:10.1103/PhysRevLett.128.051801](#).
- [348] C.-C. Li, G.-J. Ding, Implications of residual CP symmetry for leptogenesis in a model with two right-handed neutrinos, *Phys. Rev. D* 96 (7) (2017) 075005. [arXiv:1701.08508](#), [doi:10.1103/PhysRevD.96.075005](#).

- [349] A. S. Joshipura, K. M. Patel, Horizontal symmetries of leptons with a massless neutrino, *Phys. Lett. B* 727 (2013) 480–487. [arXiv:1306.1890](#), [doi:10.1016/j.physletb.2013.11.003](#).
- [350] A. S. Joshipura, K. M. Patel, A massless neutrino and lepton mixing patterns from finite discrete subgroups of $U(3)$, *JHEP* 04 (2014) 009. [arXiv:1401.6397](#), [doi:10.1007/JHEP04\(2014\)009](#).
- [351] S. F. King, P. O. Ludl, Direct and Semi-Direct Approaches to Lepton Mixing with a Massless Neutrino, *JHEP* 06 (2016) 147. [arXiv:1605.01683](#), [doi:10.1007/JHEP06\(2016\)147](#).
- [352] R. Barbieri, L. J. Hall, S. Raby, A. Romanino, Unified theories with $U(2)$ flavor symmetry, *Nucl. Phys. B* 493 (1997) 3–26. [arXiv:hep-ph/9610449](#), [doi:10.1016/S0550-3213\(97\)00134-X](#).
- [353] R. Barbieri, L. J. Hall, A. Romanino, Consequences of a $U(2)$ flavor symmetry, *Phys. Lett. B* 401 (1997) 47–53. [arXiv:hep-ph/9702315](#), [doi:10.1016/S0370-2693\(97\)00372-9](#).
- [354] M. Linster, R. Ziegler, A Realistic $U(2)$ Model of Flavor, *JHEP* 08 (2018) 058. [arXiv:1805.07341](#), [doi:10.1007/JHEP08\(2018\)058](#).
- [355] S. F. King, Predicting neutrino parameters from $SO(3)$ family symmetry and quark-lepton unification, *JHEP* 08 (2005) 105. [arXiv:hep-ph/0506297](#), [doi:10.1088/1126-6708/2005/08/105](#).
- [356] S. F. King, M. Malinsky, Towards a Complete Theory of Fermion Masses and Mixings with $SO(3)$ Family Symmetry and 5-D $SO(10)$ Unification, *JHEP* 11 (2006) 071. [arXiv:hep-ph/0608021](#), [doi:10.1088/1126-6708/2006/11/071](#).
- [357] I. de Medeiros Varzielas, G. G. Ross, $SU(3)$ family symmetry and neutrino bi-tri-maximal mixing, *Nucl. Phys. B* 733 (2006) 31–47. [arXiv:hep-ph/0507176](#), [doi:10.1016/j.nuclphysb.2005.10.039](#).
- [358] S. Antusch, S. F. King, M. Malinsky, Solving the SUSY Flavour and CP Problems with $SU(3)$ Family Symmetry, *JHEP* 06 (2008) 068. [arXiv:0708.1282](#), [doi:10.1088/1126-6708/2008/06/068](#).
- [359] F. Bazzocchi, S. Morisi, M. Picariello, E. Torrente-Lujan, Embedding $A(4)$ into $SU(3) \times U(1)$ flavor symmetry: Large neutrino mixing and fermion mass hierarchy in $SO(10)$ GUT, *J. Phys. G* 36 (2009) 015002. [arXiv:0802.1693](#), [doi:10.1088/0954-3899/36/1/015002](#).
- [360] S. Weinberg, The Problem of Mass, *Trans. New York Acad. Sci.* 38 (1977) 185–201. [doi:10.1111/j.2164-0947.1977.tb02958.x](#).
- [361] H. Fritzsch, Calculating the Cabibbo Angle, *Phys. Lett. B* 70 (1977) 436–440. [doi:10.1016/0370-2693\(77\)90408-7](#).
- [362] H. Fritzsch, Weak Interaction Mixing in the Six - Quark Theory, *Phys. Lett. B* 73 (1978) 317–322. [doi:10.1016/0370-2693\(78\)90524-5](#).
- [363] P. H. Frampton, S. L. Glashow, D. Marfatia, Zeroes of the neutrino mass matrix, *Phys. Lett. B* 536 (2002) 79–82. [arXiv:hep-ph/0201008](#), [doi:10.1016/S0370-2693\(02\)01817-8](#).
- [364] P. Chen, G.-J. Ding, F. Gonzalez-Canales, J. W. F. Valle, Classifying CP transformations according to their texture zeros: theory and implications, *Phys. Rev. D* 94 (3) (2016) 033002. [arXiv:1604.03510](#), [doi:10.1103/PhysRevD.94.033002](#).
- [365] P. Chen, S. Centelles Chuliá, G.-J. Ding, R. Srivastava, J. W. F. Valle, CP symmetries as guiding posts: revamping tri-bi-maximal mixing. Part I, *JHEP* 03 (2019) 036. [arXiv:1812.04663](#), [doi:10.1007/JHEP03\(2019\)036](#).

- [366] S. Centelles Chuliá, A. Trautner, Asymmetric tri-bi-maximal mixing and residual symmetries, *Mod.Phys.Lett.A* 35 (35) (2020) 2050292. [arXiv:1911.12043](#), [doi:10.1142/S0217732320502922](#).
- [367] P. Chen, S. Centelles Chuliá, G.-J. Ding, R. Srivastava, J. W. F. Valle, Realistic tribimaximal neutrino mixing, *Phys. Rev. D* 98 (5) (2018) 055019. [arXiv:1806.03367](#), [doi:10.1103/PhysRevD.98.055019](#).
- [368] J. Schechter, J. W. F. Valle, Majorana Neutrinos and Magnetic Fields, *Phys. Rev. D* 24 (1981) 1883–1889, [Erratum: *Phys.Rev.D* 25, 283 (1982)]. [doi:10.1103/PhysRevD.25.283](#).
- [369] L. Wolfenstein, CP Properties of Majorana Neutrinos and Double beta Decay, *Phys. Lett. B* 107 (1981) 77–79. [doi:10.1016/0370-2693\(81\)91151-5](#).
- [370] P. Chen, S. Centelles Chuliá, G.-J. Ding, R. Srivastava, J. W. F. Valle, CP symmetries as guiding posts: Revamping tribimaximal mixing. II., *Phys. Rev. D* 100 (5) (2019) 053001. [arXiv:1905.11997](#), [doi:10.1103/PhysRevD.100.053001](#).
- [371] S. M. Boucenna, S. Morisi, M. Tortola, J. W. F. Valle, Bi-large neutrino mixing and the Cabibbo angle, *Phys. Rev. D* 86 (2012) 051301. [arXiv:1206.2555](#), [doi:10.1103/PhysRevD.86.051301](#).
- [372] G.-J. Ding, S. Morisi, J. W. F. Valle, Bilarge neutrino mixing and Abelian flavor symmetry, *Phys. Rev. D* 87 (5) (2013) 053013. [arXiv:1211.6506](#), [doi:10.1103/PhysRevD.87.053013](#).
- [373] S. Roy, S. Morisi, N. N. Singh, J. W. F. Valle, The Cabibbo angle as a universal seed for quark and lepton mixings, *Phys. Lett. B* 748 (2015) 1–4. [arXiv:1410.3658](#), [doi:10.1016/j.physletb.2015.06.052](#).
- [374] P. Chen, G.-J. Ding, R. Srivastava, J. W. F. Valle, Predicting neutrino oscillations with “bi-large” lepton mixing matrices, *Phys. Lett. B* 792 (2019) 461–464. [arXiv:1902.08962](#), [doi:10.1016/j.physletb.2019.04.022](#).
- [375] S. Roy, K. Sashikanta Singh, J. Borah, Revamped Bi-Large neutrino mixing with Gatto-Sartori-Tonin like relation, *Nucl. Phys. B* 960 (2020) 115204. [arXiv:2001.07401](#), [doi:10.1016/j.nuclphysb.2020.115204](#).
- [376] H. Ishimori, T. Kobayashi, H. Ohki, H. Okada, Y. Shimizu, M. Tanimoto, An introduction to non-Abelian discrete symmetries for particle physicists, Vol. 858, 2012. [doi:10.1007/978-3-642-30805-5](#).
- [377] Y. Abe, et al., Reactor electron antineutrino disappearance in the Double Chooz experiment, *Phys. Rev. D* 86 (2012) 052008. [arXiv:1207.6632](#), [doi:10.1103/PhysRevD.86.052008](#).
- [378] S. F. King, C. Luhn, On the origin of neutrino flavour symmetry, *JHEP* 10 (2009) 093. [arXiv:0908.1897](#), [doi:10.1088/1126-6708/2009/10/093](#).
- [379] S. F. King, T. Neder, A. J. Stuart, Lepton mixing predictions from $\Delta(6n^2)$ family Symmetry, *Phys. Lett. B* 726 (2013) 312–315. [arXiv:1305.3200](#), [doi:10.1016/j.physletb.2013.08.052](#).
- [380] S. F. King, T. Neder, Lepton mixing predictions including Majorana phases from $\Delta(6n^2)$ flavour symmetry and generalised CP, *Phys. Lett. B* 736 (2014) 308–316. [arXiv:1403.1758](#), [doi:10.1016/j.physletb.2014.07.043](#).
- [381] S.-F. Ge, D. A. Dicus, W. W. Repko, \mathbb{Z}_2 Symmetry Prediction for the Leptonic Dirac CP Phase, *Phys. Lett. B* 702 (2011) 220–223. [arXiv:1104.0602](#), [doi:10.1016/j.physletb.2011.06.096](#).
- [382] S.-F. Ge, D. A. Dicus, W. W. Repko, Residual Symmetries for Neutrino Mixing with a Large θ_{13} and Nearly Maximal δ_D , *Phys. Rev. Lett.* 108 (2012) 041801. [arXiv:1108.0964](#), [doi:10.1103/PhysRevLett.108.041801](#).

- [383] D. Hernandez, A. Y. Smirnov, Lepton mixing and discrete symmetries, Phys. Rev. D 86 (2012) 053014. [arXiv:1204.0445](#), [doi:10.1103/PhysRevD.86.053014](#).
- [384] D. Hernandez, A. Y. Smirnov, Discrete symmetries and model-independent patterns of lepton mixing, Phys. Rev. D 87 (5) (2013) 053005. [arXiv:1212.2149](#), [doi:10.1103/PhysRevD.87.053005](#).
- [385] W. Grimus, M. N. Rebelo, Automorphisms in gauge theories and the definition of CP and P, Phys. Rept. 281 (1997) 239–308. [arXiv:hep-ph/9506272](#), [doi:10.1016/S0370-1573\(96\)00030-0](#).
- [386] Z.-z. Xing, Z.-h. Zhao, A review of μ - τ flavor symmetry in neutrino physics, Rept. Prog. Phys. 79 (7) (2016) 076201. [arXiv:1512.04207](#), [doi:10.1088/0034-4885/79/7/076201](#).
- [387] M.-C. Chen, M. Fallbacher, K. T. Mahanthappa, M. Ratz, A. Trautner, CP Violation from Finite Groups, Nucl. Phys. B 883 (2014) 267–305. [arXiv:1402.0507](#), [doi:10.1016/j.nuclphysb.2014.03.023](#).
- [388] G.-J. Ding, S. F. King, A. J. Stuart, Generalised CP and A_4 Family Symmetry, JHEP 12 (2013) 006. [arXiv:1307.4212](#), [doi:10.1007/JHEP12\(2013\)006](#).
- [389] S. F. King, Littlest Seesaw, JHEP 02 (2016) 085. [arXiv:1512.07531](#), [doi:10.1007/JHEP02\(2016\)085](#).
- [390] G.-J. Ding, S. F. King, C.-C. Li, Tri-Direct CP in the Littlest Seesaw Playground, JHEP 12 (2018) 003. [arXiv:1807.07538](#), [doi:10.1007/JHEP12\(2018\)003](#).
- [391] G.-J. Ding, S. F. King, C.-C. Li, Lepton mixing predictions from S_4 in the tridirect CP approach to two right-handed neutrino models, Phys. Rev. D 99 (7) (2019) 075035. [arXiv:1811.12340](#), [doi:10.1103/PhysRevD.99.075035](#).
- [392] P.-T. Chen, G.-J. Ding, S. F. King, C.-C. Li, A New Littlest Seesaw Model, J. Phys. G 47 (6) (2020) 065001. [arXiv:1906.11414](#), [doi:10.1088/1361-6471/ab7e8d](#).
- [393] C.-C. Li, J.-N. Lu, G.-J. Ding, A_4 and CP symmetry and a model with maximal CP violation, Nucl. Phys. B 913 (2016) 110–131. [arXiv:1608.01860](#), [doi:10.1016/j.nuclphysb.2016.09.005](#).
- [394] F. Feruglio, C. Hagedorn, R. Ziegler, A realistic pattern of lepton mixing and masses from S_4 and CP, Eur. Phys. J. C 74 (2014) 2753. [arXiv:1303.7178](#), [doi:10.1140/epjc/s10052-014-2753-2](#).
- [395] J.-N. Lu, G.-J. Ding, Alternative Schemes of Predicting Lepton Mixing Parameters from Discrete Flavor and CP Symmetry, Phys. Rev. D 95 (1) (2017) 015012. [arXiv:1610.05682](#), [doi:10.1103/PhysRevD.95.015012](#).
- [396] J. T. Penedo, S. T. Petcov, A. V. Titov, Neutrino mixing and leptonic CP violation from S_4 flavour and generalised CP symmetries, JHEP 12 (2017) 022. [arXiv:1705.00309](#), [doi:10.1007/JHEP12\(2017\)022](#).
- [397] G. C. Branco, I. de Medeiros Varzielas, S. F. King, Invariant approach to CP in family symmetry models, Phys. Rev. D 92 (3) (2015) 036007. [arXiv:1502.03105](#), [doi:10.1103/PhysRevD.92.036007](#).
- [398] G. C. Branco, I. de Medeiros Varzielas, S. F. King, Invariant approach to \mathcal{CP} in unbroken $\Delta(27)$, Nucl. Phys. B 899 (2015) 14–36. [arXiv:1505.06165](#), [doi:10.1016/j.nuclphysb.2015.07.024](#).
- [399] G.-J. Ding, Y.-L. Zhou, Predicting lepton flavor mixing from $\Delta(48)$ and generalized \mathcal{CP} symmetries, Chin. Phys. C 39 (2) (2015) 021001. [arXiv:1312.5222](#), [doi:10.1088/1674-1137/39/2/021001](#).
- [400] G.-J. Ding, Y.-L. Zhou, Lepton mixing parameters from $\Delta(48)$ family symmetry and generalised CP, JHEP 06 (2014) 023. [arXiv:1404.0592](#), [doi:10.1007/JHEP06\(2014\)023](#).

- [401] C.-C. Li, G.-J. Ding, Lepton Mixing in A_5 Family Symmetry and Generalized CP, JHEP 05 (2015) 100. [arXiv:1503.03711](#), [doi:10.1007/JHEP05\(2015\)100](#).
- [402] A. Di Iura, C. Hagedorn, D. Meloni, Lepton mixing from the interplay of the alternating group A_5 and CP, JHEP 08 (2015) 037. [arXiv:1503.04140](#), [doi:10.1007/JHEP08\(2015\)037](#).
- [403] P. Ballett, S. Pascoli, J. Turner, Mixing angle and phase correlations from A_5 with generalized CP and their prospects for discovery, Phys. Rev. D 92 (9) (2015) 093008. [arXiv:1503.07543](#), [doi:10.1103/PhysRevD.92.093008](#).
- [404] J. Turner, Predictions for leptonic mixing angle correlations and nontrivial Dirac CP violation from A_5 with generalized CP symmetry, Phys. Rev. D 92 (11) (2015) 116007. [arXiv:1507.06224](#), [doi:10.1103/PhysRevD.92.116007](#).
- [405] A. Di Iura, M. L. López-Ibáñez, D. Meloni, Neutrino masses and lepton mixing from $A_5 \times CP$, Nucl. Phys. B 949 (2019) 114794. [arXiv:1811.09662](#), [doi:10.1016/j.nuclphysb.2019.114794](#).
- [406] G.-J. Ding, S. F. King, Generalized CP and $\Delta(96)$ family symmetry, Phys. Rev. D 89 (9) (2014) 093020. [arXiv:1403.5846](#), [doi:10.1103/PhysRevD.89.093020](#).
- [407] C. Hagedorn, A. Meroni, E. Molinaro, Lepton mixing from $\Delta(3n^2)$ and $\Delta(6n^2)$ and CP, Nucl. Phys. B 891 (2015) 499–557. [arXiv:1408.7118](#), [doi:10.1016/j.nuclphysb.2014.12.013](#).
- [408] G.-J. Ding, S. F. King, Generalized CP and $\Delta(3n^2)$ Family Symmetry for Semi-Direct Predictions of the PMNS Matrix, Phys. Rev. D 93 (2016) 025013. [arXiv:1510.03188](#), [doi:10.1103/PhysRevD.93.025013](#).
- [409] G.-J. Ding, S. F. King, T. Neder, Generalised CP and $\Delta(6n^2)$ family symmetry in semi-direct models of leptons, JHEP 12 (2014) 007. [arXiv:1409.8005](#), [doi:10.1007/JHEP12\(2014\)007](#).
- [410] C.-C. Li, C.-Y. Yao, G.-J. Ding, Lepton Mixing Predictions from Infinite Group Series $D_{9n,3n}^{(1)}$ with Generalized CP, JHEP 05 (2016) 007. [arXiv:1601.06393](#), [doi:10.1007/JHEP05\(2016\)007](#).
- [411] C. Jarlskog, Commutator of the Quark Mass Matrices in the Standard Electroweak Model and a Measure of Maximal CP Nonconservation, Phys. Rev. Lett. 55 (1985) 1039. [doi:10.1103/PhysRevLett.55.1039](#).
- [412] G. C. Branco, L. Lavoura, M. N. Rebelo, Majorana Neutrinos and CP Violation in the Leptonic Sector, Phys. Lett. B 180 (1986) 264–268. [doi:10.1016/0370-2693\(86\)90307-2](#).
- [413] J. F. Nieves, P. B. Pal, Minimal Rephasing Invariant CP Violating Parameters With Dirac and Majorana Fermions, Phys. Rev. D 36 (1987) 315. [doi:10.1103/PhysRevD.36.315](#).
- [414] T. D. Lee, A Theory of Spontaneous T Violation, Phys. Rev. D 8 (1973) 1226–1239. [doi:10.1103/PhysRevD.8.1226](#).
- [415] G. C. Branco, J. M. Gerard, W. Grimus, Geometrical T Violation, Phys. Lett. B 136 (1984) 383–386. [doi:10.1016/0370-2693\(84\)92024-0](#).
- [416] I. de Medeiros Varzielas, D. Emmanuel-Costa, Geometrical CP Violation, Phys. Rev. D 84 (2011) 117901. [arXiv:1106.5477](#), [doi:10.1103/PhysRevD.84.117901](#).
- [417] C. Luhn, S. Nasri, P. Ramond, The Flavor group $\Delta(3n^2)$, J. Math. Phys. 48 (2007) 073501. [arXiv:hep-th/0701188](#), [doi:10.1063/1.2734865](#).
- [418] J. A. Escobar, C. Luhn, The Flavor Group $\Delta(6n^2)$, J. Math. Phys. 50 (2009) 013524. [arXiv:0809.0639](#), [doi:10.1063/1.3046563](#).

- [419] D. Adey, et al., Measurement of the Electron Antineutrino Oscillation with 1958 Days of Operation at Daya Bay, *Phys. Rev. Lett.* 121 (24) (2018) 241805. [arXiv:1809.02261](#), [doi:10.1103/PhysRevLett.121.241805](#).
- [420] Y. Abe, et al., Indication of Reactor $\bar{\nu}_e$ Disappearance in the Double Chooz Experiment, *Phys. Rev. Lett.* 108 (2012) 131801. [arXiv:1112.6353](#), [doi:10.1103/PhysRevLett.108.131801](#).
- [421] Y. Abe, et al., Improved measurements of the neutrino mixing angle θ_{13} with the Double Chooz detector, *JHEP* 10 (2014) 086, [Erratum: *JHEP* 02, 074 (2015)]. [arXiv:1406.7763](#), [doi:10.1007/JHEP02\(2015\)074](#).
- [422] G. Bak, et al., Measurement of Reactor Antineutrino Oscillation Amplitude and Frequency at RENO, *Phys. Rev. Lett.* 121 (20) (2018) 201801. [arXiv:1806.00248](#), [doi:10.1103/PhysRevLett.121.201801](#).
- [423] D. S. Ayres, et al., NOvA: Proposal to Build a 30 Kiloton Off-Axis Detector to Study $\nu_\mu \rightarrow \nu_e$ Oscillations in the NuMI Beamline [arXiv:hep-ex/0503053](#).
- [424] K. Abe, et al., The T2K Experiment, *Nucl. Instrum. Meth. A* 659 (2011) 106–135. [arXiv:1106.1238](#), [doi:10.1016/j.nima.2011.06.067](#).
- [425] K. Abe, et al., Search for CP Violation in Neutrino and Antineutrino Oscillations by the T2K Experiment with 2.2×10^{21} Protons on Target, *Phys. Rev. Lett.* 121 (17) (2018) 171802. [arXiv:1807.07891](#), [doi:10.1103/PhysRevLett.121.171802](#).
- [426] M. A. Acero, et al., First Measurement of Neutrino Oscillation Parameters using Neutrinos and Antineutrinos by NOvA, *Phys. Rev. Lett.* 123 (15) (2019) 151803. [arXiv:1906.04907](#), [doi:10.1103/PhysRevLett.123.151803](#).
- [427] K. Abe, et al., Constraint on the matter–antimatter symmetry-violating phase in neutrino oscillations, *Nature* 580 (7803) (2020) 339–344, [Erratum: *Nature* 583, E16 (2020)]. [arXiv:1910.03887](#), [doi:10.1038/s41586-020-2177-0](#).
- [428] K. Abe, et al., Measurements of neutrino oscillation parameters from the T2K experiment using 3.6×10^{21} protons on target, *Eur. Phys. J. C* 83 (9) (2023) 782. [arXiv:2303.03222](#), [doi:10.1140/epjc/s10052-023-11819-x](#).
- [429] M. A. Acero, et al., Improved measurement of neutrino oscillation parameters by the NOvA experiment, *Phys. Rev. D* 106 (3) (2022) 032004. [arXiv:2108.08219](#), [doi:10.1103/PhysRevD.106.032004](#).
- [430] B. Abi, et al., Deep Underground Neutrino Experiment (DUNE), Far Detector Technical Design Report, Volume II: DUNE Physics [arXiv:2002.03005](#).
- [431] K. Abe, et al., Physics potential of a long-baseline neutrino oscillation experiment using a J-PARC neutrino beam and Hyper-Kamiokande, *PTEP* 2015 (2015) 053C02. [arXiv:1502.05199](#), [doi:10.1093/ptep/ptv061](#).
- [432] S. T. Petcov, A. V. Titov, Assessing the Viability of A_4 , S_4 and A_5 Flavour Symmetries for Description of Neutrino Mixing, *Phys. Rev. D* 97 (11) (2018) 115045. [arXiv:1804.00182](#), [doi:10.1103/PhysRevD.97.115045](#).
- [433] M. Blennow, M. Ghosh, T. Ohlsson, A. Titov, Testing Lepton Flavor Models at ESSnuSB, *JHEP* 07 (2020) 014. [arXiv:2004.00017](#), [doi:10.1007/JHEP07\(2020\)014](#).
- [434] J. Gehrlein, M. Spinrath, Leptonic Sum Rules from Flavour Models with Modular Symmetries, *JHEP* 03 (2021) 177. [arXiv:2012.04131](#), [doi:10.1007/JHEP03\(2021\)177](#).

- [435] P. P. Novichkov, J. T. Penedo, S. T. Petcov, Double cover of modular S_4 for flavour model building, Nucl. Phys. B 963 (2021) 115301. [arXiv:2006.03058](#), [doi:10.1016/j.nuclphysb.2020.115301](#).
- [436] P. P. Novichkov, J. T. Penedo, S. T. Petcov, Fermion mass hierarchies, large lepton mixing and residual modular symmetries, JHEP 04 (2021) 206. [arXiv:2102.07488](#), [doi:10.1007/JHEP04\(2021\)206](#).
- [437] J. Gehrlein, S. Petcov, M. Spinrath, A. Titov, Testing neutrino flavor models, in: Snowmass 2021, 2022. [arXiv:2203.06219](#).
- [438] D. Marzocca, S. T. Petcov, A. Romanino, M. C. Sevilla, Nonzero $|U_{e3}|$ from Charged Lepton Corrections and the Atmospheric Neutrino Mixing Angle, JHEP 05 (2013) 073. [arXiv:1302.0423](#), [doi:10.1007/JHEP05\(2013\)073](#).
- [439] P. Ballett, S. F. King, C. Luhn, S. Pascoli, M. A. Schmidt, Testing solar lepton mixing sum rules in neutrino oscillation experiments, JHEP 12 (2014) 122. [arXiv:1410.7573](#), [doi:10.1007/JHEP12\(2014\)122](#).
- [440] J. E. Kim, M.-S. Seo, Quark and lepton mixing angles with a dodeca-symmetry, JHEP 02 (2011) 097. [arXiv:1005.4684](#), [doi:10.1007/JHEP02\(2011\)097](#).
- [441] S. K. Agarwalla, S. S. Chatterjee, S. T. Petcov, A. V. Titov, Addressing Neutrino Mixing Models with DUNE and T2HK, Eur. Phys. J. C 78 (4) (2018) 286. [arXiv:1711.02107](#), [doi:10.1140/epjc/s10052-018-5772-6](#).
- [442] I. Masina, A Maximal atmospheric mixing from a maximal CP violating phase, Phys. Lett. B 633 (2006) 134–140. [arXiv:hep-ph/0508031](#), [doi:10.1016/j.physletb.2005.10.097](#).
- [443] S. Antusch, S. F. King, Charged lepton corrections to neutrino mixing angles and CP phases revisited, Phys. Lett. B 631 (2005) 42–47. [arXiv:hep-ph/0508044](#), [doi:10.1016/j.physletb.2005.09.075](#).
- [444] P. Ballett, S. F. King, C. Luhn, S. Pascoli, M. A. Schmidt, Testing atmospheric mixing sum rules at precision neutrino facilities, Phys. Rev. D 89 (1) (2014) 016016. [arXiv:1308.4314](#), [doi:10.1103/PhysRevD.89.016016](#).
- [445] I. Girardi, S. T. Petcov, A. V. Titov, Predictions for the Leptonic Dirac CP Violation Phase: a Systematic Phenomenological Analysis, Eur. Phys. J. C 75 (2015) 345. [arXiv:1504.00658](#), [doi:10.1140/epjc/s10052-015-3559-6](#).
- [446] M. Blennow, M. Ghosh, T. Ohlsson, A. Titov, Probing Lepton Flavor Models at Future Neutrino Experiments, Phys. Rev. D 102 (11) (2020) 115004. [arXiv:2005.12277](#), [doi:10.1103/PhysRevD.102.115004](#).
- [447] G.-J. Ding, Y.-F. Li, J. Tang, T.-C. Wang, Confronting tridirect CP -symmetry models with neutrino oscillation experiments, Phys. Rev. D 100 (5) (2019) 055022. [arXiv:1905.12939](#), [doi:10.1103/PhysRevD.100.055022](#).
- [448] J. Gehrlein, M. Spinrath, Neutrino Mass Sum Rules and Symmetries of the Mass Matrix, Eur. Phys. J. C 77 (5) (2017) 281. [arXiv:1704.02371](#), [doi:10.1140/epjc/s10052-017-4817-6](#).
- [449] E. Ma, Aspects of the tetrahedral neutrino mass matrix, Phys. Rev. D 72 (2005) 037301. [arXiv:hep-ph/0505209](#), [doi:10.1103/PhysRevD.72.037301](#).
- [450] J. Barry, W. Rodejohann, Neutrino Mass Sum-rules in Flavor Symmetry Models, Nucl. Phys. B 842 (2011) 33–50. [arXiv:1007.5217](#), [doi:10.1016/j.nuclphysb.2010.08.015](#).
- [451] S. F. King, A. Merle, A. J. Stuart, The Power of Neutrino Mass Sum Rules for Neutrinoless Double Beta Decay Experiments, JHEP 12 (2013) 005. [arXiv:1307.2901](#), [doi:10.1007/JHEP12\(2013\)005](#).

- [452] J. Gehrlein, A. Merle, M. Spinrath, Renormalisation Group Corrections to Neutrino Mass Sum Rules, JHEP 09 (2015) 066. [arXiv:1506.06139](#), [doi:10.1007/JHEP09\(2015\)066](#).
- [453] J. Gehrlein, A. Merle, M. Spinrath, Predictivity of Neutrino Mass Sum Rules, Phys. Rev. D 94 (9) (2016) 093003. [arXiv:1606.04965](#), [doi:10.1103/PhysRevD.94.093003](#).
- [454] P. Huber, M. Lindner, W. Winter, Simulation of long-baseline neutrino oscillation experiments with GLoBES (General Long Baseline Experiment Simulator), Comput. Phys. Commun. 167 (2005) 195. [arXiv:hep-ph/0407333](#), [doi:10.1016/j.cpc.2005.01.003](#).
- [455] P. Huber, J. Kopp, M. Lindner, M. Rolinec, W. Winter, New features in the simulation of neutrino oscillation experiments with GLoBES 3.0: General Long Baseline Experiment Simulator, Comput. Phys. Commun. 177 (2007) 432–438. [arXiv:hep-ph/0701187](#), [doi:10.1016/j.cpc.2007.05.004](#).
- [456] R. G. Calland, A. C. Kaboth, D. Payne, Accelerated Event-by-Event Neutrino Oscillation Reweighting with Matter Effects on a GPU, JINST 9 (2014) P04016. [arXiv:1311.7579](#), [doi:10.1088/1748-0221/9/04/P04016](#).
- [457] M. Wallraff, C. Wiebusch, Calculation of oscillation probabilities of atmospheric neutrinos using nuCraft, Comput. Phys. Commun. 197 (2015) 185–189. [arXiv:1409.1387](#), [doi:10.1016/j.cpc.2015.07.010](#).
- [458] C. A. Argüelles, J. Salvado, C. N. Weaver, nuSQuIDS: A toolbox for neutrino propagation, Comput. Phys. Commun. 277 (2022) 108346. [arXiv:2112.13804](#), [doi:10.1016/j.cpc.2022.108346](#).
- [459] J. Tang, T.-C. Wang, Flavour Symmetry Embedded - GLoBES (FaSE-GLoBES), Comput. Phys. Commun. 263 (2021) 107899. [arXiv:2006.14886](#), [doi:10.1016/j.cpc.2021.107899](#).
- [460] I. Antoniadis, N. Arkani-Hamed, S. Dimopoulos, G. R. Dvali, New dimensions at a millimeter to a Fermi and superstrings at a TeV, Phys. Lett. B 436 (1998) 257–263. [arXiv:hep-ph/9804398](#), [doi:10.1016/S0370-2693\(98\)00860-0](#).
- [461] N. Arkani-Hamed, S. Dimopoulos, G. R. Dvali, The Hierarchy problem and new dimensions at a millimeter, Phys. Lett. B 429 (1998) 263–272. [arXiv:hep-ph/9803315](#), [doi:10.1016/S0370-2693\(98\)00466-3](#).
- [462] L. Randall, R. Sundrum, A Large mass hierarchy from a small extra dimension, Phys. Rev. Lett. 83 (1999) 3370–3373. [arXiv:hep-ph/9905221](#), [doi:10.1103/PhysRevLett.83.3370](#).
- [463] N. Arkani-Hamed, S. Dimopoulos, G. R. Dvali, Phenomenology, astrophysics and cosmology of theories with submillimeter dimensions and TeV scale quantum gravity, Phys. Rev. D 59 (1999) 086004. [arXiv:hep-ph/9807344](#), [doi:10.1103/PhysRevD.59.086004](#).
- [464] K. Agashe, A. Delgado, M. J. May, R. Sundrum, RS1, custodial isospin and precision tests, JHEP 08 (2003) 050. [arXiv:hep-ph/0308036](#), [doi:10.1088/1126-6708/2003/08/050](#).
- [465] K. Agashe, R. Contino, L. Da Rold, A. Pomarol, A Custodial symmetry for $Zb\bar{b}$, Phys. Lett. B 641 (2006) 62–66. [arXiv:hep-ph/0605341](#), [doi:10.1016/j.physletb.2006.08.005](#).
- [466] G. Cacciapaglia, C. Csaki, G. Marandella, J. Terning, The Gaugephobic Higgs, JHEP 02 (2007) 036. [arXiv:hep-ph/0611358](#), [doi:10.1088/1126-6708/2007/02/036](#).
- [467] Y. Grossman, M. Neubert, Neutrino masses and mixings in nonfactorizable geometry, Phys. Lett. B 474 (2000) 361–371. [arXiv:hep-ph/9912408](#), [doi:10.1016/S0370-2693\(00\)00054-X](#).

- [468] T. Gherghetta, A. Pomarol, Bulk fields and supersymmetry in a slice of AdS, Nucl. Phys. B 586 (2000) 141–162. [arXiv:hep-ph/0003129](#), [doi:10.1016/S0550-3213\(00\)00392-8](#).
- [469] R. Gatto, G. Sartori, M. Tonin, Weak Selfmasses, Cabibbo Angle, and Broken $SU(2) \times SU(2)$, Phys. Lett. B 28 (1968) 128–130. [doi:10.1016/0370-2693\(68\)90150-0](#).
- [470] N. Deutschmann, T. Flacke, J. S. Kim, Current LHC Constraints on Minimal Universal Extra Dimensions, Phys. Lett. B 771 (2017) 515–520. [arXiv:1702.00410](#), [doi:10.1016/j.physletb.2017.06.004](#).
- [471] N. Ganguly, A. Datta, Exploring non minimal Universal Extra Dimensional Model at the LHC, JHEP 10 (2018) 072. [arXiv:1808.08801](#), [doi:10.1007/JHEP10\(2018\)072](#).
- [472] F. J. Escrihuela, D. V. Forero, O. G. Miranda, M. Tortola, J. W. F. Valle, On the description of nonunitary neutrino mixing, Phys. Rev. D 92 (5) (2015) 053009, [Erratum: Phys.Rev.D 93, 119905 (2016)]. [arXiv:1503.08879](#), [doi:10.1103/PhysRevD.92.053009](#).
- [473] S. Antusch, V. Maurer, Running quark and lepton parameters at various scales, JHEP 11 (2013) 115. [arXiv:1306.6879](#), [doi:10.1007/JHEP11\(2013\)115](#).
- [474] Z.-z. Xing, H. Zhang, S. Zhou, Updated Values of Running Quark and Lepton Masses, Phys. Rev. D 77 (2008) 113016. [arXiv:0712.1419](#), [doi:10.1103/PhysRevD.77.113016](#).
- [475] S. Antusch, J. Kersten, M. Lindner, M. Ratz, M. A. Schmidt, Running neutrino mass parameters in see-saw scenarios, JHEP 03 (2005) 024. [arXiv:hep-ph/0501272](#), [doi:10.1088/1126-6708/2005/03/024](#).
- [476] N. Abgrall, et al., The Large Enriched Germanium Experiment for Neutrinoless Double Beta Decay (LEGEND), AIP Conf. Proc. 1894 (1) (2017) 020027. [arXiv:1709.01980](#), [doi:10.1063/1.5007652](#).
- [477] J. B. Albert, et al., Sensitivity and Discovery Potential of nEXO to Neutrinoless Double Beta Decay, Phys. Rev. C 97 (6) (2018) 065503. [arXiv:1710.05075](#), [doi:10.1103/PhysRevC.97.065503](#).
- [478] F. Feruglio, Are neutrino masses modular forms?, 2019, pp. 227–266. [arXiv:1706.08749](#), [doi:10.1142/9789813238053_0012](#).
- [479] T. Kobayashi, M. Tanimoto, Modular flavor symmetric models, 2023. [arXiv:2307.03384](#).
- [480] G.-J. Ding, S. F. King, Neutrino Mass and Mixing with Modular Symmetry [arXiv:2311.09282](#).
- [481] H. Cohen, F. Strömberg, **Modular Forms: A Classical Approach**, Graduate studies in mathematics, American Mathematical Society, 2017.
URL <https://books.google.com.hk/books?id=1MmctQEACAAJ>
- [482] P. P. Novichkov, S. T. Petcov, M. Tanimoto, Trimaximal Neutrino Mixing from Modular A_4 Invariance with Residual Symmetries, Phys. Lett. B 793 (2019) 247–258. [arXiv:1812.11289](#), [doi:10.1016/j.physletb.2019.04.043](#).
- [483] G.-J. Ding, S. F. King, X.-G. Liu, J.-N. Lu, Modular S_4 and A_4 symmetries and their fixed points: new predictive examples of lepton mixing, JHEP 12 (2019) 030. [arXiv:1910.03460](#), [doi:10.1007/JHEP12\(2019\)030](#).
- [484] X.-G. Liu, G.-J. Ding, Neutrino Masses and Mixing from Double Covering of Finite Modular Groups, JHEP 08 (2019) 134. [arXiv:1907.01488](#), [doi:10.1007/JHEP08\(2019\)134](#).
- [485] X.-G. Liu, C.-Y. Yao, G.-J. Ding, Modular invariant quark and lepton models in double covering of S_4 modular group, Phys. Rev. D 103 (5) (2021) 056013. [arXiv:2006.10722](#), [doi:10.1103/PhysRevD.103.056013](#).

- [486] X. Wang, B. Yu, S. Zhou, Double covering of the modular A_5 group and lepton flavor mixing in the minimal seesaw model, Phys. Rev. D 103 (7) (2021) 076005. [arXiv:2010.10159](#), [doi:10.1103/PhysRevD.103.076005](#).
- [487] C.-Y. Yao, X.-G. Liu, G.-J. Ding, Fermion masses and mixing from the double cover and metaplectic cover of the A_5 modular group, Phys. Rev. D 103 (9) (2021) 095013. [arXiv:2011.03501](#), [doi:10.1103/PhysRevD.103.095013](#).
- [488] X.-G. Liu, C.-Y. Yao, B.-Y. Qu, G.-J. Ding, Half-integral weight modular forms and application to neutrino mass models, Phys. Rev. D 102 (11) (2020) 115035. [arXiv:2007.13706](#), [doi:10.1103/PhysRevD.102.115035](#).
- [489] P. P. Novichkov, J. T. Penedo, S. T. Petcov, A. V. Titov, Generalised CP Symmetry in Modular-Invariant Models of Flavour, JHEP 07 (2019) 165. [arXiv:1905.11970](#), [doi:10.1007/JHEP07\(2019\)165](#).
- [490] T. Kobayashi, Y. Shimizu, K. Takagi, M. Tanimoto, T. H. Tatsuishi, H. Uchida, CP violation in modular invariant flavor models, Phys. Rev. D 101 (5) (2020) 055046. [arXiv:1910.11553](#), [doi:10.1103/PhysRevD.101.055046](#).
- [491] G.-J. Ding, F. Feruglio, X.-G. Liu, CP symmetry and symplectic modular invariance, SciPost Phys. 10 (6) (2021) 133. [arXiv:2102.06716](#), [doi:10.21468/SciPostPhys.10.6.133](#).
- [492] A. Baur, H. P. Nilles, A. Trautner, P. K. S. Vaudrevange, Unification of Flavor, CP, and Modular Symmetries, Phys. Lett. B 795 (2019) 7–14. [arXiv:1901.03251](#), [doi:10.1016/j.physletb.2019.03.066](#).
- [493] B. S. Acharya, D. Bailin, A. Love, W. A. Sabra, S. Thomas, Spontaneous breaking of CP symmetry by orbifold moduli, Phys. Lett. B 357 (1995) 387–396, [Erratum: Phys.Lett.B 407, 451–451 (1997)]. [arXiv:hep-th/9506143](#), [doi:10.1016/0370-2693\(95\)00945-H](#).
- [494] T. Dent, CP violation and modular symmetries, Phys. Rev. D 64 (2001) 056005. [arXiv:hep-ph/0105285](#), [doi:10.1103/PhysRevD.64.056005](#).
- [495] J. Giedt, CP violation and moduli stabilization in heterotic models, Mod. Phys. Lett. A 17 (2002) 1465–1473. [arXiv:hep-ph/0204017](#), [doi:10.1142/S0217732302007879](#).
- [496] G.-J. Ding, X.-G. Liu, C.-Y. Yao, A minimal modular invariant neutrino model, JHEP 01 (2023) 125. [arXiv:2211.04546](#), [doi:10.1007/JHEP01\(2023\)125](#).
- [497] G.-J. Ding, X.-G. Liu, J.-N. Lu, M.-H. Weng, Modular binary octahedral symmetry for flavor structure of Standard Model, JHEP 11 (2023) 083. [arXiv:2307.14926](#), [doi:10.1007/JHEP11\(2023\)083](#).
- [498] A. Baur, H. P. Nilles, A. Trautner, P. K. S. Vaudrevange, A String Theory of Flavor and CP , Nucl. Phys. B 947 (2019) 114737. [arXiv:1908.00805](#), [doi:10.1016/j.nuclphysb.2019.114737](#).
- [499] T. Kobayashi, S. Nagamoto, S. Uemura, Modular symmetry in magnetized/intersecting D-brane models, PTEP 2017 (2) (2017) 023B02. [arXiv:1608.06129](#), [doi:10.1093/ptep/ptw184](#).
- [500] T. Kobayashi, S. Nagamoto, S. Takada, S. Tamba, T. H. Tatsuishi, Modular symmetry and non-Abelian discrete flavor symmetries in string compactification, Phys. Rev. D 97 (11) (2018) 116002. [arXiv:1804.06644](#), [doi:10.1103/PhysRevD.97.116002](#).
- [501] T. Kobayashi, S. Tamba, Modular forms of finite modular subgroups from magnetized D-brane models, Phys. Rev. D 99 (4) (2019) 046001. [arXiv:1811.11384](#), [doi:10.1103/PhysRevD.99.046001](#).

- [502] Y. Kariyazono, T. Kobayashi, S. Takada, S. Tamba, H. Uchida, Modular symmetry anomaly in magnetic flux compactification, *Phys. Rev. D* 100 (4) (2019) 045014. [arXiv:1904.07546](#), [doi:10.1103/PhysRevD.100.045014](#).
- [503] H. Ohki, S. Uemura, R. Watanabe, Modular flavor symmetry on a magnetized torus, *Phys. Rev. D* 102 (8) (2020) 085008. [arXiv:2003.04174](#), [doi:10.1103/PhysRevD.102.085008](#).
- [504] S. Kikuchi, T. Kobayashi, S. Takada, T. H. Tatsuishi, H. Uchida, Revisiting modular symmetry in magnetized torus and orbifold compactifications, *Phys. Rev. D* 102 (10) (2020) 105010. [arXiv:2005.12642](#), [doi:10.1103/PhysRevD.102.105010](#).
- [505] Y. Almumin, M.-C. Chen, V. Knapp-Pérez, S. Ramos-Sánchez, M. Ratz, S. Shukla, Metaplectic Flavor Symmetries from Magnetized Tori, *JHEP* 05 (2021) 078. [arXiv:2102.11286](#), [doi:10.1007/JHEP05\(2021\)078](#).
- [506] I. de Medeiros Varzielas, S. F. King, Y.-L. Zhou, Multiple modular symmetries as the origin of flavor, *Phys. Rev. D* 101 (5) (2020) 055033. [arXiv:1906.02208](#), [doi:10.1103/PhysRevD.101.055033](#).
- [507] G.-J. Ding, F. Feruglio, X.-G. Liu, Automorphic Forms and Fermion Masses, *JHEP* 01 (2021) 037. [arXiv:2010.07952](#), [doi:10.1007/JHEP01\(2021\)037](#).
- [508] K. Ishiguro, T. Kobayashi, H. Otsuka, Spontaneous CP violation and symplectic modular symmetry in Calabi-Yau compactifications, *Nucl. Phys. B* 973 (2021) 115598. [arXiv:2010.10782](#), [doi:10.1016/j.nuclphysb.2021.115598](#).
- [509] A. Baur, M. Kade, H. P. Nilles, S. Ramos-Sanchez, P. K. S. Vaudrevange, Siegel modular flavor group and CP from string theory, *Phys. Lett. B* 816 (2021) 136176. [arXiv:2012.09586](#), [doi:10.1016/j.physletb.2021.136176](#).
- [510] H. P. Nilles, S. Ramos-Sanchez, A. Trautner, P. K. S. Vaudrevange, Orbifolds from $Sp(4, Z)$ and their modular symmetries, *Nucl. Phys. B* 971 (2021) 115534. [arXiv:2105.08078](#), [doi:10.1016/j.nuclphysb.2021.115534](#).
- [511] H. P. Nilles, S. Ramos-Sánchez, P. K. S. Vaudrevange, Eclectic Flavor Groups, *JHEP* 02 (2020) 045. [arXiv:2001.01736](#), [doi:10.1007/JHEP02\(2020\)045](#).
- [512] H. P. Nilles, S. Ramos-Sanchez, P. K. S. Vaudrevange, Lessons from eclectic flavor symmetries, *Nucl. Phys. B* 957 (2020) 115098. [arXiv:2004.05200](#), [doi:10.1016/j.nuclphysb.2020.115098](#).
- [513] F. Feruglio, V. Gherardi, A. Romanino, A. Titov, Modular invariant dynamics and fermion mass hierarchies around $\tau = i$, *JHEP* 05 (2021) 242. [arXiv:2101.08718](#), [doi:10.1007/JHEP05\(2021\)242](#).
- [514] F. Feruglio, Universal Predictions of Modular Invariant Flavor Models near the Self-Dual Point, *Phys. Rev. Lett.* 130 (10) (2023) 101801. [arXiv:2211.00659](#), [doi:10.1103/PhysRevLett.130.101801](#).
- [515] F. Feruglio, Fermion masses, critical behavior and universality, *JHEP* 03 (2023) 236. [arXiv:2302.11580](#), [doi:10.1007/JHEP03\(2023\)236](#).
- [516] M. Cvetič, A. Font, L. E. Ibanez, D. Lust, F. Quevedo, Target space duality, supersymmetry breaking and the stability of classical string vacua, *Nucl. Phys. B* 361 (1991) 194–232. [doi:10.1016/0550-3213\(91\)90622-5](#).
- [517] E. Gonzalo, L. E. Ibáñez, A. M. Uranga, Modular symmetries and the swampland conjectures, *JHEP* 05 (2019) 105. [arXiv:1812.06520](#), [doi:10.1007/JHEP05\(2019\)105](#).

- [518] T. Kobayashi, Y. Shimizu, K. Takagi, M. Tanimoto, T. H. Tatsuishi, A_4 lepton flavor model and modulus stabilization from S_4 modular symmetry, Phys. Rev. D 100 (11) (2019) 115045, [Erratum: Phys.Rev.D 101, 039904 (2020)]. [arXiv:1909.05139](#), [doi:10.1103/PhysRevD.100.115045](#).
- [519] K. Ishiguro, T. Kobayashi, H. Otsuka, Landscape of Modular Symmetric Flavor Models, JHEP 03 (2021) 161. [arXiv:2011.09154](#), [doi:10.1007/JHEP03\(2021\)161](#).
- [520] P. P. Novichkov, J. T. Penedo, S. T. Petcov, Modular flavour symmetries and modulus stabilisation, JHEP 03 (2022) 149. [arXiv:2201.02020](#), [doi:10.1007/JHEP03\(2022\)149](#).
- [521] J. M. Leedom, N. Righi, A. Westphal, Heterotic de Sitter beyond modular symmetry, JHEP 02 (2023) 209. [arXiv:2212.03876](#), [doi:10.1007/JHEP02\(2023\)209](#).
- [522] V. Knapp-Perez, X.-G. Liu, H. P. Nilles, S. Ramos-Sanchez, M. Ratz, Matter matters in moduli fixing and modular flavor symmetries, Phys. Lett. B 844 (2023) 138106. [arXiv:2304.14437](#), [doi:10.1016/j.physletb.2023.138106](#).
- [523] S. Kikuchi, T. Kobayashi, K. Nasu, Y. Yamada, Moduli trapping mechanism in modular flavor symmetric models, JHEP 08 (2023) 081. [arXiv:2307.13230](#), [doi:10.1007/JHEP08\(2023\)081](#).
- [524] S. F. King, X. Wang, Modulus stabilisation in the multiple-modulus framework [arXiv:2310.10369](#).
- [525] C. Hagedorn, S. F. King, C. Luhn, A SUSY GUT of Flavour with $S_4 \times SU(5)$ to NLO, JHEP 06 (2010) 048. [arXiv:1003.4249](#), [doi:10.1007/JHEP06\(2010\)048](#).
- [526] G.-J. Ding, Fermion Masses and Flavor Mixings in a Model with $S(4)$ Flavor Symmetry, Nucl. Phys. B 827 (2010) 82–111. [arXiv:0909.2210](#), [doi:10.1016/j.nuclphysb.2009.10.021](#).

Exploring the sensitivity to non-standard and generalized neutrino interactions through coherent elastic neutrino-nucleus scattering with a NaI detector

Sabya Sachi Chatterjee,^{1,2,*} Stéphane Lavignac,^{2,†} O. G. Miranda,^{3,‡} and G. Sanchez Garcia^{4,§}

¹*Institut für Astroteilchenphysik, Karlsruher Institut für Technologie (KIT), 76131 Karlsruhe, Germany*

²*Institut de Physique Théorique, Université Paris Saclay, CNRS, CEA, F-91191 Gif-sur-Yvette, France*

³*Departamento de Física, Centro de Investigación y de Estudios Avanzados del IPN, Apartado Postal 14-740 07000, Ciudad de Mexico, Mexico*

⁴*Instituto de Física Corpuscular (CSIC-Universitat de València), Parc Científic UV, C/ Catedrático José Beltrán, 2, 46980 Paterna, Spain*

After the first observation of coherent elastic neutrino-nucleus scattering ($\text{CE}\nu\text{NS}$) by the COHERENT collaboration, many efforts are being made to improve the measurement of this process, making it possible to constrain new physics in the neutrino sector. In this paper, we study the sensitivity to non-standard interactions (NSIs) and generalized neutrino interactions (GNIs) of a NaI detector with characteristics similar to the one that is currently being deployed at the Spallation Neutron Source at Oak Ridge National Laboratory. We show that such a detector, whose target nuclei have significantly different proton to neutron ratios (at variance with the current CsI detector), could help to partially break the parameter degeneracies arising from the interference between the Standard Model and NSI contributions to the $\text{CE}\nu\text{NS}$ cross section, as well as between different NSI parameters. By contrast, only a slight improvement over the current CsI constraints is expected for parameters that do not interfere with the SM contribution. We find that a significant reduction of the background level would make the NaI detector considered in this paper very efficient at breaking degeneracies among NSI parameters.

I. INTRODUCTION

Coherent elastic neutrino-nucleus scattering ($\text{CE}\nu\text{NS}$) [1] is a privileged process to probe new physics in the neutrino sector. So far, the only measurements of $\text{CE}\nu\text{NS}$ have been done at the Spallation Neutron Source (SNS) at Oak Ridge National Laboratory, USA, by the COHERENT collaboration. The first observation of this process was performed with a CsI detector [2, 3]. Another detector, with liquid Argon as a target, was subsequently used by the COHERENT collaboration [4].

* sabya.chatterjee@kit.edu

† stephane.lavignac@ipht.fr

‡ omar.miranda@investav.mx

§ gsanchez@fis.cinvestav.mx

These measurements allowed to test the Standard Model at low energy [5], to constrain the neutron root mean square (*rms*) radius of Cesium, Iodine [6] and Argon [7], and to probe various possible manifestations of physics beyond the Standard Model, such as non-standard neutrino interactions (NSIs) [8–11], generalized neutrino interactions (GNIs) [10, 12–14], neutrino electromagnetic properties [15–17], new light gauge bosons [13, 18–20] and sterile neutrinos [10, 21, 22], among others. Future $CE\nu NS$ experiments at spallation neutron sources [23–25] or nuclear reactors [26–29] will provide more data using different target materials. Particularly interesting is the possibility to disentangle new physics from Standard Model parameters using the interplay between experiments with different neutrino sources [30, 31]. In addition, using nuclear targets with different proportions of protons and neutrons can help reduce the parameter degeneracies arising from the interference between standard and non-standard contributions to $CE\nu NS$, e.g., in the presence of NSIs [8].

A broad class of new physics models predict low-energy effects in the lepton sector that can effectively be described in terms of NSIs or GNIs [32–35]. $CE\nu NS$ is an excellent process to test such new physics effects and to resolve the degeneracies that appear in the interpretation of neutrino oscillation data in the presence of NSIs [36, 37]. However, the possibility of constraining NSI parameters with $CE\nu NS$ is limited by the possible cancellations between standard and non-standard contributions to the cross section, as well as between different NSI couplings. It is, therefore, crucial to perform $CE\nu NS$ measurements with different neutrino sources and targets in order to break these degeneracies [8, 9, 24, 37–39].

In this work, we study the expected sensitivity to non-standard and generalized neutrino interactions of a NaI detector with characteristics similar to the one that is currently being deployed at the SNS. NaI, as opposed to CsI, has the important feature of consisting of two target nuclei with significantly different proton-to-neutron ratios ($p/n \simeq 0.72$ for Iodine and $p/n \simeq 0.92$ for Sodium). We show that this property of the NaI detector makes it particularly efficient at reducing the degeneracies between NSI parameters, provided that the signal-over-background ratio is sufficiently large. For generalized neutrino interactions and off-diagonal NSIs, no significant improvement over the constraints extracted from the current CsI data is expected, unless the signal systematic uncertainty can be reduced below 10%.

The paper is structured as follows. In Section II, we discuss the NSI and GNI contributions to the $CE\nu NS$ cross section. In Section III, we present the experimental setup at the SNS and the characteristics of the current CsI and future NaI detectors. Section IV details our analysis procedure. The expected sensitivities of the future NaI detector to NSI and GNI parameters are presented in Section V, and compared with the current CsI constraints. The impact of the statistics, signal

systematic uncertainty and background level are also studied in this section. Finally, we present our conclusions in Section VI.

II. THEORETICAL FRAMEWORK

In this section, we discuss the tools needed to probe GNIs through $\text{CE}\nu\text{NS}$ measurements. We begin by introducing the SM prediction for the $\text{CE}\nu\text{NS}$ cross section, then we discuss how this cross section is modified when GNI parameters are introduced.

A. The standard $\text{CE}\nu\text{NS}$ cross section

In the Standard Model, the cross section for the coherent elastic scattering of a neutrino or antineutrino of flavor α ($\alpha = e, \mu, \tau$) and energy E_ν off a nucleus with Z protons, N neutrons and mass M is given (up to subleading terms of order T/E_ν , $(T/E_\nu)^2$ [8] and small radiative corrections [40]) by [1]

$$\frac{d\sigma}{dT}(E_\nu, T) = \frac{G_F^2 M}{\pi} \left(1 - \frac{MT}{2E_\nu^2}\right) F^2(|\vec{q}|^2) Q_{W,\alpha}^2, \quad (1)$$

where G_F is the Fermi constant, T the nuclear recoil energy, $F(|\vec{q}|^2)$ the form factor of the nucleon distribution in the nucleus [41] (assumed to be the same for protons and neutrons) evaluated at the transferred three-momentum $|\vec{q}| \simeq \sqrt{2MT}$, and

$$Q_{W,\alpha} = Zg_V^p + Ng_V^n, \quad (2)$$

with $g_V^p = \frac{1}{2} - 2\sin^2\theta_W$ and $g_V^n = -\frac{1}{2}$, is the weak nuclear charge. Since $|\vec{q}|$ is typically very small in $\text{CE}\nu\text{NS}$, the value of the weak mixing angle is taken at zero momentum transfer ($\sin^2\theta_W = 0.23867$ [42, 43]).

The form factor $F(|\vec{q}|^2)$ describe the loss of coherence of the scattering when $|\vec{q}| \gtrsim R^{-1}$, where R is the nucleon radius. Following the COHERENT collaboration, we use the Klein-Nystrand parametrization for the nuclear form factor [44],

$$F(|\vec{q}|^2) = 3 \frac{j_1(|\vec{q}|R_A)}{|\vec{q}|R_A} \left(\frac{1}{1 + |\vec{q}|^2 a_k^2} \right), \quad (3)$$

where $j_1(x) = (\sin x - x \cos x)/x^2$ is the spherical Bessel function of order one, $a_k = 0.9 \text{ fm}$ and $R_A = 1.23A^{1/3} \text{ fm}$ is the nuclear radius, with A the total number of nucleons of the target nucleus.

B. Non-standard and generalized neutrino interactions

The CE ν NS cross section is potentially affected by any interaction between neutrinos and quarks that may be generated by new physics beyond the Standard Model. The simplest example of such interactions are the so-called (neutral-current) non-standard neutrino interactions (NC-NSIs, or NSIs for short), whose phenomenology has been widely studied [33–35, 45]. They are usually parametrized as

$$\mathcal{L}_{\text{NC-NSI}} = -\sqrt{2} G_F \left\{ \varepsilon_{\alpha\beta}^{fV} (\bar{\nu}_\alpha \gamma^\mu P_L \nu_\beta) (\bar{f} \gamma_\mu f) + \varepsilon_{\alpha\beta}^{fA} (\bar{\nu}_\alpha \gamma^\mu P_L \nu_\beta) (\bar{f} \gamma_\mu \gamma^5 f) \right\}, \quad (4)$$

where $\alpha, \beta = e, \mu, \tau$ denote the neutrino flavors, $f = u, d$ label the up and down quarks (we omit the leptonic NSIs, $f = e$, as they do not contribute to CE ν NS), summation over α, β and f is implicit, and $\varepsilon_{\alpha\beta}^{fV}, \varepsilon_{\alpha\beta}^{fA}$ are the vector and axial-vector NSI couplings, respectively. In this paper, we do not consider the axial-vector NSIs, because their contribution to the CE ν NS cross section depends on the nuclear spin and is therefore negligible for heavy nuclei [12], similarly to the contribution of the neutral current axial couplings in the SM [8, 46].

Non-standard neutrino-quark interactions can have a more general Lorentz structure than the one of Eq. (4). Namely, one may also consider scalar, pseudo-scalar and tensor couplings¹, usually dubbed “generalized neutrino interactions” (GNIs) in the literature [12, 32, 48]

$$\begin{aligned} \mathcal{L}_{\text{GNI}} = -\sqrt{2} G_F \left\{ \varepsilon_{\alpha\beta}^{qS} (\bar{\nu}_\alpha P_L \nu_\beta) (\bar{q} q) + \varepsilon_{\alpha\beta}^{qP} (\bar{\nu}_\alpha P_L \nu_\beta) (\bar{q} \gamma^5 q) \right. \\ \left. + \varepsilon_{\alpha\beta}^{qT} (\bar{\nu}_\alpha \sigma^{\mu\nu} P_L \nu_\beta) (\bar{q} \sigma_{\mu\nu} P_L q) \right\} + \text{h.c.}, \end{aligned} \quad (5)$$

where $\sigma^{\mu\nu} = \frac{i}{2} [\gamma^\mu, \gamma^\nu]$ and $q = u, d$. Generally, NSIs are also included in the GNI Lagrangian. In the following, we will refer to $\varepsilon_{\alpha\beta}^{qS}, \varepsilon_{\alpha\beta}^{qV}$ and $\varepsilon_{\alpha\beta}^{qT}$ as scalar, vector and tensor couplings, respectively (we will not consider pseudo-scalar interactions, which give a negligible contribution to CE ν NS [12, 32]). Note that hermiticity of the Lagrangian implies $\varepsilon_{\beta\alpha}^{qV} = (\varepsilon_{\alpha\beta}^{qV})^*$, while the matrices of scalar and tensor couplings do not have any particular symmetry property if neutrinos are Dirac fermions. If they are Majorana fermions, instead, one has $\varepsilon_{\beta\alpha}^{qS} = \varepsilon_{\alpha\beta}^{qS}$ and $\varepsilon_{\beta\alpha}^{qT} = -\varepsilon_{\alpha\beta}^{qT}$ (in particular, flavor-diagonal tensor couplings vanish for Majorana neutrinos).

In the presence of scalar, vector and tensor non-standard neutrino interactions, the differential CE ν NS cross section (1) for an incident neutrino of flavor α is modified to [32]

$$\begin{aligned} \frac{d\sigma}{dT}(E_\nu, T) = \frac{G_F^2 M}{\pi} F^2(|\vec{q}|^2) \sum_{\beta=e, \mu, \tau} \left[|C_{\beta\alpha}^S|^2 \frac{MT}{8E_\nu^2} + |C_{\beta\alpha}^V + Q_{W,\alpha} \delta_{\alpha\beta}|^2 \left(1 - \frac{MT}{2E_\nu^2}\right) \right. \\ \left. + 2|C_{\beta\alpha}^T|^2 \left(1 - \frac{MT}{4E_\nu^2}\right) \right], \end{aligned} \quad (6)$$

¹ The tensor operators $(\bar{\nu}_\alpha \sigma^{\mu\nu} P_L \nu_\beta) (\bar{q} \sigma_{\mu\nu} P_R q)$ vanish by Lorentz symmetry [47], hence do not appear in Eq. (5).

where subleading terms of order $T/E_\nu \ll MT/E_\nu^2$ have been omitted². For an incident antineutrino of flavor α , one should replace $C_{\beta\alpha}^S \rightarrow C_{\alpha\beta}^S$, $C_{\beta\alpha}^V \rightarrow C_{\alpha\beta}^V$ and $C_{\beta\alpha}^T \rightarrow C_{\alpha\beta}^T$ in Eq. (6). The SM contribution is contained in the weak nuclear charge $Q_{W,\alpha}$, given by Eq. (2), while the non-standard contributions are encapsulated in the coefficients $C_{\alpha\beta}^S$, $C_{\alpha\beta}^V$ and $C_{\alpha\beta}^T$, which are given by [12]

$$C_{\alpha\beta}^S = \sum_{q=u,d} \left(Z \frac{m_p}{m_q} f_q^p + N \frac{m_n}{m_q} f_q^n \right) \varepsilon_{\alpha\beta}^{qS}, \quad (7)$$

$$C_{\alpha\beta}^V = (2Z + N) \varepsilon_{\alpha\beta}^{uV} + (Z + 2N) \varepsilon_{\alpha\beta}^{dV}, \quad (8)$$

$$C_{\alpha\beta}^T = \sum_{q=u,d} (Z\delta_q^p + N\delta_q^n) \varepsilon_{\alpha\beta}^{qT}, \quad (9)$$

For the numerical coefficients appearing in Eqs. (7) and (9), we adopt the values given in Refs. [49] and [50], respectively:

$$f_u^p = 0.0208, \quad f_d^p = 0.0411, \quad f_u^n = 0.0189, \quad f_d^n = 0.0451, \quad (10)$$

$$\delta_u^p = 0.792, \quad \delta_d^p = -0.194, \quad \delta_u^n = -0.194, \quad \delta_d^n = 0.792. \quad (11)$$

As for quark masses, we use the central values given by the Particle Data Group [43], $m_u = 2.2$ MeV and $m_d = 4.7$ MeV. Given the large uncertainties associated with the light quark masses and with f_q^N and δ_q^N , many authors provide constraints on the coefficients $C_{\alpha\beta}^S$ and $C_{\alpha\beta}^T$ rather than on the Lagrangian parameters $\varepsilon_{\alpha\beta}^{qS}$ and $\varepsilon_{\alpha\beta}^{qT}$. In this paper, we choose instead to constrain the Lagrangian parameters for fixed values of m_q , f_q^N and δ_q^N . It is straightforward to translate the current bounds and future sensitivity estimates on $\varepsilon_{\alpha\beta}^{qS}$ and $\varepsilon_{\alpha\beta}^{qT}$ presented in the next sections into constraints on $C_{\alpha\beta}^S$ and $C_{\alpha\beta}^T$.

Other authors, e.g. in Ref. [10, 12, 32, 51, 52], use the symbols C_S^q , C_V^q , C_T^q instead of ε^{qS} , ε^{qV} , ε^{qT} in Eqs. (7) to (9), with depending on the normalization convention either $C_V^q = \varepsilon^{qV}$ [52] (with the CE ν NS cross section given by Eq. (6)) or $C_V^q = 2\varepsilon^{qV}$ [10, 12, 32, 51] (in which case one should replace $C_{\alpha\beta}^V$ by $\frac{1}{2} C_{\alpha\beta}^V$ in Eq. (6)).

III. EXPERIMENTAL SETUP AND DETECTORS

In this section, we describe the SNS neutrino beam and the main characteristics of the two detectors considered in this paper, namely the current CsI detector used by the COHERENT collaboration and a future NaI detector similar to the one under deployment by the same collaboration [53].

² In particular, we omit a scalar-tensor interference term in Eq. (6), which is proportional to T/E_ν and whose sign is different for neutrinos and antineutrinos [32].

A. Neutrino beam and predicted number of CE ν NS events

At the SNS, the neutrinos used for CE ν NS measurements arise from the decays at rest of the π^+ produced, together with neutrons and π^- 's, from the collision of high-energy protons on a mercury target (in which the π^- are absorbed before decaying). The SNS neutrino beam therefore consists of three components: a prompt, mono-energetic ν_μ component produced in the two-body decays of stopped positively charged pions ($\pi^+ \rightarrow \mu^+ + \nu_\mu$), and two delayed $\bar{\nu}_\mu$ and ν_e components arising from the subsequent decays at rest of the antimuons ($\mu^+ \rightarrow e^+ + \bar{\nu}_\mu + \nu_e$). These contributions can be analytically computed and are given by

$$\frac{dN_{\nu_\mu}}{dE_\nu} = \xi \delta\left(E_\nu - \frac{m_\pi^2 - m_\mu^2}{2m_\pi}\right), \quad (12)$$

$$\frac{dN_{\bar{\nu}_\mu}}{dE_\nu} = \xi \frac{64E_\nu^2}{m_\mu^3} \left(\frac{3}{4} - \frac{E_\nu}{m_\mu}\right), \quad (13)$$

$$\frac{dN_{\nu_e}}{dE_\nu} = \xi \frac{192E_\nu^2}{m_\mu^3} \left(\frac{1}{2} - \frac{E_\nu}{m_\mu}\right), \quad (14)$$

where E_ν is the neutrino energy and $\xi = rN_{\text{POT}}/4\pi L^2$ is a normalization factor that depends on several experimental features: N_{POT} , the number of protons on target (POT) throughout the operation time; r , the number of neutrinos per flavor produced by each POT; and L , the distance between the source and the detector.

Given the neutrino flux, the predicted number of CE ν NS events in the nuclear recoil energy bin $[T_i, T_{i+1}]$ is given by, for a target material consisting of a single nucleus with mass M ,

$$N_i^{\text{th}} = \mathcal{N} \int_{T_i}^{T_{i+1}} A(T) dT \int_0^{T'_{\text{max}}} \mathcal{R}(T, T') dT' \sum_{\nu=\nu_e, \nu_\mu, \bar{\nu}_\mu} \int_{E_{\text{min}}(T')}^{E_{\text{max}}} dE_\nu \frac{dN_\nu}{dE_\nu}(E_\nu) \frac{d\sigma}{dT'}(E_\nu, T'), \quad (15)$$

where $d\sigma/dT$ is the relevant CE ν NS cross section, given by Eq. (1) or (6), and $\mathcal{N} = N_A M_{\text{det}}/M_{\text{mol}}$ is the number of nuclei in the detector, which is computed from the detector mass M_{det} and the molar mass of the nucleus M_{mol} , with N_A the Avogadro constant. The lower limit of the integral over E_ν is the minimal neutrino energy that can induce a nuclear recoil of energy T' , $E_{\text{min}}(T') = \sqrt{MT'}/2$, while the upper limit E_{max} is the maximum neutrino energy, which for the SNS beam is 52.8 MeV. Notice that Eq. (15) depends on both the real (T') and the reconstructed (T) nuclear recoil energies, with $\mathcal{R}(T, T')$ the smearing function, which may be different for each detector, and the upper limit of the integral over T' is the maximal nuclear recoil energy that can be induced by a neutrino from the beam, $T'_{\text{max}} = 2E_{\text{max}}^2/M$. Finally, $A(T)$ is an acceptance function, which also depends

Target nucleus	Z	N	Z/N	M (a.m.u)
Cs	55	78	0.71	132.91
I	53	74	0.72	126.90
Na	11	12	0.92	22.99

TABLE I. Main properties of the target nuclei used in the two detectors considered in this work: number of protons (Z) and neutrons (N), proton to neutron ratio (Z/N) and mass in atomic units (M).

on the detector. If the target material consists of two nuclei, as is the case for the CsI and NaI detectors, the total number of CE ν NS events is the sum of the numbers of neutrino scatterings on each nucleus, computed separately from Eq. (15) with the appropriate values of M and M_{mol} .

When the timing information of the experiment is available, one can also bin the data in time intervals. In this case, the predicted number of events in the nuclear recoil energy bin i and time bin j is given by

$$N_{ij}^{\text{th}} = \sum_{\nu=\nu_e, \nu_\mu, \bar{\nu}_\mu} N_{\nu,i}^{\text{th}} \int_{t_j}^{t_{j+1}} f_\nu(t) \varepsilon_t(t) dt, \quad (16)$$

where $N_{\nu,i}^{\text{th}}$ is the predicted number of CE ν NS events induced by the component ν ($\nu = \nu_e, \nu_\mu, \bar{\nu}_\mu$) of the neutrino flux in the nuclear recoil energy bin $[T_i, T_{i+1}]$, $f_\nu(t)$ is the time distribution of the neutrino flux component ν taken from Ref. [54], and $\varepsilon(t)$ is the timing efficiency provided in Ref. [3]. To compute $N_{\nu,i}^{\text{th}}$, we use Eq. (15) without performing the sum over the contributions of the three components of the neutrino flux.

In our analysis, we will use the data of the current CsI detector of the COHERENT collaboration, as well as the expected future data from a NaI detector at the SNS. The main characteristics of these detectors are described in the following subsections.

B. Current CsI detector

The COHERENT collaboration performed CE ν NS measurements with a 14.6 kg CsI detector located at 19.3 m from the neutrino source [3]. The accumulated data corresponds to $N_{\text{POT}} = 3.198 \times 10^{23}$, with a number of neutrinos per flavor of $r = 0.0848$ [3]. These numbers are used to compute the neutrino fluxes through Eqs. (12), (13) and (14). Following the COHERENT collaboration, we take the smearing function $\mathcal{R}(T, T')$ in Eq. (15) to be the Gamma function given in Ref. [3] (we refer the reader to Ref. [10] for details about the smearing procedure). Finally, we take into account the timing information provided by the COHERENT collaboration in our analysis and use Eq. (16) to compute the predicted number of events in each recoil energy and time bin.

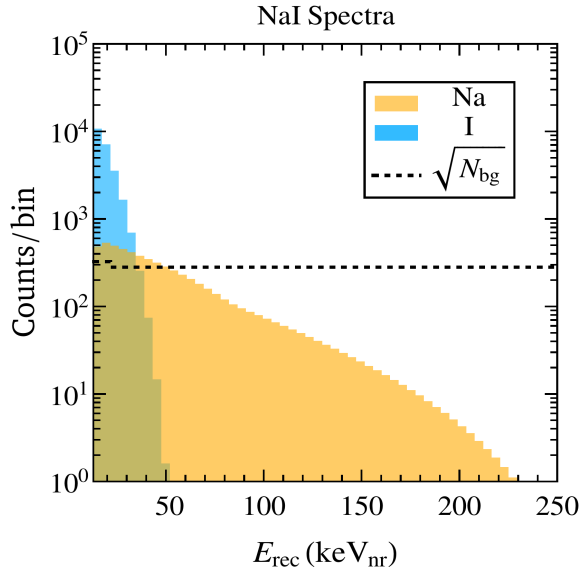


FIG. 1. Projected numbers of signal and background events in the SM as a function of the reconstructed nuclear recoil energy for the future NaI detector considered in this paper, assuming 3 years of data taking. The signal event spectra are displayed separately for the Sodium (yellow) and Iodine (light blue) target nuclei and include the contributions of the three components of the SNS neutrino beam (ν_e , ν_μ and $\bar{\nu}_\mu$). The expected steady-state background is represented by the black dashed curve, which for the sake of presentation shows the square root of the actual number of events.

C. Future NaI detector

The complete program of the COHERENT collaboration includes a NaI-based detector comprising several modules, each consisting of individual 7.7 kg NaI crystals [23]. In its final design, this detector is expected to have up to seven modules, each containing 63 crystals, giving a total mass $M_{\text{det}} = 3395.7$ kg, which we shall consider in this work. The detector is expected to be located at a distance $L = 22$ m from the neutrino source [23]. The SNS provides around 1.1×10^{23} POT per calendar year, corresponding to $\simeq 5000$ hours (208.3 days) of operation per year. In this work, we consider three years of data taking with the SNS operating at current beam power, giving a total number of protons on target $N_{\text{POT}} = 3.3 \times 10^{23}$. We also assume the current value of neutrinos per flavor, $r = 0.0848$. To compute the expected number of events, we assume a conservative constant acceptance of 80% and a Gaussian smearing function $\mathcal{R}(T, T')$ with an energy-dependent resolution $\sigma(T) = \eta \sqrt{TT_{th}}$, where³ $\eta = 0.14$ and $T_{th} = 13$ keV_{nr} is the nuclear recoil energy threshold of the detector [53].

³ This choice reproduces the energy resolution given in [55] to a good approximation.

Under these assumptions and using the properties of the Sodium and Iodine nuclei given in Table I, we obtain the event spectra shown in Fig. 1, where the width of the recoil energy bins corresponds to 1 keV_{ee} [53]. To convert an electron recoil energy of 1 keV into the equivalent nuclear recoil energy (i.e., the nuclear recoil energy giving the same number of photoelectrons as an electron recoil energy of 1 keV), we use a constant quenching factor of 0.23 (estimated from Fig. 4.12 of Ref. [53]), resulting in a bin width of 4.33 keV_{nr} . Fig. 1 displays the individual contributions of the Sodium (yellow) and Iodine (light blue) target nuclei to the signal event spectra. As can be seen, the CE ν NS signal is dominated by the Iodine contribution below $T \approx 35 \text{ keV}_{nr}$, while for larger nuclear recoil energies the Sodium contribution is dominant. This is due to the fact that the Iodine nucleus is heavier than Sodium, resulting in a larger cross section at low recoil energies, but in a lower endpoint (namely, $T_{\text{max}}(\text{I}) \approx 47 \text{ keV}_{nr}$ while $T_{\text{max}}(\text{Na}) \approx 259 \text{ keV}_{nr}$). As we will see later, the different features of the Sodium and Iodine contributions to the CE ν NS signal can help reduce the degeneracies arising in the presence of vector-type GNIs. Fig. 1 also shows the expected steady-state background, which we assumed to be flat and equal to its average value of 300 ckkd (counts per keV_{ee} per kg per day) [53], except in the first two bins where the background is larger. There, we took a conservative value of 400 ckkd. In practice, the number of background events is reduced by a factor of 8000 [53] taking into account the fact that the SNS neutrino beam is pulsed. This reduction factor has been applied in Fig. 1. It is important to mention that the background model adopted here results in a smaller signal-over-background ratio than for the current CsI detector. For comparison, the signal-over-background ratio ranges from 4.2×10^{-3} to 0.15 in the first eight recoil energy bins of Fig. 1 (the ones that contribute the most to the statistics), while it varies between 0.04 and 2.2, depending on the energy bin, for the CsI measurement. This relatively large background level will affect the expected sensitivity of the NaI detector to generalized neutrino interactions. We will see in particular that, in spite of a larger statistics, the NaI detector will not be able to significantly improve the current CsI constraints on scalar and tensor GNI parameters.

IV. ANALYSIS PROCEDURE

For the analysis of the current CsI detector data, we follow the same procedure as Ref. [10] and use the Poissonian χ^2 function

$$\chi^2(\kappa) = \min_{\xi} \left\{ 2 \sum_{i,j} \left[N_{ij}(\kappa, \xi) - \tilde{N}_{ij} + \tilde{N}_{ij} \ln \left(\frac{\tilde{N}_{ij}}{N_{ij}(\kappa, \xi)} \right) \right] + \sum_{m=1}^2 \frac{\xi_{sig,m}^2}{\sigma_{\xi_{sig,m}}^2} + \sum_{k=1}^3 \frac{\xi_{bg,k}^2}{\sigma_{\xi_{bg,k}}^2} \right\}, \quad (17)$$

where i, j run over the nuclear recoil energy and time bins, respectively, \tilde{N}_{ij} is the experimental number of events in bins (i, j) , $N_{ij}(\kappa, \xi)$ the predicted number of events in the same bins in the presence of GNIs, κ stands for the set of GNI parameters under test, and ξ is the set of nuisance parameters over which we minimize the expression within braces. $N_{ij}(\kappa, \xi)$ is computed as

$$N_{ij}(\kappa, \xi) = (1 + \xi_{sig,1})N_{ij}^{sig}(\kappa, \xi_{sig,2}, \xi_1, \xi_2) + (1 + \xi_{bg,1})N_{ij}^{BRN}(\xi_1) + (1 + \xi_{bg,2})N_{ij}^{NIN}(\xi_1) + (1 + \xi_{bg,3})N_{ij}^{SSB}, \quad (18)$$

where N_{ij}^{sig} is the number of signal events, and N_{ij}^{BRN} , N_{ij}^{NIN} and N_{ij}^{SSB} are the numbers of beam-related neutron (BRN), neutrino-induced neutron (NIN) and steady-state (SSB) background events, respectively. The signal nuisance parameter $\xi_{sig,1}$ accounts for the detector efficiency, neutrino flux, and quenching factor (QF) normalizations, while $\xi_{sig,2}$ is related to the nuclear radius. The corresponding uncertainties are $\sigma_{\xi_{sig,1}} = 11.45\%$ and $\sigma_{\xi_{sig,2}} = 5\%$ [10]. As for the nuisance parameters $\xi_{bg,k}$, they are associated with the different sources of background: BRN ($\xi_{bg,1}$), NIN ($\xi_{bg,2}$) and SSB ($\xi_{bg,3}$), with corresponding uncertainties $\sigma_{\xi_{bg,1}} = 25\%$, $\sigma_{\xi_{bg,2}} = 35\%$ and $\sigma_{\xi_{bg,3}} = 2.1\%$ [3]. Following Ref. [10], we include in Eq. (17) two additional nuisance parameters ξ_1 and ξ_2 , with no penalization term, which account for deviations in the uncertainty on the CE ν NS detection efficiency and on beam timing, respectively. By minimizing over all nuisance parameters, we obtain allowed regions at a given confidence level for the GNI parameters under test.

To assess the sensitivity of the future NaI detector to GNI parameters, we consider the following χ^2 function

$$\chi^2(\kappa) = \min_{\xi} \left[\sum_i 2 \left\{ N_i(\kappa, \xi) - \tilde{N}_i + \tilde{N}_i \ln \left(\frac{\tilde{N}_i}{N_i(\kappa, \xi)} \right) \right\} + \left(\frac{\xi_{sig}}{\sigma_{sig}} \right)^2 + \left(\frac{\xi_{bg}}{\sigma_{bg}} \right)^2 \right], \quad (19)$$

where we have divided the data in recoil energy bins labelled by i . Since we are dealing with simulated data, we compare the theoretical predictions in the absence and in the presence of GNIs. Hence, we take

$$\tilde{N}_i = N_i^{sig}(SM) + N_i^{bg}, \quad (20)$$

where $N_i^{sig}(SM)$ represents the number of signal events in bin i predicted by the SM and N_i^{bg} is the simulated steady-state background described in Section III, while

$$N_i(\kappa, \xi) = N_i^{sig}(\kappa)(1 + \xi_{sig}) + N_i^{bg}(1 + \xi_{bg}), \quad (21)$$

where $N_i^{sig}(\kappa)$ is the predicted number of signal events in bin i in the presence of GNIs, and the nuisance parameters ξ_{sig} , ξ_{bg} account for the signal and background normalizations, respectively.

For the associated systematic uncertainties, we conservatively assume $\sigma_{sig} = 10\%$ and $\sigma_{bg} = 5\%$, motivated by the known values of the uncertainties for the current CsI detector. Notice that, due to the absence of detailed information on the signal and background systematic uncertainties, for the NaI detector currently under deployment at the SNS, we only consider two nuisance parameters.

V. EXPECTED SENSITIVITIES TO GNI PARAMETERS

In this section, we study the sensitivities to GNI parameters⁴ of a future NaI detector with characteristics described in Subsection III C, and compare them with the constraints set by the COHERENT CsI detector. As discussed in Subsection II B, we consider only scalar, vector and tensor interactions and denote the corresponding couplings by $\varepsilon_{\alpha\beta}^{qS}$, $\varepsilon_{\alpha\beta}^{qV}$ and $\varepsilon_{\alpha\beta}^{qT}$, respectively, with $\alpha, \beta = e, \mu, \tau$ and $q = u, d$.

Since the SNS neutrino beam consists only of electron neutrinos, muon neutrinos and muon antineutrinos, not all of these parameters can be constrained by CE ν NS measurements. Vector GNIs, also known as NSIs, are subject to the hermiticity condition $\varepsilon_{\beta\alpha}^{qV} = \left(\varepsilon_{\alpha\beta}^{qV}\right)^*$. As a result, there are 6 independent parameters for each quark flavor, but only 5 of them can be constrained at the SNS: two real flavor-diagonal couplings, ε_{ee}^{qV} and $\varepsilon_{\mu\mu}^{qV}$, and three complex flavor off-diagonal couplings, $\varepsilon_{e\mu}^{qV}$, $\varepsilon_{e\tau}^{qV}$ and $\varepsilon_{\mu\tau}^{qV}$. In this paper, we study the sensitivities of the CsI and NaI detectors to ε_{ee}^{qV} , $\varepsilon_{\mu\mu}^{qV}$ and $\varepsilon_{e\mu}^{qV}$ ($q = u, d$), leaving aside the other off-diagonal couplings, which are less constrained⁵.

For scalar and tensor GNIs, the number of independent parameters depends on whether neutrinos are Dirac or Majorana fermions. In this paper, we assume that they are Majorana fermions, both for simplicity and because this possibility is better motivated from a theoretical point of view. Scalar couplings are therefore symmetric, and for each quark flavor, 5 out of the 6 independent ones can be constrained by CE ν NS measurements at the SNS. However, due to the absence of interference between the scalar and SM contributions to the CE ν NS cross section, the same constraints apply to ε_{ee}^{qS} and $\varepsilon_{e\tau}^{qS}$, as well as to $\varepsilon_{\mu\mu}^{qS}$ and $\varepsilon_{\mu\tau}^{qS}$. It is therefore sufficient to study the sensitivities of the CsI and NaI detectors to the scalar couplings ε_{ee}^{qS} , $\varepsilon_{\mu\mu}^{qS}$ and $\varepsilon_{e\mu}^{qS}$ ($q = u, d$). Finally, tensor couplings are antisymmetric for Majorana neutrinos, leaving only 3 independent parameters $\varepsilon_{e\mu}^{qT}$, $\varepsilon_{e\tau}^{qT}$ and $\varepsilon_{\mu\tau}^{qT}$ for each value of q , all of which can induce scatterings of SNS neutrinos off nuclei.

Throughout this paper, we assume all GNI couplings to be real. The upper bounds on these

⁴ From now on, we will collectively refer to vector, scalar and tensor couplings as GNI parameters, and we will more specifically use NSI parameters for vector couplings.

⁵ This is due to the fact that $\varepsilon_{e\mu}^{qV}$ can induce coherent scatterings for all three components of the SNS neutrino flux, while only ν_e (resp. ν_μ and $\nu_{\bar{\mu}}$) can scatter off a nucleus via $\varepsilon_{e\tau}^{qV}$ (resp. $\varepsilon_{\mu\tau}^{qV}$).

parameters obtained from the currently available CsI data and the expected sensitivity of the future NaI detector are determined following the numerical procedure described in Section IV.

A. Expected sensitivities to individual GNI parameters

We first consider the expected sensitivities of the NaI detector to individual GNI parameters, i.e. we consider a single nonvanishing coupling at a time. Note that in this case, the assumption of real couplings does not mean any loss of generality, as the $\text{CE}\nu\text{NS}$ cross section only depends on the moduli of the GNI parameters (except for diagonal vector couplings, which are real and can interfere with the SM contribution).

The results for vector couplings are shown in Fig. 2, where the $\Delta\chi^2$ functions defined in Section IV are plotted against the parameter assumed to be nonvanishing (from left to right: ε_{ee}^{qV} , $\varepsilon_{e\mu}^{qV}$ and $\varepsilon_{\mu\mu}^{qV}$, with $q = u$ in the upper panels and $q = d$ in the lower panels). The black solid curves are obtained using the currently available CsI data, and are consistent with the results obtained in Ref. [10]. The red dashed curves represent the expected sensitivities of the future NaI detector after 3 years of data taking, assuming conservatively $\sigma_{sig} = 10\%$ and $\sigma_{bg} = 5\%$. For the flavor-diagonal parameters ε_{ee}^{qV} and $\varepsilon_{\mu\mu}^{qV}$ ($q = u, d$), two minima can be observed in the $\Delta\chi^2$ profiles⁶, as a result of the interference between the SM and NSI contributions in the $\text{CE}\nu\text{NS}$ cross section, Eq. (6). The sharp rise of the $\Delta\chi^2$ for $\varepsilon_{\mu\mu}^{qV}$ between the two minima is due to the fact that when $\varepsilon_{\mu\mu}^{qV} \approx 0.2$, the NSI and SM contributions to the $\text{CE}\nu\text{NS}$ cross section almost completely cancel out for ν_μ 's and $\bar{\nu}_\mu$'s, resulting in a reduction of the predicted number of $\text{CE}\nu\text{NS}$ events by roughly 2/3, in strong tension with data. The same effect is present for ε_{ee}^{qV} , but since this coupling only affects ν_e -induced $\text{CE}\nu\text{NS}$ events, i.e. roughly 1/3 of the signal, the $\Delta\chi^2$ reaches smaller values between the two minima (especially for CsI, which suffers from a smaller statistics than the NaI detector). In Table II, we give the 90% C.L. and 2σ expected sensitivities of the future NaI detector to the vector couplings ε_{ee}^{qV} , $\varepsilon_{e\mu}^{qV}$ and $\varepsilon_{\mu\mu}^{qV}$ ($q = u, d$), as well as the constraints on these parameters from the COHERENT CsI data.

As can be seen from Fig. 2 and Table II, a clear improvement of the constraints on these diagonal vector couplings is expected from the future NaI detector, already with 3 years of data taking. This is partly due to the larger statistics of the NaI detector, as already mentioned. However, the most noticeable feature, namely the fact that the second minimum of the χ^2 function tends to

⁶ Note that for the CsI detector, the first minimum of the χ^2 function is not located at $\varepsilon_{ee}^{qV} = 0$ (resp. $\varepsilon_{\mu\mu}^{qV} = 0$).

This is due to the fact that we are analysing real data, which does not exactly match the SM prediction.

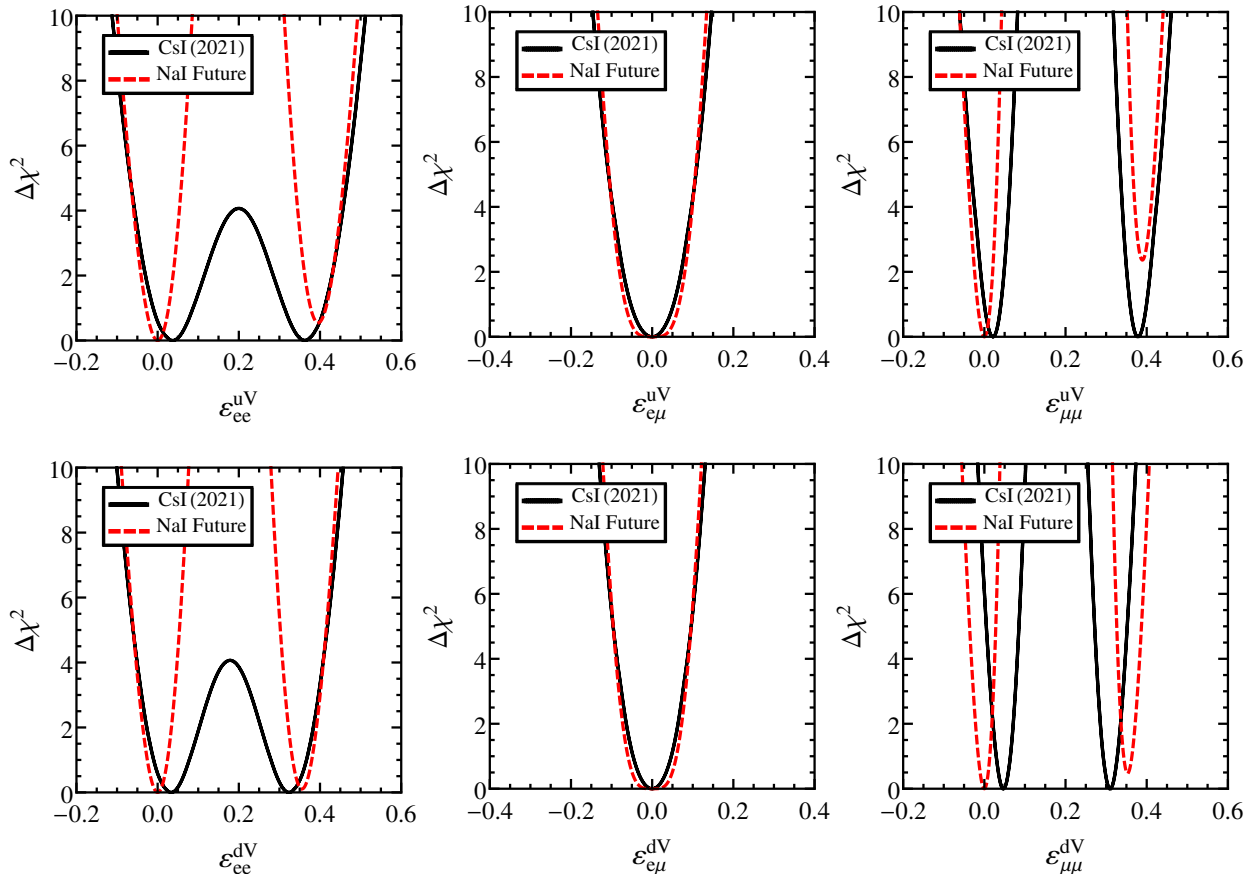


FIG. 2. One-dimensional $\Delta\chi^2$ profiles (17) and (19) for the vector coupling ε_{ee}^{qV} (left panels), $\varepsilon_{e\mu}^{qV}$ (middle panels) and $\varepsilon_{\mu\mu}^{qV}$ (right panels), with $q = u$ in the upper panels and $q = d$ in the lower panels. The black solid curves correspond to Eq. (17) and are obtained using the currently available data of the COHERENT CsI detector. The red dashed curves correspond to Eq. (19) and represent the expected sensitivities of the NaI detector described in Subsection III C, assuming 3 years of data taking at the SNS. The off-diagonal NSI parameter $\varepsilon_{e\mu}^{qV}$ is assumed to be real.

be disfavoured (mostly for the parameter $\varepsilon_{\mu\mu}^{uV}$, and to a lesser extent for ε_{ee}^{uV} and $\varepsilon_{\mu\mu}^{dV}$), cannot be explained by statistics alone. This can be understood instead by noting that the SM–NSI interference term in the CE ν Ns cross section is controlled by the quantity (where we have neglected a term suppressed by $g_V^p \ll 1$)

$$C_{\alpha\alpha}^V + Q_{W,\alpha} \simeq N \left[\left(2 \frac{Z}{N} + 1 \right) \varepsilon_{\alpha\alpha}^{uV} + \left(\frac{Z}{N} + 2 \right) \varepsilon_{\alpha\alpha}^{dV} - \frac{1}{2} \right], \quad (22)$$

and is therefore sensitive to the proton to neutron ratio of the target nucleus. In particular, the second $\Delta\chi^2$ minimum for $\varepsilon_{\alpha\alpha}^{uV}$ (resp. $\varepsilon_{\alpha\alpha}^{dV}$) is located at $\varepsilon_{\alpha\alpha}^{uV} \approx 1/(2Z/N + 1)$ (resp. $\varepsilon_{\alpha\alpha}^{dV} \approx 1/(Z/N + 2)$). While the CsI detector involves two nuclei with approximately the same proton

Detector	q	ε_{ee}^{qV}		$\varepsilon_{e\mu}^{qV}$		$\varepsilon_{\mu\mu}^{qV}$	
		90% C.L.	2σ C.L.	90% C.L.	2σ C.L.	90% C.L.	2σ C.L.
NaI	u	$[-0.047, 0.044]$ $\cup [0.356, 0.438]$	$[-0.059, 0.053]$ $\cup [0.345, 0.451]$	$[-0.088, 0.088]$	$[-0.099, 0.099]$	$[-0.027, 0.024]$ $\cup [0.380, 0.399]$	$[-0.036, 0.028]$ $\cup [0.371, 0.411]$
	d	$[-0.043, 0.039]$ $\cup [0.317, 0.398]$	$[-0.053, 0.048]$ $\cup [0.308, 0.408]$	$[-0.079, 0.079]$	$[-0.09, 0.09]$	$[-0.026, 0.021]$ $\cup [0.333, 0.376]$	$[-0.032, 0.026]$ $\cup [0.329, 0.382]$
CsI	u	$[-0.04, 0.134]$ $\cup [0.266, 0.440]$	$[-0.056, 0.186]$ $\cup [0.212, 0.456]$	$[-0.081, 0.081]$	$[-0.097, 0.097]$	$[-0.015, 0.053]$ $\cup [0.346, 0.414]$	$[-0.024, 0.060]$ $\cup [0.34, 0.424]$
	d	$[-0.035, 0.120]$ $\cup [0.237, 0.393]$	$[-0.05, 0.168]$ $\cup [0.190, 0.408]$	$[-0.073, 0.073]$	$[-0.087, 0.087]$	$[-0.016, 0.075]$ $\cup [0.282, 0.340]$	$[-0.010, 0.081]$ $\cup [0.276, 0.347]$

TABLE II. Sensitivities to the vector couplings ε_{ee}^{qV} , $\varepsilon_{e\mu}^{qV}$ and $\varepsilon_{\mu\mu}^{qV}$ ($q = u, d$) at the 90% and 2σ confidence levels with 1 degree of freedom (i.e. $\Delta\chi^2 \leq 2.71$ and $\Delta\chi^2 \leq 4$, respectively). For the CsI detector, the intervals actually correspond to the ranges of parameter values allowed by the currently available data, while for the NaI detector they represent the expected sensitivities assuming 3 years of data taking at the SNS. The off-diagonal NSI parameter $\varepsilon_{e\mu}^{qV}$ is assumed to be real.

to neutron ratio, this is not the case for the NaI detector (see Table I), making it more difficult to fit SM-like experimental data with a nonzero value of $\varepsilon_{\alpha\alpha}^{uV}$ or $\varepsilon_{\alpha\alpha}^{dV}$. The same effect is observed when combining the data collected by two detectors with target nuclei characterized by different proton to neutron ratios [24, 39]; in the case of the NaI detector, the two nuclei are present in the same target. However, the NaI detector considered in this paper is not as efficient at constraining flavor-diagonal vector couplings as expected from suitably chosen combinations of the detectors proposed for CE ν NS measurements at the European Spallation Source [24], such as CsI + Si and Xe + Si [39]. The latter indeed benefit from a large statistics and from a lower background level than the NaI detector. Also, the advantage of combining two target nuclei with different proton to neutron ratios in the same detector is counterbalanced, in the case of NaI, by the fact that the recoil energy bins in which the Na-induced scatterings contribute significantly are the ones in which the signal over background ratio is the least favorable, as can be seen from Fig. 1.

For off-diagonal vector couplings, whose contributions do not interfere with the SM one, no significant improvement on the current constraints is expected from the future NaI detector, in spite of the larger statistics (the results for $\varepsilon_{e\tau}^{qV}$ and $\varepsilon_{\mu\tau}^{qV}$ are qualitatively similar to the ones for $\varepsilon_{e\mu}^{qV}$ shown in Fig. 2). This is due to the fact that the signal-over-background ratio is significantly smaller than for the CsI detector (see the discussion at the end of Subsection III C).

Let us now move on to the results for scalar GNIs. As explained before, CE ν NS measurements

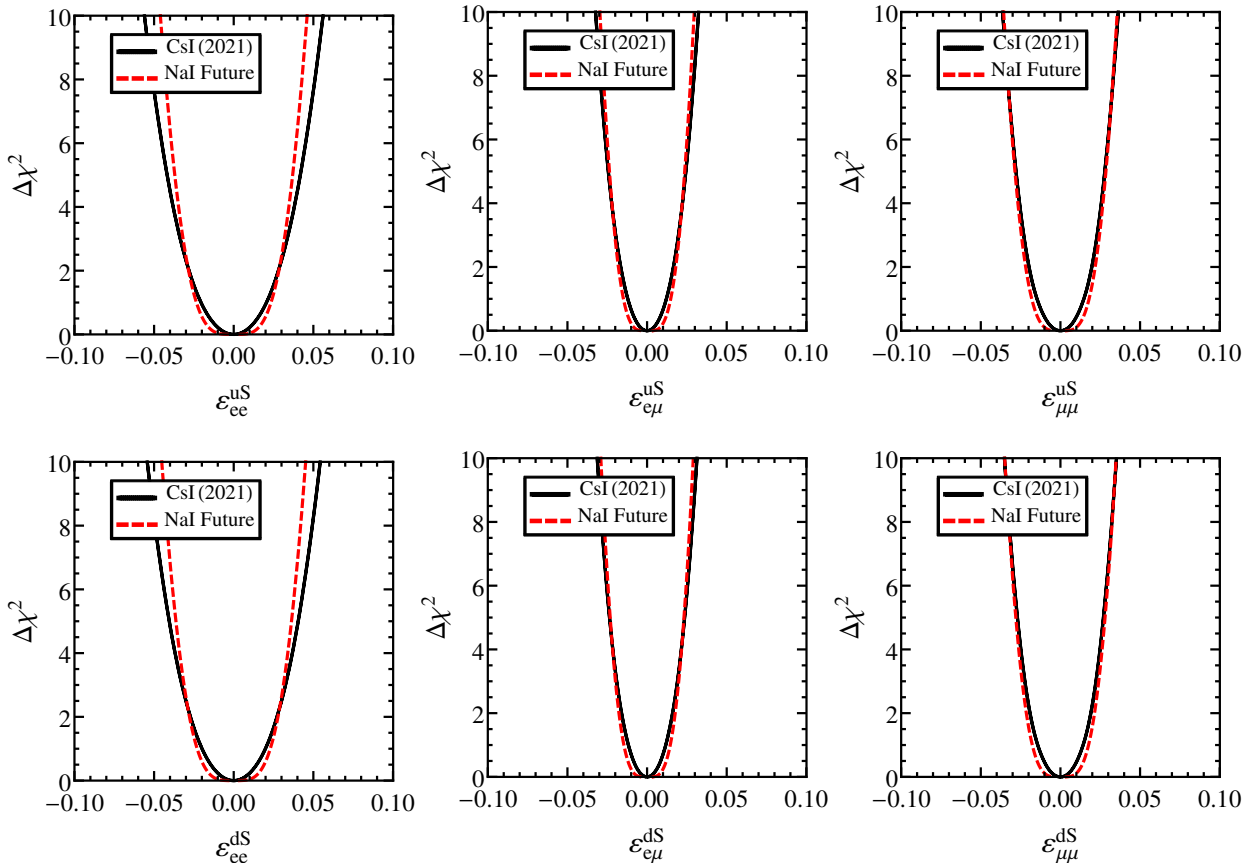


FIG. 3. Same as Fig. 2, but for the scalar couplings ε_{ee}^{qS} (left panels), $\varepsilon_{e\mu}^{qS}$ (middle panels) and $\varepsilon_{\mu\mu}^{qS}$ (right panels), with $q = u$ in the upper panels and $q = d$ in the lower panels. All couplings are assumed to be real.

Detector	q	ε_{ee}^{qS}		$\varepsilon_{e\mu}^{qS}$		$\varepsilon_{\mu\mu}^{qS}$	
		90% C.L.	2σ C.L.	90% C.L.	2σ C.L.	90% C.L.	2σ C.L.
NaI	u	[-0.031, 0.031]	[-0.034, 0.034]	[-0.02, 0.02]	[-0.022, 0.022]	[-0.024, 0.024]	[-0.027, 0.027]
	d	[-0.031, 0.031]	[-0.033, 0.033]	[-0.019, 0.019]	[-0.021, 0.021]	[-0.023, 0.023]	[-0.026, 0.026]
CsI	u	[-0.032, 0.032]	[-0.038, 0.038]	[-0.018, 0.018]	[-0.022, 0.022]	[-0.022, 0.022]	[-0.026, 0.026]
	d	[-0.031, 0.031]	[-0.037, 0.037]	[-0.018, 0.018]	[-0.022, 0.022]	[-0.022, 0.022]	[-0.025, 0.025]

TABLE III. Same as Table II, but for the scalar couplings ε_{ee}^{qS} , $\varepsilon_{e\mu}^{qS}$ and $\varepsilon_{\mu\mu}^{qS}$ ($q = u, d$).

at the SNS only give six independent constraints on scalar couplings, since $\varepsilon_{e\tau}^{qS}$ and $\varepsilon_{\mu\tau}^{qS}$ contribute the same way to the CE ν NS cross section as ε_{ee}^{qS} and $\varepsilon_{\mu\mu}^{qS}$, respectively⁷. We therefore only present results for the 6 scalar couplings ε_{ee}^{qS} , $\varepsilon_{\mu\mu}^{qS}$ and $\varepsilon_{e\mu}^{qS}$ ($q = u, d$). The $\Delta\chi^2$ profiles are displayed in Fig. 3, and the 90% C.L. and 2σ expected sensitivities of the future NaI detector, together

⁷ This statement holds for symmetric scalar couplings, hence for Majorana neutrinos (as assumed in this paper), but not for Dirac neutrinos.

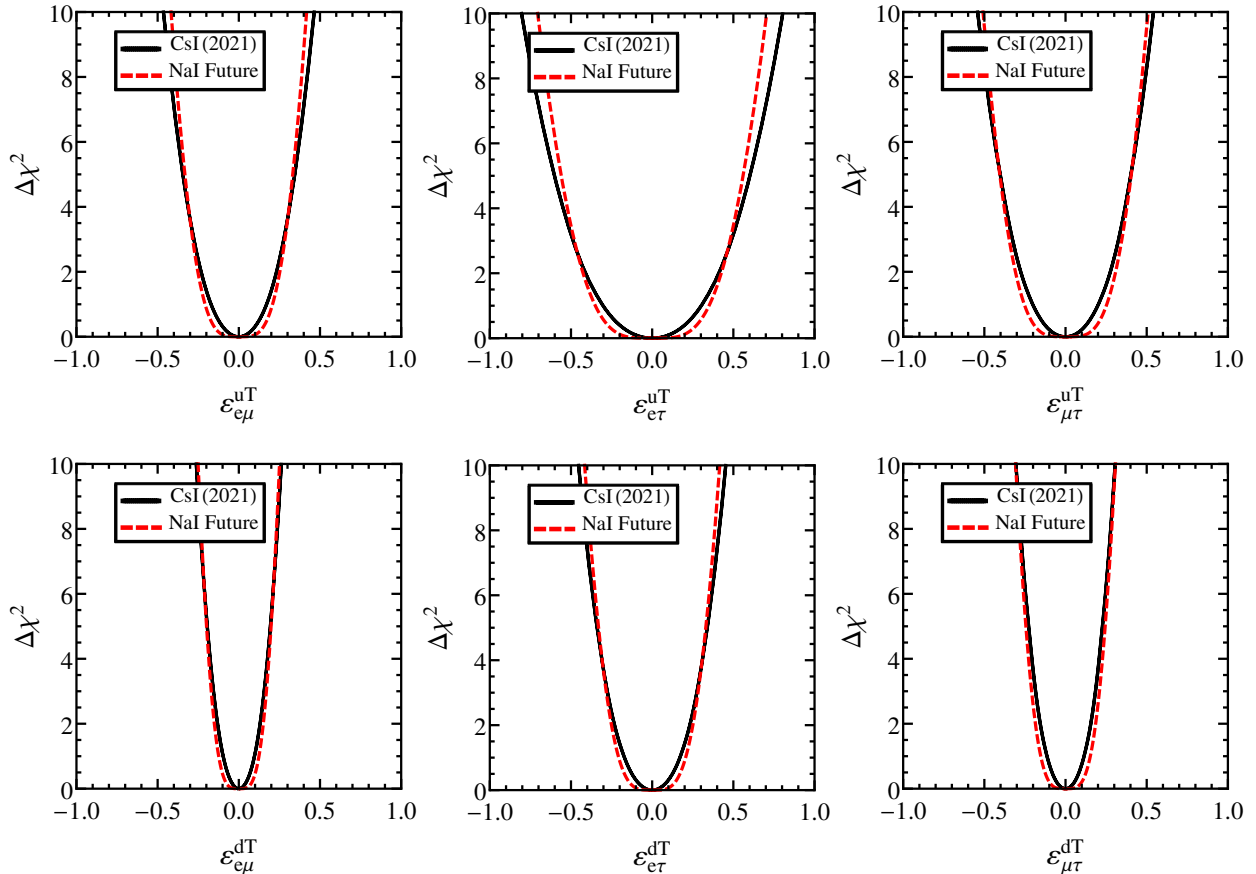


FIG. 4. Same as Fig. 2, but for the tensor couplings $\varepsilon_{e\mu}^{qT}$ (left panels), $\varepsilon_{e\tau}^{qT}$ (middle panels) and $\varepsilon_{\mu\tau}^{qT}$ (right panels), with $q = u$ in the upper panels and $q = d$ in the lower panels. All couplings are assumed to be real.

with the constraints from the COHERENT CsI data, are given in Table III. As can be seen by comparing Figs. 2 and 3, the results for scalar couplings are similar to the ones for off-diagonal vector couplings, which is not a surprise since both types of interactions share the property of not interfering with the SM contribution in the CE ν NS cross section. In particular, we do not expect the future NaI detector to significantly improve the current CsI constraints on scalar couplings within the assumptions made in our analysis (3 years of running time, $\sigma_{sig} = 10\%$ and $\sigma_{bg} = 5\%$). Note however that, at the $\gtrsim 3\sigma$ confidence level, there is a slight improvement for ε_{ee}^{uS} and ε_{ee}^{dS} .

Finally, the results for tensor GNIs are shown in Fig. 4 and Table IV. Recall that there are only 6 independent tensor couplings if, as assumed in this paper, neutrinos are Majorana fermions, namely $\varepsilon_{e\mu}^{qT}$, $\varepsilon_{e\tau}^{qT}$ and $\varepsilon_{\mu\tau}^{qT}$ ($q = u, d$). Comparing the expected sensitivities of the future NaI detector with the constraints from the COHERENT CsI data (see Table IV), we only expect a marginal improvement of the constraints on tensor GNI parameters. However, at the $\gtrsim 3\sigma$ confidence level,

Detector	q	$\varepsilon_{e\mu}^{qT}$		$\varepsilon_{e\tau}^{qT}$		$\varepsilon_{\mu\tau}^{qT}$	
		90% C.L.	2σ C.L.	90% C.L.	2σ C.L.	90% C.L.	2σ C.L.
NaI	u	[-0.275, 0.275]	[-0.310, 0.310]	[-0.465, 0.465]	[-0.525, 0.525]	[-0.337, 0.337]	[-0.380, 0.380]
	d	[-0.165, 0.165]	[-0.186, 0.186]	[-0.274, 0.274]	[-0.310, 0.310]	[-0.203, 0.203]	[-0.228, 0.228]
CsI	u	[-0.265, 0.265]	[-0.314, 0.314]	[-0.467, 0.467]	[-0.55, 0.55]	[-0.314, 0.314]	[-0.369, 0.369]
	d	[-0.15, 0.15]	[-0.177, 0.177]	[-0.264, 0.264]	[-0.310, 0.310]	[-0.177, 0.177]	[-0.208, 0.208]

TABLE IV. Same as Table II, but for the tensor couplings $\varepsilon_{e\mu}^{qT}$, $\varepsilon_{e\tau}^{qT}$ and $\varepsilon_{\mu\tau}^{qT}$ ($q = u, d$).

a slight improvement can be observed for $\varepsilon_{e\tau}^{uT}$.

B. Expected sensitivities to pairs of GNI parameters

In this section, we study the expected sensitivity of the NaI detector to pairs of GNI parameters, i.e. we consider two nonvanishing couplings at a time. As it is well known, this situation leads to degeneracies in the form of extended allowed regions in the two-dimensional GNI parameter space. Combining data on target nuclei characterized by different proton to neutron ratios can help reduce these degeneracies, as shown e.g. in Refs. [8, 24, 39]. In the case of the NaI detector studied in this paper, the two nuclei have significantly different proton to neutron ratios 0.92 (for Na) and 0.72 (for I), while the Cesium and Iodine targets of the CsI detector have approximately the same ratio.

We begin our analysis by considering the case where the two nonvanishing GNI parameters are of vector type (i.e., NSIs). Many different combinations of two NSI parameters are possible; we only present results for a few representative examples, as the other combinations are characterized by similar allowed regions. Fig. 5 shows the allowed regions at the 90% confidence level for four different pairs of vector couplings. The upper panels correspond to combinations of diagonal couplings involving the same lepton flavor but different quarks, namely $(\varepsilon_{ee}^{uV}, \varepsilon_{ee}^{dV})$ in the left panel and $(\varepsilon_{\mu\mu}^{uV}, \varepsilon_{\mu\mu}^{dV})$ in the right panel. By contrast, the lower panels correspond to pairs of vector couplings involving the same quark but different lepton flavors. The combination in the left panel, $(\varepsilon_{ee}^{uV}, \varepsilon_{\mu\mu}^{uV})$, involves two diagonal couplings, while the one in the right panel, $(\varepsilon_{e\mu}^{uV}, \varepsilon_{\mu\mu}^{uV})$, involves a diagonal and an off-diagonal coupling. In all cases, the green regions are the ones allowed by the current CsI data (these allowed regions were first presented in Ref. [10], and are shown here for reference), while the regions delimited by red lines correspond to the expected sensitivity of the NaI detector described in Subsection III C, assuming 3 years of data taking at the SNS.

In the upper panels of Fig. 5, the allowed regions consist of two parallel bands [9]. This is a

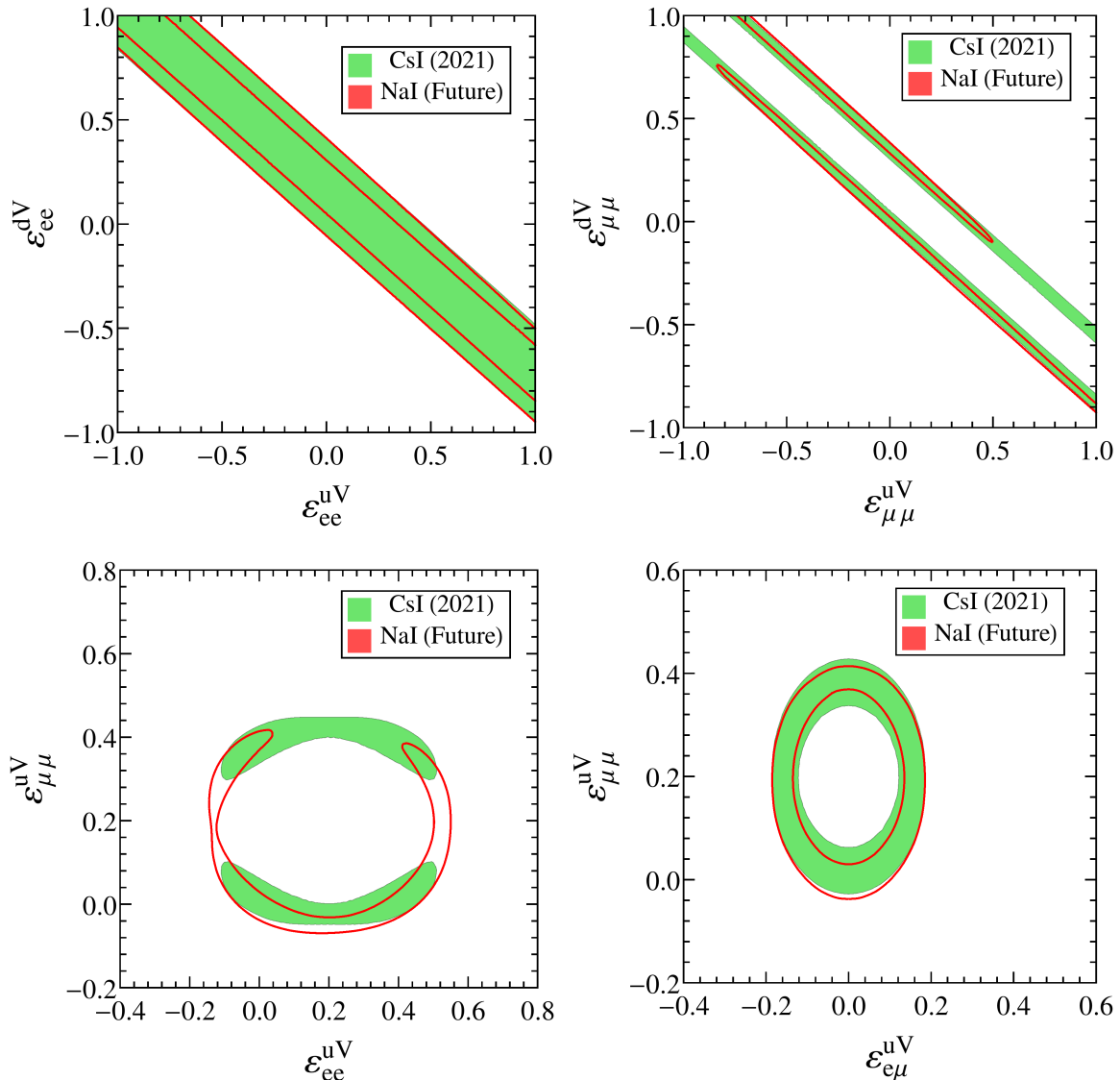


FIG. 5. 90% C.L. allowed regions (with two degrees of freedom, i.e. $\Delta\chi^2 \leq 4.61$) for different combinations of two NSI parameters: $(\varepsilon_{ee}^{uV}, \varepsilon_{ee}^{dV})$ (upper left panel), $(\varepsilon_{\mu\mu}^{uV}, \varepsilon_{\mu\mu}^{dV})$ (upper right panel), $(\varepsilon_{ee}^{uV}, \varepsilon_{\mu\mu}^{uV})$ (lower left panel) and $(\varepsilon_{e\mu}^{uV}, \varepsilon_{\mu\mu}^{uV})$ (lower right panel). The green regions correspond to the constraints from the current CsI data, while the red contours represent the expected sensitivity of the NaI detector described in Subsection III C, assuming 3 years of data taking at the SNS. The off-diagonal parameter $\varepsilon_{e\mu}^{qV}$ is assumed to be real.

consequence of the fact that, for a single-nucleus target (or a target composed of two nuclei with approximately the same proton to neutron ratio, like CsI), the CE ν NS cross section depends on NSI parameters only through the modulus of the combination (22), which can be more conveniently

rewritten as

$$C_{\alpha\alpha}^V + Q_{W,\alpha} \simeq (Z + 2N) \left(\varepsilon_{\alpha\alpha}^{dV} - m \varepsilon_{\alpha\alpha}^{uV} \right) - \frac{1}{2}, \quad m = -\frac{2Z + N}{Z + 2N}. \quad (23)$$

Thus, values of $\varepsilon_{\alpha\alpha}^{uV}$ and $\varepsilon_{\alpha\alpha}^{dV}$ lying on a straight line with slope m [8] produce the same number of CE ν NS events in each recoil energy bin. This is an example of the degeneracies mentioned above. It follows that the parameter space region allowed by SM-like experimental data at a given confidence interval (here 90% C.L.) consists of two parallel bands around the straight lines $\varepsilon_{\alpha\alpha}^{dV} - m \varepsilon_{\alpha\alpha}^{uV} = 0$ and $\varepsilon_{\alpha\alpha}^{dV} - m \varepsilon_{\alpha\alpha}^{uV} = 1/(Z + 2N)$. This is what can be observed in Fig. 5 for CsI, where the two bands overlap for $\alpha = e$ due to the limited statistics (there are twice as many ν_μ 's and $\bar{\nu}_\mu$'s as ν_e 's in the SNS neutrino beam). For NaI, the bands are thinner due to the larger statistics, and they reduce to closed or semi-closed areas in the $(\varepsilon_{\mu\mu}^{uV}, \varepsilon_{\mu\mu}^{dV})$ plane⁸. This partial breaking of the degeneracy between $\varepsilon_{\mu\mu}^{uV}$ and $\varepsilon_{\mu\mu}^{dV}$ is due to the fact that Sodium and Iodine have different proton to neutron ratios, hence different slopes m_I and m_{Na} .

The elliptic-like shape of the allowed regions in the lower panels of Fig. 5 can be understood from the expression for the predicted CE ν NS events in each reconstructed nuclear recoil energy bin [39]. Considering for instance the couplings $(\varepsilon_{ee}^{uV}, \varepsilon_{\mu\mu}^{uV})$, the predicted number of events in the recoil energy bin $[T_i, T_{i+1}]$, for a single-nucleus detector, can be written as

$$N_i^{th} = C_i^e (2Z + N)^2 \left(\varepsilon_{ee}^{uV} + \frac{Zg_V^p + Ng_V^n}{2Z + N} \right)^2 + C_i^\mu (2Z + N)^2 \left(\varepsilon_{\mu\mu}^{uV} + \frac{Zg_V^p + Ng_V^n}{2Z + N} \right)^2, \quad (24)$$

where C_i^e (resp. C_i^μ) is the number obtained by performing the integral over E_{ν_e} (resp. E_{ν_μ} and $E_{\bar{\nu}_\mu}$) and the true and reconstructed nuclear recoil energies in Eq. (15), after having factorized out $|C_{\alpha\alpha}^V + Q_{W,\alpha}|^2$. Eq. (24) is the equation of an ellipse with semi-major and semi-minor axes (given respectively by $\sqrt{N_i^{th}/C_i^e (2Z + N)^2}$ and $\sqrt{N_i^{th}/C_i^\mu (2Z + N)^2}$) that depend on both the nucleus and the energy bin (the center of the ellipse also depends on the nucleus). All sets of $(\varepsilon_{ee}^{uV}, \varepsilon_{\mu\mu}^{uV})$ values lying on this ellipse predict the same number of CE ν NS events in the i th energy bin, but not necessarily in the other bins, resulting in an approximate degeneracy between these two parameters. This explains why the 90% C.L. allowed regions in the lower left panel of Fig. 5 have the form of approximate, partly broken ellipses. The degeneracy is broken by the energy binning and, in the case of the NaI detector, by the fact that the nuclei composing the target have different numbers of protons and neutrons (while they are approximately the same for Cesium and Iodine).

From the lower left panel of Fig. 5, one can see that the CsI and NaI detectors play a complementary role in reducing the degeneracy between the vector couplings ε_{ee}^{uV} and $\varepsilon_{\mu\mu}^{uV}$. For CsI, the

⁸ The same effect should occur for $(\varepsilon_{ee}^{uV}, \varepsilon_{ee}^{dV})$ as well, but is not seen in the left panel of Fig. 5 due to the relatively smaller statistics of the ν_e beam component with respect to the $\nu_\mu + \bar{\nu}_\mu$ components.

allowed region has a symmetric shape, reflecting the fact that Cesium and Iodine have almost the same numbers of protons and neutrons. There are no allowed points around $\varepsilon_{\mu\mu}^{uV} \approx 0.2$, where the NSI and SM contributions to ν_μ - and $\bar{\nu}_\mu$ -induced CE ν NS almost completely cancel out. While an increase of the number of ν_e -induced CE ν NS events could in principle compensate for this effect, the required increase (hence the required value of ε_{ee}^{uV}) is not the same in all energy bins, so that no value of ε_{ee}^{uV} can mimic the experimental data within 90% C.L. A similar effect occurs around $\varepsilon_{ee}^{uV} \approx 0.2$, but only leads to a small shrinking of the allowed region. By contrast, the expected allowed region for NaI is not symmetric. Around $\varepsilon_{ee}^{uV} \approx 0.2$, negative values of $\varepsilon_{\mu\mu}^{uV}$ can compensate for the suppression of ν_e -induced CE ν NS events, but this is not possible for positive values of $\varepsilon_{\mu\mu}^{uV}$, as a consequence of the different proton to neutron ratios of the Sodium and Iodine nuclei⁹. Around $\varepsilon_{\mu\mu}^{uV} \approx 0.2$, the allowed region shrinks for negative values of ε_{ee}^{uV} , but the degeneracy is not completely broken.

Finally, we also observe an “ellipse-shaped” degeneracy between the vector couplings $\varepsilon_{e\mu}^{uV}$ and $\varepsilon_{\mu\mu}^{uV}$ in the lower right panel of Fig. 5, but neither the CsI nor the NaI detector are able to reduce this degeneracy. This can be understood by noting that $\varepsilon_{e\mu}^{uV}$ induces both ν_e and $\nu_\mu/\bar{\nu}_\mu$ coherent scatterings on the target nuclei, without interfering with the SM contribution. Nonvanishing values of $\varepsilon_{e\mu}^{uV}$ can therefore compensate for the destructive interference between the SM and $\varepsilon_{\mu\mu}^{uV}$ contributions to the CE ν NS cross section, which would otherwise reduce the number of $\nu_\mu/\bar{\nu}_\mu$ -induced signal events. As a result, the ellipse is not broken around $\varepsilon_{\mu\mu}^{uV} \approx 0.2$ in the case of the CsI detector, at variance with what one can see in the lower left panel. The expected sensitivity of the future NaI detector only represents a slight improvement on the CsI constraints. In particular, we do not observe a partial breaking of the degeneracy around $\varepsilon_{\mu\mu}^{uV} \approx 0.4$, unlike in the lower left panel.

Let us now consider scalar and tensor GNIs. Fig. 6 shows the 90% C.L. allowed regions for two different pairs of scalar couplings with the same lepton flavor indices, $(\varepsilon_{e\mu}^{uS}, \varepsilon_{e\mu}^{dS})$ in the left panel and $(\varepsilon_{\mu\mu}^{uS}, \varepsilon_{\mu\mu}^{dS})$ in the right panel. As in Fig. 5, the regions allowed by the current CsI data are in green, while the ones delimited by red lines correspond to the expected sensitivity of the future NaI detector, assuming 3 years of data taking at the SNS. Since the scalar couplings $\varepsilon_{\alpha\beta}^{uS}$ and $\varepsilon_{\alpha\beta}^{dS}$ contribute to the CE ν NS cross section through the linear combination $C_{\alpha\beta}^S$, given in Eq. (7), the allowed regions are straight bands around a line passing through the origin (as a consequence of the fact that scalar couplings do not interfere with the SM contribution). While the slope of this line depends on the proton to neutron ratio of the target nucleus, it is in practice very close to -1

⁹ The same asymmetric behaviour can be seen in the $\Delta\chi^2$ for $\varepsilon_{\mu\mu}^{uV}$, in the upper right panel of Fig. 2, where the second minimum is “uplifted” with respect to the first one, a feature that is not observed in the case of the CsI detector.

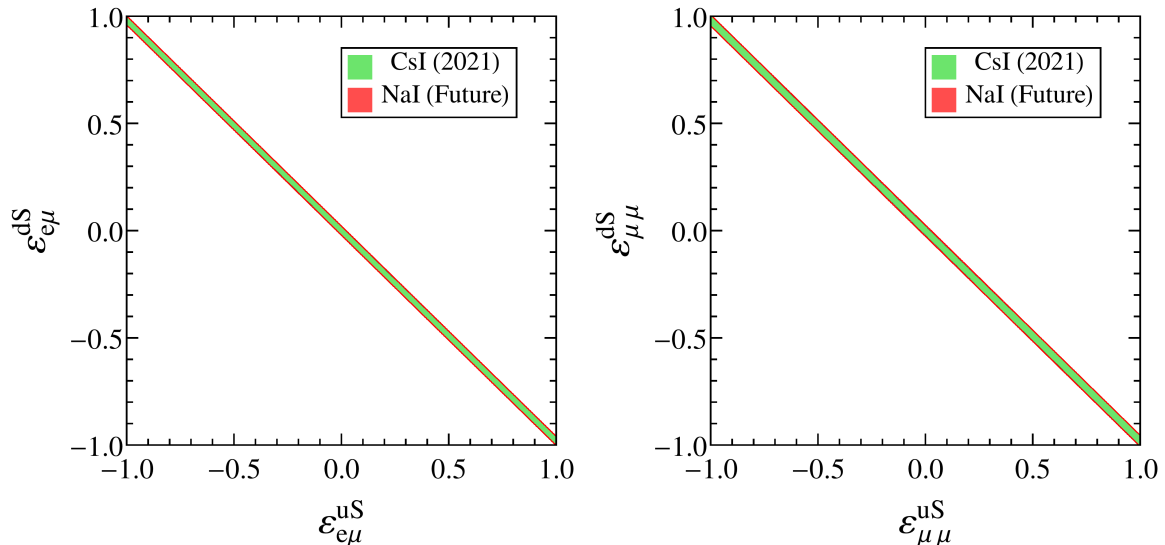


FIG. 6. 90% C.L. allowed regions for the pairs of scalar GNI parameters $(\varepsilon_{e\mu}^{uS}, \varepsilon_{e\mu}^{dS})$ (left panel) and $(\varepsilon_{\mu\mu}^{uS}, \varepsilon_{\mu\mu}^{dS})$ (right panel). The green regions correspond to the constraints from the current CsI data, while the red contours represent the expected sensitivity of the NaI detector described in Subsection III C, assuming 3 years of data taking at the SNS. All GNI parameters are assumed to be real.

for Cs, I and Na, as can be seen in Fig. 6. A consequence of this is that even though Sodium and Iodine have different proton to neutron ratios, the NaI detector is unable to reduce the degeneracy between $\varepsilon_{\alpha\beta}^{uS}$ and $\varepsilon_{\alpha\beta}^{dS}$.

Finally, Fig. 7 displays the 90% C.L. allowed regions for the pairs of tensor couplings $(\varepsilon_{e\mu}^{uT}, \varepsilon_{e\mu}^{dT})$ (left panel) and $(\varepsilon_{\mu\tau}^{uT}, \varepsilon_{\mu\tau}^{dT})$ (right panel). Qualitatively similar features to the scalar case can be observed, except that $\text{CE}\nu\text{NS}$ is much less sensitive to tensor couplings, and that the line slope has a different dependence on the proton to neutron ratio of the nucleus. This explains the shape of the NaI region, but the poor sensitivity of $\text{CE}\nu\text{NS}$ to tensor GNI parameters makes it difficult to reduce the degeneracy between $\varepsilon_{\alpha\beta}^{uT}$ and $\varepsilon_{\alpha\beta}^{dT}$ with a NaI detector.

C. Impact of statistics, systematic uncertainties and background level

In the previous subsections, we argued that the ability of the future NaI detector to set better constraints on generalized neutrino interactions than the current CsI detector was limited by its low signal-over-background ratio. In order to support this statement, and to identify other limiting factors, we now study the impact of statistics, systematic uncertainties and background level on the expected sensitivity of the future NaI detector to GNI parameters. To this end, we consider three

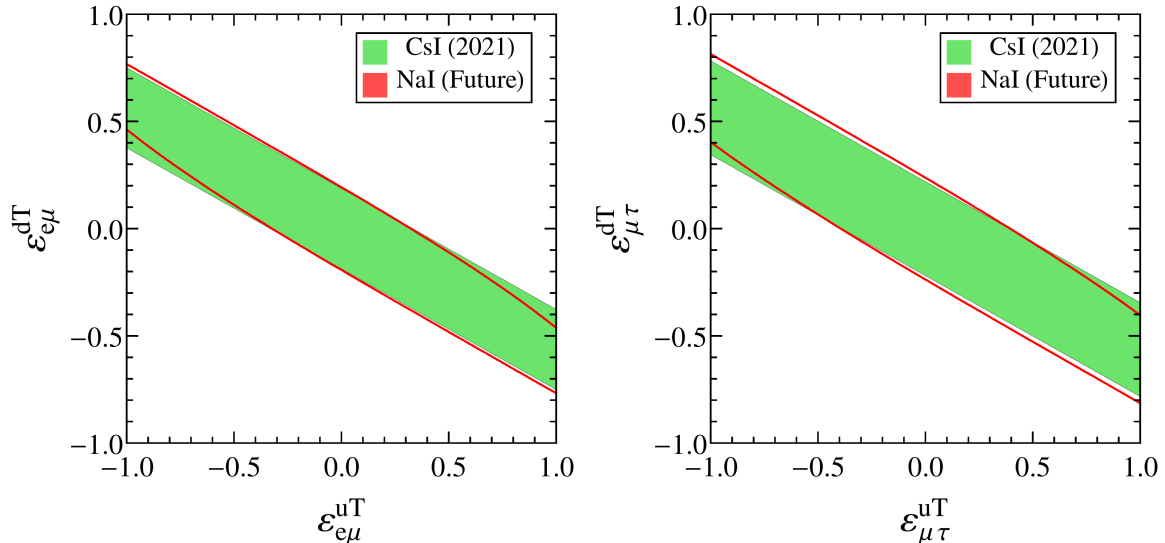


FIG. 7. Same as Fig. 6, but for the pairs of tensor GNI parameters $(\epsilon_{e\mu}^{uT}, \epsilon_{e\mu}^{dT})$ (left panel) and $(\epsilon_{\mu\tau}^{uT}, \epsilon_{\mu\tau}^{dT})$ (right panel).

scenarios characterized by more optimistic assumptions about the exposure time, signal systematic uncertainty or background control than the ones made in the previous subsections. In Scenario A, we assume five years of data taking with the same systematic errors as before (namely, $\sigma_{sig} = 10\%$ and $\sigma_{bg} = 5\%$). In Scenario B, we consider a running time of three years as in the previous subsections, but reduce the signal systematic uncertainty to $\sigma_{sig} = 5\%$, while keeping $\sigma_{bg} = 5\%$. Finally, in Scenario C, we assume a reduced background of 100 ckkd (to be compared with 400 ckkd in the first two recoil energy bins and 300 ckkd in the other bins in the previous subsections), with the same running time and systematic uncertainties as before.

Let us first discuss Scenario A. In Fig. 8, we show the expected sensitivity of the future NaI detector to some representative GNI parameters. In each panel, we compare the results of the previous subsections (red solid lines/red region) with the ones obtained with the larger statistics of Scenario A (blue dashed lines/blue contour). In the upper left panel, one can see that increasing the statistics makes it possible for the NaI detector to exclude the second minimum of the $\Delta\chi^2$ profile for the vector coupling $\epsilon_{\mu\mu}^{uV}$ at the 2σ confidence level. Similarly, in the upper right panel, the larger statistics of Scenario A allows to further reduce the degeneracy between the vector couplings ϵ_{ee}^{uV} and $\epsilon_{\mu\mu}^{uV}$, especially around $(\epsilon_{ee}^{uV}, \epsilon_{\mu\mu}^{uV}) \approx (-0.12, 0.2)$. This result illustrates the capability of a detector made of two nuclei with different proton to neutron ratios to lift degeneracies among NSI parameters, almost as efficiently as combinations of two different detectors, as discussed in Ref. [39] in the context of proposed experiments at the European Spallation Source. However, statistics

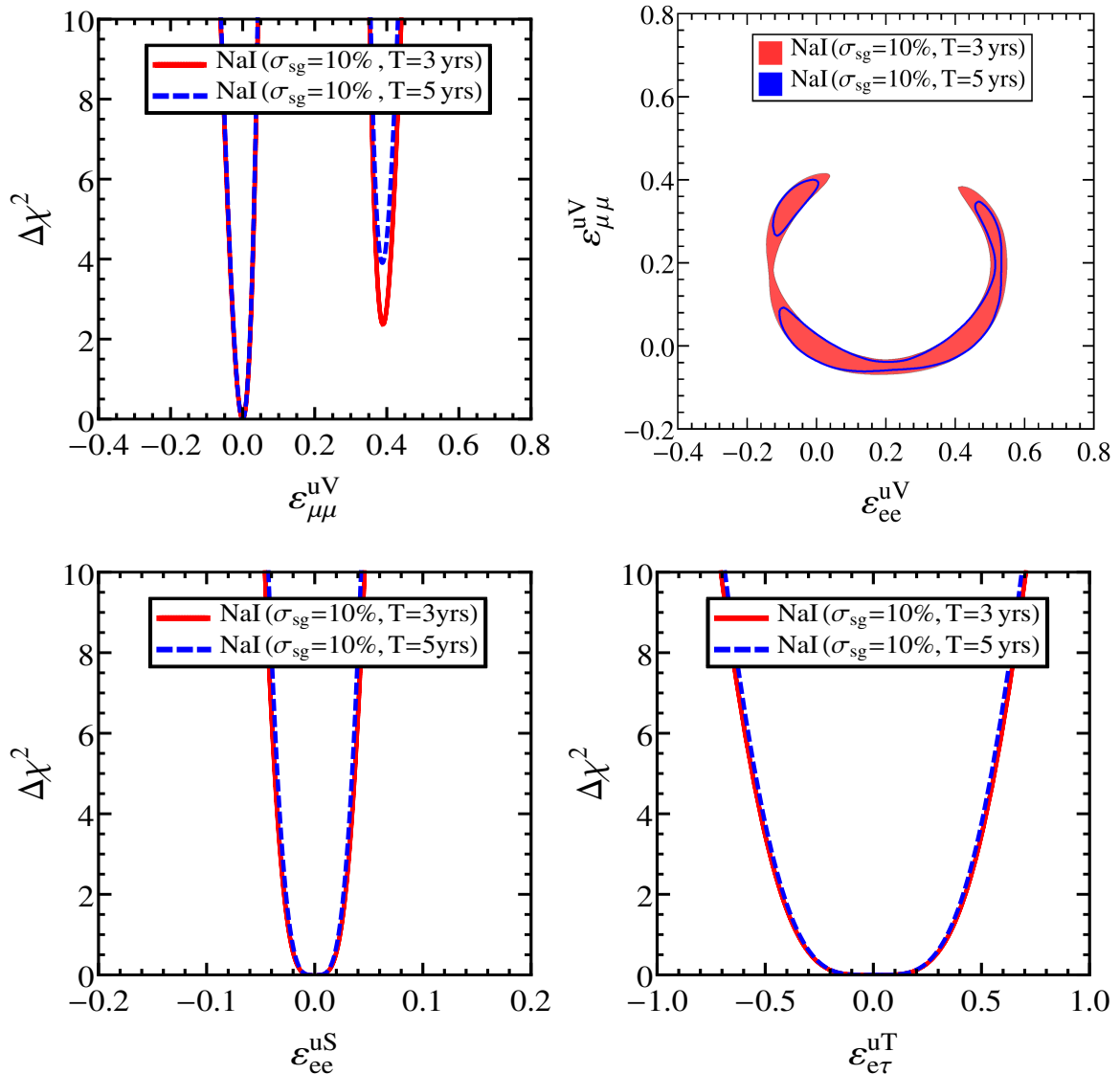


FIG. 8. Expected sensitivities of the future NaI detector to different GNI parameters, assuming 3 years (assumption of Subsections V A and V B, red solid lines/red region) or 5 years (Scenario B, blue dashed lines/blue contour) of data taking at the SNS. Upper left panel: one-dimensional $\Delta\chi^2$ profile for the vector coupling $\varepsilon_{\mu\mu}^{uV}$. Upper right panel: 90% C.L. allowed region for the pair of vector couplings $(\varepsilon_{ee}^{uV}, \varepsilon_{\mu\mu}^{uV})$. Lower panels: one-dimensional $\Delta\chi^2$ profiles for the scalar coupling ε_{ee}^{uS} (left) and tensor coupling $\varepsilon_{e\tau}^{uT}$ (right), both assumed to be real.

and (as we will see later) a good signal-over-background ratio are crucial to fully benefit from the presence of nuclei with different proton to neutron ratios in the same target material. Finally, the bottom panels of Fig. 8 show the $\Delta\chi^2$ profiles for the scalar coupling ε_{ee}^{uS} (left panel) and tensor coupling $\varepsilon_{e\tau}^{uT}$ (right panel). One can see that increasing the exposure time from 3 to 5 years does

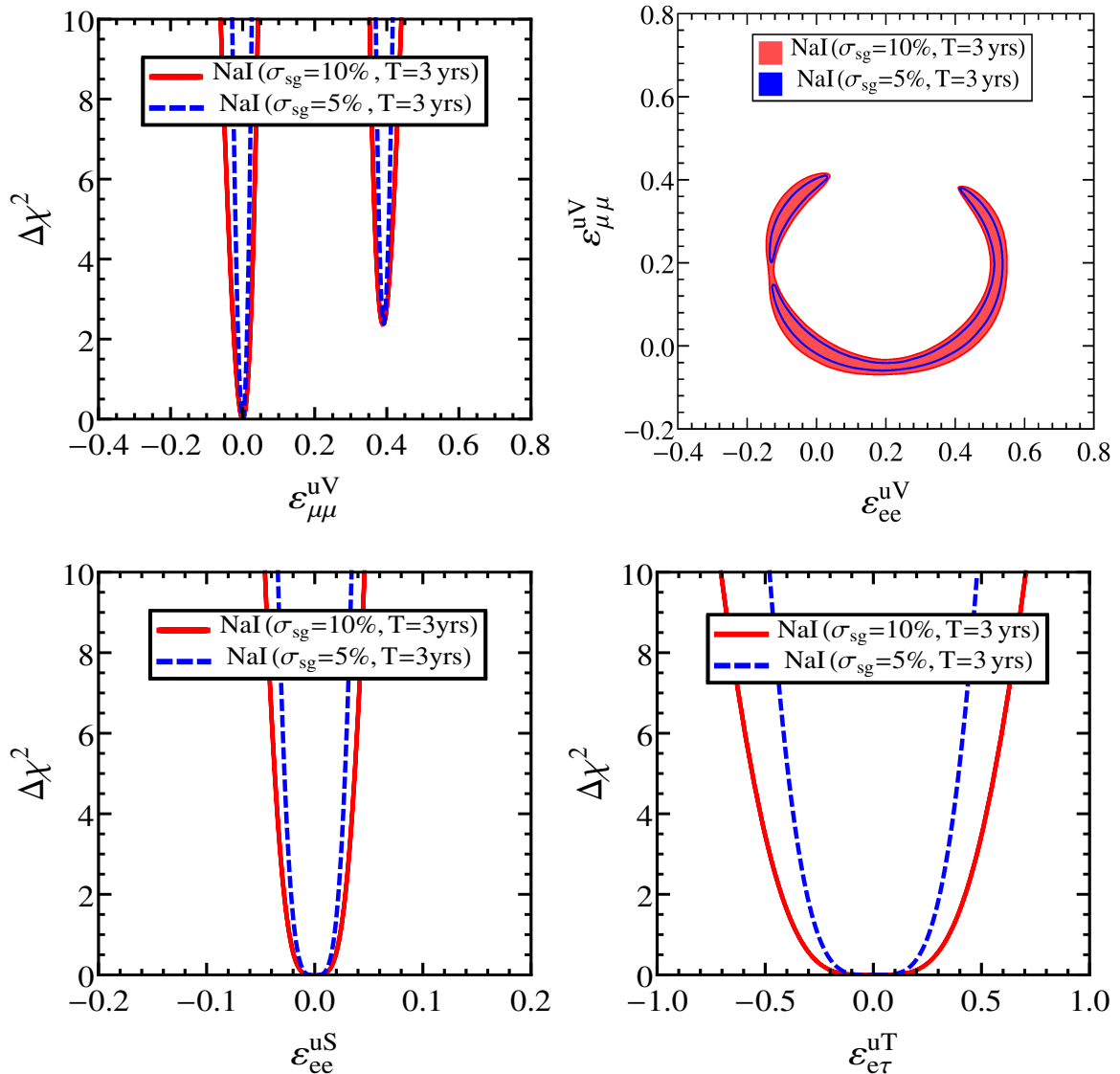


FIG. 9. Expected sensitivities of the future NaI detector to different GNI parameters, assuming a signal systematic uncertainty of 10% (assumption of Subsections VA and VB, red solid lines/red region) or 5% (Scenario B, blue dashed lines/blue contour). Upper left panel: one-dimensional $\Delta\chi^2$ profile for the vector coupling $\varepsilon_{\mu\mu}^{uV}$. Upper right panel: 90% C.L. allowed region for the pair of vector couplings $(\varepsilon_{ee}^{uV}, \varepsilon_{\mu\mu}^{uV})$. Lower panels: one-dimensional $\Delta\chi^2$ profiles for the scalar coupling ε_{ee}^{uS} (left) and tensor coupling $\varepsilon_{e\tau}^{uT}$ (right), both assumed to be real.

not result in a significant improvement of the expected sensitivity to those GNI parameters.

Let us now study the impact of the signal systematic uncertainty. In Fig. 9, we compare the results of the previous subsections (red solid lines/red region) with the ones obtained with the smaller σ_{sig} of Scenario B (blue dashed lines/blue contour), for the same GNI parameters as in Fig. 8. As can be seen, the main effect of reducing the signal systematic error is to improve the

sensitivity to GNI parameters, resulting in smaller allowed intervals or regions at a given confidence level. The impact on degeneracies is less important. In particular, the allowed region in the upper right panel is thinner for $\sigma_{sig} = 5\%$ than for $\sigma_{sig} = 10\%$ (which results in a partial breaking of the degeneracy around $(\varepsilon_{ee}^{uV}, \varepsilon_{\mu\mu}^{uV}) \approx (-0.12, 0.2)$), but the region keeps roughly the same extent. Also, the second minimum of the $\Delta\chi^2$ profile for $\varepsilon_{\mu\mu}^{uV}$ (upper left panel) is excluded at the same confidence level for $\sigma_{sig} = 5\%$ and $\sigma_{sig} = 10\%$.

Finally, we consider Scenario C, which assumes a reduced background level of 100 ckkd in all recoil energy bins, as opposed to 400 ckkd in the first two bins and 300 ckkd in the other bins in Subsections V A and V B. In Fig. 10, we present the expected sensitivity of the future NaI detector to different GNI parameters, both in Scenario C and under the assumptions of Subsections V A and V B. The running time, signal and background systematic uncertainties are the same in both cases. As can be seen from the upper right panel (see also the lower left panel for a different type of degeneracy), a reduction of the background level by 66% (75% in the first two recoil energy bins) is more efficient at breaking degeneracies between NSI parameters than an increase of the running time from 3 to 5 years (Fig. 8), or a decrease of the signal systematic uncertainty by 50% (Fig. 9). The same statement holds for the second minimum of the $\Delta\chi^2$ profile for $\varepsilon_{\mu\mu}^{uV}$ (upper left panel), which is excluded at the 99% confidence level in Scenario C. In fact, such a level of background reduction would make the future NaI detector competitive with some of the best combinations of future advanced detectors at the European Spallation Source [39]. By contrast, the sensitivity to tensor and scalar couplings of the NaI detector is only slightly ameliorated by a better background control (as illustrated in the right panel in the case of the parameter ε_{eT}^{uT}), while a reduction of the signal systematic error has a much stronger impact (see the lower panels of Fig. 9).

VI. CONCLUSIONS

In this work, we studied the potential of a NaI detector with characteristics similar to the one that is currently being deployed by the COHERENT collaboration to constrain scalar, vector, and tensor GNIs via CE ν NS measurements at the Spallation Neutron Source. Compared with the current CsI detector, this new detector has the interesting property that its target material is composed of two nuclei with significantly different proton to neutron ratios, a feature that is known to help break degeneracies among NSI parameters. Furthermore, the future NaI detector benefits from a larger statistics than the current CsI detector, but suffers from a much less favorable signal-over-background ratio. As a consequence, the NaI detector is not expected to significantly improve

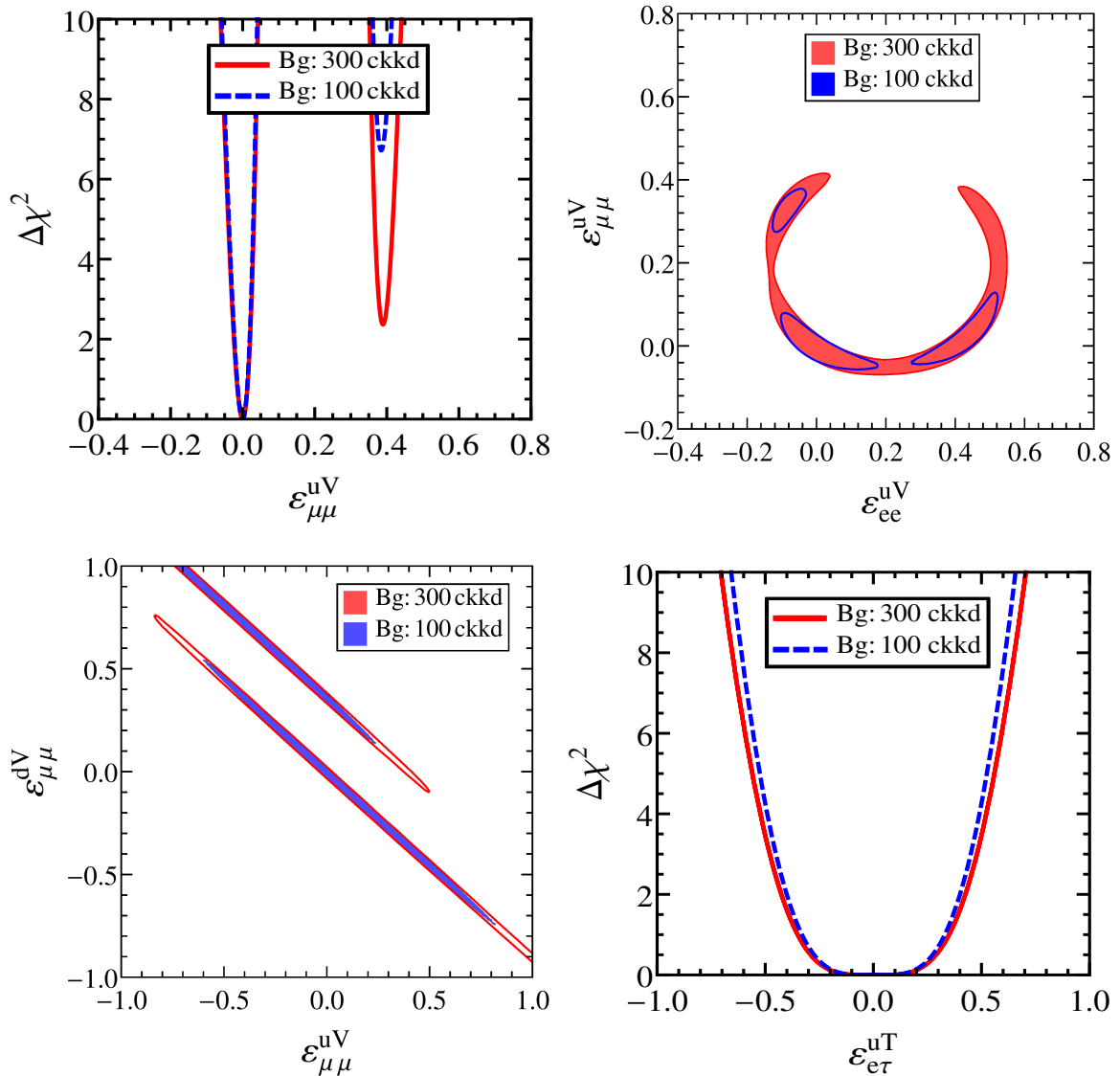


FIG. 10. Expected sensitivities of the future NaI detector to different GNI parameters, assuming the background level of Subsections VA and VB (red solid lines/red region) or 100 ckkd (Scenario C, blue dashed lines/blue contour). Upper left panel: one-dimensional $\Delta\chi^2$ profile for the vector coupling $\varepsilon_{\mu\mu}^{uV}$. Upper right panel: 90% C.L. allowed region for the pair of vector couplings $(\varepsilon_{ee}^{uV}, \varepsilon_{\mu\mu}^{uV})$. Lower left panel: 90% C.L. allowed region for the pair of vector couplings $(\varepsilon_{\mu\mu}^{uV}, \varepsilon_{\mu\mu}^{dV})$. Lower right panel: one-dimensional $\Delta\chi^2$ profile for the tensor coupling $\varepsilon_{e\tau}^{uT}$, assumed to be real.

the current CsI bounds on individual GNI parameters, except for diagonal vector couplings, whose contribution interfere with the Standard Model one in the $CE\nu\text{NS}$ cross section. The NaI detector is also able to partially break degeneracies between two diagonal vector couplings, in a way that is complementary to the current CsI detector. These results are based on the technical details about

the NaI detector given in Refs. [53, 55] and on the background studies of Ref. [53], as well as on our assumptions about signal and background systematic uncertainties.

We also studied the impact of statistics, signal systematic uncertainty and background level on the expected sensitivity of the future NaI detector to GNIs. We found that reducing the signal systematic uncertainty from 10% to 5% significantly improves the sensitivity to all GNI parameters, while increasing the running time from three to five years makes it possible to further break degeneracies among diagonal NSIs, but has little impact on the sensitivity to GNI parameters whose contribution to $CE\nu NS$ does not interfere with the SM contribution. Our results also show that a good background control is crucial to fully benefit from the different proton to neutron ratios of the Sodium and Iodine targets. More specifically, a background level of 100 counts per keV_{ee} per kg per day (ckkd), if achievable, would make the NaI detector considered in this work very efficient at breaking degeneracies among NSI parameters, already after three years of data taking.

ACKNOWLEDGMENTS

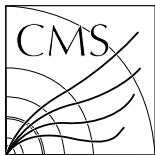
The work of S.S.C. is funded by the Deutsche Forschungsgemeinschaft (DFG, German Research Foundation) – project number 510963981. S. S. C. also acknowledges financial support from the LabEx P2IO (ANR-10-LABX-0038 - Project “BSMNu”) in the framework of the “Investissements d’Avenir” (ANR-11-IDEX-0003-01) managed by the Agence Nationale de la Recherche (ANR), France. This work has been supported by the Spanish grants PID2020-113775GB-I00 (MCIN/AEI/10.13039/501100011033) and CIPROM/2021/054 (Generalitat Valenciana). G.S.G. acknowledges financial support by the CIAPOS/2022/254 grant funded by Generalitat Valenciana. The work of SL is supported in part by the European Union’s Horizon 2020 research and innovation programme under the Marie Skłodowska-Curie grant agreement No. 860881-HIDDeN. O. G. M. was supported by the CONAHCyT grant 23238 and by SNII-Mexico.

-
- [1] D. Z. Freedman, “Coherent effects of a weak neutral current,” *Phys. Rev. D* **9** (Mar, 1974) 1389–1392. <https://link.aps.org/doi/10.1103/PhysRevD.9.1389>.
- [2] **COHERENT** Collaboration, D. Akimov *et al.*, “Observation of Coherent Elastic Neutrino-Nucleus Scattering,” *Science* **357** no. 6356, (2017) 1123–1126, [arXiv:1708.01294](https://arxiv.org/abs/1708.01294) [[nucl-ex](#)].
- [3] D. Akimov *et al.*, “Measurement of the Coherent Elastic Neutrino-Nucleus Scattering Cross Section on CsI by COHERENT,” [arXiv:2110.07730](https://arxiv.org/abs/2110.07730) [[hep-ex](#)].
- [4] **COHERENT** Collaboration, D. Akimov *et al.*, “First Measurement of Coherent Elastic Neutrino-Nucleus Scattering on Argon,” *Phys. Rev. Lett.* **126** no. 1, (2021) 012002, [arXiv:2003.10630](https://arxiv.org/abs/2003.10630) [[nucl-ex](#)].
- [5] M. Cadeddu, N. Cargioli, F. Dordei, C. Giunti, Y. F. Li, E. Picciau, C. A. Ternes, and Y. Y. Zhang, “New insights into nuclear physics and weak mixing angle using electroweak probes,” *Phys. Rev. C* **104** no. 6, (2021) 065502, [arXiv:2102.06153](https://arxiv.org/abs/2102.06153) [[hep-ph](#)].
- [6] M. Cadeddu, C. Giunti, Y. Li, and Y. Zhang, “Average CsI neutron density distribution from COHERENT data,” *Phys. Rev. Lett.* **120** no. 7, (2018) 072501, [arXiv:1710.02730](https://arxiv.org/abs/1710.02730) [[hep-ph](#)].
- [7] O. Miranda, D. Papoulias, G. Sanchez Garcia, O. Sanders, M. Tórtola, and J. Valle, “Implications of the first detection of coherent elastic neutrino-nucleus scattering (CEvNS) with Liquid Argon,” *JHEP* **05** (2020) 130, [arXiv:2003.12050](https://arxiv.org/abs/2003.12050) [[hep-ph](#)].
- [8] J. Barranco, O. G. Miranda, and T. I. Rashba, “Probing new physics with coherent neutrino scattering off nuclei,” *JHEP* **12** (2005) 021, [arXiv:hep-ph/0508299](https://arxiv.org/abs/hep-ph/0508299).
- [9] K. Scholberg, “Prospects for measuring coherent neutrino-nucleus elastic scattering at a stopped-pion neutrino source,” *Phys. Rev. D* **73** (2006) 033005, [arXiv:hep-ex/0511042](https://arxiv.org/abs/hep-ex/0511042).
- [10] V. De Romeri, O. G. Miranda, D. K. Papoulias, G. Sanchez Garcia, M. Tórtola, and J. W. F. Valle, “Physics implications of a combined analysis of COHERENT CsI and LAr data,” *JHEP* **04** (2023) 035, [arXiv:2211.11905](https://arxiv.org/abs/2211.11905) [[hep-ph](#)].
- [11] V. Bresó-Pla, A. Falkowski, M. González-Alonso, and K. Monsálvez-Pozo, “EFT analysis of New Physics at COHERENT,” *JHEP* **05** (2023) 074, [arXiv:2301.07036](https://arxiv.org/abs/2301.07036) [[hep-ph](#)].
- [12] D. Aristizabal Sierra, V. De Romeri, and N. Rojas, “COHERENT analysis of neutrino generalized interactions,” *Phys. Rev. D* **98** (2018) 075018, [arXiv:1806.07424](https://arxiv.org/abs/1806.07424) [[hep-ph](#)].
- [13] L. J. Flores, N. Nath, and E. Peinado, “Non-standard neutrino interactions in $U(1)$ ’ model after COHERENT data,” *JHEP* **06** (2020) 045, [arXiv:2002.12342](https://arxiv.org/abs/2002.12342) [[hep-ph](#)].
- [14] T. Han, J. Liao, H. Liu, and D. Marfatia, “Scalar and tensor neutrino interactions,” *JHEP* **07** (2020) 207, [arXiv:2004.13869](https://arxiv.org/abs/2004.13869) [[hep-ph](#)].
- [15] M. Cadeddu, F. Dordei, C. Giunti, Y. F. Li, and Y. Y. Zhang, “Neutrino, electroweak, and nuclear physics from COHERENT elastic neutrino-nucleus scattering with refined quenching factor,” *Phys. Rev. D* **101** no. 3, (2020) 033004, [arXiv:1908.06045](https://arxiv.org/abs/1908.06045) [[hep-ph](#)].

- [16] O. G. Miranda, D. K. Papoulias, M. Tórtola, and J. W. F. Valle, “Probing neutrino transition magnetic moments with coherent elastic neutrino-nucleus scattering,” [JHEP 07 \(2019\) 103](#), [arXiv:1905.03750 \[hep-ph\]](#).
- [17] M. Cadeddu, F. Dordei, C. Giunti, Y. F. Li, E. Picciau, and Y. Y. Zhang, “Physics results from the first COHERENT observation of coherent elastic neutrino-nucleus scattering in argon and their combination with cesium-iodide data,” [Phys. Rev. D 102 no. 1, \(2020\) 015030](#), [arXiv:2005.01645 \[hep-ph\]](#).
- [18] Y. Farzan, M. Lindner, W. Rodejohann, and X.-J. Xu, “Probing neutrino coupling to a light scalar with coherent neutrino scattering,” [JHEP 05 \(2018\) 066](#), [arXiv:1802.05171 \[hep-ph\]](#).
- [19] L. M. G. de la Vega, L. J. Flores, N. Nath, and E. Peinado, “Complementarity between dark matter direct searches and CE ν NS experiments in U(1)’ models,” [JHEP 09 \(2021\) 146](#), [arXiv:2107.04037 \[hep-ph\]](#).
- [20] E. Bertuzzo, G. Grilli di Cortona, and L. M. D. Ramos, “Probing light vector mediators with coherent scattering at future facilities,” [JHEP 06 \(2022\) 075](#), [arXiv:2112.04020 \[hep-ph\]](#).
- [21] B. Dutta, Y. Gao, R. Mahapatra, N. Mirabolfathi, L. E. Strigari, and J. W. Walker, “Sensitivity to oscillation with a sterile fourth generation neutrino from ultra-low threshold neutrino-nucleus coherent scattering,” [Phys. Rev. D 94 no. 9, \(2016\) 093002](#), [arXiv:1511.02834 \[hep-ph\]](#).
- [22] T. S. Kosmas, D. K. Papoulias, M. Tortola, and J. W. F. Valle, “Probing light sterile neutrino signatures at reactor and Spallation Neutron Source neutrino experiments,” [Phys. Rev. D 96 no. 6, \(2017\) 063013](#), [arXiv:1703.00054 \[hep-ph\]](#).
- [23] D. Akimov *et al.*, “The COHERENT Experimental Program,” in [Snowmass 2021](#). 4, 2022. [arXiv:2204.04575 \[hep-ex\]](#).
- [24] D. Baxter *et al.*, “Coherent Elastic Neutrino-Nucleus Scattering at the European Spallation Source,” [JHEP 02 \(2020\) 123](#), [arXiv:1911.00762 \[physics.ins-det\]](#).
- [25] CCM Collaboration, A. A. Aguilar-Arevalo *et al.*, “First Dark Matter Search Results From Coherent CAPTAIN-Mills,” [arXiv:2105.14020 \[hep-ex\]](#).
- [26] CONUS Collaboration, H. Bonet *et al.*, “Novel constraints on neutrino physics beyond the standard model from the CONUS experiment,” [JHEP 05 \(2022\) 085](#), [arXiv:2110.02174 \[hep-ph\]](#).
- [27] CONNIE Collaboration, A. Aguilar-Arevalo *et al.*, “Results of the Engineering Run of the Coherent Neutrino Nucleus Interaction Experiment (CONNIE),” [JINST 11 no. 07, \(2016\) P07024](#), [arXiv:1604.01343 \[physics.ins-det\]](#).
- [28] ν GeN Collaboration, I. Alekseev *et al.*, “First results of the ν GeN experiment on coherent elastic neutrino-nucleus scattering,” [Phys. Rev. D 106 no. 5, \(2022\) L051101](#), [arXiv:2205.04305 \[nucl-ex\]](#).
- [29] D. Y. Akimov, I. Alexandrov, R. Alyev, V. Belov, A. Bolozdynya, A. Etenko, A. Galavanov, E. Glagovsky, Y. Gusakov, A. Khromov, *et al.*, “The red-100 experiment,” [Journal of Instrumentation 17 no. 11, \(2022\) T11011](#).

- [30] B. C. Canas, E. A. Garces, O. G. Miranda, A. Parada, and G. Sanchez Garcia, “Interplay between nonstandard and nuclear constraints in coherent elastic neutrino-nucleus scattering experiments,” [Phys. Rev. D](#) **101** no. 3, (2020) 035012, [arXiv:1911.09831 \[hep-ph\]](#).
- [31] R. R. Rossi, G. Sanchez Garcia, and M. Tórtola, “Probing nuclear properties and neutrino physics with current and future CE ν NS experiments,” [arXiv:2311.17168 \[hep-ph\]](#).
- [32] M. Lindner, W. Rodejohann, and X.-J. Xu, “Coherent Neutrino-Nucleus Scattering and new Neutrino Interactions,” [JHEP](#) **03** (2017) 097, [arXiv:1612.04150 \[hep-ph\]](#).
- [33] T. Ohlsson, “Status of non-standard neutrino interactions,” [Rept. Prog. Phys.](#) **76** (2013) 044201, [arXiv:1209.2710 \[hep-ph\]](#).
- [34] O. G. Miranda and H. Nunokawa, “Non standard neutrino interactions: current status and future prospects,” [New J. Phys.](#) **17** no. 9, (2015) 095002, [arXiv:1505.06254 \[hep-ph\]](#).
- [35] Y. Farzan and M. Tortola, “Neutrino oscillations and Non-Standard Interactions,” [Front. in Phys.](#) **6** (2018) 10, [arXiv:1710.09360 \[hep-ph\]](#).
- [36] O. G. Miranda, M. A. Tortola, and J. W. F. Valle, “Are solar neutrino oscillations robust?,” [JHEP](#) **10** (2006) 008, [arXiv:hep-ph/0406280](#).
- [37] P. Coloma and T. Schwetz, “Generalized mass ordering degeneracy in neutrino oscillation experiments,” [Phys. Rev. D](#) **94** no. 5, (2016) 055005, [arXiv:1604.05772 \[hep-ph\]](#). [Erratum: [Phys.Rev.D](#) 95, 079903 (2017)].
- [38] A. Galindo-Uribarri, O. G. Miranda, and G. S. Garcia, “Novel approach for the study of coherent elastic neutrino-nucleus scattering,” [Phys. Rev. D](#) **105** no. 3, (2022) 033001, [arXiv:2011.10230 \[hep-ph\]](#).
- [39] S. S. Chatterjee, S. Lavignac, O. G. Miranda, and G. Sanchez Garcia, “Constraining nonstandard interactions with coherent elastic neutrino-nucleus scattering at the European Spallation Source,” [Phys. Rev. D](#) **107** no. 5, (2023) 055019, [arXiv:2208.11771 \[hep-ph\]](#).
- [40] O. Tomalak, P. Machado, V. Pandey, and R. Plestid, “Flavor-dependent radiative corrections in coherent elastic neutrino-nucleus scattering,” [JHEP](#) **02** (2021) 097, [arXiv:2011.05960 \[hep-ph\]](#).
- [41] J. D. Lewin and P. F. Smith, “Review of mathematics, numerical factors, and corrections for dark matter experiments based on elastic nuclear recoil,” [Astropart. Phys.](#) **6** (1996) 87–112.
- [42] J. Erler and R. Ferro-Hernández, “Weak Mixing Angle in the Thomson Limit,” [JHEP](#) **03** (2018) 196, [arXiv:1712.09146 \[hep-ph\]](#).
- [43] **Particle Data Group** Collaboration, R. L. Workman *et al.*, “Review of Particle Physics,” [PTEP](#) **2022** (2022) 083C01.
- [44] S. R. Klein and J. Nystrand, “Exclusive vector meson production in relativistic heavy ion collisions,” [Phys. Rev. C](#) **60** (Jun, 1999) 014903. <https://link.aps.org/doi/10.1103/PhysRevC.60.014903>.
- [45] C. Giunti, “General COHERENT constraints on neutrino nonstandard interactions,” [Phys. Rev. D](#) **101** no. 3, (2020) 035039, [arXiv:1909.00466 \[hep-ph\]](#).

- [46] O. G. Miranda, G. Sanchez Garcia, and O. Sanders, “Coherent elastic neutrino-nucleus scattering as a precision test for the Standard Model and beyond: the COHERENT proposal case,” [Adv. High Energy Phys.](#) **2019** (2019) 3902819, [arXiv:1902.09036 \[hep-ph\]](#).
- [47] E. E. Jenkins, A. V. Manohar, and P. Stoffer, “Low-Energy Effective Field Theory below the Electroweak Scale: Operators and Matching,” [JHEP](#) **03** (2018) 016, [arXiv:1709.04486 \[hep-ph\]](#).
- [48] I. Bischer and W. Rodejohann, “General Neutrino Interactions at the DUNE Near Detector,” [Phys. Rev. D](#) **99** no. 3, (2019) 036006, [arXiv:1810.02220 \[hep-ph\]](#).
- [49] M. Hoferichter, J. Ruiz de Elvira, B. Kubis, and U.-G. Meißner, “High-Precision Determination of the Pion-Nucleon σ Term from Roy-Steiner Equations,” [Phys. Rev. Lett.](#) **115** (2015) 092301, [arXiv:1506.04142 \[hep-ph\]](#).
- [50] T. Bhattacharya, V. Cirigliano, S. Cohen, R. Gupta, H.-W. Lin, and B. Yoon, “Axial, Scalar and Tensor Charges of the Nucleon from 2+1+1-flavor Lattice QCD,” [Phys. Rev. D](#) **94** no. 5, (2016) 054508, [arXiv:1606.07049 \[hep-lat\]](#).
- [51] L. J. Flores, N. Nath, and E. Peinado, “ $CE\nu NS$ as a probe of flavored generalized neutrino interactions,” [Phys. Rev. D](#) **105** no. 5, (2022) 055010, [arXiv:2112.05103 \[hep-ph\]](#).
- [52] A. Majumdar, D. K. Papoulias, R. Srivastava, and J. W. F. Valle, “Physics implications of recent Dresden-II reactor data,” [Phys. Rev. D](#) **106** no. 9, (2022) 093010, [arXiv:2208.13262 \[hep-ph\]](#).
- [53] S. C. Hedges, [Low Energy Neutrino-Nucleus Interactions at the Spallation Neutron Source](#). PhD thesis, Duke U., 2021 (<https://hdl.handle.net/10161/24413>).
- [54] E. Picciau, [Low-energy signatures in DarkSide-50 experiment and neutrino scattering processes](#). PhD thesis, Cagliari U., 2022.
- [55] S. C. Hedges, “The NaI[Tl] COHERENT Detector,”. Talk at the Magnificent $CE\nu NS$ Workshop 2018 ([doi:10.5281/zenodo.3462345](https://doi.org/10.5281/zenodo.3462345)).



Observation of the $\Xi_b^- \rightarrow \psi(2S)\Xi^-$ decay and studies of the Ξ_b^{*0} baryon in proton-proton collisions at $\sqrt{s} = 13$ TeV

The CMS Collaboration*

Abstract

The first observation of the decay $\Xi_b^- \rightarrow \psi(2S)\Xi^-$ and measurement of the branching ratio of $\Xi_b^- \rightarrow \psi(2S)\Xi^-$ to $\Xi_b^- \rightarrow J/\psi\Xi^-$ are presented. The J/ψ and $\psi(2S)$ mesons are reconstructed using their dimuon decay modes. The results are based on proton-proton colliding beam data from the LHC collected by the CMS experiment at $\sqrt{s} = 13$ TeV in 2016–2018, corresponding to an integrated luminosity of 140 fb^{-1} . The branching fraction ratio is measured to be $\mathcal{B}(\Xi_b^- \rightarrow \psi(2S)\Xi^-)/\mathcal{B}(\Xi_b^- \rightarrow J/\psi\Xi^-) = 0.84_{-0.19}^{+0.21} (\text{stat}) \pm 0.10 (\text{syst}) \pm 0.02 (\mathcal{B})$, where the last uncertainty comes from the uncertainties in the branching fractions of the charmonium states. New measurements of the Ξ_b^{*0} baryon mass and natural width are also presented, using the $\Xi_b^- \pi^+$ final state, where the Ξ_b^- baryon is reconstructed through the decays $J/\psi\Xi^-$, $\psi(2S)\Xi^-$, $J/\psi\Lambda K^-$, and $J/\psi\Sigma^0 K^-$. Finally, the fraction of the Ξ_b^- baryons produced from Ξ_b^{*0} decays is determined.

Submitted to Physical Review D

1 Introduction

The Ξ_b family consists of baryons that form isodoublets composed of a triplet of b , s , and q quarks, where q corresponds to a u or d quark for the Ξ_b^0 and Ξ_b^- states, respectively. Three such isodoublets that are neither orbitally nor radially excited should exist [1]. These include one with the spin of the light diquark $j_{qs} = 0$ and spin-parity of the baryon $J^P = 1/2^+$ (Ξ_b ground states), one with $j_{qs} = 1$ and $J^P = 1/2^+$ (Ξ_b'), and another with $j_{qs} = 1$ and $J^P = 3/2^+$ (Ξ_b^*). The ground states were discovered more than a decade ago at the Fermilab Tevatron [2–4] via their decays to $J/\psi \Xi^-$ and $\Xi_c^+ \pi^-$. Three of the four states with $j_{qs} = 1$ have been observed during the last decade at the CERN LHC [5–7] via their $\Xi_b^- \pi^+$ and $\Xi_b^0 \pi^-$ decays, as expected from theoretical predictions [8–10]. The fourth state, $\Xi_b'^0$, is expected to have a mass lower than the $\Xi_b^- \pi^+$ mass threshold, making a strong decay to the Ξ_b^- baryon kinematically impossible. Several other more massive Ξ_b resonances were also observed recently by the CMS and LHCb Collaborations [11–15] via their decays to $\Xi_b^0 \pi^-$, $\Xi_b^- \pi^+$, $\Xi_b^- \pi^+ \pi^-$, $\Xi_b^0 \pi^+ \pi^-$, $\Lambda_b^0 K^-$, and $\Lambda_b^0 K^- \pi^+$. Various theoretical models and calculations predict a spectrum of excited Ξ_b baryons [8–10, 16–27], and the observed resonances are considered to be $1P$ isodoublets of Ξ_b or Ξ_b' states, and a $1D$ doublet. However, larger data samples are needed to measure the quantum numbers of these resonances. There is also the possibility that some of the observed wide resonances could instead be unresolved overlapping narrow states.

Besides the searches for excited Ξ_b states, the LHCb Collaboration has observed new ground-state Ξ_b decays and determined some of their branching fractions [28–33]. The spectrum of excited Ξ_b baryons can be classified relatively easily, especially with the guidance of the similar and well-established Ξ_c baryons [34]. By contrast, the wide variety of decay modes available in the weak decay of the ground-state baryons presents a significant theoretical challenge, and predictions of the branching fractions to various final states are less straightforward. Multi-body decays of Ξ_b baryons can contain rich resonant structures, including both conventional and exotic resonances, such as excited Ξ^- states and the $P_{\psi s}^\Lambda(4459)^0$ pentaquark reported in the $\Xi_b^- \rightarrow J/\psi \Lambda K^-$ decay [35]. The search for new Ξ_b decays is also important in the quest for observing possible CP violation [36]. In general, both weak decays of heavy baryons and their strongly decaying excitations can be described in the framework of heavy-quark effective theory (HQET) [37–41]. Measurements of the decays and properties of both ground and excited Ξ_b states provide coherent and complementary input to HQET, which could improve our understanding of the quantum chromodynamic (QCD) mechanisms responsible for quark dynamics and the formation of hadrons.

In this paper, we study Ξ_b^- and $\Xi_b'^0$ baryon states using a sample of proton-proton (pp) collisions from the LHC, collected by the CMS experiment in 2016–2018 at $\sqrt{s} = 13$ TeV, corresponding to an integrated luminosity of 140 fb^{-1} [42–44]. The inclusion of charge-conjugate states is implied throughout this paper, unless otherwise noted. We report the first observation of the $\Xi_b^- \rightarrow \psi(2S) \Xi^-$ decay and the measurement of its branching fraction with respect to the well-known $\Xi_b^- \rightarrow J/\psi \Xi^-$ decay. In both signal and normalization channels, the charmonium states are reconstructed through their dimuon decay modes, and Ξ^- decays to $\Lambda \pi^-$ with the following $\Lambda \rightarrow p \pi^-$ are used. Thus, the relative branching ratio R is measured using the following expression:

$$R = \frac{\mathcal{B}(\Xi_b^- \rightarrow \psi(2S) \Xi^-)}{\mathcal{B}(\Xi_b^- \rightarrow J/\psi \Xi^-)} = \frac{N(\Xi_b^- \rightarrow \psi(2S) \Xi^-)}{N(\Xi_b^- \rightarrow J/\psi \Xi^-)} \frac{\epsilon(\Xi_b^- \rightarrow J/\psi \Xi^-)}{\epsilon(\Xi_b^- \rightarrow \psi(2S) \Xi^-)} \frac{\mathcal{B}(J/\psi \rightarrow \mu^+ \mu^-)}{\mathcal{B}(\psi(2S) \rightarrow \mu^+ \mu^-)}, \quad (1)$$

where N and ϵ represent the measured number of signal events in data and the total efficiency from Monte Carlo (MC) simulation, respectively, for each of the respective decay modes. The

values of the branching fractions \mathcal{B} in the last term are taken from the PDG [34]. Even though the value of $\mathcal{B}(\Xi_b^- \rightarrow J/\psi \Xi^-)$ is not known, the choice of this normalization channel is quite natural since it has the same topology and similar kinematic properties as the signal channel, reducing the systematic uncertainty in the ratio related to the reconstruction of the muons and the other charged particle tracks from the Ξ_b^- decays.

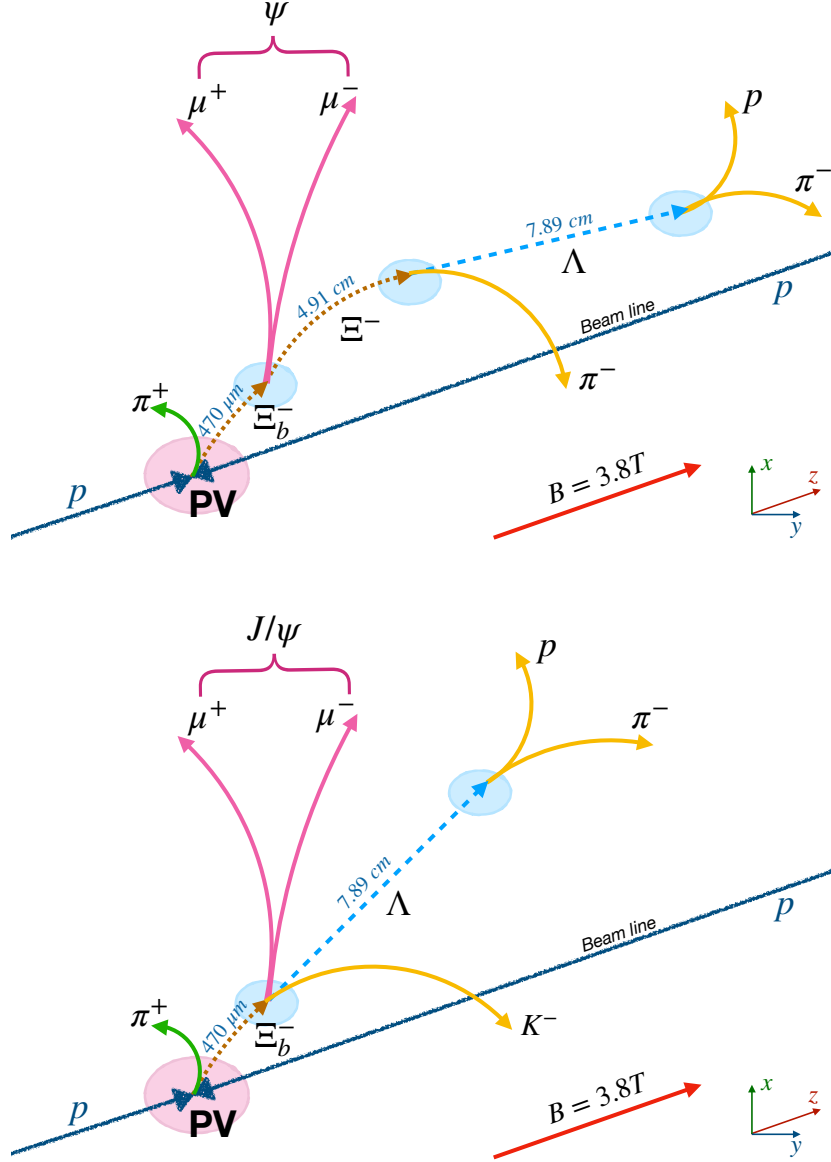


Figure 1: The $\Xi_b^{*0} \rightarrow \Xi_b^- \pi^+$ decay topology, where the Ξ_b^- baryon decays to $\psi \Xi^-$ with $\psi \rightarrow \mu^+ \mu^-$ (upper) or $J/\psi \Lambda K^-$ (lower), where ψ refers to the J/ψ and $\psi(2S)$ mesons. The distances given are the average decay lengths, $c\tau$.

We also determine the Ξ_b^{*0} baryon mass and natural width, using the $\Xi_b^{*0} \rightarrow \Xi_b^- \pi^+$ decay. The ground-state Ξ_b^- is reconstructed via its decays to $J/\psi \Xi^-$, $\psi(2S) \Xi^-$, and $J/\psi \Lambda K^-$. For the $\Xi_b^- \rightarrow \psi(2S) \Xi^-$ decay, both $\psi(2S) \rightarrow J/\psi \pi^+ \pi^-$, with $J/\psi \rightarrow \mu^+ \mu^-$, and $\psi(2S) \rightarrow \mu^+ \mu^-$ modes are used in the analysis, and Ξ^- is again reconstructed via the $\Lambda \pi^-$ channel. For the $\Xi_b^- \rightarrow J/\psi \Lambda K^-$ decay, the presence of the partially reconstructed mode $J/\psi \Sigma^0 K^-$, where the

low-energy photon from the $\Sigma^0 \rightarrow \Lambda \gamma$ decay is undetected, is included in the fit to the $\Xi_b^- \pi^+$ invariant mass spectrum. Pictorial representations of the decay topologies for $\Xi_b^{*0} \rightarrow \Xi_b^- \pi^+$ are shown in Fig. 1.

We also measure the ratio of the production cross sections $R_{\Xi_b^{*0}}$ for Ξ_b^{*0} and Ξ_b^- using the expression:

$$R_{\Xi_b^{*0}} = \frac{\sigma(\text{pp} \rightarrow \Xi_b^{*0} X) \mathcal{B}(\Xi_b^{*0} \rightarrow \Xi_b^- \pi^+)}{\sigma(\text{pp} \rightarrow \Xi_b^- X)} = \frac{N(\Xi_b^{*0} \rightarrow \Xi_b^- \pi^+)}{N(\Xi_b^-)} \frac{\epsilon(\Xi_b^-)}{\epsilon(\Xi_b^{*0} \rightarrow \Xi_b^- \pi^+)}, \quad (2)$$

where N and ϵ refer to similar quantities as those in Eq. (1). Following an analogous CMS measurement of the $B_c(2S)^+$ and $B_c^*(2S)^+$ production cross section ratios [45], the Ξ_b^- baryon is reconstructed in the phase space region defined by the Ξ_b^- baryon transverse momentum $p_T > 15$ GeV and rapidity $|y| < 2.4$; however, this measured ratio is intended to be representative of the entire phase space, given the small mass difference between the Ξ_b^{*0} and Ξ_b^- particles. The Ξ_b^{*0} baryon was the first new particle observed by the CMS Collaboration, using 5 fb^{-1} of data from 2011 [5]. With this paper we significantly improve and enrich our previous results for this state. Tabulated results are provided in the HEPData record for this analysis [46].

2 The CMS detector and simulated event samples

The central feature of the CMS apparatus is a superconducting solenoid of 6 m internal diameter, providing a magnetic field of 3.8 T. Within the solenoid volume are a silicon pixel and strip tracker, a lead tungstate crystal electromagnetic calorimeter, and a brass and scintillator hadron calorimeter, each composed of a barrel and two endcap sections. Forward calorimeters extend the pseudorapidity (η) coverage provided by the barrel and endcap detectors. Muons are measured in gas-ionization detectors embedded in the steel flux-return yoke outside the solenoid. A more detailed description of the CMS detector, together with a definition of the coordinate system used and the relevant kinematic variables, can be found in Ref. [47]. More recent changes to the detector are described in Ref. [48]

Muons are measured in the range $|\eta| < 2.4$, with detection planes made using three technologies: drift tubes, cathode strip chambers, and resistive plate chambers. The single-muon trigger efficiency exceeds 90% over the full η range, whereas the efficiency to reconstruct and identify muons is greater than 96%. Matching muons identified in the muon system to tracks measured in the silicon tracker results in a relative p_T resolution for muons with p_T up to 100 GeV of 1% in the barrel and 3% in the endcaps [49]. The silicon tracker used in 2016 measured charged particles within the range $|\eta| < 2.5$. For nonisolated particles of $1 < p_T < 10$ GeV and $|\eta| < 1.4$, the track resolutions were typically 1.5% in p_T and 25–90 (45–150) μm in the transverse (longitudinal) impact parameter [50]. At the start of 2017, a new pixel detector was installed [51]; the upgraded tracker measured particles up to $|\eta| < 3$ with typical resolutions of 1.5% in p_T and 20–75 μm in the transverse impact parameter [52] for nonisolated particles of $1 < p_T < 10$ GeV. The default track selection used in CMS analyses is the “high-purity” requirement. Because low momentum and displaced tracks share some features with nongenuine tracks such as not pointing back to the pp collision vertex and having fewer measurement points, the high-purity selection is less efficient for these tracks and so the less-restrictive “loose” requirement is often used.

Events of interest are selected using a two-tiered trigger system [53]. The first level (L1), composed of custom hardware processors, uses information from the calorimeters and muon detectors to select events at a rate of around 100 kHz within a fixed latency of about 4 μs [54]. The

second level, known as the high-level trigger (HLT), consists of a farm of computing processors running a version of the full event reconstruction software optimized for fast processing, and reduces the event rate to around 1 kHz before data storage. The events used in this analysis were selected at L1 by requiring the presence of at least two muons, and at the HLT by requiring that the two muons have opposite sign (OS), with various $|\eta|$ and p_T thresholds, compatible with being produced in the dimuon decay of J/ψ or $\psi(2S)$ mesons by requiring the corresponding invariant mass windows.

The PYTHIA 8.240 package [55] with the CP5 underlying event tune [56] is used to simulate the production of the Ξ_b^- and Ξ_b^{*0} states (where the Σ_b^0 baryon, with a modified mass value, is used as a proxy for the Ξ_b^{*0} state). The $\Xi_b^{*0} \rightarrow \Xi_b^- \pi^+$, $\Xi_b^- \rightarrow J/\psi \Xi^-$, $\Xi_b^- \rightarrow \psi(2S) \Xi^-$, $\Xi_b^- \rightarrow J/\psi \Lambda K^-$ (including $\Xi_b^- \rightarrow J/\psi \Sigma^0 K^-$, $\Sigma^0 \rightarrow \Lambda \gamma$), $\psi(2S) \rightarrow \mu^+ \mu^-$, $\psi(2S) \rightarrow J/\psi \pi^+ \pi^-$, and $J/\psi \rightarrow \mu^+ \mu^-$ decays are modeled with EVTGEN 1.6.0 [57], where final-state photon radiation is included using PHOTOS 3.61 [58, 59]. The generated MC events are then passed to a detailed GEANT4-based simulation [60] of the CMS detector, which includes the long-lived hyperon decays $\Xi^- \rightarrow \Lambda \pi^-$ and $\Lambda \rightarrow p \pi^-$. The simulated events are then put through the same trigger and reconstruction algorithms used for the collision data. The simulation includes effects from multiple pp interactions in the same or nearby bunch crossings (pileup) with a multiplicity distribution matching that in data.

3 Event reconstruction and selection

The Ξ_b^- ground state is reconstructed using two main decay modes: $\Xi_b^- \rightarrow \psi \Xi^-$ (followed by $\psi \rightarrow \mu^+ \mu^-$), where ψ refers to the J/ψ and $\psi(2S)$ mesons, or $\Xi_b^- \rightarrow J/\psi \Lambda K^-$. We also reconstruct the decay chain $\Xi_b^- \rightarrow \psi(2S) \Xi^-$, $\psi(2S) \rightarrow J/\psi \pi^+ \pi^-$ to increase the number of events for the $\Xi_b^- \pi^+$ studies. In all the cases, the J/ψ meson is identified through its dimuon decay. The selection criteria, described below, are mainly inherited from Ref. [13].

The reconstruction chain requires two OS muons forming a good-quality vertex, passing the CMS soft-muon selection [49], and with each having $p_T(\mu) > 3 \text{ GeV}$ and $|\eta(\mu)| < 2.4$. To be of good quality, the fit to a dimuon common vertex must have a χ^2 vertex fit probability greater than 1%. These requirements reinforce those applied at the trigger level during the online data taking. A J/ψ or $\psi(2S)$ candidate is required to have a dimuon invariant mass within 100 MeV of the corresponding world-average mass [34], which is about 3 times the mass resolution. Further, a kinematic constraint to the known ψ meson mass [34] is applied to the selected dimuon candidates.

The Λ candidates are formed from displaced two-prong vertices, assuming the decay $\Lambda \rightarrow p \pi^-$, as described in Ref. [61]. The higher-momentum track is associated with the proton and the lower-momentum track with the pion. A Λ candidate must have $p_T > 1.8 \text{ GeV}$, and the $p \pi^-$ invariant mass must be within 10 MeV of the known Λ mass [34] after the tracks are refit to a common vertex, corresponding to about 3 times the mass resolution. The vertex fit is then repeated with the $p \pi^-$ invariant mass constrained to the Λ mass, and its momentum recomputed. The χ^2 probability of this fit must be greater than 1%.

For the $\Xi_b^- \rightarrow \psi \Xi^-$ channel, the Ξ^- candidates are reconstructed by combining each selected Λ candidate with a charged particle track, assumed to be a pion. The track must have $p_T > 0.3 \text{ GeV}$ and satisfy the loose requirement [50]. A kinematic vertex fit of the $\Xi^- \rightarrow \Lambda \pi^-$ decay is performed, and the χ^2 probability is required to be greater than 1%. The $\Lambda \pi^-$ invariant mass must be within 10 MeV of the known Ξ^- mass [34], which is about 3 times the mass resolution. The resulting Ξ^- candidate must have $p_T > 2.5 \text{ GeV}$. Because Λ particles mainly

decay much further from the Ξ^- decay vertex than our vertex resolution, we set a requirement on the pointing angle $\cos \alpha(\Lambda, \Xi^-) > 0.99$ between the momentum of the Λ candidate and the vector from the Ξ^- decay vertex to the Λ decay vertex in the plane perpendicular to the beam direction (the transverse plane).

To reconstruct the decay chain $\Xi_b^- \rightarrow \psi(2S)\Xi^-, \psi(2S) \rightarrow J/\psi\pi^+\pi^-$, two additional OS tracks passing the high-purity requirement [50] are assigned the charged pion mass and added to the process. The higher-momentum pion must have $p_T > 0.6$ GeV, and the other pion $p_T > 0.35$ GeV. The invariant mass of the $\psi(2S)$ candidate, calculated via the formula $M(\mu^+\mu^-\pi^+\pi^-) - M(\mu^+\mu^-) + m^{\text{PDG}}(J/\psi)$, is required to be within 18 MeV of the known $\psi(2S)$ mass [34], corresponding to about 3 times the mass resolution. Using this variable removes the $J/\psi \rightarrow \mu^+\mu^-$ detector invariant mass resolution from the measurement of the $M(\mu^+\mu^-\pi^+\pi^-)$ invariant mass. Here, and throughout the paper, the symbol M represents a reconstructed invariant mass and m^{PDG} the PDG world-average mass [34].

The Ξ_b^- candidates are selected by using the μ^+ , μ^- , and Ξ^- particles in a kinematic fit that constrains their momentum vectors to a common vertex and the dimuon invariant mass to the world-average J/ψ or $\psi(2S)$ mass [34]. For the decay chain $\Xi_b^- \rightarrow \psi(2S)\Xi^-, \psi(2S) \rightarrow J/\psi\pi^+\pi^-$, the two additional pions described above are added to the Ξ_b^- vertex fit. From all the reconstructed pp collision vertices in an event, the primary vertex (PV) is chosen as the one with the smallest pointing angle. The pointing angle is the angle between the Ξ_b^- candidate momentum and the vector joining the PV with the reconstructed Ξ_b^- candidate decay vertex. If any of the tracks used in the Ξ_b^- candidate reconstruction are included in the fit of the chosen PV, they are removed, and the PV is refit. The selected Ξ_b^- candidates are required to have $p_T(\Xi_b^-) > 10$ GeV and a χ^2 vertex fit probability greater than 1%. The pion from the $\Xi^- \rightarrow \Lambda\pi^-$ decay must satisfy an impact parameter significance requirement $d_{xy}/\sigma_{d_{xy}} > 1$, where d_{xy} is the closest distance between the track and the chosen PV in the transverse plane, and $\sigma_{d_{xy}}$ is its uncertainty. For the decay chain $\Xi_b^- \rightarrow \psi(2S)\Xi^-, \psi(2S) \rightarrow J/\psi\pi^+\pi^-$, we require that the two pion tracks each have $d_{xy}/\sigma_{d_{xy}} > 0.4$. The pointing angle α between the Ξ^- momentum and the vector from the Ξ_b^- decay vertex to the Ξ^- vertex in the transverse plane must satisfy $\cos \alpha(\Xi^-, \Xi_b^-) > 0.999$. The analogous angle between the Ξ_b^- momentum and the vector from the PV to the Ξ_b^- vertex is required to have $\cos \alpha(\Xi_b^-, \text{PV}) > 0.99$. Additionally, the distance L_{xy} between the PV and the Ξ_b^- decay vertex in the transverse plane must fulfill the requirement $L_{xy}/\sigma_{L_{xy}} > 3$, where $\sigma_{L_{xy}}$ is its uncertainty.

For the $\Xi_b^- \rightarrow J/\psi\Lambda K^-$ decay channel, the J/ψ and Λ candidates are reconstructed in the same way as described above, with the additional requirement $p_T(\Lambda) > 2$ GeV. However, instead of adding a pion track to the subsequent $\Xi^- \rightarrow \Lambda\pi^-$ fit, a charged particle track with a kaon mass assignment is selected. The track must have $p_T > 1.4$ GeV and satisfy the high-purity requirement [50]. The Ξ_b^- candidates are obtained by performing a kinematic vertex fit to the μ^+ , μ^- , Λ , and K^- candidates, along with the same J/ψ mass constraint and PV selection as for the $\Xi_b^- \rightarrow \psi\Xi^-$ channel. The kaon impact parameter significance must satisfy $d_{xy}/\sigma_{d_{xy}} > 0.5$ with respect to the chosen PV. Because of the higher background in this channel more restrictive kinematic and topological requirements are applied: $p_T(\Xi_b^-) > 15$ GeV and $\cos \alpha(\Xi_b^-, \text{PV}) > 0.999$, along with the same requirements as above on the vertex fit and $L_{xy}/\sigma_{L_{xy}}$.

Since the lifetime of the excited Ξ_b^- states is expected to be negligible, the $\Xi_b^- \pi^+$ candidates are formed by combining the selected Ξ_b^- candidates with each charged particle track originating from the PV and satisfying the loose requirement [50] as done in Ref. [62], which are given the charged pion mass. The pion charge must be opposite to that of the pion from $\Xi^- \rightarrow \Lambda\pi^-$

or the kaon from $\Xi_b^- \rightarrow J/\psi \Lambda K^-$. The mass difference variable $\Delta M = M(\Xi_b^- \pi^+) - M(\Xi_b^-) - m_{\pi^+}^{\text{PDG}}$ is used instead of $M(\Xi_b^- \pi^+)$ since it is characterized by a better mass resolution as the effect of the Ξ_b^- mass resolution is removed. From simulation studies, this variable is found to be insensitive to potential mass shifts caused by the missing low-energy photon from the $\Sigma^0 \rightarrow \Lambda \gamma$ decay. As developed in Ref. [63], the Ξ_b^- candidate and all the tracks forming the PV are refit to a common vertex, further improving the $\Xi_b^- \pi^+$ invariant mass resolution from 1.07 ± 0.07 to 0.74 ± 0.04 MeV (statistical uncertainties only), as determined from simulation studies. If multiple Ξ_b^{*0} candidates (where the multiplicity comes from the soft pion reconstruction) in an event pass the selection requirements (which happens in 10–15% of events depending on the Ξ_b^- channel), only the highest p_T candidate is kept, which is found from simulation studies to improve the signal purity.

4 Observation of the $\Xi_b^- \rightarrow \psi(2S) \Xi^-$ decay and studies of the Ξ_b^- signal

The invariant mass distributions of the selected $J/\psi \Xi^-$, $J/\psi \Lambda K^-$, and $\psi(2S) \Xi^-$ (with both $\psi(2S) \rightarrow \mu^+ \mu^-$ and $\psi(2S) \rightarrow J/\psi \pi^+ \pi^-$) candidates are shown in Fig. 2. An unbinned extended maximum likelihood fit is performed on each of these distributions. For all four channels, the signal component is described using the sum of two Gaussian functions with a common mean, whose widths and ratio between them are fixed to those determined from MC simulation. However, both widths are allowed to scale by the same free parameter in the fit to give a better description of the data. The background is described with a first-order polynomial for the $J/\psi \Xi^-$ and $\psi(2S) \Xi^-$ channels, and an exponential function for the $J/\psi \Lambda K^-$. In the latter fit, the signal contribution from the partially reconstructed $\Xi_b^- \rightarrow J/\psi \Sigma^0 K^-$ decays is taken into account by including an asymmetric Gaussian (also known as skew normal) function in the fit, whose shape parameters are fixed to those found from simulation studies.

Table 1: The number of signal events N , the mean Ξ_b^- mass $m_{\Xi_b^-}^{\text{fit}}$, and the effective Ξ_b^- width σ_{eff} from the fits to the Ξ_b^- invariant mass distributions for each of the Ξ_b^- decay channels. The uncertainties are statistical only.

Decay channel	N	$m_{\Xi_b^-}^{\text{fit}}$ (MeV)	σ_{eff} (MeV)
$\Xi_b^- \rightarrow J/\psi \Xi^-$	846 ± 40	5797.1 ± 0.6	16.3 ± 1.0
$\Xi_b^- \rightarrow J/\psi \Lambda K^-$	920 ± 98	5798.8 ± 0.9	11.9 ± 1.5
$\Xi_b^- \rightarrow J/\psi \Sigma^0 K^-$	880 ± 170	—	—
$\Xi_b^- \rightarrow \psi(2S) \Xi^-$ (with $\psi(2S) \rightarrow \mu^+ \mu^-$)	74 ± 11	5797.7 ± 1.4	11.1 ± 2.0
$\Xi_b^- \rightarrow \psi(2S) \Xi^-$ (with $\psi(2S) \rightarrow J/\psi \pi^+ \pi^-$)	90 ± 14	5797.2 ± 1.7	13.1 ± 2.8

The number of signal events N , the mean Ξ_b^- mass $m_{\Xi_b^-}^{\text{fit}}$, and the effective Ξ_b^- width σ_{eff} from the fit are given in Table 1 for each of the Ξ_b^- decay channels, along with their statistical uncertainties. The value of σ_{eff} is calculated as $\sqrt{f_1 \sigma_1^2 + (1 - f_1) \sigma_2^2}$, where σ_1 (σ_2) is the width of the first (second) Gaussian, and f_1 is the fraction of signal events from the fit associated with the first Gaussian function. The measured resolution of the different channels is within the expectations from the available phase space and the final state threshold proximity. The fitted Ξ_b^- mass values are consistent with the world-average value $m_{\Xi_b^-}^{\text{PDG}} = 5797.0 \pm 0.6$ MeV [34].

This is the first observation of the $\Xi_b^- \rightarrow \psi(2S) \Xi^-$ decay. Its local statistical significance is eval-

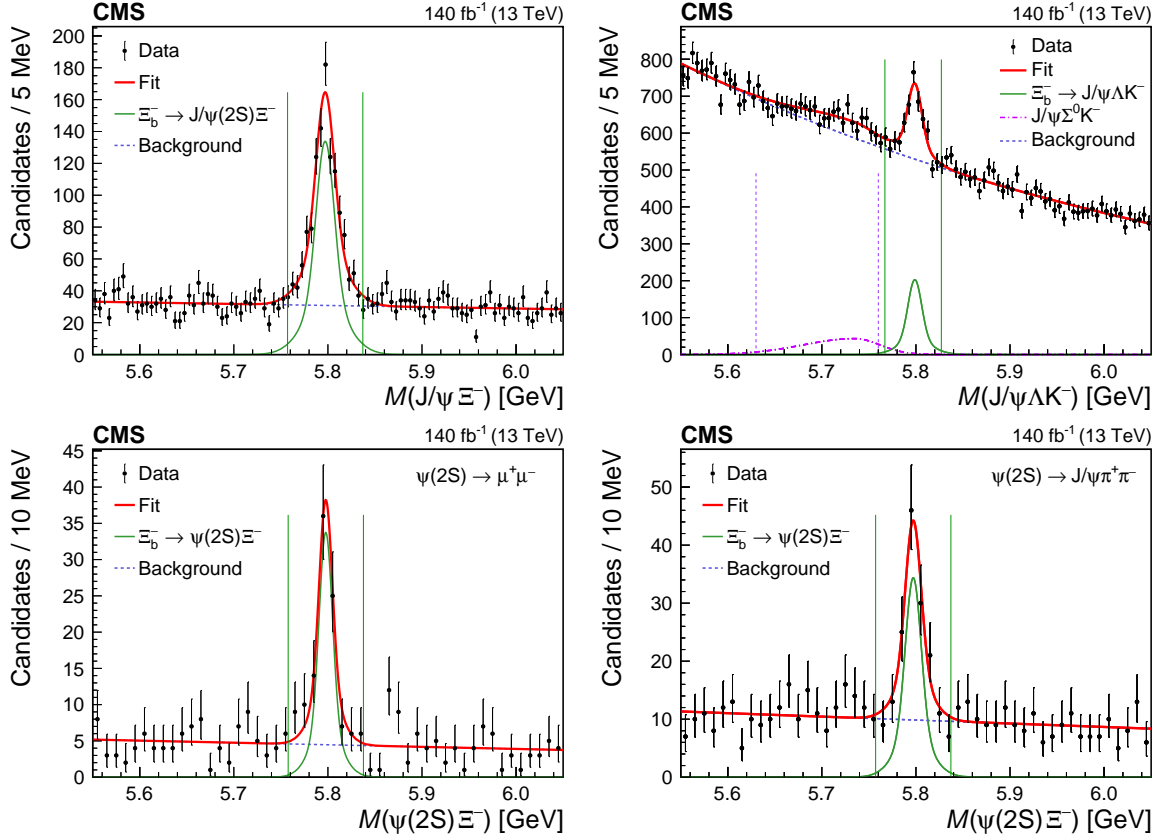


Figure 2: Invariant mass distributions of the selected $J/\psi \Xi^-$ (upper left), $J/\psi \Lambda K^-$ (upper right), and $\psi(2S) \Xi^-$ [lower row, with $\psi(2S) \rightarrow \mu^+ \mu^-$ (left) and $\psi(2S) \rightarrow J/\psi \pi^+ \pi^-$ (right) candidates]. The data are shown by the points, while the vertical bars represent the statistical uncertainties. The overall fit result is shown by the solid red curve, with the signal and background contributions given by the solid green and dashed blue curves, respectively. The vertical lines around each peak display the mass window required for a Ξ_b^- candidate to be used in the Ξ_b^{*0} studies. The dotted-dashed curve in the upper right plot shows the fitted contribution from the $\Xi_b^- \rightarrow J/\psi \Sigma^0 K^-$ decay, with the accompanying vertical dotted lines indicating the mass window for this mode.

uated with the likelihood ratio technique, comparing the likelihood value from a fit to a signal-plus-background hypothesis to that for a background-only hypothesis. Since the conditions of Wilks' theorem [64] are satisfied, the asymptotic formulae of Ref. [65] (Eqs. (12) and (52)) are used to determine the $\Xi_b^- \rightarrow \psi(2S) \Xi^-$ signal significance, which is found to be well above 5 standard deviations for both the $\psi(2S) \rightarrow \mu^+ \mu^-$ and $\psi(2S) \rightarrow J/\psi \pi^+ \pi^-$ modes.

For the $\Xi_b^- \pi^+$ studies described in the next section, the Ξ_b^- candidates must have an invariant mass within 40 (30) MeV of the $m_{\Xi_b^-}^{\text{fit}}$ value for the $J/\psi \Xi^-$ and $\psi(2S) \Xi^-$ ($J/\psi \Lambda K^-$) decay channels. This corresponds to about (2.5–3) times σ_{eff} , as shown by the solid vertical lines around the peaks in Fig. 2. For the partially reconstructed $J/\psi \Sigma^0 K^-$ decay channel, a mass window of 5.63–5.76 GeV, as in Ref. [13] and shown by the vertical dotted lines in Fig. 2 (upper right), is used for the reconstructed Ξ_b^- mass.

5 Studies of the Ξ_b^{*0} baryon

The measured ΔM distributions found by combining the selected Ξ_b^- candidates, as defined in Section 4, with charged particle tracks, consistent with coming from the PV and assumed to be pions, are shown in Fig. 3. The distributions are shown separately for the $\Xi_b^- \rightarrow J/\psi \Xi^-$, $\Xi_b^- \rightarrow \psi(2S) \Xi^-$ (combined $\psi(2S) \rightarrow J/\psi \pi^+ \pi^-$ and $\psi(2S) \rightarrow \mu^+ \mu^-$ modes), $\Xi_b^- \rightarrow J/\psi \Lambda K^-$, and $\Xi_b^- \rightarrow J/\psi \Sigma^0 K^-$ channels. A significant near-threshold peak is evident in all 4 distributions, in agreement with previous CMS [5] and LHCb [6, 15] results. The ΔM distribution for the same-sign $\Xi_b^- \pi^-$ control sample is also displayed in Fig. 3. It shows no evidence of a peak and is consistent with the $\Xi_b^- \pi^+$ combinatorial background. No other structures are observed in this ΔM region for either the $\Xi_b^- \pi^+$ or $\Xi_b^- \pi^-$ distributions.

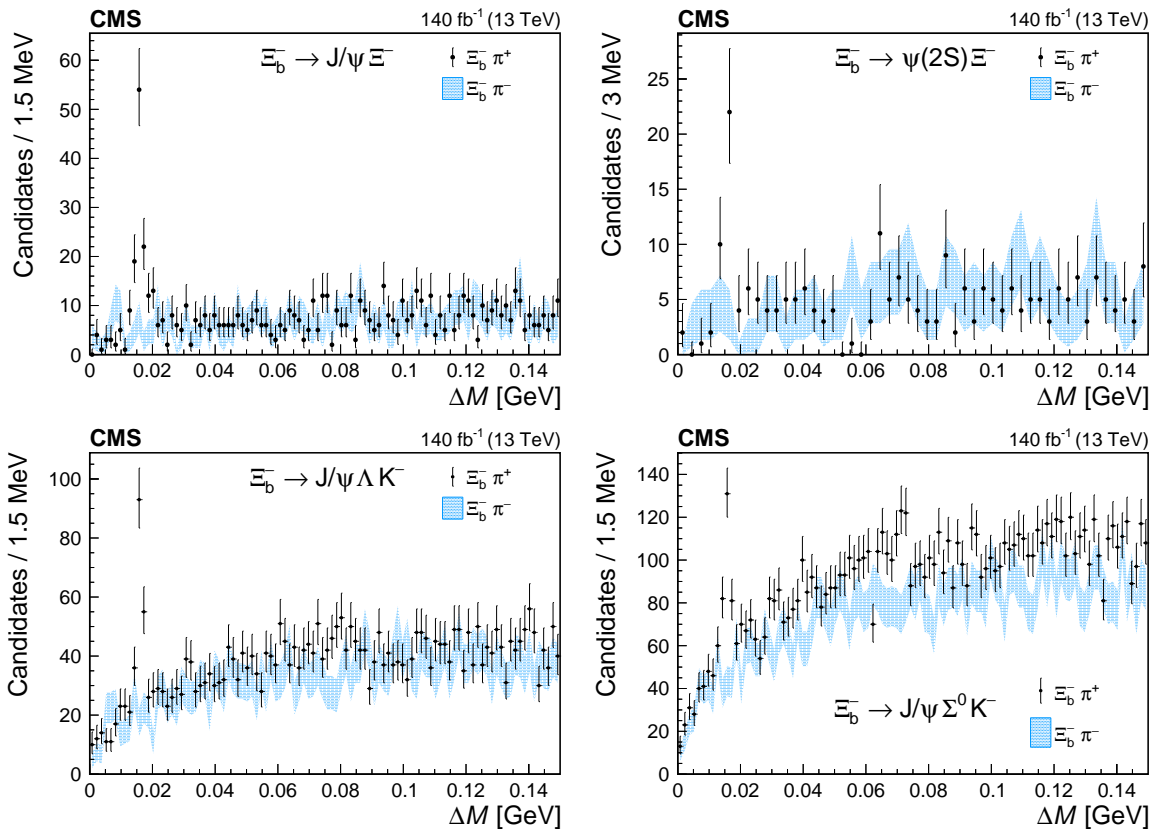


Figure 3: The mass difference ΔM distribution of the selected $\Xi_b^- \pi^\pm$ candidates for the decay channel labeled on each plot. The points show the correct-sign combinations and the blue bands the wrong-sign. The vertical bars on the points and the length of the bands represent the statistical uncertainties in each distribution, respectively.

We fit the Ξ_b^{*0} signal using a relativistic Breit–Wigner function, which accounts for the non-negligible natural width $\Gamma(\Xi_b^{*0})$, convolved with a Gaussian function describing the invariant mass resolution, whose parameters are extracted from MC simulation. Lattice QCD calculations [66] give $\Gamma(\Xi_b^{*0}) = 0.51 \pm 0.16$ MeV, the 3P_0 model predicts 0.85 MeV [67], and the latest LHCb result finds $\Gamma(\Xi_b^{*0}) = 0.87 \pm 0.06 \pm 0.05$ MeV [15]. The simulation studies predict that the invariant mass resolution is slightly different for each Ξ_b^- baryon decay channel, except for the $\Xi_b^- \rightarrow J/\psi \Sigma^0 K^-$ mode, where the missing low-energy photon from the Σ^0 baryon decay produces a much wider peak with a 26% larger mass resolution. In all cases, the measured widths from the fully reconstructed decay modes are in agreement within their uncertainties.

An unbinned extended maximum likelihood simultaneous fit of all four channels is applied, where the Ξ_b^{*0} mass and natural width are constrained to be equal for all the channels, while the mass resolutions, yields, and background parameters are different. The background component is modeled with a threshold function $(\Delta M)^\alpha$, where α is a free parameter. The fit results are shown in Fig. 4, and the fitted signal yields are given in Table 2.

The measured mass difference and natural width of the Ξ_b^{*0} state are $\Delta M^{\text{fit}} = 15.810 \pm 0.077$ MeV and $\Gamma(\Xi_b^{*0}) = 0.87^{+0.22}_{-0.20}$ MeV, respectively, where the uncertainties are statistical only.

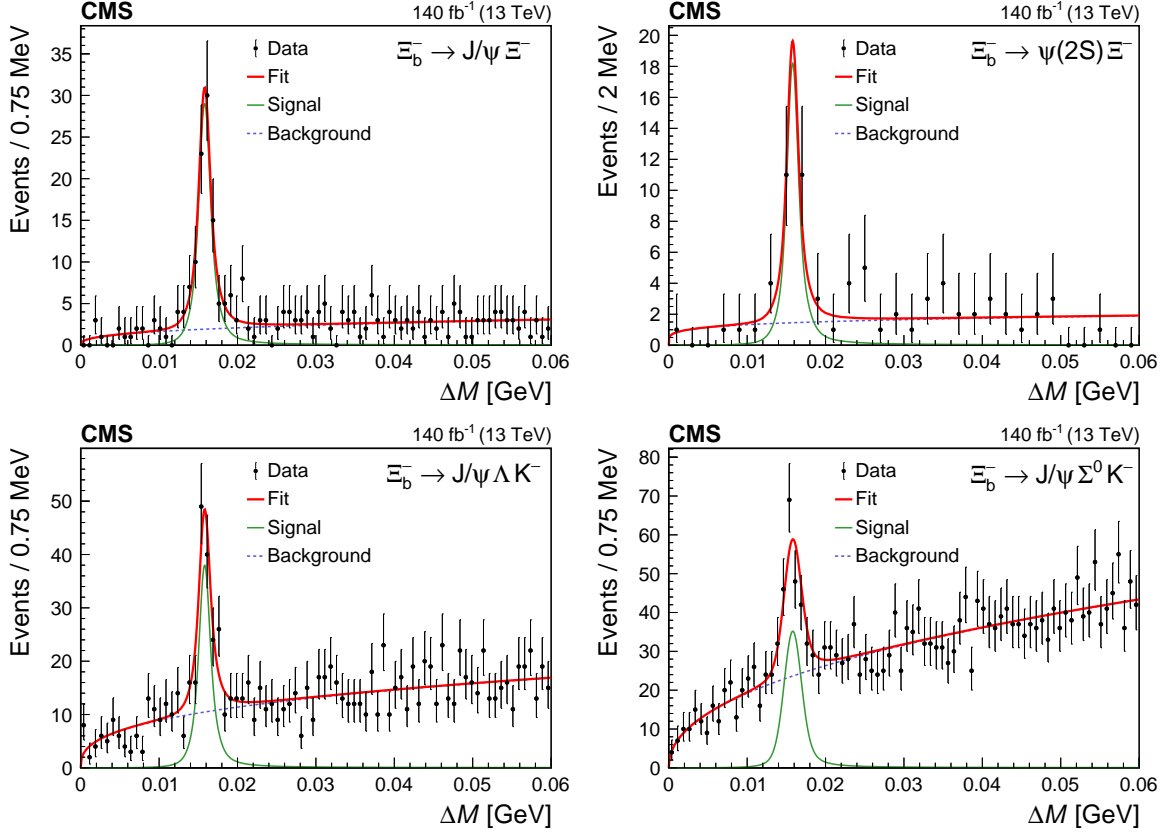


Figure 4: Results of the simultaneous fits to the ΔM invariant mass distributions for the Ξ_b^{*0} candidates in the decay channels given in each plot. The points show the data, with the vertical bars representing the statistical uncertainty. The solid red curve displays the overall fit result, with the solid green and dashed blue curves showing the signal and background contributions, respectively.

Table 2: The fitted signal yields of the $\Xi_b^{*0} \rightarrow \Xi_b^- \pi^+$ decay for each of the listed Ξ_b^- decay channels. Uncertainties are statistical only.

Decay channel	$N(\Xi_b^{*0})$
$\Xi_b^- \rightarrow J/\psi \Xi^-$	97^{+13}_{-12}
$\Xi_b^- \rightarrow \psi(2S) \Xi^-$	24^{+6}_{-5}
$\Xi_b^- \rightarrow J/\psi \Lambda K^-$	124^{+17}_{-16}
$\Xi_b^- \rightarrow J/\psi \Sigma^0 K^-$	155^{+22}_{-20}

6 Efficiency and production ratio measurements

While in general the analysis uses events collected by a combination of different dimuon HLT paths, for the measurements of the ratios of efficiencies and the resulting branching fractions and production cross sections, a single dedicated trigger suitable for the decay topology is required in order to simplify the efficiency estimations and reduce the trigger-related systematic uncertainty. For the $\Xi_b^- \rightarrow J/\psi \Xi^-$ and $\Xi_b^- \rightarrow \psi(2S) \Xi^-$ channels, we use an inclusive dimuon HLT path, requiring the presence in the event of a J/ψ ($\psi(2S)$) meson with p_T exceeding 25 (18) GeV and decaying into two OS muons. This HLT path is only used for the 2017–2018 sample, while for the 2016 sample the similar trigger requires a minimum p_T of 20 (13) GeV for the J/ψ ($\psi(2S)$) meson. In the case of the $\Xi_b^- \rightarrow J/\psi \Lambda K^-$ channel, we use an HLT path requiring the presence of a $J/\psi \rightarrow \mu^+ \mu^-$ decay and an additional track consistent with originating from the dimuon vertex and having $d_{xy}/\sigma_{d_{xy}} > 2$. The dimuon vertex must also be displaced from the PV, by requiring $L_{xy}/\sigma_{L_{xy}} > 3$.

These requirements are much stricter than those discussed in Section 3 — most ψ from Ξ_b^- decays are populated within the 10–20 GeV range of p_T . Thus, using them causes a significant decrease in the signal yields for the $\psi \Xi^-$ channels. Redoing the fitting procedure with the new requirements leads to total signal yields of 103_{-13}^{+14} and 38_{-7}^{+8} for $\Xi_b^- \rightarrow J/\psi \Xi^-$ and $\Xi_b^- \rightarrow \psi(2S) \Xi^-$ ($\psi(2S) \rightarrow \mu^+ \mu^-$ mode), respectively. The $\Xi_b^- \rightarrow J/\psi \Lambda K^-$ signal with the tighter HLT requirement results in 606_{-64}^{+67} events. The fits to the $\Xi_b^{*0} \rightarrow \Xi_b^- \pi^+ \Delta M$ distributions are performed separately for each of the decay channels, with $\Gamma(\Xi_b^{*0})$ fixed to the value found from the simultaneous fit. The resulting signal yields are 13 ± 4 and 74 ± 11 for the $J/\psi \Xi^-$ and $J/\psi \Lambda K^-$ decay modes, respectively.

The efficiencies for the signal and normalization channels are calculated using simulated MC samples of events that have passed the more-restrictive HLT paths described above. The total efficiency includes several factorizable contributions such as the trigger, detector acceptance, and decay channel reconstruction efficiencies. The detector acceptance term is calculated as the ratio of the number of generator-level events within the CMS kinematic acceptance to the number of generated events without any restrictions (within the full phase space region). Efficiencies for different years of data taking are estimated separately and then combined with weights corresponding to the integrated luminosity collected in each year.

Since we measure branching fractions and production cross sections with respect to normalization channels, only the ratios of such efficiencies are needed. Thus, for example, the systematic uncertainties associated with the muon, charged particle track, and Λ candidate reconstruction are reduced. Table 3 reports three efficiency ratios, where the first is used in measuring the quantity R , the ratio of branching fractions defined in Eq. (1), and the latter two for finding the Ξ_b^{*0}/Ξ_b^- production cross section ratio using two different decay channels: $J/\psi \Xi^-$ and $J/\psi \Lambda K^-$.

Table 3: The measured efficiency ratios and their statistical uncertainties.

Efficiency ratio	Value
$\epsilon(\Xi_b^- \rightarrow J/\psi \Xi^-)/\epsilon(\Xi_b^- \rightarrow \psi(2S) \Xi^-, \psi(2S) \rightarrow \mu^+ \mu^-)$	0.304 ± 0.014
$\epsilon(\Xi_b^- \rightarrow J/\psi \Xi^-)/\epsilon(\Xi_b^{*0} \rightarrow \Xi_b^- \pi^+, \Xi_b^- \rightarrow J/\psi \Xi^-)$	1.645 ± 0.108
$\epsilon(\Xi_b^- \rightarrow J/\psi \Lambda K^-)/\epsilon(\Xi_b^{*0} \rightarrow \Xi_b^- \pi^+, \Xi_b^- \rightarrow J/\psi \Lambda K^-)$	1.941 ± 0.085

Using the measured signal yields, the efficiency ratio, and Eq. (1), we determine the ratio R of the branching fraction for the newly observed $\Xi_b^- \rightarrow \psi(2S) \Xi^-$ decay to that of the $\Xi_b^- \rightarrow$

$J/\psi \Xi^-$ decay to be

$$R = 0.84^{+0.21}_{-0.19},$$

where the uncertainty is coming from the uncertainty in the measured yields. The uncertainty in the ratio of efficiencies is treated separately as a systematic uncertainty, as described in Section 7.1.

Applying Eq. (2), the ratio $R_{\Xi_b^{*0}}$ of the Ξ_b^{*0} to Ξ_b^- production is separately measured using two Ξ_b^- decay channels: $J/\psi \Xi^-$ and $J/\psi \Lambda K^-$. The results are

$$R_{\Xi_b^{*0}}^{J/\psi \Xi^-} = 0.21 \pm 0.07$$

and

$$R_{\Xi_b^{*0}}^{J/\psi \Lambda K^-} = 0.24 \pm 0.04,$$

where the uncertainties are statistical only (again, the efficiency uncertainties are discussed in Section 7.1). Both values, obtained with fully independent data and simulation samples, are in good agreement with each other and with the previous measurement by the LHCb Collaboration [6].

7 Systematic uncertainties

The systematic uncertainties in the measurements given above are divided into two categories. The first is related to the uncertainties in the measured efficiency ratios and the Ξ_b^- and Ξ_b^{*0} signal yields. The second covers the uncertainties in the measured mass difference and natural width of the Ξ_b^{*0} baryon.

7.1 Systematic uncertainties in the measured ratios

Many systematic uncertainties related to muon reconstruction and identification, trigger effects and efficiencies, and charged particle track and Λ candidate reconstruction cancel out in the measured ratio R due to the identical topologies of the $\Xi_b^- \rightarrow \psi(2S)\Xi^-$ and $\Xi_b^- \rightarrow J/\psi \Xi^-$ decays. There is a similar cancellation in the determination of the production cross section ratio $R_{\Xi_b^{*0}}$, where the only topological difference between Ξ_b^{*0} and Ξ_b^- is an additional track from the $\Xi_b^{*0} \rightarrow \Xi_b^- \pi^+$ decay.

The systematic uncertainty related to the choice of fit functions used to describe the signal and background shapes in the invariant mass fits is evaluated by varying the functions used and recording the change in the number of signal events. For the three Ξ_b^- decay channels, we first perform the fit with the resolution scaling parameter for the sum of two Gaussian functions set to unity and note the change in the fit results. We then use a Student's t distribution [68] to model the signal, with the mean and the width allowed to be free and the n parameter (corresponding to the number of degrees of freedom) fixed from the simulation. This function, being symmetric and bell-shaped, also models a heavy-tailed distribution and thus is found to be a reliable alternative to the sum of two Gaussian functions. A single Gaussian function with free parameters is also tried for fitting the $\psi(2S)\Xi^-$ and $J/\psi \Xi^-$ signals. Using the largest change in the number of events, the resulting systematic uncertainty in R from this source is 8.8%.

Two alternative background functions are considered in fitting the $J/\psi \Xi^-$ and $\psi(2S)\Xi^-$ invariant mass distributions: an exponential function and a second-order polynomial. For the more

complicated background shape in the $J/\psi\Lambda K^-$ distribution, we switch from an exponential function to a second-order polynomial. The resulting systematic uncertainty in R from this source is estimated as 4.5%. The combined signal-plus-background Ξ_b^- fit model uncertainties are estimated as 4.0 and 6.9% in the $R_{\Xi_b^{*0}}^{J/\psi\Xi^-}$ and $R_{\Xi_b^{*0}}^{J/\psi\Lambda K^-}$ values, respectively.

The alternative functions used in fitting the $\Xi_b^{*0} \rightarrow \Xi_b^- \pi^+$ ΔM distribution are described in the next subsection when the systematic uncertainties in the measured Ξ_b^{*0} mass and width are discussed. The resulting systematic uncertainties due to the fitting functions in the $R_{\Xi_b^{*0}}$ production cross section ratio are 7.7 and 6.7% for the $J/\psi\Xi^-$ and $J/\psi\Lambda K^-$ decay modes, respectively.

For the R measurement, given that we are using different HLT paths for the $\Xi_b^- \rightarrow J/\psi\Xi^-$ and the $\Xi_b^- \rightarrow \psi(2S)\Xi^-$ signals, a cross-check of the correctness and robustness of such a procedure is performed. The similar branching fraction ratio $R_{B^+} = \mathcal{B}(B^+ \rightarrow \psi(2S)K^+)/\mathcal{B}(B^+ \rightarrow J/\psi K^+)$ was measured with the triggers we use for the Ξ_b^- signals, and the resulting value of 0.601 ± 0.030 is consistent with the world-average value [34] 0.605 ± 0.021 . The 5% precision of the R_{B^+} value is taken conservatively as an additional systematic uncertainty in the R measurement.

As mentioned above, an additional source of uncertainty in the $R_{\Xi_b^{*0}}$ measurement comes from identifying the extra pion in the $\Xi_b^{*0} \rightarrow \Xi_b^- \pi^+$ decay. The uncertainty in the tracking reconstruction efficiency for the low- p_T pion is estimated as 5.2% [69].

The uncertainty related to the finite size of the MC samples is also considered as a systematic uncertainty. It is estimated from the statistical uncertainty in the determinations of the efficiency ratios from the MC simulation. This corresponds to a systematic uncertainty of 4.6% in R , and 6.5 and 4.4% in $R_{\Xi_b^{*0}}$ for the $J/\psi\Xi^-$ and $J/\psi\Lambda K^-$ modes, respectively.

The systematic uncertainties in the R and $R_{\Xi_b^{*0}}$ measurements are summarized in Tables 4 and 5, respectively, along with the total systematic uncertainties, calculated from the sum in quadrature of the individual sources.

Table 4: Systematic uncertainties in percent in the ratio R from the different sources and the total uncertainty.

Source	Uncertainty (%)
Signal model	8.8
Background model	4.5
R_{B^+} uncertainty	5.0
MC finite size	4.6
Total	12.0

7.2 Systematic uncertainties in the Ξ_b^{*0} baryon mass and width measurements

Several sources of systematic uncertainty are considered in the simultaneous measurement of the Ξ_b^{*0} baryon mass difference and natural width. To evaluate the systematic uncertainties related to the choice of functions used to fit the $\Xi_b^{*0} \Delta M$ distributions, alternative functions are chosen and the maximum changes in the results of the fit are used to estimate the corresponding systematic uncertainty. We use a Student's t-distribution [68] as the alternative function to describe the invariant mass resolution, with the shape parameters determined from MC

Table 5: Systematic uncertainties in percent in the ratio $R_{\Xi_b^{*0}}$ from the different sources and the total uncertainty, separately for the $J/\psi\Xi^-$ and $J/\psi\Lambda K^-$ decay modes.

Source	$J/\psi\Xi^-$ (%)	$J/\psi\Lambda K^-$ (%)
Ξ_b^- fit model	4.0	6.9
Ξ_b^{*0} fit model	7.7	6.7
Tracking efficiency	5.2	5.2
MC finite size	6.5	4.4
Total	12.0	11.8

simulation. Fitting the data distributions leads to estimates for the systematic uncertainty of ± 0.003 MeV in the mass difference, while the change in the natural width is negligible.

We also vary the function used to describe the background in the fit. We use the threshold function described earlier, multiplied by a first-order polynomial, except for the $\Xi_b^- \rightarrow \psi(2S)\Xi^-$ decay channel, where the number of events is too small to allow a reasonable fit to the background for functions with more parameters. Another alternative model uses the baseline background model to fit the same-sign $\Xi_b^- \pi^-$ distributions. The α values obtained in these fits are then used as fixed parameters of the simultaneous fit. From this, we estimate systematic uncertainties from this source of ± 0.002 and ± 0.04 MeV in the mass difference and natural width, respectively.

The systematic uncertainty coming from the choice of the fit range is estimated by varying the ΔM fit region from $[0, 0.05]$ to $[0, 0.09]$ GeV. The maximum deviation of the fit parameters is used as the systematic uncertainty, giving ± 0.023 and ± 0.13 MeV in the mass difference and natural width, respectively.

The signal shape for the $\Xi_b^{*0} \Delta M$ distribution is fit with a Gaussian resolution function, convolved with a relativistic Breit–Wigner (RBW) and a Blatt–Weisskopf barrier factor [70], with the radial parameter in these functions set to $r = 3.5 \text{ GeV}^{-1}$ and the angular momentum (spin) to $\ell = 1$. To determine the systematic uncertainty associated with these choices, the fit is repeated with the value of r varied in the range 1–5 GeV^{-1} and ℓ set to 0 or 2. The change in r has a negligible effect, while the spin change leads to systematic uncertainties of ± 0.022 and ± 0.02 MeV in the mass difference and natural width measurements, respectively.

For the $\Xi_b^- \rightarrow J/\psi\Xi^-$ channel, we verify that the mass resolutions obtained in data and simulation agree to within the combined uncertainty of 7.5%. We obtain a systematic uncertainty associated with any potential disagreement in the ΔM mass resolution between data and simulation by repeating the Ξ_b^{*0} fit with the resolutions from MC scaled up or down by 1.075. The resulting systematic uncertainties are ± 0.004 and ± 0.08 MeV for the mass difference and natural width, respectively.

The systematic uncertainties described above are summarized in Table 6, together with the total systematic uncertainties, found from the quadrature sum of those from the individual sources.

8 Results

Our final result for the ratio of the branching fractions for the $\Xi_b^- \rightarrow \psi(2S)\Xi^-$ decay with respect to the $\Xi_b^- \rightarrow J/\psi\Xi^-$ normalization mode is

$$R = \frac{\mathcal{B}(\Xi_b^- \rightarrow \psi(2S)\Xi^-)}{\mathcal{B}(\Xi_b^- \rightarrow J/\psi\Xi^-)} = 0.84_{-0.19}^{+0.21} (\text{stat}) \pm 0.10 (\text{syst}) \pm 0.02 (\mathcal{B}),$$

Table 6: The systematic uncertainties in MeV in the measurement of the Ξ_b^{*0} mass difference and natural width from each of the sources, along with the total uncertainties.

Source	ΔM (MeV)	$\Gamma(\Xi_b^{*0})$ (MeV)
Signal model	0.003	< 0.01
Background model	0.002	0.04
Fit range	0.023	0.13
RBW shape	0.022	0.02
Mass resolution	0.004	0.08
Total	0.032	0.16

where the uncertainties are statistical, systematic, and related to the uncertainties in the J/ψ and $\psi(2S)$ branching fractions, respectively. For the last term of Eq. (1), we used the lepton universality assumption of $\mathcal{B}(J/\psi \rightarrow \mu^+\mu^-)/\mathcal{B}(\psi(2S) \rightarrow \mu^+\mu^-) = \mathcal{B}(J/\psi \rightarrow e^+e^-)/\mathcal{B}(\psi(2S) \rightarrow e^+e^-) = 7.53 \pm 0.17$ from the PDG [34], since the dielectron modes are measured more precisely than the dimuon ones.

Including the systematic uncertainties described in the previous section, the Ξ_b^{*0} mass difference and natural width are found to be

$$M(\Xi_b^{*0}) - M(\Xi_b^-) - m^{\text{PDG}}(\pi^\pm) = 15.810 \pm 0.077 (\text{stat}) \pm 0.032 (\text{syst}) \text{ MeV},$$

$$\Gamma(\Xi_b^{*0}) = 0.87^{+0.22}_{-0.20} (\text{stat}) \pm 0.16 (\text{syst}) \text{ MeV}.$$

Using the world-average Ξ_b^- baryon mass [34], our ΔM^{fit} value corresponds to a Ξ_b^{*0} mass of $5952.4 \pm 0.1 (\text{stat+syst}) \pm 0.6 (m_{\Xi_b^-})$ MeV, where the first uncertainty includes the statistical and systematic components and the last comes from the uncertainty in the Ξ_b^- mass. These measurements of the Ξ_b^{*0} baryon mass and width are significantly more precise than the previous CMS results [5] and in agreement with those obtained by the LHCb experiment [6, 15]. Their recent measurement, using data corresponding to an integrated luminosity of 9 fb^{-1} , reported $\Delta M = 15.80 \pm 0.02 \pm 0.01$ MeV and $\Gamma(\Xi_b^{*0}) = 0.87 \pm 0.06 \pm 0.05$ MeV [15].

Finally, our measurement of the inclusive ratio of the Ξ_b^{*0} and Ξ_b^- production cross sections gives

$$R_{\Xi_b^{*0}} = \frac{\sigma(\text{pp} \rightarrow \Xi_b^{*0} X) \mathcal{B}(\Xi_b^{*0} \rightarrow \Xi_b^- \pi^+)}{\sigma(\text{pp} \rightarrow \Xi_b^- X)} = 0.23 \pm 0.04 (\text{stat}) \pm 0.02 (\text{syst}),$$

where we used the BLUE procedure [71–73] to combine the results from the $\Xi_b^- \rightarrow J/\psi \Xi^-$ and $\Xi_b^- \rightarrow J/\psi \Lambda K^-$ decay modes. The statistical and systematic uncertainties are assumed to be uncorrelated, except for the tracking efficiency, which we treat as correlated.

9 Summary and conclusions

In this article, we present the first observation of the $\Xi_b^- \rightarrow \psi(2S) \Xi^-$ decay. We use data from LHC proton-proton (pp) collisions at $\sqrt{s} = 13$ TeV, collected by the CMS experiment during 2016–2018, corresponding to an integrated luminosity of 140 fb^{-1} . We measure the ratio of the branching fraction for the new decay to that for $\Xi_b^- \rightarrow J/\psi \Xi^-$ to be

$$R = \frac{\mathcal{B}(\Xi_b^- \rightarrow \psi(2S) \Xi^-)}{\mathcal{B}(\Xi_b^- \rightarrow J/\psi \Xi^-)} = 0.84^{+0.21}_{-0.19} (\text{stat}) \pm 0.10 (\text{syst}) \pm 0.02 (\mathcal{B}),$$

where the last uncertainty comes from the uncertainties in the J/ψ and $\psi(2S)$ branching fractions.

This result is consistent with analogous measured ratios from $B_{(s)}$ and Λ_b^0 decays such as $B^+ \rightarrow \psi K^+$, $B^0 \rightarrow \psi K_S^0$, $B_s^0 \rightarrow \psi \phi$, and $\Lambda_b^0 \rightarrow \psi \Lambda$, whose values are in the range 0.5–0.6 [34] (here ψ refers to the J/ψ and $\psi(2S)$ mesons). In general, currently existing results for such ratios do not form any clear and unambiguous pattern. New measurements, such as the one reported here, and corresponding theoretical predictions are required to build a robust model that can reliably describe b hadron decays to charmonium states.

We reconstruct Ξ_b^{*0} candidates using the $\Xi_b^{*0} \rightarrow \Xi_b^- \pi^+$ decay mode by combining tracks from the proton-proton collision vertex with Ξ_b^- candidates from four different decay modes. A simultaneous fit of all decay modes is used to extract the mass difference and natural width, which are consistent with our previous results [5], but with much better precision. They are also in agreement with the LHCb measurements [6, 15]. Using the world-average value for the Ξ_b^- baryon mass [34], we measure the mass of the Ξ_b^{*0} baryon to be

$$M(\Xi_b^{*0}) = 5952.4 \pm 0.1 \text{ (stat+syst)} \pm 0.6 (m_{\Xi_b^-}) \text{ MeV},$$

where the last uncertainty comes from the uncertainty in the Ξ_b^- baryon mass. We measure the natural width to be $\Gamma(\Xi_b^{*0}) = 0.87_{-0.20}^{+0.22} \text{ (stat)} \pm 0.16 \text{ (syst)} \text{ MeV}$.

Finally, our determination of the Ξ_b^{*0} / Ξ_b^- relative production rate $R_{\Xi_b^{*0}} = 0.23 \pm 0.04 \text{ (stat)} \pm 0.02 \text{ (syst)}$ is in good agreement with the LHCb result [6] of $0.28 \pm 0.03 \pm 0.01$ and is of a similar precision. From the measured values of this ratio, we conclude that about 1/4 of Ξ_b^- baryons are produced from the $\Xi_b^{*0} \rightarrow \Xi_b^- \pi^+$ decay. The other major Ξ_b^{*0} decay is $\Xi_b^{*0} \rightarrow \Xi_b^0 \pi^0$. Since $\mathcal{B}(\Xi_b^* \rightarrow \Xi_b \pi)$ should be close to 100%, we expect $\mathcal{B}(\Xi_b^{*0} \rightarrow \Xi_b^- \pi^+) \approx 2 \mathcal{B}(\Xi_b^{*0} \rightarrow \Xi_b^0 \pi^0) \approx 2/3$, where the factor of 2 comes from isospin differences and the Clebsch–Gordan coefficients [34]. Incorporating this estimate of $\mathcal{B}(\Xi_b^{*0} \rightarrow \Xi_b^- \pi^+)$ into our results for the ratio of production cross sections, we find that $\sigma(\text{pp} \rightarrow \Xi_b^{*0} X) / \sigma(\text{pp} \rightarrow \Xi_b^- X) \approx 1/3$. If the relative production rate for Ξ_b^{*-} to Ξ_b^- follows the same scheme, the corresponding ratio can be estimated as $R_{\Xi_b^{*-}} = [\sigma(\text{pp} \rightarrow \Xi_b^{*-} X) \mathcal{B}(\Xi_b^{*-} \rightarrow \Xi_b^- \pi^0)] / \sigma(\text{pp} \rightarrow \Xi_b^- X) \approx 1/3 \times 1/3 = 1/9$. Thus, we can conclude that about a third of the Ξ_b^- baryons are produced from Ξ_b^* decays.

Since decays from higher-mass excited Ξ_b baryons are also possible, such as the $\Xi_b(6227)$ doublet reported by the LHCb experiment [11, 12], less than two thirds of the Ξ_b^- baryons are expected to be directly produced from pp collisions. It is clear that further studies of different ground- and excited-state Ξ_b baryons are needed to fully understand this family of baryons.

Acknowledgments

We congratulate our colleagues in the CERN accelerator departments for the excellent performance of the LHC and thank the technical and administrative staffs at CERN and at other CMS institutes for their contributions to the success of the CMS effort. In addition, we gratefully acknowledge the computing centers and personnel of the Worldwide LHC Computing Grid and other centers for delivering so effectively the computing infrastructure essential to our analyses. Finally, we acknowledge the enduring support for the construction and operation of the LHC, the CMS detector, and the supporting computing infrastructure provided by the following funding agencies: SC (Armenia), BMBWF and FWF (Austria); FNRS and FWO (Belgium); CNPq, CAPES, FAPERJ, FAPERGS, and FAPESP (Brazil); MES and BNSF (Bulgaria); CERN; CAS, MoST, and NSFC (China); MINCIENCIAS (Colombia); MSES and CSF (Croatia); RIF (Cyprus); SENESCYT (Ecuador); ERC PRG, RVTT3 and MoER TK202 (Estonia);

Academy of Finland, MEC, and HIP (Finland); CEA and CNRS/IN2P3 (France); SRNSF (Georgia); BMBF, DFG, and HGF (Germany); GSRI (Greece); NKFIH (Hungary); DAE and DST (India); IPM (Iran); SFI (Ireland); INFN (Italy); MSIP and NRF (Republic of Korea); MES (Latvia); LMTLT (Lithuania); MOE and UM (Malaysia); BUAP, CINVESTAV, CONACYT, LNS, SEP, and UASLP-FAI (Mexico); MOS (Montenegro); MBIE (New Zealand); PAEC (Pakistan); MES and NSC (Poland); FCT (Portugal); MESTD (Serbia); MCIN/AEI and PCTI (Spain); MOSTR (Sri Lanka); Swiss Funding Agencies (Switzerland); MST (Taipei); MHESI and NSTDA (Thailand); TUBITAK and TENMAK (Turkey); NASU (Ukraine); STFC (United Kingdom); DOE and NSF (USA).

Individuals have received support from the Marie-Curie program and the European Research Council and Horizon 2020 Grant, contract Nos. 675440, 724704, 752730, 758316, 765710, 824093, 101115353, and COST Action CA16108 (European Union); the Leventis Foundation; the Alfred P. Sloan Foundation; the Alexander von Humboldt Foundation; the Science Committee, project no. 22r1-037 (Armenia); the Belgian Federal Science Policy Office; the Fonds pour la Formation à la Recherche dans l'Industrie et dans l'Agriculture (FRIA-Belgium); the Agentschap voor Innovatie door Wetenschap en Technologie (IWT-Belgium); the F.R.S.-FNRS and FWO (Belgium) under the "Excellence of Science – EOS" – be.h project n. 30820817; the Beijing Municipal Science & Technology Commission, No. Z191100007219010 and Fundamental Research Funds for the Central Universities (China); the Ministry of Education, Youth and Sports (MEYS) of the Czech Republic; the Shota Rustaveli National Science Foundation, grant FR-22-985 (Georgia); the Deutsche Forschungsgemeinschaft (DFG), under Germany's Excellence Strategy – EXC 2121 "Quantum Universe" – 390833306, and under project number 400140256 - GRK2497; the Hellenic Foundation for Research and Innovation (HFRI), Project Number 2288 (Greece); the Hungarian Academy of Sciences, the New National Excellence Program - ÚNKP, the NKFIH research grants K 124845, K 124850, K 128713, K 128786, K 129058, K 131991, K 133046, K 138136, K 143460, K 143477, 2020-2.2.1-ED-2021-00181, and TKP2021-NKTA-64 (Hungary); the Council of Science and Industrial Research, India; ICSC – National Research Center for High Performance Computing, Big Data and Quantum Computing, funded by the EU NexGeneration program (Italy); the Latvian Council of Science; the Ministry of Education and Science, project no. 2022/WK/14, and the National Science Center, contracts Opus 2021/41/B/ST2/01369 and 2021/43/B/ST2/01552 (Poland); the Fundação para a Ciência e a Tecnologia, grant CEECIND/01334/2018 (Portugal); the National Priorities Research Program by Qatar National Research Fund; MCIN/AEI/10.13039/501100011033, ERDF "a way of making Europe", and the Programa Estatal de Fomento de la Investigación Científica y Técnica de Excelencia María de Maeztu, grant MDM-2017-0765 and Programa Severo Ochoa del Principado de Asturias (Spain); the Chulalongkorn Academic into Its 2nd Century Project Advancement Project, and the National Science, Research and Innovation Fund via the Program Management Unit for Human Resources & Institutional Development, Research and Innovation, grant B37G660013 (Thailand); the Kavli Foundation; the Nvidia Corporation; the SuperMicro Corporation; the Welch Foundation, contract C-1845; and the Weston Havens Foundation (USA).

References

- [1] D. Ebert, T. Feldmann, C. Kettner, and H. Reinhardt, "A diquark model for baryons containing one heavy quark", *Z. Phys. C* **71** (1996) 329, doi:10.1007/BF02906991, arXiv:hep-ph/9506298.

- [2] D0 Collaboration, “Direct observation of the strange b baryon Ξ_b^- ”, *Phys. Rev. Lett.* **99** (2007) 052001, doi:10.1103/PhysRevLett.99.052001, arXiv:0706.1690.
- [3] CDF Collaboration, “Observation and mass measurement of the baryon Ξ_b^- ”, *Phys. Rev. Lett.* **99** (2007) 052002, doi:10.1103/PhysRevLett.99.052002, arXiv:0707.0589.
- [4] CDF Collaboration, “Observation of the Ξ_b^0 baryon”, *Phys. Rev. Lett.* **107** (2011) 102001, doi:10.1103/PhysRevLett.107.102001, arXiv:1107.4015.
- [5] CMS Collaboration, “Observation of a new Ξ_b baryon”, *Phys. Rev. Lett.* **108** (2012) 252002, doi:10.1103/PhysRevLett.108.252002, arXiv:1204.5955.
- [6] LHCb Collaboration, “Measurement of the properties of the Ξ_b^{*0} baryon”, *JHEP* **05** (2016) 161, doi:10.1007/JHEP05(2016)161, arXiv:1604.03896.
- [7] LHCb Collaboration, “Observation of two new Ξ_b^- baryon resonances”, *Phys. Rev. Lett.* **114** (2015) 062004, doi:10.1103/PhysRevLett.114.062004, arXiv:1411.4849.
- [8] E. E. Jenkins, “Model-independent bottom baryon mass predictions in the $1/N_c$ expansion”, *Phys. Rev. D* **77** (2008) 034012, doi:10.1103/PhysRevD.77.034012, arXiv:0712.0406.
- [9] M. Karliner, B. Keren-Zur, H. J. Lipkin, and J. L. Rosner, “The quark model and b baryons”, *Ann. Phys.* **324** (2009) 2, doi:10.1016/j.aop.2008.05.003, arXiv:0804.1575.
- [10] D. Ebert, R. N. Faustov, and V. O. Galkin, “Masses of excited heavy baryons in the relativistic quark model”, *Phys. Lett. B* **659** (2008) 612, doi:10.1016/j.physletb.2007.11.037, arXiv:0705.2957.
- [11] LHCb Collaboration, “Observation of a new Ξ_b^- resonance”, *Phys. Rev. Lett.* **121** (2018) 072002, doi:10.1103/PhysRevLett.121.072002, arXiv:1805.09418.
- [12] LHCb Collaboration, “Observation of a new Ξ_b^0 state”, *Phys. Rev. D* **103** (2021) 012004, doi:10.1103/PhysRevD.103.012004, arXiv:2010.14485.
- [13] CMS Collaboration, “Observation of a new excited beauty strange baryon decaying to $\Xi_b^- \pi^+ \pi^-$ ”, *Phys. Rev. Lett.* **126** (2021) 252003, doi:10.1103/PhysRevLett.126.252003, arXiv:2102.04524.
- [14] LHCb Collaboration, “Observation of two new excited Ξ_b^0 states decaying to $\Lambda_b^0 K^- \pi^+$ ”, *Phys. Rev. Lett.* **128** (2022) 162001, doi:10.1103/PhysRevLett.128.162001, arXiv:2110.04497.
- [15] LHCb Collaboration, “Observation of new baryons in the $\Xi_b^- \pi^+ \pi^-$ and $\Xi_b^0 \pi^+ \pi^-$ systems”, *Phys. Rev. Lett.* **131** (2023) 171901, doi:10.1103/PhysRevLett.131.171901, arXiv:2307.13399.
- [16] W. Roberts and M. Pervin, “Heavy baryons in a quark model”, *Int. J. Mod. Phys. A* **23** (2008) 2817, doi:10.1142/S0217751X08041219, arXiv:0711.2492.
- [17] D. Ebert, R. N. Faustov, and V. O. Galkin, “Spectroscopy and Regge trajectories of heavy baryons in the relativistic quark-diquark picture”, *Phys. Rev. D* **84** (2011) 014025, doi:10.1103/PhysRevD.84.014025, arXiv:1105.0583.

-
- [18] H. Garcilazo, J. Vijande, and A. Valcarce, “Faddeev study of heavy baryon spectroscopy”, *J. Phys. G* **34** (2007) 961, doi:10.1088/0954-3899/34/5/014, arXiv:hep-ph/0703257.
- [19] B. Chen, K.-W. Wei, and A. Zhang, “Assignments of Λ_Q and Ξ_Q baryons in the heavy quark-light diquark picture”, *Eur. Phys. J. A* **51** (2015) 82, doi:10.1140/epja/i2015-15082-3, arXiv:1406.6561.
- [20] I. L. Grach, I. M. Narodetskii, M. A. Trusov, and A. I. Veselov, “Heavy baryon spectroscopy in the QCD string model”, in *Particles and Nuclei. Proceedings, 18th International Conference, PANIC08, Eilat, Israel*. 2008. arXiv:0811.2184.
- [21] Q. Mao et al., “QCD sum rule calculation for P-wave bottom baryons”, *Phys. Rev. D* **92** (2015) 114007, doi:10.1103/PhysRevD.92.114007, arXiv:1510.05267.
- [22] Z.-G. Wang, “Analysis of the $1/2^-$ and $3/2^-$ heavy and doubly heavy baryon states with QCD sum rules”, *Eur. Phys. J. A* **47** (2011) 81, doi:10.1140/epja/i2011-11081-8, arXiv:1003.2838.
- [23] K.-L. Wang, Y.-X. Yao, X.-H. Zhong, and Q. Zhao, “Strong and radiative decays of the low-lying S- and P-wave singly heavy baryons”, *Phys. Rev. D* **96** (2017) 116016, doi:10.1103/PhysRevD.96.116016, arXiv:1709.04268.
- [24] Y. Kawakami and M. Harada, “Singly heavy baryons with chiral partner structure in a three-flavor chiral model”, *Phys. Rev. D* **99** (2019) 094016, doi:10.1103/PhysRevD.99.094016, arXiv:1902.06774.
- [25] Z.-Y. Wang, J.-J. Qi, X.-H. Guo, and K.-W. Wei, “Spectra of charmed and bottom baryons with hyperfine interaction”, *Chin. Phys. C* **41** (2017) 093103, doi:10.1088/1674-1137/41/9/093103, arXiv:1701.04524.
- [26] K. Thakkar, Z. Shah, A. K. Rai, and P. C. Vinodkumar, “Excited state mass spectra and Regge trajectories of bottom baryons”, *Nucl. Phys. A* **965** (2017) 57, doi:10.1016/j.nuclphysa.2017.05.087, arXiv:1610.00411.
- [27] K.-W. Wei et al., “Spectroscopy of singly, doubly, and triply bottom baryons”, *Phys. Rev. D* **95** (2017) 116005, doi:10.1103/PhysRevD.95.116005, arXiv:1609.02512.
- [28] LHCb Collaboration, “Studies of beauty baryon decays to $D^0 p h^-$ and $\Lambda_c^+ h^-$ final states”, *Phys. Rev. D* **89** (2014) 032001, doi:10.1103/PhysRevD.89.032001, arXiv:1311.4823.
- [29] LHCb Collaboration, “Evidence for the strangeness-changing weak decay $\Xi_b^- \rightarrow \Lambda_b^0 \pi^-$ ”, *Phys. Rev. Lett.* **115** (2015) 241801, doi:10.1103/PhysRevLett.115.241801, arXiv:1510.03829.
- [30] LHCb Collaboration, “Observation of the decay $\Xi_b^- \rightarrow p K^- K^-$ ”, *Phys. Rev. Lett.* **118** (2017) 071801, doi:10.1103/PhysRevLett.118.071801, arXiv:1612.02244.
- [31] LHCb Collaboration, “Observation of the $\Xi_b^- \rightarrow J/\psi \Lambda K^-$ decay”, *Phys. Lett. B* **772** (2017) 265, doi:10.1016/j.physletb.2017.06.045, arXiv:1701.05274.
- [32] LHCb Collaboration, “Measurement of branching fractions of charmless four-body Λ_b^0 and Ξ_b^0 decays”, *JHEP* **02** (2018) 098, doi:10.1007/JHEP02(2018)098, arXiv:1711.05490.


- [33] LHCb Collaboration, “Isospin amplitudes in $\Lambda_b^0 \rightarrow J/\psi\Lambda(\Sigma^0)$ and $\Xi_b^0 \rightarrow J/\psi\Xi^0(\Lambda)$ decays”, *Phys. Rev. Lett.* **124** (2020) 111802, doi:10.1103/PhysRevLett.124.111802, arXiv:1912.02110.
- [34] Particle Data Group, “Review of particle physics”, *PTEP* **2022** (2022) 083C01, doi:10.1093/ptep/ptac097.
- [35] LHCb Collaboration, “Evidence of a $J/\psi\Lambda$ structure and observation of excited Ξ^- states in the $\Xi_b^- \rightarrow J/\psi\Lambda K^-$ decay”, *Sci. Bull.* **66** (2021) 1278, doi:10.1016/j.scib.2021.02.030, arXiv:2012.10380.
- [36] LHCb Collaboration, “Search for CP violation in $\Xi_b^- \rightarrow pK^-K^-$ decays”, *Phys. Rev. D* **104** (2021) 052010, doi:10.1103/PhysRevD.104.052010, arXiv:2104.15074.
- [37] A. G. Grozin, “Heavy quark effective theory”. Springer Berlin, Heidelberg, 2004. doi:10.1007/b79301.
- [38] N. Isgur and M. B. Wise, “Spectroscopy with heavy quark symmetry”, *Phys. Rev. Lett.* **66** (1991) 1130, doi:10.1103/PhysRevLett.66.1130.
- [39] M. A. Shifman and M. B. Voloshin, “Preasymptotic effects in inclusive weak decays of charmed particles”, *Sov. J. Nucl. Phys.* **41** (1985) 120.
- [40] N. Isgur and M. B. Wise, “Weak decays of heavy mesons in the static quark approximation”, *Phys. Lett. B* **232** (1989) 113, doi:10.1016/0370-2693(89)90566-2.
- [41] I. I. Y. Bigi, N. G. Uraltsev, and A. I. Vainshtein, “Nonperturbative corrections to inclusive beauty and charm decays: QCD versus phenomenological models”, *Phys. Lett. B* **293** (1992) 430, doi:10.1016/0370-2693(92)90908-M, arXiv:hep-ph/9207214. [Erratum: doi:10.1016/0370-2693(92)91287-J].
- [42] CMS Collaboration, “Precision luminosity measurement in proton-proton collisions at $\sqrt{s} = 13$ TeV in 2015 and 2016 at CMS”, *Eur. Phys. J. C* **81** (2021) 800, doi:10.1140/epjc/s10052-021-09538-2, arXiv:2104.01927.
- [43] CMS Collaboration, “CMS luminosity measurement for the 2017 data-taking period at $\sqrt{s} = 13$ TeV”, CMS Physics Analysis Summary CMS-PAS-LUM-17-004, 2018.
- [44] CMS Collaboration, “CMS luminosity measurement for the 2018 data-taking period at $\sqrt{s} = 13$ TeV”, CMS Physics Analysis Summary CMS-PAS-LUM-18-002, 2019.
- [45] CMS Collaboration, “Measurement of $B_c(2S)^+$ and $B_c^*(2S)^+$ cross section ratios in proton-proton collisions at $\sqrt{s} = 13$ TeV”, *Phys. Rev. D* **102** (2020) 092007, doi:10.1103/PhysRevD.102.092007, arXiv:2008.08629.
- [46] HEPData record for this analysis, 2024. doi:10.17182/hepdata.146756.
- [47] CMS Collaboration, “The CMS experiment at the CERN LHC”, *JINST* **3** (2008) S08004, doi:10.1088/1748-0221/3/08/S08004.
- [48] CMS Collaboration, “Development of the CMS detector for the CERN LHC Run 3”, 2023. arXiv:2309.05466. Accepted by *JINST*.

- [49] CMS Collaboration, “Performance of the CMS muon detector and muon reconstruction with proton-proton collisions at $\sqrt{s} = 13$ TeV”, *JINST* **13** (2018) P06015, doi:10.1088/1748-0221/13/06/P06015, arXiv:1804.04528.
- [50] CMS Collaboration, “Description and performance of track and primary-vertex reconstruction with the CMS tracker”, *JINST* **9** (2014) P10009, doi:10.1088/1748-0221/9/10/P10009, arXiv:1405.6569.
- [51] CMS Tracker Group, “The CMS Phase-1 pixel detector upgrade”, *JINST* **16** (2021) P02027, doi:10.1088/1748-0221/16/02/P02027, arXiv:2012.14304.
- [52] CMS Collaboration, “Track impact parameter resolution for the full pseudorapidity coverage in the 2017 dataset with the CMS Phase-1 pixel detector”, CMS Detector Performance Note CMS-DP-2020-049, 2020.
- [53] CMS Collaboration, “The CMS trigger system”, *JINST* **12** (2017) P01020, doi:10.1088/1748-0221/12/01/P01020, arXiv:1609.02366.
- [54] CMS Collaboration, “Performance of the CMS level-1 trigger in proton-proton collisions at $\sqrt{s} = 13$ TeV”, *JINST* **15** (2020) P10017, doi:10.1088/1748-0221/15/10/P10017, arXiv:2006.10165.
- [55] T. Sjöstrand et al., “An introduction to PYTHIA 8.2”, *Comput. Phys. Commun.* **191** (2015) 159, doi:10.1016/j.cpc.2015.01.024, arXiv:1410.3012.
- [56] CMS Collaboration, “Extraction and validation of a new set of CMS PYTHIA8 tunes from underlying-event measurements”, *Eur. Phys. J. C* **80** (2020) 4, doi:10.1140/epjc/s10052-019-7499-4, arXiv:1903.12179.
- [57] D. J. Lange, “The EVTGEN particle decay simulation package”, *Nucl. Instrum. Meth. A* **462** (2001) 152, doi:10.1016/S0168-9002(01)00089-4.
- [58] E. Barberio, B. van Eijk, and Z. Wąs, “PHOTOS: A universal Monte Carlo for QED radiative corrections in decays”, *Comput. Phys. Commun.* **66** (1991) 115, doi:10.1016/0010-4655(91)90012-A.
- [59] E. Barberio and Z. Wąs, “PHOTOS: A universal Monte Carlo for QED radiative corrections. version 2.0”, *Comput. Phys. Commun.* **79** (1994) 291, doi:10.1016/0010-4655(94)90074-4.
- [60] GEANT4 Collaboration, “GEANT4 — a simulation toolkit”, *Nucl. Instrum. Meth. A* **506** (2003) 250, doi:10.1016/S0168-9002(03)01368-8.
- [61] CMS Collaboration, “CMS tracking performance results from early LHC operation”, *Eur. Phys. J. C* **70** (2010) 1165, doi:10.1140/epjc/s10052-010-1491-3, arXiv:1007.1988.
- [62] CMS Collaboration, “Observation of two excited B_c^+ states and measurement of the $B_c^+(2S)$ mass in pp collisions at $\sqrt{s} = 13$ TeV”, *Phys. Rev. Lett.* **122** (2019) 132001, doi:10.1103/PhysRevLett.122.132001, arXiv:1902.00571.
- [63] CMS Collaboration, “Study of excited Λ_b^0 states decaying to $\Lambda_b^0 \pi^+ \pi^-$ in proton-proton collisions at $\sqrt{s} = 13$ TeV”, *Phys. Lett. B* **803** (2020) 135345, doi:10.1016/j.physletb.2020.135345, arXiv:2001.06533.









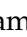


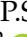


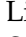
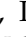


- [64] S. S. Wilks, "The large-sample distribution of the likelihood ratio for testing composite hypotheses", *Annals Math. Statist.* **9** (1938) 60, doi:10.1214/aoms/1177732360.
- [65] G. Cowan, K. Cranmer, E. Gross, and O. Vitells, "Asymptotic formulae for likelihood-based tests of new physics", *Eur. Phys. J. C* **71** (2011) 1554, doi:10.1140/epjc/s10052-011-1554-0, arXiv:1007.1727. [Erratum: doi:10.1140/epjc/s10052-013-2501-z].
- [66] W. Detmold, C.-J. D. Lin, and S. Meinel, "Calculation of the heavy-hadron axial couplings g_1 , g_2 and g_3 using lattice QCD", *Phys. Rev. D* **85** (2012) 114508, doi:10.1103/PhysRevD.85.114508, arXiv:1203.3378.
- [67] C. Chen et al., "Strong decays of charmed baryons", *Phys. Rev. D* **75** (2007) 094017, doi:10.1103/PhysRevD.75.094017, arXiv:0704.0075.
- [68] S. Jackman, "Bayesian analysis for the social sciences". John Wiley & Sons, New Jersey, USA, 2009. doi:10.1002/9780470686621.
- [69] CMS Collaboration, "Measurement of prompt open-charm production cross sections in proton-proton collisions at $\sqrt{s} = 13$ TeV", *JHEP* **11** (2021) 225, doi:10.1007/JHEP11(2021)225, arXiv:2107.01476.
- [70] J. M. Blatt and V. F. Weisskopf, "Theoretical nuclear physics". Springer, New York, 1952. doi:10.1007/978-1-4612-9959-2, ISBN 978-0-471-08019-0.
- [71] L. Lyons, D. Gibaut, and P. Clifford, "How to combine correlated estimates of a single physical quantity", *Nucl. Instrum. Meth. A* **270** (1988) 110, doi:10.1016/0168-9002(88)90018-6.
- [72] R. Nisius, "On the combination of correlated estimates of a physics observable", *Eur. Phys. J. C* **74** (2014) 3004, doi:10.1140/epjc/s10052-014-3004-2, arXiv:1402.4016.
- [73] R. Nisius, "BLUE: combining correlated estimates of physics observables within ROOT using the best linear unbiased estimate method", *SoftwareX* **11** (2020) 100468, doi:10.1016/j.softx.2020.100468, arXiv:2001.10310.

A The CMS Collaboration




Yerevan Physics Institute, Yerevan, Armenia

A. Hayrapetyan, A. Tumasyan¹ 

Institut für Hochenergiephysik, Vienna, Austria

W. Adam , J.W. Andrejkovic, T. Bergauer , S. Chatterjee , K. Damanakis , M. Dragicevic , P.S. Hussain , M. Jeitler² , N. Krammer , A. Li , D. Liko , I. Mikulec , J. Schieck² , R. Schöfbeck , D. Schwarz , M. Sonawane , S. Templ , W. Waltenberger , C.-E. Wulz² 









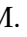
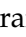




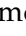

Universiteit Antwerpen, Antwerpen, Belgium

M.R. Darwish³ , T. Janssen , P. Van Mechelen 




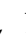






Vrije Universiteit Brussel, Brussel, Belgium

E.S. Bols , J. D'Hondt , S. Dansana , A. De Moor , M. Delcourt , S. Lowette , I. Makarenko , D. Müller , S. Tavernier , M. Tytgat⁴ , G.P. Van Onsem , S. Van Putte , D. Vannerom 





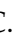



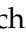



Université Libre de Bruxelles, Bruxelles, Belgium

B. Clerbaux , A.K. Das, G. De Lentdecker , H. Evard , L. Favart , P. Gianneios , D. Hohov , J. Jaramillo , A. Khalilzadeh, F.A. Khan , K. Lee , M. Mahdavihorrani , A. Malara , S. Paredes , L. Thomas , M. Vanden Bemden , C. Vander Velde , P. Vanlaer 







Ghent University, Ghent, Belgium

M. De Coen , D. Dobur , Y. Hong , J. Knolle , L. Lambrecht , G. Mestdach, K. Mota Amarilo , C. Rendón, A. Samalan, K. Skovpen , N. Van Den Bossche , J. van der Linden , L. Wezenbeek 




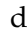





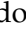









Université Catholique de Louvain, Louvain-la-Neuve, Belgium

A. Benecke , A. Bethani , G. Bruno , C. Caputo , C. Delaere , I.S. Donertas , A. Giammanco , Sa. Jain , V. Lemaitre, J. Lidrych , P. Mastrapasqua , T.T. Tran , S. Wertz 

Centro Brasileiro de Pesquisas Fisicas, Rio de Janeiro, Brazil

G.A. Alves , E. Coelho , C. Hensel , T. Menezes De Oliveira , A. Moraes , P. Rebello Teles , M. Soeiro

Universidade do Estado do Rio de Janeiro, Rio de Janeiro, Brazil

W.L. Aldá Júnior , M. Alves Gallo Pereira , M. Barroso Ferreira Filho , H. Brandao Malbouisson , W. Carvalho , J. Chinellato⁵, E.M. Da Costa , G.G. Da Silveira⁶ , D. De Jesus Damiao , S. Fonseca De Souza , R. Gomes De Souza, M. Macedo , J. Martins⁷ , C. Mora Herrera , L. Mundim , H. Nogima , J.P. Pinheiro , A. Santoro , A. Sznajder , M. Thiel , A. Vilela Pereira 

Universidade Estadual Paulista, Universidade Federal do ABC, São Paulo, Brazil

C.A. Bernardes⁶ , L. Calligaris , T.R. Fernandez Perez Tomei , E.M. Gregores , P.G. Mercadante , S.F. Novaes , B. Orzari , Sandra S. Padula 

Institute for Nuclear Research and Nuclear Energy, Bulgarian Academy of Sciences, Sofia, Bulgaria

A. Aleksandrov , G. Antchev , R. Hadjiiska , P. Iaydjiev , M. Misheva , M. Shopova , G. Sultanov 




University of Sofia, Sofia, Bulgaria

A. Dimitrov , L. Litov , B. Pavlov , P. Petkov , A. Petrov , E. Shumka 

Instituto De Alta Investigación, Universidad de Tarapacá, Casilla 7 D, Arica, Chile

S. Keshri , S. Thakur 












Beihang University, Beijing, China

T. Cheng , T. Javaid , L. Yuan 

Department of Physics, Tsinghua University, Beijing, China

Z. Hu , J. Liu, K. Yi^{8,9} 


Institute of High Energy Physics, Beijing, China

G.M. Chen¹⁰ , H.S. Chen¹⁰ , M. Chen¹⁰ , F. Iemmi , C.H. Jiang, A. Kapoor¹¹ , H. Liao , Z.-A. Liu¹² , R. Sharma¹³ , J.N. Song¹², J. Tao , C. Wang¹⁰, J. Wang , Z. Wang¹⁰, H. Zhang 

State Key Laboratory of Nuclear Physics and Technology, Peking University, Beijing, China

A. Agapitos , Y. Ban , A. Levin , C. Li , Q. Li , Y. Mao, S.J. Qian , X. Sun , D. Wang , H. Yang, L. Zhang , C. Zhou 

Sun Yat-Sen University, Guangzhou, China

Z. You 

University of Science and Technology of China, Hefei, China

K. Jaffel , N. Lu 

Nanjing Normal University, Nanjing, China

G. Bauer¹⁴

Institute of Modern Physics and Key Laboratory of Nuclear Physics and Ion-beam Application (MOE) - Fudan University, Shanghai, China

X. Gao¹⁵ 





Zhejiang University, Hangzhou, Zhejiang, China

Z. Lin , C. Lu , M. Xiao 





Universidad de Los Andes, Bogota, Colombia

C. Avila , D.A. Barbosa Trujillo, A. Cabrera , C. Florez , J. Fraga , J.A. Reyes Vega

Universidad de Antioquia, Medellin, Colombia

J. Mejia Guisao , F. Ramirez , M. Rodriguez , J.D. Ruiz Alvarez 

University of Split, Faculty of Electrical Engineering, Mechanical Engineering and Naval Architecture, Split, Croatia

D. Giljanovic , N. Godinovic , D. Lelas , A. Sculac 









University of Split, Faculty of Science, Split, Croatia

















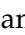








































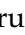












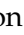

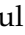














M. Kovac , T. Sculac 


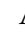








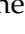
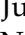


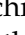








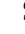
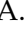





















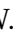







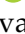
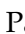




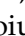


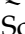
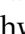
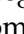
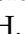














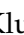

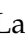
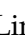




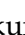



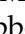



Institute Rudjer Boskovic, Zagreb, Croatia

P. Bargassa , V. Brigljevic , B.K. Chitroda , D. Ferencek , K. Jakovcic, S. Mishra , A. Starodumov¹⁶ , T. Susa 

University of Cyprus, Nicosia, Cyprus

A. Attikis , K. Christoforou , A. Hadjiagapiou, S. Konstantinou , J. Mousa , C. Nicolaou, L. Paizanos, F. Ptochos , P.A. Razis , H. Rykaczewski, H. Saka , A. Stepennov 

Charles University, Prague, Czech RepublicM. Finger , M. Finger Jr. , A. Kveton **Escuela Politecnica Nacional, Quito, Ecuador**E. Ayala **Universidad San Francisco de Quito, Quito, Ecuador**E. Carrera Jarrin **Academy of Scientific Research and Technology of the Arab Republic of Egypt, Egyptian Network of High Energy Physics, Cairo, Egypt**Y. Assran^{17,18}, S. Elgammal¹⁸**Center for High Energy Physics (CHEP-FU), Fayoum University, El-Fayoum, Egypt**M.A. Mahmoud , Y. Mohammed **National Institute of Chemical Physics and Biophysics, Tallinn, Estonia**K. Ehataht , M. Kadastik, T. Lange , S. Nandan , C. Nielsen , J. Pata , M. Raidal , L. Tani , C. Veelken **Department of Physics, University of Helsinki, Helsinki, Finland**H. Kirschenmann , K. Osterberg , M. Voutilainen **Helsinki Institute of Physics, Helsinki, Finland**S. Bharthuar , E. Brücken , F. Garcia , K.T.S. Kallonen , R. Kinnunen, T. Lampén , K. Lassila-Perini , S. Lehti , T. Lindén , L. Martikainen , M. Myllymäki , M.m. Rantanen , H. Siikonen , E. Tuominen , J. Tuominiemi **Lappeenranta-Lahti University of Technology, Lappeenranta, Finland**P. Luukka , H. Petrow **IRFU, CEA, Université Paris-Saclay, Gif-sur-Yvette, France**M. Besancon , F. Couderc , M. Dejardin , D. Denegri, J.L. Faure, F. Ferri , S. Ganjour , P. Gras , G. Hamel de Monchenault , V. Lohezic , J. Malcles , F. Orlandi , L. Portales , J. Rander, A. Rosowsky , M.Ö. Sahin , A. Savoy-Navarro¹⁹ , P. Simkina , M. Titov , M. Tornago **Laboratoire Leprince-Ringuet, CNRS/IN2P3, Ecole Polytechnique, Institut Polytechnique de Paris, Palaiseau, France**F. Beaudette , A. Buchot Perraguin , P. Busson , A. Cappati , C. Charlot , M. Chiusi , F. Damas , O. Davignon , A. De Wit , I.T. Ehle , B.A. Fontana Santos Alves , S. Ghosh , A. Gilbert , R. Granier de Cassagnac , A. Hakimi , B. Harikrishnan , L. Kalipoliti , G. Liu , J. Motta , M. Nguyen , C. Ochando , R. Salerno , J.B. Sauvan , Y. Sirois , A. Tarabini , E. Vernazza , A. Zabi , A. Zghiche **Université de Strasbourg, CNRS, IPHC UMR 7178, Strasbourg, France**J.-L. Agram²⁰ , J. Andrea , D. Apparau , D. Bloch , J.-M. Brom , E.C. Chabert , C. Collard , S. Falke , U. Goerlach , C. Grimault, R. Haeberle , A.-C. Le Bihan , M. Meena , G. Saha , M.A. Sessini , P. Van Hove **Institut de Physique des 2 Infinis de Lyon (IP2I), Villeurbanne, France**S. Beauceron , B. Blancon , G. Boudoul , N. Chanon , D. Contardo , P. Depasse , C. Dozen²¹ , H. El Mamouni, J. Fay , S. Gascon , M. Gouzevitch , C. Greenberg, G. Grenier , B. Ille , I.B. Laktineh, M. Lethuillier , L. Mirabito, S. Perries, A. Purohit , M. Vander Donckt , P. Verdier , J. Xiao 

Georgian Technical University, Tbilisi, GeorgiaI. Lomidze , T. Toriashvili²² , Z. Tsamalaidze¹⁶ **RWTH Aachen University, I. Physikalisches Institut, Aachen, Germany**V. Botta , L. Feld , K. Klein , M. Lipinski , D. Meuser , A. Pauls , N. Röwert , M. Teroerde **RWTH Aachen University, III. Physikalisches Institut A, Aachen, Germany**S. Diekmann , A. Dodonova , N. Eich , D. Eliseev , F. Engelke , J. Erdmann, M. Erdmann , P. Fackeldey , B. Fischer , T. Hebbeker , K. Hoepfner , F. Ivone , A. Jung , M.y. Lee , F. Mausolf , M. Merschmeyer , A. Meyer , S. Mukherjee , D. Noll , F. Nowotny, A. Pozdnyakov , Y. Rath, W. Redjeb , F. Rehm, H. Reithler , U. Sarkar , V. Sarkisovi , A. Schmidt , A. Sharma , J.L. Spah , A. Stein , F. Torres Da Silva De Araujo²³ , S. Wiedenbeck , S. Zaleski**RWTH Aachen University, III. Physikalisches Institut B, Aachen, Germany**C. Dziwok , G. Flügge , W. Haj Ahmad²⁴ , T. Kress , A. Nowack , O. Pooth , A. Stahl , T. Ziemons , A. Zotz **Deutsches Elektronen-Synchrotron, Hamburg, Germany**H. Aarup Petersen , M. Aldaya Martin , J. Alimena , S. Amoroso, Y. An , S. Baxter , M. Bayatmakou , H. Becerril Gonzalez , O. Behnke , A. Belvedere , S. Bhattacharya , F. Blekman²⁵ , K. Borrás²⁶ , A. Campbell , A. Cardini , C. Cheng, F. Colombina , S. Consuegra Rodríguez , G. Correia Silva , M. De Silva , G. Eckerlin, D. Eckstein , L.I. Estevez Banos , O. Filatov , E. Gallo²⁵ , A. Geiser , A. Giraldi , V. Guglielmi , M. Guthoff , A. Hinzmann , A. Jafari²⁷ , L. Jeppe , B. Kaech , M. Kasemann , C. Kleinwort , R. Kogler , M. Komm , D. Krücker , W. Lange, D. Leyva Pernia , K. Lipka²⁸ , W. Lohmann²⁹ , F. Lorkowski , R. Mankel , I.-A. Melzer-Pellmann , M. Mendizabal Morentin , A.B. Meyer , G. Milella , A. Mussgiller , L.P. Nair , A. Nürnberg , Y. Otariid, J. Park , D. Pérez Adán , E. Ranken , A. Raspereza , D. Rastorguev , B. Ribeiro Lopes , J. Rübenach, A. Saggio , M. Scham^{30,26} , S. Schnake²⁶ , P. Schütze , C. Schwanenberger²⁵ , D. Selivanova , K. Sharko , M. Shchedrolosiev , R.E. Sosa Ricardo , D. Stafford, F. Vazzoler , A. Ventura Barroso , R. Walsh , Q. Wang , Y. Wen , K. Wichmann, L. Wiens²⁶ , C. Wissing , Y. Yang , A. Zimmermann Castro Santos **University of Hamburg, Hamburg, Germany**A. Albrecht , S. Albrecht , M. Antonello , S. Bein , L. Benato , S. Bollweg, M. Bonanomi , P. Connor , K. El Morabit , Y. Fischer , E. Garutti , A. Grohsjean , J. Haller , H.R. Jabusch , G. Kasieczka , P. Keicher, R. Klanner , W. Korcar , T. Kramer , V. Kutzner , F. Labe , J. Lange , A. Lobanov , C. Matthies , L. Moureaux , M. Mrowietz, A. Nigamova , Y. Nissan, A. Paasch , K.J. Pena Rodriguez , T. Quadfasel , B. Raciti , M. Rieger , D. Savoie , J. Schindler , P. Schleper , M. Schröder , J. Schwandt , M. Sommerhalder , H. Stadie , G. Steinbrück , A. Tews, M. Wolf **Karlsruher Institut fuer Technologie, Karlsruhe, Germany**S. Brommer , M. Burkart, E. Butz , T. Chwalek , A. Dierlamm , A. Droll, N. Faltermann , M. Giffels , A. Gottmann , F. Hartmann³¹ , R. Hofsaess , M. Horzela , U. Husemann , J. Kieseler , M. Klute , R. Koppenhöfer , J.M. Lawhorn , M. Link, A. Lintuluoto , B. Maier , S. Maier , S. Mitra , M. Mormile , Th. Müller , M. Neukum, M. Oh , E. Pfeffer , M. Presilla , G. Quast , K. Rabbertz , B. Regnery , N. Shadskiy 

I. Shvetsov , H.J. Simonis , M. Toms , N. Trevisani , R.F. Von Cube , M. Wassmer ,
S. Wieland , F. Wittig, R. Wolf , X. Zuo 





Institute of Nuclear and Particle Physics (INPP), NCSR Demokritos, Aghia Paraskevi, Greece

G. Anagnostou, G. Daskalakis , A. Kyriakis, A. Papadopoulos³¹, A. Stakia 

National and Kapodistrian University of Athens, Athens, Greece

P. Kontaxakis , G. Melachroinos, Z. Painesis , A. Panagiotou, I. Papavergou ,
I. Paraskevas , N. Saoulidou , K. Theofilatos , E. Tziaferi , K. Vellidis , I. Zisopoulos 






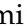
National Technical University of Athens, Athens, Greece

G. Bakas , T. Chatzistavrou, G. Karapostoli , K. Kousouris , I. Papakrivopoulos ,
E. Siamarkou, G. Tsiopolitis, A. Zacharopoulou


University of Ioánnina, Ioánnina, Greece

K. Adamidis, I. Bestintzanos, I. Evangelou , C. Foudas, C. Kamtsikis, P. Katsoulis,
P. Kokkas , P.G. Kosmoglou Kioseoglou , N. Manthos , I. Papadopoulos , J. Strologas 



HUN-REN Wigner Research Centre for Physics, Budapest, Hungary

M. Bartók³² , C. Hajdu , D. Horvath^{33,34} , K. Márton, A.J. RádI³⁵ , F. Sikler ,
V. Veszpremi 

MTA-ELTE Lendület CMS Particle and Nuclear Physics Group, Eötvös Loránd University, Budapest, Hungary

M. Csanád , K. Farkas , M.M.A. Gadallah³⁶ , Á. Kadlecsek , P. Major , K. Mandal ,
G. Pásztor , G.I. Veres 




Faculty of Informatics, University of Debrecen, Debrecen, Hungary

P. Raics, B. Ujvari , G. Zilizi 






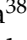


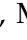
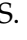
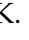



Institute of Nuclear Research ATOMKI, Debrecen, Hungary

G. Bencze, S. Czellar, J. Molnar, Z. Szillasi

Karoly Robert Campus, MATE Institute of Technology, Gyongyos, Hungary

T. Csorgo³⁷ , F. Nemes³⁷ , T. Novak 


Panjab University, Chandigarh, India

J. Babbar , S. Bansal , S.B. Beri, V. Bhatnagar , G. Chaudhary , S. Chauhan ,
N. Dhingra³⁸ , A. Kaur , A. Kaur , H. Kaur , M. Kaur , S. Kumar , K. Sandeep ,
T. Sheokand, J.B. Singh , A. Singla 














University of Delhi, Delhi, India

A. Ahmed , A. Bhardwaj , A. Chhetri , B.C. Choudhary , A. Kumar , A. Kumar ,
M. Naimuddin , K. Ranjan , S. Saumya 



Saha Institute of Nuclear Physics, HBNI, Kolkata, India

S. Baradia , S. Barman³⁹ , S. Bhattacharya , S. Dutta , S. Dutta, S. Sarkar







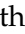
Indian Institute of Technology Madras, Madras, India

M.M. Ameen , P.K. Behera , S.C. Behera , S. Chatterjee , P. Jana , P. Kalbhor ,
J.R. Komaragiri⁴⁰ , D. Kumar⁴⁰ , P.R. Pujahari , N.R. Saha , A. Sharma , A.K. Sikdar ,
S. Verma 





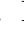






Tata Institute of Fundamental Research-A, Mumbai, India

S. Dugad, M. Kumar , G.B. Mohanty , P. Suryadevara










Tata Institute of Fundamental Research-B, Mumbai, India

A. Bala , S. Banerjee , R.M. Chatterjee, R.K. Dewanjee⁴¹ , M. Guchait , Sh. Jain ,
A. Jaiswal, S. Kumar , G. Majumder , K. Mazumdar , S. Parolia , A. Thachayath 

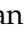
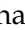

National Institute of Science Education and Research, An OCC of Homi Bhabha National Institute, Bhubaneswar, Odisha, India

S. Bahinipati⁴² , C. Kar , D. Maity⁴³ , P. Mal , T. Mishra , V.K. Muraleedharan Nair Bindhu⁴³ , K. Naskar⁴³ , A. Nayak⁴³ , P. Sadangi, S.K. Swain , S. Varghese⁴³ ,
D. Vats⁴³ 

Indian Institute of Science Education and Research (IISER), Pune, India

S. Acharya⁴⁴ , A. Alpana , S. Dube , B. Gomber⁴⁴ , P. Hazarika , B. Kansal ,
A. Laha , B. Sahu⁴⁴ , S. Sharma , K.Y. Vaish

Isfahan University of Technology, Isfahan, Iran

H. Bakhshiansohi⁴⁵ , E. Khazaie⁴⁶ , M. Zeinali⁴⁷ 













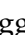
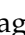
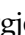

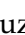













Institute for Research in Fundamental Sciences (IPM), Tehran, Iran

S. Bashiri, S. Chenarani⁴⁸ , S.M. Etesami , M. Khakzad , M. Mohammadi Najafabadi ,
S. Tizchang 


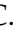

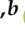

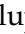




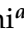






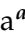







University College Dublin, Dublin, Ireland

M. Grunewald 

INFN Sezione di Bari^a, Università di Bari^b, Politecnico di Bari^c, Bari, Italy

M. Abbrescia^{a,b} , R. Aly^{a,c,49} , A. Colaleo^{a,b} , D. Creanza^{a,c} , B. D'Anzi^{a,b} ,
N. De Filippis^{a,c} , M. De Palma^{a,b} , A. Di Florio^{a,c} , W. Elmetenawee^{a,b,49} ,
L. Fiore^a , G. Iaselli^{a,c} , M. Louka^{a,b}, G. Maggi^{a,c} , M. Maggi^a , I. Margjeka^{a,b} ,
V. Mastrapasqua^{a,b} , S. My^{a,b} , S. Nuzzo^{a,b} , A. Pellecchia^{a,b} , A. Pompili^{a,b} ,
G. Pugliese^{a,c} , R. Radogna^a , G. Ramirez-Sanchez^{a,c} , D. Ramos^a , A. Ranieri^a ,
L. Silvestris^a , F.M. Simone^{a,b} , Ü. Sözbilir^a , A. Stamerra^a , R. Venditti^a ,
P. Verwilligen^a , A. Zaza^{a,b} 











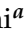

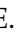



INFN Sezione di Bologna^a, Università di Bologna^b, Bologna, Italy

G. Abbiendi^a , C. Battilana^{a,b} , D. Bonacorsi^{a,b} , L. Borgonovi^a , P. Capiluppi^{a,b} ,
A. Castro^{a,b} , F.R. Cavallo^a , M. Cuffiani^{a,b} , G.M. Dallavalle^a , T. Diotallevi^{a,b} ,
F. Fabbri^a , A. Fanfani^{a,b} , D. Fasanella^{a,b} , P. Giacomelli^a , L. Giommi^{a,b} ,
C. Grandi^a , L. Guiducci^{a,b} , S. Lo Meo^{a,50} , L. Lunerti^{a,b} , S. Marcellini^a ,
G. Masetti^a , F.L. Navarria^{a,b} , A. Perrotta^a , F. Primavera^{a,b} , A.M. Rossi^{a,b} ,
T. Rovelli^{a,b} , G.P. Siroli^{a,b} 

INFN Sezione di Catania^a, Università di Catania^b, Catania, Italy

S. Costa^{a,b,51} , A. Di Mattia^a , R. Potenza^{a,b}, A. Tricomi^{a,b,51} , C. Tuve^{a,b} 

INFN Sezione di Firenze^a, Università di Firenze^b, Firenze, Italy

P. Assiouras^a , G. Barbagli^a , G. Bardelli^{a,b} , B. Camaiani^{a,b} , A. Cassese^a ,
R. Ceccarelli^a , V. Ciulli^{a,b} , C. Civinini^a , R. D'Alessandro^{a,b} , E. Focardi^{a,b} ,
T. Kello^a, G. Latino^{a,b} , P. Lenzi^{a,b} , M. Lizzo^a , M. Meschini^a , S. Paoletti^a ,
A. Papanastassiou^{a,b}, G. Sguazzoni^a , L. Viliani^a 














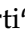









INFN Laboratori Nazionali di Frascati, Frascati, Italy

L. Benussi , S. Bianco , S. Meola⁵² , D. Piccolo 










INFN Sezione di Genova^a, Università di Genova^b, Genova, Italy

P. Chatagnon^a , F. Ferro^a , E. Robutti^a , S. Tosi^{a,b} 









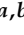
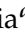
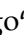




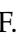
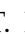




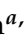
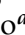






INFN Sezione di Milano-Bicocca^a, Università di Milano-Bicocca^b, Milano, Italy

A. Benaglia^a , G. Boldrini^{a,b} , F. Brivio^a , F. Cetorelli^a , F. De Guio^{a,b} , M.E. Dinardo^{a,b} , P. Dini^a , S. Gennai^a , R. Gerosa^{a,b} , A. Ghezzi^{a,b} , P. Govoni^{a,b} , L. Guzzi^a , M.T. Lucchini^{a,b} , M. Malberti^a , S. Malvezzi^a , A. Massironi^a , D. Menasce^a , L. Moroni^a , M. Paganoni^{a,b} , S. Palluotto^{a,b} , D. Pedrini^a , B.S. Pinolini^a, G. Pizzati^{a,b}, S. Ragazzi^{a,b} , T. Tabarelli de Fatis^{a,b} 












INFN Sezione di Napoli^a, Università di Napoli 'Federico II'^b, Napoli, Italy; Università della Basilicata^c, Potenza, Italy; Scuola Superiore Meridionale (SSM)^d, Napoli, Italy

S. Buontempo^a , A. Cagnotta^{a,b} , F. Carnevali^{a,b}, N. Cavallo^{a,c} , F. Fabozzi^{a,c} , A.O.M. Iorio^{a,b} , L. Lista^{a,b,53} , P. Paolucci^{a,31} , B. Rossi^a , C. Sciacca^{a,b} 



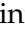
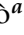
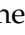




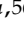

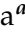
INFN Sezione di Padova^a, Università di Padova^b, Padova, Italy; Università di Trento^c, Trento, Italy

R. Ardino^a , P. Azzi^a , N. Bacchetta^{a,54} , A. Bergnoli^a , D. Bisello^{a,b} , P. Bortignon^a , G. Bortolato^{a,b}, A. Bragagnolo^{a,b} , A.C.M. Bulla^a , R. Carlin^{a,b} , P. Checchia^a , T. Dorigo^a , F. Gasparini^{a,b} , U. Gasparini^{a,b} , E. Lusiani^a , M. Margoni^{a,b} , F. Marini^a , A.T. Meneguzzo^{a,b} , M. Migliorini^{a,b} , J. Pazzini^{a,b} , P. Ronchese^{a,b} , R. Rossin^{a,b} , F. Simonetto^{a,b} , G. Strong^a , M. Tosi^{a,b} , A. Triossi^{a,b} , M. Zanetti^{a,b} , P. Zotto^{a,b} , A. Zucchetta^{a,b} , G. Zumerle^{a,b} 

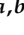


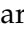
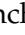






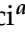

















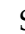


INFN Sezione di Pavia^a, Università di Pavia^b, Pavia, Italy

S. Abu Zeid^{a,55} , C. Aimè^{a,b} , A. Braghieri^a , S. Calzaferri^a , D. Fiorina^a , P. Montagna^{a,b} , V. Re^a , C. Riccardi^{a,b} , P. Salvini^a , I. Vai^{a,b} , P. Vitulo^{a,b} 











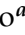





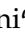




INFN Sezione di Perugia^a, Università di Perugia^b, Perugia, Italy

S. Ajmal^{a,b} , G.M. Bilei^a , D. Ciangottini^{a,b} , L. Fanò^{a,b} , M. Magherini^{a,b} , V. Mariani^{a,b} , M. Menichelli^a , F. Moscatelli^{a,56} , A. Rossi^{a,b} , A. Santocchia^{a,b} , D. Spiga^a , T. Tedeschi^{a,b} 

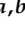

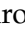





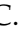


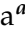










INFN Sezione di Pisa^a, Università di Pisa^b, Scuola Normale Superiore di Pisa^c, Pisa, Italy; Università di Siena^d, Siena, Italy








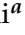








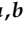

P. Asenov^{a,b} , P. Azzurri^a , G. Bagliesi^a , R. Bhattacharya^a , L. Bianchini^{a,b} , T. Boccali^a , E. Bossini^a , D. Bruschini^{a,c} , R. Castaldi^a , M.A. Ciocci^{a,b} , M. Cipriani^{a,b} , V. D'Amante^{a,d} , R. Dell'Orso^a , S. Donato^a , A. Giassi^a , F. Ligabue^{a,c} , D. Matos Figueiredo^a , A. Messineo^{a,b} , M. Musich^{a,b} , F. Palla^a , A. Rizzi^{a,b} , G. Rolandi^{a,c} , S. Roy Chowdhury^a , T. Sarkar^a , A. Scribano^a , P. Spagnolo^a , R. Tenchini^a , G. Tonelli^{a,b} , N. Turini^{a,d} , F. Vaselli^{a,c} , A. Venturi^a , P.G. Verdini^a 

INFN Sezione di Roma^a, Sapienza Università di Roma^b, Roma, Italy



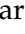
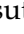


C. Baldenegro Barrera^{a,b} , P. Barria^a , C. Basile^{a,b} , M. Campana^{a,b} , F. Cavallari^a , L. Cunqueiro Mendez^{a,b} , D. Del Re^{a,b} , E. Di Marco^a , M. Diemoz^a , F. Errico^{a,b} , E. Longo^{a,b} , P. Meridiani^a , J. Mijuskovic^{a,b} , G. Organtini^{a,b} , F. Pandolfi^a , R. Paramatti^{a,b} , C. Quaranta^{a,b} , S. Rahatlou^{a,b} , C. Rovelli^a , F. Santanastasio^{a,b} , L. Soffi^a 

INFN Sezione di Torino^a, Università di Torino^b, Torino, Italy; Università del Piemonte Orientale^c, Novara, Italy








N. Amapane^{a,b} , R. Arcidiacono^{a,c} , S. Argiro^{a,b} , M. Arneodo^{a,c} , N. Bartosik^a , R. Bellan^{a,b} , A. Bellora^{a,b} , C. Biino^a , C. Borca^{a,b} , N. Cartiglia^a , M. Costa^{a,b} , R. Covarelli^{a,b} , N. Demaria^a , L. Finco^a , M. Grippo^{a,b} , B. Kiani^{a,b} , F. Legger^a , F. Luongo^{a,b} , C. Mariotti^a , L. Markovic^{a,b} , S. Maselli^a , A. Mecca^{a,b} 

E. Migliore^{a,b} , M. Monteno^a , R. Mulargia^a , M.M. Obertino^{a,b} , G. Ortona^a ,
L. Pacher^{a,b} , N. Pastrone^a , M. Pelliccioni^a , M. Ruspa^{a,c} , F. Siviero^{a,b} ,
V. Sola^{a,b} , A. Solano^{a,b} , A. Staiano^a , C. Tarricone^{a,b} , D. Trocino^a , G. Umoret^{a,b} ,
E. Vlasov^{a,b} , R. White^a 

INFN Sezione di Trieste^a, Università di Trieste^b, Trieste, Italy

S. Belforte^a , V. Candelise^{a,b} , M. Casarsa^a , F. Cossutti^a , K. De Leo^a ,
G. Della Ricca^{a,b} 


Kyungpook National University, Daegu, Korea

S. Dogra , J. Hong , C. Huh , B. Kim , D.H. Kim , J. Kim, H. Lee, S.W. Lee ,
C.S. Moon , Y.D. Oh , M.S. Ryu , S. Sekmen , Y.C. Yang 





Department of Mathematics and Physics - GWNNU, Gangneung, Korea

M.S. Kim 


Chonnam National University, Institute for Universe and Elementary Particles, Kwangju, Korea

G. Bak , P. Gwak , H. Kim , D.H. Moon 

Hanyang University, Seoul, Korea

E. Asilar , J. Choi , D. Kim , T.J. Kim , J.A. Merlin

Korea University, Seoul, Korea

S. Choi , S. Han, B. Hong , K. Lee, K.S. Lee , S. Lee , J. Park, S.K. Park, J. Yoo 



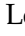

Kyung Hee University, Department of Physics, Seoul, Korea

J. Goh , S. Yang 





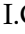


Sejong University, Seoul, Korea

H. S. Kim , Y. Kim, S. Lee



Seoul National University, Seoul, Korea

J. Almond, J.H. Bhyun, J. Choi , W. Jun , J. Kim , S. Ko , H. Kwon , H. Lee , J. Lee ,
J. Lee , B.H. Oh , S.B. Oh , H. Seo , U.K. Yang, I. Yoon

University of Seoul, Seoul, Korea

W. Jang , D.Y. Kang, Y. Kang , S. Kim , B. Ko, J.S.H. Lee , Y. Lee , I.C. Park , Y. Roh,
I.J. Watson 

Yonsei University, Department of Physics, Seoul, Korea

S. Ha , H.D. Yoo 





Sungkyunkwan University, Suwon, Korea

M. Choi , M.R. Kim , H. Lee, Y. Lee , I. Yu 


**College of Engineering and Technology, American University of the Middle East (AUM),
Dasman, Kuwait**

T. Beyrouthy

Riga Technical University, Riga, Latvia

K. Dreimanis , A. Gaile , G. Pikurs, A. Potrebko , M. Seidel 

University of Latvia (LU), Riga, Latvia

N.R. Strautnieks 




Vilnius University, Vilnius, Lithuania

M. Ambrozias , A. Juodagalvis , A. Rinkevicius , G. Tamulaitis 







National Centre for Particle Physics, Universiti Malaya, Kuala Lumpur, Malaysia

N. Bin Norjoharuddeen , I. Yusuff⁵⁷ , Z. Zolkapli

Universidad de Sonora (UNISON), Hermosillo, Mexico

J.F. Benitez , A. Castaneda Hernandez , H.A. Encinas Acosta, L.G. Gallegos Maríñez, M. León Coello , J.A. Murillo Quijada , A. Sehwat , L. Valencia Palomo 





Centro de Investigacion y de Estudios Avanzados del IPN, Mexico City, Mexico

G. Ayala , H. Castilla-Valdez , H. Crotte Ledesma, E. De La Cruz-Burelo , I. Heredia-De La Cruz⁵⁸ , R. Lopez-Fernandez , C.A. Mondragon Herrera, A. Sánchez Hernández 


Universidad Iberoamericana, Mexico City, Mexico

C. Oropeza Barrera , M. Ramírez García 

Benemerita Universidad Autonoma de Puebla, Puebla, Mexico

I. Bautista , I. Pedraza , H.A. Salazar Ibarguen , C. Uribe Estrada 

University of Montenegro, Podgorica, Montenegro

I. Bubanja, N. Raicevic 

University of Canterbury, Christchurch, New Zealand

P.H. Butler 



National Centre for Physics, Quaid-I-Azam University, Islamabad, Pakistan

A. Ahmad , M.I. Asghar, A. Awais , M.I.M. Awan, H.R. Hoorani , W.A. Khan 







AGH University of Krakow, Faculty of Computer Science, Electronics and Telecommunications, Krakow, Poland

V. Avati, L. Grzanka , M. Malawski 

National Centre for Nuclear Research, Swierk, Poland

H. Bialkowska , M. Bluj , B. Boimska , M. Górski , M. Kazana , M. Szeper , P. Zalewski 






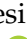
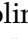









Institute of Experimental Physics, Faculty of Physics, University of Warsaw, Warsaw, Poland

K. Bunkowski , K. Doroba , A. Kalinowski , M. Konecki , J. Krolikowski , A. Muhammad 



Warsaw University of Technology, Warsaw, Poland

K. Pozniak , W. Zabolotny 

Laboratório de Instrumentação e Física Experimental de Partículas, Lisboa, Portugal

M. Araujo , D. Bastos , C. Beirão Da Cruz E Silva , A. Boletti , M. Bozzo , T. Camporesi , G. Da Molin , P. Faccioli , M. Gallinaro , J. Hollar , N. Leonardo , T. Niknejad , A. Petrilli , M. Pisano , J. Seixas , J. Varela , J.W. Wulff

Faculty of Physics, University of Belgrade, Belgrade, Serbia


























P. Adzic , P. Milenovic 

VINCA Institute of Nuclear Sciences, University of Belgrade, Belgrade, Serbia

M. Dordevic , J. Milosevic , V. Rekovic

Centro de Investigaciones Energéticas Medioambientales y Tecnológicas (CIEMAT), Madrid, Spain





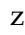









M. Aguilar-Benitez, J. Alcaraz Maestre , Cristina F. Bedoya , Oliver M. Carretero 

M. Cepeda , M. Cerrada , N. Colino , B. De La Cruz , A. Delgado Peris , A. Escalante Del Valle , D. Fernández Del Val , J.P. Fernández Ramos , J. Flix , M.C. Fouz , O. Gonzalez Lopez , S. Goy Lopez , J.M. Hernandez , M.I. Josa , D. Moran , C. M. Morcillo Perez , Á. Navarro Tobar , C. Perez Dengra , A. Pérez-Calero Yzquierdo , J. Puerta Pelayo , I. Redondo , D.D. Redondo Ferrero , L. Romero, S. Sánchez Navas , L. Urda Gómez , J. Vazquez Escobar , C. Willmott


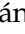
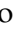

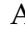
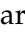

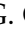











Universidad Autónoma de Madrid, Madrid, Spain

J.F. de Trocóniz 

Universidad de Oviedo, Instituto Universitario de Ciencias y Tecnologías Espaciales de Asturias (ICTEA), Oviedo, Spain

B. Alvarez Gonzalez , J. Cuevas , J. Fernandez Menendez , S. Folgueras , I. Gonzalez Caballero , J.R. González Fernández , P. Leguina , E. Palencia Cortezon , C. Ramón Álvarez , V. Rodríguez Bouza , A. Soto Rodríguez , A. Trapote , C. Vico Villalba , P. Vischia 


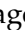

Instituto de Física de Cantabria (IFCA), CSIC-Universidad de Cantabria, Santander, Spain

S. Bhowmik , S. Blanco Fernández , J.A. Brochero Cifuentes , I.J. Cabrillo , A. Calderon , J. Duarte Campderros , M. Fernandez , G. Gomez , C. Lasaosa García , R. Lopez Ruiz , C. Martinez Rivero , P. Martinez Ruiz del Arbol , F. Matorras , P. Matorras Cuevas , E. Navarrete Ramos , J. Piedra Gomez , L. Scodellaro , I. Vila , J.M. Vizan Garcia 








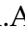





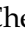


























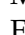








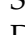

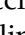
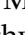

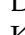
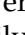
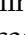
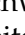

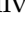
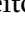


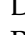
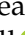
University of Colombo, Colombo, Sri Lanka

M.K. Jayananda , B. Kailasapathy⁵⁹ , D.U.J. Sonnadara , D.D.C. Wickramarathna 



University of Ruhuna, Department of Physics, Matara, Sri Lanka

W.G.D. Dharmaratna⁶⁰ , K. Liyanage , N. Perera , N. Wickramage 





CERN, European Organization for Nuclear Research, Geneva, Switzerland





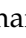







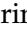
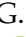
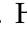

D. Abbaneo , C. Amendola , E. Auffray , G. Auzinger , J. Baechler, D. Barney , A. Bermúdez Martínez , M. Bianco , B. Bilin , A.A. Bin Anuar , A. Bocci , C. Botta , E. Brondolin , C. Caillol , G. Cerminara , N. Chernyavskaya , D. d'Enterria , A. Dabrowski , A. David , A. De Roeck , M.M. Defranchis , M. Deile , M. Dobson , L. Forthomme , G. Franzoni , W. Funk , S. Giani, D. Gigi, K. Gill , F. Glege , L. Gouskos , M. Haranko , J. Hegeman , B. Huber, V. Innocente , T. James , P. Janot , O. Kaluzinska , S. Laurila , P. Lecoq , E. Leutgeb , C. Lourenço , L. Malgeri , M. Mannelli , A.C. Marini , M. Matthewman, A. Mehta , F. Meijers , S. Mersi , E. Meschi , V. Milosevic , F. Monti , F. Moortgat , M. Mulders , I. Neutelings , S. Orfanelli, F. Pantaleo , G. Petrucciani , A. Pfeiffer , M. Pierini , D. Piparo , H. Qu , D. Rabadý , M. Rovere , H. Sakulin , S. Scarfi , C. Schwick, M. Selvaggi , A. Sharma , K. Shchelina , P. Silva , P. Sphicas⁶¹ , A.G. Stahl Leitner , A. Steen , S. Summers , D. Treille , P. Tropea , A. Tsiros, D. Walter , J. Wanczyk⁶² , J. Wang, S. Wuchterl , P. Zehetner , P. Zejdl , W.D. Zeuner

Paul Scherrer Institut, Villigen, Switzerland









T. Bevilacqua⁶³ , L. Caminada⁶³ , A. Ebrahimi , W. Erdmann , R. Horisberger , Q. Ingram , H.C. Kaestli , D. Kotlinski , C. Lange , M. Missiroli⁶³ , L. Noehte⁶³ , T. Rohe 

ETH Zurich - Institute for Particle Physics and Astrophysics (IPA), Zurich, Switzerland



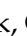


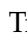
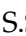
T.K. Aarrestad , K. Androsov⁶² , M. Backhaus , G. Bonomelli, A. Calandri , C. Caz-

zaniga , K. Datta , A. De Cosa , G. Dissertori , M. Dittmar , M. Donegà , F. Eble , M. Galli , K. Gedia , F. Glessgen , C. Grab , N. Härringer , T.G. Harte , D. Hits , W. Luster , A.-M. Lyon , R.A. Manzoni , M. Marchegiani , L. Marchese , C. Martin Perez , A. Mascellani⁶² , F. Nessi-Tedaldi , F. Pauss , V. Perovic , S. Pigazzini , C. Reissel , T. Reitspiess , B. Ristic , F. Riti , R. Seidita , J. Steggemann⁶² , D. Valsecchi , R. Wallny



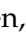
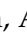


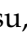

Universität Zürich, Zurich, Switzerland

C. Amsler⁶⁴ , P. Bäertschi , M.F. Canelli , K. Cormier , J.K. Heikkilä , M. Huwiler , W. Jin , A. Jofrehei , B. Kilminster , S. Leontsinis , S.P. Liechti , A. Macchiolo , P. Meiring , U. Molinatti , A. Reimers , P. Robmann , S. Sanchez Cruz , M. Senger , E. Shokr , F. Stäger , Y. Takahashi , R. Tramontano


National Central University, Chung-Li, Taiwan

C. Adloff⁶⁵ , D. Bhowmik , C.M. Kuo , W. Lin , P.K. Rout , P.C. Tiwari⁴⁰ , S.S. Yu 




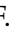
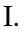
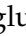


National Taiwan University (NTU), Taipei, Taiwan

L. Ceard , Y. Chao , K.F. Chen , P.s. Chen , Z.g. Chen , A. De Iorio , W.-S. Hou , T.h. Hsu , Y.w. Kao , S. Karmakar , R. Khurana , G. Kole , Y.y. Li , R.-S. Lu , E. Paganis , X.f. Su , J. Thomas-Wilsker , L.s. Tsai , H.y. Wu , E. Yazgan

High Energy Physics Research Unit, Department of Physics, Faculty of Science, Chulalongkorn University, Bangkok, Thailand

C. Asawatangtrakuldee , N. Srimanobhas , V. Wachirapusanand 

Çukurova University, Physics Department, Science and Art Faculty, Adana, Turkey

D. Agyel , F. Boran , Z.S. Demiroglu , F. Dolek , I. Dumanoglu⁶⁶ , E. Eskut , Y. Guler⁶⁷ , E. Gurpinar Guler⁶⁷ , C. Isik , O. Kara , A. Kayis Topaksu , U. Kiminsu , G. Onengut , K. Ozdemir⁶⁸ , A. Polatoz , B. Tali⁶⁹ , U.G. Tok , S. Turkcapar , E. Uslan , I.S. Zorbakir

Middle East Technical University, Physics Department, Ankara, Turkey

G. Sokmen , M. Yalvac⁷⁰ 

Bogazici University, Istanbul, Turkey

B. Akgun , I.O. Atakisi , E. Gülmez , M. Kaya⁷¹ , O. Kaya⁷² , S. Tekten⁷³ 

Istanbul Technical University, Istanbul, Turkey

A. Cakir , K. Cankocak^{66,74} , G.G. Dincer , Y. Komurcu , S. Sen⁷⁵ 

Istanbul University, Istanbul, Turkey

O. Aydilek²⁴ , S. Cerci⁶⁹ , V. Epshteyn , B. Hacisahinoglu , I. Hos⁷⁶ , B. Kaynak , S. Ozkorucuklu , O. Potok , H. Sert , C. Simsek , C. Zorbilmez

Yildiz Technical University, Istanbul, Turkey

B. Isildak⁷⁷ , D. Sunar Cerci⁶⁹ 

Institute for Scintillation Materials of National Academy of Science of Ukraine, Kharkiv, Ukraine

A. Boyaryntsev , B. Grynyov 

National Science Centre, Kharkiv Institute of Physics and Technology, Kharkiv, Ukraine


















L. Levchuk 

University of Bristol, Bristol, United Kingdom







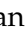
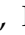


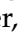












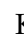





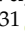
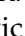
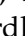

D. Anthony , J.J. Brooke , A. Bundock , F. Bury , E. Clement , D. Cussans 

H. Flacher , M. Glowacki, J. Goldstein , H.F. Heath , M.-L. Holmberg , L. Kreczko , S. Paramesvaran , L. Robertshaw, S. Seif El Nasr-Storey, V.J. Smith , N. Stylianou⁷⁸ , K. Walkingshaw Pass




Rutherford Appleton Laboratory, Didcot, United Kingdom

A.H. Ball, K.W. Bell , A. Belyaev⁷⁹ , C. Brew , R.M. Brown , D.J.A. Cockerill , C. Cooke , K.V. Ellis, K. Harder , S. Harper , J. Linacre , K. Manolopoulos, D.M. Newbold , E. Olaiya, D. Petyt , T. Reis , A.R. Sahasransu , G. Salvi , T. Schuh, C.H. Shepherd-Themistocleous , I.R. Tomalin , T. Williams 

Imperial College, London, United Kingdom

R. Bainbridge , P. Bloch , C.E. Brown , O. Buchmuller, V. Cacchio, C.A. Carrillo Montoya , G.S. Chahal⁸⁰ , D. Colling , J.S. Dancu, I. Das , P. Dauncey , G. Davies , J. Davies, M. Della Negra , S. Fayer, G. Fedi , G. Hall , M.H. Hassanshahi , A. Howard, G. Iles , M. Knight , J. Langford , J. León Holgado , L. Lyons , A.-M. Magnan , S. Malik, M. Mieskolainen , J. Nash⁸¹ , M. Pesaresi , B.C. Radburn-Smith , A. Richards, A. Rose , K. Savva, C. Seez , R. Shukla , A. Tapper , K. Uchida , G.P. Uttley , L.H. Vage, T. Virdee³¹ , M. Vojinovic , N. Wardle , D. Winterbottom 




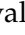

Brunel University, Uxbridge, United Kingdom

K. Coldham, J.E. Cole , A. Khan, P. Kyberd , I.D. Reid 

Baylor University, Waco, Texas, USA

S. Abdullin , A. Brinkerhoff , B. Caraway , E. Collins , J. Dittmann , K. Hatakeyama , J. Hiltbrand , B. McMaster , S. Sawant , C. Sutantawibul , J. Wilson 


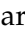


















Catholic University of America, Washington, DC, USA

R. Bartek , A. Dominguez , C. Huerta Escamilla, A.E. Simsek , R. Uniyal , A.M. Vargas Hernandez 












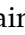

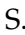



The University of Alabama, Tuscaloosa, Alabama, USA

B. Bam , R. Chudasama , S.I. Cooper , S.V. Gleyzer , C.U. Perez , P. Rumerio⁸² , E. Usai , R. Yi 







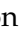







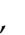


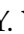

Boston University, Boston, Massachusetts, USA

A. Akpinar , D. Arcaro , C. Cosby , Z. Demiragli , C. Erice , C. Fangmeier , C. Fernandez Madrazo , E. Fontanesi , D. Gastler , F. Golf , S. Jeon , I. Reed , J. Rohlf , K. Salyer , D. Sperka , D. Spitzbart , I. Suarez , A. Tsatsos , S. Yuan , A.G. Zecchinelli 


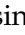

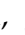



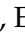


Brown University, Providence, Rhode Island, USA

G. Benelli , X. Coubez²⁶, D. Cutts , M. Hadley , U. Heintz , J.M. Hogan⁸³ , T. Kwon , G. Landsberg , K.T. Lau , D. Li , J. Luo , S. Mondal , M. Narain[†] , N. Pervan , S. Sagir⁸⁴ , F. Simpson , M. Stamenkovic , N. Venkatasubramanian, X. Yan , W. Zhang

University of California, Davis, Davis, California, USA

S. Abbott , J. Bonilla , C. Brainerd , R. Breedon , H. Cai , M. Calderon De La Barca Sanchez , M. Chertok , M. Citron , J. Conway , P.T. Cox , R. Erbacher , F. Jensen , O. Kukral , G. Mocellin , M. Mulhearn , D. Pellett , W. Wei , Y. Yao , F. Zhang 




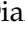

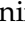





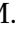
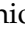
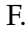



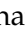
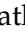




University of California, Los Angeles, California, USA

M. Bachtis , R. Cousins , A. Datta , G. Flores Avila, J. Hauser , M. Ignatenko , M.A. Iqbal , T. Lam , E. Manca , A. Nunez Del Prado, D. Saltzberg , V. Valuev 


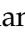
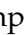













University of California, Riverside, Riverside, California, USA

R. Clare , J.W. Gary , M. Gordon, G. Hanson , W. Si , S. Wimpenny[†] 

University of California, San Diego, La Jolla, California, USA

J.G. Branson , S. Cittolin , S. Cooperstein , D. Diaz , J. Duarte , L. Giannini , J. Guiang , R. Kansal , V. Krutelyov , R. Lee , J. Letts , M. Masciovecchio , F. Mokhtar , S. Mukherjee , M. Pieri , M. Quinnan , B.V. Sathia Narayanan , V. Sharma , M. Tadel , E. Vourliotis , F. Würthwein , Y. Xiang , A. Yagil 









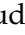


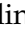



University of California, Santa Barbara - Department of Physics, Santa Barbara, California, USA

A. Barzdukas , L. Brennan , C. Campagnari , J. Incandela , J. Kim , A.J. Li , P. Masterson , H. Mei , J. Richman , U. Sarica , R. Schmitz , F. Setti , J. Sheplock , D. Stuart , T.Á. Vami , S. Wang 



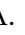
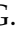










California Institute of Technology, Pasadena, California, USA

A. Bornheim , O. Cerri, A. Latorre, J. Mao , H.B. Newman , G. Reales Gutiérrez, M. Spiropulu , J.R. Vlimant , C. Wang , S. Xie , R.Y. Zhu 


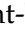



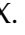
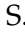

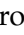







Carnegie Mellon University, Pittsburgh, Pennsylvania, USA

J. Alison , S. An , M.B. Andrews , P. Bryant , M. Cremonesi, V. Dutta , T. Ferguson , A. Harilal , C. Liu , T. Mudholkar , S. Murthy , P. Palit , M. Paulini , A. Roberts , A. Sanchez , W. Terrill 



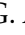
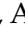

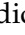










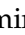


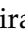









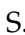



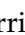









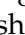

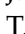





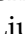




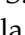
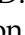
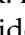


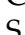
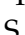



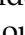
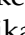

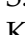
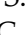
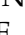

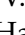
University of Colorado Boulder, Boulder, Colorado, USA

J.P. Cumalat , W.T. Ford , A. Hart , A. Hassani , G. Karathanasis , N. Manganelli , A. Perloff , C. Savard , N. Schonbeck , K. Stenson , K.A. Ulmer , S.R. Wagner , N. Zipper , D. Zuolo 




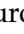

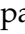


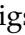









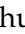
Cornell University, Ithaca, New York, USA

J. Alexander , S. Bright-Thonney , X. Chen , D.J. Cranshaw , J. Fan , X. Fan , S. Hogan , P. Kotamnives, J. Monroy , M. Oshiro , J.R. Patterson , J. Reichert , M. Reid , A. Ryd , J. Thom , P. Wittich , R. Zou 
















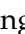
Fermi National Accelerator Laboratory, Batavia, Illinois, USA

M. Albrow , M. Alyari , O. Amram , G. Apollinari , A. Apresyan , L.A.T. Bauerdick , D. Berry , J. Berryhill , P.C. Bhat , K. Burkett , J.N. Butler , A. Canepa , G.B. Cerati , H.W.K. Cheung , F. Chlebana , G. Cummings , J. Dickinson , I. Dutta , V.D. Elvira , Y. Feng , J. Freeman , A. Gandrakota , Z. Gecse , L. Gray , D. Green, A. Grummer , S. Grünendahl , D. Guerrero , O. Gutsche , R.M. Harris , R. Heller , T.C. Herwig , J. Hirschauer , L. Horyn , B. Jayatilaka , S. Jindariani , M. Johnson , U. Joshi , T. Klijnsma , B. Klima , K.H.M. Kwok , S. Lammel , D. Lincoln , R. Lipton , T. Liu , C. Madrid , K. Maeshima , C. Mantilla , D. Mason , P. McBride , P. Merkel , S. Mrenna , S. Nahn , J. Ngadiuba , D. Noonan , V. Papadimitriou , N. Pastika , K. Pedro , C. Pena⁸⁵ , F. Ravera , A. Reinsvold Hall⁸⁶ , L. Ristori , E. Sexton-Kennedy , N. Smith , A. Soha , L. Spiegel , S. Stoynev , J. Strait , L. Taylor , S. Tkaczyk , N.V. Tran , L. Uplegger , E.W. Vaandering , A. Whitbeck , I. Zoi 










University of Florida, Gainesville, Florida, USA

C. Aruta , P. Avery , D. Bourilkov , L. Cadamuro , P. Chang , V. Cherepanov , R.D. Field, E. Koenig , M. Kolosova , J. Konigsberg , A. Korytov , K. Matchev , N. Menendez , G. Mitselmakher , K. Mohrman , A. Muthirakalayil Madhu , N. Rawal , D. Rosenzweig , S. Rosenzweig , J. Wang 





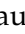



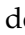




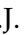







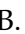





Florida State University, Tallahassee, Florida, USA

T. Adams , A. Al Kadhim , A. Askew , S. Bower , R. Habibullah , V. Hagopian , R. Hashmi , R.S. Kim , S. Kim , T. Kolberg , G. Martinez , H. Prosper , P.R. Prova , M. Wulansatiti , R. Yohay , J. Zhang 



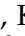


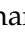





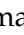



Florida Institute of Technology, Melbourne, Florida, USA

B. Alsufyani , M.M. Baarmand , S. Butalla , S. Das , T. Elkafrawy⁵⁵ , M. Hohlmann , R. Kumar Verma , M. Rahmani , E. Yanes 



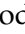








University of Illinois Chicago, Chicago, USA, Chicago, USA

M.R. Adams , A. Baty , C. Bennett , R. Cavanaugh , R. Escobar Franco , O. Evdokimov , C.E. Gerber , M. Hawksworth , A. Hingrajiya , D.J. Hofman , J.h. Lee , D. S. Lemos , A.H. Merrit , C. Mills , S. Nanda , G. Oh , B. Ozek , D. Pilipovic , R. Pradhan , E. Prifti , T. Roy , S. Rudrabhatla , M.B. Tonjes , N. Varelas , M.A. Wadud , Z. Ye , J. Yoo 


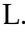

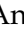
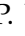





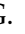
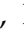
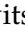











The University of Iowa, Iowa City, Iowa, USA

M. Alhusseini , D. Blend , K. Dilsiz⁸⁷ , L. Emediato , G. Karaman , O.K. Köseyan , J.-P. Merlo , A. Mestvirishvili⁸⁸ , J. Nachtman , O. Neogi , H. Ogul⁸⁹ , Y. Onel , A. Penzo , C. Snyder , E. Tiras⁹⁰ 




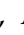


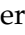


Johns Hopkins University, Baltimore, Maryland, USA

B. Blumenfeld , L. Corcodilos , J. Davis , A.V. Gritsan , L. Kang , S. Kyriacou , P. Maksimovic , M. Roguljic , J. Roskes , S. Sekhar , M. Swartz 

The University of Kansas, Lawrence, Kansas, USA

A. Abreu , L.F. Alcerro Alcerro , J. Anguiano , P. Baringer , A. Bean , Z. Flowers , D. Grove , J. King , G. Krintiras , M. Lazarovits , C. Le Mahieu , J. Marquez , N. Minafra , M. Murray , M. Nickel , M. Pitt , S. Popescu⁹¹ , C. Rogan , C. Royon , R. Salvatico , S. Sanders , C. Smith , Q. Wang , G. Wilson 






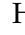





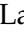




Kansas State University, Manhattan, Kansas, USA

B. Allmond , R. Gujju Gurunadha , A. Ivanov , K. Kaadze , A. Kalogeropoulos , Y. Maravin , J. Natoli , D. Roy , G. Sorrentino 





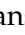

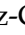














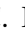



Lawrence Livermore National Laboratory, Livermore, California, USA

F. Rebassoo , D. Wright 



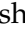










University of Maryland, College Park, Maryland, USA

A. Baden , A. Belloni , Y.M. Chen , S.C. Eno , N.J. Hadley , S. Jabeen , R.G. Kellogg , T. Koeth , Y. Lai , S. Lascio , A.C. Mignerey , S. Nabili , C. Palmer , C. Papageorgakis , M.M. Paranipe , L. Wang 

Massachusetts Institute of Technology, Cambridge, Massachusetts, USA

J. Bendavid , I.A. Cali , M. D'Alfonso , J. Eysermans , C. Freer , G. Gomez-Ceballos , M. Goncharov , G. Grosso , P. Harris , D. Hoang , D. Kovalskiy , J. Krupa , L. Lavezzo , Y.-J. Lee , K. Long , A. Novak , C. Paus , D. Rankin , C. Roland , G. Roland , S. Rothman , G.S.F. Stephans , Z. Wang , B. Wyslouch , T. J. Yang 













University of Minnesota, Minneapolis, Minnesota, USA

B. Crossman , B.M. Joshi , C. Kapsiak , M. Krohn , D. Mahon , J. Mans , B. Marzocchi , S. Pandey , M. Revering , R. Rusack , R. Saradhy , N. Schroeder , N. Strobbe 

University of Mississippi, Oxford, Mississippi, USA

L.M. Cremaldi 










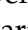





University of Nebraska-Lincoln, Lincoln, Nebraska, USA

K. Bloom , D.R. Claes , G. Haza , J. Hossain , C. Joo , I. Kravchenko , J.E. Siado ,
W. Tabb , A. Vagnerini , A. Wightman , F. Yan , D. Yu 




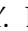


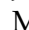

State University of New York at Buffalo, Buffalo, New York, USA

H. Bandyopadhyay , L. Hay , I. Iashvili , A. Kharchilava , M. Morris , D. Nguyen ,
S. Rappoccio , H. Rejeb Sfar, A. Williams 





















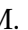





Northeastern University, Boston, Massachusetts, USA

G. Alverson , E. Barberis , J. Dervan, Y. Haddad , Y. Han , A. Krishna , J. Li ,
M. Lu , G. Madigan , R. Mccarthy , D.M. Morse , V. Nguyen , T. Orimoto ,
A. Parker , L. Skinnari , D. Wood 





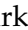


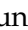
Northwestern University, Evanston, Illinois, USA

J. Bueghly, Z. Chen , S. Dittmer , K.A. Hahn , Y. Liu , Y. Miao , D.G. Monk ,
M.H. Schmitt , A. Taliercio , M. Velasco











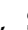

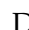





University of Notre Dame, Notre Dame, Indiana, USA

G. Agarwal , R. Band , R. Bucci, S. Castells , A. Das , R. Goldouzian , M. Hildreth ,
K.W. Ho , K. Hurtado Anampa , T. Ivanov , C. Jessop , K. Lannon , J. Lawrence ,
N. Loukas , L. Lutton , J. Mariano, N. Marinelli, I. Mcalister, T. McCauley , C. Mcgrady ,
C. Moore , Y. Musienko¹⁶ , H. Nelson , M. Osherson , A. Piccinelli , R. Ruchti ,
A. Townsend , Y. Wan, M. Wayne , H. Yockey, M. Zarucki , L. Zygalá 


The Ohio State University, Columbus, Ohio, USA

A. Basnet , B. Bylsma, M. Carrigan , L.S. Durkin , C. Hill , M. Joyce , M. Nunez Ornelas ,
K. Wei, B.L. Winer , B. R. Yates 
















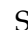



Princeton University, Princeton, New Jersey, USA

F.M. Addesa , H. Bouchamaoui , P. Das , G. Dezoort , P. Elmer , A. Frankenthal ,
B. Greenberg , N. Haubrich , G. Kopp , S. Kwan , D. Lange , A. Loeliger ,
D. Marlow , I. Ojalvo , J. Olsen , A. Shevelev , D. Stickland , C. Tully 



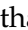
University of Puerto Rico, Mayaguez, Puerto Rico, USA

S. Malik 





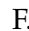






Purdue University, West Lafayette, Indiana, USA

A.S. Bakshi , V.E. Barnes , S. Chandra , R. Chawla , A. Gu , L. Gutay, M. Jones ,
A.W. Jung , D. Kondratyev , A.M. Koshy, M. Liu , G. Negro , N. Neumeister ,
G. Paspalaki , S. Piperov , V. Scheurer, J.F. Schulte , M. Stojanovic , J. Thieman ,
A. K. Viridi , F. Wang , W. Xie 








Purdue University Northwest, Hammond, Indiana, USA






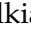












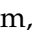



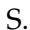
















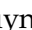


J. Dolen , N. Parashar , A. Pathak 

Rice University, Houston, Texas, USA

D. Acosta , T. Carnahan , K.M. Ecklund , P.J. Fernández Manteca , S. Freed, P. Gardner,
E.J.M. Geurts , W. Li , O. Miguel Colin , B.P. Padley , R. Redjimi, J. Rotter ,
E. Yigitbasi , Y. Zhang 

University of Rochester, Rochester, New York, USA

A. Bodek , P. de Barbaro , R. Demina , J.L. Dulemba , A. Garcia-Bellido ,
O. Hindrichs , A. Khukhunaishvili , N. Parmar, P. Parygin⁹² , E. Popova⁹² , R. Taus 

The Rockefeller University, New York, New York, USAK. Goulianos **Rutgers, The State University of New Jersey, Piscataway, New Jersey, USA**B. Chiarito, J.P. Chou , S.V. Clark , D. Gadkari , Y. Gershtein , E. Halkiadakis , M. Heindl , C. Houghton , D. Jaroslowski , O. Karacheban²⁹ , I. Laflotte , A. Lath , R. Montalvo, K. Nash, H. Routray , P. Saha , S. Salur , S. Schnetzer, S. Somalwar , R. Stone , S.A. Thayil , S. Thomas, J. Vora , H. Wang **University of Tennessee, Knoxville, Tennessee, USA**H. Acharya, D. Ally , A.G. Delannoy , S. Fiorendi , S. Higginbotham , T. Holmes , A.R. Kanuganti , N. Karunarathna , L. Lee , E. Nibigira , S. Spanier **Texas A&M University, College Station, Texas, USA**D. Aebi , M. Ahmad , O. Bouhali⁹³ , R. Eusebi , J. Gilmore , T. Huang , T. Kamon⁹⁴ , H. Kim , S. Luo , R. Mueller , D. Overton , D. Rathjens , A. Safonov **Texas Tech University, Lubbock, Texas, USA**N. Akchurin , J. Damgov , V. Hegde , A. Hussain , Y. Kazhykarim, K. Lamichhane , S.W. Lee , A. Mankel , T. Peltola , I. Volobouev **Vanderbilt University, Nashville, Tennessee, USA**E. Appelt , Y. Chen , S. Greene, A. Gurrola , W. Johns , R. Kunnawalkam Elayavalli , A. Melo , F. Romeo , P. Sheldon , S. Tuo , J. Velkovska , J. Viinikainen **University of Virginia, Charlottesville, Virginia, USA**B. Cardwell , B. Cox , J. Hakala , R. Hirosky , A. Ledovsky , C. Neu , C.E. Perez Lara **Wayne State University, Detroit, Michigan, USA**S. Bhattacharya , P.E. Karchin **University of Wisconsin - Madison, Madison, Wisconsin, USA**A. Aravind, S. Banerjee , K. Black , T. Bose , S. Dasu , I. De Bruyn , P. Everaerts , C. Galloni, H. He , M. Herndon , A. Herve , C.K. Koraka , A. Lanaro, R. Loveless , J. Madhusudanan Sreekala , A. Mallampalli , A. Mohammadi , S. Mondal, G. Parida , L. Pétré , D. Pinna, A. Savin, V. Shang , V. Sharma , W.H. Smith , D. Teague, H.F. Tsoi , W. Vetens , A. Warden **Authors affiliated with an institute or an international laboratory covered by a cooperation agreement with CERN**S. Afanasiev , V. Andreev , Yu. Andreev , T. Aushev , M. Azarkin , I. Azhgirey , A. Babaev , A. Belyaev , V. Blinov⁹⁵ , E. Boos , V. Borshch , D. Budkouski , V. Chekhovsky, R. Chistov⁹⁵ , M. Danilov⁹⁵ , A. Dermenev , T. Dimova⁹⁵ , D. Druzhkin⁹⁶ , M. Dubinin⁸⁵ , L. Dudko , A. Ershov , G. Gavrilo , V. Gavrilo , S. Gninenko , V. Golovtsov , N. Golubev , I. Golutvin , I. Gorbunov , A. Gribushin , K. Ivanov , Y. Ivanov , V. Kachanov , V. Karjavine , A. Karneyev , V. Kim⁹⁵ , M. Kirakosyan, D. Kirpichnikov , M. Kirsanov , V. Klyukhin , O. Kodolova⁹⁷ , D. Konstantinov , V. Korenkov , V. Korotkikh, A. Kozyrev⁹⁵ , N. Krasnikov , A. Lanev , P. Levchenko⁹⁸ , N. Lychkovskaya , V. Makarenko , A. Malakhov , V. Matveev⁹⁵ , V. Murzin , A. Nikitenko^{99,97} , S. Obraztsov , V. Oreshkin , V. Palichik , V. Perelygin , S. Petrushanko , S. Polikarpov⁹⁵ , V. Popov , O. Radchenko⁹⁵ , R. Ryutin, M. Savina , V. Savrin , V. Shalaev , S. Shmatov , S. Shulha , Y. Skovpen⁹⁵ , S. Slabospitskii , V. Smirnov , A. Snigirev , D. Sosnov , V. Sulimov , E. Tcherniaev , A. Terkulov

O. Teryaev , I. Tlisova , A. Toropin , L. Uvarov , A. Uzunian , A. Vorobyev[†],
N. Voytishin , B.S. Yuldashev¹⁰⁰, A. Zarubin , I. Zhizhin , A. Zhokin 

†: Deceased

¹Also at Yerevan State University, Yerevan, Armenia

²Also at TU Wien, Vienna, Austria

³Also at Institute of Basic and Applied Sciences, Faculty of Engineering, Arab Academy for Science, Technology and Maritime Transport, Alexandria, Egypt

⁴Also at Ghent University, Ghent, Belgium

⁵Also at Universidade Estadual de Campinas, Campinas, Brazil

⁶Also at Federal University of Rio Grande do Sul, Porto Alegre, Brazil

⁷Also at UFMS, Nova Andradina, Brazil

⁸Also at Nanjing Normal University, Nanjing, China

⁹Now at The University of Iowa, Iowa City, Iowa, USA

¹⁰Also at University of Chinese Academy of Sciences, Beijing, China

¹¹Also at China Center of Advanced Science and Technology, Beijing, China

¹²Also at University of Chinese Academy of Sciences, Beijing, China

¹³Also at China Spallation Neutron Source, Guangdong, China

¹⁴Now at Henan Normal University, Xinxiang, China

¹⁵Also at Université Libre de Bruxelles, Bruxelles, Belgium

¹⁶Also at an institute or an international laboratory covered by a cooperation agreement with CERN

¹⁷Also at Suez University, Suez, Egypt

¹⁸Now at British University in Egypt, Cairo, Egypt

¹⁹Also at Purdue University, West Lafayette, Indiana, USA

²⁰Also at Université de Haute Alsace, Mulhouse, France

²¹Also at Department of Physics, Tsinghua University, Beijing, China

²²Also at Tbilisi State University, Tbilisi, Georgia

²³Also at The University of the State of Amazonas, Manaus, Brazil

²⁴Also at Erzincan Binali Yildirim University, Erzincan, Turkey

²⁵Also at University of Hamburg, Hamburg, Germany

²⁶Also at RWTH Aachen University, III. Physikalisches Institut A, Aachen, Germany

²⁷Also at Isfahan University of Technology, Isfahan, Iran

²⁸Also at Bergische University Wuppertal (BUW), Wuppertal, Germany

²⁹Also at Brandenburg University of Technology, Cottbus, Germany

³⁰Also at Forschungszentrum Jülich, Juelich, Germany

³¹Also at CERN, European Organization for Nuclear Research, Geneva, Switzerland

³²Also at Institute of Physics, University of Debrecen, Debrecen, Hungary

³³Also at Institute of Nuclear Research ATOMKI, Debrecen, Hungary

³⁴Now at Universitatea Babeş-Bolyai - Facultatea de Fizica, Cluj-Napoca, Romania

³⁵Also at MTA-ELTE Lendület CMS Particle and Nuclear Physics Group, Eötvös Loránd University, Budapest, Hungary

³⁶Also at Physics Department, Faculty of Science, Assiut University, Assiut, Egypt

³⁷Also at HUN-REN Wigner Research Centre for Physics, Budapest, Hungary

³⁸Also at Punjab Agricultural University, Ludhiana, India

³⁹Also at University of Visva-Bharati, Santiniketan, India

⁴⁰Also at Indian Institute of Science (IISc), Bangalore, India

⁴¹Also at Birla Institute of Technology, Mesra, Mesra, India

⁴²Also at IIT Bhubaneswar, Bhubaneswar, India

⁴³Also at Institute of Physics, Bhubaneswar, India

- ⁴⁴Also at University of Hyderabad, Hyderabad, India
- ⁴⁵Also at Deutsches Elektronen-Synchrotron, Hamburg, Germany
- ⁴⁶Also at Department of Physics, Isfahan University of Technology, Isfahan, Iran
- ⁴⁷Also at Sharif University of Technology, Tehran, Iran
- ⁴⁸Also at Department of Physics, University of Science and Technology of Mazandaran, Behshahr, Iran
- ⁴⁹Also at Helwan University, Cairo, Egypt
- ⁵⁰Also at Italian National Agency for New Technologies, Energy and Sustainable Economic Development, Bologna, Italy
- ⁵¹Also at Centro Siciliano di Fisica Nucleare e di Struttura Della Materia, Catania, Italy
- ⁵²Also at Università degli Studi Guglielmo Marconi, Roma, Italy
- ⁵³Also at Scuola Superiore Meridionale, Università di Napoli 'Federico II', Napoli, Italy
- ⁵⁴Also at Fermi National Accelerator Laboratory, Batavia, Illinois, USA
- ⁵⁵Also at Ain Shams University, Cairo, Egypt
- ⁵⁶Also at Consiglio Nazionale delle Ricerche - Istituto Officina dei Materiali, Perugia, Italy
- ⁵⁷Also at Department of Applied Physics, Faculty of Science and Technology, Universiti Kebangsaan Malaysia, Bangi, Malaysia
- ⁵⁸Also at Consejo Nacional de Ciencia y Tecnología, Mexico City, Mexico
- ⁵⁹Also at Trincomalee Campus, Eastern University, Sri Lanka, Nilaveli, Sri Lanka
- ⁶⁰Also at Saegis Campus, Nugegoda, Sri Lanka
- ⁶¹Also at National and Kapodistrian University of Athens, Athens, Greece
- ⁶²Also at Ecole Polytechnique Fédérale Lausanne, Lausanne, Switzerland
- ⁶³Also at Universität Zürich, Zurich, Switzerland
- ⁶⁴Also at Stefan Meyer Institute for Subatomic Physics, Vienna, Austria
- ⁶⁵Also at Laboratoire d'Annecy-le-Vieux de Physique des Particules, IN2P3-CNRS, Annecy-le-Vieux, France
- ⁶⁶Also at Near East University, Research Center of Experimental Health Science, Mersin, Turkey
- ⁶⁷Also at Konya Technical University, Konya, Turkey
- ⁶⁸Also at Izmir Bakircay University, Izmir, Turkey
- ⁶⁹Also at Adiyaman University, Adiyaman, Turkey
- ⁷⁰Also at Bozok Universitetesi Rektörlüğü, Yozgat, Turkey
- ⁷¹Also at Marmara University, Istanbul, Turkey
- ⁷²Also at Milli Savunma University, Istanbul, Turkey
- ⁷³Also at Kafkas University, Kars, Turkey
- ⁷⁴Now at Istanbul Okan University, Istanbul, Turkey
- ⁷⁵Also at Hacettepe University, Ankara, Turkey
- ⁷⁶Also at Istanbul University - Cerrahpasa, Faculty of Engineering, Istanbul, Turkey
- ⁷⁷Also at Yildiz Technical University, Istanbul, Turkey
- ⁷⁸Also at Vrije Universiteit Brussel, Brussel, Belgium
- ⁷⁹Also at School of Physics and Astronomy, University of Southampton, Southampton, United Kingdom
- ⁸⁰Also at IPPP Durham University, Durham, United Kingdom
- ⁸¹Also at Monash University, Faculty of Science, Clayton, Australia
- ⁸²Also at Università di Torino, Torino, Italy
- ⁸³Also at Bethel University, St. Paul, Minnesota, USA
- ⁸⁴Also at Karamanoğlu Mehmetbey University, Karaman, Turkey
- ⁸⁵Also at California Institute of Technology, Pasadena, California, USA
- ⁸⁶Also at United States Naval Academy, Annapolis, Maryland, USA

⁸⁷Also at Bingol University, Bingol, Turkey

⁸⁸Also at Georgian Technical University, Tbilisi, Georgia

⁸⁹Also at Sinop University, Sinop, Turkey

⁹⁰Also at Erciyes University, Kayseri, Turkey

⁹¹Also at Horia Hulubei National Institute of Physics and Nuclear Engineering (IFIN-HH), Bucharest, Romania

⁹²Now at an institute or an international laboratory covered by a cooperation agreement with CERN

⁹³Also at Texas A&M University at Qatar, Doha, Qatar

⁹⁴Also at Kyungpook National University, Daegu, Korea

⁹⁵Also at another institute or international laboratory covered by a cooperation agreement with CERN











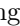


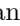


















⁹⁶Also at Universiteit Antwerpen, Antwerpen, Belgium

⁹⁷Also at Yerevan Physics Institute, Yerevan, Armenia

⁹⁸Also at Northeastern University, Boston, Massachusetts, USA

⁹⁹Also at Imperial College, London, United Kingdom

¹⁰⁰Also at Institute of Nuclear Physics of the Uzbekistan Academy of Sciences, Tashkent, Uzbekistan

A. Vinokurova , V. S. Vismaya , L. Vitale , V. Vobbilisetti , R. Volpe , B. Wach , M. Wakai , S. Wallner ,
 E. Wang , M.-Z. Wang , X. L. Wang , Z. Wang , A. Warburton , S. Watanuki , C. Wessel , E. Won ,
 X. P. Xu , B. D. Yabsley , S. Yamada , W. Yan , S. B. Yang , J. Yelton , J. H. Yin , K. Yoshihara ,
 C. Z. Yuan , Y. Yusa , B. Zhang , V. Zhilich , Q. D. Zhou , X. Y. Zhou , V. I. Zhukova , and R. Žlebčák 
 (The Belle II Collaboration)

We present GFlaT, a new algorithm that uses a graph-neural-network to determine the flavor of neutral B mesons produced in $\Upsilon(4S)$ decays. It improves previous algorithms by using the information from all charged final-state particles and the relations between them. We evaluate its performance using B decays to flavor-specific hadronic final states reconstructed in a 362 fb^{-1} sample of electron-positron collisions collected at the $\Upsilon(4S)$ resonance with the Belle II detector at the SuperKEKB collider. We achieve an effective tagging efficiency of $(37.40 \pm 0.43 \pm 0.36)\%$, where the first uncertainty is statistical and the second systematic, which is 18% better than the previous Belle II algorithm. Demonstrating the algorithm, we use $B^0 \rightarrow J/\psi K_S^0$ decays to measure the mixing-induced and direct CP violation parameters, $S = (0.724 \pm 0.035 \pm 0.014)$ and $C = (-0.035 \pm 0.026 \pm 0.013)$.

PACS numbers:

I. INTRODUCTION

In the standard model, CP violation arises from an irreducible complex phase in the Cabibbo-Kobayashi-Maskawa (CKM) matrix [1]. Measurements of mixing-induced CP violation in B^0 meson decays constrain the values of the CKM-unitarity-triangle angles ϕ_1 and ϕ_2 ,¹ helping us probe for sources of CP violation beyond the standard model. For example, we learn ϕ_1 from $B^0 \rightarrow J/\psi K^0$ [2–4] and ϕ_2 from $B^0 \rightarrow (\pi\pi)^0$ [5–7], $(\rho\rho)^0$ [8–10]. These measurements require knowledge of the neutral B meson flavor. At B factory experiments, B^0 and \bar{B}^0 mesons are produced in pairs from e^+e^- collisions at the $\Upsilon(4S)$ resonance. Since their states are entangled, tagging the flavor of one of the mesons, B_{tag} , at the time of its decay determines the flavor of the other one, B_{sig} , at the same time [11, 12].

The Belle II [13] experiment reported results using a flavor tagger [14–16] based on algorithms developed by the Belle and BABAR experiments [2, 17]. It uses the kinematic, topology, particle-identification, and charge information of charged final-state particles in the B_{tag} decay to infer if they originated from categories of flavor-specific decays. For instance, a charged particle is assigned as being a μ^+ in a $B^0 \rightarrow D\mu^+\nu_\mu X$ decay or a K^+ in the subsequent $D \rightarrow K^+Y$ decay, the charge of which correlates to the B_{tag} flavor. This category-based flavor tagger selects the most probable assignment in each category, discards all other possibilities in that category, and then combines the probabilities of the selected assignments to predict the B_{tag} flavor.

In this paper, we present a new algorithm, the graph-neural-network flavor tagger, GFlaT, which uses a dynamic-graph-convolutional-neural-network [18] to combine the information from all charged final-state par-

ticles. It improves flavor tagging by accounting for the discarded information in the category-based flavor tagger and correlations between information from final-state particles.

To demonstrate GFlaT, we measure the CP parameters of $B^0 \rightarrow J/\psi K_S^0$ from which we calculate ϕ_1 . The probability density to observe B_{sig} decay at a time Δt from when B_{tag} decays with flavor q_{tag} (1 for B^0 , -1 for \bar{B}^0) is

$$P(\Delta t, q_{\text{tag}}) = \frac{e^{-|\Delta t|/\tau}}{4\tau} \left\{ 1 + q_{\text{tag}}(1 - 2w)[S \sin(\Delta m_d \Delta t) - C \cos(\Delta m_d \Delta t)] \right\}, \quad (1)$$

where q_{tag} is determined by the flavor tagger, w is the probability to wrongly determine it, τ is the B^0 lifetime, and Δm_d is the difference of masses of the B^0 mass eigenstates.² Here S and C , the parameters of interest, quantify mixing-induced and direct CP violation, respectively. In the standard model, $S = \sin 2\phi_1$ and $C = 0$ to good precision [19–21]. At B factories, the B mesons are boosted and have significant momentum in the lab frame, so Δt is determined from the relative displacement of their decay vertices.

To measure CP parameters in tagged B^0 decays, we must know w . We determine it from events with the flavor-specific B_{sig} decaying as $B^0 \rightarrow D^{(*)-}\pi^+$, for which

$$P(\Delta t, q_{\text{sig}}, q_{\text{tag}}) = \frac{e^{-|\Delta t|/\tau}}{4\tau} \left\{ 1 - q_{\text{sig}}q_{\text{tag}}(1 - 2w) \cos(\Delta m_d \Delta t) \right\}, \quad (2)$$

where q_{sig} equals the charge of the pion from the B_{sig} decay, neglecting the $\mathcal{O}(10^{-4})$ wrong-sign contribution

¹ These angles are also known as β and α .

² We use a system of units in which $\hbar = c = 1$ and mass and frequency have the same dimension.

from $B^0 \rightarrow D^{(*)+}\pi^-$ [22–24]; we implicitly include charge conjugated decays here and throughout. Here we assume w is independent of the B_{sig} decay mode. Flavor taggers also determine the quality of their flavor assignments by the dilution factor, $r \in [0, 1]$ which approximates $1 - 2w$. We determine w in seven contiguous disjoint intervals (r bins) defined by the edges $[0.0, 0.1, 0.25, 0.45, 0.6, 0.725, 0.875, 1.0]$, as in Ref. [15], and calculate the effective tagging efficiency,

$$\varepsilon_{\text{tag}} = \sum_i \varepsilon_i (1 - 2w_i)^2, \quad (3)$$

where ε_i is the average of the efficiencies to tag B^0 and \bar{B}^0 in r bin i . An increase in ε_{tag} improves statistical precision for parameters measured in tagged B^0 decays, for example, the statistical uncertainties on S and C are proportional to $1/\sqrt{\varepsilon_{\text{tag}}}$. The effective tagging efficiency is thus a convenient metric for evaluating tagger performance.

We reconstruct the flavor-specific $B^0 \rightarrow D^{(*)-}\pi^+$ decays from $D^- \rightarrow K^+\pi^-\pi^-$ and $D^{*-} \rightarrow \bar{D}^0\pi^-$ with $\bar{D}^0 \rightarrow K^+\pi^-$, $K^+\pi^-\pi^0$, or $K^+\pi^-\pi^+\pi^-$. We fit the background-subtracted Δt distributions to extract flavor tagger parameters, including w , and determine the Δt resolution model.

For the measurements of S and C , we reconstruct the B_{sig} candidates by combining $K_S^0 \rightarrow \pi^+\pi^-$ with $J/\psi \rightarrow e^+e^-$ or $\mu^+\mu^-$. The values of S and C are extracted via a fit to the background-subtracted Δt distribution using the flavor tagger parameters and Δt resolution model determined from the study of $B^0 \rightarrow D^{(*)-}\pi^+$.

This paper is organized as follows. We first discuss the Belle II detector and the simulation software used in the study in Sec. II. Section III describes the GFlaT algorithm, including input variables, training procedure, and a discussion on the improvement from the category-based flavor tagger. Section IV presents the evaluation of GFlaT’s performance using the flavor-specific process, $B^0 \rightarrow D^{(*)-}\pi^+$. We describe the measurement of S and C for $B^0 \rightarrow J/\psi K_S^0$ to demonstrate GFlaT’s effectiveness in Sec. V and conclude in Sec. VI.

II. DETECTOR AND SIMULATION

We evaluate GFlaT’s performance using a $(362 \pm 2) \text{ fb}^{-1}$ data set collected with the Belle II detector in 2019–2022. The Belle II detector is located at SuperKEKB, which collides electrons and positrons at and near the $\Upsilon(4S)$ resonance [25]. It is cylindrical and includes a two-layer silicon-pixel detector (PXD) surrounded by a four-layer double-sided silicon-strip detector [26] and a 56-layer central drift chamber (CDC). These detectors reconstruct trajectories of charged particles (tracks). Only one sixth of the second layer of the PXD was installed for the data analyzed here. The symmetry axis of these detectors, z , is nearly coincident

with the direction of the electron beam. Surrounding the CDC, which also measures dE/dx ionization energy-loss, is a time-of-propagation detector [27] in the barrel and an aerogel-based ring-imaging Cherenkov detector in the forward ($+z$) endcap region. These detectors provide information for charged-particle identification. Surrounding them is an electromagnetic calorimeter (ECL) based on CsI(Tl) crystals that primarily measures the energies and times of detection of photons and electrons. Outside it is a superconducting solenoid magnet that provides a 1.5 T field in the z direction. Its flux return is instrumented with resistive-plate chambers and plastic scintillator modules to detect muons, K_L^0 , and neutrons.

We use simulated data to train GFlaT, estimate reconstruction efficiencies and background contributions, and construct fit models. We generate $e^+e^- \rightarrow \Upsilon(4S) \rightarrow B\bar{B}$ using EVTGEN [28] and PYTHIA8 [29] and $e^+e^- \rightarrow q\bar{q}$ with q indicating a u, d, c , or s quark using KKMC [30] and PYTHIA8. We simulate particle decays using EVTGEN interfaced with PYTHIA8, and the interaction of particles with the detector using GEANT4 [31]. Our simulation includes effects of beam-induced backgrounds [32]. Events in both simulation and data are reconstructed using the Belle II analysis software framework [33, 34].

III. GFLAT

GFlaT is designed to run after B_{sig} is reconstructed and uses information from the tracks and energy deposits in the ECL (clusters) not associated with B_{sig} , in the same manner as the category-based flavor tagger [14]. We refer to these tracks and clusters as the rest of the event (ROE), which mostly originates from B_{tag} . Tracks from the ROE must be within the CDC and have points of closest approach (POCAs) to the e^+e^- interaction region (IR) that are less than 3 cm from the IR in the z direction and less than 1 cm from it in the transverse plane. The shape and location of the IR are determined from $e^+e^- \rightarrow \mu^+\mu^-$ events in 30-minute intervals. We retain only the first 16 charged particles in the ROE, ordered by decreasing momentum in the lab frame. According to simulation, the average number of charged particles in the ROE is 4.8, and less than 0.001% of events have more than 16 charged particles.

GFlaT uses 25 input variables for each ROE charged particle: the lab-frame Cartesian components of its momentum and the displacement of its POCA from the IR; particle-identification likelihoods for each of the six possible charged final-state particles, e, μ, π, K , proton, and deuteron; and the products of the charge of the particle and the output of the category-based flavor tagger for each of its 13 categories.³ The input variables have the

³ corresponding to $q_{\text{cand}}y_{\text{cat}}$ defined in Ref. [14].

same distributions for B^0 and \bar{B}^0 except for differences in the detection and reconstruction efficiency for negative and positive charged particles.

GFlaT uses a dynamic-graph-convolutional-neural-network that has been used for jet tagging at LHC experiments [35]. GFlaT first processes the input variables using the EdgeConv algorithm [18], which consists of three neural networks: edge and node networks run in parallel, and a weight network runs on their output. In the context of graph-neural-networks, the set of ROE charged particles is a graph with each particle a node and each pair an edge. The node network processes the variables of each particle to update them. The edge network processes the variables of each pair of particles to update the variables of each particle. To reduce computational resources, with no impact on performance, the edge network processes information from pairs formed from only the five nearest neighbors to each particle. The weight network processes the outputs of the edge and node networks with a squeeze-and-excitation algorithm that calculates weights based on variable importance [36]. The output of the EdgeConv consists of the updated variables for each particle that are improved to more accurately reflect the characteristics of each particle.

GFlaT runs EdgeConv twice. The first run processes the measured particle variables, with its edge network finding nearest neighbors based on POCAs. The second run processes the output of the first run, with its edge network finding nearest neighbors based on particle similarity using the updated particle variables. To keep output reasonably symmetric between B^0 and \bar{B}^0 , the output variables of each particle from the second EdgeConv are multiplied by its charge. The averages, maxima, and minima of the outputs are processed with a final network, the event network, which outputs one variable, qr_{GFlaT} , which is in $[-1, 1]$, with $q_{\text{tag}} = \text{sign}(qr_{\text{GFlaT}})$ and $r = |qr_{\text{GFlaT}}|$.

We train GFlaT using simulated events in which B_{tag} decays generically according to known (if known) or assumed (otherwise) branching fractions [37] and B_{sig} decays to $\nu\bar{\nu}$, so that all reconstructed tracks and ECL clusters form the ROE. The training data set consists of 5×10^6 events; the independent validation data set consists of 8×10^5 events. We minimize binary cross-entropy loss with the Adam optimizer [38] and train with a one-cycle learning schedule [39]. The learning rate increases linearly from 5×10^{-4} to 3×10^{-3} over five epochs, then decreases linearly to its initial value over five epochs, and finally decreases linearly over ten epochs to 10^{-6} .

Figure 1 shows the qr distributions for true B^0 and \bar{B}^0 for independent test data consisting of 1×10^5 events from GFlaT and the category-based flavor tagger. The latter has more reliable tagging information than reported in Ref. [14], due to recent improvements in particle identification and parameter tuning. GFlaT better distinguishes between B^0 and \bar{B}^0 than the category-based flavor tagger: the peaks at $|qr| \approx 1$ are higher and the bumps at $|qr| \approx 0$ and $|qr| \approx 0.65$ are smaller.

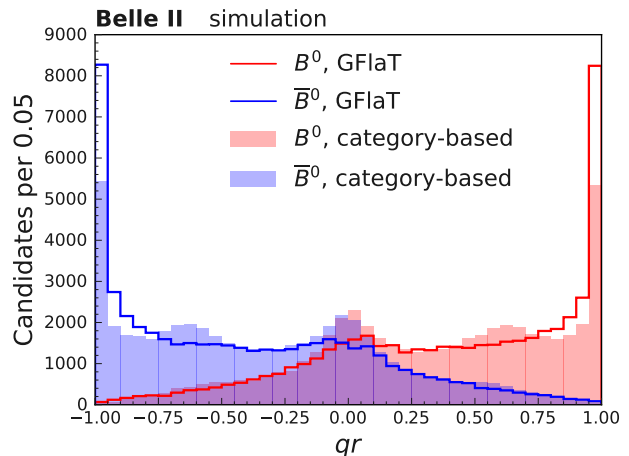


Figure 1. Distributions of qr for true B^0 and \bar{B}^0 from GFlaT and the category-based flavor tagger in simulated data.

Figure 2 shows the qr distributions for events classified according to the presence of charged leptons or kaons in the ROE. The ROE contains a charged lepton and a charged kaon in 22.2% of events, a charged lepton and no charged kaon in 22.9%, a charged kaon and no charged lepton in 31.5%, and neither in 23.4%. The distributions indicate that performance is optimal when both a lepton and a kaon are present, with the contribution from leptons being particularly significant. The distributions also reveal that the bump at $|qr| \approx 0.65$ in the category-based flavor tagger is due to events with charged kaons, which indicates that flavor assignment in such events is less reliable since a K^- , predominantly associated with \bar{B}^0 decays, can also originate from a B^0 decay, for example through decay to a D^- with $D^- \rightarrow \bar{K}^0 K^-$. Since GFlaT accounts for the relationships between final-state particles, it can better discern the origin of the tracks; and so its output does not peak at $|qr| \approx 0.65$ for those events, but instead at $|qr| \approx 1$. Both flavor taggers perform poorly for events with neither a charged lepton nor a charged kaon, consisting mostly of pions, but GFlaT's output still exhibits a visible improvement. A charged pion from B^0 decay, such as $B^0 \rightarrow D^- \pi^+$, or through an intermediate resonance that decays via the strong force, correlates with the B flavor. The GFlaT algorithm exploits this correlation more effectively to improve performance.

IV. CALIBRATION AND PERFORMANCE

We evaluate GFlaT's performance using events in which B_{sig} decays to the $D^{(*)-} \pi^+$ final state. The flavor of B_{sig} is determined by the charge of the pion, neglecting the wrong-sign contribution. We fit the Δt probability density model to the background-subtracted Δt distribution, accounting for resolution effects, to determine the

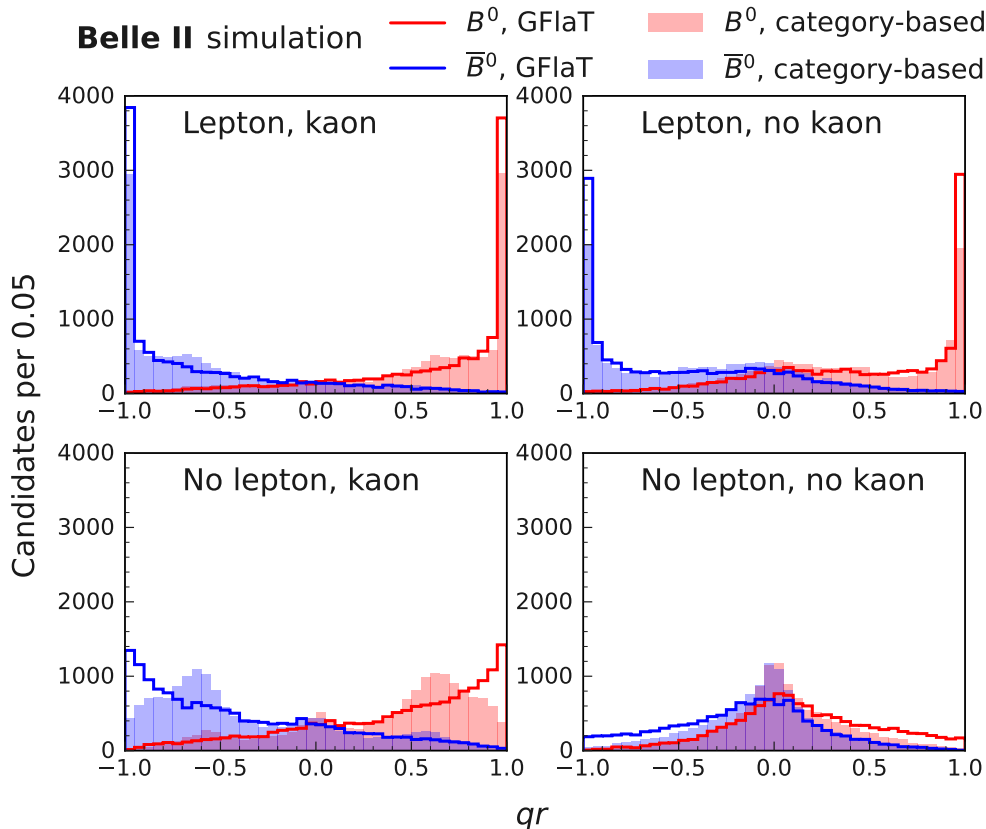


Figure 2. Distributions of qr for true B^0 and \bar{B}^0 from GFlaT and the category-based flavor tagger for events classified according to the presence of charged leptons or charged kaons in the ROE in simulation data.

wrong-tag probability w in each r bin. We subtract the background with $sWeight$ [40, 41] using the B energy as a discriminating variable.

We reconstruct D^- candidates via $D^- \rightarrow K^+\pi^-\pi^-$ and D^{*-} via $D^{*-} \rightarrow \bar{D}^0\pi^-$ with $\bar{D}^0 \rightarrow K^+\pi^-$, $K^+\pi^-\pi^0$, or $K^+\pi^-\pi^+\pi^-$. Tracks must originate from the IR and have polar angles within the CDC.

We reconstruct π^0 candidates via $\pi^0 \rightarrow \gamma\gamma$, forming photon candidates from ECL clusters not associated with any tracks. To suppress beam-background photons, we require each cluster have an energy greater than 120 MeV, 30 MeV, or 80 MeV if it is in the forward, barrel, or backward region of the ECL, which corresponds to the lab-frame polar angle ranges $[12.4, 31.4]^\circ$, $[32.2, 128.7]^\circ$, and $[130.7, 155.1]^\circ$, respectively. The angle between the photon momenta must be less than 52° in the lab frame and the diphoton mass must be in the range $[121, 142]$ MeV, which is centered on the known π^0 mass and is six units of diphoton mass resolution wide.

One of the D 's decay products must be consistent with being a K^+ , but no particle-identification requirements are placed on the other charged particles. Each D^- candidate must have a mass in $[1.860, 1.880]$ GeV, which is centered on the known D^- mass and is a $\pm 3\sigma$ range, with σ being the mass resolution. Each \bar{D}^0

candidate reconstructed from $K^+\pi^-$ ($\pi^+\pi^-$) must have a mass in $[1.845, 1.885]$ GeV, which is centered on the known \bar{D}^0 mass and is a $\pm 5\sigma$ range. Each \bar{D}^0 candidate reconstructed from $K^+\pi^-\pi^0$ must have a mass in $[1.810, 1.895]$ GeV, which is an asymmetric range of $+2.5\sigma$ and -4σ around the known \bar{D}^0 mass to account for energy losses in photon reconstruction.

The π^- from a D^{*-} candidate decay must have momentum below 300 MeV in the e^+e^- center-of-mass (c.m.) frame. Each D^{*-} candidate must have an energy release, $m(D^{*-}) - m(\bar{D}^0) - m_{\pi^-}$, in $[4.6, 7.0]$ MeV, which is centered around the known energy release and six units of its resolution wide.

We reconstruct a B^0 candidate from a $D^{(*)-}$ candidate and a track that is consistent with being a π^+ . For each B^0 candidate, we fit the trajectories and momenta of its decay products according to its decay chain with TREEFIT [42], constraining the B^0 to originate from the IR and the $D^{(*)-}$ to its known mass [37]. We reject B^0 candidates whose fits do not converge. The fraction of rejected signal candidates is 0.4%. We define the signal region from a beam-constrained mass

$$M_{bc} \equiv \sqrt{E_{\text{beam}}^2 - |\vec{p}|^2} \quad (4)$$

and energy difference, $\Delta E \equiv E - E_{\text{beam}}$, where E_{beam} , E , and \vec{p} are the beam energy and B^0 energy and momentum in the c.m. frame, respectively. The criteria for the signal region are $M_{\text{bc}} > 5.27$ GeV and $\Delta E \in [-0.10, 0.25]$ GeV.

We determine the decay position of B_{tag} by fitting the trajectories of ROE tracks with RAVE [43]. Unlike TREEFIT, RAVE accounts for the unknown B_{tag} decay chain by reducing the impact of a displaced vertex due to potential intermediate D 's, constraining the B_{tag} vertex position to be consistent with the origin and direction of B_{sig} . We reject events in which this fit does not converge, which rejects 3.4% of the signal events.

To suppress events not coming from $e^+e^- \rightarrow B\bar{B}$, such as $e^+e^- \rightarrow q\bar{q}$, we exploit their topological differences, by requiring the ratio of the second to the zeroth Fox-Wolfram moment, R_2 , be less than 0.4 [44]. After applying all selection requirements, the average number of candidates per event is 1.05 and all candidates are retained.

Events passing the above criteria are either correctly identified B_{sig} decays or backgrounds from $B\bar{B}$ and $q\bar{q}$ events. To separate signal from background, we fit to the ΔE distribution using an extended unbinned likelihood, combining data from B_{sig} and \bar{B}_{sig} and all r intervals.

We model the signal contribution as the sum of a Gaussian function and a double-sided Crystal-Ball function [45]. Their parameters and their admixture are fixed to values obtained from fitting to simulated data, but a common shift of their peak values and common scaling of their widths are left free to account for differences between data and simulation.

Events in which B_{sig} decays to the $D^{(*)-}K^+$ final state, with the K^+ misidentified as a π^+ , peak at -50 MeV in the ΔE distribution. According to simulation studies, the fraction of these events to the signal is 2.5%. We model this contribution as a double-sided Crystal Ball function, whose parameters are fixed to values obtained from fitting to simulated data, including the ratio of its yield to the signal, except for the shift of its peak value and the scaling of its width, which are the same as for the signal. Since these events have the same Δt distribution as $B^0 \rightarrow D^{(*)-}\pi^+$, we use this contribution as signal in the $sWeight$ calculation.

We model the $B\bar{B}$ background contribution as a second-order polynomial, with the ratio of its yield to that of the signal fixed to a value obtained from simulated data. We model the $q\bar{q}$ background contribution as an exponential function. To constrain the parameters of the $q\bar{q}$ component, we simultaneously fit to the ΔE distribution in a sideband, $M_{\text{bc}} \in [5.20, 5.24]$ GeV, populated predominantly by $q\bar{q}$ events. We confirm via simulation studies that the ΔE distributions of the $q\bar{q}$ component in the signal and sideband regions are sufficiently similar to warrant a simultaneous fit.

Figure 3 shows the ΔE distributions in the signal region and sideband and the fit results. The fit agrees well with the data. Yields in the signal region are 77130 ± 320 events for the signal (for the sum of the $D^{(*)-}\pi^+$ and

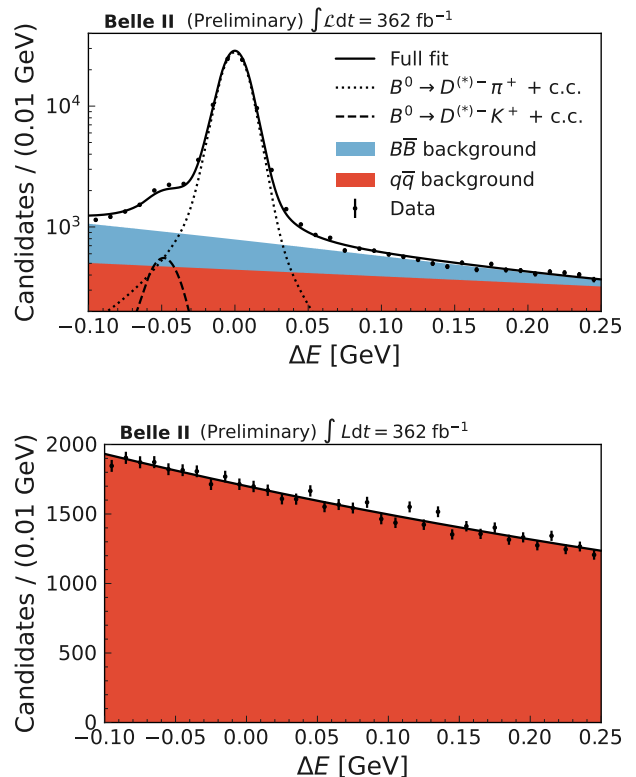


Figure 3. Distributions of ΔE for $B^0 \rightarrow D^{(*)-}\pi^+$ reconstructed in data in the signal region (top) and sideband (bottom) and the best-fit function, with background components stacked.

$D^{(*)-}K^+$ final states), 8620 ± 40 for the $B\bar{B}$ background, and 14200 ± 230 for the $q\bar{q}$ background.

We modify equation (2) to account for differences in the wrong-tag probabilities for B_{tag} and \bar{B}_{tag} , by introducing $w(B^0) \equiv \bar{w} + \frac{1}{2}\Delta w$ and $w(\bar{B}^0) \equiv \bar{w} - \frac{1}{2}\Delta w$ and reconstruction efficiency asymmetries for B_{sig} and \bar{B}_{sig} , a_{sig} and a_{tag} , with $a_x \equiv [\varepsilon(B_x^0) - \varepsilon(\bar{B}_x^0)] / [\varepsilon(\bar{B}_x^0) + \varepsilon(B_x^0)]$, where x indicates ‘tag’ or ‘sig’,

$$\begin{aligned}
 P(\Delta t, q_{\text{sig}}, q_{\text{tag}}) = & \\
 & (1 + a_{\text{sig}}q_{\text{sig}}) \frac{e^{-|\Delta t|/\tau}}{4\tau} \left\{ 1 + q_{\text{tag}}[a_{\text{tag}}(1 - 2\bar{w}) - \Delta w] \right. \\
 & \left. + q_{\text{sig}}q_{\text{tag}}(1 - 2\bar{w} + q_{\text{tag}}a_{\text{tag}} - a_{\text{tag}}\Delta w) \cos(\Delta m_d \Delta t) \right\}. \quad (5)
 \end{aligned}$$

We determine a_{sig} by fitting the ΔE distributions for B_{sig} and \bar{B}_{sig} separately, using the same model as for their combined fit, without selection criteria on B_{tag} to avoid a bias from using B_{tag} information. We measure $a_{\text{sig}} = (-2.53 \pm 0.39)\%$, which we attribute to charge asymmetries in kaon identification and low-momentum track finding.

We calculate a per-candidate signal probability using $sWeight$ from the ΔE -fit results, allowing us to statisti-

cally subtract background contributions to the Δt distributions. This requires that ΔE , Δt , and r be independent, which is confirmed in simulation studies.

We calculate Δt from the distance, $\Delta \ell$, of the B_{sig} vertex from that of B_{tag} along the $\Upsilon(4S)$ boost direction,

$$\Delta t = \frac{\Delta \ell}{\beta \gamma \gamma_B}, \quad (6)$$

where $\beta \gamma = 0.28$ is the Lorentz boost of the $\Upsilon(4S)$ in the lab frame and $\gamma_B = 1.002$ is the Lorentz factor of the B in the c.m. frame.

To account for resolution and bias in measuring $\Delta \ell$, we convolve equation (5) with the resolution function introduced in Ref. [15]. The resolution function consists of a core component modeled by a Gaussian function, a tail component modeled by a weighted sum of a Gaussian and two exponentially modified Gaussian functions, and an outlier component modeled by a Gaussian function. Parameters of the resolution function are shared by all r bins, except for the highest r bin. This bin is mostly populated by semileptonic B_{tag} decays, which have a better resolution.

We fit simultaneously to the binned background-subtracted Δt distributions in 28 subsets of the data defined by the 7 r intervals, 2 flavors of B_{sig} , and 2 flavors of B_{tag} . The fit has seven free resolution-function parameters and 21 free flavor-tagger parameters, a_{tag} , \bar{w} , and Δw in each of the 7 r bins. The uncertainty on the Δt measurement, $\sigma_{\Delta t}$, is computed for each event and is a conditional variable in the resolution function. We use a histogram with 500 bins in each data subset as the probability density function for this variable. We fix Δm_d and τ to their world average values [37]. Figure 4 shows the Δt distribution in each r interval and the result of the fit.

Figure 5 shows the qr_{GFlaT} distribution in background-subtracted data and correctly reconstructed simulated events normalized to the data signal yield. Figure 6 shows the dilution factors, $1 - 2w_i$, for each r bin i for both B_{tag}^0 and \bar{B}_{tag}^0 . It shows that r is a good estimator of $1 - 2w$ for both tag flavors. The effective tagging efficiency is $\varepsilon_{\text{tag}} = (37.40 \pm 0.43)\%$, where the uncertainty is statistical only. Table II in Appendix A lists a_{tag} , \bar{w} , and Δw for each r bin.

V. MEASUREMENT OF $\sin 2\phi_1$ IN $B^0 \rightarrow J/\psi K_S^0$

We demonstrate GFlaT by measuring S and C in $B^0 \rightarrow J/\psi K_S^0$ decays. We reconstruct J/ψ candidates via $J/\psi \rightarrow e^+e^-$ or $\mu^+\mu^-$. The leptons must fulfill the same track requirements as described for the decay products of $B^0 \rightarrow D^{(*)-}\pi^+$ and be consistent with both being electrons or both being muons. To account for energy loss due to bremsstrahlung, the four-momenta of photons with lab-frame energy in [75, 1000] MeV detected within 50 mrad of the initial direction of an electron are added to

the electron's four-momentum. Each $J/\psi \rightarrow e^+e^-$ candidate must have a mass in [2.90, 3.14] GeV; each $J/\psi \rightarrow \mu^+\mu^-$ candidate must have a mass in [3.00, 3.14] GeV. The resolutions at masses above and below the known J/ψ mass are 8.0 MeV and 9.0 MeV for electron pairs and 6.3 MeV and 8.3 MeV for muon pairs.

We reconstruct K_S^0 candidates via $K_S^0 \rightarrow \pi^+\pi^-$. The pions must have polar angles within the CDC. Each K_S^0 candidate must have a mass in the range [0.45, 0.55] GeV, a successful vertex fit, and a decay vertex displaced from the IR by at least five units of the displacement's uncertainty. The reconstructed K_S^0 mass resolution is 2.0 MeV.

We fit the trajectories and momenta of B^0 decay products with TREEFIT, constraining the B^0 to originate from the IR and the J/ψ to have its known mass [37]. Each B^0 candidate must have M_{bc} greater than 5.27 GeV and ΔE in $[-0.10, 0.25]$ GeV. The B_{tag} vertex position is determined as described for $B_{\text{sig}}^0 \rightarrow D^{(*)-}\pi^+$ above. We require R_2 be less than 0.4 to remove $q\bar{q}$ background. After applying all selection requirements, the average number of candidates per event is 1.01. All candidates are retained for further analysis.

To validate our analysis, we also measure S and C for $B^0 \rightarrow J/\psi K^*(892)^0$, for which we expect $S = 0$, as this decay mode is flavor-specific, and $C = 0$ as with $B^0 \rightarrow J/\psi K_S^0$. Hereafter, $K^*(892)^0$ is written as K^{*0} . We reconstruct K^{*0} candidates via $K^{*0} \rightarrow K^+\pi^-$, requiring the positively charged particle be consistent with a K^+ and the negatively charged particle be consistent with a π^- . Each K^{*0} candidate must have a mass in [0.8, 1.0] GeV, corresponding to approximately four times the K^{*0} natural width [37]. All selection criteria on J/ψ and B^0 candidates are the same as for $B^0 \rightarrow J/\psi K_S^0$, except that the B^0 must have ΔE in a reduced range, $[-0.10, 0.10]$ GeV, to reject background from $B^+ \rightarrow J/\psi K^+$ with a π^- from B_{tag} reconstructed as part of B_{sig} .

We perform extended unbinned likelihood fits to the ΔE distributions to determine signal and background yields and shapes that we use to statistically isolate the signal Δt distributions using $sWeight$. We model the signal components as double-sided Crystal-Ball functions with tail parameters fixed to values determined from fits to simulated data and peak values and widths freely determined by the fits to data. We model the background components taking into account both $B\bar{B}$ and $q\bar{q}$, as exponential functions, whose parameters are freely determined by the fits to data.

Figure 7 shows the ΔE distributions and the fit results. The best-fit results agree well with the data. For $B^0 \rightarrow J/\psi K_S^0$, the signal yield is 6390 ± 90 and the background yield is 570 ± 40 . For $B^0 \rightarrow J/\psi K^{*0}$, the signal yield is 12660 ± 130 and the background yield is 1900 ± 70 .

We determine S and C by performing a simultaneous fit to the background-subtracted Δt distributions in 14 subsets defined by the 7 r intervals and 2 flavors of B_{tag} . To take into account detection and tagging asymmetries,

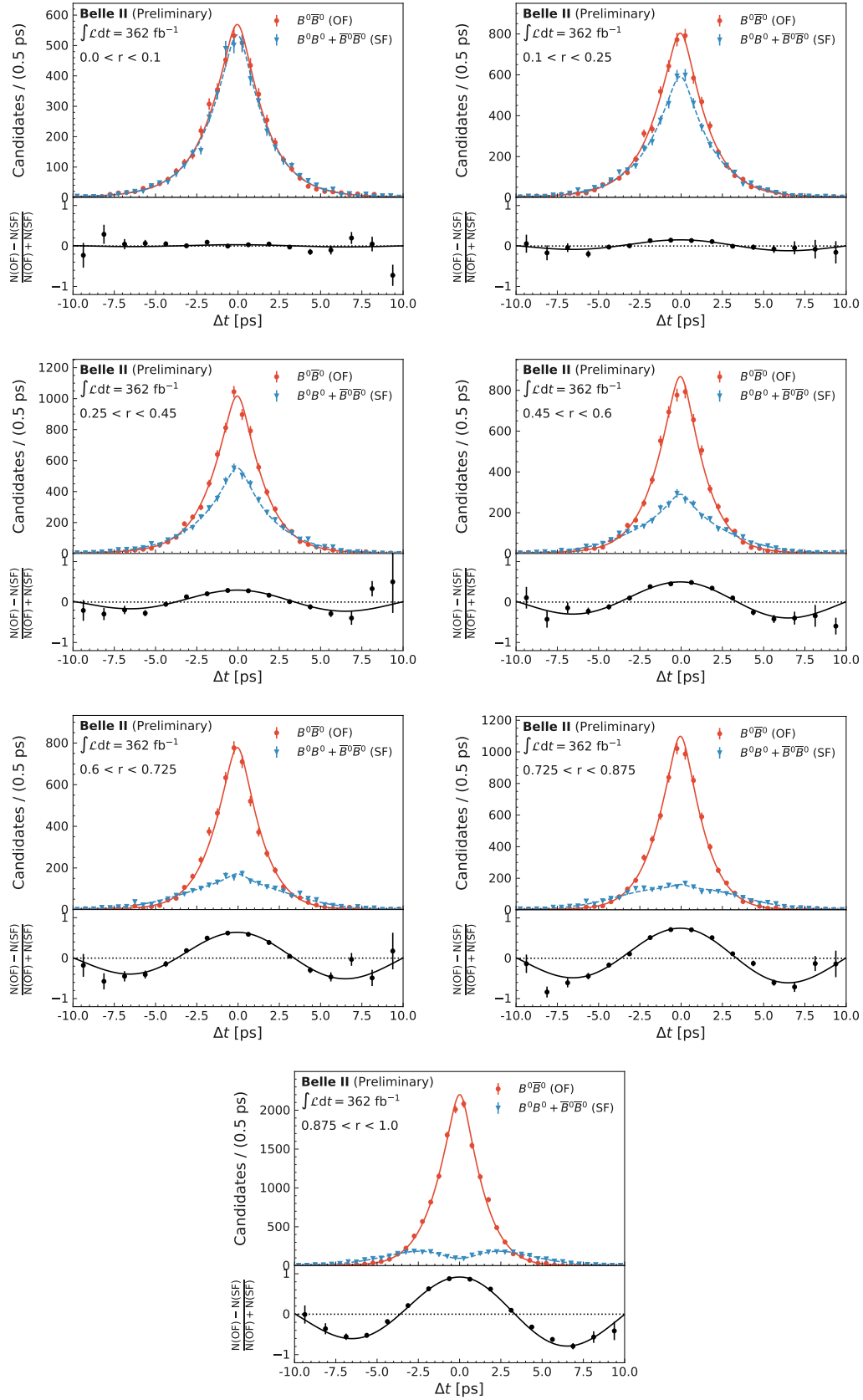


Figure 4. Background-subtracted Δt distributions of $B^0 \rightarrow D^{(*)-} \pi^+$ reconstructed in data in each of the seven r intervals (points) and the best-fit functions for opposite- and like-flavor B pairs with the corresponding asymmetries.

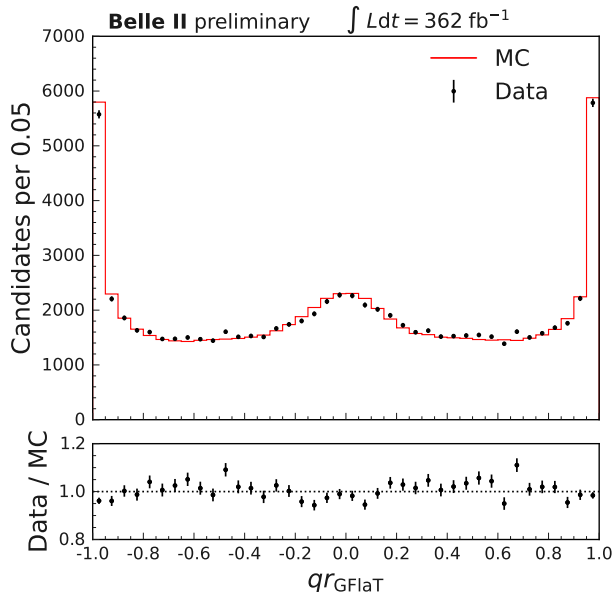


Figure 5. Distributions of qr_{GFlaT} for $B^0 \rightarrow D^{(*)-}\pi^+$ in background-subtracted data and correctly reconstructed simulated events normalized to the data signal yield.

we modify equation (1),

$$P(\Delta t, q_{\text{tag}}) = \frac{e^{-|\Delta t|/\tau}}{4\tau} \left\{ 1 + q_{\text{tag}} [a_{\text{tag}}(1 - 2\bar{w}) - \Delta w] + q_{\text{tag}} (1 - 2\bar{w} + q_{\text{tag}} a_{\text{tag}} - a_{\text{tag}} \Delta w) \times [S \sin(\Delta m_d \Delta t) - C \cos(\Delta m_d \Delta t)] \right\}. \quad (7)$$

To account for resolution and bias in determining Δt , we use the resolution function of the $B^0 \rightarrow D^{(*)-}\pi^+$ decays without the outlier component, which shows no impact on the results. The a_{tag} , \bar{w} , Δw , and resolution-function parameters are fixed to the values determined from the study of $B^0 \rightarrow D^{(*)-}\pi^+$, so that the only parameters left free to vary in the Δt fit are S and C . Figure 8 shows the background-subtracted Δt distributions (combining all r intervals) and the result of the fits. For $B^0 \rightarrow J/\psi K_S^0$, $S = (0.724 \pm 0.035)$ and $C = (-0.035 \pm 0.026)$. The statistical correlation between S and C is 0.32. For $B^0 \rightarrow J/\psi K^{*0}$, $S = (-0.018 \pm 0.026)$ and $C = (0.008 \pm 0.019)$; as expected, both are consistent with zero. The uncertainties are statistical only.

Additionally, we fit the $B^0 \rightarrow J/\psi K_S^0$ candidates without distinguishing between B_{tag} and \bar{B}_{tag} , therefore removing the ability to observe $\bar{C}P$ violation, with τ free. This checks for potential problems in the modeling of the resolution function, which would likely result in τ being biased from its expected value. We measure the B^0 lifetime to be (1.514 ± 0.022) ps, which agrees with the

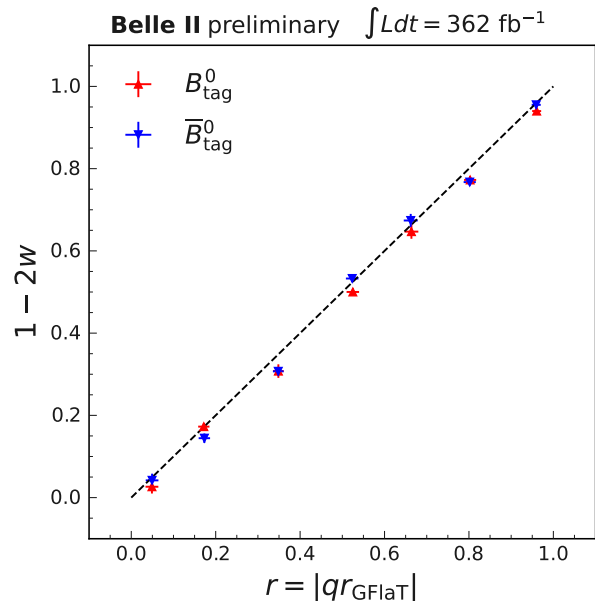


Figure 6. Dilution factors $1 - 2w$ of $B^0 \rightarrow D^{(*)-}\pi^+$ as functions of their GFlaT predictions, r for B_{tag}^0 , $1 - 2\bar{w} - \Delta w$, and \bar{B}_{tag}^0 , $1 - 2\bar{w} + \Delta w$; the dashed line shows $r = 1 - 2w$.

current world average [37]. The uncertainty is statistical only.

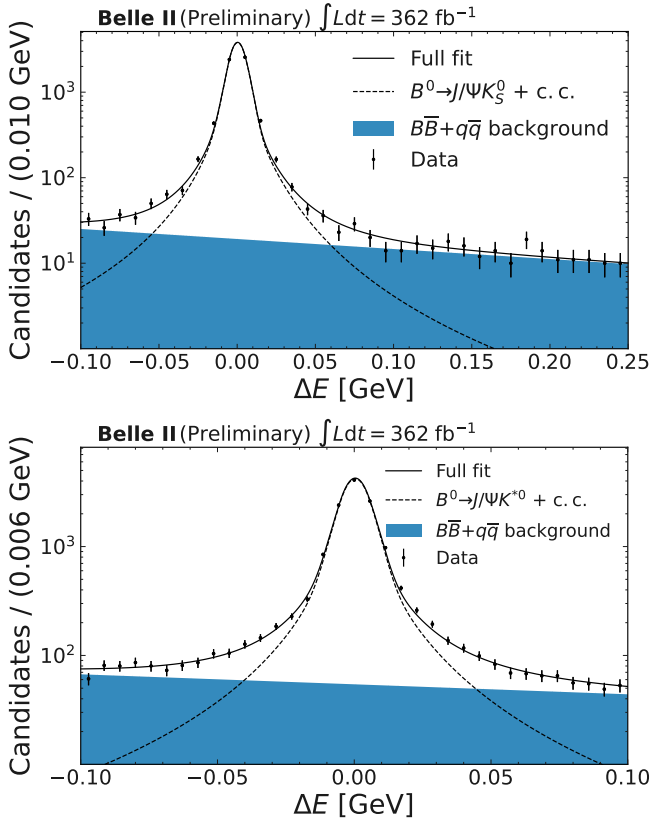
Table I lists the statistical and systematic uncertainties on ε_{tag} for $B^0 \rightarrow D^{(*)-}\pi^+$ and S and C for $B^0 \rightarrow J/\psi K_S^0$. Statistical uncertainties are computed by bootstrapping [46], resampling the $B^0 \rightarrow D^{(*)-}\pi^+$ and $B^0 \rightarrow J/\psi K_S^0$ data 1000 times each. The statistical uncertainties are larger than the sum in quadrature of all the individual systematic uncertainties.

Uncertainties on the alignment of the tracking system of Belle II detector [47], the shape and location of the IR, and the e^+e^- beam energy propagate to uncertainties on Δt , resulting in potential changes to ε_{tag} , S , and C . We determine ε_{tag} , S , and C from simulated events reconstructed assuming four detector misalignment scenarios and take their changes, added in quadrature, as systematic uncertainties. Both the IR and beam energy are determined from $e^+e^- \rightarrow \mu^+\mu^-$ events in 30-minute intervals. We determine ε_{tag} , S , and C with the parameters of the IR and beam energy varied by their uncertainties and take the shifts as systematic uncertainties.

Uncertainties on ΔE -fit component shapes propagate to uncertainties on the background-subtracted Δt distributions, resulting in potential changes to ε_{tag} , S , and C . We fit using various models and take any resulting shifts, added in quadrature, as systematic uncertainties. For the fit to $B^0 \rightarrow D^{(*)-}\pi^+$ data, these models are inclusion of an additional Gaussian function to model a small peaking background from $B\bar{B}$ events, variation of the fixed ratio of $B\bar{B}$ events to $B^0 \rightarrow D^{(*)-}\pi^+$ events by $\pm 20\%$, and the

Table I. Systematic and statistical uncertainties on ε_{tag} for $B^0 \rightarrow D^{(*)-} \pi^+$ and, S and C for $B^0 \rightarrow J/\psi K_S^0$.

Source	ε_{tag} [%]	S	C
Detector alignment	0.08	0.005	0.003
Interaction region	0.16	0.002	0.002
Beam energy	0.03	< 0.001	0.001
ΔE -fit background model	0.11	0.001	0.001
ΔE -fit signal model	0.08	0.003	0.006
$sWeight$ background subtraction	0.24	0.001	0.001
Fixed resolution-function parameters	0.07	0.004	0.004
τ and Δm_d	0.06	0.001	< 0.001
$\sigma_{\Delta t}$ binning	0.04	< 0.001	< 0.001
Δt -fit bias	0.09	0.002	0.005
CP violation in B_{tag} decay		0.011	0.006
$B^0 \rightarrow D^{(*)-} \pi^+$ sample size		0.004	0.007
Total systematic uncertainty	0.36	0.014	0.013
Statistical uncertainty	0.43	0.035	0.026

Figure 7. Distributions of ΔE for $B^0 \rightarrow J/\psi K_S^0$ (top) and $B^0 \rightarrow J/\psi K^{*0}$ (bottom) and the best-fit functions.

freeing of the ratio of $B^0 \rightarrow D^{(*)-} K^+$ to $B^0 \rightarrow D^{(*)-} \pi^+$ events. Variations to the background models in the fits to $B^0 \rightarrow J/\psi K_S^0$ data have negligible impact. For the signal components, we varied fixed parameters within their uncertainties one by one.

The process of subtracting the backgrounds using $sWeight$ is itself a source of uncertainty. For $B^0 \rightarrow$

$J/\psi K_S^0$, it is accounted for in the Δt -fit bias discussed below. We account for the uncertainty in the background subtraction in $B^0 \rightarrow D^{(*)-} \pi^+$ by determining ε_{tag} , S , and C replacing the Δt distributions with those from 1 ab^{-1} of simulated $B^0 \rightarrow D^{(*)-} \pi^+$ data that either contain signal events or signal and background events with background subtraction using $sWeight$, and take the differences as systematic uncertainties. This is the dominant systematic uncertainty on ε_{tag} .

Uncertainties on Δt -fit shape parameters directly propagate to changes to ε_{tag} , S , and C . We repeat the fits with fixed resolution-function parameters freed one at a time and take the resulting changes to ε_{tag} , S , and C , added in quadrature, as systematic uncertainties. We also repeat the fits with τ and Δm_d varied within their known uncertainties [37] and take the resulting changes, added in quadrature, as systematic uncertainties. Finally, we repeat the fits with the numbers of bins for the $\sigma_{\Delta t}$ histogrammed probability density functions varied between 200 and 1000 and take the largest changes as systematic uncertainties.

The Δt fits have biases that we determine from fits to simulated data sets equivalent in size to the real data, 20 such sets for $B^0 \rightarrow D^{(*)-} \pi^+$ and 290 for $B^0 \rightarrow J/\psi K_S^0$. We take the quadratic sum of the biases and their uncertainties as systematic uncertainties.

Equation (7) does not account for CP violation in B_{tag} decays [48]. This yields a systematic uncertainty determined in Ref. [3], which is the dominant systematic uncertainty on S . We propagate the statistical uncertainties on GFLaT's parameters and resolution-function parameters, arising from the $B^0 \rightarrow D^{(*)-} \pi^+$ sample size, to uncertainties on S and C by repeating the fits for each $B^0 \rightarrow D^{(*)-} \pi^+$ bootstrap sample.

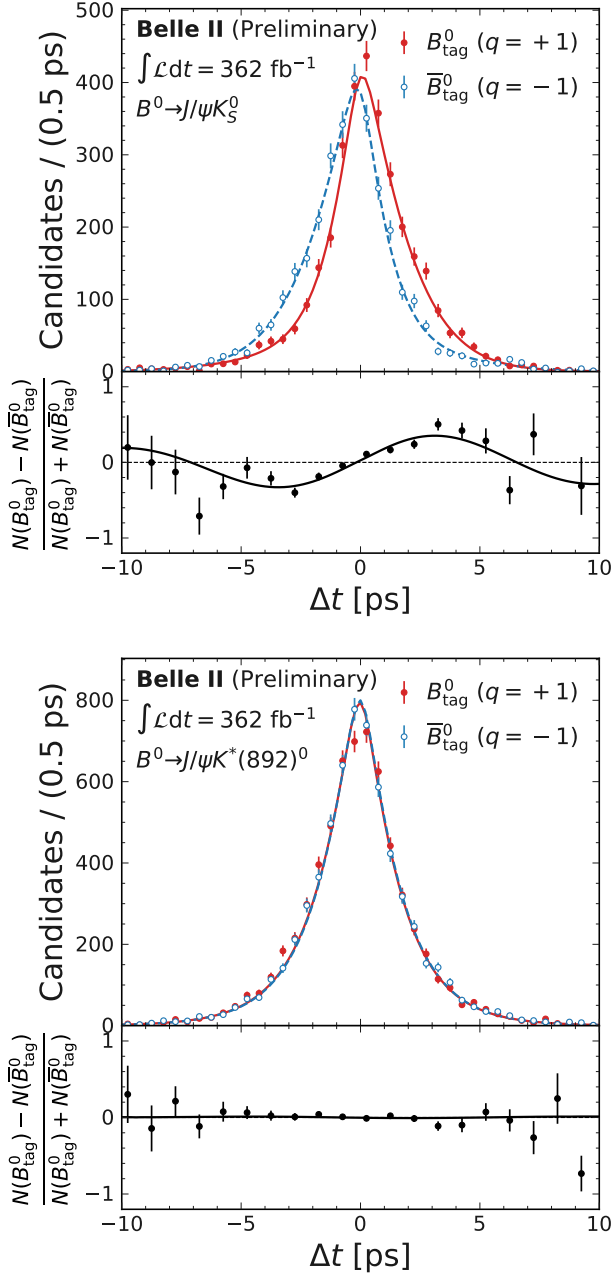


Figure 8. Background-subtracted Δt distributions for $B^0 \rightarrow J/\psi K_S^0$ (top) and $B^0 \rightarrow J/\psi K^{*0}$ (bottom) in the full r range (points) and the best-fit function (lines) for opposite- and like-flavor B pairs and the corresponding asymmetries.

VI. SUMMARY

We report on a new B flavor tagger, GFlaT, for Belle II that uses a graph-neural-network to account for the correlated information among the decay products of the tag-side B . We calibrate it using flavor-specific hadronic B decays reconstructed in a $(362 \pm 2) \text{ fb}^{-1}$ sample of Belle II

data and determine an effective tagging efficiency of

$$\varepsilon_{\text{tag}} = (37.40 \pm 0.43 \pm 0.36)\%, \quad (8)$$

where the first uncertainty is statistical and the second is systematic. For comparison, using the same data, we determine $\varepsilon_{\text{tag}} = (31.68 \pm 0.45)\%$ for the Belle II category-based flavor tagger.⁴ The GFlaT algorithm thus has an 18% better effective tagging efficiency.

We demonstrate GFlaT by measuring S and C for $B^0 \rightarrow J/\psi K_S^0$,

$$S = 0.724 \pm 0.035 \pm 0.014, \quad (9)$$

$$C = -0.035 \pm 0.026 \pm 0.013, \quad (10)$$

with a statistical correlation between S and C of 0.32, which agree with previous measurements [2–4, 37]. The statistical uncertainties are 8% and 7% smaller, respectively, than they would be if measured using the category-based flavor tagger, as expected given GFlaT’s higher effective tagging efficiency. From S , we calculate $\phi_1 = (23.2 \pm 1.5 \pm 0.6)^\circ$.⁵

ACKNOWLEDGEMENTS

This work, based on data collected using the Belle II detector, which was built and commissioned prior to March 2019, was supported by Higher Education and Science Committee of the Republic of Armenia Grant No. 23LCG-1C011; Australian Research Council and Research Grants No. DP200101792, No. DP210101900, No. DP210102831, No. DE220100462, No. LE210100098, and No. LE230100085; Austrian Federal Ministry of Education, Science and Research, Austrian Science Fund No. P 31361-N36 and No. J4625-N, and Horizon 2020 ERC Starting Grant No. 947006 “InterLeptons”; Natural Sciences and Engineering Research Council of Canada, Compute Canada and CANARIE; National Key R&D Program of China under Contract No. 2022YFA1601903, National Natural Science Foundation of China and Research Grants No. 11575017, No. 11761141009, No. 11705209, No. 11975076, No. 12135005, No. 12150004, No. 12161141008, and No. 12175041, and Shandong Provincial Natural Science Foundation Project ZR2022JQ02; the Czech Science Foundation Grant No. 22-18469S; European Research Council, Seventh Framework PIEF-GA-2013-622527, Horizon 2020 ERC-Advanced Grants No. 267104 and No. 884719, Horizon 2020 ERC-Consolidator

⁴ Systematic uncertainties were not explicitly computed for the category-based flavor tagger, as they are expected to be very similar to and fully correlated with those from GFlaT.

⁵ The other solution $\pi/2 - \phi_1$ is excluded from independent measurements [49]

Grant No. 819127, Horizon 2020 Marie Skłodowska-Curie Grant Agreement No. 700525 “NIOBE” and No. 101026516, and Horizon 2020 Marie Skłodowska-Curie RISE project JENNIFER2 Grant Agreement No. 822070 (European grants); L’Institut National de Physique Nucléaire et de Physique des Particules (IN2P3) du CNRS and L’Agence Nationale de la Recherche (ANR) under grant ANR-21-CE31-0009 (France); BMBF, DFG, HGF, MPG, and AvH Foundation (Germany); Department of Atomic Energy under Project Identification No. RTI 4002, Department of Science and Technology, and UPES SEED funding programs No. UPES/R&D-SEED-INFRA/17052023/01 and No. UPES/R&D-SOE/20062022/06 (India); Israel Science Foundation Grant No. 2476/17, U.S.-Israel Binational Science Foundation Grant No. 2016113, and Israel Ministry of Science Grant No. 3-16543; Istituto Nazionale di Fisica Nucleare and the Research Grants BELLE2; Japan Society for the Promotion of Science, Grant-in-Aid for Scientific Research Grants No. 16H03968, No. 16H03993, No. 16H06492, No. 16K05323, No. 17H01133, No. 17H05405, No. 18K03621, No. 18H03710, No. 18H05226, No. 19H00682, No. 20H05850, No. 20H05858, No. 22H00144, No. 22K14056, No. 22K21347, No. 23H05433, No. 26220706, and No. 26400255, the National Institute of Informatics, and Science Information NETwork 5 (SINET5), and the Ministry of Education, Culture, Sports, Science, and Technology (MEXT) of Japan; National Research Foundation (NRF) of Korea Grants No. 2016R1D1A1B02012900, No. 2018R1A2B3003643, No. 2018R1A6A1A06024970, No. 2019R1I1A3A01058933, No. 2021R1A6A1A-03043957, No. 2021R1F1A1060423, No. 2021R1F1A-1064008, No. 2022R1A2C1003993, and No. RS-2022-00197659, Radiation Science Research Institute, Foreign Large-Size Research Facility Application Supporting project, the Global Science Experimental Data Hub Center of the Korea Institute of Science and Technology Information and KREONET/GLORIAD; Universiti Malaya RU grant, Akademi Sains Malaysia, and Ministry of Education Malaysia; Frontiers of Science Program Contracts No. FOINS-296, No. CB-221329, No. CB-236394, No. CB-254409, and No. CB-180023, and SEP-CINVESTAV Research Grant No. 237 (Mexico); the Polish Ministry of Science and Higher Education and the National Science Center; the Ministry of Science and Higher Education of the Russian Federation and the HSE University Basic Research Program, Moscow; University of Tabuk Research Grants No. S-0256-1438 and No. S-0280-1439 (Saudi Arabia); Slovenian Research Agency and Research Grants No. J1-9124 and No. P1-0135; Agencia Estatal de Investigacion, Spain Grant No. RYC2020-029875-I and Generalitat Valenciana, Spain Grant No. CIDEGENT/2018/020; National Science and Technology Council, and Ministry of Education (Taiwan); Thailand Center of Excellence in Physics; TUBITAK ULAKBIM (Turkey); National Research

Foundation of Ukraine, Project No. 2020.02/0257, and Ministry of Education and Science of Ukraine; the U.S. National Science Foundation and Research Grants No. PHY-1913789 and No. PHY-2111604, and the U.S. Department of Energy and Research Awards No. DE-AC06-76RLO1830, No. DE-SC0007983, No. DE-SC0009824, No. DE-SC0009973, No. DE-SC0010007, No. DE-SC0010073, No. DE-SC0010118, No. DE-SC0010504, No. DE-SC0011784, No. DE-SC0012704, No. DE-SC0019230, No. DE-SC0021274, No. DE-SC0021616, No. DE-SC0022350, No. DE-SC0023470; and the Vietnam Academy of Science and Technology (VAST) under Grants No. NVCC.05.12/22-23 and No. DL0000.02/24-25.

These acknowledgements are not to be interpreted as an endorsement of any statement made by any of our institutes, funding agencies, governments, or their representatives.

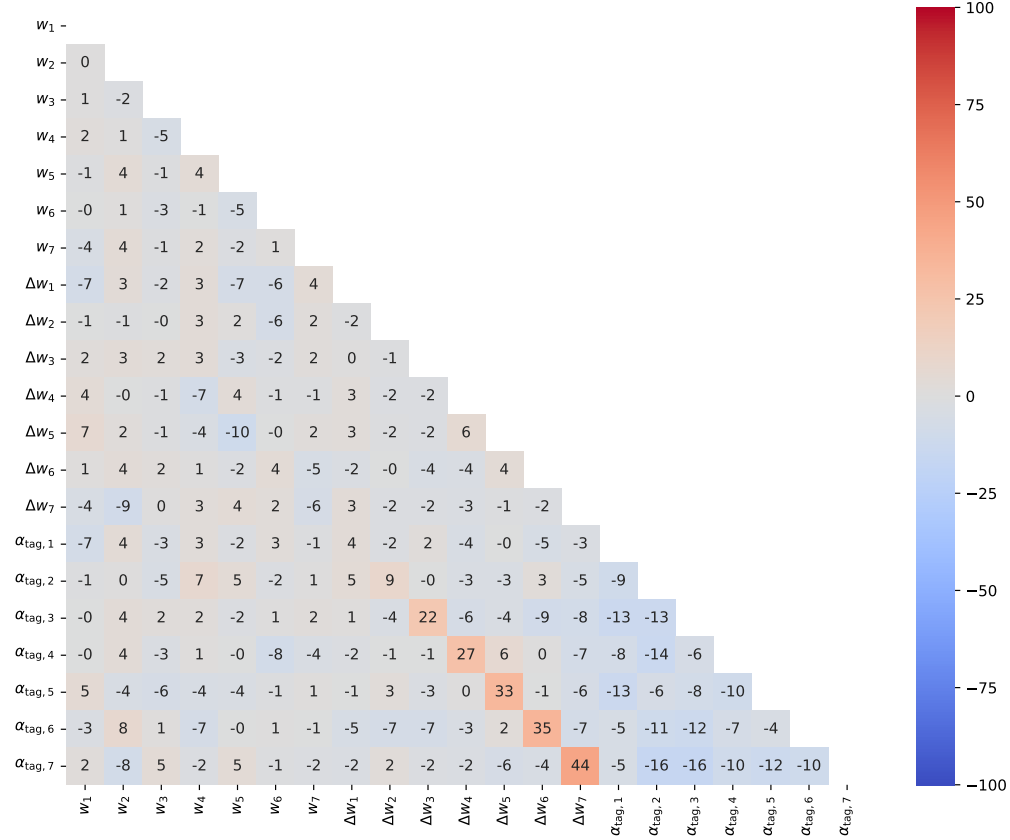
We thank the SuperKEKB team for delivering high-luminosity collisions; the KEK cryogenics group for the efficient operation of the detector solenoid magnet; the KEK computer group and the NII for on-site computing support and SINET6 network support; and the raw-data centers at BNL, DESY, GridKa, IN2P3, INFN, and the University of Victoria for off-site computing support.

Appendix A: GF1aT parameters

Table II lists a_{tag} , \bar{w} , and Δw for each r bin, measured from events with $B^0 \rightarrow D^{(*)-}\pi^+$. The sources of systematic uncertainty are the same as listed in Table I for ε_{tag} . Figure 9 shows the statistical correlation coefficients between the parameters that are used as inputs to estimate systematic uncertainties for S and C .

Table II. GFLaT parameters in each r bin.

r bin	$a_{\text{tag}} [\%]$	$\bar{w} [\%]$	$\Delta w [\%]$
[0.0, 0.1]	$-1.72 \pm 1.47 \pm 1.32$	$48.29 \pm 0.78 \pm 0.75$	$0.78 \pm 1.16 \pm 0.71$
[0.1, 0.25]	$-0.94 \pm 1.36 \pm 1.45$	$42.07 \pm 0.72 \pm 0.32$	$-1.41 \pm 1.06 \pm 0.92$
[0.25, 0.45]	$-0.28 \pm 1.28 \pm 1.46$	$34.63 \pm 0.61 \pm 0.61$	$-0.04 \pm 0.97 \pm 1.28$
[0.45, 0.6]	$3.21 \pm 1.44 \pm 1.50$	$24.17 \pm 0.68 \pm 0.36$	$1.64 \pm 1.13 \pm 0.52$
[0.6, 0.725]	$1.17 \pm 1.58 \pm 1.47$	$16.98 \pm 0.68 \pm 0.92$	$1.36 \pm 1.15 \pm 0.72$
[0.725, 0.875]	$-1.13 \pm 1.30 \pm 1.55$	$11.50 \pm 0.53 \pm 0.39$	$-0.26 \pm 0.92 \pm 0.71$
[0.875, 1.0]	$-0.18 \pm 0.91 \pm 1.30$	$2.62 \pm 0.27 \pm 0.14$	$0.75 \pm 0.53 \pm 0.60$

Figure 9. Correlation coefficients, in 10^{-2} , between the GFLaT parameters. Subscripts indicate r bins.

- [1] M. Kobayashi and T. Maskawa, *CP* violation in the renormalizable theory of weak interaction, *Prog. Theor. Phys.* **49**, 652 (1973).
- [2] B. Aubert *et al.* (BaBar collaboration), Measurement of Time-Dependent *CP* Asymmetry in $B^0 \rightarrow c\bar{c}K^{(*)0}$ Decays, *Phys. Rev. D* **79**, 072009 (2009), arXiv:0902.1708 [hep-ex].
- [3] I. Adachi *et al.* (Belle collaboration), Precise measurement of the *CP* violation parameter $\sin 2\phi_1$ in $B^0 \rightarrow (c\bar{c})K^0$ decays, *Phys. Rev. Lett.* **108**, 171802 (2012), arXiv:1201.4643 [hep-ex].
- [4] R. Aaij *et al.* (LHCb collaboration), Measurement of *CP* violation in $B^0 \rightarrow \psi(\rightarrow \ell^+\ell^-)K_S^0(\rightarrow \pi^+\pi^-)$ decays, *Phys. Rev. Lett.* **132**, 021801 (2024), arXiv:2309.09728 [hep-ex].
- [5] J. P. Lees *et al.* (BaBar collaboration), Measurement of *CP* Asymmetries and Branching Fractions in Charmless Two-Body *B*-Meson Decays to Pions and Kaons, *Phys. Rev. D* **87**, 052009 (2013), arXiv:1206.3525 [hep-ex].
- [6] I. Adachi *et al.* (Belle collaboration), Measurement of the *CP* violation parameters in $B^0 \rightarrow \pi^+\pi^-$ decays, *Phys. Rev. D* **88**, 092003 (2013), arXiv:1302.0551 [hep-ex].
- [7] R. Aaij *et al.* (LHCb collaboration), Observation of *CP* violation in two-body $B_{(s)}^0$ -meson decays to charged pions and kaons, *JHEP* **03**, 075, arXiv:2012.05319 [hep-ex].

- [8] B. Aubert *et al.* (BaBar collaboration), A Study of $B^0 \rightarrow \rho^+ \rho^-$ Decays and Constraints on the CKM Angle α , *Phys. Rev. D* **76**, 052007 (2007), arXiv:0705.2157 [hep-ex].
- [9] P. Vanhoefer *et al.* (Belle collaboration), Study of $B^0 \rightarrow \rho^+ \rho^-$ decays and implications for the CKM angle ϕ_2 , *Phys. Rev. D* **93**, 032010 (2016), [Addendum: *Phys.Rev.D* 94, 099903 (2016)], arXiv:1510.01245 [hep-ex].
- [10] B. Aubert *et al.* (BaBar collaboration), Measurement of the Branching Fraction, Polarization, and CP Asymmetries in $B^0 \rightarrow \rho^0 \rho^0$ Decay, and Implications for the CKM Angle α , *Phys. Rev. D* **78**, 071104 (2008), arXiv:0807.4977 [hep-ex].
- [11] I. I. Y. Bigi and A. I. Sanda, Notes on the Observability of CP Violations in B Decays, *Nucl. Phys. B* **193**, 85 (1981).
- [12] P. Oddone, Detector considerations, *UCLA Linear-Collider BB Factory Concep. Design: Proceedings*, eConf **C870126**, 423 (1987).
- [13] T. Abe *et al.* (Belle II collaboration), Belle II technical design report, arXiv:1011.0352 [physics.ins-det] (2010).
- [14] F. Abudinén *et al.* (Belle II collaboration), B-flavor tagging at Belle II, *Eur. Phys. J. C* **82**, 283 (2022), arXiv:2110.00790 [hep-ex].
- [15] F. Abudinén *et al.* (Belle II collaboration), Measurement of the B^0 lifetime and flavor-oscillation frequency using hadronic decays reconstructed in 2019–2021 Belle II data, *Phys. Rev. D* **107**, L091102 (2023), arXiv:2302.12791 [hep-ex].
- [16] I. Adachi *et al.* (Belle II collaboration), Measurement of decay-time-dependent CP violation in $B^0 \rightarrow J/\psi K_S^0$ decays using 2019-2021 Belle II data, arXiv:2302.12898 [hep-ex] (2023).
- [17] H. Kakuno *et al.* (Belle collaboration), Neutral B flavor tagging for the measurement of mixing induced CP violation at Belle, *Nucl. Instrum. Meth. A* **533**, 516 (2004), arXiv:hep-ex/0403022.
- [18] Y. Wang, Y. Sun, Z. Liu, S. E. Sarma, M. M. Bronstein, and J. M. Solomon, Dynamic graph cnn for learning on point clouds, *ACM Trans. Graph.* **38**, 10.1145/3326362 (2019).
- [19] K. De Bruyn and R. Fleischer, A Roadmap to Control Penguin Effects in $B_d^0 \rightarrow J/\psi K_S^0$ and $B_s^0 \rightarrow J/\psi \phi$, *JHEP* **03**, 145, arXiv:1412.6834 [hep-ph].
- [20] M. Z. Barel, K. De Bruyn, R. Fleischer, and E. Malami, In pursuit of new physics with $B_d^0 \rightarrow J/\psi K^0$ and $B_s^0 \rightarrow J/\psi \phi$ decays at the high-precision Frontier, *J. Phys. G* **48**, 065002 (2021), arXiv:2010.14423 [hep-ph].
- [21] M. Z. Barel, K. De Bruyn, R. Fleischer, and E. Malami, Penguin Effects in $B_d^0 \rightarrow J/\psi K_S^0$ and $B_s^0 \rightarrow J/\psi \phi$, *PoS CKM2021*, 111 (2023), arXiv:2203.14652 [hep-ph].
- [22] I. Dunietz, Clean CKM information from $B_d(t) \rightarrow D^{*\mp} \pi^\pm$, *Phys. Lett. B* **427**, 179 (1998), arXiv:hep-ph/9712401.
- [23] A. Das *et al.* (Belle collaboration), Measurements of Branching Fractions for $B^0 \rightarrow D_s^+ \pi^-$ and $\bar{B}^0 \rightarrow D_s^+ K^-$, *Phys. Rev. D* **82**, 051103 (2010), arXiv:1007.4619 [hep-ex].
- [24] B. Aubert *et al.* (BaBar collaboration), Measurement of the Branching Fractions of the Rare Decays $B^0 \rightarrow D_s^{(*)+} \pi^-$, $B^0 \rightarrow D_s^{(*)+} \rho^-$, and $B^0 \rightarrow D_s^{(*)-} K^{(*)+}$, *Phys. Rev. D* **78**, 032005 (2008), arXiv:0803.4296 [hep-ex].
- [25] K. Akai, K. Furukawa, and H. Koiso, SuperKEKB collider, *Nucl. Instrum. Meth.* **A907**, 188 (2018), arXiv:1809.01958 [physics.acc-ph].
- [26] K. Adamczyk *et al.* (Belle II SVD collaboration), The design, construction, operation and performance of the Belle II silicon vertex detector, *JINST* **17** (11), P11042, arXiv:2201.09824 [physics.ins-det].
- [27] D. Kotchetkov *et al.*, Front-end electronic readout system for the Belle II imaging Time-Of-Propagation detector, *Nucl. Instrum. Meth. A* **941**, 162342 (2019), arXiv:1804.10782 [physics.ins-det].
- [28] D. J. Lange, The EvtGen particle decay simulation package, *Proceedings, 7th International Conference on B physics at hadron machines (BEAUTY 2000): Maagan, Israel, September 13-18, 2000*, *Nucl. Instrum. Meth.* **A462**, 152 (2001).
- [29] T. Sjöstrand, S. Ask, J. R. Christiansen, R. Corke, N. Desai, P. Ilten, S. Mrenna, S. Prestel, C. O. Rasmussen, and P. Z. Skands, An Introduction to PYTHIA 8.2, *Comput. Phys. Commun.* **191**, 159 (2015), arXiv:1410.3012 [hep-ph].
- [30] S. Jadach, B. F. L. Ward, and Z. Wąs, The precision Monte Carlo event generator KK for two-fermion final states in e^+e^- collisions, *Comput. Phys. Commun.* **130**, 260 (2000), arXiv:hep-ph/9912214 [hep-ph].
- [31] S. Agostinelli *et al.* (GEANT4 collaboration), GEANT4: A simulation toolkit, *Nucl. Instrum. Meth.* **A506**, 250 (2003).
- [32] P. M. Lewis *et al.*, First Measurements of Beam Backgrounds at SuperKEKB, *Nucl. Instrum. Meth. A* **914**, 69 (2019), arXiv:1802.01366 [physics.ins-det].
- [33] T. Kuhr, C. Pulvermacher, M. Ritter, T. Hauth, and N. Braun (Belle II Framework Software Group), The Belle II Core Software, *Comput. Softw. Big Sci.* **3**, 1 (2019), arXiv:1809.04299 [physics.comp-ph].
- [34] Belle II collaboration, Belle II Analysis Software Framework (basf2), <https://doi.org/10.5281/zenodo.5574115>.
- [35] H. Qu and L. Gouskos, ParticleNet: Jet Tagging via Particle Clouds, *Phys. Rev. D* **101**, 056019 (2020), arXiv:1902.08570 [hep-ph].
- [36] J. Hu, L. Shen, and G. Sun, Squeeze-and-excitation networks, *CoRR* **abs/1709.01507** (2017), 1709.01507.
- [37] R. L. Workman *et al.* (Particle Data Group), Review of Particle Physics, *PTEP* **2022**, 083C01 (2022).
- [38] D. P. Kingma and J. Ba, Adam: A method for stochastic optimization, arXiv:1412.6980 [cs.LG] (2017).
- [39] L. N. Smith, A disciplined approach to neural network hyper-parameters: Part 1 – learning rate, batch size, momentum, and weight decay, arXiv e-prints , arXiv:1803.09820 (2018), arXiv:1803.09820 [cs.LG].
- [40] M. Pivk and F. R. Le Diberder, sPlot: A statistical tool to unfold data distributions, *Nucl. Instrum. Meth.* **A555**, 356 (2005), arXiv:physics/0402083 [physics.data-an].
- [41] H. Dembinski, M. Kenzie, C. Langenbruch, and M. Schmelling, Custom Orthogonal Weight functions (COWs) for event classification, *Nucl. Instrum. Meth. A* **1040**, 167270 (2022), arXiv:2112.04574 [stat.ME].
- [42] J.-F. Krohn *et al.* (Belle II Analysis Software Group), Global decay chain vertex fitting at Belle II, *Nucl. Instrum. Meth.* **A976**, 164269 (2020), arXiv:1901.11198 [hep-ex].

- [43] W. Waltenberger, W. Mitaroff, F. Moser, B. Pflugfelder, and H. V. Riedel, The RAVE/VERTIGO vertex reconstruction toolkit and framework, *J. Phys. Conf. Ser.* **119**, 032037 (2008).
- [44] G. C. Fox and S. Wolfram, Observables for the Analysis of Event Shapes in e^+e^- Annihilation and Other Processes, *Phys. Rev. Lett.* **41**, 1581 (1978).
- [45] T. Skwarnicki, *A study of the radiative CASCADE transitions between the Upsilon-Prime and Upsilon resonances*, Ph.D. thesis, Cracow, INP (1986).
- [46] B. Efron, Bootstrap Methods: Another Look at the Jackknife, *Annals Statist.* **7**, 1 (1979).
- [47] T. Bilka *et al.*, Alignment for the first precision measurements at Belle II, *EPJ Web Conf.* **245**, 02023 (2020).
- [48] O. Long, M. Baak, R. N. Cahn, and D. P. Kirkby, Impact of tag side interference on time dependent CP asymmetry measurements using coherent $B^0\bar{B}^0$ pairs, *Phys. Rev. D* **68**, 034010 (2003), arXiv:hep-ex/0303030.
- [49] A. Abdesselam *et al.* (BaBar, Belle), First Observation of CP Violation in $\bar{B}^0 \rightarrow D_{CP}^{(*)}h^0$ Decays by a Combined Time-Dependent Analysis of BABAR and Belle Data, *Phys. Rev. Lett.* **115**, 121604 (2015), arXiv:1505.04147 [hep-ex].

EUROPEAN ORGANISATION FOR NUCLEAR RESEARCH (CERN)



CERN-EP-2024-051
February 28, 2024

K_S^0 meson production in inelastic $p+p$ interactions at 31, 40 and 80 GeV/c beam momentum measured by NA61/SHINE at the CERN SPS

The NA61/SHINE Collaboration

Measurements of K_S^0 meson production via its $\pi^+\pi^-$ decay mode in inelastic $p+p$ interactions at incident projectile momenta of 31, 40 and 80 GeV/c ($\sqrt{s_{NN}} = 7.7, 8.8$ and 12.3 GeV, respectively) are presented. The data were recorded by the NA61/SHINE spectrometer at the CERN Super Proton Synchrotron. Double-differential distributions were obtained in transverse momentum and rapidity. The mean multiplicities of K_S^0 mesons were determined to be $(5.95 \pm 0.19(stat) \pm 0.22(sys)) \times 10^{-2}$ at 31 GeV/c, $(7.61 \pm 0.13(stat) \pm 0.31(sys)) \times 10^{-2}$ at 40 GeV/c and $(11.58 \pm 0.12(stat) \pm 0.37(sys)) \times 10^{-2}$ at 80 GeV/c. The results on K_S^0 production are compared with model calculations (EPOS1.99, SMASH 2.0 and PHSD) as well as with published data from other experiments.

Contents

1	Introduction	4
2	Experimental setup	5
3	Analysis	6
3.1	Data sets	6
3.2	Analysis method	7
3.3	Event selection	7
3.4	Track and topology selection	7
3.5	Raw K_S^0 yields	8
3.6	Correction factors	9
3.7	Statistical uncertainties	11
3.8	Systematic uncertainties	12
3.9	Mean lifetime measurements	14
4	Results	15
4.1	Transverse momentum spectra	15
4.2	Rapidity distributions and mean multiplicities	15
5	Comparison with published world data and model calculations	18
6	Summary	23

N. Abgrall²⁹, H. Adhikary¹³, P. Adrich¹⁵, K.K. Allison²⁶, N. Amin⁵, E.V. Andronov²², T. Antičić³, I.-C. Arsene¹², M. Bajda¹⁶, Y. Balkova¹⁸, M. Baszczyk¹⁷, D. Battaglia²⁵, A. Bazgir¹³, S. Bhosale¹⁴, M. Bielewicz¹⁵, A. Blondel⁴, M. Bogomilov², Y. Bondar¹³, N. Bostan²⁵, A. Brandin²², A. Bravar²⁹, W. Bryliński²¹, J. Brzychczyk¹⁶, M. Buryakov²², A.F. Camino²⁸, M. Čirković²³, M. Csanád⁸, J. Cybowska²¹, T. Czopowicz¹³, C. Dalmazzone⁴, N. Davis¹⁴, A. Dmitriev²², P. von Doetinchem²⁷, W. Dominik¹⁹, P. Dorosz¹⁷, J. Dumarchez⁴, R. Engel⁵, G.A. Feofilov²², L. Fields²⁵, Z. Fodor^{7,20}, M. Friend⁹, M. Gaździcki^{13,6}, O. Golosov²², V. Golovatyuk²², M. Golubeva²², K. Grebieszko²¹, F. Guber²², A. Haesler²⁹, S.N. Igoekin²², S. Ilieva², A. Ivashkin²², A. Izvestnyy²², K. Kadija³, N. Kargin²², N. Karpushkin²², E. Kashirin²², M. Kielbowicz¹⁴, V.A. Kireyeu²², H. Kitagawa¹⁰, R. Kolesnikov²², D. Kolev², A. Korzenev²⁹, Y. Koshio¹⁰, V.N. Kovalenko²², S. Kowalski¹⁸, B. Kozłowski²¹, A. Krasnoperov²², W. Kucewicz¹⁷, M. Kuchowicz²⁰, M. Kuich¹⁹, A. Kurepin²², A. László⁷, M. Lewicki²⁰, G. Lykasov²², V.V. Lyubushkin²², M. Maćkowiak-Pawłowska²¹, Z. Majka¹⁶, A. Makhnev²², B. Maksiak¹⁵, A.I. Malakhov²², A. Marcinek¹⁴, A.D. Marino²⁶, H.-J. Mathes⁵, T. Matulewicz¹⁹, V. Matveev²², G.L. Melkumov²², A. Merzlaya¹², Ł. Mik¹⁷, A. Morawiec¹⁶, S. Morozov²², Y. Nagai⁸, T. Nakadaira⁹, M. Naskręt²⁰, S. Nishimori⁹, V. Ozvenchuk¹⁴, O. Panova¹³, V. Paolone²⁸, O. Petukhov²², I. Pidhurskyi^{13,6}, R. Płaneta¹⁶, P. Podlaski¹⁹, B.A. Popov^{22,4}, B. Pórfy^{7,8}, M. Posiadła-Zezula¹⁹, D.S. Prokhorova²², D. Pszczel¹⁵, S. Puławski¹⁸, J. Puzović^{23†}, R. Renfordt¹⁸, L. Ren²⁶, V.Z. Reyna Ortiz¹³, D. Röhrich¹¹, E. Rondio¹⁵, M. Roth⁵, Ł. Rozpłochowski¹⁴, B.T. Rumberger²⁶, M. Romyantsev²², A. Rustamov^{1,6}, M. Rybczynski¹³, A. Rybicki¹⁴, K. Sakashita⁹, K. Schmidt¹⁸, A.Yu. Seryakov²², P. Seyboth¹³, U.A. Shah¹³, Y. Shiraishi¹⁰, A. Shukla²⁷, M. Słodkowski²¹, P. Staszal¹⁶, G. Stefanek¹³, J. Stepianiak¹⁵, M. Strikhanov²², H. Ströbele⁶, T. Šušar³, L. Swiderski¹⁵, J. Szewiński¹⁵, R. Szukiewicz²⁰, A. Taranenko²², A. Tefelska²¹, D. Tefelski²¹, V. Tereshchenko²², A. Toia⁶, R. Tsenov², L. Turko²⁰, T.S. Tveter¹², M. Unger⁵, M. Urbaniak¹⁸, F.F. Valiev²², D. Veberič⁵, V.V. Vechernin²², V. Volkov²², A. Wickremasinghe²⁴, K. Wójcik¹⁸, O. Wyszynski¹³, A. Zaitsev²², E.D. Zimmerman²⁶, A. Zviagina²², and R. Zwaska²⁴

[†] *deceased*

The NA61/SHINE Collaboration

¹ National Nuclear Research Center, Baku, Azerbaijan

² Faculty of Physics, University of Sofia, Sofia, Bulgaria

³ Ruđer Bošković Institute, Zagreb, Croatia

⁴ LPNHE, University of Paris VI and VII, Paris, France

⁵ Karlsruhe Institute of Technology, Karlsruhe, Germany

⁶ University of Frankfurt, Frankfurt, Germany

⁷ Wigner Research Centre for Physics, Budapest, Hungary

⁸ Eötvös Loránd University, Budapest, Hungary

⁹ Institute for Particle and Nuclear Studies, Tsukuba, Japan

¹⁰ Okayama University, Japan

¹¹ University of Bergen, Bergen, Norway

¹² University of Oslo, Oslo, Norway

¹³ Jan Kochanowski University, Kielce, Poland

¹⁴ Institute of Nuclear Physics, Polish Academy of Sciences, Cracow, Poland

¹⁵ National Centre for Nuclear Research, Warsaw, Poland

¹⁶ Jagiellonian University, Cracow, Poland

¹⁷ AGH - University of Science and Technology, Cracow, Poland

¹⁸ University of Silesia, Katowice, Poland

- ¹⁹ University of Warsaw, Warsaw, Poland
²⁰ University of Wrocław, Wrocław, Poland
²¹ Warsaw University of Technology, Warsaw, Poland
²² Affiliated with an institution covered by a cooperation agreement with CERN
²³ University of Belgrade, Belgrade, Serbia
²⁴ Fermilab, Batavia, USA
²⁵ University of Notre Dame, Notre Dame, USA
²⁶ University of Colorado, Boulder, USA
²⁷ University of Hawaii at Manoa, Honolulu, USA
²⁸ University of Pittsburgh, Pittsburgh, USA
²⁹ University of Geneva, Geneva, Switzerland¹

1 Introduction

The measurement of hadron production in proton-proton interactions plays a key role in understanding nucleus-nucleus collisions. In particular, it can shed some light on the creation process of Quark Gluon Plasma (QGP), on its properties, and on the characterization of the phase transition between hadronic matter and the QGP. One of the key signals of QGP creation is the enhanced production of s and \bar{s} quarks, carried mostly by kaons [1]. The experimental results indicate that the creation of the QGP starts in nucleus-nucleus collisions at centre of mass energies from 10 to 20 GeV [2], which is the realm of the NA61/SHINE experiment at CERN. To explore this region systematically NA61/SHINE studies observables indicative of the QGP by a two-dimensional scan in collision energy and nuclear mass number of the colliding nuclei. Since 2009, NA61/SHINE has collected data on $p+p$, $p+\text{Pb}$, $\text{Be}+\text{Be}$, $\text{Ar}+\text{Sc}$, $\text{Xe}+\text{La}$ and $\text{Pb}+\text{Pb}$ interactions in the beam momentum range from 13A to 158A GeV/c [3]. Results on neutral kaon spectra in $p+p$ at 158 GeV/c can be found in Ref. [4], while results on charged kaon spectra in $p+p$ at 31, 40, 80 and 158 GeV/c can be found in Ref. [5]. In this paper, we present the results of K_S^0 production in $p+p$ collisions at 31, 40, and 80 GeV/c, which will be compared with K_S^0 production at 158 GeV/c [4] and constitute the baseline for the interpretation of results obtained in heavier systems collected with the NA61/SHINE detector. Thanks to high statistics, large acceptance, and good momentum resolution the results presented here have, in general, higher precision than previously published measurements at SPS energies.

The paper is organised as follows. In Sec. 2, details of the NA61/SHINE detector system are presented. Section 3 is devoted to describing the analysis method. The results are shown in Sec. 4. In Sec. 5, they are compared to published world data and model calculations. Section 6 closes the paper with a summary and outlook.

The following units, variables and definitions are used in this paper. The particle mass and energy are presented in GeV, while particle momentum is shown in GeV/c. The particle rapidity y is calculated in the proton-proton collision center of mass system (cms), $y = 0.5 \cdot \ln[(E + cp_L)/(E - cp_L)]$, where E and p_L are the particle energy and longitudinal momentum. The transverse component of the momentum is denoted as p_T . The momentum in the laboratory frame is denoted p_{lab} and the collision energy per nucleon pair in the centre of mass by $\sqrt{s_{NN}}$.

¹ No longer affiliated with the NA61/SHINE collaboration

2 Experimental setup

The NA61/SHINE collaboration uses a large acceptance spectrometer located in the CERN North Area. The schematic layout of the NA61/SHINE detector during the $p+p$ data-taking is shown in Fig. 1. A detailed description of the experimental setup can be found in Ref. [6], while the details on the simulation in describing the detector performance across different kinematic variables as well as its inefficiencies can be found in Ref. [7].

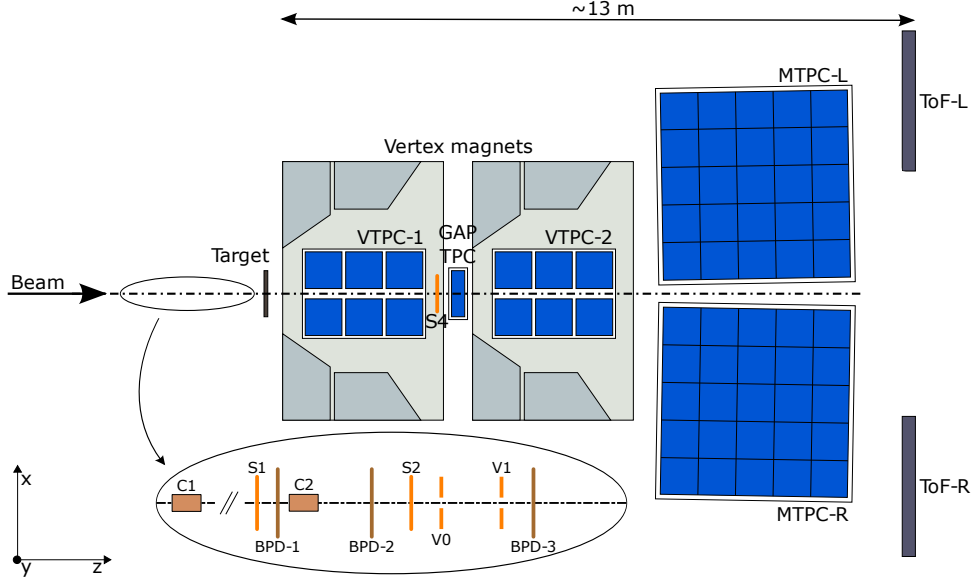


Figure 1: (Color online) The schematic layout of the NA61/SHINE experiment at the CERN SPS during $p+p$ data taking (horizontal cut, not to scale). The beam and trigger detector configuration used for data taking in 2009 is shown in the inset (see Refs. [6–8] for a detailed description). The chosen coordinate system is drawn on the lower left: its origin lies in the middle of the VTPC-2 on the beam axis.

The main components of the NA61/SHINE spectrometer are four large-volume Time Projection Chambers (TPCs). Two of them, the vertex TPCs (VTPC-1 and VTPC-2), are located in the magnetic fields of two super-conducting dipole magnets with a maximum combined bending power of 9 Tm, which corresponds to about 1.5 T and 1.1 T in the upstream and downstream magnets, respectively. This field strength was used for data taking at 158 GeV/c and scaled down in proportion to the lower beam momenta to obtain similar $y - p_T$ acceptance at all beam momenta. Two large main TPCs (MTPC-L and MTPC-R) and two walls of pixel Time-of-Flight (ToF-L/R) detectors are positioned symmetrically to the beamline downstream of the magnets. A GAP-TPC (GTPC) is placed between VTPC-1 and VTPC-2 directly on the beamline. It closes the gap between the beam axis and the sensitive volumes of the other TPCs. The TPCs are filled with Ar and CO₂ gas mixtures in proportions 90:10 for the VTPCs and 95:5 for the MTPCs. Particle identification in the TPCs is based on measurements of the specific energy loss (dE/dx) in the chamber gas. Typical values for the momentum resolution are $\sigma(p)/p^2 = 7 \times 10^{-4} (\text{GeV}/c)^{-1}$ for low-momentum tracks measured only in VTPC-1 ($p \leq 8 \text{ GeV}/c$) and $3 \times 10^{-3} (\text{GeV}/c)^{-1}$ for tracks traversing the full detector up to and including the MTPCs ($p \geq 8 \text{ GeV}/c$).

Secondary beams of positively charged hadrons at momenta of 31, 40 and 80 GeV/c were used to collect the data for the analysis presented in this paper. These beams were produced from a 400 GeV/c proton

beam extracted from the SPS in a slow extraction mode with a flat-top of 10 seconds. The beam momentum and intensity were adjusted by appropriate settings of the H2 beam line magnet currents and collimators. Protons from the secondary hadron beam are identified by two Cherenkov counters, C1 [9] and C2 (THC). The C1 counter, using a coincidence of six out of the eight photomultipliers placed radially along the Cherenkov ring, provides identification of protons, while the THC, operated at a pressure lower than the proton threshold, is used in anti-coincidence in the trigger logic. A selection based on the signals from the Cherenkov counters allowed to identify beam protons with a purity of about 99%, as demonstrated by a measurement of the specific ionization energy loss dE/dx of the beam particles by bending the 31 GeV/c beam into the TPCs using the full magnetic field strength [10]. A set of scintillation (S1, S2 and V0, V1) and beam position detectors (BPDs) upstream of the spectrometer provide timing reference, and position measurements of incoming beam particles. The trigger scintillation counter S4 placed downstream of the target has a diameter of 2 cm. It is used to trigger the readout whenever an incoming beam particle, which is registered upstream of the target, does not hit S4, which indicates that an interaction occurred in the target area.

A cylindrical target vessel of 20.29 cm length and 3 cm diameter was placed upstream of the entrance window of VTPC-1 (center of the target is at $z = -581$ cm in the NA61/SHINE coordinate system). The vessel was filled with liquid hydrogen corresponding to an interaction length of 2.8%. The liquid hydrogen had a density of approximately 0.07 g/cm³. Data were taken with the vessel filled with liquid hydrogen and being empty. Here, only events recorded with the target vessel filled with hydrogen were analyzed.

3 Analysis

3.1 Data sets

The presented results on K_S^0 production in inelastic $p+p$ interactions at $p_{beam} = 31, 40$ and 80 GeV/c are based on data recorded in 2009. Table 1 summarizes basic information about data sets used in the analysis, the number of events selected by interaction trigger and the number of events after analysis cuts. The event numbers recorded with the interaction trigger were 2.85M, 4.37M and 3.80M, respectively. The drop in event numbers after cuts is caused mainly by BPD reconstruction inefficiencies and off-target interactions accepted by the trigger logic.

p_{beam} (GeV/c)	$\sqrt{s_{NN}}$ (GeV)	Number of recorded events with interaction trigger	Number of events after selection criteria
31	7.7	2.85×10^6	0.83×10^6
40	8.8	4.37×10^6	1.24×10^6
80	12.3	3.80×10^6	1.48×10^6

Table 1: Data sets used for the analysis of K_S^0 production. The beam momentum is denoted by p_{beam} , whereas $\sqrt{s_{NN}}$ is the energy available in the center-of-mass system for the nucleon pair. The events selection criteria are described in Sec. 3.3.

3.2 Analysis method

The event vertex and the produced particle tracks were reconstructed using the standard NA61/SHINE software. Details of the track and vertex reconstruction procedures can be found in Refs. [7, 8, 11]. Detector parameters were optimized by a data-based calibration procedure, which also considered their time dependence; for details, see Refs. [5, 12]. The following section enumerates the criteria for selecting events, tracks and the K_S^0 decay topology. Then, the simulation-based correction procedure is described and used to quantify the losses due to reconstruction inefficiencies and limited geometrical acceptance.

3.3 Event selection

The criteria for selection of inelastic $p+p$ interactions are the following:

- (i) An event was accepted by the trigger logic (see Refs. [7, 8]) as an interaction candidate event.
- (ii) No off-time beam particle was detected within a time window of $\pm 2 \mu\text{s}$ around the trigger particle.
- (iii) Beam particle trajectory was measured in at least three planes out of four of BPD-1 and BPD-2 and in both planes of BPD-3.
- (iv) The primary interaction vertex fit converged.
- (v) The z position of the interaction vertex (fitted using the beam trajectory and TPC tracks) not farther away than 9 cm from the center of the target vessel.
- (vi) Events with a single, well-measured, positively charged track with absolute momentum close to the beam momentum ($p > p_{beam} - 1 \text{ GeV}/c$) were rejected.

The background due to elastic interactions was removed via cuts (iv) and (vi). The contribution from off-target interactions was reduced by cut (v). The simulations corrected the losses of inelastic $p+p$ interactions due to the event selection procedure.

The numbers of events left after the selection criteria described in the text above are given in Table 1.

3.4 Track and topology selection

Neutral strange particles are detected and measured using their weak decay into charged particles. The K_S^0 decays into $\pi^+ + \pi^-$ with a branching ratio of 69.2% [13] are used here. The decay particles form the so-called V^0 topology. K_S^0 decay candidates (V^0 s) are obtained by pairing all positively with all negatively charged pion candidates. The tracks of the decay pions and the V^0 topology are subject to the following additional selection criteria:

- (i) For each candidate track, the minimum number of measured clusters in VTPC-1 and VTPC-2 must be 15.
- (ii) All pion tracks must have a measured specific energy loss (dE/dx) in the TPCs within $\pm 3\sigma$ around the nominal Bethe-Bloch value for charged pions. Here, σ represents the typical standard deviation of a Gaussian fitted to the dE/dx distribution of pions. Since only small variations of σ were observed for different bins and beam momenta, a constant value $\sigma = 0.052$ is used [14]. This selection criterion applies only to experimental data, not MC-simulated events (see below).

- (iii) The distance $|\Delta z|$ between the z-coordinates of the primary production and the K_S^0 decay vertices is required to lie in the rapidity dependent range: $|\Delta z| > e^{a+b \cdot y_{lab}}$, with y_{lab} the rapidity in the laboratory and a and b constants which amount to 1.91 and 0.99 for the $p_{beam} = 31$ GeV/c, 1.71 and 0.95 for $p_{beam} = 40$ GeV/c, and 1.85 and 0.90 for $p_{beam} = 80$ GeV/c data sets, respectively.
- (iv) The distance of closest approach (DCA) in the x and y directions of the straight line given by the K_S^0 momentum vector in the laboratory and the primary vertex must be smaller than 0.25 cm, with DCA given by $\sqrt{(b_x/2)^2 + b_y^2}$.
- (v) The cosine of the angle between the V^0 and π^+ momentum vectors in the K_S^0 rest frame has to be in the range: $-0.97 < \cos\Theta^* < 0.85$.

The quality of the aforementioned track and topology selection criteria is illustrated in Fig. 2. The population of K_S^0 decay candidates is shown as a function of the two Armenteros-Podolansky variables p_T^{Arm} and α^{Arm} [15] and after all track and topology selection criteria. The quantity p_T^{Arm} is the transverse momentum of the decay particles with respect to the direction of motion of the V^0 candidate and $\alpha^{Arm} = (p_L^+ - p_L^-)/(p_L^+ + p_L^-)$, where p_L^+ and p_L^- are the longitudinal momenta of the positively and negatively charged V^0 daughter particles, measured with respect to the V^0 's direction of motion. From the plots (see Fig. 2) one can see that contributions of Λ and $\bar{\Lambda}$ hyperons are removed by the topological selection criteria.

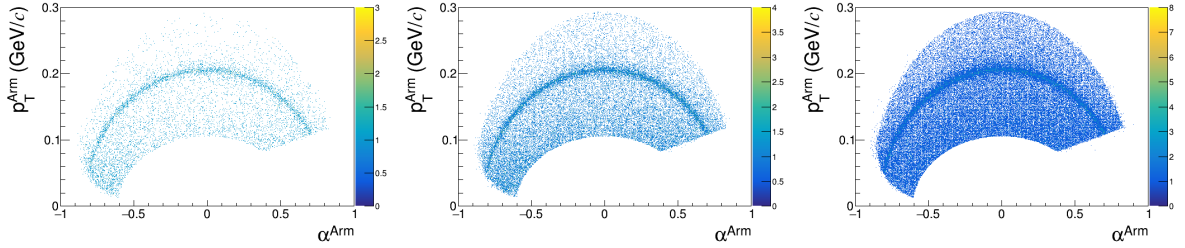


Figure 2: Armenteros-Podolanski plots of V^0 candidates after all track and topology selection criteria for $p_{beam} = 31, 40$ and 80 GeV/c from left to right. The boundaries on the plots' left and right sides result from using the $\cos\Theta^*$ cut, while the upper and lower boundaries are shaped by selecting a certain invariant mass range.

3.5 Raw K_S^0 yields

The double differential uncorrected yields of K_S^0 are determined by studying the invariant mass distributions of the accepted pion pairs in bins of rapidity and transverse momentum (examples are presented in Fig. 3). The K_S^0 decays will appear as a peak over a smooth combinatorial background. The K_S^0 yield was determined in each bin using a fit function that describes both the signal and the background. A Lorentzian function was used for the signal:

$$L(m) = A \frac{1}{\pi} \frac{\frac{1}{2}\Gamma}{(m - m_0)^2 + (\frac{1}{2}\Gamma)^2}, \quad (1)$$

where A is the normalization factor, Γ is the full width at half maximum of the signal peak, and m_0 is the mass parameter. The background contribution is described by a polynomial function of 2^{nd} order.

Figure 3 shows examples of $\pi^+\pi^-$ invariant mass distributions obtained from the $p_{beam} = 40$ GeV/c data set after all V^0 selection cuts for real data (*left*) and for simulated events (*right*).

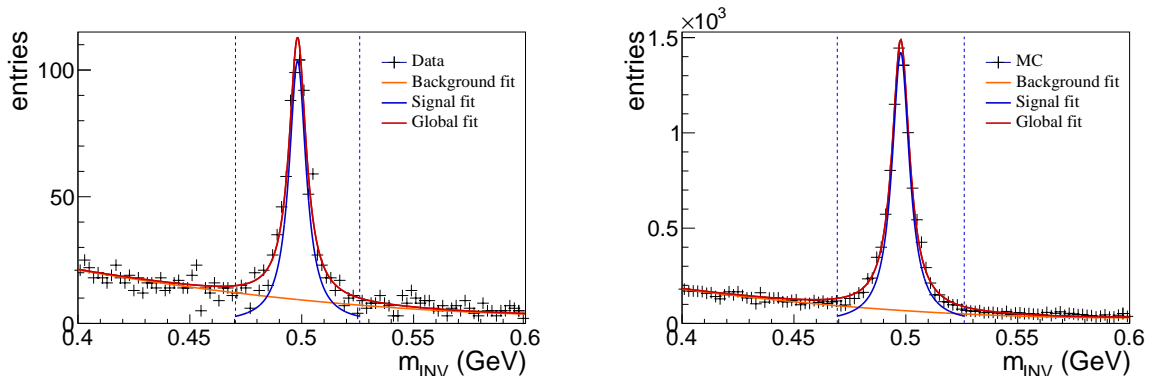


Figure 3: The invariant mass distribution of K_S^0 candidates for experimental data (*left*) and MC (*right*) for the $p_{beam} = 40$ GeV/c data set for $-0.25 \leq y < 0.25$ and $0.2 \leq p_T < 0.4$ after all selection criteria. The dashed-blue vertical lines indicate the regions where the K_S^0 signal was integrated. The signal data points are black, the fitted background is orange, the fitted signal is blue, and the total fit results are red. Mass resolutions obtained from the fits are: $\sigma = (0.00925 \pm 0.00064)$ GeV for the experimental data and $\sigma = (0.00946 \pm 0.00017)$ GeV for the MC.

The procedure of fitting the histograms proceeds in three steps. In the first step, the background outside the signal peak ($[0.475-0.525]$ GeV) is fitted with a polynomial of 2^{nd} order. This step is necessary to obtain starting values for the parameters of the background function. In the next step, a full invariant mass spectrum fit is performed with the sum of the Lorentzian and the background function. The initial parameter values for the background function are taken from the previous step, the mass parameter is fixed to the PDG value of $m_0 = 0.497614(24)$ GeV [13], and the width is allowed to vary between 0.005 and 0.03 GeV. Finally, in the last step, all parameters are free, and the fitting region is $[0.35-0.65]$ GeV. The orange and blue curves in Fig. 3 show the fitted polynomial background and the Lorentzian signal function. To minimize the sensitivity of the K_S^0 yield to the integration window, the uncorrected number of K_S^0 was calculated by subtracting bin-by-bin the fitted background (B) and summing the background-subtracted signal in the mass window $m_0 \pm 3\Gamma$ (dashed vertical lines), where m_0 is the fitted mass of the K_S^0 . Figure 3 shows that the simulation reproduces the central value of the K_S^0 mass distribution and its width agree with the data within uncertainties. The Γ parameter fitted to the simulation was used to calculate the signal from the simulation. Thus, a possible bias due to differences between the data and the simulation is reduced; see Sec. 3.8.

The uncorrected bin-by-bin K_S^0 multiplicities and their statistical uncertainties are shown in Fig. 4.

3.6 Correction factors

A correction for interactions of the incident protons with the target vessel is not needed, because the distributions of the primary vertex coordinates show no sign of such events after the event and track selection cuts. A detailed Monte Carlo simulation was performed to compute the corrections for losses due to the trigger bias, geometrical acceptance, reconstruction efficiency, and the selection criteria applied in the analysis. The correction factors are based on 20×10^6 inelastic $p+p$ events at each beam momenta

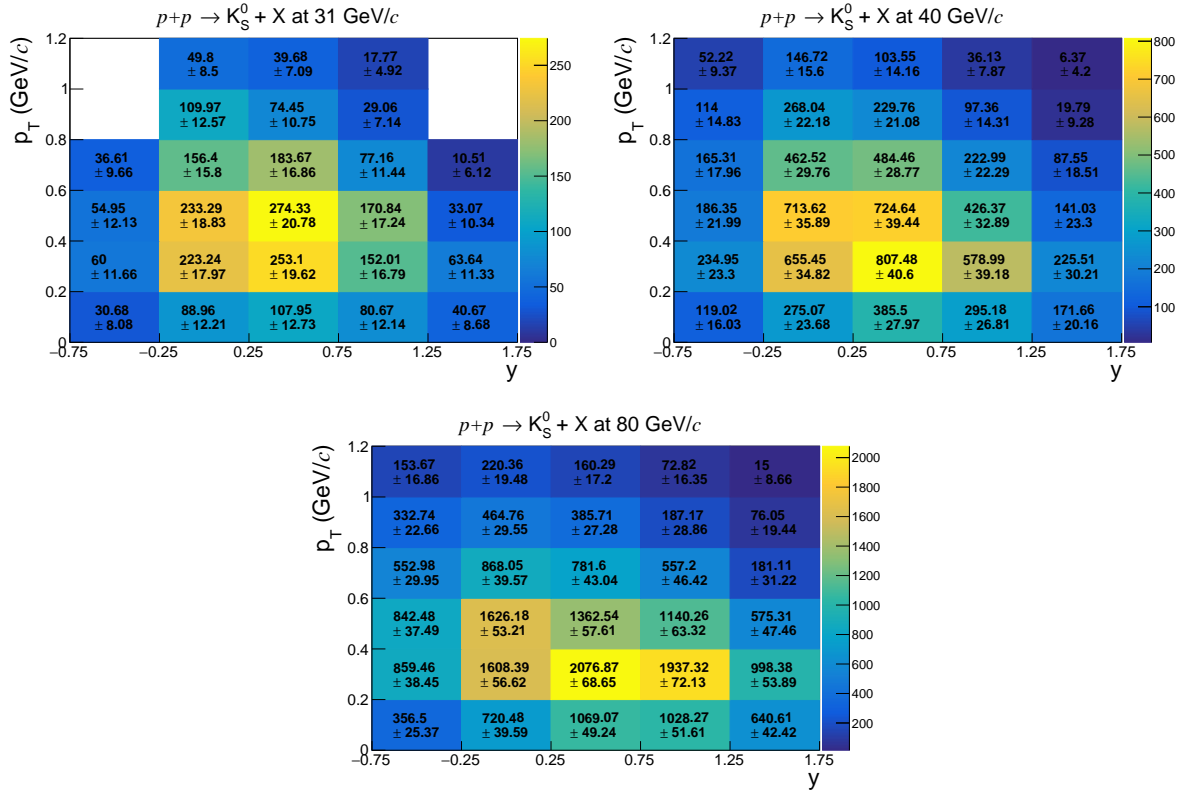


Figure 4: Uncorrected bin-by-bin multiplicities of K_S^0 with their statistical uncertainties for $p_{beam} = 31$ GeV/c (left), $p_{beam} = 40$ GeV/c (right) and $p_{beam} = 80$ GeV/c (bottom).

$p_{beam} = 31, 40$ and 80 GeV/c produced by the EPOS1.99 event generator [16, 17]. Particles in the generated events were tracked through the NA61/SHINE apparatus using the GEANT3 package [18]. The TPC response was simulated by dedicated software packages that account for known detector effects. The simulated events were reconstructed with the same software as the real events, and the same selection cuts were applied. However, dE/dx identification was replaced by matching reconstructed tracks to simulated ones. The branching ratio of K_S^0 decays is taken into account in the GEANT3 software package. For each y and p_T bin, the correction factor $c_{MC}(y, p_T)$ was calculated as:

$$c_{MC}(y, p_T) = \frac{n_{MC}^{gen}(y, p_T)}{N_{MC}^{gen}} \bigg/ \frac{n_{MC}^{acc}(y, p_T)}{N_{MC}^{acc}}, \quad (2)$$

where:

- $n_{MC}^{gen}(y, p_T)$ is the number of K_S^0 generated in a given (y, p_T) bin,
- $n_{MC}^{acc}(y, p_T)$ is the number of reconstructed K_S^0 in a given (y, p_T) bin.
- N_{MC}^{gen} is the number of generated inelastic $p+p$ interactions (20×10^6),
- N_{MC}^{acc} is the number of accepted $p+p$ events (about 13.5×10^6 for all three beam momenta).

The loss of the K_S^0 mesons due to the dE/dx cut is corrected with an additional factor:

$$c_{dE/dx} = \frac{1}{\varepsilon^2} = 1.005, \quad (3)$$

where $\varepsilon = 0.9973$ is the probability for the pions to be detected within $\pm 3\sigma$ around the nominal Bethe-Bloch value.

The double-differential yield of K_S^0 per inelastic event in bins of (y, p_T) is calculated as follows:

$$\frac{d^2n}{dydp_T}(y, p_T) = \frac{c_{dE/dx} \cdot c_{MC}(y, p_T)}{\Delta y \Delta p_T} \cdot \frac{n_{K_S^0}(y, p_T)}{N_{events}}, \quad (4)$$

where:

- $c_{dE/dx}$, $c_{MC}(y, p_T)$ are the correction factors described above,
- Δy and Δp_T are the bin widths,
- $n_{K_S^0}(y, p_T)$ is the uncorrected number of K_S^0 , obtained by the signal extraction procedure described in Sec. 3.5. The corresponding values are presented in Fig. 4,
- N_{events} is the number of events left in the sample after selection criteria.

3.7 Statistical uncertainties

The statistical uncertainties of the corrected double-differential yields (see Eq. 4) receive contributions from the statistical uncertainty of the correction factor $c_{MC}(y, p_T)$ and the statistical uncertainty of the uncorrected number of K_S^0 ($\Delta n_{K_S^0}(y, p_T)$). The statistical uncertainty of the former receives two contributions, the first, α , caused by the loss of inelastic interactions due to the event selection and the second, β , connected with the loss of K_S^0 candidates due to the V^0 selection:

$$c_{MC}(y, p_T) = \frac{n_{MC}^{gen}(y, p_T)}{N_{MC}^{gen}} \bigg/ \frac{n_{MC}^{acc}(y, p_T)}{N_{MC}^{acc}} = \frac{N_{MC}^{acc}}{N_{MC}^{gen}} \bigg/ \frac{n_{MC}^{acc}(y, p_T)}{n_{MC}^{gen}(y, p_T)} = \frac{\alpha}{\beta(y, p_T)}, \quad (5)$$

The error of α is calculated assuming a binomial distribution:

$$\Delta\alpha = \sqrt{\frac{\alpha(1-\alpha)}{N_{MC}^{gen}}}, \quad (6)$$

The error of β is calculated according to the formula:

$$\Delta\beta(y, p_T) = \sqrt{\left(\frac{\Delta n_{MC}^{acc}(y, p_T)}{n_{MC}^{gen}(y, p_T)}\right)^2 + \left(\frac{n_{MC}^{acc}(y, p_T) \cdot \Delta n_{MC}^{gen}(y, p_T)}{(n_{MC}^{gen}(y, p_T))^2}\right)^2}, \quad (7)$$

where $\Delta n_{MC}^{acc}(y, p_T) = \sqrt{S+B}$ see Sec. 3.5, and $\Delta n_{MC}^{gen}(y, p_T) = \sqrt{n_{MC}^{gen}(y, p_T)}$. The equation for $\Delta c_{MC}(y, p_T)$ can be written as:

$$\Delta c_{MC}(y, p_T) = \sqrt{\left(\frac{\Delta\alpha}{\beta}\right)^2 + \left(-\frac{\alpha \cdot \Delta\beta}{\beta^2}\right)^2}. \quad (8)$$

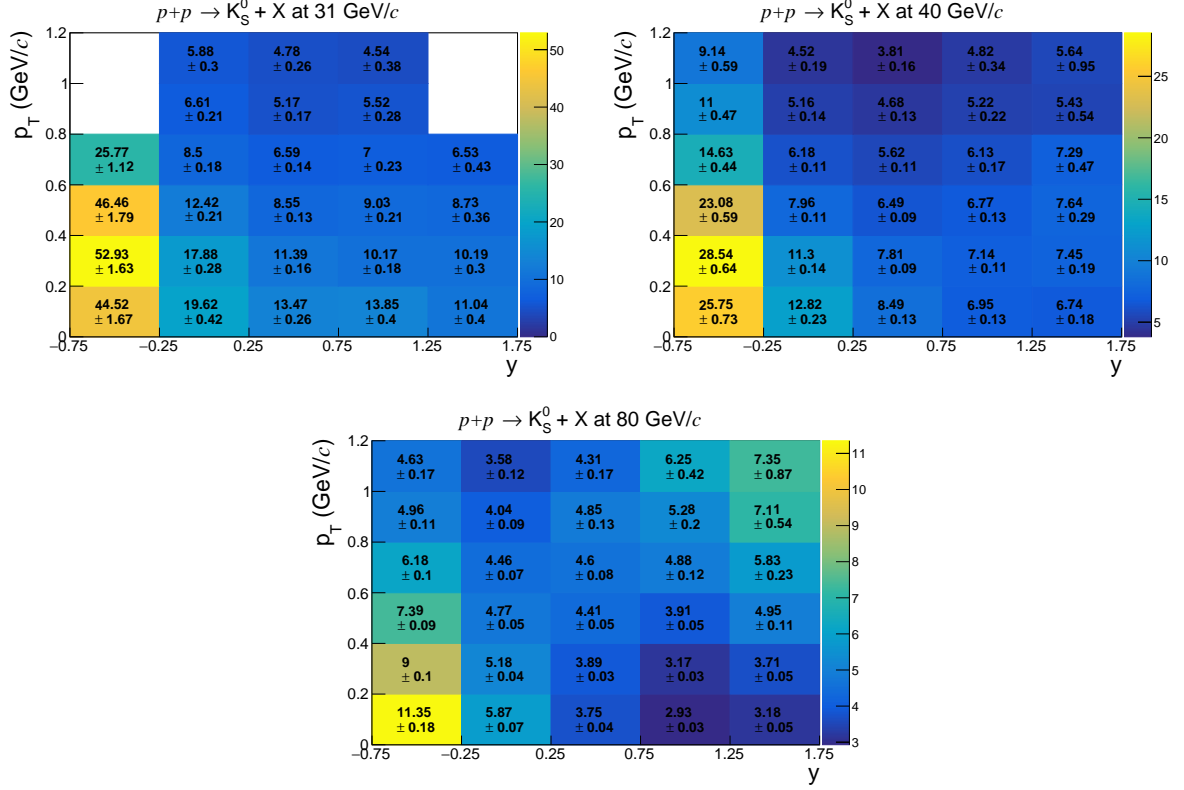


Figure 5: Monte-Carlo correction factors (see Eq. 2) with their statistical uncertainties (see Eq. 8) in each (y, p_T) bin for $p_{beam} = 31$ GeV/c (left), $p_{beam} = 40$ GeV/c (right) and $p_{beam} = 80$ GeV/c (bottom).

Finally, the statistical uncertainties $\Delta n_{K_S^0}(y, p_T)$ of the corrected number of K_S^0 are:

$$\Delta \frac{d^2n}{dy dp_T}(y, p_T) = \sqrt{\left(\frac{c_{dE/dx} \cdot c_{MC}(y, p_T)}{N_{events} \Delta y \Delta p_T}\right)^2 \Delta n_{K_S^0}^2(y, p_T) + \left(\frac{c_{dE/dx} \cdot n_{K_S^0}(y, p_T)}{N_{events} \Delta y \Delta p_T}\right)^2 \Delta c_{MC}^2(y, p_T)}. \quad (9)$$

3.8 Systematic uncertainties

Three possible contributions to the systematic uncertainties related to the event selection criteria, the track and V^0 selection criteria and the signal extraction procedure were considered.

- (i) The uncertainties related to the event selection criteria (see Sec. 3.3) were estimated by performing the analysis with the following changes:

- Simulations were done with and without the S4 trigger condition for all inelastic $p+p$ interactions. One-half of the difference between these two results was taken as the contribution to the systematic uncertainty, which amounts to up to 3%.
 - The allowed range of the vertex z position was changed from $-590 < z \text{ (cm)} < -572$ to $-588 < z \text{ (cm)} < -574$ and $-592 < z \text{ (cm)} < -570$. The uncertainty due to the variation of the selection window amounts to up to 4%.
- (ii) The uncertainties related to the track and V^0 selection criteria were estimated by performing the analysis with the following changes compared to the original values (see Sec. 3.4):
- the minimum required number of clusters in both VTTPCs for V^0 daughters was changed from 15 to 12 and 18, indicating a possible bias of up to 2%,
 - the standard dE/dx cut used for identification of V^0 daughters was changed from $\pm 3\sigma$ to $\pm 2.5\sigma$ and $\pm 3.5\sigma$ from the nominal Bethe-Bloch value indicating a possible bias of up to 3%,
 - the Δz cut was changed by varying the parameters a and b from 1.91 to 2.01 and 1.81 for parameter a and from 0.99 to 0.98 and 1.00 for parameter b for $p_{beam} = 31 \text{ GeV}/c$, from 1.71 to 1.91 and 1.51 for parameter a and from 0.95 to 0.93 and 0.97 for parameter b for $p_{beam} = 40 \text{ GeV}/c$ and from 1.85 to 2.05 and 1.65 for parameter a and from 0.90 to 0.88 and 0.92 for parameter b for $p_{beam} = 80 \text{ GeV}/c$, indicating a possible bias of up to 2%,
 - the allowed distance of closest approach of the K_S^0 trajectory to the primary vertex was varied from 0.25 to 0.20 and 0.30 cm, indicating a possible bias of up to 3%,
 - the $\cos\Theta^*$ range for accepted candidates was changed from $-0.97 < \cos\Theta^* < 0.85$ to $-0.99 < \cos\Theta^* < 0.87$ and $-0.95 < \cos\Theta^* < 0.83$ indicating a possible bias of up to 3%.
- (iii) The uncertainty due to the signal extraction procedure (see Sec. 3.5) was estimated by:
- changing the background fit function from a 2^{nd} order to a 3^{rd} order polynomial indicating a possible bias of up to 4%,
 - changing the invariant mass range over which the uncorrected number of K_S^0 was integrated from $m_0 \pm 3\Gamma$ to $m_0 \pm 2.5\Gamma$ and $m_0 \pm 3.5\Gamma$ indicating a possible bias of up to 2%,
 - calculating the uncorrected number of K_S^0 as the sum of entries after background fit subtraction instead of the integral of the Lorentzian signal function indicating a possible bias of up to 2%,
 - changing the region of the fit from $[0.35-0.65] \text{ GeV}/c^2$ to $[0.38-0.62] \text{ GeV}/c^2$ indicating a possible bias of up to 2%.

The maximum deviations are determined separately for each group of contributions to the systematic uncertainty. The systematic uncertainty was calculated as the square root of the sum of squares of the maximum deviations. This procedure was used to estimate systematic uncertainties of all final quantities presented in this paper: yields in (y, p_T) bins, inverse slope parameters of transverse momentum spectra, yields in rapidity bins, and mean multiplicities.

3.9 Mean lifetime measurements

The reliability of the K_S^0 reconstruction and the correction procedure was validated by studying the lifetime distribution of the analyzed K_S^0 . The lifetime ($c\tau$) of each identified K_S^0 was calculated from the V^0 path length and its velocity. The corrected number of K_S^0 was then determined in bins of $c\tau/c\tau_{PDG}$, and for the five rapidity bins of the $p_{beam} = 40$ GeV/c and 80 GeV/c data sets and in the whole rapidity range ($-0.75 < y < 1.75$) of the $p_{beam} = 31$ GeV/c data set (see Fig. 6). The straight lines in Fig. 6 represent the results of exponential fits, which provide mean lifetime values (normalized to the known PDG value [13]) as a function of rapidity. The thus determined mean lifetimes are shown in Fig. 7 as a function of rapidity. The measured mean K_S^0 lifetimes agree within uncertainties with the PDG value and thus confirm the quality of the analysis.

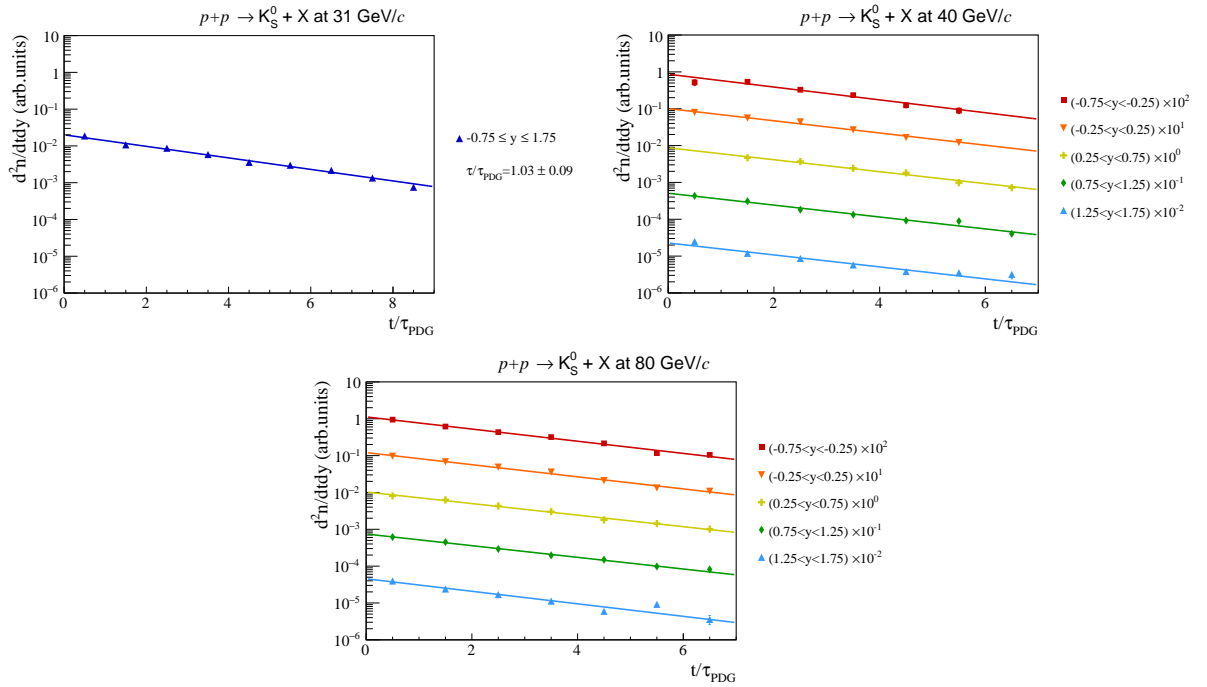


Figure 6: (Color online) Corrected lifetime distributions for K_S^0 mesons produced in inelastic $p+p$ interactions at beam energies of $p_{beam} = 31$ GeV/c (top left), $p_{beam} = 40$ GeV/c (top right), and $p_{beam} = 80$ GeV/c (bottom). The straight lines show the results of exponential fits used to obtain the mean lifetimes (normalized to the PDG value) in rapidity bins. Statistical uncertainties are smaller than the marker size and are not visible on the plots.

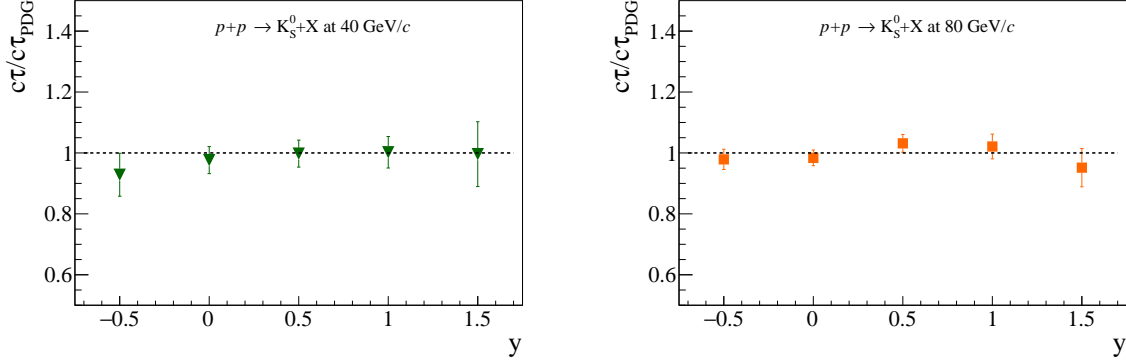


Figure 7: (Color online) Mean K_S^0 lifetimes (normalized to the PDG value) obtained from fits to the lifetime distributions of Fig. 6 for the $p_{beam} = 40$ GeV/c (left) and $p_{beam} = 80$ GeV/c (right) data sets versus the rapidity y . The error bars indicate the statistical uncertainties.

4 Results

This section presents new NA61/SHINE results on inclusive K_S^0 meson production from inelastic $p+p$ interactions at beam momenta of 31, 40 and 80 GeV/c. Transverse momentum and rapidity spectra are obtained from the analysis of the weak decays of K_S^0 mesons into two charged pions.

4.1 Transverse momentum spectra

Double differential K_S^0 yields listed in Table 2 represent the main result of this paper. Yields are determined in five consecutive rapidity bins in the interval $-0.75 < y < 1.75$ and six transverse momentum bins in the interval $0.0 < p_T$ (GeV/c) < 1.2 . The transverse momentum distributions at mid-rapidity ($y \approx 0$) are shown in Fig. 8.

An exponential function was fitted to the transverse momentum spectra. It reads:

$$f(p_T) = A \cdot p_T \cdot \exp\left(-\frac{\sqrt{p_T^2 + m_0^2}}{T}\right), \quad (10)$$

where m_0 is the mass of the K_S^0 and T is the inverse slope parameter. The resulting values of T in each rapidity bin are listed in Table 3.

4.2 Rapidity distributions and mean multiplicities

Kaon yields in each rapidity bin were obtained from the measured transverse momentum distributions. The small fraction of K_S^0 at high p_T outside of the acceptance was determined using Eq. 10. The resulting $\frac{dn}{dy}$ spectra of K_S^0 mesons produced in inelastic $p+p$ interactions at 31, 40 and 80 GeV/c are presented in Fig. 9 together with the previous NA61/SHINE results obtained for $p+p$ interactions at 158 GeV/c [4].

Momentum		Results $\frac{d^2n}{dydp_T} \times 10^3$		
$p_{beam} = 31 \text{ GeV}/c$	$p_T \text{ (GeV}/c)$	(0.0;0.2)	(0.2;0.4)	(0.4;0.6)
	y			
	(-0.75;-0.25)	$19.2 \pm 5.1 \pm 6.6$	$44.6 \pm 8.8 \pm 7.0$	$35.9 \pm 8.0 \pm 11.7$
	(-0.25;0.25)	$24.5 \pm 3.4 \pm 4.4$	$56.1 \pm 4.6 \pm 3.9$	$40.7 \pm 3.4 \pm 2.6$
	(0.25;0.75)	$20.4 \pm 2.5 \pm 1.7$	$40.5 \pm 3.2 \pm 2.0$	$33.0 \pm 2.6 \pm 2.4$
	(0.75;1.25)	$15.7 \pm 2.4 \pm 4.6$	$21.7 \pm 2.5 \pm 1.9$	$21.7 \pm 2.3 \pm 2.1$
	(1.25;1.75)	$6.3 \pm 1.4 \pm 2.5$	$9.1 \pm 1.7 \pm 1.2$	$4.1 \pm 1.3 \pm 1.0$
	$p_T \text{ (GeV}/c)$	(0.6;0.8)	(0.8;1.0)	(1.0;1.2)
	y			
	(-0.75;-0.25)	$13.3 \pm 3.6 \pm 3.8$	-	-
	(-0.25;0.25)	$18.7 \pm 2.0 \pm 1.6$	$10.2 \pm 1.2 \pm 1.6$	$4.2 \pm 0.8 \pm 0.7$
	(0.25;0.75)	$17.0 \pm 1.6 \pm 1.3$	$5.4 \pm 0.8 \pm 0.6$	$2.7 \pm 0.5 \pm 0.4$
	(0.75;1.25)	$7.6 \pm 1.2 \pm 0.5$	$2.3 \pm 0.6 \pm 0.7$	$1.2 \pm 0.4 \pm 0.2$
	(1.25;1.75)	$1.0 \pm 0.6 \pm 0.3$	-	-
$p_{beam} = 40 \text{ GeV}/c$	$p_T \text{ (GeV}/c)$	(0.0;0.2)	(0.2;0.4)	(0.4;0.6)
	y			
	(-0.75;-0.25)	$24.8 \pm 3.5 \pm 7.3$	$54.3 \pm 5.6 \pm 7.6$	$34.9 \pm 4.3 \pm 4.3$
	(-0.25;0.25)	$28.6 \pm 2.6 \pm 1.6$	$60.0 \pm 3.3 \pm 2.9$	$46.0 \pm 2.4 \pm 1.4$
	(0.25;0.75)	$26.5 \pm 2.0 \pm 2.4$	$51.1 \pm 2.7 \pm 2.8$	$38.1 \pm 2.2 \pm 2.6$
	(0.75;1.25)	$16.6 \pm 1.6 \pm 0.7$	$33.5 \pm 2.4 \pm 3.0$	$23.4 \pm 1.9 \pm 1.5$
	(1.25;1.75)	$9.4 \pm 1.2 \pm 1.1$	$13.6 \pm 1.9 \pm 2.6$	$8.7 \pm 1.5 \pm 1.3$
	$p_T \text{ (GeV}/c)$	(0.6;0.8)	(0.8;1.0)	(1.0;1.2)
	y			
	(-0.75;-0.25)	$19.6 \pm 2.3 \pm 2.1$	$10.2 \pm 1.4 \pm 1.7$	$3.9 \pm 0.8 \pm 0.8$
	(-0.25;0.25)	$23.2 \pm 1.6 \pm 1.6$	$11.2 \pm 1.0 \pm 0.9$	$5.4 \pm 0.7 \pm 0.6$
	(0.25;0.75)	$22.1 \pm 1.4 \pm 1.8$	$8.7 \pm 0.9 \pm 1.2$	$3.2 \pm 0.5 \pm 0.4$
	(0.75;1.25)	$11.1 \pm 1.2 \pm 1.0$	$4.1 \pm 0.7 \pm 0.5$	$1.4 \pm 0.4 \pm 0.3$
	(1.25;1.75)	$5.2 \pm 1.2 \pm 2.3$	$0.9 \pm 0.5 \pm 0.2$	$0.3 \pm 0.2 \pm 0.1$
$p_{beam} = 80 \text{ GeV}/c$	$p_T \text{ (GeV}/c)$	(0.0;0.2)	(0.2;0.4)	(0.4;0.6)
	y			
	(-0.75;-0.25)	$35.2 \pm 2.5 \pm 3.5$	$64.2 \pm 2.9 \pm 2.6$	$51.8 \pm 2.4 \pm 2.9$
	(-0.25;0.25)	$35.0 \pm 2.0 \pm 2.1$	$68.6 \pm 2.5 \pm 2.0$	$63.8 \pm 2.2 \pm 1.9$
	(0.25;0.75)	$33.0 \pm 1.6 \pm 0.9$	$67.6 \pm 2.3 \pm 1.7$	$49.7 \pm 2.2 \pm 3.0$
	(0.75;1.25)	$23.6 \pm 1.3 \pm 1.0$	$50.8 \pm 2.0 \pm 1.6$	$35.3 \pm 2.1 \pm 1.7$
	(1.25;1.75)	$15.5 \pm 1.2 \pm 0.6$	$30.8 \pm 1.7 \pm 1.4$	$20.5 \pm 1.9 \pm 1.6$
	$p_T \text{ (GeV}/c)$	(0.6;0.8)	(0.8;1.0)	(1.0;1.2)
	y			
	(-0.75;-0.25)	$28.0 \pm 1.6 \pm 1.7$	$13.4 \pm 1.0 \pm 0.6$	$5.6 \pm 0.7 \pm 0.5$
	(-0.25;0.25)	$31.6 \pm 1.5 \pm 1.9$	$15.4 \pm 1.0 \pm 1.1$	$6.4 \pm 0.6 \pm 0.5$
	(0.25;0.75)	$29.3 \pm 1.7 \pm 1.6$	$14.7 \pm 1.2 \pm 1.0$	$5.4 \pm 0.7 \pm 0.4$
	(0.75;1.25)	$22.0 \pm 2.0 \pm 1.3$	$7.4 \pm 1.3 \pm 0.9$	$3.4 \pm 0.9 \pm 0.3$
	(1.25;1.75)	$8.5 \pm 1.6 \pm 1.5$	$4.6 \pm 1.2 \pm 1.3$	$0.8 \pm 0.6 \pm 0.2$

Table 2: Double differential K_S^0 yields in bins of (y, p_T) . The first uncertainty is statistical, while the second one is systematic.

The mean multiplicities of K_S^0 mesons were calculated as the sum of the measured data points in Fig. 9 scaled by the ratio between measured and unmeasured regions obtained from the Monte-Carlo simulation. The statistical uncertainties of $\langle K_S^0 \rangle$ were calculated as the square root of the sum of the squares of the statistical uncertainties of the contributing bins. The systematic uncertainties were calculated as the square

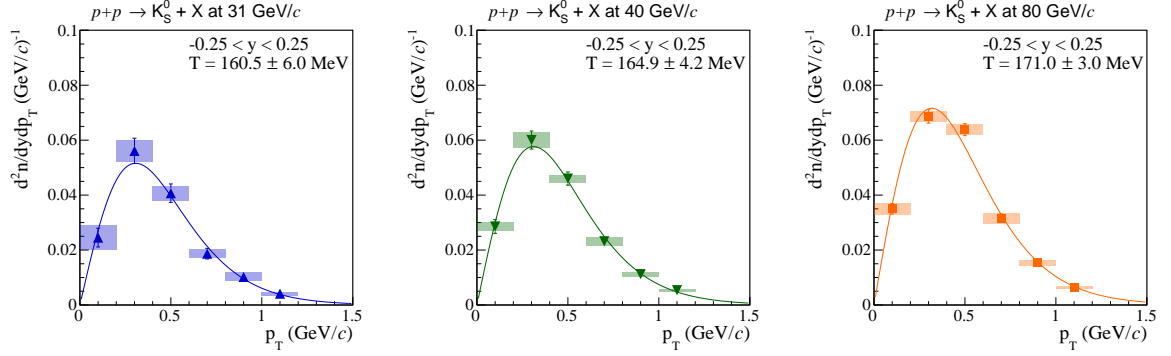


Figure 8: (Color online) Double-differential K_S^0 spectra in inelastic $p+p$ interaction at 31 GeV/c (*left*), 40 GeV/c (*middle*) and 80 GeV/c (*right*) at mid-rapidity ($y \approx 0$) calculated according to Eq. 4. Measured points are shown as blue full triangles up (for $p_{beam} = 31$ GeV/c), green full triangles down (for $p_{beam} = 40$ GeV/c) and orange full squares (for $p_{beam} = 80$ GeV/c). The solid curves are fitted to the data points using the exponential function (Eq. 10). Vertical bars indicate statistical uncertainties (for some points smaller than the symbol size). Shaded boxes show systematic uncertainties. Only statistical uncertainties are taken into account in the fit, because the systematic uncertainties do not depend on p_T . The numerical values of the data points are listed in Table 2.

	y	T (MeV)	$\frac{dn}{dy} \times 10^3$
	$p_{beam} = 31$ GeV/c	(-0.75;-0.25)	$149.4 \pm 18.7 \pm 21.8$
	(-0.25;0.25)	$160.5 \pm 5.9 \pm 5.7$	$31.3 \pm 1.5 \pm 1.7$
	(0.25;0.75)	$152.5 \pm 4.9 \pm 3.7$	$24.1 \pm 1.1 \pm 1.0$
	(0.75;1.25)	$137.0 \pm 6.2 \pm 8.1$	$14.1 \pm 0.9 \pm 0.8$
	(1.25;1.75)	$93.5 \pm 11.7 \pm 11.2$	$4.2 \pm 0.6 \pm 0.8$
	y	T (MeV)	$\frac{dn}{dy} \times 10^3$
	$p_{beam} = 40$ GeV/c	(-0.75;-0.25)	$162.6 \pm 6.8 \pm 9.7$
	(-0.25;0.25)	$164.8 \pm 4.2 \pm 1.9$	$35.5 \pm 1.0 \pm 1.4$
	(0.25;0.75)	$157.4 \pm 3.7 \pm 4.0$	$30.4 \pm 0.9 \pm 1.8$
	(0.75;1.25)	$143.6 \pm 4.5 \pm 2.6$	$18.2 \pm 0.8 \pm 1.0$
	(1.25;1.75)	$122.2 \pm 7.6 \pm 6.2$	$7.6 \pm 0.6 \pm 0.7$
	y	T (MeV)	$\frac{dn}{dy} \times 10^3$
	$p_{beam} = 80$ GeV/c	(-0.75;-0.25)	$165.8 \pm 3.6 \pm 2.3$
	(-0.25;0.25)	$171.0 \pm 3.0 \pm 1.7$	$45.1 \pm 0.9 \pm 1.5$
	(0.25;0.75)	$168.0 \pm 3.4 \pm 2.4$	$40.7 \pm 0.8 \pm 1.2$
	(0.75;1.25)	$159.9 \pm 4.7 \pm 4.0$	$28.9 \pm 0.8 \pm 0.7$
	(1.25;1.75)	$140.6 \pm 6.2 \pm 3.9$	$16.2 \pm 0.7 \pm 0.7$

Table 3: Numerical values of T and dn/dy for K_S^0 mesons produced in $p+p$ interactions at 31, 40 and 80 GeV/c. The first column indicates the data set. The second column shows the rapidity range. The values of the inverse slope parameter are listed in the third column, along with their statistical and systematic uncertainties. The last column shows the numerical values of the p_T -integrated yields presented in Fig. 9 with statistical and systematic uncertainties.

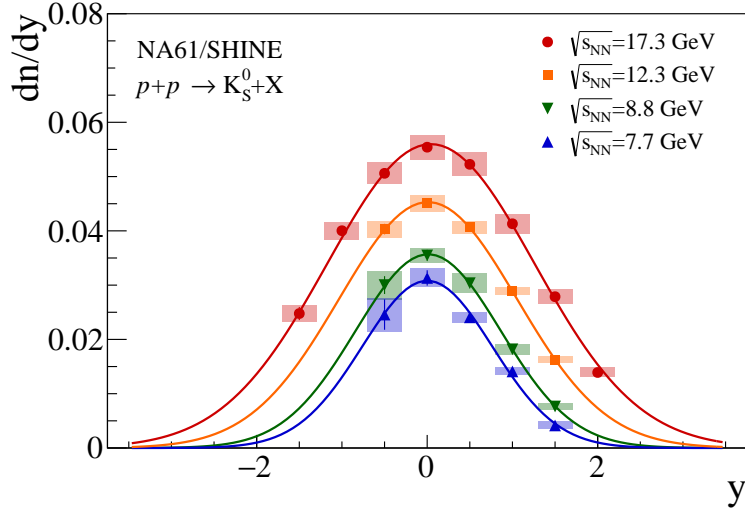


Figure 9: (Color online) Rapidity distribution dn/dy obtained by p_T -integration of data and extrapolation. Statistical uncertainties are shown by vertical bars (often smaller than the marker size), while shaded boxes indicate systematic uncertainties. The curves indicate the result of the Gaussian fit to the measured points. Points for $p+p$ at $\sqrt{s_{NN}} = 17.3$ GeV are taken from [4].

root of squares of systematic uncertainties described in Sec. 3.8. To estimate the systematic uncertainties of the method used to determine the mean multiplicities of K_S^0 , the rapidity distributions were also fitted using a single Gaussian or two Gaussians symmetrically displaced from mid-rapidity. The deviations of the results of these fits from $\langle K_S^0 \rangle$ are included as an additional contribution to the final systematic uncertainty. The mean multiplicities of K_S^0 mesons in inelastic $p+p$ collisions were found to be $0.0595 \pm 0.0019(stat) \pm 0.0022(sys)$ at 31 GeV/c, $0.0761 \pm 0.0013(stat) \pm 0.0031(sys)$ at 40 GeV/c and $0.1158 \pm 0.0012(stat) \pm 0.0037(sys)$ at 80 GeV/c.

5 Comparison with published world data and model calculations

This section compares the new NA61/SHINE measurements of K_S^0 production in inelastic $p+p$ interactions at 31, 40 and 80 GeV/c with world data as well as with microscopic model calculations (EPOS1.99 [16, 17], SMASH 2.0 [19] and PHSD [20, 21]). The K_S^0 rapidity spectra from NA61/SHINE are compared in Fig. 10 to the results from Blobel *et al.* [22] as well as with results from Ammosov *et al.* [23]. The results from Blobel *et al.* at 24 GeV/c are significantly below the NA61/SHINE 31 GeV/c data in the central rapidity part. The results from Ammosov *et al.* at 69 GeV/c are located between the measured NA61/SHINE points of the 40 and 80 GeV/c data sets, as expected.

Recently NA61/SHINE reported an excess of charged over neutral kaon production in Ar+Sc collisions at 75A GeV/c [24]. The precise and detailed results on K_S^0 production in $p+p$ interactions reported here, together with the corresponding results on charged kaons [5], may contribute to the understanding of this puzzle. To this end the rapidity distributions of K_S^0 are compared with two predictions derived from K^+ and K^- yields obtained from the same data sets [5]. The first prediction is based on valence- and sea-quark counting arguments [25] and leads to the equation $N_{K_S^0} = \frac{1}{4}(N_{K^+} + 3 \cdot N_{K^-})$. This relation was used in the

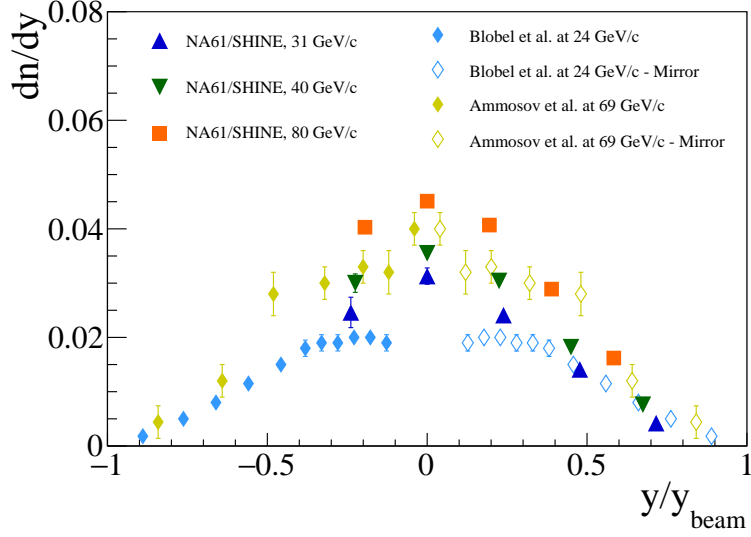


Figure 10: (Color online) dn/dy as a function of scaled rapidity y/y_{beam} of K_S^0 mesons in inelastic $p+p$ interactions at 31, 40 and 80 GeV/c. Measured points are shown as blue full triangles up (for $p_{beam} = 31$ GeV/c), green full triangles down (for $p_{beam} = 40$ GeV/c) and orange full squares (for $p_{beam} = 80$ GeV/c). Results from other experiments are shown as azure-colored diamonds (for Blobel *et al.* at 24 GeV/c) and yellow-colored diamonds (for Ammosov *et al.* at 69 GeV/c). Vertical bars indicate statistical uncertainties (for some points smaller than the symbol size).

past to estimate the neutral kaon flux in the fragmentation region for K^0 beam studies [26]. The second prediction assumes isospin symmetry of the different charge states of the kaon: $N_{K_S^0} = \frac{1}{2}(N_{K^+} + N_{K^-})$. The K_S^0 rapidity distributions are compared to these two predictions in Fig. 11. The prediction based on valence quark counting describes the K_S^0 rapidity distributions significantly better than the one assuming isospin symmetry.

Figure 12 compares the NA61/SHINE measurements with model calculations from EPOS1.99, PHSD and SMASH 2.0. EPOS1.99 overpredicts the experimental data at all three data beam momenta. PHSD overpredicts the measured $p_{beam} = 80$ GeV/c data, while for the remaining two data sets it shows fair agreement. SMASH 2.0 describes the experimental $p_{beam} = 80$ GeV/c data very well but underpredicts the remaining two data sets. All models exhibit the same shape of the rapidity distribution as the experimental data. The energy dependence of K_S^0 production seems to be well reproduced by EPOS1.99, whereas PHSD and SMASH 2.0 both exhibit a stronger rise than observed in the data.

The mean multiplicity of K_S^0 mesons in $p+p$ collisions at $\sqrt{s_{NN}} = 7.7, 8.8, 12.3$ GeV, reported here, and the published result at $\sqrt{s_{NN}} = 17.3$ GeV [4] are compared in Fig. 13 with the world data in the range from 3 - 32 GeV. The measured values are seen to rise linearly with collision energy $\sqrt{s_{NN}}$.

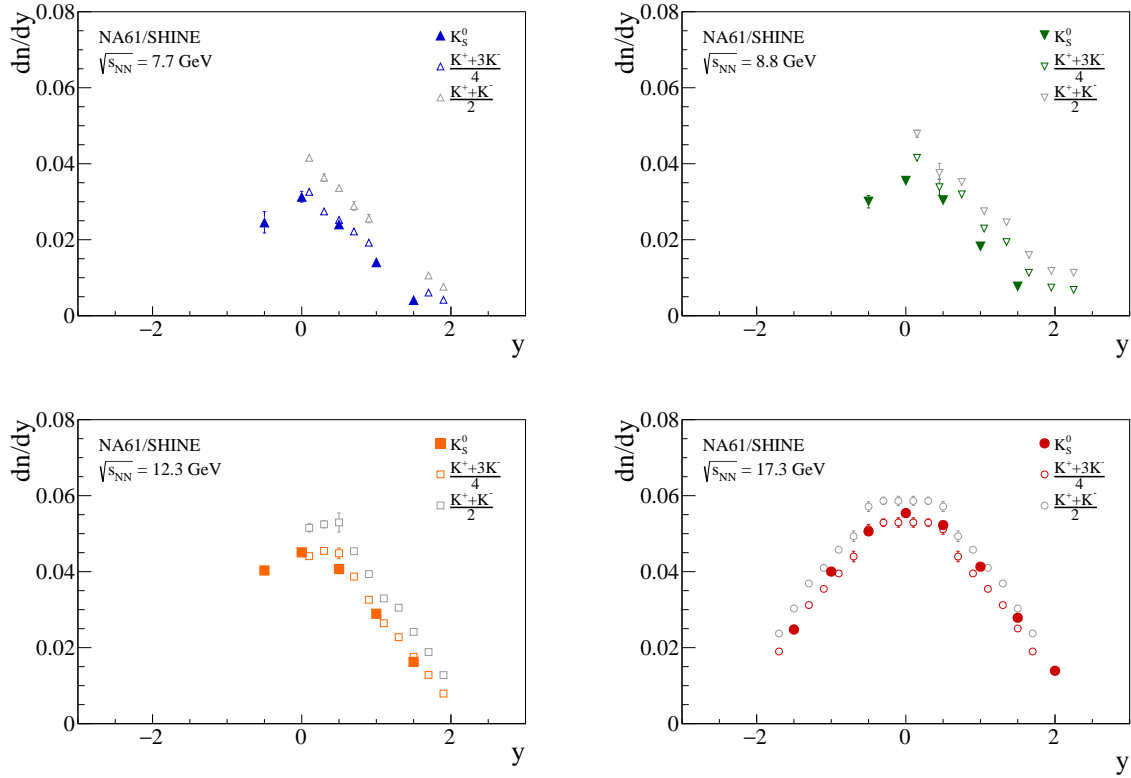


Figure 11: (Color online) Rapidity distribution dn/dy of K_S^0 mesons in inelastic $p+p$ interactions at 31, 40, 80 and 158 GeV/c. Measured points are shown as blue full triangles up for $p_{beam} = 31$ GeV/c (top left), green full triangles down for $p_{beam} = 40$ GeV/c (top right), orange full squares for $p_{beam} = 80$ GeV/c (bottom left) and red full circles for $p_{beam} = 158$ GeV/c (bottom right). Results for charged kaons obtained by formula $\frac{1}{4}(N_{K^+} + 3 \cdot N_{K^-})$ are shown by open colored symbols for all data sets, while the results obtained by formula $\frac{1}{2}(N_{K^+} + N_{K^-})$ are shown by grey opened symbols. Vertical bars indicate statistical uncertainties (for some points smaller than the symbol size).

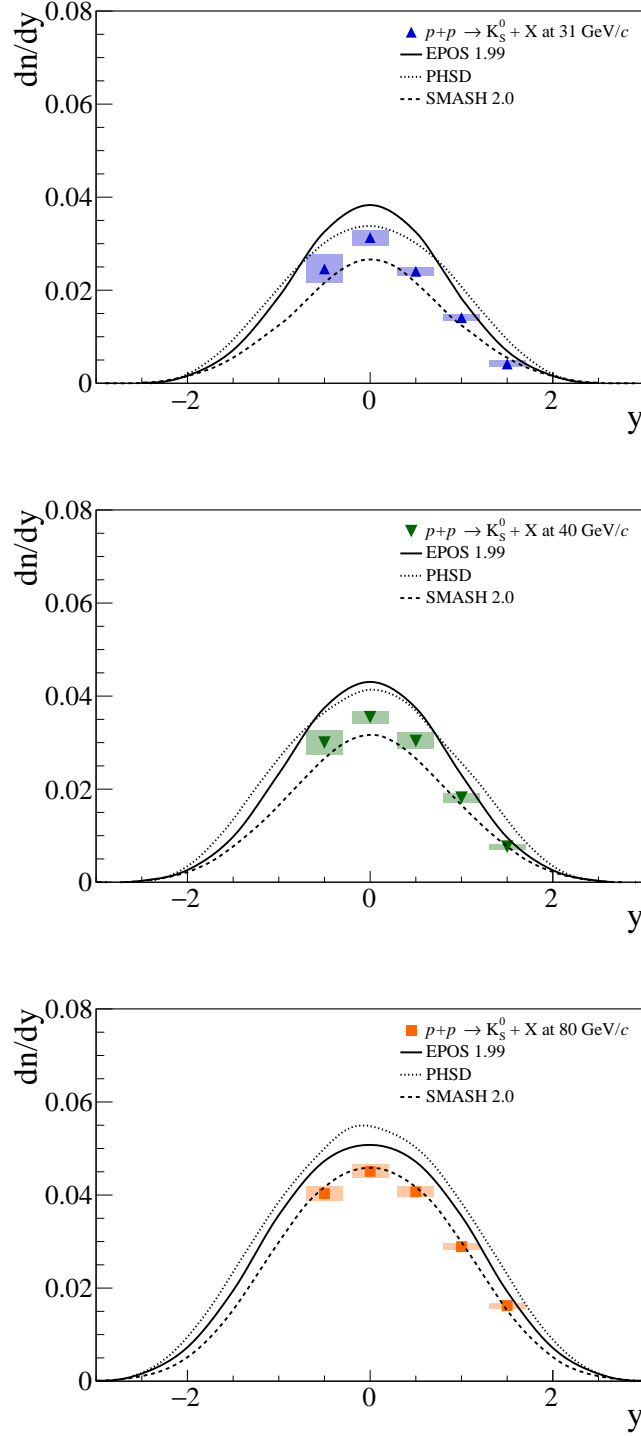


Figure 12: (Color online) Comparison of the experimental K_S^0 rapidity distributions with model calculations. Colored symbols show the new measurements of NA61/SHINE as follows: $p_{beam} = 31$ GeV/c (*top*), $p_{beam} = 40$ GeV/c (*middle*) and $p_{beam} = 80$ GeV/c (*bottom*). The black curves show the result of the model calculations: EPOS1.99 (solid), PHSD (dotted) and SMASH 2.0 (dashed).

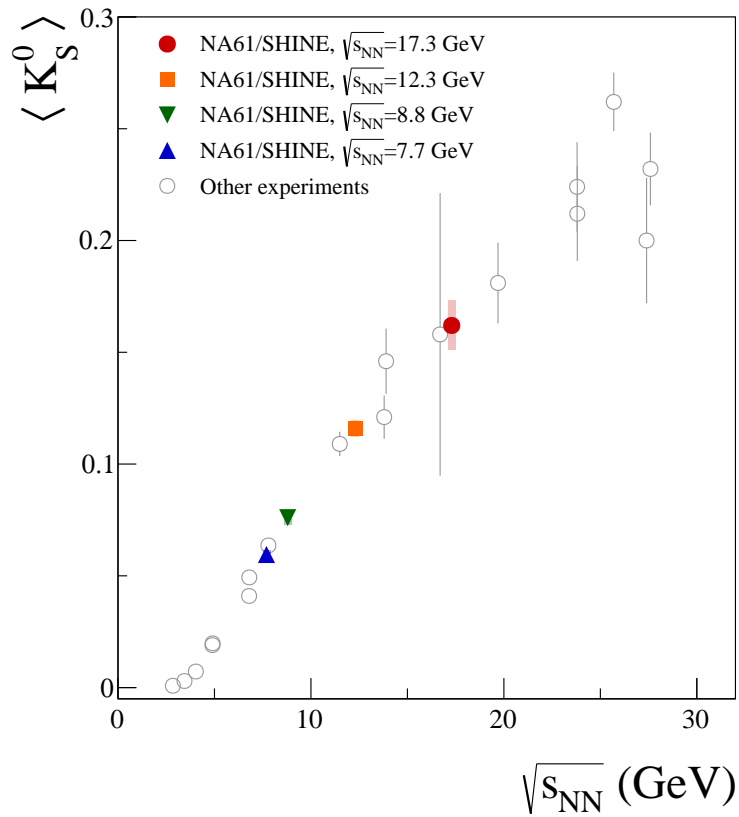


Figure 13: (Color online) Collision energy dependence of mean multiplicity of K_S^0 mesons produced in $p+p$ interactions. The measurements from NA61/SHINE are shown with colored symbols as follows: blue full triangle up for $p_{beam} = 31$ GeV/ c , green full triangle down for $p_{beam} = 40$ GeV/ c , orange full square for $p_{beam} = 80$ GeV/ c and red full circle for $p_{beam} = 158$ GeV/ c [4]. The results published by other experiments are shown by the grey open circles [22, 23, 27–40]. Statistical uncertainties are smaller than the marker size, while shaded boxes indicate systematic uncertainties.

6 Summary

This paper presents the new NA61/SHINE measurement of K_S^0 mesons via their $\pi^+\pi^-$ decay mode in inelastic $p+p$ collisions at beam momenta of 31, 40 and 80 GeV/ c ($\sqrt{s_{NN}} = 7.7, 8.8$ and 17.3 GeV). Spectra of transverse momentum (up to 1.2 GeV/ c), as well as a distributions of rapidity (from -0.75 to 1.75), are presented. The mean multiplicities, obtained from p_T -integrated spectra and extrapolated rapidity distributions, are $(5.95 \pm 0.19 \pm 0.22) \times 10^{-2}$ at 31 GeV/ c , $(7.61 \pm 0.13 \pm 0.31) \times 10^{-2}$ at 40 GeV/ c and $(11.58 \pm 0.12 \pm 0.37) \times 10^{-2}$ at 80 GeV/ c , where the first uncertainty is statistical and the second systematic. The measured K_S^0 lifetime agrees within uncertainties with the PDG value and thus confirms the quality of the analysis. The mean multiplicities from model calculations deviate by up to 10% from the measurements. The SMASH 2.0 model provides the best results for $p_{beam} = 31$ and 80 GeV/ c , while the PHSD model has the best agreement with measured data for $p_{beam} = 40$ GeV/ c . The results of K_S^0 production in proton-proton interactions presented in this paper significantly improve, with their high statistical precision, the knowledge of strangeness production in elementary interactions and will serve as a reference for studies of strange hadron production in nucleus-nucleus collisions.

Acknowledgments

We would like to thank the CERN EP, BE, HSE and EN Departments for the strong support of NA61/SHINE.

This work was supported by the Hungarian Scientific Research Fund (grant NKFIH 138136/137812/138152 and TKP2021-NKTA-64), the Polish Ministry of Science and Higher Education (DIR/WK/2016/2017/10-1, WUT ID-UB), the National Science Centre Poland (grants 2014/14/E/ST2/00018, 2016/21/D/ST2/01983, 2017/25/N/ST2/02575, 2018/29/N/ST2/02595, 2018/30/A/ST2/00226, 2018/31/G/ST2/03910, 2020/39/O/ST2/00277), the Norwegian Financial Mechanism 2014–2021 (grant 2019/34/H/ST2/00585), the Polish Minister of Education and Science (contract No. 2021/WK/10), the European Union’s Horizon 2020 research and innovation programme under grant agreement No. 871072, the Ministry of Education, Culture, Sports, Science and Technology, Japan, Grant-in-Aid for Scientific Research (grants 18071005, 19034011, 19740162, 20740160 and 20039012,22H04943), the German Research Foundation DFG (grants GA 1480/8-1 and project 426579465), the Bulgarian Ministry of Education and Science within the National Roadmap for Research Infrastructures 2020–2027, contract No. D01-374/18.12.2020, Serbian Ministry of Science, Technological Development and Innovation (grant OI171002), Swiss Nationalfonds Foundation (grant 200020117913/1), ETH Research Grant TH-01 07-3, National Science Foundation grant PHY-2013228 and the Fermi National Accelerator Laboratory (Fermilab), a U.S. Department of Energy, Office of Science, HEP User Facility managed by Fermi Research Alliance, LLC (FRA), acting under Contract No. DE-AC02-07CH11359 and the IN2P3-CNRS (France).

The data used in this paper were collected before February 2022.

References

- [1] J. Letessier and J. Rafelski, *Hadrons and Quark–Gluon Plasma*. Oxford University Press, 2002.
- [2] M. Gazdzicki and M. I. Gorenstein, “On the early stage of nucleus-nucleus collisions,” *Acta Phys. Polon.* **B30** (1999) 2705, [arXiv:hep-ph/9803462](https://arxiv.org/abs/hep-ph/9803462) [hep-ph].
- [3] M. Gazdzicki, Z. Fodor, and G. Vesztegombi, [NA49-future Collaboration Collab.], “Study of Hadron Production in Hadron-Nucleus and Nucleus-Nucleus Collisions at the CERN SPS,” Tech. Rep. CERN-SPSC-2006-034. SPSC-P-330, CERN, Geneva, Nov, 2006. <https://cds.cern.ch/record/995681>. revised version submitted on 2006-11-06 12:38:20.
- [4] A. Acharya *et al.*, [NA61/SHINE Collab.], “ K_S^0 meson production in inelastic p+p interactions at 158 GeV/c beam momentum measured by NA61/SHINE at the CERN SPS,” *Eur. Phys. J. C* **82** no. 1, (2022) 96, [arXiv:2106.07535](https://arxiv.org/abs/2106.07535) [hep-ex].
- [5] A. Aduszkiewicz *et al.*, [NA61/SHINE Collab.], “Measurements of π^\pm , K^\pm , p and \bar{p} spectra in proton-proton interactions at 20, 31, 40, 80 and 158 GeV/c with the NA61/SHINE spectrometer at the CERN SPS,” *Eur. Phys. J. C* **77** no. 10, (2017) 671, [arXiv:1705.02467](https://arxiv.org/abs/1705.02467) [nucl-ex].
- [6] N. Abgrall *et al.*, [NA61 Collab.], “NA61/SHINE facility at the CERN SPS: beams and detector system,” *JINST* **9** (2014) P06005, [arXiv:1401.4699](https://arxiv.org/abs/1401.4699) [physics.ins-det].
- [7] N. Abgrall *et al.*, [NA61/SHINE Collab.], “Measurement of negatively charged pion spectra in inelastic p+p interactions at $p_{lab} = 20, 31, 40, 80$ and 158 GeV/c,” *Eur. Phys. J. C* **74** no. 3, (2014) 2794, [arXiv:1310.2417](https://arxiv.org/abs/1310.2417) [hep-ex].
- [8] A. Aduszkiewicz *et al.*, [NA61/SHINE Collab.], “Multiplicity and transverse momentum fluctuations in inelastic proton-proton interactions at the CERN Super Proton Synchrotron,” *Eur. Phys. J. C* **76** no. 11, (2016) 635, [arXiv:1510.00163](https://arxiv.org/abs/1510.00163) [hep-ex].
- [9] A. P. C. Bovet, R. Maleyran and M. Placidi, “The cedar (cerenkov differential counters with achromatic ring focus) project,” *IEEE Transactions on Nuclear Science* **25** no. 1, (1978) 572–576.
- [10] C. Strabel, *Evaluation of Particle Yields in 30 GeV Proton-Carbon Inelastic Interactions for Estimating the T2K Neutrino Flux*. PhD thesis, Frankfurt U., 2011.
- [11] A. Aduszkiewicz *et al.*, [NA61/SHINE Collab.], “Two-particle correlations in azimuthal angle and pseudorapidity in inelastic p + p interactions at the CERN Super Proton Synchrotron,” *Eur. Phys. J. C* **77** no. 2, (2017) 59, [arXiv:1610.00482](https://arxiv.org/abs/1610.00482) [nucl-ex].
- [12] N. Abgrall, [NA61 Collab.], “Calibration and Analysis of the 2007 Data,” tech. rep., CERN, Geneva, 2008. <https://cds.cern.ch/record/1113279>.
- [13] M. Tanabashi *et al.*, [Particle Data Group Collab.], “Review of Particle Physics,” *Phys. Rev. D* **98** no. 3, (2018) 030001.
- [14] A. Aduszkiewicz *et al.*, [NA61/SHINE Collab.], “ $K^*(892)^0$ meson production in inelastic p+p interactions at 158 GeV/c beam momentum measured by NA61/SHINE at the CERN SPS,” *Eur. Phys. J. C* **80** no. 5, (2020) 460, [arXiv:2001.05370](https://arxiv.org/abs/2001.05370) [nucl-ex].
- [15] J. Podolanski and R. Armenteros, “III. Analysis of V-events,” *The London, Edinburgh, and Dublin Philosophical Magazine and Journal of Science* **45** no. 360, (1954) 13–30. <https://doi.org/10.1080/14786440108520416>.
- [16] K. Werner, F. M. Liu, and T. Pierog, “Parton ladder splitting and the rapidity dependence of transverse momentum spectra in deuteron-gold collisions at RHIC,” *Phys. Rev. C* **74** (2006) .
- [17] T. Pierog and K. Werner, “EPOS Model and Ultra High Energy Cosmic Rays,” *Nucl. Phys. B Proc.* **196** (2009) 102–105.
- [18] R. Brun *et al.*, *GEANT: Detector Description and Simulation Tool; Oct 1994*. CERN, Geneva, 1993. <https://cds.cern.ch/record/1082634>. Long Writeup W5013.
- [19] J. Mohs, S. Ryu, and H. Elfner, “Particle Production via Strings and Baryon Stopping within a Hadronic Transport Approach,” *J. Phys. G* **47** no. 6, (2020) 065101, [arXiv:1909.05586](https://arxiv.org/abs/1909.05586) [nucl-th].

- [20] W. Cassing and E. L. Bratkovskaya, “Parton transport and hadronization from the dynamical quasiparticle point of view,” *Phys. Rev. C* **78** (2008) 034919, [arXiv:0808.0022 \[hep-ph\]](#).
- [21] W. Cassing and E. L. Bratkovskaya, “Parton-Hadron-String Dynamics: an off-shell transport approach for relativistic energies,” *Nucl. Phys. A* **831** (2009) 215–242, [arXiv:0907.5331 \[nucl-th\]](#).
- [22] V. Blobel *et al.*, “Multiplicities, topological cross sections, and single particle inclusive distributions from pp interactions at 12 and 24 GeV/c,” *Nuclear Physics B* **69** (1974) 454–492.
- [23] V. V. Ammosov *et al.*, “Neutral Strange Particle Production in p p Interactions at 69-GeV/c,” *Nucl. Phys. B* **115** (1976) 269–286.
- [24] H. Adhikary, [NA61 Collab.], “Excess of charged over neutral K meson production in high-energy collisions of atomic nuclei,” tech. rep., CERN, Geneva, 2023. [arXiv:2312.06572](#). <https://cds.cern.ch/record/2883229>. 18 pages, 6 figures.
- [25] J. Stepaniak and D. Pszczel, “On the relation between K_s^0 and charged kaon yields in proton–proton collisions,” *Eur. Phys. J. C* **83** no. 10, (2023) 928, [arXiv:2305.03872 \[hep-ph\]](#).
- [26] L. Gagnon, “Design and Tuning of Secondary Beamlines in the CERN North and East Areas,” <https://cds.cern.ch/record/2730780>.
- [27] R. I. Louttit, T. W. Morris, D. C. Rahm, R. R. Rau, A. M. Thorndike, W. J. Willis, and R. M. Lea, “Production of strange particles in $p - p$ collisions at 2.85 GeV,” *Phys. Rev.* **123** (Aug, 1961) 1465–1471. <https://link.aps.org/doi/10.1103/PhysRev.123.1465>.
- [28] G. Alexander *et al.*, “Proton-Proton Interactions at 5.5 GeV/c,” *Phys. Rev.* **154** (1967) 1284–1304.
- [29] M. Firebaugh *et al.*, “Strange-particle production in 8-GeV/c proton-proton interactions,” *Phys. Rev.* **172** (1968) 1354–1369.
- [30] H. Fesefeldt *et al.*, “Strangeness-transfer distributions in proton-proton collisions at 12 and 24 GeV/c,” *Nuclear Physics B* **147** (1979) 317–335.
- [31] M. Y. Bogolyubsky *et al.*, “Study of Neutral Strange Particle Production in pp Interactions at 32-GeV/c and Comparison With $\bar{p}p$ Data,” *Sov. J. Nucl. Phys.* **50** (1989) 424.
- [32] M. Alston-Garnjost *et al.*, “Neutral particle production in π^+p and pp collisions at 100 GeV/c,” *Phys. Rev. Lett.* **35** (Jul, 1975) 142–145.
- [33] J. W. Chapman *et al.*, “Production of γ , Λ^0 , K_S^0 and $\bar{\Lambda}^0$ in pp collisions at 102 GeV/c,” *Physics Letters B* **47** (1973) 465–468.
- [34] D. Brick *et al.*, “Inclusive production of neutral strange particles by 147-GeV/c $\text{Pi}^+ \text{K}^+ p$ interactions in hydrogen,” *Nucl. Phys. B* **164** (1980).
- [35] K. Jaeger *et al.*, “Characteristics of V^0 and γ production in pp interactions at 205 GeV/c,” *Phys. Rev. D* **11** (May, 1975) 2405–2425.
- [36] A. Sheng *et al.*, “ pp interactions at 300 GeV/c: γ and neutral-strange-particle production,” *Phys. Rev. D* **11** (Apr, 1975) 1733–1742.
- [37] F. LoPinto *et al.*, “Inclusive K^0 , Λ^0 , $K^{*\pm}$ (890), and $\Sigma^{*\pm}$ (1385) production in pp collisions at 300 GeV/c,” *Phys. Rev. D* **22** (Aug, 1980) 573–581.
- [38] M. Asai *et al.*, [EHS-RCBC, Bombay-CERN-Genoa-Innsbruck-Japan-Madrid-Mons-Rutgers-Serpukhov-Tennessee-Vienna Collab.], “Inclusive K_S^0 , Λ and $\bar{\Lambda}$ Production in 360-GeV/c pp Interactions Using the European Hybrid Spectrometer,” *Z. Phys. C* **27** (1985) 11.
- [39] R. D. Kass *et al.*, “Charged- and neutral-particle production from 400-GeV/c pp collisions,” *Phys. Rev. D* **20** (Aug, 1979) 605–614.
- [40] H. Kichimi *et al.*, “Inclusive study of strange-particle production in pp interactions at 405 GeV/c,” *Phys. Rev. D* **20** (Jul, 1979) 37–52.

Estimation of the electromagnetic field in intermediate-energy heavy-ion collisions

Hidetoshi Taya,^{1,*} Toru Nishimura,^{2,3} and Akira Ohnishi³

¹*RIKEN iTHEMS, RIKEN, Wako 351-0198, Japan*

²*Department of Physics, Osaka University, Toyonaka, Osaka, 560-0043, Japan*

³*Yukawa Institute for Theoretical Physics, Kyoto University, Kyoto, 606-8317, Japan*

We estimate the spacetime profile of the electromagnetic field in head-on heavy-ion collisions at intermediate collision energies $\sqrt{s_{\text{NN}}} = \mathcal{O}(3 - 10 \text{ GeV})$. Using a hadronic cascade model (JAM; Jet AA Microscopic transport model), we numerically demonstrate that the produced field has strength $eE = \mathcal{O}((30 - 60 \text{ MeV})^2)$, which is supercritical to the Schwinger limit of QED and is non-negligibly large compared even to the hadron/QCD scale, and survives for a long time $\tau = \mathcal{O}(10 \text{ fm}/c)$ due to the baryon stopping. We show that the produced field is nonperturbatively strong in the sense that the nonperturbativity parameters (e.g., the Keldysh parameter) are sufficiently large, which is in contrast to high-energy collisions $\sqrt{s_{\text{NN}}} \gtrsim 100 \text{ GeV}$, where the field is merely perturbative. Our results imply that the electromagnetic field may have phenomenological impacts on hadronic/QCD processes in intermediate-energy heavy-ion collisions and that heavy-ion collisions can be used as a new tool to explore strong-field physics in the nonperturbative regime.

I. INTRODUCTION

Super dense matter, such as that realized inside a neutron star or even denser, can be produced on Earth by colliding heavy ions at intermediate collision energies $\sqrt{s_{\text{NN}}} = \mathcal{O}(3 - 10 \text{ GeV})$. Such collision experiments have been performed in the Beam Energy Scan program at RHIC [1] and are planned worldwide (e.g., FAIR [2], NICA [3], HIAF [4], J-Parc-HI [5]) to reveal the extreme form of matter in the dense limit and to develop a better understanding of strong interaction, or quantum chromodynamics (QCD). These experimental programs have motivated various theoretical studies, which are mainly aimed at investigating the consequences of the high-density matter and the dynamics of how it can be created during the collisions, e.g., novel phases of QCD at finite density (see Ref. [6] for a review) and the development of various transport models to simulate the real-time collision dynamics such as RQMD [7], UrQMD [8, 9], JAM [10], and SMASH [11].

The purpose of this paper is, rather than pursuing the high-density physics as previously discussed, to point out that a strong electromagnetic field can be created in intermediate-energy heavy-ion collisions. The generation of such a strong electromagnetic field is of interest not only to hadron/QCD physics but also to the area of strong-field physics. For hadron/QCD physics, electromagnetic observables such as di-lepton yields [12–15], which are promising probes of nontrivial processes induced by the high-density matter, are naturally affected by the presence of a strong electromagnetic field. A correct estimation of the electromagnetic-field profile (and also its implementation into transport-model simulations; cf. Ref. [16, 17]) is, therefore, important when extracting/interpreting signals of the high-density matter from the actual experimental data. As for strong-

field physics, the generation of a strong electromagnetic field would provide a unique and novel opportunity to study quantum electrodynamics (QED) in the nonperturbative regime beyond the Schwinger limit $eE_{\text{cr}} := m_e^2 = (0.511 \text{ MeV})^2$ (with $e = |e|$ being the elementary electric charge, E electric field strength, and m_e the electron mass). Currently, strong-field physics is driven mainly by high-power lasers (see, e.g., Refs. [18, 19] for reviews). The focused laser intensity of $I = 1 \times 10^{23} \text{ W/cm}^2$ (corresponding to $E \approx 10^{-3} E_{\text{cr}}$) is the current world record [20], which is envisaged to be surpassed by the latest and future facilities such as Extreme Light Infrastructure (ELI) $I = \mathcal{O}(10^{25} \text{ W/cm}^2)$ [21]. Although the laser intensity is growing rapidly, it is and will remain, for at least the next decade, several orders of magnitude below the Schwinger limit E_{cr} . Therefore, it is difficult to study strong-field phenomena with current lasers. This means that a novel method or physical system to realize a strong electromagnetic field is highly demanded.

There exist a number of studies on the generation of a strong electromagnetic field at low- and high-energies both theoretically and experimentally. Let us briefly review them, so as to clarify our motivation to go to the intermediate energy. At low energies, due to the baryon stopping (i.e., the Landau picture [22, 23]), the collided ions stick together at the collision point and form up a gigantic ion with large atomic number $Z = \mathcal{O}(100)$, and thereby creates a strong Coulomb electric field of the order of $eE \sim (e^2/4\pi)Z/R^2 = \mathcal{O}((20 \text{ MeV})^2)$, where $R = \mathcal{O}(10 \text{ fm})$ is the typical radius of the gigantic ion. The produced field is weak compared to the hadron/QCD scale but is far surpassing the Schwinger limit of QED. Thus, it is expected to induce intriguing nonlinear QED processes such as the vacuum decay (see Ref. [24] for a recent analysis), experimental investigation of which has been done around 1980s but is not conclusive yet (see, e.g., Ref. [25] for possible interpretations of the experimental results). On the other hand, at high energies, the Bjorken picture [26] is valid rather than the Landau picture. The colliding ions penetrate with each other

* hidetoshi.taya@riken.jp

without sticking, and hence they do not form up a gigantic ion with large Z , unlike the low-energy case. Nevertheless, high-energy heavy-ion collisions are able to produce a very strong electromagnetic field with a different mechanism. Namely, due to a strong Lorentz contraction, the charge density ρ of the incident ions are enhanced by the Lorentz factor $\gamma \approx (\sqrt{s_{\text{NN}}}/1 \text{ GeV})/2$ as $\rho \rightarrow \gamma\rho \approx \gamma e\rho_0/2$, where $\rho_0 \approx 0.168 \text{ fm}^{-3}$ is the nuclear saturation density and we halved it because roughly the half of the ions is composed of charged nucleons (i.e., proton). Due to this enhancement, at central collision events, a strong Coulomb electric field with peak strength $eE \sim e\rho R$, which can exceed the hadron/QCD scale at the RHIC/LHC energy scale $\sqrt{s_{\text{NN}}} = \mathcal{O}(100 - 1000 \text{ GeV})$ and can achieve $eE = \mathcal{O}(100 - 1000 \text{ MeV})$ [27], is produced at the instant of when the colliding ions maximally overlap with each other [and also a strong magnetic field can be produced in non-central events at the moment when the ions pass through each other due to the Ampère law (see Ref. [28] for a review), which is experimentally utilized to test intriguing nonlinear QED processes such as the photon-photon scattering [29] and the linear Breit-Wheeler process [30, 31]].

Besides the field strength, there is a crucial difference between the low- and high-energy cases: the lifetime of the produced field. The lifetime of the field is long at low energies due to the baryon stopping. For example, it has been shown that the lifetime τ can reach $\tau = \mathcal{O}(100 - 1000 \text{ fm}/c)$ for collision energies close to the Coulomb barrier [32–34]. In contrast, the lifetime is extremely short at high energies. The produced field can survive only for the instance that the colliding ions pass through each other, which is strongly suppressed by the Lorentz factor as $\tau \sim R/\gamma = \mathcal{O}(0.1 - 0.01 \text{ fm}/c)$ at the RHIC/LHC energy.

The shortness of the lifetime τ significantly affects the *nonperturbativity* of the physics induced by the strong field. Namely, no matter how strong a field is, the physics has to be perturbative if it is short-lived. The low-order perturbation theory becomes sufficient in such a limit, and therefore the physics becomes “trivial” in the sense that it is not very different from the usual electromagnetic processes in the vacuum. Intuitively, this is simply because there is no time for the finite field to have multiple interactions with a particle. To be more quantitative, suppose we have, as an example, an electric field with peak strength E_0 and lifetime τ , and consider the vacuum pair production by such a strong electric field, vacuum $+ E \rightarrow e^+ + e^-$. For this case, the interplay between the nonperturbative and perturbative pair production is controlled by two dimensionless quantities [35–44],

$$\xi(m) := \frac{eE_0\tau}{m} \quad \text{and} \quad \nu := eE_0\tau^2. \quad (1)$$

Note that the parameter ξ is known as the Keldysh parameter [45] and, depending on the context, is also called the classical nonlinearity parameter [19]. The mass m is the mass of the particle to be produced. For enough

strong and long-lived fields such that $\xi, \nu \gg 1$, the pair production becomes nonperturbative in the sense that the rate of the pair production acquires a non-analytic dependence in e and E_0 as $\propto \exp[-(\text{const.}) \times (m^2/eE_0)]$. In the opposite limit, $\xi, \nu \ll 1$, it becomes purely perturbative, i.e., the low-order perturbative treatment becomes sufficient, meaning that the rate only has the power dependence in e and E_0 as $\propto (eE_0/m^2)^n$ ($n \in \mathbb{N}$). This example of the vacuum pair production clearly demonstrates that the supercriticality $eE_0 \gtrsim m^2$ is not sufficient to guarantee the nonperturbativity of strong-field processes. One must, thus, pay attention to the magnitude of the lifetime τ , or the resulting ξ and ν , as well, in addition to the strength E_0 . In terms of these nonperturbativity parameters (1), high-energy heavy-ion collisions at the typical RHI/LHC scale correspond to $\nu = \mathcal{O}(0.1)$ and $\xi = \mathcal{O}(100)$ for electron $m = m_e$ and $\mathcal{O}(1)$ for pion $m = m_\pi \approx 140 \text{ MeV}$. This means, although ξ can be nonperturbatively large for the QED scale $m = m_e$ due to the largeness of the field strength, ν always remains perturbatively small due to the shortness of the lifetime. For the hadron/QCD scale $m = m_\pi$, neither ξ nor ν can be nonperturbative. Therefore, in either case of QED or QCD, the pair production cannot be nonperturbative, implying that strong-field physics in the nonperturbative regime cannot be explored with the field produced in high-energy heavy-ion collisions. This naive argument, based on the “order parameters” of the vacuum pair production, is consistent with the actual experimental results. There have been observations of next-leading-order QED processes such as light-by-light scattering [29] and linear Breit-Wheeler pair production [30], in which the experimental results are consistent with perturbative QED calculations and no signatures of higher-order nonlinear effects have been detected.

We are now in a position to address the advantage of going to intermediate energies. It is natural to expect that the electromagnetic field generated in intermediate-energy heavy-ion collisions should have characteristics between the low- and high-energy cases. Namely, although the field strength would be weaker than that in the high-energy case, it should be stronger than that in the low-energy case. This means that the produced field will remain much stronger than the Schwinger limit of QED and may still be comparable to the hadron/QCD scale. As for lifetime, we can naturally expect that the field produced at intermediate energies should survive longer than the high-energy field. If this is true, it overcomes the problem of the short lifetime in the high energy limit, while maintaining a sufficiently large field strength. Hence, it enables us to access the strong-field physics in the nonperturbative regime. It is therefore worthwhile to investigate the generation of a strong electromagnetic field in intermediate-energy heavy-ion collisions and to make a realistic estimate to clarify whether this is the case, and, if so, how important it is.

Based on the motivations explained thus far, we would like to make a realistic estimate of the electromagnetic

field in intermediate-energy heavy-ion collisions based on a hadron-transport-model simulation. Indeed, neither the Landau nor the Bjorken picture is complete at intermediate energies (cf. Ref. [46] as a related for vorticity estimation). Accordingly, the generation mechanism of the electromagnetic field is more involved compared to the low- and high-energy limits, and hence it is impossible to carry out a simple analytic estimate at intermediate energies. In particular, dynamical effects become more important than the other energy regimes. For example, both elastic- and inelastic- multiple collision processes among the constituent nucleons are important to determine the sticking or non-sticking of the colliding ions. Hadrons are produced or decay during the time evolution through the inelastic processes, meaning that the simple but widely-used modeling based the Liénard-Wiechert potential of the electromagnetism is not applicable¹. The Lorentz contraction comes into play, unlike at the low energy limit, but is not as strong as that at the high energy, and therefore hadrons consisting of the colliding ions need to be treated as anisotropic objects with finite size. All of those dynamical effects can be taken into account systematically by using established hadron-transport models of heavy-ion collisions. In this work, we adopt JAM (Jet AA Microscopic transport model) [10, 47]. JAM is a hadronic cascade model to simulate the realtime dynamics of heavy-ion collisions. In addition to elastic hadron-hadron scatterings, inelastic processes are implemented in JAM via resonance production, soft-string excitation, and multiple mini-jet production, so that it can be applied to a wide range of collision energies from $\sqrt{s_{\text{NN}}} = \mathcal{O}(2 \text{ GeV})$ up to $\mathcal{O}(100 \text{ GeV})$. More details of JAM, including its comparison with other models, can be found in, e.g., Ref. [48].

This paper is organized as follows. We first explain our numerical setup and how we calculate the electromagnetic field with JAM in Sec. II. We then present the numerical results in Sec. III that include the spacetime profiles of the charge density (Sec. III A) and the resulting electromagnetic field (Sec. III B), the time evolution of the peak strength (Sec. III C), and the corresponding nonperturbativity parameters ξ and ν to demonstrate that the field is nonperturbatively strong (Sec. III D).

Notation: Our metric is the mostly minus, i.e., $g^{\mu\nu} := \text{diag}(+1, -1, -1, -1)$. Spatial three vectors are indicated by the bold letters, e.g., $x^\mu := (t, \mathbf{x})$ for spacetime coordinates and $A^\mu = (A^0, \mathbf{A})$ for the four-vector potential. We take the z -axis along the beam direction and write $\mathbf{x} =: (x, y, z) =: (\mathbf{x}_\perp, z)$.

II. NUMERICAL RECIPE

A. Calculation program

We wish to calculate the electric \mathbf{E} and magnetic \mathbf{B} fields in heavy-ion collisions at intermediate collision energies. The electromagnetic fields are given by

$$\mathbf{E} := -\partial_t \mathbf{A} - \nabla A^0 \quad \text{and} \quad \mathbf{B} := \nabla \times \mathbf{A}, \quad (2)$$

where A^μ is the retarded vector potential,

$$A^\mu(t, \mathbf{x}) := \frac{1}{4\pi} \int d^3 \mathbf{x}' \frac{J^\mu(t - |\mathbf{x} - \mathbf{x}'|, \mathbf{x}')}{|\mathbf{x} - \mathbf{x}'|}, \quad (3)$$

with J^μ being the total electric current carried by the charged particles in the collisions. In the present paper, we focus on the event-averaged values of $O = \mathbf{E}, \mathbf{B}$ and take the event averaging of Eq. (2) as

$$O := \frac{1}{N} \sum_{i=1}^N O_i, \quad (4)$$

where O_i is the event-by-event result and N is the total number of the events. Note that event-by-event fluctuations may be important in actual experiments (see also Ref. [27] for the high-energy case). For example, it has been argued in Refs. [49–51] that the maximum value of the baryon density can fluctuate event-by-event by more than 30 % at intermediate energies. Such large fluctuations of the baryon density ρ_B imply that the charge density $\rho/e \approx \rho_B/2$ should also fluctuate, and so does the resulting electromagnetic field. We shall report the event-by-event fluctuations of the electromagnetic fields in intermediate-energy heavy-ion collisions in a forthcoming paper.

We evaluate the electromagnetic field (2) numerically as follow. We first calculate the electric current J^μ with JAM. JAM calculates the phase-space distributions of hadrons in heavy-ion collisions $(\mathbf{x}_n(t), p_n^\mu(t))$, where the subscript n labels the hadrons in a collision event. The electric current J^μ at a position (t', \mathbf{x}') is then given in terms of the JAM phase-space distribution as

$$J^\mu(t', \mathbf{x}') := \sum_{n \in \text{all hadrons}} \frac{p_n^\mu(t')}{p_n^0(t')} \rho_n(t', \mathbf{x}'), \quad (5)$$

where ρ_n is the charge density of a single charged hadron. In JAM, hadrons are treated as if they are point-like, and hence the charge density of each hadron is localized strictly at \mathbf{x}_n . Hadrons are finite-sized in reality, motivated by which we smear the charge density by using the (relativistic) Gaussian distribution:

$$\rho_n(t', \mathbf{x}') := q_n \frac{\gamma_n(t')}{(\sqrt{2\pi}\sigma)^3} \times \exp \left[-\frac{|\mathbf{x}' - \mathbf{x}_n(t')|^2 + \gamma_n^2(t') (\mathbf{v}_n(t') \cdot (\mathbf{x}' - \mathbf{x}_n(t')))^2}{2\sigma^2} \right],$$

¹ The Liénard-Wiechert potential is explicitly dependent on time-derivatives of the trajectory of a charged particle $\mathbf{r}(t)$. Therefore, it is valid only if $\mathbf{r}(t)$ does not have any singularities, which means the particle cannot decay nor be produced during the time evolution.

where q_n is the electric charge, σ the smearing width, and $\gamma := \sqrt{1 - \mathbf{v}_n^2} := \sqrt{1 - (\mathbf{p}_n/p_n^0)^2}$ the Lorentz factor for the n -th hadron.

Once the electric current J^μ is obtained with JAM, can we calculate the retarded vector potential $A^\mu(t, \mathbf{x})$ by carrying out the \mathbf{x}' integration according to Eq. (3) at each spacetime point (t, \mathbf{x}) . This can be done with the standard numerical integration schemes, e.g., the Gauss-Legendre quadrature method, which we have adopted in this work.

In the default setting of JAM, the simulation starts from some initial time $t_{\text{in}} =: 0$, around which the incident ions start to collide. The JAM hadron phase-space data is, thus, available only later than t_{in} , so is the electric current J^μ (5). To perform the integration (3), the information of the electric current at time $t' = t - |\mathbf{x} - \mathbf{x}'|$, which can be earlier than t_{in} (when $|\mathbf{x} - \mathbf{x}'| > t - t_{\text{in}}$), is needed. To get the electric current before the initial time t_{in} , we extrapolate the phase-space data at the initial time $t = t_{\text{in}}$ by assuming that the hadrons that constitutes the incident ions go straight trajectories in the phase-space without any interactions:

$$\begin{aligned} \mathbf{x}_n(t < t_{\text{in}}) &:= \mathbf{x}_n(t_{\text{in}}) + (t - t_{\text{in}}) \frac{\mathbf{p}_n(t_{\text{in}})}{p_n^0(t_{\text{in}})}, \\ p_n^\mu(t < t_{\text{in}}) &:= p_n^\mu(t_{\text{in}}). \end{aligned} \quad (6)$$

Having calculated the retarded vector potential A^μ (3), can we obtain the electromagnetic fields via the differentiation (2). We in this work have adopted the standard central difference method with discretizing the \mathbf{x} coordinates with uniform meshes.

B. Numerical parameters

We summarize the numerical parameters adopted in the present work in Table I.

Using JAM, we simulate head-on (i.e., the impact parameter b is strictly fixed at $b = 0$) collisions of gold ions at the intermediate energies $\sqrt{s_{\text{NN}}} = 2.4, 3.0, 3.5, 3.9, 4.5, 5.2, 6.2, 7.2, 7.7, 9.2$, and 11.5. Several advanced options are available in JAM (such as the mean-field potential and hybrid hydrodynamic simulation), which we switch off and run JAM with the default setting to carry out the most basic hadronic cascade simulation. Note that, although we have concentrated on gold collisions as a first step to study the electromagnetic-field physics in intermediate-energy heavy-ion collisions, it is an interesting question to consider other ion species. In particular, deformed ions such as uranium and also asymmetric collisions such as Au + Cu (see, e.g., Refs. [52–54] at high energies) would be of interest, in which case the resulting electromagnetic fields should have a preferred direction due to the collision geometry, leading to observable effects such as a charged v_1 flow. The impact parameter dependence is also an interesting issue. With finite impact parameters

magnetic field shall dominate, while electric field does so in head-on events as we shall demonstrate below. We shall report the interplay of the dominance between the electric and magnetic fields in a future publication.

We have five numerical parameters in the evaluation of the electromagnetic field outlined in Sec. II A: the event number N , the smearing width σ , and the discretizations of t , \mathbf{x} , and \mathbf{x}' . To reduce the numerical cost, we are reluctant to take a relatively small event number $N = 100$, although the residual event-by-event fluctuations do not look very significant after the event averaging as we show later. We shall use the particular value of the smearing width $\sigma = 1$ fm for all hadron species, which is physically motivated by that the typical size of a nucleon is of the order of 1 fm and is a common choice in the literature. We have checked that the numerical results are less sensitive to the value of σ after taking the event averaging. We have also carefully checked that the lattice volumes of \mathbf{x} and \mathbf{x}' and the mesh sizes Δt , $\Delta \mathbf{x}$, and $\Delta \mathbf{x}'$ are sufficiently large and fine, respectively, in such a way that the numerical results are not sensitive to them. Note that, for the present parameters, a single numerical simulation (per energy) consumes $\mathcal{O}(20$ GB) RAM and takes about a few days with a standard GPU computer available on the market.

III. NUMERICAL RESULTS

We present the numerical results obtained with the recipe outlined in Sec. II. The main result is that an electric field which is non-perturbatively strong and long-lived can be created in intermediate-energy heavy-ion collisions; see Sec. III D, in particular Fig. 4. Before getting there, we discuss the generation of such a strong electric field step by step. We first demonstrate in Sec. III A that a highly-charged matter $\rho/e = \mathcal{O}(0.5 \text{ fm}^{-3})$, as a reminiscent of the dense baryon matter, is realized at intermediate energies. The highly-charged matter sources a strong electric field, whose spacetime profile shall be discussed in Sec. III B. We shall discuss the intensity and the lifetime of the produced electric field in detail in Sec. III C and show in Sec. III D that it can be nonperturbatively strong and long-lived, in contrast to what is realized at high energies.

A. Spacetime profile of the charge density

Fig. 1 shows the spacetime profile of the charge density. The key observation is that intermediate-energy heavy-ion collisions can realize a high charge density, typically of the order of $\rho/e = \mathcal{O}(0.5 \text{ fm}^{-3})$, for a relatively long time $\tau = \mathcal{O}(10 \text{ fm}/c)$. The magnitude of the charge density is roughly $\mathcal{O}(5)$ times greater than that of an usual charged ion at rest $\rho/e \approx \rho_0/2 \approx 0.08 \text{ fm}^{-3}$. This highly-charged matter sources a strong electric field, as we shall demonstrate later.

Ion species	^{197}Au
Collision energy $\sqrt{s_{\text{NN}}}$	2.4, 3.0, 3.5, 3.9, 4.5, 5.2, 6.2, 7.2, 7.7, 9.2, and 11.5 GeV
Impact parameter b	0 fm
Gaussian smearing width σ	1 fm
Total event number N	100
Discretization of time t	$t \in [0, 30]$ fm/c with $\Delta t = 0.5$ fm/c
Discretization of $\mathbf{x} = (x, y, z)$	$x, y, z \in [-30, +30]$ fm with $(n_x, n_y, n_z) = (121, 121, 121)$ sites (a uniform 3D lattice with $\Delta x = \Delta y = \Delta z = 0.5$ fm)
Discretization of $\mathbf{x}' = (x', y', z')$	$x', y', z' \in [-30, +30]$ fm with $(n_{x'}, n_{y'}, n_{z'}) = (120, 120, 120)$ sites (a non-uniform 3D lattice for the Gauss-Legendre quadrature method)

TABLE I. Parameters adopted in the numerical simulation.

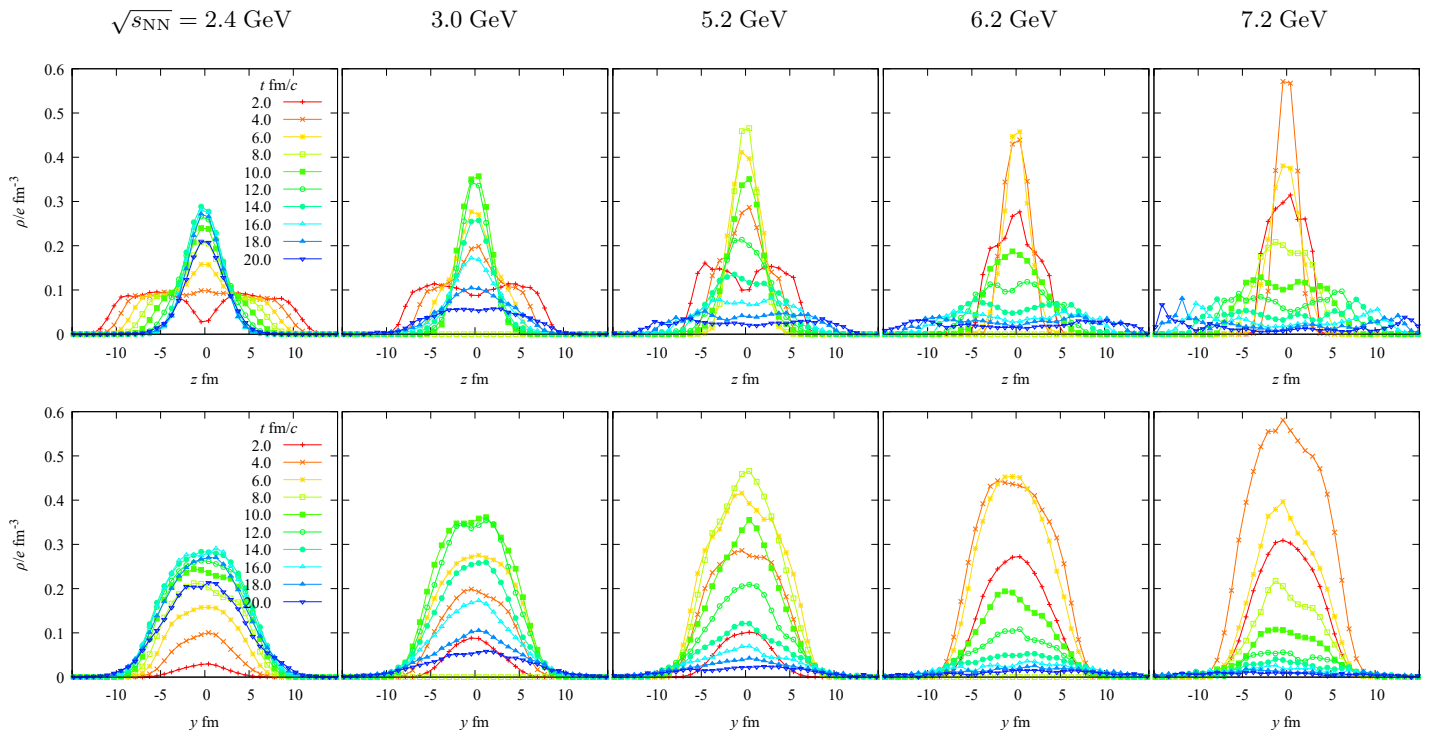


FIG. 1. The spacetime profile of electric charge density ρ/e at some selected collision energies ($\sqrt{s_{\text{NN}}} = 2.4, 3.0, 5.2, 6.2,$ and 7.2 GeV). The different colors indicate different time slices, ranging from 2 fm/c (red) to 20 fm/c (blue) with the increment of 2 fm/c. The top and bottom panels correspond to the distributions in the beam z direction at fixed $x = y = 0$ fm and in the transverse y direction at fixed $x = z = 0$ fm, respectively.

There are two important physics that contribute to the creation of the highly-charged matter. The first one is the Lorentz contraction. Due to the Lorentz contraction in the beam direction, the incident ions are not spherical, but anisotropic, and the longitudinal size is shortened as $R \rightarrow R/\gamma \approx (13 \text{ fm})/(\sqrt{s_{\text{NN}}}/1 \text{ GeV})$, where $R \approx (1.1 \text{ fm}) \times A^{1/3} \approx 6.4 \text{ fm}$ is the radius of a gold ion $A = 197$ at rest and we used $2\gamma \approx (\sqrt{s_{\text{NN}}}/1 \text{ GeV})$. Accordingly, the charge density is enhanced from that at rest by the Lorentz factor γ and hence becomes larger with collision energy as $\rho/e \approx \gamma \times \rho_0/2 \approx (0.04 \text{ fm}^{-3}) \times (\sqrt{s_{\text{NN}}}/1 \text{ GeV})$. The collision dynamics can roughly

be understood as an overlapping process of these two Lorentz-contracted ions. The maximum charge density is then achieved when the two ions maximally overlap with each other. As a zero-th order approximation, we may neglect the interaction between the ions and hence assume that they just pass through each other during a collision. Then, the maximum can be estimated as $\max \rho/e \approx 2 \times \rho/e \approx (0.08 \text{ fm}^{-3}) \times (\sqrt{s_{\text{NN}}}/1 \text{ GeV})$ and the time of which achieved as $t_{\text{max}} \approx 2R/\gamma \approx (26 \text{ fm}/c)/(\sqrt{s_{\text{NN}}}/1 \text{ GeV})$. These estimates are in rough agreement with the numbers shown Fig. 1.

The second is the interaction (i.e., the baryon stop-

ping), which is especially important in determining the lifetime of the highly-charged matter. The importance of the interaction is evident in Fig. 1. If it is non-interacting, the charge density should exhibit a two-peak structure after the maximum, i.e., the collided ions pass through each other and leave nothing in the mid-rapidity $z \approx 0$ (the Bjorken picture [26]). This is not the case in Fig. 1, which shows that the density is single-peaked at the mid-rapidity after the collision. In other words, the interaction makes it difficult for the colliding ions to penetrate each other, instead causing them to merge at the point of collision (the Landau picture [22, 23]). The interaction makes the lifetime τ of the highly-charged matter longer, compared to what is naively expected from the Bjorken picture $\tau \approx 2R/\gamma \approx (26 \text{ fm}/c)/(\sqrt{s_{\text{NN}}}/1 \text{ GeV})$. For example, at $\sqrt{s_{\text{NN}}} = 3.0 \text{ GeV}$, a relatively dense charge state $\rho/e \gtrsim 0.1 \text{ fm}^{-3}$ appears around $t \approx 2 \text{ fm}/c$ and survives until $t \approx 18 \text{ fm}/c$, whose lifetime $\tau \approx 18 - 2 \text{ fm}/c = 16 \text{ fm}/c$ is much longer than the naive Bjorken estimate $\tau \approx 26/3 \text{ fm}/c \approx 9 \text{ fm}/c$. The interaction effect is non-negligible and hence a highly-charged matter with a relatively long lifetime is realized in the intermediate energy values $\sqrt{s_{\text{NN}}} = \mathcal{O}(3 - 10 \text{ GeV})$.

B. Spacetime profile of the produced field

The highly-charged matter created in intermediate-energy heavy-ion collisions (see Fig. 1) produces a strong electric field. To show this, we plot, in Fig. 2, an electromagnetic Lorentz invariant,

$$\mathcal{F} := \mathbf{E}^2 - \mathbf{B}^2. \quad (7)$$

Note that the other invariant $\mathcal{G} := \mathbf{E} \cdot \mathbf{B}$ is found to be vanishing (up to residual event-by-event fluctuations). This is reasonable, since we have no electric current \mathbf{J} to produce a macroscopic magnetic field in central collision events and hence $\mathbf{B} \approx \mathbf{0}$. This also means

$$\mathcal{F} \approx \mathbf{E}^2. \quad (8)$$

That is, the produced field is electric, which is also evident in Fig. 2 that the sign of \mathcal{F} is always positive. It is thus convenient to introduce an *effective* electric field strength E_{eff} such that

$$E_{\text{eff}} := \sqrt{\mathcal{F}}. \quad (9)$$

Fig. 2 shows that the typical strength of the produced electric field is $e^2\mathcal{F} = \mathcal{O}(10^{6-7} \text{ MeV}^4)$, corresponding to $eE_{\text{eff}} = \mathcal{O}((30 - 60 \text{ MeV})^2)$. The created field is strong in the sense that it is far beyond the Schwinger limit of QED, $eE_{\text{cr}} = m_e^2 = (0.511 \text{ MeV})^2$. It is not supercritical to the hadron/QCD scale, $m_\pi \approx 140 \text{ MeV}$, but still is non-negligibly strong $eE_{\text{eff}} = \mathcal{O}((30\% \times m_\pi)^2)$, implying that it can affect hadron/QCD processes. The produced field also has a sufficiently large spacetime volume $\tau \times V = \mathcal{O}(10 \text{ fm}/c) \times \mathcal{O}((10 \text{ fm})^3)$ because of the baryon

stopping and of that the highly-charged matter has a macroscopically large spatial volume $\propto R^3/\gamma$.

Let us have a closer look at the spacetime structure of the produced field. First, the produced field has a donuts-like spatial structure, with peaks located around where the charge density vanishes (see Fig. 1). Namely, the effective field strength E_{eff} is zero at the collision point $\mathbf{x} \approx \mathbf{0}$, and, as going away from the collision point, E_{eff} increases almost linearly $\propto |\mathbf{x}|$ and then decreases quadratically $\propto 1/|\mathbf{x}|^2$ after it gets peaked. These are the direct consequences of the Gauss law $\text{div } \mathbf{E} = \rho$ (and is similar to the textbook exercise of the electric field produced by a uniformly charged sphere; see, e.g., Jackson [55]).

Second, the field strength in the transverse plane (the bottom panel in Fig. 2) increases with collision energy $\sqrt{s_{\text{NN}}}$, while that along the beam direction (the top panel in Fig. 2) is less sensitive to $\sqrt{s_{\text{NN}}}$ and is weaker than that in the transverse plane. This is reminiscent of the anisotropic structure of the charged matter due to the Lorentz contraction (see Fig. 1) and can be understood simply with the Gauss law. For simplicity, let us model the matter as a uniformly charged short cylinder, with radius $|\mathbf{x}_\perp| \leq R$ and length $|z| \leq R/\gamma$. Then, the Gauss law tells us that the field strength is maximized along the longitudinal direction at the ends of the charged cylinder $|z| = R/\gamma$ and the corresponding strength is $E = \rho R/\gamma$. Similarly, the maximum in the transverse plane is $E = \rho R/2$ at $|\mathbf{x}_\perp| = R$. Thus, the field strength in the transverse plane is enhanced by the anisotropy factor γ compared to that along the longitudinal axis.

Note that the charge density ρ can roughly be estimated as a simple overlapping of two Lorentz-contracted ions $\rho/e \approx \gamma\rho_0$ (see Sec. III A). Therefore, the maximum field strength over the space can be estimated, by using the simple modeling in the last paragraph, as $eE \approx e^2\gamma\rho_0 R/2 \approx ((\sqrt{s_{\text{NN}}}/1 \text{ GeV})^{1/2} \times 31 \text{ MeV})^2$. This simple estimate is in rough agreement with the actual numbers shown in Fig. 2 (albeit a bit overestimating, which we discuss in Sec. III C).

Third, the produced field expands faster with increasing collision energy. For lower energies $\sqrt{s_{\text{NN}}} \lesssim 5 \text{ GeV}$, the expansion is negligible and the field is roughly staying around the original position created. In contrast, for higher energies $\sqrt{s_{\text{NN}}} \gtrsim 5 \text{ GeV}$, the expansion becomes significant and the field moves almost at the speed of light. For the longitudinal expansion, this is a natural consequence that the Bjorken picture begins to be effective for higher energies. Although the Landau picture dominates in the intermediate-energy regime as we have explained in Sec. III A, it is also true that the Bjorken picture is becoming effective for higher energies, which can be observed in Fig. 1 from that the charged matter expands in the beam direction after created and begins to exhibit a two-peak structure at, e.g., $\sqrt{s_{\text{NN}}} = 7.2 \text{ GeV}$. The expansion also becomes faster in the transverse direction, simply because the typical kinetic energy of the particles in the collision system increases with collision

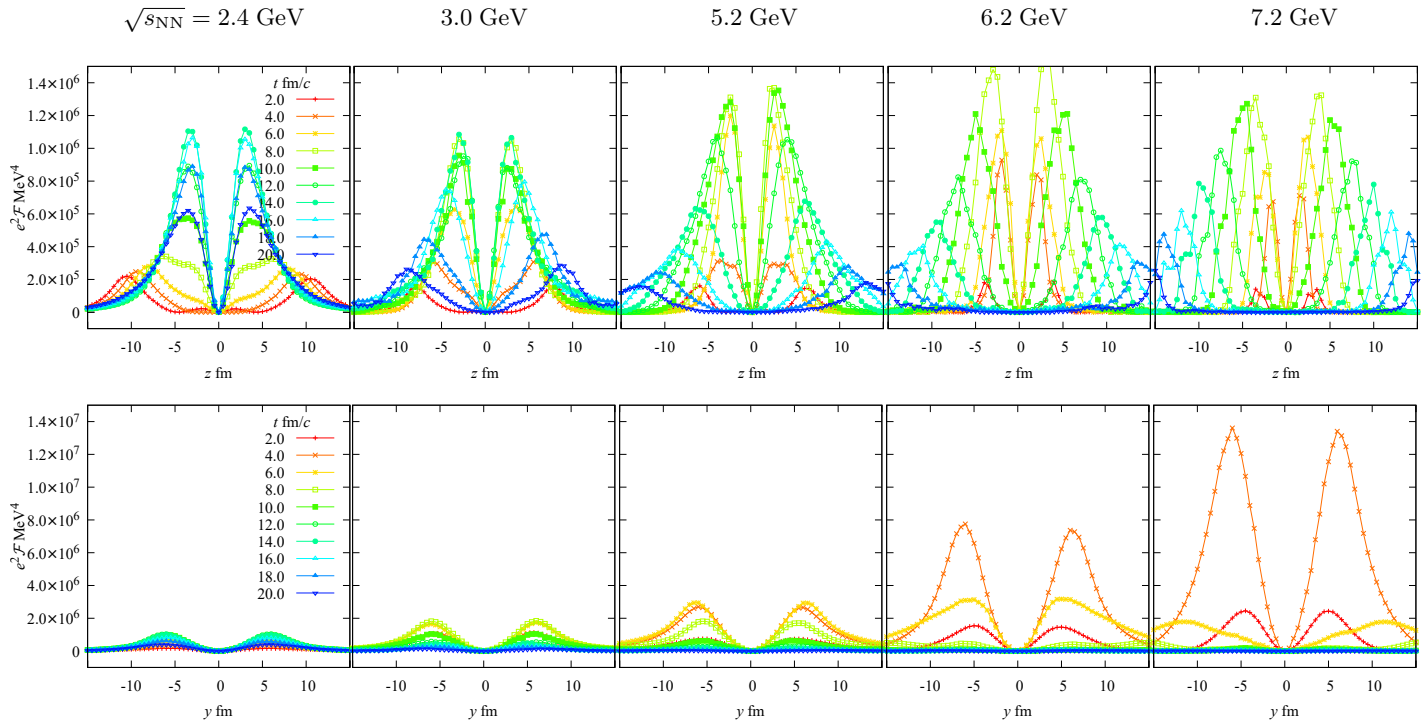


FIG. 2. The typical spacetime profile of the Lorentz invariant $\mathcal{F} = \mathbf{E}^2 - \mathbf{B}^2$ in intermediate-energy heavy-ion collisions. The plotting style is the same as Fig. 1: the time slices are indicated by the colors, and the top and bottom panels correspond to the distributions in the z and y directions, respectively. Note that the vertical scale is ten times greater in the bottom than in the top.

energy, allowing them to move faster.

C. Field strength

Having observed the generation of a strong electric field in intermediate-energy heavy-ion collisions, we turn to discuss more quantitative aspects of the produced field, in particular the peak field strength over the space.

We first discuss the time evolution of the field strength; see Fig. 3 (i). The strength gets maximized when the incident ions overlap with each other the most and shows up a sharp peak at around $t \approx (26 \text{ fm}/c)/(\sqrt{s_{\text{NN}}}/1 \text{ GeV})$ (within the non-interacting estimate; see Sec. III A). After the peak, the field strength decays rather slowly, as the collision remnant can survive in the mid-rapidity region due to the baryon stopping, and consequently the field can maintain its strength for a relatively long time. For example, a single ion at rest has a field strength of $eE \lesssim e^2(\rho_0/2)R/3 \approx 25 \text{ MeV}$, above which strength is kept for more than $\mathcal{O}(15 \text{ fm}/c)$ in intermediate-energy heavy-ion collisions.

The peak in Fig. 3 (i) becomes larger and sharper with increasing collision energy. This is also evident in Fig. 3 (ii) and (iii), which show, respectively, the maximum strength of the peak, $\max E_{\text{eff}}$, and the full width at the

half maximum of E_{eff} (FWHM),

$$\tau := \int_{E_{\text{eff}}(t) > \max E_{\text{eff}}/2} dt. \quad (10)$$

Note that the FWHM (10) can naturally be regarded as the lifetime of the field produced, and so we use Eq. (10) to *define* the lifetime in what follows.

The maximum peak field strength increases with collision energy [see Fig. 3 (ii)], as anticipated with the simple estimate $eE \approx e^2\gamma\rho_0R/2 \approx ((\sqrt{s_{\text{NN}}}/1 \text{ GeV})^{1/2} \times 31 \text{ MeV})^2$ that we made in Sec. III B. The key point is the enhancement of the charge density by the Lorentz contraction, which yields to the energy dependence. Although the simple estimate can capture the qualitative feature of the peak field strength, it fails at the quantitative level mainly because the modeling with a uniformly-charged short cylinder is crude. In particular, the actual charge distribution (see Fig. 1) is tailed and thus the charge extends more than the rigid cylinder distribution, which makes the actual peak field strength smaller than the simple estimate. Indeed, we find

$$\max \sqrt{eE_{\text{eff}}} = \left(\frac{\sqrt{s_{\text{NN}}}}{1 \text{ GeV}} \right)^{1/2} \times 22.38 \text{ MeV}, \quad (11)$$

which has the smaller coefficient (31 MeV \rightarrow 22 MeV), can fit the numerical result well.

The lifetime (10) decreases with collision energy [see Fig. 3 (ii)], which is essentially due to the Lorentz

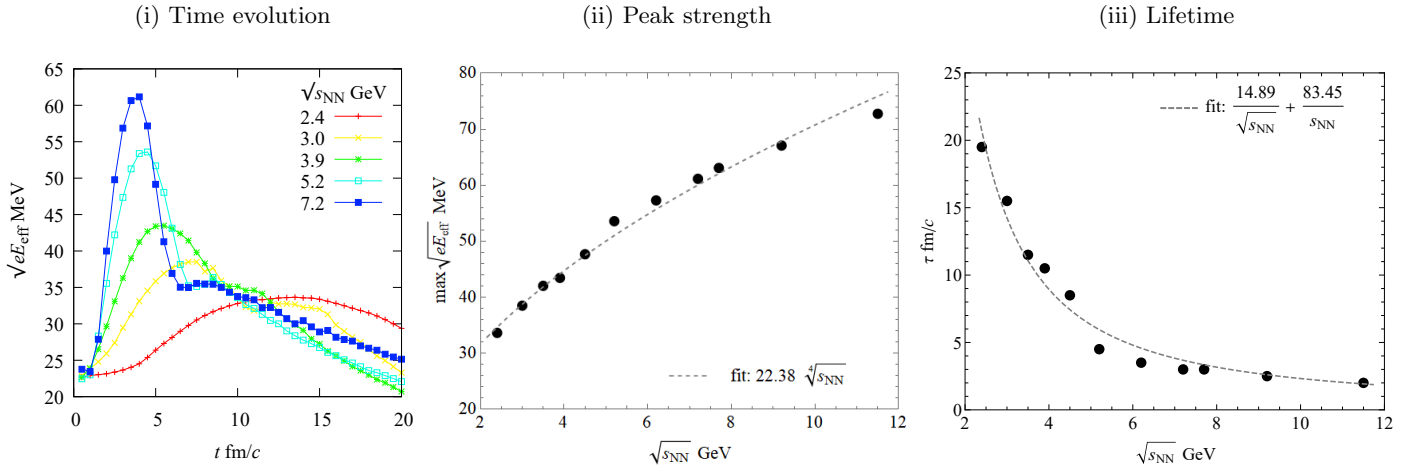


FIG. 3. The effective electric-field strength E_{eff} in intermediate-energy heavy-ion collisions. (i) The time evolution of E_{eff} for some selected collision energies. (ii) The maximum peak strength of E_{eff} , extracted from (i), plotted against collision energy $\sqrt{s_{\text{NN}}}$. (iii) The lifetime of the field, defined as FWHM of E_{eff} (10). The dashed lines in (ii) and (iii) are the numerical fittings of the obtained results.

contraction. The typical lifetime of the field is determined by that of the highly-charged matter. Therefore, $\tau \approx 2R/\gamma \approx (26 \text{ fm}/c)/(\sqrt{s_{\text{NN}}}/1 \text{ GeV})$ in the non-interacting limit (see Sec. III A). In reality, however, the interaction is important, especially for lower energies $\sqrt{s_{\text{NN}}} \lesssim 5 \text{ GeV}$, and thus the naive non-interacting estimate only gives a poor fit at the quantitative level. The interaction makes the lifetime considerably longer. We numerically find that such an interaction effect can be reproduced well with a higher-order term $\propto s_{\text{NN}}^{-1}$, added to the naive $s_{\text{NN}}^{-1/2}$ dependence, and the best fitting curve is found to be

$$\tau = \left(\frac{\sqrt{s_{\text{NN}}}}{1 \text{ GeV}} \right)^{-1} \times 14.89 \text{ fm}/c + \left(\frac{\sqrt{s_{\text{NN}}}}{1 \text{ GeV}} \right)^{-2} \times 83.45 \text{ fm}/c. \quad (12)$$

Note that the fitting curve (12) does not reproduce the coefficient of the naive estimate, 26 fm/c, even in the limit of $\sqrt{s_{\text{NN}}} \rightarrow \infty$. This can be understood as an indication that the Bjorken picture cannot be complete and the interaction is important at intermediate energies.

We emphasize that the lifetime is affected significantly by the interaction and made considerably longer, while the peak strength is less affected. Accordingly, the lifetime is more dependent on collision energy than the peak strength is. As we see shortly below, this shall be the essence why we can have a nonperturbatively strong electric field in intermediate-energy heavy-ion collisions, in particular for $\sqrt{s_{\text{NN}}} \lesssim 5 \text{ GeV}$, where the interaction becomes more important.

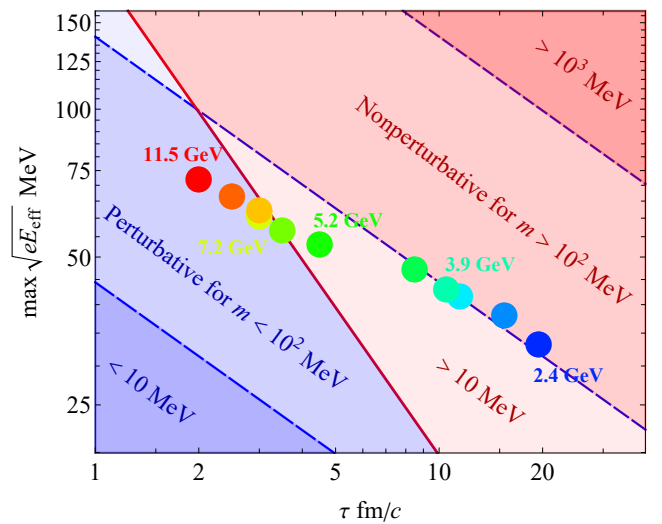


FIG. 4. Sensitivity plot for nonperturbativity of the produced electric field in intermediate-energy heavy-ion collisions. The dots represent the characteristics of the field ($\tau, \max \sqrt{eE_{\text{eff}}}$) extracted from Fig. 3 at each collision energy $\sqrt{s_{\text{NN}}}$, ranging from $\sqrt{s_{\text{NN}}} = 2.4 \text{ GeV}$ (blue), 3.0, 3.5, 3.9, 4.5, 5.2, 6.2, 7.2, 7.7, 9.2, to 11.5 GeV (red). The lines represent the nonperturbativity parameters (1): $1 = \xi(10 \text{ MeV})$ (bottom blue dashed), $1 = \xi(10^2 \text{ MeV})$ (middle blue dashed), $1 = \xi(10^3 \text{ MeV})$ (top blue dashed), and $1 = \nu$ (red). Those lines set “phase boundaries” of the nonperturbativity (of the vacuum pair production). The red regions $\xi(m), \nu > 1$ are nonperturbative (for mass scales m), while it is perturbative in the blue regions $\xi(m), \nu < 1$.

D. Nonperturbativity

As one of the possible “order parameters” for the nonperturbativity of a strong field, we calculate the non-

perturbativity parameters ξ and ν (1) and discuss the sensitivity region in intermediate-energy heavy-ion collisions. The result is shown in Fig. 4. It clearly shows that intermediate-energy heavy-ion collisions, in particular with $\sqrt{s_{\text{NN}}} \lesssim 5$ fm/c, can access the nonperturbative regime. Namely, although higher collision energies $\sqrt{s_{\text{NN}}} \gtrsim 5$ fm/c are advantageous in that the field strength is strong, which can be comparable even to the hadron/QCD scale, it is disadvantageous in that the lifetime gets extremely short and accordingly the physics has to be purely perturbative. On the other hand, although the achievable field strength is weaker in lower collision energies $\sqrt{s_{\text{NN}}} \lesssim 5$ fm/c, it is still much stronger than the critical strength of QED and is non-negligible to the hadron/QCD scale, and also the lifetime can be very long, allowing us to enter the nonperturbative regime.

Using the fitting results, Eq. (11) for $\max \sqrt{eE_{\text{eff}}}$ and Eq. (12) for τ , we find that the nonperturbativity parameters ξ and ν can be parametrized as

$$\xi = \frac{37.27 \text{ MeV} + \left(\frac{\sqrt{s_{\text{NN}}}}{1 \text{ GeV}}\right)^{-1} \times 208.93 \text{ MeV}}{m}, \quad (13)$$

$$\nu = \left(9.34 \times s_{\text{NN}}^{-3/4} + 1.67 \times s_{\text{NN}}^{-1/4}\right)^2 \approx 87.18 \times s_{\text{NN}}^{-3/2}.$$

It is clear that both ξ and ν increase with decreasing collision energy $\sqrt{s_{\text{NN}}}$, i.e., lowering the energy is more beneficial for the nonperturbativity. The interaction effect in the Landau stopping regime gives a significant contribution here, as the dominant $s_{\text{NN}}^{-1/2}$ and $s_{\text{NN}}^{-3/2}$ dependencies in ξ and ν , respectively, arise from the s_{NN}^{-1} term in the lifetime τ (12), which we have added to account for the interaction effect.

For clarity, we remark that the meaning of the “nonperturbative” in Fig. 4 is just that the physical observable (or, to be precise, the number of particle and anti-particle pairs with mass m produced from the vacuum by a strong electric field E [35–44]) acquires a nonperturbative dependence $\propto \exp[-(\text{const}) \times m^2/eE]$. In other words, being in the nonperturbative regime does not necessarily guarantee the significance of the nonperturbative effect and/or its detectability in actual experiments. In fact, unless we have a field strength comparable to or exceeding the mass scale $eE \gtrsim m^2$, the effect is strongly suppressed by the exponential $\propto \exp[-(\text{const}) \times m^2/eE]$ and is simply negligible. For example, the lowest energy $\sqrt{s_{\text{NN}}} = 2.4$ GeV is nonperturbative for $m \approx 100$ MeV, but the field strength is at most $eE = \mathcal{O}((30 \text{ MeV})^2)$ and therefore the corresponding nonperturbative effect is suppressed as $\propto \exp[-(100/30)^2] = \mathcal{O}(10^{-5})$. The exponential suppression becomes mild for $m^2 \lesssim eE$ and hence $m \lesssim 30$ MeV is the mass region for $\sqrt{s_{\text{NN}}} = 2.4$ GeV such that the nonperturbative effect becomes significant and/or would be detectable in actual experiments. In this sense of the significance/detectability, the highest collision energy closest to the phase boundary is the most advantageous to observe a nonperturbative effect with the largest m . According to Fig. 4, such a collision energy

is $\sqrt{s_{\text{NN}}} \approx 5$ GeV and the corresponding mass region is $m \lesssim 50$ MeV.

IV. SUMMARY AND DISCUSSION

We have studied the generation of a strong electric field in head-on collisions of gold ions at intermediate energies $\mathcal{O}(3 - 10 \text{ GeV})$, based on a hadron transport-model simulation JAM. Our main statement is that intermediate-energy heavy-ion collisions are useful not only to study the densest matter on Earth but also to study strong-field physics in the nonperturbative regime. Namely, we have shown that the produced electric field is as strong as $eE_{\text{eff}} = \mathcal{O}((30 - 60 \text{ MeV})^2)$ (see Figs. 2 and 3), which is supercritical to the Schwinger limit of QED and is still non-negligibly strong compared to the hadron/QCD scale. The produced field is sufficiently long-lived and enables us to explore the nonperturbative regime of strong-field physics up to mass scale of $m \lesssim 50$ MeV (see Fig. 4), which is inaccessible with any other experiments at the present such as high-power lasers and high-energy heavy-ion collisions.

The present work is just a first step, e.g., towards realistic estimations of nonperturbative strong-field effects and/or modifications to hadron/QCD dynamics in intermediate-energy heavy-ion collisions. Let us briefly discuss possible directions and outlook below.

First, it is a very exciting possibility that we can study strong-field physics by using intermediate-energy heavy-ion collisions, since such a truly strong-field regime above the QED critical field strength cannot be achieved with any other experiments at the present. One of the most intriguing targets is the Schwinger effect, i.e., the nonperturbative vacuum pair production, which was predicted more than seventy years ago [56, 57] and applied to various contexts, including the Hawking radiation in a black hole [58], but has never been observed in actual experiments yet. As we have shown, intermediate-energy heavy-ion collisions generate a nonperturbatively strong electric field that is able to induce the Schwinger effect, and therefore can in principle be used as a new experimental setup to test it. It is, therefore, an important task to predict possible experimental signatures of the Schwinger effect in heavy-ion collisions. Naively, we can expect a thermal-like excess in electron/positron yields (and possibly muon/antimuon as well) in the very low-momentum regime $|\mathbf{p}| \lesssim \sqrt{eE}$, where $eE \approx \mathcal{O}((50 \text{ MeV})^2)$ for intermediate energies, as the celebrated Schwinger formula [57] says that the momentum spectrum of the produced pairs is $\propto \exp[-\pi(m^2 + \mathbf{p}^2)/eE]$. It is worthwhile to quantify this excess, the zero-th order evaluation of which can be done with the Schwinger formula, or the locally-constant-field approximation [43, 59–63]. For a more realistic estimation, it would be necessary to include various modifications due to, e.g., spatial inhomogeneities, polarization of the field, and event-by-event fluctuations in actual ex-

periments. Meanwhile, such a low-momentum spectrum would naturally be contaminated by hadronic processes such as the Dalitz decay, $\pi^0 \rightarrow \gamma + e^- + e^+$, and therefore it poses an experimental challenge how to eliminate those backgrounds to test the Schwinger effect with heavy-ion collisions.

Second, from the standpoint of studying the densest matter and/or the QCD phase diagram with intermediate-energy heavy-ion collisions, the existence of the strong electric field is a noise that needs to be tamed, since electromagnetic observables such as charged flow and di-lepton yields are naturally affected. For example, it has been argued in Ref. [14] that di-lepton yields are considerably enhanced due to the existence of the QCD critical point in the low invariant-mass regime $\lesssim 100$ MeV and that such an enhancement can be used as an experimental signature of the QCD critical point. Meanwhile, it is natural to expect additional contributions to such a low-energy di-lepton spectrum due to strong-field effects, including the Schwinger effect that we have mentioned in the last paragraph and other effects such as the nonlinear Breit-Wheeler process $\gamma + E \rightarrow e^+ + e^-$, but they have never been estimated. Considering the fact that so far no clear signals of the critical point, or novel phases of QCD, have been found in the Beam Energy Scan program at RHIC [1], it is reasonable to assume that the signals, if they exist, should be small. Therefore, possible contaminations must be removed beforehand as much as possible, which of course

applies to the strong-field effects.

Third, our result suggests that intermediate-energy heavy-ion collisions may provide a unique opportunity to study QCD in a new extreme condition characterized by a strong electric field. Although it would be difficult to have something very nontrivial for the hadronic scale $m = \mathcal{O}(100 - 1000 \text{ MeV})$, which is greater than the achievable field strength $eE = \mathcal{O}((30 - 60 \text{ MeV})^2)$, it is very reasonable to expect nonperturbative changes in the deconfined phase of QCD, where the typical mass scale m is the current quark mass $\mathcal{O}(1 \text{ MeV})$. There are a number of studies of QCD in a strong magnetic field and it has been predicted that the QCD phase diagram is modified significantly (see, e.g., Ref. [64]). In contrast, only a few exist for a strong electric field [65, 66] and there has been no consensus on what would happen, meaning that it requires further theoretical study.

ACKNOWLEDGMENTS

The authors thank Kensuke Homma, Asanosuke Jinno, Masakiyo Kiatazawa, and Yasushi Nara for enlightening discussions. This work is supported by JSPS KAKENHI under grant No. 22K14045 (HT), the RIKEN special postdoctoral researcher program (HT), JST SPRING (grant No. JPMJSP2138) (TN), and Multidisciplinary PhD Program for Pioneering Quantum Beam Application (TN).

-
- [1] A. Aparin (STAR Collaboration), STAR Experiment Results From Beam Energy Scan Program, *Phys. Atom. Nucl.* **86**, 758 (2023).
- [2] <https://fair-center.de/>.
- [3] <https://nica.jinr.ru/>.
- [4] <https://english.imp.cas.cn/research/facilities/HIAF/>.
- [5] <https://asrc.jaea.go.jp/soshiki/gr/hadron/jparc-hi/index.html>.
- [6] K. Fukushima and T. Hatsuda, The phase diagram of dense QCD, *Rept. Prog. Phys.* **74**, 014001 (2011), [arXiv:1005.4814 \[hep-ph\]](https://arxiv.org/abs/1005.4814).
- [7] H. Sorge, Flavor production in Pb (160-A/GeV) on Pb collisions: Effect of color ropes and hadronic rescattering, *Phys. Rev. C* **52**, 3291 (1995), [arXiv:nucl-th/9509007](https://arxiv.org/abs/nucl-th/9509007).
- [8] S. A. Bass *et al.*, Microscopic models for ultrarelativistic heavy ion collisions, *Prog. Part. Nucl. Phys.* **41**, 255 (1998), [arXiv:nucl-th/9803035](https://arxiv.org/abs/nucl-th/9803035).
- [9] M. Bleicher *et al.*, Relativistic hadron hadron collisions in the ultrarelativistic quantum molecular dynamics model, *J. Phys. G* **25**, 1859 (1999), [arXiv:hep-ph/9909407](https://arxiv.org/abs/hep-ph/9909407).
- [10] Y. Nara, N. Otuka, A. Ohnishi, K. Niita, and S. Chiba, Study of relativistic nuclear collisions at AGS energies from p + Be to Au + Au with hadronic cascade model, *Phys. Rev. C* **61**, 024901 (2000), [arXiv:nucl-th/9904059](https://arxiv.org/abs/nucl-th/9904059).
- [11] J. Weil *et al.* (SMASH), Particle production and equilibrium properties within a new hadron transport approach for heavy-ion collisions, *Phys. Rev. C* **94**, 054905 (2016), [arXiv:1606.06642 \[nucl-th\]](https://arxiv.org/abs/1606.06642).
- [12] C. Sasaki, Signatures of chiral symmetry restoration in dilepton production, *Phys. Lett. B* **801**, 135172 (2020), [arXiv:1906.05077 \[hep-ph\]](https://arxiv.org/abs/1906.05077).
- [13] O. Savchuk, A. Motornenko, J. Steinheimer, V. Vovchenko, M. Bleicher, M. Gorenstein, and T. Galatyuk, Enhanced dilepton emission from a phase transition in dense matter, *J. Phys. G* **50**, 125104 (2023), [arXiv:2209.05267 \[nucl-th\]](https://arxiv.org/abs/2209.05267).
- [14] T. Nishimura, M. Kitazawa, and T. Kunihiro, Enhancement of dilepton production rate and electric conductivity around the QCD critical point, *PTEP* **2023**, 053D01 (2023), [arXiv:2302.03191 \[hep-ph\]](https://arxiv.org/abs/2302.03191).
- [15] T. Nishimura, Y. Nara, and J. Steinheimer, Enhanced Dilepton production near the color superconducting phase and the QCD critical point, (2023), [arXiv:2311.14135 \[hep-ph\]](https://arxiv.org/abs/2311.14135).
- [16] Y. Sun, Y. Wang, Q. Li, and F. Wang, Effect of internal magnetic field on collective flow in heavy ion collisions at intermediate energies, *Phys. Rev. C* **99**, 064607 (2019), [arXiv:1905.12492 \[nucl-th\]](https://arxiv.org/abs/1905.12492).
- [17] G.-F. Wei, C. Liu, X.-W. Cao, Q.-J. Zhi, W.-J. Xiao, C.-Y. Long, and Z.-W. Long, Necessity of self-consistent calculations for the electromagnetic field in probing the nuclear symmetry energy using pion observables in heavy-ion collisions, *Phys. Rev. C* **103**, 054607 (2021), [arXiv:2105.01866 \[nucl-th\]](https://arxiv.org/abs/2105.01866).

- [18] A. Di Piazza, C. Muller, K. Z. Hatsagortsyan, and C. H. Keitel, Extremely high-intensity laser interactions with fundamental quantum systems, *Rev. Mod. Phys.* **84**, 1177 (2012), arXiv:1111.3886 [hep-ph].
- [19] A. Fedotov, A. Ilderton, F. Karbstein, B. King, D. Seipt, H. Taya, and G. Torgrimsson, Advances in QED with intense background fields, *Phys. Rept.* **1010**, 1 (2023), arXiv:2203.00019 [hep-ph].
- [20] J. W. Yoon, Y. G. Kim, I. W. Choi, J. H. Sung, H. W. Lee, S. K. Lee, and C. H. Nam, Realization of laser intensity over 10^{23} w/cm², *Optica* **8**, 630 (2021).
- [21] The white paper of ELI can be find at <https://www.eli-np.ro/whitebook.php>.
- [22] E. Fermi, High Energy Nuclear Events, *Progress of Theoretical Physics* **5**, 570 (1950), <https://academic.oup.com/ptp/article-pdf/5/4/570/5430247/5-4-570.pdf>.
- [23] L. D. Landau, On the multiparticle production in high-energy collisions, *Izv. Akad. Nauk Ser. Fiz.* **17**, 51 (1953).
- [24] I. A. Maltsev, V. M. Shabaev, R. V. Popov, Y. S. Kozhedub, G. Plunien, X. Ma, T. Stöhlker, and D. A. Tumafov, How to observe the vacuum decay in low-energy heavy-ion collisions, *Phys. Rev. Lett.* **123**, 113401 (2019), arXiv:1903.08546 [physics.atom-ph].
- [25] J. Rafelski, J. Kirsch, B. Müller, J. Reinhardt, and W. Greiner, Probing QED Vacuum with Heavy Ions, *FIAS Interdisc. Sci. Ser.*, 211 (2017), arXiv:1604.08690 [nucl-th].
- [26] J. D. Bjorken, Highly Relativistic Nucleus-Nucleus Collisions: The Central Rapidity Region, *Phys. Rev. D* **27**, 140 (1983).
- [27] W.-T. Deng and X.-G. Huang, Event-by-event generation of electromagnetic fields in heavy-ion collisions, *Phys. Rev. C* **85**, 044907 (2012), arXiv:1201.5108 [nucl-th].
- [28] K. Hattori and X.-G. Huang, Novel quantum phenomena induced by strong magnetic fields in heavy-ion collisions, *Nucl. Sci. Tech.* **28**, 26 (2017), arXiv:1609.00747 [nucl-th].
- [29] M. Aaboud *et al.* (ATLAS), Evidence for light-by-light scattering in heavy-ion collisions with the ATLAS detector at the LHC, *Nature Phys.* **13**, 852 (2017), arXiv:1702.01625 [hep-ex].
- [30] J. Adam *et al.* (STAR), Measurement of e^+e^- Momentum and Angular Distributions from Linearly Polarized Photon Collisions, *Phys. Rev. Lett.* **127**, 052302 (2021), arXiv:1910.12400 [nucl-ex].
- [31] J. D. Brandenburg, J. Seger, Z. Xu, and W. Zha, Report on progress in physics: observation of the Breit–Wheeler process and vacuum birefringence in heavy-ion collisions, *Rept. Prog. Phys.* **86**, 083901 (2023), arXiv:2208.14943 [hep-ph].
- [32] T. Maruyama, A. Bonasera, M. Papa, and S. Chiba, Formation and decay of superheavy systems, *Eur. Phys. J. A* **14**, 191 (2002), arXiv:nucl-th/0107021.
- [33] V. I. Zagrebaev, Y. T. Oganessian, M. G. Itkis, and W. Greiner, Superheavy nuclei and quasi-atoms produced in collisions of transuranium ions, *Phys. Rev. C* **73**, 031602 (2006).
- [34] J. Tian, X. Wu, K. Zhao, Y. Zhang, and Z. Li, Properties of the composite systems formed in the reactions of U-238 + U-238 and Th-232 + Cf-250, *Phys. Rev. C* **77**, 064603 (2008).
- [35] V. S. Popov, Production of e^+e^- Pairs in an Alternating External Field, *JETP Lett.* **13**, 185 (1971).
- [36] V. S. Popov, Pair production in a variable external field (quasiclassical approximation), *Zh. Eksp. Teor. Fiz.* **61**, 1334 (1971).
- [37] E. Brezin and C. Itzykson, Pair Production in Vacuum by an Alternating Field, *Phys. Rev. D* **2**, 1191 (1970).
- [38] G. V. Dunne and C. Schubert, Worldline instantons and pair production in inhomogeneous fields, *Phys. Rev. D* **72**, 105004 (2005), arXiv:hep-th/0507174.
- [39] G. V. Dunne, Q.-h. Wang, H. Gies, and C. Schubert, Worldline instantons. II. The Fluctuation prefactor, *Phys. Rev. D* **73**, 065028 (2006), arXiv:hep-th/0602176.
- [40] T. Oka, Nonlinear doublon production in a Mott insulator: Landau-Dykhne method applied to an integrable model, *Phys. Rev. B* **86**, 075148 (2012), arXiv:1105.3145 [cond-mat.str-el].
- [41] H. Taya, H. Fujii, and K. Itakura, Finite pulse effects on e^+e^- pair creation from strong electric fields, *Phys. Rev. D* **90**, 014039 (2014), arXiv:1405.6182 [hep-ph].
- [42] F. Gelis and N. Tanji, Schwinger mechanism revisited, *Prog. Part. Nucl. Phys.* **87**, 1 (2016), arXiv:1510.05451 [hep-ph].
- [43] I. A. Aleksandrov, G. Plunien, and V. M. Shabaev, Locally-constant field approximation in studies of electron-positron pair production in strong external fields, *Phys. Rev. D* **99**, 016020 (2019), arXiv:1811.01419 [hep-ph].
- [44] H. Taya, T. Fujimori, T. Misumi, M. Nitta, and N. Sakai, Exact WKB analysis of the vacuum pair production by time-dependent electric fields, *JHEP* **03**, 082, arXiv:2010.16080 [hep-th].
- [45] L. V. Keldysh, Ionization in the Field of a Strong Electromagnetic Wave, *J. Exp. Theor. Phys.* **20**, 1307 (1965).
- [46] X.-G. Deng, X.-G. Huang, Y.-G. Ma, and S. Zhang, Vorticity in low-energy heavy-ion collisions, *Phys. Rev. C* **101**, 064908 (2020), arXiv:2001.01371 [nucl-th].
- [47] The latest version of JAM (JAM2) is publically available at <https://gitlab.com/transportmodel/jam2>.
- [48] H. Wolter *et al.* (TMEP), Transport model comparison studies of intermediate-energy heavy-ion collisions, *Prog. Part. Nucl. Phys.* **125**, 103962 (2022), arXiv:2202.06672 [nucl-th].
- [49] A. Ohnishi, Physics of heavy-ion collisions at JHF, in *Workshop on Nuclear Physics at JHF* (2002) pp. 56–65.
- [50] A. Ohnishi, Approaches to qcd phase diagram; effective models, strong-coupling lattice qcd, and compact stars, in *Journal of Physics: Conference Series*, Vol. 668 (IOP Publishing, 2016) p. 012004.
- [51] A. Jinno, M. Kiatazawa, Y. Nara, T. Nishimura, and H. Taya, Spacetime volume of the dense baryon matter in intermediate-energy heavy-ion collisions, .
- [52] Y. Hirono, M. Hongo, and T. Hirano, Estimation of electric conductivity of the quark gluon plasma via asymmetric heavy-ion collisions, *Phys. Rev. C* **90**, 021903 (2014), arXiv:1211.1114 [nucl-th].
- [53] V. Voronyuk, V. D. Toneev, S. A. Voloshin, and W. Cassing, Charge-dependent directed flow in asymmetric nuclear collisions, *Phys. Rev. C* **90**, 064903 (2014), arXiv:1410.1402 [nucl-th].
- [54] L. Adamczyk *et al.* (STAR), Charge-dependent directed flow in Cu+Au collisions at $\sqrt{s_{NN}} = 200$ GeV, *Phys. Rev. Lett.* **118**, 012301 (2017), arXiv:1608.04100 [nucl-ex].
- [55] J. D. Jackson, *Classical Electrodynamics* (Wiley, 1998).
- [56] F. Sauter, Über das Verhalten eines Elektrons im homogenen elektrischen Feld nach der relativistischen Theorie

- Diracs, *Z. Phys.* **69**, 742 (1931).
- [57] J. S. Schwinger, On gauge invariance and vacuum polarization, *Phys. Rev.* **82**, 664 (1951).
- [58] S. W. Hawking, Particle Creation by Black Holes, *Commun. Math. Phys.* **43**, 199 (1975), [Erratum: *Commun. Math. Phys.* 46, 206 (1976)].
- [59] S. S. Bulanov, N. B. Narozhny, V. D. Mur, and V. S. Popov, On $e^+ e^-$ pair production by a focused laser pulse in vacuum, *Phys. Lett. A* **330**, 1 (2004), [arXiv:hep-ph/0403163](#).
- [60] H. Gies and F. Karbstein, An Addendum to the Heisenberg-Euler effective action beyond one loop, *JHEP* **03**, [arXiv:1612.07251](#) [hep-th].
- [61] S. P. Gavrilov and D. M. Gitman, Vacuum instability in slowly varying electric fields, *Phys. Rev. D* **95**, 076013 (2017), [arXiv:1612.06297](#) [hep-th].
- [62] F. Karbstein, Heisenberg-Euler effective action in slowly varying electric field inhomogeneities of Lorentzian shape, *Phys. Rev. D* **95**, 076015 (2017), [arXiv:1703.08017](#) [hep-ph].
- [63] D. G. Sevostyanov, I. A. Aleksandrov, G. Plunien, and V. M. Shabaev, Total yield of electron-positron pairs produced from vacuum in strong electromagnetic fields: validity of the locally constant field approximation, (2020), [arXiv:2012.10751](#) [hep-ph].
- [64] J. O. Andersen, W. R. Naylor, and A. Tranberg, Phase diagram of QCD in a magnetic field: A review, *Rev. Mod. Phys.* **88**, 025001 (2016), [arXiv:1411.7176](#) [hep-ph].
- [65] A. Yamamoto, Lattice QCD with strong external electric fields, *Phys. Rev. Lett.* **110**, 112001 (2013), [arXiv:1210.8250](#) [hep-lat].
- [66] G. Endrodi and G. Marko, QCD phase diagram and equation of state in background electric fields, *Phys. Rev. D* **109**, 034506 (2024), [arXiv:2309.07058](#) [hep-lat].

On the significance of radiative corrections on measurements of the EMC effect

S. Moran,¹ M. Arratia,¹ J. Arrington,² D. Gaskell,³ and B. Schmookler¹

¹*Department of Physics and Astronomy, University of CA, Riverside, California 92521, USA*

²*Lawrence Berkeley National Laboratory, Berkeley, CA 94720, USA*

³*Thomas Jefferson National Accelerator Facility, Newport News, VA 23606, USA*

(Dated: February 28, 2024)

Analyzing global data on the EMC effect, which denotes differences in parton distribution functions in nuclei compared to unbound nucleons, reveals tensions. Precise measurements at Jefferson Lab, studying both x and A dependence, show systematic discrepancies among experiments, making the extraction of the A dependence of the EMC effect sensitive to the selection of datasets. By comparing various methods and assumptions used to calculate radiative corrections, we have identified differences that, while not large, significantly impact the EMC ratios and show that using a consistent radiative correction procedure resolves this discrepancy, leading to a more coherent global picture, and allowing for a more robust extraction of the EMC effect for infinite nuclear matter.

INTRODUCTION

Precision measurement of deep-inelastic scattering (DIS) from nucleons and nuclei allows for an extraction of parton distribution functions (pdfs). Early measurements of the nuclear pdfs demonstrated that the quark distributions in iron were not simply the sum of the distribution arising from its constituent protons and neutrons [1]. Since the initial observation of this “EMC effect”, additional measurements have been made for a wide range of nuclei [2–8] and many different explanations have been proposed to explain this observation [6, 9–13]. One of these measurements [4] demonstrated an unexpected, non-trivial dependence on nuclear structure in light nuclei [4] which corresponded to a similar dependence in the number of short-range correlations (SRCs) [14, 15], renewing interest in precision measurements of the A dependence of the EMC effect.

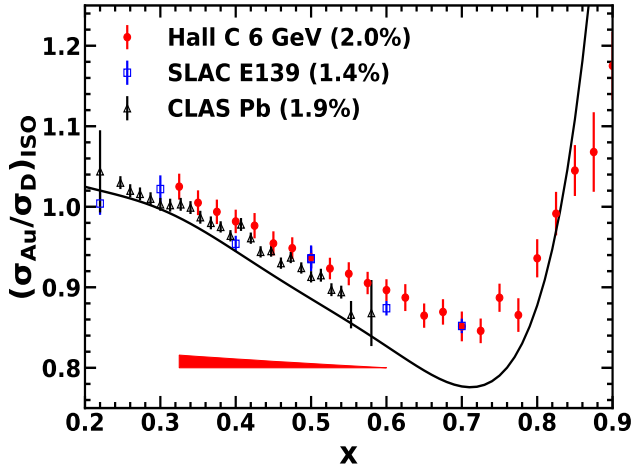


FIG. 1. EMC ratios for gold and lead [2, 5, 6] after applying uniform isoscalar corrections from [6]. The number in parentheses is the normalization uncertainty, the solid curve is the parameterization of Ref. [2], and the red band indicates the correlated systematic uncertainty for Ref. [6].

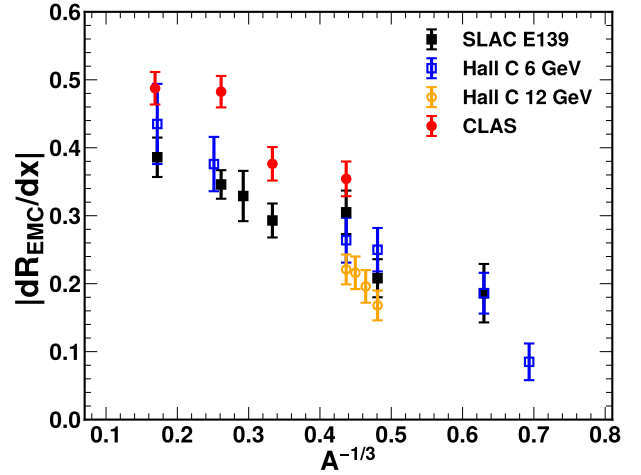


FIG. 2. EMC slopes from world’s data, with the common isoscalar correction from Ref. [6] applied to all data sets.

Figure 1 shows the EMC ratios from various experiments for heavy ($A \approx 200$) nuclei after applying consistent isoscalar corrections [6]. The size of the EMC effect is typically parameterized by taking the slope of the EMC ratios for $0.3 \leq x \leq 0.7$, and a comparison of world data on the EMC slopes is shown in Figure 2. As noted in Ref. [6] the CLAS slopes [5] are systematically higher, even when applying identical isoscalar corrections. Some fraction of the experimental uncertainty will be correlated across the slopes from a given measurement, as they all use common deuterium data. However, the CLAS slopes are systematically higher by roughly 0.10, much larger than the total quoted uncertainties of ~ 0.02 .

Because the CLAS measurement [5] includes only heavier nuclei, the inclusion of this data yields a significant change in the required A dependence over the full range of nuclei measured [6]. Even excluding ^3He , the inclusion of the CLAS data yields a significant difference in the A dependence. A linear fit of the EMC slope vs $A^{-1/3}$ for the data shown in Fig. 2 (excluding ^3He and

^4He) yields a large reduced chi-squared value, $\chi_\nu^2 = 4.06$ when including the CLAS data, and $\chi_\nu^2 = 1.07$ without the CLAS points. Inclusion of the CLAS results increases the slope parameter (A dependence) of the fit by 22%, a 2σ increase, and the extrapolation to $A = \infty$, corresponding to the EMC slope for infinite nuclear matter, is 15% higher (2.8σ) than without the CLAS data. The impact of the CLAS data on both the result and quality of the fit demonstrates the importance of understanding potential differences between the various experiments. In this work, we examine the world's data on the EMC effect at large x to try to understand these inconsistencies, as such differences can have a significant impact on understanding the A dependence of the EMC effect.

There are several differences between CLAS and the other experiments. CLAS has a lower beam energy and lower Q^2 values, a somewhat different x range, and uses a large-acceptance detector as opposed to small-acceptance spectrometers. In addition, the experiments used somewhat different radiative corrections in extracting the cross-section ratios [6].

Some of these are straightforward to rule out as a significant contribution to the discrepancy. The CLAS data have a greater slope even when comparing over $0.3 \leq x \leq 0.6$, where all measurements have data, as seen in Fig. 1. While published results from different experiments applied different isoscalar corrections and Coulomb corrections, the cross-section ratios and slopes in Figs. 1 and 2 include identical isoscalar corrections [6], and the CLAS and JLab data used identical Coulomb corrections with the same corrections applied to the SLAC data in Ref. [6]. Ref. [6] also examined other effects that will be different at the lower Q^2 values of the CLAS measurement, e.g. quasielastic (QE) contribution to the EMC region and target-mass corrections, and showed that these do not explain a significant part of the observed difference. While the acceptance corrections are large, they have significant cancellations in the ratio. So for the EMC ratios, the systematic uncertainties of the measurement [5] are small enough that they cannot explain a large part of the discrepancy, even if the x dependence is assumed to maximize the impact on the slopes.

RADIATIVE CORRECTIONS

Having argued that several differences are unlikely to explain the discrepancy, we focus on the difference in the radiative corrections (RCs). These are a natural candidate as the RCs introduce a target-dependent correction to the x -dependence of the EMC ratios. Because the EMC effect relies on precision comparisons of the x dependence for different nuclei, it is sensitive to any correction that is x and A dependent. Radiative corrections can have a significant x dependence and are sensitive to the

radiation length of the target. Several things about the CLAS radiative correction procedure are different from the other experiments. In addition to using a different RC formalism, the corrections will be different due to the lower beam energy of the CLAS measurement and the large acceptance (yielding a large Q^2 range contributing to each x bin). In addition, the experiment used a dual-target system, where the liquid deuterium (LD2) target is in the beam upstream of one of the solid targets, leading to modified radiative corrections due to the LD2 target acting as an additional radiator for the solid target.

The JLab Hall A and C measurements [4, 6–8] use the RC code “EXTERNALS”, which is based on the Mo and Tsai formalism [16] with details of the implementation described in Ref. [3]. This is essentially the same code that was used for radiative corrections for the SLAC E139 [2] and E140 [3] experiments, with only minor modifications. The CLAS analysis [5] also used RCs based on the Mo and Tsai formalism, but these were implemented in the code “INCLUSIVE” [17]) that makes different approximations.

The primary difference between the EXTERNALS and INCLUSIVE RC evaluation is how they evaluate the corrections over the full phase space that can contribute to a given event. Events can radiate in from a 2D region in $(E_{beam}, E_{e'})$ space, where the initial beam energy (E_{beam}) is higher than the energy at the scattering vertex and/or the scattered electron energy at the vertex is higher than observed at the detector ($E_{e'}$) due to the emission of real photons. EXTERNALS integrates the contribution over the full 2D region, while INCLUSIVE uses the so-called “energy-peaking approximation” that replaces the 2D integral with a pair of 1D integrals. Further details and a more technical comparison of the two approaches are provided in the supplementary material [18].

In addition to using a different prescription for the radiative correction calculation, INCLUSIVE does not allow for materials other than the target to contribute to the external Bremsstrahlung. This is particularly relevant for the CLAS measurements since the experiment used a target system that allowed the insertion of the liquid deuterium target and various solid targets in the beam at the same time [19]. When calculating the radiative corrections for the solid targets, the INCLUSIVE program does not include the effects of external radiation in the upstream deuterium target.

We examined the impact of the RC calculation by comparing the INCLUSIVE calculation, as applied in Ref. [5], to the result from the EXTERNALS code used in the analysis of the other JLab extractions [4, 6, 8]. As a first step, we calculated the RC for the CLAS measurement using the INCLUSIVE code, with all parameters and settings matching those of the original publication, and verified that we obtained consistent results. This tests our procedure for taking the cross-section weighted aver-

age RC as a function of x , integrated over the CLAS Q^2 acceptance, reproduces the original calculation. We then compare our INCLUSIVE RC factors to those obtained using EXTERNALS, with the inclusion of the liquid deuterium (LD2) target upstream of the solid target.

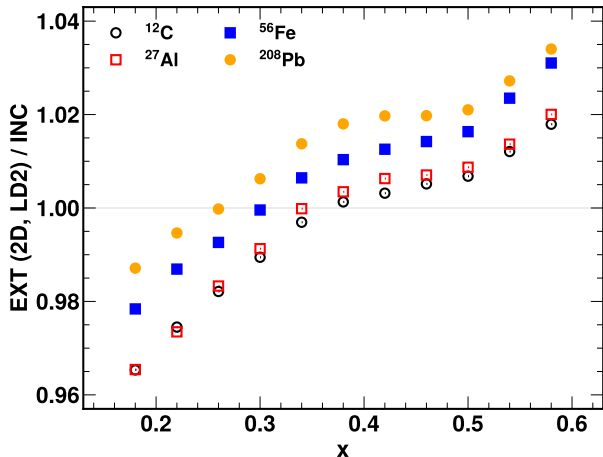


FIG. 3. Impact of the RC procedure (EXTERNALS, including upstream LD2 target) vs original (INCLUSIVE, no LD2 target) on the EMC ratios.

Figure 3 shows the change to the RC factors for the EMC ratios when applying the calculation of EXTERNALS (including the upstream LD2 target), as opposed to the INCLUSIVE corrections [5]. The C and Al (hollow symbols) targets have thicknesses below 1% of a radiation length (RL), while the Fe and Pb targets (solid symbols) have thicknesses of $\approx 2\%$ RL. The modification to the EMC ratio is typically $\lesssim 2\%$ and has a systematic x dependence that is similar for all of the targets, decreasing the extracted EMC slopes.

The largest correction comes from the difference between the EXTERNALS and INCLUSIVE RC procedures. This introduces a 3% x -dependence, roughly linear in x . It also introduces a small overall offset between low- and high-radiation length targets. The inclusion of the LD2 target as an upstream radiator yields a nearly identical correction for all targets, as expected, with a minimal impact on the RCs at larger x and a reduction of 2% at $x \approx 0.2$. This yields a common distortion in the shape below $x = 0.4$ for all targets but has only a small reduction in the EMC slopes when fitting over $0.3 \leq x \leq 0.7$. The supplemental material [18] shows separately the impact of changing to the EXTERNALS correction code and the impact of including the LD2 target upstream.

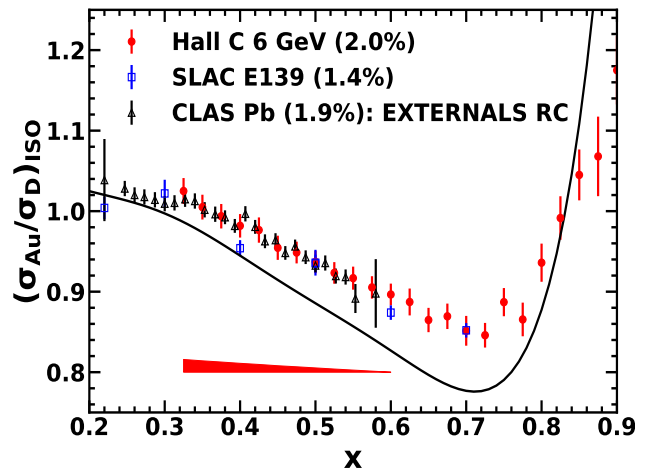


FIG. 4. EMC ratios for gold and lead [2, 5, 6] with common isoscalar corrections from [6] and the radiative correction procedure described in the text applied to the CLAS data. Symbols as in Fig. 1.

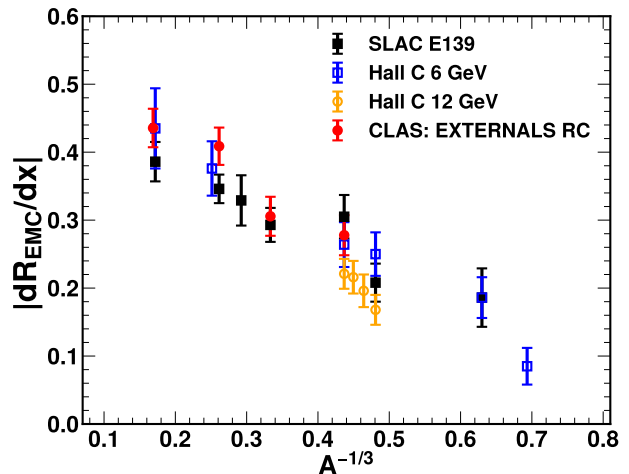


FIG. 5. EMC slopes from world's data, with the common isoscalar correction from Ref. [6] and the radiative correction procedure described in the text applied to the CLAS data. Symbols as in Fig. 2.

IMPACT ON THE EMC RATIOS

We note that there was also a cryogenic isolation foil between the LD2 target and the solid targets which we do not include in this study, but its radiation length was very small compared to the LD2 target and the upstream material had minimal impact except at very low x [18], so this has a negligible impact on our study. In addition, the upstream LD2 target was empty for the Aluminum data taking, reducing its radiation length and thus the impact on the radiative corrections. So the correction for the Aluminum target slightly overestimates the effect, but again the upstream radiator has minimal impact on the

EMC slope.

Given that the EXTERNALS calculation yields a different correction factor for the CLAS data, we now evaluate the impact of these changes on the extracted EMC ratios and slopes. To ensure that all other aspects of the analysis are unchanged, we start with the published cross-section ratios from [5], which used the INCLUSIVE RCs. We then divide out our INCLUSIVE RC factor and multiply by the EXTERNALS RC factor to provide EMC ratios based on the EXTERNALS correction. To ensure a consistent comparison with other measurements, we follow the approach of Ref. [6] and ensure that all data sets use the same correction.

While the uncertainty in the x -dependent radiative correction will partially cancel between different targets, this cancellation will not be perfect. We add 0.5% uncorrelated uncertainty to each point to account for uncertainties in our procedure that could introduce a potential bias in the x dependence of the ratios. The sensitivity to the quasielastic model is somewhat smaller than that seen for the Hall C measurement (red band in Fig. 1), due to the lower Q^2 of the CLAS measurements and lower radiation length targets.

Figure 4 shows the cross-section ratios for world's data on Au and Pb, using the ratios from Ref. [6] and applying the EXTERNALS RC to the CLAS data. We added in quadrature our estimated uncertainty for the radiative correction procedure. Figure 5 shows the EMC slopes from fitting the EXTERNALS-corrected CLAS EMC ratios for $x \geq 0.3$. The EXTERNALS-corrected result yields better agreement in the EMC ratios and the EMC slope for all nuclei measured. The slopes are reduced by a significant amount, as seen in the comparison to Fig. 2, and are now in good agreement with the remaining world's data. The supplemental material [18] includes the data shown in Figs. 3-5.

Repeating the linear fit of EMC slope vs $A^{-1/3}$ for $A \geq 9$ nuclei using the EXTERNALS-corrected CLAS slopes yields $\chi^2_\nu = 1.22$, only slightly above the value for the fit excluding CLAS, and the slope and intercept of the fit are within 1σ of the values for the fit without the CLAS results. This gives an EMC slope for $A = \infty$ of 0.542 ± 0.023 .

RADIATIVE CORRECTIONS FOR QUASIELASTIC SCATTERING AT $x > 1$

Having observed that the RC procedure has a significant impact on the EMC ratios and their x dependence, we performed a similar comparison of the RCs in the region where scattering from short-range correlations (SRCs) are expected to dominate [13, 15, 20–22]. Ref. [5] extracted these ratios in addition to the DIS ratios at lower x , and so the same differences that changed the EMC ratios could also modify the ratios in the SRC

region. We repeat the comparisons presented above for the data in the SRC region to determine if it leads to similar systematic differences in the comparison to previous SRC measurements [14, 23, 24]. In this region, the goal is to examine the ratio of the cross-section from heavy nuclei to the deuteron, which is expected to be constant for large x and Q^2 , where scattering is dominated from quasielastic-scattering off of high-momentum nucleons from SRCs [13, 23].

In this case, there is less reason to expect that the impact will be large. While the inclusion of the LD2 target upstream could produce a systematic shift in the ratios, the uncertainties in the average cross-section ratios in the SRC region, $a_2(A)$, are roughly 5%. So the 2% level changes observed in the DIS region would have a much less significant impact on the relative precision of the SRC measurements. In addition, because the radiative corrections at $x > 1$ are dominated by the loss of high- x events that radiate into lower- x kinematics, with very little radiating in from higher x where the cross sections are highly suppressed, there is less sensitivity to the cross-section model. This would tend to reduce the A dependence but not the potential dependence on the target thickness. Figures showing the impact on the cross-section ratios at $x > 1$ and modified versions of the extracted $a_2(A)$ ratios are included in the supplemental material [18]. The main impact is a systematic decrease in the extracted $a_2(A)$ values of up to 1-2%, compared to the ~ 2 -3% uncertainty in the original extraction. Thus, it is a small effect, although not negligible given that it is partially correlated between the different nuclei, as shown in the supplemental material [18].

CONCLUSIONS

In conclusion, we have performed comparisons of the INCLUSIVE and EXTERNALS radiative correction procedures, and find that the use of the more complete EXTERNALS formalism on the CLAS data [5] appears to resolve the discrepancies between the EMC ratios from this measurement and those reported by SLAC and Jefferson Lab Hall C experiments. Focusing on the CLAS [5] experiment, we find that employing an improved numerical-integration implementation of the Mo and Tsai radiative correction procedures, as done in EXTERNALS, yields corrections of up to 2-3% with a systematic x dependence. Additionally, the inclusion of the upstream CLAS LD2 target introduces a distortion in the shape at low x . While these corrections are relatively small, they are significant given the precision of the data [5]. Because of the nearly linear x dependence, these effects combine to give a systematic reduction in the slope of the EMC effect for all targets. The adoption of this alternative radiative correction procedure aligns the CLAS EMC slopes with earlier SLAC and Hall-C

measurements. This yields more consistent results for individual targets, as well as making global fits to the A dependence of the EMC effect less sensitive to whether or not the CLAS results are included.

These studies can also inform future measurements of hadron production in nuclear DIS such as Refs. [25–28], which typically feature observables that are normalized relative to the inclusive DIS cross-sections. They may also be of importance for other experiments that collect data with multiple targets in the beam.

ACKNOWLEDGEMENTS

This material is based upon work supported by the U.S. Department of Energy, Office of Science, Office of Nuclear Physics under contracts DE-AC05-06OR23177, DE-AC02-05CH11231, and DE-SC0022324.

-
- [1] J. J. Aubert *et al.* (European Muon), Phys. Lett. B **123**, 275 (1983).
 - [2] J. Gomez *et al.*, Phys. Rev. D **49**, 4348 (1994).
 - [3] S. Dasu, P. deBarbaro, A. Bodek, H. Harada, M. Krasny, *et al.*, Phys. Rev. D **49**, 5641 (1994).
 - [4] J. Seely *et al.*, Phys. Rev. Lett. **103**, 202301 (2009).
 - [5] B. Schmookler *et al.*, Nature **566**, 354 (2019).
 - [6] J. Arrington *et al.*, Phys. Rev. C **104**, 065203 (2021).
 - [7] D. Abrams *et al.* (Jefferson Lab Hall A Tritium), Phys. Rev. Lett. **128**, 132003 (2022), arXiv:2104.05850 [hep-ex].
 - [8] A. Karki *et al.*, Phys. Rev. C **108**, 035201 (2023).
 - [9] S. Malace, D. Gaskell, D. W. Higinbotham, and I. Cloet, Int. J. Mod. Phys. E **23**, 1430013 (2014).
 - [10] J. Arrington, EPJ Web Conf. **113**, 01011 (2016), arXiv:1508.05042 [nucl-ex].
 - [11] O. Hen, G. A. Miller, E. Piassetzky, and L. B. Weinstein, Rev. Mod. Phys. **89**, 045002 (2017), arXiv:1611.09748 [nucl-ex].
 - [12] I. C. Cloët *et al.*, J. Phys. G **46**, 093001 (2019).
 - [13] J. Arrington, N. Fomin, and A. Schmidt, Ann. Rev. Nucl. Part. Sci. **72**, 307 (2022).
 - [14] N. Fomin *et al.*, Phys. Rev. Lett. **108**, 092502 (2012).
 - [15] J. Arrington *et al.*, Phys. Rev. C **86**, 065204 (2012).
 - [16] Y. S. Tsai, (1971), SLAC-PUB-848.
 - [17] M. Sargsian, “Computer Code for Inclusive (e,e’) Electro-production Reactions and Radiative Corrections,” (1990), CLAS Note 90-007, https://www.jlab.org/Hall-B/notes/clas_notes-all.html.
 - [18] “Supplemental Material,” (2023).
 - [19] H. Hakobyan *et al.*, Nucl. Instrum. Meth. A **592**, 218 (2008).
 - [20] L. Frankfurt and M. Strikman, Phys. Rept. **160**, 235 (1988).
 - [21] M. M. Sargsian *et al.*, J. Phys. **G29**, R1 (2003).
 - [22] N. Fomin, D. Higinbotham, M. Sargsian, and P. Solvignon, Ann. Rev. Nucl. Part. Sci. **67**, 129 (2017).
 - [23] L. L. Frankfurt, M. I. Strikman, D. B. Day, and M. Sargsyan, Phys. Rev. C **48**, 2451 (1993).
 - [24] S. Li *et al.*, Nature **609**, 41 (2022), arXiv:2210.04189 [nucl-ex].
 - [25] S. Moran *et al.* (CLAS), Phys. Rev. C **105**, 015201 (2022), arXiv:2109.09951 [nucl-ex].
 - [26] T. Chetry *et al.* (CLAS), Phys. Rev. Lett. **130**, 142301 (2023).
 - [27] A. Airapetian *et al.* (HERMES), Eur. Phys. J. C **20**, 479 (2001), arXiv:hep-ex/0012049.
 - [28] A. Airapetian *et al.* (HERMES), Eur. Phys. J. A **47**, 113 (2011), arXiv:1107.3496 [hep-ex].
 - [29] P. Bosted and V. Mamyan, arXiv:1203.2262 (2012).

SUPPLEMENTAL MATERIAL

Differences between the INCLUSIVE and EXTERNALS radiative corrections prescriptions

The primary difference between the EXTERNALS and INCLUSIVE programs is how each treats the so-called radiative correction “triangle”. The phase space of initial and scattered electron energies that can contribute to the cross-section at $(E_{beam}, E_e) = (E_s, E_p)$ after radiation is illustrated in Figure 6. Any point encompassed by the red curve and black lines in the figure (which includes nuclear elastic, quasielastic, and inelastic processes) can contribute to the measured cross-section. So a complete calculation of the radiated cross-section at (E_s, E_p) requires a two-dimensional integral of the appropriately weighted cross-section over the phase space. The EXTERNALS program performs this two-dimensional integral while the INCLUSIVE program makes use of the so-called “energy-peaking approximation”, which allows the simplification of the full two-dimensional integral to a pair of one-dimensional integrals along the E_s and E_p contours. This approximation is useful in cases in which there is insufficient existing data to constrain the cross-section away from the point of the measurement. However, the “energy-peaking approximation” is inadequate in certain cases, in particular for large radiation-length targets.

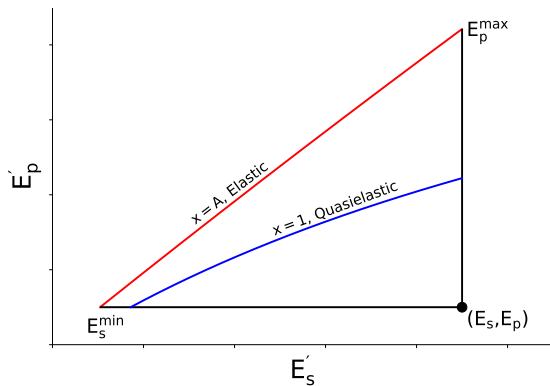


FIG. 6. Radiative corrections triangle. This diagram shows the phase space of initial and scattered electrons (after radiation) that can contribute to the radiated cross-section at $(E_{beam}, E_e) = (E_s, E_p)$. The red line denotes the elastic limit where $x = A$ and the blue line is the location of the quasielastic contribution. In principle, nuclear-excited states can populate the region between the elastic and quasielastic, while the inelastic contributes to the region between the quasielastic and the measured point. In the energy-peaking approximation, the full two-dimensional integral over this phase space is simplified to two one-dimensional integrals along the E'_s and E'_p axes.

As described in Ref. [16], the measured radiated cross-

section from a target of thickness T , at a beam energy $E_b = E_s$ and scattered electron energy $E'_e = E_p$ is given by,

$$\sigma_{exp}(E_s, E_p) = \int_0^T \frac{dt}{T} \int_{E_s^{min}}^{E_s} dE'_s \int_{E_p}^{E_p^{max}} dE'_p I(E_s, E'_s, t) \sigma_I(E'_s E'_p) I(E'_p, E_p, T - t), \quad (1)$$

where $\sigma_I(E'_s E'_p)$ is the cross section including internal radiative corrections and $I(E, E - \delta, t)$ is the probability of an electron with energy E to lose an amount of energy δ in material of thickness t due to Bremsstrahlung and ionization energy loss. The limits of integration are given by,

$$E_p^{max}(E'_s) = \frac{E'_s}{1 + \frac{E'_s}{M}(1 - \cos\theta)}, \quad (2)$$

and

$$E_s^{min}(E_p) = \frac{E_p}{1 - \frac{E_p}{M}(1 - \cos\theta)}, \quad (3)$$

where M is the target mass and θ is the electron scattering angle.

The program EXTERNALS calculates the two-dimensional integral in Eq. 1 over the full phase space, calculating σ_I (the cross section including internal radiative corrections) using the so-called equivalent radiator approximation.

The energy-peaking approximation employed by INCLUSIVE reduces the two-dimensional integration to line integrals along the E_p and E_s axes. In some cases, this approximation does not result in large changes to the radiated cross section (on the order of 1%). For thick targets and certain kinematics, the effects can be significant, though.

A comparison of the radiated cross section calculated with and without the energy-peaking approximation is shown in Figure 7. These calculations were done as part of the analysis of Hall C experiment E03103 [4, 6] at Jefferson Lab. In this experiment, measurements were made of the EMC effect at $E_{beam} = 5.776$ GeV for several targets (^3He , ^4He , ^9Be , ^{12}C , Cu, and ^{197}Au). The ^9Be and ^{12}C targets had relatively small radiation lengths (1.6-3%), while the Cu and ^{197}Au targets were thicker (6%). Fig. 7 shows the ratio of radiated cross sections calculated with and without the energy-peaking approximation for the $\approx 1.6\%$ RL carbon target (top) and the 6% RL gold target (bottom). The radiative effects shown in Fig. 7 were calculated using the same parametrization for the inelastic and quasielastic contributions [29], the only difference being the application (or not) of the energy-peaking approximation. The impact of using the energy-peaking approximation is clearly larger for the larger RL target and at a larger scattering angle (larger Q^2). At large x the difference is only a few percent, but at smaller

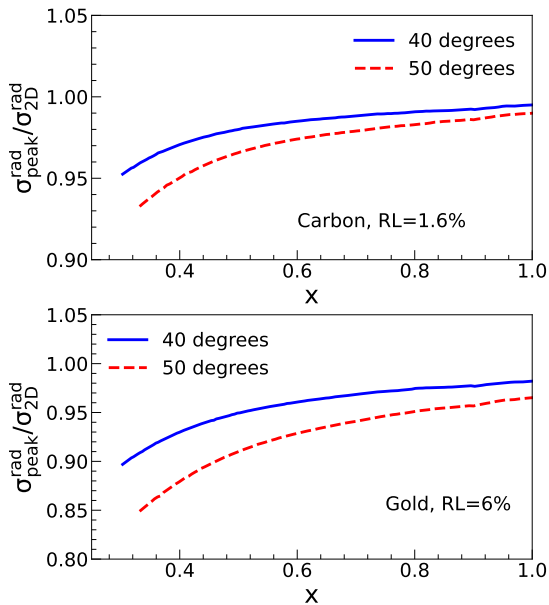


FIG. 7. Ratio of radiated cross section calculated using the energy-peaking approximation ($\sigma_{\text{peak}}^{\text{rad}}$) to that from the full 2-dimensional integral over the radiative corrections “triangle” (σ_{2D}^{rad}). Calculations were performed at the kinematics of the Hall C 6 GeV EMC effect measurements (E03103) using the nominal carbon and gold target thicknesses (1.6% and 6% RL respectively). Effects can be significant for certain kinematics (large angle and low x) and for thicker targets.

x (≈ 0.3), the difference can grow to more than 10%, so the energy-peaking approximation was not used in the E03103 analysis. The kinematics of the CLAS measurement are similar to those from the Hall C measurement, suggesting that the use of the energy-peaking approximation might induce biases.

Detailed radiative correction comparisons

The main paper shows the impact of using the EXTERNALS radiative correction procedure and including the upstream LD2 target (Fig. 3) on the EMC ratios. Here, we break down the different contributions to the modification of the radiative corrections. Figure 8 shows the impact of switching from the INCLUSIVE to EXTERNALS RC code, without the inclusion of the upstream LD2 target as an additional external radiator. For all targets, this introduces a correction that is roughly linear in x and decreases the falloff of the EMC ratio from $x=0.3-0.7$ by 2–3%, thus reducing the EMC slope. The x dependence of the modification to the EMC ratios is similar for all of the targets, although the thick targets have a 1–2% change in the overall normalization of the correction. These changes bring the slope in better agreement with world’s data, and also explain some of the normalization difference [6].

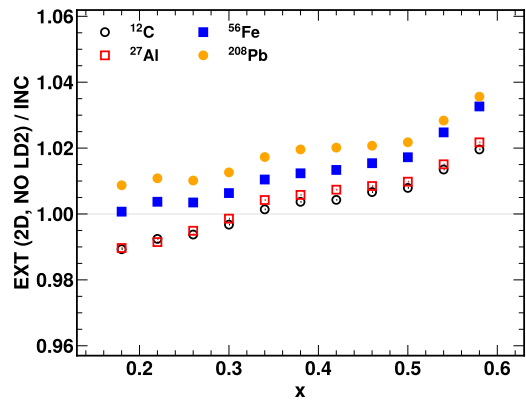


FIG. 8. Ratio of radiative correction factors for the targets used in the CLAS EMC effect extraction calculated using the EXTERNALS program (but without including the LD2 target that was upstream of the solid targets) relative to the RC factor calculated using INCLUSIVE (i.e., making use of the energy peaking approximation).

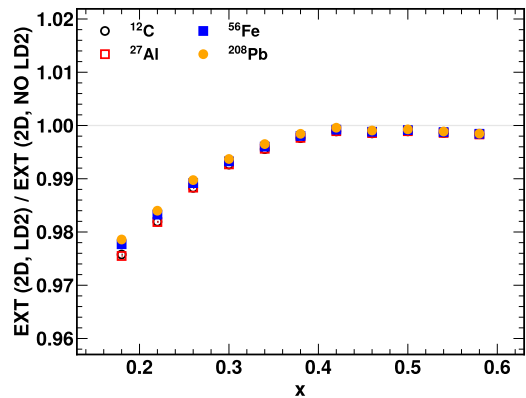


FIG. 9. Ratio of radiation correction factors calculated using EXTERNALS with and without the upstream LD2 target included in the calculation.

Figure 9 shows the impact of adding the LD2 target upstream of the solid target position, evaluated using the EXTERNALS code. The main impact is a reduction of the EMC ratio at low x values, mainly below $x = 0.4$. The correction is nearly A independent, and is generally a 1% effect or less in the EMC region ($x \geq 0.3$), yielding a small reduction in the EMC slope that is largely target independent. If data below $x = 0.3$ is used in fitting the EMC effect, or as a consistency check with other data sets, the impact would be larger - up to 2.5% for the lowest x values.

The total impact to the RC shown in Fig. 3 consists of combining the contributions shown in Figs. 8 and 9. This can then be applied as a multiplicative correction to the CLAS EMC ratios from Ref. [6] which after applying common isoscalar corrections for all data sets.

Corrections for quasielastic scattering at $x > 1$

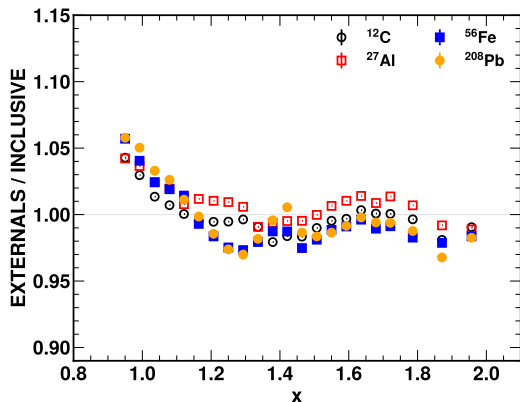


FIG. 10. Comparison of the EXTERNALS RC correction (including upstream LD2 target) vs original (INCLUSIVE, no LD2 target) in the SRC region.

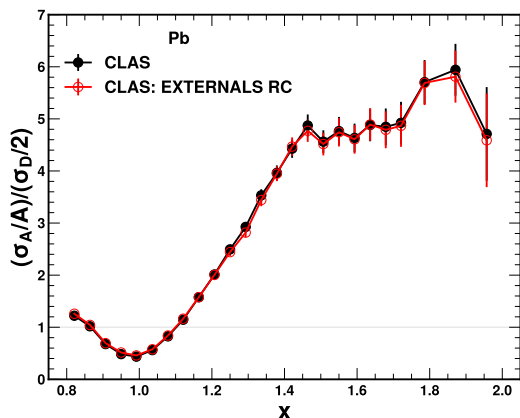


FIG. 11. Pb/D ratio for $x > 1$ for the CLAS data [5] using the INCLUSIVE (black) and EXTERNALS (red) radiative corrections.

Next, we present a similar study for quasielastic scattering at $x > 1$. In this case, the physics interpretation of the data in terms of short-range correlation does not require the same level of precision as in the DIS region. Thus, even if the difference between EXTERNALS and INCLUSIVE could be as large or even larger, the impact is likely to be less. Figure 10 shows the change to the A/D ratios when converting from INCLUSIVE to EXTERNALS, where the EXTERNALS code includes the addition of the upstream LD2 target. The correction is largest near the top of the QE peak, where the rapidly changing cross-section (and ratio) in the QE peak region makes the corrections more sensitive to the RC procedure.

The correction is small and relatively Q^2 independent above $x = 1.3$, the region of interest for SRC studies.

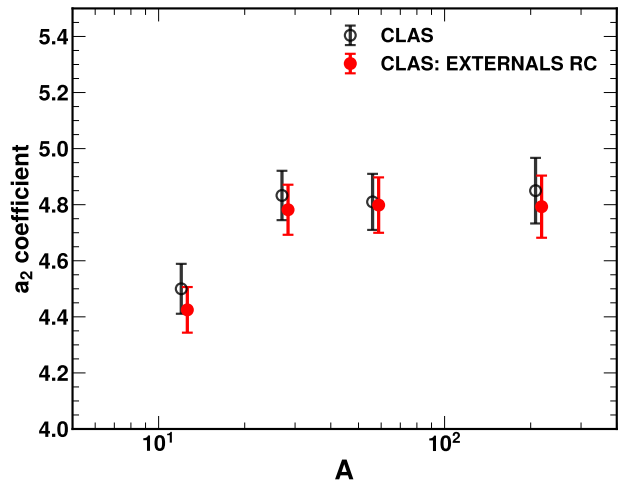


FIG. 12. Impact of RC procedures described in the text on SRC plateau values, $a_2(A)$. The a_2 values based on the EXTERNALS RC are offset slightly for clarity.

The overall impact in this region is a reduction of up to 2% in the cross-section ratio that is somewhat larger for the heavy (higher radiation length) targets.

Figure 11 shows the Pb/D ratio as published [5] (“CLAS”) and after the application of the EXTERNALS radiative correction, and Figure 12 shows the impact on the extracted value of $a_2(A)$ for all four nuclei measured in the CLAS experiment. While the RC changes led to a reduction of up to 2% in the SRC-dominated region, this is not large compared to the experimental uncertainties on the a_2 extraction. Nonetheless, because it is a systematic reduction for all nuclei, with some A dependence, it is not completely negligible.

Table I give the EMC slopes extracted from the EXTERNALS-corrected CLAS ratios, as shown in Fig. 5. Table II shows the ratio of EXTERNALS to INCLUSIVE radiative corrections from Fig. 8 and the EXTERNALS-corrected EMC ratios from Fig. 4.

Target	Slope (EXTERNALS)	$a_2(A)$ (EXTERNALS)
^{12}C	0.278 ± 0.030	4.43 ± 0.081
^{27}Al	0.306 ± 0.029	4.78 ± 0.089
^{56}Fe	0.409 ± 0.027	4.80 ± 0.099
^{208}Pb	0.436 ± 0.028	4.79 ± 0.110

TABLE I. EMC slopes (absolute value) and $a_2(A)$ for the EXTERNALS-corrected CLAS data, using the isoscalar corrections from Ref. [6]

x	$\langle Q^2 \rangle$ [GeV ²]	¹² C/D		²⁷ Al/D		⁵⁶ Fe/D		²⁰⁸ Pb/D	
		EXT/INC	EMC ratio	EXT/INC	EMC ratio	EXT/INC	EMC ratio	EXT/INC	EMC ratio
0.220	1.62	0.9750	1.0276(490)	0.9730	0.9785(518)	0.9870	1.0129(506)	0.9950	1.0386(510)
0.247	1.72	0.9797	1.0111(094)	0.9798	0.9869(093)	0.9910	1.0112(094)	0.9984	1.0281(095)
0.260	1.77	0.9820	1.0036(094)	0.9830	0.9835(093)	0.9930	1.0087(094)	1.0000	1.0201(095)
0.273	1.81	0.9843	1.0020(094)	0.9856	0.9893(093)	0.9953	1.0095(094)	1.0019	1.0176(095)
0.287	1.86	0.9867	0.9956(094)	0.9884	0.9905(094)	0.9977	1.0045(094)	1.0041	1.0141(095)
0.300	1.90	0.9890	0.9939(094)	0.9910	0.9903(094)	1.0000	1.0022(094)	1.0060	1.0093(095)
0.313	1.94	0.9916	0.9995(094)	0.9939	0.9896(094)	1.0019	1.0058(095)	1.0086	1.0103(095)
0.327	1.98	0.9944	1.0033(094)	0.9971	0.9980(094)	1.0041	1.0074(095)	1.0114	1.0148(095)
0.340	2.02	0.9970	1.0020(094)	1.0000	0.9971(094)	1.0060	1.0027(095)	1.0140	1.0126(095)
0.353	2.05	0.9983	0.9923(094)	1.0010	0.9812(094)	1.0073	0.9892(094)	1.0153	1.0017(095)
0.367	2.08	0.9997	0.9887(094)	1.0020	0.9795(094)	1.0087	0.9859(094)	1.0167	0.9962(095)
0.380	2.11	1.0010	0.9860(094)	1.0030	0.9776(094)	1.0100	0.9835(094)	1.0180	0.9924(086)
0.393	2.16	1.0016	0.9776(094)	1.0040	0.9707(094)	1.0110	0.9737(094)	1.0187	0.9817(086)
0.407	2.24	1.0023	0.9933(094)	1.0050	0.9871(094)	1.0120	0.9854(094)	1.0193	0.9967(095)
0.420	2.33	1.0030	0.9829(094)	1.0060	0.9782(094)	1.0130	0.9775(094)	1.0200	0.9805(086)
0.433	2.41	1.0036	0.9625(094)	1.0063	0.9564(093)	1.0133	0.9567(085)	1.0200	0.9626(086)
0.447	2.50	1.0043	0.9612(094)	1.0067	0.9581(094)	1.0137	0.9534(085)	1.0200	0.9640(086)
0.460	2.60	1.0050	0.9547(093)	1.0070	0.9474(093)	1.0140	0.9438(085)	1.0200	0.9481(085)
0.473	2.70	1.0056	0.9614(094)	1.0076	0.9564(094)	1.0150	0.9492(085)	1.0203	0.9562(085)
0.487	2.80	1.0063	0.9460(093)	1.0083	0.9369(093)	1.0160	0.9331(085)	1.0207	0.9428(085)
0.500	2.91	1.0070	0.9456(093)	1.0090	0.9428(093)	1.0170	0.9251(084)	1.0210	0.9325(085)
0.513	3.02	1.0086	0.9562(102)	1.0106	0.9435(093)	1.0193	0.9369(085)	1.0231	0.9356(094)
0.527	3.14	1.0104	0.9457(102)	1.0124	0.9218(093)	1.0217	0.9176(084)	1.0254	0.9194(093)
0.540	3.25	1.0120	0.9422(102)	1.0140	0.9276(093)	1.0240	0.9138(084)	1.0275	0.9182(094)
0.553	3.37	1.0139	0.9186(198)	1.0159	0.8967(198)	1.0263	0.8974(180)	1.0296	0.8915(180)
0.580	3.60	1.0180	0.9427(471)	1.0200	0.9481(482)	1.0310	0.9360(466)	1.0340	0.8978(426)

TABLE II. The ratio of the EXTERNALS RC factor to that from INCLUSIVE, along with the CLAS A/D per-nucleon cross-section ratio with the EXTERNALS RCs applied.